2002

Proceedings of the 24th Seismic Research Review:
Nuclear Explosion Monitoring: Innovation and Integration

Vol. I

Proceedings of the 24th Seismic Research Review -- Nuclear Explosion Monitoring: Innovation and Integration

September 17-19, 2002

Ponte Vedra Beach, Florida

Volume I

Seismic Regional Characterization and Wave Propagation
Seismic Event Detection and Location
Seismic Identification and Source Characterization

Approved for Public Release; further dissemination unlimited.

LA-UR-02-5048

To view these Proceedings online, visit

http://www.nemre.nn.doe.gov/review2002

Table of Contents - Volume I

1. Seismic Regional Characterization and Wave Propagation 1

1-01 **Ammon, C., G. Randall, J. Julia, R. Herrmann, and E. Arias**
Systematic Inversion of Receiver Functions & Surface-wave Dispersion for Crustal Structure in Central Asia 3

1-02 **Ammon, C., R. Herrmann, M. Pasyanos, W. Walter, and M. Kosarian**
Simultaneous Inversion of Receiver Functions, Multi-Mode Dispersion, and Travel-Time Tomography for Lithospheric Structure Beneath the Middle East and North Africa 12

1-03 **Brown, W., D. Doser, and R. Keller**
The Use of Gravity Models to Constrain Regional Velocity Models for the Libya Area 21

1-04 **Chan, W. and R. Wagner**
Seismic Monitoring System Calibration Using Ground Truth Database 29

1-05 **Chan, W., R. Herrmann, and W. Jiao**
High-Frequency Ground Motion Scaling in the Yunnan Region 34

1-06 **Cormier, V. and A. Stoujkova**
Source-Specific Corrections Modeled by Dynamic Ray Tracing in 3-D Earth Models 45

1-07 **Harris, D., F. Ringdal, E. Kremenetskaya, S. Mykkeltveit, D. Rock, and J. Schweitzer**
Ground Truth Collection for Mining Explosions in Northern Fennoscandia and Russia 54

1-08 **Herrmann, R., C. Ammon, K. Lee, and H. Yoo**
Algorithms for Regional Structure - Progress and Application 61

1-09 **Jemberie, A. and B. Mitchell**
Shear-wave Q and its Frequency Dependence in the Crust of Southeastern Asia from Surface-Wave Attenuation 70

1-10 **Jiao, W., W. Chan, and R. Wagner**
The Broadband Seismic Experiment In Yunnan, Southwest China 78

1-11 **Lay, T. and G. Fan**
Improving Discriminants for Source Identification 86

1-12 **Levshin, A., J. Stevens, M. Ritzwoller, and D. Adams**
Short-Period (7-s to 15-s) Group Velocity Measurements and Maps in Central Asia 97

1-13 **Mackey, K., K. Fujita, L. Steck, and H. Hartse**
Seismic Regionalization in Northeast Russia 107

1-14 **Morozov, I., S. Smithson, H. Li, and J. Duenow**
Amplitude Analysis and Modeling of Peaceful Nuclear Explosion Recordings 117

1-15 **O'Boyle, J., S. Ruppert, T. Hauk, D. Dodge, M. Firpo, and F. Ryall**
Middle East, North Africa and Western Eurasia Seismic Research Database 125

1-16 **Priestley, K., A. Maggi, V. Gaur, S. Mitra, J. Bonner, and J. Lewkowicz**
Broadband Seismic Studies in Southern Asia: Source and Path Characterization 134

1-17 **Pulliam, J., M. Sen, C. Frohlich, and S. Grand**
Waveform Modeling of the Crust and Upper Mantle Using S, Sp, SsPmP and Shear-Coupled PL Waves 144

1-18 **Rautian, T. and W. Leith**
Developing Composite Regional Catalogs of the Seismicity of the Former Soviet Union 154

1-19 **Rodgers, A. and A. Al-Amri**
Calibration Data for PS38 in the Central Arabian Peninsula 168

1-20 **Russian Federation/United States Calibration Working Group,**
Refinement of Regional Seismic Events Location in Northern Eurasia Using 3-D Crustal and Upper Mantle Velocity Model 176

1-21 **Smithson, S., I. Morozov, E. Morozova, and L. Solodilov**
Deep Seismic Sounding Data Sets for Seismic Calibration of Northern Eurasia 186

1-22 **Stump, B., C. Hayward, and R. Zhou**
A Comparative Study of Natural and Man-Induced Seismicity in the Yanqing-Huailai Basin and the Haicheng Area 192

1-23 **Toksöz, M., S. Kuleli, C. Schultz, D. Harris, C. Gürbüz, D. Kalafat, and A. Isikara**
Calibration of Regional Seismic Stations in the Middle East With Shots in Turkey 200

1-24 **Wu, R., X. Xie, X. Wu, and T. Lay**
Quantifying Source Excitation and Path Effects for High-Frequency Regional Waves 209

1-25 **Xie, J., R. Gok, J. Ni, and Y. Aoki**
Lateral Variations of Lg Q in the Tibetan Plateau 219

2. Seismic Event Detection and Location 229

2-01 **Armbruster, J., V. Burlacu, M. Fisk, V. Khalturin, W. Kim, I. Morozov, E. Morozova, P. Richards, D. Schaff, and F. Waldhauser**
Seismic Location Calibration for Thirty International Monitoring System Stations in Eastern Asia 231

2-02 **Ballard, S. and P. Reeves**
Improved Seismic Event Location Resolution Using a Damped Least Squares Algorithm 242

2-03 **Bergman, E. and E. Engdahl**
Probability Density Functions for Secondary Seismic Phase Arrivals 252

2-04 **Engdahl, E., E. Bergman, M. Ritzwoller, N. Shapiro, and A. Levshin**
A Reference Data Set for Validating 3-D Models 261

2-05 **Gitterman, Y., V. Pinsky, A. Shapira, M. Ergin, D. Kalafat, C. Gürbüz, and K. Solomi**
Improvement in Detection, Location, and Identification of Small Events Through Joint Data Analysis by Seismic Stations in the Middle East/Eastern Mediterranean Region 271

2-06 **Hipp, J., R. Simons, L. Jensen, L. Lindsey, and M. Chown**
The GNEM R&E Parametric Grid Software Suite: Tools for Data Creation, Access, Managment, Viewing, and Export 283

2-07 **Husebye, E., Y. Fedorenko, and E. Beketova**
Enhanced CTBT Monitoring Through Modeling, Processing and Extraction of Secondary Phase Information at High Signal Frequencies 292

2-08 **Kohl, B., R. North, J. Murphy, M. Fisk, and G. Beall**
Demonstration of Advanced Concepts for Nuclear Test Monitoring Applied to the Nuclear Test Site at Lop Nor, China 302

2-09 **Kovalenko, V. and M. Mamsurov**
Permissible Spatio-Temporal Errors of Seismic Event Location Accuracy in the Context of Nuclear-Explosion-Monitoring Requirements 313

2-10 **McLaughlin, K., I. Bondar, X. Yang, J. Bhattacharyya, H. Israelsson, R. North, V. Kirichenko, R. Engdahl, M. Ritzwoller, A. Levshin, N. Shapiro, E. Bergman, M. Antolik, A. Dziewonski, G. Ekström, H. Ghalib, I. Gupta, R. Wagner, W. Chan, W. Rivers, A. Hofstetter, A. Shapira, and G. Laske**
Seismic Location Calibration in the Mediterranean, North Africa, Middle East and Western Eurasia 320

2-11 **Merchant, B., J. Drake, D. Hart, and C. Young**
Multiple Algorithm Signal Detection Using Neural Networks 330

2-12 **Murphy, J., W. Rodi, M. Johnson, J. Sultanov, T. Bennett, M. Toksöz, C. Vincent, V. Ovtchinnikow, B. Barker, A. Rosca, and Y. Shchukin**
Seismic Calibration of Group 1 International Monitoring System (IMS) Stations in Eastern Asia for Improved Event Location 340

2-13 **Myers, S., M. Flanagan, M. Pasyanos, W. Walter, P. Vincent, and C. Schultz**
Location Calibration in Western Eurasia and North Africa: Ground Truth Improved Earth Models, Bayesian Kriging, Regional Analysis, Location Algorithms, Array Calibration, and Validation 351

2-14 **Nyblade, A., R. Brazier, C. Schultz, and M. Pasyanos**
Ground Truth Events from Regional Seismic Networks in Northeastern Africa 361

2-15 **Randall, G., H. Hartse, and L. Steck**
Attempts to Enhance Array Detection Capability: A Search for Systematic Array Residuals 368

2-16 **Reiter, D., J. Bonner, C. Vincent, and J. Britton**
Incorporating Secondary Phases in 3D Regional Seismic Event Location: Application to the Sparse Network Problem 375

2-17 **Ringdal, F., T. Kvaerna, E. Kremenetskaya, V. Asming, C. Lindholm, and J. Schweitzer**
Research in Regional Seismic Monitoring 385

2-18 **Rodi, W., C. Schultz, W. Hanley, S. Sarkar, and S. Kuleli**
Grid-Search Location Methods for Ground-Truth Collection from Local and Regional Seismic Networks 394

2-19 **Rodi, W., R. Engdahl, E. Bergman, F. Waldhauser, G. Pavlis, H. Israelsson, J. Dewey, and M. Toksoz**
A New Grid-Search Multiple-Event Location Algorithm and a Comparison of Methods 403

2-20 **Saikia, C., H. Thio, G. Ichinose, and B. Woods**
Regional Wave Propagation and Influence of Model-Based and Empirical SSSCs on Locations In and Around The Indian Subcontinent 412

2-21 **Saikia, C., R. Lohman, G. Ichinose, D. Helmberger, M. Simons, and P. Rosen**
Ground Truth Locations - A Synergy of Seismic and Synthetic Aperture Radar Interferometric Methods 420

2-22 **Steck, L., H. Hartse, C. Bradley, C. Aprea, A. Velasco, G. Randall, and J. Franks**
Regional Location Calibration in Asia 430

2-23 **Thurber, C., H. Zhang, C. Rowe, and W. Lutter**
Methods For Improving Seismic Event Location Processing 438

2-24 **Wallace, T., F. Vernon, and G. Pavlis**
Collaborative Research: Seismic Catalogue Completeness and Accuracy 448

3. Seismic Identification and Source Characterization 457

3-01 **Ammon, C., G. Randall, J. Julia, and E. Arias**
Improving Estimates of Depth, Magnitude, and Faulting Parameters of Earthquakes in Central Asia 459

3-02 **Baumgardt, D., Z. Der, M. Keohane, and A. Freeman**
Development and Investigation of Transportable Regional Discriminants 467

3-03 **Bonner, J., D. Harris, S. Rieven, I. Tibuleac, and J. Britton**
Development of a Mining Explosion Database for Southern Asia 478

3-04 **Bonner, J., J. Orrey, and A. Rosca**
Modeling Short-Period Surface Waves from Small Explosions at the Shagan Test Site 488

3-05 **Hedlin, M.**
Seismic Monitoring of Blasting Activity in Russia 498

3-06 **Kim, W., J. Granville, and P. Richards**
Discrepancies among PIDC, ISC, and USGS Seismic Magnitudes 507

3-07 **Mayeda, K., T. Eken, A. Hofstetter, J. O'Boyle, N. Turkelli, and W. Walter**
Stable and Transportable Regional Magnitudes Based on Coda-Derived Moment-Role Spectra 517

3-08 **Murphy, J., B. Barker, and W. Rodi**
Improved Focal Depth Determination for Use in Nuclear-Explosion Monitoring 522

3-09 **Phillips, W., H. Patton, C. Aprea, H. Hartse, and S. Taylor**
Regional Magnitude Studies in China and Surrounding Areas 530

3-10 **Renwald, M., T. Wallace, and S. Taylor**
Transfer Functions and Seismic Discrimination 536

3-11 **Sammis, C.**
Generation of High-Frequency P and S Wave Energy by Rock Fracture During a Buried Explosion: Its Effect on P/S Discriminants at Low Magnitude 542

3-12 **Stevens, J., D. Adams, and G. Baker**
Improved Surface Wave Dispersion Models And Azimuth Estimation Techniques 552

3-13 **Stevens, J., N. Rimer, H. Xu, G. Baker, J. Murphy, G. Kocharyan, and B. Ivanov**
Near-field and Regional Modeling of Explosions at the Degelen Test Site 562

3-14 **Stump, B., S. McKenna, C. Hayward, and T. Kim**
Seismic and Infrasound Data and Models at Near-Regional Distances 572

3-15 **Tibuleac, I., J. Bonner, E. Herrin, and D. Harkrider**
Calibration of the Ms:mb Discriminant at NVAR 582

3-16 **Walter, W., A. Rodgers, M. Pasyanos, K. Mayeda, and A. Sicherman**
Identification in Western Eurasia: Regional Body-Wave Corrections and Surface-Wave Tomography Models to Improve Discrimination 592

3-17 **Walter, W., K. Smith, S. Ruppert, T. Hauk, J. O'Boyle, F. Ryall, M. Firpo, and D. Dodge**
Improving the Fundamental Understanding of Regional Seismic Signal Processing with a Unique Western US Dataset 601

3-18 **Yang, X., S. Taylor, H. Patton, M. Maceira, and A. Velasco**
Evaluation of Intermediate-Period (10- to 30-Sec) Rayleigh-Wave Group-Velocity Maps for Central Asia 609

Seismic Regional Characterization and Wave Propagation

SYSTEMATIC INVERSION OF RECEIVER FUNCTIONS & SURFACE-WAVE DISPERSION FOR CRUSTAL STRUCTURE IN CENTRAL ASIA

Charles J. Ammon,[1] George E. Randall,[2] Jordi Julia,[1] Robert B. Herrmann,[3] Eliana Arias[1]

Penn State University,[1] Los Alamos National Laboratory,[2] and Saint Louis University[3]

Sponsored by National Nuclear Security Administration
Office of Nonproliferation Research and Engineering
Office of Defense Nuclear Nonproliferation

Contract No. DE-FC03-02SF22498[1,3] and W-7405-ENG-36[2]

ABSTRACT

We report on our initial investigations into the seismic structure of the lithosphere in central Asia using surface waves and receiver functions. We are relying on global and regional tomographic analyses for long-period surface-wave dispersion constraints on the structure, which we supplement with short-period observations measured directly from regional signals (when available). We plan to present an overview of receiver function complexity across the region using results from previous studies and receiver functions from many of the permanent stations. We will also present preliminary results from a small-scale short-period tomographic analysis of sparse observations across the Tibetan Plateau. The short period information is critical to tight constraints on shallow shear-wave velocity structure, but the measurements are sensitive to source location and origin time uncertainties. We will illustrate the combined inversion of surface-waves and receiver functions using a variety of model constraints. Our initial efforts will focus on permanent stations and temporary stations for which data are already in hand.

OBJECTIVES

Our objectives are the construction of shear-velocity profiles for regions surrounding broadband seismic stations throughout central Asia. Application of the technique in the region provides an opportunity to revise models of the crust and upper mantle structure throughout the region and to exploit the global and regional work of previous seismic verification research (*e.g.* Pasyanos *et al.*, 2001; Ritzwoller & Levshin, 1998, Larson and Ekstrom, 2001, Stevens and McLaughlin, 2001). The resulting shear-velocity models provide a single structure consistent with a range of observations and that can be tested as a tool for the construction of mode isolation filters that can help improve surface-wave magnitude estimates. We also plan to explore the possibility of adding data to our inversions of receiver functions, surface-wave dispersion. The diverse seismic activity throughout the region will facilitate cross-validation of the mode isolation filters with simple empirical filters constructed using larger events with adequate signal-to-noise ratios.

Background

Much of the background for this project is identical to that found in Simultaneous Inversion Of Receiver Functions, Multi-Mode Dispersion, And Travel-Time Tomography For Lithospheric Structure Beneath The Middle East And North Africa , by Ammon *et al.*, which appears elsewhere in these Proceedings. We refer the reader to this other work for general background information and use this space to provide more details on the inversion method and constraints that we have incorporated into the technique.

The Joint Inversion of Receiver Functions and Surface-Wave Dispersion Curves

The receiver function is sensitive to velocity transitions and vertical travel times. Surface-wave dispersion measurements are sensitive to averages of the velocities, and relatively insensitive to sharp velocity contrasts. The complementary nature of the signals makes them ideal selections for joint study because they can fill in resolution gaps of each data set. Ammon and Zandt (1993) pointed this out in a study of the Landers region of southern California (although for their specific case, available observations were unsuitable to resolve subtle features in the lower crust) and Ozalaybey *et al*. (1997) and Last *et al*. (1997) have performed complementary analyses of surface-wave dispersion and receiver functions and Du and Foulger (1999) implemented a joint inversion of these data types. The mechanics of the inversion are relatively simple since partial derivatives of dispersion observations (Herrmann, 1995) and receiver functions waveforms *(e.g.*, Randall, 1989, Ammon *et. al*, 1990) can be calculated quickly and accurately.

The inversion is formulated to allow convenient adjustment of the relative importance of the different signals on the resulting models. We use an iterative least-squares approach to minimize a functional, *S(x)*, which contains two terms corresponding to the two sets of observations (*N* receiver function sample points, y, and *M* dispersion observations, *z*) adjusted to an approximate unit variance. A control parameter, *p*, is used to adjust the importance of each set of observations.

$$\mathbf{S(x)} = \left\{ \frac{(1-\mathbf{p})}{\mathbf{N}} \cdot \sum_{\mathbf{i}=1}^{\mathbf{N}} \left(\frac{\mathbf{y_i} - \mathbf{A x_i}}{\sigma_{\mathbf{y_i}}} \right)^2 + \frac{\mathbf{p}}{\mathbf{M}} \cdot \sum_{\mathbf{i}=1}^{\mathbf{M}} \left(\frac{\mathbf{z_j} - \mathbf{B x_j}}{\sigma_{\mathbf{z_j}}} \right)^2 \right\} \quad (1)$$

No *a priori* approach is available to select an optimal weighting parameter, and the choice is made best after a systematic study of the inversions produced with a range of weights on each set of observations. At times the appropriate value of the trade-off parameter can be made by studying the fits. You may not want to fit part of a waveform that you know may be corrupted by off-azimuth arrivals, or you may not want to fit a rough portion of a noisy dispersion curve. These seismological decisions are not easily coded, but the decisions are easy after a careful study of the matches to the signals for a range of inversion weights. The overriding philosophy is simply to construct a model that suitably matches the observed dispersion and receiver functions.

Iterative "Jumping" Inversion Scheme. We use a jumping algorithm to jointly invert receiver functions and surface-wave observations for shear-wave velocity (Constable *et al.*, 1987). The jumping scheme allows us to implement a smoothness constraint in the inversion by minimizing a model roughness norm (Constable *et al.*, 1987; *Ammon et al.*, 1990) that can trade off with the prediction error. Our inversion weighting scheme accounts for the different num-

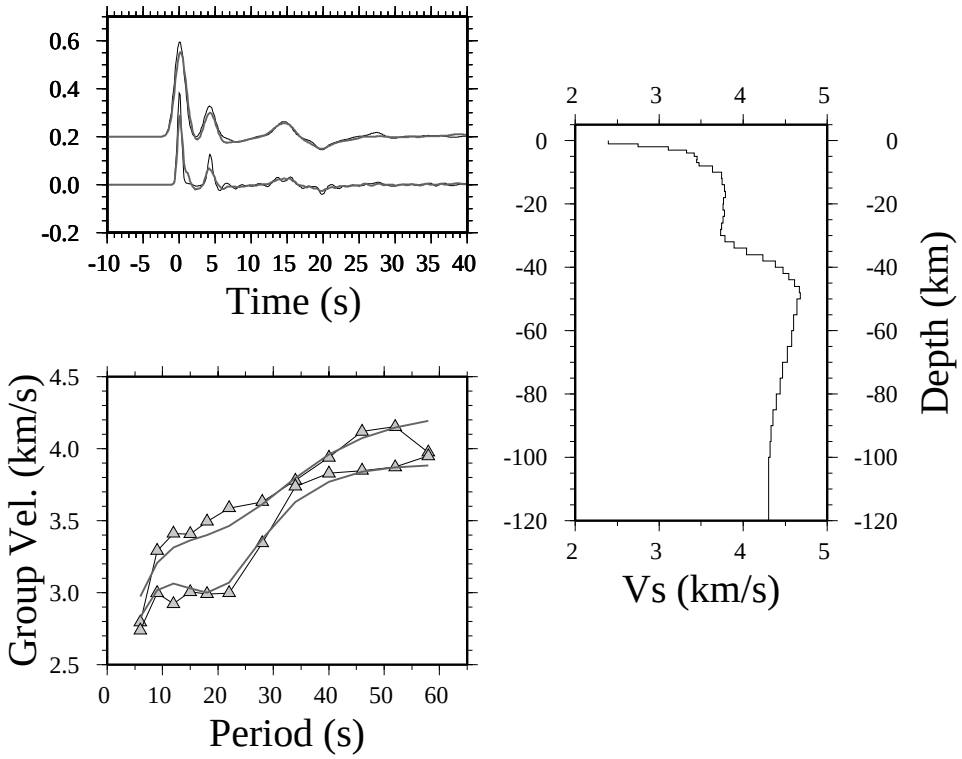

Figure 1. Observations, predictions, and shear-velocity model resulting from the joint inversion of receiver functions and fundamental-mode surface-wave dispersion measurements corresponding to station SODA located on the western Arabian Shield. The combination of the two data sets results in a simple crust with relatively smooth features but strong gradients despite the use of thin layers.

ber of data points and different physical units of each data set, and incorporates an *a priori* parameter that allows us to investigate the relative influence of each data set in the resulting models (Julia *et al.* 2000). Our model parameters are velocities of fixed-thickness layers overlying a half-space. The system of equations to be inverted is

$$\begin{bmatrix} \mathbf{pD_s} \\ \mathbf{qD_r} \\ \sigma\Delta \end{bmatrix} \cdot \mathbf{m} = \begin{bmatrix} \mathbf{pr_s} \\ \mathbf{qr_r} \\ 0 \end{bmatrix} + \begin{bmatrix} \mathbf{pD_s} \\ \mathbf{qD_r} \\ 0 \end{bmatrix} \cdot \mathbf{m}_0 \qquad (2)$$

where $\mathbf{D_s}$ and $\mathbf{D_r}$ are the partial derivative matrices for the dispersion measurements and the receiver function estimates, respectively, $\mathbf{r_s}$ and $\mathbf{r_r}$ are the corresponding vectors of residuals, $\mathbf{m}$ is the vector of S-wave velocities, $\mathbf{m}_0$ is the starting model, and Δ is a matrix that constructs the second difference of the model. The partial derivative matrices and the vectors of residuals are normalized to equalize the different number of data points and physical units in the data sets. A number of trade-off parameters must be specified before inversion. The influence factor, $\mathbf{p}$, controls the trade-off between fitting receiver functions and dispersion curves, and the smoothness parameter, σ, controls the trade-off between data fitting and model smoothness. The parameter $\mathbf{q} = 1 - \mathbf{p}$, so that $\mathbf{p}$ is meaningless outside the range $0 \le \mathbf{p} \le 1$.

We begin with an example illustrating the inversion. Although the example data are not from Asia, they serve the present need to illustrate the value of constraints in the joint inversion. Figure 1 is a plot of the observed and predicted radial receiver functions and fundamental mode group velocity values for station SODA located near the western edge of the Arabian Shield. The receiver function sampled the structure into the Shield and away from the coast. The resulting shear-velocity profile is shown on the right. The shear-velocity model layers are 1 km thick for depths down

to 8 km, 2-km thick from 8- to 50-km depth, and 5 km thick from 50- to 100-km depth, beneath which is a uniform half-space. The trade-off parameters for the inversion, $\mathbf{p} = 0.4$ and $\sigma = 1.0$, were chosen empirically, after a systematic study of the inversion results produced for a range of values, as described in Julia *et al.* (2000). The starting model was a uniform 8.0 km/s P-wave velocity half-space. The resulting model is relatively simple, with a strong, shallow velocity gradient with a two-layer crust underlain by a transitional lower crust. The upper mantle is smooth, but contains a low-velocity zone below 50 km.

Although simple, this model poses some interpretational challenges. First the shallow structure appears to be too slow when compared with more detailed models of shallow shield structure that suggest an average velocity of 3.2 km/s for the top kilometer (Mokhtar *et al.*, 1988). Our surface low-velocity structure is 3 to 4 km thick, much more than the 400-m layer in higher-frequency studies. After considerable numerical experimentation, we found it necessary to omit the shortest periods for Love waves (T = 5 and 9 s) to remain consistent with geologic and seismic constraints on shallow structure of the Shield (e.g. Mokhtar *et al.*, 1988). We believe that the likely source of the problem is an overly smoothed tomography that produces slower than true group velocities in the shield, a result of compromising between the adjacent fast shield and slow platform on the western Arabian peninsula.

Also worth close inspection is the need for the decrease in velocity throughout the upper mantle in the model. The half-space velocity is significantly low for a shield, and a simple check of the long-period dispersion shows values that are much lower than those commonly observed. The model's deepest velocities are controlled by the long-period Rayleigh waves, and not surprisingly, since our longest period is 60 s, we cannot uniquely resolve much of the deeper structure in the model. However, although our observations cannot unambiguously constrain the deep structure, they are sensitive to deep features in the model, particularly an infinitely deep half-space located at such a shallow depth. Our concern is that the anomalous structure in the mantle may still trade off with features in the crust. To minimize the extent that deep velocity features may influence crustal features, we decided to constrain our results to transition smoothly into *a priori* mantle structures. Although we do not know *a priori* the deep structure, we are confident that PREM (Dziewonski and Anderson, 1980) or slight modifications from PREM velocities are certainly a better choice than an unconstrained component in our band-limited inversion. In practice we can implement constraints to be consistent with global aspherical shear velocity models since we need only know the values of deeper mantle shear velocity beneath the station (which we can get for the shear-wave models). Of course we could include longer-period tomographic dispersion measurements from other studies into our inversion to also help alleviate the problem.

Constraining The Solution

The upper mantle. The upper mantle low-velocity zone in Figure 2 may be a consequence of the limited resolving power at depth of our data set. To test the hypothesis, we incorporated *a priori* information to compel the deepest layers in our model to resemble values from global mantle models like S12WM13 (Su *et al.*, 1994). We chose to constrain our solution by appending the following set of equations to the original system (1) (Jackson, 1972),

$$\mathbf{W} \cdot \mathbf{m} = \mathbf{W} \cdot \mathbf{m}_{\mathbf{a\ priori}} \tag{3}$$

where $\mathbf{W}$ is a diagonal matrix of constraint weights and $\mathbf{m}_{\mathbf{a\ priori}}$ contains *a priori* predefined velocity values. We also thicken the model to move the half-space to a depth of 500 km, well below the depth of influence in our band width. The resulting models are satisfactory in that they predict dispersion values more consistent with global observations than do the truncated-depth models. The results of an inversion using a constrained upper mantle are shown in Figure 2. The constrained inversions incorporate *a priori* estimates of mantle velocities for depths greater than 100 km (down to 500 km), but prohibit the receiver function data to influence this part of the model. The starting model from the surface to 100-km depth and the parameters $\mathbf{p}$ and σ were identical to those used in the unconstrained inversion (Figure 2). The receiver functions for all the resulting models are essentially identical, and show good agreement with the data, and the predicted dispersion values are effectively identical up to 3-s period. The constraint still allows acceptable fits to our observations and insures that our models are close to those required by longer period surface-wave observations.

The shallow crust. Short-period ($\mathbf{T} < 10\mathbf{s}$) dispersion observations provide strong constraints on shallow shear-wave structure. The previous inversions have illustrated that a consequence of fitting the shortest period dispersion values

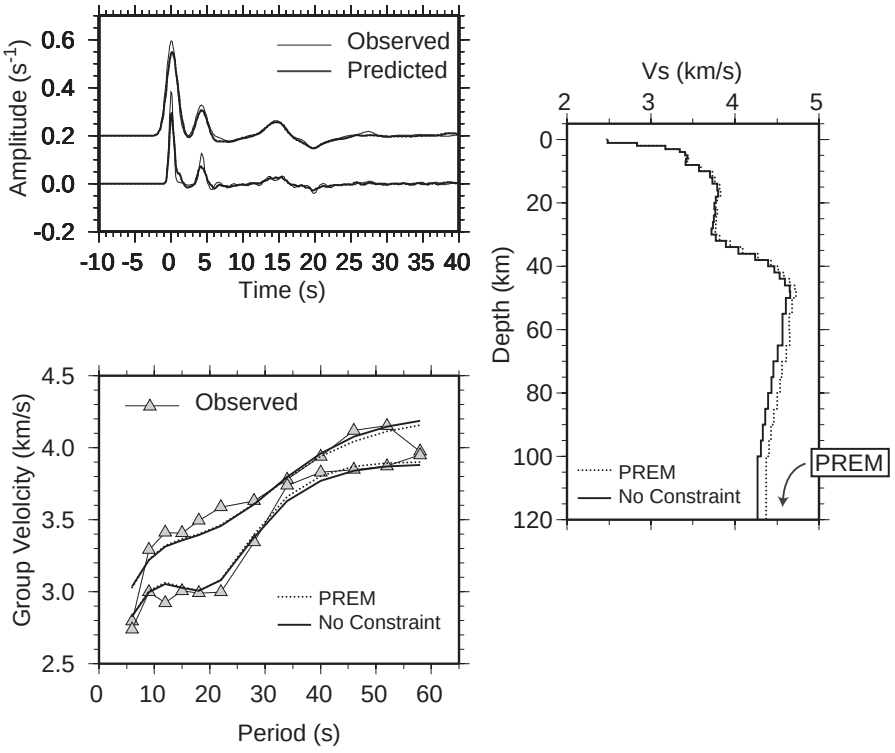

Figure 2. Results of the joint inversion of the receiver function and the intermediate-period Rayleigh group velocity values recorded near station SODA, Saudi Arabia (*p = 0.6*). The observed (solid line) and predicted (dashed line) receiver functions are shown in the upper left, the dispersion on the lower left, and the resulting shear velocity model on the right. The receiver functions were computed with Gaussian filter width factors of 1.0 and 2.5 to emphasize and exploit the frequency dependence of features in the response. The starting model was a uniform layered half-space.

from the tomographic models is unexpectedly slow velocities in the uppermost crust, inconsistent with the average 3.2 km/s that Mokhtar *et al.* (1988) inferred for the top kilometer from high-frequency (1-20 Hz) Rayleigh waves. Using thinner layers or an adaptive smoothness constraint near the surface did not alleviate the discrepancy, but numerical experiments suggested that the low velocities in our models were a consequence of the slow Love-wave group velocities for periods less than 10 seconds. Since these values are not well resolved by the tomographic study (Mokhtar, *et al.,* 2001) we repeated the inversion excluding the short-period (6 and 9 s) Love wave group velocities. Figure 3 is a comparison of the inversion results thus obtained with the full dispersion curve with an inversion excluding the 6-9 s period Love wave group velocities. We also increased the smoothing in the upper crust ($\sigma = 2.0$ for the upper 8 km, $\sigma = 1.0$ otherwise). The effects on the shallow crust are substantial, but the new results are more consistent with high-frequency Rayleigh dispersion analysis of Mokhtar *et al.* (1988) and with the geology of the Shield. The faster upper crust also improves the match to the peak P-wave amplitude on the broadband receiver function. As expected an increase in near-surface velocity deepens the shallowest velocity contrast, a clear example of the receiver function depth-velocity trade off (Ammon *et al.*, 1990), but the size of the upper crustal contrast is unchanged. Slight changes in the lower crust and upper mantle are noticeable.

RESEARCH ACCOMPLISHED

Receiver Function Computation

The first step in the project is the selection of target stations and the computation of receiver functions at those stations. To begin, we have selected a subset of permanent stations that have relatively long recording histories and thus will have substantial data already available. We plan to include all available temporary and permanent stations within the central Asian mainland. More recently installed stations and operating temporary stations will be added later in

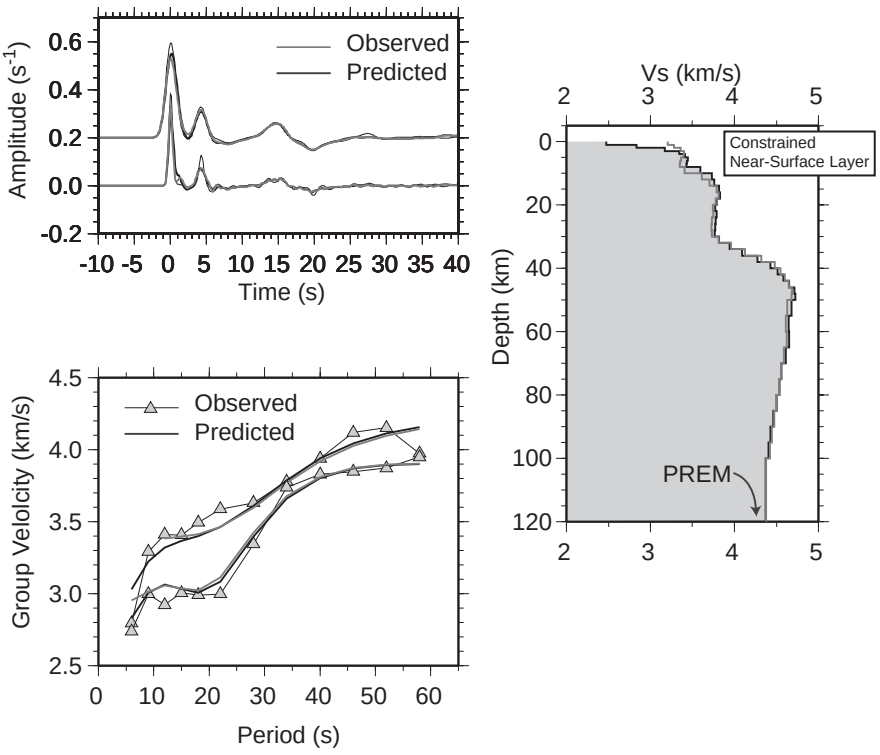

Figure 3. Inversion results with a requirement that the deep structure resemble an adjusted PREM (actually slightly modified to match Harvard Model SH12WM13 (Su *et al*., 1994) and that the shallow structure match to *a priori* information on near-surface velocities for the Shield. The constrained model produces a faster near surface layer at the expense of not fitting the shortest period Love wave dispersion from the tomography. The change in the upper crust shifts the mid-crustal boundary down about 2 km but does little else to the model.

the project. Data that we have begun to process at the time this report was written are shown in Figure 4. Example receiver functions for station BRVK in central Asia are shown in Figure 5. Receiver functions generally vary with azimuth and ray parameter and so we summarize our observations in two profiles to show the variation with each. As a first order approximation of the structure, we ve ignored azimuthal variation and performed a stacking procedure to use the waveforms to estimate the thickness and Poisson s ratio of the crust (assuming that Vp ~ 6.2 km/s) using the method of Zhu and Kanamori (2000). The resulting fits are reasonable, with a thickness value of about 45 km and a Poisson s ratio of 0.26. We will perform similar analyses and inversions for each station with suitable data. When necessary (or possible), we will split the data as a function of azimuth to produce estimates of the lateral heterogeneity associated with each site.

CONCLUSIONS AND RECOMMENDATIONS

Since we have just begun work in this project in the last few months, conclusions and recommendations are premature.

ACKNOWLEDGEMENTS

We thank P. Wessel and W. H. F. Smith, the authors of GMT for producing easy-to-use, quality software for making maps and charts.

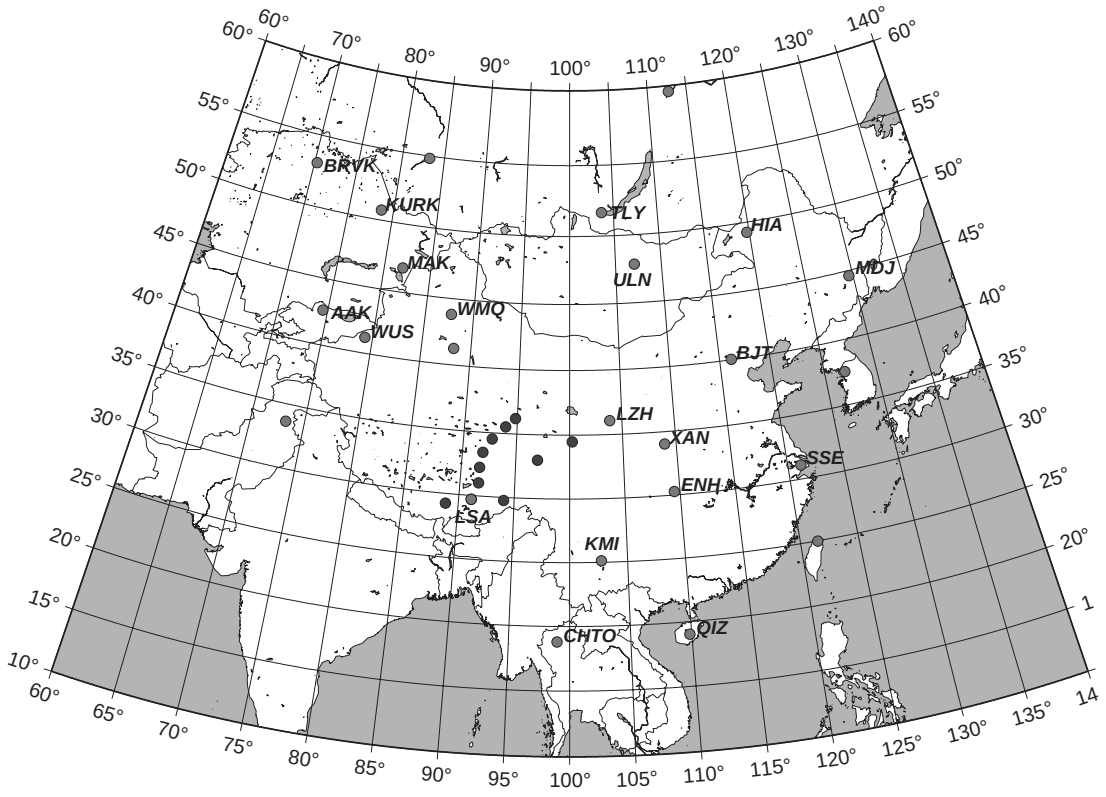

Figure 4. Open stations that we have targeted for analysis as part of this project. The stations are located in a range of environments, and most have some regional activity nearby that we can use to add short-period dispersion measurements and to test the resulting shear-velocity models.

REFERENCES

Ammon, C.J., G.E. Randall, and G. Zandt (1990), On the non-uniqueness of receiver function inversions, *J. Geophys. Res.*, **95**, 15303-15318.

Ammon, C. J., and G. Zandt (1993), The receiver structure beneath the southern Mojave Block, *Bull. Seism. Soc. Am.*, **83**, 737-755.

Constable, S.C., R.L. Parker, and C.G. Constable (1987), Occam's inversion: A practical algorithm for generating smooth models from electromagnetic sounding data, *Geophysics*, **52**, 289-300.

Du, Z.J. and G.R. Foulger (1999), The crustal structure beneath the northwest fjords, Iceland, from receiver functions and surface waves, *Geophys. J. Int.*, **139**, 419-432.

Dziewonski, A.M., and D.L. Anderson (1981), Preliminary reference Earth model, *Phys. Earth Planet. Int.*, **25**, 297-356.

Herrmann, R. B., *Computer Programs in Seismology, 1995*, Saint Louis University, St. Louis, MO, USA.

Jackson, D.D., Interpretation of inaccurate, insufficient, and inconsistent data (1972), *Geophys. J. R. Astron. Soc.*, **28**, 97-109.

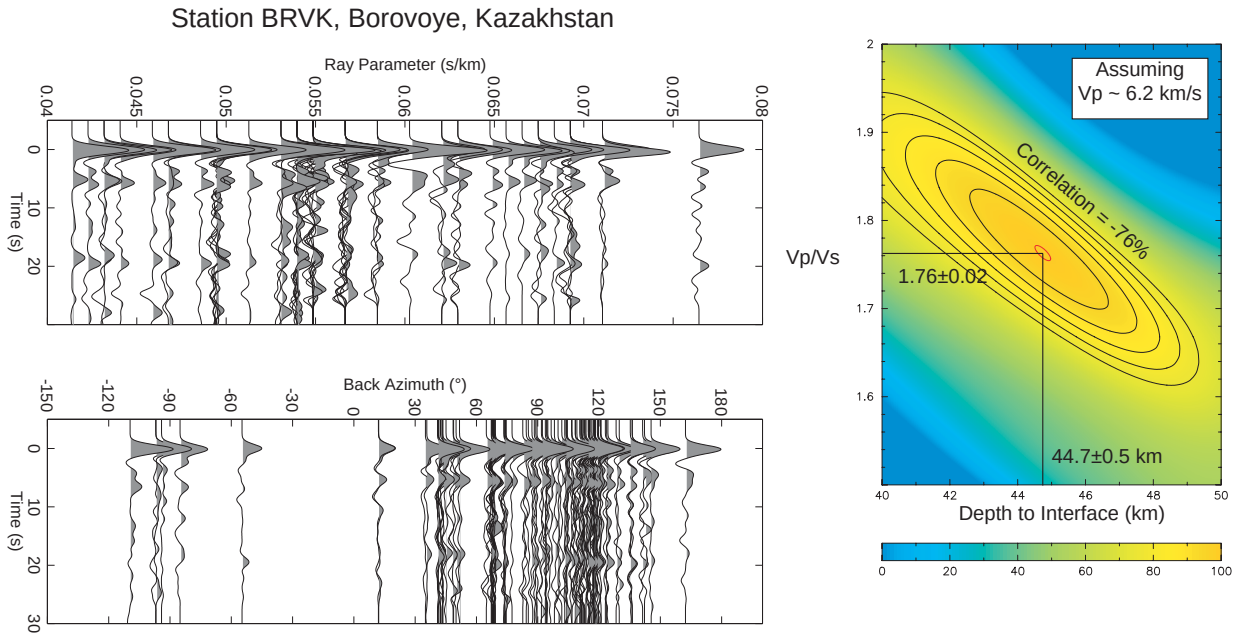

Figure 5. Sample receiver function observations and a limited analysis of Poisson's ratio and crustal thickness (assuming Vp ~ 6.2 km/s). The observed receiver functions are shown as a function of ray parameters (sin of the P-wave incident angle) and as a function of back azimuth. The data do not sample the azimuthal structure uniformly as teleseisms are predominantly observed from western Pacific subduction zones. The ray parameter sampling is good, and identifiable conversions and multiples are seen clearly for a range of incident angles. The image on the right shows the results of stacking all waveforms to identify the crust-mantle transition. Uncertainties were estimated using a jack-knifing technique. These uncertainties are conservative since they also depend on the assumed P-velocity of the crust. As a result of azimuthal sampling, the results are most reflective of the structure to the east of the station.

Julia, J., C. J. Ammon, R. B. Herrmann, and A. M. Correig (2000), Joint Inversion of receiver function and surface-wave dispersion observations, *Geophys. J. Int.* **143**, 99-112.

Larson, E. W. F. and G. Ekstr m (2001), Global Models of Group Velocity, *Pure and Applied Geophys.*, **158**, 1377-1399.

Last, R. J., A. A. Nyblade, C. A. Langston and T. J. Owens (1997), Crustal structure of the East African Plateau from receiver functions and Rayleigh wave phase velocities, *J. Geophys. Res.*, 102, 24,469-24,483.

Mokhtar, T. A., R. B. Herrmann, and D. R. Russell (1988), Seismic velocity and Q model for the shallow structure of the Arabian shield from short-period Rayleigh waves, *Geophysics*, **53**, 1379-1387.

Mokhtar, T. A., C. J. Ammon, R. B. Herrmann (2001), and H. A. A. Ghalib, Lithospheric structure beneath Arabia, *Pure and Applied Geophys*, **158**, 1445-1474.

Nalaybey, S., M.K. Savage, A.F. Sheehan, J.N. Louie, and J.N. Brune (1997), Shear-wave velocity structure in the northern Basin and Range Province from the combined analysis of receiver functions and surface waves, *Bull. Seismol. Soc. Am.*, **87**, 183-199.

Pasyanos, M.E., W.R. Walter, and S.E. Hazler (2001), A Surface wave dispersion study of the Middle East and North Africa for Monitoring the Comprehensive Nuclear-Test-Ban Treaty, *Pure and Applied Geophys*, **158**, 1445-1474.

Randall, G. E. (1989), Efficient calculation of differential seismograms for lithospheric receiver functions, *Geophys. J. Int.*, **99**, 469-481.

Ritzwoller, M. H. and A. L. Levshin (1998), Eurasian surface wave tomography: Group velocities, *J. Geophys. Res.*, **103**, 1839-1878.

Stevens, J. L. and K. L. McLaughlin (2001), Optimization of Surface Wave Identification and Measurement, *Pure and Applied Geophys*., **158**, 1547-1582

Su, W., R. L. Woodward, and A. M. Dziewonski (1994), Degree 12 model of shear velocity heterogeneity in the mantle, *Nature*, **99**, 6945-6980.

Zhu, L., and H. Kanamori (2000), Moho depth variation in Southern California from teleseismic receiver functions, *J. Geophys. Res.*, **105** (2), 2969-2980.

SIMULTANEOUS INVERSION OF RECEIVER FUNCTIONS, MULTI-MODE DISPERSION, AND TRAVEL-TIME TOMOGRAPHY FOR LITHOSPHERIC STRUCTURE BENEATH THE MIDDLE EAST AND NORTH AFRICA

Charles J. Ammon,[1] Robert B. Herrmann,[2] Michael E. Pasyanos,[3] William R. Walter,[3] Minoo Kosarian[1]

Penn State University,[1] Saint Louis University,[2] Lawrence Livermore National Laboratory[3]

Sponsored by Defense Threat Reduction Agency [1]
and
The National Nuclear Security Administration
Office of Nonproliferation Research and Engineering
Office of Defense Nuclear Nonproliferation[2,3]

Contracts No.: DTRA01-02-C-0038[1] & ROA01-31-LLNL[2,3]

ABSTRACT

We report on our initial investigations into the seismic structure of the lithosphere in the Middle East and North Africa using surface waves and receiver functions. We have initiated the collection of prior work in the region and computing receiver functions for use in the joint inversion. Critical to the joint inversion are surface-wave dispersion information localized to approximately the same region sampled by receiver functions. We continue to improve our surface wave dispersion model of Western Eurasia and North Africa. We have developed group velocity maps at 2-degree resolution for both Love and Rayleigh waves from 10- to 100-s period. The model shows excellent relationship to tectonic structure, and group velocity variations correlate well with orogenic zones, cratons, sedimentary basins, and rift zones. We have recently implemented a variable-resolution tomography and have pushed the resolution of the model down to 1 degree in areas with sufficient density sampling. We plan to present information on the complexity of receiver structure at many permanent sites in the region as well as several illustrative inversions for lithospheric structure. Other work on the combination of additional observations (body-wave travel times, higher-mode observations, surface-wave polarization information) is planned for the future stages of the project, but we include illustrations outlining our ideas for the use of these data to help further constrain the seismic structure of the lithosphere.

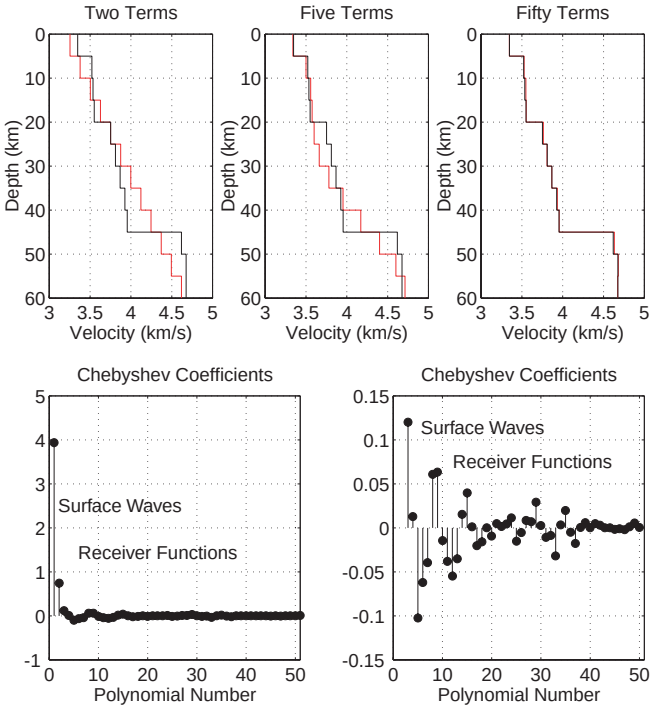

Figure 1. Expansion of a shear-velocity model (dark line in top panel) in terms of Chebyshev Coefficients. The top panel shows the sum of two, five and fifty terms respectively. The lower panels show the model spectra, that on the right focuses on the smaller amplitude, higher wave number coefficients. The point is that to image the structure, we must have data that can control the entire spectrum of the structure.

OBJECTIVES

Our objectives are the construction of shear-velocity profiles for regions surrounding broadband seismic stations throughout the Middle East, north Africa (MENA), central Africa, and parts of western Europe. Application of the technique in the MENA region provides an opportunity to revise models of the crust and upper mantle structure throughout the region and to exploit the global and regional work of previous seismic verification research (*e.g.* Pasyanos *et al.*, 2001; Ritzwoller & Levshin, 1998, Larson *et al.*, 2001). The resulting shear-velocity models provide a single structure consistent with a range of observations and which can be tested as a tool for the construction of mode isolation filters that can help improve surface-wave magnitude estimated. We also plan to explore the possibility of adding further data to our inversions of receiver functions, surface-wave dispersion. The diverse seismic activity throughout the region will facilitate cross-validation of the mode isolation filters with simple empirical filters constructed using larger events with adequate signal-to-noise ratios.

Background

Subsurface geology generally has a broad wave number spectrum (Figure 1) containing sharp, or high wave number, changes in velocity near Earth s major geologic boundaries and smooth low-wave number variations in regions of relatively uniform geologic structure. Access to the full spectrum of earth structure requires that we exploit signals that span a wide frequency range and that are sensitive to the entire spectrum of heterogeneity. Surface waves, travel times, and direct-wave amplitudes, for example, are sensitive to smooth variations in earth structure; reflected and converted waves are sensitive to velocity contrasts. Combining seismic data in joint inversions is an obvious approach to improve estimates of earth structure. To successfully combine data in an inversion, we must insure that all the data are sensitive to the same (or related) physical quantities and that they sample or average structure over comparable length scales. Recent advances in surface-wave tomography have provided an opportunity to combine localized surface-wave dispersion estimates with other data such as P- and S-wave receiver functions. Ammon and

Zandt (1993) used surface-wave dispersion observations to try and distinguish between competing models of the Mojave Desert, but zalaybey *et al.*, (1997) pioneered a formal, joint inversion of these data. They nicely illustrated the value of even a limited band of dispersion values to help reduce the trade-off between crustal thickness and velocity inherent in receiver function analyses. Specifically, they used Rayleigh-wave phase velocities in the 20- to 25-s period range to help produce stable estimates of crustal thickness in the northern and central Basin and Range. The limited bandwidth did not permit resolution of details in the crust and they limited their inversion (or at least their interpretation) to depths above 40 km. More recent authors have exercised the approach and combined the data with additional *a priori* model constraints (Du and Foulger, 1999; Julia *et al.*, 2000). Recent accomplishments in global and regional tomography now provide a more complete band of dispersion measurements to combine with receiver functions that allow us to improve the resolution of earlier works.

Surface-wave dispersion measurements are sensitive to broad averages, or low wave number components of earth structure. They provide valuable information on the absolute seismic shear velocity but are relatively insensitive to sharp, high-wave number velocity changes. Generally surface-wave inversions must be constrained using a particular layer parameterization (*e.g.* near-surface, upper-crust, lower crust, mantle lid, deep mantle), resemble an *a priori* model, or be substantially smoothed to stabilize earth-structure estimation. Despite these drawbacks, surface-wave dispersion values contain important constraints on the subsurface structure, and the general increase in depth sensitivity with depth allows an intuitive understanding of their constraints on structure. Additionally, modeling dispersion values facilitates a broadband inversion by reducing the dominance of Airy phases, which pose problems when constructing broadband misfit norms to model seismograms directly. Perhaps most important for our application is the ability to localize Earth s dispersion properties using seismic tomography. The idea is now well established, and global dispersion models exist for a broad range of frequencies (*e.g.* Larson and Ekstr m, 2001; Stevens *et al.*, 2001). The localization of dispersion allows us to isolate the variations in properties spatially, and global models of surface-wave dispersion exist and are readily available for application to other studies such as the proposed work.

Receiver functions are time/series computed from three-component body-wave seismograms, which show the relative response of Earth structure near the receiver (*e.g.* Langston, 1979). Source, near-source structure, and mantle propagation effects are removed from the seismograms using a deconvolution that sacrifices P-wave information for the isolation of near-receiver effects (Langston, 1979; Owens *et al.*, 1984; Ammon, 1991; Cassidy, 1992). Receiver function waveforms are a composite of P-to-S (or S-to-P) converted waves that reverberate within the structure near the seismometer. Modeling the amplitude and timing of those reverberating waves can supply valuable constraints on the underlying geology. In general, the receiver functions sample the structure over a range of tens of kilometers from the station in the direction of wave approach (the specific sample width depends on the depth of the deepest contrast). Stations sited near geologic boundaries can produce different responses for different directions. Recent innovations in receiver function analysis include more detailed modeling of receiver function arrivals from sedimentary basin structures (*e.g.* Clitheroe *et al.*, 2000), anisotropic structures (*e.g.* Levin and Park, 1997; Savage 1998), estimation of Poisson s ratio (*e.g.* Zandt *et al.*, 1995; Zandt and Ammon, 1995; Zhu and Kanamori, 2000, Ligorr a, 2000), reflection-like processing of array receiver functions (*e.g.* Chevrot and Girardin, 2000; Ryberg and Weber, 2000) and joint inversions (*e.g.* zalaybey *et al.*, 1997; Du and Foulger, 1999; Julia *et al.*, 2000).

Our joint inversion method is similar to that of zalaybey *et al.* (1997) except that we use jumping, smoothness, and constraints to include as much *a priori* information into the inversion as is available. We combine the receiver function and surface-wave observations into a single algebraic equation and account for their different physical units and equalize their importance in the misfit norm by weighting each data set by an estimate of the uncertainty in the observations and the number of data. We also append smoothness constraints and *a priori* model constraints on the deepest part of the model. Although we cannot resolve fine details in the deep upper mantle, these regions can impact our results since surface-wave dispersion values at intermediate and longer periods are somewhat sensitive to this deeper structure. We believe that it is important to have a reasonable basement structure so that our results are more consistent with global models. We extend our models to about 500—700*km* to insure this consistency. The resulting inversion equations are

$$\begin{bmatrix} \mathbf{p}\mathbf{D_s} \\ \mathbf{q}\mathbf{D_r} \\ \sigma\Delta \\ \mathbf{W} \end{bmatrix} \cdot \mathbf{m_{i+1}} = \begin{bmatrix} \mathbf{p}\mathbf{r_s} \\ \mathbf{q}\mathbf{r_r} \\ 0 \\ \mathbf{W}\mathbf{m_a} \end{bmatrix} + \begin{bmatrix} \mathbf{p}\mathbf{D_s} \\ \mathbf{q}\mathbf{D_r} \\ 0 \\ 0 \end{bmatrix} \cdot \mathbf{m_i} \qquad (1)$$

where $\mathbf{p}$, $\mathbf{q} = 1 - \mathbf{p}$, σ, and $\mathbf{W}$ are weights that control the relative importance of receiver functions, dispersion values, smoothness, and *a priori* model constraints in the norm minimized during the inversion. The data comprise the vectors $\mathbf{r_s}$ and $\mathbf{r_r}$, and the partial derivatives fill the matrices $\mathbf{D_r}$ and $\mathbf{Ds}$. The matrix Δ is a finite-difference stencil that computes model roughness, and the matrix $\mathbf{W}$ is a layer-dependent weight that is used to insure the model blends smoothly into the *a priori* model, $\mathbf{m_a}$, at depth. The second term on the right is added to create the jumping inversion scheme (*e.g.* Constable *et al.*, 1987; Ammon *et al.*, 1990) and allows us to solve for (and constrain) the shear-velocity models as opposed to shear-velocity correction vectors. Equation (1) is solved in a least-squares sense for the model, $\mathbf{m_{i+1}}$, starting with an initial model $\mathbf{m}_0$. The procedure generally converges in a few iterations.

RESEARCH ACCOMPLISHED

Receiver Function Computation

The first step in the project is the selection of target stations and the computation of receiver functions at those stations. To begin, we have selected a subset of permanent stations that have relatively long recording histories and thus will have substantial data already available. More recently installed stations and operating temporary stations will be added later in the project. Data processed at the time this report was written (July 2002) are shown in Figure 2. We plan to include all available temporary and permanent stations within central and northern Africa, the Middle East, and parts of Europe.

When the data are high quality and the receiver structure is not too complex, the choice of a deconvolution procedure does not make much difference. However, when the noise in the seismograms is substantial, or the receiver structure is complex, different deconvolution approaches have strengths and weaknesses. We will compute receiver functions using the iterative time-domain deconvolution procedure described by Ligorr a and Ammon (1999). We prefer the iterative approach, which is based on the Kikuchi and Kanamori (1982) source-time function estimation algorithm, for several reasons. First, in the iterative approach the receiver function is constructed by a sum of Gaussian pulses, which produces a flat spectrum at the longest periods. The flat long-period spectrum can be viewed as *a priori* information that helps reduce side-lobes that may result from spectral or singular-value truncation stabilization procedures. The reduction of side-lobes eases the interpretation and helps stabilize low-frequency receiver functions. Second, the iterative approach constructs a causal receiver function, which is what we expect in all cases of reasonable earth structure. This is a subtle difference from spectral techniques (*e.g.* Langston, 1979; Park and Levin, 2000) which can always introduce a component to the signal before the P-wave. The acausal component of the spectral signal may be small but still important to the satisfaction of the convolutional model that defines a receiver function, *i.e.:*

$$\mathbf{R(t)} = \mathbf{Z(t)} * \mathbf{E_R(t)}. \qquad (2)$$

In equation (2), $\mathbf{R(t)}$ and $\mathbf{Z(t)}$ are the radial and vertical seismograms, and $\mathbf{E_R(t)}$ is the radial receiver function (a similar equation holds for the transverse component). The point is that even when the receiver function estimation is unstable, spectral deconvolutions may satisfy (2) quite well. The iterative time-domain approach, which can be restricted to produce the best *causal* solution, may not always satisfy (2). Experienced modelers have always been able to identify failed receiver functions, but the misfit to (2) available from iterative deconvolutions provides quantitative information that can be used when stacking signals, or in extreme cases, to discard obviously failed deconvolu-

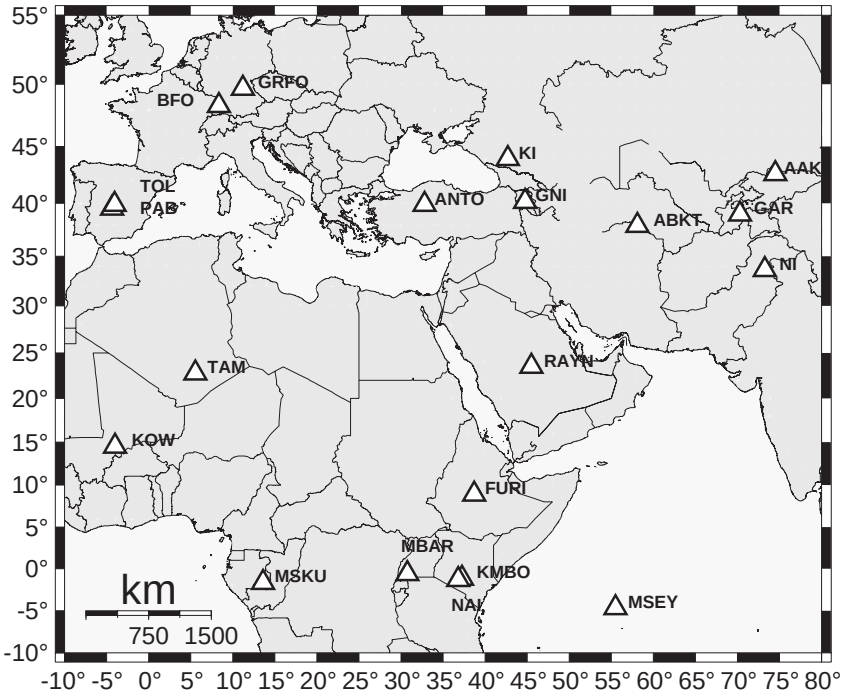

Figure 2. Stations for which we have already computed receiver functions (as of the date of this report). The eventual target stations include all available permanent and temporary three-component seismic stations.

tions. In our case we find using a threshold cut-off of 80-90% of the radial power fit allows us to quickly discard poorly constrained deconvolution results, enabling an efficient and objective selection of the data to include in further analysis.

Tomographic Imaging of Group-Velocity Variations

We have performed a large-scale study of surface wave group velocity dispersion across Western Eurasia and North Africa (Pasyanos, 2002). This study expands the coverage area northwards relative to previous work (Pasyanos *et al.*, 2001), which covered only North Africa and the Middle East. As a result, we have increased by about 50% the number of seismograms examined and group velocity measurements made. We have now made good quality dispersion measurements for about 10,000 Rayleigh wave and 6000 Love wave paths, and have incorporated measurements from several other researchers into the study. We use a conjugate gradient method to perform a group velocity tomography.

We have improved our inversion from the previous study by adopting a variable smoothness (Pasyanos, 2002). This technique allows us to go to higher resolution where the data allow without producing artifacts. Our current results include both Love and Rayleigh wave inversions across the region for periods from 10 to 100 s. Figure 3 shows inversion results for Rayleigh waves at periods of 20 and 50 s. Short-period group velocities are sensitive to slow velocities associated with large sedimentary features such as the Russian Platform, Mediterranean Sea, and Persian Gulf. Intermediate periods are sensitive to differences in crustal thickness, such as those between oceanic and continental crust or along orogenic zones. At longer periods, we find fast velocities beneath cratons and slow upper mantle velocities along rift systems and the Tethys Belt.

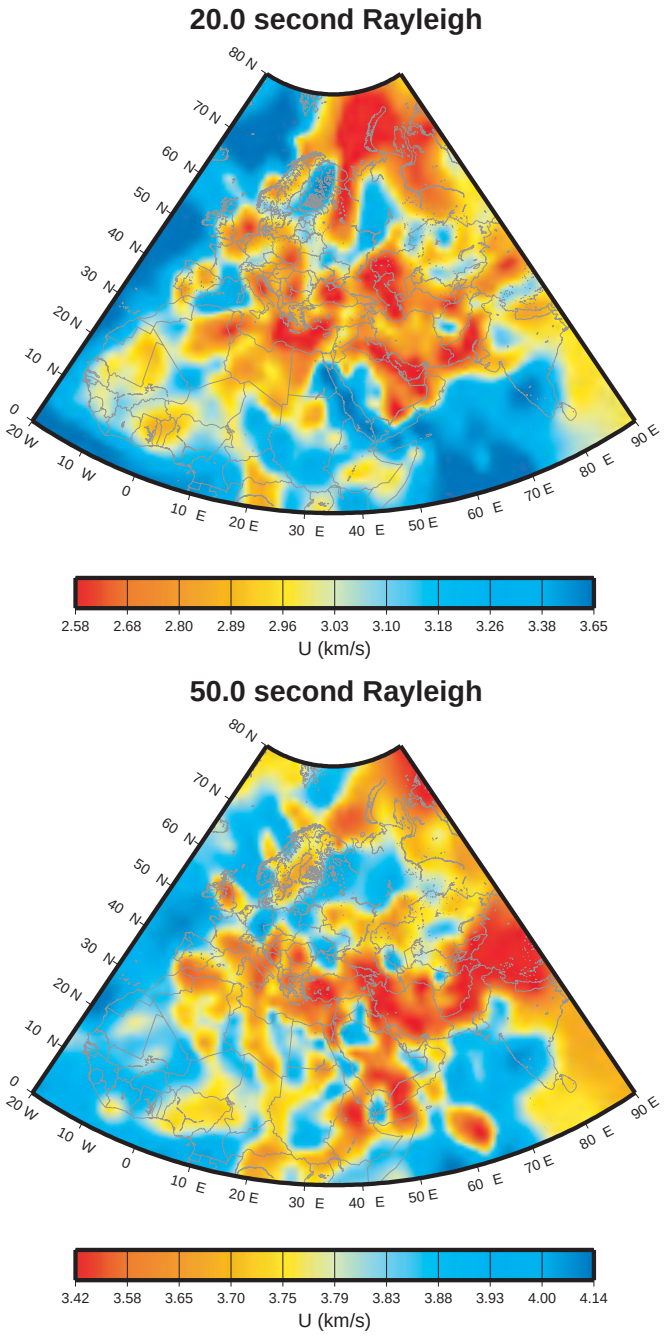

Figure 3. Tomographic imaging results for the Middle-East, North Africa, and western Europe. The upper diagram shows the lateral group velocity variations in 20-second period Rayleigh waves, the lower 50-second period Rayleigh waves.

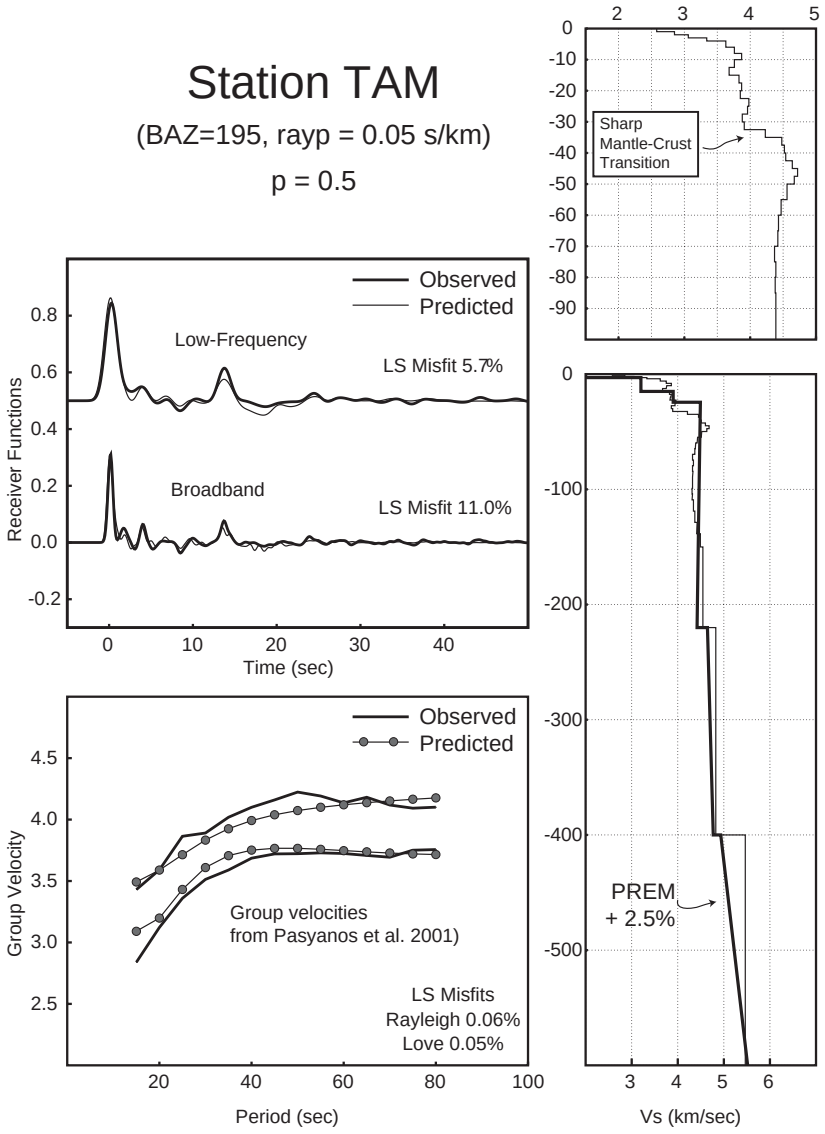

Figure 4. Preliminary inversion results for station TAM, located in north-central Africa. The receiver function in two bandwidths (low- and broad- frequency band) are inverted simultaneously to weight lower-frequency signals more. The group velocities from Pasyanos *et al.*, 2001 and the corresponding fits are shown on the lower left. The fit is generally good to all the observations although some systematic misfits between Love and Rayleigh wave dispersion are apparent. The structure is relatively simple and constrained to blend gradually into a modified PREM model.

An Example, Station TAM, North Africa

We illustrate the ideas with an example. We computed receiver functions for GEOSCOPE station TAM using events from the 1990 s. We extracted intermediate-period (period ‡ 12 s) group velocity dispersion measurements from the Lawrence Livermore National Laboratory (LLNL) MENA group velocity map (Pasyanos *et al.*, 2001). The joint inversion results for the station are shown in Figure 4. The observations are shown on the left, the models on the right. The receiver functions for this station are relatively simple, dominated by converted phases and a sharp multi-

ple from the crust-mantle transition. The results are not optimal in the sense that for the preliminary calculation we fixed the deepest parts of the model to resemble a coarsely-layered structure with a velocity of about 2.5% faster than PREM, which corresponds to the values in Harvard Shear-Wave Model S12WM13 (Su *et al.*, 1996). We can adapt the solution to match the IASPEI-91 model to be more consistent with body-wave travel times, or use velocity-depth profiles extracted from global aspherical models. The crustal velocity structure is a little rough, which reflects small arrivals in the broadband receiver function. The crust is also relatively thin, about 35 km, which is roughly consistent, but slightly thinner than the 38 –0.0 (< 1.0) km estimated by Sandvol *et al.*, (1998). The relatively slow shallow structure is dictated by the surface waves and is much slower than the values in MENA 1.1 region 5. Including local dispersion at shorter periods from paths of nearby earthquakes (of which there are few in this case) would help to verify these values.

CONCLUSIONS AND RECOMMENDATIONS

Since we have just begun work in this project in the last few months, conclusions and recommendations are premature.

ACKNOWLEDGEMENTS

We thank P. Wessel and W. H. F. Smith (1990), the authors of GMT for producing easy-to-use, quality software for making maps and charts.

REFERENCES

Ammon, C.J., G.E. Randall, and G. Zandt (1990), On the non-uniqueness of receiver function inversions, *J. Geophys. Res.*, **95**, 15303-15318.

Ammon, C.J. (1991), The isolation of receiver effects from teleseismic P waveforms, *Bull. Seism. Soc. Am.*, **81**, 2504-2510.

Ammon, C. J., and G. Zandt (1993), The receiver structure beneath the southern Mojave Block, *Bull. Seism. Soc. Am.*, **83**, 737-755.

Cassidy, J.F., Numerical experiments in broadband receiver function analysis, *Bull. Seismol. Soc. Am.*, **82**, 1453-1474, 1992.

Chevrot, S., and N. Girardin (2000), On the detection and identification of converted and reflected phases from receiver functions, *Geophys. J. Int.*, **141** (3), 801-808.

Clitheroe, G., O. Gudmundsson, and B.L.N. Kennett (2000), Sedimentary and upper crustal structure of Australia from receiver functions, *Australian Journal of Earth Sciences*, **47** (2), 209-216.

Constable, S.C., R.L. Parker, and C.G. Constable (1987), Occam's inversion: A practical algorithm for generating smooth models from electromagnetic sounding data, *Geophysics*, **52**, 289-300.

Du, Z.J. and G.R. Foulger (1999), The crustal structure beneath the northwest fjords, Iceland, from receiver functions and surface waves, *Geophys. J. Int.*, **139**, 419-432.

Julia, J., C. J. Ammon, R. B. Herrmann, and A. M. Correig (2000), Joint Inversion of receiver function and surface-wave dispersion observations, *Geophys. J. Int.* **143**, 99-112.

Kikuchi, M., and H. Kanamori, Inversion of complex body waves (1982), *Bull. Seism. Soc. Am.*, **72**, 491-506, 1982.

Langston, C.A. (1979), Structure under Mount Rainier, Washington, inferred from teleseismic body waves, *J. Geophys. Res.*, **84**, 4749-4762.

Larson, E. W. F. and G. Ekstr m (2001), Global Models of Group Velocity, *Pure and Applied Geophys.*, **158**, 1377-1399.

Levin, V., and J. Park (1997), Crustal anisotropy in the Ural Mountains from teleseismic receiver functions, *Geophysical Research Letters*, **24** (11), 1283-1286.

Ligorr a, J.P. (2000), An Investigation of the Crust-Mantle Transition Beneath North America and the Bulk Composition of the North American Crust, *Ph.D. Thesis, Saint Louis University,* 261 pages.

Ligorr a, J.P. and C. J. Ammon (1999), Iterative deconvolution and receiver function estimation, *Bull. Seismol. Soc. Am.*, **89**, 1395-1400.

Myers, S.C., and S.L. Beck (1994), Evidence for a local crustal root beneath the Santa Catalina metamorphic core complex, Arizona, *Geology*, **22**, 223-226.

Owens, T.J., G. Zandt, and S.R. Taylor (1984), Seismic evidence for an ancient rift beneath the Cumberland Plateau, Tennessee: A detailed analysis of broadband teleseismic P waveforms, *J. Geophys. Res.*, **89**, 7783-7795.

zalaybey, S., M.K. Savage, A.F. Sheehan, J.N. Louie, and J.N. Brune (1997), Shear-wave velocity structure in the northern Basin and Range Province from the combined analysis of receiver functions and surface waves, *Bull. Seismol. Soc. Am.*, **87**, 183-199.

Park, J., and V. Levin (2000), Receiver functions from multiple-taper spectral correlation estimates, *Bull. Seismol. Soc. Am.*, **90** (6), 1507-1520.

Pasyanos, M.E., W.R. Walter, and S.E. Hazler (2001), A Surface wave dispersion study of the Middle East and North Africa for Monitoring the Comprehensive Nuclear-Test-Ban Treaty, *Pure and Applied Geophys*, **158**, 1445-1474.

Pasyanos, M.E. (2002), A Variable-resolution Surface Wave Dispersion Study of Western Eurasia and North Africa, submitted to *Journal of Geophysical Research*.

Ritzwoller, M. H. and A. L. Levshin (1998), Eurasian surface wave tomography: Group velocities, *J. Geophys. Res.*, **103**, 1839-1878.

Ryberg, T., and M. Weber (2000), Receiver function arrays; a reflection seismic approach, *Geophys. J. Int.*, **141** (1), 1-11.

Sandvol, E., D. Seber, A. Calvert, M. Barazangi (1998), Grid search modeling of receiver functions: Implications for crustal structure in the Middle East and North Africa, *J. Geophys. Res.*, **103**, 26,899-26,917.

Savage, M.K. (1998), Lower crustal anisotropy or dipping boundaries? Effects on receiver functions and a case study in New Zealand, *J. Geophys. Res.*, **103** (7), 15,069-15,087, 1998.

Stevens, J. L. and K. L. McLaughlin (2001), Optimization of Surface Wave Identification and Measurement, *Pure and Applied Geophys*., **158**, 1547-1582

Su, W., R. L. Woodward, and A. M. Dziewonski (1994), Degree 12 model of shear velocity heterogeneity in the mantle, *Nature*, **99**, 6945-6980.

Zandt, G., and C. J. Ammon (1995), Continental Crustal composition constrained by measurements of crustal Poisson's ratio, *Nature*, **374**, 152-154.

Zandt, G., S.C. Myers, and T.C. Wallace (1995), Crust and mantle structure across the Basin and Range-Colorado Plateau boundary at 37 degrees N latitude and implications for Cenozoic extensional mechanism, *J. Geophys. Res.*, **100** (6), 10,529-10,548.

Zhu, L., and H. Kanamori (2000), Moho depth variation in Southern California from teleseismic receiver functions, *J. Geophys. Res.*, **105** (2), 2969-2980.

THE USE OF GRAVITY MODELS TO CONSTRAIN REGIONAL VELOCITY MODELS FOR THE LIBYA AREA

Wesley A. Brown, Diane I. Doser, and G. Randy Keller

University of Texas at El Paso

Sponsored by Defense Threat Reduction Agency

Contract No. DTRA01-01-C-0058

ABSTRACT

The tectonic evolution of Libya has yielded a complex crustal structure, which is composed of a series of basins and uplifts. A considerable amount of oil exploration has been undertaken in the area and numerous studies have been published on the shallow (<10-km depth) geology and geophysics of the region. In addition, over 6000 gravity measurements are available for the northern Libya region. We are using these data in conjunction with other geologic and geophysical controls to construct a three-dimensional (3-D) model of density/geology for northern Libya and surrounding regions. Northern Libya is the most seismologically active portion of the country. This 3-D model will then be used to develop a regional velocity model that can be verified/modified by analysis of regional waveform data we are collecting from earthquakes occurring within northern Libya.

OBJECTIVE

Introduction

Libya sits at the northern extreme of the African continent and includes classic examples of continental rifts and domal uplifts. Throughout the year to come, we will be carrying out further studies to investigate lithospheric thickness and structure of the African continent beneath Libya. However, at this stage, the study is still in its infancy. In order to set the stage for this project, we are in the process of constructing a 3-D gravity model of density/geology for northern Libya and its surrounding regions. Further analysis of waveform data will be used to construct a reliable velocity model. Previous studies have used seismic and gravity data (e.g., Dial, 1998) to investigate variations in the lithosphere throughout the northern portion of the African continent.

Although geological and geophysical studies in the Libya region of northern Africa are adding to the growing database of knowledge in the region, few data are available on the lithospheric structure of the region (Dial, 1998). Using existing geological (Figure 1) and geophysical data as a foundation, this project ultimately seeks to construct updated lithospheric models for the Libya region employing integrated gravity modeling, waveform modeling, remote sensing data, well logs and all other available geological or geophysical data.

RESEARCH ACCOMPLISHED

Data Collection

Waveform modeling has become one of the most powerful tools available to seismologists for refining Earth structure models and understanding the fault rupture processes. Waveform modeling will be one of the primary tools used in this study. For the body waveform modeling section of this study, we are in the process of collecting hard copies of seismograms from California Institute of Technology's (Caltech's) microfiche collection of seismograms from stations that were members of WWSSN (see Table 1 and Figure 2). The seismograms collected are those of magnitude 4.5 or greater. In addition, we will be downloading digitally recorded seismograms for the more recent events from reliable seismic data collection agencies.

Over 6000 reduced gravity data points have already been compiled and will be used in this study. These gravity points were collected from a number of databases. The majority of these points were collected from the worldwide gravity database maintained by the National Imagery and Mapping Agency (NIMA). The other points were pulled from our local database here at the University of Texas at El Paso (UTEP). Figure 3 shows a Generic Mapping Tool (GMT) plot of the location of the gravity points that will be used in the study.

Remotely sensed images collected by the Landsat 4 and Landsat 5 instruments will be incorporated to better understand structural features within the study area. Landsat 4 and 5 refer to the dataset collected by the unmanned satellites that were launched in the 1980s. The Landsat images that were ordered for this project were carefully selected in order to minimize the expense while optimizing the coverage. The satellite images have not been delivered at the time this paper was written; therefore, not much more can be said about this section of the study.

A vast number of well logs is available, owing to the fact that Libya has been extensively drilled for the purpose of oil exploration. Some of these wells will be critical in the characterization of the subsurface geology. The well logs will be consulted during and after processing to make sure that the models are geologically feasible.

Processing

Once collected, the seismograms will be scanned and digitized using either SEISCAN (Liberty and Pelton, 1995), which is a Matlab (version 5) based program or 'mapdig', a UNIX-based program developed at the University of Texas El Paso (UTEP), which involves manually digitizing the seismograms on a digitizing board followed by processing by another UNIX based program called 'xydig'. Once processed, the inversion technique of Baker and Doser (1988) will be used to carry out the waveform modeling, which will determine fault orientation, focal depth and rupture process. In general, waveform modeling is an iterative process in which differences between the observed and adjusted Earth structure or source representation minimizes synthetic seismograms. The synthetic

seismogram is a mathematical construction that uses wave propagation effects, source effects and characteristics of the seismometer to predict the character of a seismogram in a realistic model of the earth (Lay and Wallace, 1995).

The gravity data used in this study covers an area extending from 8°E, 35°N to 26°E, 19°N. The data will be gridded as a 5 by 5 grid constructed using a minimum curvature technique. These data were reduced to Bouguer anomaly values using a standard density of 2.67g/cm^3. Gravity station locations (over 6000 stations) are shown in Figure 3, and this figure shows the high density of coverage that exists in the northern regions as opposed to a sparse coverage existing in southern regions.

The program "SURFGRAV" will be used to construct the 3-D gravity model. SURFGRAV is a general-purpose 3-D gravity-modeling program. The computation is based on representing the Earth's surface as a gridded Digital Elevation Model (DEM) with an associated grid derived from mapped geologic units. For this computation, Figure 1 has been gridded and will be used in conjunction with the DEM shown in Figure 4. The output computed gravity (a kernel file) is presented as a matrix or spreadsheet data set with each row a gravity station, and the columns containing unit-density gravity contributions for each of the geologic units in the area of computation. Spreadsheet, Matlab or other specialized software can then combine these kernel files to give terrain-corrections, regional/local contributions, tests of forward models at different densities, or the Jacobian for use in inverse algorithms (Baker 2001). The results of the 3-D gravity modeling will be correlated with well logs to check for validity.

CONCLUSIONS AND RECOMMENDATIONS

We believe that our integrated analysis will be the most comprehensive study of the Libyan lithosphere ever undertaken. Thus, we believe that it will provide significant insight on the tectonics and wave propagation in the area.

REFERENCES

Baker, M. R., and D. I. Doser, 1988, Joint inversion of regional and teleseismic earthquake waveforms, *J. Geophys. Res.* **93**, 2037-2045.

Dial, P., 1998, An integrated geophysical study of North Africa and Mediterranean and lithospheric structure, *PhD. Dissertation,* p.1-38.

Hearn, P. Jr., *et al*, 2001, *Global GIS Database: Digital Atlas of Africa*, USGS. Digital Data Series (DDS-62-B).

Lay, T. and T. C. Wallace, *Modern Global Seismology*, 1995, Academic Press, p. 310-430.

Wessel, P. and W. H. F. Smith, 1995, New version of the generic mapping tools released, *EOS Trans. Amer. Geophys. U.*, **76**, 329.

Table 1 Location time of occurrence and magnitude of the earthquake events that will be used to do the waveform modeling.

Date	Time	Location		
YYYY:MM:DD	HH:MM:SS.SS	Lat.	Long.	Magnitude
1935:04:19	15:23:24	31.00	15.20	7.1
1935:04:19	20:31:39	30.80	15.50	6.0
1935:04:20	05:10:56	30.81	15.51	6.5
1963:02:21	17:14:31	32.69	20.97	5.5
1963:02:21	18:32:55	32.00	20.60	4.5
1963:02:21	20:26:39	32.66	21.10	4.5
1964:03:31	21:38:37.20	33.23	21.40	4.5
1967:01:02	08:19:37.00	32.44	22.62	4.6
1967:03:09	19:54:38.00	31.00	18.00	4.7
1968:05:24	17:57:22.00	23.90	11.90	4.6
1968:05:26	00:05:44.00	26.70	14.60	4.6
1972:03:27	13:33:30.29	32.1586	21.7809	4.6
1972:09:02	14:53:47.75	31.3939	16.0939	5.1
1974:09:04	06:29:13.97	33.0899	13.5020	5.2
1975:11:13	03:07:20.48	33.4177	22.8430	5.1
1976:12:19	21:21:52.66	33.0098	13.9704	4.5

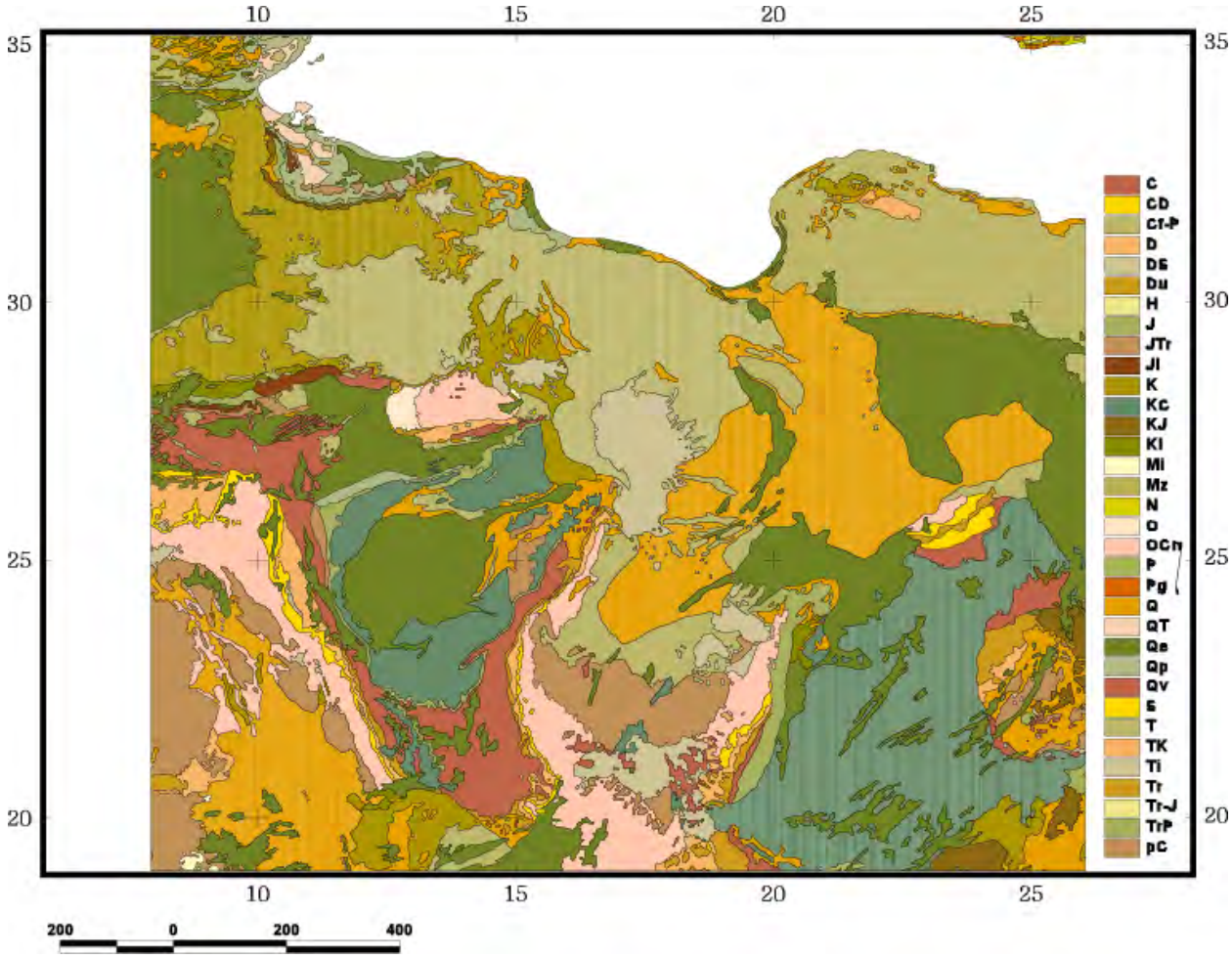

Figure 1. Geologic map of Libya and adjacent areas (modified from Hearn, 2001)

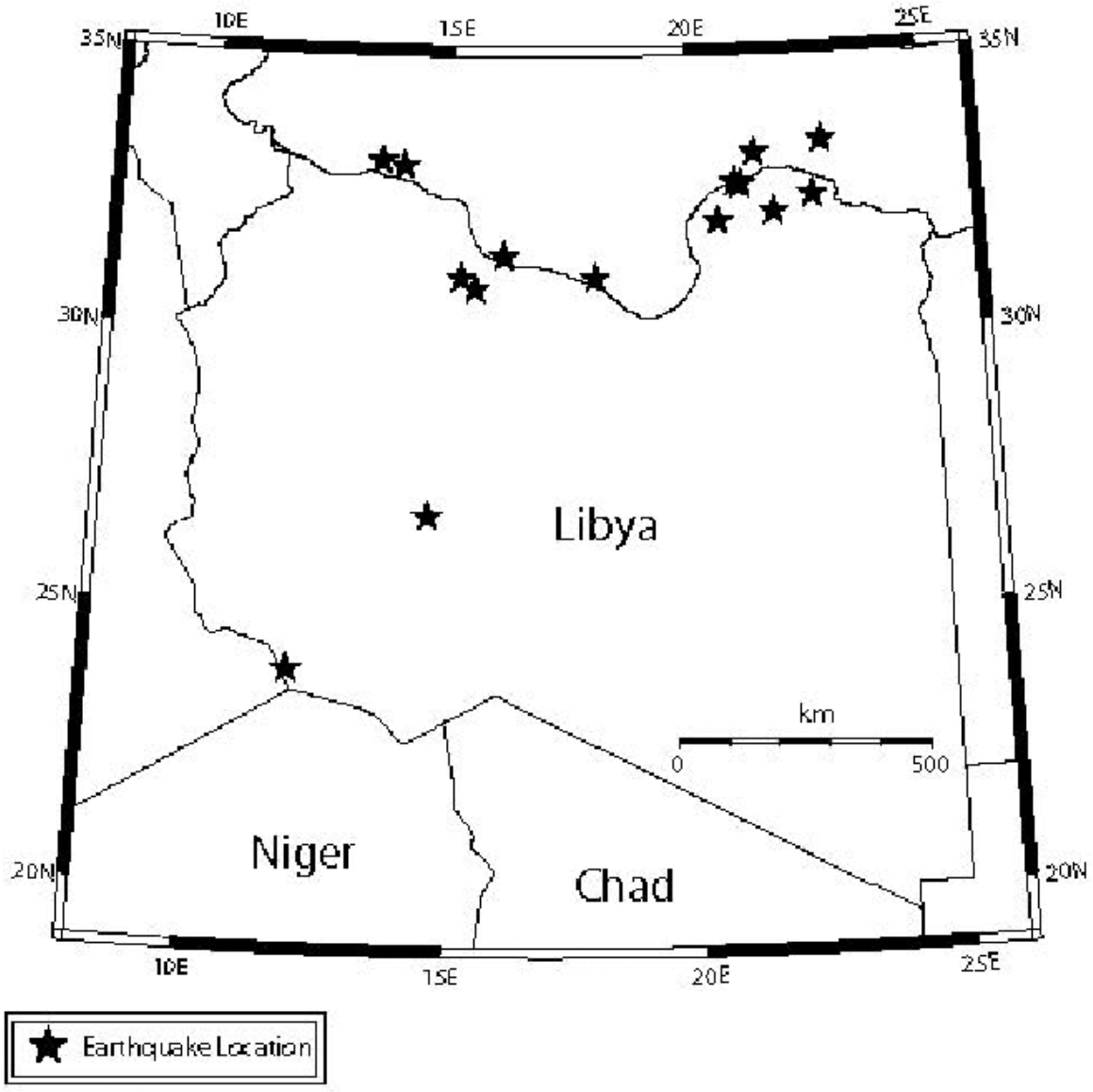

Figure 2. This figure shows the location of the earthquakes that will be used to do the waveform modeling in the Libya region.

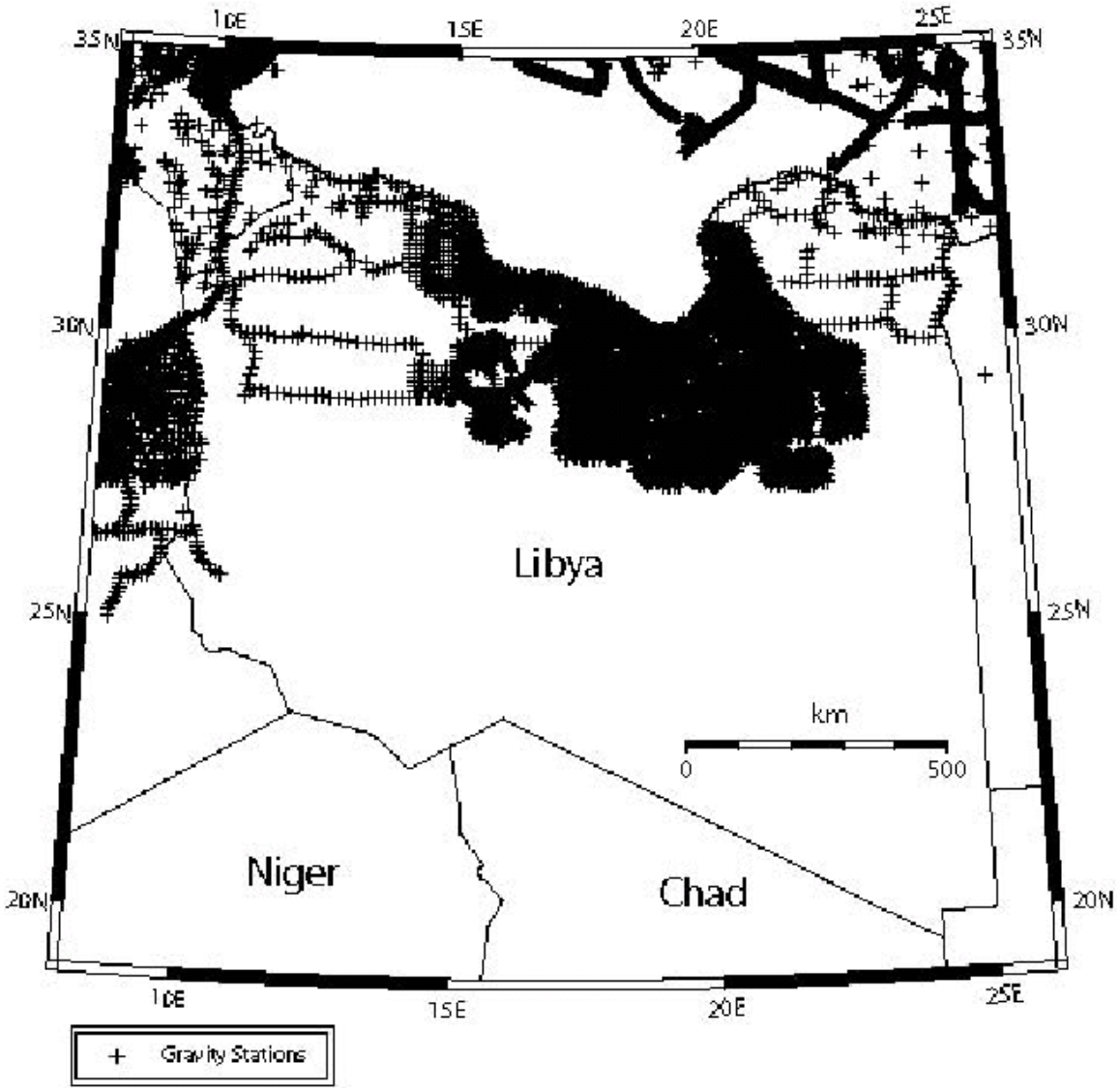

Figure 3. Map of Libya showing the locations of the gravity stations that have been reduced and will be used in the gravity study.

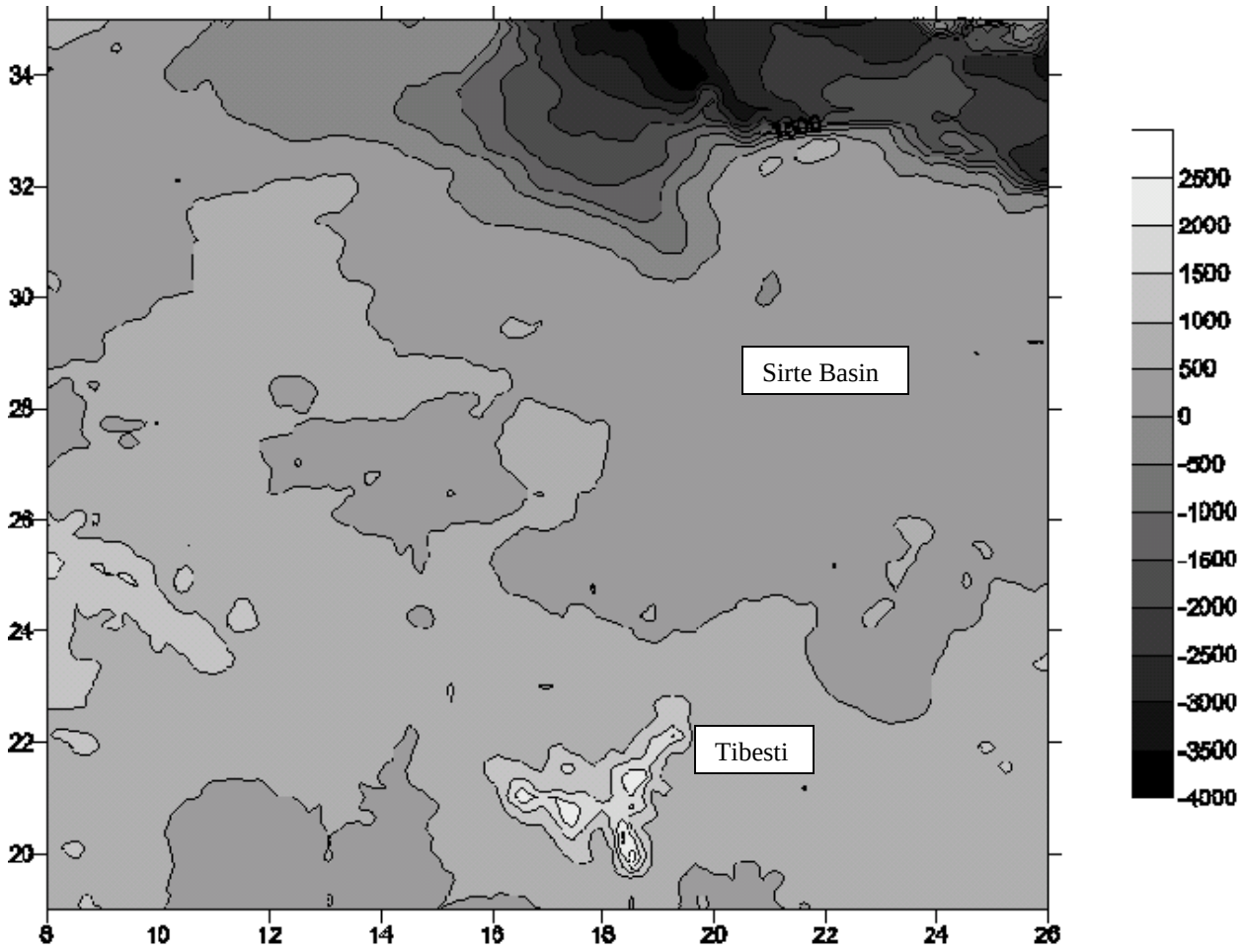

Figure 4. Contour map of the Libya region. The data used to plot this contour map have been gridded to be used as the digital elevation model to be used in SURFGRAV.

SEISMIC MONITORING SYSTEM CALIBRATION USING GROUND TRUTH DATABASE

Winston Chan and Robert Wagner

Multimax Inc.

Sponsored by US Department of Energy

Contract No. DE-FG02-99-ER82837

ABSTRACT

Calibration of a seismic monitoring system remains a major issue due to the lack of ground truth information and uncertainties in the regional geological parameters. Rapid and accurate identification of seismic events is currently not feasible due to the absence of a fundamental framework allowing immediate access to ground truth information for many parts of the world. Precise location and high-confidence identification of regional seismic events are the primary objectives of monitoring research in seismology. In the Department of Energy Knowledge Base (KB), ground truth information addresses these objectives and will play a critical role for event relocation and identification using advanced seismic analysis tools. Maintaining the KB with systematic compilation and analysis of comprehensive sets of geophysical data from various parts of the world is vital.

The goal of this project is to identify a comprehensive database for China using digital seismic waveform data that are currently unavailable. These data may be analyzed along with ground truth information that becomes available. To date, arrival times for all regional phases are determined on all events above Mb 4.5 that occurred in China in 2000 and 2001. Travel-time models are constructed to compare with existing models. Seismic attenuation models may be constructed to provide better understanding of regional wave propagation in China with spatial resolution that has not previously been obtained.

OBJECTIVE

Introduction

Calibration of a seismic monitoring system remains a major issue due to the lack of ground truth information and uncertainties in the regional geological parameters. Rapid and accurate identification of suspicious events is currently not feasible due to the absence of a fundamental framework regarding the thorough and comprehensive knowledge of ground truth information for many parts of the world.

In this project, we identify a comprehensive database for all of China. Digital seismic waveform data from the newly operational China National Digital Seismic Network (CNSDN) may be analyzed along with the seismic bulletins prepared from this network. Tomographic inversion may be performed to obtain regional three-dimensional velocity models for calculation of travel-time correction surfaces.

RESEARCH ACCOMPLISHED

Data Collection and Processing

We have been successful in extending our collaborative research with the Chinese scientists on seismic data exchange. In the initial phase of the study, we focus on the collection of seismic waveform data that have recently come online from the China National Digital Seismic Network (CNDSN). This network comprises 48 three-component seismic stations utilizing the latest broadband sensors developed by the Chinese seismologists and engineers. All data are transmitted via satellite to the principal receiving center in Beijing for archive and distribution. All data are archived in the SEED format either as event data or as continuous data in time segments. The event data archive all significant events that occur within China and its vicinity. The continuous data archive in two-hour segments can be retrieved through query.

All the stations in the CNSDN are plotted in Figure 1 along with the events that are recorded in 2000 and 2001. These 48 stations replace the original CDSN stations that were installed by the USGS in the 1980's. The coverage of the CNSDN expands the original CDSN coverage by almost 5 times and has a broader distribution that is best suited for regional studies. The network started its formal operation in September 2000. These data have not been widely distributed and have not been used for any notable research as yet. There remains ambiguity in the official data exchange of these data, especially on the station coordinates of all the 48 stations.

Instrument response is critical to obtaining the true ground motion. The seismometers employed in the Chinese National Digital Seismic Networks prior to late 2001 were of KJ-3 type manufactured by the China Seismological Bureau. This type of instrument has proved successful in obtaining high-quality and reliable digital seismic data from permanent deployments in various parts of China for the last several years. These instruments are three-component mid-band sensors with high dynamic range of greater than 120 dB and low power consumption (250mW). Since late 2001, these sensors have been upgraded to the DFD-V/H high sensitive broadband feedback seismometers. These force-balance instruments have a high dynamic range of over 140 dB. The sensitivity of the broadband output to ground velocity is 2,000 volts-sec/meter with a critical damping of 0.707. A shielding against variations in temperature, air pressure and magnetic field is also provided. These instruments have the ideal response for regional seismic recording ranging from 50 seconds to 20 Hz, as shown in Fig. 2.

The data acquisition system consists of a PC and the associated data acquisition, graphics, local area network (LAN), and storage devices. The system is characterized by:

1. 24-bit (140 dB) A/D converter;
2. A sampling rate up to 100 Hz per channel;
3. A digital oscilloscope capable of displaying any 32 pre-selected channels;
4. The ability to record data either continuously or by event triggering;
5. An automatic event locator based on automatic P phase picking;
6. A 2 mega-baud LAN to link the data acquisition and processing/archiving systems;
7. A processing/archiving system capable of performing real-time interactive analysis;
8. An effective archiving sub-system to store the digital waveform and associated data.

There are a total of 116 events above Mb 4.1 for a 12-month period. The locations of these events are shown in Figure 1 along with the stations. The overall quality of the data is quite good and the azimuthal coverage of these events is unprecedented. This is the first time that seismic events are recorded digitally with such a dense regional coverage using that many broadband stations in China. Sample waveforms of two of these events are shown in Figures 3 through 4.

CONCLUSIONS AND RECOMMENDATIONS

The study has exhibited the expansiveness of the Chinese National Seismic Data Network, whose data are of relatively good quality. A comprehensive database for China using digital seismic waveform data will provide important input to the NNSA Knowledge Base of ground truth information in event relocation and identification using advanced seismic analysis tools. The analysis of these data will yield important parameters to provide better understanding of regional wave propagation in China with resolution that was previously not achievable.

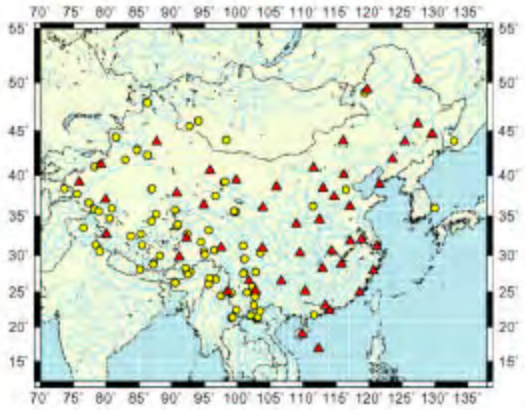

Figure 1. Locations of the China National Digital Seismic Network (triangles) and events recorded (circles).

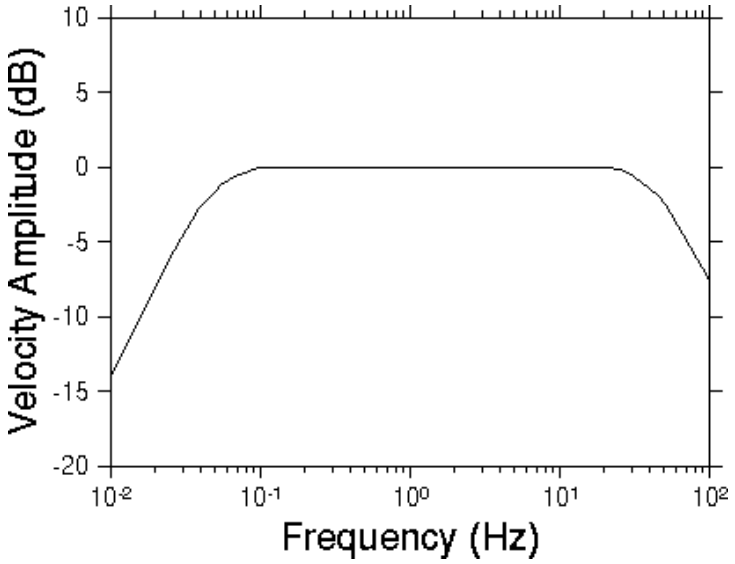

Figure 2. Instrument response for the broadband seismometer in the Chinese digital seismic networks.

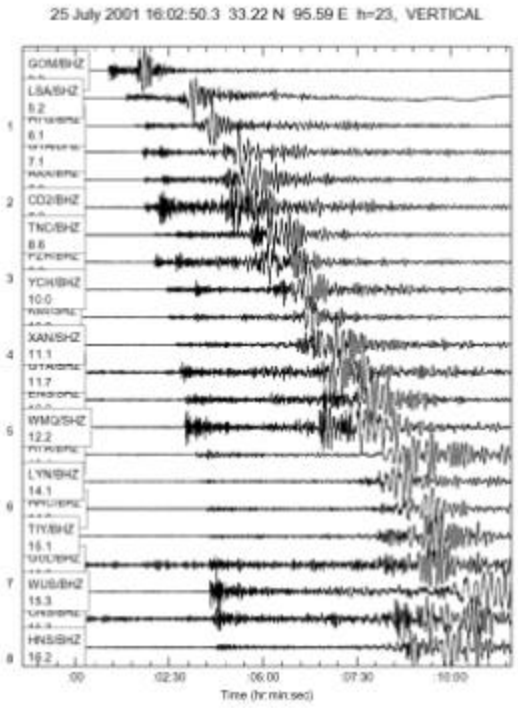

Figure 3. Vertical component seismograms for the July 25, 2001, event near the Tibet-Sichuan border, China.

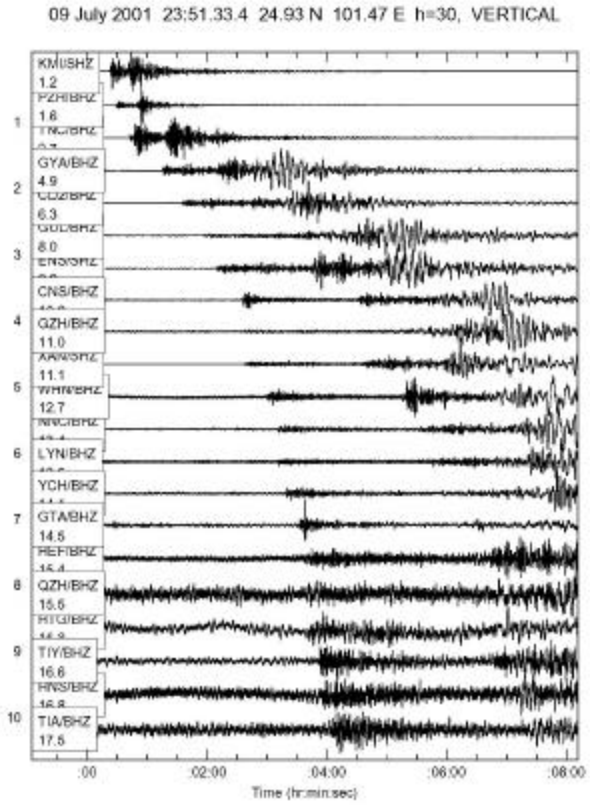

Figure 4. Vertical component seismograms for the July 9, 2001, event in Yunnan Province, China

HIGH-FREQUENCY GROUND MOTION SCALING IN THE YUNNAN REGION

Winston Chan,[1] Robert Herrmann,[2] and Wenjie Jiao[1]

Multimax Inc.,[1] Saint Louis University[2]

Sponsored by Defense Threat Reduction Agency

Contract No. DTRA01-00-C-0068

ABSTRACT

Vertical component velocity seismograms from the Yunnan digital seismic provincial network are used to characterize high-frequency S-wave propagation. The signals are processed to examine the peak ground motion and Fourier velocity spectra in the frequency range of 1 - 12 Hz. Analysis involves a two-step process: first, modeling of peak S-wave motions in terms of EXCITATION, DISTANCE, and SITE terms; this is followed by a parameterization in terms of geometrical spreading, frequency dependent Q and distance-dependent duration. The data set consists of over 6000 waveforms from 23 stations and 325 events. Observations are in the distance range of 30 - 700km. The data are processed for purposes of defining the parameters needed for the application of Random Vibration Theory to predict high-frequency earthquake motions.

OBJECTIVE

Introduction

The Lg/Pg ratio has been shown to improve discriminant performance as the frequency content increases, with frequencies higher than 5 Hz leading to good separation of explosion and earthquake populations in most regions where it has been tested (National Research Council, 1997). For example, in their study of discrimination between Nevada Test Site (NTS) explosions and earthquakes, Walter *et al*. (1995) noted improved performance at higher frequencies. Other examples are the regional discrimination study of explosions and earthquakes in the eastern United States and in southern Russia by Kim *et al*. (1997), who observed significantly improved discrimination capability of the amplitude ratio P/Lg in the 5- to 25-Hz band over the lower frequency bands. Several recent studies (e.g., Baumgardt and Schneider, 1997; Rodgers and Walter, 1997; Walter *et al*. 1997) have observed significant variability of regional phase ratios, such as Pn/Lg or Pg/Lg, which are generally powerful regional discriminants. Their characteristics vary significantly from one tectonic or geographic region to another and may also be strongly dependent on frequency (e.g. Baumgardt and Der, 1994). Southwestern China is known to have complex geology with large Q variations (e.g. Qin and Kan, 1986), so that several combinations of distinct source and receiver regions will need to be calibrated. It is important to understand and quantify these differences in order to accomplish improved regional discrimination in a region of complex geology, such as the Yunnan Province in southwestern China.

In order to systematically perform the spectral ratio study, we have to apply the magnitude and distance corrections to the signals. We propose to apply the techniques for characterizing high-frequency S-wave motion to improve the effectiveness of the regional seismic discriminants and extend the application to P-wave also. The procedures used in the analysis were developed by Yazd (1993) and then extended to the current processing and interpretation described in Raoof *et al* (1999) and Malagnini (1999). At present the central US, southern Great Basin surrounding NTS, southern California, the US Pacific Northwest, Italy, and Germany have been studied using the same methodology. Studies on Switzerland, Utah, Valle de Mexico, and Turkey are underway or just starting. The goal of processing to date is to use regional network data in Yunnan Province from small to moderate earthquakes to constrain ground motion estimates for large earthquakes. Data analysis consists of processing a very large set of waveforms (~1000-2000) distributed uniformly from short to large distances to characterize the high-frequency motion. The result of this analysis is an empirical *D(r)*, *Site* and *Excitation* term.

RESEARCH ACCOMPLISHED

Data Collection and Processing

We have constructed a large database of short-period waveform data from the Yunnan regional network in southwestern China. Figure 1 shows the event location and stations used for the analysis of high-frequency ground motion. A prerequisite for successful regression is the requirement for each station to observe events at different distances, and that each event be observed by many stations with overlapping distance distributions, as shown in Fig. 2. This is required for the data to define the actual distance dependence of motion independently of station site/instrument effects.

The specifics of the Regression Model are:

- Use filtered vertical component velocity at 1, 2, 3, 4, 6, 8, 10 and 12 Hz (DT = 0.02 s)
- Use Coda normalization as an independent test of distance term.
- Perform regression on Peak Velocities and Fourier Velocity Spectra at each frequency for the model $\log A = D(r) + E(r_{ref}) S$

where A is observed motion, $D(r)$ is distance term, $E(r_{ref})$ is the excitation term at the reference distance, and S is a site term, and the following constraints apply: $\sum Si = 0$; $D(40\ km) = 0$; $D(r)$ is a piecewise linear continuous function defined by distance nodes. A smoothing constraint is applied to $D(r)$.

Stable regression requires a non-singular set of equations. The data define the actual distance variation. A reference distance is chosen to be within the range of observed distances. This reference distance is chosen to be 40 km, which is large enough that errors in hypocentral distance due to poor event depths will not be important and is less than the distance at which supercritical reflections from the Moho become important. The net effect of these constraints indicates that the $E(r_{ref})$ is the network average motion at that distance. The $D(r)$ then corrects that level of motion

to the desired distance and the $S(f)$ term provides a local correction for a site for component of motion. Regression results for processing the peak S motion at 1.0 Hz are shown in Fig. 3. The uniform distribution of residuals and the lack of significant outliers indicate uniform calibration of instruments. The distance distribution indicates that the regression can only constrain high-frequency motion in the 30- to 800-km distance range.

To indicate the frequency dependence of D(r), the regression is performed separately at each frequency under the constraint that D(r) = 0 at r = 40 km (Fig. 4). Because of the lack of data at short distances, curves are not plotted for r < 30 km. Given the excitation at 40 km, this figure is used to predict the level of motion at other distances as a function of frequency. This figure is for the regression of filtered peak velocities. A similar figure results from the regression of the Fourier velocity spectra observations.

Duration is defined as the length of time that bounds the 5% and 75% bounds of $TS \int s(t)2dt$. The Fourier velocity spectra are generated from the signal within this window, and the combination of the spectra and duration are used with Random Vibration Theory to predict the peak motion. Fig. 5 shows all durations whose corresponding observed peak motion are within the 5-95% range of predicted values. There are still outliers at large distances. A least-squares estimate of duration is plotted on top of the observations. Outliers affect the least squares estimate, and hence the regression curve deviates from the dense trend of observations at large times. The increase of duration with distance is related to crustal structure. Fig. 6 shows the comparison of distance dependence for the various frequencies. The durations for frequencies > 1.0 Hz are very similar, whereas the duration at 1.0 Hz is greater at shorter distances. This may be due to the fact that the 1.0-Hz signal contains scattered surface waves at the lowest frequency.

Modeling

The predicted Fourier velocity spectra for a frequency f and a distance r is:

$$a(r, f) = s(f, \mathbf{M}_W) g(r) e^{-\pi f r / Q(f) \beta} V(f) e^{-\pi f \kappa_0}$$

where $a(r, f)$ is the Fourier velocity spectra, $s(f, \mathbf{M}_W)$ is the source excitation as a function of moment-magnitude, $g(r)$ is the geometrical spreading function, $Q(f)$ is the frequency dependent quality factor, which equals $Q_0(f/1.0)^{\eta}$, Q_0 is the quality factor at 1.0 Hz, $V(f)$ is a frequency dependent site amplification, and κ_0 controls site dependent attenuation of high frequency. This is a phenomenological description that conceptually includes everything that affects the observed signal. Usually little is known about the site and the $V((f)exp(-\pi f \kappa)$ is lumped together as a $exp(-\pi f \kappa_{eff})$ term as a simplification which is valid since this a reasonable approximation over the limited frequency band of observations.

A comparison to the regression model shows the following correspondence for the Fourier Velocity spectra:

$$10E = s(f, \mathbf{M}_W) g(r_{ref}) e^{-\pi f r_{ref} / Q(f) \beta} V(f) e^{-\pi f \kappa_0}$$
$$10D = g(r) e^{-\pi f r / Q(f) \beta} g(r_{ref}) e^{-\pi f r_{ref} / Q(f) \beta}$$
$$10Si = V(f) e^{-\pi f \kappa_0} V(f) e^{-\pi f \kappa_0},$$

where $V(f) e^{-\pi f \kappa_0} f$ is the network average site effect arising from the $\sum Si = 0$ constraint. This interpretation is tied to the constraints used in the inversion: the use of a reference distance and the $\sum Si = 0$ constraint.

The modeling procedures include:

Model Fourier Velocity. Start with $g(r)$, Q_0 and η. Next look at small event E terms to get κ_0.
Include duration to model time domain $D(r)$. Compare observed and predicted $D(r)$'s. Compare observed and predicted $E(r_{ref}, f)$'s.

Use events with known M_W to constrain the $g(r)$ from the source to the first observation distance, here about 40 km. The initial effort is to model the $D(r)$ term in terms of the $g(r)$ and the $Q(f)$. The rationale is that these terms are separable for the Fourier Velocity and approximately so for the time domain observations. Once these are defined, only the source spectrum and the site term affect the observed level of motion at the reference distance. For $M_W <$ 2.5, the source spectrum is independent of stress drop in the frequency range of 1 - 12 Hz for stress drops > 50 bars

or so. Thus, only the site term affects the unmatched part of the $E(r_{ref})$. Note we cannot separate the effect of the site term from the source spectrum; we do so for convention. It may be possible to see different site terms with some data sets (New Madrid) by comparing the *E()* functions for ΣSZ = 0 and ΣSH = 0 regressions. The real unknown is the *g(r)* required to get the motion from the source to the first observation distance. This is usually assumed to be of the form r^{-1} - but synthetic seismogram modeling indicates that the decay may be slightly more rapid. If we independently have an M_W and have sufficient observations at lower frequencies so that unknown stress drop does not affect us, we can use this additional evidence to define the proper g(r) for distances outside our observations.

Comparison of model fit to the Fourier velocity excitation terms is shown in Fig. 7. The high-frequency level for small events is not a function of stress drop. The largest events in the data set had moment magnitudes of 5 - 5.5. The averages are used to be able to see the trends. Comparison of model fit to the Fourier velocity *D(r)* term is shown in Fig. 8. To highlight the frequency dependence, the deviation from a *1/r* trend is plotted. Remember data only for r > 30. Fig. 9 shows the comparison of model fit to the filtered time domain velocity *D(r)* term. To highlight the frequency dependence, the deviation from a *1/r* trend is plotted. Remember data only for r > 30.

Model Parameters:

k_0 = 0. 050 *s; Q*(*f*) = 200(*f* /1. 0)0.49; *VS*(for*Q*) = 3. 5 *km*/*s; VS*(*source*) = 3. 5 *km*/*s;*
r= 2. 8 *gm*/*cm*3; *f*max = 100 *Hz;* Δs= 100 *bars; V*(*f*) = 1.0

$$g(r) = \begin{cases} r^{-1} & 1\ km \le r \le 40 km \\ r^{-1.2} & 40\ km \le r \le 90\ km \\ r^{0} & 90\ km \le r \le 150\ km \\ r^{-0.5} & R \le 150\ km \end{cases}$$

$$T(r) = \begin{cases} s & r = 0\ km \\ 5\ s & r = 50\ km \\ 8\ s & r = 200\ km \\ 15\ s & r = 500\ km \\ 18\ s & r = 1000\ km \end{cases}$$

In performing the regression, the site term constraint can be taken to be ΣZ = 0, with no constraint on the horizontal components. This means that both the vertical and the horizontal data constrain the *D(r)* term, but only the vertical components define the *E(r)*. We can now form the *log H/Z* ratio subtracting the horizontal S term from the corresponding vertical at a station (Fig. 10). The ratio depends on the earth model and predominant focal mechanism. Any frequency dependence would be indicative of very strong site effects that are seen in this data set. We see that log(H/Z) ~ 0.2 for this data set. Fig. 11 shows the plot of site terms for the regression on peak-filtered motions. A positive site term represents a motion greater than expected for the network average. This could be due either to an actual size effect due to local structure or to absolute instrument calibration.

CONCLUSIONS AND RECOMMENDATIONS

This study indicates that modeling of small event distance dependence and excitation terms is independent of stress drop and source scaling and the modeling of large events requires a source model. Moments from larger events are needed to further constrain *g*(*r*) and *S*(*f*). This study has provided constraints on the amplitude-distance relation of 1- to 12-Hz high-frequency ground motion in the distance range of 30 - 600 km in Yunnan and surrounding provinces. More work is required on the absolute scaling of ground motion in terms of the source. We hope to use waveform modeling to define focal mechanisms, source depths and seismic moments for many of the larger events. This may help define the correct geometrical spreading from the source to the first observations at 30 km and also constrain the stress drop of these events. This study is an important first step in predicting ground motion for large magnitude earthquakes in the region.

REFERENCES

Baumgardt, D. R. and Z. A. Der (1994), Investigation of the transportability of the P/S ratio discriminant to different tectonic regions, PL-TR-94-2299, Phillips Laboratory, Hanscom Air Force Base, Massachusetts.

Baumgardt, D. R. and C. M. Schneider (1997), Multivariate canonical correlation of P/S ratios and propagation path parameters for Iran, *Proc. 19th Annual Seismic Research Symposium on Monitoring a Comprehensive Test Ban Treaty* (Editors: M. J. Shore, R. S. Jih, A. Dainty, and J. Erwin), Defense Special Weapons Agency, Alexandria, 14-23.

Kim, W. Y., V. Aharonian, A. L. Lerner-Lam, and P. G. Richards (1997), Discrimination of earthquakes and explosions in southern Russia using regional high-frequency three-component data from the IRIS/JSP Caucasus Network, *Bull. Seism. Soc. Am* **87**, 569-588.

Malagnini, L. (1999), Ground Motion Scaling in Italy and Germany, *Ph. D. Dissertation*.

National Research Council (1997), Research Required to Support Comprehensive Test Ban Treaty Monitoring, National Academy Press, Washington, D.C.

Qin, J. Z. and R. J. Kan (1986), Q Values and Seismic Moments Estimates Using the Coda Waves of Near Earthquakes in the Kunming and Surrounding Regions, *Chinese J. Geophy*., **29**(2): 145-155.

Raoof, M., R. B. Herrmann, and L. Malagnini (1999), Attenuation and excitation of three-component ground motion in Southern California, *Bull. Seism. Soc. Am.* **89**, (Aug. 99) preprint.

Rodgers, A. and W. Walter (1997), Regionalization and calibration of seismic discriminants, path effects, and signal-to-noise for station ABKT, *Proc. 19th Annual Seismic Research Symposium on Monitoring a Comprehensive Test Ban Treaty* (Editors: M. J. Shore, R. S. Jih, A. Dainty, and J. Erwin), Defense Special Weapons Agency, Alexandria, 143-151.

Walter, W. R, K. M. Mayeda, and H. J. Patton (1995), Phase and spectral ratio discrimination between NTS earthquakes and explosions. Part1: empirical observations, *Bull. Seism.Soc.Am* **85**, 1050-1067.

Walter, W. R., D. B. Harris, and S. C. Myers (1997), Seismic discrimination between earthquakes and explosions in the Middle East and North Africa, *Proc. 19th Annual Seismic Research Symposium on Monitoring a Comprehensive Test Ban Treaty* (Editors: M. J. Shore, R. S. Jih, A. Dainty, and J. Erwin), Defense Special Weapons Agency, Alexandria, 459-468.

Yazd, M. R. S. (1993), Ground motion studies in the Southern Great Basin of Nevada and California, *Ph. D. Dissertation*, Saint Louis University, 189p.

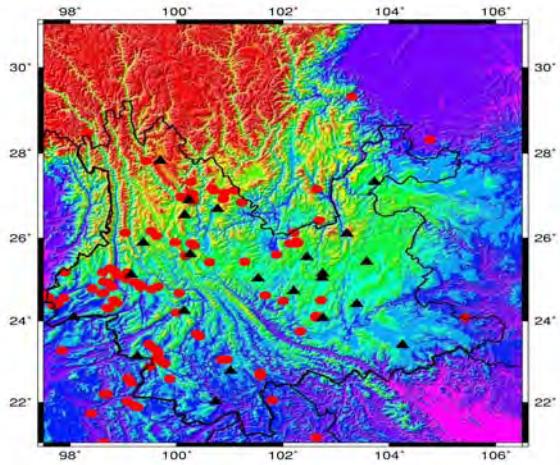

Figure 1. Plot of events, left, and stations, right, used for the analysis of high frequency ground motion in the Yunnan region of southwestern China.

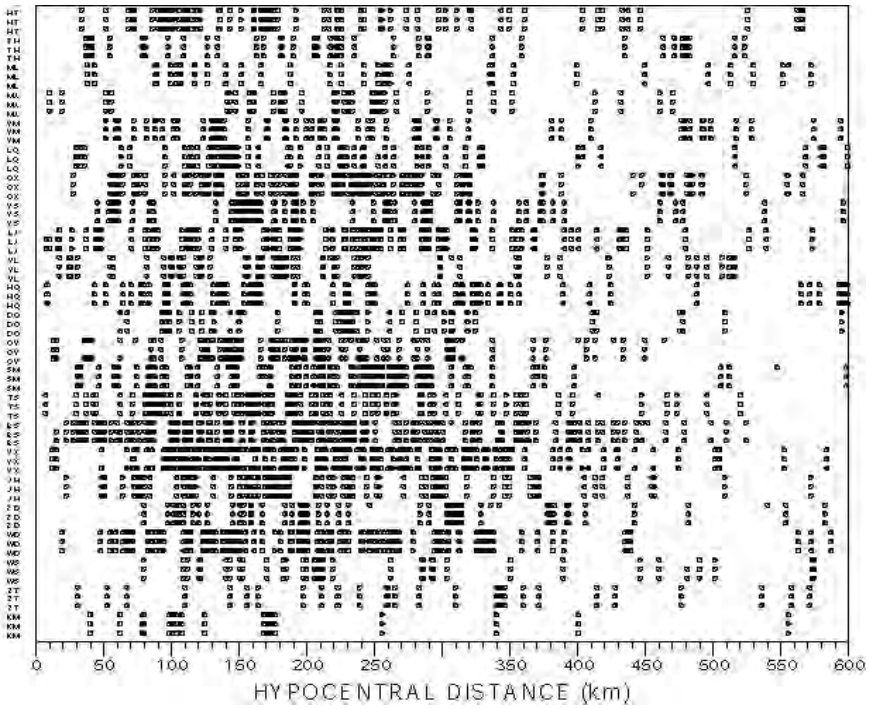

Figure 2. Distribution of observed events for each station at different distances indicates that each event can be observed by many stations, and that the distance distributions overlap.

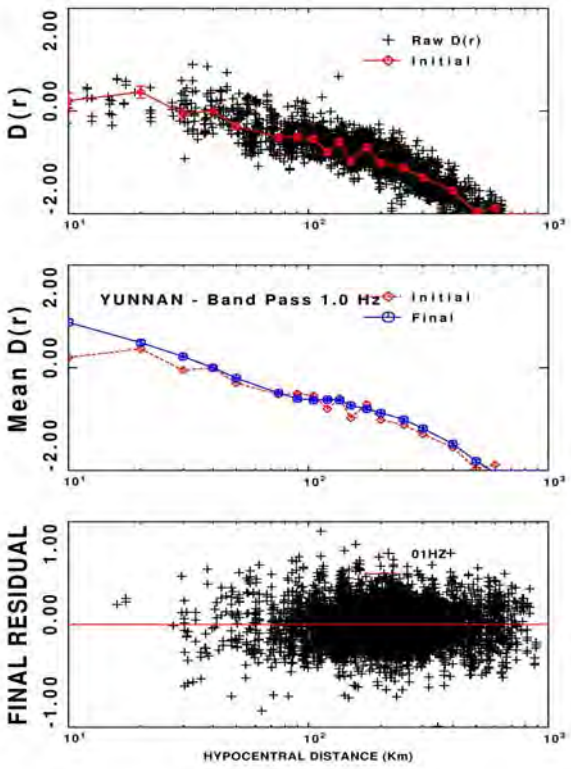

Figure 3. Regression results for processing the peak S motion at 1.0 Hz. top). Estimate of the D(r) term using the coda normalization technique; middle), Comparison of coda normalization (red) and regression (blue) results; bottom) regression residuals as a function of distance.

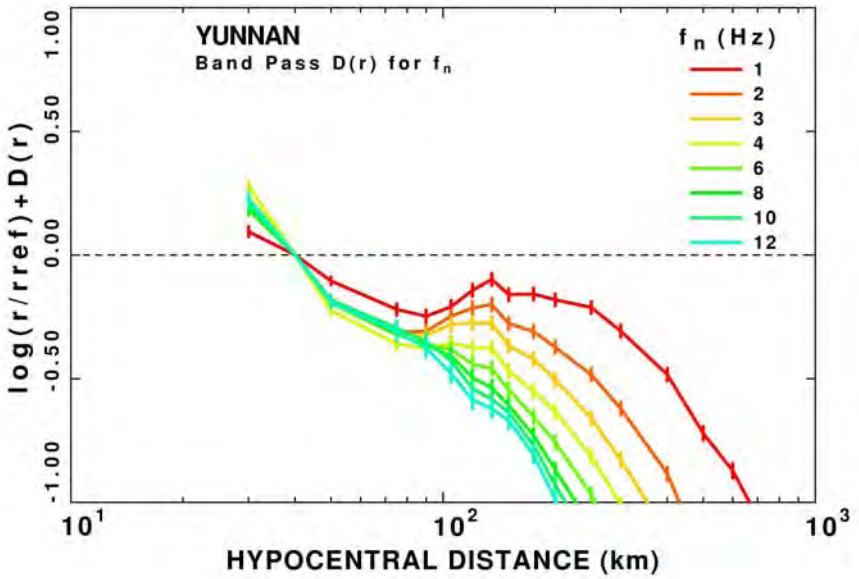

Figure 4. This figure compares the D(r) for each frequency of the regression of filtered peak velocities. Because of the lack of data at short distances, curves are not plotted for r < 30 km.

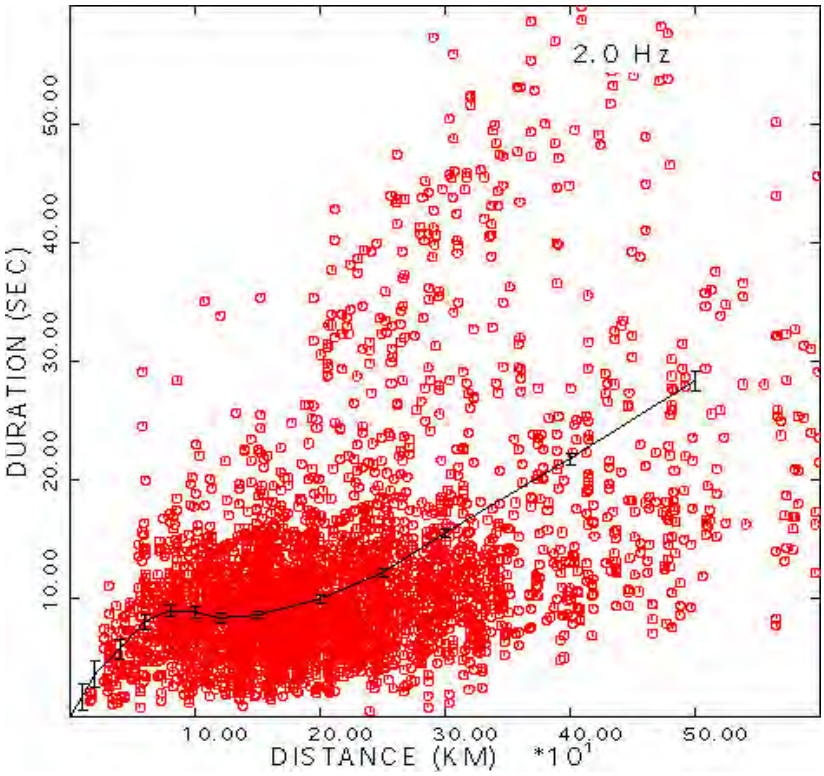

Figure 5. Distance Dependent Duration for a frequency of 2 Hz. A least-squares estimate of duration is plotted on top of the observations.

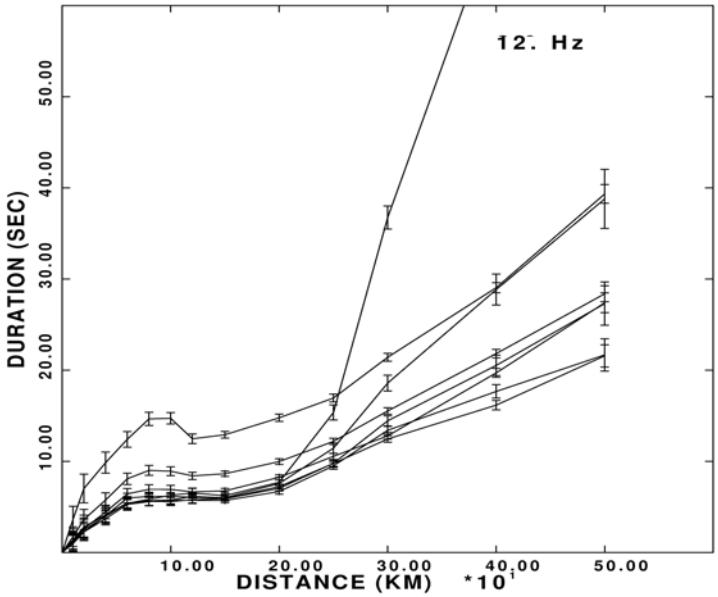

Figure 6. Comparison of duration versus distance at various frequencies.

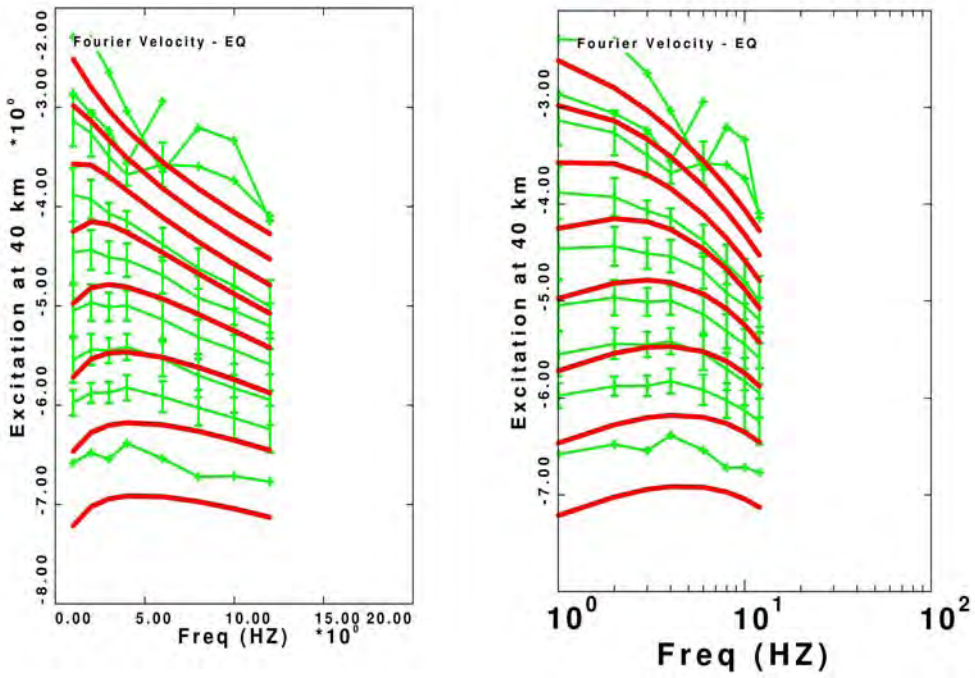

Figure 7. Comparison of model fit to the Fourier velocity excitation terms. The green lines are averages of the regression excitation terms into groups that are separated by 0.5 log units in level at 3.0 Hz. The red curves are the predicted excitation terms for the model for moment magnitudes of 2.0 - 5.5 at increments of 0.5 moment magnitude units.

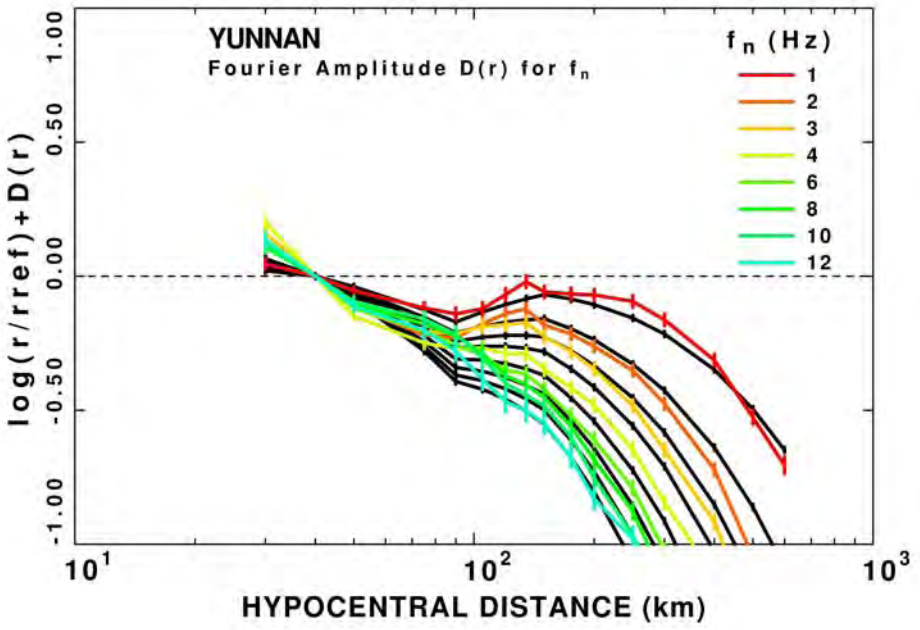

Figure 8. Fourier D(r): Comparison of model fit to the Fourier velocity *D(r)* term. The regression results (color) are plotted on top of the predicted values (black). To highlight the frequency dependence, the deviation from a *1/r* trend is plotted. Remember data only for r > 30.

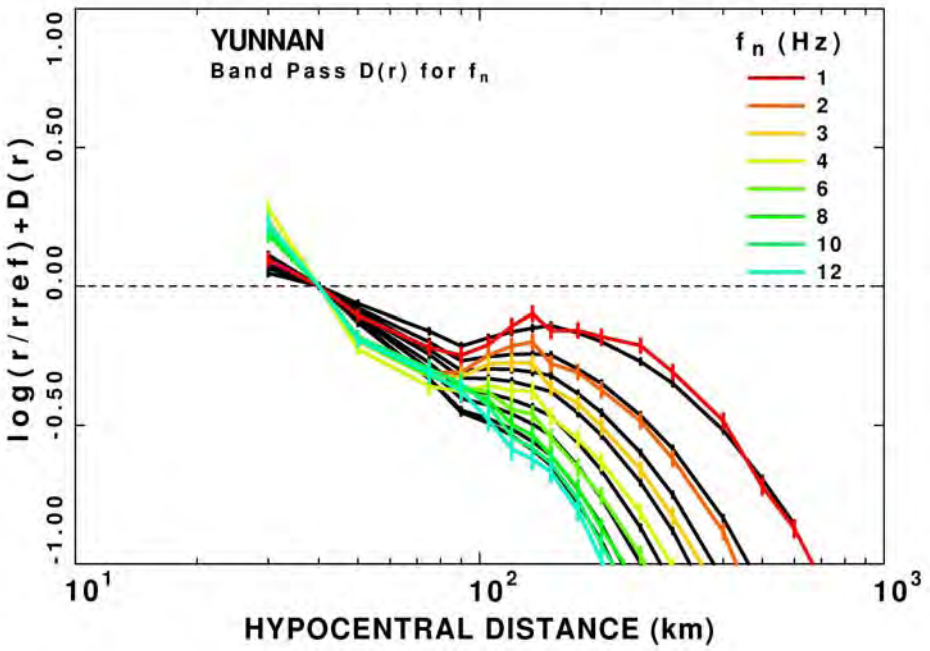

Figure 9. Comparison of model fit to the filtered time domain velocity *D(r)* term. The regression results (color) are plotted on top of the predicted values (black). To highlight the frequency dependence, the deviation from a *1/r* trend is plotted.

H/Z Ratio

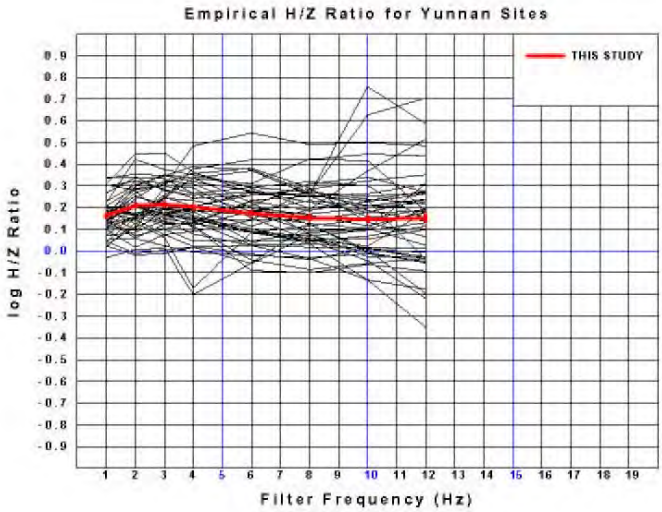

Figure 10. H/Z Ratio: In performing the regression, the site term constraint can be taken to be Z = 0, with no constraint on the horizontal components. The ratio depends on the earth model and predominant focal mechanism. Any frequency dependence that would be indicative of very strong site effects are seen in this data set.

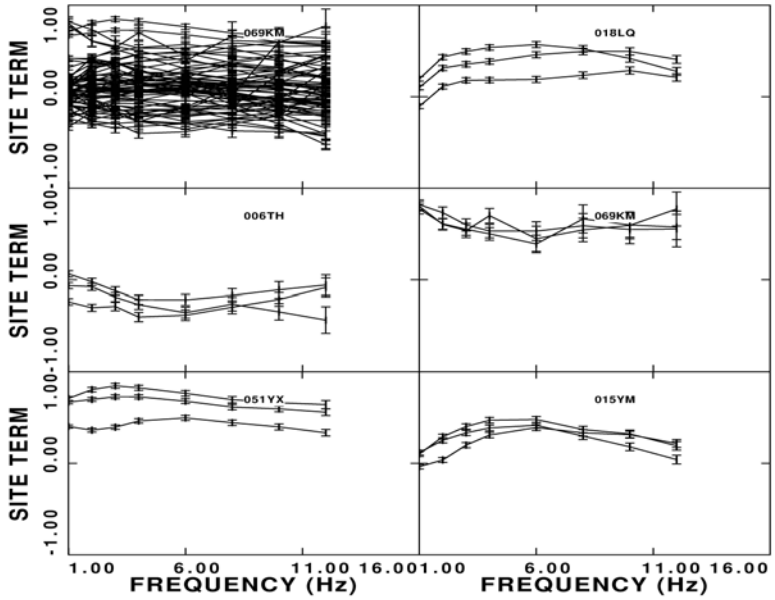

Figure 11. Plot of site terms for the regression on peak-filtered motions. Site terms for all components are plotted at the upper left. The remaining panels display the site terms for selected stations with large deviations from 0.

SOURCE-SPECIFIC STATION CORRECTIONS MODELED BY DYNAMIC RAY TRACING IN 3-D EARTH MODELS

Vernon Cormier, Anastasia Stroujkova

University of Connecticut

Sponsored by Defense Threat Reduction Agency

Contract No.: DTRA01-00-C-29

ABSTRACT

Source-specific station corrections (SSSCs) to travel-time tables have been constructed for International Monitoring System (IMS) stations in Eastern Asia by ray tracing in three-dimensional (3-D) earth structure. Three-dimensional models are parameterized by tetrahedra, with linear interpolation of velocities between tetrahedron vertices. This parameterization allows analytic integration of kinematic and dynamic ray tracing equations. Two types of 3-D models have been tested: (1) a model consisting of 22 1-D velocity regions with lateral transition zones between regions and (2) a model constructed from CRUST 2 and RUM upper mantle. SSSC's are generated on 1 x 1 degree grids from 0-, 10-, 50-, 100-, and 150-km depth sources. In tests of relocation accuracy against ground truth locations, type (1) model, consisting of 1-D velocity profiles with lateral transition zones, performs better than the hybrid CRUST2 + RUM model. We find that travel times beyond the 1- to 2-degree range are more sensitive to structure in the upper mantle than the crust. A comparison of the SSSC's computed assuming a realistic Moho topography versus that predicted by lateral transitions between 1-D models is in progress.

OBJECTIVE

This work is a part of the Lamont-Doherty IMS calibration consortium. This consortium is charged with improving earthquake locations for 30 proposed stations in the International Monitoring System (IMS). The task assigned to the University of Connecticut is to develop algorithms for constructing three-dimensional models of the crust and upper mantle, to compute travel times, and to quantify the errors in estimated travel times for regional seismic waves propagating in these models. The incorporation of three-dimensional structure is needed to overcome the effects of off-azimuth paths on travel times and to estimate these effects. 3-D ray-tracing is particularly important in areas with strong lateral variations of velocity and/or Moho topography (e. g. Tibet). Three-dimensional modeling is also useful for SSSC computation for buried sources in regions where little ground truth information is available.

RESEARCH ACCOMPLISHED

Three-dimensional velocity models

Two types of velocity models were tested. One type is constructed from published models for the crust and upper mantle of eastern Asia. CRUST2 by Mooney *et al* (1998) incorporates many published refraction studies in a global 7 layer crust at 2 x 2 degree resolution and is a refinement of CRUST5.1. This crustal model was merged with the Regionalized Upper Mantle (RUM) model (Sambridge and Gudmundsson, 1998). Although this latter model is reported on 2 x 2 degree grid, it has been obtained primarily by inverting teleseismic data and therefore has lower resolution.

The second type of model is based upon partitioning of the whole region (Eastern Asia) into 22 sub-regions (Figure 1; Khalturin, unpublished). Each of these sub-regions corresponds to a geologic province with relatively homogenous lateral velocities. Available travel-time information (Kirichenko and Kraev, 2001) has been used to construct 1-D velocity model for each region (West, 2001). The 3-D model was then created with the assumption that each of the regions has a 1-D model with properties that change abruptly at region boundaries. Figure 2 shows velocity profiles corresponding to these models beneath station Borovoye. Seismic velocities in the upper mantle are higher for the regionalized model than for both the IASPEI-91 model and CRUST/RUM hybrid. This is important because Pn travel times computed with the IASPEI-01 model in Asia are typically longer than the ground truth travel times.

Parameterization and 3-D ray-tracing

The models, initially defined as functions of latitude, longitude and depth, were projected onto 3-D Cartesian grid tracking the spherical shape of the Earth. The earth was not flattened. Model input formats were converted for 3-D ray tracing codes (Menke, 2002), which requires quasi-layered structure with a constant number of nodes in each direction. The grid was discretized at 0.5 by 0.5 degrees. Each parallelepiped of 8 nodes is then divided into 5 tetrahedra with velocity defined in each vertex. The velocity inside each tetrahedron is a linear function of coordinates. A ray path in such medium is an arc of a circle and the travel time along such an arc can be computed exactly. The limitation of this method is that it requires non-zero velocity gradient in each tetrahedron and does not allow velocity discontinuities.

The error of this method is contributed by two major effects. The first source of errors is the tetrahedral parameterization of the Earth, which implies an approximation of the surface of the Earth by a multifaceted surface (Figure 3 b). It is possible to roughly estimate the magnitude of this error. Figure 3 c shows a simplified 2-D geometry for this case. The deviation of the model surface from the surface of the sphere at both source and receiver is $dz = R(1-\cos(\delta/2)/\cos\gamma)$, where R is the radius of the Earth, δ is the angular distance between nodes of the grid, and γ is the smallest angular distance to the node. This corresponds to a travel-time perturbation equal to $dt = dz\cos i/V_0$, where V_0 is the velocity at the source or receiver and *i* is a takeoff or arrival angle respectively. This type of error is largest in the center of a grid cell and gets smaller toward its nodes and goes to zero as we approach the nodes.

The second error comes from the velocity approximation. To examine the relative importance of these two types of errors, we compared the ray-tracing results using the well-known IASPEI-91 model with theoretical travel times. The results are shown in Figure 3c and d for grid sampling of 0.5 and 1 degree respectively. Subtraction of the theoretical error from the observed error yields the error caused by velocity approximation, which in the case of one-degree grid spacing was below 0.1 s for distances between 2 and 15 degrees. For distances less than 2 degrees, it can be as large as 2 s, and beyond 15 degrees, it becomes less than 0.05 s. For a 0.5×0.5 degree grid, the error beyond 2 degrees stays less than about 0.07 s. The velocity approximation error, however, stays large for distances less than about 2 degrees.

Results and ground truth validation

P-wave travel-time tables were generated for paths of regional seismic phases within and to area 1 IMS stations in Eurasia on 1 × 1 degree grid for different depths (0 km, 10 km, 50 km, 100 km and 150 km). Figure 4 shows travel-time differences between computed and theoretical (IASPEI-91) travel times for station Borovoye. For most stations the differences are ±8s. The magnitude of the corrections with respect to IASPEI-91 is greater for the regionalized model. CRUST/RUM hybrid converges with the IASPEI model as depth increases. Therefore the magnitude of the corrections decreases with growing distance.

The ray-tracing results for deeper sources suffer from lack of convergence at certain points of 1 × 1 degree grid. To overcome this problem, we are testing different schemes of travel-time interpolation to fill in shadow zones, including tension spline interpolation.

The validation of the travel-time estimates was performed using ground truth data from several sources (Murphy *et al*, 1997; Sultanov *et al*, 1999). The large part of the dataset comes from 83 Soviet peaceful nuclear explosions (PNE), 80 underground nuclear tests (UNT) from Semipalatinsk, and 7 UNT from Lop Nor (China). We also included data from Indian and Pakistani tests and well-located earthquakes (GT5-GT10, Yang et al., 2000). Another part of the dataset, which covers vast aseismic regions of Russia, comes from the Deep Seismic Sounding (DSS) program in the form of profiles from 19 PNEs and 2 weapon explosions (over 4600 travel-time picks made by the University of Wyoming research group).

The ground truth data were used for further refinement of the velocity model. We performed a travel-time inversion with software ray-traced (Menke, 2002). This software was chosen because it uses the same ray-tracing algorithm that was used to compute travel times. The model parameterization was performed as follows. We chose the regionalized model as a starting point. The model parameters were layer velocities in each region covered with data points. Each layer in the model was permitted to vary as a whole during the inversion. Overall 26% reduction of travel-time residuals was achieved as the result of the inversion. This improved velocity structure region was used to compute the SSSCs.

Performance of different velocity models in predicting actual travel times compared to the reference (IASPEI-91) model is summarized in Table 1. The travel-time residuals are the smallest for almost all of the stations, except NRI and FRU. The IASPEI 91 yields the best fit for NRI, and the CRUST/RUM hybrid gives good results for stations AAK and FRU. The overall mean and standard deviation of the travel-time residuals is the smallest for the regionalized velocity model. The IASPEI model has the greatest bias in estimate of travel times (mean residual is 1.53 s) and typically over predicts the true values.

Table 1. Travel time residuals for ground truth events for selected auxiliary stations, shown in Figure 1.

Station	Latitude N	Longitude E	IASPEI		CRUST+RUM		Regionalized	
			mean	rms	mean	rms	mean	rms
AAK	42.6300	74.4800	2.23	2.73	0.27	1.47	-0.92	1.01
ARU	56.4302	58.5625	1.29	2.16	-2.09	3.02	-0.16	1.04
BOD	57.8500	114.1830	-0.51	0.94	-3.67	4.23	-0.14	0.67
BRVK	53.0581	70.2828	1.28	1.87	0.30	1.93	0.33	1.18
ELT	53.2500	86.2670	1.69	2.06	0.75	2.00	0.79	1.38
FRU	42.8330	74.6170	2.12	3.26	0.21	0.89	-0.26	1.69
KURK	50.7000	78.6000	1.49	1.54	0.87	2.77	-0.18	0.64
MAKZ	46.8080	81.9770	2.12	2.17	1.19	1.68	0.51	0.93
NIL	33.6500	73.2512	3.56	3.87	0.7	1.24	-0.61	0.92
NRI	69.4430	88.0830	0.07	1.92	-2.68	4.34	0.33	2.34
OBN	55.1167	36.6000	1.16	1.59	-3.04	3.36	0.98	1.47
ZAL	53.9367	84.7981	2.01	2.04	2.69	2.71	1.24	1.29
Total	-	-	1.53	2.32	-0.45	2.34	0.03	1.56

CONCLUSIONS AND RECOMMENDATIONS

1. Source-specific station corrections (SSSCs) to travel-time tables have been constructed for IMS stations in Eastern Asia by ray tracing in three-dimensional earth structure. The ray-tracing procedure and velocity models were verified using available ground-truth information. The ground truth data were used for refining the velocity structure in the area of work. After testing different velocity models we found that the velocity model constructed of laterally homogeneous regions provided the best fit to the available data.

2. Ray-tracing in the medium with known travel times has shown that grid discretized at 0.5 by 0.5 degree provides adequate accuracy.

3. P-wave travel-time tables were generated for 30 IMS stations in Eurasia on 1×1 degree grid based upon the improved regionalized velocity model.

ACKNOWLEDGEMENTS

The authors would like to thank Prof. W. Menke of Lamont Doherty Earth Observatory for providing the ray-tracing code. We also appreciate help from other members of the Consortium.

REFERENCES

Cerveny, V. (2001), Seismic Ray Theory, *Cambridge University Press*.

Kirichenko, V.V., and Y.A. Kraev (2001), Results of 1-D location calibration studies related to the territory of Northern Eurasia, *23rd Seismic Research Review: Worldwide Monitoring of Nuclear Explosions – October 2-5, 2001*, 70-79.

Menke, W. (2002), Case studies of seismic tomography in a regional context, in Seismic Data Analysis and Imaging With Global and Local Arrays, Alan Levander and Guust Nolet, Eds., American Geophysical Union, submitted 2002.

Mooney, W. D., G. Laske and T. G. Masters (1998), Crust 5.1: a global crustal model at 5x5 degrees, *J. Geophys. Res*, **103**, 727-747.

Murphy, J. R., Sultanov D. D., B. W. Barker, I. O. Kitov, and M. E. Marshall (1997), Further Analyses of Regional Seismic Data Recorded From the Soviet PNE Program: Implications with Respect to CTBT Monitoring, PL-TR-97-2141.

Sambridge, M., and O. Gudmundsson (1998), A Regionalized Upper Mantle (RUM) model, *J. Geophys. Res*., **103**, pp 7121-7136.

Sultanov, D. D., J. R. Murphy, and Kh. D. Rubinstein (1999), A Seismic Source Summary for Soviet Peaceful Nuclear Explosions, *Bull. Seism. Soc. Am*., **89**, pp 640-647.

West, M (2001). http://www.ldeo.columbia.edu/~mwest.

Yang X., I. Bondar, and C. Romney (2000), PIDC GT Event Database, CDMR Technical Report 00/15.

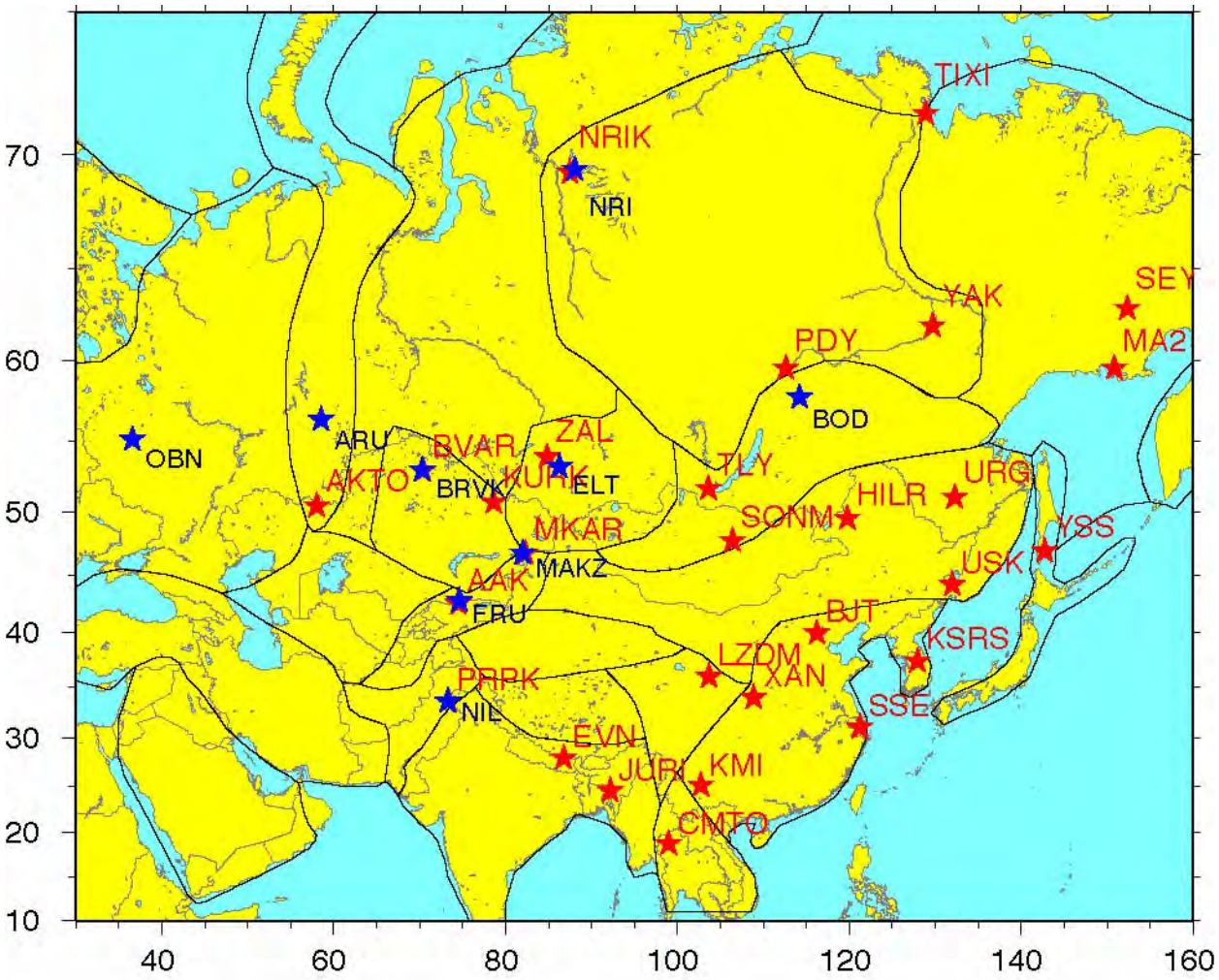

Figure 1. Map showing 30 IMS stations (red) and additional stations used for travel-time verification (blue).

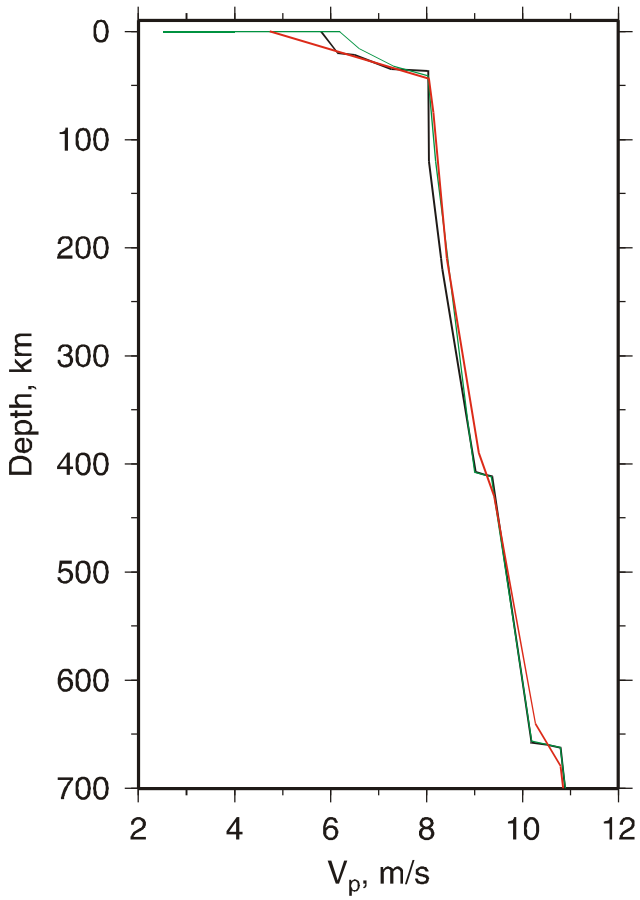

Figure 2. Velocity profiles beneath station Borovoye. Black line shows reference IASPEI velocity, red line – RUM/CRUST hybrid velocity, green line – 1-D velocity in the region surrounding station Borovoye.

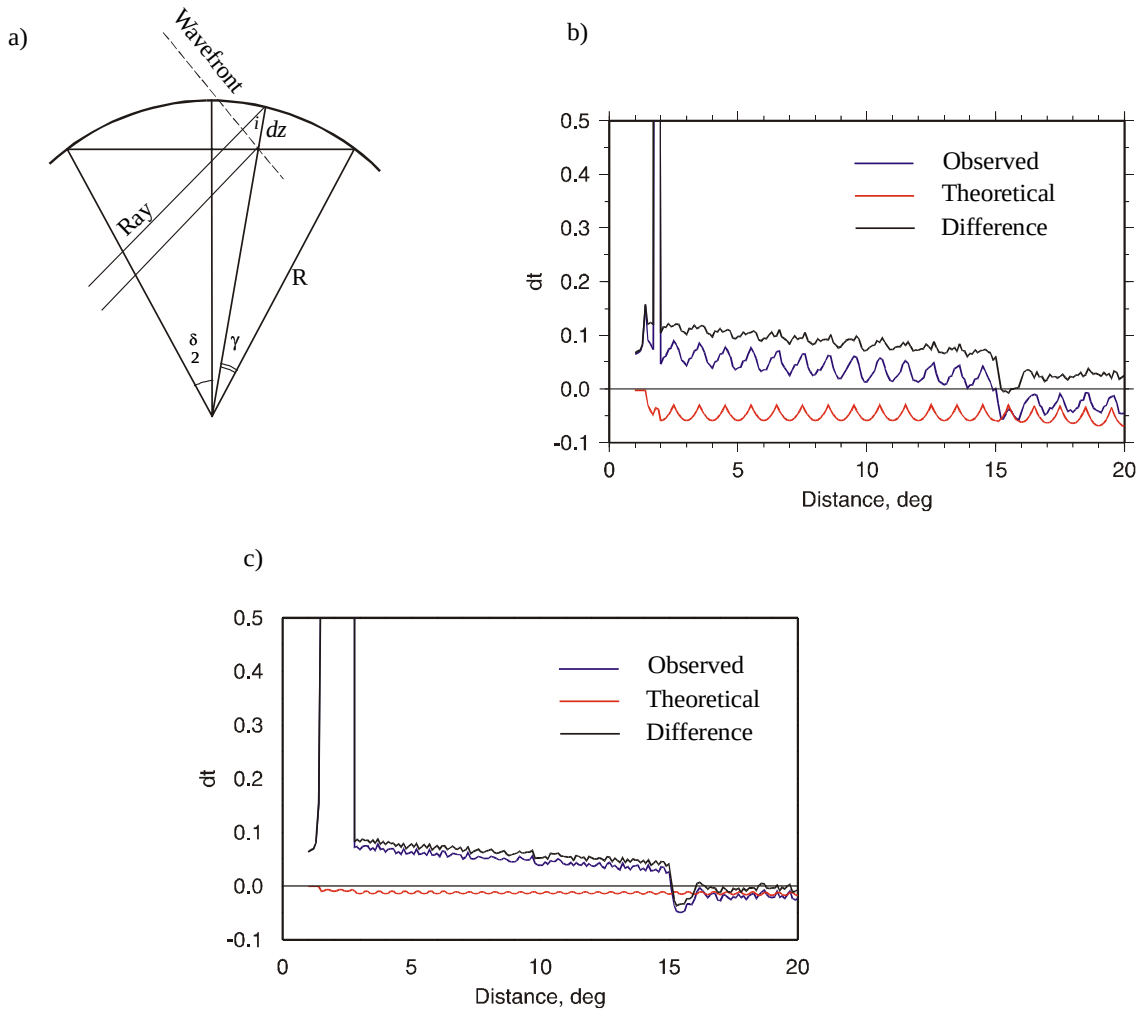

Figure 3. a) Geometry of a ray near the surface in the spherical earth approximated by tetrahedra. b) Difference between theoretical and computed travel times for IASPEI-91 model with 1 degree between nodes. Blue line shows the difference between ray traced and theoretical travel times, red line shows predicted error due to surface approximation, and black line is the difference between actual and predicted error. c) Same as b, except node spacing is reduced to 0.5 degree.

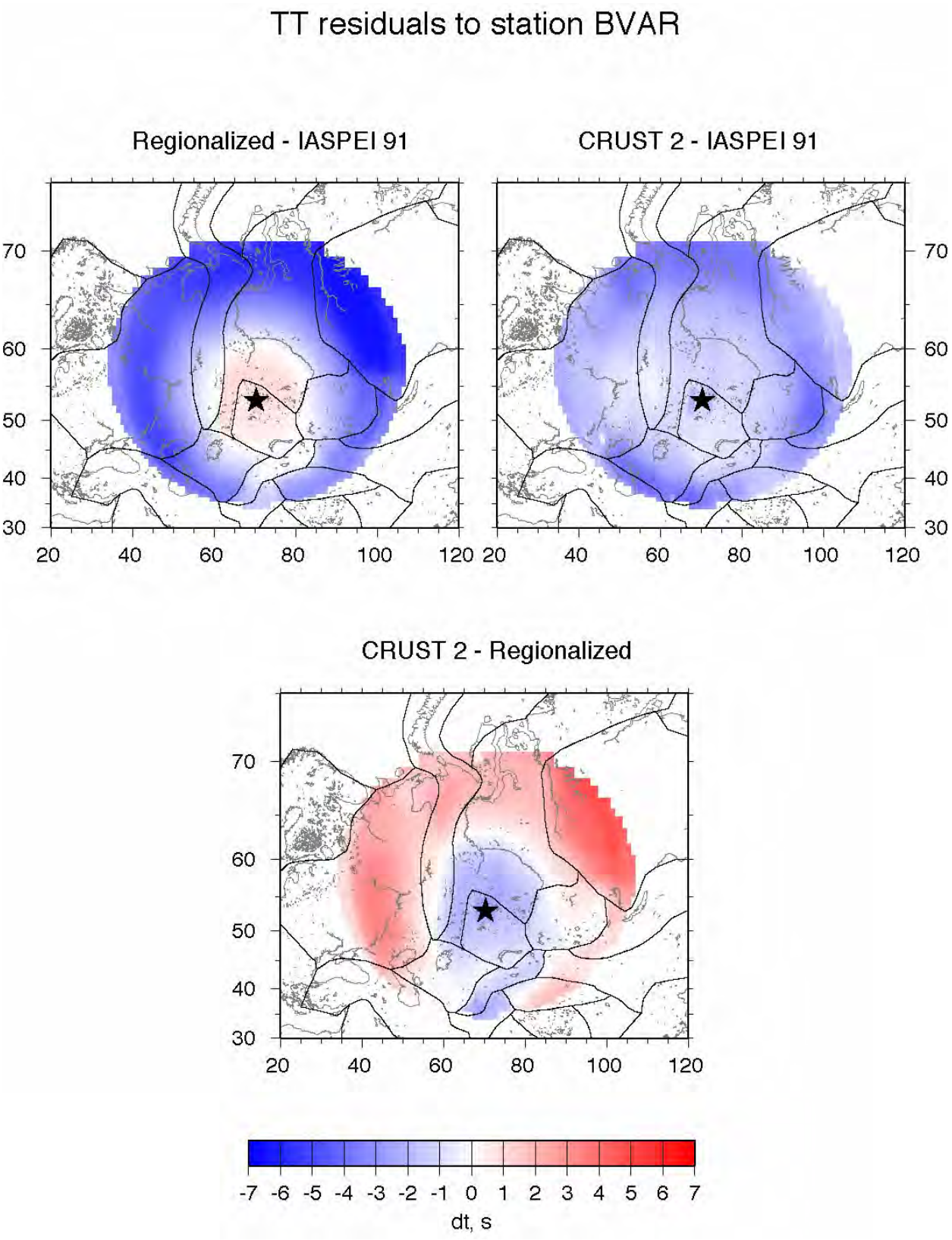

Figure 4. Travel-time differences between different velocity models computed for IMS station BVAR (Borovoye).

GROUND TRUTH COLLECTION FOR MINING EXPLOSIONS IN NORTHERN FENNOSCANDIA AND RUSSIA

David B. Harris,[1] Frode Ringdal,[2] Elena Kremenetskaya,[3] Svein Mykkeltveit,[2]
Donald W. Rock,[1] Johannes Schweitzer[2]

Lawrence Livermore National Laboratory,[1] NORSAR,[2] Kola Regional Seismological Centre[3]

Sponsored by National Nuclear Security Administration
Office of Nonproliferation Research and Engineering
Office of Defense Nuclear Nonproliferation

Contract No. W-7405-ENG-48[1] and DE-FC03-01SF22420[2,3]

ABSTRACT

This three-year project, which began on 1 September 2001, focuses on the collection of ground truth information on explosions at the principal mines within 500 km of the ARCES seismic array in northern Norway. Ground truth is being collected directly by deploying seismic stations at the mines and also by polling mine operators for shot information. In addition, two lines of seismic instruments are planned to be deployed in August 2002, extending from the Khibiny Massif of the Kola Peninsula to two points in Norway (one line includes ARCES). Observations of mining explosions collected by these instruments will enable researchers to examine the range (distance) dependence of seismic discriminants. The line will be operated for a year. In the third year of the project, the seismic stations will be redeployed to selected mines in northern Norway, Sweden, and parts of northwestern Russia to collect origin times and locations of additional commercial mining explosions.

To date, we have collected ground truth information on several hundred explosions in mines of the Khibiny Massif for a period of seven months. The data provided for each event include a seismically determined origin time, the mine conducting the explosion, the total yield of the explosion, and an indication of whether the shot was conducted on the surface or underground. The origin times are determined with data from a local network, including stations in the immediate vicinity of the mines. Frequently additional information is provided, such as the distribution of yields for individual shots in a multiple explosion event. The ground-truth catalog drives event waveform extraction for a collection of regional stations including ARCES, Lovozero (LVZ), Kevo (KEV), and Apatity stations (the Apatity array APAES and the broadband station APAZ9). Our goal is to assemble a ground truth set of waveforms useful for studying the effect of different shooting practices (e.g. underground compact explosions and ripple-fired surface explosions) on seismic observables. The mines of the Khibiny Massif are a highly desirable natural laboratory for examining this issue, since surface and underground mines conducting a variety of shot types are co-located and at regional distance from a major International Monitoring System (IMS) array -- ARCES.

Another objective of this project is to develop a strategy for allocating calibration resources in a region with many mines. Fennoscandia and western Russia illustrate the problem of resource allocation since hundreds of mines exist within regional distance of major monitoring stations. How many should be instrumented for ground truth collection and in what order are reasonable concerns for any monitoring organization. Our approach to this problem is to rank mines by their frequency of observation by the monitoring stations in question. This frequency can be determined by plotting event density geographically using automated and analyst-reviewed bulletins developed for the stations and then associating geographic clusters of events with known mine locations. This form of cluster analysis and association may be refined with waveform correlation techniques. We present an analysis of the geographic distributions of events detected and located by the ARCES array and by the Fennoscandian array network for the purpose of ranking the observability of mines in Fennoscandia and western Russia.

OBJECTIVE

The collection of ground truth on mining explosions in northern Fennoscandia and northwest Russia underpins three efforts of interest to monitoring agencies:

1. the calibration of discriminants and location algorithms,
2. the construction of templates for event screening, and
3. the development of empirical and theoretical linkage between explosion source phenomena and observed seismic waveform characteristics.

RESEARCH ACCOMPLISHED

Ground truth and associated waveform data collection for events in the Khibiny Massif

One partner in this project, the Kola Regional Seismic Centre (KRSC), has begun collecting ground truth information on explosions from the major mines of the Kola Peninsula. The mines of this region provide a natural laboratory for exploring the effects of different shooting practices at mines on observed seismic signals. In particular, the Khibiny Massif (an alkaline intrusion occupying 1300 square kilometers in the Kola) contains five large mines producing apatite-nepheline ores for the superphosphate and aluminum industries. Both surface and underground mines are in close proximity in this group, and these conduct a variety of large and small explosions. The underground explosions range from small, compact shots of 2-3 tons of explosive having only a few delays to large ripple-fired shots of 120-240 tons with many delays of 20-35 milliseconds. The surface explosions range from small shots at the Kirovsk and Rasvumchorr mines in the 3- to 15-ton class up to large ripple-fired explosions averaging 150-180 tons at the Central and Koashva mines.

The information that we routinely are able to collect includes, for each explosion, the origin (which mine), a seismically determined origin time, the amount of explosive used, whether the shot was on the surface or underground, and frequently some information on the character of the explosion. The character may include whether the explosion was conducted as several distinct smaller shots (and the amount of explosive used for each) or whether it was conducted as a relatively compact explosion consisting of at most a few delays. Figure 1 shows the mines included in the study.

To improve the quality of origin time determinations and to provide some information on source time histories, KRSC has deployed several stations in the Khibiny Massif adjacent to or in operating mines. Data from their permanent stations APA and AP0 also contribute to the solutions.

As of this writing, we have information on 409 explosions covering the time period from September 2001 through March 2002, inclusive, split roughly equally between surface, open-pit explosions (212) and underground explosions (197). One hundred eighty-one compact underground explosions have been reported. The breakout of ground truth information by mine is given in Table 1. Note that one mine (Kirovsk) has explosions both at the surface and underground, and that the fairly compact group of Khibiny mines has large numbers of both types of events in close proximity. These events should permit studies of source effects of observed seismic signals.

Table 1. Reported Explosions by Mine

	Surface	Underground	Total
Khibiny Group	(95)	(197)	(292)
Kirovsk	10	118	128
Rasvumchorr	0	79	79
Koashva	29	0	29
Norpakh	14	0	14
Central	42	0	42
Olenogorsk Group			
Olenogorsk	14	0	14
Kirovogorsk	14	0	14
Bauman	11	0	11
Komsomolsk	6	0	6
Kovdor	30	0	30
Zapolyarny Group			
Zapadny	19	0	19
Zapolyarny Central	15	0	15

The ground truth information is being used to extract observation time histories for regional stations including KEV, LVZ, ARCES, and the Apatity stations. Figure 2 shows ARCES observations of eight representative small (3-10 tons) surface explosions and eight compact (1-5 tons) underground explosions conducted at the Kirovsk mine. Differences in signal frequency content between the surface and underground shots are apparent in Figure 2a (3-6 Hz) and 2b (6-9 Hz). Not surprisingly, the underground shots, though generally smaller, have similar signal amplitudes to those of the surface shots in the lower frequency band but are substantially richer in high-frequency components than the signals from the surface explosions.

One application of a database of collected waveforms is to develop waveform signatures for each of the mines observed by ARCES. Such signatures may be used as the basis for a bank of correlation detectors that screens out the background of mining explosions at that station. We plan a test of this screening operation later this year, validated by the ground truth being collected for the Kola mines.

Developing a strategy for allocating ground truth collection resources

One possible principle for ranking mines for ground truth resource allocation is to identify the mines that have the greatest seismic visibility to a monitoring network (in the sense of being most frequently observed and/or generating the largest signals). We are testing a data-driven approach to identifying such mines, consisting of four steps: (1) detection of geographic event clusters in NORSAR network bulletins, (2) refined waveform-correlation clustering of identified event groups, (3) relocation of the refined clusters with single-station location methods calibrated to

reduce bias in order to associate the clusters with a mine, and (4) ranking the mines according to the numbers and size of the events in the associated clusters.

Our search for geographic clusters in NORSAR's bulletins is yielding significant results. Figures 3a and 3b show the result of mapping event density using two NORSAR bulletins, an automatic single-array bulletin generated from the ARCES data stream and an analyst-reviewed bulletin developed from the network of Fennoscandian arrays. Both show clearly defined clusters that, for the most part, map directly to known mining districts. The event density map from the automatic ARCES bulletin shows considerable background scatter and only delineates clusters in northernmost Fennoscandia and Russia. The second map displays considerably less scatter and more clearly defines clusters throughout Fennoscandia. The reduced scatter obviously is a function of the overlapping coverage of multiple stations and the screening effect of analyst review.

Preparations for deployment of a line of stations between ARCES and the Khibiny Massif

To enable studies of the evolution of phase amplitudes and discriminants with range, nine sets of 3-component instruments available to this project will be deployed temporarily on profile lines originating in the Khibiny Massif. Three systems will be deployed on the Kola Peninsula, and six systems will be deployed in Finland and Norway. A site survey is underway at this writing (July 2002); potential deployment sites are being ranked according to the availability of bedrock, local noise conditions, and the availability of power and access during winter months. Much of the area between the Khibiny Massif and ARCES is covered by lakes and also not accessible by roads. The current plan for deployment, as shown in Figure 4, consists of two lines from the Khibiny Massif, one running through the ARCES array and one passing to the north of ARCES. The deployment of two lines will allow studies of the azimuthal dependence of discriminants, in addition to range dependence. Current plans call for the lines to be deployed in late August 2002; data will be recorded continuously over a period of one full year.

CONCLUSIONS AND RECOMMENDATIONS

The ground truth collection effort is progressing very well, yielding explosion data at a faster rate than originally anticipated. We expect to build a regional waveform database containing on the order of a thousand explosions with ground truth sufficient to perform statistical studies on the effects of firing practices at mines on regional discriminants. Initial geographic clustering results indicate that the principal observable mining groups around ARCES are identifiable from seismic bulletins, both automated and analyst reviewed. Further refinement of the clusters by waveform correlation analysis is anticipated to resolve individual mines. The methodology appears viable for identifying the most active mines for ground truth collection.

ACKNOWLEDGEMENTS

The authors would like to thank Terri Hauk for assembling available waveform and parameter data into a database for subsequent display and analysis.

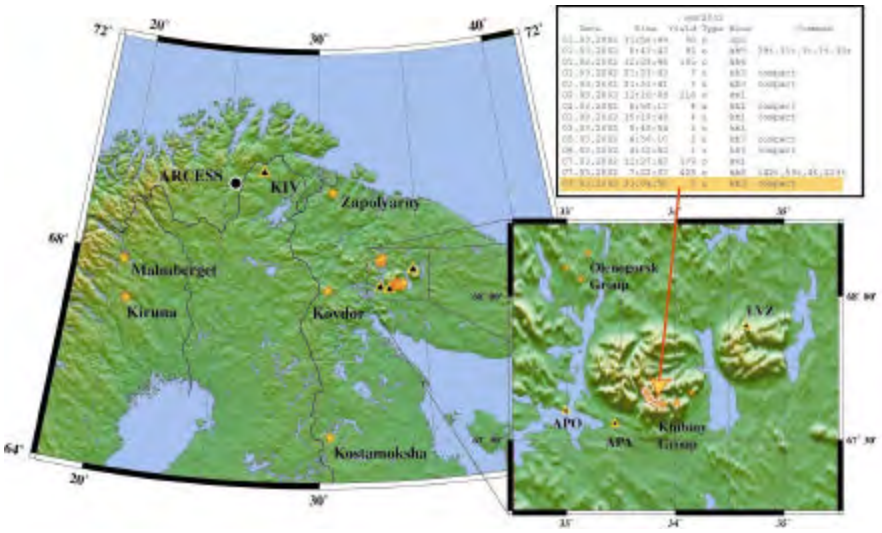

Figure 1. Map showing the mines for which ground truth information on explosions is being collected as part of this study and the stations from which waveform observations of the explosions are being compiled. The stations are indicated as triangles and the mines are shown as stars (those surrounded by circles are possibly underground as well as on the surface). A sample of available ground truth information is shown at upper right.

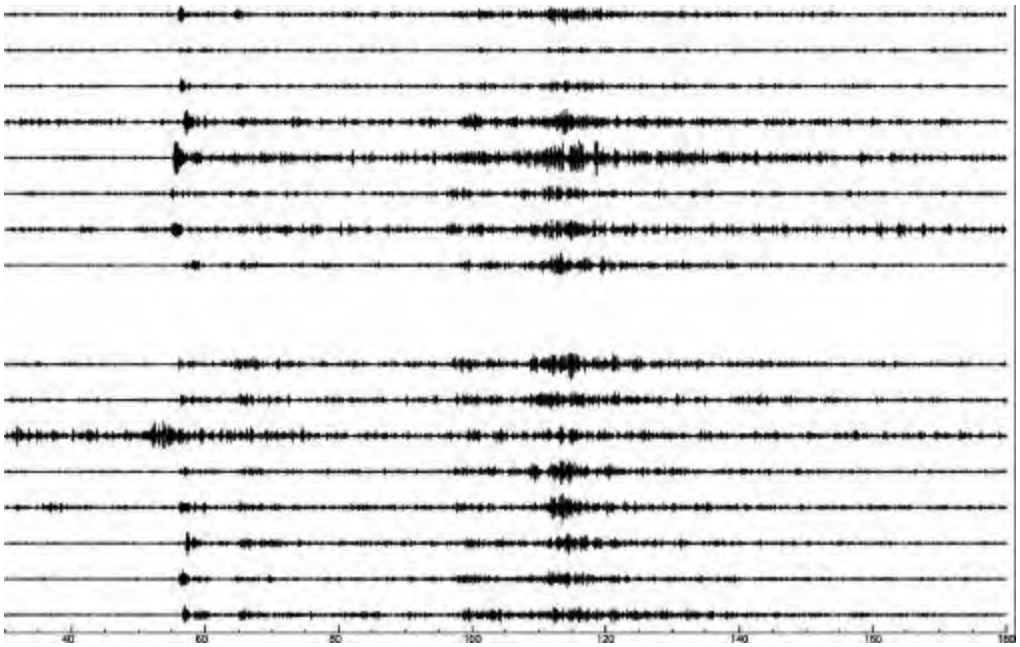

Figure 2a. ARCES waveform observations (single channel, A0 vertical) for 16 shots at the Kirovsk mine, filtered into the 3- to 6-Hz band. The top eight traces correspond to small surface explosions, and the bottom eight to subterranean explosions. Pn, Pg, Sn and Lg phase are evident in most of the seismograms. The observation range is approximately 410 km.

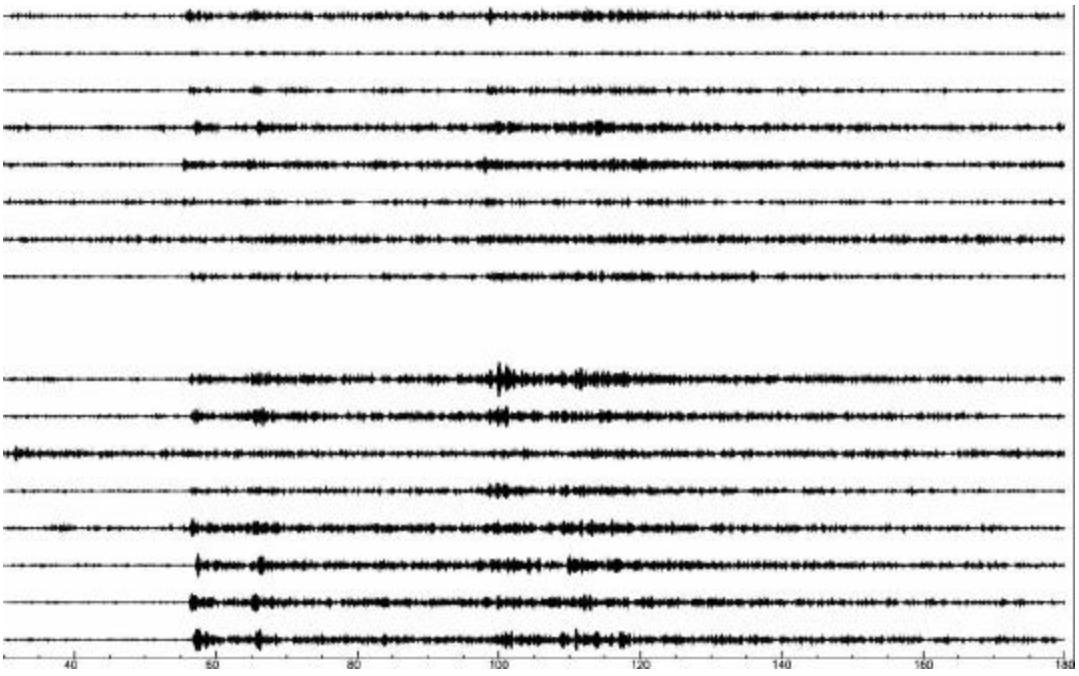

Figure 2b. The same events filtered into the 6- to 9-Hz band. Note the increase in energy in the underground explosions (bottom) relative to the surface explosions (top) at this higher frequency.

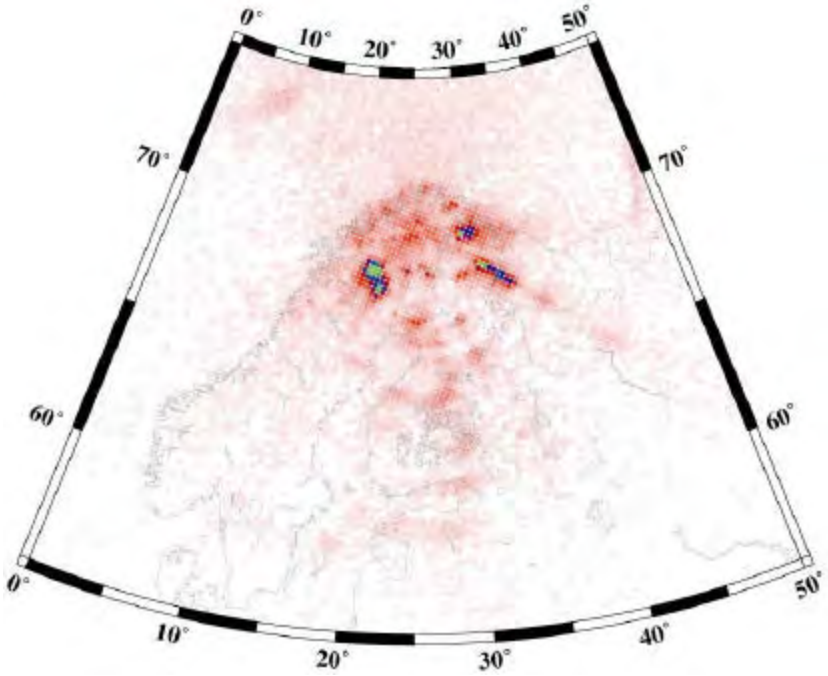

Figure 3a. Event density map generated from the ARCES automatic bulletin. This map clearly shows the major mines of northern Fennoscandia (especially two mines in Sweden), and the mines of the Kola Peninsula.

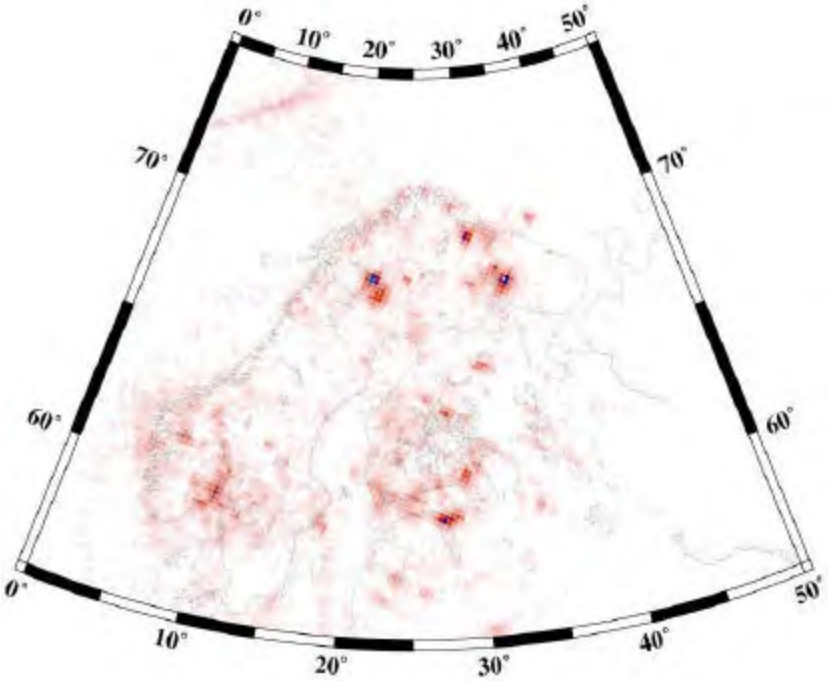

Figure 3b. Event density map developed from the NORSAR analyst-reviewed bulletin for the Fennoscandian array network. Major mining districts throughout Fennoscandia and Russia are much clearer in this map, because analyst review and redundant network observations eliminate artifacts that appear in the previous figure. Natural seismicity is apparent along the Arctic ridge and along the west coast of Norway. A cluster of events around the Kursk disaster site appears north of the Kola Peninsula.

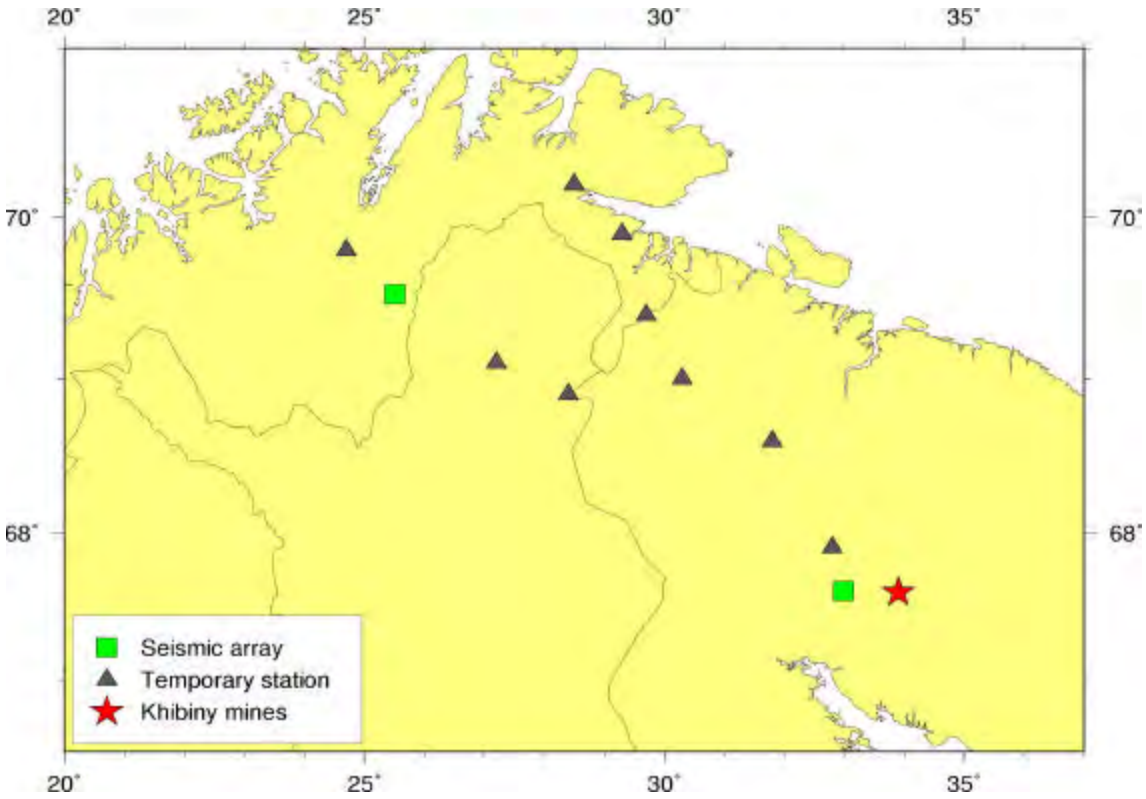

Figure 4. Approximate map of station sites for the year-long line deployment between the Khibiny mines and ARCES. A perfect line is not possible because of logistical, maintenance and access considerations.

ALGORITHMS FOR REGIONAL STRUCTURE – PROGRESS AND APPLICATION

Robert B. Herrmann,[1] Charles J. Ammon, [2] Kiehwa Lee,[3] Hyun-Jae Yoo[3]

Saint Louis University,[1] Pennsylvania State University,[2] Seoul National University[3]

Sponsored by Defense Threat Reduction Agency

Contract No. DTRA01-00-C-0214

ABSTRACT

Significant progress has been made in the development and documentation of standardized algorithms for analysis of regional Earth structure. *Computer Programs in Seismology – 3.15* was released in February 2002 to the research community. This distribution includes the new program suites **surf96**, **rftn96** and **joint96** for determining crustal structure from the inversion of surface-wave dispersion and/or teleseismic P-wave receiver functions. The programs have been applied to regional data sets in eastern Turkey and in the Republic of Korea.

Receiver functions were determined at all current broadband station locations in Korea except for the Incorporated Research Institutions for Seismology (IRIS) INCN and the KSAR stations. The time domain deconvolution tool of Ligorria and Ammon (1999) provides stable, causal and consistent receiver functions for inversion. Except for the stations on two islands, the receiver functions are very similar, attesting to the uniformity of the crust on the southern part of the Korean peninsula. The receiver functions require a uniform velocity model for the crust with a sharp, within resolution, crust-mantle transition. A test of the new programs **rftn96** and **joint96** was made using the data set at the Seoul National University station – the initial inversions highlight the non-uniqueness of receiver function inversion unless *a priori* crustal model information or other independent data, such as surface-wave dispersion, are introduced.

Computer Programs in Seismology – 3.16 will be released at the 24th Seismic Research Review, September 2002. This version includes the following: wavenumber integration synthetics for transversely isotropic media, newly adapted programs for regional focal mechanism determination using surface wave radiation patterns and broadband waveforms. The programs can be used for determination of local structure and seismic event source parameters. An outline of new codes to be developed with continuing support will also be presented.

OBJECTIVE

The objective of this effort is to develop regional scale crustal models that are precise enough to be used for waveform inversion of regional signals to characterize the source. Waveform inversion, even at low frequencies, requires an earth model specification much more detailed than required for location. Waveform inversion is important since this is the only means of calibrating local magnitude scales to teleseismic observations. To accomplish this task software development is tied to the analysis of real data sets.

RESEARCH ACCOMPLISHED

R. Herrmann visited Seoul National University (SNU) in 2000 (5 days), 2001 (2 weeks) and 2002 (2 weeks) for the purpose of establishing a cooperative relationship that permits access to both Korean Meteorological Administration (KMA) and Korean Institute of Geology and Mining (KIGAM) broadband data. The P.I. works with the SNU graduate students in the analysis of data. This year's trip led to the acquisition of a large data set for receiver function determination.

The geology of Korea consists largely of Pre-Cambrian rocks, such as granite gneisses and other metamorphics. Two separate blocks of Paleozoic strata are found in South and North Korea. Korea is stable land with no active volcanoes and rare earthquake shocks, although the islands of Ullungdo (station ULL) and Chejudo (stations SOG SGP) are of volcanic origin. The Pre-Cambrian basement of the peninsula is tectonically related to that of Manchuria and China. The generalized geology map of the peninsula is shown in Figure 1.

KMA has recently installed a modern digital seismic network in South Korea. This network consists of broadband STS-2, short period SS-1 and Episensor accelerometer sensors. The broadband station locations are given in Table 1 and their locations are plotted in Figure 2. Some stations were moved in 2001 to avoid overlap with KIGAM stations, to provide more even geographical coverage and to occupy quieter sites.

Teleseismic data were collected from earthquakes in three regions: India-Pakistan-Afghanistan, Indonesia-Philippines, and the Aleutians. Preprocessing consisted of windowing, removing the linear trend, rotation of horizontals and highpass filtering at 0.02 Hz. P-wave receiver functions were computed using the Ligorria and Ammon (1999) time domain deconvolution using the program saciterd. A total of 1127 receiver functions were obtained for the 25-station network. One aspect of the Ligorria and Ammon (1999) algorithm is the computation of a goodness of fit parameter that indicates the fit of the predicted radial component to the observed as a percentage. Receiver functions were computed for each event using Gaussian filter parameters of 0.5, 1.0 and 2.5, corresponding to low pass corners of 0.15, 0.30 and 0.75 Hz, respectively.

To compare the individual station receiver functions, a stack of the better receiver functions was made for each station. The selection criterion was that the goodness of fit be 80% and 95% for Gaussian filter parameters 1.0 and 2.5. This sieved data set is used for receiver function inversion for each station. The stack was made irrespective of the ray parameter since it varied little among the observations. Figure 3 presents the stacked receiver functions for each of the two filters. The station code is given to the left and the number of qualified waveforms used in the stack is indicated to the right of each stack. The waveforms window is [-5, 25] seconds with respect to the direct-P contribution.

The receiver functions of each station are very similar except ULL, SOG and SGP, which are on islands. To focus on the slight differences in the receiver function at each station, the stacked similar receiver functions are superimposed in Figure 4 for each filter parameter. The rainbow color scheme is alphabetical with BRD - red and ULJ - blue. Slight difference seen in the amplitude of the first peak may indicate local variations in upper crustal velocities. The slight shift in the second peak may indicate slight differences in local crustal thickness. Both causes are enhanced in the third peak halfway down the trace.

Although the seismicity levels in South Korea are low, some efforts have been made to define the crustal velocity structure using existing seismic network data. Kim *et al* (1998), Kim and Lee (2001) and Yoo and Lee (2001) used these models as a starting point for their receiver function studies at the broadband stations sites in Korea. Except for the ULL, SOG and SGP stations, the models are similar, as they should be because of the similarity of receiver functions seen in Figures 3 and 4. In a different study, Song and Lee (2001) used the program VELEST with 178 P-wave first arrivals from 29 local earthquakes recorded from 1991-1998 by the KMA analog-telemetry network. The

latter study was hampered by the small number of observations but concluded that the average crustal P-wave velocity in the southern part of the peninsula is 6.3 km/s, the upper mantle P-wave velocity is near 7.9 km/s and that the crustal thickness is about 33 km.

To test the new inversion code and the capability of receiver functions to uniquely define the crustal velocity structure, the initial focus was on the recordings at SNU (Seoul National University). Receiver functions from 31 events were inverted under the assumption that nothing was known about the crust. The initial model consisted of a layered halfspace with a layer thickness of 2.5 km, P- and S-wave velocities of 8.0 and 4.7 km/s, respectively. The inversion applied a differential smoothness constraint and ten iterations were performed. The inversion constraints were that the halfspace velocity and the Poisson ratio in each layer were fixed. Next the same inversion was performed using the stacked receiver functions for the station and the same final model resulted. As expected because of the detail permitted in the model, the receiver function fits of the stacked data were perfect. Figure 5 presents the results of this inversion.

Next the receiver function data were combined with the Stevens (1999) Rayleigh-wave group velocity estimates for the peninsula and inverted jointly using the new program **joint96**. The resultant model and comparison of the model predictions to the observations are presented in Figures 6 and 7. The receiver-function and joint inversions share a similar sharp discontinuity that defines the Moho because the receiver functions require this feature. The receiver function model has higher crustal velocities (Figure 8) than the joint inversion model.

The program **timmod96 was** used to compare predicted P-wave first-arrival times for a surface focus event for the Song and Lee (2001), **rftn96** and **joint96** models (Figure 9). The joint inversion model is similar to the VELEST model except for the 0.5 sec delay, which is caused by the lower velocities in the upper crust. The upper crust velocities are controlled by the Stevens (1999) dispersion estimates and seem low for an essentially exposed arcane structure. The shallow part of the VELEST model is not well controlled either because of the lack of data at short distances from shallow foci events. These time delays are crucial since then will control the apparent depths of shallow events.

CONCLUSIONS AND RECOMMENDATIONS

A significant receiver function data set is now available. The inversion programs work, although more testing is required to document an effective methodology for inversion. Future work by SNU graduate students will use the regional earthquake arrival time for 2000-2002 in another application of VELEST for joint hypocenter and 1-D crustal velocity model determination since sufficient data should now exist from the broadband, short-period and accelerometer networks operated by KMA. Dispersion studies will focus on using teleseismic surface wave recordings to define Rayleigh- and Love-wave phase velocity dispersion as well as local Rg waves recorded at short distances. The recurrence rate of magnitude 4 - 5 events in Korea indicate that recording for waveform inversion for source parameters will be available in the next few years. Continued work on the Korean broadband data will permit a robust specification of crustal structure.

ACKNOWLEDGEMENTS

The authors wish to thank the Korean Meteorological Administration and the Korean Institute for Geology and Mining for the use of their broadband seismic data.

REFERENCES

Ammon, C. J., G. Randall and G. Zandt (1990). On the nonuniqueness of receiver function inversions, *J. Geophys. Res.*, 95, No. B10, 15303-15318.

Julia, J., C. J. Ammon, R. B. Herrmann and A. M. Correig (2000). Joint inversion of receiver function and surface wave dispersion observations, *Geophys. J. Int.*, 143, 1-19.

Kim, S. G., S. K. Lee, M. S. Jun and I. B. Kang (1998). Crustal structure of the Korean Peninsula from broadband teleseismic records using receiver function, *Econ. Environ. Geol.*, 31, No. 1, 21-29.

Kim. S. G., and S. K. Lee (2001). Moho receiver function methods studies beneath the broadband stations using receiver functions in South Korea, Korea *Society of Hazard Mitigation,* 6, No. 1. 139-155.

Ligorria, J. P., and C. J. Ammon (1999). Iterative deconvolution of teleseismic seismograms and receiver function estimation, *Bull. Seism. Soc. Am.,* 89, 1395-1400.

Song, S., and K. Lee (2001). Crustal structure of the Korean peninsula by travel time inversion of local earthquakes, *J. Korean Geophysical Society*, 4, No. 1, 21-33.

Stevens, J. L. (2001). Global Rayleigh wave dispersion article, *PAGEOPH*, in press.

Yoo, H., and K. Lee (2001). Crustal structure under the Taejon (TJN) station by receiver function methods, *J. Korean Geophysical Society*, 4, No. 1, 35-46.

Table 1. Broadband station locations in Republic of Korea.

Name	Latitude	Longitude	Elevation	Comment
TJN	36.3805	127.3615	161	KIGAM
SNU	37.4509	126.9566	161	KIGAM
GKP	35.8863	128.6083	46.51	KIGAM
BGD	34.1569	126.5575	5.7	KIGAM
KSA	38.5953	128.3512		KIGAM
HDB	35.7307	129.4012	Borehole	KIGAM
PUS	35.1010	129.0339	69.23	KMA Closed and moved to BUS in 2001
TAG	35.8750	128.6194	57.64	KMA Closed and moved to DAG in 2001
SOG	33.2390	126.5671	50.47	KMA Closed and moved to SGP in 2001
CHU	37.8904	127.7308	120.00	KMA Closed and moved to CHC in 2001
TEJ	36.3681	127.3712	68.28	KMA Closed and moved to CHJ in 2001
SEO	37.4879	126.9188	33.51	KMA
SES	36.7893	126.4531	99.1	KMA
KWJ	35.1599	126.9910	213.0	KMA
KAN	37.7425	128.8893	25.91	KMA Closed and moved to DGY in 2001
ULJ	36.7021	129.4084	77.1	KMA
ULL	37.4738	130.9008	218	KMA
BUS	35.2487	129.1125	91	
DAG	35.7685	128.8970	262	
CHC	37.7775	127.8145	245	
CHJ	36.8730	127.9748	227	
DGY	37.6904	128.6742	791	
SGP	33.2587	126.4994	222	
BRD	37.9677	124.6303	169	New 2002

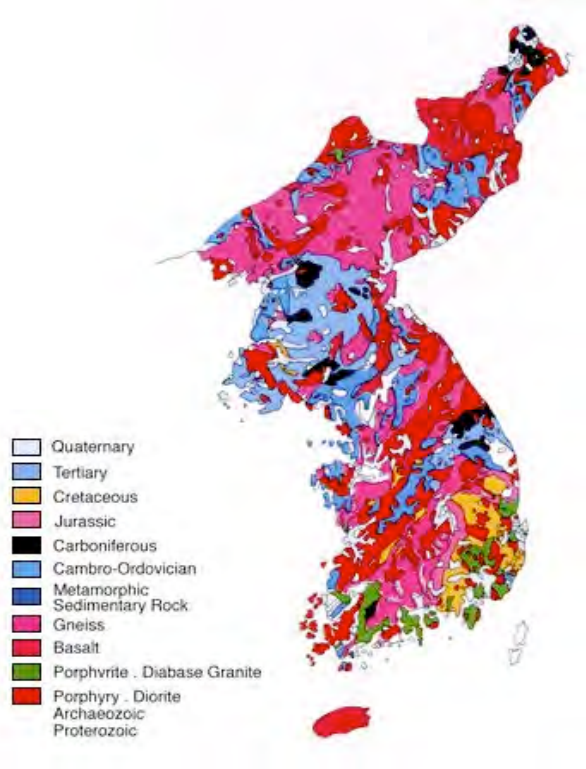

Figure 1. Geology of the Korean Peninsula http://cinema.sangji.ac.kr/WINDOW/window/win00000.htm

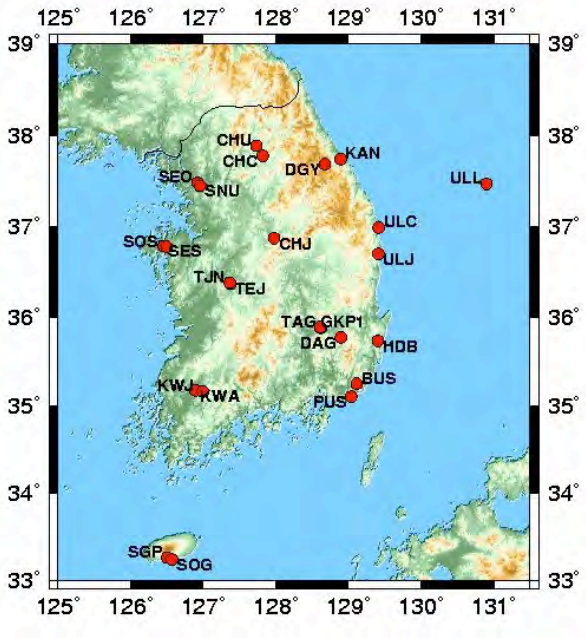

Figure 2. Location of broadband stations used in surface wave dispersion receiver function analysis of the Korean Peninsula.

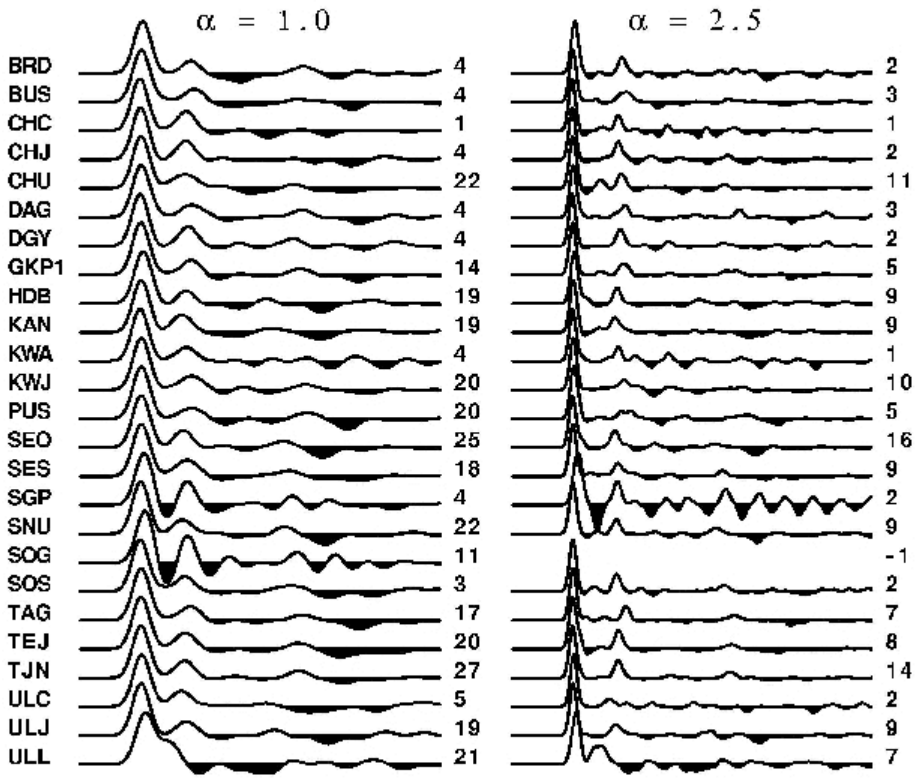

Figure 3. Stacked receiver functions all stations listed for each of the two Gaussian filter parameters. Traces begin 5 seconds before and 25 seconds after the direct P. The number to the right of each trace is the number of traces used in the stack.

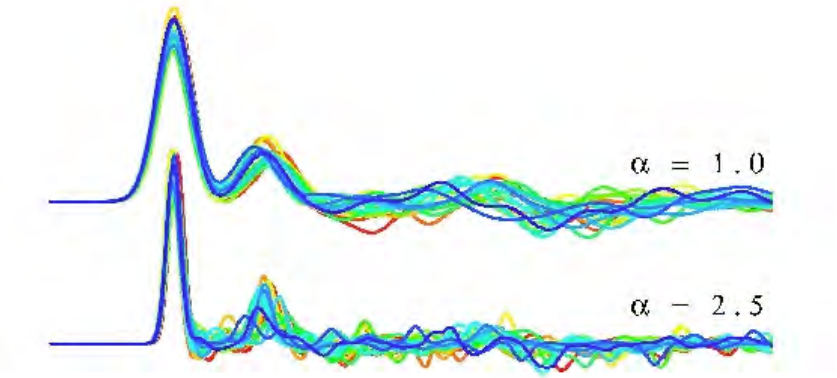

Figure 4. Overlay of stacked receiver functions for all stations except ULL, SOG and SGP. The color rainbow represents stations alphabetically with BRD 9red) and ULJ (blue). The time window is as above.

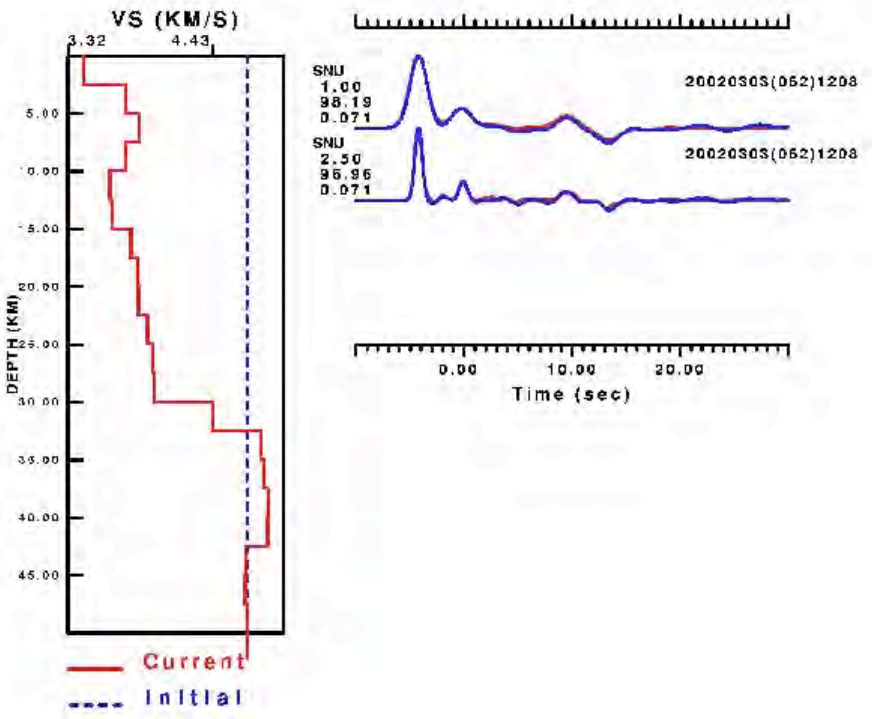

Figure 5. Inversion results using program rftn96 and the stacked receiver function data at SNU. The initial model is a uniform halfspace (blue). The final model is shown in red. The halfspace velocity was fixed. The model explains 97% of the observed receiver function.

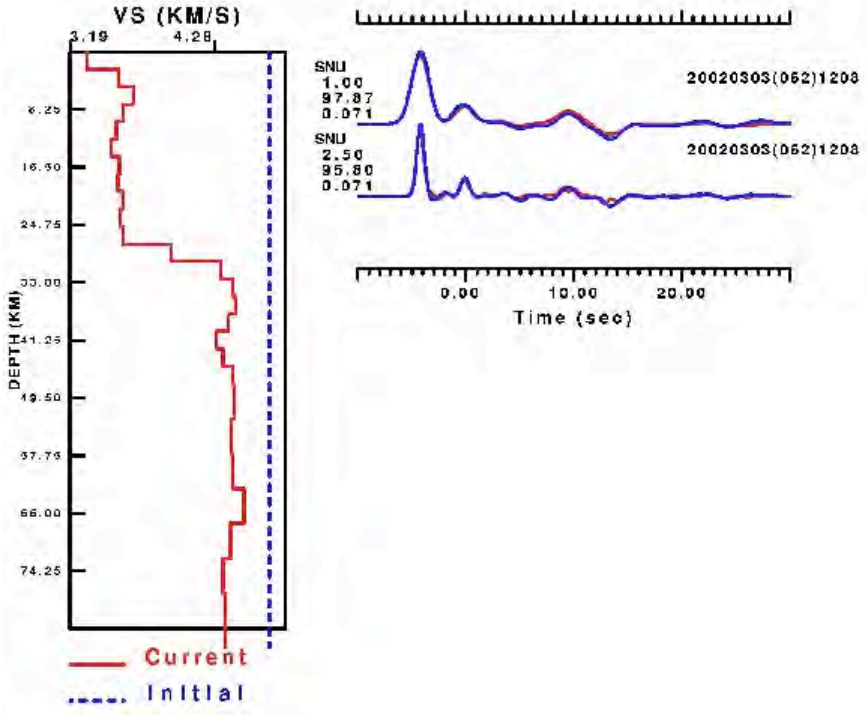

Figure 6. Inversion results using program joint96 with the same stacked receiver functions. The dispersion data are shown in Figure 7. The halfspace constraint used is weaker than above in Figure 6.

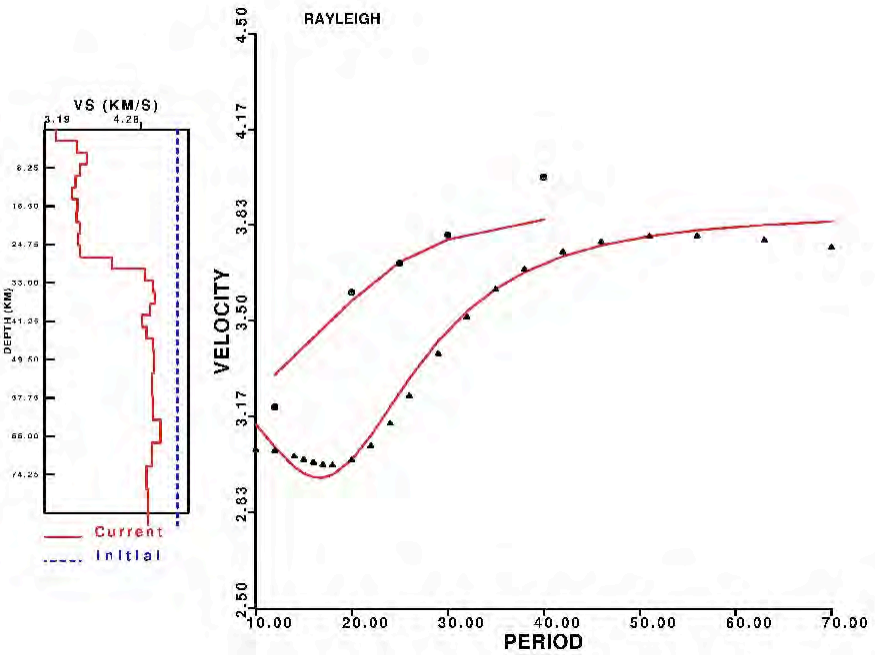

Figure 7. Rayleigh-wave groupd velocity dispersion data (Steven, 1999) and fit used with joint96. The phase velocity data are from a p-tau stack of selected broadband recordings of teleseismic surface waves.

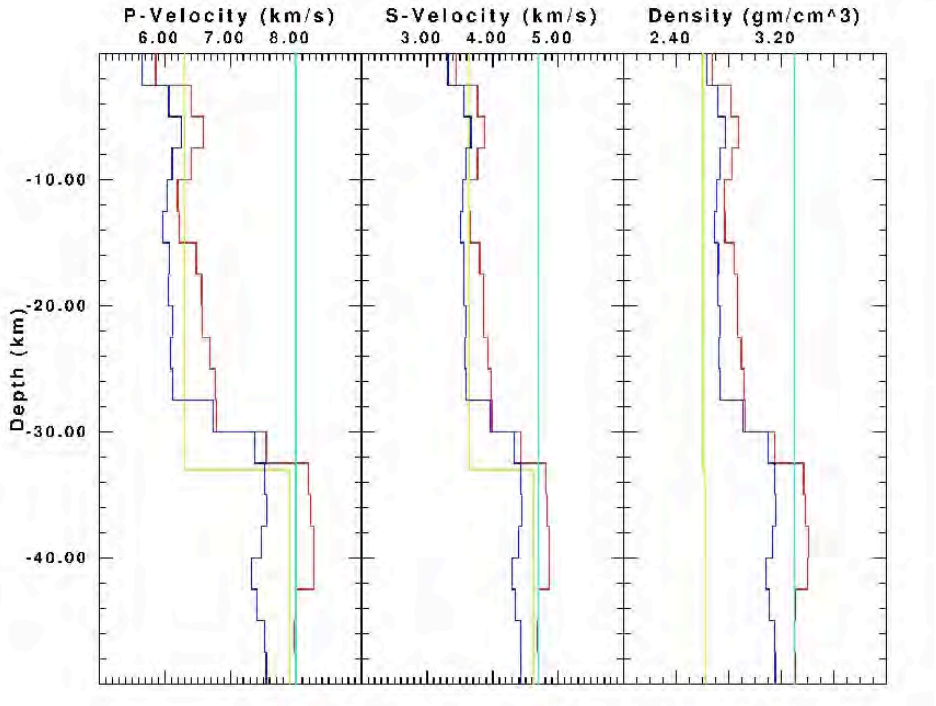

Figure 8. Overlay of models. The initial halfspace (aqua), VELEST of Song and Lee, 2001, model (yellow), the receiver function only (red) and joint inversion (blue) models are shown. The rftn96 and joint96 inversions share the Moho discontinuity at 30 km but differ in an absolute sense because of the effect of the dispersion data.

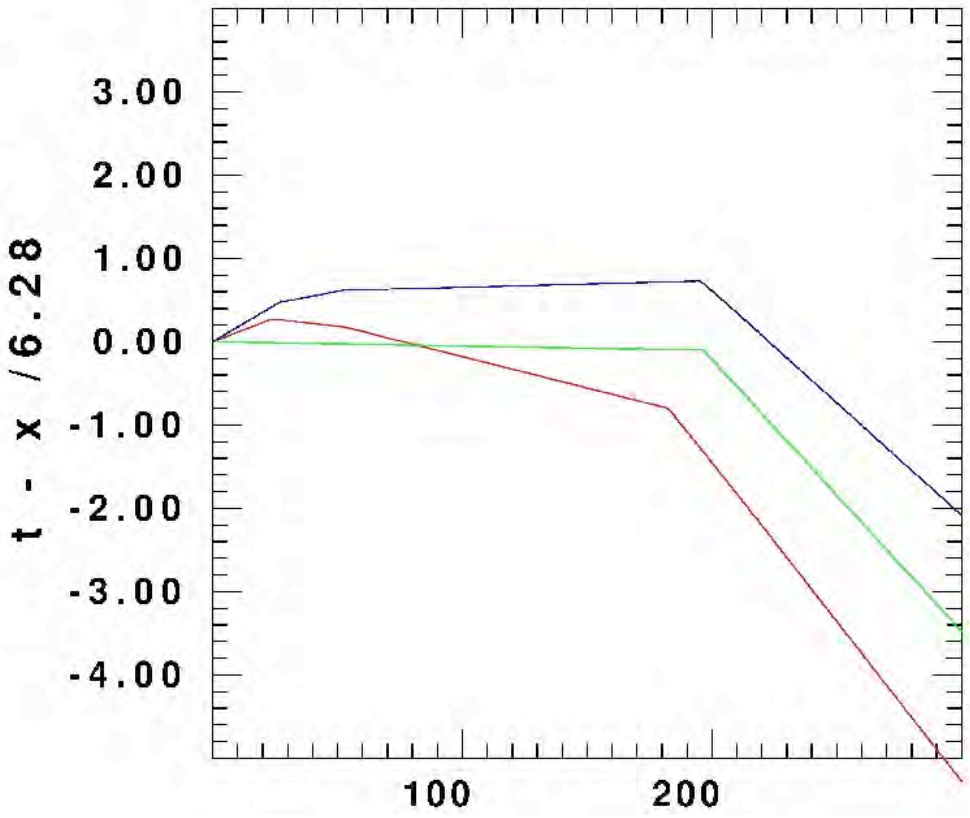

Figure 9. Comparison of predicted P-wave first arrival times for surface-focus and surface-receivers for the Song and Lee, 2001 VELEST (green), rftn96 receiver function only (red) and joint96 joint inversion models. The addition of surface wave dispersion applies a strong constraint on the receiver function inversion.

SHEAR-WAVE Q AND ITS FREQUENCY DEPENDENCE IN THE CRUST OF SOUTHEASTERN ASIA FROM SURFACE-WAVE ATTENUATION

Alemayehu L. Jemberie and Brian J. Mitchell

Saint Louis University

Sponsored by Defense Threat Reduction Agency

Contract No. DTRA-01-00-C-0213

ABSTRACT

Models of shear-wave Q (Q_μ) have been obtained for the crust over a broad region of southeastern Asia, including China and portions of surrounding countries, using a single-station multi-mode method. Event and station coverage is sufficient to allow the mapping of Q_μ variations for three depth ranges in the crust and, in some sub-regions, the uppermost mantle. In layer 1 (10 km thick) Q_μ is highest in southeastern China, where it attains values of about 250. These values are consistent with the relatively high values of Lg coda Q found in earlier work. Q_μ decreases from east to west and reaches a minimum of about 40 in parts of western China, including part of the Tibetan Plateau. Further west, Q_μ increases in a region that comprises the Tarim Basin and parts of southwestern China. Layer 2 (20 km thick) exhibits highest values of Q_μ (140) in eastern China and lowest values (about 60) in the eastern portion of the Tibetan Plateau and in southernmost central China (about 80). A band of relatively high values (with a minimum of about 140) lies between those two regions and extends northward to Mongolia. Layer 3 (30 km thick) contains a concentrated zone of high Q values (up to 200) in north-central China and another (with values up to 160) in northwestern China. They are separated by a north-south band of lower Q_μ values (about 100).

We have computed Q at 1 Hz (Q_o) and the value of frequency dependence (η) that would be predicted by shear-wave models in various sub-regions of southeastern Asia and compared them to previously measured values of Lg coda Q and their frequency dependence in the same regions. For most cases, in order to match predicted and observed values, shear-wave frequency dependence values between 0.0 and 0.6 are required. For most sub-regions adequate agreement can be achieved by assuming the η is constant with depth, but a few cases suggest a depth-variable η.

OBJECTIVE

Q values for seismic shear waves (Q_μ) that propagate in the crust are known to vary laterally by as much as an order of magnitude or more (Mitchell, 1995) and to vary with frequency at least at frequencies near 1 Hz and higher (Mitchell, 1980). Differences in Q_μ will produce path-dependent amplitudes and waveforms for regional phases. If the Q variations are large enough and are not corrected for, magnitude and moment estimates for regional events could be greatly in error. If Q is very low in a region, small signals may be lost in noise and events that generated them could go undetected when epicentral paths are too great. Moreover, if depth variations of Q_μ differ from those assumed to occur, discrimination studies that use amplitude ratios for regional phases that travel predominantly at different depths could give incorrect results.

Our objectives are (1) to use seismic surface waves to determine depth-dependent regional variations of Q_μ over distances that are as small as possible, and (2) to estimate frequency dependence values (ζ) for Q_μ that explain the attenuation observed for surface waves at intermediate periods (about 5-50s) and values of Q_o (Q_{Lg} at 1 Hz) and η (the frequency dependence of Q_{Lg} at 1 Hz). This information will allow us to extend our results on regional variations of Q_μ using surface waves to frequencies that are important for regional phases.

RESEARCH ACCOMPLISHED

The method used in our research requires Rayleigh waves that have traveled over regional distances between seismic events and stations and that have not been greatly affected by major lateral variations in velocity structure. We investigated the spectra for all events that occurred in our region of study between 1990 and 1999 and found 34 that provided useful spectra for our research. They were recorded at one or more of the 13 seismic stations in our region of study and had magnitudes between 4.9 and 6.2. Figure 1 shows locations for events and stations used in the study as well as paths between them. The paths range in distance between 300 and 3000 km and cover a region that extends between about 25 and 55 degrees north latitude and between about 60 and 130 degrees east longitude.

Our method matches theoretically predicted fundamental-mode and higher-mode Rayleigh-wave spectra computed for sources with known depths, moments, and focal mechanism solutions with the corresponding observed spectra. The theoretical spectral were computed using the equations of Anderson *et al* (1965). We used fundamental mode spectra at periods between about 5 and 50 s and higher mode spectra, consisting of super-positions of many individual higher modes, at periods between about 3 and 10 s. We assumed an initial Q model and adjusted it until a good fit was achieved between theoretical and observed spectra. We initially tried to use published focal depths and moments in our computations, but we sometimes had to adjust the values of those parameters to obtain a good fit. We started our spectral fitting process by varying values of Q_μ in layer 1, which we took to be 10 km thick, and holding Q_μ at greater depths at high values. We found a value of Q_μ that provided the best possible agreement in the short-period portion of the theoretical and observed spectra. We then held Q_μ in layer 1 at the derived value and adjusted Q_μ in layer 2 to obtain the best spectral fit at longer periods for the fundamental Rayleigh mode. Fixing Q_μ in both layers 1 and 2, we then determined Q_μ in layer 3 in the same way.

Figure 2 exhibits comparisons between observed and theoretical for nine paths. About half of them show that theoretical and observed spectra agree well for the fundamental mode over the entire period range but for others the observed spectra are higher than those observed at periods greater than 20 or 30 s. This can be attributed to low signal/noise ratios at the longer periods. In these nine examples Q_μ in layer 1 varies between 55 and 150, Q_μ in layer 2 varies between 40 and 120, and Q_μ in layer 3 varies between 80 and 200. Figure 3 shows the models that were obtained by the spectral fits for the same nine sets of spectra. The standard deviations for the Q_μ values in each layer were obtained using the method described by Cheng and Mitchell (1981). The method adapts the equation of Anderson *et al* (1965) to error estimation using rms misfits between theoretical and observed spectra. The models exhibit wide variations in Q_μ values in all three layers and in the nature of Q_μ depth variation; Q_μ sometimes increases and sometimes decreases with depth.

Figures 4-6 map Q_μ variation for the three depth ranges chosen for our study. For layer 1 the highest values (as high as 240) correspond to a stable region that is termed the Southeast China Block and lowest values (40-60) correspond to the Tibetan Plateau and adjacent regions, as well as to a region near the Baikal Rift. A second region of relatively high Q_μ values lies in western Mongolia and southernmost Siberia at longitudes between about 90^o and 100^o. There are three centers of low Q_μ in layer 2, one in the southern portion of the Tibetan Plateau, one centered in northern

Myanmar and southernmost China, and one in the region of the Baikal Rift. High values extend from central China to southeastern-most Siberia. Since error bars for many of our Q_μ models indicate that large uncertainties characterize layer 3, we consider only broad-scale variations to be significant. Relatively high values underlie Mongolia and the Baikal Rift, and small regions of southern China, and western-most China.

Almost all mechanisms that explain variations of Q_μ in the Earth predict that Q_μ should vary with frequency (e.g. Jackson and Anderson, 1970). This frequency dependence has been observed in laboratory experiments and has been required to simultaneously explain measured Q_μ values for free oscillations of the Earth and for 1-Hz body waves. It is also required to simultaneously explain the attenuation of Rayleigh waves at intermediate periods (5-100s) and Lg waves at 1 Hz. It is important to determine frequency dependence values for Q_μ for frequency ranges that are important in monitoring the Comprehensive Nuclear-Test-Ban treaty. If this can be determined we will be able to extrapolate values of Q determined from surface waves to the higher frequencies that characterize regional phases at shorter distances.

As a first step toward determining the frequency dependence of Q_μ and how it may vary with depth we wave developed a method by which the frequency dependence can be obtained for our crustal models using a combined forward modeling/formal inversion procedure. It is a variation of a previously developed procedure (Mitchell and Xie, 1994) and obtains a frequency dependence value that reconciles Q_μ values at 1 Hz with those obtained at surface-wave periods (5-50s). The process proceeds as follows:

1. Compute attenuation coefficients for the fundamental Rayleigh mode, as a function of period, for the three-layer Q_μ model and corresponding velocity model of interest.

2. Assume a depth distribution for the frequency dependence, ζ, of Q_μ and determine the attenuation coefficients obtained in step 1 to obtain a Q_μ model.

3. Calculate the fundamental-mode Rayleigh-wave attenuation coefficient values which are predicted by the model from step 2 and compare them with the values of step 1. An example appears in Figure 7. If they agree within reasonable uncertainties go to step 4; if not, try a new distribution of ζ.

4. Compute synthetic Lg seismograms at several distances from a seismic source using the appropriate velocity and Q_μ models from step 2.

5. Apply the stacked spectral ratio (SSR) method of Xie and Nuttli (1998) to the set of synthetic seismograms in step 4 to obtain values of Q_o and η predicted by the derived Q_μ model and compare them with measured values from maps of Eurasia (Mitchell *et al*, 1997).

6. If necessary, change the depth distribution of ζ in step 2 and go through the procedure again.

7. From the results of step 5, compute Q_μ at frequencies of interest (1 Hz for the present study).

Four examples of results using this procedure appear in Figure 8. The solid lines in the left-hand side of each pair of boxes are frequency-independent Q_μ models obtained from spectral matching and the dashed lines show models at 1Hz using our procedure to obtain Q_μ frequency dependence. The boxes on the right-hand side of each pair show the assumed distributions of ζ with depth. In all but one of the examples, a constant value of ζ produced acceptable results. Values of Qo and η predicted by the models for Lg attenuation at 1 Hz appear below each set of models. Note that, as shown by the model on the upper left of the figure, a model with frequency-independent Q_μ can still produce a frequency-dependent Q value for Lg if Q_μ increases rapidly at mid-crustal depths. This phenomenon was shown to occur in the crust of the Basin and Range province of the United States (Mitchell, 1991).

CONCLUSIONS AND RECOMMENDATIONS

Three-layer models of shear-wave Q (Q_μ) have been obtained for a broad portion of southeastern Asia. Layer 1 extends through the upper 10 km of the crust, layer 2 through the depth range 10-30 km, and layer 3 through

30-60 km. The models therefore include the uppermost mantle in some regions, but in the Tibetan Plateau correspond only to the crust. Values of Q_μ in layer 1, from a frequency-independent determination, vary between 55 and 150, are lowest in the Tibetan Plateau and highest in the Southeast China Block. A zone of relatively high Q_μ lies in western Mongolia and southern Siberia. In layer 2 Q_μ varies between 40 and 120 and contains three centers of low values, one in the southern part of the Tibetan Plateau, one centered in northern Myanmar and southernmost China, and one near the Baikal rift. High values extend through much of central and eastern China and southeastern Siberia. Only the broad-scale variation Q_μ are taken to be significant and vary between 80 and 200 with relatively high values underlying Mongolia and the Baikal Rift, and beneath small portions of southern and westernmost China.

Frequency-dependent models of Q_μ were obtained that explain both the observed attenuation of fundamental-mode Rayleigh waves and measured values of Lg coda Q. Variations of the frequency-dependence parameter (ζ) for Q_μ vary between 0.0 and 0.6. Both this Q_μ frequency dependence and the depth distribution of Q_μ values contribute to values of the frequency dependence (η) of Q_{Lg}.

ACKNOWLEDGEMENTS

Lianli Cong, now at Yunnan University, wrote the programs for plotting amplitude spectra and Robert Herrman developed the code for their computation.

REFERENCES

Anderson, D.L., A. Ben-Menahem and C.B. Archambeau (1965), Attenuation of seismic energy in the upper mantle, *J. Geophys. Res*., **70**, 1441-1448.

Chen, C.C., and B.J. Mitchell (1981), Crustal Q structure in the United States from multi-mode surface waves, *Bull. Seism. Soc. Am.*, **71**, 161-181.

Cong, L., and B.J. Mitchell (1998), Seismic velocity and Q structure of the Middle Eastern crust and upper mantle from surface-wave dispersion and attenuation, *Pure App. Geophys*., **153**, 503-538.

Jackson, D.D., and D.L. Anderson (1970), Physical mechanisms for seismic wave attenuation, *Rev. Geophys.*, **8**, 1-63.

Mitchell, B.J. (1980), Frequency dependence of shear wave internal friction in the continental crust of eastern North America, *J. Geophys. Res.*, **85**, 5212-5218.

Mitchell, B.J. (1991), Frequency dependence of QLg and its relation to crustal anelasticity in the Basin and Range province, *Geophys. Res. Lttrs*., **18**, 621-624.

Mitchell, B.J. (1995), Anelastic structure and evolution of the continental crust and upper mantle from seismic surface wave attenuation, *Rev. Geophys*. **33**, 441-462.

Mitchell, B.J., Y. Pan, J. Xie and L. Cong (1997), Lg coda Q variation across Eurasia and its relation to crustal evolution, *J. Geophys. Res*., **102**, 22767-22779.

Xie, J., and O.W. Nuttli (1988), Interpretation of high-frequency coda at large distances: Stochastic modeling and method of inversion, *Geophys. J*., **95**, 579-595.

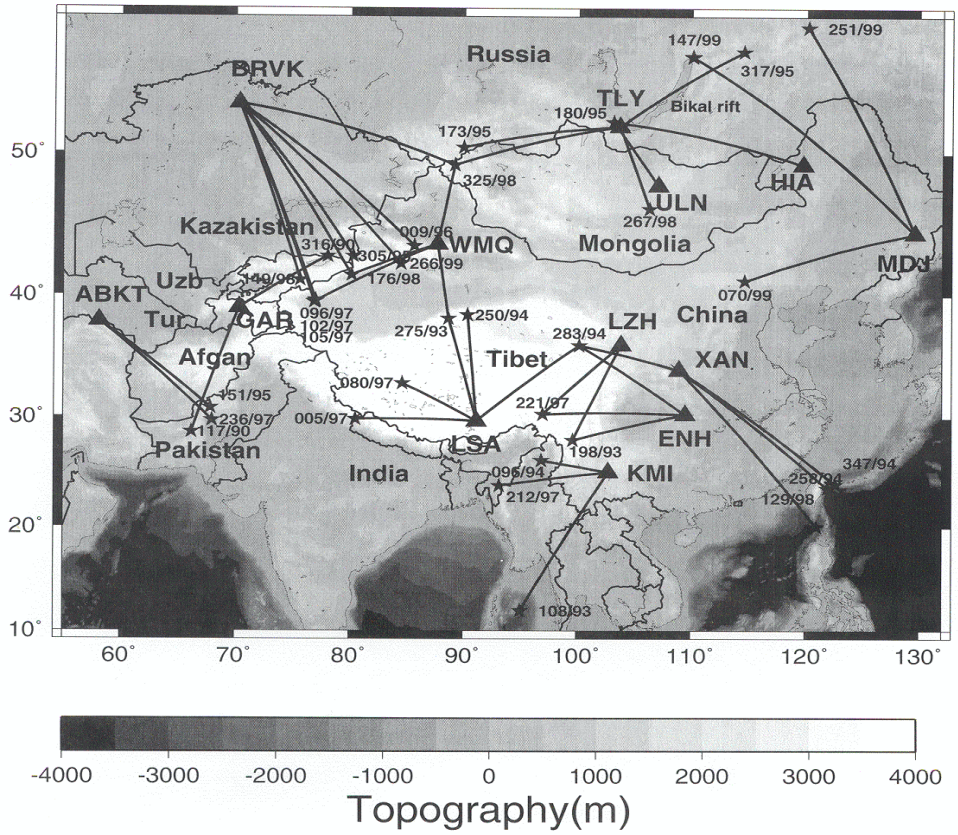

Figure 1. Map of southeastern Asia showing events (stars), stations (triangles), and paths between them.

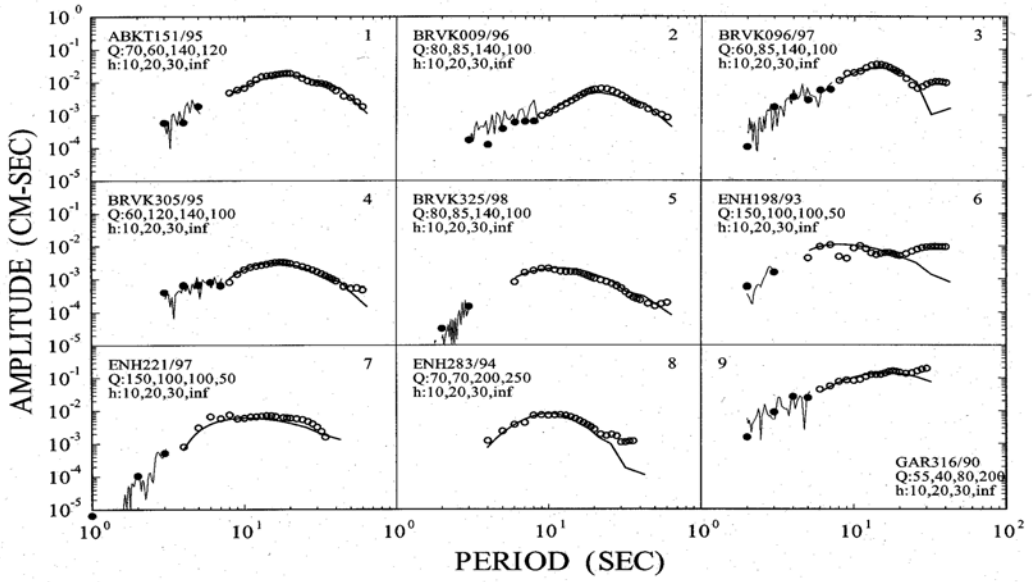

Figure 2. Comparison of theoretical and observed amplitude spectra for nine event-station paths. Open circles denote spectra for fundamental mode spectra and solid circles denote spectra for a superposition of higher modes. The notation in each box gives the station name and event date (in julian day), shear-wave Q values, for three layers and the underlying half-space, and the thicknesses of the layers.

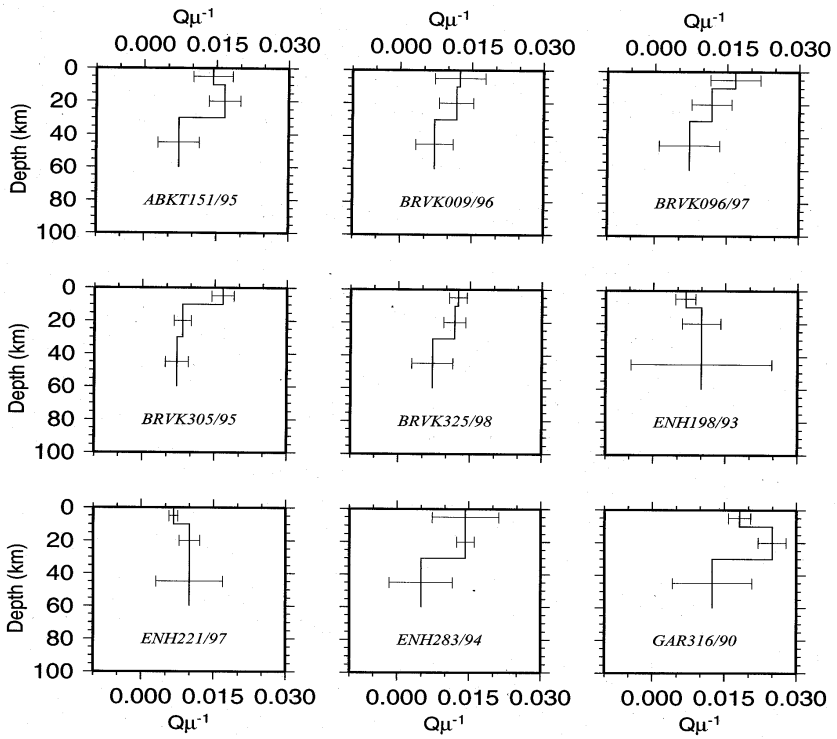

Figure 3. Three-layer models of shear-wave Q with error estimates derived from the spectral matching technique and the spectra of Figure 2.

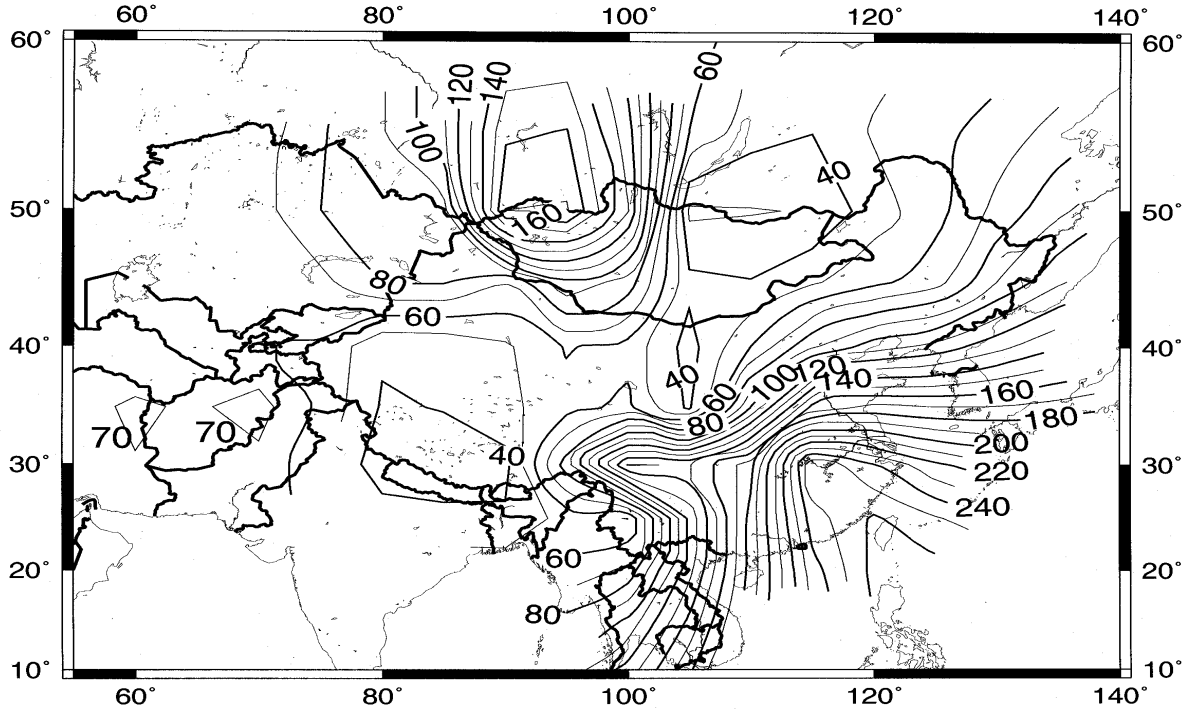

Figure 4. Map of shear-wave Q variations in layer 1 (10 km thick).

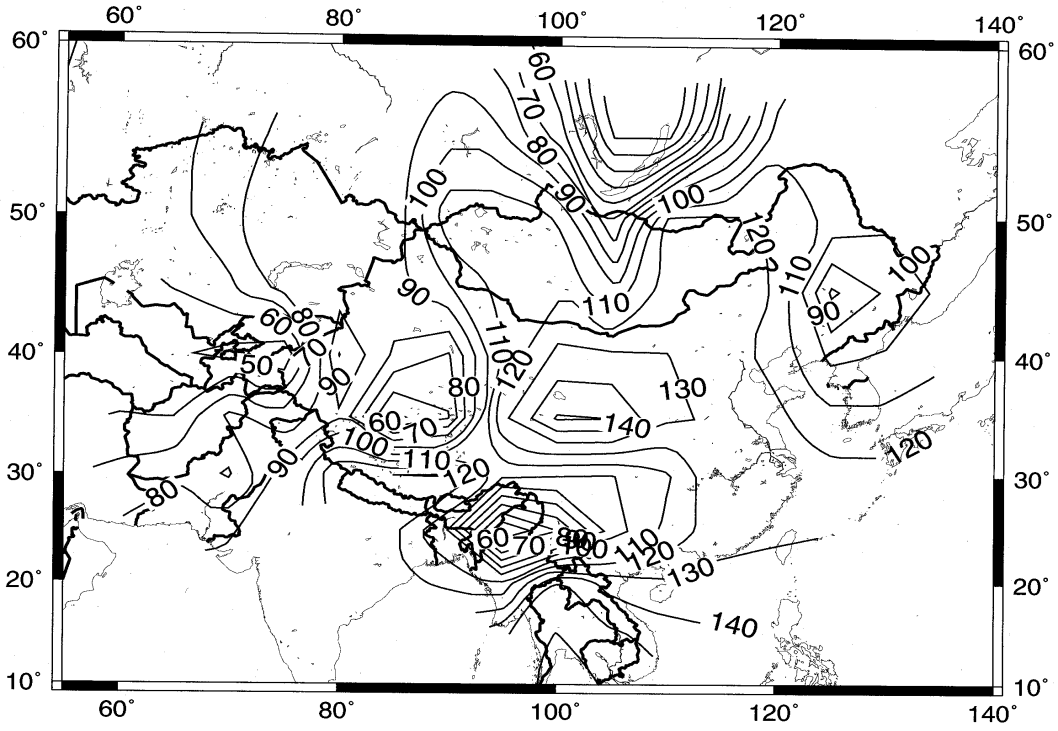

Figure 5. Map of shear-wave Q variations in layer 2 (20 km thick).

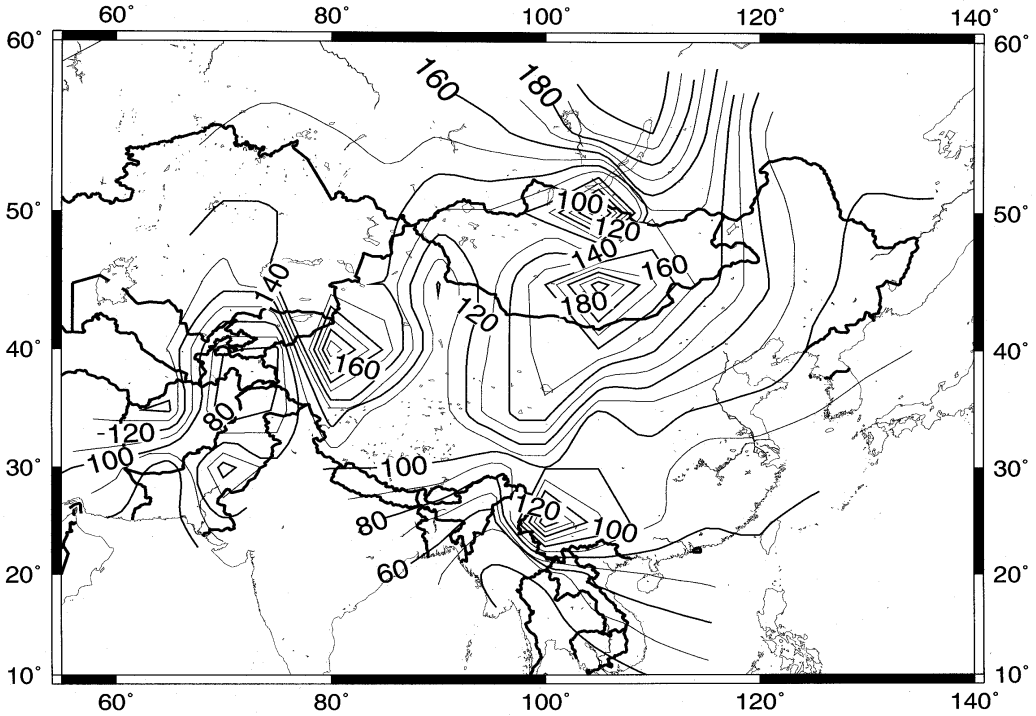

Figure 6. Map of shear-wave Q variations in layer 3 (30 km thick).

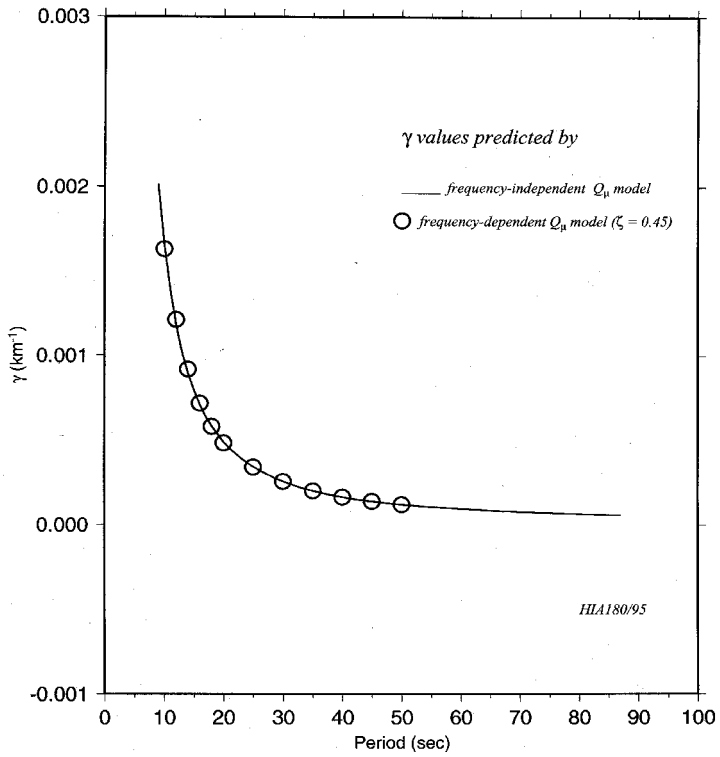

Figure 7. Comparison of Rayleigh-wave attenuation coefficients predicted by the three-layer frequency-independent model of shear-wave Q with a frequency-dependent model for spectra obtained at station HIA for the event of day 180 in 1995.

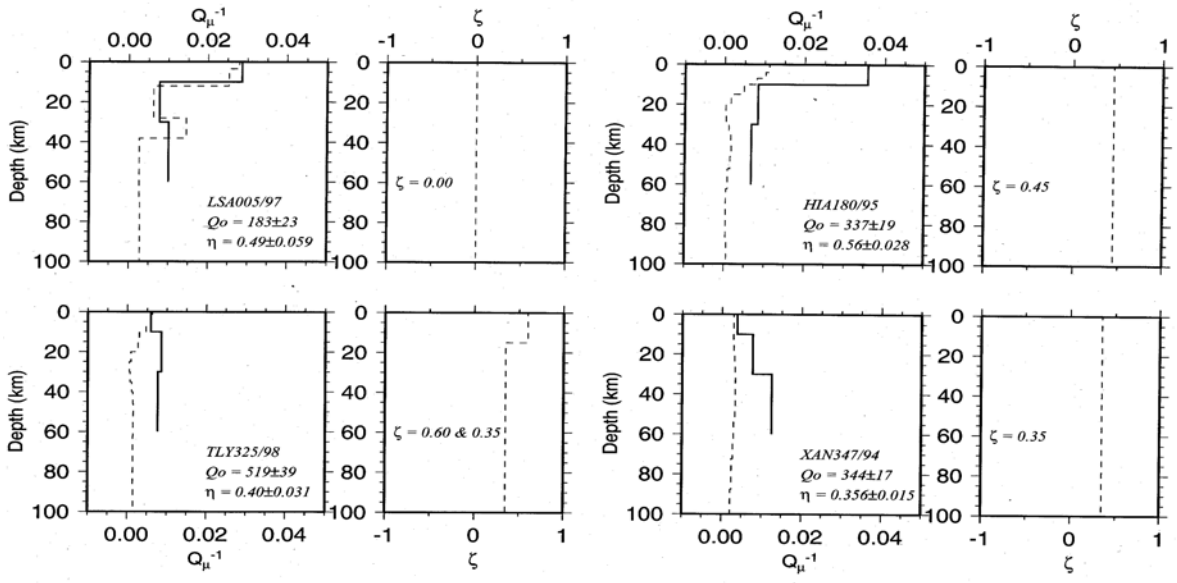

Figure 8. Comparison of frequency-independent (solid lines) and frequency-dependent (dashed lines) models of shear-wave Q for four cases obtained for the ς distribution plotted next to each pair of models. Values of Q_o and η for Q_{Lg} at 1 Hz predicted by the models are given for all cases.

THE BROADBAND SEISMIC EXPERIMENT IN YUNNAN, SOUTHWEST CHINA

Wenjie Jiao, Winston Chan, and Robert Wagner

Multimax, Inc.

Sponsored by Defense Threat Reduction Agency

Contract No. DTRA01-00-C-0081

ABSTRACT

Since August 2001, a broadband portable seismic network has been operating in Yunnan, southwest China, to collect seismic data for advanced studies on regional crustal and mantle structures, earthquake prediction, characteristics of wave propagation, and earthquake and explosion sources. The area of interest in southwest China is situated in a transitional tectonic region between the uplifted Tibetan plateau to the west and the Yangtze continental platform to the east. The region displays varying crustal thickness from 35 km to over 60 km with seismic activity strongly associated with the mapped active faults. The portable seismic network, consisting of nine stations equipped with the STS-2 seismometers and RefTek data loggers, and ten stations with the Chinese broadband instruments, is deployed in the region of 98°E-105°E, 21°N-29°N. There are also 23 permanent digital broadband seismic stations recording in the region. Yunnan has the strongest intra-plate seismic activities in China. Moreover, Yunnan is a very interesting area considering its position relative to several strong seismic zones in China, such as Tibet, Xinjiang, Sichuan, and northern China, as well as those in the rest of the world, like Burma, India-Pakistan, Tonga-Fiji, Japan, and the west coast of South and North America. So far, we have recorded several moderate (M=4.5-6) local earthquakes, including one located only 100 km north from the auxiliary International Monitoring System (IMS) station KMI. These moderate earthquakes are well surveyed by the provincial Yunnan Seismological Bureau and yield high-quality ground truth information. A large amount of local events are routinely recorded, among which, many are believed to be industrial explosions. Moderate to large earthquakes in other parts of China, as well as large events worldwide, are also routinely recorded, including

- the November 14, 2001, Ms=8.0 Qinghai earthquake,
- the December 18, 2001, Ms=7.3 Taiwan earthquake,
- the September 11, 2001, Ms=6.4 Iranian earthquake,
- the October 12, 2001, Ms=7.3 Mariana earthquake,
- the January 2, 2002, Ms=7.6 Vanuatu Islands earthquake, and
- the March 3, 2002 Ms=7.2 Hindu-Kush earthquake.

The waveforms recorded in this project are being processed and analyzed to provide very useful information on the source, path and site terms for regional seismic studies.

OBJECTIVE

The major purpose of this project is to collect fundamental ground truth data for advanced studies on regional crustal and mantle structures, earthquake prediction, and regional characteristics of wave propagation and seismic sources in Yunnan, China, through deploying a broadband portable seismic network there. The area of interest in southwest China is situated in an evolving tectonic region transitioning between the uplifted Tibetan plateau to the west and the Yangtze continental platform to the east. The region displays varying crustal thickness from 35 km to over 60 km with seismic activity strongly associated with the mapped active faults. Figure 1 shows the topography of the Yunnan province and the layout of our broadband network. The red triangles are STS-2 seismometers from the US, while the red circles are Chinese broadband instruments (the long-period corner at 20s) from our Chinese collaborators. Please notice that we modified the distribution of the stations a little from the original pattern that was reported last year in order to provide better coverage of more interesting areas with respect to tectonics and ground truth sources. Yunnan has the strongest intra-plate seismic activities in China. There are several strong seismic zones in its surrounding areas, such as Tibet, Sichuan, Burma, and India. There is also an abundance of mining activities in this area. Moreover, the distances from the Yunnan area to many of the strongest seismic zones in the world, such as Tonga-Fiji, the west coast of North and South America, and the Japan-Kuril region (Figure 2), make the Yunnan area an ideal place top record various seismic phases for tectonic and structural studies. Therefore, the strong seismicity and the intensive mining activities in Yunnan and its surrounding areas, as well as its unique position relative to many strongest seismic zones in the world, provide the foundation for success of this deployment.

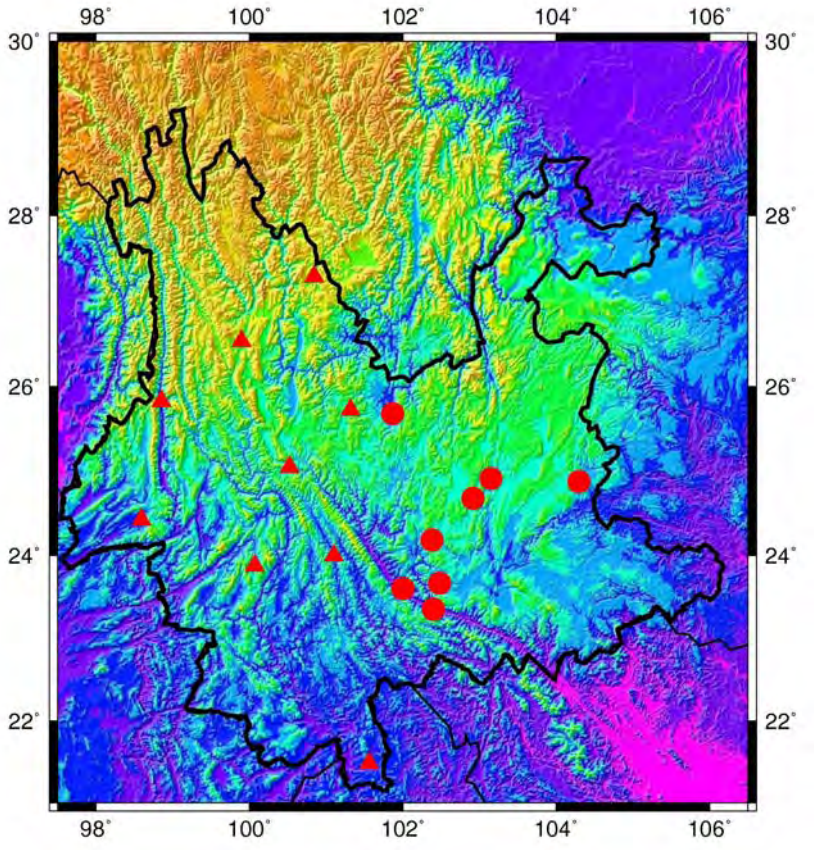

Figure 1. The topography of the Yunnan province and the layout of our broadband network. The red triangles are STS-2 seismometers, while the red circles are Chinese broadband instruments (the long-period corner at 20 s).

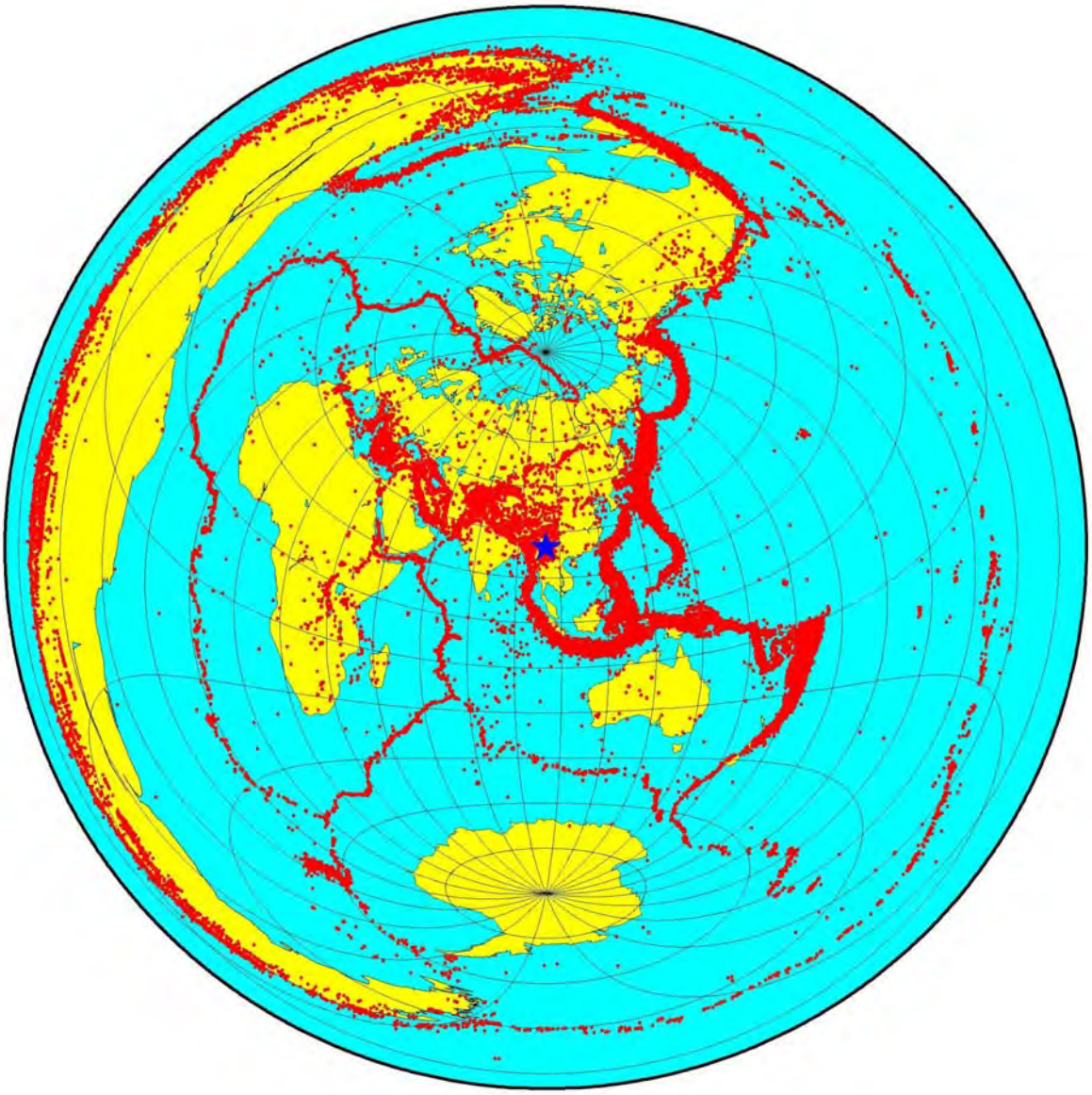

Figure 2. Yunnan province (the blue star in the middle) and its relative position to other strong seismic zones in the world. The small red dots are seismic activities in the world (United States Geological Survey data).

RESEARCH ACCOMPLISHED

All the instruments except at one station are deployed alongside the existing short-period analog seismic stations of the Yunnan Seismological Bureau. The instruments are installed in vaults that are typically 30 m deep extending horizontally into the hillside. Since these piers were usually built professionally by seismological standards, the data quality of this deployment is, on average, very high. The local provincial bureaus provide support for security and maintenance of the instruments. The deployment and data collection ends at the end of June of 2002.

At the present stage of research, the data are being routinely processed. Our analysts are screening all the waveforms recorded and constructing a ground truth database. Basically, the database consists of the waveforms of three kinds of events: small to moderate local/regional earthquakes, industrial explosions, and moderate to large earthquakes at teleseismic distances.

Local Earthquakes

Several moderate local earthquakes occurred during our experiment. After such an event, the Yunnan Seismological Bureau usually dispatches exploration teams to do an on-site geological and geophysical survey. Therefore, they provide excellent ground truth information. Figure 3 is the vertical waveform recorded across our network for a M=5 earthquake at Jinggu on September 4, 2001. The epicentral distances to the stations in our network are from 50 km to 400 km.

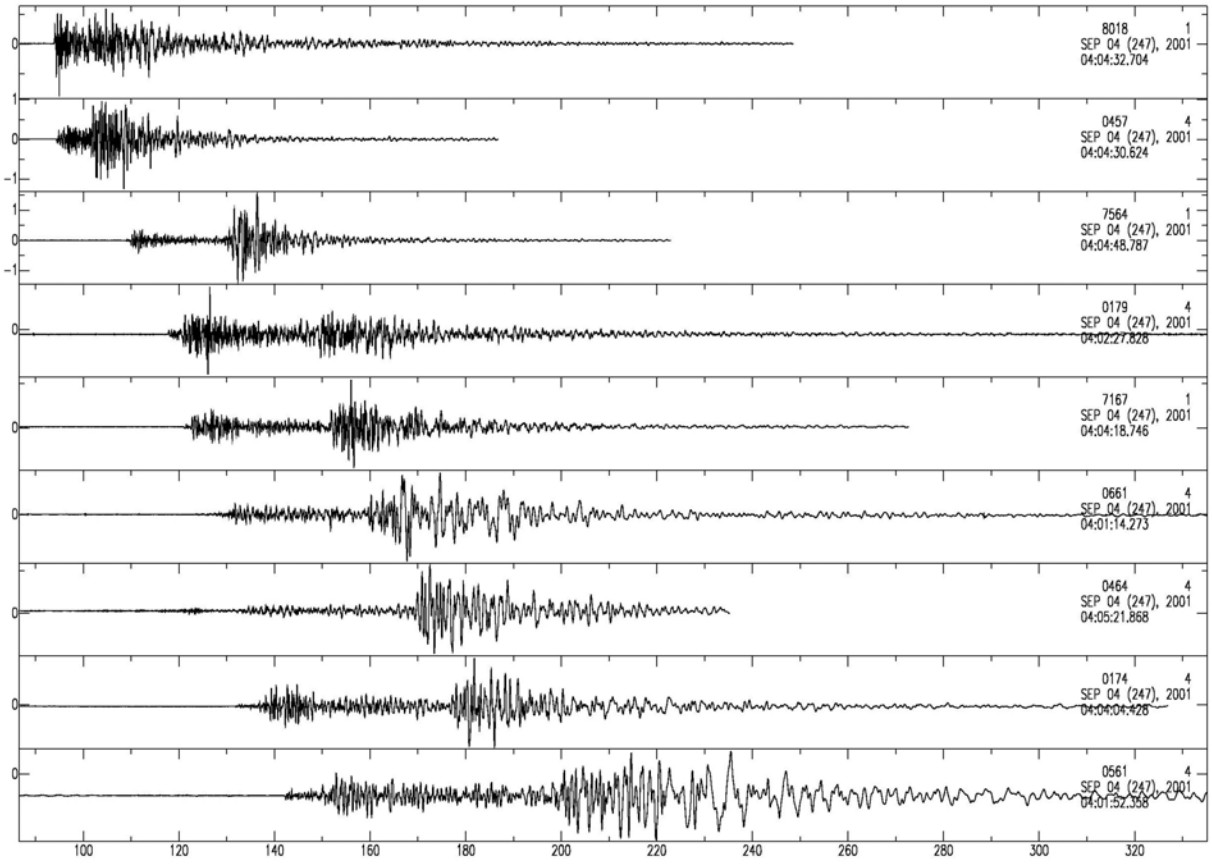

Figure 3. The vertical component of the waveforms of the September 4, 2001, Jinggu earthquake recorded across the network. The epicentral distances to the stations in our network are from 50 km (Lincang, the top trace, to 400 km, Ninglang, the bottom trace).

Screening of Industrial Explosions

The provincial earthquake catalog, compiled on the recordings from the high-density short-period analog seismic network in Yunnan province, as well as the provincial digital seismic network of 23 broadband stations, is a complete list of all the earthquakes with magnitude greater than 1 in Yunnan and its proximity. Of all the 4,144 waveforms we have processed so far, about 923 among them could neither be associated with any earthquakes in the catalog nor be associated with any other events in the global PDE catalog. Figures 4 and 5 show two examples of

such waveforms. These events are most likely to be the local and regional industrial explosions that need to be studied further.

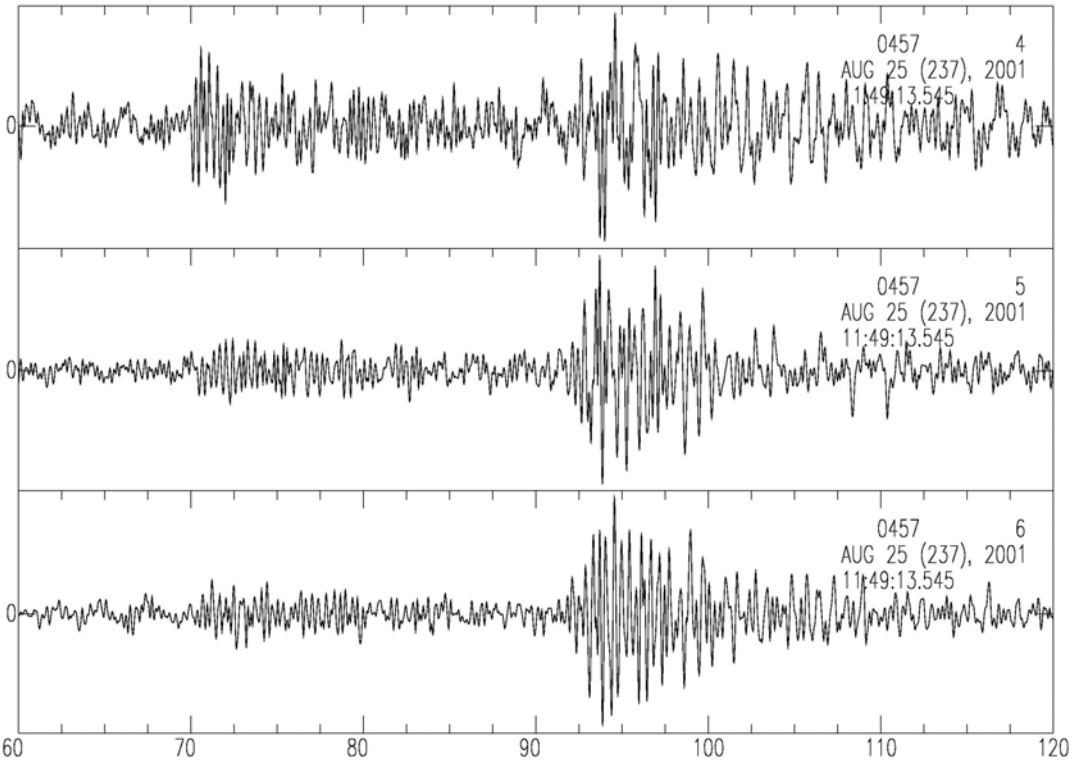

Figure 4. An example of waveforms of a potential industrial explosion recorded at station Zhenyuan.

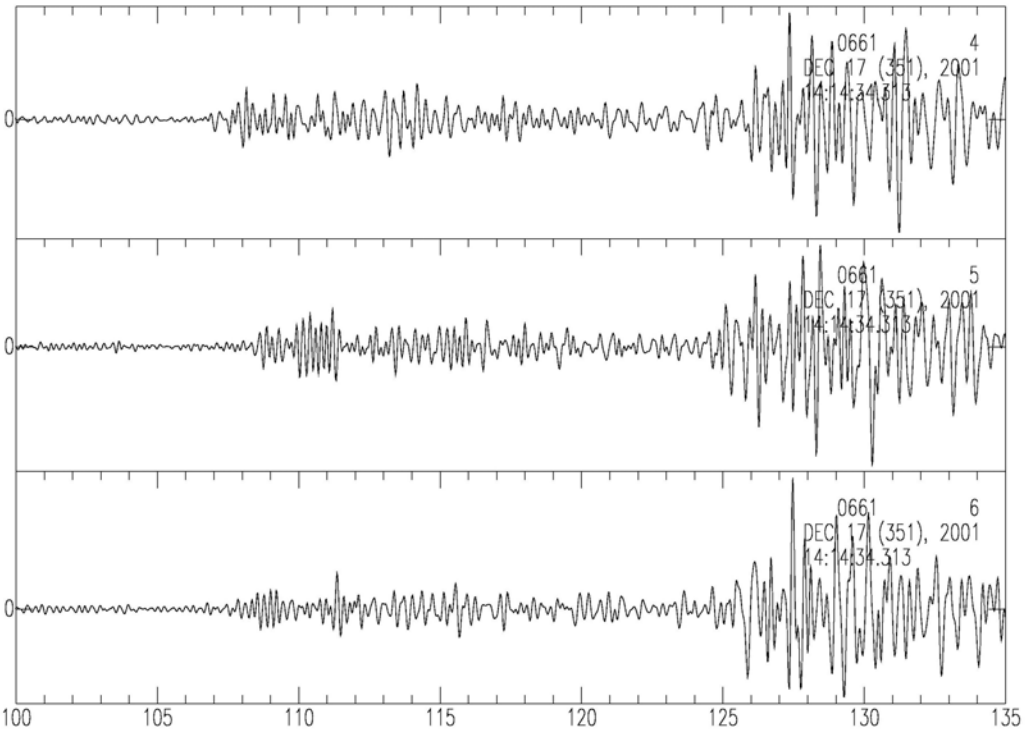

Figure 5. An example of waveforms of a potential industrial explosion recorded at station Mengla.

Moderate to Large Earthquakes at Teleseismic Distances

Moderate to large earthquakes in the world are routinely recorded, including the November 14, 2001, Ms=8.0 Qinghai, China, earthquake; the December 18, 2001, Ms=7.3 Taiwan earthquake; the September 11, 2001, Ms=6.4 Iranian earthquake; the October 12, 2001, Ms=7.3 Mariana earthquake; the January 2, 2002, Ms=7.6 Vanuatu Islands earthquake; and the March 3, 2002, Ms=7.2 Hindu-Kush earthquake, etc. These waveforms are valuable for studying wave propagation along the paths from southwest China to many interesting regions in the world, as well as for studying the source mechanism of large earthquakes. Figure 6 shows the waveforms of the October 12, 2001, Ms=7.3 Mariana earthquake recorded at the network.

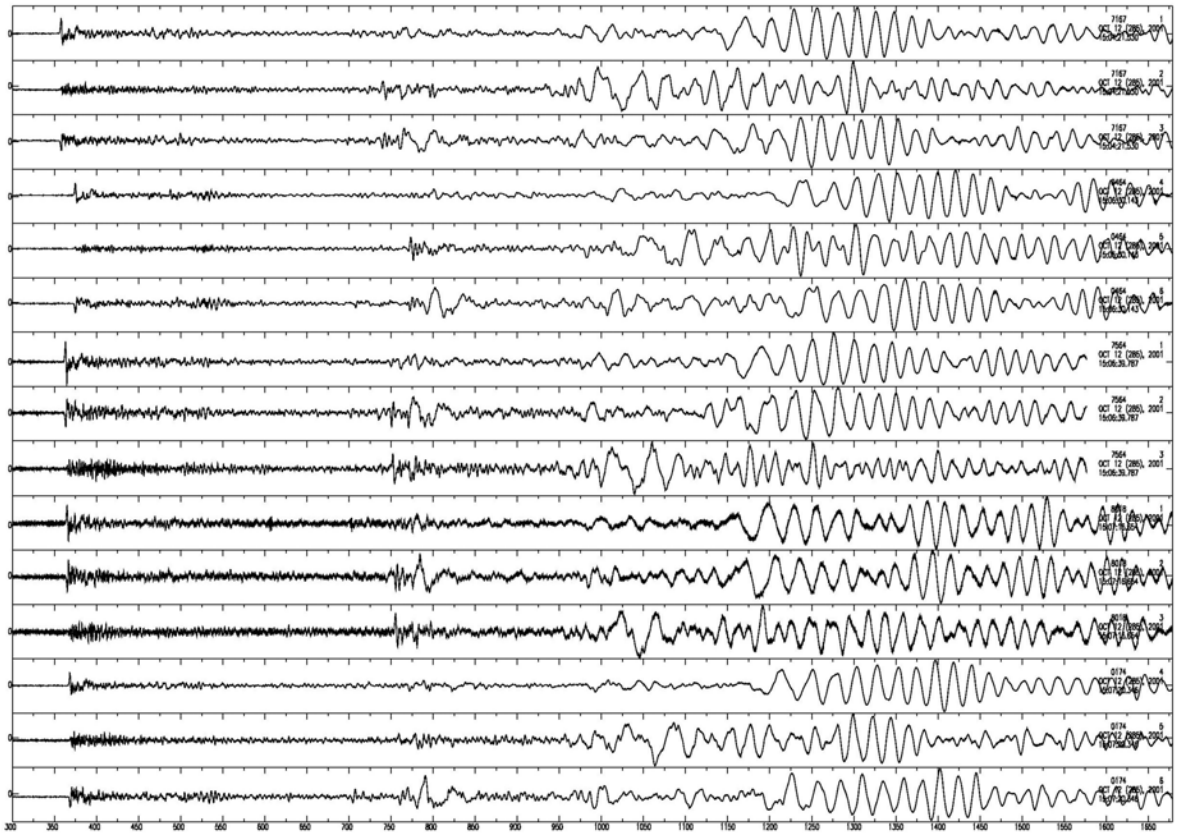

Figure 6. The waveforms of the October 12, 2001, Mariana earthquake recorded at the network.

CONCLUSIONS AND RECOMMENDATIONS

The Yunnan broadband seismic experiment is very successful. A high-quality, unique database of waveforms recorded in this experiment has been building up. In the database, there are basically waveforms of three kinds of events: small to moderate local/regional earthquakes, industrial explosions, and moderate to large earthquakes at teleseismic distances. A screening of the waveforms shows that more than 20% of the events could be industrial explosions. This database includes tremendous ground truth information and provides excellent opportunities for studying regional wave propagation, seismic source discriminants, and active tectonics in the eastern portion of the Tibetan Plateau and seismic hazard reduction in the Yunnan area.

ACKNOWLEDGEMENTS

We thank Peter Goldstein at Lawrence Livermore National Laboratory for providing us with the Seismic Analysis Code (SAC) under Linux for field use. We also thank the IRIS/PASSCAL instrument center, as well as Refraction Technology Inc., for providing a great deal of technical help.

REFERENCES

Aki, K. (1980), Attenuation of shear waves in the lithosphere for frequencies from 0.05 to 25 Hz, *Phys. Earth Planet. Inter*., **21**, 50-60.

Chen, P. S., F. T. Liu, Q. Li, and J. Z. Qin (1991), The lateral inhomogeneity in Yunnan province. China, *Science in China (Series B)*, **34** (5), 630-640.

Cui, Z.Z., D.Y. Du, J.P. Chen, Z.Y. Zhang, and L.Y. Huang (1987), The Deep Structure and Tectonic Features of the Crust in Panxi Area, *Chinese J. Geophy*., **30** (6): 566-580 (in Chinese).

Ge, B.R., and K.Y. Yang (1990), Mesozoic-Cenozoic Tectonic Features in Panzhihua-Xichang Area, *Chinese J. Geophy*., **33** (1): 64-69 (in Chinese).

Herrmann, R.B., and C.J. Ammon (1997). Faulting parameters of earthquakes in the New Madrid, Missouri region, *Engineering Geology* **46,** 299-311.

Hu, H.X., *et al.* (1986), Explosion Investigation of the Crustal Structure in Western Yunnan Province. *Chinese J. Geophy*., **29** (2), 133-144 (in Chinese).

Hu, H.X., Z.Y. Lin, Y.J. Bian, C.Y. Wang and L.B. Zhu (1996), Study on the Characteristics of Crust-Mantle Transition Zone in Western Yunnan Province, *Acta Seismologica Sinica*, **18** (4): 444-450 (in Chinese).

Lin, Z., *et al*. (1993), The Preliminary Interpretation of Deep Seismic Sounding in Western Yunnan, Acta Seismologica Sinica, **15** (4): 427-440 (in Chinese).

Liu, R.F., P.S. Chen, and Q. Li (1993), Three-Dimensional Velocity Images in Yunnan and Its Neibouring District, *Acta Seismologica Sinica*, **15** (1): 61-67 (in Chinese).

Liu, Z., R.B. Herrmann, J. Xie, and E.D. Cranswick (1991), Waveform characteristics and focal mechanisms of five aftershocks of the 1983 Goodnow, New York, earthquake by polarization analysis and waveform modeling, *Seism. Res. Letters*, **62**, 123-133.

Malagnini, L. (1999), *Ground Motion Scaling in Italy and Germany*, Ph.D. Dissertation.

National Research Council (1997), *Research Required to Support Comprehensive Test Ban Treaty Monitoring*, National Academy Press, Washington, D.C.

Qin, J.Z., and R.J. Kan (1986), Q Values and Seismic Moments Estimates Using the Coda Waves of Near Earthquakes in the Kunming and Surrounding Regions, *Chinese J. Geophy.*, **29** (2): 145-155 (in Chinese).

Raoof, M., R.B. Herrmann, and L. Malagnini (1999), Attenuation and excitation of three-component ground motion in Southern California, *Bull. Seism. Soc. Am.* **89**, (Aug. 99) preprint.

Rodgers, A. and W. Walter (1997), Regionalization and calibration of seismic discriminants, path effects, and signal-to-noise for station ABKT, *Proc. 19th Annual Seismic Research Symposium on Monitoring a Comprehensive Test Ban Treaty* (Editors: M. J. Shore, R. S. Jih, A. Dainty, and J. Erwin), Defense Special Weapons Agency, Alexandria, 143-151.

Sun, K.Z., J.W. Teng, D.M. Jin, and Y. Zheng (1987), Q-Value and Its Lateral Variations in Pan-xi Tectonic Belt, *Chinese J. Geophy*., **30** (1): 101-104 (in Chinese).

Wang, C.Y., X.L. Wang, and Q.Z. Yan (1994), Tree Dimensional Velocity Structure Beneath the Kunming Telemetered Seismic Network. Acta Seismologica Sinica, 1994, **16** (2): 167-175 (in Chinese).

Xiong, S.B., J.W. Teng, Z.X. Yin, M.H. Lai , and Y.P. Huang (1986), Explosion Seismological Study of the Structure of the Crust and Upper Mantle at Southern Part of the Panxi Tectonic, Belt, *Chinese J. Geophy*., **29** (3), 235-244 (in Chinese).

Xiong, S.B., et al. (1993), The 2-D Structure and Its Tectonic Implications of the Crust in the Lijiang£-Panzhihua£-Zhehai Region, *Chinese J. Geophy*., **36** (4), 434-444 (in Chinese).

Yazd, M.R.S. (1993), *Ground motion studies in the Southern Great Basin of Nevada and California*, Ph.D. Dissertation, Saint Louis University, 189p.

Zhu, P.D., Y.M. Li, L.M. Zhang, P.Y. Shu and S.H. Liang (1986), On the Study of the Seismic Telemetry Network in South Sichuan and North Yunnan Provinces, *Chinese J. Geophy*., **29** (3), 245-254 (in Chinese).

IMPROVING DISCRIMINANTS FOR SOURCE IDENTIFICATION

Thorne Lay and Guangwei Fan

University of California, Santa Cruz

Sponsored by Defense Threat Reduction Agency

Contract No. DTRA01-00-C-0211

ABSTRACT

Regional phases in the Tibetan Plateau have anomalous discriminant performance due to low shear wave (Sn, Lg) amplitudes for paths traversing the northern portion of the Plateau. Our investigation of the mechanism responsible for this lack of shear wave energy indicates that strong attenuation in the crust and upper mantle is responsible rather than waveguide blockage effects such as thinning of the crust. This is based on observation of progressive, path-length dependent evolution of the Lg spectra over paths within the Plateau. Anelastic losses, rather than scattering by waveguide disruption, for both Lg and Sn preclude mitigating strategies such as using P/Smax measurements. Thus, improving discrimination for sources in this seismically active region requires improved understanding of the magnitude and spatial variations in shear wave attenuation. In the initial phases of this investigation, reported on last year, we utilized progressive Lg spectral shifts with distance from station WMQ to estimate the attenuation effects for Lg, exploiting the severity of the attenuation to offset the lack of control on source radiation intrinsic to single-station methods. Our preliminary results indicated Lg attenuation with Q_o (1 Hz) values of 85-90 in northern central Tibet, with whole-Tibet path averages of 122-149 for the reliable 0.2-0.5 Hz passband. These values are 2 to 3 times lower than prior published values, most of which omit paths with strong attenuation, suggesting that regional phase attenuation in Tibet has been seriously underestimated, and the resultant problems for discrimination efforts also underestimated. To improve the confidence of our attenuation estimates and to extend the spatial sampling, we have augmented the WMQ observations with observations from LSA, KMI and LZH. These stations provide paths within central Tib*et al*ong with extended sampling of eastern Tibet. As a first-order check on our WMQ observations, we established that all of these stations display strong spectral shifts for the Lg group velocity window as functions of propagation distance. The data from LZH closely parallel those from WMQ, while data for KMI show a slightly lower distance dependence, but still much stronger than observed in China. The LSA observations parallel the trend for WMQ and LZH, but with a baseline shift to lower corner frequencies consistent with having paths entirely within the strongly attenuating Plateau crust. The similarity of the spectral trends results in comparable path averaged attenuation values in the frequency band 0.2-1.0 Hz, but in all cases the signal bandwidth is insufficient to reliably constrain the frequency dependent coefficient of Lg Q. As a result there is some ambiguity in relating our relatively low-frequency results to estimates available for east-central Tibet (about which there is significant controversy, with about a factor of 3 range in reported Q_o values for the same data set). Generally, the data favor a southward increase in Lg Q relative to the very low values found in northernmost Tibet. The latter area spans the region of Cenozoic volcanism in the Plateau along with the region of strong Sn attenuation established in many studies. We have applied a two-station, two-source (close to great-circle) method to estimate Lg Q more accurately on certain paths. Observations at LSA and WMQ have been combined to estimate the Lg Q of northernmost Tibet, resulting in Q_o values of 94 ± 3 and $\eta = 0.29 \pm 0.04$ for the passband 0.2-1.0 Hz. This is very consistent with the results found for WMQ alone. We are currently applying similar analysis to the fundamental mode Rayleigh waves at WMQ and LSA for those events for which focal mechanism estimates are available, in an effort to develop a vertical profile of Q_s in the crust. The two-station method has been applied to WMQ and KMI Lg data as well, providing new constraints on the attenuation in Eastern Tibet. For paths traversing most of the Plateau, we find $Q_o = 183$ for the passband 0.2-1.0 Hz, but as in Central Tibet, there appears to be a strong increase in Q_o toward the south, with the northern region yielding $Q_o = 123$ and the southern region yielding $Q_o = 392$. On the basis of this, we find support for the relatively high Q_o values estimated for east-central Tibet by McNamara *et al*. While efforts to fully map out the Tibetan attenuation structure are continuing, it is clear that the strong regional variations in crustal attenuation will give variable discriminant performance, with paths traversing northern Tibet being particularly prone to anelastic loss of shear wave energy. The effect is so pronounced that path calibration efforts (parametric inversions, kriging, cap-averaging) are not adequate, and one must either calibrate and utilize lower frequency Lg or Sn energy or rely on discriminants other than P/S measures.

OBJECTIVE

Prior work has established that extensive areas of Tibet have very inefficient transmission of *S* waves, for both crustal (*Lg*) and upper mantle (*Sn*) paths. This greatly complicates application of regional seismic discriminants involving *P/S* ratios in the region, and makes Tibet an area of primary concern for seismic monitoring of underground nuclear testing. As part of our multi-year analysis of regional discriminant path corrections in Eurasia, we have been conducting an analysis of *Lg* attenuation within the Tibetan Plateau using the low-frequency passband of 0.2-1.0 Hz to overcome the depletion of high-frequency *Lg* signals within the Plateau. The regional signals for events within the Plateau recorded at stations outside the Plateau often appear rather explosion-like due to the weak *Sn* and *Lg* arrivals, and our work has established that this is most likely due to strong attenuation of shear waves within the crust rather than a structural blockage effect on the Plateau margins. We now believe that there is an extensive region of northern Tibet with 1-Hz Lg attenuation values of 90 –100, which is responsible for the apparent 'blockage' of high-frequency Lg phases observed for paths traversing the northern boundary of the Plateau (Ruzaikin *et al.*, 1977, Ni and Barazangi, 1983; Rapine *et al.* 1977; Fan and Lay, 2002).

McNamara *et al.* (1996) analyzed data recorded at 11 broadband stations in eastern central Tibet, finding that high-frequency *Lg* is generated by events within the Plateau, and this energy can propagate to distances of at least 600 km; however, they did not observe the *Lg* phase for even shorter paths traversing western or central Tibet or for events in the Himalayas traveling across the southern margin of the Plateau. For eastern central Tibet, where sufficient high-frequency *Lg* signal-to-noise ratios were observed, a frequency-dependent *Q* function given by $Q(f) = (366\pm37)f^{(0.45\pm0.06)}$ was estimated for the passband (0.5-16 Hz) (McNamara *et al.*, 1996). This is comparable to the estimate of $Q(f)=(448\pm82)f^{(0.426\pm0.157)}$ estimated for 1-6 s *Lg* waves traversing Tibet by Shih *et al.* (1994). This latter value is likely also dominated by eastern Tibet paths, as 'blocked' observations were omitted from the calculation. Similar 1-Hz Q_o value was also estimated to be 340 for events north of LSA using spectral methods by assuming a constant Q_o model (Reese *et al.*, 1999). These attenuation values are typical of tectonically active areas and are not low enough to cause rapid extinction of 1-Hz *Lg* over just a few hundred kilometers, as observed for paths traversing the northern margin of Tibet. We believe the explanation is that Q_{Lg} has substantial lateral variations within Tibet. Indeed one might expect this to be the case, for it is true of *Sn* attenuation, which is strongest in northern central Tibet. The possibility of stronger *Lg* attenuation in northern and central Tibet is suggested by the lack of high-frequency *Lg* detections for events to the west of the broadband stations in the data set of McNamara *et al.* (1996). Furthermore, a recent reanalysis of the data set used by McNamara *et al.* (1996) indicates a much lower *Lg Q* in eastern central Tibet, with Q_o = 126 (Xie, 2002). The latter value is almost a factor of 3 lower than the earlier result, which Xie suggested may be due to instabilities in the inversion for source and receiver terms in the formulation by McNamara *et al.* (1996).

Our current work resolves this issue, demonstrating the presence of very strong attenuation in the region of north-central Tibet, an area where other work has demonstrated the presence of partial melt in the crust. We also find average Q_o values for paths traversing the Plateau of about 150, much lower than proposed in earlier work.

RESEARCH ACCOMPLISHED

Work reported on last year utilized regional waveforms recorded at broadband station WMQ, the westernmost station of the Chinese Digital Seismic Network. This station lies just north of the Tarim Basin, about 650 km from the northern boundary of the Tibetan Plateau. While three-component data were obtained, we restricted our analysis to the vertical component seismograms due to the attenuated nature of the *Lg* phases traversing Tibet, which leads to confusion with fundamental mode Love wave energy on the transverse components. We examine energy in the standard *Lg* group velocity window of 3.6 to 3.0 km/s, which precedes short and intermediate period fundamental mode Rayleigh wave energy. We analyzed recordings for 90 earthquakes with magnitudes of $4.4 \le m_b \le 6.4$ that occurred between 1987 and 1999 in the Tibetan Plateau and around its margins. Progressive shifts of frequency content with propagation distance were observed for the WMQ data, leading us to estimate *Lg* attenuation in the 0.2-1.0-Hz frequency band. Given that propagation effects appear to dominate over any plausible source effects, we applied a single-station, multi-event stacking method to obtain the 1-Hz *Lg* attenuation values (Q_o) summarized in Figure 1. The distribution of events enabled whole-Plateau path estimates to be obtained in western, central, and eastern Tibet, along with a more localized estimate for northern-central Tibet. The preferred whole-Plateau estimates, obtained from the passband 0.2-0.5 Hz, involve Q_o values of 122-146, much lower than previously reported within Tibet, with particularly strong attenuation noted for northern central Tibet, where Q_o is about 90.

The concentration of strong attenuation in the northern region of Tibet implies that Q_o in southern central Tibet is actually much higher than the whole-path average, and a value of 316 was determined. It is plausible that there are comparable north-to-south gradients in the western and eastern areas of Tibet; however, the value of 122 found as an average for Eastern Tibet is in close agreement with the value of 126 estimated by Xie (2002), so this need not be the case.

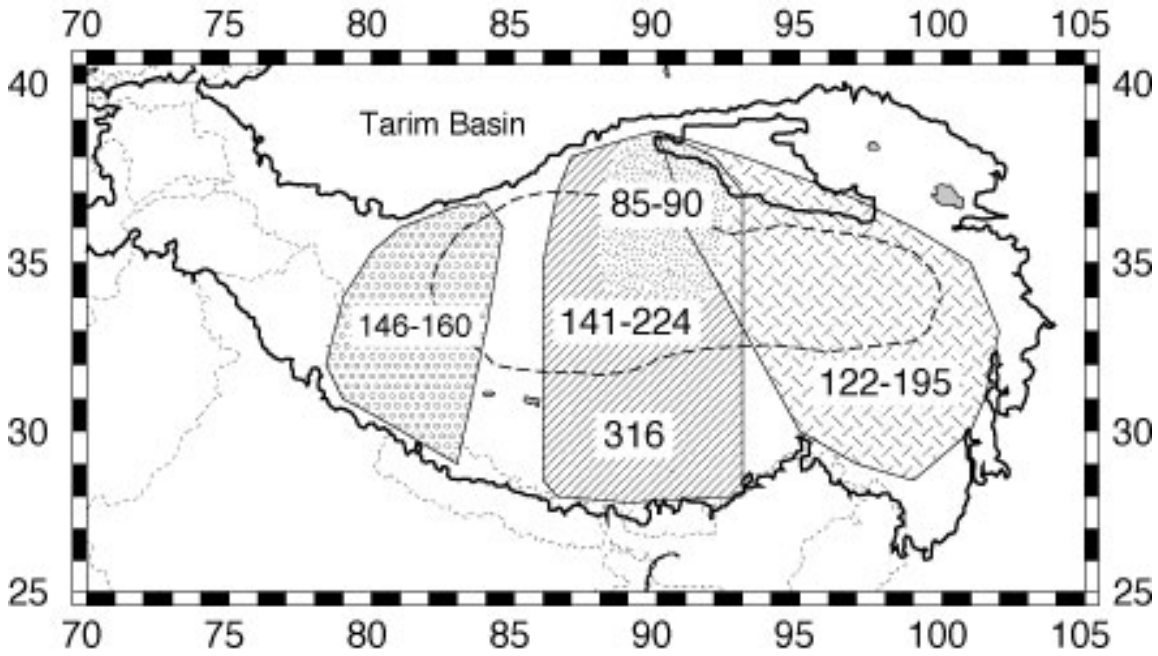

Figure 1. Estimates of *Lg* Q_o variations within the Tibetan Plateau based on single station analysis for data at WMQ. These results were reported on last year, and are based on progressive distance-dependent spectral decay of *Lg* signals for events at the southern edge of each province relative to the northern edge. The first number in each range corresponds to the more reliable spectral range from 0.2-0.5 Hz, with the second number, if given, corresponding to results for the spectral band 0.2-1.0 Hz. The latter band is contaminated by scattered high-frequency *S* energy. In central Tibet, paths traversing the whole Plateau yield overall estimates of 141-224; however, this is resolved to be an average of intense attenuation in the northern third of central Tibet, with much lower attenuation in southern central Tibet. Results are from Fan and Lay (2002).

In this year's continuation of this research, our focus has been on corroborating the results of the single-station analysis for station WMQ, along with extending the spatial coverage using additional broadband stations. We sought all available recordings of Tibetan earthquakes for stations LSA, KMI and LZH. As for WMQ, we began by inspecting systematic range-dependence relative to each station, ignoring source variations. A total of 31 events yielded useful data for LSA, 37 for LZH and 30 for KMI, with the latter two stations yielding extensive coverage of eastern Tibet, while LSA samples the entire Plateau (Figure 2). We estimated an effective 'Lg corner frequency', corresponding to the onset of strong amplitude decrease apparent in all spectra, and regressed the measured values on total path length to each station. As shown in Figure 2 for station LSA, these spectral corners shift very systematically with path length for each station, with distance correlation coefficients of -0.91 for LSA, -0.90 for LZH and -0.95 for KMI, compared to –0.82 for WMQ. We believe that strong attenuation throughout the Plateau is responsible for these spectral shifts with propagation distance that overwhelm any source variations. Tightly fitting regression curves for each station are shown in Figure 3, where it is apparent that the data for WMQ are not anomalous despite all associated paths traversing the northern margin of the Plateau, so any form of crustal structure blockage near the northern boundary is not responsible for this trend.

Given that the attenuation analysis for WMQ suggests average Plateau *Qo* values of around 140, we infer from Figure 3 that similar general results will hold for all 4 stations. However, we note that the WMQ data do appear to

involve averaging of subregions of lower *Q* and subregions of higher *Q*, so mapping out the spatial patterns within the Plateau is essential. The geometry of the event distributions for stations LSA, LZH and KMI is less favorable

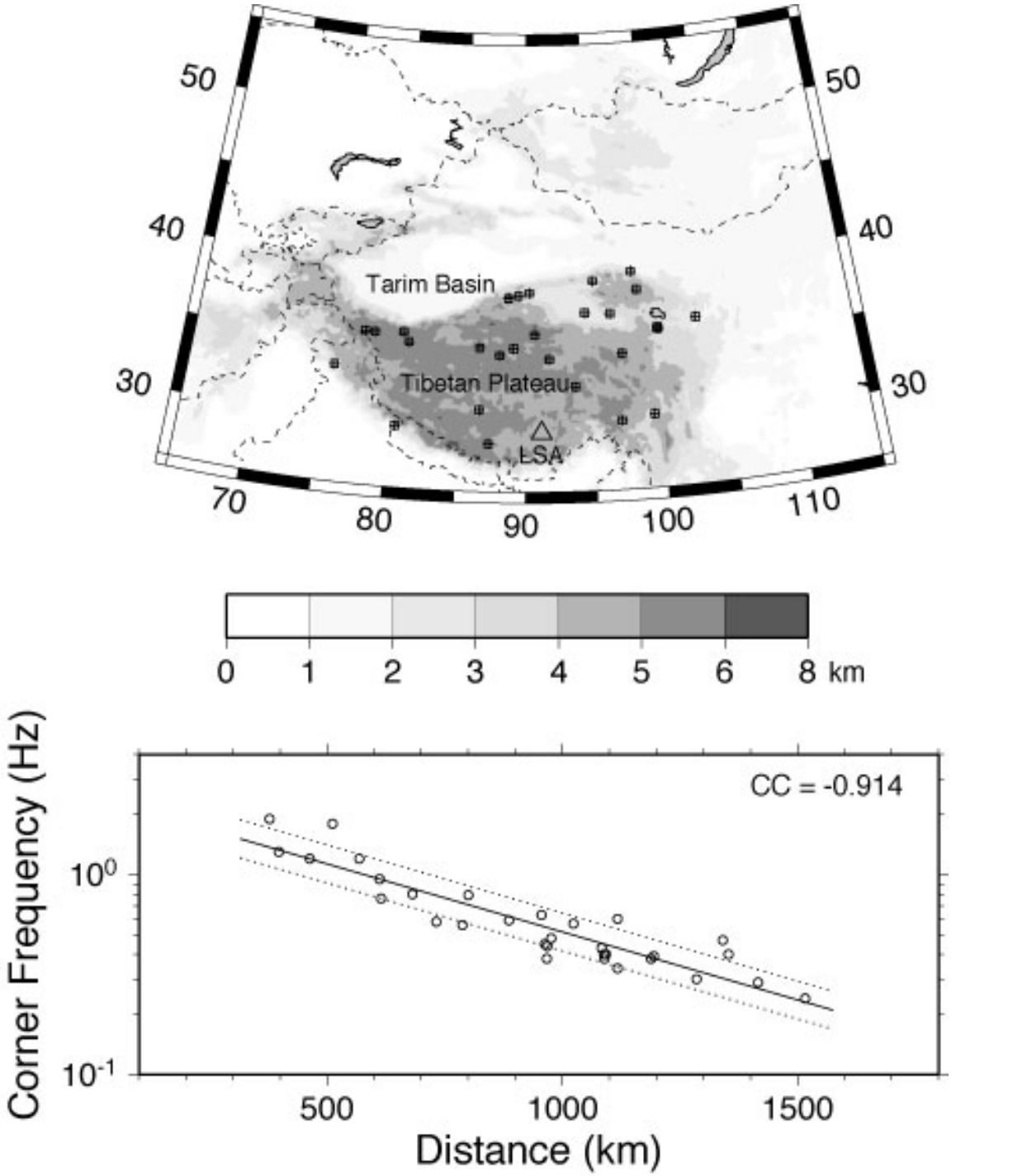

Figure 2. Top: Map showing the location of events yielding useful recordings at station LSA. The associated paths give extensive sampling of the Tibetan Plateau but none of the paths traverse the northern boundary of the Plateau. Bottom: The apparent corner frequency of the *Lg* spectra for each seismogram at LSA is plotted as a function of total path length between source and receiver. The linear correlation coefficient (CC) is indicated at the upper right. The solid line is the result of linear regression, with the dotted lines being ±1 standard deviation about the regression.

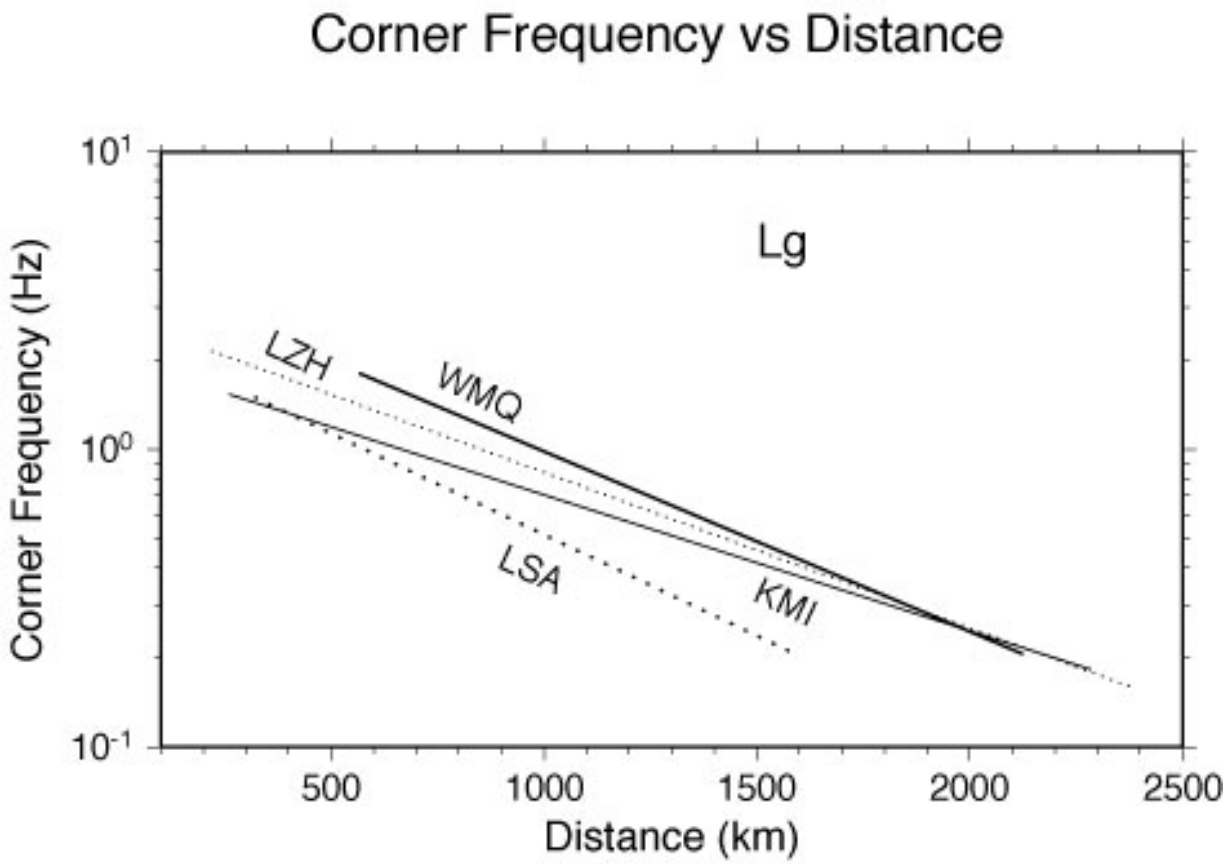

Figure 3. Summary of the regression curves obtained for *Lg* corner frequency versus propagation distance for each of the four stations providing numerous observations of Tibetan events. LSA and WMQ have the most uniform sampling of Tibet, and nearly equivalent regression slopes are found. At a given distance, the entire path to LSA is within the Plateau, while for WMQ, there is at least a 600-km additional path through high *Q* crust north of the Plateau, which accounts for the baseline shift. Paths to LZH and KMI also have portions outside the Plateau, in presumably higher crust as well.

to the single-station spectral stacking approach that was used for WMQ, and we desire to make more precise, spatially resolved estimates of *Lg* attenuation, so we have applied a more restrictive, two-station, two-event method, for the limited geometries in which stations and events are close to a great-circle path. As shown in Figure 4, this is viable using WMQ and LSA, and for WMQ and KMI. The basic approach is that of Chun *et al*. (1987), applied to vertical component *Lg* spectra in the passband 0.2-1.0 Hz. For the geometrical spreading function, we use $d^{-0.5}$, where *d* is the propagation length, as appropriate for spectral observations (Shin and Herrmann, 1987). This procedure explicitly cancels source spectral effects (and azimuthal patterns, to the extent that data are on a great-circle path), and explicitly cancels receiver terms (except to the extent that incoming signals have slightly differing back-azimuths and/or incidence angles). While the assumption of nearly isotropic radiation pattern for *Lg* would allow many more event-station combinations, we feel that it is prudent to restrict this application to nearly great-circle geometries, and this allows us to localize our results to the region between events, given that our stations are always the outer pair of the double combination. Stacking of multiple sets of two-station, two-event spectral estimates further stabilizes the spectral estimates, and reduces any errors associated with slight departures from great-circle geometry. This results in somewhat extended bandwidth at the higher frequency end (between 0.5-1.0 Hz), relative to the single-station spectral stacks for which source corrections were not made.

Our first targeted area was for northern central Tibet where the WMQ results indicated Q_o values near 90. This region is directly along the great-circle between WMQ and LSA (Figure 4), enabling a direct comparison of the

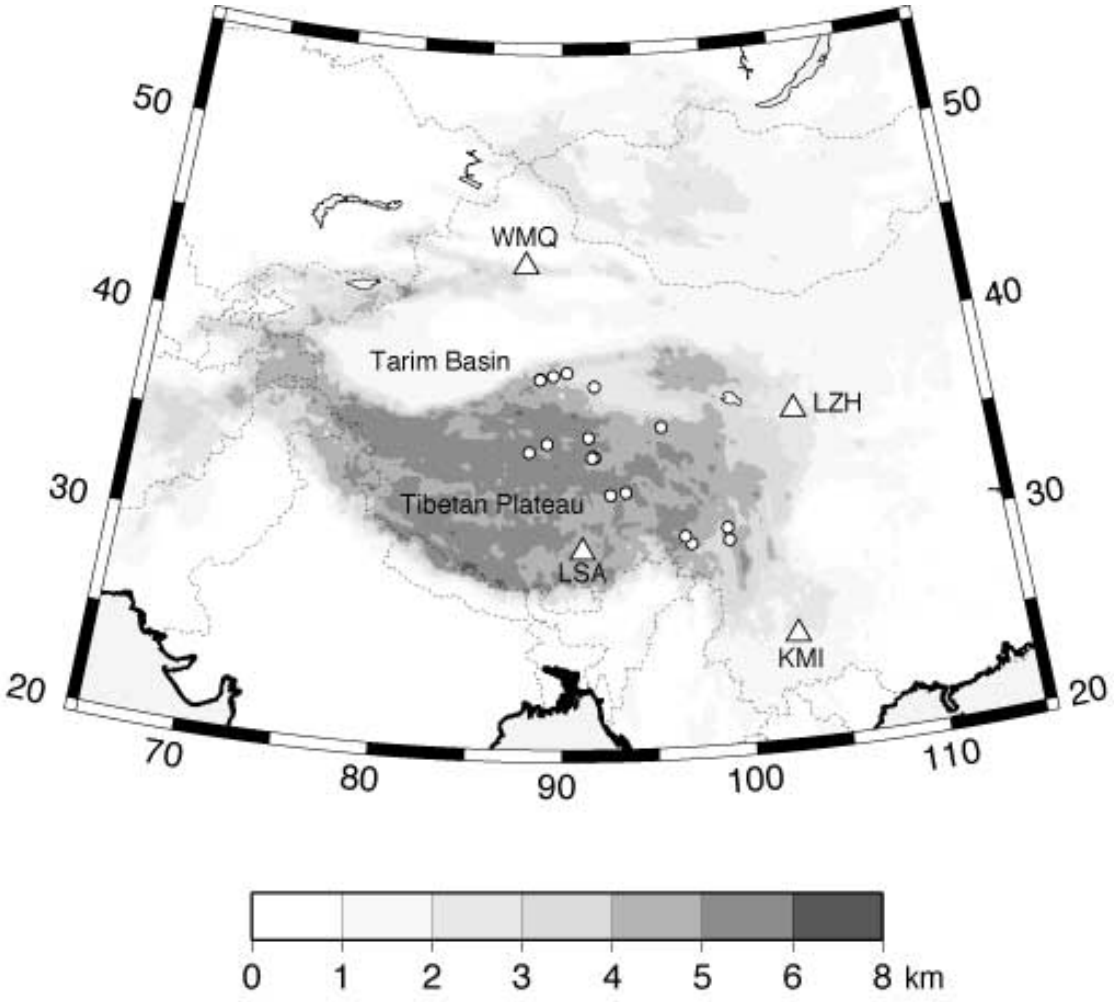

Figure 4. Base map of the study area, showing the topography in Western China and the Tibetan Plateau as well as the location of stations used (triangles) and epicenters of events used for the two-station, two-event applications.

results for one-station, two-event and two-station, two-event methods. Figure 5 shows high-frequency band-passed waveforms for events near the northern boundary of Tibet and about 400 km to the south, as recorded at WMQ and LSA. Note that for the event closer to WMQ, there is clear high-frequency *Lg* energy at WMQ, but no signal above the background noise at LSA, while the opposite is true for the event closer to LSA. This indicates that there is strong depletion of the *Lg* frequency content as a function of increasing distance from LSA, even though the paths never cross the northern boundary of the Tibetan Plateau. This confirms that structural blockage is not responsible, and that a progressive path effect such as attenuation is the explanation for the rapid loss of *Lg* energy in the region. The northern event has a larger *Lg* at WMQ than does the southern event at LSA. This is consistent with a high *Q* path across the Tarim basin to the north, and a moderate attenuation path across southern Tibet to LSA. If the low *Q* region between the two events extended further to the south, the LSA recording from the southern event would be much more depleted in high-frequency *Lg* than is the case. The *Lg/P* ratios indicated in the figure indicate that the primary loss of high-frequency energy is for the shear waves in the *Lg* phase, as high-frequency *P* wave energy does manage to reach stations both to the north and south from each event. The basic strategy of the two-station, two-event method is to compute spectral ratios of the pairs of seismograms for each event (with the more distant station in the numerator) and multiply the spectral ratios, thereby canceling both source and receiver effects. With a correction for geometric spreading over the path length between the sources, the spectra are reduced to a function of the *Lg* attenuation along the path between the sources. The resulting spectra, in the form of the *Lg* attenuation coefficient, are shown in Figure 6, spanning the frequency band 0.2-1.0 Hz. Higher frequency energy in the 1-5 Hz

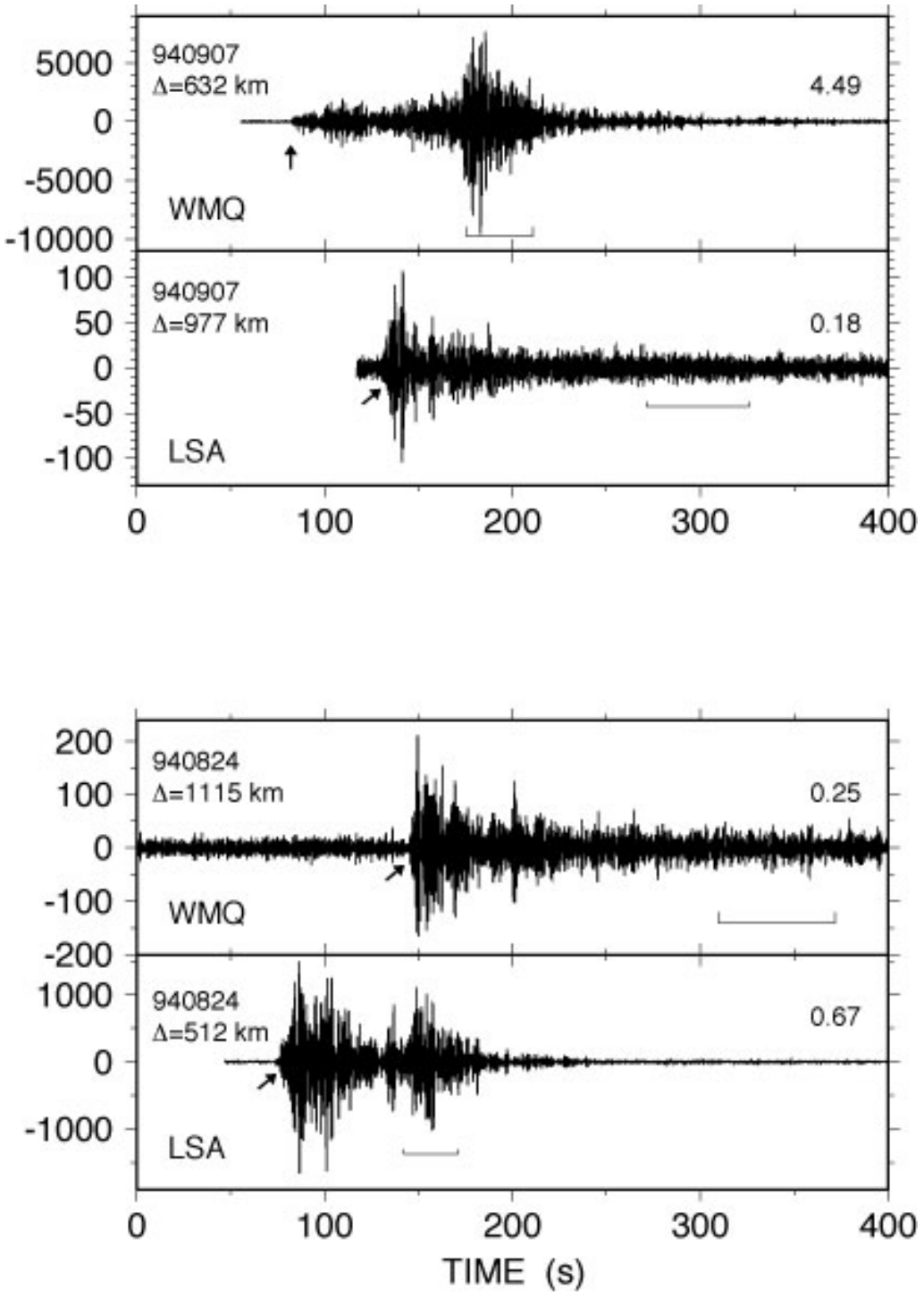

Figure 5. Bandpass (1-5 Hz) filtered seismograms for events recorded by both WMQ and LSA. The upper panels are for an event at the northern edge of Tibet, closer to WMQ. Note the presence of high-frequency energy in the *Lg* window (underlying brackets indicate the *Lg* group velocity window) at WMQ, and its absence at LSA. The amplitude ratio of energy in the Lg window relative to the Pn window is shown on the right (the onset of Pn is marked by the arrowheads). The lower panel is for an event several hundred kilometers to the south, in northern central Tibet. Note the presence of high-frequency *Lg* energy in the LSA recording, but its absence in the WMQ recording. The region between the two sources causes strong attenuation of Lg energy.

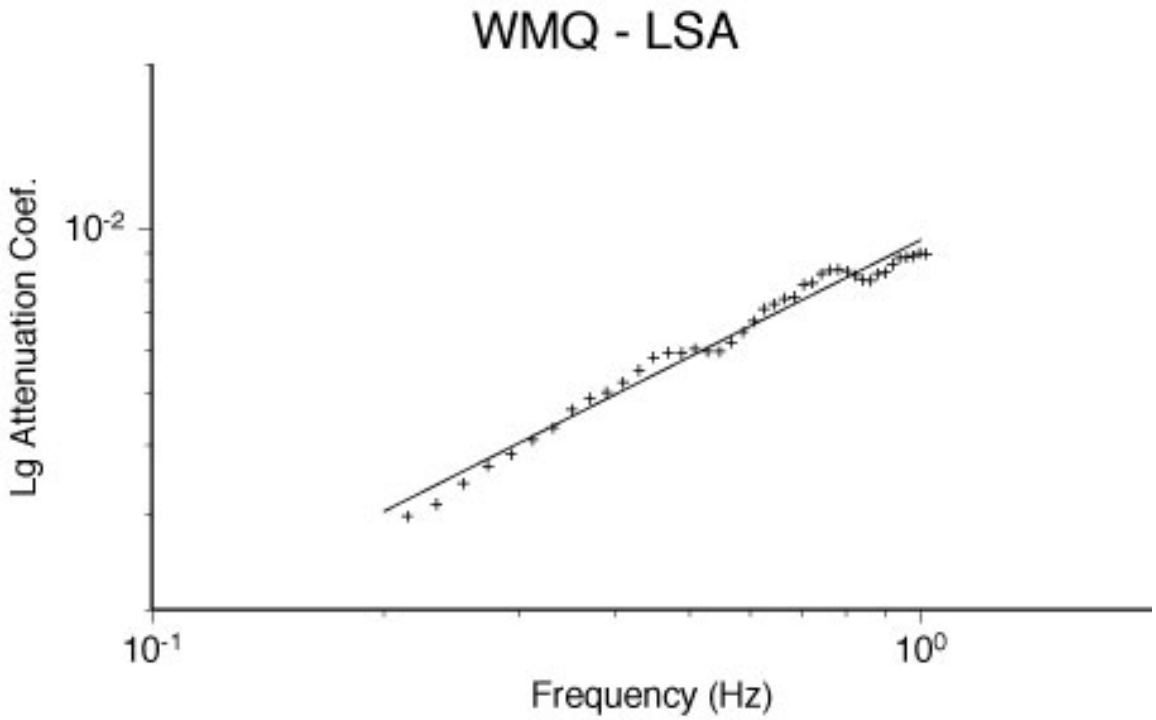

Figure 6. *Lg* attenuation coefficients in the 0.2-1.0 Hz band for the two-station, two-event stacking method WMQ and LSA observations. Twelve event pairs were averaged to give these spectra, so they are very robust. The regression curve is used to estimate Q_o and the frequency dependent parameter η. These spectra give Q_o = 94± 3 and η = 0.29±0.04 for the passband 0.2-1.0 Hz.

band is at the noise level for the more distant observations in each pair (see Figure 5), so we do not extend to higher frequencies. Doing so results in a flattening curve due to contamination from the high-frequency *P* or *Sn* coda seen in the *Lg* window in Figure 5, and that biases the attenuation to higher *Q* estimates. There were 4 events at the north end of this profile and three at the southern end, so a total of 12 spectra processed by the two-event, two-station method were stacked, resulting in the smooth attenuation coefficients shown in Figure 6. The results for velocity spectra in the passband 0.2 to 1.0 Hz are Q_o = 94±3 and η = 0.29±0.04. Processing of displacement spectra gives almost identical results (Q_o = 92±3 and η = 0.28±0.03). The single-station results from WMQ were Q_o = 85±2 (0.2-1.0 Hz) and 90±20 (0.2-0.5 Hz), which is remarkably consistent, given the lack of source corrections. Thus, the LSA-WMQ analysis confirms our result of strong *Lg* attenuation in northern central Tibet.

Corresponding analysis was made for WMQ-KMI combinations sampling eastern Tibet. In this case, the distribution of sources (Figure 4) enables four profiles to be examined, tolerating deviation of up to 30° from the great-circle path. All combinations in eastern Tibet are included in Profile III (named to correspond to the regionalization used in the WMQ analysis). The attenuation coefficient estimates are shown in Figure 7. Table 1

Table 1. The values of *Lg* attenuation in different parts of eastern Tibet.

		Profile III (WMQ)	**Profile III (WMQ-KMI)**	**Profile III (W) (WMQ-KMI)**	**Profile III (NW) (WMQ-KMI)**	**Profile III (SE) (WMQ-KMI)**
0.2-0.5 Hz	Q_o	122±20	119±17	--	--	--
	η	-0.19±0.15	-0.20±0.13	--	--	--
0.2-1.0 Hz	Q_o	195±14	183±13	--	--	--
	η	0.24±0.08	0.22±0.09	--	--	--
0.35-1.0 Hz	Q_o	--	--	199±15	123±3	344±54
	η	--	--	0.28±0.06	0.29±0.05	0.16±0.16

shows the estimated attenuation parameters and compares them to the results from single-station analysis of WMQ. Five event in the north and 4 events in the south were used for Profile III (20 spectral estimates were stacked). The spectra flatten above 0.5 Hz, so the Q_o estimate is very dependent on the frequency range fit, as was found for the WMQ data (Table 1). Given the source cancellation, we have confidence in the 0.2-1.0 Hz results, which give Q_o = 183±13 in eastern Tibet. The western portion of Profile III has higher source density, and whole-Plateau path estimates were made using three northern events and two southern events. Profile III(W) yields a slightly higher Q_o of 199 (Table 1, Figure 7). This portion of the profile is further subdivided into a northwestern section and a southeastern section, with 3x2 and 2x2 event combinations each (the first number indicates number of events at the northern end of each profile and the second number indicates the number of events at the southern end; their product is the total number of spectral estimates that are stacked for each region). Regressions over the 0.35-1.0 Hz range give the results in Table 1, with a strong north-south gradient being present. Again, it appears that very strong attenuation in the northern portion of the Plateau lowers the Plateau-wide averages. The Q_o estimates are shown in map view in Figure 8 for comparison with the results from WMQ analysis in Figure 1. We find it interesting that the relative high Q_o in Profile III (SE) is found in the immediate vicinity of the studies by McNamara *et al*. (1996)

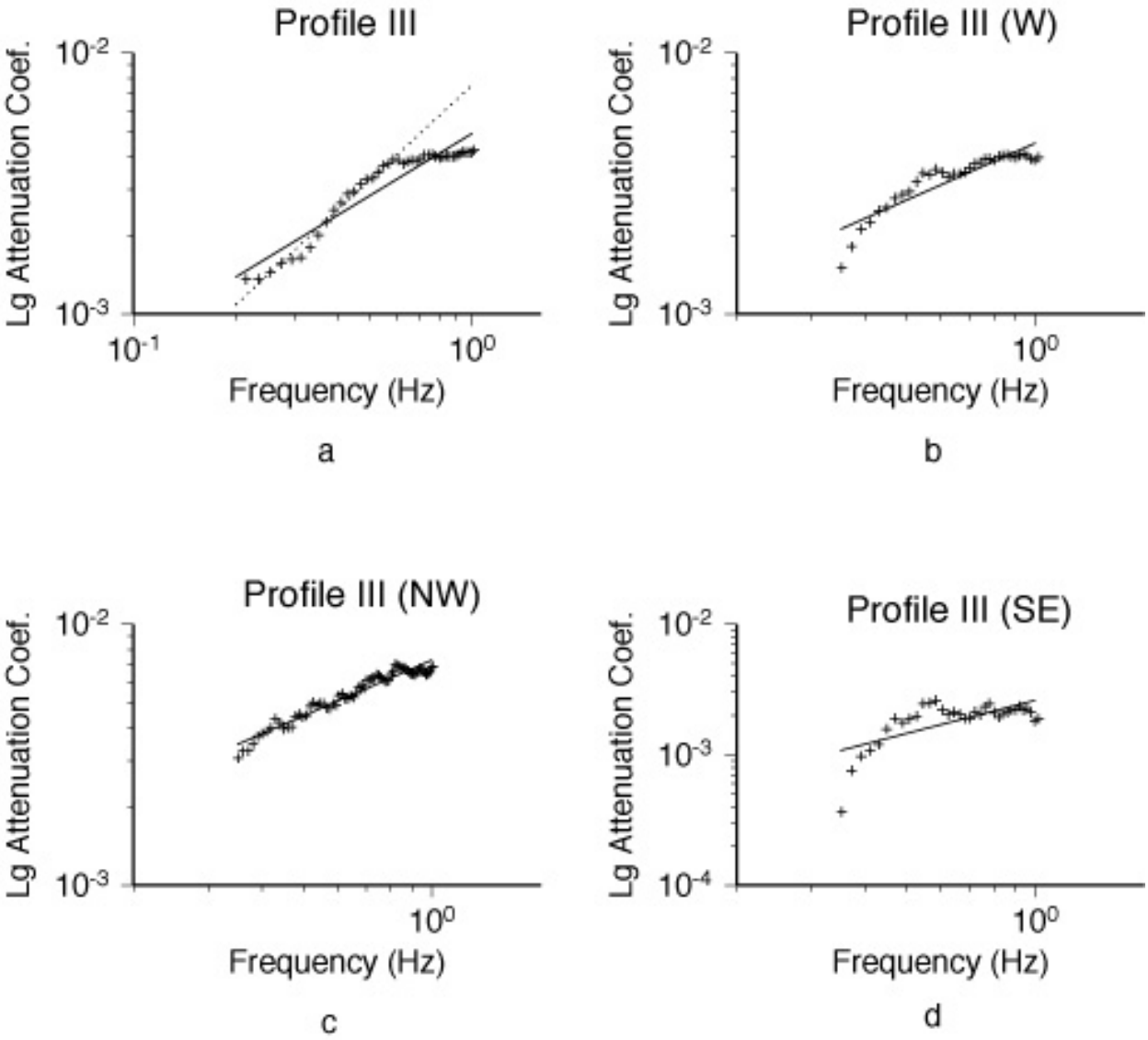

Figure 7. Lg attenuation coefficient estimates from stacking of two-station, two-event combinations for WMQ-KMI recordings. Profile III samples all of eastern Tibet, Profile III (W) is confined to a narrow corridor traversing the entire Plateau in the western portion of Profile III, and Profile III (NW) and (SE) are subdivisions of Profile III (W).

and Xie (2002). Our result is very consistent with the results from McNamara *et al*. (1996), which gave Q_o = 366±37 and η = 0.45±0.06. Our result is also consistent with the work of Reese *et al*. (1999). The results by Xie (2002) warrant further investigation, as the large discrepancy with other results is not clearly explained.

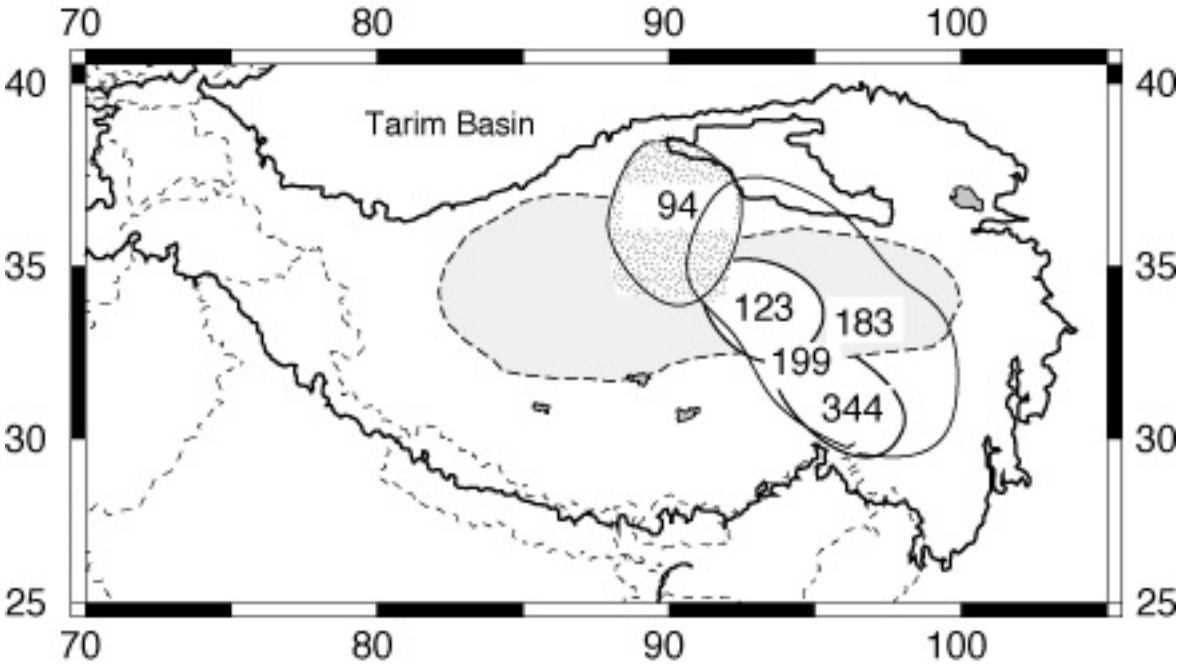

Figure 8. Map of Tibet highlighting regions where 1-Hz *Lg* attenuation coefficient has been estimated by stacking results of two-source/two-station analysis. These results can be compared with Figure 1, obtained by single station analysis of WMQ data. There is a broad region of very low *Q* in northern Tibet with the lowest values in the central region. Average values of *Q* for eastern Tibet are in the 183-218 range, but this is biased low by weighted averaging of the lower *Q* values of the north and the higher *Q* values of the south. The shaded area with dashed line corresponds to the region of inefficient *Sn* propagation in northern Tibet.

CONCLUSIONS AND RECOMMENDATIONS

Tibet has broad regions with some of the strongest *Lg* attenuation values of any continental area [comparably low *Q* values have been reported for the Altiplano in Bolivia (Baumont *et al*., 1999)]. This causes effective extinction of high-frequency *Lg* energy over path lengths of just a few hundred kilometers in northern Tibet. There is substantial spatial variation in attenuation, with the strongest attenuation located in northern central Tibet, the primary region of Cenozoic magmatism within Tibet (Molnar, 1988; Turner *et al*., 1993, 1996; Arnaud *et al*., 1992). Localized regions in southern Tibet appear to have comparably strong *Lg* attenuation over relatively localized regions (Xie, in preparation). Partial melting of the deep crust may be responsible for the strong *Lg* attenuation. There is evidence for a lower crustal low-velocity zone with anomalous Poisson's ratio in northern Tibet (Owens and Zandt, 1997), along with a broad region of inefficient *Sn* propagation (Figure 8; Ni and Barazangi, 1983; McNamara *et al*., 1995) and low Pn velocity (McNamara *et al*., 1997). There is some evidence for partial melt and crustal low-velocity zones north of the Tsangpo suture in southern Tibet (Nelson *et al*., 1996; Kind *et al*., 1996; Cotte *et al*., 1999), so regions of strong *Lg* attenuation in southern Tibet may not have been resolved by our data distribution. Phillips *et al*. (2000) also find north to south gradients in *Lg* attenuation. It is also important to recognize that our results are for the relatively low-frequency band, and due to their narrow-band nature, we cannot place very good results on the frequency variations; thus extrapolation of our values to higher frequency may be erroneous. Nonetheless, we are confident that one cannot invoke uniformly low Q_o values over all of Tibet without violating many observations of high-frequency *Lg* energy at distances where it would be precluded. Systematic mapping of the spatial and

frequency dependence of *Lg* attenuation throughout the Plateau is essential prior to full assessment of the implications for regional discriminant performance in the region.

REFERENCES

Arnaud, N. O., P. Vidal, P. Tapponnier, P. Matte, and M. Deng (1992), The high K_2O volcanism of northwestern Tibet: Geochemistry and tectonic implications, *Earth Planet. Sci. Lett*., **111**, 355-367.

Baumont, D., A. Paul, S. Beck, and G. Zandt (1999). Strong crustal heterogeneity in the Bolivian Altiplano as suggested by attenuation of Lg waves, *J. Geophys. Res*., **104**, 20287-20305.

Chun, K-Y., G. F. West, R. J. Kokoski, and C. Samson (1987), A novel technique for measuring Lg attenuation – Results from Eastern Canada between 1 to 10 Hz, *Bull. Seism. Soc. Am*., **77**, 398-419.

Cotte, N., H. Pedersen, M. Campillo, J. Mars, J.F. Ni, R. Kind, E. Sandvol., and W. Zhao (1999), Determination of the crustal structure in southern Tibet by dispersion and amplitude analysis of Rayleigh waves, *Geophys. J. Int*., **138,** 809-819.

Fan, G., and T. Lay (2002). Characteristics of Lg attenuation in the Tibetan Plateau, *J. Geophys. Res*., in press.

Kind, R., *et al.* (1996), Evidence from earthquake data for a partially molten crustal layer in southern Tibet, *Science*, **274**, 1652-1654.

McNamara, T. J. Owens, and W. R. Walter (1995), Observations of regional phase propagation across the Tibetan Plateau, *J. Geophys. Res.*, **100**, 22215-22229.

McNamara, W. R. Walter, T. J. Owens, and C. J. Ammon (1997), Upper mantle velocity structure beneath the Tibetan Plateau from Pn travel time tomography, *J. Geophys. Res.*, **102**, 493-505.

McNamara, D. E., T. J. Owens, and W. R. Walter (1996), Propagation characteristics of L_g across the Tibetan plateau, *Bull. Seism. Soc. Am*., **86**, 457-469.

Molnar, P. (1988), A review of geophysical constraints on the deep structure of the Tibetan Plateau, the Himalaya and the Karakoram, and their tectonic implications, *Trans. R. Soc*. London, Ser. A, 327, 33-88.

Nelson, K. D., *et al*. (1996), Partially molten middle crust beneath southern Tibet: Synthesis of project INDEPTH results, *Science*, **274**, 1684-1688.

Ni, J. and M. Barazangi (1983), High-frequency seismic wave propagation beneath the Indian Shield, Himalayan Arc, Tibetan Plateau and surrounding regions: high uppermost mantle velocities and efficient S_n propagation beneath Tibet, *Geophys. J. R. astr. Soc*., **72**, 665-689.

Owens, T. J. and G. Zandt (1997), Implications of crustal property variations for models of Tibetan plateau evolution, *Nature*, **387**, 37-43.

Phillips, W. S., H. E. Hartse, S. R. Taylor, and G. E. Randall (2000), 1 Hz *Lg* Q tomography in central Asia, *Geophys. Res. Let*., **27**, 3425-3428.

Rapine, R. R., J. F. Ni, and T. M. Hearn (1997), Regional wave propagation in China and its surrounding regions, *Bull. Seism. Soc. Am*., **87**, 1622-1636.

Reese, C. C., Rapine, R. R., and J. F. Ni (1999), Lateral variation of Pn and Lg attenuation at the CDSN station LSA, *Bull. Seism. Soc. Am*., **89**, 325-330.

Ruzaikin, A. I., L. Nersesov, V. I. Khalturin, and P. Molnar (1977), Propagation of *Lg* and lateral variations in crustal structure in Asia, *J. Geophys. Res*., **82**, 307-316.

Shih, X. R., K.-Y. Chun, and T. Zhu (1994), Attenuation of 1-6 s *Lg* waves in Eurasia, *J. Geophys. Res*., **99**, 23859-23874.

Shin, T.-C. and R. B. Herrmann (1987), *Lg* attenuation and source studies using 1982 Miramichi data, *Bull. Seism. Soc. Am*., **77**, 384-397.

Turner, S., C. J. Hawkesworth, J. Liu, N. Rogers, S. Kelley, and P. van Calsteren (1993). Timing of Tibetan uplift constrained by analyis of volcanic rocks, *Nature*, **364**, 5053.

Turner, S., N. Arnaud, J. Liu, N. Rogers, C. Hawkesworth, N. Harris, S. Kelley, P. van Calsteren, and W. Deng (1996), Post-collision, shoshonitic volcanism on the Tibetan Plateau: Implications for convective thinning of the lithosphere and the source of ocean island basalts, *J. Petrology*, **37**, 45-71, 1996.

Xie, J. (2002), *Lg* Q in the Eastern Tibetan Plateau, *Bull. Seism. Soc. Am*., **92** 871-876.

SHORT-PERIOD (7-s TO 15-s) GROUP VELOCITY MEASUREMENTS AND MAPS IN CENTRAL ASIA

Anatoli L. Levshin,[2] Jeffry L. Stevens,[1] Michael H. Ritzwoller,[2] and David A. Adams [1]

Science Applications International Corporation,[1] University of Colorado at Boulder[2]

Sponsored by Defense Threat Reduction Agency

Contract No. DTRA01-00-C-0026

ABSTRACT

This research program is a joint project between the University of Colorado (CU) and SAIC. CU has measured a large number of surface wave dispersion curves for paths crossing central Asia. The data analysis has concentrated on short-period (7- to 15-s) measurements, which allow finer resolution than previous studies, which were performed at longer periods. The region studied includes western China, northern India, and Pakistan. Surface wave data have been obtained from more than 1600 events recorded on 240 stations of the GSN, GEOSCOPE, KNET, KAZNET, CDSN, GEOFON and MEDNET networks. In addition, data have been acquired from temporary PASSCAL networks in Saudi Arabia and Tibet. A total of 7,800 Rayleigh wave dispersion curves and 5,400 Love wave dispersion curves were recovered from the data. The Rayleigh wave dispersion measurements are organized into two groups. One group (65484 points) consists of one dispersion curve per ray path, while the other one (48590 points) is made up of summary dispersion curves found by averaging measurements made over similar paths. Two paths are defined as similar when their end points lie within 55 km of one another. In addition, Station-Specific Source Corrections (SSSC's) have been derived for Rayleigh waves at periods of 7-20 seconds for 50 International Monitoring System (IMS) acting and reserved stations. Both the dispersion data sets and SSSC's will be delivered to the Center for Monitoring Research (CMR) at the conclusion of the project.

SAIC's role in this project is to perform validation of CU's dispersion curves by testing them on IMS data at the CMR. This is being accomplished by reviewing the dispersion curves and comparing with both predicted values and other measurements along similar paths. Predictions made after incorporating the new data are then compared with a larger set of data including IMS data in addition to the input data. Predictions are made using a global earth model similar to the models used in the operational system at the International Data Centre (IDC). These models are developed by inversion of a large data set of dispersion measurements using a modification of the Crust 2.0 earth model over AK135 as a starting model. Dispersion curves calculated from the models are used for surface wave detection. The new dispersion curves being measured by CU are added to the global data set. The predictions of the model are used to perform an initial assessment of the validity of the measured dispersion curves, and then the measured dispersion curves are used to improve the models and the predicted dispersion curves. In our initial assessment of the effect of the higher frequency data on the earth models, we found that it was necessary to increase the number of crustal layers in the starting models and decrease their thickness in order to match the higher frequency dispersion data. New models were also required to match some difficult regions, such as the Tarim Basin, which strongly affect the surface wave dispersion curves. The final stage of validation will be to construct phase-matched filters from the predicted dispersion curves and then apply them to IMS data that were not part of the initial data set and assess the data compression and detection performance of the predictions.

OBJECTIVE

This research program is a joint project between the University of Colorado (CU) and SAIC. The primary objective is to measure and validate high-frequency (7-s to 15-s) surface wave dispersion curves and develop group velocity maps and earth models for Western/Central Asia, including Western China, North India, and Pakistan. The dispersion maps are then used to develop SSSC's and phase-matched filters to improve surface wave detection and measurement.

RESEARCH ACCOMPLISHED

In this project we develop improved group velocity dispersion curves and maps for West/Central Asia covering the region approximately from 10 to 50 degrees north latitude and 20 to 140 degrees east longitude. We refine existing dispersion curves; extend the curves to higher frequency (7- to 15-s period) and measure new dispersion curves. A total of 7,800 Rayleigh wave dispersion curves and 5,400 Love wave dispersion curves were recovered from the data.

Data

We acquired waveform data from IRIS DMC, GEOSCOPE and GEOFON data centers for the seismic events that occurred in 1996-2000. Altogether data from more than 1600 events recorded by about 260 stations of the GSN, GEOSCOPE, KNET, KAZNET, CDSN, GEOFON, MEDNET, and temporary PASSCAL networks in Saudi Arabia and Tibet have been acquired and analyzed. Figure 1 shows the locations of stations and events used in this study.

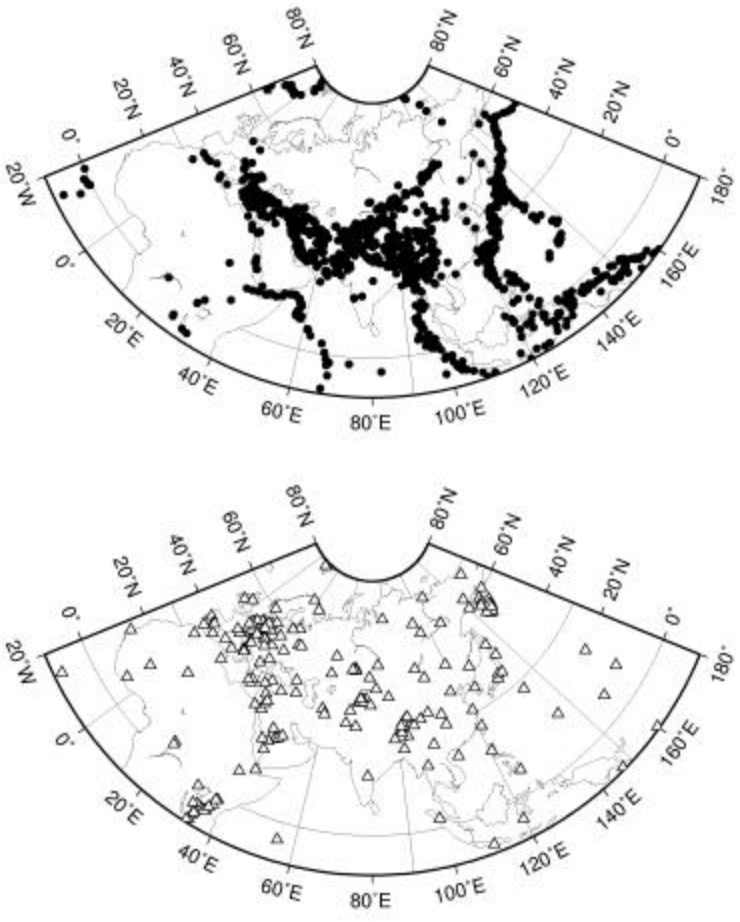

Figure 1. Locations of events (top) and stations (bottom) used in this study.

Surface wave dispersion measurements

Waveform data and accompanying information were converted into the CSS 3.0 format database. After preprocessing, these data were used for measuring group velocities of Rayleigh and Love waves in period range 7-15 s. All data were processed by seismic analysts in a semi-automatic regime using the frequency-time analysis package FTAN developed at CU (Dziewonski *et al*., 1968; Levshin *et al*., 1972; Russell *et al*., 1988; Levshin *et al*., 1992; Ritzwoller *et al*., 1995) to obtain group travel-time, phase travel-time, and spectral amplitude measurements. Group velocities and phase velocities were then computed from these travel times and distances between the receiver and the Harvard-CMT location (Dziewonski *et al*., 1981) when it existed, or, alternatively, the receiver and the PDE location. As part of FTAN, an analyst interactively designed a group velocity-period filter to reduce contamination from other waves and coda, chose the frequency band for each measurement, and assigned a qualitative grade (A - F) to each measurement. These new data were combined with an existing data set to form the input for tomographic inversion. Altogether, more than 7,800 dispersion curves of Rayleigh waves and 5,400 dispersion curves of Love waves were obtained.

Dispersion measurements were passed through several post-processing procedures for quality control. Evident outliers were rejected by comparison of observed travel times with predictions from reference group velocity maps corresponding to CU's recent global model (Shapiro and Ritzwoller, 2002). Then the measurements for close paths were combined into single common path measurements by averaging observed group velocities and rejecting outliers. The number of individual and declustered measurements as a function of period is shown in Figure 2. Declustering allows the accuracy of individual measurements to be estimated. RMS scatter of measurements at different periods is between 0.020-0.025 km/s both for Rayleigh and Love waves.

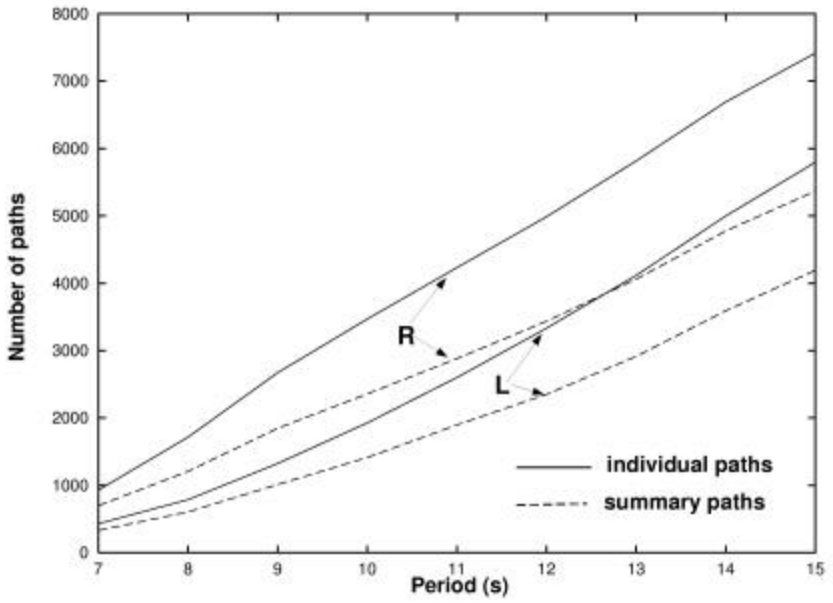

Figure 2. Number of individual and declustered measurements as a function of period for Rayleigh (R) and Love (L) waves.

The coverage of the studied region by surface wave observations varies geographically and with period. At 7 s almost all observations concentrate around KNET. At 15 s the path density is quite homogeneous across the region with an exception in Southern India. Maps of Rayleigh wave path density for several periods are shown in Figure 3.

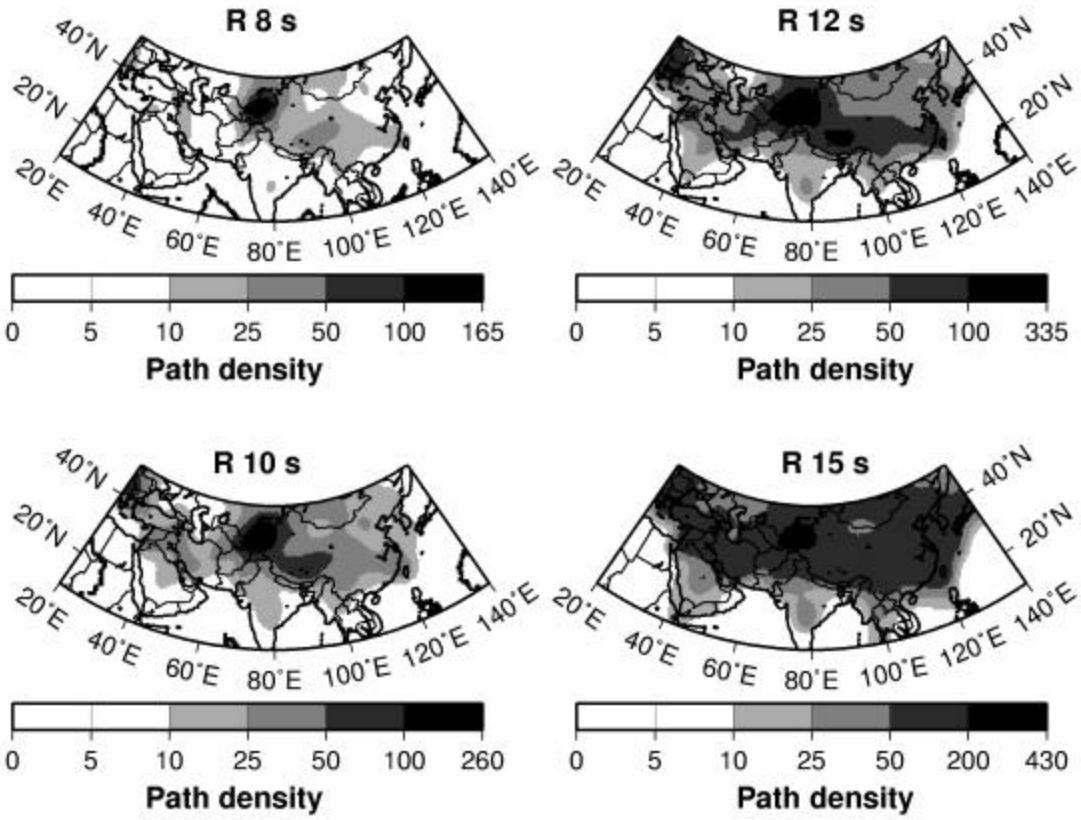

Figure 3. Rayleigh wave path density. Path density is defined as the number of paths crossing 2-degree cells.

CU Dispersion Maps and Station-Specific Source Corrections

Declustered data sets were converted to tomographic maps using the techniques described in Barmin *et al*. (2001). We produced tomographic group velocity maps for periods 7, 8, 9, 10, 11, 12, 13, 14, 15 s for Rayleigh and Love waves. As reference maps we used smoothed maps predicted by the CU global models (Shapiro and Ritzwoller, 2002). The resulting maps are accompanied by path density, resolution and amplitude bias maps, and differential maps characterizing additional signals contained in the new set of group velocity maps relative to the reference maps. The maps at 7 s are very close to the reference maps as the low density of observations penalizes perturbations relative to the initial model. As the period increases the difference between the initial maps and our tomographic maps becomes more and more significant, especially for Pakistan, Western China and N. India, indicating the presence of new information in the short-period data obtained in this study. Analysis of resolution maps demonstrates that spatial resolution changes from 300-400 km to 100-200 km with increasing period.

We calculated SSSCs for Rayleigh waves at periods of 7-20 s for 50 IMS acting and reserved stations. The SSSCs contain values of group velocity perturbation and travel time perturbation relative to the reference curve values on the one degree grid for a distance range of up to 30 degrees from the stations. An example of the SSSC for several periods is shown in Figure 4.

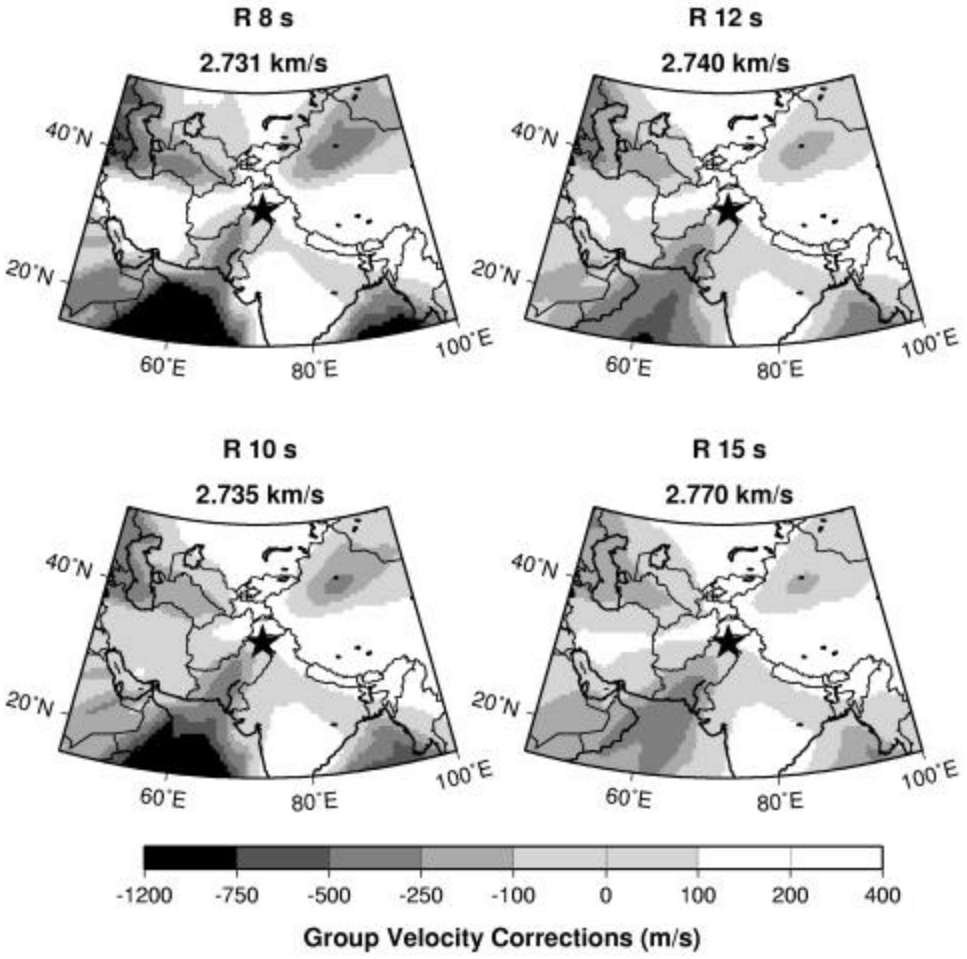

Figure 4. Rayleigh wave site-specific station corrections for station PAK0 at several periods. Values of reference velocities are shown above the maps.

Comparison of CU and SAIC dispersion maps

SAIC is performing validation of CU's dispersion curves by testing them on IMS data at CMR. This is being accomplished by reviewing the dispersion curves and comparing with both predicted values and other measurements along similar paths. Predictions made after incorporating the new data are then compared with a larger set of data, including IMS data in addition to the input data. Predictions are made using a global earth model similar to the models used in the operational system at the International Data Centre (IDC) (Stevens and McLaughlin, 2001). These models are developed by inversion of a large data set of dispersion measurements using a modification of the Crust 2.0 earth model (Laske, *et al*, 2001) over AK135 (Kennett *et al*, 1995) as a starting model (Stevens *et al*., 2002). Dispersion curves calculated from the models are used for surface wave detection. The new dispersion curves being measured by CU are added to the global data set. The predictions of the model are used to perform an initial assessment of the validity of the measured dispersion curves, and then the measured dispersion curves are used to improve the models and the predicted dispersion curves.

The SAIC dispersion maps are derived as described above by determining a set of earth structures and then calculating the dispersion. The CU maps in contrast are determined by inverting group velocity measurements to get group velocity maps for a set of periods without determining an earth model. The SAIC data set is a superset of the CU data set, incorporating other data for this region including dispersion curves derived from IMS data and explosions at the Shagan River and Novaya Zemlya test sites. Consequently, a comparison of the maps provides a good check on each. Figure 5 shows the SAIC and CU dispersion maps at periods of 10 and 20 seconds. Although there are some differences, in general they are in good agreement.

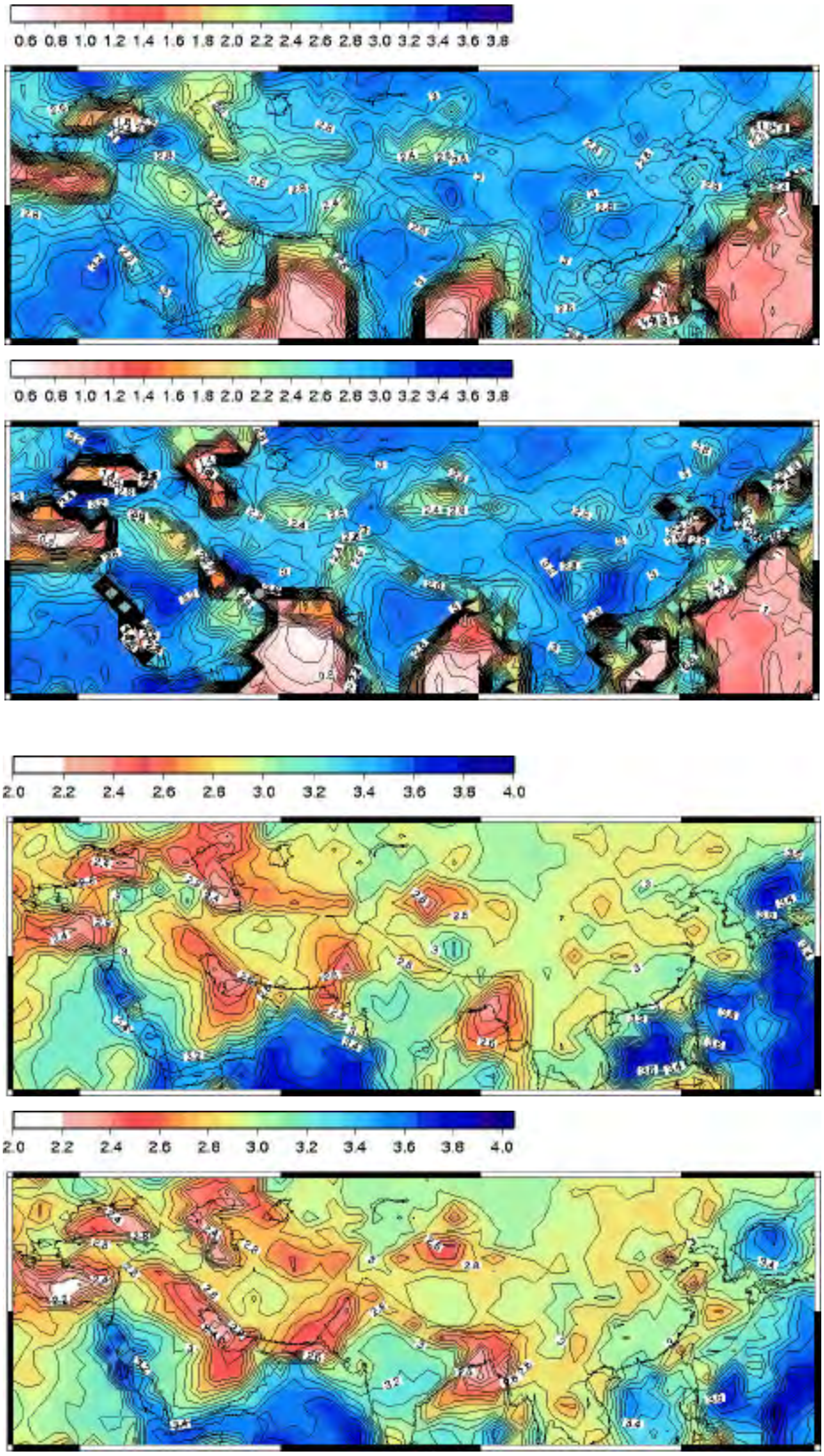

Figure 5. Group velocity maps for 10-s (top two maps) and 20-s (bottom two maps) period. Top map of each is derived using the SAIC procedure, bottom using CU procedure.

Tarim Basin group velocities

For most of the data set, we get good agreement between predicted and observed values after inversion. The Tarim Basin region in Western China, however, has proven to be difficult, so we discuss this area in some detail here. Most of the Tarim Basin data was recorded at the KNET array in Kyrgyzstan. Figure 6 shows raypaths of data recorded at this station in two frequency bands. The paths are color coded according to the slowness residual $1\text{-}s_o/s_p$ where s_o and s_p are the observed and predicted group slownesses. Blue paths indicate observed group velocity slower than predicted, red faster than predicted. In the low-frequency band (period>22 seconds), there is some variation in the residuals, but there are no large, consistent regions of data misfit. In contrast, in the high-frequency band of 0.08 to 0.15 Hz, there is a striking feature of blue rays centered in a southeast direction and passing through the Tarim Basin.

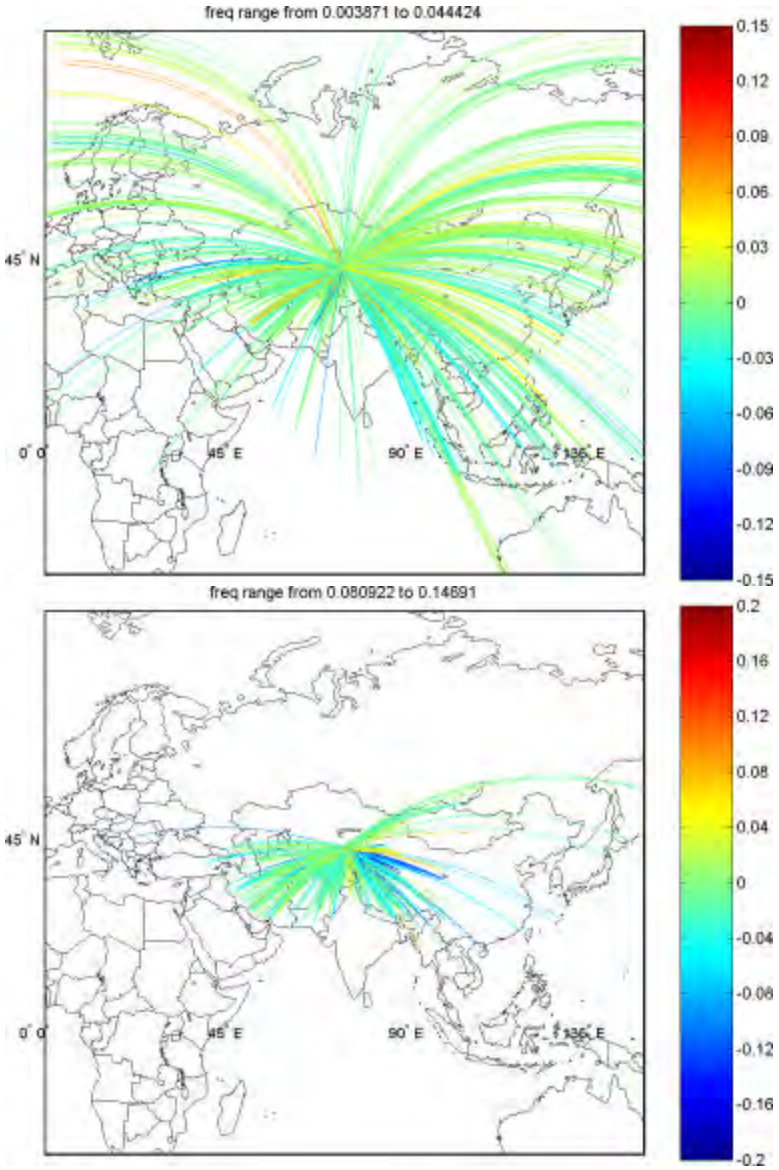

Figure 6. Paths color-coded according to residuals for group velocity dispersion curves for periods greater than 22 s (top) and for periods of 7-13 s (bottom) recorded at the station cluster in and near Kyrgyzstan.

Figure 7 shows the dispersion curves associated with these same paths. Notice the very wide range of group velocities at the higher frequencies, differing by as much as 40% over this narrow band of paths. The most northerly paths, which just skirt the Tarim Basin, are faster than the model, while the ones pointing more southerly are slower than the model.

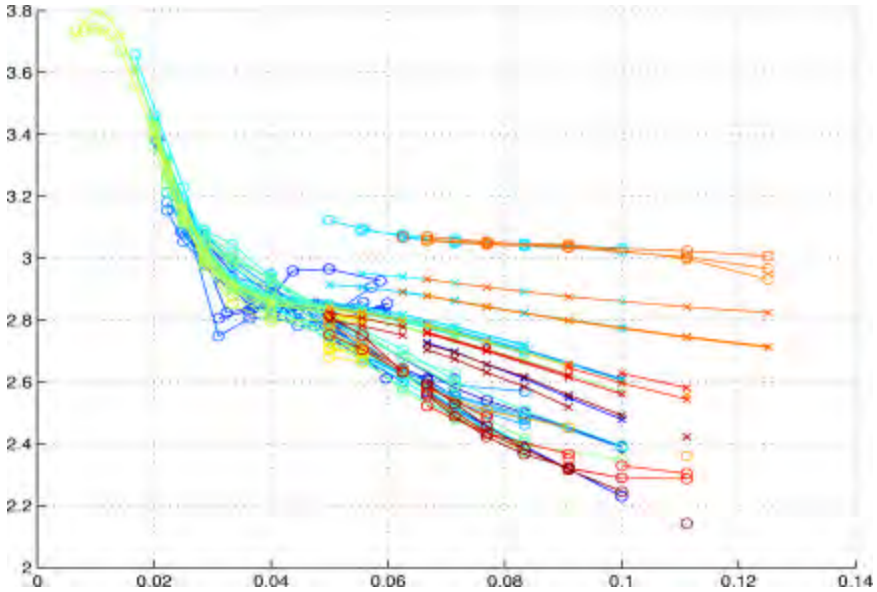

Figure 7. Group velocity dispersion curves recorded at the cluster of stations in the Kyrgyzstan cluster from sources located across the Tarim Basin. The "x"s and "o"s are predicted and observed velocities respectively. The colors are for cross-referencing between observed and predicted velocities and with the raypaths shown in Figure 8.

Figure 8 shows some of these paths plotted against the depth of sediments. The difficulty with these dispersion curves is caused by a geophysical effect – a large change in earth structure over a very small change in azimuth that causes a large change in high-frequency surface wave dispersion. In this case it is necessary to refine the model types and locations so that they accurately follow the basin boundary in order to be able to predict the dispersion.

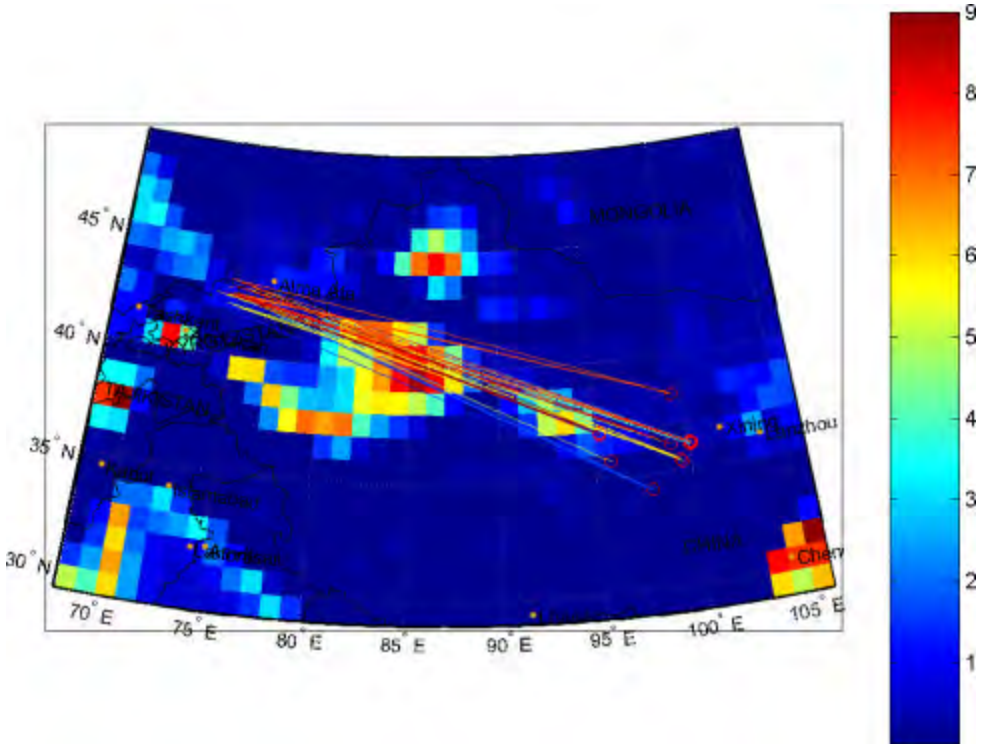

Figure 8. Paths of group velocity dispersion measurements across the Tarim Basin made at the cluster of stations in Kyrgyzstan. The color scale shows sedimentary thickness in kilometers. The ray color corresponds to the dispersion curve color in Figure 7.

Importance of high-frequency data

The higher frequency data is important for measuring low amplitude surface waves at regional distances because most of the observable surface wave energy will be in the higher frequency band. In order to predict the higher frequency dispersion and construct phase-matched filters, it is necessary to have high frequency data to constrain the models. An example is shown in Figure 9. Here we show one dispersion curve for a path running southwest of the Tarim Basin together with the predicted dispersion curve from models determined before and after addition of the new data. Without the high frequency data, the dispersion is determined primarily by the background model, and is nearly flat between 0.05 and 0.1 Hz. With the high frequency data it is clear that there is more variation in the dispersion curve at these higher frequencies, and the model adjusts to match the dispersion data.

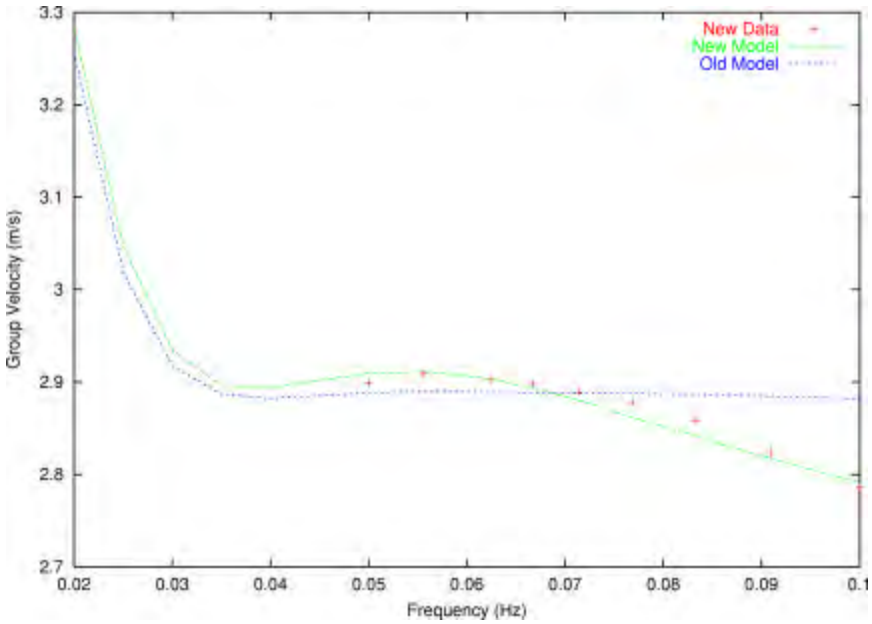

Figure 9. Dispersion curves before and after addition of new high-frequency data.

Plans

This project is nearing its conclusion. CU has completed its database of dispersion curves, tomographic inversions, and development of SSSCs. Most of the remaining effort will be on validation of the results. After completing model development as discussed above, this will be accomplished by applying phase-matched filters derived from this data set to an independent data set of IMS data traversing this region. The data set and inversion results will be delivered to CMR for distribution to other researchers at the end of the project.

CONCLUSIONS AND RECOMMENDATIONS

The high frequency dispersion data set measured by CU provides important information about earth structure and surface wave properties in Central Asia. This level of detail cannot be resolved with more typical lower frequency dispersion data. The Tarim Basin example illustrates how the high frequency surface wave data resolves the fine structure of the earth, and how strongly these structural differences can affect the surface waves. This is important because recovery of low amplitude surface waves through phase-matched filtering depends on accurate prediction of the dispersion. The results of this project will therefore lead to improved capability for identification of surface waves at a lower threshold.

REFERENCES

Bassin, C., G. Laske, and G. Masters, (2000), The Current Limits of Resolution for Surface Wave Tomography in North America, *EOS Trans AGU*, **81**, F897.

Dziewonski, A. M., S. Bloch, and M. Landisman, 1969. A technique for the analysis of transient seismic signals, *Bull. Seism. Soc. Am.*, **59**, 427 - 444.

Dziewonski, A. M., T.-A. Chou, and J. H. Woodhouse, 1981. Determination of earthquake source parameters from waveform data for studies of global and regional seismicity, *J. Geophys. Res.*, **86**, 2825 - 2852.

Kennett, B.L.N., E. R. Engdahl, R. Buland (1995), Constraints on seismic velocities in the Earth from travel times, *Geophys J Int*, **122**, 108-124.

Laske, G., and G. Masters (1997), A Global Digital Map of Sediment Thickness, *EOS Trans. AGU*, **78**, F483.

Laske, G., G. Masters, and C. Reif, Crust 2.0 (2001), A new global crustal model at 2x2 degrees, http://mahi.ucsd.edu/Gabi/rem.html.

Levshin, A. L., V. F. Pisarenko, and G. A. Pogrebinsky (1972), On a frequency-time analysis of oscillations, *Ann. Geophys.*, **28**, 211 - 218.

Levshin, A. L., M. H. Ritzwoller, M. P. Barmin, and J. L. Stevens (2001), Short Period Group Velocity Measurements and Maps in Central Asia, *Proceedings of the 23rd Seismic Research Review*, Vol. I, 258 - 269.

Ritzwoller, M. H., A. L. Levshin, S. S. Smith, and C. S. Lee (1995), Making accurate continental broadband surface wave measurements, in *Proceedings of the 17th Seismic Research Symposium on Monitoring a CTBT*, (ed. J. F. Lewkowicz, J. M. McPhetres, and D. T. Reiter), Phillips Lab., Hanscom AFB, Mass., 482 - 490.

Russell, D. W., R. B. Herrman, and H. Hwang (1988), Application of frequency-variable filters to surface wave amplitude analysis, *Bull. Seismol. Soc. Am.*, **78**, 339 - 354.

Shapiro, N. M. and M. H. Ritzwoller (2002), Monte-Carlo inversion of surface waves (Inversion of broad-band surface-waves with the a-priori information), *J. Geophys. Res.*, in press.

Stevens, J. L., W. L. Rodi, J. Wang, B. Shkoller, E. J. Halda, B. F. Mason, and J. B. Minster (1982), Surface wave analysis package and Shagan river to SRO station path corrections, S-CUBED topical report submitted to VELA Seismological Center, SSS-R-82-5518, April.

Stevens, J. L. and K. L. McLaughlin (2001), Optimization of surface wave identification and measurement, *Pure and Applied Geophysics*, **158**, no. 7, pp 1547-1582.

Stevens, J. L., D. A. Adams, and G. E. Baker (2001), Phase-matched filtering with a one degree dispersion model, *Proceedings of the 23rd Seismic Research Review*, Vol. I, 420 - 430.

Stevens, J. L., D. A. Adams, and G. E. Baker (2002), Improved surface wave dispersion models and azimuth estimation techniques, *Proceedings of the 24th Seismic Research Reveiw*.

SEISMIC REGIONALIZATION IN NORTHEAST RUSSIA

Kevin G. Mackey,[1] Kazuya Fujita,[1] Lee K. Steck,[2] and Hans E. Hartse[2]

Michigan State University,[1] Los Alamos National Laboratory[2]

Sponsored by National Nuclear Security Administration
Office of Nonproliferation Research and Engineering
Office of Defense Nuclear Nonproliferation

Contract No. DE-FC03-02SF22490[1] and W-7405-ENG-36[2]

ABSTRACT

In an effort to characterize seismicity in support of nuclear explosion monitoring for the continental regions of northeast Russia, we have been analyzing information obtained from regional seismic network operators. Our goal is to merge catalog, bulletin, waveform, and other ground truth data from several regional networks into a comprehensive data set that we will use for various seismic research projects. To date we have compiled a bulletin from published and unpublished event data of about 200,000 events and over 150,000 arrival times. We have also determined that the Russian regional network catalogs are contaminated with mining-explosion events. Hence, one of our primary efforts is to identify mining events when possible and move them into a separate bulletin from the natural earthquakes.

We have extended our preliminary analysis of explosion contamination of Russian seismicity catalogs using temporal analysis into the Irkutsk and Chita districts and the Buryat Republic. Based on analysis of epicenters and origin times reported in *Material po Seismichnost' Sibiri* for 1970 – 1993, it is likely that considerable explosion contamination occurs in the gold (Bodaibo, northern Irkutsk Region, and in the Chita region), mica (Vitim, northern Irkutsk Region), and other mining areas (Bushulei, Nerchinsk, and Petrovsk in the Buryat and Chita areas). Explosion contamination is also observed in northernmost Mongolia in the mining and industrial district near Darkhan. Explosions associated with the construction of the Baikal-Amur Mainline Railroad are likely, as was observed in the Amur district; however, the amount of natural seismicity dominates the activity and makes it impossible to resolve the railroad separately.

In conjunction with the Magadan Seismic Network operators, we have deployed a small network of digital stations to aid in our calibration efforts. We have been obtaining digital waveforms from this deployment for several years. As part of our current project, we will be deploying additional stations in other regions of Siberia. In the later stages of this three-year project, we will derive regional velocity models, calibrate regional magnitude scales [such as mb(Lg) and mb(coda)], test regional event discriminants, and rank ground truth events for calibration of far-regional and teleseismic stations.

OBJECTIVE

The objective of our research is to improve event location and identification capability in northeast Russia in support of nuclear-explosion and treaty monitoring. We plan to reach our objectives through (1) collection, analysis, and merging of regional catalogs and bulletins, (2) deployment of additional digital seismic stations in northeast Russia, (3) relocating events and estimating appropriate correction surfaces for improved locations, and (4) analysis of waveform characteristics to identify effective regional event discriminants.

RESEARCH ACCOMPLISHED

This is a newly-funded project that has been underway for only a few months. However, to date we have obtained bulletins and catalogs, begun merging and analysis of the bulletins, and deployed new stations in northeast Russia.

We have expanded our previous seismicity catalog (Mackey and Fujita, 2001a) for northeast Russia (Figure 1; approximately 200,000 events) to include the Irkutsk district, the Buryat Autonomous Republic, and the Chita district. These areas are under the auspices of the Irkutsk regional seismic network. Catalog data were obtained from *Materialy po Seismichnost' Sibiri* (1970-1993; Data on the Seismicity of Siberia; hereafter *Materialy*), a bi-monthly publication with both epicenter lists and phase data for the continental seismic networks in Siberia (Irkutsk, Magadan, Yakutsk, Amur (1979-1993) and Altai). We have supplemented this listing with catalog data from the Irkutsk regional network (1993-1996). For the Irkutsk network, the catalog is generally complete for K-class greater than about 8 (approximately magnitude 2 ¾; Figure 2). Data for the Kamchatka peninsula were obtained from the Kamchatka seismic network.

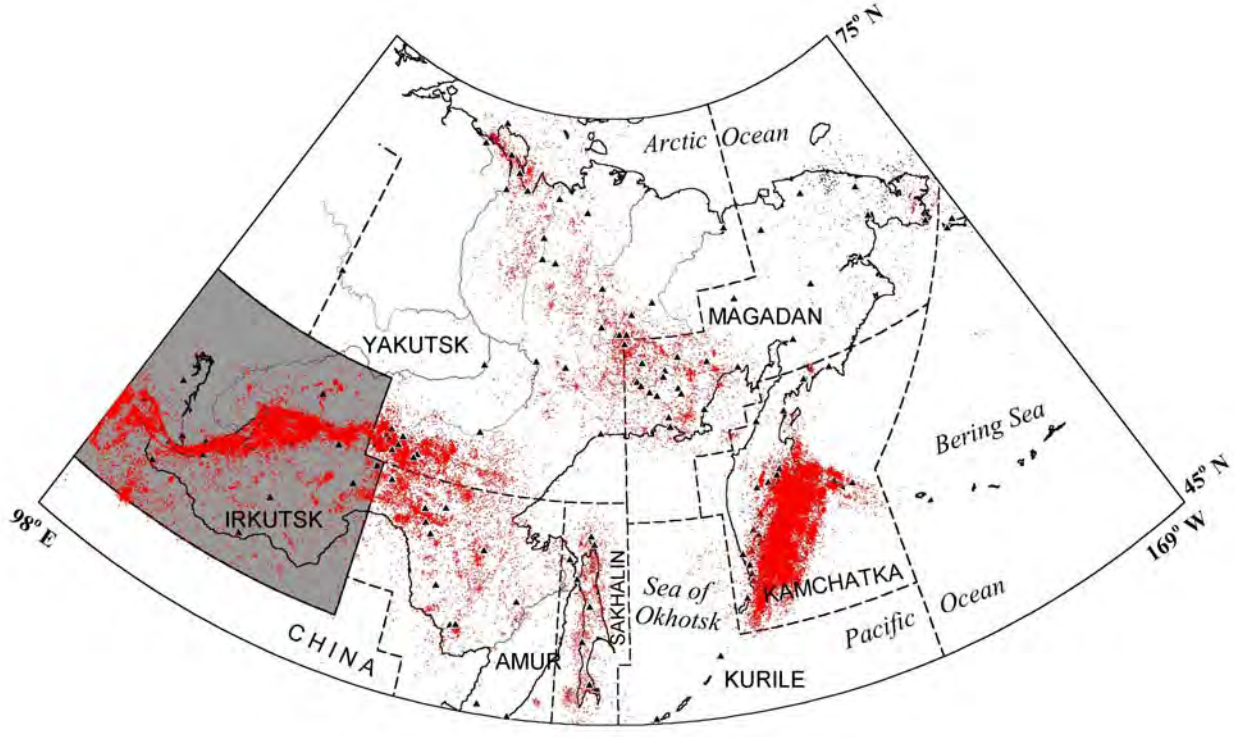

Figure 1. Seismicity catalog of northeast Russia depicting approximately 200,000 events. Events of the Irkutsk network (shaded gray) were recently incorporated into the catalog. Seismic network boundaries are depicted by dashed lines and historically operated seismic stations by triangles.

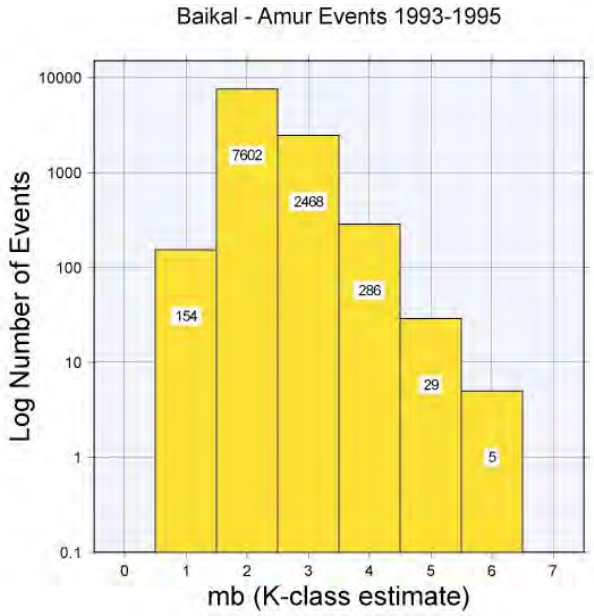

Figure 2. Histogram for the earthquakes in the Irkutsk network (1993-1995) showing magnitude (derived from K-class) versus number of events. This indicates that the catalog is complete for events larger than magnitude 2.5 or 3.0, which corresponds to a K-class of about 8.

Explosion Contamination

The seismicity catalog for the Irkusk, Buryat, and Chita regions is presumed to be contaminated by a large number of industrial explosions (e.g., Godzikovskaya, 1995) in a manner similar to other areas discussed in our previous study (Mackey and Fujita, 1999). As in the rest of eastern Russia, explosions occur in mica, iron, tin, coal, and placer gold mines, as well as in prospecting and the construction of roads, railways, and dams. In the study area, many of the active mines are located outside highly seismically active regions, which makes identification of regions contaminated by mining explosions relatively easy. However, much of the blasting associated with the construction of the Baikal-Amur railroad (BAM) occurs in regions of high tectonic activity that mask all but the highest levels of explosion contamination. Contamination of the seismicity catalog with explosions here, as elsewhere, results in an erroneous perception of the level and distribution of natural seismicity.

As in our previous study (Mackey and Fujita, 1999), a qualitative estimate of the level of explosion contamination and levels of natural seismicity can be obtained by examining the spatial and temporal characteristics of earthquakes located by the regional networks (e.g., Agnew, 1990). The study area was divided into cells in which the percentages of daytime earthquakes are calculated. Cells containing fewer than ten events were not considered to be statistically significant, and were not analyzed. The 12-hour local “day” has been shifted according to time zones. Light blue (light gray) areas in Figure 3 represent regions where seismicity is roughly balanced between night and day, and dark blue (dark gray) areas are those in which seismicity is concentrated during local night (>65%). There are several areas of night time-biased seismicity, most of which are in seismically less active regions and away from seismic stations. This is not unexpected since almost all seismic stations in the area are located in populated areas, and thus have lower cultural noise during the night.

Pink (medium gray) areas on Figure 3 represent regions where more than 65% of the seismicity occurs during local “day”. Many of the regions with predominantly daytime events are found in discrete clusters or trends of seismicity, most of which can be associated with mining or construction related blasting. Several clusters of seismicity in the Patom Highlands region have more than 90% of the events occurring during local day. Below, we examine several regions, shown in Figure 3, of daytime bias that can be positively related to explosion contamination.

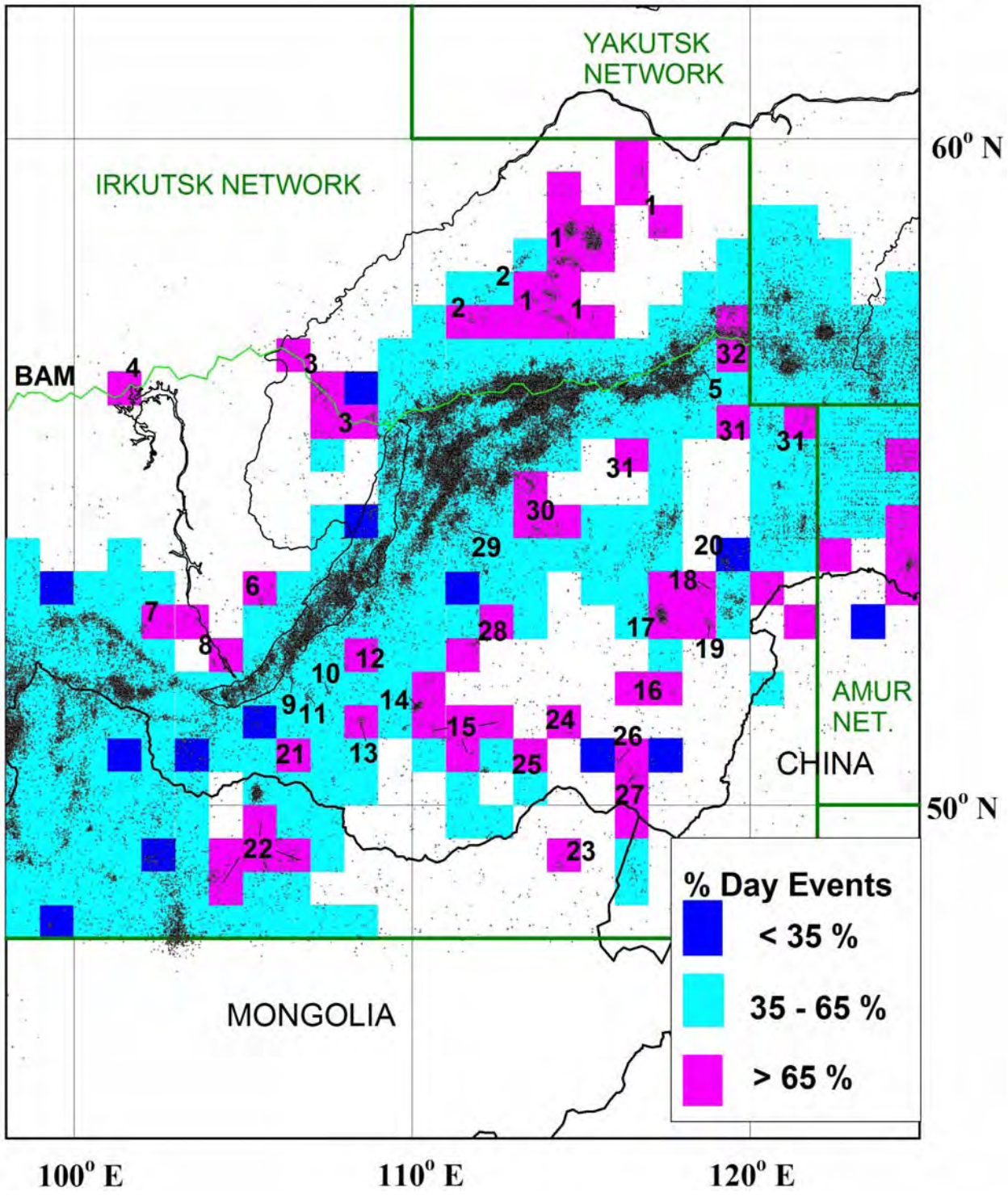

Figure 3. Seismicity of the Irkutsk network showing percentages of daytime events by cell. Explosion contamination of the seismicity catalog is suspected where cells are pink (> 65% of the events occur during local daytime). Numbers are keyed to text. The green line depicts the Baikal Amur Mainline railroad (BAM).

Recently, there have been attempts to filter explosions and many areas of explosion activity have been identified for the late 1990s (Masal'sky, pers. com.); however, analysis of temporal distributions remains the best way to study contamination of the historical seismicity catalog. Industrial explosions locatable by the regional networks have magnitudes of about 1.5 - 3.0 and occur during the local day (Godzikovskaya, 1995; Odinets, 1996). Placer deposit explosions are also concentrated during the late winter and early spring, when frozen ground is broken up for the summer processing season. Because few explosions exceed magnitude 3.5, teleseismically recorded events in the historical catalog are not likely to be contaminated. A small, but not statistically significant, number of explosions are also known to occur at night (Godzikovskaya, 1995) since Russian law requires that explosives loaded into boreholes can not be kept overnight, but must be detonated (V. N. Kovalev, pers. comm.). This results in some night blasting, and is supported by a small number of night time explosions listed in the network bulletins.

Explosion Contamination by Region

Possible anthropogenic origins of explosion contamination identified in the compiled seismicity catalog were researched using various publications on tourism and economic geography of eastern Russia, 1:200,000 Soviet military topographic maps, and 1:500,000 and 1:1,000,000 US air navigation charts.

One of the clearest regions of explosion contamination is the **Patom Highlands** (Area 1, Figure 3). Here, almost all of the seismicity is biased towards local daytime. This is an extensive region of placer gold mining (Shabad, 1969). The clusters of seismicity are centered on mining centers located at Marakan, Kropotkin, Svetlyi, Artemovsky, and Bodaibo. Additional areas of probable gold mining activity are located along the road between Perevoz and Chapaevo, near Bul'bukhta, and along the Pravyi Mamakan River. It is possible that some events could be related to construction of the dams on the Pravy Mamakan River. Analysis of events from the mid-1990s indicates that there is a tremendous bias with almost all events occurring between 2100 and 1400 UTC, and no events between 1400 and 2100 UTC (Figure 4). Events, however, appear to occur seven days a week, but with a peak in mid-week.

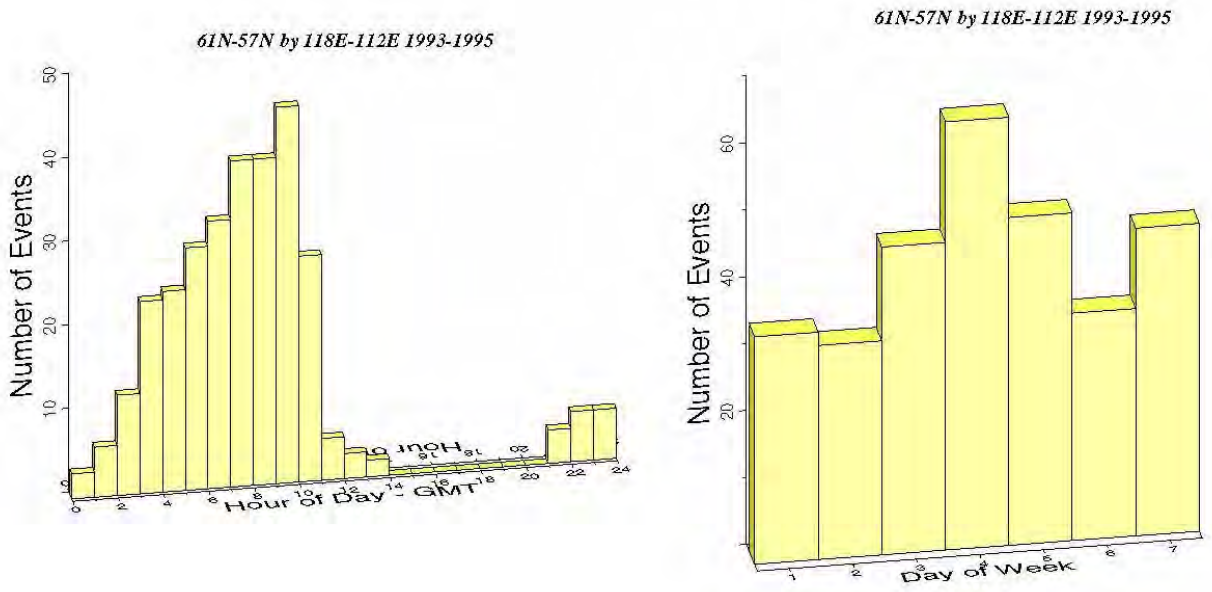

Figure 4. Histograms of reported earthquakes in the Patom Highlands region. The left histogram depicts number of events vs. time of day, with almost all events occurring during local day (GMT 0-11 hours). The right histogram depicts number of events vs. day of week, showing an increase in activity mid-week.

A series of phlogopite mica mines lies along the **Mama and Vitim Rivers** (area 2; Shabad, 1969). The northern part of this trend, near the Vitim River, shows no temporal seismicity bias, although events occur along the mining trend. A cluster of daytime biased events, however, occurs south and southeast of Gorno-Chuisk at the southern end of the mica mining district.

A series of grid squares located along the **BAM** (area 3) between Ust' Kut and Severo Baikal'sk show daytime biases. A small cluster at the eastern end near the now abandoned settlement of Granitnyi may be associated with the construction of the Del'bichinda Tunnel, which was completed in 1984 (Yates and Zvegintzov, 2001). Further west, a cluster of events is found slightly offset to the southwest of the BAM between Nebel' and Okunaisky. As no mining is known in this area and construction of the BAM here occurred in the late 1970s and early 1980s, these events are likely associated with construction, as is the cluster of events east of Ust' Kut.

A daytime biased cluster is also located near **Bratsk** (area 4), the site of the Bratsk hydroelectric station as well as a large industrial complex. As no nighttime events occur here, it is presumed that these represent explosions related either to construction or to other industrial activity; mining is not associated with this area.

No events are associated with two large iron mining complexes in the area, at Zelenogorsk-Ilimsk and Rudnogorsk (Yates and Zvegintzov, 2001); thus, they must either be too small to be recorded at the network (the closest stations are 400-500 km away), or the operators are able to identify these events.

No strong signal is observed near the **Udokan** copper mines (area 5); however, they lie in an area of high tectonic activity. It is possible that a detailed search of the area would identify either exploratory blasting or blasting associated with infrastructure being built in the area (Yates and Zvegintzov, 2001).

An unexplained cluster of daytime events occurs near Bayandai (area 6) in the **Bayandaevskii Raion** of the Ust' Ordynskii Buryat Autonomus Okrug, which is close to a cluster of explosions identified by the Irkutsk network at the Kharanut coal mine (Gorkin, 1998). A smaller cluster is located northeast of Bayandai near the town of Khogot. The only mineral deposit reported in the Bayandai area consists of white clay (Gorkin, 1998).

A cluster of daytime activity occurs at **Onot** (area 7), the site of talc production (Sherbakov, 1991). There is no significant signal from the nearby coal mines in the Cheremkhovo area.

Daytime biases with a small amount of seismicity are associated with the industrial cities along the **Angara River** (area 8; Usol'e Sibirskoe, Angarsk, and Irkutsk). As no significant mining occurs in these areas, it is presumed that these are explosions related to industrial activity.

South of the active Baikal seismic belt, there are numerous areas of presumed explosion contamination. Many of them lie along the Trans-Siberian Railroad and along its two major branches, the Trans-Mongolian and Trans-Manchurian routes. We discuss these from west to east along the rail lines.

Although not identified in our statistical calculations, a cluster of daytime bias stands out just off of the eastern coast of Lake Baikal between **Bol'shaya Rechka** (area 9) and Selenga. The events trend to the east-southeast, but probably are due to an east-west striking chain of limestone quarries located south of the Selenga River.

A small cluster of events also identifies the town of **Ulan Ude** (area 10), a major manufacturing center, while an unattributed cluster of daytime events occurs near the settlement of **Khuramsha** (area 11), 40 km to the southwest; no mining or industrial activity has yet been attributed to this area.

To the northeast of Ulan Ude, a diffuse cluster is located in the southern part of the **Ulan Burgassy Range** (area 12). These may be associated with the Balbagar iron ore deposit (Thiel, 1957), but are offset to the north and west; alternatively they may be exploratory blasting.

The next cluster of presumed explosions is in the area to the west of **Petrovsk-Zabailak'sky** (area 13). There are a number of mining towns in this area associated with deposits of gold, tungsten, tin, lead, zinc, molybdenum, and lithium (Thomas, 1997). Specific clusters appear to center on the towns of Shabur, Kusoty, and Khonkholoi. There is no contamination associated with the coal mines along the Khilok River (e.g., Kataevo, Balyaga, Kuli, Tarbagatai, and the large pit at Novo Pavlovsk)

A cluster along the Trans-Siberian Railroad near Glinka and Zhipkhegen is elongated along the railroad line (area 14). However, the main locus of possible explosion activity is a mine just to the north of **Zhipkhegen**. Either the location procedures cause a smearing of the blast locations or there may have been expansion of the mining area along the foothills of the Tsagan-Kurtei Range. Resources in the region include sand, clay, gravel, coal, and some minerals (Gorkin, 1998).

To the southeast, daytime bias is found along the highway between Chita and Khilok along the upper **Ingoda** and **Arei Rivers**, including the settlement of Leninsk (area 15). Known mineral deposits in this area include gold ore, tungsten, uranium, and coal (Gorkin, 1998). Although the region was developed as an agricultural base, it is probable that there has been recent development or exploration in some of these deposits.

A very small and perhaps statistically marginal cluster of events is found around **Nerchinsk** and to the east (area 16). Nerchinsk is an old gold and silver mining area. No noticeable events are associated with gold mining at Balei to the south and Vershino-Darasunsky to the northwest (Shabad, 1969).

The largest cluster of daytime biased events occurs in the area of **Bushulei** (area 17), a gold and molybdenum mining district (Thomas, 1997) located on the Trans-Siberian railroad. The main mines are located to the east of the railroad. There is no significant signal from the coal mines at Bukachacha (Shabad, 1969) to the northwest of Bushulei .

A diffuse cluster of events lies along the **Chernaya River** valley (area 18), southeast of Sbega. As of about 1990, no development was known in this area. However, given the proximity of gold mining districts to the northeast and south, it is possible that this represents some exploratory activity. The compact cluster to the south is associated with the **Ust' Kansk** (area 19) gold mining district (Thomas, 1997).

A cluster that does not appear in the grid search, but is apparent by inspection, is located south of the Trans-Siberian railroad in the area of the Davenda molybdenum mine and the **Klyuchevsky** gold mine (area 20; Shabad, 1969). The open pit mine at Klyuchevsky is a more likely site for larger explosions; however, in 1999-2000, the Irkutsk network identified activity as being dominantly from Davenda.

Along the Trans-Mongolian railroad south of Ulan Ude, a small cluster of daytime biased events is found near **Novoselenginsk** and southeast of Ozero Gusinoe (area 21). Although these events may be associated with coal mining at the Kholboldzhinsky mine on the southeast edge of Ozero Gusinoe, the fact that explosions from all other coal mines seem to have been excluded from the catalog makes it unlikely that events from this large complex would be included; thus, an alternate cause is suspected.

Further south, presumed mining and industrial events occur in **northern Mongolia**, in particular near the huge copper mine at Erdenet, and the industrial and mining towns of Ornon, Darkhan, and Sharyn Gol (area 22; Mayhew, 2001). The Irkutsk network has also identified numerous explosions from Darkhan and Erdenet in the past few years. However, a cluster in an uninhabited area of northeast Mongolia **north of Choibalsan** (area 23) is difficult to explain.

Several clusters of presumed industrial explosions are found along and near the route of the Trans-Manchurian Railroad. Southeast of Chita there is a cluster of activity near **Orlovsk** (area 24), the site of a tantalum mine (Shabad, 1969). Another cluster, which can not be attributed at this time, occurs near **Taptanai** (area 25); however, deposits of tungsten and gold are reported in the area (Gorkin, 1998).

A compact cluster of daytime events is located near **Mirnaya** (area 26), and a larger cluster near **Sherlovaya Gora** (area 27). Tin and coal mining is concentrated near the latter town (Shabad, 1969). Other mining in the area associated with flourspar (Kalangui and Klicha) and lithium (Akatui, Gornyi Zerentui, and others), do not register in our analysis.

Finally, several clusters of presumed industrial events are found north of the Trans-Siberian and south of BAM, mainly in the Buryat Autonomous Republic. Two centers of presumed explosions are located about 100 km

northwest of Chita. These events cluster around the towns of **Sosnovo-Ozerskoe and Isinga** (area 28). Limestone quarrying is known in the Sosnovo-Ozerskoe area and polymetallic ores are found in the region (Gorkin, 1998).

A small cluster of daytime bias is noted near the settlement of **Karaftit** (area 29) where there is a gold mine (Shabad, 1969), although the search grid box is statistically dominated by the tectonic activity of the Baikal rift zone. Further east, large clusters of daytime events are located around **Tsipikan**, Bagdarin, Severnyi, Mongoi, and Rossoshino (area 30). These areas are alluvial deposits worked by dredging (Thiel, 1957).

Three grid squares (areas 31) with greater than 65% daytime events are found in the far northern part of the Chita oblast. None of these can be associated with mining or construction. Only one square, encompassing **Kalakan**, is associated with a populated point. These may be due to the small number of statistics or to exploratory drilling.

Finally two grid squares bracketing the BAM (area 32) are found around **Mururin**. It is surprising that these two grid squares alone along the tectonically active part of the BAM yielded strong daytime biases. Since there is a significant amount of nighttime seismicity here as well, there is likely both natural and anthropogenic activity. One possible explanation is that this section of the BAM is the highest (Yates and Zvegintzov, 2001) and considerable blasting was likely required in its construction.

Based on the above analysis, it is apparent that explosions at coal and iron mines have been fairly well filtered, even prior to the late-1990s, and are not included in the seismicity catalogs. Explosions associated with placer gold and construction, and some quarrying, however, are still prevalent in the catalogs.

Digital networks and deployments

Our current research will incorporate data recorded by existing digital stations throughout eastern Russia. Currently the Irkutsk network operates 19 (excluding the IRIS station TLA) and the Yakutsk network four (excluding the IRIS stations YAK and TIXI) digital stations (Figure 5). We will also continue development of our digital station network in northeastern Russia to improve epicenter locations and begin a program to develop seismic discriminants in support of nuclear-explosion and treaty monitoring by digitally recording local explosions and earthquakes. Deployment of these stations began under a previous project (Mackey and Fujita, 2001a). At present, we have eight permanent stations deployed in and operated in conjunction with the Magadan and Yakutsk networks of northeast Russia (Figure 5). All stations are 3-component, with three stations recording broadband instruments. The remaining stations use short-period Russian seismometers (SKM-3 or SM3-KV). All seismometer outputs are digitized at 30 samples per second with 24-bit resolution and logged on a PC. Our current project will deploy additional digital stations throughout northeastern Russia, primarily supplementing existing digital stations in the Irkutsk and Yakutsk networks (Figure 5). Most of these new stations will use Geotech Instruments KS-2000 broadband seismometers. To aid in the acquisition of ground truth data, three additional portable digital stations will be maintained for temporary deployment at mine sites or in aftershock studies. Ultimately, one aspect of this project will be to combine digital waveform data from all digital stations in northeast Russia into a single database containing both earthquakes and explosions.

Using the existing deployed stations in the Magadan network, we have thus far recorded several hundred earthquakes, and mine blasts from many locations throughout the Magadan region with yields ranging up to or exceeding 40 T. To obtain ground truth information on explosions, we have either visited or deployed temporary stations at mine sites, and we have been able to obtain information on blast size and location. Additional information and seismograms from early stages of this deployment can be found in Mackey and Fujita, 2000, and Mackey and Fujita, 2001 a,b. In addition, we plan to deploy our temporary stations at mine sites as we expand our digital network and use data acquired for ground truth studies.

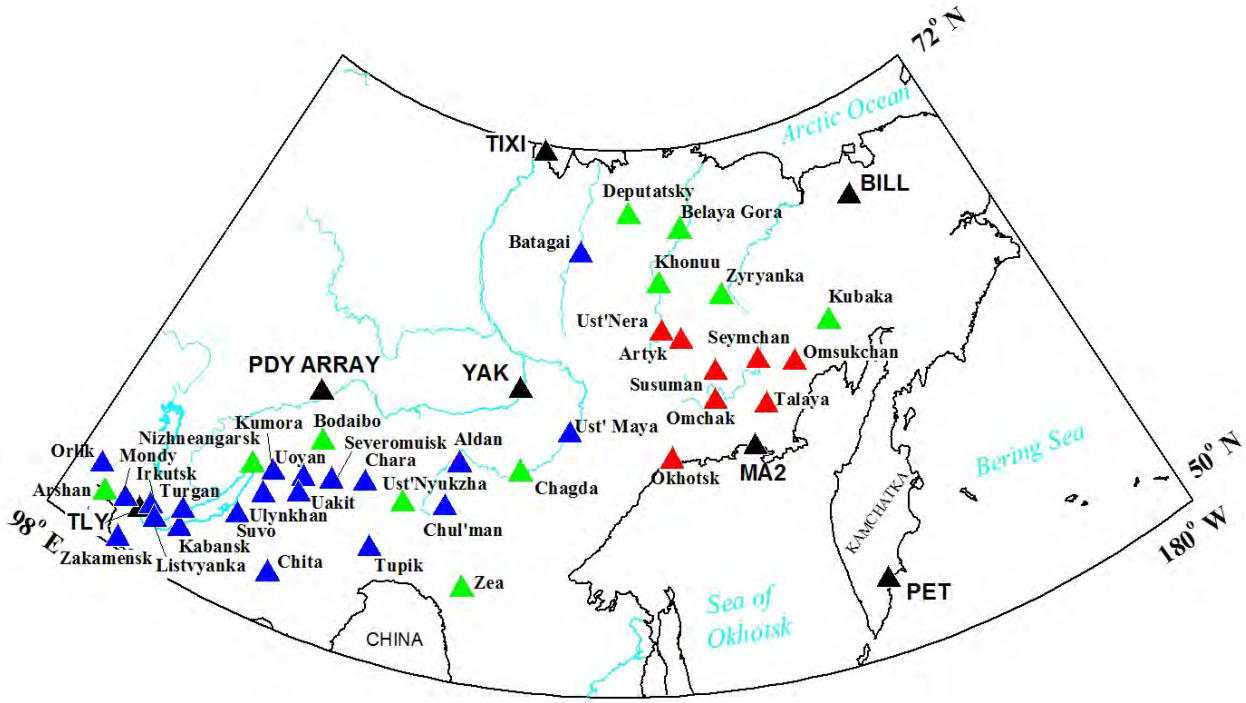

Figure 5. Digital stations in northeastern Russia to be used in this study. Red triangles – digital stations operated jointly between Michigan State University and local seismic networks. Black triangles – IRIS and International Monitoring System stations. Blue triangles – digital stations operated by Russian seismic networks. Green triangles – preliminary sites for additional stations to be deployed as a part of this study.

CONCLUSIONS AND RECOMMENDATIONS

We have begun an ambitious project to compile a complete seismic catalog and bulletin for northeast Russia to use for ground truth studies and develop velocity models for the region. We are also in the process of deploying a digital seismic network in northeast Russia in cooperation with local network operators. Waveform data from our network will be combined with that from other existing digital stations to improve monitoring in the area and develop seismic discriminants. Additional portable digital stations will be maintained in the region for rapid deployment at active mine sites to record explosions or to record aftershocks from large events if the opportunity arises.

ACKNOWLEDGEMENTS

We thank the operators and seismologists of the Irkutsk, Yakutsk, Magadan, and Kamchatka seismic networks for assistance in compiling this database.

REFERENCES

Agnew, D.C., (1990). The use if time-of-day seismicity maps for earthquake/explosion discrimination by local networks, with an application to the seismicity of San Diego county, *Bulletin of the Seismological Society of America*, v. **80**, p. 747-750.

Godzikovskaya, A.A., (1995). *Local Explosions and Earthquakes*: Rossiskoe Aksionernoe Obshchestvo Energy and Electrification “EES Rossii” Moscow, p. 55-66 (In Russian).

Gorkin, A. P., ed., (1998). *Geography of Russia*: Bol’shaya Rossiiskaya Entsiklopediya, Moscow, 799 pp.

Mackey, K.G., and K. Fujita, (1999). The northeast Russia seismicity database and explosion contamination of the Russian earthquake catalog, *in Proceedings of the 21st Seismic Research Symposium: Technologies for Monitoring The Comprehensive Nuclear-Test-Ban Treaty*, v.1, p.151-161.

Mackey, K.G., and K. Fujita, (2000). Event relocations and seismic calibration in northeast Russia, *in 22nd Annual DoD/DOE Seismic Research Symposium: Planning for Verification of and Compliance with the Comprehensive Nuclear-Test-Ban Treaty (CTBT), Proceedings*, vol. 2: *US Department of Defence*, Dulles, VA, p. 223-232.

Mackey, K.G., and K. Fujita, (2001a). *Seismicity Characterization and Velocity Structure of Northeast Russia, Final Scientific Report*: Michigan State University, East Lansing, xviii + 162.

Mackey, K.G., and K. Fujita, (2001b). Seismic calibration and discrimination in northeast Russia, *in Proceedings of the 23rd Seismic Research Review: Worldwide Monitoring of Nuclear Explosions*, vol. 1**:** National Nuclear Safety Administration, *US Department of Energy*, p. 80-89.

Materialy po Seismichnost' Sibiri, 1970-1993: Academy of Sciences of the USSR, Siberian Branch, Irkutsk (bi-monthly, in Russian).

Mayhew, B., (2001). *Mongolia*: Lonely Planet Publications, Melbourne, 319 pp.

Odinets, M.G., (1996). The problem of polluting the earthquake catalog with industrial blasts in northeastern Russia, *in* Lin'kova, T.I., and Bobrobnikov, V.A., eds., *Geophysical Models of Geologic Processes in Northeast Russia*: NEISRI, Magadan, p. 90-99 (in Russian).

Shabad, T., (1969). *Basic Industrial Resources of the USSR*: Columbia University Press, New York, xiv+393 pp.

Sherbakov, L. M., (1991). Mineral Resources of the USSR, in Kozlovsky, E. A., ed., *Mining Encyclopedia: Sovetskaya Entsiklopediya*, Moscow, v. 5.

Thiel, E., (1957). *The Soviet Far East*: Frederick A. Praeger, New York, 388 pp.

Thomas, B., (1997). *Trans-Siberian Handbook (4th Edition)*: Trailblazer Publications, Surrey, 416 pp.

Yates, A., and Zvegintsov, N., (2001). *Siberian BAM Guide*: Trailblazer Publications, Surrey, 384 pp.

AMPLITUDE ANALYSIS AND MODELING OF PEACEFUL NUCLEAR EXPLOSION RECORDINGS

Igor B. Morozov, Scott B. Smithson, Hongyan Li, and Joel N. Duenow

University of Wyoming

Sponsored by Defense Threat Reduction Agency

Contract No. DTRA01-01-C-0057

ABSTRACT

For a number of years, in cooperation with the Centre of Regional Geophysical and Geological Research (Centre GEON), Moscow, Russia, the Reflection Seismology group at the University of Wyoming has been analyzing the unique recordings of Peaceful Nuclear Explosions (PNEs) in Russian Eurasia. Recent studies included imaging two-dimensional velocity, reflectivity, and P-wave attenuation of the upper mantle to ~700-km depth, interpretation of high-frequency scattering, and seismic coda. In this new project, we focus specifically on the analysis of the spectral properties of *Lg*, crustal and upper mantle attenuation using the spectral and coda decay information extracted from the PNE records.

At this early development stage of the project, we present plans of data measurement and modeling techniques. Relative spectral amplitudes for both attenuation and coda studies are derived using multi-taper techniques designed to increase the stability of the estimates in respect to the effects of noise. Owing to a generalized formulation of the spectral estimation problem (implemented in an object-oriented code using C++ programming language), virtually the same technique is used for the measurements of both *P*-wave spectral attenuation (t*), *Lg Q*, and *Lg* coda *Q*. Preliminary results using five of the available PNE profiles show *Lg* coda *Q* values similar to those obtained previously in our studies of a part of profile QUARTZ. From these measurements, we plan to produce crustal and upper mantle *Q* values that are required for large-scale simulation of propagation of the regional phases (*Lg*, *Pg*, *P*, and *S*) across Northern Eurasia

Our current modeling effort is targeting simulation of a realistic, three-component coda created by a distant PNE source. Since, as we have argued previously, three-dimensional (3-D) simulations are required for a correct description of short-period coda of PNE arrivals, we perform our modeling in 3-D by employing a single-scattering (Born) approximation. To achieve this, we first pre-compute the Green's functions for the source and for the scattering point using 1- or 2-D finite-difference simulation, and then convolve them multiplied by the surface scattering potential in order to obtain the desired scattered response. This modeling technique both correctly accounts for 3-D geometric spreading, for the complexity and three-component character of the wavefield, and also captures coda amplitude irregularities caused by heterogeneity of the scattering potential (associated, for example, with variations in topography, crustal faults, or boundaries of sedimentary basins). We expect that such modeling could be used to calibrate our measurements.

OBJECTIVES

In cooperation with Centre GEON, Moscow, Russia, the University of Wyoming has obtained a substantial part of the unique Deep Seismic Sounding (DSS) data including systematic and continuous profiling of Peaceful Nuclear Explosions (PNEs) in Northern Eurasia (**Figure 1**). Along with reversed recording of the PNEs to over 3000-km ranges, 30 to 80 chemical explosions were recorded in each of the ultra-long profiles, making these datasets unparalleled in terms of both detailed coverage of the crust and upper mantle and also as comprehensive collections of seismic recordings of explosions at regional distances. Recent studies of the data included imaging two-dimensional velocity, reflectivity, and P-wave attenuation of the upper mantle to ~700-km depth, interpretation of high-frequency scattering and seismic coda. In this new project, we focus specifically on the analysis of the spectral properties of *Lg*, crustal and upper mantle attenuation using the spectral and coda decay information extracted from the PNE records.

At this early stage of the project, we present plans of data measurement and modeling techniques. The principal objectives of this work include:

1) Development of amplitude and spectral measurement techniques taking into account the character of PNE recordings using portable, 3-component, densely spaced instruments. These methods include measurements of spectra, spectral ratios, relative amplitudes, and amplitude decay parameters for the different phases. Below, we describe our techniques for estimations of power spectra and effective attenuation.
2) Development of methods for modeling of the PNE waveforms and amplitudes, with accounting for the complexity of the observed waveforms and propagation paths. Specifically, we need to develop modeling methods for short-period (~1-2 Hz) crustal-guided phases (*Pg*, *Lg*) propagating to ~2000 km along crustal paths that are heterogeneous in a 3D sense. Since the straightforward 3D modeling problem of this scale is not tractable and also not supported by sufficient data at present, we propose several approximate approaches that could produce interpretable and useful results. Below, we describe our ongoing work on one of these approximations of the PNE arrival coda using the first-order Born scattering in 3D.

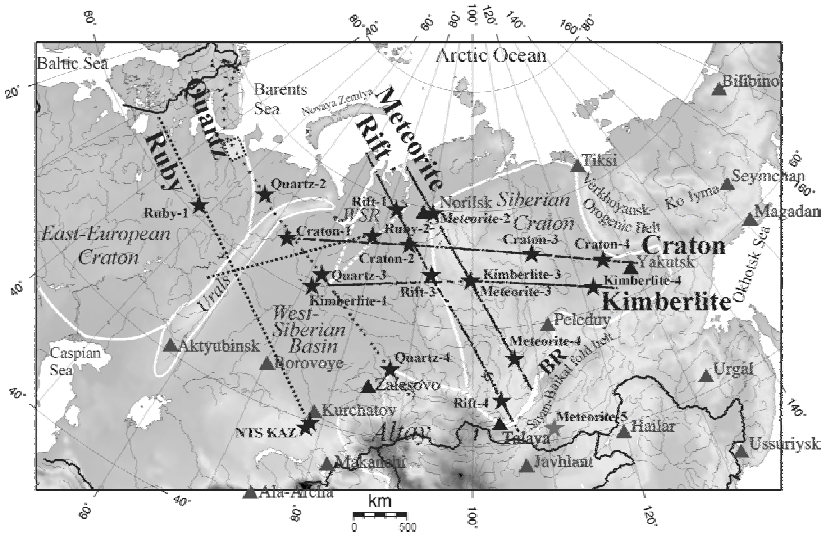

Figure 1. DSS PNE profiles under study at the University of Wyoming: QUARTZ, CRATON, KIMBERLITE, RIFT, METERORITE, and RUBY (two lines, obtained recently). Large stars are the PNEs; small stars (for profile QUARTZ only) are the chemical explosions. Profile RUBY is shown schematically. The coordinates and other parameters of the PNEs used in these profiles were reported by Sultanov et al (1999). White contours show the major tectonic units (labeled: WSR – West Siberian Rift, BR – Baikal Rift). Note the extent of systematic, continuous profiling, with PNEs detonated at the intersections of the 3000–4000-km long profiles. The profiles are close to some of the IMS stations (labeled triangles). The profile QUARTZ has been studied extensively for the upper mantle and crustal structure, for seismic coda effects and crustal reverberations. The box NW of PNE QUARTZ 2 indicates the area where crustal attenuation was measured using coda amplitude analysis.

RESEARCH ACCOMPLISHED

Below, we describe our approaches to the attribute extraction and approximate 3D coda modeling. As this is work in progress, we concentrate on the methodologies and applications in the project.

Measurements of spectra and effective *Q* from PNE records.

Relative spectral amplitudes for both attenuation and coda studies are derived using a broad class of multitaper techniques similar to the one used by Xie et al. (1988). Multiple spectral estimates in shorter sub-windows increase the stability of the estimates in respect to the effects of noise (Figure 2). This increase is achieved at the expense of reduced spectral resolution resulting from using shorter time sub-windows for spectral analysis. Such a reduction, however, is quite acceptable for PNE records in which the signal typically exhibits little coherency over time period exceeding ~5 s; consequently, we estimate that a time window of ~5 s is the appropriate choice for spectral sampling. This choice results in a ~0.2 s resolution of the spectra and allows us using 4-8 sub-windows for *Lg*, *Sn*, and *Pg*. Also, most importantly, this generalized multiple tapering technique provides for an estimation of the effective spectral decay (attenuation) within the analysis time gate (Figure 2).

Our spectral estimation method is an extension of the common spectrum technique described by Morozov et al. (1998). First, in each of the tapered sub-windows *i*, we compute the amplitude FFT spectrum of the signal, $A_i(f)$ (Figure 2). By selecting a set of pairs of sub-windows, (i,j) (choosing this set is yet another option of the algorithm), we form their associated spectral ratios: $SR_{i,j}=A_i(f)/A_j(f)$. By assuming the usual model of the spectra:

$$A_i(f) = A_0(f) e^{-pft_i/Q},$$

and taking a logarithm of the spectral ratios, we obtain a linear inverse problem for $1/Q$:

$$\ln SR_{i,j}(f) = -\frac{pf}{Q}(t_i - t_j). \qquad (1)$$

This linear system (for a range of frequencies *f* and pairs of time sub-windows *i* and *j*) is solved using the Least Squares approach. This method is also suitable to invert for a frequency-dependent attenuation: by replacing $1/Q$ in

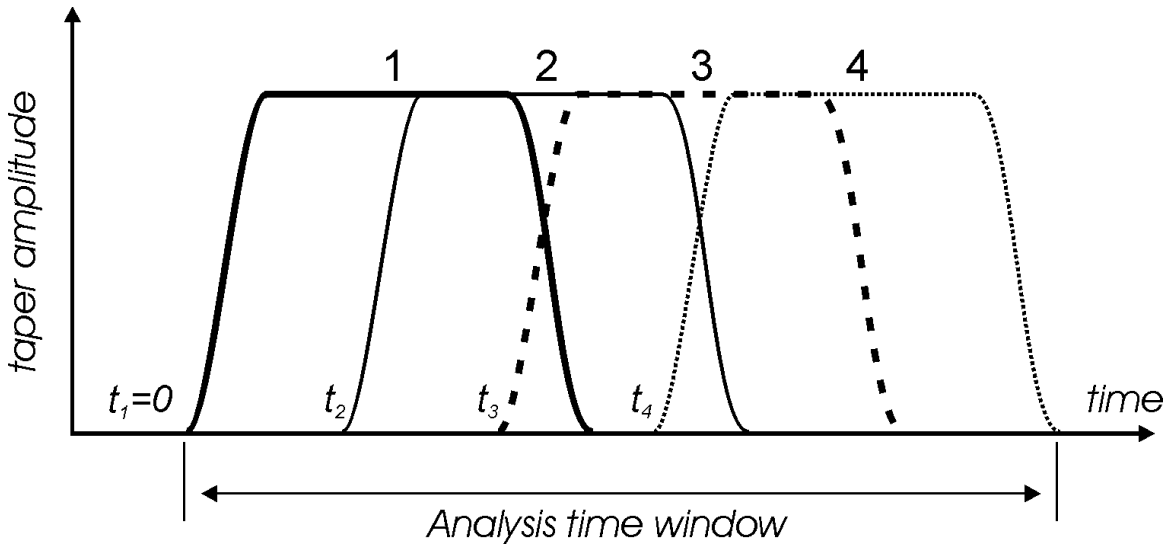

Figure 2.Multiple-taper spectral analysis windows. The spectral analysis time gate is subdivided into a number of overlapping sub-windows (libeled with numbers). Although the tapers do not have to be trapezoidal and equally spaced, in this example, we are using four identical Hanning windows. Increasing number of tapers improves the statistical significance of the results at the expense of spectral resolution (reduced because of using shorter FFT analysis gates).

equation (1) with $1/Q_0 + hf$, we obtain:

$$\ln SR_{i,j}(f) = -\frac{pf}{Q_0}(t_i - t_j) - hf^2(t_i - t_j), \quad (2)$$

which is also a linear inverse problem in respect to $1/Q_0$ and h. In order to avoid complications caused by spectral holes, we exclude from the above analysis the frequencies at which any of the (normalized) spectra $A_i(f)$ becomes lower than some predefined threshold (Morozov et al., 1998).

After the (possibly, frequency-dependent) value of $1/Q$ is estimated, the final "common", time-independent, spectrum $A_0(f)$ is estimated simply by averaging the sub-window spectra corrected for the attenuation:

$$A_0(f) = \frac{1}{N}\sum_{i=1}^{N} A_i(f) e^{pft_i/Q}. \quad (3)$$

Here, N is the number of time sub-windows (Figure 2). Note that spectral holes do not need to be excluded from expression (3), and thus we obtain a uniform estimate of both the spectral amplitude and Q throughout the entire frequency range.

A three-component analog of the expressions (1-3) above can be obtained by using spectra averaged over the three displacement directions:

$$A_0(f) = \overline{A}_0(f) = \sqrt{\sum_{i=x,y,z}(A^i)^2}.$$

Our preliminary tests of this procedure using synthetic data and records from profile Kimberlite show that the resulting estimates of Q are stable and the *Lg* Q (spectral attenuation across the *Lg* window) and *Lg* coda Q are similar to each other. Preliminary results using five of the available PNE profiles show *Lg* coda Q values similar to those obtained previously in our studies of a part of profile QUARTZ. From these measurements, we plan to produce crustal and upper mantle Q values that are required for large-scale simulation of propagation of the regional phases (*Lg*, *Pg*, *P*, and *S*) across Northern Eurasia

Simulations of PNE arrival coda in 3D.

The motivation for our coda modeling effort is illustrated in Figure 3. As a number of previous attempts for finite-difference modeling of the coda of long-range PNE arrivals (Tittgemeyer, 1996; Ryberg et al., 2000,) indicated, neither 1D nor 2D simulations are able to explain the observed amplitude patterns of PNE arrivals at regional to teleseismic distances (Morozov and Smithson, 2000; Morozov, 2001). Therefore, three-dimensional (3D) simulations are required for a correct description of short-period coda of PNE arrivals (Figure 3).

Our current modeling is targeting simulations of a realistic, three-component wavefield recorded from a distant PNE source. Since the full 3D modeling problem is not tractable at present, we perform our modeling by employing a single-scattering (Born) approximation. This modeling technique both correctly accounts for 3D geometric spreading, for the complexity and three-component character of the wavefield. Also, by using such an approximation, we could potentially identify regions of increased scattering in the PNE records and associate them with the major tectonic or topographic features (such as crustal faults, mountain ranges, or boundaries of sedimentary basins; Figure 4). Thus we expect that such modeling could be used to calibrate the above measurements.

Scattering, as shown in Figure 4, is dominated by the out-of-plane effects, and it cannot be modeled correctly by conventional 2D numerical modeling. Nevertheless, as we are mainly interested in RMS average energy decay in the coda, we can estimate the recorded signal at any surface point by convolving the incident wavefield with an "empirical Green's function" that would describe the propagation of scattered waves, multiplied by some "scattering potential" (Revenaugh, 1995):

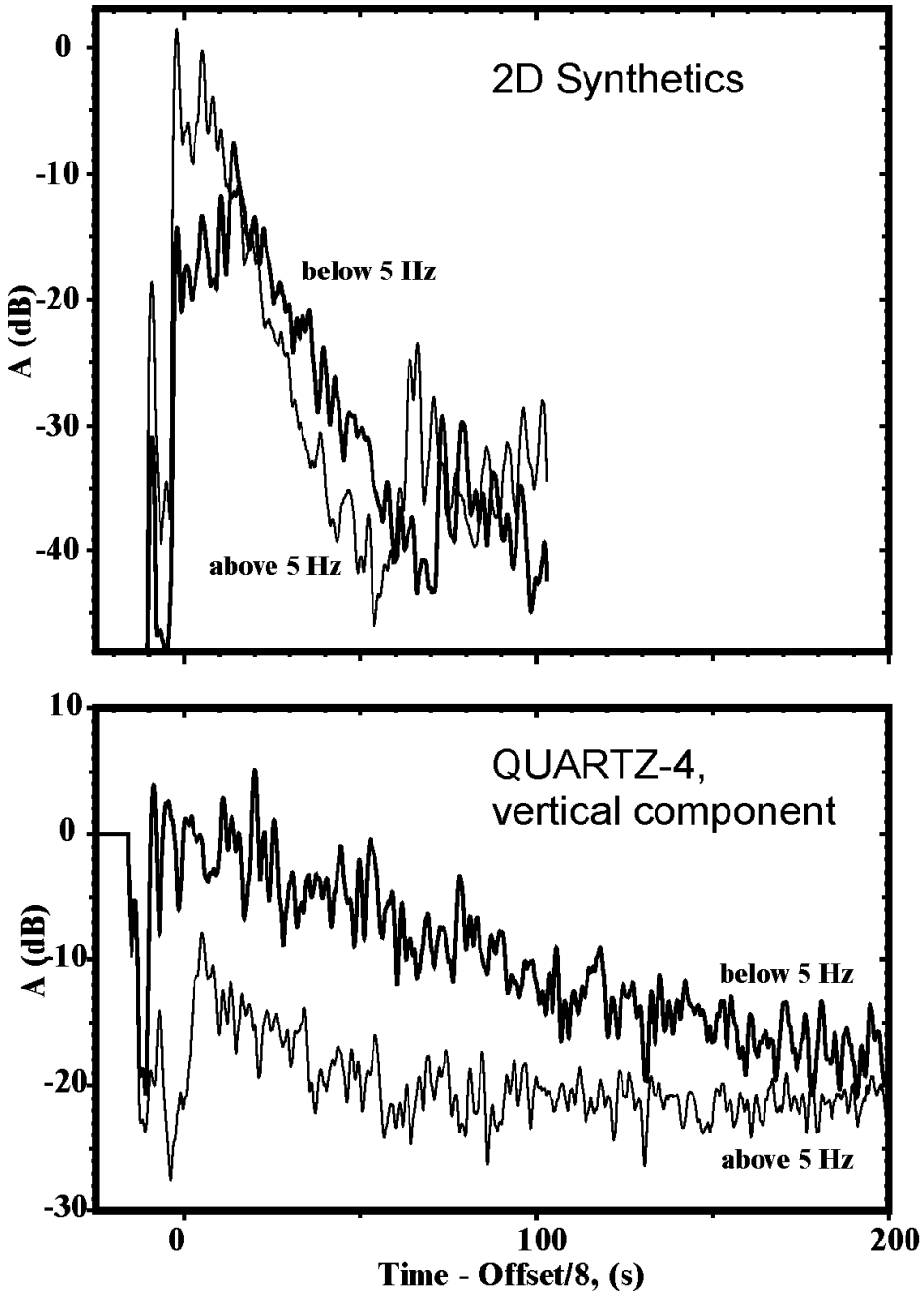

Figure 3. Comparison of the amplitude decay observed in PNE QUARTZ-4 (bottom) and modeled using an elastic 2D finite-difference method (modelling performed by Lars Nielsen, University of Copenhagen; unpublished). Note that the observed coda is significantly longer than the one obtained from 2D synthetics, both at higher and lower frequencies. As we argue (Morozov and Smithson, 2000), only some kind of 3D simulation could provide an adequate model of the coda.

$$\tilde{u}(r,t) = R\left(\int_S ds\, dt\, A(s)\, u(s,t) * G(s,t \mid r,t)\right), \quad (1)$$

where *s* is the surface integration point, u() is the source function, and *A* is the scattering potential, and R is the receiver factor, and '*' denotes time convolution (Figure 4).

Both the direct wave response at point *S* and the Green's function *G*(…) in equation (1) can be estimated from 2D or 1D synthetics. At present, we precompute the Green's functions for the source and for the scattering point using the 1D finite-difference modeling program modified after Fuchs and Muller (1971). The scattering potential in equation (1) can be simulated either as a stochastic function or based on an empirical correlation with topography, crustal faulting, and seismicity (Revenaugh, 1995, 2000).

For any recording point at the surface, *R*, we simulate the seismic trace coda by attributing its form to the effect of point scattering of seismic waves from surface scattering points (Figure 4). A seismic wave travels outward from the seismic source S. Part of this energy is received at scatter point *Sc* and reflected from the point to receiver R. The waveform recorded at R is a function of the source waveform, source-scatterer distance, and scatterer-receiver distance. In this simulation, the source waveform is a synthetic IASP-91 seismic section. Several scatterers may be arranged to simulate various geologic scattering bodies; for instance, a linear array of scatterers may simulate a mountain range (Figure 4), a boundary of a sedimentary basin, or a coastline. We specify a linear array of receivers to act as a seismic line.

The synthetic coda due to surface point-scattering effects is computed by summing over the convolution of two synthetic traces for each scatterer-receiver pair. The first trace represents the seismic signal at the offset of the scattering point from the seismic source. The second trace contains the signal at the offset of the receiver from the scattering point (Figure 4). The traces are determined from the synthetic seismic section using a *t-p* interpolation

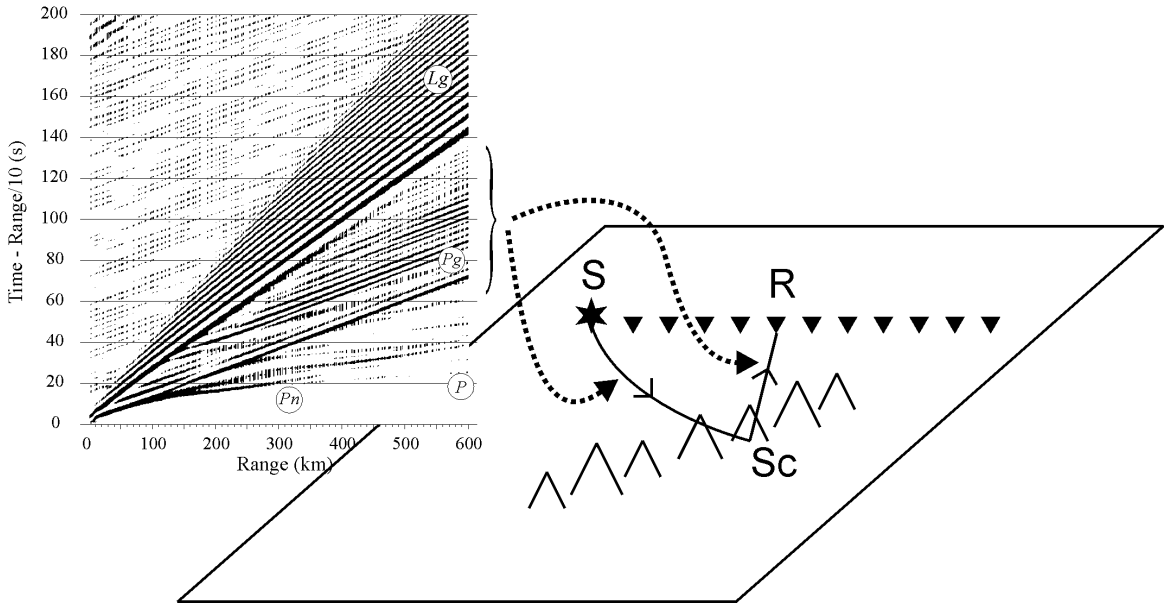

Figure 4. Simulation of first-order scattering responses. The wavefield at receiver location ® is approximated as a combination of the direct wavefield from the source (S) and an integral over the positions of the scatterers (*Sc*) located near the Earth's surface. At present, we approximate the direct source field and both legs of the scattering path *S_Sc_R* using an empirical Green's function (shown here as a data section) computed using a 1D reflectivity synthetic (Fuchs and Muller, 1971). Note that since a dominant contribution to the coda comes from the waves trapped within the crustal layers and propagating generally horizontally, their amplitude decay with distance is compensated by the increasing area of scattering (Morozov and Smithson, 2000). As a result, coda energy is collected from a large area and its decay is slow.

routine which allows us to compute the trace values more accurately because a more accurate offset value is used in each calculation. Rather than using the nearest trace to the offset distance from the synthetic section for each of the two traces in the convolution, new traces are interpolated between traces of the synthetic section for the source-scatterer and scatterer-receiver distances and convolved. The source-scatterer and scatterer-receiver traces, when convolved, give the scattering response at receiver *R*. These convolution calculations are repeated for each scatterer-receiver pair. All the resulting convolved trace values from each scatterer-receiver pair are summed together at each receiver to give the total response due to point scattering.

Implementation

The above procedures are implemented in a very general form of programmable seismic processing flows (Morozov and Smithson, 1997; http://w3.uwyo.edu/~seismic/sia) allowing the use of arbitrary configurations of receivers and a variety of choices of scattering regions. In principle, the procedure also allows iterating the scattering steps thereby extending our modeling beyond the single-scattering Born approximation. However, such iteration would require a significantly greater computing power and thus it still has not been investigated.

In developing our signal processing and modeling approaches, a considerable effort is applied to achieving sufficient portability and scalability of the methods. Owing to a highly generalized formulation of the spectral estimation problem (implemented in an object-oriented code using C++ programming language), virtually the same technique is used for the measurements of both *P*-wave spectral attenuation (t^*), *Lg Q*, and *Lg* coda *Q*. The codes are completely portable and implemented on several platforms ranging from a multi-processor SGI and Sun systems to a PC Linux notebook (interestingly, the latter yielding the highest performance!). The codes include hundreds of useful C++ classes, over 140 seismic processing tools, and are equipped with a system maintenance package and automated on-line documentation (http://w3.uwyo.edu/~seismic/sia). In the near future, we are planning to extend the package with a capability for operation on multiprocessor platforms (Beowulf clusters) using the Message Passing Interface (MPI).

CONCLUSIONS AND RECOMMENDATIONS

In this report, we present our ongoing development of methods for quantitative amplitude and spectral analysis and modeling of PNE arrivals recorded by the Deep Seismic Sounding profiles in the former Soviet Union. The importance of this research is emphasized by the great variety of the tectonic structures covered by the profiling and also by the fact that DSS recordings cover largely aseismic regions of Northern Eurasia where virtually no other data is available for seismic calibration ( ). The DSS data sets contain abundant 3-component recordings of the full spectrum of regional phases that hold significant potential for seismic calibration and discrimination. At present, we have implemented and tested on synthetics procedures for (1) spectral measurements of PNE arrivals using multiple tapering and allowing estimations of (optionally) frequency-dependent effective attenuation, and (2) approximate modeling of the amplitude decay of PNE arrivals in 3D using the first-order, Born approximation.

Further research will involve: (1) space and time-variant measurements of the amplitude decay, (2) interpretation of the resulting database and inversion of the amplitude and spectral decay parameter for variations in the regional crustal attenuation structure and correlation with tectonics; (3) modeling of *Lg* propagation using an extended, 3D variant of the Generalized Screen Propagator (e.g., Wu et al., 2000), and (4) integration of the resulting *Lg* waveforms with our surface scattering model. The above studies should result in a comprehensive modeling capability that could be utilized for interpretation of both average and region-specific character of regional wave propagation in Northern Eurasia.

REFERENCES

Morozov, I. B. (2001). Comment on “High-frequency wave propagation in the uppermost mantle” by T. Ryberg and F. Wenzel, J. Geophys. Res., 106, 30,715-30,718.

Morozov, I., B., E. A. Morozova, S. B. Smithson, and L. N. Solodilov, 1998. 2D image of seismic attenuation beneath the Deep Seismic Sounding profile QUARTZ, Russia, Pure Appl. Geoph, 153, 311-343.

Revenaugh, J. (1995). The contribution of topographic scattering to teleseismic coda in Southern California, Geophys. Res. Lett., 22, 543-546.

Ryberg, T., M. Tittgemeyer, and F. Wenzel (2000). Finite-difference modelling of P-wave scattering in the upper mantle, Geophys. J. Int, 141, 787-800.

Sultanov, D. D., J. R. Murphy, and K. D. Rubinstein (1999). A seismic source summary for Soviet Peaceful Nuclear Explosions, Bull. Seism. Soc. Am., 89, 640-647.

Tittgemeyer, M., F. Wenzel, K. Fuchs, and T. Ryberg (1996). Wave propagation in a multiple-scattering upper mantle—observations and modeling, Geophys. J. Int., 127, 492-502.

Wu, R.-S., S. Jin, and X.-B. Xie (2000). Energy partition and attenuation of *Lg* waves by numerical simulation using screen propagators, Phys. Earth. Planet. Inter., 120, 227-243.

Xie, J., et al., (1998), Interpretation of high-frequency coda at large distances: Stochastic modeling and method of inversion. Geophysical Journal.95, 579-595.

MIDDLE EAST, NORTH AFRICA AND WESTERN EURASIA SEISMIC RESEARCH DATABASE

Jennifer L. O'Boyle, Stanley D. Ruppert, Teresa F. Hauk, Douglas A. Dodge,
Michael A. Firpo, and Flori Ryall

Lawrence Livermore National Laboratory

Sponsored by National Nuclear Security Administration
Office of Nonproliferation Research and Engineering
Office of Defense Nuclear Nonproliferation

Contract No. W-7405-ENG-48

ABSTRACT

The National Nuclear Security Administration (NNSA) Ground-Based Nuclear Explosion Monitoring Research and Engineering (GNEM R&E) Program has made significant progress populating a comprehensive Seismic Research Database (SRDB) used for deriving seismic calibration parameters for the Middle East, North Africa and Western Eurasia (ME/NA/WE) regions. In addition to an overview of select individual information products, we present an overview of our visualization, integration, validation, and organizational processes. Development of these processes and the SRDB was necessitated by both the very large amount of data and information involved (over 2 terabytes) and the varied data and research result formats utilized. The SRDB allows for the collection of raw and contextual seismic data used in research, provides an interface for researchers to access data, provides a framework to store research results and integrate data sets, and supports assembly, integration and dissemination of data sets to the NNSA Knowledge Base (KB).

The SRDB is a flexible and extensible framework consisting of a relational database (RDB), Geographical Information System (GIS), and associated product/data visualization and data management tools. This framework is designed to accommodate large volumes of data in diverse formats from many sources (both in-house-derived research and integrated products), in addition to maintaining detailed quality control and metadata. In order to efficiently organize information within the SRDB, it was necessary to automate procedures needed to create and update database tables, but a large effort is still required by technicians and scientists to load special data sets, review results of automated processing and resolve quality issues. The SRDB currently has 3 million reconciled event origins and arrivals from several global, regional and local seismic bulletins and 3.5 million waveforms from 100,000 seismic events of interest. We also use the SRDB for integration and have developed procedures, algorithms, and tools allowing us to merge data sets and maintain quality control as well as integrate data or products at a range of levels from data sets to databases to the NNSA KB. This suite of tools is now being used throughout the NNSA GNEM R&E Program. It enables us to include data from contractors, universities, and NNSA collaborators in our research and to provide coherent, reconciled and integrated results to the NNSA KB. The SRDB integration framework also supports and facilitates other NNSA collaborative projects.

The SRDB provides the basis for synergistic development of all NNSA GNEM R&E Program research. The SRDB provides not only a coherent framework in which to store and organize very large volumes of collected seismic waveforms, associated event parameter information, and spatial contextual data, but also provides an efficient data processing/research environment for deriving a wide range of information products required to support the ME/NA/WE regionalization program. Products assembled, integrated and validated using the SRDB are grouped into five main categories: Reference and Contextual Information, Detection Data, Calibration and Ground Truth Data, Event Location Products and Event Identification Products. Using the SRDB, we are combining travel-time observations, event characterization studies, and regional tectonic models to assemble a library of ground-truth information and phenomenology (e.g. travel-time and amplitude) correction surfaces. Corrections and parameters distilled from the SRDB provide essential contributions to the NNSA KB for the ME/NA/WE region and facilitate calibration of seismic monitoring stations, thereby improving capabilities for underground nuclear explosion monitoring.

OBJECTIVE

The primary objective of the Seismic Research Database (SRDB) is to facilitate development of information products for the Ground-Based Nuclear Explosion Monitoring Research and Engineering (GNEM R&E) Middle East, North Africa and Western Eurasia (ME/NA/WE) regionalization program. The SRDB provides efficient access to, and organization of, thousands of seismic events and associated waveforms, while also providing the framework to store, organize, integrate and disseminate information products for delivery into the National Nuclear Security Administration Knowledge Base (NNSA KB).

The SRDB provides a unified framework for all seismic data and information products as outlined in Figure 1. This requires the reconciliation and merging of data derived from different sources and methods and of varying quality, along with the ranking of the data sets based on relative quality. Integration occurs on many levels in order to generate data, data sets, databases or knowledge bases. The SRDB also allows for the integration of research with contractor research products and other available data sets. In order to efficiently organize information within the SRDB, it was necessary to automate procedures needed to create and update database tables, but a large effort is still required by technicians and scientists to load special data sets, review results of automated processing and resolve quality issues. Sufficient metadata (including measurement procedures, codes, comments and measurement errors) are stored at each step in the data creation and analysis process to allow re-creation or verification of results at any stage in the processing flow.

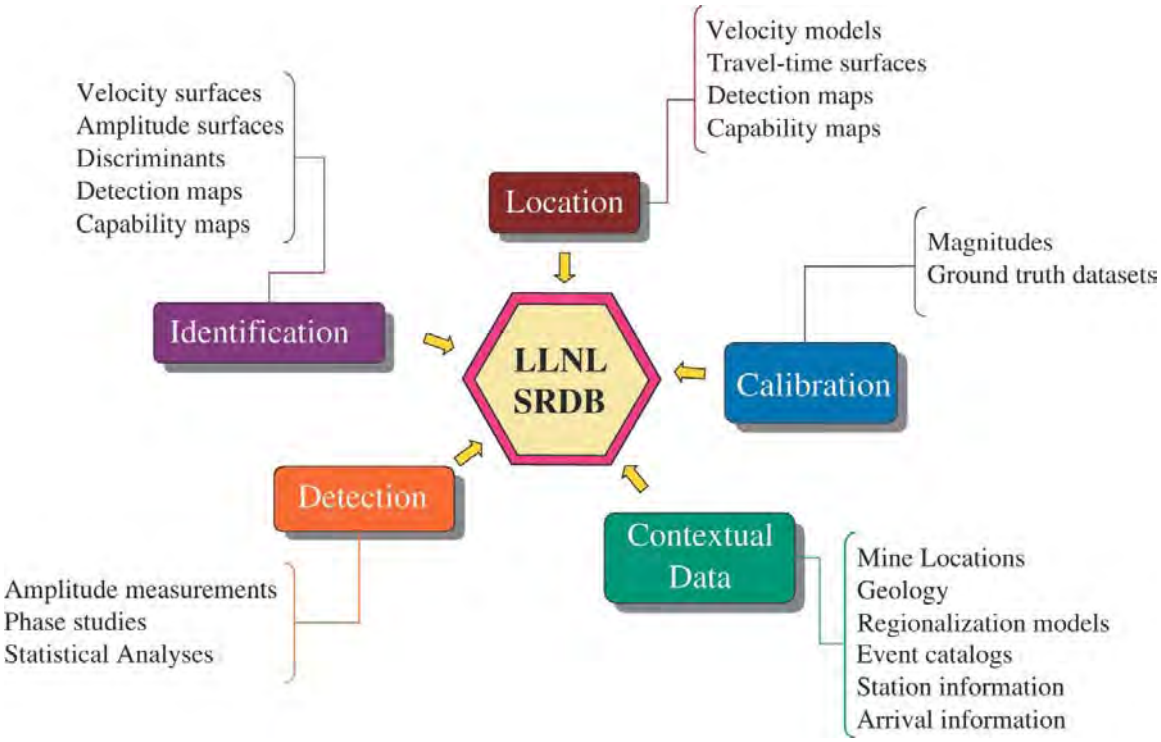

Figure 1. The SRDB provides a unified framework for contextual/reference data and information products. The SRDB provides efficient access to, and organization of, thousands of seismic events and associated waveforms, while also providing the framework to store, organize, integrate and disseminate information products for delivery into the National Nuclear Security Administration Knowledge Base (NNSA KB).

Information products created using the SRDB may be grouped under two major categories: primary data products and derived products. The primary products are those developed in the process of collecting the raw materials for calibration: ground truth data, waveform data, event catalogs, phase pick information, regional station information and instrument responses. The derived products (distilled from the organized raw seismological data) are models and corrections that improve detection, location and identification functions. In order to calibrate seismic monitoring stations, the SRDB must incorporate and organize the following categories of primary and derived measurements, data and metadata:

Contextual and Raw Data

1. Station Parameters and Instrument Responses
2. Global and Regional Earthquake Catalogs
3. Selected Calibration Events
4. Event Waveform Data
5. Geologic/Geophysical Data sets
6. Geophysical Background Model

Measurements and Research Results

1. Phase Picks
2. Travel-time and Velocity Models
3. Rayleigh and Love Surface Wave Group Velocity Measurements
4. Phase Amplitude Measurements and Magnitude Calibrations
5. Detection and Discrimination Parameters

Corrections and parameters distilled from the SRDB provide needed contributions to the NNSA KB for the ME/NA/WE region and will improve capabilities for underground nuclear explosion monitoring. The contributions support critical functions in detection, location, feature extraction, discrimination, and analyst review. Figure 2 outlines the processes of data collection, research and integration that result in contributions to the NNSA KB.

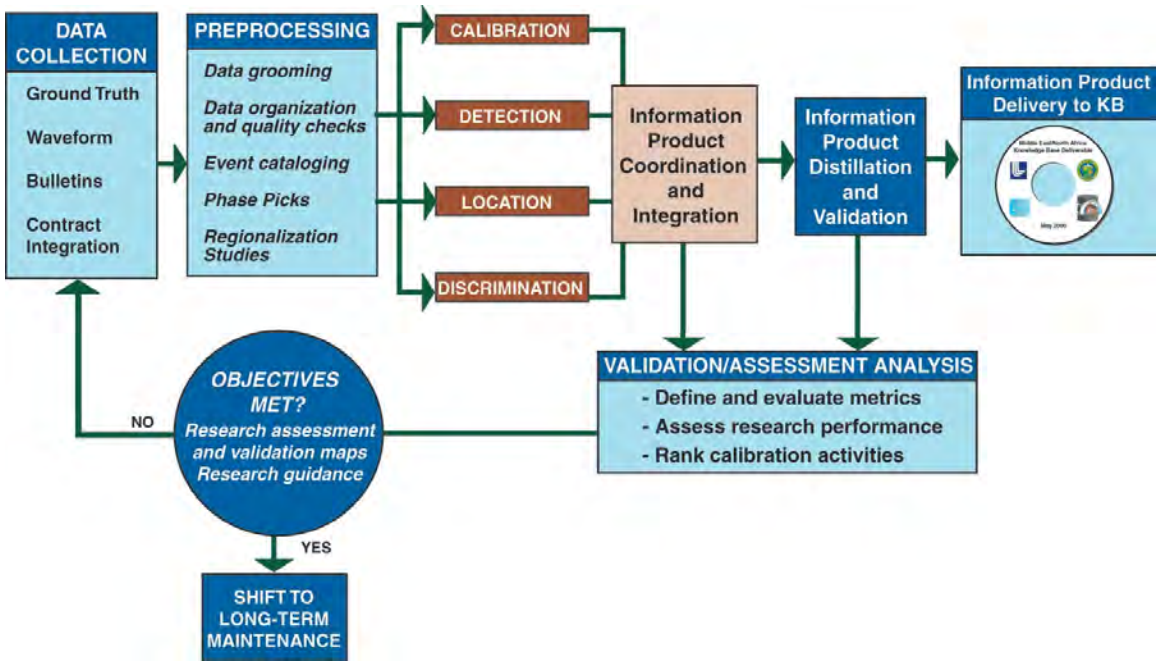

Figure 2. Seismic Research Database (SRDB) process flow. The SRDB is the framework that supports development of information products related to seismic calibration research. Integration and synergy of data and research and visualization tools are made possible through the SRDB.

RESEARCH ACCOMPLISHED

The SRDB is a framework consisting of an ORACLE relational database (RDB), Geographical Information System (GIS), and associated product/data visualization and data management tools. The SRDB is necessary for the storage and organization of very large volumes of collected seismic waveforms, associated event parameter information, and spatial contextual data. It also provides an efficient data processing/research environment for deriving location and discrimination correction surfaces. Figure 3 outlines the interaction among all components of the SRDB. The relational database is organized in CSS3.0 (Center for Seismic Studies Version 3.0) format with custom extensions. This format provides parameter-defined tables for different elements of seismic data, such as event and station information, as well as allowing for customized tables to be developed for specific research needs or results and the compatibility with other organizations.

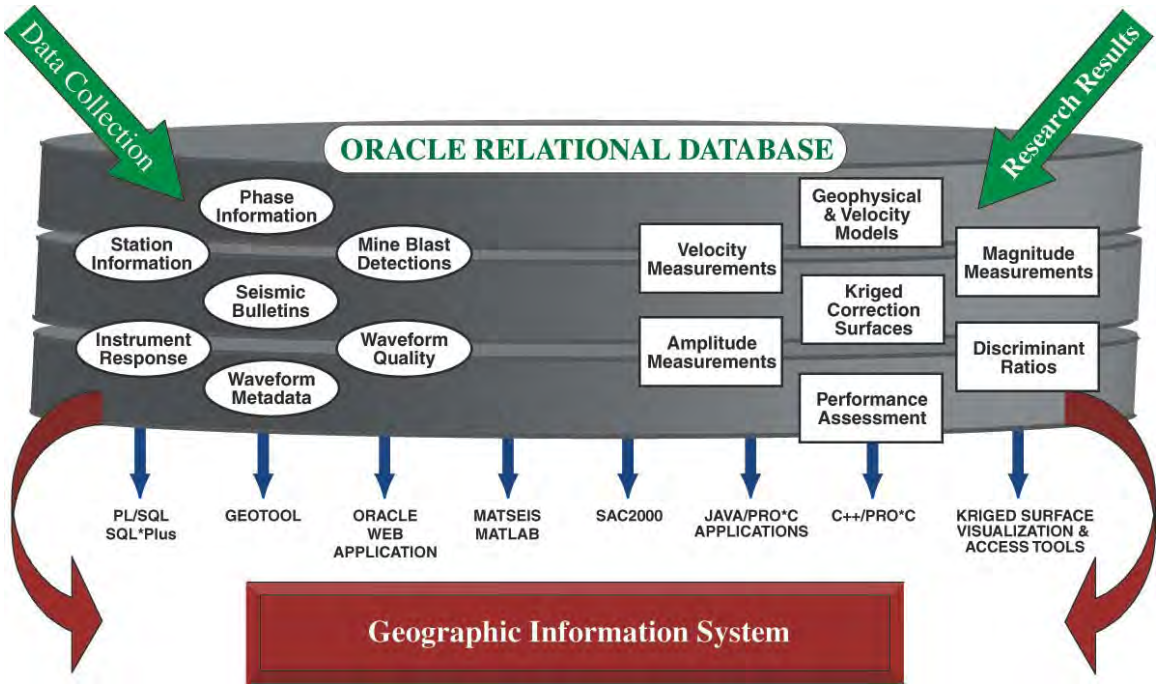

Figure 3. The LLNL SRDB integrates a relational database, a Geographic Information System (GIS) and visualization/data management processes. Many aspects of GNEM R&E are contained within the database and can be accessed using a wide variety of tools.

This extensible framework uses modern object-oriented and database programming practices to combine a number of tools and libraries that incorporate automation where possible to streamline the data set loading, reconciliation, and integration processes. This framework also provides the primary mechanism for merging and reconciling derived calibration data from contractors, individual researchers, and NNSA laboratories into a single product. There are six main classes of products that require integration effort and four main reconciliation issues for each class summarized below:

Data Set Class	Reconciliation Issue
Core tables / Core files (e.g. velocity models)	Initial merge
Catalogs	Updating
Waveforms	Validation
Derived products (internal and external)	Back propagation / synchronization
Spatial/Contextual information	
Assembled databases / Knowledge bases	

To assist us in the integration and reconciliation tasks related to calibration research, we have written a set of 130 C++ classes designed primarily as components of computer programs for use by the GNEM R&E program. A class is a software abstraction of an entity from the problem domain, which combines all of the attributes and actions of a single entity into one data type. This allows programmers to work at a higher level of abstraction, thus improving productivity and software maintainability. Of the classes we designed, about 10 are service classes with no specific seismological capability, *e.g.* time class, architecture class, etc. All the remaining classes are specialized to some degree for use in seismological applications. All of the collection classes have database-aware specializations as well, since most of the programs developed with the classes interact extensively with the SRDB database. The class library has built-in support for the CSS3.0, SAC, GSE2.0, and PC-SUDS data formats. Using the classes has proven to be an effective means of building the utility programs required to support the SRDB as described in the following paragraphs.

We have developed an automated method/tool (Orloader) to load various seismic bulletins of different formats into native-format database tables, which retain many of the fields provided in the original bulletin, as well as assign a unique origin identifier (*orid*) to each event. Individual bulletins are then merged into a single CSS3.0 **origin** table retaining the author of the original bulletin. The native tables are linked to the origin and event tables created by Orloader through a remap table. Using the remap table, any origin in the target CSS3.0 table can be uniquely associated with the corresponding native origin. Because the same event may often be reported by different organizations, there will be instances in which new origins correspond to origins that are already in the database. A space-time correlation algorithm is used to reconcile events between individual catalogs. Events common to multiple bulletins will be assigned common event identifiers (*evid*) while retaining unique *orid*s. The **event** table stores the preferred origin for each event based on a ranked list of catalog preferences. Phase arrivals provided with native catalogs are loaded into the **assoc** and **arrival** tables.

To generate the event waveforms for the SRDB, we have developed automated methods/tools (Ddload, UpdateMrg) for extracting event waveforms from continuous data and inserting them into the appropriate database tables. Event selection can be restricted by time, location, event magnitude or a specific list of *evids*. Ddload extracts waveforms from continuous data in the native format, converts the data to CSS3.0 format and creates entries in staging tables (**wfdisc**, **wftag**). The **wfdisc** table contains pointers to the waveform files and the **wftag** table associates the waveform file with the *evid* used in the extraction. Currently, we can perform waveform extraction on data in SAC, SEED, CSS, SEGY and GSE formats. The UpdateMrg program is used to insert the staged **wfdisc** and **wftag** records into the target tables. During the insertion process, UpdateMrg checks waveforms for poor or missing signals, which are then recorded in a metadata table. If waveforms for a specific event are segmented, the segments will be merged together; if a gap exists between segments, the space will be filled with zero-value data points. If two segments that are being inserted overlap or a segment for an overlapping time period already exists in the target tables, a correlation test is done before the two segments are joined.

The SRDB also provides the framework to perform end-to-end process validation and testing of research results. Validation and assessment tasks include the definition and evaluation of specific metrics, analysis and use of metrics to define the stopping criteria for particular location and identification tasks, and ranking and performance evaluation of calibration activities. Success and efficient implementation of validation and assessment tasks require a framework that ties research results to data and measurements used to create each calibration product and that also supports statistical and visualization tools for performing the validation tasks. The metadata inherent in the SRDB allow multiple realizations of calibration products, created with different processes and assumptions, to be created, stored, and compared with one another. Thus, the SRDB facilitates the distillation, documentation, and delivery of information products.

As part of our validation and automation processes, we have developed a suite of consistency tests and related updating/repair procedures (DBcheck / DBfix) to assist both the data set loading staff and researchers in maintaining the highest quality collection of data possible. These test procedures consist of PL/SQL stored procedures used for identifying and resolving inconsistencies between data sets (core tables and measurement tables) to be integrated as well as maintaining consistency in the final SRDB and products to be delivered.

Contextual and Raw Data

Station Parameters

Seismic station information is a metadata requirement needed to support all stages of seismic waveform analysis. These metadata include such parameters as station operation dates, location and elevation, type of channels and instruments, sampling rates, and instrument responses. Our main source of this information is Incorporated Research Institutes for Seismology (IRIS) "data-less" SEED files, which are provided by each of the networks affiliated with IRIS. Other station information has been obtained through Internet station books and AutoDRM systems. CSS3.0 **site** and **sitechan** table entries (listing station location, available channels, sensor orientations, operation dates, etc.) were created for almost all IRIS-affiliated networks as well as many other stations with waveforms in the SRDB. All station parameters are reviewed among existing information sources, and conflicts must be resolved between sources and in reference to waveforms available before database tables are updated. Over 1800 station and array element table entries have been updated, but reliable parameter data do not exist for some stations if only minimal or inconsistent information is available. **Instrument** and **sensor** tables are used to document instrument type and response for each station and channel. The Seismic Analysis Code (SAC) has been modified to interpret response information in RESP or FAP format for use in performing instrument response corrections on waveform data by using the EVALRESP software library available from IRIS.

Event Bulletins

Reference event locations and origin time information are necessary in most stages of our seismic processing and research. Bulletin information from many global, local, and regional earthquake catalogs has been incorporated into the SRDB and provides a much larger source for event selection. This combined and reconciled source facilitates comparison of event parameters provided by multiple networks with different degrees of location accuracy and provides a wider range of magnitudes and event types. The global catalogs include: United States Geological Survey (USGS) Monthly (Final) Preliminary Determination of Epicenters (PDE) catalog, Bulletin of the International Seismological Centre (ISC), Harvard Centroid Moment Tensor (CMT) catalog, and the International Data Centre Reviewed Event Bulletin (REB). We have also compiled numerous regional and local catalogs for the ME/NA/WE region, including Jordan, Israel, Scandinavia/ European Arctic and the Kola Peninsula. Figure 5 shows a map of the event location coverage provided by several of the bulletins in the ME/NA/WE region. We have established a number of collaborative agreements with countries and institutes in our study region to obtain both local seismic catalogs and ground truth information as well as seismic waveform data.

Waveforms

We are collecting seismic data from IMS primary and auxiliary stations, as well as surrogate stations (for IMS stations not yet installed) and other stations needed to support calibration in the region of study. We have obtained up to 10 years of continuous data for important ME/NA/WE stations from IRIS; the Institut de Physique du Globe de Paris GEOSCOPE program; the GEO-Forschungs Zentrum/Potsdam, Germany GEOFON program; and other data centers. Data for particular events have been obtained from the prototype International Data Center (PIDC) and the United States National Data Center (US NDC). The Center for Monitoring Research (CMR) and NORSAR have provided waveforms for special regions/events, such as the Novaya Zemlya test site. Stations in the ME/NA/WE region with event waveforms stored in the SRDB are shown in Figure 4.

Most of the archived waveforms in the SRDB are from events located within the ME/NA/WE region and occurring between 1976 and 2001. Although the continuous data remain archived on tapes, data segments for seismic events are extracted from the continuous waveforms. The number of waveforms in the SRDB is now almost 3.5 million, which represents 100,000 seismic events.

Other Reference and Ground Truth Data Sets

Projects to develop reference data sets include waveform correlation and subspace detectors to provide statistics on mining activity and a regionalization model based on *a priori* geophysical knowledge used as a reference model for model-based correction surfaces. Collaborations with Cornell University, USGS and other organizations allow us to obtain reference data sets useful as background and supporting information for research. Most of these data sets are provided as Geographic Information System (GIS) products, which allow us to integrate them with our data sets. The data sets include geographic, geopolitical, mining industry, geologic and tectonic information for the ME/NA/WE region. We also collect photographs and satellite imagery to support ground truth determination.

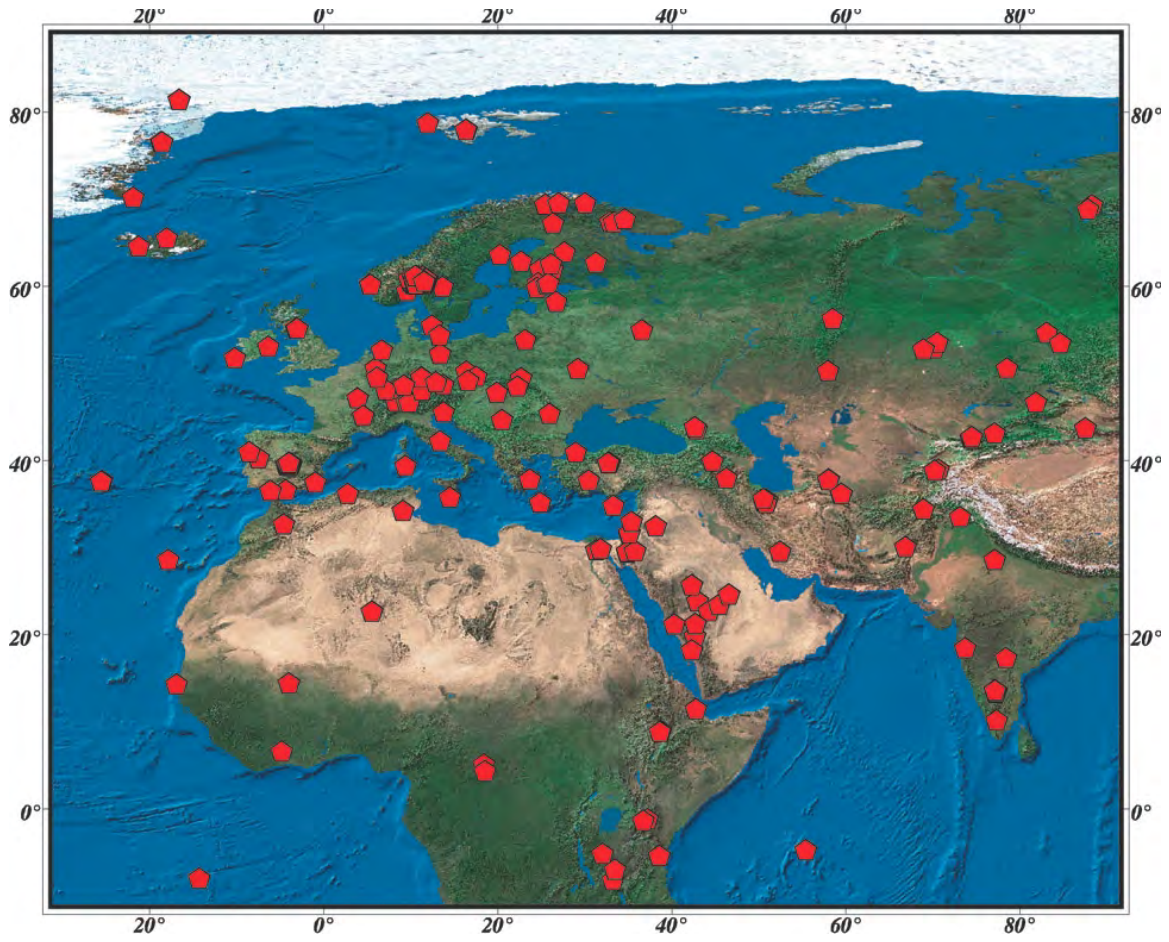

Figure 4. Seismic stations in the ME/NA/WE region with event waveforms stored in the SRDB.

Measurements and Research

Phase Information

Our researchers and analysts have made phase picks for over 1500 events to yield over 20,000 travel-time observations available to the research team for location and discrimination projects. Phase information is recorded in the **arrival** and **assoc** tables, along with pick and waveform quality and other comments that are recorded in a **remark** table. Augmenting the picks, we added 30 million ISC phase arrival measurements from 1964-1998, almost 2 million REB arrivals to be used for travel-time correction studies and picks from a few regional bulletins.

Seismic Location Research

Seismic location researchers utilize event catalogs (especially ground truth), waveforms and phase picks to develop travel-time corrections. Improvement in seismic location is accomplished by combining model-based and empirical travel-time corrections. After a calibration model is applied, empirical corrections are calculated using the Modified Bayesian Kriging algorithm with travel-time residuals for suitably well located calibration events. The travel-time and velocity models developed through this research are an important part of the SRDB. See Myers *et al*., 2002, this Proceedings, for more details about these aspects of the GNEM R&E research.

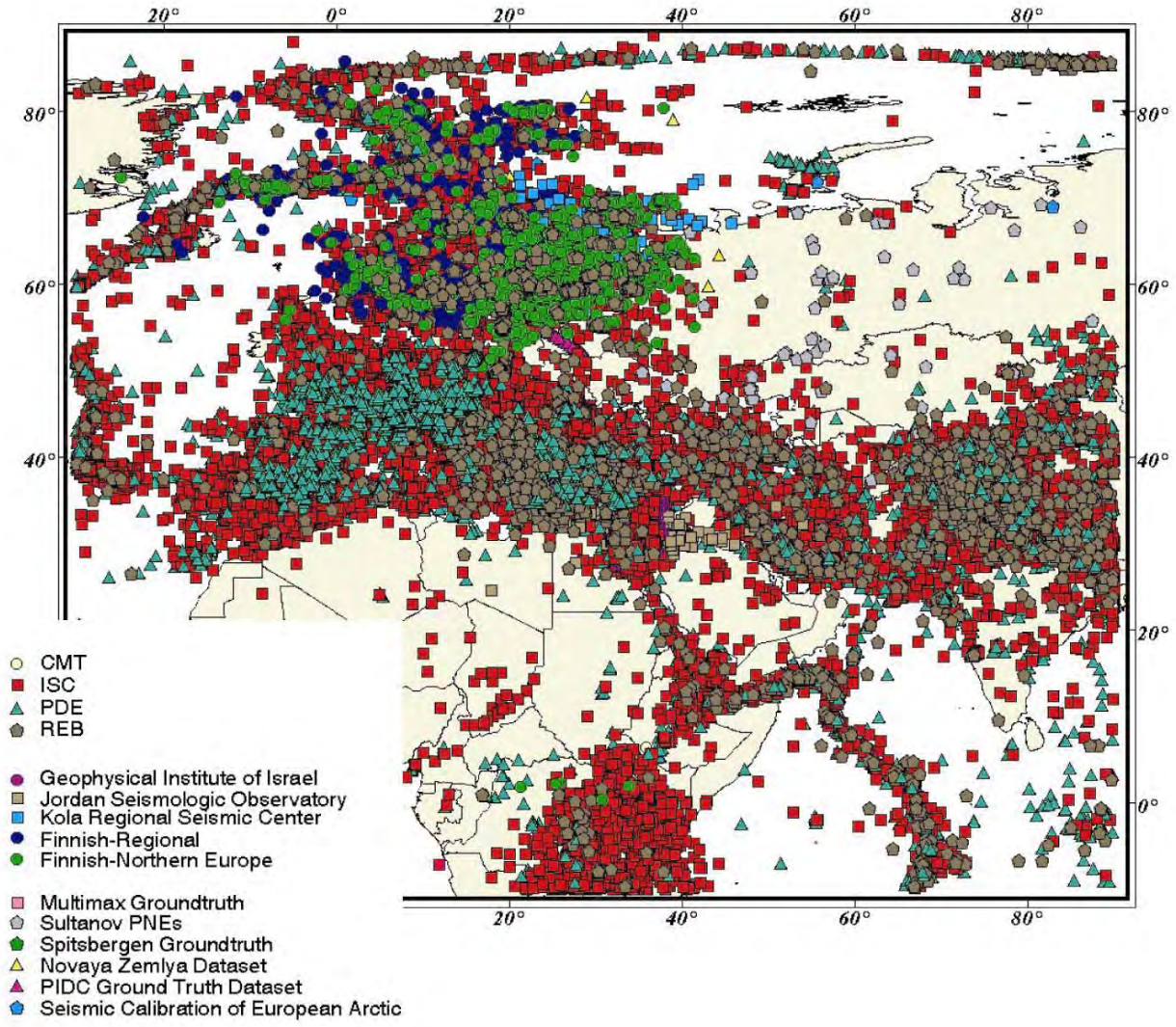

Figure 5. Plot of seismic events in the ME/NA/WE region. The SRDB contains multiple seismic event catalogs that have been reconciled into one database table. These catalogs range in scope from global to regional to special ground truth data sets and provide a much broader range of event magnitudes and event types than any single catalog.

Event Identification and Magnitude Research

The event identification researchers also use event catalogs, waveforms and phase picks to develop products that provide seismological information to improve the ability to identify underground nuclear explosions, by discriminating them from the background of earthquakes. The magnitude research results in calibration products and magnitudes for 1-Hz regional phases, broadband coda waves, and long-period surface waves. This provides the necessary calibration information for regional data in order to calculate seismic magnitudes for use by nuclear monitoring functions (detection, location, identification, and characterization). Custom tables in the SRDB database store measurements and related parameters for surface wave group velocities, body wave amplitudes and

magnitudes. See Walter *et al*., 2002, this Proceedings for more details about these aspects of the GNEM R&E research.

Data Access

Different researcher needs for data and metadata require that subsets of data be provided in a format easily accessible to many diverse types of software and analysis tools. Therefore, the SRDB access tools have been designed to utilize the power of the relational database to facilitate efficient queries and data retrieval. The Seismic Analysis Code (SAC) software used by researchers provides direct access to database table information and waveforms and uses the response files to perform instrument response corrections. For spatial queries and organization, we have adopted a Geographic Information System (GIS), which provides a framework to store and manipulate spatially defined data. The GIS is linked with the ORACLE database to provide joint spatial and relational queries. We have integrated a large number of our research and contextual data sets into the GIS products in conjunction with other data sets, including contractor products. Researchers can use the GIS to browse many of their research data sets combined with integrated data sets, and also perform basic comparisons, queries, and analyses.

Given the large quantity of data now managed by the SRDB, the need arose to create the efficient "production" level seismic data selection, processing and visualization tools necessary to meet programmatic and NNSA KB needs. These tools, along with data browsers to allow visualization and quick access to both data and delivered information products, were developed in collaboration with Sandia National Laboratories. The tools provide such functionality as deriving location corrections, making amplitude and magnitude measurements, and developing discriminants.

CONCLUSIONS AND RECOMMENDATIONS

We have made a major effort to provide a product development environment that encourages the natural synergies among each of the separate research efforts of the GNEM R&E researchers. The derivation of reference and ground truth data sets and location and identification products takes place in an integrated environment with changes and improvements in one area being used to facilitate development of the remaining areas. We utilize the SRDB as an integrating framework to provide the basis for synergistic development of all GNEM R&E products. By combining travel-time observations, event characterization studies, and regional wave-propagation studies for ground truth and regional events, we have assembled a substantial library of ground truth information (origin times, locations, depths, magnitudes), mine explosion statistics, tomographic models and travel-time and body-wave correction surfaces.

The SRDB allows for the collection of raw and contextual seismic data to be used in research, provides an interface for the researchers to access data, provides a framework to store research results and integrate data sets, and supports assembly and dissemination of data sets to the NNSA KB. A wide range of information products required to support the ME/NA/WE regionalization program is being derived from waveforms, station parameters, and event origin information contained in the SRDB. Corrections and parameters derived, assembled, integrated and validated using the SRDB provide essential contributions to the NNSA Knowledge Base for the ME/NA/WE region and will improve capabilities for underground nuclear explosion monitoring by supporting critical functions in detection, location, feature extraction, identification, and analyst review in the Middle East, North Africa and Western Eurasia.

REFERENCES

Myers, S., M. Flanagan, M. Pasyanos, C. Schultz (2002), Location Calibration in Western Eurasia and North Africa: Ground Truth Improved Earth Models, Bayesian Kriging, Regional Analysis, Location Algorithms, Array Calibrations and Validation, Proceedings of the 24th Seismic Research Review.

Walter, W., A. Rodgers, M. Pasyanos, K. Mayeda, A. Sicherman (2002), Identification in Western Eurasia: Regional Body-Wave Corrections and Surface-Wave Tomography Models to Improve Discrimination Validation, Proceedings of the 24th Seismic Research Review.

BROADBAND SEISMIC STUDIES IN SOUTHERN ASIA: SOURCE AND PATH CHARACTERIZATION

Keith Priestley,[1] Alessia Maggi,[1] Vinod K. Gaur,[2] Supriyo Mitra,[1] Jessie L. Bonner,[3] and James F. Lewkowicz[3]

Cambridge University,[1]
Center for Mathematical Modeling and Computational Sciences, Bangalore, India,[2] and
Weston Geophysical Corporation[3]

Sponsored by Defense Threat Reduction Agency

Contract No. DTRA01-00-C-0028

ABSTRACT

We have deployed a sparse network of nine broadband stations in India to collect seismic data for studies of the crust and upper mantle velocity and attenuation structure, regional wave propagation characteristics, seismic sources, and seismic hazards. To date, our primary focus has been the installation and operation of the seismic stations, the determination of crustal structure of the southern Indian shield, and waveform modeling of earthquake sequences.

Travel times between sources and stations in the Indian shield are used to develop *P*- and *S*-wave velocity models for the Indian peninsula. Arrival times are measured in the distance range 200 to 2400 km. We minimize travel-time errors by only using sources whose hypocentral parameters are constrained with local seismic data. At near-regional distances the *Pn* and *Sn* velocities are 8.10 km/sec and 4.70 km/sec, which agree with previous results from receiver function studies. These new and/or updated velocity models have been integrated into WINPAK3D (Reiter *et al*., 2001) and are currently being validated using various sources of ground truth data in the region.

We have modeled teleseismic and regional waveforms of the 26 January 2001 Bhuj mainshock and its aftershocks. The propagation paths to the regional seismographs were calibrated by using the source mechanism and depth determined by inverting the teleseismic P- and SH- body waves of the large aftershock that occurred on 28 January 2001 and inverting the regional waveforms for the propagation characteristics of the path. We then use the regional waveforms and the calibration information for the regional paths to determine mechanisms and depths for the smaller aftershocks. We use an adaptive forward modeling approach, which efficiently samples the entire space of focal parameters and converges to the minimum misfit solution. This approach is similar to the neighborhood algorithm of Sambridge (1999). The variation in aftershock location and mechanisms suggests that more than one fault was active during the Bhuj earthquake sequence.

OBJECTIVES

The objectives of our research effort are fourfold. The first is to increase the amount of high quality seismic data that are available by deploying additional seismic stations in the India/Pakistan region. The second is to use these data to refine the regional attenuation characteristics, the regional travel time corrections, and the crust and upper mantle structure of the region. The third is to use the analysis of these data to refine Weston's 3D velocity model for India and Pakistan (WINPAK3D) and to validate the model. The fourth is to provide a cooperative forum for the exchange of information and ideas on the analysis of the data and modeling of the region.

RESEARCH ACCOMPLISHED

Operation of Broadband Seismographs in India

We currently have nine broadband seismic stations collecting seismic data in India as shown in Figure 1. This includes three new stations (BOMD, ALMO, and NAPG) together with six stations that have been in operation intermittently since early 2001. These stations are operated by Cambridge University in conjunction with the Indian Institute of Astrophysics (IIA) at Bangalore. Each station consists of a Guralp CMG-3T digital output seismometer with a velocity response between 0.008 and 50 Hz. The stations continuously sample data at 100 samples/sec, and the data are archived on 9 GB disks. Several of the stations suffered mechanical and power failures during the past year, resulting in modifications to the systems. As a result, dial-up capabilities were developed and will be installed at most of the stations by September 2002 in order to give the operators easy access to troubleshooting the systems. As we enter the final year of this project, the entire network has been deployed and is in operation.

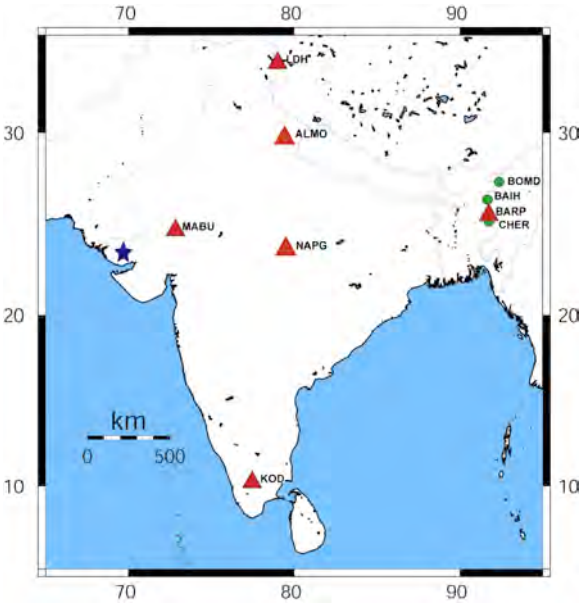

Figure 1. (Left) Locations of the Cambridge University/IIA broadband seismic stations. The stations marked with red triangles will remain deployed for the duration of the experiment while the green circles show stations that will be redeployed for optimal data coverage.

Updating the WINPAK3D Velocity Model

We continue to use the products derived from these new data collected in southern Asia to update Weston Geophysical Corporation's INdia and PAKistan 3D velocity model, referenced as WINPAK3D. The initial 3D velocity model was developed through synthesis of pertinent data from approximately 69 published references on the velocity structure, geology, and tectonics throughout the region. The references utilized included data such as seismic refraction and reflection studies, interpretations of gravity data, surface wave studies, and receiver function analyses. Stable shield regions make up a significant portion of the model to the SE, while continental collision has complicated much of the structure in the north. Recently, the model was updated using a fully 3-D tomographic inversion as described in Reiter *et al.*, (2001).

Station MABU is located in northwestern India (Figure 1) approximately 300 km northwest of the Mw=7.6 Bhuj earthquake that occurred on 26 January 2001 (blue star in Figure 1). The station was deployed after the mainshock on 18 March 2001 and immediately started recording aftershocks from this region including a M_s=4.9 that occurred on 19 March 2001 (Figure 2). During the initial three weeks of MABU operation, we noted over 700 detections associated with aftershocks from this region. Figure 2 shows an example of further WINPAK3D development using these new data. We then used WINPAK3D as the starting model and inverted the Rayleigh dispersion curves for shear wave velocity structure. The results show the crustal thickness in this region is approximately 40 km and there are differences between the inverted model and WINPAK3D in the upper and middle crust. We continue to examine the events in this region for further constraints on velocity structure in northwestern India.

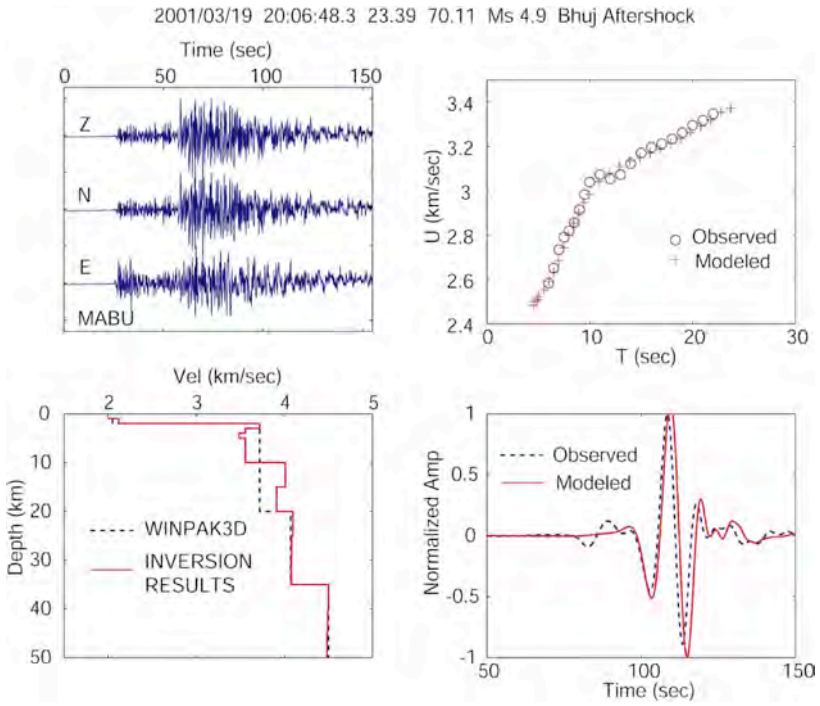

Figure 2. (Upper Left) Three-component seismograms at MABU for a Bhuj earthquake. (Upper Right) Observed and modeled dispersion curves for the Rayleigh waves from this aftershock. (Lower Left) Initial (WINPAK3D) and final model from the inversion of the Rayleigh wave dispersion curves. (Lower Right) Comparison of observed and modeled surface waves using the final model from the inversions.

<u>Source Mechanisms of Bhuj Aftershocks from Regional Waveform Modeling</u>

The Mw 7.6 earthquake of 26 January 2001 occurred in the Kachcch Peninsula (Figure 3), an area with a long history of strong earthquakes (Bapat *et al*., 1983). The region is bordered to the north and south by rift systems, created during the initial separation of the Indian subcontinent from Pangea. These structures are now subjected to compressional stress and reverse faulting resulting from the India - Eurasian collision (Talwani and Gangopadhyay, 2001). The 1819 Allah Bund earthquake, which occurred on a fault bounding the northern side of the Great Rann, was the first large earthquake in this region for which some focal mechanism information is available (Bilham, 1998). There have been other significant earthquakes in this region, the best located being the 1956 event near the town of Anjar (Figure 3).

In the following study, we examine source mechanisms for the mainshock and larger aftershocks of the Bhuj earthquake sequence. We invert teleseismic P- and SH-waveforms to determine the mainshock mechanism. We determine the mechanisms of the moderate size aftershocks from inversion of regional waveforms after calibrating the propagation paths.

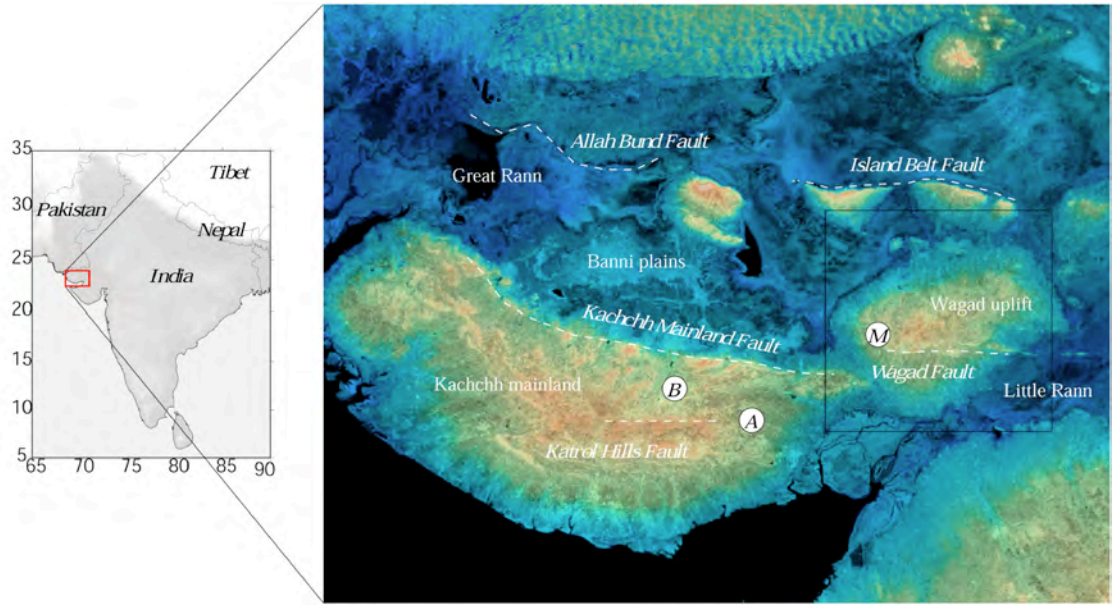

Figure 3. (Left) Geographical location of the Kachchh region and topography (right) from the Shuttle Radar Topography Mission (NASA/JPL/NIMA). Superimposed on the topography image are the locations of the major faults and the towns mentioned in this paper (B: Bhuj, A: Anjar, M: Manfara).

Teleseismic waveform modeling

The focal mechanism and depth of moderate-sized earthquakes can be determined through teleseismic body wave modeling. We invert P- and SH-waveform data for strike, dip, rake, centroid depth, seismic moment and source time function for the Bhuj mainshock and the largest aftershock (28 January). Another aftershock, 19 February, was well recorded at a few teleseismic stations and we used these data to confirm our regional solution for this event.

The Bhuj mainshock waveforms are fit by a single double couple source (Figure 4a). The minimum misfit solution is an EW trending thrust (strike 281°, dip 42°, rake 107°), with a centroid depth of ~20km. The centroid depth is constrained by the width of the larger pulses in both the P- and SH-waveforms, while the strike of the fault plane is primarily constrained by the polarity and amplitude of the SH arrivals. Our solution is consistent with the Harvard CMT solution (strike 298°, dip 39°, slip 136°). Fault-slip distribution studies (Yagi and Kikuchi, 2001; Antolik and Dreger, 2001) found that most of the slip occurred at depths of 18-25 km, with almost no slip occurring at the surface, consistent with the lack of a substantial surface faulting (Wesnousky *et al*., 2001). The rupture nucleated in the bottom half of the fault plane, and propagated westwards about 40 km and upwards about 20 km.

The 28 January event was the largest aftershock of the Bhuj earthquake, and occurred at the northern edge of the Wagad Uplift (Figure 3). The teleseismic waveforms for this earthquake (Figure 4b) are similar to those for the mainshock, except for the narrower width of the first pulse, which is controlled by both the depth and duration of the event. The body wave inversion (Figure 4b) solution for this event gives an E-W trending thrust fault (strike 81°, dip 50°, rake 87°) with a centroid depth of ~9 km and a 4 second duration. The strike of the solution is controlled by the SH waves, but is less well constrained than that of the mainshock, because the seismograms are noisier.

Regional waveform modeling

Method: The remaining large aftershocks did not produce sufficient good quality teleseismic body-waveforms to determine their source parameters from body wave modeling, and we have instead constrained their source parameters by regional waveform modeling. The character of a seismic waveform is determined by both the seismic structure along the propagation path and the earthquake source. It is more difficult to determine source properties from regional data because of the greater propagation path complexity, but source parameters can be determined from regional seismic data if the contribution from the propagation path is known. We calibrate the propagation paths to the regional stations (Figure 5) using the seismograms of the 28 January event, and then using these calibrated propagation characteristics, extract focal parameter information from the regional seismograms of the

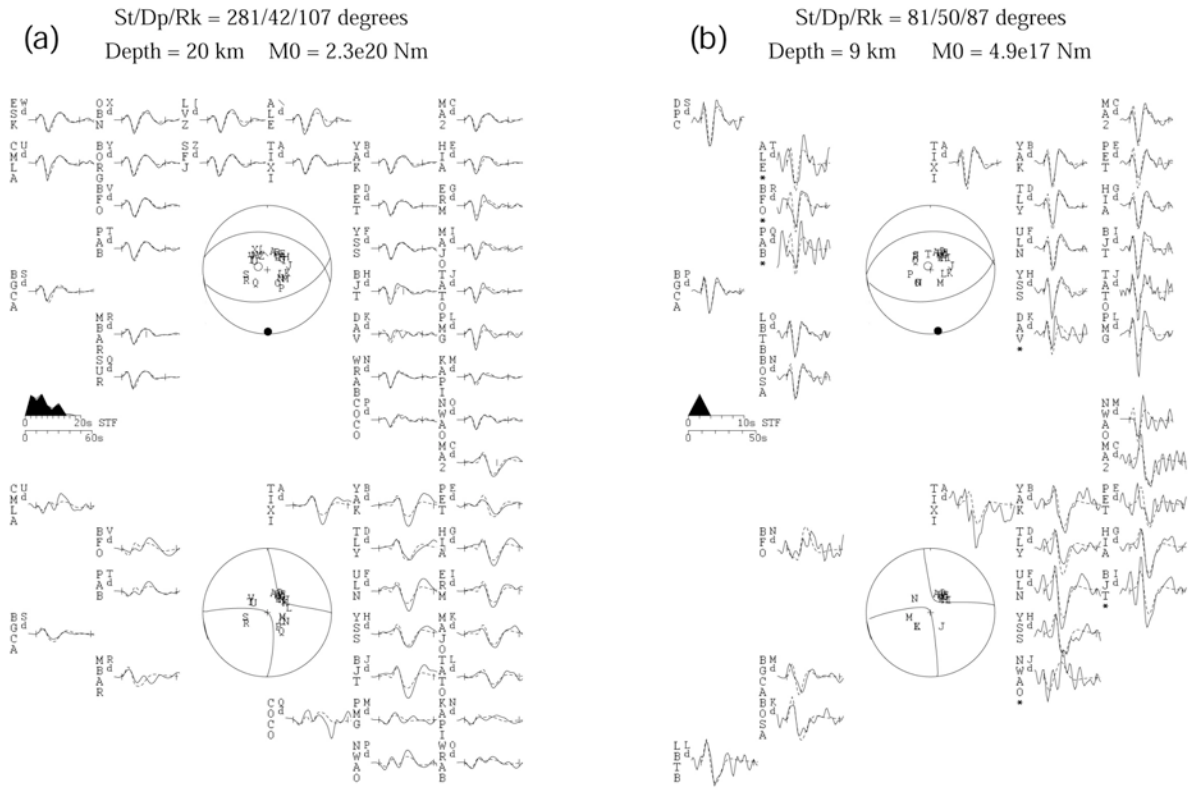

Figure 4. (a) Minimum misfit solution for the Bhuj mainshock. The upper sphere shows the P-wave radiation pattern and the lower sphere the SH-wave radiation patter. Both are lower hemisphere projections. The station code by each waveform is accompanied by a letter corresponding to its position in the focal sphere. The positions are ordered clockwise by azimuth. The solid lines are the observed waveforms, the dashed lines are the synthetic waveforms. The inversion window is marked by solid bars at either end of the waveform. P and T axes within the sphere are represented by solid and open circles, respectively. The source time function is shown below the P focal sphere, with the waveform time scale below it. (b) Minimum misfit solution for Mw 5.7 aftershock of 28 January is shown in the same format as (a).

smaller events. We calibrate the propagation paths using the 28 January aftershock rather than the mainshock because of the extended rupture of the mainshock and because the recordings at several of the closer stations were clipped.

We use a surface-waveform fitting algorithm (Nolet, 1990), which applies perturbations to depth-parameterized 1D starting models to fit multimode surface waves in increasingly wide frequency bands. We create starting models for each path by integrating along Crust2 (Bassin *et al*, 2000) and adding this to the upper mantle structure of PREM, and have parameterized both shear wave velocity (b) and Moho depth. We have calibrated Rayleigh and Love waves separately since we require the propagation characteristics and not the velocity model. The locations of the stations and an example of path calibration are shown in Figure 5. Only three of these stations are part of the Global Seismograph Network (GSN); other data are from proprietary data sources.

Adaptive grid search: Having calibrated the propagation characteristics of paths to regional stations, we then extract focal mechanism information from surface wave recordings of the aftershocks at these stations. We use an adaptive forward modeling approach, which efficiently samples the entire space of focal parameters (strike, dip, rake, depth). This approach is similar to the neighborhood algorithm of Sambridge (1999) and is summarized in Figure 6.

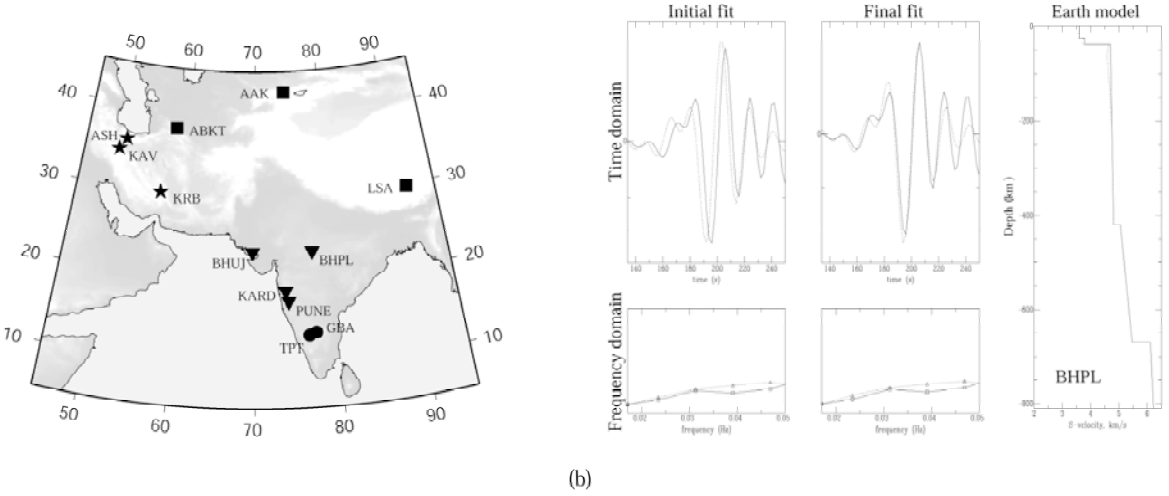

Figure 5. (a) Location of broadband stations within regional distances of Bhuj. GSN stations are shown as squares, while other data sources are shown as stars, circles, and triangles. The station at Bhuj is also plotted for reference. (b) Love wave calibration of the path to central India, showing the initial and final fit of synthetic (dotted lines) seismograms and spectra to the data (solid lines). The right hand panel contains the starting (solid) and final (dotted) Earth models.

We take a random sample of points in parameter space, calculate forward synthetic seismograms by modal summation for all stations that recorded the event using the calibrated structure for each path, and compare the synthetic seismograms to the observed records to give a single misfit value per point in parameter space. We then subdivide the entire parameter space into subspaces around each sample point, such that each point within a subspace is closer to the sample point at its center than any other sample point (subdivision into Voronoi cells). 'Closeness' is defined by a Euclidean distance metric which is normalized by the a priori variances of the single parameters. We rank the sample points according to misfit, and take new random samples within the Voronoi cells around the best few sample points (best 10%). By iterating this procedure, it is possible to quickly and efficiently converge to the minimum misfit region of parameter space, mapping out deep local minima, but not getting trapped in them.

We measure the misfit, *e*, between an observed record and its synthetic seismogram by cross-correlation (Wallace, 1986):

$$e = 1 - \frac{s \, f \, d}{(s \, f \, d)^{\frac{1}{2}} (d \, f \, d)^{\frac{1}{2}}}, \qquad (1)$$

where *s* is the synthetic seismogram, *d* is the observed seismogram and f indicates 'the maximum value of the correlation function'. Comparing seismograms in this manner allows us to cope with errors in the epicentral locations of the events. Errors in epicentral location cause the synthetic seismograms to be shifted in time with respect to the observed seismograms. These time shifts translate directly into the lag of the cross-correlation function, but do not affect its amplitude or the misfit *e*.

Results: We use this method outlined to extract focal parameter information for six of the larger aftershocks of the Bhuj earthquake. The resulting focal mechanisms and depths are listed in Table 1 and examples of the analyses are shown in Figures 7 and 8. As a test of the method, we first analyzed the 28 January aftershock. The mechanism determined from the regional seismic data for this event (Figure 7a) agrees very well with the teleseismic solution (Figure 4b) for both focal mechanism and depth. Both depth and dip have wide minima; the minimum misfit region spans depths from 5 to 12 km, and dips from 25° to 60°. There is an indication of trade-off between strike and rake, although the minimum is narrow in both these parameters. The fits to the 10 Rayleigh and 7 Love waves observed for this event at regional stations are excellent.

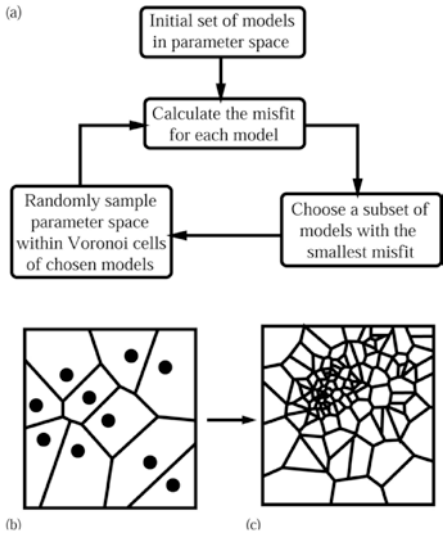

Figure 6. The neighborhood algorithm. (a) Flowchart of the adaptive grid-searching method. (b) Example of an initial distribution of parameters within a parameter space. (c) Example of a final distribution of parameters within a parameter space. (b) and (c) are reproduced from Sambridge (1999).

Table 1. Locations and focal mechanisms of the Bhuj mainshock and larger aftershocks.

DATE	TIME	LAT. N	LON. E	M_W	DEPTH	FOCAL MECHANISM
26-01-2001	03:16:40	23.415	70.322	7.5	20	281/42/107ß
27-01-2001	04:36:06	23.404	70.107	5.2	13	104/39/105
28-01-2001	01:02:12	23.541	70.587	5.7	9	096/48/107
03-02-2001	03:04:35	23.712	70.525	5.1	1	127/33/056
08-02-2001	16:54:42	23.705	70.475	5.2	5	141/65/167
19-02-2001	08:24:21	23.596	70.158	5.2	4	004/28/136
04:03:2001	07:54:22	23.134	70.493	5.0	11	036/86/332

Epicenters from Engdahl and Bergman (2001) except aftershock on 27-01-2001 (proprietary data). Depths and mechanisms from regional waveform inversion except the mainshock (ß - teleseismic waveform inversion).

Although the 27 January, 2001 (Mw 5.2) event was well recorded at six regional stations, the minimum misfit solution shows good fits to both Love and Rayleigh waveforms (Figure 7b) at stations AAK, ABKT, LSA, and (though to lower frequency) TPT. The fits at stations GBA and PUNE are less convincing. Although the minimum misfit region is small, the 10% acceptability contour encompasses a wide range of depths (0-15 km) and dips (20-70). The minimum misfit focal mechanism, an E-W trending thrust, is similar to both the mainshock and the January 28 aftershock.

The mechanism for the 19 February, 2001 (Mw 5.2) event determined from the regional seismograms is shown in Figure 8. Fits to all seismograms are good, although the synthetic seismograms do not fit the long period start of the Love wave at ABKT or the tail of the Rayleigh wave at ASH very well. This event was large enough to have a Harvard CMT solution: an E-W trending thrust mechanism also at a depth of 4 km, significantly different from the mechanism shown in Figure 8a (a NW-SE trending thrust). Figure 8b-c compare our solution with the Harvard CMT solution. Synthetic seismograms for the Harvard mechanism (Figure 8b) produces poorer fits at all stations, except for the Love wave at ABKT. This event was also large enough to produce several teleseismic P- and SH-waveforms which could be modeled. Figure 8c compares fits for four P and two SH waveforms for our mechanism and the Harvard CMT mechanism. Both solutions fit the seismograms reasonably well, with our mechanism giving a synthetic waveform fitting significantly better only at LBTB.

CONCLUSIONS AND RECOMMENDATIONS

The regional waveform grid-search analysis of the larger aftershocks of the Bhuj earthquake finds that the depths of the events are poorly constrained by the surface wave data. After depth, fault dip is the least well-constrained parameter, while fault strike and slip (rake) direction can be very well constrained by the surface wave data. Only

Figure 7. (a) Regional waveform solution for the 28 January aftershock. The focal parameters for the minimum misfit solution are shown under the event date. The six upper panels show slices through the misfit volume taken through the minimum, with two different parameters fixed at the minimum misfit values. Regions with misfits of less than 1% are shown in black, and regions with misfits of less than 10% are surrounded by a white contour. The regional and teleseismic mechanisms are shown below the panels, and are followed by the fits of synthetic (red dotted) to observed (solid) seismograms for all the available data. The letters (L) and (R) after the station names indicate the seismograms are Love and Rayleigh waves respectively. All parameters are very well constrained, and the resulting focal mechanism is almost identical to the teleseismic solution. (b) Regional waveform solution for the 27 January aftershock in the same format as (a). All parameters are well constrained, despite the low number of waveforms available (7), but the dip and depth have broad 10% contours. The minimum misfit focal mechanism is almost identical to the mainshock.

Figure 8. Regional waveform solution for the 19 February aftershock. Comparison with the Harvard CMT solution for the 19 February aftershock. (b) Fits to the regional data: the seismograms are less well matched at all stations, except for ABKT, where the long period precursor to the Love waves is better matched by the CMT solution. (c) Fits to the teleseismic data. The first line shows the synthetics from the regional mechanism for 8 P and 5 SH waveforms. The second line shows the fit of synthetics for the Harvard CMT mechanism. Strike, dip, rake, depth (km) and seismic moment (Nm) are shown above the P and SH focal mechanisms in each line.

two of the larger aftershocks of the Bhuj earthquake sequence (27 January and 28 January) had mechanisms (E-W trending thrusts) similar to that of the mainshock (Table 1). The 27 January (Mw 5.1) event occurred just north of the Kachcch Mainland fault, at the edge of the Banni Plain, and took up N-S compression along an E-W trending trust fault. The 28 January (Mw 5.7) event occurred on the north Wagad peninsula, probably on an E-W structure parallel to the northern boundary of the peninsula itself. Two of the aftershocks (8 February, 4 March) have well constrained strike slip mechanisms (Table 1) with N-S P-axes that can take up N-S shortening. The epicenters of these events to the north and south of the Wagad uplift, respectively (Figure 3), place them in the salt plains and tidal regions of the Rann. There is no obvious surface expression of the faults that ruptured in these small events (Mw 5.2 and 5.0 respectively). Wesnousky *et al.* (2001) reported that although they found no primary surface faulting reflecting large reverse motion, they did observe one tectonic rupture showing strike slip motion, along the western boundary of the Wagad uplift, near the town of Manfara. This surface rupture zone strikes NW for about 8 km, and shows primarily right lateral motion with up to 32 centimeters of slip. Given the location of the fault, between the Kachcch mainland and the Wagad uplift, Wesnousky *et al.* (2001) speculated that this strike slip rupture occurred on a pre-existing fault, related to a structural discontinuity or tear between the two uplifted blocks. The 3 February and 19 February aftershocks are both thrust events with a strike-slip component. The mechanism of the 3 February (Mw 5.1) event indicates either near-vertical slip on a high angle eastward dipping fault, or westward slip on a low angle southwest dipping fault. The mechanism of the 19 February (Mw 5.2) event is similar to that of the 3rd February, though the fault planes are reversed (the shallow plane dips east while the steep plane dips south west). The epicenters of these two events are both within the flat-lying tidal range of the Rann of Kachcch, and there is no obvious surface expression of the faults on which they occurred.

The source mechanism and depth can be further constrained by adding Pnl to the source mechanism inversion procedure. We have calibrated the Pnl propagation to the regional stations and are now incorporating Pnl in the source mechanism inversion routine.

REFERENCES

Antolik, M. and D.S. Dreger. (2001), Source rupture process of the 26 January, 2001 Bhuj, India, earthquake (M 7.6). *EOS Trans. AGU*, 82 (47), Fall Meet. Suppl.

Bapat, A., R.C. Kulkarni, and S.K. Gutha. (1983), Catalog of earthquakes in India and neighborhood from historical period up to 1979. Technical report, India. Soc. Earthq. Tech.

Bassin, B., G. Laske, and G. Masters, (2000), The current limits of resolution for surface wave tomography in North America. *EOS Trans. AGU*, 81: 897.

Bilham, R., (1998), Slip parameters for the Rann of Kachchh, India, 16 June 1819, earthquake, quantified from contemporary accounts. In I.S. Stewart and C. Vita-Finzi, editors, Coastal Tectonics, volume 146, pages 295-319. Geological Society, London, Special Publications.

Chung, W-Y. and H. Gao, (1995), Source parameters of the Anjar earthquake of July 21, 1956, India, and its seismotectonic implications for the Kutch rift basin. *Tectonophysics*, 242: 281-292.

Engdahl, E.R. and E.A. Bergman, (2001), Validation and generation of reference events by cluster analysis. In Proceedings of the 23rd Seismic Research Review: Worldwide Monitoring of Nuclear Explosions, Volume 1, pages 205-214. NNSA, DTRA.

Nolet, G., (1990), Partitioned waveform inversion ant two-dimensional structure under the Network of Autonomously Recording Seismographs. *J. Geophys. Res.*, 95: 8499-8512, 1990.

Reiter, D. T., M. Johnson, A. Rosca, C. Vincent (2001), Development of a regional 3-D velocity model of the Pakistan region for improved seismic event location. Final Report, Weston Geophysical, 27 p.

Sambridge, M. (1999), Geophysical inversion with a neighborhood algorithm - I: searching a parameter space. Geophys. J. Int., 138: 479-494.

Talwani, P. and A. Gangopadhyay, (2001), Tectonic framework of the Kachchh earthquake of 26 January 2001. *Seism. Res. Lett.*, 72: 336-345.

Wallace, T.C. (1986), Inversion of long period regional body waves for crustal structure. *Geophy. Res. Lett.*, 13.

Wesnousky, S. G., L. Seeber, T.K. Rockwell, V. Thakur, R. Briggs, S. Kumar, and D. Ragona (2001), Eight days in Bhuj: field report bearing on surface rupture and genesis of the 26 January 2001 earthquake in India. *Seism. Res. Lett.*, 72 514-523.

Yagi, Y. and M. Kikuchi (2001), Results of rupture process for January 26, 2001 western India earthquake (ms 7.9). WWW:http://wwweic.eri.u-tokyo.ac.jp/yuji/southindia/index.html, March 2001.

WAVEFORM MODELING OF THE CRUST AND UPPER MANTLE USING S, Sp, SsPmP AND SHEAR-COUPLED PL WAVES

Jay Pulliam, Mrinal K. Sen, Cliff Frohlich, and Steve Grand

University of Texas at Austin

Sponsored by the Defense Threat Reduction Agency

Contract No. DTRA01-00-C-0060

ABSTRACT

Phases that arrive near the direct SV phase, including Sp (converted at the base of the Moho), SsPmP, and shear-coupled PL (SPL) waves, collectively sample the Earth's crust and upper mantle at oblique angles and therefore have the potential to produce an accurate lateral average of structural properties than teleseismic P waves. SPL waves essentially mimic the propagation characteristics of regional PL phases, with the important difference that the number of events available for modeling is often greater for relatively aseismic regions, since sources are located at teleseismic distances. SPL waves are sensitive to crust and upper mantle structure, including seismic velocity gradients, Vp/Vs, impedance contrast across the Moho, and layer thicknesses. The first-arriving Sp and relatively large-amplitude SsPmP phases can often be identified and modeled simultaneously with SPL, which offers stronger overall constraints on the model.

The high frequencies and long time-series required for these phases, their deep penetration into the Earth and observation at teleseismic distances make the computation of synthetic seismograms time-consuming. We have parallelized and optimized a synthetic seismogram code based on the reflectivity method and are now able to compute complete seismograms up to 0.5 Hz in just over two minutes using eight DEC Alpha processors. The speed-up in computation time is nearly linear with the number of processors used, so a larger cluster and/or faster processors will further increase computation speed significantly.

In the past year we calibrated our reflectivity code against two widely-used codes and implemented a waveform-fitting global optimization algorithm. We are currently modeling observations of S, Sp, SsPmP, and SPL recorded for five deep earthquakes located at distances of 31°--59° from stations of the China Digital Seismographic Network (CDSN). The waveform-fitting process is controlled by a variant of Simulated Annealing (SA) that speeds up the annealing process by drawing each new model from a temperature dependent Cauchy-like distribution centered on the current model. This change with respect to SA has two fundamental effects. First, it allows for larger sampling of the model space at the early stages of the inversion and much narrower sampling in the model space as the inversion converges and the temperature decreases, while still allowing the search to escape from local minima. Second, each model parameter can have its own cooling schedule and model-space sampling scheme. In our case, each modeling run performs roughly a thousand iterations of forward calculations. Such a broad search of the model space, combined with analyses of sensitivity, resolution, and uncertainty, allows tradeoffs between model parameters to be evaluated, which helps build confidence in the final models.

OBJECTIVE

The conventional S phase is the initial, relatively sharp and pulse-like arrival that signals the beginning of a wavetrain with generally longer periods and normal dispersion. The particle motion associated with the S phase is rectilinear and all three components of motion are in phase. The dispersive wavetrain that follows S exhibits prograde elliptical particle motion that is confined to the vertical plane. Oliver (1961) named this wavetrain "shear-coupled PL" because it is analogous to the PL wavetrain, which appears between P and S arrivals at regional distances. Oliver (1961) presented a theory, based on the observed group and phase velocity of SPL that explained the phase as coupling between S and the fundamental leaking mode of Rayleigh waves in the crustal waveguide. According to this theory, shear energy generated by an earthquake (or explosion) travels through the Earth's mantle as a body wave, whereupon it impinges upon the Moho. Afterward a portion travels through the crustal waveguide as trapped P-waves and leaky SV-waves (Figure 2). The only difference between a PL phase, which is observed at regional distances from a source, and SPL phases, which are observed at teleseismic distances, is that SPL is generated by a shear wave impinging upon the Moho at regional distances from the observing station. In addition to producing SPL as it impinges on the Moho, a portion of the incident S wave converts to P as well, which then travels through the crust to arrive at the station as a precursor to S (Figure 1). This phase is called Sp and it has been used to model the crust by Jordan and Frazer (1975). Its sampling is much more localized to the station than is SPL's, making its sensitivity less representative of the broader region and more similar to that of P-coda receiver functions. SsPmP arrives at the base of the crust as a shear wave, travels upward through the crust as a shear wave, converts to a P wave at its surface reflection and bounces once off the Moho as a P wave. Langston (1996), while demonstrating that it can be highly useful for regional crustal modeling, showed that SsPmP can arrive before or after direct S, with either larger or smaller amplitude, and can also distort the S arrival pulse. We will attempt to simultaneously model S, Sp, and SsPmP which essentially isolates differences to the P structure of the crust, for data collected for SPL modeling. Because receiver function methods typically deconvolve the vertical seismogram, which is most sensitive to compressional wave energy, from the radial seismogram, constraints on P velocity are essentially sacrificed in order to obtain clean records of shear phases. The data we propose to model will provide a valuable check of receiver functions, in that they constrain the bulk properties of the crust—average P velocity and crustal thickness

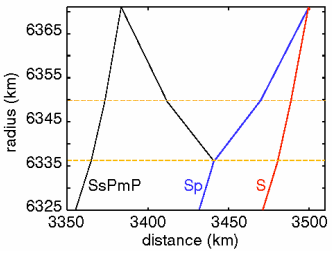

Figure 1. Typical raypaths for S, Sp, and SsPmP. These body wave phases provide constraints on crustal thickness, P and S velocities near the station.

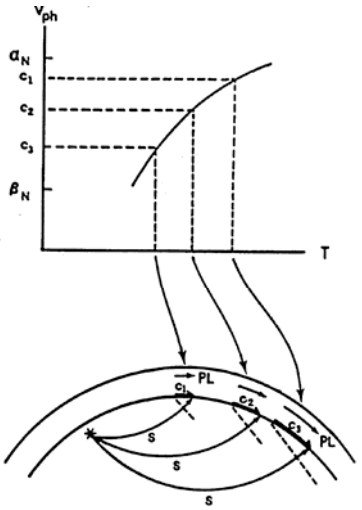

Excitation of *SPL*-waves with distance and corresponding period–phase velocity curve. α_N, β_N: velocities of *P*- and *S*-waves at the Moho, *T*: period, V_{ph}: phase velocity.

Figure 2. Propagation characteristics of shear-coupled PL phases (from Baag and Langston, 1985). Note that the distance of propagation of SPL, and therefore its sampling, depends on characteristics of the velocity structure, including the slope of velocities below the Moho and attenuation. The earliest-arriving and largest-amplitude SPL waves are those that have converted from S nearest to the station, so our modeling will weight local sampling more highly than distant sampling but the wavefield still averages structure laterally.

(Sp and SsPmP)—and upper mantle (SPL). If the broad model search turns out to be too time-consuming or impractical, a fall-back strategy would be to first obtain a basic starting model by modeling Sp and SsPmP, then automating the SPL modeling using the Sp/SsPmP model as a starting point. Since reflectivity is a full-waveform method, there is no need to specify which phases should be included (nor need we identify or "pick" specific arrivals) in the waveform fitting procedure. While the waveform fitting itself will be automated, a great deal of exploration will be required to determine optimal window lengths, frequency content, and, perhaps, variable weighting functions for different portions of the seismograms.

We are evaluating the usefulness of S, Sp, SsPmP (Figure 1), and shear-coupled PL (SPL) phases (Figure 2) for modeling crustal and upper mantle structure using real and synthetic data, developing a waveform inversion technique based on a novel implementation of the reflectivity method and global optimization algorithms, and applying this method to data recorded in China. We have made substantial progress in speeding up the synthetic seismogram computations to the point where a global optimization is feasible. The reflectivity calculation involves computation of reflectivity matrices for a stack of layers as a function of ray parameter (or wavenumber) and frequency. The computation of reflectivity responses for different ray parameters and frequencies are completely independent of each other. We took advantage of this independence to develop a reflectivity code that runs on parallel computer architectures. Our code loops over ray parameters, i.e., to each node we assign a certain number of ray parameters to compute. At the end, the master node assembles the partial responses and performs the inverse transformation to generate synthetic seismograms at the required azimuths and distances. We used MPI for message passing and ran our code on a PC cluster consisting of 16 nodes; each node is a 660MHz alpha processor with 8MB cache and 1GB of RAM. A Myrinet interconnect is used to communicate between nodes.

Figure 3 shows synthetic seismograms computed using our parallelized reflectivity code for a distance of 50° and an earthquake at 600 km focal depth. Since the reflectivity algorithm is "embarrassingly parallel" in that the response for each frequency or ray parameter can be computed on independent processors, without communication between processors, on a parallel machine computation speed increases nearly linearly with the number of processors (Figure 4). In a side-by-side comparison for various distances, source depths, and model complexity, our code matched results of the Fuchs-Muller code very well.

Our modeling method retains the time and cost advantages of P-coda receiver function methods but which uses types of data that are more appropriate for CTBT purposes: Shear-coupled PL phases (SPL), Sp phases converted at the Moho, and SsPmP. SPL samples the crust and upper mantle in the vicinity of a station most broadly compared to Sp, SsPmP and P and it emulates the propagation of regional phases, which reflect at more oblique angles (or are refracted by these layers) than are the more steeply arriving body phases typically used in receiver function modeling. In short, because of the data they use, the models produced by receiver function methods may be inadequate for the purposes of CTBT monitoring. These

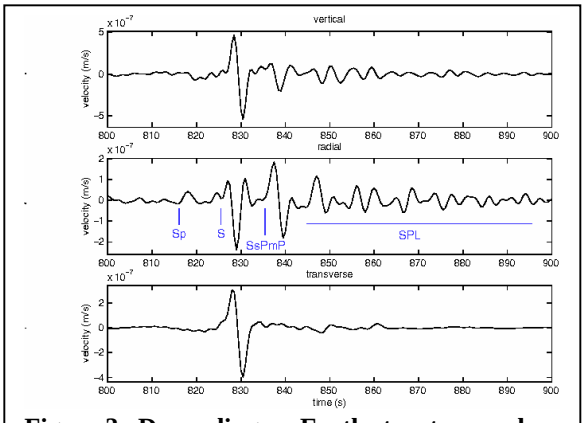

Figure 3. Depending on Earth structure and an earthquake's radiation pattern, the phases Sp, S, SsPmP, and SPL may appear prominently on the radial component seismogram at distances between 30° and 75°.

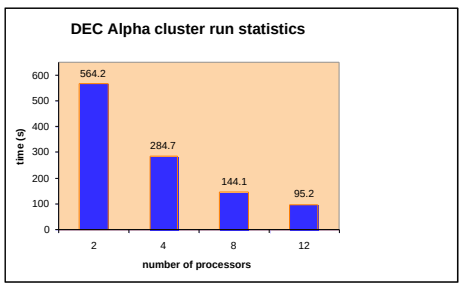

Figure 4. Statistics of an example run to compute complete seismograms for frequencies from 0 to 0.5 Hz (number of frequencies = 2000, number of layers=192, number of ray-parameters=1000) on the DEC Alpha cluster. Note the near linear speedup of the algorithm with the increase in the number of processors.

latter phases sample only a narrow cone beneath the station (e.g., Zhao and Frohlich, 1996). Modeled simultaneously (where they exist), SPL, Sp, and SsPmP offer the potential for producing azimuthally-dependent structural models.

We are pursuing this strategy because efforts to determine the locations of small, regional seismic events are hampered, in most parts of the world, by insufficient knowledge of the crust and upper mantle. Also, while focal depths are often a highly useful discriminant between explosions and earthquakes, their determination is quite sensitive to crustal structure. The most encouraging approaches to determining focal depths require precise modeling of seismic waveforms, particularly for small-magnitude events, in which travel time picks are relatively more prone to errors than for larger events. Yet, a precise modeling of waveforms at regional distances requires an accurate model of the crust and upper mantle along the propagation path between source and receiver.

RESEARCH ACCOMPLISHED

Forward Modeling

In order to explore the sensitivity of each phase we computed synthetics for a variety of distances using different crust and upper mantle models, including PREM (Dziewonski and Anderson, 1981; Figure 5), SNA (Grand and Helmberger, 1986; Figure 6), TNA (Grand and Helmberger, 1986; Figure 7), ECH (Zhao et al., 1991; Figure 8), and WCH (Beckers et al., 1999; Figure 9). Differences between these results point to sensitivity on the parts of these phases to distinct parts of the models' structure. Figure 10 shows an expanded comparison of waveforms produced using the different models for a single epicentral distance.

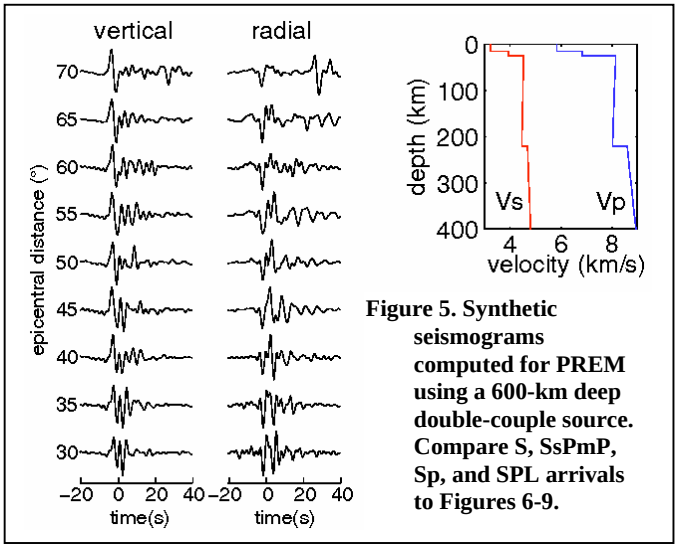

Figure 5. Synthetic seismograms computed for PREM using a 600-km deep double-couple source. Compare S, SsPmP, Sp, and SPL arrivals to Figures 6-9.

Figure 11 shows differences in waveform features to be expected from structural variations within China alone. The models at upper right were produced by Mangino et al. (1999) by modeling receiver functions for structure beneath stations of the China Digital Seismographic Network. The models differ primarily in the lower crust. One can see from the synthetics at left that these model differences are reflected by differences in the S coda, largely in SsPmP and SPL, for the distance range 30°-50°. These synthetics were produced for a 600-km deep event. This suggests that the relative timing of SsPmP-S and the phase and amplitudes of SPL phases are sensitive to the lower crust.

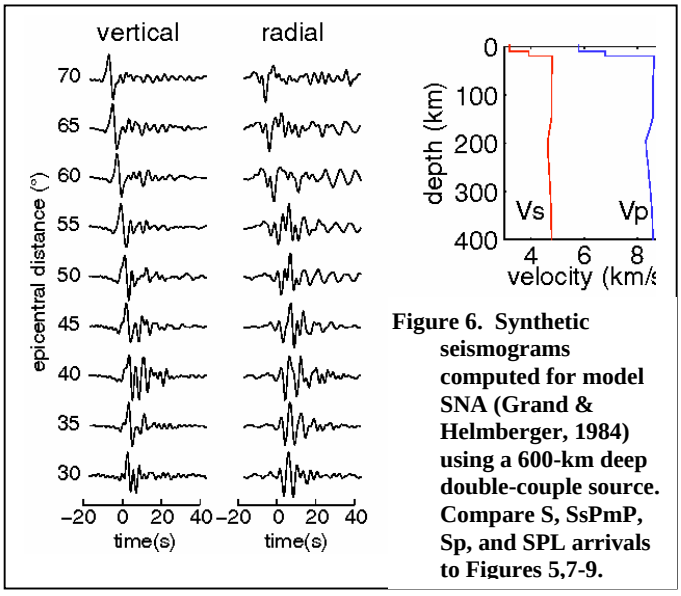

Figure 6. Synthetic seismograms computed for model SNA (Grand & Helmberger, 1984) using a 600-km deep double-couple source. Compare S, SsPmP, Sp, and SPL arrivals to Figures 5,7-9.

Inverse Modeling

Our modeling process is controlled by a global optimization algorithm called Very Fast Simulated Annealing (VFSA) (e.g., Sen and Stoffa, 1995). Simulated annealing (SA) is analogous

to the natural process of crystal annealing when a liquid gradually cools to a solid state. The SA technique starts with an initial model m_0, with associated error or energy $E(m_0)$. It draws a new model m_{new} from a flat distribution of models within the predefined limits. The associated energy $E(m_{new})$ is then computed and compared against $E(m_0)$. If the energy of the new state is less than the energy of the initial state, the new model is accepted and it replaces the initial model. However, if the energy of the new state is higher than the initial state, m_{new} is accepted with the probability of $\exp\left(\left(E\left(\mathbf{m}_{new}\right) - E\left(\mathbf{m}_0\right)\right)/T\right)$, where T is a control parameter called temperature. This rule of probabilistic acceptance (called the Metropolis rule) allows SA to escape local minima. The process of model generation and acceptance is repeated a large number of times with the annealing temperature gradually decreasing according to a predefined cooling schedule. A variant of SA, called Very Fast Simulated Annealing (VFSA) speeds up the annealing process by drawing new models from a temperature dependent Cauchy-like distribution centered on the current model. This change with respect to SA has two fundamental effects. First, it allows for larger sampling of the model space at the early stages of the inversion (when "temperature" is high), and much narrower sampling in the model space as the inversion converges and the temperature decreases, while still allowing the search to escape from local minima. Second, each model parameter can have its own cooling schedule and model-space sampling scheme. VFSA therefore allows for individual control of each parameter and the incorporation of a priori information. The model is parameterized in terms of layers, in which layer thickness is a free parameter, as are Vp, Vs, and density for each layer. In our modeling so far we have kept attenuation fixed, although it could be allowed to vary as well.

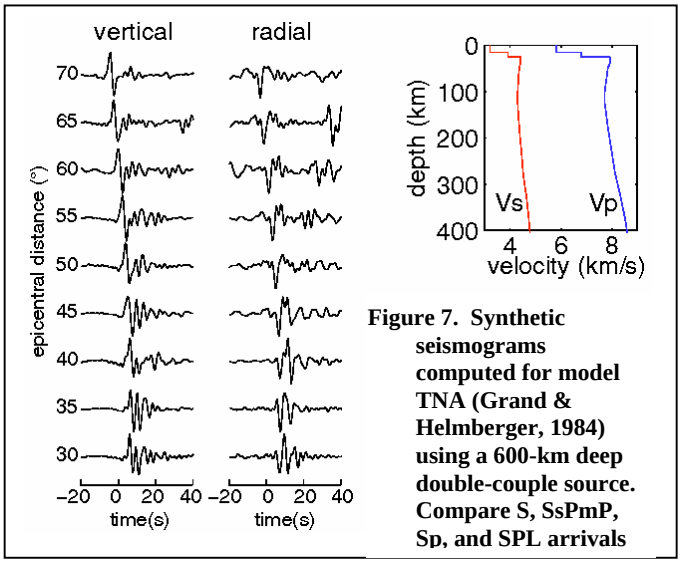

Figure 7. Synthetic seismograms computed for model TNA (Grand & Helmberger, 1984) using a 600-km deep double-couple source. Compare S, SsPmP, Sp, and SPL arrivals

Figure 12 shows the results of a synthetic inversion in which synthetic seismograms were computed for the input model shown in Figure 13 and then modeled. The result is a very good fit between output and input seismograms but the model that corresponds to the best-fitting waveforms shows some differences compared to the input model (Figure 13). However, the modeling produced accurate bulk properties for the crust, including average velocities and thickness and generally put layer boundaries close to their true locations. The differences between input and output models suggest that there is some tradeoff between parameters of different layers. These tradeoffs are the sort of information that our uncertainty estimation scheme is designed to evaluate. The goal is to produce quantitative estimates of the strengths of constraints and the uniqueness of the modeling.

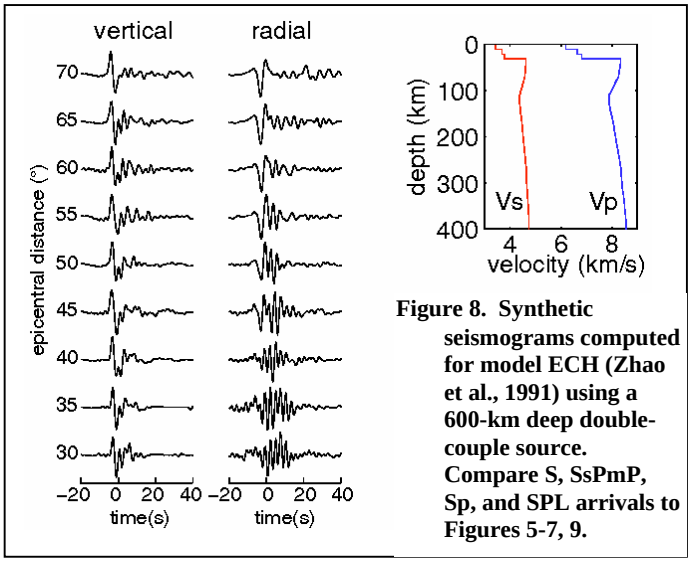

Figure 8. Synthetic seismograms computed for model ECH (Zhao et al., 1991) using a 600-km deep double-couple source. Compare S, SsPmP, Sp, and SPL arrivals to Figures 5-7, 9.

Uncertainty Estimation: PPD, Posterior Covariance and Correlation

In seismic waveform inversion, more than one model can often explain the observed data equally well and trade-offs between different model parameters are common. It is therefore important not only to find a single, best-fitting solution but also to find the uncertainty and level of uniqueness of that solution. A convenient way to address these issues is to cast the inverse problem in a Bayesian framework (e.g., Tarantola, 1987; Sen and Stoffa, 1995) in which the posterior probability density function (PPD) is the answer to the inverse problem. "Importance sampling" based on a Gibbs sampler or a Metropolis rule (Sen and Stoffa, 1998) can be used effectively to evaluate the necessary multi-dimensional integrals and to estimate PPD, posterior mean, covariance and correlation matrices. The posterior covariance and correlation matrices quantify the trade-off between different model parameters. Sen and Stoffa (1995) showed that multiple VFSA runs with different random starting models could be used to sample models from the most significant parts of the model space. This "poor man's" importance sampling, which is computationally highly efficient, results in estimates that are fairly close to the values obtained by theoretically-correct Gibbs sampling.

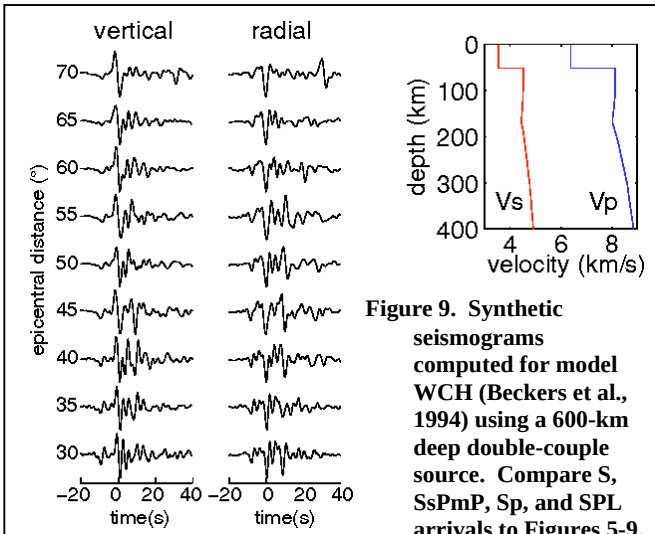

Figure 9. Synthetic seismograms computed for model WCH (Beckers et al., 1994) using a 600-km deep double-couple source. Compare S, SsPmP, Sp, and SPL arrivals to Figures 5-9.

Application to Data from the China Digital Seismographic Network

Figure 14 shows the result of modeling radial and vertical records from station BJT of the 9/28/1994 event in Indonesian (see Table 1). Subjective choices must be made in the modeling about which parts of the seismogram to try to fit. Regions with strong lateral variations or anisotropy, it may be that no single 1D model will predict all the phases adequately. Requiring the modeling to try to fit each phase similarly will result in a model that does not predict any single phase well. Given the sampling produced by the various phases, we tried to prioritize fits in the following order: SPL, SsPmP, SV, and Sp. Given the broad sampling and lateral averaging performed by SPL we believe that the single 1D model that fits SPL best will be the most useful for locating earthquakes regionally. SsPmP also has a broad sample and constrains Vp, so it's second in priority. This priority order reflects a starting point—an initial preference—and will be evaluated as a strategy.

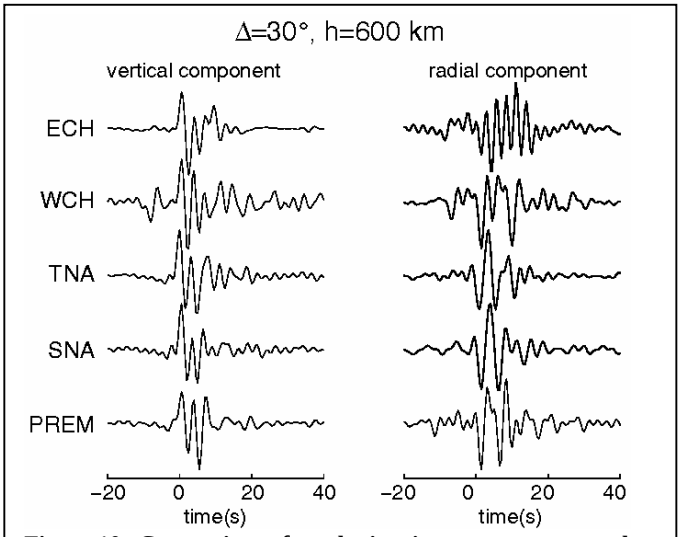

Figure 10. Comparison of synthetic seismograms computed using the models shown in Figures 5-9 for the same deep, double-couple source at an epicentral distance of 30°. Differences in the arrival times and amplitudes of S, Sp, SsPmP and SPL indicate those phases' sensitivity to structure near the receiver.

To implement this strategy we successively try to fit broader time windows of the data waveforms. Figure 14 shows the results of 600 iterations in which only the window between 815 s and 860 s is evaluated

for correlation at each iteration. The BJT receiver function model of Mangino et al. (1999) is shown for comparison, although it is not a "reference" or "starting" model in any sense. In our procedure we specify the search limits (also shown in Figure 14) and the first candidate model is chosen randomly. Figure 16 shows an attempt to fit a broader window that includes SV and Sp. Differences between the two final models shown in Figures 14 and 15 are again concentrated in the lower crust, between 30 and 50 km depth. Figure 16 shows the result of a 600-iteration run to model records from BJT of the 11/15/1994 Indonesia event (Table 1), in which the time interval fit is restricted to include SsPmP and SPL. Figure 17 shows the results of a 600-iteration run to fit a broader window, as in Figure 15. Figure 18 shows results for a third event (Table 1), also recorded at BJT. Figure 19 compares the models produced for the region containing BJT with Mangino et al.'s (1999) receiver function model, in the context of the imposed search limits. Figure 20 shows the potential applications of this technique worldwide.

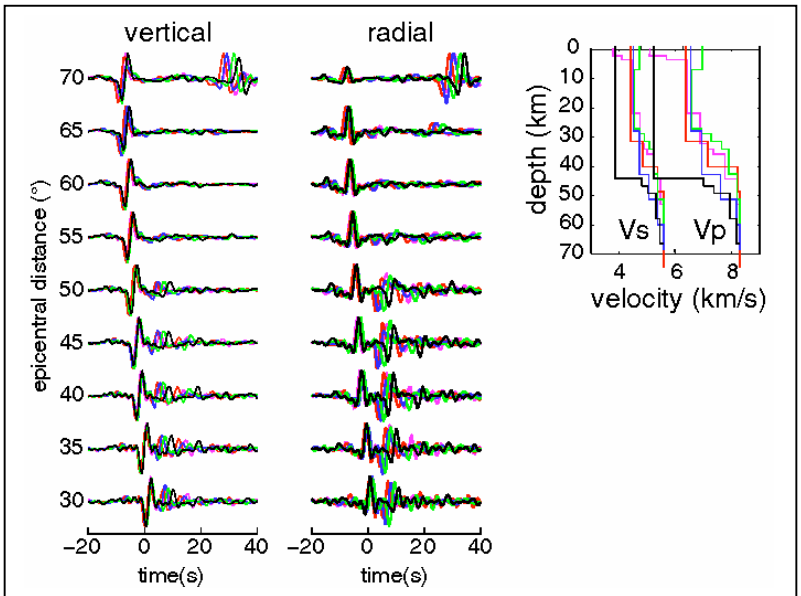

Figure 11. Synthetic seismograms computed for various receiver function models of the crust and upper mantle beneath China (models from Mangino et al., 1999). The primary differences between the seismograms are in the S coda, including SsPmP and SPL, which indicates these phases are highly sensitive to distinguishing structural details of these models.

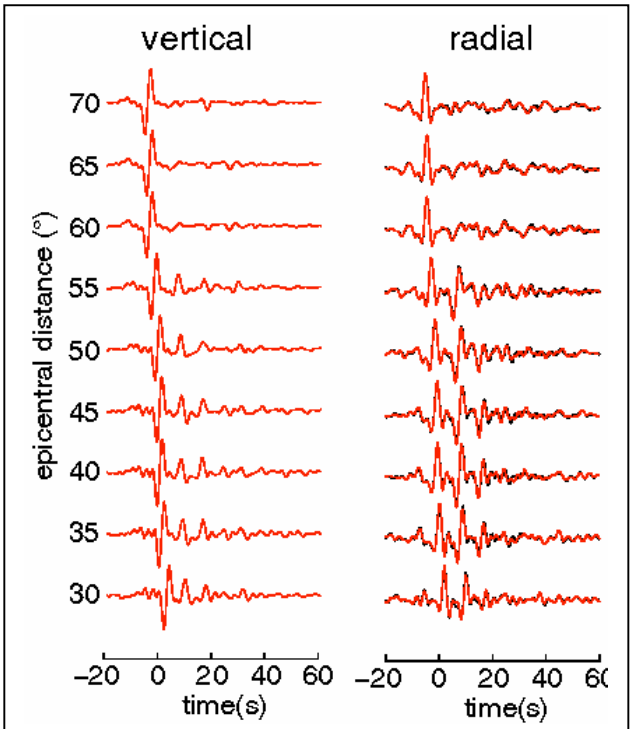

Figure 12. Waveform fits resulting from a synthetic inversion of seismograms computed for an input model shown in Figure 14 (black). Best-fitting seismograms after 400 iterations are shown in red.

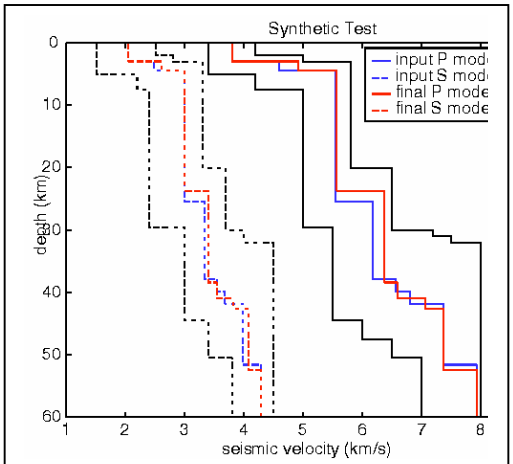

Figure 13. Input (blue) and output (red) models from the synthetic inversion test. Differences between inputs and outputs point to poor sensitivity of the phases to these parts of the model, and non-uniqueness in the inversion.

CONCLUSIONS AND RECOMMENDATIONS

We believe that modeling shear-coupled PL along with associated phases is a fruitful strategy for producing models of the crust and upper mantle that are most appropriate for locating regional seismic events. We have shown that the modeling scheme we proposed is feasible and practical but, for wide application and to evaluate uncertainties as proposed we need further increases in computational speed. We will further increase computational throughput by using additional processors (we have been unable to use all 16 processors due to minor hardware difficulties), a new cluster of faster processors, tailoring the number of ray parameters more carefully to the structure being modeled, and by pre-computing and storing reflectivity matrices for deeper parts of the mantle that will not vary in our modeling. The high frequencies needed to compute body waves accurately over the distances to which SPL is observed contribute to the time requirements for computing SPL. We plan to remove these complications by storing pre-computed products for fixed parts of the Earth model. A new cluster of processors at our institute will make our proposed approach even more practical. Evaluating objective functions and computing posterior marginal density functions and model covariance's require a negligible amount of computation time. For estimating uncertainty, we cast the inverse problem in a Bayesian framework such that, given prior information on data and model, the a posteriori probability density (PPD) function describes the answer to the inverse problem (Tarantola, 1987). Obtaining a complete description of the PPD, i.e., choosing how to sample models from the PPD, is the most challenging task. Due to the nonlinearity of the problem, an "importance sampling" approach based on Gibbs' sampler is the correct choice (Sen and Stoffa, 1998). However, this method is computationally very expensive. Sen and Stoffa (1995) have shown that the models sampled

Table 1. Events used in this study.

	Year	Month	Day	Hour	Min	Sec	Latitude (°)	Longitude (°)	Depth (km)	Mag
1	1990	5	24	20	9	23.2	-7.363	120.363	588.9	6.4
2	1994	9	28	16	39	51.7	-5.786	110.352	637.5	6.6
3	1994	11	15	20	18	11.3	-5.589	110.186	560.6	6.5

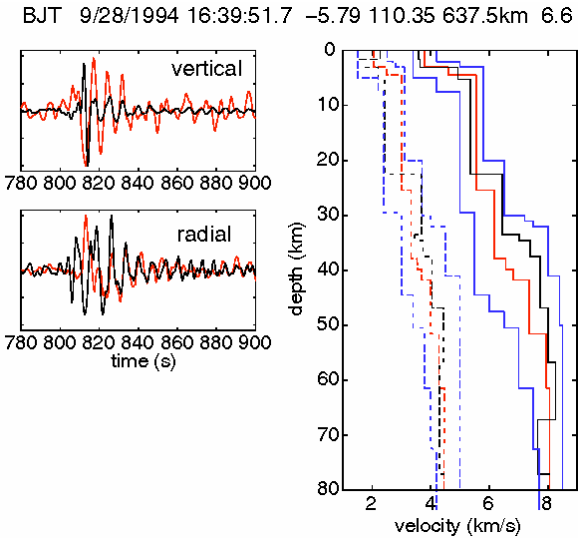

Figure 14. Optimization results after 600 iterations for fitting synthetics (black) to BJT vertical and radial records (red) of the 9/28/1994 event, using the time interval 815-860 s. Best-fitting model (black), search bounds (blue), and receiver function model by Mangino et al. (1999) (red).

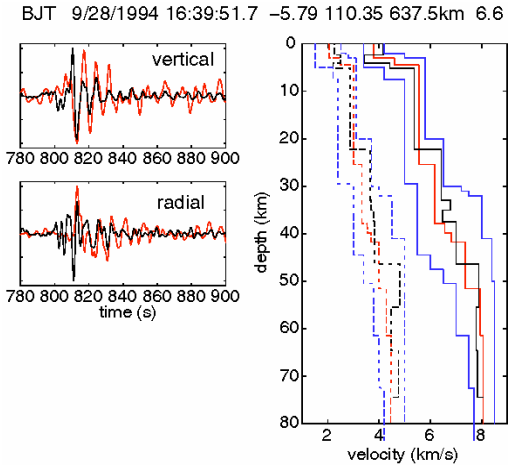

Figure 15. Same as in Figure 14 except that the interval 800-860 s was used in the waveform fitting.

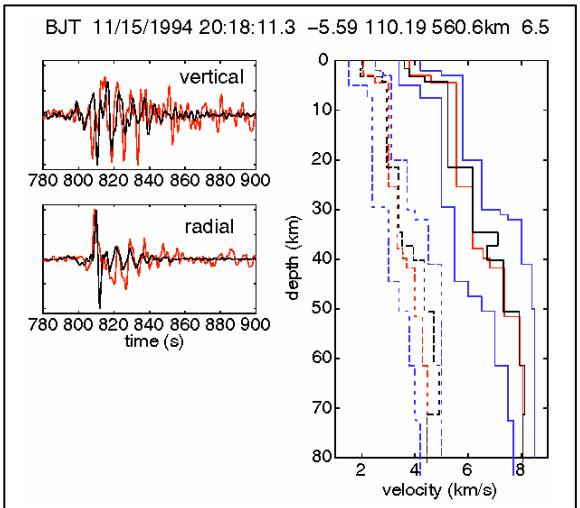

Figure 16. Optimization results after 600 iterations for fitting synthetics (black) to BJT vertical and radial records (red) of the 11/15/1994 event, using the time interval 815-860 s. Best-fitting model (black), search bounds (blue), and receiver function model by Mangino et al. (1999) (red).

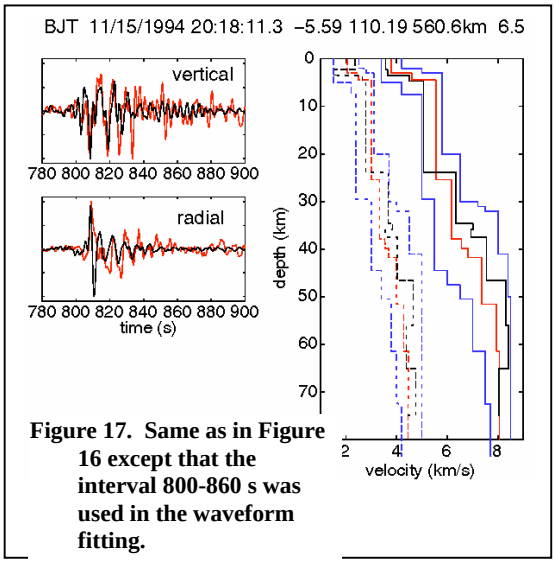

Figure 17. Same as in Figure 16 except that the interval 800-860 s was used in the waveform fitting.

by multiple modeling runs can be used to obtain quick estimates of the PPD that give fairly accurate estimates of the posterior model covariance's and correlation, although individual variances may be underestimated. We propose to use multiple VFSA runs to estimate the marginal PPD, mean and posterior covariance's, which will aid tremendously in the interpretation of our results. We will also employ the theoretically correct Gibbs' sampling approach with a narrow search range for a limited number of model layers.

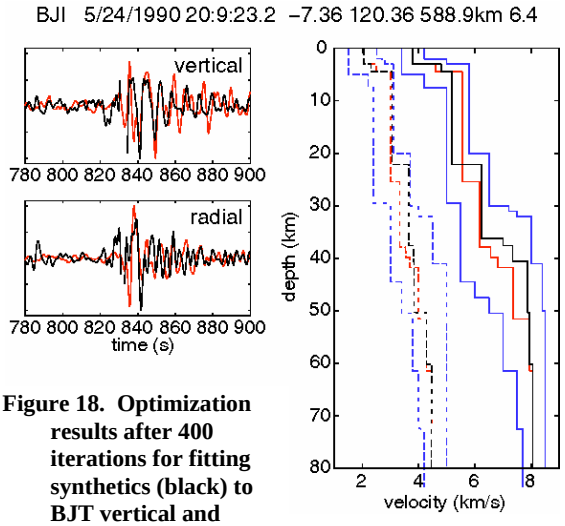

Figure 18. Optimization results after 400 iterations for fitting synthetics (black) to BJT vertical and radial records (red) of the 5/24/1994 event, using the time interval 835-870 s. See Figure 16 for other details.

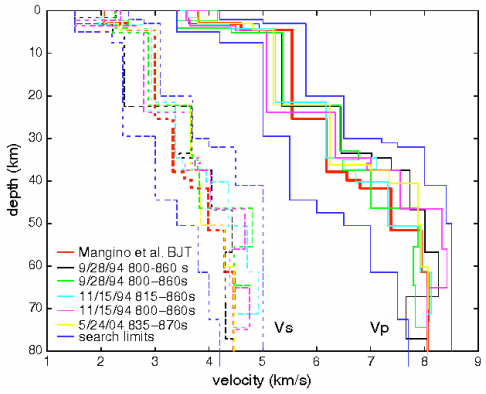

Figure 19. Comparison of models for the crust and upper mantle in the vicinity of station BJT resulting from waveform fits to various data (see legend), Mangino et al.'s (1999) receiver function model (red), and the simulated annealing search limits (blue).

REFERENCES

Baag, C.-E. and C.A. Langston, Shear-coupled PL, *Geophys. J. R. Astr. Soc.*, **80**, 363-385, 1985.

Beckers, J., S. Schwartz, and T. Lay, *Geophys. J. Int*., **119**, 574-594, 1994

Chander, R., Alsop, L.E., and Oliver, J., On the synthesis of shear coupled PL waves, *Bull. Seism. Soc. Am.*, **58**, 1849-1877, 1968.

Crotwell, H.P., T.J. Owens, and J. Ritsema, The TauP toolkit; flexible seismic travel-time and ray-path utilities, Seism. Res. Lett., **70**, 154-160, 1999.

Dziewonski, A. M., Anderson, D. L., Preliminary reference Earth model, *Phys. Earth. Planet. Int.*, **25**, p. 297-356, 1981.

Frazer, L.N., Synthesis of shear coupled PL. *Ph.D. thesis*, Princeton University, 54 pp., 1977.

Grand, S.P., and D. Helmberger, Geophys. *J. R. Astr. Soc.*, **76**, 399-438, 1984

Helmberger, D.V., and G.R. Engen, Upper mantle shear structure, *J. Geophys. Res.*, **79**, 4017-4028, 1974.

Jordan, T.H., and L.N. Frazer, Crustal and upper mantle structure from Sp phases, J. Geophys. Res., **80**, 1504-1518, 1975

Langston, C.A., The SsPmP phase in regional wave propagation, *Bull. Seism. Soc. Am*., **86**, 133-143, 1996.

Mangino, S., K. Priestley, and J. Ebel, The receiver structure beneath the China Digital Seismograph Network Station, *Bull. Seism. Soc. Am.*, **89**, 1053-1076, 1999

Oliver, J., On the long period character of shear waves, *Bull. Seism. Soc. Am.*, **51**, 1-12,1961.

Sen, M., and P. L. Stoffa, 1995, **Global Optimization Methods in Geophysical Inversion**, Elsevier Science Publishing Company, The Netherlands.

Swenson, J.L., Beck, S.L., Zandt, G., Regional distance shear-coupled PL propagation within the northern Altiplano, Central Andes, *Geophys. J. Int.*, **139**, p. 743-753, 1999.

Tarantola, A., **Inverse Problem Theory: Methods for Data Fitting and Model Parameter Estimation**, 613 pp., Elsevier, Amsterdam, 1987.

Zhao, L.-S., D. Helmberger, and D.V. Harkrider, *Geophys. J. Int.*, **105**, 713-730, 1991

Zhao, L.-S. and C. Frohlich. Teleseismic body waveforms and receiver structures beneath seismic stations, *Geophys. J. Int.*, **124**, 525-540, 1996.

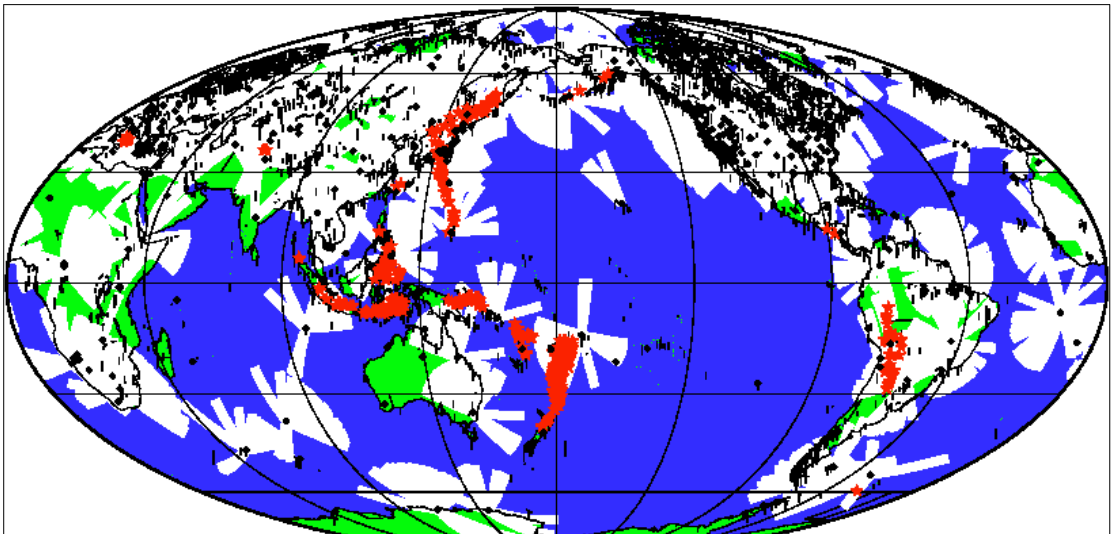

Figure 20. Potential global sampling of SPL waves using earthquakes (red stars) with source depths greater than 200 km for the years 1970-2002. Black triangles indicate broadband seismographic stations for which data are generally available. This testifies to the attractive potential for using SPL to model crustal and upper mantle structure beneath the continents. However, not all of these events will produce useful SPL phases. The amplitude of SPL depends on structural characteristics (e.g., a low-

DEVELOPING COMPOSITE REGIONAL CATALOGS OF THE SEISMICITY OF THE FORMER SOVIET UNION

Tatyana Rautian[1] and William S. Leith[2]

Institute of Physics of the Earth, Moscow, Russia,[1] U.S. Geological Survey[2]

Sponsored by United States Geological Survey

ABSTRACT

Seismological studies by institutions of the former Soviet Union during the 20th century employed standard instrumentation and methods of data processing for determining standardized parameters to describe seismic sources, resulting in the production of regular summary publications. For most of the century, bulletin data were published only in Russian and were generally unavailable to the Western scientific community. Yet, for many regions of this vast territory, earthquakes with magnitudes less than 2 were routinely located and characterized, especially since the early 1960s. A great volume of data on the seismicity of the Eurasian land mass is therefore available, although to date only in scattered publications and for incomplete periods of time. To address this problem, we have undertaken a comprehensive compilation, documentation and evaluation of catalogs of seismicity of the former Soviet Union. These include four principal, Soviet-published catalog sources, supplemented by other publications. We view this as the first step in compiling a complete catalog of all known seismic events in this large and important region. To make these data more useful for regional seismic investigations, as well as to be consistent with their provenance, we have prepared *composite regional catalogs* in digital form, dividing the territory of the former Soviet Union into 24 regions. For each of these regions, all the data available from the basic and supplementary catalog sources have been combined and evaluated. For regions with low seismicity, we have included the historical, non-instrumental (macro-seismic) data. Completion of this work will require digitizing the remaining catalogs of the various regional seismological institutes.

OBJECTIVE

During the 20th century, seismological studies by institutions of the former Soviet Union employed standard instrumentation and methods of data processing for determining standardized parameters to describe seismic sources, resulting in the production of regular summary publications. For most of the century, event data were published only in Russian and were generally unavailable to the Western scientific community. Yet for many regions of this vast territory, earthquakes with magnitudes less than 2 were routinely located and characterized, especially since the early 1960s. A great volume of data on the seismicity of the Eurasian landmass is therefore available, although to date only in scattered publications and for incomplete periods of time.

To address this problem, we have undertaken a comprehensive compilation, documentation and evaluation of catalogs of seismicity of the former Soviet Union. These include four principal, Soviet-published catalog sources, supplemented by other publications. We view this as the first step in compiling a complete catalog of all known seismic events in this large and important region. Completion of this work will require digitizing the remaining catalogs of the various regional seismological institutes.

To make these data more useful for regional seismic investigations, as well as to be consistent with their provenance, we have prepared composite regional catalogs, dividing the territory of the former Soviet Union into 24 regions. For each of these regions, all the data available from the basic catalog sources (see below) have been combined and evaluated. Note that, for regions with low seismicity, the historical (non-instrumental, macro-seismic) data are of increased importance. Such information, if not included in any summary, were taken from various publications and marked as "historical".

RESEARCH ACCOMPLISHED

Brief History of Seismological Study in Russia and the Former Soviet Union

The first substantial summary of earthquakes in Russia and adjacent territories was the catalog of I.V. Mushketov and A.P. Orlov [1893; Figure 1], which was based solely on macroseismic data. The beginning of regular seismic observations in Russia was marked by the issuance of a noteworthy publication --the Bulletin of the Permanent Central Seismological Commission (or PCSK [2]), published from 1902-1908 under the direction of G.V. Levitskaya. Being aware of imperfections in the seismic instrumentation used at that time, the compilers of the PCSK Bulletin did everything possible to preserve the main quantitative characteristics of these records –the amplitude and duration of vibrations– in the most complete form. Macroseismic data were collected under the direction of the PCSK, and were combined with instrumental data in a separate publication, in order to simplify the use of the materials in the PCSK Bulletin.

From 1908 to 1928, periods and amplitudes were published in the first Soviet summary bulletin of the network of seismic stations [3]. Because of the exceptionally high quality of seismogram analysis, reflected in the individual bulletins of the best seismic stations (e.g., Pulkovo and the independent stations of Anapa, Grozniy, Pyatigorsk, Samarkand and others), it is still possible to calculate accurate earthquake magnitudes for events in this time period. Beginning in 1923, the bulletins of the individual seismic stations were published in Moscow by the Institute of Physics of the Earth.

By 1911, macroseismic observations were being separated from instrumental data, and their publication in the bulletins became of secondary importance. Macroseismic data were collected and analyzed, but published independently, without cross-reference. Eventually, however, the boom in construction brought to the forefront the problem of seismic risk, and aroused new interest in historic strong earthquakes. In these early years, the Caucasian seismologist Eu.I. Bius compiled an exceptionally detailed and complete catalog of Earthquakes In Transcaucasia [4], and a number of other data collections were published [5-8]. Changes were also made to the summaries of instrumental data. For example, the inability to accurately calculate true ground displacement was considered sufficient reason to remove the dynamic characteristics of waves from event summaries.

A landmark publication was the 1962 Atlas of Earthquakes in the U.S.S.R [9], a compilation and presentation of earthquakes that occurred in the period of 1911-1957. This volume, which included a catalog of seismicity and detailed maps, served to summarize this early period in the development of Soviet observational seismology.

After the 1948 devastating Ashkabad earthquake, the expansion of the seismic network was undertaken, as well as the replacement of the seismographs of the Nikiforov system with what were then the advanced broadband seismographs of the Kirnos system (CK). This created a new foundation for improving the analysis of observations. Substantially more precise calculation of amplitude of ground displacement soon made it possible to incorporate the earthquake magnitude into seismological practice. After 1956, the sensitivity of seismic stations was further increased and the dynamic and frequency

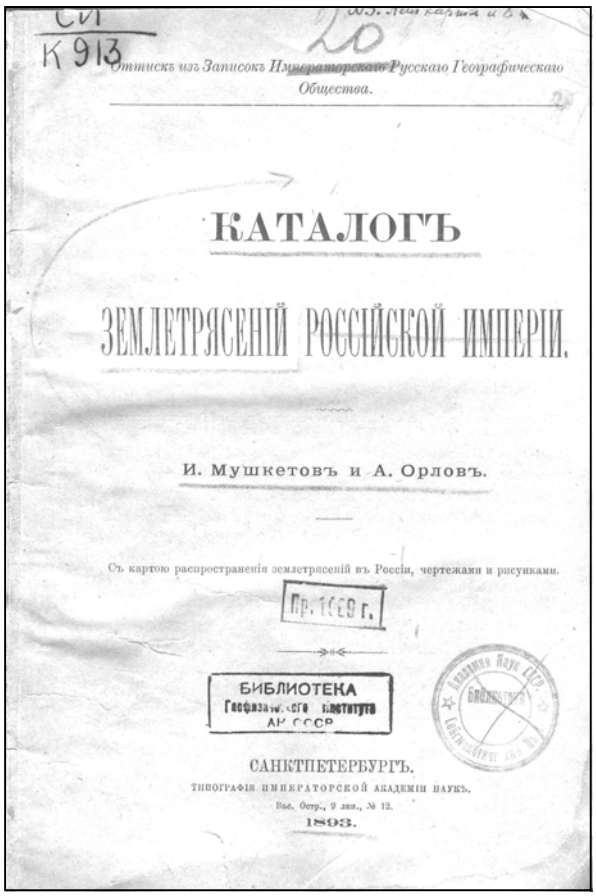

ranges of the recorded signals were widened. Short-period seismographs of high sensitivity were installed at the network stations, as well as long-period instruments and seismographs for recording strong ground motions. In the 1970s, the sensitivity of the equipment was increased again, with the dynamic range of instruments increasing to 100 dB. An increase in the number of stations was accompanied by unification and standardization of seismic observations. With a few exceptions, the instrumental and macroseismic data were not cross-correlated or jointly analyzed.

Principal Catalog Sources

By the end of the 20th century, four principal earthquake catalogs had been compiled and published (one electronically):

- The Obninsk Bulletin, issued every 10 days in the period from 1955 through 1999;
- The annual series, "Earthquakes in the USSR" (and since 1991, "Earthquakes in Northern Eurasia"), consisting of the regional catalogs of the ESSN, or Unified System of Seismic Observation. Published annually in Russian since 1962, a recent issue, published in 2000, was for earthquakes in 1994.
- The "New Catalog of Strong Earthquakes in the USSR," compiled by Shebalin and Kondorskaya [1974].
- The "General Catalog of Earthquakes in North Eurasia", compiled by the Institute of Physics of the Earth under the direction of W. Ulomov (and a nearly inclusive extension of the "New Catalog").

Figure 1. Cover of the first comprehensive catalog of earthquakes in Russia (Mushketov and Orlov, 1893, *"Catalog of the Earthquakes of the Russian Empire"*).

Additional event data were taken from the catalog published by *SevMorGeo* [10], the book, "The Seismic Regionalization of USSR Territory" [11], and various other publications. Some non-instrumental data were taken from a collection of felt earthquakes by Nikonov and Ananin (still being compiled). At present, not all of the available data are in digital format. For example, some of the most seismically active regions, such as Kopetdagh, Central Asia and the Far East, the smallest earthquakes (M < 3.5) are not yet available. A diagram illustrating the provenance and publication histories of the various catalogs is shown in Figure 2, and summarized in Table 1. A comparison of the number of events per year in the principal catalog sources and in the regional catalogs is shown in Figure 3.

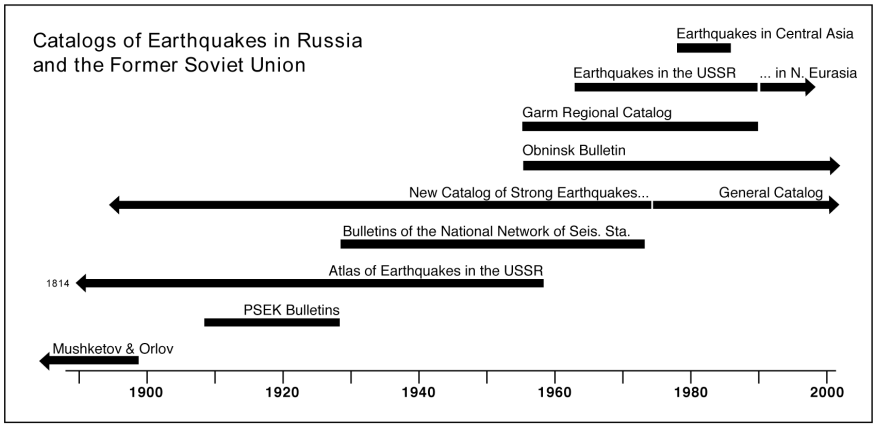

Figure 2. Time periods included in the various catalog sources of seismicity data for Russia and the Former Soviet Union.

Table 1. Summary of the principal catalogs of seismic events in the former USSR.

Short Name	Full Name (in translation)	Abbr.	Date Range Avail.
Obninsk Bulletin	Bulletin of the SEME GS RAS	OBN	1955-present
The Annuals	Earthquakes in the USSR Earthquakes in Northern Eurasia	ESSN	1962-1994
The New Catalog	New Catalog of Strong Earthquakes in the USSR [1973]	NEW	Historic through 1973
The General Catalog	General Catalog of Earthquakes in Northern Eurasia (digital)	GNRL	Historic through 1999

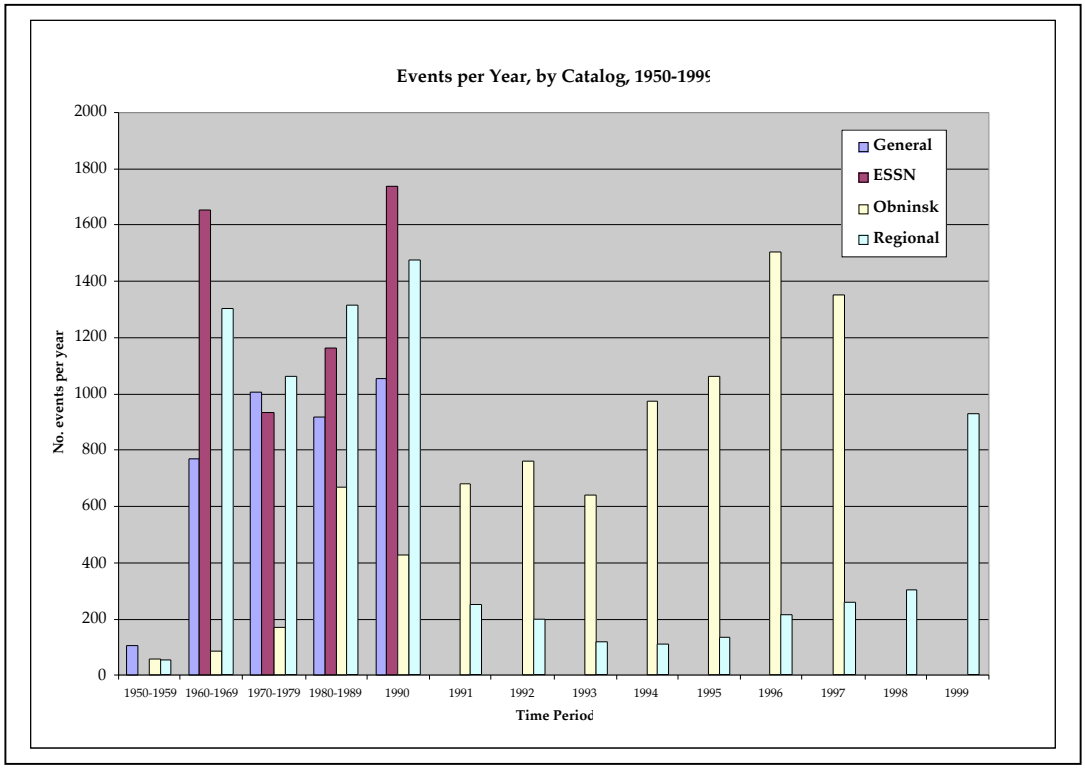

Figure 3. Numbers of events per year in the three principal catalog sources and in the regional catalogs we have compiled. Note that the Obninsk Bulletin is of earthquakes worldwide.

The Obninsk Bulletin

The "decadal" (Russian for 10-day) catalog was first issued by the Moscow Institute of Physics of the Earth, beginning in 1955. This catalog was compiled by the Seismological Expedition of the Geophysical Survey of the Russian Academy of Sciences (SEME GS RAS). Its publication was delayed only a few months, issued in about 50 paper copies, and sent to all the seismological centers of the former USSR. The Obninsk Observatory later became responsible for preparing the publication (now referred to as the Obninsk Bulletin), and it is now available in electronic format in its entirety.

The Bulletin includes the earthquakes recorded by numerous seismic stations (45, as of Dec. 2000) belonging to the Geophysical Survey of the Russian Academy of Sciences. At present, these stations include: 19 digital broadband stations; 2 micro-arrays; and 24 analog, three-component stations equipped with short-period, middle-period and long-period seismometers with analog galvanometer recording on photo paper. The broadband digital stations include 12 IRIS GSN stations and seven stations of Russian manufacture, known as the Seismic Digital Acquisition Station (SDAS). The analog stations of the network are equipped with short period (SKM) and long period (SK and SKD) instruments. The data from the teleseismic network of analog stations are transferred to the Obninsk processing center in the form of station summaries in alert and operation modes by regular telephone and teletype lines. The quality of digital station operations is monitored continually, but only periodically for the analog stations. No seismic event parameters are automatically determined.

For the digital recordings, the processing and analysis are done at the Obninsk processing center (CEME GS RAS). For analog seismograms, the operator of the station(s) does the analysis with subsequent transfer of results to Obninsk. The decadal catalog is available after a delay of about 30 days. It includes earthquakes in Russia with M > ~4.5; for the whole of Northern Eurasia, M > ~5.0; and for the globe, with M > ~5.5. The Bulletin is sent throughout Russia and to foreign data centers (e.g., in the USA, the USGS National Earthquake Information Center (NEIC), and in the U.K., the International Seismological Center (ISC)). Currently, the Obninsk Bulletin (through 1999) consists of about 41,550 earthquakes, worldwide. About 16,600 events are in the region roughly from 34-90N and 00-195E, including the former USSR and surrounding areas. A comparison of the number of earthquakes in the Obninsk Bulletin in this region during three five-year periods is as follows:

Years	No Eqs
1955-1959	258
1975-1979	1,011
1995-1999	6,055

The Obninsk Bulletin reports origin times, coordinates, depth and magnitudes. Three magnitudes are traditionally reported: a surface wave magnitude MLH; a P- wave magnitude from short-period instruments (Mpsp; earlier called MPVA) and a long-period P-wave magnitude (Mplp, earlier called MPVB). Most events have no magnitudes; these are usually at about 4 < M < 4.5. The intensity data published in the Obninsk Bulletin are taken only from seismic stations as "alert" information, and not included in our composite regional catalogs.

The Annual "Earthquakes In The USSR" (ESSN)

By 1962, the creation and development of regional seismic surveys lead to a tremendous increase in the number of earthquakes detected in northern Eurasia (see Figure 3). Subsequently, the Institute of Physics of the Earth began publication of a new yearly summary, "Earthquakes in USSR" (Zemletriasenniia v SSSR), which was a collection of bulletin data from the regional seismological institutes, along with articles on the seismicity of the various geographic regions of the USSR.

Increased coverage, as a result of using regional and local stations, resulted in catalogs that had lower detection thresholds and higher epicentral location accuracies than that of the global catalogs (such as the ISC and USGS), which were based only on teleseismic observations. The much greater resolution of the Annuals is evident the a comparison of these data with the ISC Bulletin made by Simpson and Lerner-Lam [1992] for the years 1962-1986, which showed that the annuals have about five times as many events as the ISC Bulletin in that time period.

The data in the Annuals is based on observations solely from stations located within the former USSR. Coverage therefore decreases to the south and southeast. Epicenters are also reported only to the nearest 0.1 or 0.01 degree (11 or 1.1 km), resulting in a gridded pattern on maps of high-seismicity areas when viewed at large scales. Another problem with the catalog is the lack of resolution in depth determinations, which is especially prominent near the boundaries of regions covered by the regional networks. Many events are given zero or no depth (i.e., blank).

Recent Contributors to the Annual

Current contributors to the annual include the Geophysical Survey Russian Academy of Sciences and its Central Experimental-Methodical Expedition, as well as ten regional surveys operated under the management of Obninsk:

- Kamchatka Experimental-Methodical Seismological Department Geophysical Survey Russian Academy of Sciences
- Sakhalin Experimental-Methodical Seismological Department Geophysical Survey Russian Academy of Sciences
- Magadan Experimental-Methodical Seismological Department Geophysical Survey Russian Academy of Sciences
- Dagestan Experimental-Methodical Seismological Department Geophysical Survey Russian Academy of Sciences
- Kola Regional Seismological Center Geophysical Survey Russian Academy of Sciences
- Siberian Geophysical Survey, Branch of Russian Academy of Sciences
- Baikal Experimental-Methodical Seismological Expedition Geophys Survey Siberian Branch Russian Academy of Sci.
- Yakutiya Experimental-Methodical Seismological Dept Geophysical Survey Siberian Branch Russian Academy of Sci.
- Altai-Sayans Exp-Methodical Seismological Expedition Geophys Survey Siberian Branch Russian Academy of Sci
- North Caucasus - Central Experimental-Methodical Expedition of Geophysical Survey Russian Academy of Sciences

The additional contributors from outside Russia to Obninsk are:

- Carpathian Institute of Geophysics of the Ukranian Academy of Sciences;
- Crimea Institute of Geophysics of the Ukranian Academy of Sciences;
- Kopetdag Institute of Seismology of the Academy of Sciences of Turkmenistan;

- Central Asian Institute of Seismology of the Academy of Sciences of Kyrgyzstan;
- Institute of Seismology of the Academy of Sciences of Kazakhstan;
- Institute of Seismology of the Academy of Sciences of Uzbekistan
- North Tien Shan Institute of Seismology of the Academy of Sciences of Kazakhstan;
- Gruziya Institute of Geophysics of the Academy of Sciences of Georgia;
- Institute of Geophysics and Engineering Seismology of the Academy of Sciences of Armenia;
- Institute of Geology of the Azerbaijan Republic.

The structure of the Annual

The catalogs completed by each regional survey are only a part of the Annual volume. It includes as well the papers describing the seismicity on each zone, special paper with detail study of macroseismic data of strong earthquakes with isoseismal maps, separate paper about large (M>6) earthquakes in the world, tables of fault plain solutions and spectral content. As an example of the typical content of the annual "Earthquakes in the USSR," the contents of the 1990 volume are given in Appendix I.

The number of earthquakes in the Annual

Because the monitored regions differ both in terms of their seismic activity and their areal extent, the yearly number of earthquakes in the various regional catalogs range from a few tens of events to thousands of events. Table 2 compares the number of earthquakes listed in each zone in 1990 and 1993:

Table 2. Comparison of numbers of earthquakes reported in two years of the Annual.

Zone	in 1990	1n 1993
Carpathians	50	37
Crimea	100	11
Caucasus	300	330
Kopetdag	270	263
Central Asia and Kazakhstan	970	617
North Tien Shan	330	475
Altai and Sayan	110	117
Baikal	230	263
Primorie	320	136
Sakhalin	40	24
Kuril-Okhotsk	630	667
Kamchatka and Komandorskaya Isl.	550	880
North-East	70	40
Yakutia	260	255
Baltic Shield and Arctic	53	2
Large earthquakes in the World	113	100
Total for the year is about	4,400	4,200

These numbers vary in time not only because of variations in seismicity and changes in the number of operating stations, but also because of changes in a cutoff value of the lower magnitude (or "Energy Class", *K* [12,13]) for earthquakes that were included in Annual Catalog. In 1967, a decision was made to raise the lower energy class limit of earthquakes from 7 to 9, in order to make the ESSN catalog "representative" (comparable) at all geographic zones. While the small events were still characterized at the regional seismic centers, they were not reported in this publication. For example, in 1990, the Altai & Sayan zone ESSN Catalog listed 110 earthquakes with Energy Class (K) of 8.5 or larger, while that year about 870 small earthquakes (5 <= K <= 8) were characterized but not published. In the Caucasus, about 1300 small earthquakes (K=5-8) were processed but not included in that year's ESSN publication. In the relatively small area monitored by the Garm expedition (100 by 150 km), more than 80,000 earthquakes were compiled in the expedition catalog for the time period from 1955 to 1990 (over 2200 per year). However, only a small fraction of these events were included in the ESSN catalog for Central Asia. For example, in 1964, only 84 earthquakes were reported with energy class, K > 9.

The parameters reported in regional ESSN catalogs

As a rule, the following data are included in the Regional Catalogs:

- Origin date and time to (GMT)
- Coordinates of epicenter

- Depth (in km)
- Energy Class, K = log E (in joules)

The Energy Class (from the Russian, Klass) determination is standard in most geographic zones (Carpathians, Caucasus, Kopetdag, Central Asia, Kazakhstan, Altai-Sayans, Baikal, Yakutia, and North East), but differs slightly in the catalogs for the Crimean region [14]. In the Far East, regional versions of K were created; these are KFS (after S.Fedotov, Kamchatka) and KC (for Sakhalin, after Soloviev & Solovieva [15]).

Unfortunately, when comparing these scales with the more widely used K (called KR, or K after Rautian) via teleseismic magnitudes, the regional versions were found to have a systematical discrepancy:

KR = KFS + 0.7
KR = KC + 1.6

In 1980, a new movement appeared in the regional seismological surveys, which begin to create their own versions of P-wave magnitude scales for regional distances. The MLH scale was extended to local and regional distances (10- 100s km), and the surveys begin to include values of these magnitudes in the Annual Catalogs. Unfortunately, these regional scales (MPVA) have the same name used for the classic teleseismic scale in the Obninsk Bulletin. It would be not bad if the values of regional MPVA were in a good accordance with traditional teleseismic MPVA. But our preliminary study shows, that it is not. It is well known that the P-wave, amplitude-distance dependence is extremely unstable at regional distances. Local MPVA is therefore not accordant with its teleseismic namesake, and is of high scattering in the correlation with other magnitude scale data. In contrast, the K scale, based on the maximum phase of P and S (mainly Lg) wave, is much more stable. The regional variation of amplitude-distance relation is small and negligible. To avoid confusion, the name MPVA now means regional P-wave scale. The teleseismic P wave scale is named Mpsp and Mplp (short- and long-period Mp). MPVA are not included in our Composite Regional Catalogs. The main scale used in ESSN was taken to be K (with its Far East and Crimean modifications [15,16]). K also determines the magnitudes of deep Hundu Kush earthquakes. Note that K was estimated for nearly 100 % of the earthquakes in the regional catalogs. For deep, Carpathian earthquakes the MSH scale was used, based on the max amplitude of the S wave (horizontal component of the short-period instrument).

The "New Catalog of Strong Earthquakes"

The New Catalog of Strong Earthquakes in the USSR (Shebalin and Kondorskaya, 1974), was the first attempt to collect all the data for strong earthquakes together, both for seismological and macroseismic observations. In 1984, data through 1977 were added and the New Catalog was translated in English [16].

The New Catalog consists of a huge volume of data, carefully collected and critically analyzed. The macroseismic and instrumental data were made compatible by development of the method of estimation of the epicenter, depth, and magnitudes from macroseismic data (details are explained in the New Catalog). When one uses data from the General Catalog, one can feel this methodical basis of the New Catalog.

Note that, in the General Catalog, the New Catalog was not used in its entirety. Of all the earthquakes that were taken, the format was nearly the same. However, not all the data from the New Catalog were included in the General Catalog. Specifically, no comments, references or information on macroseismic effects were included, and only some of the maximum intensity (Io) determinations.

Sources of data

The main principles used in preparing the New Catalog were to use all available information for each earthquake, and to estimate the most probable values for each of the basic focal parameters. The compilers did not limit themselves to using basic, well-known sources. Attempts were made to seek additional information, through research done in archives and elsewhere. Even for the period 1911- 1957, covered by the "Atlas of Earthquakes In the USSR", many “new” earthquakes were found. The list of references used as sources of data comprises 20 pages of the published Russian text, and about 30 pages in foreign-language versions.

To compile a chronological foundation for the New Catalog, data were taken from:

- the "Atlas of Earthquakes in the U.S.S.R."
- the bulletins of the National Network of Seismic Stations for (1902-12) and (1928-73);
- the International Seismological Service (ISS);
- the bulletins of the BCIS and the Preliminary Determination of Epicenters of GSUS;
- publications of the International Seismological Centre (ISC);
- individual bulletins of domestic stations (1911-27) and foreign stations (1900-70);

- numerous summaries of macroseismic data, beginning with the catalogs of A. Perrey and A.P. Orlov (both as published and in manuscript form).

In addition, even more numerous papers and investigations dealing with individual earthquakes were reviewed, as well as archive materials, reports of seismic correspondents, extracts from geographic descriptions by travelers and regional specialists, reports in the Soviet and foreign newspapers, etc. One specific task of the work with the sources was the elimination of errors, mainly in dating, because every error in date, particularly in early sources, is then repeated in subsequent summaries making one earthquake appear as two events.

Processing of macroseismic data

In using historic and archival data, the help of historians was particularly important in evaluating the sources and separating true information from anachronisms and fabrications caused by emotional, political, and other factors. Special control of determination basic parameters from macroseismic data was used. Analysis of the earthquake was made first on the basis on macroseismic data only. Then the results compared with the basic parameters of the earthquake determined from instrumental data. This analysis showed that the procedure for treatment of macroseismic data does make it possible to determine the basic parameters of the focus with adequate reliability. The rigid formalism in choosing the parameter and estimation of its error is the most important for macroseismic data during the pre-instrumental period (as described in the New Catalog). The following general principles were used in selecting the final values for the basic parameters and in estimating their precision:

1) Each parameter was determined in several ways where possible;
2) The value of each parameter was chosen to eliminate or minimize contradictions with the raw data;
3) If estimates coincided, the value obtained for the parameter was taken as final, and its error was taken as the minimum of the errors determined by different methods;
4) If estimates differ and the ranges of error overlapped, the final value was chosen in the common range of errors and the value of the error was taken as the minimum;
5) If estimates differ and the ranges of error did not overlap, the one with the least error was taken as the final value and the spread of the determinations was taken as the error;
6) If direct calculation of a parameter was not possible, the realistic extreme possible values were taken as the limits, and the final value of the parameter was chosen as the mean In this interval;
7) All errors were rounded upward in a given system of gradations.

Intensity was estimated based on the European MSK-64 scale. If the data were originally given in the Rossi-Forel or JMA scale and the observational data were unavailable, a-priori re-determination of intensity was impossible. In such cases, the values of intensity were converted into MSK-64 by graphic relations compiled by Shebalin (see Figure 6). The range of error in intensity was assigned based on the quality and quantity of initial macroseismic data.

Origin Time. Using the macro-seismic data, origin times were assigned based on the individual reports. Dates were converted to modern format (accounting for differences from century to century), and dates according to the Muslim calendar were translated to the European chronology. Times were converted to Greenwich Mean Time. In this process, local time was taken to be that of the local time zone, which is not always accurate. Before the end of the 19th century, the time in nearby major cities was used as local time, with an error generally not more than 30 minutes. Because the quality of time estimates for older earthquakes were low, we ignored this difference. After the introduction of daylight-saving time in 1931, the corresponding 1-hour corrections were incorporated.

The epicenter, depth and magnitude of earthquake estimation was based on the so called “equation of the macroseismic field”:

$$I = B*M - A \log R + C$$

where H is depth and R is hypocentral distance (R = (H2 + D2)1/2), with the empirical parameters A, B and C. These parameters were initially estimated as B = 1.5, A = 3.5, and C = 3.0. The epicenter of large earthquakes with rich data was taken as a center of first isoseismal with an error equal to its average radius. For poor data, and if there were no macroseismic information from epicenter (located at sea or in an uninhabited area, etc.), the Golenetski method was used. The equation:

$$Ii - Ik = a \log (Ri2/Rk2)$$

describes a circle as the locus of the possible position of the epicenter. If the coefficient a is known, the epicenter can be found with the Wadati method as the intersection of loci for several pairs of points. The error of epicenter, estimated this way, was taken from 0.2° to 0.5°, depending on magnitude. For earthquakes found by paleoseismic studies, the epicenter was taken as the center of the dislocation, with a location error of half of the dislocation length.

The focal depth was determined by two methods: from the decrease of intensity with distance (using a nomograph), and/or from magnitude and intensity "Io" at the epicenter. The magnitude was determined from intensity in epicenter Io if found from initial data and depth. If the depth cannot be estimated, the magnitude determined from the intensity far from the epicenter (where epicentral and hypocentral distances are similar). In this manner, the parameters of time, location, depth and magnitude were calculated and "non- instrumental" earthquakes became compatible with instrumental ones.

The New Catalog includes the radii of isoseismals and, in some cases, comments about destructive effects, such as landslides, collapse of ancient buildings (churches, fortress) and human loss, if these were mentioned in original sources. There are also comments about reliability or errors in the referenced sources (note that the latter were not included in the General Catalog, see below).

The "General" Catalog

As noted above, the "General Catalog of Earthquakes in North Eurasia" is an extension of the previous "New Catalog" by Shebalin and Kondorskaya (1974) It was compiled by the Institute of Physics of the Earth under the direction of W. Ulomov, but never published, and exists only in electronic form. As a source in our Composite Regional Catalogs, it is referred to as "General" (or shortened to "Gnrl").

The General Catalog provides data for 31,821 events that occurred during the time period from 1900 to 1990 in the region of Eurasia from 30°-90° N and 0°-190° E. Earthquakes that occurred before 1955, when Obninsk began to issue its Bulletin, are mostly taken from the New Catalog, supplemented by macroseismic information and from some local station Bulletins (the sources of data are not documented in the catalog).

The General Catalog contains a seismic magnitude M, which has been calculated from various kinds of data, as follows:

- the Soviet surface wave magnitude MLH (later renamed to Ms, but not identical to western Ms), which is determined not from amplitude but from A/T; both A and T correspond to the maximum A on surface wave records (and not necessarily to 20-second period waves).
- the p-wave magnitude, MPVA (taken from SKM instrumentation, at periods To=1.5-2 sec) and MPVB (taken from SD instrumentation, To=15-20 sec) were used for calculation of M.

The magnitudes of the smaller events were initially characterized by Energy Class (K) as determined by the local surveys. This makes the number of earthquakes in the General Catalog more than twice that of the Obninsk Bulletin; further, all events in the General Catalog have a value of M.

The General Catalog has been divided into regions, corresponding to those of the Obninsk Catalog (see Table 3). The table below shows the distribution of events versus regions and the magnitude range of earthquakes in each region. Note that the total number of events in all the regions listed below (23,467) are less than in the whole General Catalog, since no data for the active regions Central Asia and Turkmenia were included.

Table 3. Magnitude Ranges for Events in the GENERAL catalog, by region.

Region	N	Lat	Lon	M
Aldan	249	52-60	122-142	6.6-3.3
Alti	474	43-60	80-90	8.0-3.5
Arctic*	334	70-90	0-170	6.8-3.5
Baikal	1967	50-60	102-122	7.6-3.3
Baltic	12	52-60	20-30	4.7-3.5
Caucasus-East	1074	38-45	44-51	6.9-3.3
Caucasus-West	317	40-45	37-44	6.8-3.3
Central Asia	7662	35-44	65-80	8.3-3.2
Chukotka	37	59-70	165-190	5.8-3.5
Cremea	45	44-46	28-37	6.8-3.5
Kamchatka	6767	50-60	155-165	8.5-3.5
Kazakhstan NE	15	45-60	65-80	5.8-3.6
Kurile Islands	1954	45-51	145-164	

Table 3. Continued

Region	N	Lat	Lon	M
Primorie-E	649	42-52	131-142	7.8-3.2
Primorie-W	6	48-52	127-131	6.0-3.6
Russia Central	3	52-60	30-54	4.6-3.5
Russia North	13	60-70	30-54	4.9-3.0
Russia South	12	45-52	37-54	5.4-3.5
Sakhalin	660	46-55	142-146	7.0-3.3
Sayans	924	50-60	90-102	7.0-3.5
Siberia East	240	59-72	115-165	7.1-3.3
Siberia West	0	60-72	66-115	
Ukraine	45	46-52	20-37	5.5-3.4
Urals	15	45-70	54-66	5.5-3.2

*including the Laptev Sea

Sources of data

The General Catalog was converted to electronic format in the 1990s. The compilers at IPE combined data from the New Catalog, the Obninsk Bulletin and the annuals (ESSN data), with the goal of making the catalog as homogeneous as possible in terms of the magnitude distribution of events. If two of three sources reported the same event, only one version was included, as decided by the compiler. The origin time and coordinates were taken from these sources, choosing the most reliable version, or after revising the data. They converted all the various magnitude scales and energy classes as well as macroseismic data into unified magnitude M. The available information on errors was included for all the parameters. The parameters included in General Catalog are:

t_o, the origin time:
Year, Mon, day, hour, min, sec;
Er-t:
error in time, and units of measure the error (sec, min, etc.)
Latitude and Longitude:
coordinates of epicenter, in degrees;
Er-ep:
error in the epicenter, in degrees;
Dep:
depth of origin, in km;
Er-D:
Error in depth, measured in relation to depth and ranging from 0.05 to 2 times the depth

Meth:
method of depth determination, as follows:
(0) - instrumental
(1) - macroseismic
(2) - assumed

Earthquake energy and magnitude determinations

Earthquake magnitudes were determined by a number of methods, some of which have been described in earlier sections of this report. A full documentation of the magnitude relationships used by the various regions and for various event depths will be included in the final report. Note that, in our compilations of regional catalogs, if more than one estimation of magnitude is available, the following order of priority was established:

1) The magnitude, obtained from surface waves (with a correction for depth added)
2) The magnitude from seismic moment
3) The magnitude from P wave,
4) The magnitude from S wave

Composite Regional Catalogs

As described above, the compilers of the four principal source catalogs (New, Obninsk, ESSN, General) took different approaches in the compilation of their data, which are reflected in the content and scope of their products. For example,

the New Catalog attempted to make instrumental and non-instrumental data mutually compatible, and the events therein are described with the same language. Macroseismic data are a significant part the New Catalog, since it was constructed as the home of strong earthquakes.

The Obninsk Bulletin can be considered to be "conservative", in that only teleseismic data were used for characterizing events. The Bulletin therefore contains only moderate and large earthquakes and only classical (teleseismic) magnitudes. While growth in the number of stations over the second half of the 20th century greatly increased the number of earthquakes cataloged by Obninsk, it did not break the principle of stability and conservatism.

In contrast, the Regional (ESSN) surveys worked to characterize as many earthquakes as possible, with the goal of elucidating the detailed spatial distribution of regional seismicity and its relation with regional geological structure.

The General catalog was undertaken with the goal of merging all data into a single complete catalog. Adopting a "unified magnitude," with the standard lower cutoff of M=3.5, was proposed as the basic description of seismicity for the territory.

Approach

Our principal goal in compiling the Composite Regional Catalogs is to archive as much of the available information as possible, with no lower magnitude cutoff and no "standardization" of magnitudes. When integrating the data from the various "ancestral" catalogs, the following approach was taken:

1. If, for particular seismic event, two (or three) source catalogs report identical origin time and coordinates, the event occupies a single record in the database. Other parameters are placed in different columns. In the column "Source" these two or three initial catalogs are pointed in "chronological order" of publication (OBN, ESSN, NEW/GNRL). Other parameters, from different surveys are placed in the same record, in different fields. They are:

from the ESSN:	K = energy class
	M(K) = magnitude calculated from K : M(K)=(K-4)/1.8]
from Obninsk:	MLH, Mpsp, and Mplp magnitudes
from General:	M = the "unified magnitude"
	M(_) = indicating the parameter used to calculate M
	Io = intensity at the epicenter
	Azim = azimuth

2. If the times and/or coordinates are different in initial catalogs (estimated independently), two events are reported, with each source data in a separate record.
3. Events are assigned to a geographic region. The "regionalization" of the Catalog does not precisely coincide with the zones for which each of the separate regional surveys is or was responsible. For example, the Baikal Survey processed and included in its catalog some events with longitudes less than 100°, they were incorporated into the Sayan Regional Catalog. Another example is the situation for Siberia, where the Yakutsk survey is responsible for the huge area, including the Aldan, East Siberia and Chukotka.
4. For several regions (Turkmenia, Central Asia, Primorie & Priamurie, Sakhalin, Kurile, Kamchatka), ESSN data are not yet available in digital form, so only the Obninsk and General catalogs were used in the compilations to date.

The catalogs can be divided into two time periods: "historical" (prior to 1962) and "modern (from 1962 through 1999). The first period includes the available data on errors, as estimated or assumed by the compilers of the New and General catalogs. In the so-called "modern observation period," the errors are smaller then in the historical period. Note also that error estimates were not included in all of the regional catalogs, and when they were reported, they were mostly assumed values. For example, the density of seismic stations was generally not sufficient to discriminate a depth of 5, 10, or even from 15 km. Therefore, the depths of many events are presumed. The accuracy of these determinations can be evaluated by comparing separate analyses of the data for events that were recorded and processed by neighboring surveys, by regional and independent (e.g., Obninsk) determinations, or by comparing with the revised estimations by authors of the General Catalog or other special studies. For these reasons, the data about accuracy are not included in 1962-99 Catalogs.

Parameters included in Composite Catalog.

The catalogs for the early time periods have nearly the same parameters as those in the General catalog, and are included in the same format. But there is a difference: because the Obninsk Bulletin begins in 1955, the magnitudes MLH were included in it. Therefore, we have included an additional column, "MLH," in the Composite Regional Catalogs.

The recent part of catalogs consists of time, coordinates, depth, energy class (K, from the Annuals/ESSN), M(K) (calculated by us for completeness), M and M(K) from the General Catalog, the three classical magnitudes (MLH, Mpsp and Mplp) from the Obninsk Bulletin, and Io and Azim (from the General Catalog). The data from the Annuals are marked in the Composite Catalogs as "ESSN" (from the Russian abbreviation for "Unified Survey of Seismic Observation"). Note that the identifier, "ESSN," was used for all the regional data published in Annual "Earthquakes in the USSR" (described above), without mention of which regional center provided the data.

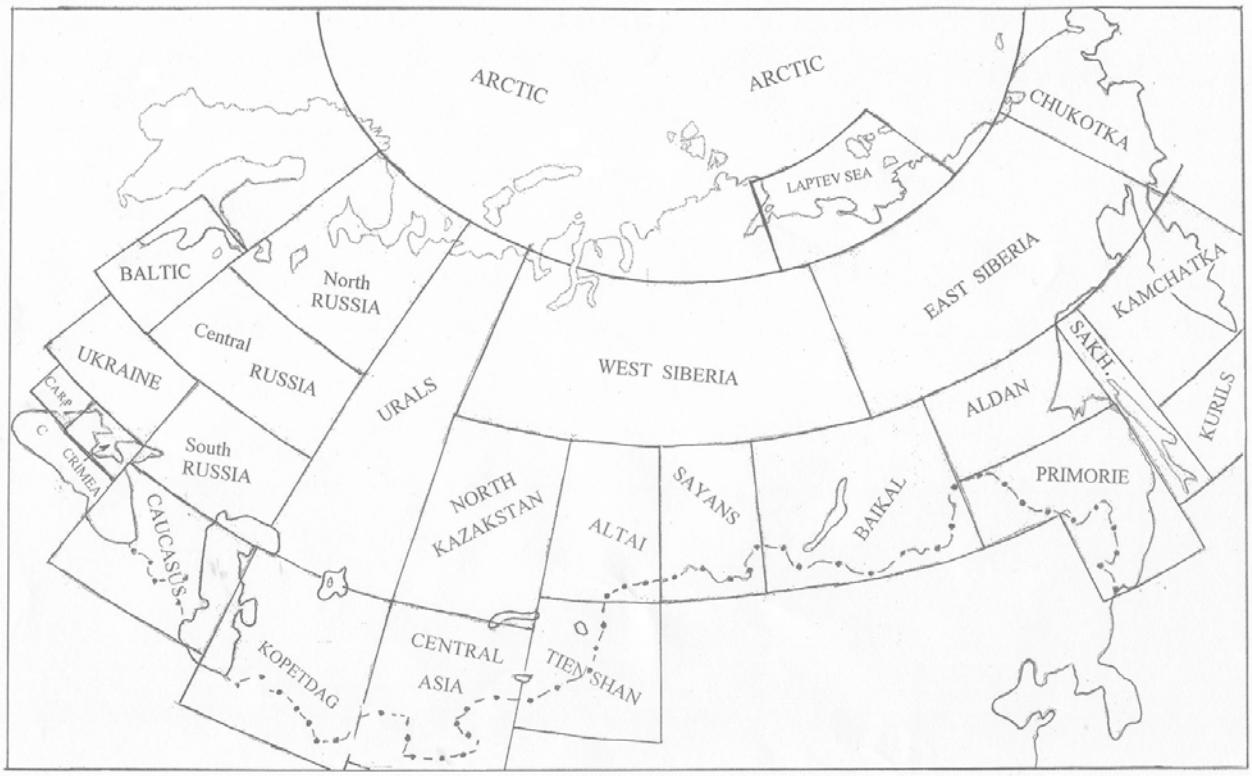

Figure 4. Sketch map of the former Soviet Union, showing the regions we have used in building the composite catalogs.

The regionalization

The system of regional networks, and the responsibilities of the regional seismological centers for monitoring the seismicity and characterizing events in their regions, was established mainly for political and administrative reasons. Some broad territories, like Central Russia and the Urals, were designated as one of the regions, but without any regional network or survey.

The boundaries between the various Soviet/Russian administrative regions were important for regional surveys, defining their areas of responsibility. However, these politically-based geographic divisions are not particularly useful to Earth scientists ("earthquakes know only natural boundaries"). Therefore, in the Composite Regional Catalogs, we have defined regions based not only on historical reporting responsibilities, network distributions and basic geographic features, but also on the spatial distribution of seismicity and tectonic features.

The entire territory of the former Soviet Union is divided into contiguous regions, although some low-seismicity regions are poorly reported in the available catalog sources and appear as "blank spots" on seismicity maps. Also, Russia, the Urals, West Siberia, and North Kazakhstan have a low and poorly-studied seismicity, but are known for intensive blasting. Most of the available information on events in these regions is for non-instrumentally recorded earthquakes. An example showing epicenters from the composite regional catalog for the Baykal region is shown in Figure 5.

A map of the epicenters of events in the General and composite regional catalogs is shown in Figure 6. In this presentation, the epicenters of events in the regional catalogs overlay the epicenters of events in the general catalog. This emphasizes the spatial distribution of events in the regional catalogs.

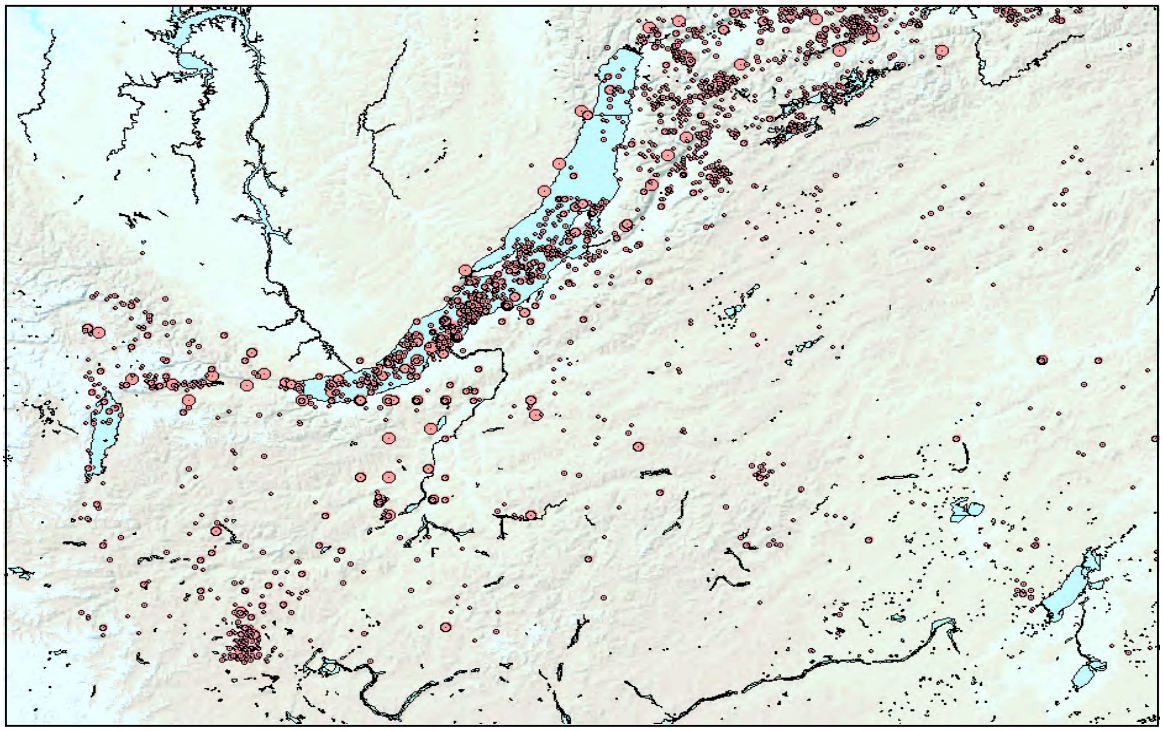

Figure 5. Map of epicenters in the Baykal Lake region, from the composite regional catalog of seismicity of that region.

CONCLUSIONS AND RECOMMENDATIONS

We have made substantial progress toward the goal of completing uniform regional catalogs of seismicity of Russian and the former Soviet Union, using and documenting all the available major catalog sources, with no standardization of magnitudes and no lower magnitude cutoff. These catalogs therefore contain the best available representation of the seismicity of the former Soviet Union, particularly at low magnitudes. Completion of this work will require digitizing the remaining catalogs of the various regional seismological institutes. A prototype web site for the distribution of these data is available through the U.S. Geological Survey, at: http://geology.er.usgs.gov/gmapeast/kaz/.

ACKNOWLEDGEMENTS

We gratefully acknowledge support from the U.S. Geological Survey. This work benefited greatly from the expertise, contributions and reviews of Vitaliy Khalturin, and from the contribution of papers by and discussions with David Simpson. We also thank Kim Buttleman and Steve Schindler, for assistance in building and maintaining the web site.

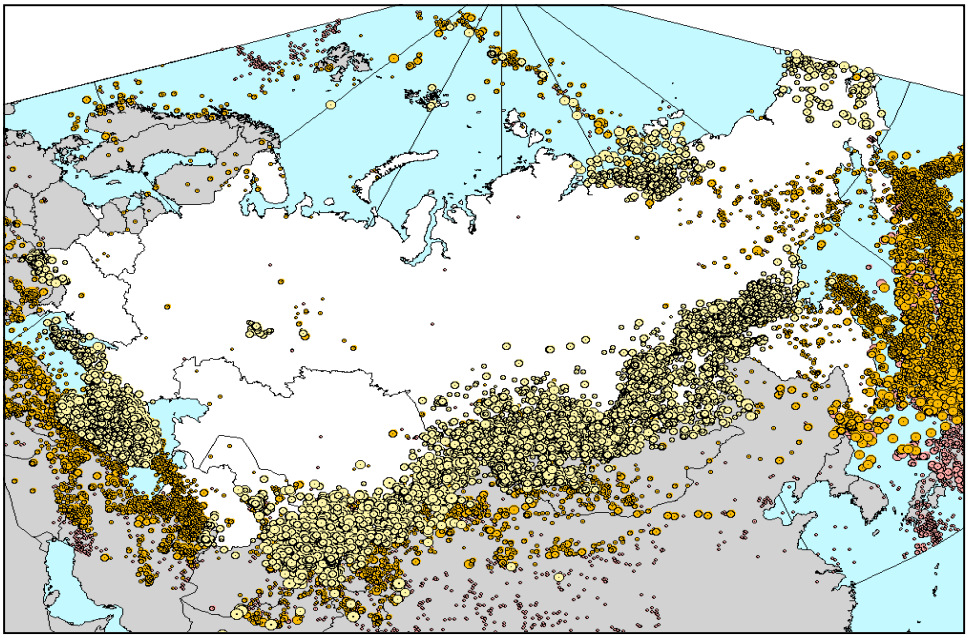

Figure 6. Map of the epicenters in the Obninsk Bulletin (pink), overlain by those of the General Catalog (ochre), overlain by epicenters of events in the Annual (ESSN) catalogs (yellow).

REFERENCES

1) Musketov IV and AP Orlov. The Catalog of Earthquakes in the Russian Empire. Russ. Geogr. Soc., St. Petersburg (1893)
2) Bulletin of the Central Seismological Committee of Russian Acad. of Science (1902-1908; 1911-1913).
3) Bulletin of the First-Class Seismic Stations: Pulkovo (1912-1915, 1923-1927). Sverdlovsk (Ekaterinburg), (1913-1916, 1923-1927); Irkutsk (1902, 1913-1914, 1923-1927); Baku (1912, 1924, 1927); Tashkent (1913-1915, 1923, 1924, 1927) Makeyevka (1925-1927); Leningrad (1925-1927).
4) Bius, Eu. I., Seismic conditions of the Trans-Caucasus, Tbillisi Acad. Sci. USSR, Parts 1,2,3 (1948,1950, 1955).
5) Vvedenskaya N.A., Catalog of Strong Earthquakes in the Tien Shan, Inst. Phys. Earth Acad. Sci. USSR, Moscow, 1962.
6) Seismotectonics and Seismicity in Southeastern Sayans, Nauka, Novosibirsk. 1975.
7) Golinski. G. L., Chronological Catalog of Earthquakes Felt in Turkmenia from 2,000 BC to 1973 A.D. Inst. Phys. and Earth Atmosphere Acad. Sci TSSR Ashhabad 1974.
8) Atlas of Earthquakes in USSR. Acad. Sci. USSR, Moscow, 1962.
9) Earthquakes in the USSR (called “Earthquakes in Northern Eurasia” as published annually since 1993). Nauka, Moscow, (1962-1994).
10) Avetisov, G.P., Seismoactive Zones of Arctic, Inst. Oceangeology, St. Petersburg, 1996, 185 pp.
11) The Seismic Regionalization of the Territory of the USSR.
12) Rautian, T.G., The energy of earthquakes, in Methods of Detailed Study of Seismicity, Trudy Inst. Phys. Earth, no. 176, Moscow, Nauka, p.75-114 (1960).
13) Rautian, T.G., On the estimation of earthquake energy at distances up to 3,000 km. Trudy Inst. Phys. Earth, No. 32 Moscow Nauka P.88-93 (1964).
14) Pustovitenko, B.G. and B.E. Kulchitski, Estimation of energy of Crimean earthquakes, in Magnitude and Energy of Earthquakes, v.2, Moscow, Nauka, p. 113-124 (1974).
15) Soloviev, S.L. and O.N. Solovieva, The relation between magnitude and energy class for Kuril earthquakes. Phys. Earth, No.2 (1967), p.13-22.
16) Shebalin, N.V. and N.V. Kondorskaya. The New Catalog of strong earthquakes in the USSR from ancient times through 1974.
17) Shebalin, N.V., Methods of application of seismic engineering data for regional seismicity, in Regional seismicity in the USSR, (1968) Moscow, Nauka.

CALIBRATION DATA FOR PS38 IN THE CENTRAL ARABIAN PENINSULA

Arthur J. Rodgers[1] and Abdullah M. S. Al-Amri[2]

Lawrence Livermore National Laboratory,[1]
Seismic Studies Center and Geology Department, King Saud University[2]

Sponsored by National Nuclear Security Administration
Office of Nonproliferation Research and Engineering
Office of Defense Nuclear Nonproliferation

Contract No. W-7405-ENG-48[1] and DE-FC03-01SF22418[2]

ABSTRACT

In order to improve monitoring of explosions in the Middle East, we are collecting calibration waveform data near the site of primary seismic array PS38 in central Saudi Arabia. This site is located on the Arabian Shield near the town of Halban and was host to a station deployed by the US Department of Energy-funded University of California at San Diego Broadband Deployment 1995-1997 (Vernon and Berger, 1998). Noise surveys found this site to be very quiet (Mellors, 1998; Al-Amri *et al*., 1999). We re-occupied the same vault in January 2002 with a broadband Guralp CMG-3T three-component seismometer. Data are recorded to a REFTEK 72A 24-bit digitizer and saved on a 1-Gigabyte SCSI (small computer system interface) field disk. King Saud University Seismic Studies Center personnel service the station every 6-8 weeks. Data from this station will be made available for analysis as a surrogate station for the planned International Monitoring System (IMS) primary seismic array PS38. This station has been sited and a noise survey has been performed by the King Abdulaziz City for Science and Technology (KACST), although the installation and certification dates are not yet known. As part of a separate effort, we are performing analysis of broadband data recorded by our station and others in Saudi Arabia to support location and identification efforts.

OBJECTIVE

The objective of this project is to collect raw waveform data for empirical calibration of the International Monitoring System (IMS) primary seismic array (PS38) planned near the town of Halban in central Saudi Arabia.

RESEARCH ACCOMPLISHED

Introduction

The IMS of the Comprehensive Nuclear Test-Ban Treaty Organization (CTBT0) will rely on seismic stations and arrays to monitor nuclear explosions. An IMS primary seismic array is being planned near the town of Halban on the Arabian Shield in central Saudi Arabia. Figure 1 shows a map of the Middle East with existing and planned IMS seismic stations.

A Department of Energy (DOE) Research Opportunity Announcement (ROA) project was funded to collect calibration data for explosion monitoring of the Arabian Peninsula. A main part of this project ("Ground Truth Event and Waveform Data Collection for Seismic Calibration of the Arabian Peninsula and Surrounding Regions - Project #35) is to collect calibration data for the primary array near Halban, Saudi Arabia. During the week of January 21-27, 2002, Lawrence Livermore National Laboratory (LLNL) and King Saudi University (KSU) seismologists deployed an autonomous broadband seismic station near Halban. This deployment took advantage of the vault built for station HALM by the 1995-1997 University of California, San Diego (UCSD) Saudi Broadband Deployment (Vernon and Berger, 1998; also funded by DOE). Noise characteristics from the UCSD Deployment indicated that the HALM site was very quiet (Mellors, 1997; Al-Amri *et al*., 1999). Table 1 summarizes seismic station deployments near Halban.

Table 1. Summary of Seismic Station Deployments near Halban, central Saudi Arabia.

Station Code	Institution	On Date	Off Date	Latitude	Longitude	Elevation	Sensor
HALM	UCSD	1995/327	1997/060	22.8454	44.3173	930 m	STS-2
HALB	LLNL/KSU	2002/021	present	22.8452	44.3173	930 m	Guralp-3T
PS38	KACST	To be determined	To be determined	23.4349	44.4894	???	array

Instrumentation

The deployment features a Guralp CMG-3T three-component broadband seismometer (passband 0.008-50 Hz or 125-0.02 s). Data are recorded by a Reftek 72A 24-bit digitizer onto a 1-Gigabyte SCSI field disk. The sample rate is 40/second. Timing is determined every hour by global positioning satellite (GPS) at the site. The system is powered by a 12-V (100-Amp) battery that is recharged by a solar panel. The sensor and digitizer are placed in a vault built for the 1995-1997 UCSD-Saudi Broadband Deployment (Vernon and Berger, 1999). Figure 2 shows the site after installation.

IMS Array Site

The IMS primary seismic station (PS38) is being planned near Halban (Table 1, Figure 3). In April 2001 the Preparatory Commission for the CTBTO and King Abdulaziz City of Science and Technology (KACST) performed a site survey at the KACST-proposed site. During the LLNL-KSU deployment, we learned that the KACST-proposed site is approximately 65 km away from our site. The KACST site is much closer to the highway and the town of Halban. There are many Bedouin encampments closer to the highway and security may be an issue. The array site will require a 4-km by 4-km footprint to be enclosed by a fence. The Hadabat Al-Marhi site is more remote and less likely to be disturbed. Once the site of the array is chosen and secured with a fence, we would like to deploy a station at the exact IMS site. We will then be able to compare observations at both the Hadabat Al-Marhi and IMS array sites to estimate the transfer function between the two sites.

Noise Characteristics and Instrument Response

Noise survey of the 1995-7 Saudi Broadband Deployment found the Halban site to have very low seismic background noise (Mellors, 1997; Al-Amri *et al*., 1999). We compared the noise in a 100-s window for our deployment with a similar window for roughly the same time of day and day of year. The results (Figure 4) show that the noise levels are very similar between our Guralp CGM-3T seismometer and the STS-2 of the 1995-7 Deployment. The noise window for our deployment was taken during the first few days after deployment and the instrument could still have been settling. More analysis will be done as additional data become available.

In order to test the instrument calibration, we computed synthetic seismograms for a moderately large earthquake in the Southern Zagros Mountains (February 17, 2002, M_W 5.3, Harvard CMT). A calibrated model for the Arabian Platform from our previous work (Rodgers *et al*., 1998) was used for the synthetics. Results (Figure 5) show that the data agree well with the synthetics both in amplitude and phase. This indicates that the instrument response and timing have no major problems.

CONCLUSIONS AND RECOMMENDATIONS

We are collecting data for empirical calibration of the Arabian Peninsula at a single broadband station near the planned IMS primary array in central Saudi Arabia (PS38). The deployment is expected to record many events in the seismically active regions surrounding the Arabian Peninsula (e.g. Turkish-Iranian Plateau, Zagros Mountains, Gulf of Aden, Red Sea and Dead Sea Transform). Preliminary analysis of the data show that the noise levels are comparable with the 1995-7 Saudi Broadband Deployment station and that instrument responses are properly calibrated. More data and analysis will be shown at the meeting. Data from the deployment will be distributed on CD ROM.

ACKNOWLEDGEMENTS

Pat Lewis provided essential assistance with the instrumentation before and during the deployment. Don Rock prepared the equipment and loan documentation. Rob Mellors and Frank Vernon kindly provided their field notes and maps to help locate the site. Ahmad Rabie Khalil (KSU) helped set-up the KSU computer system and read the field disks. The primary author thanks the staff of the KSU Seismic Studies Center for their kind hospitality during our visit to Saudi Arabia

REFERENCES

Al-Amri, A. M., R. Mellors and F. Vernon (1999). Broadband seismic noise characteristics of the Arabian Shield, *The Arabian Journal for Science and Engineering*, **24**, 2A, 99-113.

Mellors, R. (1997). Preliminary noise survey and data report of Saudi Arabian data, Lawrence Livermore National Laboratory Informal Document, UCRL-ID-128949.

Rodgers, A., W. Walter, R. Mellors, A. M. S. Al-Amri and Y.-S. Zhang (1999). Lithospheric structure of the Arabian Shield and Platform from complete regional waveform modeling and surface wave group velocities, *Geophys. J. Int*., **138**, 871-878.

Vernon, F. and J. Berger (1998). Broadband seismic characterization of the Arabian Shield, Final Scientific Technical Report, Department of Energy Contract No. F 19628-95-K-0015, 36 pp.

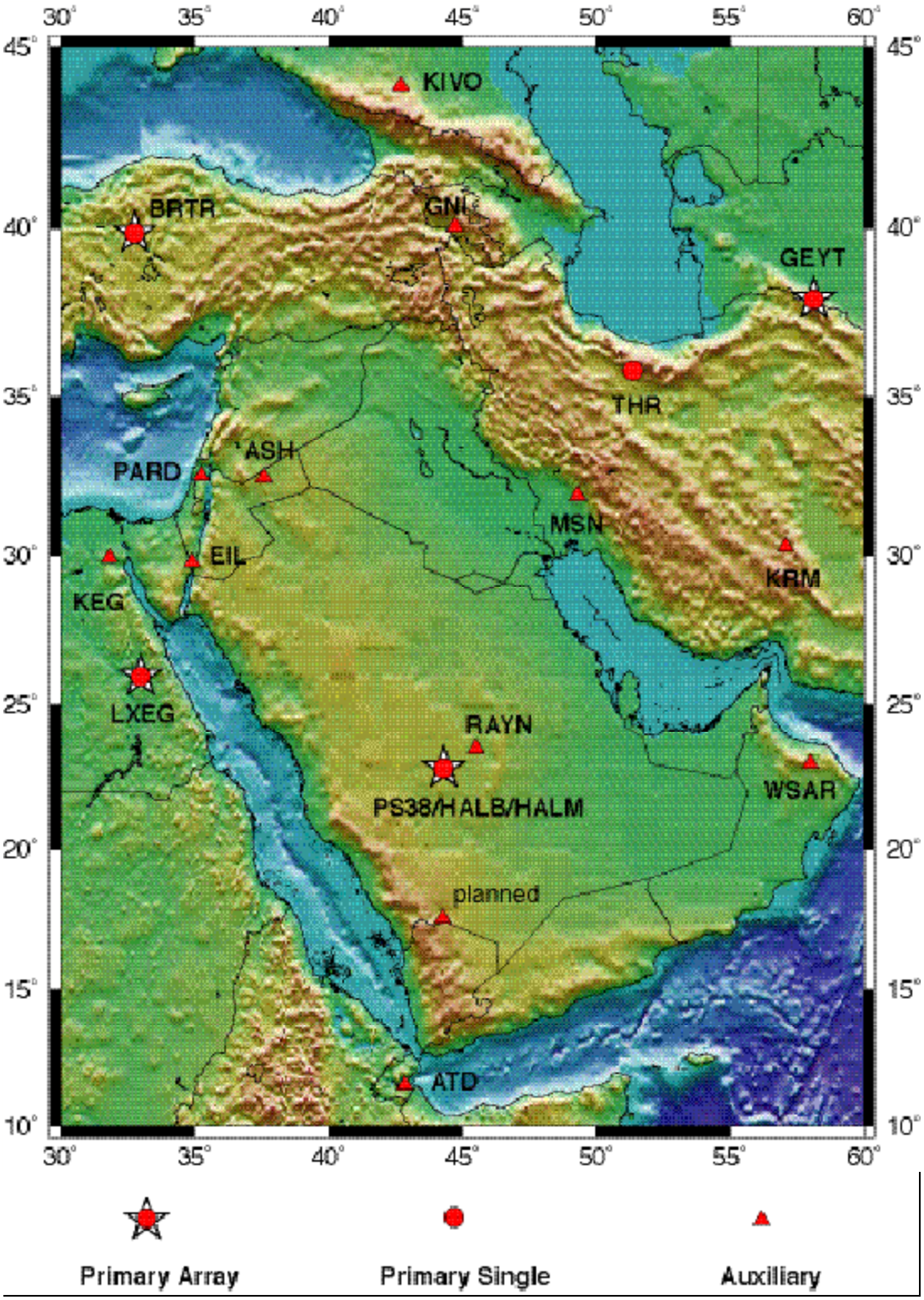

Figure 1. Map of International Monitoring System stations in the Middle East.

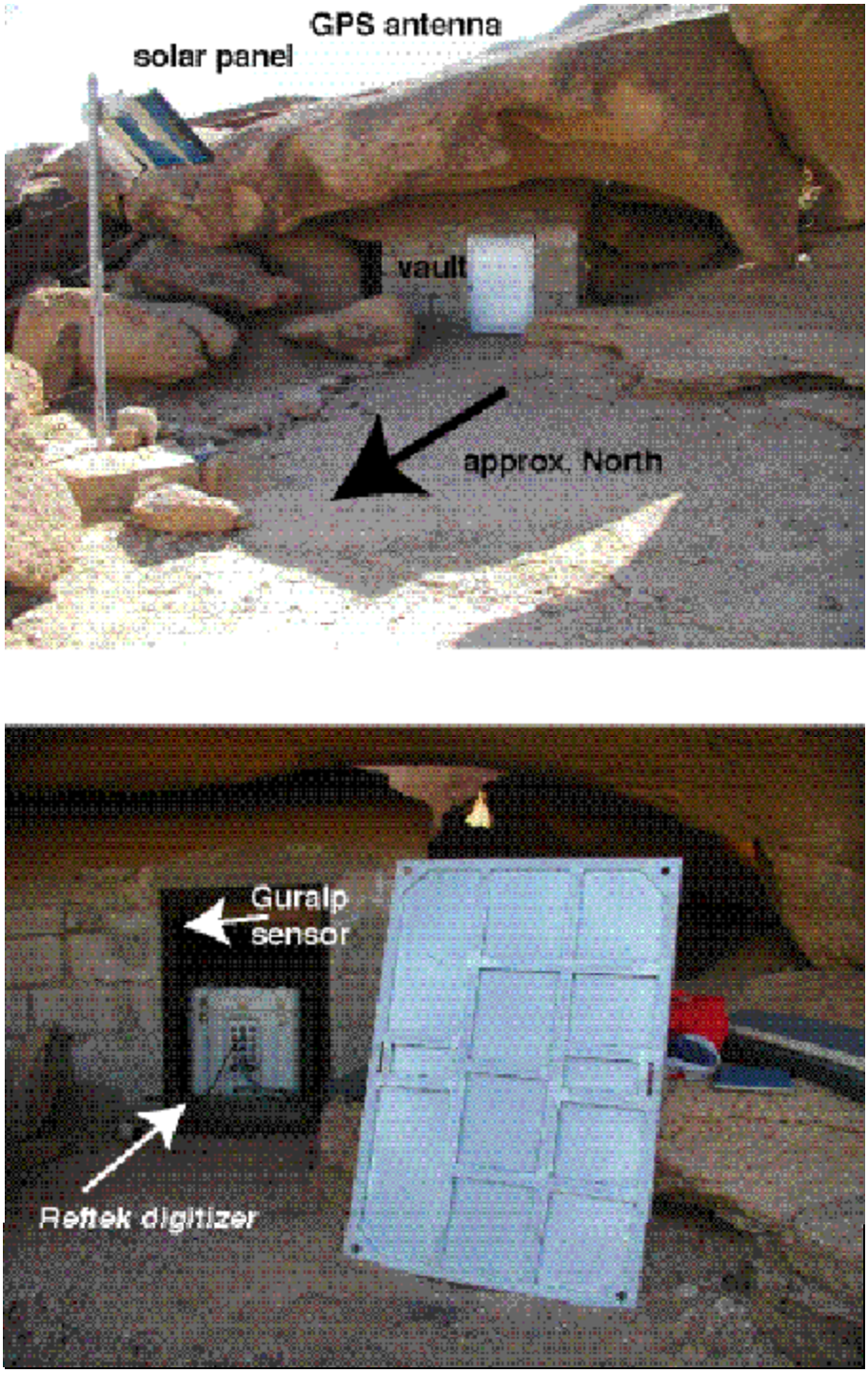

Figure 2. HALB station site. (a) Overview of site showing the vault, solar panel and mast. The GPS antenna is located on the overhanging rock above the vault. The vault door has slots that fit over two protruding U-bolts. Pad locks through the U-bolts secure the door to the frame. (b) Close-up of the vault with the door open. There is a concrete pad inside the vault for the sensor and digitizer.

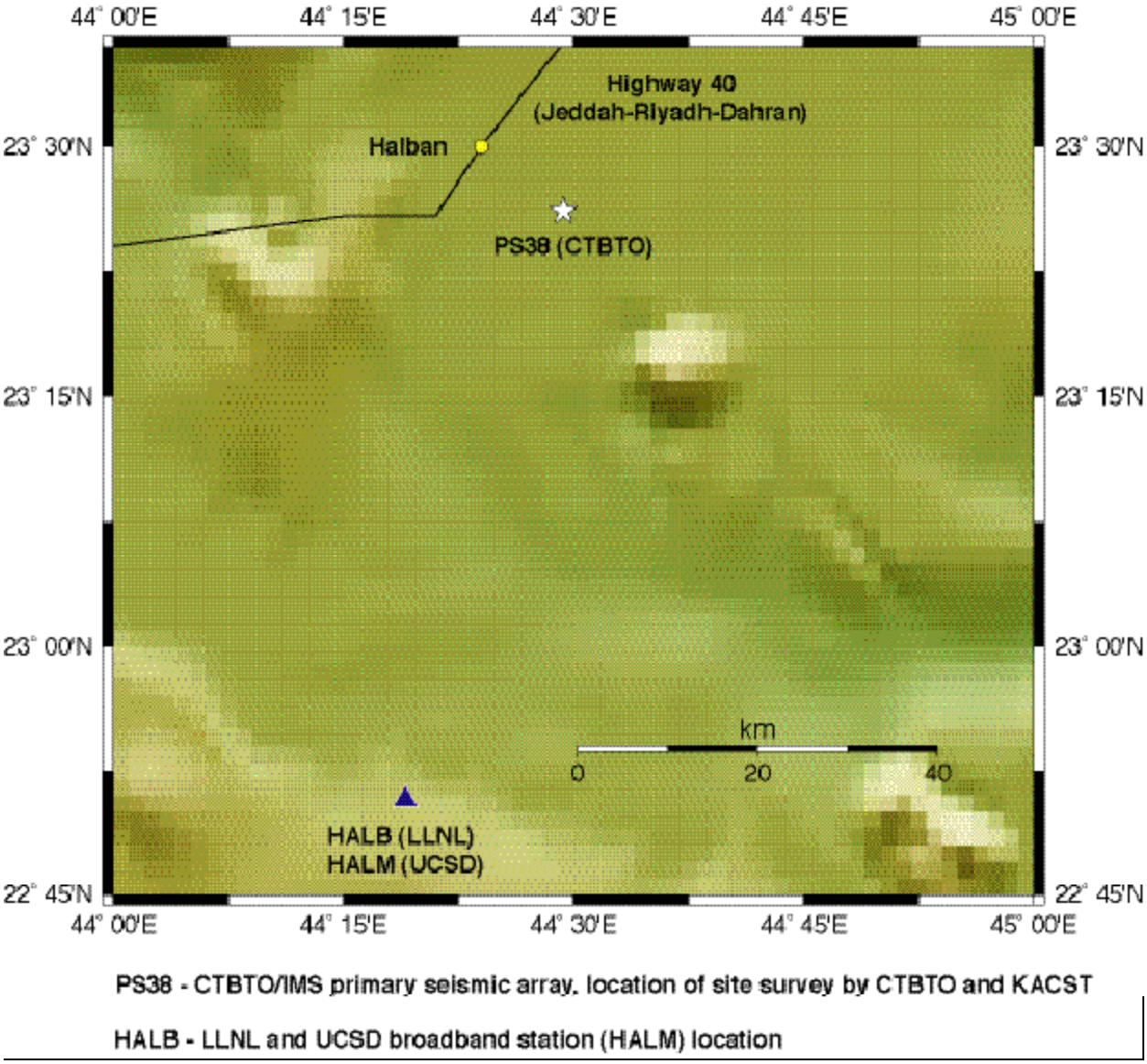

Figure 3. Locations of seismic station deployments, past, present and future, near the town of Halban in central Saudi Arabia.

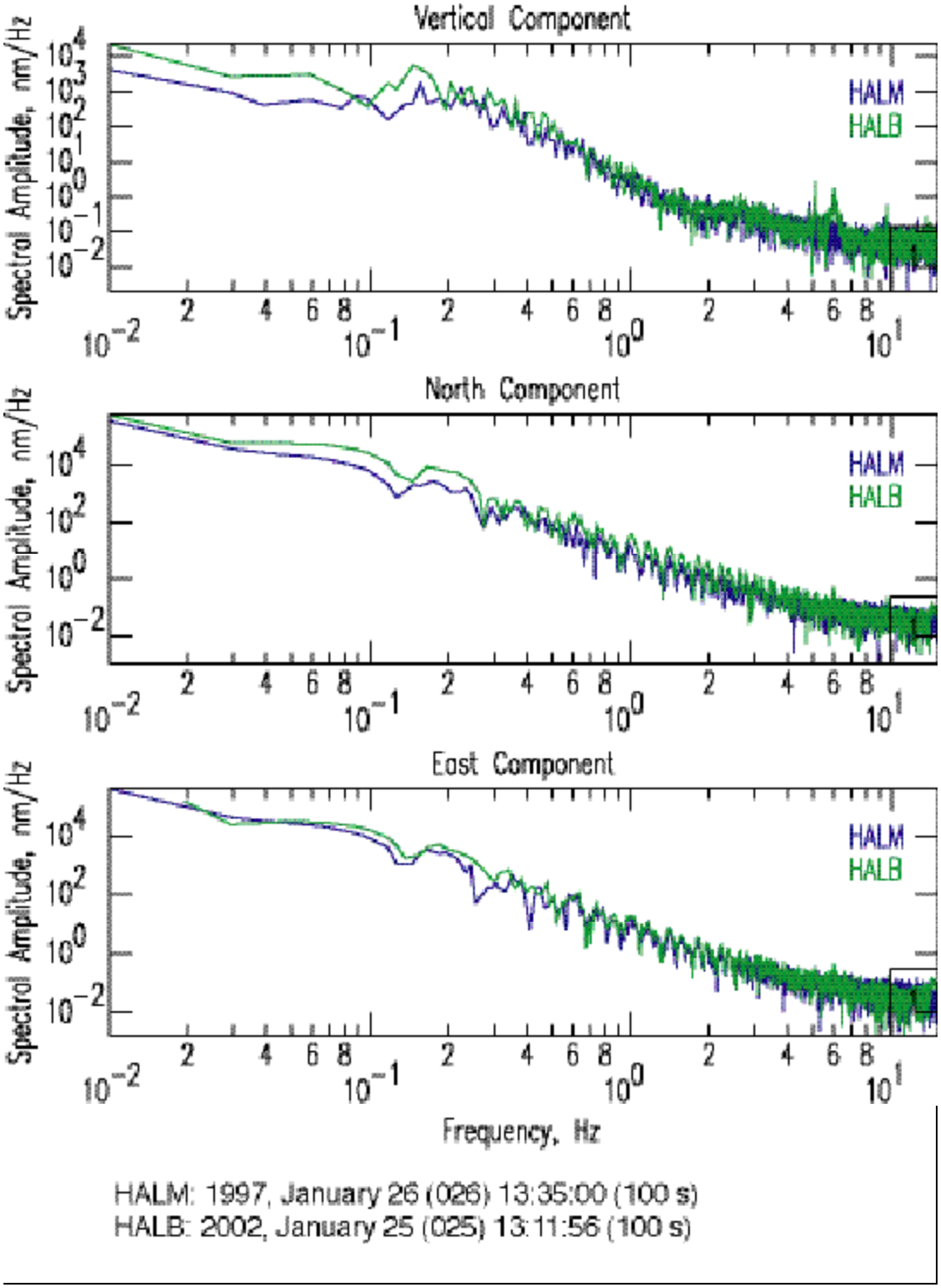

Figure 4. Comparison of noise spectra at HALB (this deployment) and HALM (the 1995-7 Saudi Broadband Deployment, Vernon and Berger, 1998). The comparison was done for a 100-s window at roughly the same time of day and day of year. This plot shows that the noise characteristics of our deployment with a Guralp CGM-3T seismometer are comparable to the STS-2 deployment of Vernon and Berger. More extensive analysis will be performed as more data become available.

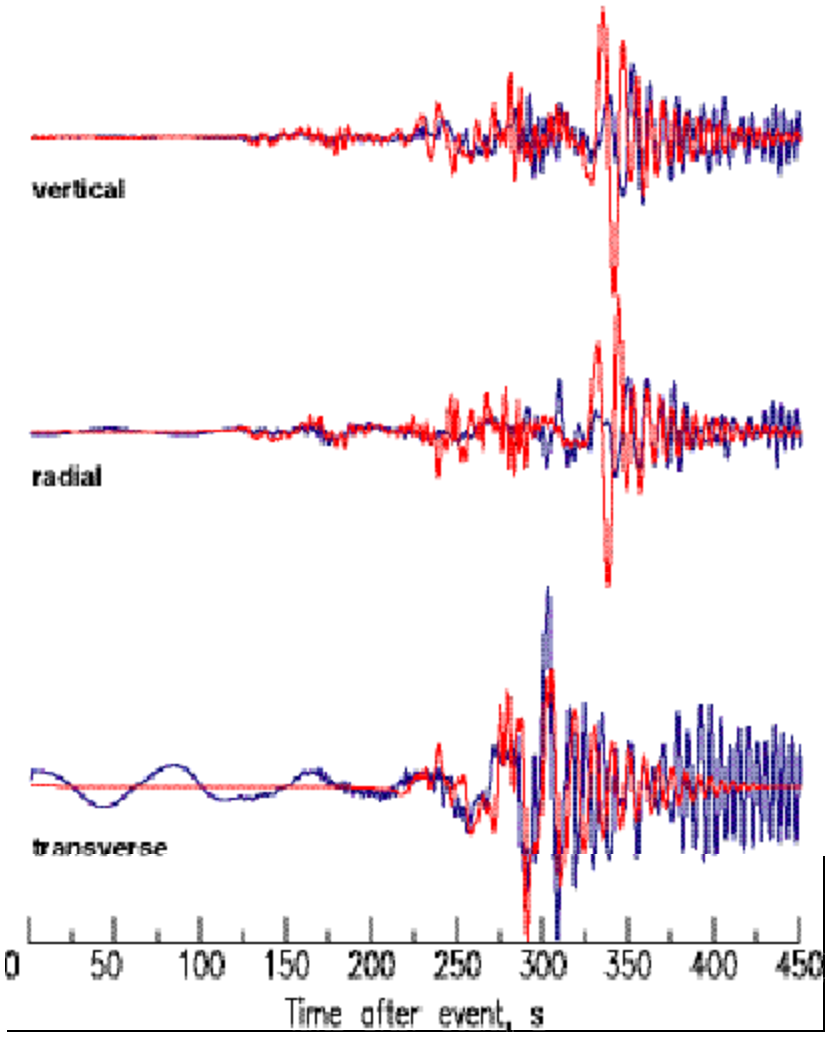

Figure 5. Waveform modeling of the 2002 February 17 (048) Southern Zagros Mountains earthquake. Synthetics were computed from a model derived from similar paths across the Arabian Platform (Rodgers *et al*., 1998). The data (blue) and synthetic (red) were both filtered in the band 80-3 seconds. The focal mechanism and moment were taken from the Harvard CMT Project.

REFINEMENT OF REGIONAL SEISMIC EVENT LOCATION IN NORTHERN EURASIA USING 3-D CRUSTAL AND UPPER MANTLE VELOCITY MODEL

Russian Federation/United States Calibration Working Group[1]

Sponsored by Defense Threat Reduction Agency

Contract No. DTRA01-01-C-0028

ABSTRACT

This study was performed within the framework of the United States/Russian Federation (US/RF) Joint Program of Seismic Calibration of the International Monitoring System (IMS) in Northern Eurasia and North America. The Joint Research Program was signed on 18 March 1997 between the Nuclear Treaty Programs Office of the Department of Defense (DoD), USA, and the Special Monitoring Service of the Ministry of Defense (MoD), Russian Federation. To implement the Joint Research Program, a Working Group has been established. This paper summarizes results for calibration of the IMS for Northern Eurasia using a 3-D velocity model developed for the area stretching from the Atlantic Ocean (western border) to the Pacific Ocean (eastern border) and from approximately 40^o N to 75^o N. Approximately 200 nuclear and large chemical explosions with known location and origin time have been used in this work.

The 3-D crustal and upper mantle velocity model developed for Northern Eurasia is based on previous results of deep seismic studies and is derived by fitting a model to observed travel-time residuals of regional waves from ground-truth (GT) GT0-GT1 nuclear and chemical explosions with known location and origin time. The model was used to generate a set of Source-Specific Station Corrections (SSSCs) for 28 IMS stations and some additional stations needed for relocation experiments for Pn, Pg, and Sn phases. The program "SSSC2" was used to compute SSSCs up to distance 20^o for Pn and up to distance 8.5^o for Pg. Corrections were derived for Sn by using a relationship between Pn and Sn travel times derived from the Center for Monitoring Research (CMR) GT database and the IASPEI[2]-91 tables. In regions where no information on deep velocity structure was available, tectonic regionalization was used to extrapolate and/or interpolate seismic data from other regions where the velocity structure was known.

To develop the 3-D velocity model we collected and analyzed travel times of regional phases recorded from 35 calibration events with known location and origin time within Northern Eurasia. These events were recorded within different tectonic units of the territory under investigation. Abrupt and unreasonable variations of travel times from reversed, overlapping, or repeated observations were used as criteria to identify outliers. Maps of deviations of the observed travel times from the IASPEI-91 travel-time tables were made for all calibration events. These maps indicate travel-time variations as a function of distance and azimuth within different geological provinces and provide a basis for the derivation of the 3-D velocity model.

To validate the location accuracy improvement achieved by application of the SSSCs, we relocated 167 GT events (nuclear explosions, announced chemical explosions, mine blasts, and earthquakes) with well-known location and origin time from the CMR GT database and from archived data. These relocation events, located within different tectonic provinces, were completely independent from the calibration GT data that were used to derive the 3-D model. Results of the relocation experiments using Pn, Pg, and Sn phases clearly indicate that the event location estimates were substantially improved, and 90% error ellipse areas were decreased when the SSSCs were applied. Although these results indicate significant improvement in the relocations, the model and validation datasets are still quite sparse in the region, especially for Siberia and the Far East, and the network used contains large gaps between seismic stations. Continued efforts are ongoing to collect additional data for model refinement and validation.

---

[1] The RF members of the Working Group (WG): Colonel A. Nikitin (chairman), Colonel A. Kuznetsov, Colonel V. Jacushevich, Lt. Colonel D. Bobrov, Lt. Colonel D. Zaporozhets, and Major K. Kichigin. The US members of the WG: Dr. A. Dainty (chairman), Dr. D. Baumgardt, Mr. J. Murphy, Dr. R. North, and Dr. V. Ryaboy.

[2] International Association of Seismology and Physics of the Earth's Interior.

OBJECTIVES

To improve location accuracy of seismic events, the IMS has to be calibrated. Travel times of seismic waves used for event location must take into account the 3-D velocity structure of the Earth, as has been demonstrated previously by Firbas (2000), Ryaboy et al. (2001), and other work. The aim of this study is to improve regional seismic event location within Northern Eurasia using a 3-D crustal and upper mantle velocity model. In comparison with previous IMS calibration studies of Northern Eurasia [Russian Federation (RF)/United States (US), 2001], this work is for a larger area stretching from the Atlantic Ocean to the Pacific Ocean and from approximately 40^o N to 75^o N, and uses a substantially greater number of ground-truth (GT) nuclear and chemical explosions recorded within Northern Eurasia. In this study, we used approximately 200 events with precisely known location and origin times. Many references to other regionalization studies may be found in the following papers (RF/US, 2001; Ryaboy et al., 2001). The primary objectives of the present study for the area under investigation are the following:

- Inventory and collection of results of deep seismic studies relevant to the IMS calibration.
- Evaluation of Pn travel times for GT0, GT1 nuclear and large chemical explosions and analysis of the travel-time deviations from the IASPEI-91 tables.
- Development of a 3-D crustal and upper mantle velocity model (preliminary version) and SSSC calculations for IMS stations and additional stations needed for relocation experiments.
- Relocation experiments with GT0-GT2 nuclear and chemical explosions, mine blasts, and earthquakes to validate location accuracy improvement using the SSSCs calculated from the 3-D velocity model.

RESEARCH ACCOMPLISHED

Tectonic maps of Northern Eurasia were generalized and digitized to assist interpolation and comparison of seismic data for different tectonic provinces. The generalized tectonic map is also used as a starting point for 3-D model development. The following tectonic provinces exist within Northern Eurasia: East-European and Siberian Pre-Cambrian platforms, including the Baltic, Ukrainian, Aldan, and Anabar ancient shields; West-European, West-Siberian, Skifsko-Turanean, and Timan-Pechora Paleozoic platforms; Kazakh shield; Paleozoic folded belts (Urals, Taimyr, Tien-Shan, Altay, Sayany), and Alpine tectonic systems (Pamirs, Kopet-Dagh, Alps, Kamchatka, Sakhalin, and Kuril regions). There are sedimentary basins within Northern Eurasia with depth to basement up to 10 km and greater (South Barents, Dnieper-Donets, Pre-Caspian, South Caspian, Kopet-Dagh and Ural fore deeps and other sedimentary depressions). These sedimentary basins can also cause anomalies of seismic wave parameters. Figure 1 shows that the primary and auxiliary IMS seismic stations are located in different tectonic provinces of Northern Eurasia and event-station paths intersect major tectonic boundaries.

Detailed seismic studies of the Earth's crust and upper mantle have been carried out in the different regions and published in numerous reports, papers and monographs. Results of these studies show that the Moho depth within Northern Eurasia varies from 55-65 km beneath young mountains (Pamirs, Tien-Shan, Alps) to 30-35 km beneath the West-European platform and North-Caspian sedimentary basin. Pn velocity within Northern Eurasia varies from approximately 7.8-8.0 km/s to 8.3-8.4 km/s and greater. The largest values of the Pn velocity were measured beneath the East-European and Siberian Pre-Cambrian platforms (8.1-8.5 km/s). The smallest values of the Pn velocity (7.7-7.8 km/s) were measured beneath the Baikal rift zone, southern regions of Siberia and the central part of the Paleozoic West-Siberian platform. Comparative analysis of tectonic maps and seismic data showed that major tectonic provinces of Northern Eurasia are characterized by different average values of the Moho depth and seismic velocities of the Earth's crust and upper mantle and different travel times of regional seismic waves.

Analysis of Pn travel-time curves and maps of Pn travel-time deviations from the IASPEI-91 travel-time tables showed that large regional travel-time variations, of the order of 5-10 seconds for Pn waves, were observed at epicentral distances of 1000-2000 km. Pn travel times for the Pre-Cambrian platforms (East-European and Siberian platforms including ancient shields) are the fastest Pn. Tectonically active regions of the southern and eastern areas of Northern Eurasia (Alps, Caucasus, Pamirs, Tien-Shan, Altay, Saiany, Baikal rift zone, Kamchatka and Sakhalin) are characterized by substantially slower travel times. Results of analysis of the observed Pn travel times were used for the upper mantle velocity regionalization.

Our goal was to derive a 3-D crustal and upper mantle velocity model for Northern Eurasia capable of predicting Pn travel times with an accuracy of approximately 1.0-1.5 seconds [root mean square (rms)]. The simplest 3-D velocity

models were sought from a family of 3-D models that simultaneously fit the observed Pn travel times for calibration events. The computer program "SSSC2" (Firbas, 2000) was used to compute the SSSCs for Pn and Pg up to distances of 20^o and 8.5^o, respectively, based on 3-D velocity models. The SSSCs for Sn were calculated from the SSSCs for Pn using a relationship between Pn and Sn travel times inferred from the CMR GT database and the IASPEI-91 travel-time tables. To better match the observations we fixed the 3-D crustal velocity model (Laske et al., 2000) and the Moho depth maps inferred from published and archived data of deep seismic studies and changed the 3-D upper mantle velocity model in a series of forward iterations. We applied the iterative process by combining and interpolating regional 1-D velocity-depth sections of the upper mantle. The 3-D velocity model developed for Northern Eurasia can be used to calculate SSSCs for the IMS stations and for other stations needed for relocation experiments.

To develop the 3-D velocity model we selected 35 GT0 and GT1 calibration events with accurate location and origin time. Figure 1 shows the location of these events (stars) and the location of the IMS stations (triangles), respectively. The thin lines are Pn event-station paths. The ray paths connecting the data points and sources provide good coverage for the territory under consideration. Dashed lines designate long-range profiles. One-dimensional upper mantle velocity sections inferred from these profiles were used for development of the 3-D velocity model.

As the first step, the initial 3-D model for P-waves was based on a new global crustal model (Laske et al., 2000) and the 3-D upper mantle velocity model based on results of deep seismic studies. These models have $2^o \times 2^o$ resolution. Moho depth was taken from published and archived maps for Northern Eurasia with a resolution $1^o \times 1^o$. Comparison of the maps of the observed Pn travel-time deviations from the IASPEI-91 tables revealed that variations in Pn travel times are correlated with tectonic regionalization. Observed and calculated Pn travel times fit better when we use tectonic regionalization and 1-D velocity models developed for different tectonic provinces for constructing the 3-D model. Figure 2 shows an example of evaluation of the 3-D velocity model developed for Northern Eurasia. The top of this figure shows discrete plots of deviations of the observed Pn travel times from the global IASPEI-91 travel-time tables. The shot point is shown as a star. The color coding of these triangles corresponds to the magnitude of travel-time deviations from IASPEI-91. Platform regions on these maps are usually characterized within the distance range from 1000 km to 2000 km by early Pn arrivals (from –3.0 s to –7.0 s in comparison with IASPEI-91 tables). The bottom part of the figure shows the difference between Pn travel times observed and calculated for the 3-D velocity model. These maps of the travel-time difference show that the 3-D model developed fits observed Pn travel times well (rms usually less than 1.0 s – 1.5 s). These maps were plotted for all calibration events. Our studies also showed that Pn travel times measured from peaceful nuclear explosions (PNEs) along the Tiksi-Norilsk / Norilsk-Tiksi long-range profile fit well with the Pn travel times calculated along the long-range profile for the Siberian platform using the 3-D velocity model.

Figure 3 shows the final result of our iterative procedure used for 3-D model development. All the territory of Northern Eurasia under investigation was separated into 30 units (top), and each of these units was characterized by one 1-D upper mantle velocity model (bottom) derived by the iterative procedure described above. Numbers on the map (top) refer to numbers on the 1-D velocity models (bottom). This 3-D velocity model developed for Northern Eurasia can be used to calculate maps of SSSCs for IMS stations and additional stations needed for relocation experiments. An updated set of SSSCs was calculated for 28 IMS stations and some additional stations located within Northern Eurasia. To have reasonable resolution and size of the SSSCs files, we calculated time corrections and modeling errors with different latitude/longitude grids for each station. The SSSCs files have grid 0.5^o for the latitude axis. The grid for the longitude axis has a constant value within the range from 0.5^o to 1.2^o for each station depending on the latitude of the station. Modeling error was calculated as the weighted average of the rms deviation for each region between the grid point and the station. Maps of the modeling errors of the Pn, Sn, and Pg waves were used for modeling error calculations. As an example, Figure 4 shows maps of SSSCs and modeling errors calculated for Pn (top) and Sn (bottom) waves for the ARU station.

Relocation experiments were performed to evaluate the influence of the SSSCs for Pn, Pg, and Sn on regional seismic event locations within Northern Eurasia and to estimate the improvement both in terms of location accuracy and in the reduction of the size of the 90% error ellipses. The LocSAT program was used for seismic event location experiments. A total of 167 events in two sets were relocated (Figure 5). These data were independent from the data used to develop the 3-D model. Only Pn, Pg, and Sn phases were used for relocation experiments. Lg travel times were not used because there is no reliable method for Lg arrival-time measurement available. We did not use teleseismic phases because we wanted to demonstrate location capabilities using only regional phases.

Set 1 includes 102 events from the CMR GT0-GT2 database. These event locations are shown on Figure 5 by small stars. The events are mainly located within the European part of Northern Eurasia. Time arrivals of the Pn, Pg, and Sn phases for relocation experiments were used from the Reviewed Event Bulletin (REB). It was found that the median mis-location changed from 15.7 km to 7.2 km, and the median 90% error ellipse decreased from 3,543 km^2 to 652 km^2. Set 2 of relocation events includes 65 historical nuclear explosions. As for set 1, only Pn, Pg, and Sn phases were used for relocation experiments. These event locations are shown on Figure 5 by large stars. The events were relocated using additional stations in the IMS. Additional stations were used to substitute for IMS stations for which data were not available. These stations are up to 200-250 km from the IMS stations and may be used for the IMS network simulation. Averaged results of relocations for set 2 show that the median mis-location changed from 22.5 km to 6.1 km and the median 90% error ellipse decreased from 3,003 km^2 to 665 km^2 . For example, Figure 6 shows some results of relocation experiments. One can see that the event location estimates were improved and the 90% error ellipse area was decreased when SSSCs were used.

CONCLUSIONS AND RECOMMENDATIONS

1. An inventory of seismic and tectonic data relevant to the IMS calibration of Northern Eurasia was performed. Travel times of regional phases recorded from 202 GT events were collected and carefully analyzed. Travel-time anomalies were recorded and plotted.
2. A 3-D crustal and upper mantle preliminary velocity model of Northern Eurasia was developed. This model was evaluated by comparison of observed and calculated travel times of regional phases and may be improved by using additional observational data.
3. The 3-D velocity model derived in this study was used to calculate SSSCs for Pn, Pg, and Sn waves for 28 IMS stations and some additional stations in Northern Eurasia.
4. The SSSCs were used to relocate two sets of 167 GT events. These sets of relocation events were independent from the calibration GT data that were used to derive the 3-D velocity model.
5. Results of relocation experiments using Pn, Pg, and Sn phases for events located in different regions of Northern Eurasia clearly indicate that the event location estimates were improved when SSSCs were applied. Efforts are ongoing to collect additional data for model refinement and validation.

ACKNOWLEDGEMENT

The authors are grateful to Dr. Petr Firbas for his “SSSC2” program that was used during this study.

REFERENCES

Firbas, P. (2000), Location Calibration Based on 3-D Modeling. *Advances in Seismic Event Location* (Thurber, C.H., Rabinowitz N. – editors), Kluwer Academic Publishers, 135-161.

Laske, G., T.G. Masters, and C. Reif (2000), Crust 2.0. A New Global Crustal Model at 2 x 2 Degrees. *http://mahi.ucsd.edu/Gabi/rem.html*, 2000.

RF/US Calibration Working Group (2001). Analysis of the IMS Location Accuracy in Northern Eurasia and North America Using Regional and Global Pn Travel-Time Tables. *Pure and Applied Geophysics*, 158, 59-77.

Ryaboy, V., D.R. Baumgardt, P. Firbas, and A.M. Dainty (2001), Application of 3-D Crustal and Upper Mantle Velocity Model of North America for Location of Regional Seismic Events. *Pure and Applied Geophysics*, 158, 79-103.

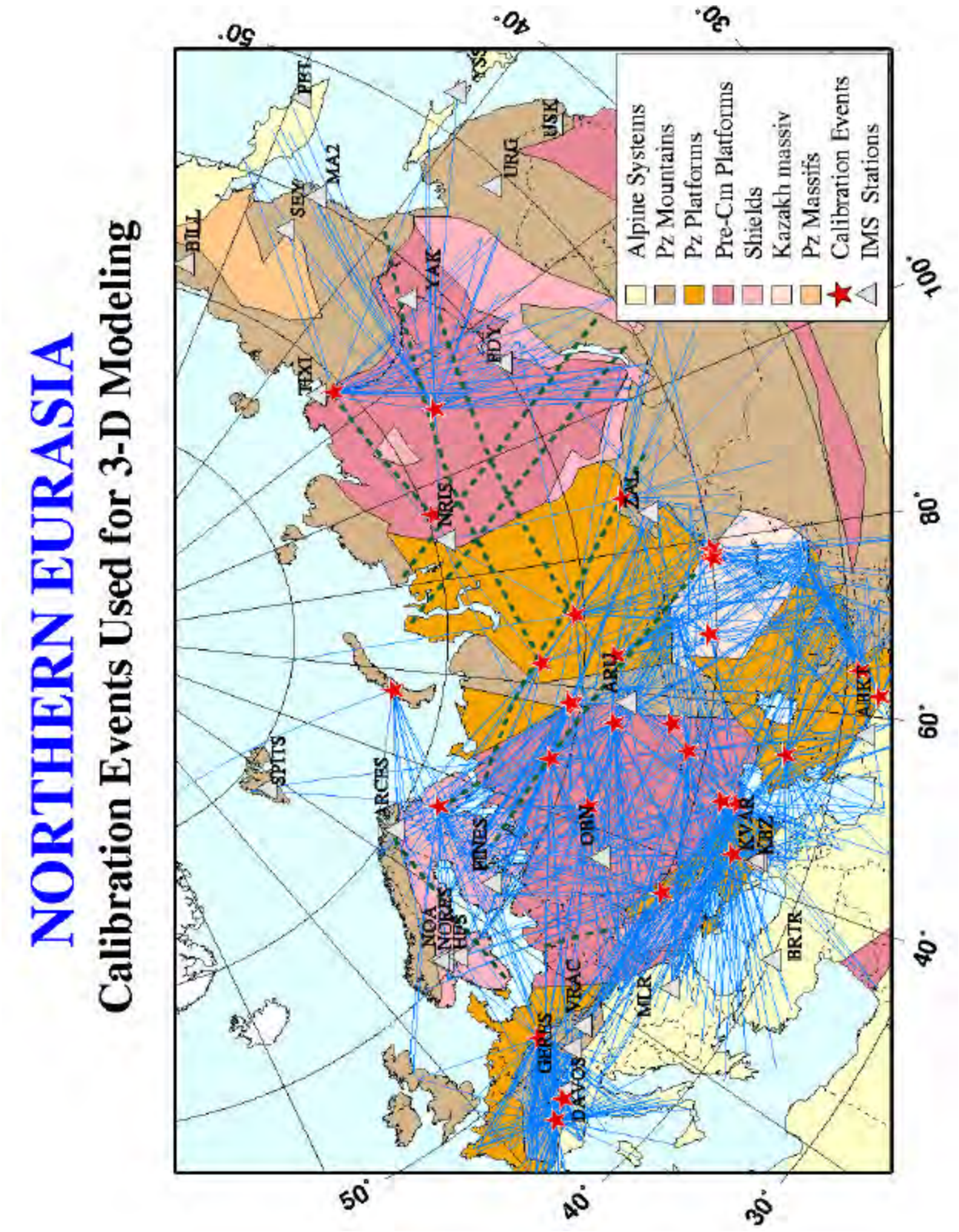

Figure 1. Map of the calibration events and IMS stations. Thin lines are Pn event-station paths. Dashed lines are long-range profiles used for the 3-D model development.

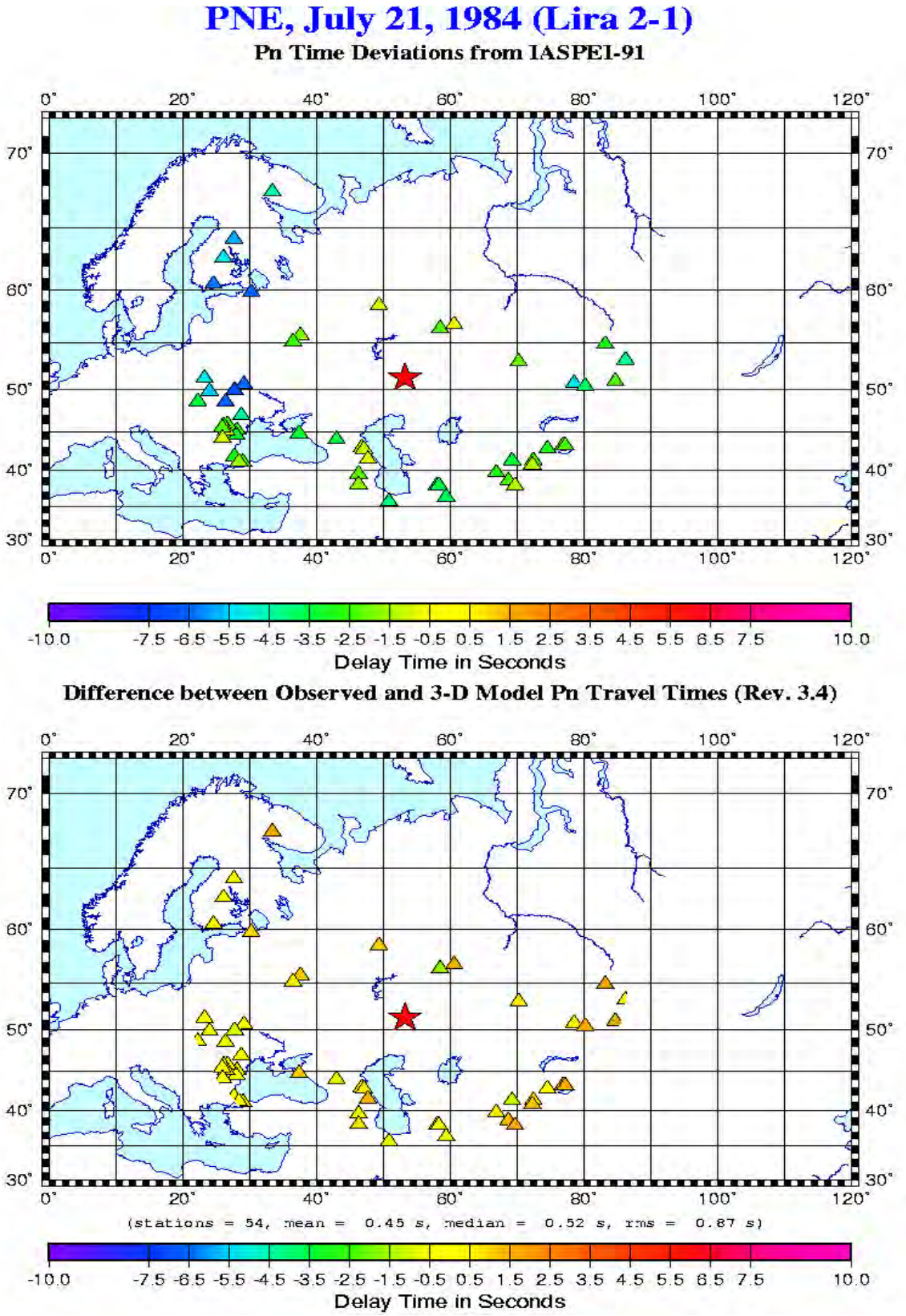

Figure 2. Pn travel-time deviations from IASPEI-91 (top), and difference between observed and calculated Pn travel times for 3-D model developed (bottom).

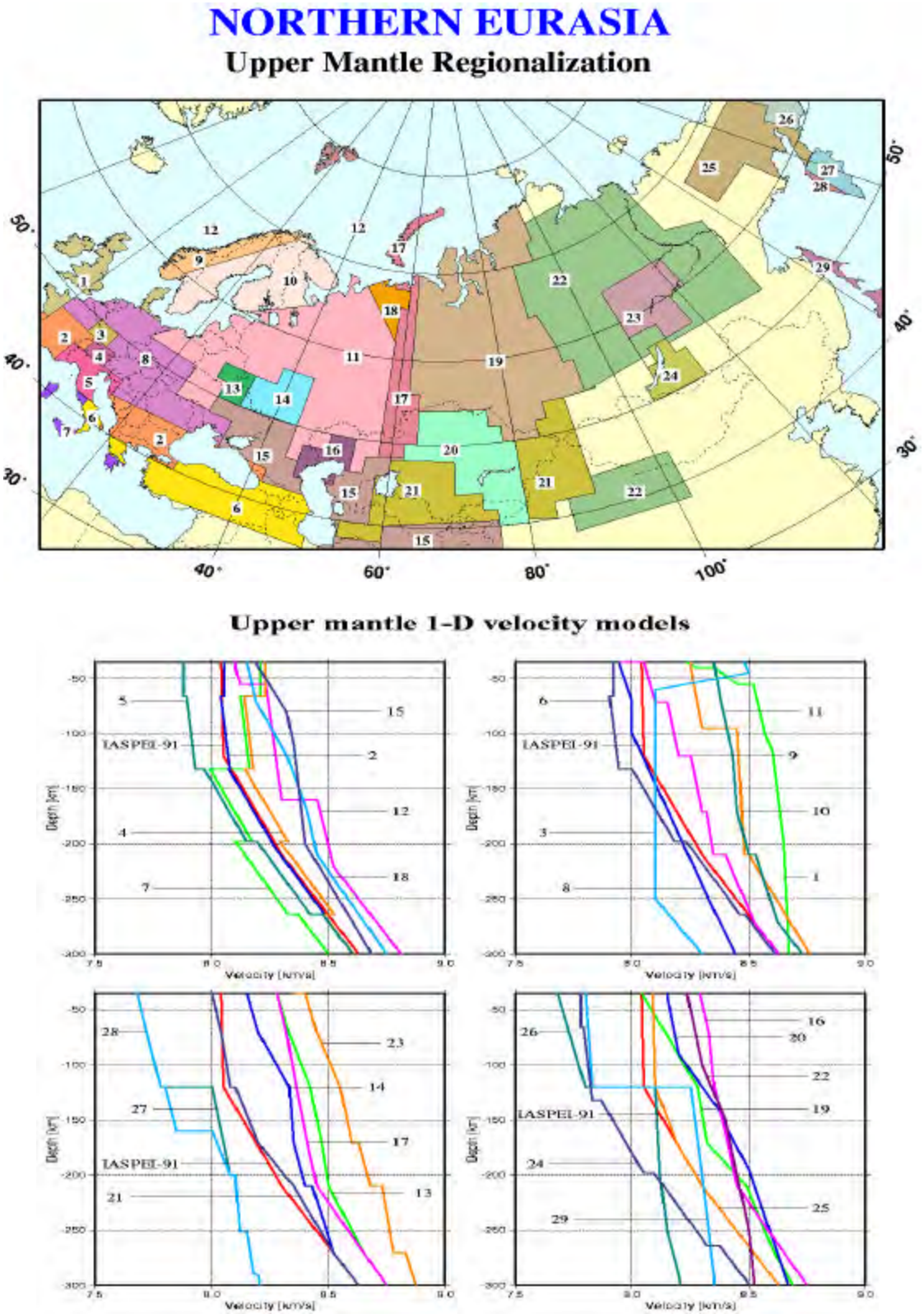

Figure 3. Final for this work an upper mantle P-velocity regionalization map (top), and 1-D upper mantle velocity models (bottom) were used for the 3-D model development.

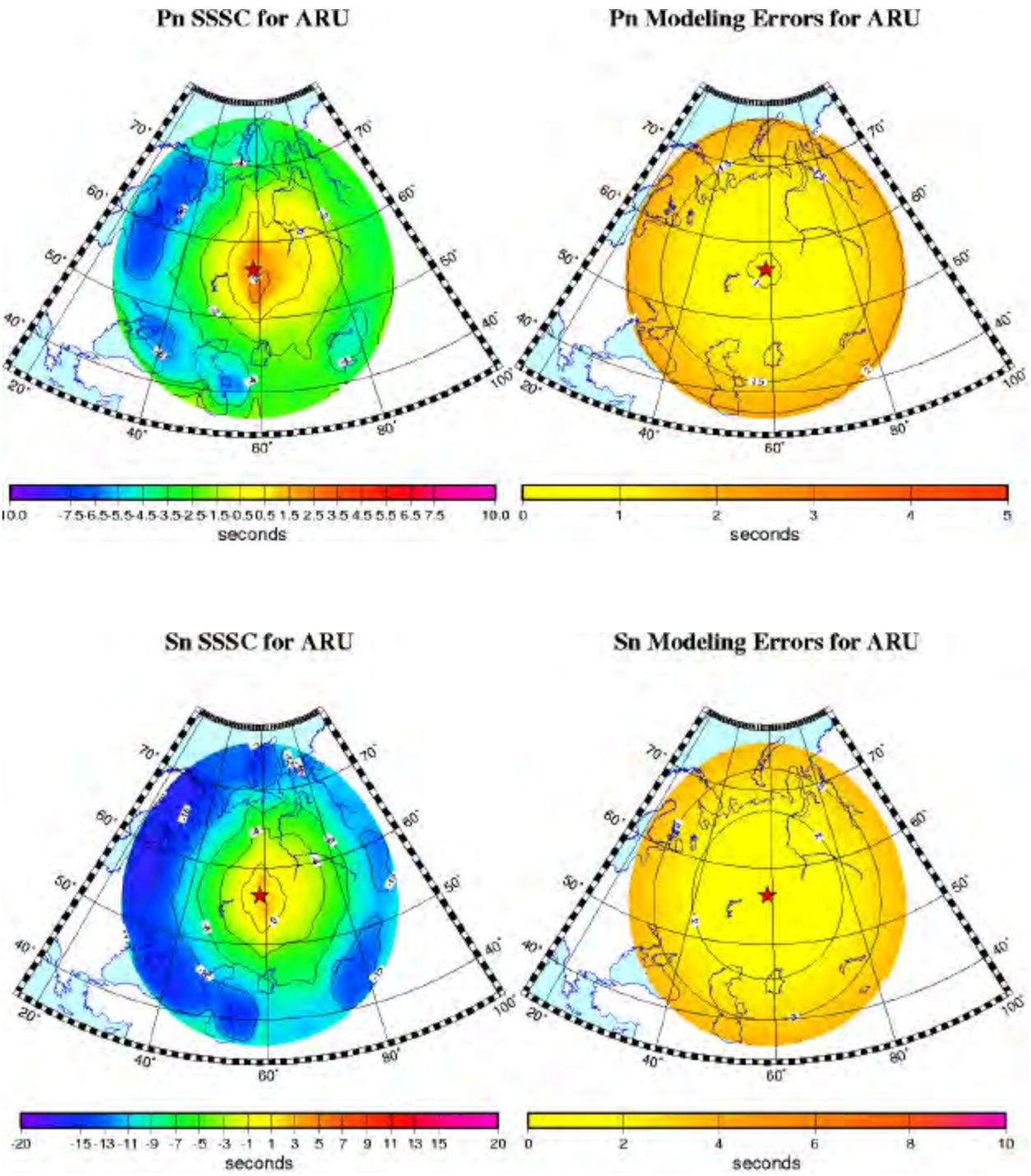

Figure 4. ARU station. SSSCs and modeling errors calculated for Pn (top) and Sn (bottom) phases.

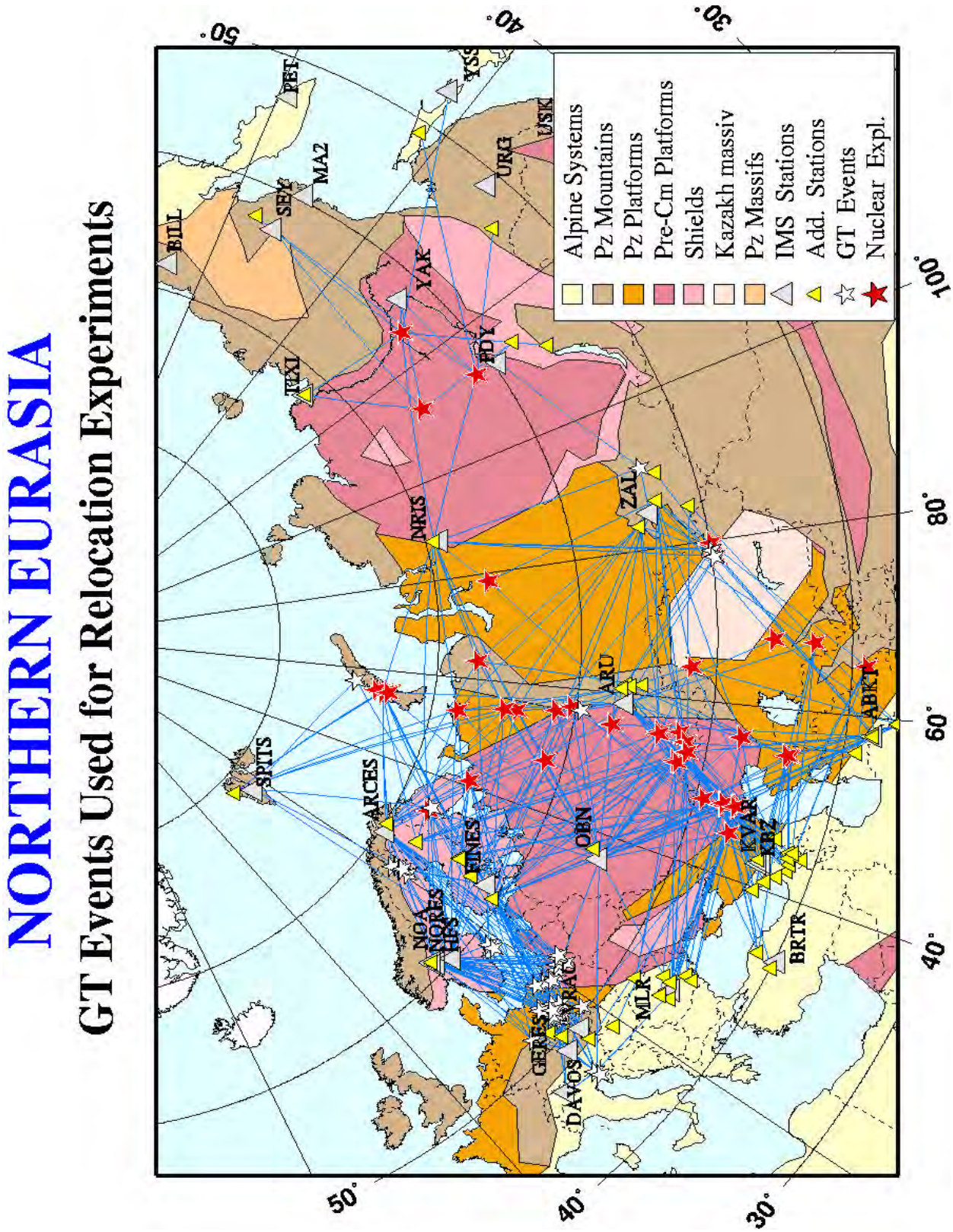

Figure 5. Map of two sets of GT events used for relocation experiments. Thin lines connect the GT events with seismic stations at regional distances used for relocation experiments.

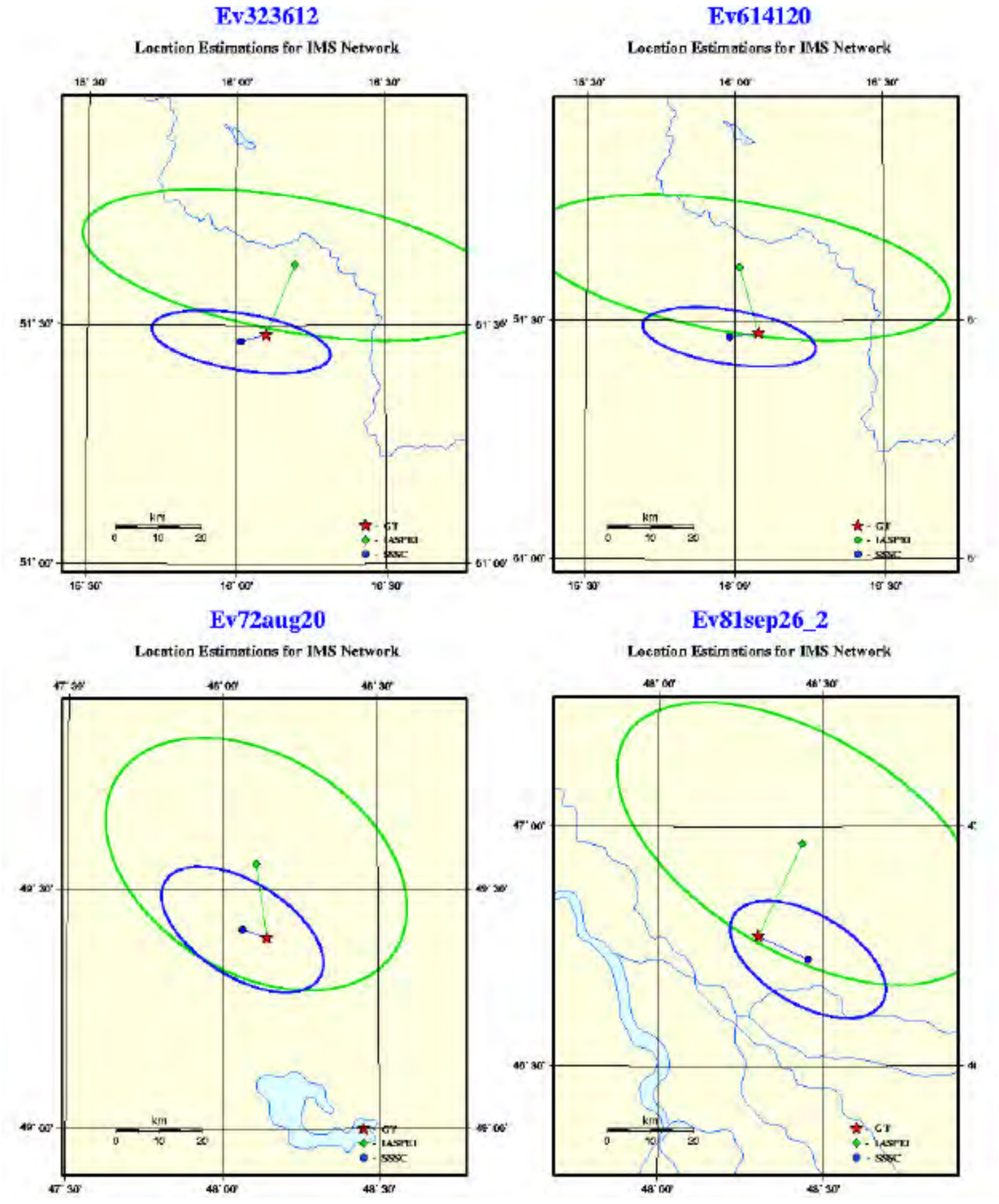

Figure 6. Examples of location maps of GT events.

DEEP SEISMIC SOUNDING DATA SETS FOR SEISMIC CALIBRATION OF NORTHERN EURASIA

Scott B. Smithson,[1] Igor B. Morozov,[1] Elena A. Morozova,[1] and Leonid. N. Solodilov[2]

University of Wyoming;[1] Centre GEON, Moscow, Russia[2]

Sponsored by Defense Threat Reduction Agency,[1] National Science Foundation[2]

Contract No. DTRA01-01-C-0081[1] and EAR-0092744[2]

ABSTRACT

Over the next three years, in cooperation with the Centre of Regional Geophysical and Geological Research (GEON), Moscow, Russia, the University of Wyoming will obtain, preprocess, and transfer to the Incorporated Research Institutions in Seismology (IRIS) a series of unique long-range Deep Seismic Sounding (DSS) profiles. These datasets will include nine major DSS projects using 22 Peaceful Nuclear Explosions (PNEs), several hundred of chemical explosions, and recordings of natural seismicity in Northern Eurasia. This project is jointly supported by the Defense Threat Reduction Agency (DTRA01-01-C-0081; 75% of funding) and the National Science Foundation (EAR-0092744; 25%). The data from project QUARTZ have already been transferred to IRIS.

The profiles were recorded between the early 1970's and late 1980's using ~400 three-component analog instruments, with recordings of 2-4 PNEs and several dozens of chemical explosions (per profile) at the same locations. Long listening times (up to ~600 sec after the first arrivals) allowed recording of the secondary phases (*S*, *Lg*, *Pg*, *Rg*) that are critical for nuclear explosion monitoring. The energies of the PNE sources (magnitudes >5) were sufficient for reliable recordings beyond 3000 km; including several reflections from the core-mantle boundary.

DSS PNE data have been widely recognized as an unparalleled source of seismic information about the detailed structure of the upper mantle down to 400- to 800-km depth and even to the Earth's core. DSS data present an unparalleled source of such information that is practically impossible to obtain by other means. The core PNE data sets of the DSS program cover an intermediate distance range between 0 – 3200 km bridging the gap between the conventional controlled source, earthquake, and nuclear–explosion-monitoring seismology. The dense, linear systems of PNEs and chemical explosions allow obtaining unusually detailed models of the crust and uppermost mantle over 4000-km long geotraverses. These datasets provide virtually the only dense three-component recordings of regional phases in aseismic regions of Northern Eurasia.

Numerous publications (primarily by GEON, Russian Academy of Sciences, the University of Wyoming, Potsdam/Karlsruhe, and Copenhagen groups) have presented velocity, reflectivity, attenuation, scattering, and receiver function models inspired by these profiles. When made broadly accessible for nuclear test monitoring research, the datasets will boost research on seismic calibration of the region and on transportable seismic discriminants in Asia. From a broader scientific perspective, the digitized DSS recordings and models of the upper mantle could also provide ideal reference and calibration data sets for the detailed structure of the upper mantle targeted by the initiative of USArray.

OBJECTIVE

Over the past three decades, Russian scientists acquired a network of dense, linear, long-range, three-component Deep Seismic Sounding (DSS) profiles using conventional and Peaceful Nuclear Explosions (PNEs) over a large territory of Northern Eurasia. These historic data provide unique opportunities to calibrate existing seismic nuclear discrimination techniques by studying regional wave propagation through complex lithospheric structures.

The objective of this research is to complete digitization, verify, edit and make broadly available through IRIS data repository a significant part of the unique collection of DSS PNE datasets currently stored at Centre GEON. The data processed and transferred to IRIS over four years of this work will include 22 PNEs recorded by nine major seismic projects (Figure 1). For the first time, this effort will deliver to the broad seismological and seismic monitoring community a set of unparalleled recordings of a large number of nuclear explosions recorded across a variety of propagation paths to the distances of ~3000 km.

RESEARCH ACCOMPLISHED

DSS PNE data have been widely recognized as an unparalleled source of seismic information about the detailed structure of the upper mantle down to 400- to 800-km depth and even to the Earth's core. DSS data present an unparalleled source of such information that is practically impossible to obtain by other means. The core PNE data sets of the DSS program cover an intermediate distance range between 0 – 3200 km bridging the gap between the

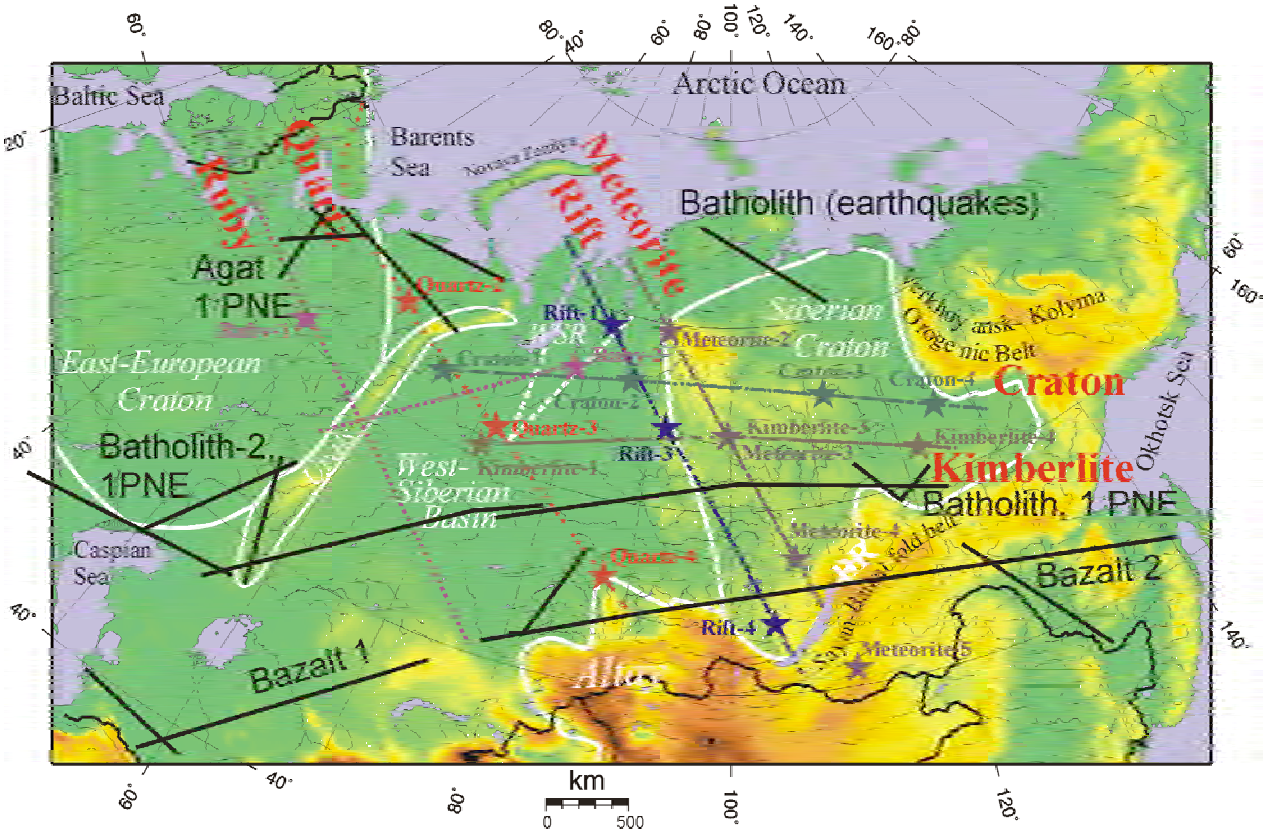

Figure 1 Nine DSS PNE projects to be delivered to IRIS as a result of this project. The data from profile QUARTZ and the PNEs from profile CRATON have already been delivered to IRIS. Colored lines and stars indicate the profiles and PNEs that have been digitized previously, black lines are the profiles to be digitized in this work. The coordinates and other parameters of the PNEs used in these profiles were reported by Sultanov et al. (1999). Major tectonic units are indicated. Note the extent of systematic, continuous profiling, with PNEs detonated at the nodes of a 2-D recording grid. Note that the profiles cover a vast asiesmic area that would be difficult to calibrate by other means.

conventional controlled source, earthquake, and nuclear explosion monitoring seismology. The dense, linear systems of PNEs and chemical explosions allow obtaining unusually detailed models of the crust and uppermost mantle over 4000-km long geotraverses. These datasets provide virtually the only dense three-component recordings of regional phases in aseismic regions of Northern Eurasia.

The data are being digitized at Centre GEON, Moscow, and preprocessed and edited at the University of Wyoming. PNE yields were between 7-23 kton providing reliable seismic recording throughout the full recording ranges (Figure 1). Continuous and often reversed PNE recordings allow observations of seismic phases diving to depths of ~800 km (e.g., Egorkin et al, 1987; Ryaboy, 1989; Kozlovsky, 1990; Morozova et al., 1999). On a typical PNE profile, 3-4 nuclear explosions were recorded at up to 400 of three-component seismograph stations with nominal spacing of 10 to 15 km. About 50-80 chemical explosions (typically, each 3000 – 5000 kg) per profile were also recorded to enable interpretation of crustal and uppermost mantle structures. The locations, depths, yields, and times of the PNEs, and characterizations of the source conditions were recently reported by Sultanov et al., (1999).

DSS profiles cross a variety of contrasting tectonic structures in Northern Eurasia and their studies have resulted in detailed images of the crust and uppermost mantle (Yegorkin, 1992). Some of the recent interpretations were performed by Egorkin and Mikhaltsev (1990), Mechie et al. (1993, 1997), Cipar et al. (1993), Priestley et al., (1994), Ryberg et. al. (1995, 1996), Schueller et al., (1997), Lorenz et al. (1997), Morozov et al. (1998a), and Morozova et al. (1999). The interpretations of the profile QUARTZ (Figure 2) by the University of Wyoming utilized the full spectrum of seismic data, including refractions and reflections from all 51 explosions of the dataset, lithospheric multiples, crustal-guided phases, seismic attenuation (Morozov et al., 1998b), coda amplitude decay (Morozov and

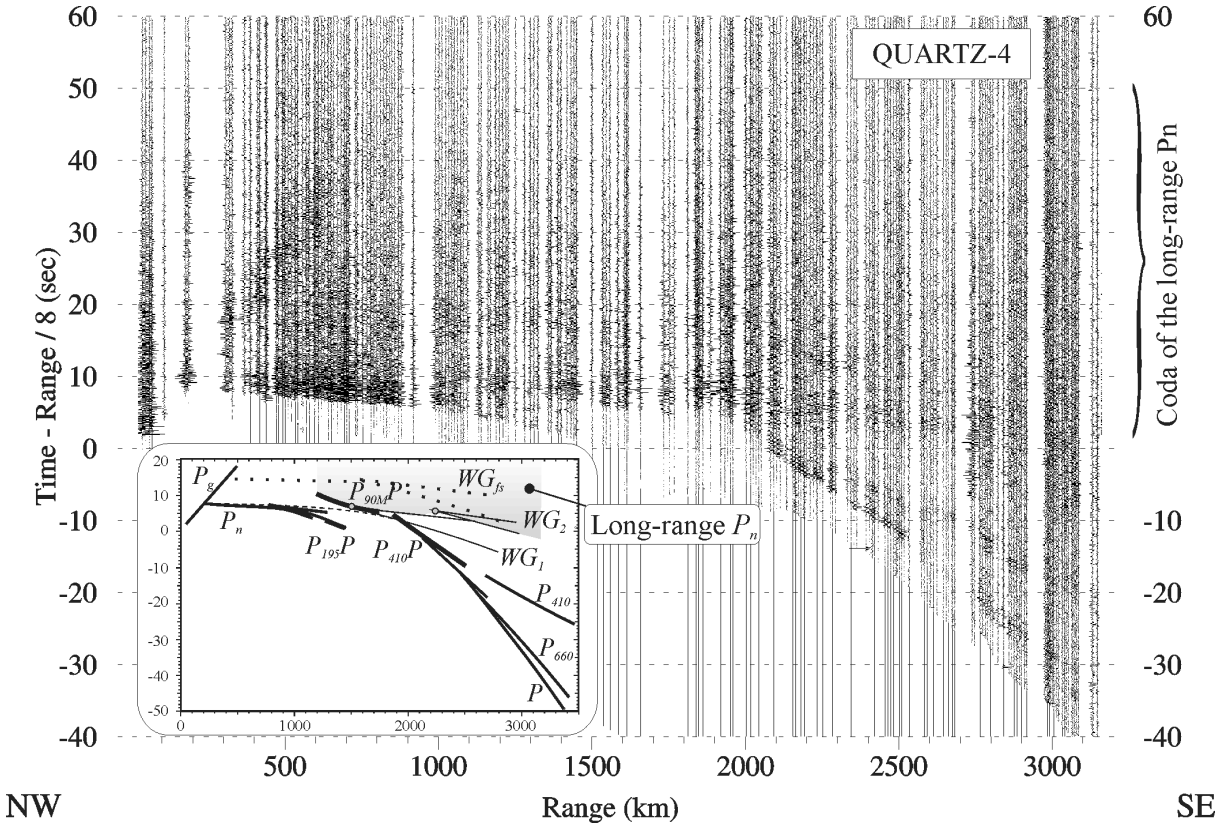

Figure 2. Vertical component record from PNE QUARTZ-4 (Figure 1). Inset shows a sketch of seismic phases identified in the wavefield. Note the free-surface and Moho *P*-wave multiples (*PP*, or whispering-gallery modes) labeled *WGfs* and *WG*, respectively. These phases were interpreted as caused by strong scattering within the uppermost mantle (Ryberg et al., 1995); however, in another interpretation, they may be due to a strong velocity gradient and mantle layering beneath the East European platform and the southern part of the West Siberian Basin (Morozov, 2001). Both of these inferences might have significant implications for nuclear test monitoring along the critical NW-SE paths across the East European Platform.

Smithson, 2000), receiver functions (Morozov et al, in press), and empirical travel-time regionalization (Morozov et al., in final preparation). Using travel-time, amplitude, and attenuation data, this study resulted in unusually well constrained images of crustal and mantle heterogeneity (Schueller et al., 1997; Morozov et al. 1998a, 1998b; Morozova et al., 1999). PNE data served as a basis for a new class of stochastic models of the uppermost mantle (e.g., Ryberg et al., 1995; Enderle et al., 1997), which, however, also resulted in a significant controversy (Morozov et al., 1998a; Morozov, 2001) and are being actively debated at present. The datasets contain spectacular and unusually continuous, three-component recordings of regional phases (Figure 3) still hold great potential for nuclear explosion monitoring research (for more detail, see our reports to several previous SRR symposia).

According to the schedule, to date, we have delivered to IRIS digitized seismic data from profile QUARTZ and PNE records from profile CRATON (Figure 1). The schedule for further planned data deliveries is given in the following table.

#	Data set (Figure 1)	Edited and reduced data delivered to IRIS DMS (months after November 2001)
1	QUARTZ	1
2	CRATON	9
3	KIMBERLITE	12
4	RIFT	18
5	METEORITE	24
6	RUBY	30
7	BATHOLITH-1,2	36
8	BAZALT-1,2	42
9	AGATE (5 profiles)	48

CONCLUSIONS AND RECOMMENDATIONS

Preliminary examination of the newly obtained Russian PNE records from the Siberian DSS PNE profiles demonstrates that the data provide valuable information for the analysis of the propagation of L_g and other phases for their use in nuclear explosion monitoring and calibration studies. When made broadly accessible for nuclear explosion monitoring research, the datasets will boost research on seismic calibration of the region and on transportable seismic discriminants in Asia. Greater availability of the unique PNE recordings would foster current research on several DoD-sponsored projects and facilitate extension of such research in the future. Also, from a broader scientific perspective, the digitized DSS recordings and models of the upper mantle could also provide ideal reference and calibration data sets for the detailed structure of the upper mantle targeted by the initiative of USArray.

REFERENCES

Cipar, J., K. F. Priestley, A. V. Egorkin, and N. I. Pavlenkova (1993). The Yamal Peninsula-Lake Baikal deep seismic sounding profile, *Geophys. Res. Lett.*, 20 (15), 1631-1634.

Egorkin, A. V. and A. V. Mikhaltsev (1990). The Results of Seismic Investigations along Geotraverses, in Super-Deep Continental Drilling and Deep Geophysical Sounding, K. Fuchs, Y. A. Kozlovsky, A. I. Krivtsov and M. D. Zoback (Editors), Super-Deep Continental Drilling and Deep Geophysical Sounding, Springer, Berlin, 111-119.

Enderle, U., M. Tittgemeyer, M. Itzin, C. Prodehl, and K. Fuchs (1997). Scales of structure in the lithosphere - Images of processes, Tectonophysics, 275, 165-198.

Kozlovsky, Y. A. (1990). The USSR Integrated Program of Continental Crust Investigations and Studies of the Earth's Deep Structure under the Globus Project, in Super-Deep Continental Drilling and Deep Geophysical Sounding, Fuchs K., Kozlovsky Y. A., Krivtsov A. I. and Zoback M. D. (Editors), Springer, Berlin, 90-103.

Lorenz, F., F. Wenzel, and J. Mechie (1997). Lateral heterogeneity implications from 2-D nuclear-seismic travel-time inversion, in: Fuchs, K. (Ed.) Upper mantle heterogeneities from active and passive seismology, pp. 237-248, Kluwer Academic Publ., Dordrecht.

Mechie, J., A. V. Egorkin, K. Fuchs, T. Ryberg, L. Solodilov, and F. Wenzel (1993). P-wave velocity structure beneath northern Eurasia from long-range recordings along the profile Quartz, Phys. Earth Planet Inter., 79, 269-286.

Mechie, J., A. V. Egorkin, L. Solodilov, K. Fuchs, F. Lorenz, and F. Wenzel (1997). Major features of the mantle velocity structure beneath northern Eurasia from long-range seismic recordings of peaceful nuclear explosions, in: Fuchs, K. (Ed.) Upper mantle heterogeneities from active and passive seismology, pp. 33-50, Kluwer Academic Publ., Dordrecht.

Morozov I. B, E. A. Morozova, S. B. Smithson, P. G. Richards, V. I. Khalturin, A. Stroikova, V. Cormier, and L. N. Solodilov, Regional travel time model of Northern Eurasia using Deep Seismic Sounding data sets, Bull. Seism. Soc. Am, in final preparation.

Morozov, I. B., and S. B. Smithson (2000). Coda of long-range arrivals from nuclear explosions, Bull. Seism. Soc. Am., 90, 929-939.

Morozov, I. B., E. A. Morozova, and S. B. Smithson, (1998a). On the nature of the teleseismic Pn phase observed in the recordings from the ultra-long range profile “Quartz”, Russia, Bull. Seism. Soc. Am, 88 (1), 62-73.

Morozov, I. B., E. A. Morozova, S. B. Smithson, and L. N. Solodilov. (1998b), 2-D image of seismic attenuation beneath the Deep Seismic Sounding profile “Quartz”, Russia, Pure and Applied Geoph., 153, 311-348.

Morozov, I. B., S. B. Smithson, and L. N. Solodilov, Imaging crustal structure along refraction profiles using multicomponent recordings of first-arrival coda, Bull. Seism. Soc. Am., in press.

Morozova, E. A., I. B. Morozov, S. B. Smithson, and L. N Solodilov (1999). Heterogeneity of the uppermost mantle beneath the ultra-long range profile “Quartz,” Russian Eurasia, *J. Geophys. Res.*, 104 (B9), 20,329-20,348.

Priestley, K. F., J. Cipar, A. Egorkin, and N. I. Pavlenkova (1994). Upper-mantle velocity structure beneath the Siberian Platform, Geophysical Journal International, 118 (2), 369-378.

Ryaboy, V. (1989). Upper mantle structure studies by explosion seismology in the USSR, Delphic Associates, 138 pp.

Ryberg, T., F. Wenzel, J. Mechie, A. Egorkin, K. Fuchs, and L. Solodilov (1996). Two-dimensional velocity structure beneath Northern Eurasia derived from the super long-range seismic profile Quartz, Bull. Seismol. Soc. Am., 86, 857-867.

Ryberg, T., K. Fuchs, A. V. Egorkin, and L. Solodilov (1995). Observations of high-frequency teleseismic Pn on the long-range Quartz profile across northern Eurasia, J. Geophys. Res., 100, 18151-18163.

Schueller, W., I. B. Morozov, and S. B. Smithson (1997). Crustal and uppermost mantle velocity structure of northern Eurasia along the profile Quartz, Bull. Seismol. Soc. Am., 87, 414-426.

Sultanov, D. D., J. R. Murphy, and K. D. Rubinstein (1999). A seismic source summary for Soviet Peaceful Nuclear Explosions, Bull. Seism. Soc. Am., 89, 640-647.

Yegorkin, A. V. (1992). Crustal structure along seismic geotraverses, International Geology Review, 34 (4), 345-362.

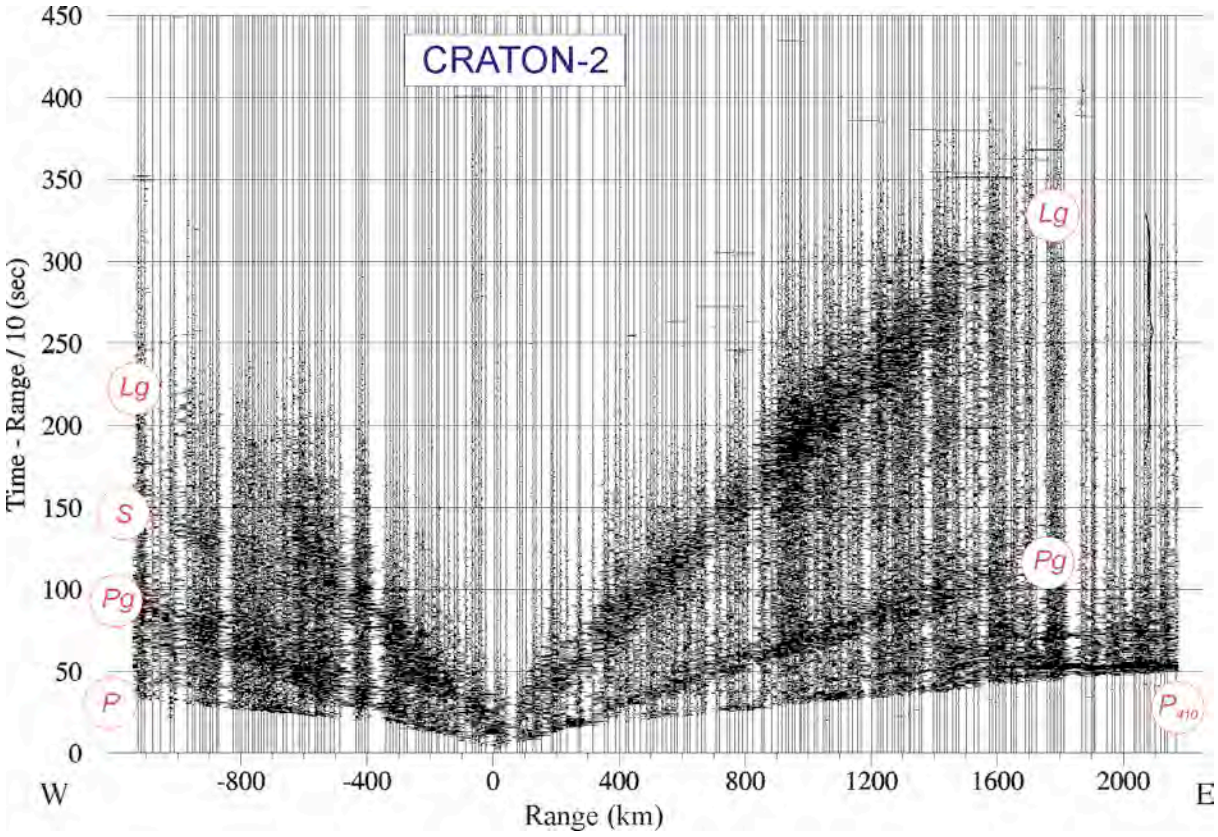

Figure 3. Vertical-component record from PNE CRATON-2 (Figure 1). Note the continuity of arrivals extending to the transition zone discontinuities. Also note the strong *Lg* and *Pg* propagating to the ranges exceeding 1600 – 1700 km, and the differences between the character of *S* wave and *Lg* in two directions from the PNE. *Lg* is very strong east of the shot point (under the Siberian Craton) whereas the mantle *S*-wave propagates efficiently to the west, under the West Siberian basin (Figure 1).

A COMPARATIVE STUDY OF NATURAL AND MAN-INDUCED SEISMICITY IN THE YANQING-HUAILAI BASIN AND THE HAICHENG AREA

Brian Stump, Christopher Hayward, and Rong-mao Zhou

Southern Methodist University

Sponsored by Defense Threat Reduction Agency

Contract No. DTRA01-02-C-0003

ABSTRACT

Natural earthquakes and mine-induced seismicity are health, life, and economic hazards. Seismic wave studies from such sources provide a mechanism for understanding local propagation path effects and constraints upon source mechanism dynamics. The geographic focus of this investigation is in two areas, the Yanqing-Huailai Basin around Beijing and northeast China along the Tan-Lu fault near the area of the 1975 Haicheng earthquake. Several regional stations and arrays from the Chinese Digital Seismic Network (CDSN) and the International Monitoring System (IMS) are available. A local network supplemented by a new high-frequency array already exists within the Yanqing-Huailai region. Within the Yanqing-Huailai Basin, earthquake risk and propagation path assessment are important because of Yanqing-Huailai Basin's high historical seismicity and Beijing's large population. Numerous underground mines regularly experience rock bursts and collapses resulting in mining operation disruptions, injury and occasional fatalities. The Haicheng area, the location of the first successfully predicted earthquake, is naturally seismically active as well. Mining operations are common in this region. Existing broadband regional data are being gathered and combined with local network data to provide an initial assessment of the earthquake and mine-induced seismicity in each region. The key to this study is the separation of propagation and source effects for these events. Once the background activity is quantified and understood, the path-source separation will be addressed with an experimental program. Plans call for an initial deployment of broadband instruments in the late summer.

OBJECTIVE

The goal of this collaborative study between Southern Methodist University (SMU) and the Institute of Geophysics, China Seismological Bureau, is to develop a ground-truth database that can be used to improve regional event locations, to characterize the nature of the event and to provide a physical understanding of the source. These goals contribute to earthquake risk assessments and mine safety issues, and this synergy motivated the collaborative empirical study. The two regions of focus (outlined in Figure 1) are the Yanqing-Huailai Basin near Beijing and the area around Haicheng along the Tan-Lu fault. Each region has an existing digital network that can provide limited ground-truth.

Our scientific goal is to use near-source instrumentation in combination with regional broadband instruments to assess path and source effects in the two regions. As part of the study, we are deploying portable instruments at both near-source and regional distances. These near-source recordings will significantly improve the source characterization and interpretation of the accompanying regional signals.

Regional signals recorded from events in Yanqing-Huailai Basin near Beijing and the area around Haicheng are strongly affected by crust and upper mantle structure that varies over the broad region diagramed in Figure 1. Geologic structure introduces path complexities that make it difficult to separate source and propagation effects in high-frequency regional signals. Thus, the signal interpretation becomes ambiguous. Simple effects, such as a regional travel-time variation, directly affect the location and origin time estimation. More complex effects lead to phase misidentification, poor magnitude estimates, and problems in event characterization.

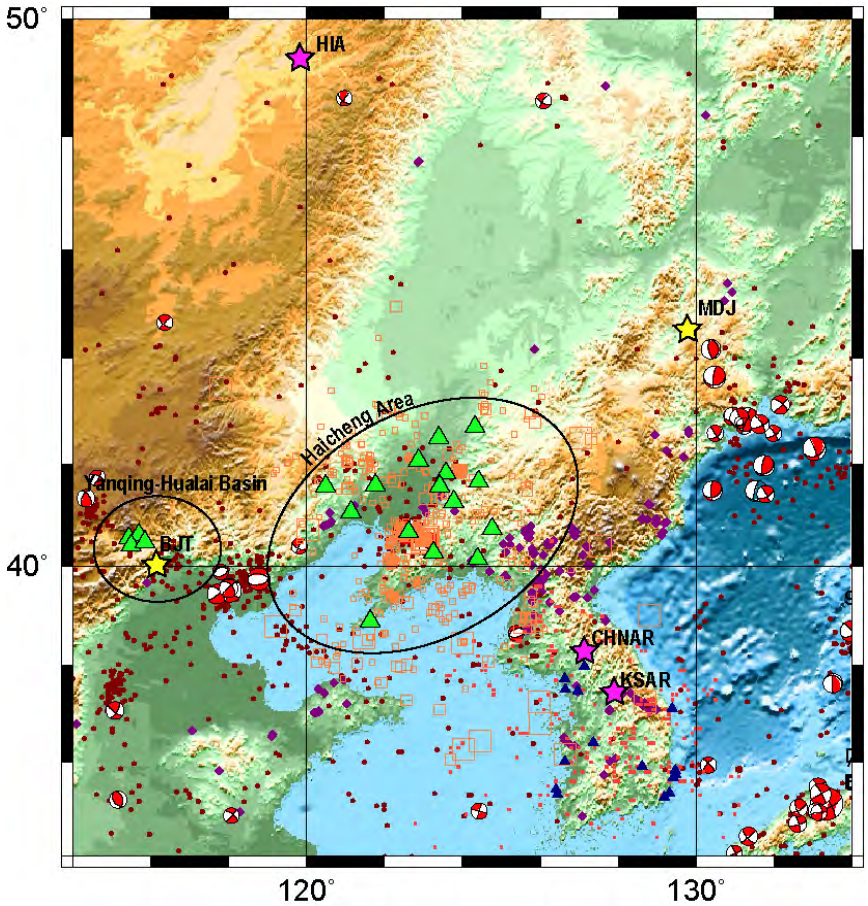

Figure 1: Map summarizing the two study areas (black circles). Regional CDSN and IMS stations (yellow stars) and arrays (purple stars) will be utilized in the study. Local seismicity is shown as brown squares and ISC locations purple circles. Fault plane solutions are from Harvard.

RESEARCH ACCOMPLISHED

Yanqing-Huailai Basin

The seismically active Huailai basin, northwest of Beijing, is the (Figure 1) initial region of focus in this work. Recent historical seismicity in the region illustrates the clustering of activity around the basin and motivates the instrument deployment (Figure 2). Fault plane and moment tensor studies of events in this region suggest that the faulting is consistent with the regional stress field, which is compressive in the ENE-WSW direction and tensile in the NNW-SSE direction. Mapped faults in the region are consistent with normal faults across the basin reflective of the NNW-SSE tensile stress directions (Yongkang *et al.*, 1995, 1996).

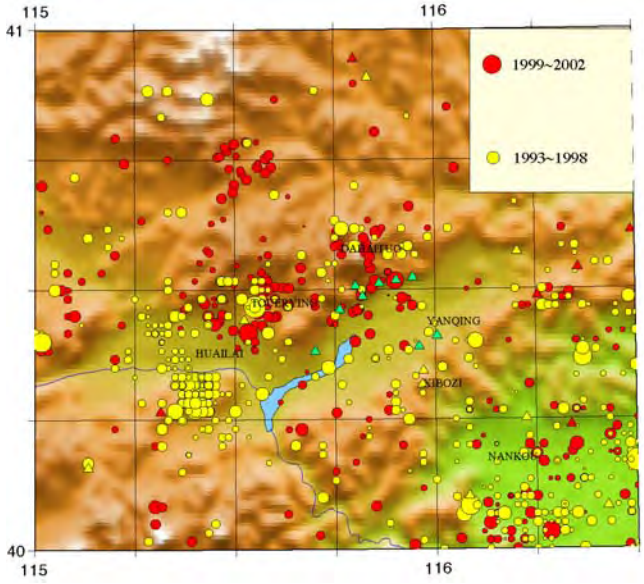

Figure 2: Locations of recent seismicity in the Huailai Basin.

Locations for the new near-source and regional broadband stations have been chosen with instrument deployment planned for the fall. Figure 3a illustrates the planned five near-source sites (crosses) while the planned regional sites are illustrated in Figure 3b. In each of these maps, the associated permanent seismic stations in the regions are denoted by triangles. This station distribution is designed to quantify near-source effects so that they can be separated from the regional propagation path effects.

Preliminary work is underway in developing and assessing source and propagation path effects in this region. A preliminary velocity model has been developed from a near-by reflection survey. This model and a simplified version are reproduced in Figure 4. This velocity model has been used for predicting arrival times. Near-source data from an earthquake within the Huailai basin is compared to the predictions in Figure 4. This starting model appears to be good for our initial studies.

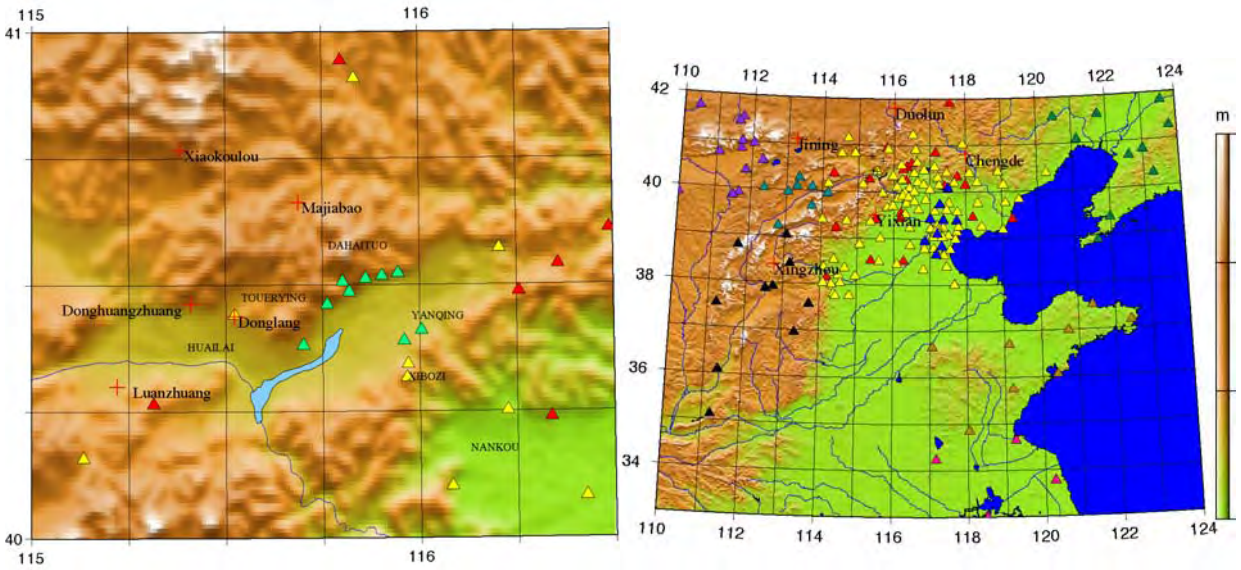

Figure 3a: Locations of planned near-source stations (crosses) and existing stations (triangles) in and around the Huailai Basin. 3b: Planned regional broadband stations (crosses).

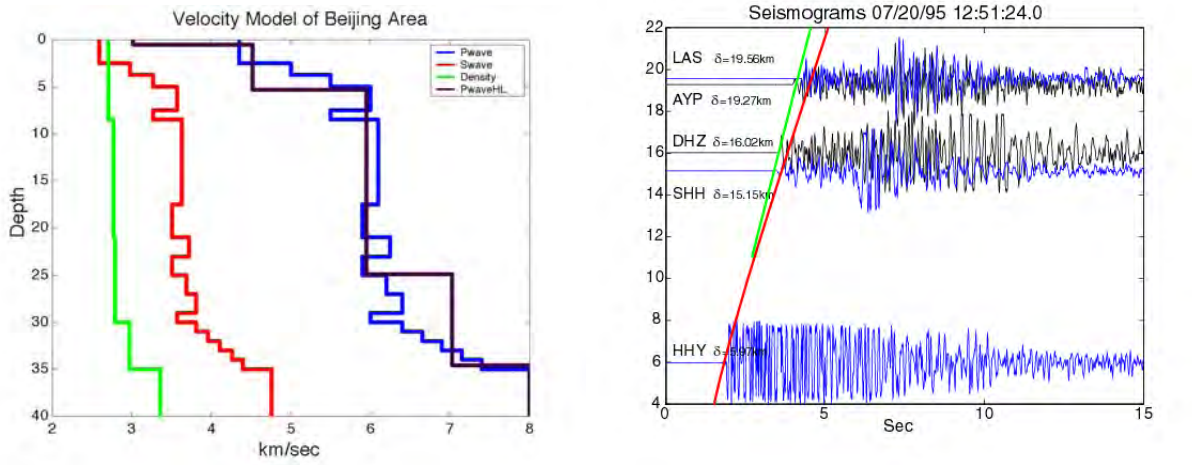

Figure 4: Preliminary velocity model for the Huailai Basin (left). Predicted arrival times are compared to near-source data generated by an earthquake within the basin.

In the Huailai Basin one of the local resources is the five, three-component station network of the Sino-European Cooperative Huailai Digital Seismograph Network (HDSN). Local sources in this region have been characterized using an empirical Green's function approach (Xu, Chen and Wang, 1999). Important source scaling information can thus be derived for regional signal interpretation. Three close-by events from this study are summarized in Table 1.

Table 1: Source Parameters for Sample Events from HDSN

	Latitude (^{0}N)	Longitude (^{0}E)	Depth (km)	M_L
Event 1	40.326	115.448	5.5	3.4
Event 2	40.323	115.447	5.1	2.0
Event 3	40.323	115.445	5.1	2.1

The basis of the Xu *et al.*, 1999 study used the fact that these events are less than a kilometer apart in their empirical Green's function source study. Figure 5 illustrates the near-source vertical waveforms from one event documenting the propagation path effects.

To illustrate the utility of near-source data in constraining earthquake source scaling effects, full record spectra were estimated for each of the three near-by events (Table 1) recorded at one of the near-source stations (Figure 6). These spectral data can be used to develop source scaling and source moment estimates for the events. Xu *et al.*, 1999, have used such data to constrain source models of the larger events. We believe that similar results will be useful in establishing magnitude-moment relations. The planned near-source stations illustrated in Figure 3a will provide additional data for constraining the sources. These data will be critical to the interpretation of the regional data and separation of propagation path and source effects.

The velocity models illustrated in Figure 4 can be used to develop synthetics for comparison to the near-source observations. Preliminary models were developed and compared to some of the near-source data recorded by the HDSN. Figure 5 summarizes these simple comparisons. The focus in this comparison is on the longer period data (2-10 sec) since the models are simple and preliminary. The two synthetics are similar to the observations and illustrate that the starting model for the Huailai Basin is consistent with the near-source recordings of the earthquakes as well as arrival times.

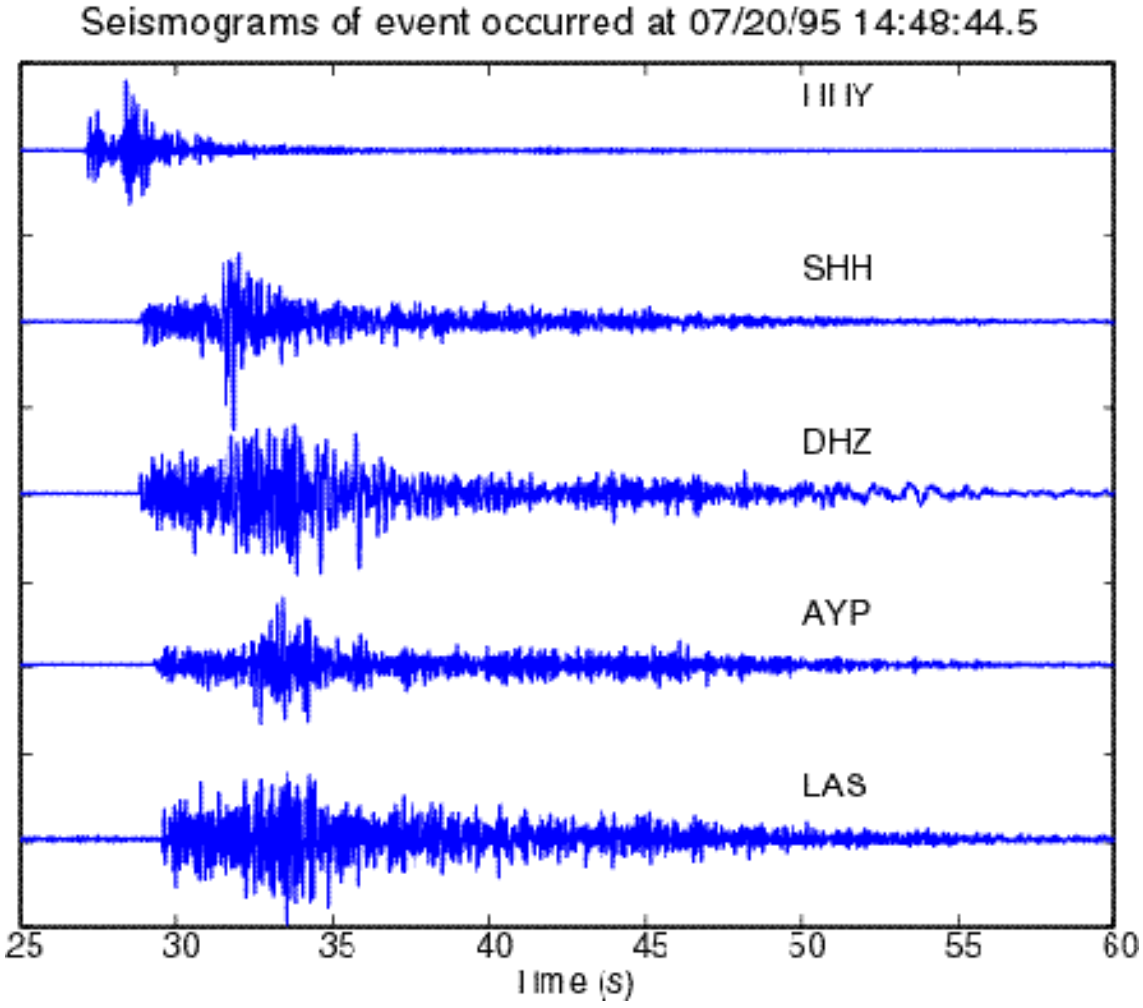

Figure 5: Vertical velocity waveforms from Event 2 (Table 1), the smallest in the sequence.

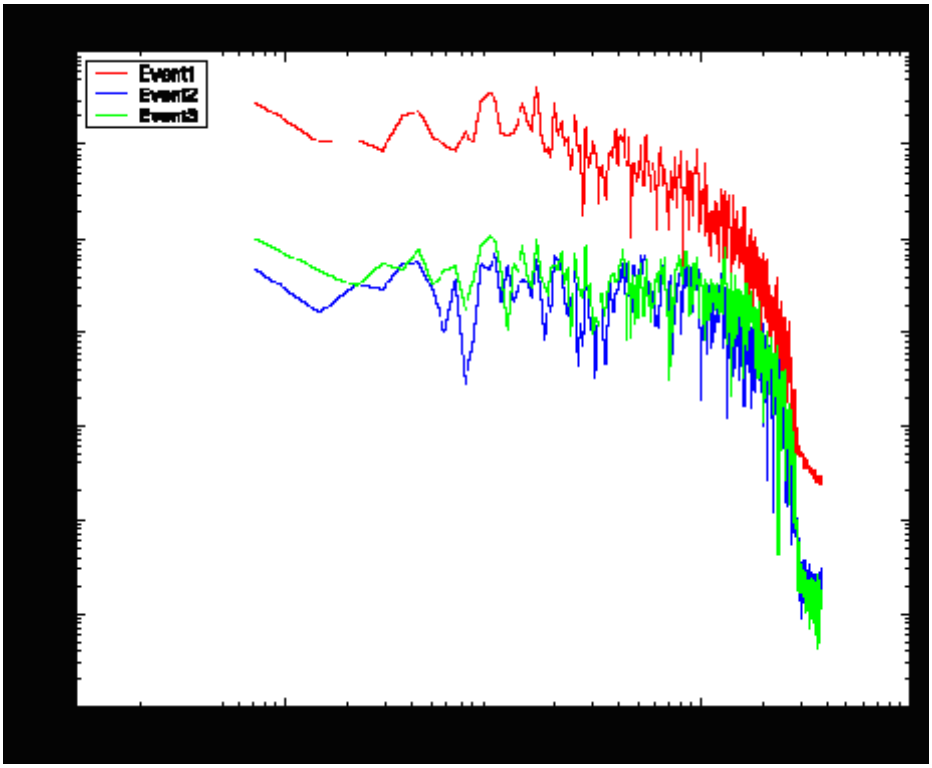

Figure 6: Vertical velocity spectrum from Events 1-3 (Table 1) recorded at AYP.

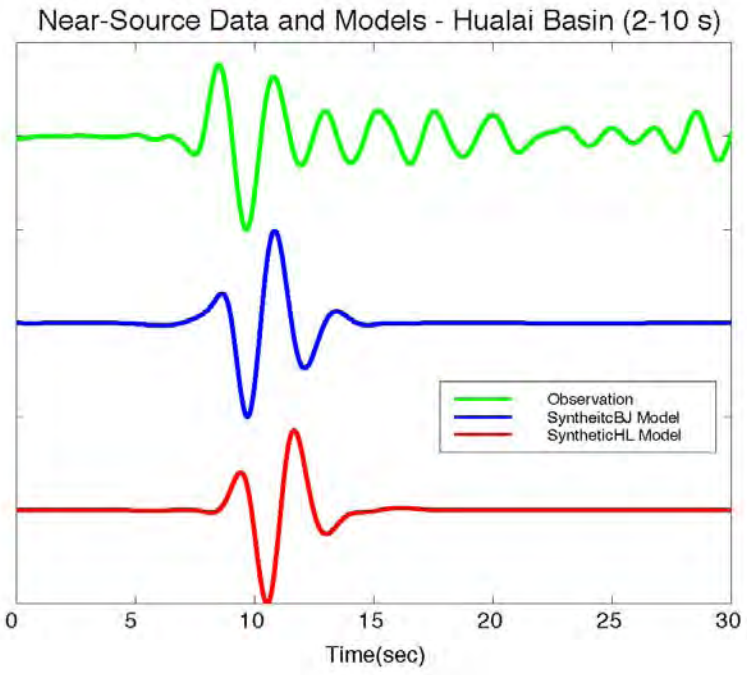

Figure 7: Comparison between long period observations (green) and synthetics developed from the preliminary velocity models for the Hualai Basin illustrated in Figure 4.

Heicheng Area

The second area for our combined near-source and regional broadband deployments is the Heicheng Area (Figure 1). Northeastern China can be divided into two primary tectonic blocks, the North China Block and the South China Block (Gilder *et. al.*, 1999). Some believe that the Tancheng-Lujiang (Tan-Lu) fault system is a boundary between these blocks extending from South China to the Bay of Okhotsk.

The 1975 Heicheng Earthquake, the first predicted in China, occurred in this region and motivates an interest to understand seismicity for hazard reduction. This earthquake was preceded by nearly 500 foreshocks for several days prior to the main event (Jones *et. al.*, 1982). The localized nature of these events and similarity in fault mechanisms (Xu *et al.*, 1982) led to the prediction. Despite the general NNE trend of faults and seismicity in the region (Figure 8), which is consistent with tectonic models for the region, the Haicheng earthquake occurred on a fault trend $N67^0W$ (Jones *et al.*, 1982).

Our plan is to focus upon the Heicheng instrumentation deployment in the second year of our cooperative work. As a result, there has been little preliminary work in developing propagation path effects for this region.

Planned Instrumentation

In both areas we will deploy Global Positioning System (GPS) locked Quanterra Q330 instruments with one STS-2 seismometer in an appropriate vault at each site. Several of the broadband sites are co-located with existing short-period stations and therefore will be able to make use of existing vaults and facilities. New stations will be deployed in temporary shallow hard rock vaults. The Q330 data acquisition system is a three-channel (as configured here) 24-bit recorder with auxiliary lower resolution channels for mass position and state-of-health variables such as temperature. For this installation, systems will be configured as stand-alone data loggers. All systems (even those close to commercial power) will use solar power and recorded data will be stored locally. Data will be recovered and quality controlled by in-country personnel on a rolling schedule with data recovery occurring at least once every few months.

Because the Q330 is a new system and has been rarely fielded, the first 10 stations will be installed in the Huailai Basin near Beijing where they can be easily monitored and maintained. Once experience demonstrates their reliability. The second deployment will be done in the Heicheng area.

CONCLUSIONS AND RECOMMENDATIONS

A combined near-source and regional study of seismicity in the Huailai Basin and Heicheng Area has been described. This work is intended to quantify seismic sources in these regions with the near-source instrumentation providing data for separating source and propagation path effects at regional distances.

This cooperative project with the Institute of Geophysics, China Seismological Bureau and Southern Methodist University includes the planned deployment of broadband stations in both regions. The year 2003 will focus upon the deployment and operation of these stations in the Huailai Basin followed by a deployment to the Heicheng Area in 2004.

The sites for both the near-source and regional deployment in and around the Huailai Basin have been identified. Plans call for the instrument deployment in the fall of 2002.

Preliminary work has been done in developing velocity models for the Huailai Basin. The model is consistent with observed near-source travel times in the regions. These starting models also show promise in modeling long-period (2- to 10-s) near-source waveforms.

ACKNOWLEDGEMENTS

This project is done in cooperation with the Institute of Geophysics, China Seismological Bureau. Particular cooperation of Prof. Chen, Dr. Yang, Ms. You and Mr. Bai is noted.

REFERENCES

Gilder, S.A., P.H. Leloup, V. Courtillot, Y. Chen, R.S. Coe, X. Zhao, W. Xiao, N. Halim, J.-P. Cogne, R. Zhu, 1999. Tectonic evolution of the Tancheng-Lujiang (Tan-Lu) fault vis middle Triassic to early Cenozoic paleomagnetic data, *J. Geophys. Res.*, **104,** 15365-15390.

Jones, L.M., B. Wang, S. Xu, and T.J. Fitch, 1982. The foreshock sequence of the February 4, 1975, Heicheng Earthquake (M=7.3), *J. Geophys. Res.*, **87**, 4575-4584.

Xu, S., L. Yang, M. Jones, X. Ma, and P. Shen, 1982. The foreshock sequence of Haicheng earthquake and earthquake swarm – The use of foreshock sequences in earthquake prediction, *Tectonophysics*, **85**, 91-105.

Xu, X.-T., Y.-T. Chen, P.-D. Wang, 1999. Rupture process of the M_L = 4.1 earthquake in Huailai Basin on July 20, 1995, *Acta Seis. Sinica*, **12**, 619-631.

Yongkang, R.., F. Zhongjing, L. Zhiyi, W. Jingbo, L. Rucheng, 1995. Paleoseismicity and Segmentation Along the Active Fault at the Northern Boundary of Huailai-Zhuolu Basin, Hebei Province, *Earthquake Research in China*, **9**, *November 1, 1995.*

Yongkang, R., F. Zhougjing, D. Ruitao, L. Zhiyi, W. Jingbo, Y. Zhe, J. Fengju, and L. Jianping, 1996. Model for Paleoearthquake Recurrence Along Baying Segment of the North Margin Fault of Fanshan Basin in Hebei Province, *Earthquake Research in China*, **10**, *November 1, 1996.*

CALIBRATION OF REGIONAL SEISMIC STATIONS IN THE MIDDLE EAST WITH SHOTS IN TURKEY

M. Nafi Toksöz,[1] Sadi Kuleli,[1] Craig A. Schultz,[2] David B. Harris,[2]
Cemil Gürbüz,[3] Dogan Kalafat,[3] and Ahmet M. Isikara[3]

Massachusetts Institute of Technology;[1] Lawrence Livermore National Laboratory;[2] Bogazici University[3]

Sponsored by National Nuclear Security Administration
Office of Nonproliferation Research and Engineering
Office of Defense Nuclear Nonproliferation

Contract No. DE-FC03-01SF22398[1, 3] and W-7405-ENG-48[2]

ABSTRACT

Two sets of calibration shots are planned in Turkey in 2002 and 2003 for the calibration of regional seismic stations and to improve knowledge of earth models in the region. The shots will be at Keskin in central Turkey, and at Lake Van in eastern Turkey. Keskin is where the short-period array of the Belbasi Station is located. Belbasi Station comprises a long-period array located in Ankara, and the aforementioned short-period array located in Keskin. The Keskin short-period array is designated as an International Monitoring System (IMS) station (PS43). The primary objectives of the experiments are: (1) calibrate the regional travel times and propagation characteristics of seismic waves across the Middle East and Eastern Mediterranean region; (2) calibrate local and regional models for specific IMS stations in Turkey; (3) conduct a reciprocal experiment to provide dense local and near regional calibration of the Keskin Belbasi IMS array in Turkey; and (4) provide data to enhance IMS detection, location, and discrimination capabilities.

The first calibration shot (two tons of explosives in boreholes) will be conducted near Keskin in October 2002. We expect that the shot will be recorded within a radius of about 500 km. It will provide reciprocal calibration for the nearby Keskin short-period array, Incorporated Research Institutes in Seismology (IRIS) station ANTO, and the long-period Belbasi array.

In this paper we present detailed three dimensional (3-D) crustal models of the region, calculated travel times, and synthetic seismograms. Well located (GT-5) local and regional earthquakes around the Keskin array are identified and areas of anticipated seismic activity will be instrumented. The information will guide the deployment of stations for the recording of the Keskin shot, and expedite the analysis of the data.

OBJECTIVES

The primary objectives of the project are to: (1) calibrate the regional travel times and propagation characteristics of seismic waves across the Middle East and Eastern Mediterranean region; (2) calibrate local and regional models for specific IMS stations in Turkey; (3) conduct a reciprocity experiment to provide dense local and near regional calibration of the Keskin Belbasi IMS array in Turkey; and (4) provide data to enhance IMS detection, location, and discrimination capabilities.

A two-ton shot will be fired in boreholes near the Keskin array (an IMS station) in central Anatolia (Asian part of Turkey) in November 2002, for calibration of stations within 300-500 km. This shot will provide a reciprocal calibration for the Keskin array, as well as for nearby IRIS station ANTO, and the long-period array operated jointly by AFTAC and Turkey. The long-period array is located around Ankara. Figures 1a and 1b show the general tectonic setting and the arrays, respectively. Turkish national network stations are also shown in Figure 1b.

RESEARCH ACCOMPLISHED

The primary activity during this period has been the planning of the experiment site selection for the shot, deployment plan for portable instruments, and gathering of data for generating local and regional models for seismic wave propagation. Using these models, 3-D travel-time calculations are carried out, for local (up to 500 km) and regional (up to 2,000 km) distances. Synthetic seismograms are calculated for the Keskin shot.

Three-Dimensional Velocity Model

Turkey and surrounding areas form a tectonically complicated region. Crustal and upper mantle structures in the region are influenced by the thermal and mechanical processes related to motions between the several plates in the region. The Keskin array is located in the middle of the Anatolian Plate surrounded by major plate boundaries as well as significant active intra-plate deformation as shown in Figure 1a.

Crustal structure and seismic attenuation vary greatly in the region (Ginzburg *et al*., 1981; Sholpo, 1993; Hofstetter *et al*., 1991; Laske *et al*., 2001; Hearn and Ni, 1994; Priestly, 1997; Mangino and Priestly, 1998; Shapiro and Ritzwoller, 2001.) Crustal thickness averages about 35-40 km in the Anatolian plateau, 40-50 km in the east toward the Iranian Plateau (Nowroozi, 1971; Bird *et al*., 1975). Hearn and Ni (1994) used a tomographic technique to obtain Pn velocities for Anatolia and surrounding regions. They used data from the International Seismological Centre (ISC) catalog and found that Pn velocity is approximately 7.8 km/s in central Anatolia. Sandvol *et al.* (1998) used receiver function inversion to determine site-specific crustal velocity and thickness models. They found crustal thickness values of 37 km in central Anatolia (ANTO), 43 km in northeastern Caucasus (KIV), and 64 km in central Caucasus (GNI).

Gurbuz and Evans (1991) determined basement depths to be between 6 and 10 km with a velocity of 6.15 km/s in the Salt Lake (Tuz Golu) basin, located approximately 150 km SSE of Ankara. Mindevalli and Mitchell (1989) measured fundamental mode Rayleigh and Love wave group velocities in the 8- to 50-s period range for the ANTO seismic station. They found the shear wave (Sn) velocity to be 4.2 km/s and an approximate crustal thickness of 40 km. Necioglu *et al.* (1981) analyzed travel times from 43 earthquakes occurring in western Turkey recorded by a number of regional stations and found the Pn velocity to be 7.80 in the vicinity of Ankara. Canitez and Toksoz (1980), using travel-time residuals of teleseismically recorded P wave velocities, concluded that P wave velocities in the uppermost mantle are 7.9 km/s in central and eastern Turkey. Turkelli *et al*. (1996) applied a two-station method for stations in east Anatolia and found that Pg and Pn velocities vary between 5.5-6.6 km/s and 7.6-7.9 km/s, respectively. Similarly, they found Sg and Sn wave speeds varying between 3.3-3.9 km/s and 4.3-4.8 km/s, respectively.

Using receiver function waveform inversion and dispersion of surface waves in western Turkey, Saunders et al. (1998) found ~37.5 km crustal thickness beneath Ankara. Shear velocities were between about 3.3 km/s and 3/5 km/s in the lower crust and 4.5 km in the uppermost mantle. Similarly, Sandvol et al. (1998) used a grid-search

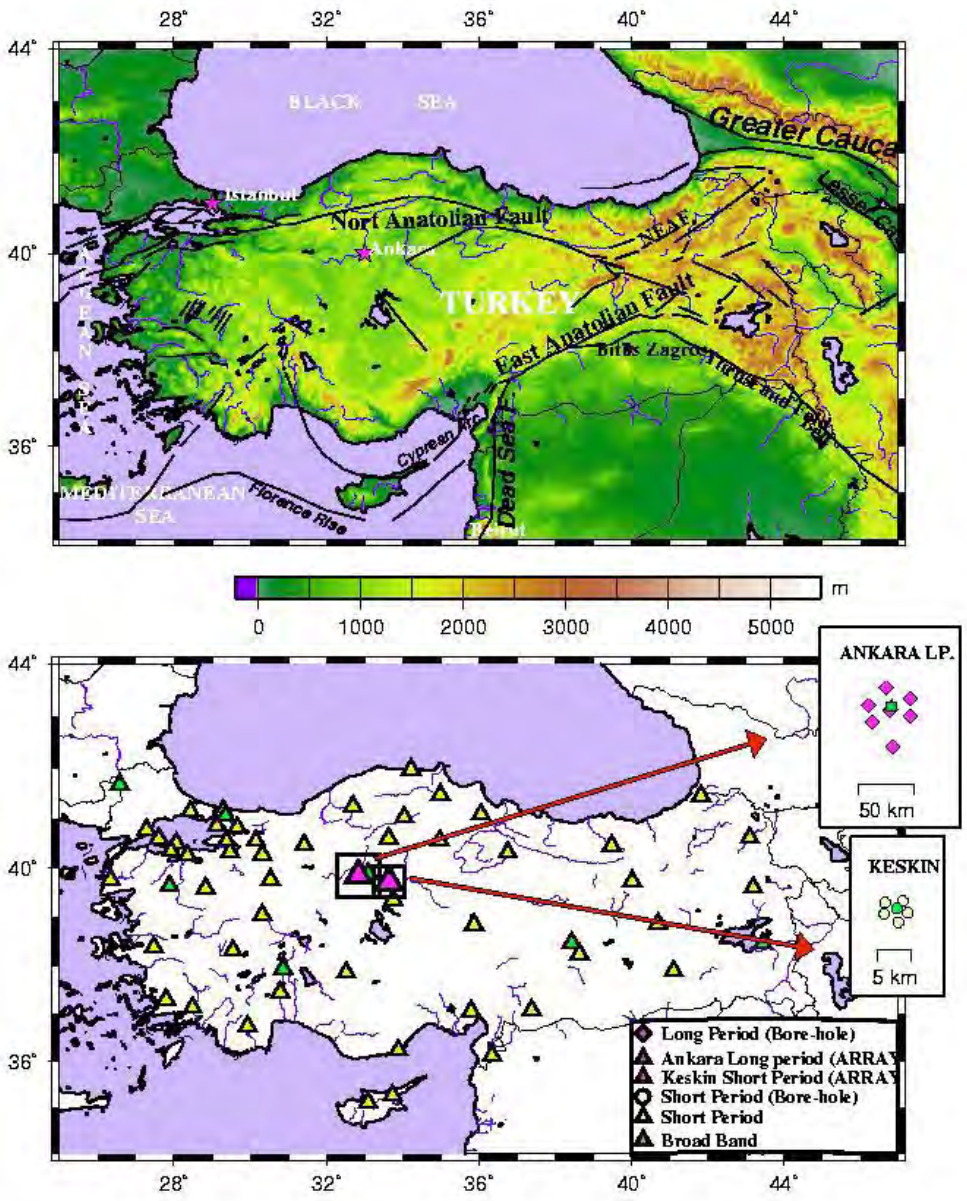

Figure 1. (a) Morphology (GTOPO30) and active tectonics features of the Turkish plate and surroundings. (b) Permanent seismic station network of Kandilli Observatory and Earthquake Research Center (KOERI). Enlarged inserts show the Belbasi long-period array (upper box) and the Keskin short-period seismic array (lower box) (Kuleli *et al*., 2001).

approach to receiver function waveform modeling and found a crustal thickness of 37.0 and an average crustal shear velocity of 3.6 km/s. South of the Marmara Sea, Gurbuz *et al*. (1980) obtained a crustal thickness of 28-29 km and a Pn velocity of 8.1 km/s from a quarry blast experiment. A complementary study in the greater Marmara region by Kalafat *et al.* (1987) using the Pn phase reading at stations operated by KOERI in southwest Turkey indicated that the seismic Pn velocity is about 7.8 km/s. Crampin and Ucer (1975) investigated seismic velocities beneath the

Marmara Sea by examining four earthquake recordings at 35 seismic stations. In this study the crustal velocities were 5.8-6.0 km/s.

Saunders *et al*. (1998) found a normal upper mantle velocity, approximately 8.1 km/s, at Kula in western Turkey. Taymaz (1996) used S-P wave travel-time residuals, which confirmed the lateral velocity variation in the region, and found higher velocity beneath the Crete and lower velocity beneath the Aegean Sea than the J-B model. Kuleli *et al.* (1997) and Spakman (1991) found high (8.1 km/s) uppermost mantle velocities beneath the northern Aegean coast where Hearn and Ni (1994) found a lower velocity of about 7.9 km/s. Beneath the Marmara region, the Hearn and Ni values are about 8 km/s. Other studies extended the coverage into Greece (Allesandrini *et al*., 1997; Papazachos *et al*., 1995; Papazachos and Nolet, 1997), reporting that the velocity distribution in the shallow layers is strongly influenced by the variation of the depth of the Moho discontinuities.

Model-Based Station-Specific Source Correction for the Keskin Array

A 3-D regional velocity model was generated for Δ=20° distance around the Keskin array using the global models of Laske *et al.* (2001), Shapiro and Ritzwoller (2001) and others cited in the previous section. The model-based travel times were calculated using a 3-D ray tracer. Travel-time corrections relative to IASPEI91 were calculated. The region around the Keskin array for which travel times are calculated, Pn velocities in the region, and travel-time corrections relative to IASPEI are shown in Figure 2.

These calculations are repeated for a smaller region (about 500-km radius) around Keskin using a more detailed crustal model. The model and travel-time corrections are shown in Figures 3a and 3b.

Seismic Attenuation

There have been numerous studies of the attenuation of Sn and Lg waves in the region (Nuttli, 1980; Kadinsky-Cade *et al*., 1981; Seber and Mitchell, 1992; Rogers *et al*., 1997; Gok *et al.*, 2000; Sandvol *et al*., 2001). These studies show high attenuation in eastern and some parts of central Turkey. Plans for deployment of portable stations take into account the attenuation properties. Synthetic seismograms were calculated using an averaged 1-D velocity model with the discrete wave number code and different attenuation values. A typical set of seismograms is shown in Figure 3c. We expect to obtain both travel times and attenuation values from the Keskin shot. A number of well-located earthquakes that are within a radius of 500 km from Keskin that qualify as GT-5 have been selected. Figure 4 shows a subset of such events and distribution of local network stations used for their locations. Each event location is validated by observed surface faulting or isoseismals. The epicenters will be instrumented for reciprocity experiments.

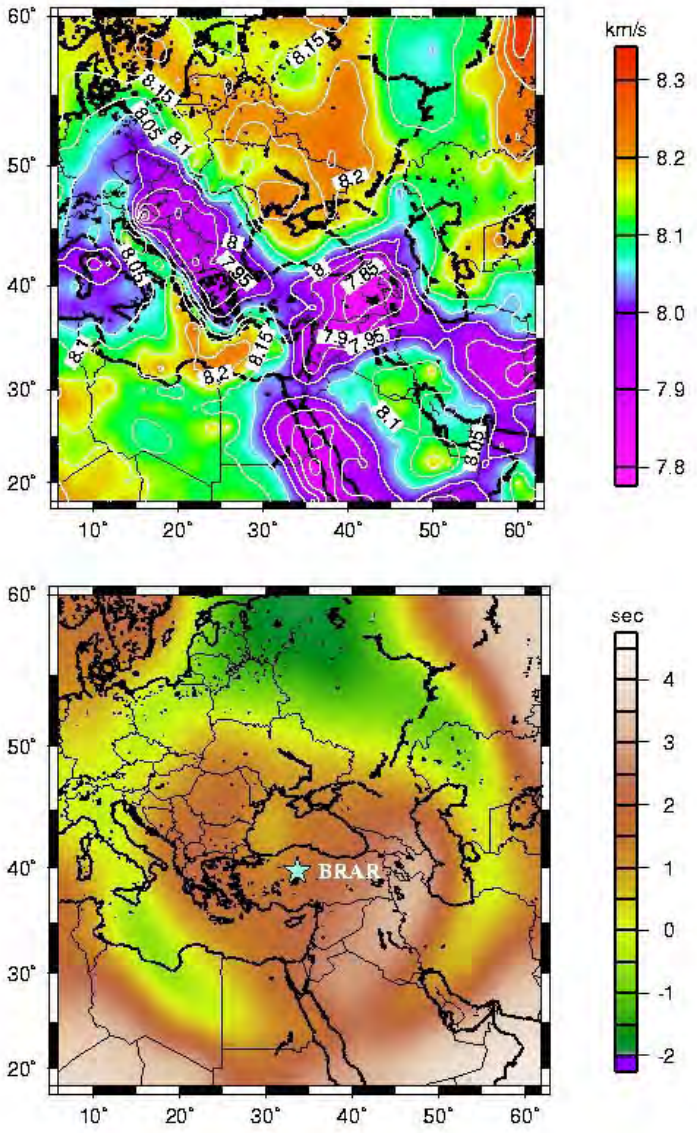

Figure 2. Model-based source specific station corrections for the IMS station BRAR (e.g., Keskin array). The crust upper mantle regional velocity model is from Laske et al. (2001) and Shapiro and Ritzwoller (2001) and others cited in the text. Three-dimensional ray tracing is used to calculate travel times. (a) Pn velocities of the regional model. (b) Travel-time corrections relative to IASPEI-91.

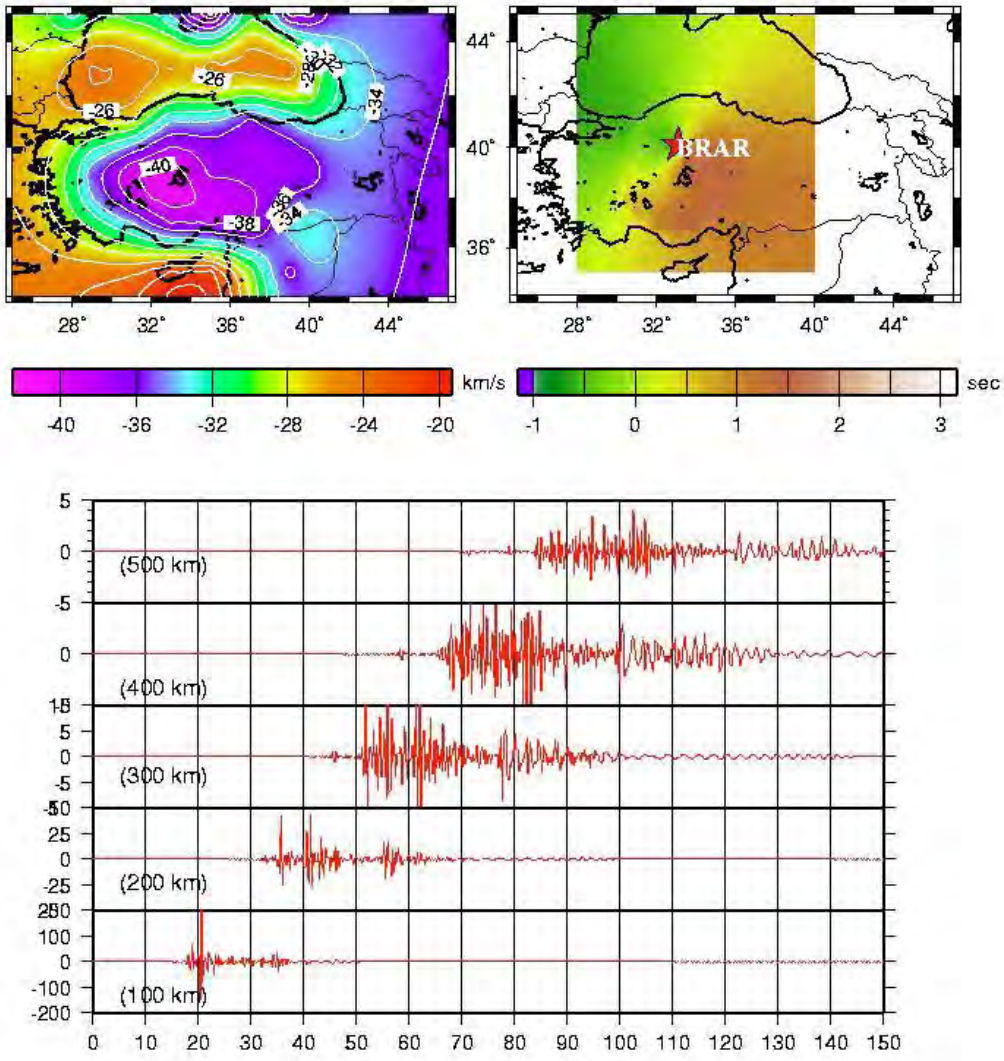

Figure 3. Local crustal model and travel-time corrections for BRAR. (a) Depth to Moho. (b) Travel-time residuals relative to IASPEI91 generated using a 0.5° x 0.5° grid local model. (c) Synthetic seismograms calculated for an explosive source at 100-m depth. An averaged 1-D velocity model (based on Figure 3a) is used for calculations.

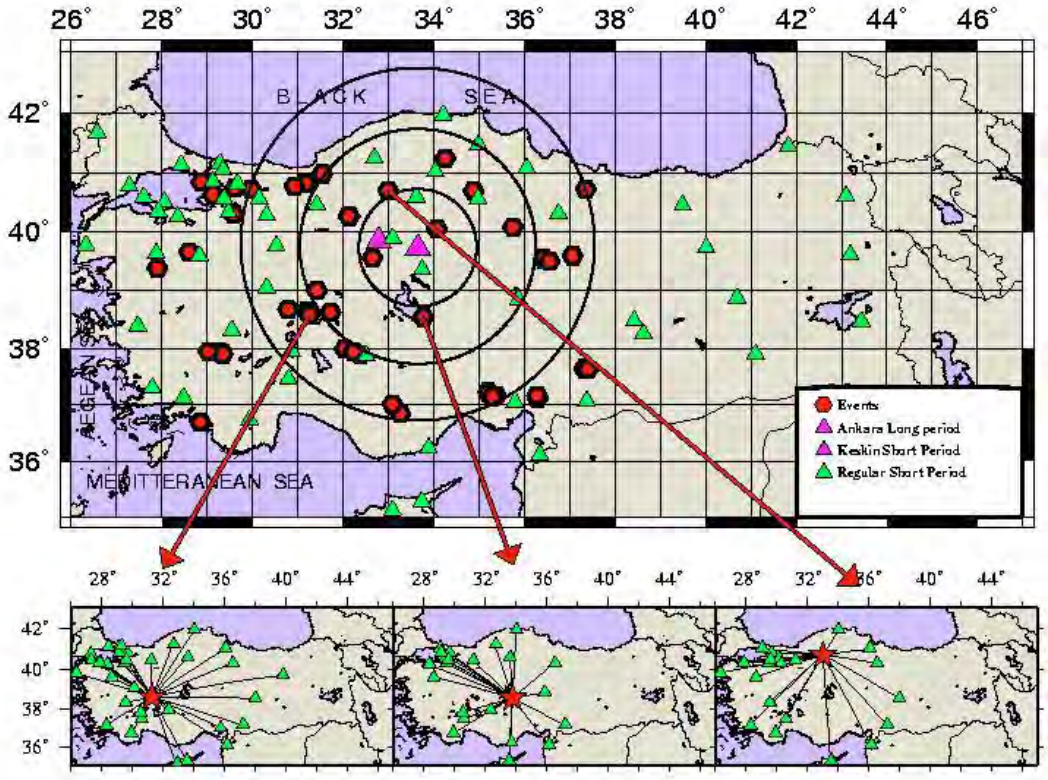

Figure 4. Selected GT events for reciprocity experiments. Events are selected using the KOERI database for the period 1985–2002. Circles indicate 1, 2, 3 degree radius from the Keskin station.

CONCLUSIONS AND RECOMMENDATIONS

Preliminary studies have been carried out to guide the distribution of portable network instruments around the Keskin shot that will take place in November 2002. These studies will expedite the analysis of the data from the shot.

REFERENCES

Allensendrini, B., L. Beranzoli, G. Drakatos, C. Falcone, G. Karantonis, F.M. Mele, and G. Stavrakaki (1997), Back arcs basins and P-wave crustal velocity in the Ionian and Aegean regions, *Geophys. Res. Let.*, **24**, 525-530.

Bird, P., M.N. Toksoz, and N. Sleep (1975), Thermal and mechanical models of continent-continent convergence zones, *J. Geophys. Res.*, **80**, 4405-4416.

Bouchon, M. (1981), A simple method to calculate Green's functions for elastic layered media, *Bull. Seismol. Soc. Am.*, **71**, 959-971.

Canitez, N. and M.N. Toksoz (1980), Crustal structure beneath Turkey, *EOS Trans. Am. Geophys.*, **61**, 290.

Crampin, S. and B. Ucer (1975), The seismicity of the Marmara Sea Region of Turkey, *Geophys. J. R. Astron. Soc.*, **40,** 269-288.

Ginzburg, A., J. Makris, K Fuchs, and C Prodehtl (1981), The structure of the crust and upper mantle in the Dead Sea Rift, *Tectonophysics***, 80**, 109-119.

Gok, R., N. Türkelli, E. Sandvol, D. Seber, and M. Barazangi, (2000). Regional wave propagation in Turkey and surrounding regions, *Geophys. Res. Lett.*, **27**, 429-432.

Gurbuz, C. and J.R. Evans, (1991). A seismic refraction study of the western Tuz Golu basin, central Turkey, *Geophys. J. Int.*, **106**, 239-251.

Gurbuz, C., B. Ucer, and H. Ozdemir (1980), Preview results about Query blasts around Adapazan region, Deprem Arasirm.

Hearn, T.M. and J. F. Ni, (1994). Pn velocities beneath continental collision zones: the Turkish-Iranian plateau, *Geophys. J. Int.*, **117**, 273-283.

Hofstetter, A. L. Feldman, and Y. Rotstein, (1991). Crustal Structure of Israel: Constrains from teleseismic and gravity data, *Geophys. J. Int.*, **104,** 371-379.

Kadinsky-Cade, K., M. Barazangi, J. Oliver, and B. Isacks (1981), Lateral Variations of High-Frequency Seismic Wave Propagation At regional Distances Across The Turkish and Iranian Plateaus, *J. Geophysical Research*, **86**, 9377-9396.

Kalafat, D., C.. Gurbuz, and B. Ucer (1987), Bati Turkiyede kabuki ve Ust Manto Yapisinin arastirilmasi., *Deprem Arastirma Bulteni*, **59**, 43-64. (Turkish).

Kuleli, H.S., C. Gürbüz. and M.N. Toksöz, (1997), Seismic velocity distribution in the Aegean region, In: *Proceedings of International Earth Sciences Colloquium on the Aegean region*, edited by O. Piskin, M. Ergun, M.Y. Savasci, G. Tarcan, **1,** 241-254, Izmir, Turkey.

Kuleli, S., E. Zor, N. Turkelli, E. Sandvol, D. Seber, and M. Barazangi (2001), The IMS Belbasi Array (BRAR) in Central Turkey. *Seismological Research Letters,* **72.**

Laske, G., G. Masters and Reif (2001), CRUST 2.0: A new global crustal model at 2X2 degrees, http://mahi.ucsd.edu/Gabi/rem.html.

Mangino, S. and K. Priestley (1998), Crustal structure in the Caspian Sea region, *Geophys. J. Int.,* **133**, 640-648.

Mindevalli, O.Y. and B.J. Mitchell (1989), Crustal structure and possible anisotropy in Turkey from seismic surface-wave dispersion, *Geophys. J. Int.*, **98**, 93-106.

Nacioglu, A., B. Maddison, and N. Turkelli (1981), A study of crustal and upper mantle structure of north-western Turkey, *Geophys. Res. Letts*., **8**, 33-35.

Nowroozi, A. (1971), Seismotectonics of the Persian Plateau,eastern Turkey, Caucasus, and Hindu-Kush regions, *Bull. Seismol, Sc. Am.*, **61**, 315-341.

Nuttli, O.W. (1980), The excitation and attenuation of seismic crustal phases in Iran, *Bull. Seismo. Soc. Am.,* **70,** 469-485.

Papazachos, C.B., P.M. Hatzidimitriou, D.G. Panagiotopoulos, and G.N. Tsokas (1995), Tomogrpahy of the crust and upper mantle in southeast Europe, *J. Geophys. Res.,* **100**, 12405-12422.

Papazachos, C. and G. Nolet (1991), P and S deep velocity structure of the Hellenic area obtained by robust-nonlinear inversion of traveltimes, *J. Geophys. Res.,* **102**, 8349-8367.

Priestly, K. (1997), An integrated study of lithospheric structure, regional seismic wave propogation, and seismic discrimination, Final Report, DOE, PL-TR-97-2161,199 pp.

Rodgers, A., J. Ni, T. Hearn (1997).,Propagation characteristics of short period Sn and Lg in the Middle East, *Bull. Seism. Soc. Am.,* **87**, 396-413.

Sandvol, E., D. Seber, A. Calvet and M. Barazangi, (1998), Grid search modeling of receiver functions: Implications for crustal structure in the Middle East and North Africa, *J. Geophys. Res.,* **103** *(B11) 26*, 899-26,917.

Sandvol, E., Al-Damegh, K. Calvert, D. Seber, M. Barazangi, R. Mohamad, R. Gok, N. Türkelli, C. Gürbüz, (2000), Tomographic imaging of Lg and Sn propagation in the Middle East, *Pure and Applied Geophysics*.

Seber, D. and B.J. Mitchell (1992), Attenuation of surface waves across the Arabian Peninsula, *Tectonophysics*, **204**, 137-150.

Shapiro, N.M. and M.H. Ritzwoller (2001), Monte-Carlo inversion of broadband surface wave dispersion for global shear velocity model of the crust and upper mantle, submitted to *Geophys. J. Int.*, 142.

Sholpo, V.N., (1993), Structure of inversion anticlinoria in the core of the Greater Caucasus: An advanced hypothesis, *Geotectonics*, **27,** 245-251.

Spakman, W. (1991), Delay-time tomography of the upper mantle below Europe, the Mediterranean and Asia Minor, *Geophys. J. Int.,* **107**, 309-332.

Taymaz, T., J.A. Jackson and D. MacKenzie (1991), Active tectonics of the north and central Aegean Sea, *Geophys. J. Int.,* **106,** 433-490.

Turkelli, N., G. Harasan, H.D. Kuleli, and D. Reiter (1996), Preliminary results of velocity distribution study in eastern Turkey, *EOS, Trans. Am. Geophys.*, **77**, F477.

QUANTIFYING SOURCE EXCITATION AND PATH EFFECTS FOR HIGH-FREQUENCY REGIONAL WAVES

Ru-Shan Wu, Xiao-Bi Xie, Xianyun Wu and Thorne Lay

University of California, Santa Cruz

Sponsored by Defense Threat Reduction Agency

Contract No. DTRA01-01-C-0076

ABSTRACT

The current year study covers two main research directions: Lg wave excitation by explosion sources and Lg wave attenuation and blockage.

Investigation of the excitation of Lg waves by explosions is essential for both understanding Lg wave energy attenuation and for discriminating explosions and earthquakes. Two-dimensional finite-difference calculation and the slowness analysis technique are used to investigate Rg-Lg coupling as an Lg wave excitation mechanism. The method allows us to investigate Lg wave excitation and propagation not only in the space domain, but also in wave number domain. The advantage of the slowness analysis is that it can be applied at close range, before Lg is formed at large distances. This feature is especially useful for the finite-difference approach. Shallow heterogeneous layers are introduced to generate the coupling between the Rg and Lg waves. Heterogeneity models with different scales, different root-mean-square (rms) values, located either near the source or along the entire path, are tested. Their contributions to Lg wave formation are analyzed in the space, slowness and frequency domains.

The half-space screen method developed in the previous project can be used to model Lg wave propagation in complex wave guides including irregular topography, large-scale geological structures and small-scale random heterogeneities. Compared with finite-difference and boundary-element methods, the screen method is very efficient in both computation speed and memory requirements. It is especially useful for Lg wave simulations for high frequencies and regional distances. In this study, anelasticity has been introduced into the screen propagators to handle the effects of intrinsic attenuation for regional Lg. Both P-wave quality factor Q_P and S-wave quality factor Q_S are incorporated into SH wave and P-SV wave calculations. Different attenuation mechanisms including intrinsic attenuation, leakage due to rough topography and Moho discontinuity, and scattering due to small-scale random heterogeneities are simulated and investigated separately. Then, their combined effects on Lg wave propagation in near-realistic crustal wave guides are evaluated and the corresponding apparent Lg quality factors Q_{LG} are calculated.

OBJECTIVE

Introduction

The regional seismic phase Lg is one of the most useful phases for event discrimination and magnitude estimation associated with nuclear explosion and treaty monitoring. The characteristics of Lg are strongly affected by the excitation conditions in the source region and by path effects controlled by waveguide structures of different scales. To obtain a comprehensive understanding of Lg signals, it is crucial to do research on both the excitation and propagation of Lg for realistic crustal models. The Regional Wave Synthetic Seismogram Program in the IGPP branch at the University of California, Santa Cruz, has done extensive work on the excitation and propagation of regional phases, and has developed theory and methods for the investigation of these problems.

A new slowness analysis method allows us to investigate Lg wave excitation in the slowness domain (Xie and Lay, 1994). The main advantage of this method is that it can be applied at close range, before Lg is formed at large distances. This allows us to include fine structure into the model and to study their effects on the Pg to Lg and Rg to Lg coupling. A highly efficient Lg propagation algorithm based on the GSP (Generalized Screen Propagators) method has been developed (Wu et al., 2000) which can propagate high-frequency waves (up to 25 Hz) to long distance (> 1000 km) using a workstation. Wu *et al* (1999) and Wu and Wu (2001) extended the screen method to handle topographic effects by performing conformal or non-conformal transforms. Wu *et al* (2000) extended P-SV screen propagators for Lg simulation by incorporating plane wave reflection coefficients into the screen method. In this paper we report new progress in the following aspects: Rg to Lg scattering as an excitation mechanism for explosion Lg-wave, and simulation of Lg wave attenuation and blockage for complicated crustal waveguide models.

RESEARCH ACCOMPLISHED

Lg-Wave Excitation Through Near Source Rg-Lg Coupling

Lg predominantly comprises shear wave energy trapped in the crust. Explosion sources are expected to be less efficient for excitation of Lg phases than earthquakes to the extent that the source can be approximated as isotropic. Shallow explosions generate relatively large Rg phases compared to deeper earthquakes, and Rg is readily disrupted by crustal heterogeneity. Rg energy may thus scatter into trapped crustal S-waves near the source region and contribute to low-frequency Lg wave (Gupta et al., 1991, 1992). In this study, finite-difference simulations are conducted to generate synthetic seismograms at near regional distance. Random velocity patches are added to the layered crustal model to provide coupling between the Rg and Lg waves. Slowness analysis (Xie and Lay, 1994) is used to investigate the coupling between Rg and Lg, as well as between Pg and Lg, as the excitation mechanisms for explosion generated Lg.

We use a layered velocity structure that resembles East Kazakh crust as the background model. This is a typical high velocity crust with its upper crust P-wave velocity larger than the upper mantle S-wave velocity. For such a velocity structure, very little energy generated from an explosion source can be trapped in the waveguide to form the Lg-wave. To investigate the near source Rg to Lg coupling as the Lg excitation candidate, we add some small random velocity patches near the source region. These random patches are 10 km wide, 2.5 km thick, located at epicentral distance 5-15 km and at different depths. The rms velocity fluctuation for these patches is 20 % with a 1 km correlation length for both vertical and horizontal directions. Figure 1 shows the near source velocity structure with several random velocity patches for different numerical experiments.

The explosion source is located at a depth of 500 m. A Gaussian derivative source time function is used for calculating the synthetic seismograms. The effective frequency band is roughly 0 to 6 Hz. Synthetic seismograms are collected from two receiver arrays for different investigations. The first is a 50x40 array with 0.5 km spacing located at an epicentral distance of 50 km. The second is a 50x40 array with 1 km spacing located at an epicentral distance of 150 km. Synthetic seismograms are generated using a 2D elastic finite-difference code (Xie and Lay, 1994).

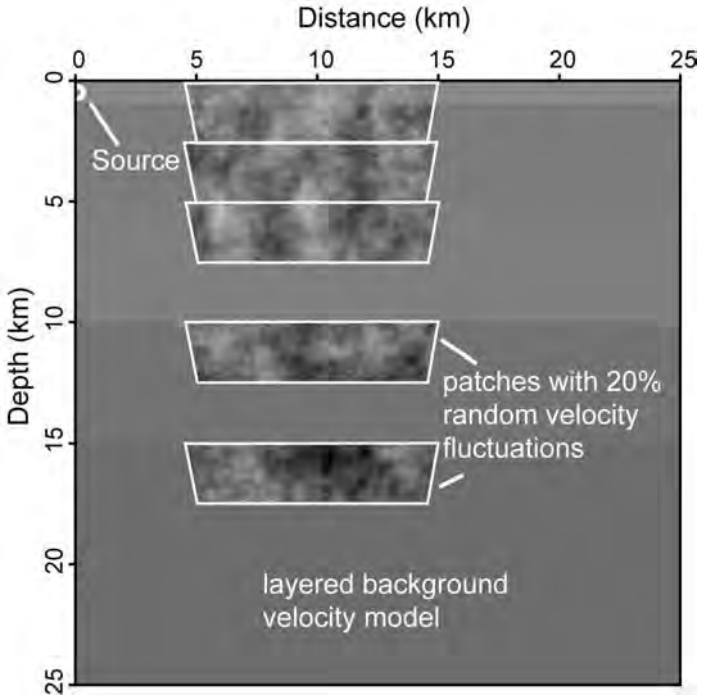

Figure 1. Near source velocity model used for finite-difference simulation. The background velocity is a typical crustal model for East Kazakh. Patches with 20% rms velocity fluctuations are added to the background velocity to generate Pg to Lg scattering and Rg to Lg coupling. These random patches are for different simulations although they are shown here simultaneously.

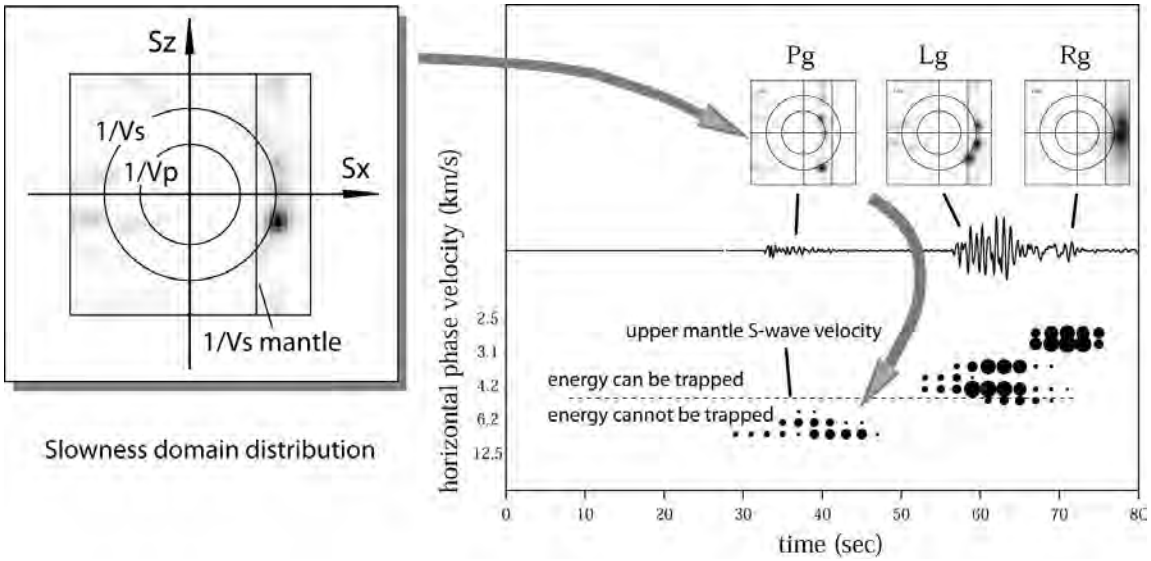

Figure 2. Sketch showing the slowness analysis process.

Synthetic seismograms computed at the receiver arrays are used for the slowness analysis. The size of the sub array for slowness analysis is 10x10. The spacing between the receivers is 0.5 km or 1.0 km, depending on the target wavelengths. Figure 2 is a sketch showing the process of slowness analysis. Shown on the left is the distribution of wave energy in the slowness domain. It is obtained by using a stacking technique and reveals the properties of the propagating waves. Shown in the middle of the right panel is the synthetic seismogram from the center receiver. Shown on the top are energy distributions in the slowness domain for Pg, Lg and Rg group velocity windows. In the Pg window, most energy is P-wave energy and P to S converted wave energy. Since the background model is a

layered crust, the P and S-waves have the same horizontal slowness. In the Lg window, most of the energy is S-wave energy and located on the right side of the upper mantle S-wave velocity (marked with a vertical line). In the Rg window, energy propagates near horizontally and its phase velocities slower than the S-wave velocity. In the lower part of the right panel, the solid circles are energy picked from the slowness domain and stacked from the entire cross section. The size of the circle is proportional to the energy. The vertical axis is apparent horizontal velocity, or equivalently, the reverse horizontal slowness. The dashed line is the upper mantle S-wave velocity. Seismic energy with slowness above this line can be trapped in the crustal waveguide and forms the Lg-wave at larger distance. The energy located below this line cannot be trapped in the crust and will leak to the upper mantle through multiple reflections. It clearly shows the Pg-wave has the lowest slowness; the Rg-wave has the highest slowness, and the Lg-energy is located above the dashed line.

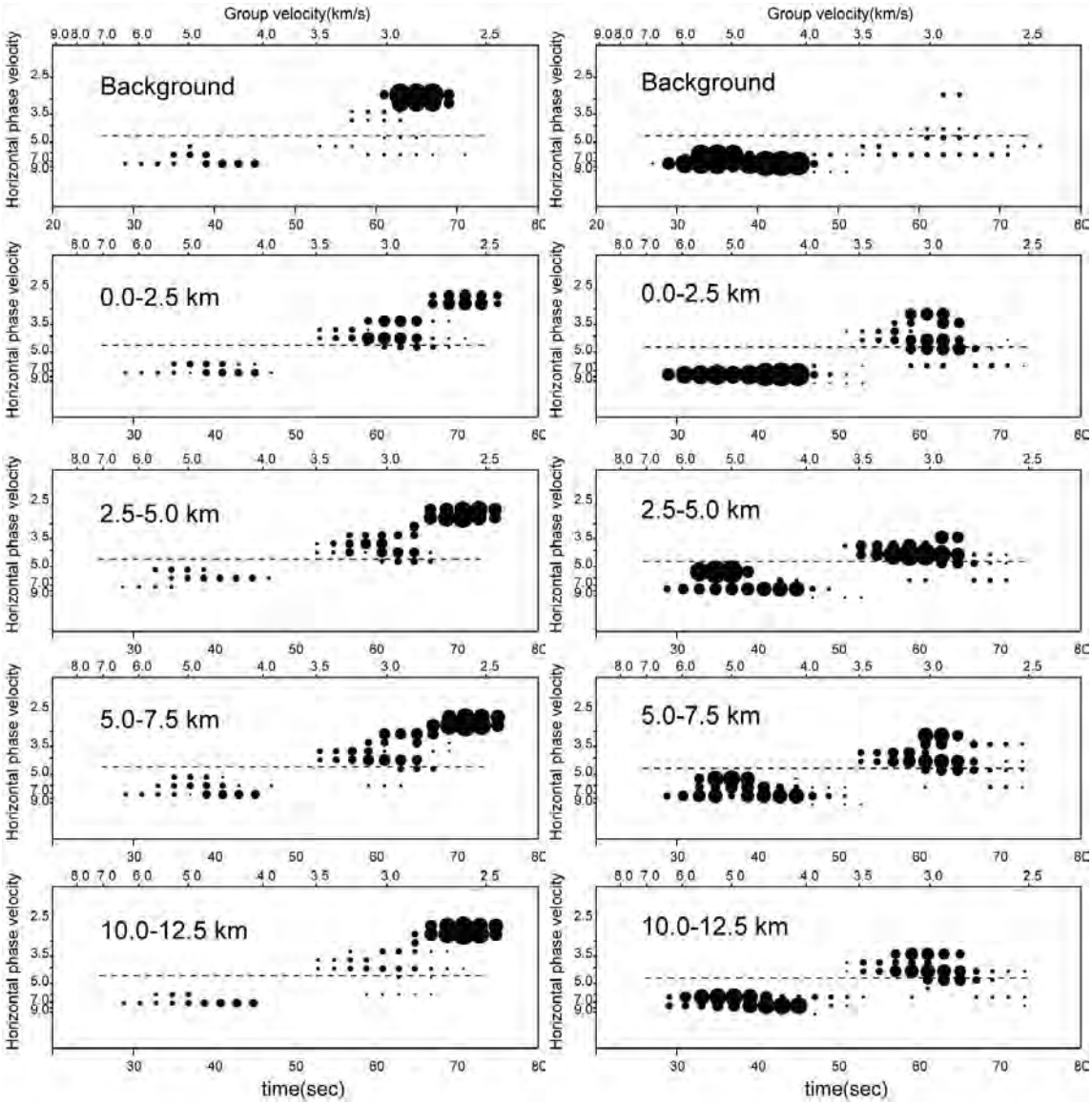

Figure 3. Slowness analysis for velocity models with random patches located at different depths. The left column is for the low-frequency band (0.3-1.5 Hz) and the right column is for the high-frequency band (2.0-5.0 Hz). The top panels are for background velocity model, and the rest of the panels are for random patches at different depths. For details see the text.

To investigate Rg to Lg scattering, a set of random velocity patches are added to the background velocity model. Then, slowness analysis is conducted using synthetic seismograms generated from different models, and for

different frequencies. Figure 3 shows the results for a cross section at 180 km in the crustal waveguide. In each panel, the vertical axis is the horizontal phase velocity. The horizontal axis is time. The group velocity is also marked on the top of each panel. The dashed line marks the upper mantle S-wave velocity. The solid circles are energy picked from the slowness domain and summed up for the entire cross section. The left column is for low frequency (0.3 -1.5 Hz) and the right column is for high-frequency (2.0-5.0 Hz). The top panel is for background velocity model. A dominant feature is that Rg mainly appears as low-frequency signal and Pg mainly appears as high-frequency signal. We first focus on the low-frequency results. From the top panel we can see some Pg-wave and strong fundamental mode Rg-wave. However, such a high velocity crust generate very poor Lg-wave. Within the Lg wave window, only very weak energy can be observed which may be generated by the S*-wave. In the second panel, a random velocity patch located at depth 0.0-2.5 km is added to the background model (refer to Figure 1). Compared with the background model, considerable energy is transferred from the Rg-wave to the Lg-wave through scattering. Panels 3 to 5 are similar to panel 2, except random patches are located at depths 2.5-5.0 km, 5.0-7.5 km and 10.0-12.5 km, respectively. Similar to the case in the second panel, energy is transferred from Rg-wave to Lg-wave. The tendency is: the shallower the random patch the more energy is transferred from Rg to Lg. This also provides additional evidence that the low-frequency Lg energy is coming from the Rg-wave, since the Rg energy is mostly concentrated at shallow depth.

Figure 4 gives the relationship between the depth of the random patch and the low-frequency Rg to Lg scattering. The horizontal axis is the depth of random patches. The upper panel shows the normalized Lg energy, which has the maximum value for the shallowest random patch. With increase of the depth of the random patch, Lg energy decreases toward its background value. The second panel is for normalized Rg energy. It has the lowest energy for the shallowest random patch. With the increase of the depth of the random patch, the Rg energy recovers to its background value. The bottom panel shows the Lg to Rg energy ratio. Its tendency shows the Rg to Lg coupling becoming weaker with increase of the depth of the random patches, which is consistent with the Rg energy distribution in the shallow crust.

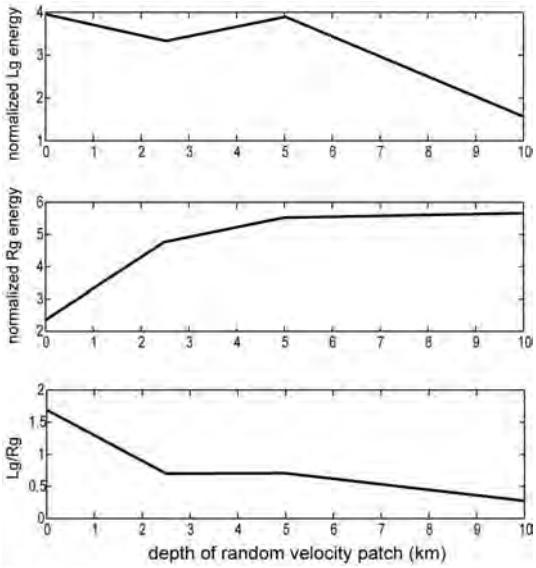

Figure 4. Comparison of normalized energy of Lg and Rg-waves for models with their random velocity patches at different depths.

The right column in Figure 3 is for high-frequency band. From the top panel (background velocity model), we see that the Rg-wave falls outside of this frequency band, and Pg-wave is very strong since it is mainly composed of high-frequency energy. When we add random patches into the background model, considerable high-frequency Lg-wave is generated from the near source scattering of Pg-wave. The strength of the Pg generated Lg-wave does not show strong variation with the depth of the random patches. The numerical simulation and slowness analysis show that near source heterogeneity is responsible for both Rg-Lg coupling and the Pg-Lg scattering. The former contribute to the low-frequency Lg-wave, and the later contribute to the high-frequency energy. The energy partitioning may depends on properties of the source and near source structure.

Simulation of Lg Wave Propagation and Blockage Using Screen Method

Many observed data have shown that regional Lg phase attenuation is related to many factors such as laterally heterogeneous velocity structure, changes in crustal discontinuities, crustal thickness, topographic features, anelastic attenuation, etc. However, the mechanism of Lg wave attenuation has not fully been understood, especially for tectonically active regions that have abnormally low Lg Q. For example in the eastern Tibetan Plateau 1 Hz Lg Q is about 126 (Xie, 2002); and it is about 200 – 267 in various regions of the western United States (Xie and Mitchell, 1990; Xie, 1998), prior numerical simulation results tend to under predict Lg attenuation or blockage. This can be attributed to two reasons. On one hand, realistic crustal models are quite complex so that the parameterized models could be poor approximations. On the other hand, the existing simulation approaches may not have the capacity to handle the effects of the various factors mentioned above.

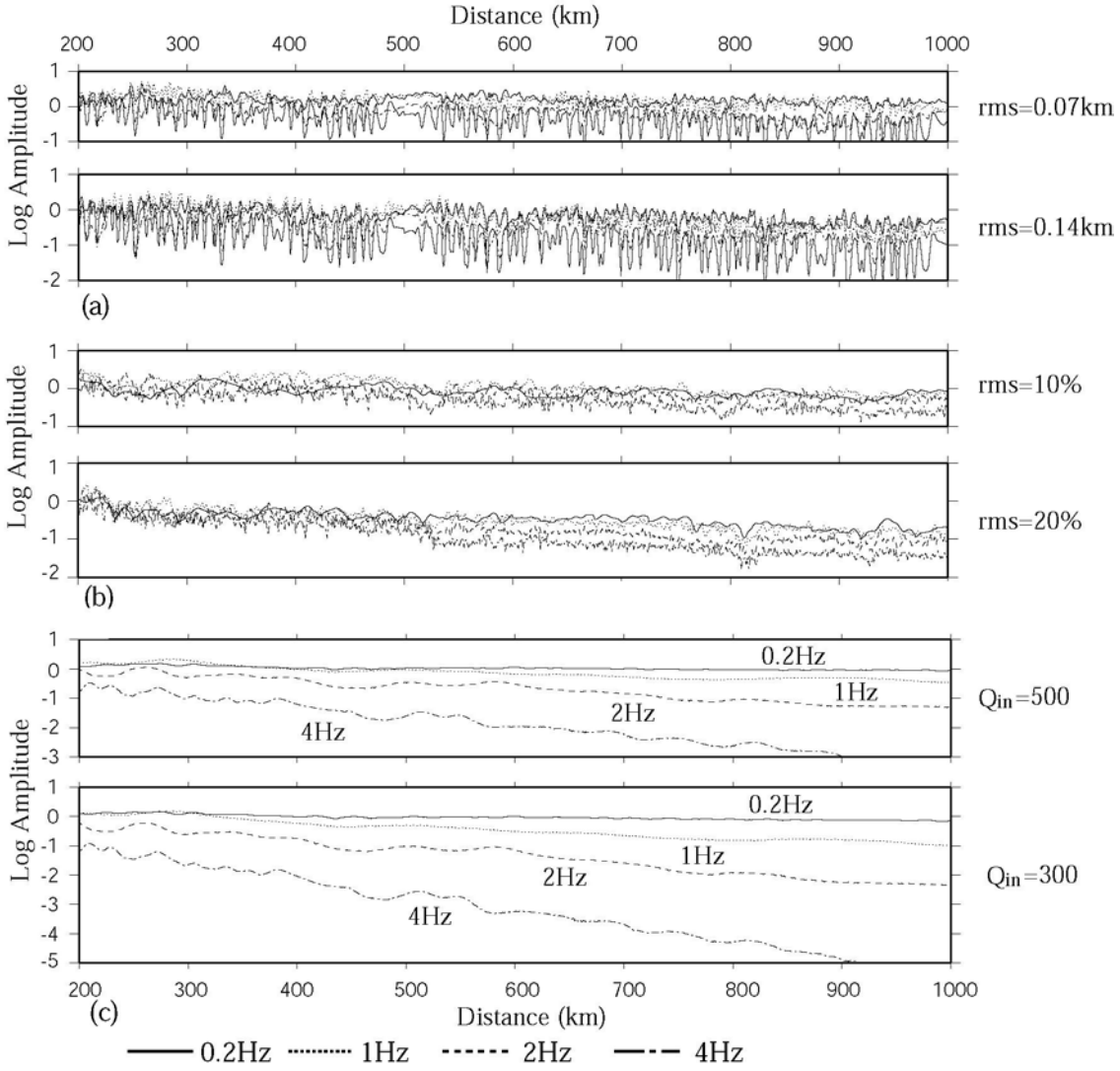

Figure 5 Lg spectral amplitudes at four different frequencies versus distance for crustal models with topographies only (a), crustal heterogeneities only (b), and intrinsic attenuation only (c). Topography with rms=0.07km has a fluctuation of 0.87~-0.75km in height. Q_{in} denotes quality factor of shear wave.

In this section, using the screen method incorporated with anelastic quality factor Q_{in}, Lg wave simulations including the effects of random topographies, crustal heterogeneities and anelastic attenuation are conduced,

separately. We estimate apparent Lg Q and its power-law frequency dependence associated with different attenuation mechanisms. Then, we synthesize Lg wave responses to a real crustal geometry in the Tibetan Plateau, assuming different heterogeneities and intrinsic attenuations. Preliminary simulation results reveal high Lg attenuation or blockage after introducing low Q_{in} (intrinsic quality factor of shear wave) into the model.

A. Scattering, anelasticity, and Lg Q

The crustal model for simulations consists of a crustal layer and a half-space mantle. The parameters of the crust and mantle are $V_{crust} = 3.5km/s$, $\rho_{crust} = 2.8g/cm^3$, $V_{mantle} = 4.5km/s$, and $\rho_{mantle} = 3.1g/cm^3$. The thickness of the crust is 32km. Two random topographies used have the same correlation length of 2.5 km but different rms fluctuations: rms=0.07km (height: 0.87~-0.75km) and rms=0.14km (height: 1.75~-1.5km). A random medium with an exponential correlation function is used to model crustal heterogeneity. Its correlation lengths are 10 km in range and 5 km in depth. The rms values used are 10% and 20%, respectively. A source is located at a depth of 8 km and has a spectrum function given by:

$$S(f) = \frac{1}{1 + (f / f_c)^2}$$

where f is frequency and $f_c = 2Hz$ is the dominant frequency. For the screen method computation, the step length for each forward step is 125 m. The spatial sampling in depth is 250 m. The number of samples in depth is 512. The number of screens is 8000 corresponding to a regional distance of 1000km. We calculate 6 sets of Lg synthetic seismograms for different crustal models. Figure 5 shows spectral amplitudes versus distance for four different frequencies: 0.2, 1., 2., and 4Hz. Figure 5a involves the scattering effect of irregular surface only. Fluctuation of Lg spectral amplitudes versus distance increases as frequency and/or topographies increase, while the averaged spectral amplitudes show a weak attenuation for either low or high frequencies. Figure 5b involves the scattering effect of heterogeneities only. Fluctuation of Lg spectral amplitudes is weak compared with those in Figure 5a. Figures 5a and b show that although topographies and crustal heterogeneities may directly affect Lg wave behavior, they cannot fully account for high Lg attenuation or blockage. Figure 5c involves only the effect of anelastic attenuation. We see that Lg spectral amplitudes vary smoothly with distance, and high-frequency Lg waves shows strong attenuation.

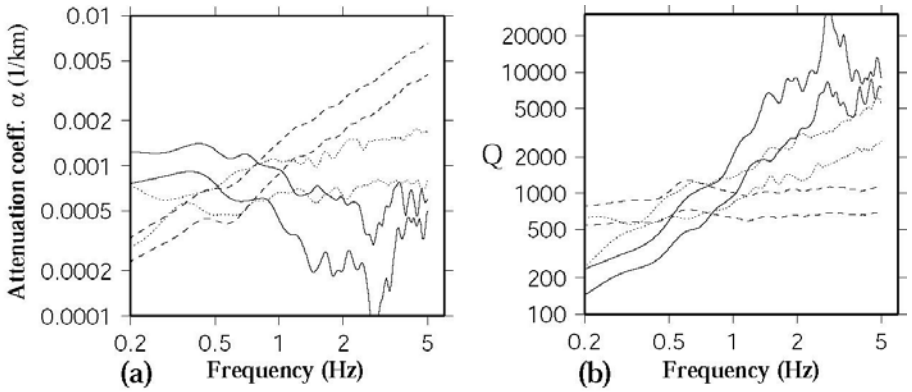

Figure 6. (a) Attenuation coefficient versus frequency, (b) Apparent Lg Q versus frequency. Solid lines correspond to the models with random topographies, dotted lines to models with random heterogeneities, and dashed lines to the anelastic crustal wave guides.

Assume that in 2-D, the Lg spectral amplitude can be expressed by:

$$A_{Lg}(f) = S(f)e^{-\frac{\pi f}{Q}\frac{x}{v}} = s(f)e^{-\alpha x}$$

where α is attenuation coefficient, x propagation distance, v Lg group velocity, and Q is apparent Lg Q being frequency-dependent. Then we can calculate attenuation coefficient and Lg Q by linearly fitting Lg spectral amplitudes shown in Figure 5. Figure 6 shows the estimated attenuation coefficients and apparent Lg Q's versus frequency. Solid lines correspond to the models with random topographies, dotted lines to the models with random heterogeneities, and dashed lines to anelastic crustal wave guides. We see that apparent Lg Q's show different frequency-dependent relations for different attenuation mechanisms.

The Lg Q has often been observed to fit a power-law frequency dependence as:

$$Q_{Lg}(f) = Q_0 f^{\eta}$$

where Q_0 and η are Lg Q at 1 Hz and its power-law frequency dependence. Using the above relation and Figure 6b, we can estimate Q_0 and η (listed in Table 1). From Table 1 we see that the Lg frequency dependence η for homogeneous anelastic crusts is much smaller than those ($0.3 < \eta < 0.6$) for most practical earthquakes and explosions, while the η associated with scattering by random topographies or random heterogeneities varies strongly. It may be possible to generate appropriate η by combining intrinsic attenuation and the attenuation due to scattering.

Table 1. Estimated Q_0 and η

	Topography		Heterogeneity		Intrinsic Q_{in}	
	D*=0.07km	D=0.14km	B**=10%	B=20%	500	300
Q_0	2029	945	1345	827	508	313
η	2.320	1.700	0.888	0.73	0.057	0.056

*D denotes the rms for random topography and B** denotes the rms for random medium.

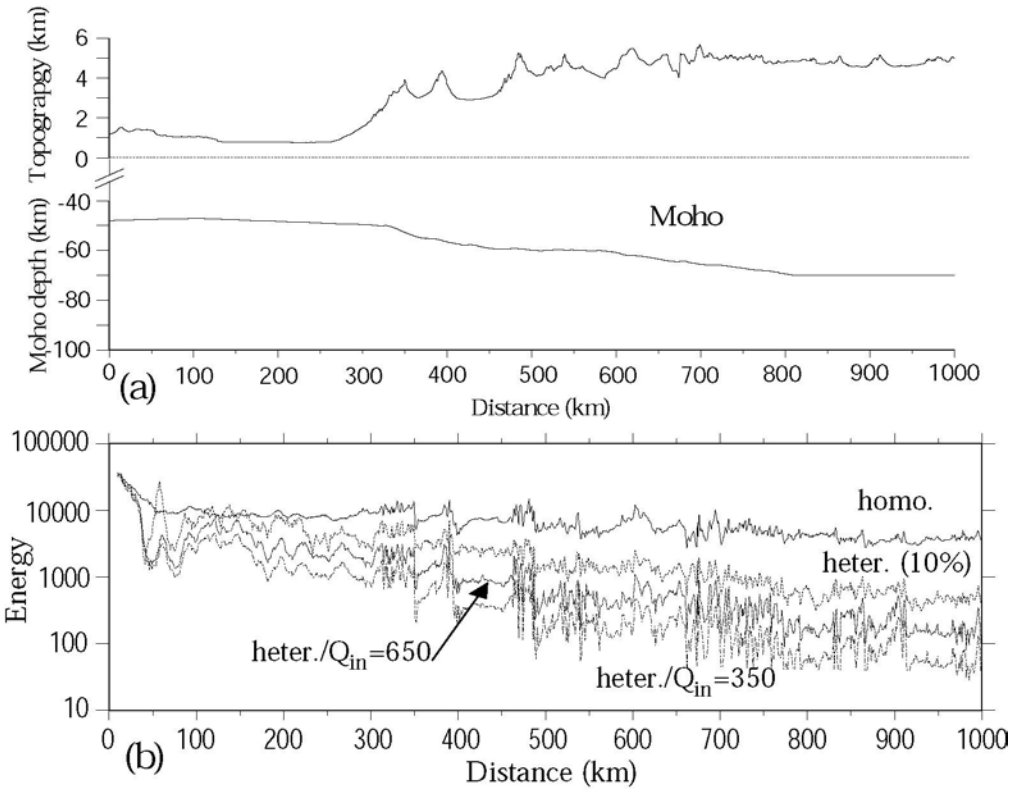

Figure 7 (a) A cross-section profile of a real crust in the Tibetan Plateau (a segment of the crust given in Fan and Lay, 1998). (b) Lg wave energy versus distance for the crustal model with different heterogeneities and anelastic attenuations. Solid line corresponds to a homogeneous elastic waveguide, dashed line to the crust with rms=10% heterogeneities, and dotted and dotted-dashed lines to the crusts with different intrinsic attenuation Q_{in}: 500 and 300, in addition to rms=10% heterogeneities.

B. Lg wave simulation with real crustal wave guides

Although the propagation of Lg has been observed across most of Asia, Lg has not been observed for paths crossing the Tibetan Plateau. It has been demonstrated that Lg has abnormally strong attenuation in these regions. Figure 7a shows a cross-section profile of a real crust in the Tibetan Plateau (Part segment of the crust given in Fan and Lay, 1998). This crust has severe topography and great changes in lateral velocity structure. Also we will introduce certain heterogeneities and anelastic attenuation into the crustal model to investigate the mechanism of Lg attenuation or blockage. Topography data have a resolution of 1 km in range and Moho depth data have a resolution of 10 km in range. For numerical computation using the screen method, both data sets are linearly interpolated up to a sampling interval of 0.125 km. Other parameters are the same as used in Figure 5. We first synthesize full seismograms for regional distances up to 1000 km and calculate Lg wave energy (excluding Sn) by summing up the energy of all frequency components of Lg waves for each receiver. Figure 7b shows Lg wave energy versus distance for the crusts with rms=10% heterogeneities and different anelastic attenuations. The solid line corresponds to an elastic homogeneous waveguide. Lg energy fluctuation is closely related to topography but Lg energy attenuation is weak in the whole range. Even at the distance of 1000 km, high-frequency Lg phase is still strong (see Figure 8b). The dashed line corresponds to the crust with rms=10% heterogeneities; the dotted and dotted-dashed lines to the crusts with different intrinsic attenuation Q_{in}: 500 and 300, as well as rms=10% heterogeneities. We see that after introducing anelastic attenuation, Lg waves show high attenuation. Note that Lg energy for the crust with Q_{in} =300 at far receivers (> 600 km), mainly comes from low-frequency Lg waves (see Figure 8a).

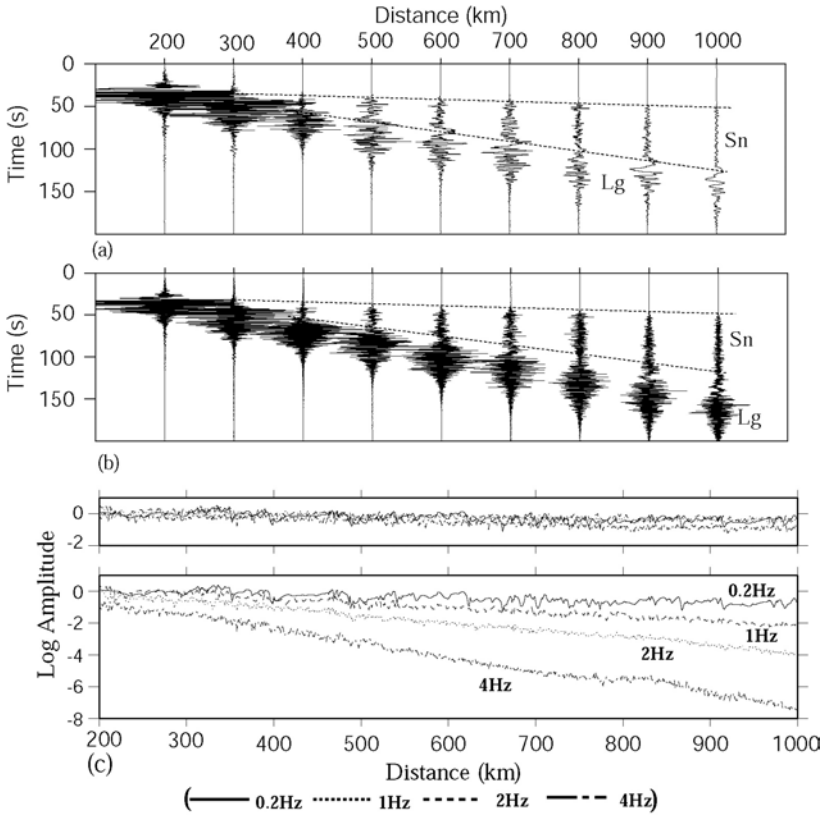

Figure 8 (a) Synthetic seismograms for the crust with variable anelastic attenuation along the path, (b) synthetic seismograms for the elastic crust with rms=10% heterogeneities, and (c) Lg spectral amplitudes versus distance at 4 different frequencies calculated from (a) and (b), respectively.

Another example is that, assuming anelastic attenuation to be variable along the path, we let Q_{in} be 450 for a range below 300 km, 250 for a range between 300 – 800 km, and 125 for a range greater than 800 km. Corresponding synthetic seismograms are shown in Figure 8a. The time axis is reduced by a velocity of 6 km/s. We see that high-frequency Lg waves are weak at the distance of 800 km, and absent at 1000 km. For comparison, synthetic seismograms for an elastic heterogeneous waveguide are given in Figure 8b. High-frequency Lg waves are very

strong at far receivers up to 1000 km. Figure 8c shows Lg spectral amplitudes at four different frequencies versus distance calculated from Figures 8a and b. We see that the slope of high-frequency Lg spectral amplitudes varies for different segments of the path.

CONCLUSIONS AND RECOMMENDATIONS

In conclusion, the existence of near source heterogeneities provides coupling between the Rg- and Lg-waves, as well as Pg- and Lg-waves. The numerical simulation and slowness analysis show that the near source scattering of fundamental mode Rg-wave can generate low-frequency Lg-wave. This is consistent with the previous observation from real data. The near source heterogeneities can also cause the scattering of high-frequency Pg-wave and contribute to the high-frequency Lg-wave. However, the low- and high-frequency Lg waves may have different attenuation patterns in their later propagation stage. Combining the excitation and propagation investigations together will give a complete description for Lg-wave.

Apparent Lg Q produced by intrinsic attenuation and scattering due to topography and random heterogeneities, shows different frequency dependence. Intrinsic attenuation shows a quite small apparent η (nearly constant Q), while scattering due to topography and heterogeneities may generate large η. Either intrinsic attenuation or scattering attenuation alone cannot satisfactorily explain the observed frequency dependence of apparent Lg Q. A combination of different attenuation mechanisms may be required. Lg wave simulation for a real crust in the Tibetan Plateau shows that anelastic attenuation, combined with scattering by heterogeneities may cause high Lg attenuation even blockage.

REFERENCES

Fan G. and T. Lay (1998), Statistical analysis of irregular wave-guide influences on regional seismic discriminants in China: Additional results for P_n / S_n, P_n / Lg, and P_g / S_n, *Bull. Seis. Soc. Am.* **88** (6), 1504-1510.

Gupta, I.N., W.W. Chan, and R.A. Wagner (1992), A comparison of regional phases from underground nuclear explosions at east Kazakh and Nevada test sites, *Bull. Seism. Soc. Am*., **8**2, 352-382.

Gupta, I.N., T.W. McElfresh, and R.A. Wagner (1991), Near source scattering of Rayleigh to P in teleseismic arrivals from Pahute Mesa (NTS) shots, in *Explosion Source Phenomenology*, edited by, Taylor, S.R., Patton, H.J. and Richards, P.G., American Geophysical Union, Washington, DC.

Wu, R.S., S. Jin, X.B. Xie (2000), Seismic wave propagation and scattering in heterogeneous crustal wave guides using screen propagators: I SH waves, *Bull. Seis. Soc. Am*., **90**, 401-413.

Wu, X.Y., and R.S. Wu (2001), Lg-wave simulation in heterogeneous wave guides with surface topography using screen propagators, *Geophys. J. Int*., **146**, 670-678.

Xie, J. (1998), Spectral inversion of Lg from earthquakes: A modified method with application to the 1995, western Texas earthquake sequence, *Bull. Seis. Soc. Am*., **88**, 1525-1537.

Xie, J. (2002), Lg Q in the Eastern Tibetan Plateau, *Bull. Seis. Soc. Am*., **92**, 871-876.

Xie, J., and B.J. Mitchell (1996), Attenuation of multiphase surface waves in the Basin and Range province. I. Lg and Lg Coda, *Geophys. J. Int*., **102**, 121-137.

Xie, X.B. and T. Lay (1994), The excitation of Lg waves by explosions: A finite-difference investigation, *Bull. Seism. Soc. Am*., **84**, 324-342.

Xie, X.B. and T. Lay (1995), The log(rms Lg)-mb scaling law slope, *Bull. Seism. Soc. Am*, **85**, 834-844.

LATERAL VARIATIONS OF LG Q IN THE TIBETAN PLATEAU

Jiakang Xie,[1] Rengin Gok,[2] James Ni,[2] and Yosuke Aoki[1]

Lamont-Doherty Earth Observatory, Columbia University;[1] New Mexico State University[2]

Sponsored by The Defense Threat Reduction Agency

Contract No. DTRA01-00-C-0048

ABSTRACT

In the past year we have been processing a large amount of regional wave data from various broad-band seismic stations in eastern Eurasia. Fourier spectra of the Lg waves are computed for many events and paths to study path attenuations. Among the Lg spectra that are obtained are those from (a) the 1991-1992 PASSCAL Tibetan Plateau, the INDEPTH II and III experiments, (b) some new Chinese digital seismic stations (with spectra processed in China), and (c) the broad-band Incorporated Research Institutions for Seismology (IRIS) and regional network stations archived at the IRIS Data Management Center (DMC). We estimate values of Q_0 and _ (Lg Q at 1 Hz and its power-law frequency dependence, respectively) in the Tibetan Plateau and its surrounding regions using various methods. Using a standard two-station method, we consistently find low inter-station Lg Q_0 values (typically < 200) in various parts of the Plateau. We also find that Q_0 values vary laterally by at least a factor of two inside the plateau. A least-squares inversion method was adapted to map lateral variations in Lg Q_0 along the INDEPTH profiles. The average value of Q_0 is about 126 over the southeastern part of the plateau, and drops to below 100 in the central part where the INDEPTH III experiment was conducted. In the southern part of the plateau, Q_0 becomes even lower (60-90) in the vicinity of the Yalong-Tsangbu Suture behind the crest of the High Himalayas. This kind of low (two-digit) Lg Q_0 is extremely rare in continental areas; it causes the Lg to be blocked within a propagation distance of about 100 km. The area where the lowest Lg Q_0 is found coincides with the prominent mid-crust reflectors found during the active-source element of the INDEPTH II experiment. Those reflectors were interpreted as being the top of a molten layer. Thus the well-kown phenomenon of Lg blockage across the southern boundary of the plateau is likely caused by a mid-crustal melting, rather than strong scatterings caused by a three-dimensional (3D) Moho topography underneath the high Himalayas. The generally low Lg Q_0 values found in the entire plateau are consistent with high temperature and/or fluid content in the Tibetan crust.

Work is underway to further improve the path coverage in and around the Tibetan Plateau, so that a tomographic mapping of Lg Q may be conducted. An effort is also being made to resolve depth variations in the crustal Q using available surface wave data.

OBJECTIVE

Introduction

The primary objective of this research is to quantify propagation and attenuation of high frequency waves in and around the Tibetan plateau. We wish to measure the laterally-variable Lg and Pn Q, and the travel times of Pn and mantle P waves from ground-truth events to southern and eastern Tibet. Additionally, we wish to invert fundamental-mode surface waves to obtain depth-variations of crustal Q in localized regions inside the plateau, such as the regions behind the high Himalayas where Lg blockage appears to take place.

This research provides an important input to the world-wide monitoring of nuclear explosions. The Q and travel times can be used for the calculation of source spectral characteristics, and location of any future seismic event to infer its nature and size. The depth-varying Q will also enable us to search for a physical mechanism, such as a molten mid-crust, for the well-known phenomenon of Lg blockage observed in several continental areas. Examples of areas of Lg blockage related to low Q include those in the Tibetan plateau just behind the crest of the high Himalayas, and regions with extensive rifting such as eastern Africa.

RESEARCH ACCOMPLISHED

Lateral variations of Lg Q

Xie (2002) calculated the average Lg Q for northeastern Tibet using data from the 1991-1992 PASSCAL Tibetan plateau experiment. He obtained the following result:

$$Q_{Lg}(f) = Q_0 f^{-} = (126 \pm 9) f^{(0.37 \pm 0.02)}$$

between frequencies of 0.2 and 3.6 Hz. The 1 Hz Lg Q (Q_0)of 126 is about the lowest ever reported for any continental regions that are of comparable size to northeastern Tibet (Figure 1 of Xie, 2002). The low Q_0 is also consistent with a higher-than normal temperature or fluid content in the crust under northeastern Tibet.

More recently we have estimated Lg Q_0 in central and southern Tibet, using data from the 1994 INDEPTH II and 1998-1999 INDEPTH III experiments (Figures 1 through 3; see also Nelson *et al*., 1996). Here we report the preliminary results of these estimates. They are subject to refinement and the readers are referred to Gok *et al.* (2002) for the final results. In the INDEPTH II and III experiments, multiple stations are deployed approximately along great-circle profiles. These profiles both recorded Lg from regional moderate events that are off, but aligned with, the profiles. These Lg recordings allow us to measure inter-station Lg Q_0 values between various pairs of the two stations using the standard two-station method (Xie and Michell, 1990b, Xie, 2002). We then input these two-station Q_0 values into a least-squares inverse method to map the lateral variations of Lg Q_0 along the profiles. This inverse method is adapted from the 2D inversion method used by Xie and Mitchell (1990b) and Zhao and Xie (1993), and is described in more detail by Gok *et al.* (2002).

Figure 2 shows the INDEPTH III stations in central Tibet and the great-circle profile (A-A') that goes through them. Two regional events are recorded along the profile and provide Lg spectra for the Q inversion. The bottom of Figure 2 shows the result of the inversion, including the laterally varying Lg Q_0 values along profile A-A', and the estimated error and resolution. The Q_0 values vary between about 80 and 100 along the profile. The errors are below 10 in the central portion of the profile, and increase to about 20 near the two ends. The resolution varies between about 20 km near the ends and over 100 km in the middle. No significant lateral variations in Q_0 are found along this profile when the amount of error is taken into account. In fact one can draw a flat line at a Q_0 of about 90 in Figure 2 that, within the errors, fits all the Q_0 values. The average values of Q_0 of about 90 are lower than the average value for the northeastern Tibet (Xie, 2002), indicating a decrease of Q_0 from northeastern to central Tibet.

Figure 3 shows the INDEPTH II stations in southern Tibet and the great-circle profile (A-A') that goes through these stations. Lg spectra from one regional event (M_b=5.5) is recorded along the profile (Figures 1 and 3). There is a severe Lg attenuation from the northern end into the middle of the profile, visible in the raw seismograms and Lg spectra (bottom of Figure 3). The attenuation is so high that near the southern end of the profile the Lg is almost

eliminated (blocked) at stations near point A. We measured inter-station Lg Q_0 values among several two-station pairs. The lowest Q_0 of 65 is found between stations BB05 and BB14. We input these Q_0 values into the least-squares inversion algorithm. The resulting laterally varying Lg Q_0 values, together with the estimated errors and resolution, are shown in Figure 4. The lateral resolution along the INDEPTH II profile varies between about 100 and 200 km, and is generally poorer than that along the INDEPTH III profile. Even with this limited resolution the resulting Lg Q_0 shows a considerable lateral variation along the INDEPTH II profile. Q_0 is about 60 near the northern end (point A'), and increases to above 100 near the southern end (point A). Even when the large error near the southern end (point A) is taken into account, it is certain that Q_0 increases to at least 90 south of the Indus-Yalong Suture (IYS; also known as the Yalong-Tsangbu suture). The segment of low Lg Q_0 of about 60 south of the IYS coincides with the prominent mid-crust reflectors found during the active source element of the INDEPTH II experiment (Nelson *et al.*, 1996; also see the bottom of Figure 4). Nelson *et al.* have previously interpreted these reflectors as being the top of a molten layer. It appears that that molten layer (or layer of terrestrial fluid as an alternative) is the cause of the low Lg Q_0 that is responsible for the virtual Lg blockage across the INDEPTH II profile (Figure 3). Therefore we have pinpointed a zone of low Lg Q behind the crest of the high-Himalayas, which might have been responsible for Lg blockage observed earlier (Ruzaikin *et al*., 1977; Ni and Barazangi, 1983).

Depth-varying shear wave Q from fundamental mode surface waves

To explore the depth range in which low shear wave Q owing to the melting or terrestrial fluid occurs, we have started to invert for depth-varying Q using fundamental-mode surface waves. Applying a two-station method to shorter period (5-20 s) Rayleigh waves from a regional event recorded by the INDEPTH II stations, we detected a layer of extremely low shear wave Q of about 10. The top of the layer is at 10 to 15 km in depth and coincides with the mid-crust reflector. At greater depths the shorter-period Rayleigh waves lose resolution. A work is going on to use teleseismic Rayleigh waves at periods longer than 20 s to resolve Q at depths greater than about 15-20 km, so that the thickness of the low Q layer can be constrained.

Pn travel times and Q from the 1994 explosions to southern Tibet

The June 10 and Oct. 7, 1994 nuclear explosions north of Tibet are recorded by the INDEPTH II stations. Fisk *et al.* (2002) and Waldhauser (2001) provided high-quality relocations of the explosions. Since Fisk *et al.* jointly used satellite image and seismic signals, their absolute locations should subject to smaller (sub-kilometer) errors. We read the Pn arrivals at the INDEPTH II stations, and calculated the respective Pn travel times from the Fisk et al. locations to these stations, as well as to the Kyrghistan network (KNET) stations (Figure 4). The travel times to the INDEPTH II stations are used to fit an average apparent Pn velocity of 8.42 (± 0.1) km/s.

Previously there has been a disagreement on whether P velocity in the uppermost 150 km of the Tibetan mantle has a gradient (Zhao and Xie, 1993, here after referred to as XZ93; McNamara *et al.*, 1997). Here we examine whether the apparent velocity of 8.42 km/s is compatible with the model of ZX93, in which the uppermost mantle has an average gradient of 3.1×10^{-3} s^{-1}. First we calculate the P wave velocity near the Pn ray turning point using our measured apparent velocity of 8.42 km/s. Since the average distance from the explosions to the to INDEPTH II stations is about 1368 km (Figure 1), the Pn rays should bottom at the maximum depths of about 100-150 km below Moho. Considering the Earth's sphericity, the apparent Pn velocity of 8.42 km/s corresponds to P velocities of 8.14 to 8.20 km/s at the ray turning point if that point is located at a depth of 100 to 150 km below Moho. Geographically, the Pn ray turning points (the mid-points between the explosions and the INDEPTH II stations; Figure 1) are located under central Tibet.

Now we estimate the P velocity at the location based on the model of ZX93, who found a low sub-Moho velocity of 7.78 km in central Tibet. Using this value and the average gradient of 3.1×10^{-3} s^{-1}, the P velocity at 100 to 150 km below Moho in central Tibet is predicted to be 8.09 km/s at 100 km below Moho, and 8.25 km/s at 150 km below Moho. These predictions based on the ZX93 model are very compatible to the estimates of 8.14 to 8.20 km/s made in this study. If the Tibetan mantle has no gradient (McNamara *et al*., 1997), our measured apparent Pn velocity would have a very different physical meaning, which will be discussed elsewhere.

Amplitude spectra are calculated using Pn from the two Lop Nor explosions at the INDEPTH II stations. These are shown in Figure 5, together with the previously calculated Pn spectra at the KNET stations by Xie and Patton (1999). The average distance of 1368 km to the INDEPTH II stations is similar to the average distance of 1194 km

to the KNET stations. Xie and Patton (1999) estimated the Pn seismic moment of the two explosions using the KNET data. Using these estimates and the geometrical spreading of the form of equation (3) of Xie and Patton (1999), we estimate average Pn Q from Lop Nor to the southern Tibetan (INDEPTH II) stations to be

$$Q_{Pn}(f) = (284 \pm 60)f^{(-0.1\pm0.2)}$$

The low _ value of -0.1±0.2 means Pn Q does not grow with frequency. This is contrary to most observations made in other regions and suggests very low Pn Q at higher frequencies (> 1 Hz). The low high-frequency Pn Q is responsible for the rapid decay of Pn spectra at INDEPTH II stations above 1 Hz (Figure 5; note the difference in decay rates of the INDEPTH II and KNET spectra). We note that the Pn Q is estimated with the specific geometrical spreading term, which may not be accurate (Sereno and Given, 1990, Zhu et al, 1991; Xie and Patton, 1999). Nevertheless, the low average _ value to the INDEPTH II stations, when compared to the value of 0.5 to the KNET stations to the west of the explosions, indicate that Pn attenuation at higher-frequencies (above 1 Hz) in the Tibetan mantle is significantly higher than the mantle under the Tarim basin and Tianshan.

CONCLUSIONS AND RECOMMENDATIONS

Lg Q_0 values are measured using high-quality data from three PASSCAL experiments in Tibet, with a two-station method that is a simple, yet the most reliable method. A least-squares inverse method is adapted to map lateral variations of Lg Q_0 along the INDEPTH II and III profiles. The resulting Lg Q_0 values are generally low in the entire Tibetan Plateau, indicating higher-than normal temperature and/or fluid content in the Tibetan crust. The real average of Lg Q_0 is about 126 in northeastern Tibet. Q_0 values drop to below 100 in central Tibet with no resolvable variations across the Bangong-Nujiang Suture. In southern Tibet, Q_0 values decrease further. In a localized zone south of the Indus Yalong Suture and/or Kangmar Dome, Q_0 reaches the lowest value of about 60. This low Q_0 visibly causes a virtual blockage of Lg over a segment of about 100 km-long along the INDEPTH II profile. Further south into the High-Himalayas, Q_0 appears to increase to reach the level of 100 or higher. Therefore we have pinpointed a Lg blockage zone which coincides with the previously mapped prominent mid-crustal reflectors marking the top of a fluid layer. Shear wave Q in this layer as determined by inverting regional Rayleigh waves is as low as 10. It seems that a mid-crust layer of fluid with low shear wave, rather than strong scattering along the high-Himalayas, is responsible for the Lg blockage near the southern boundary of the Tibetan plateau.

Pn travels times are measured over paths that traverse the entire plateau in an N-S direction from two LTS explosions to the INDEPTH II stations. An apparent Pn velocity of 8.42 (± 0.1) km is obtained. Taking into account the mantle velocity gradient and Earth's sphericity, this value is highly consistent with the P velocity model by Zhao and Xie (1993). Pn Q in the uppermost mantle is lower under Tibet than under the Tarim Basin and Tianshan, particularly at higher frequencies (> 1 Hz).

Data from more events and stations in and around Tibet is currently increasing from more temporary and permanent stations. Future research should be directed to analyzing more seismic data in the plateau with reliable methods, to resolve details of the lateral variations of $Q_{Lg}(f)$, $Q_{Pn}(f)$, shear wave Q and seismic velocities under the plateau.

REFERENCES

Fisk, M., (2002). Accurate locations of nuclear explosions at the Lop Nor test site using alignment of seismograms and IKONOS satellite imagery, *Bull. Seism. Soc. Am.*, Submitted.

Gok, R., J. Xie, and J. Ni (2002), Lg Attenuation in the Tibetan Plateau, paper in preparation.

McNamara, D., W. R. Walter, T. J. Owens, and C. J. Ammon (1997), Upper mantle velocity structure beneath the Tibetan Plateau from Pn travel time tomography, *J. Geophys. Res.*, **102**, 493-505.

Nelson, K.D., W. Zhao, L. Chen, L. D. Brown, J. Kuo, J. Che, X. Liu, S. L. Klemperer, Y. Makovsky, R. Meissner, J. Mechie, R. Kind, F. Wenzel, J. Ni, J. Nabelek, L. Chen, H. Tan, W. Wei, A. G. Jones, J. Booker, M. Unsworth, W. S. F. Kidd, M. Hauck, D. Alsdorf, A. Ross, M. Cogan, C. Wu, E. Sandvol, and M. Edwards (1996), Partially molten middle crust beneath southern Tibet: Synthesis of Project INDEPTH Results, *Science*, **274**, 1684-1688.

Ni, J. and M. Barazangi (1983), High-frequency seismic wave propagation beneath the Indian shield, Himalayan arc, Tibetan plateau and surrounding regions: high uppermost mantle velocities and efficient Sn propagation beneath Tibet, *Geophys. J. R. Astr. Soc*, **72**, 665-689.

Ruzaikin, A.I., I. L. Nersesov, V. I. Khalturin, and P. Molnar (1977), Propagation of Lg and lateral variation in crustal structure in Asia, *J. Geophys. Res*., **82**, 307-316.

Sereno, T.J. and J. W. Given (1990), Pn attenuation for a spherically symmetric Earth model, *Geophys. Res. Lett.*, **17**, 1141-1144.

Waldhauser, F., W.Y. Kim, P, G, Richards, and D. Schaff (2001), Double-difference location of underground nuclear explosions at the Lop Nor test site, *EOS Trans. AGU*, **82** (47), F815.

Xie, J. (2002), Lg Q in the Eastern Tibetan Plateau, *Bull. Seism. Soc. Am*, **92**, 871-876.

Xie, J. and B.J. Mitchell (1990a), A back projection method for imaging large scale lateral variation in Lg coda Q with application to continental Africa, *Geophys. J. Int.*, **100**, 161-181.

Xie, J. and B.J. Mitchell (1990b), Attenuation of multiphase surface waves in the Basin and Range Province, part I: Lg and Lg coda, *Geophys. J. Int.*, **102**, 121-137.

Zhao, L.S. and J. Xie (1993), Lateral variations in compressional velocities beneath the Tibetan Plateau from Pn travel time tomography, *Geophys. J. Int.*, **115**, 1970-1084.

Zhu, T.F., K.Y. Chun, and G.F. West, Geometrical spreading and Q of Pn waves: An investigative study in eastern Canada. *Bull. Seismol. Soc. Am.*, **81**, 882-896, 1991.

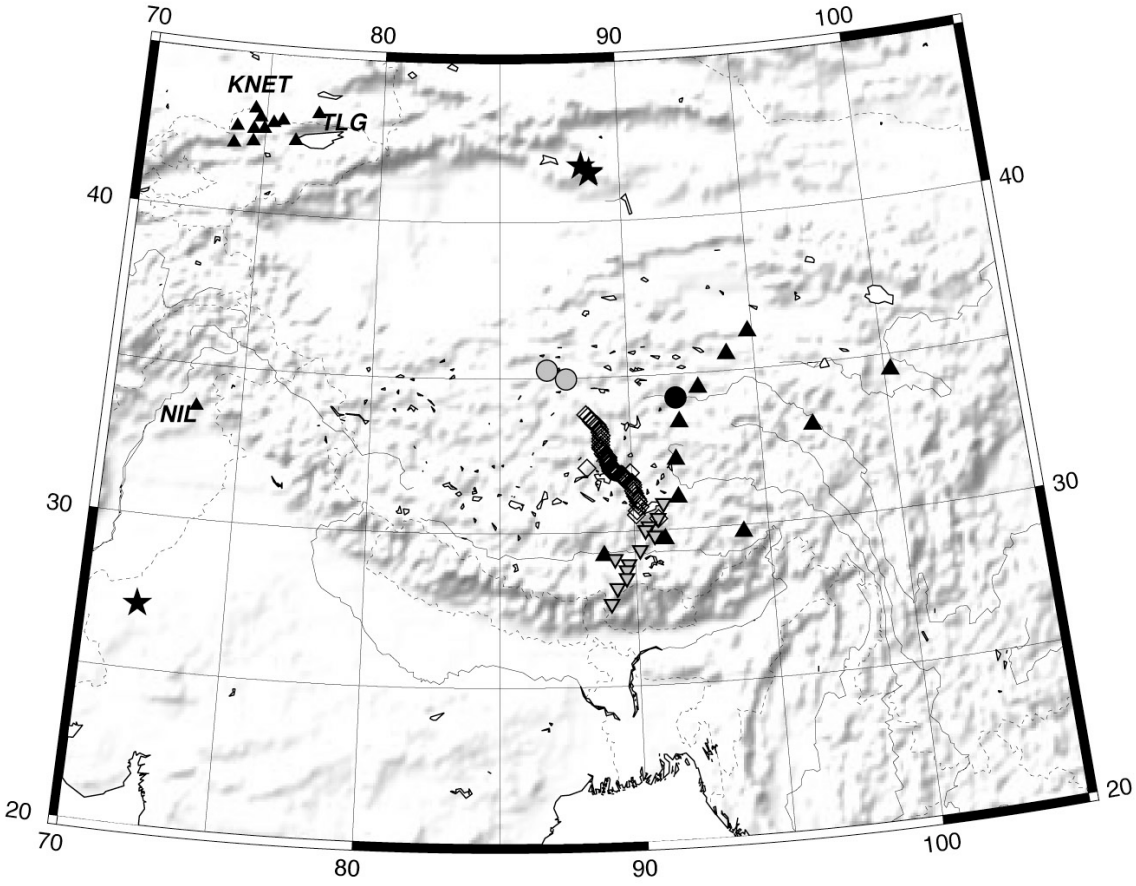

Figure 1. Map showing seismic stations and sources used in this study. Solid triangles are stations deployed during the 1991-1992 Tibetan Plateau experiment. Diamonds and inverted triangles are the INDEPTH II and III PASSCAL experiment stations. Stars are explosions. Gray and filled circles are earthquakes recorded by the INDEPTH III and II stations (Figures 2 and 3), respectively. TLG and KNET are permanent stations in Kyrghistan or Kazakhstan.

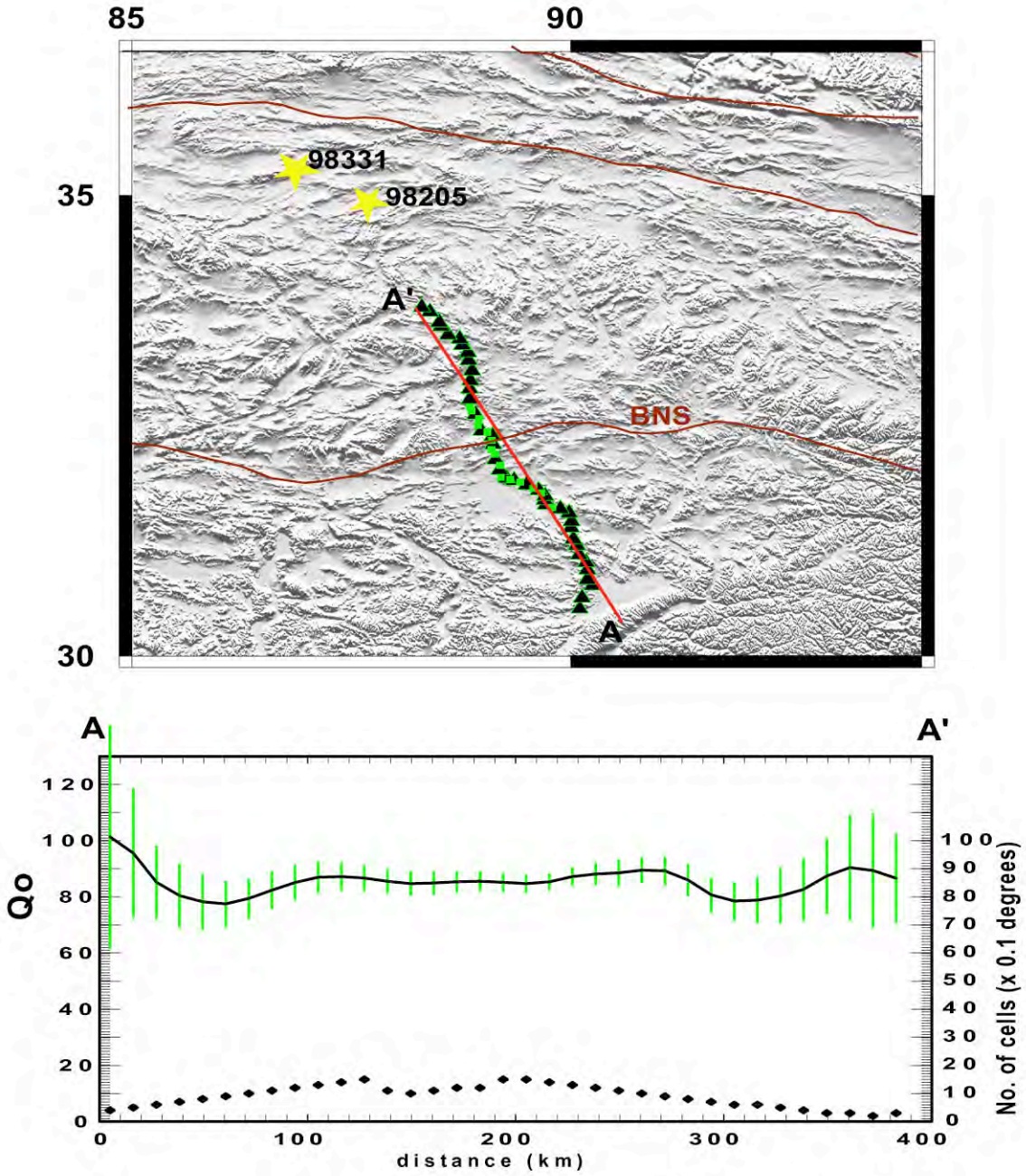

Figure 2. Top: Map showing locations of two regional events and profile A-A' through the INDEPTH III stations. "BNS" stands for Bangong-Nujiang Suture. Bottom: Variations of Lg Q_0 along profile A-A' from least square inversion, error bars and resolution (plotted as dots in the unit of 0.1 degrees).

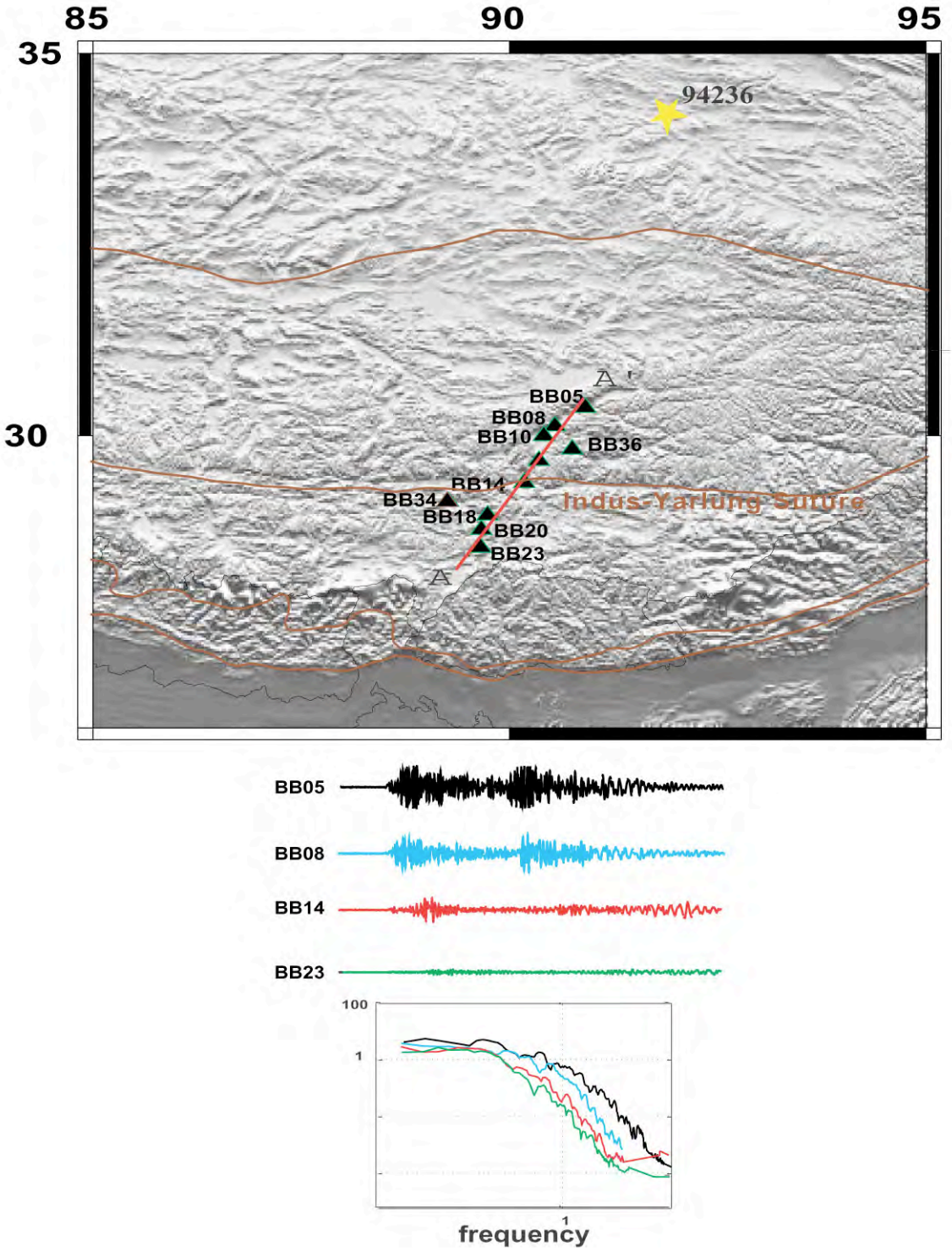

Figure 3. Top: Map showing locations of event 84236 and profile A-A' through the INDEPTH II stations. Bottom: Waveforms and Lg spectra from four stations along profile A-A'. Note the loss of energy over short distances.

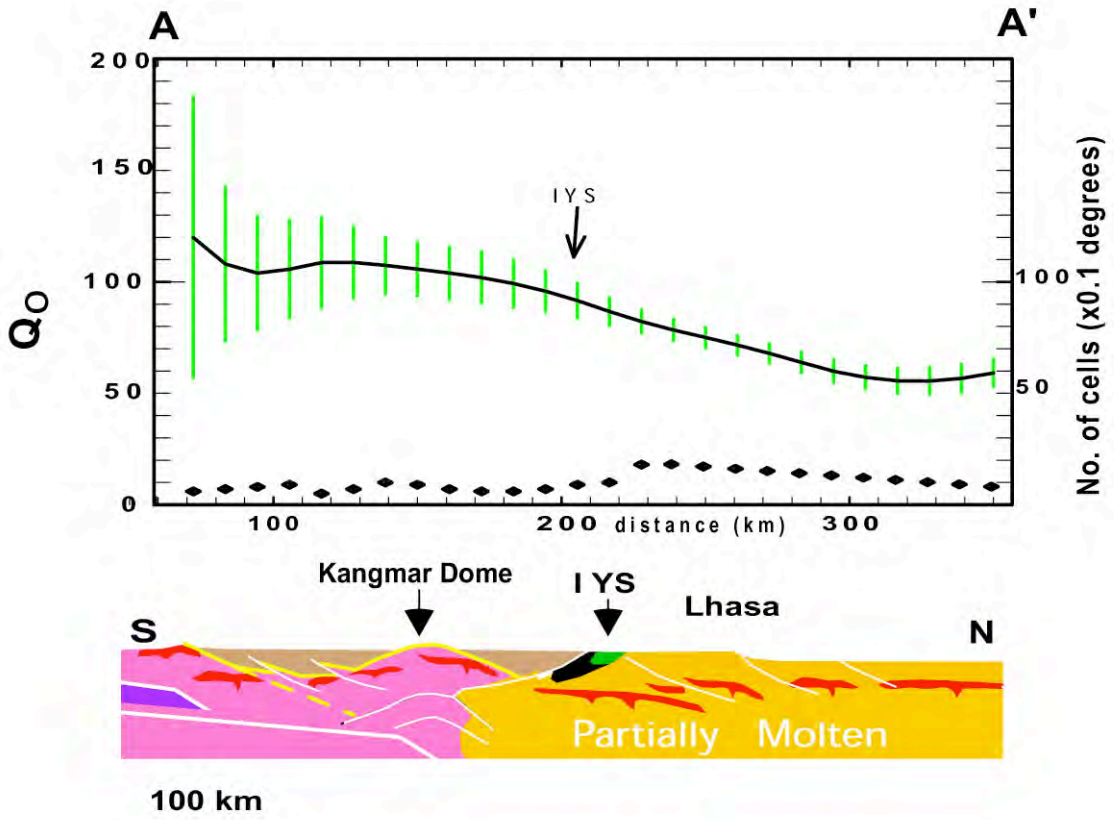

Figure 4. Top: Variations of Lg Q_0 along profile A-A' from least-squares inversion, error bars and resolution (plotted as dots in the unit of 0.1 degrees). Bottom: Cartoon showing along-profile geological structure and mid-crustal bright reflectors (Nelson *et al.* 1996). "IYS" stands for the Indus Yalong Suture.

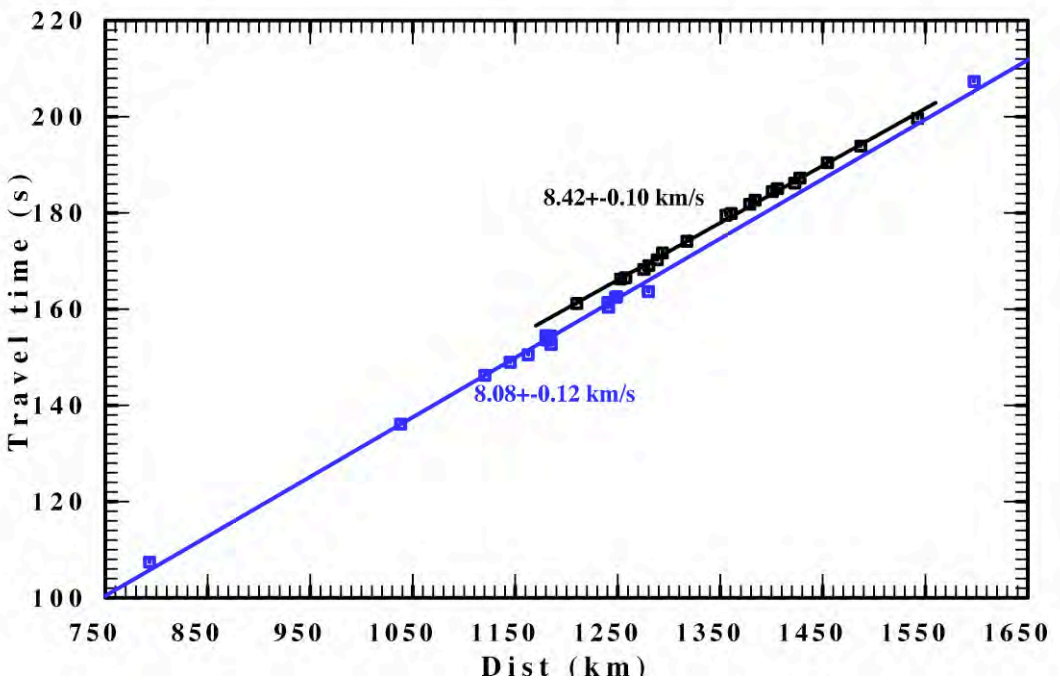

Figure 5. Pn travel time from the two Lop Nor explosions to Kyrghistan, Kazakhstan stations (lower points and line-fit) and INDEPTH II stations (upper points and line-fit). GT0 locations from Fisk *et al.* (2002) were used. Pn apparent velocity from INDEPTH II stations (from the linear fitting) is 8.42 km/s.

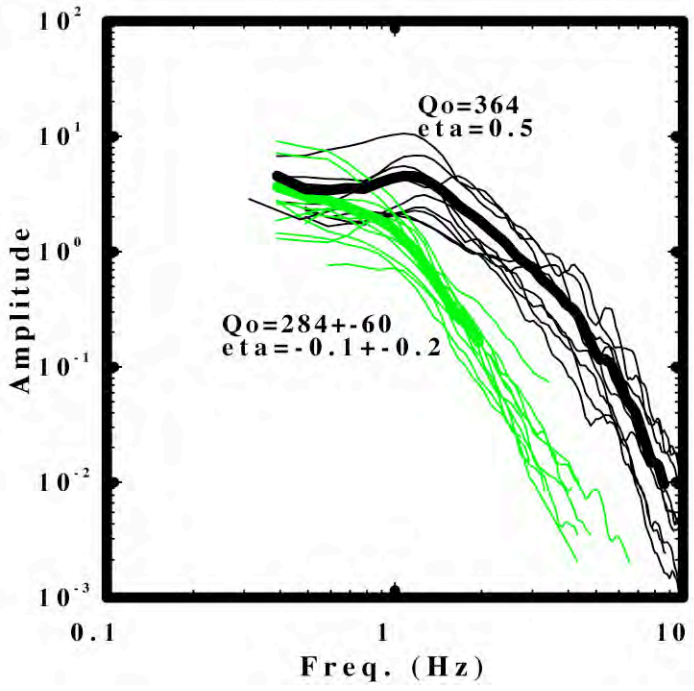

Figure 6. Individual Pn spectra from the Oct. 7, 1994 Lop Nor explosion (thin curves) and their average (thick curves), Black curves are for paths to the west (mainly Kyrghistan stations) and green curves are to the north (INDEPTH II stations). Average Pn Q_0 and n to the west and north are written near the curves.

Seismic Event Detection and Location

SEISMIC LOCATION CALIBRATION FOR THIRTY INTERNATIONAL MONITORING SYSTEM STATIONS IN EASTERN ASIA

John Armbruster,[1] Valeriu Burlacu,[2] Mark Fisk,[2] Vitaly I Khalturin,[1] Won-Young Kim,[1]
Igor Morozov,[3] Elena Morozova,[3] Paul G. Richards,[1] David Schaff,[1] and Felix Waldhauser[1]

Lamont-Doherty Earth Observatory of Columbia University, [1]
Mission Research Corporation, [2] University of Wyoming[3]

Sponsored by Defense Threat Reduction Agency

Contract No. DTRA01-00-C-0031

ABSTRACT

We review preliminary results of a three-year consortium effort to improve the capability to locate seismic events based on data acquired by 30 International Monitoring System (IMS) stations in Eastern Asia.

We have developed and tested Station-Specific Source Corrections (SSSCs) for Pn travel times at IMS stations (or suitable surrogates) in Asia, including AAK, AKTO, BRVK, KURK, MAKZ, NIL, ZAL, MAG, NRIS (NRI), SEY, TIXI (TIK), TLY, YAK, JAVM (ULN), and about 90 other stations used for validation testing. The SSSCs were initially computed by the method of Bondár (1999), using regionalized 1-D travel-time curves established by Khalturin et al. (2001) after extensive review of published studies including many from the Russian literature. These model-based SSSCs were refined empirically by applying a kriging algorithm to travel-time residuals for ground-truth (GT) events. Off-line validation tests were performed by evaluating travel-time residuals and by relocating GT events, with and without using SSSCs. To test the validity of the model directly, relocation tests were first performed using model-based SSSCs without kriging. Tests were then performed to evaluate the kriged SSSCs, using a leave-one-out approach so that events were not simultaneously used to both compute and test the SSSCs.

Using Pn arrival times for our GT events, we relocated 157 explosions (most from the Soviet era) recorded by various combinations of 94 regional stations. Mislocations were reduced for 63% of the events using the model-based SSSCs, and for 93% of the events using model-based and kriged SSSCs. Median mislocation improved from 12.2 km to 9.5 km and 2.7 km, respectively. Median error ellipse area was reduced from 1,596 km^2 to 450 km^2 and 196 km^2, respectively. Error ellipse coverage (percentage of GT locations within 90% error ellipses) was 97% without using SSSCs, 94% using model-based SSSCs, and 100% using kriged SSSCs.

Working with Cormier and Stroujkova (see their separate paper, this meeting — they are part of our Lamont consortium), we are now able to use 3D ray tracing (rather than the Bondár method) to obtain model-based SSSCs. Future efforts will focus largely on generating and testing SSSCs at IMS stations in China and nearby countries, and for secondary regional phases (Pg, Sn, Lg). To obtain reference events in China, we have carried out several studies of the Lop Nor underground nuclear explosions (UNEs) using waveform cross-correlations and IKONOS satellite images as well as conventional phase pick data, allowing us to obtain locations that are of GT1 quality or better for almost all these events.

We have also begun a series of studies based on phase pick data contained in the Annual Bulletin of Chinese Earthquakes (ABCE). Preliminary SSSCs for stations BJI, CHG, HLR, KMI, LZH, SSE, and XAN are computed from the reported first-arriving phase travel times of earthquakes within 2000 km from each of these stations. To improve the relative location of events within the ABCE we use the double-difference (DD) approach to relocate multiple events simultaneously. We have applied the DD method to several areas on mainland China where seismicity is dense enough to link earthquakes together over short distances (< 10 km). Twenty clusters of 50 or more events are formed, the largest of which is located in western China and includes more than 450 events. Initial results indicate that within these clusters the average relative location precision is improved by more than an order of magnitude, and averages about 500 m and 850 m in the horizontal and vertical directions, respectively. In some areas the seismicity correlates with surface traces from a fault map. It is also possible to use intensity maps to infer absolute locations. In this way we are building up numerous reference events, expected to be of GT5 quality.

OBJECTIVE

The goal of this project is to improve the accuracy of estimates of the location of seismic events — and to reduce the uncertainty of such estimates — on the basis of an interpretation of the arrival times of regional seismic waves observed at 30 stations of the International Monitoring System (IMS) located in Eastern Asia.

RESEARCH ACCOMPLISHED

Introduction

Our project began in March 2000. It is a three-year collaborative academic-industry research project led by Lamont Doherty Earth Observatory and involving a consortium of five institutions. Details of our work are described in Richards et al. (2000) and Conrad et al. (2001).

Web pages at http://www.LDEO.columbia.edu/~richards/consortium.html include the list of 30 stations we are studying, their locations, relevant maps, comments on pertinent datasets, and downloadable files describing our work in some detail. During the second year of work, we have focussed on the derivation of Pn SSSCs for 14 IMS stations in and near Russia and Central Asia, and we have begun to develop similar results for IMS stations in and near China. Table 1 lists these stations. This paper describes results from our second year.

Table 1. IMS stations for which preliminary Pn SSSCs have been computed

IMS Code	Country	Station Name	Station Code
PS23	Kazakhstan	Makanchi	MKAR
PS25	Mongolia	Javhlant	JAVM
PS29	Pakistan	Pari	NIL
PS33	Russian Federation	Zalesovo	ZAL
PS34	Russian Federation	Norilsk	NRIS
AS57	Kazakhstan	Borovoye	BRVK
AS58	Kazakhstan	Kurchatov	KURK
AS59	Kazakhstan	Aktyubinsk	AKTO
AS60	Kyrgyzstan	Ala-Archa	AAK
AS86	Russian Federation	Seymchan	SEY
AS87	Russian Federation	Talaya	TLY
AS88	Russian Federation	Yakutsk	YAK
AS91	Russian Federation	Tiksi	TIXI
AS93	Russian Federation	Magadan	MAG

Our overall plan has been:

a. to develop regional models with their associated travel times for about 25 sub-regions of East Asia;
b. to compute regional travel times for paths that cross between sub-regions and thus to obtain model-based SSSCs;

c. to obtain empirical travel times for IMS stations (or their surrogates), using reference events (ground truth);
d. to apply kriging methods (with the model-based SSSCs as background) to obtain new SSSCs.

Then
e. there is the final work of assessing relocation performance, which again uses ground truth, and sampling methods (leave-one-out, etc.). This final step is by far the hardest, since, for example, it entails iterations back to the earlier steps, especially in the context of seeking additional data to improve results in particular sub-regions. Our two previous papers (Richards *et al*., 2000; Conrad *et al*., 2001) have covered items (a) – (c) and have described our principal datasets. In this paper, we present preliminary results for (d) and (e).

We have quantified relocation performance using metrics that conform with the guidelines from the 1999 IMS Location Calibration Workshop (CTBT/WGB/TL-2/18) held in Oslo, Norway, which stipulated that:

- the median mislocation of ground truth (GT) events should be significantly reduced;
- mislocation should be reduced by 20% or more for the majority of events;
- median confidence ellipses should be reduced in area, and the coverage should be the same or better;
- confidence ellipses should be reduced by 20% or more for the majority of events;
- variance of travel-time residuals should be similar or smaller.

Our preliminary model-based SSSCs were computed by the method of Bondár (1999), using regionalized 1-D travel-time curves for Asia based on published studies. We then applied a kriging algorithm (e.g., Bottone *et al*., 2002) to empirical travel-time observations from events with ground truth locations. The resulting kriged SSSCs (grid files with one-degree resolution, extending out to 20 degrees from a given station) represent travel-time corrections relative to the IASPEI91 travel-time tables. We want IASPEI91 travel times plus SSSCs plus origin time plus possible corrections for elevation and ellipticity to predict observed arrival times.

Description of Results from Off-line Testing

Figure 1 shows a map of the GT event locations (red stars) and the stations that recorded them (triangles), along with great circle paths between events and stations. There are 174 events shown on the map, including 156 underground nuclear explosions (peaceful nuclear explosions [PNEs] and weapons tests) in the Former Soviet Union and 18 explosions (chemical explosions in Kazakhstan and UNEs in China, India, and Pakistan) in a separate data set that we have assembled. Further details on these datasets are given in Conrad *et al*. (2001) and from files available at http://www.LDEO.columbia.edu/~richards/consortium.html

Table 2. Comparison of Pn travel-time residuals for station BRVK

BRVK Pn Travel Time Residuals

Case	IASPEI91		SSSC		SSSC+Kriging	
	$\mu_{\Delta T}$	$\sigma_{\Delta T}$	$\mu_{\Delta T}$	$\sigma_{\Delta T}$	$\mu_{\Delta T}$	$\sigma_{\Delta T}$
STS UNE's	+0.51	0.45	+0.11	0.44	-0.02	0.30
Soviet PNE's	-3.91	1.96	-0.51	1.35	-0.05	1.09
Lop Nor UNE's	-2.52	0.04	0.85	0.04	0.02	0.04
Overall	-1.56	2.56	-0.15	1.01	-0.02	0.76

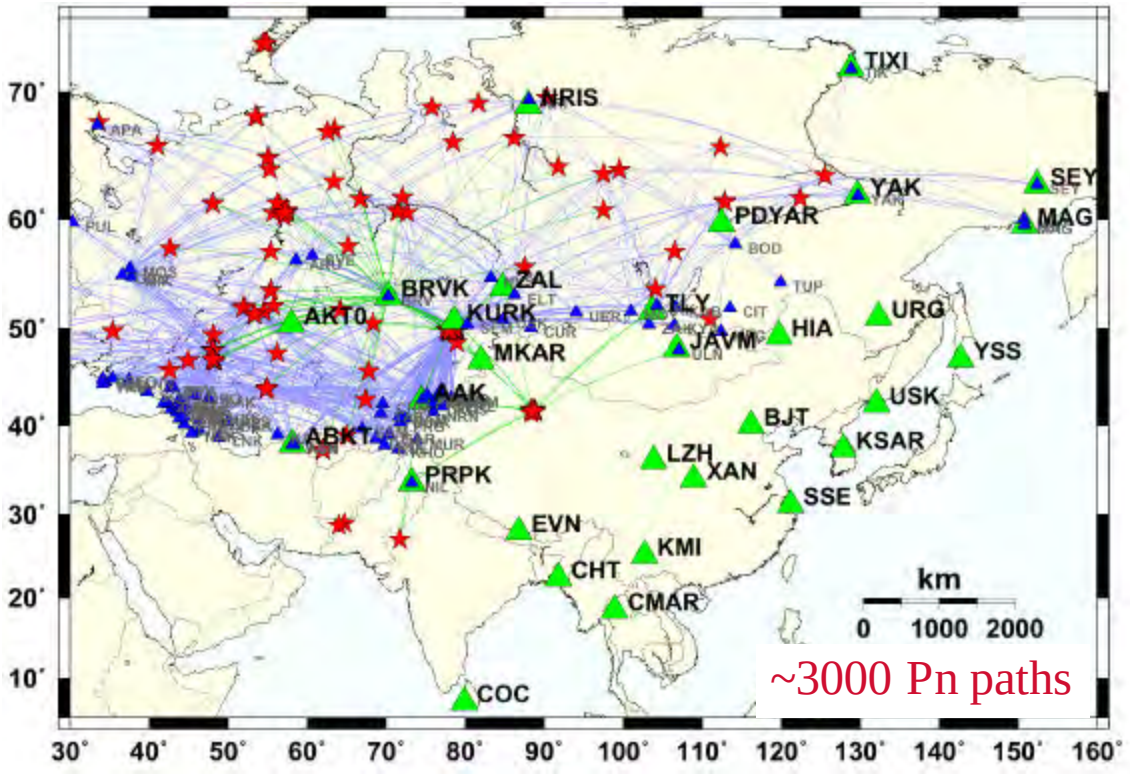

Figure 1. Map showing locations of 174 GT explosions (stars) and the recording seismographic stations (triangles) used for validation tests. Also shown are great circle paths between the events and 93 stations for which we have obtained arrival times for these events. The large (green) triangles represent the 30 IMS stations for which our consortium is generating SSSCs.

The main objective of off-line testing was to use GT events to validate the Pn SSSCs by evaluating:

- travel-time residuals before and after corrections and
- location performance (mislocation errors, error ellipse size, and coverage).

Table 2 shows travel-time residuals for 145 Pn arrivals at station BRVK, corresponding to Soviet-era PNEs and UNEs at the Semipalatinsk and Lop Nor nuclear test sites. These results are given in terms of the mean and standard deviation of the Pn travel-time residuals for the various sets of explosions, and the overall results. In all cases, both the mean travel-time bias and the standard deviation of the travel-time residuals are progressively reduced by applying the model-based SSSCs and the model-based plus kriged SSSCs. Although these results for BRVK are shown because of the good geographical distribution of GT events and the quantity and quality of the Pn phase picks for this station — which we carefully reviewed by inspection of the waveforms — they are qualitatively representative of reductions in mean travel-time bias and residual variance that we obtain at other stations in Asia.

To evaluate location performance of our SSSCs, we looked at two key aspects: (1) model validation; and (2) evaluation of the kriged SSSCs. The first is to validate the regionalized travel-time model and model-based SSSCs computed by Bondár's method. The goal here is to demonstrate that our regional model and our method of computing travel times provide an effective representation of travel times in Central Asia. This is a critical step in the validation process because events may occur at locations far from calibration points used by the kriging algorithm, where grids are asymptotically equivalent to the model-based SSSCs. The second goal is to assess the location performance using the kriged SSSCs. To do this, we relocated the GT events using the kriged SSSCs with a leave-one-out procedure (to avoid using the same events to both compute and test the grids), and we then quantified our results in terms of the same performance metrics used in the model validation. The results were compared to those in which the relocations were performed without SSSCs, and with the purely model-based SSSCs computed by Bondár's method.

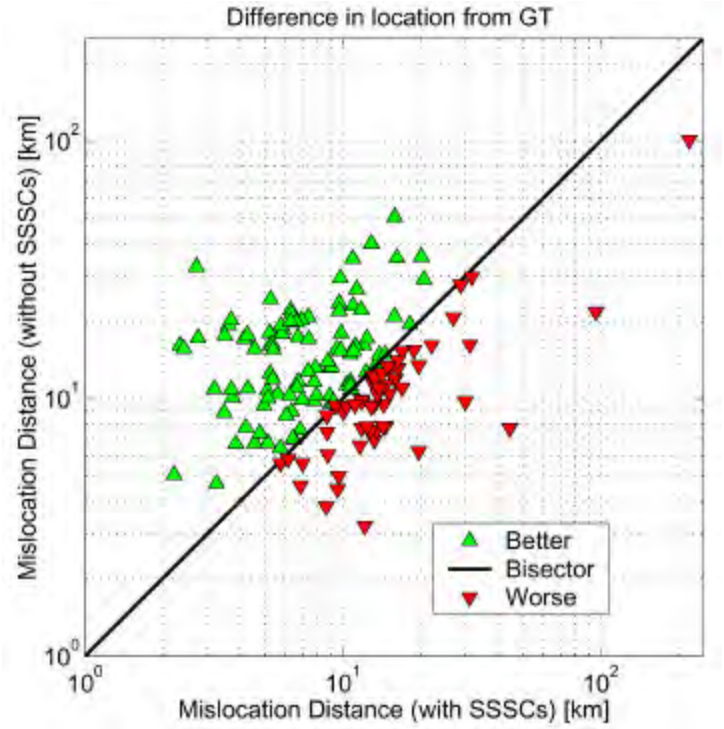

63% improved

37% deteriorated

53% improved by > 20%

24% deteriorated by > 20%

Median mislocation:

12.2 km → 9.5 km

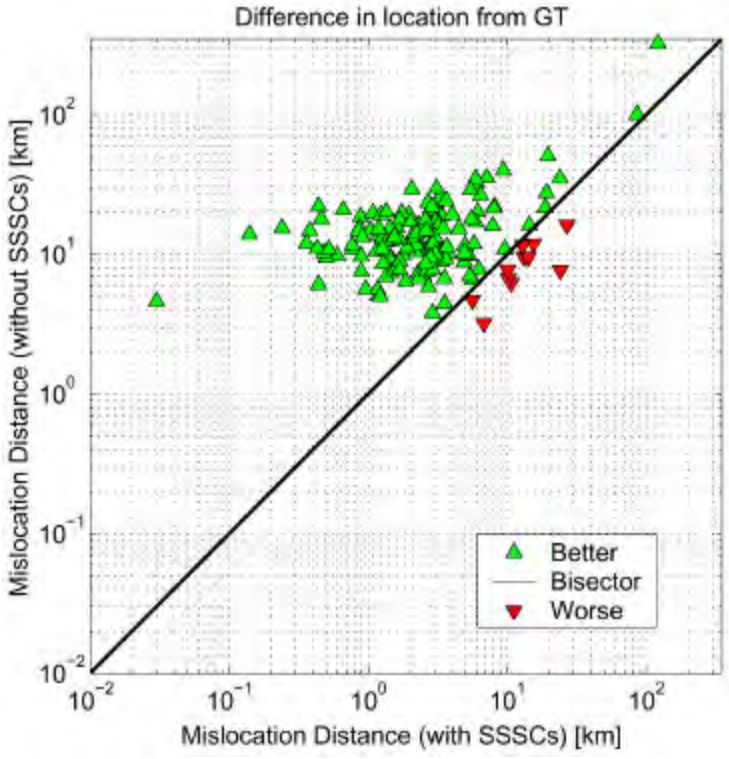

93% improved

7% deteriorated

90% improved by > 20%

6% deteriorated by > 20%

Median mislocation:

12.2 km → 2.7 km

Figure 2. Map showing reductions in mislocation. The upper panel and summary results show the reduction using model-based SSSCs. The lower panel/results shows the reduction using kriged SSSCs.

For model validation we used 156 events recorded at 93 stations (a major subset of Figure 1, namely the underground nuclear explosions in the Former Soviet Union for which we have good ground truth and numerous regional phase picks). The test consisted of relocating these events using Pn arrivals (2626 picks). All the relocations were performed with depth fixed at the surface. The relocation procedure was first applied using the IASPEI91 travel-time tables, without any SSSCs. This was followed by relocating the same events using the SSSCs. Running the program EvLoc with and without SSSCs resulted in 156 events with location estimates that converged.

Mislocation is expressed as the distance between the GT location and the location obtained by EvLoc. Of the 156 events, the locations using SSSCs improved for 99 events (63%) and deteriorated for 57 events (37%). The median mislocation was reduced from 12.2 km to 9.5 km. For 82 events (53%) the solutions improved by more than 20%, while for 37 events (24%) the deterioration is more than 20%. The upper panel of Figure 2 shows these results. To evaluate location performance using the kriged SSSCs, we used a "leave-one out" procedure in which the event to be relocated was excluded from the kriging calculation of the SSSCs. We then relocated each of the 156 events with kriged SSSCs that were re-computed for each event so that the same data were not used to both compute and test the SSSCs. Since the kriged SSSCs approach the model-based SSSCs far from calibration data, we expect that the kriged SSSCs should perform at least as well as the model-based SSSCs, and much better for areas close to calibration data. The lower panel of Figure 2 shows significant improvement with kriging. The median mislocation has been reduced from about 12 km to about 3 km.

Figure 3 (upper panel) shows the differences of mislocations, without and with the model-based SSSCs, versus number of defining phases (on the left) and azimuthal gap (on the right). Green (red) markers indicate solutions with smaller (larger) mislocations when SSSCs are used. Large mislocation errors when using the SSSCs generally occur when the number of defining phases is less than 6 and the gap is greater than 200 degrees. In such cases the locations are poorly constrained with or without use of model SSSCs. Figure 3 (lower panel) shows corresponding results with kriged SSSCs, and again there is great improvement over the use of purely model-based SSSCs.

The error ellipses are systematically reduced in area by using SSSCs. The difference in the error ellipse calculations for the two cases (with and without SSSCs) is due to a difference in modeling errors. Since the modeling error for the SSSCs is always less than for IASPEI91, we expect the error ellipses using our model SSSCs will always be smaller than for the IASPEI91 case. In fact, all 156 solutions (100%) are improved by more than 20% (Figure 4, upper panel). The decrease in the median error ellipse area is 1,146 km^2 (from 1,596 km^2 to 450 km^2). Error ellipse coverage is defined as the percentage of GT event locations that fall within the corresponding 90%-confidence error ellipse. For relocation solutions without using SSSCs, 151 events (97%) have 90%-confidence ellipses that contain the GT locations. Using our model SSSCs, 146 events (94%) have 90%-confidence ellipses that contain the GT locations. Although the coverage is slightly lower when using the SSSCs, in both cases they are above the target of 90%, while the median area of the error ellipses is reduced substantially for all the events relocated with SSSCs.

Given the large number of source regions, stations, and ray paths that sample very diverse and extensive geological structures (represented by our 25 sub-regions of Eastern Asia with corresponding travel times), we expect that SSSCs computed by Bondár's method for other stations in the same general area of Asia will, on average, perform as well as for the stations used to compile these evaluation metrics.

Using kriged SSSCs, the error ellipse area as shown in the lower panel of Figure 4 is reduced for 153 of 156 solutions (98%), 152 of which (97%) are improved by more than 20%. Only three solutions (2%) do not have smaller error ellipses. The median ellipse area is reduced from 1,596 km^2 to 196 km^2. Error ellipse coverage, computed as the percentage of GT event locations contained within the 90%-confidence error ellipses, is 100% (all 156 GT events) when using the kriged SSSCs, as compared to 97% (151 GT events) without using SSSCs (i.e., using IASPEI91 only).

The relocation results using kriged SSSCs show significant improvements for all location performance metrics. Specifically, Figure 4 shows that

- 93% of the events are located closer to the GT location (median mislocation errors down from 12.2 km to 2.7 km);
- error ellipse area is reduced by 20% or more for 97% of the events;
- median error ellipse area is reduced from 1,596 km^2 to 196 km^2, while achieving 100% coverage.

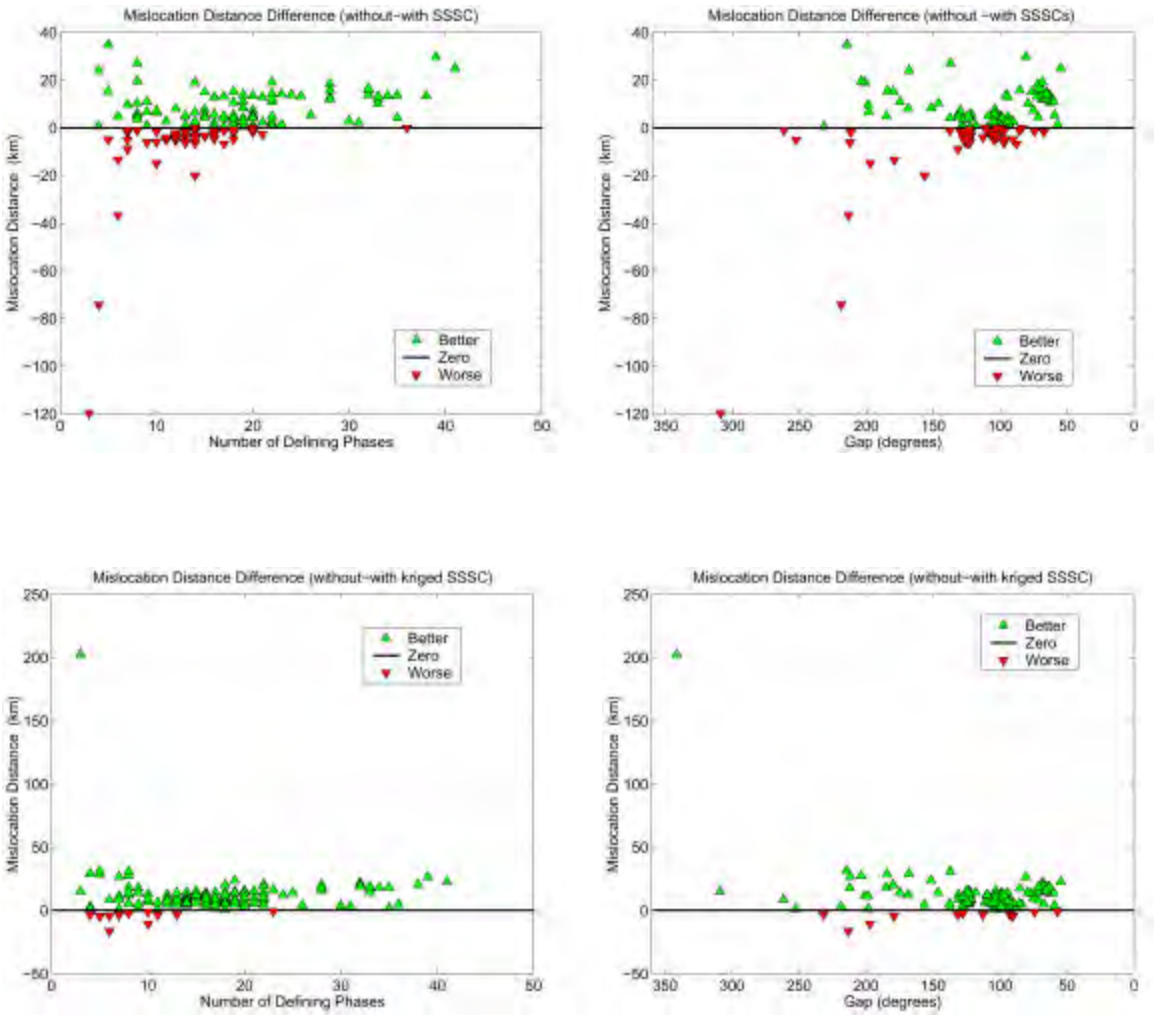

Figure 3. Mislocation distance differences (without SSSCs – with SSSCs), shown as a function of the number of defining phases (on left side), and as a function of gap (right side). The upper panel is for model-based SSSCs. The lower panel is for kriged SSSCs. Kriging gives significantly improved results.

Because we had regional Pn phase data for about 100 stations in our analysis of the phase associated with Figure 1, we developed SSSCs for far more than the 14 IMS stations (or IMS surrogates) listed in Table 1. Figure 5 shows the dependence of error ellipse area on the number of defining phases (using various subsets of the available stations), and on the gap. Again we see a notable improvement with use of kriged SSSCs. Because we are using Pn only in this analysis, the number of defining phases is equal to the number of stations.

The work summarized here in Figures 2, 3, 4, 5 was presented on May 23, 2002, as a proposal to the Configuration Control Board of the Center for Monitoring Research, and accepted as the basis for 14 Pn SSSCs of IMS stations listed in Table 1. The actual (kriged) SSSCs are available from the authors, along with extensive documentation.

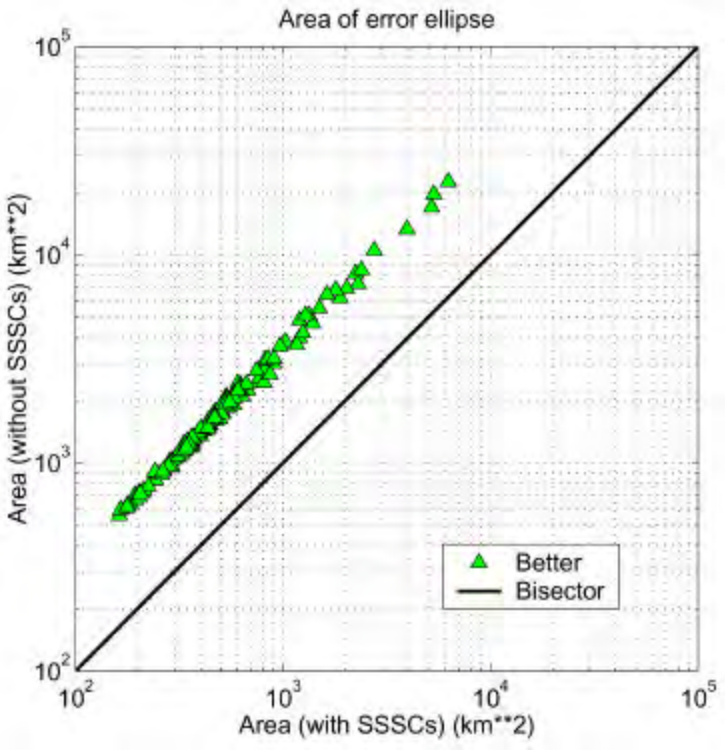

100% improved by > 20%

Median area:

1,596 km^2 → 450 km^2

Coverage 97% to 94%

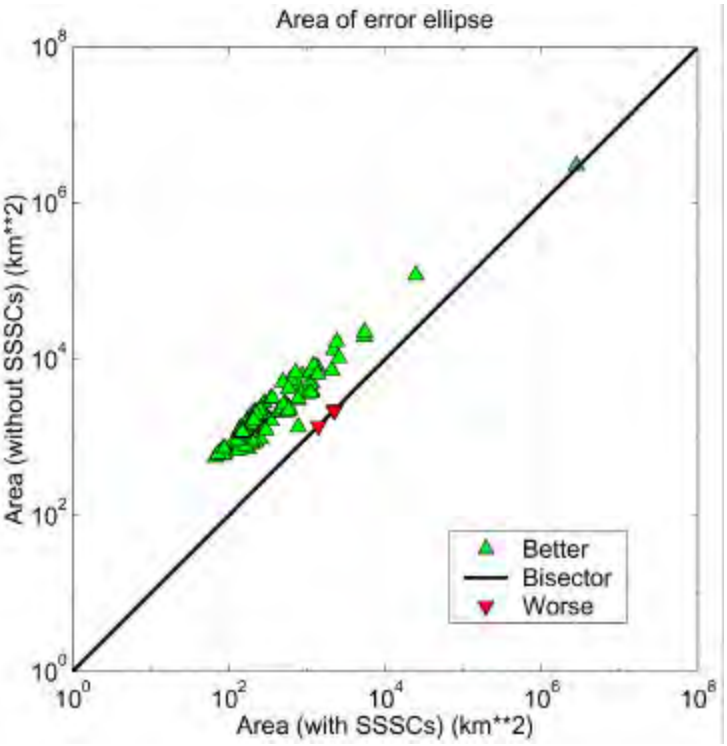

98% improved

2% deteriorated

98% improved by > 20%

0% deteriorated by > 20%

Median area:

1,596 km^2 → 196 km^2

Coverage 97% to 100%

Figure 4. Illustration of the reduction in error ellipse area, with use of SSSCs. The upper panel shows results using model-based SSSCs. The lower panel shows even better results with kriged SSSCs.

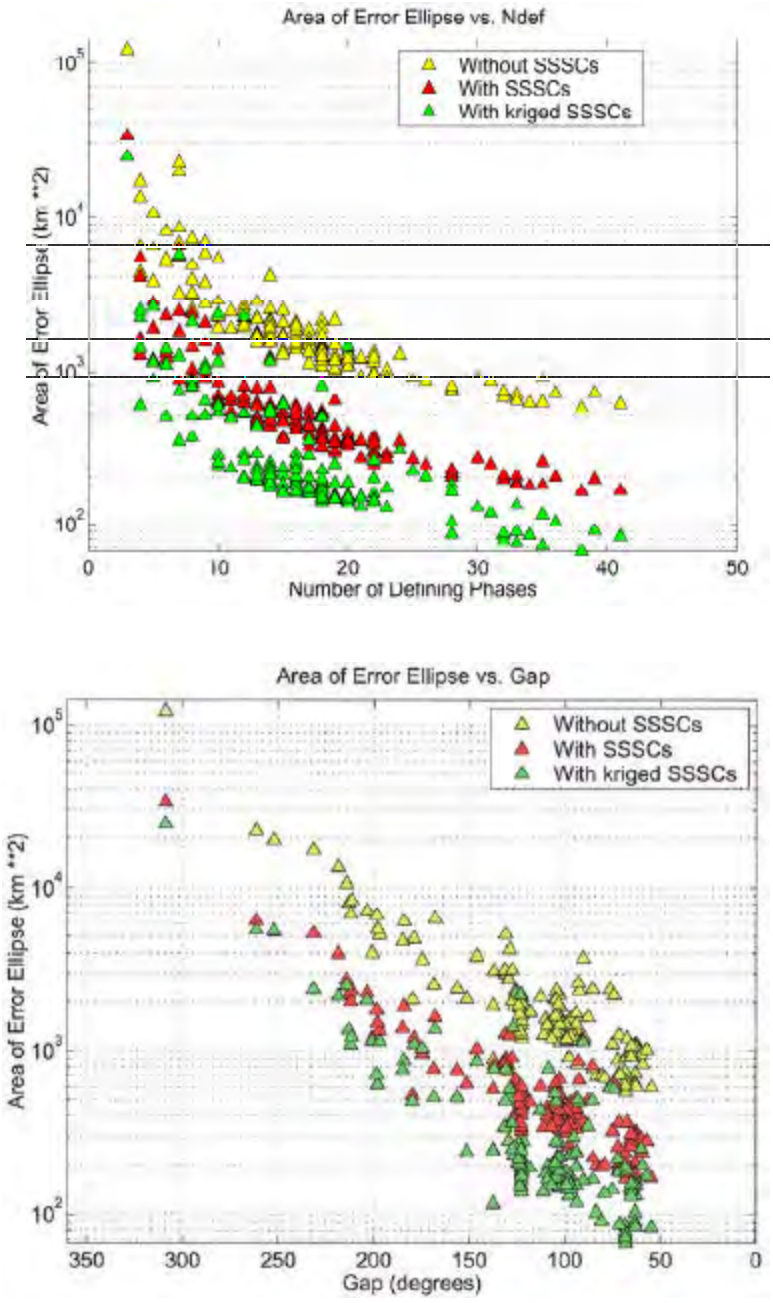

Figure 5. Illustration of the reduction in eror ellipse area, with use of SSSCs. The upper panel shows results as a function of the number of defining phases. The lower panel shows results as a function of gap.

Brief review of our work on GT events in China, and on empirical SSSC for an IMS station in China

We have worked with about 500,000 Pn phase picks for seismic events in China during 1985–1999 reported by 170 stations in and near China. These are derived from the Annual Bulletin of Chinese Earthquakes (ABCE). We are using these data to obtain GT5 quality events and empirical SSSCs in this major sub-region of East Asia. Figure 6 shows the great merit of locating events, with these data, not one-at-a-time, but all together using the double difference algorithm of Waldhauser and Ellsworth (2000). Also shown in Figure 6 are fault traces from data provided by the US Geological Survey, derived from the volumes on regional geology of China provinces published by the Geological Publishing House (Beijing, 1984 – 1993). In this case, knowledge of the position of a major fault enables us to have some confidence in treating our relocations as absolute relocations.

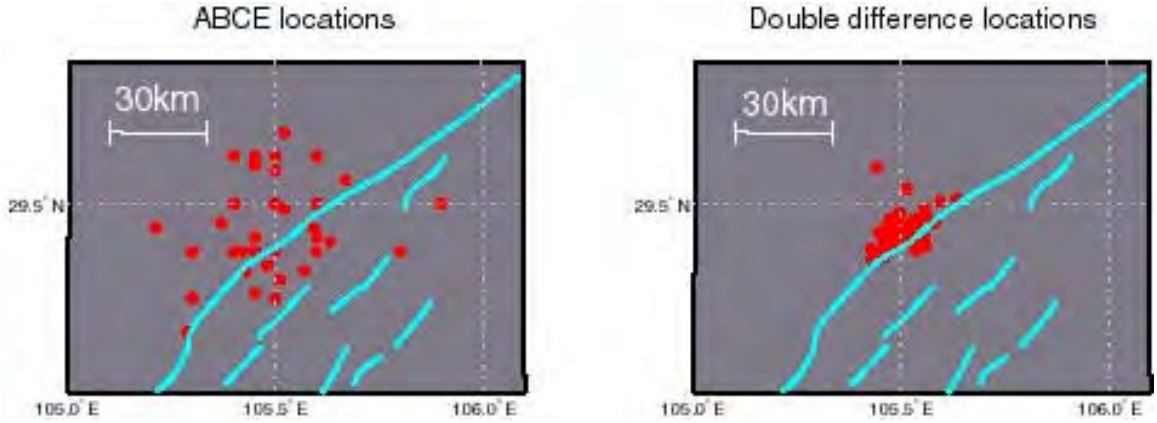

Figure 6. On the left are shown locations of a cluster of earthquakes in China, published in the Annual Bulletin of Chinese Earthquakes, compared (right) with results of a multi-event relocation.

We have carried out a similar analysis for several earthquake clusters in China. Because all of the IMS stations planned for China are at sites that have long operated as stations used for the ABCE, we can use numerous reported phase picks at these particular stations, together with ABCE event locations, to obtain empirical SSSCs for all IMS stations in China. Thus, Figure 7 shows empirical SSSCs for two stations in China that have been identified as sites for IMS stations: HLR (Hailar) as a primary station and XAN (Xi'an) as an auxiliary. Black dots are seismic events reported by the station in the ABCE (4324 for XAN, 154 for HLR). We use the reported arrival times to obtain empirical SSSCs as observed arrival times minus expected (on the basis of ABCE hypocenters and the IASPEI91 model). Of several stations for which we have made these plots, the coverage is best for XAN and worst for HLR.

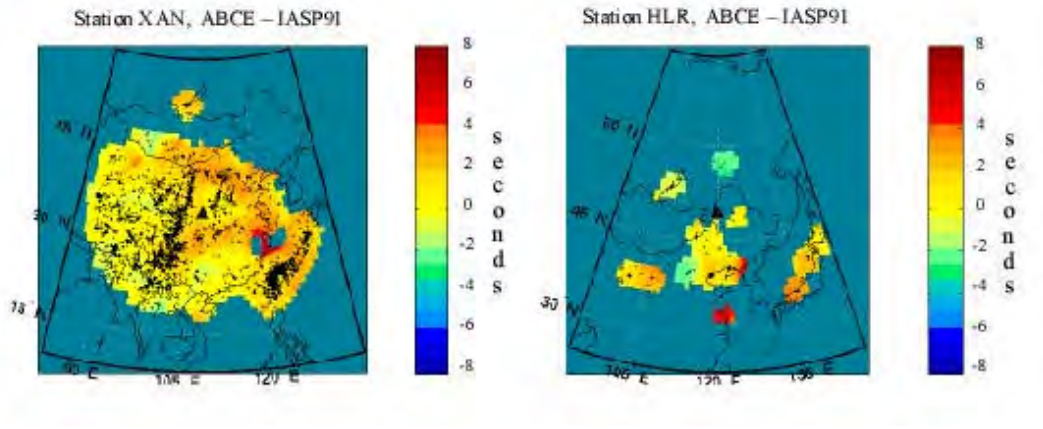

Figure 7. Empirical SSSCs based on phase picks reported in the Annual Bulletin of Chinese Earthquakes.

CONCLUSIONS AND RECOMMENDATIONS

Our principal conclusions are that ground truth data described in Figure 1, for stations in and near Russia and Central Asia, are a basis for obtaining Pn SSSCs at stations listed in Table 1, using analysis presented in Figures 2 through 5. Using these data, we have documented significant location improvement. Use of kriged SSSCs results in median mislocation error being reduced down from 12.2 km to 2.7 km, error ellipse areas reduced by 20% or more for 97% of the events, and median error ellipse area reduced from a median of 1,596 km^2 down to 196 km^2, while achieving 100% coverage. We recommend that continued analyses of these data be applied to phases other than Pn to obtain SSSCs for additional phases.

Because of the extensive experience (since 1966) of seismometer operation with digital recording at the Borovoye Geophysical Observatory, Kazakhstan, and the associated archive of sets of digital records for more than 700 underground nuclear explosions from this site, we conclude that when this site begins operation as an IMS station, it has the potential to become the best calibrated of all IMS stations. Because the station has demonstrated a capability to detect a significant fraction of global seismicity, it will have, as an IMS array station, the potential to have a significant effect upon the performance of the global system for monitoring nuclear explosions.

We have also found that regional phases routinely reported in the Annual Bulletin of Chinese Earthquakes are likely to be an adequate basis for location calibration of IMS stations in and near China. These data may be used both to establish a significant number of reference events, and to obtain empirical SSSCs for IMS stations.

ACKNOWLEDGEMENTS

We thank Drs. Bob Engdahl and Eric Bergman for general advice and for assistance in acquiring and assessing ground truth data and associated arrival times for purposes of location calibration.

REFERENCES

Bondár, I (1999), Combining 1-D models for Regional Calibration, in *Proceedings of a Workshop on IMS Location Calibration*, Oslo, January 1999.

Bottone, S., M. Fisk, and G. McCartor (2002), Regional Seismic Event Characterization using a Bayesian Formulation of Simple Kriging, in press, *Bull. Seism. Soc. Am.*

Conrad, C., M. Fisk, V. Khalturin, W.-Y. Kim, I. Morozov, E. Morozova, P. Richards, D. Schaff, and F. Waldhauser (2001), Seismic Location Calibration for 30 International Monitoring System Stations in Eastern Asia, in *Proceedings, 23rd Seismic Research Symposium*, Jackson Hole, Wyoming.

Richards, P., W.-Y. Kim, and V. Khalturin (2000), A Plan for Seismic Location calibration of 30 IMS Stations in Eastern Asia, in *Proceedings, 22nd Seismic Research Symposium*, New Orleans, Louisiana.

Waldhauser, F. and W. Ellsworth (2000), A Double-Difference Earthquake Location Algorithm: Method and Application to the Northern Hayward Fault, *Bull. Seism. Soc. Am.*, **90**, 1353–1368.

IMPROVED SEISMIC EVENT LOCATION USING A DAMPED LEAST SQUARES ALGORITHM

Sanford Ballard and Paul C. Reeves

Sandia National Laboratories

Sponsored by National Nuclear Security Administration
Office of Nonproliferation Research and Engineering
Office of Defense Nuclear Nonproliferation

Contract No. DE-AC04-94-AL85000

ABSTRACT

Perhaps the most important seismic parameter needed to distinguish explosions from natural earthquakes is the depth of the seismic event. Unfortunately, without seismic observations obtained quite close to the seismic event epicenter, this parameter is difficult to resolve precisely because of the inherent coupling between event depth and origin time. In this paper we will explore techniques to improve the location resolution of the iterative linear least squares location algorithm, which is currently the standard technique for locating seismic events.

To locate seismic events we are using a new code called LOCOO (LOCator Object Oriented). LOCOO uses an iterative least squares inversion procedure that employs singular value decomposition (SVD) to solve the associated matrix equations (Geiger, 1910). This algorithm is essentially identical to the one implemented in LocSAT and EVLoc, which are standard codes that are widely used to locate global and regional seismic activity.

For poorly constrained events, i.e., events that were observed by relatively few, distant stations, the location frequently oscillates during implementation of the iterative least squares algorithm, between two competing solutions, neither of which is the best fit to the available data in a least squares sense. In order to converge, the system must be damped such that a stable solution can be achieved that is near the point in solution space characterized by the minimum sum squared residuals. The details of how such damping is applied are critical to obtaining the best possible solution. We have developed an evolutionary scheme for selecting the proper amount of damping to apply such that a stable solution is achieved. Application of this algorithm in test cases indicates that with this code, we are able to resolve depth much more frequently than existing codes, without having to resort to arbitrarily fixing depth, and that the solutions obtained often display significantly lower residuals.

OBJECTIVE

The most widely used algorithm for estimating seismic event hypocenters and origin times, and the confidence bounds on those quantities, is the linear least squares inversion algorithm solved using singular value decomposition. This technique is described in detail by Menke (1989) and Lay and Wallace (1995) and is the basis for seismic event location applications and a next-generation application called LOCOO under development at Sandia National Laboratories. In this paper we review the mathematical basis of the algorithm, discuss the major assumptions made in its derivation, and explore the utility of using damping to improve the performance of the location algorithm in cases where some of the assumptions inherent in the algorithm have been violated.

RESEARCH ACCOMPLISHED

Formulation of the Inverse Problem

The seismic event location problem can be described as follows: We are presented with N observations of seismic arrival times, station-to-event azimuth, and horizontal slowness, which we denote as a vector $\mathbf{d}$ of length N, and we wish to determine the location in time and space of the seismic event which produced the observations. The location is described by a vector $\mathbf{m}$, of length $M = 4$, which contains the event latitude, longitude, depth and origin time. In order to determine $\mathbf{m}$, N must be $\geq M$ and we need an operator $\mathbf{F}$, which relates the event location to the observations:

$$\mathbf{F(m) = d} \tag{1}$$

For the seismic event location problem, $\mathbf{F}$ is an earth model as defined by the geometry of the Earth and a set of travel timetables with associated corrections. Equation 1 is a statement of the forward problem: given an Earth model and a seismic event location, we can use it to calculate a set of observations. The problem we wish to solve is the inverse problem: given an Earth model, $\mathbf{F}$, and a set of observations $\mathbf{d}$, find $\mathbf{m}$, the location of the seismic event that produced the observations. Since $\mathbf{F}$ is non-linear, we cannot solve the inverse problem directly. The standard approach is to start with an initial estimate of the event location, $\mathbf{m}_0$, and try to deduce an appropriate perturbation to that location, $\delta\mathbf{m}$, such that

$$\mathbf{m}_0 + \delta\mathbf{m} = \mathbf{m} \tag{2}$$

In other words, find the change in event location which will move the event location from the initial estimate of the event location to the event location that, when operated on by the Earth model, will produce the observations. Combining Equations 1 and 2 we have

$$\mathbf{F}(\mathbf{m}_0 + \delta\mathbf{m}) = \mathbf{d} \tag{3}$$

To solve Equation 3 for $\delta\mathbf{m}$, we first linearize it by expanding the left hand side into a Taylor series

$$\mathbf{F}(\mathbf{m}_0 + \delta\mathbf{m}) = \mathbf{F}(\mathbf{m}_0) + \left[\frac{\partial \mathbf{F}(\mathbf{m}_0)}{\partial \mathbf{m}_0}\right]\delta\mathbf{m} + \left[\frac{\partial^2 \mathbf{F}(\mathbf{m}_0)}{\partial \mathbf{m}_0^2}\right]\frac{\delta\mathbf{m}^2}{2!} + \left[\frac{\partial^3 \mathbf{F}(\mathbf{m}_0)}{\partial \mathbf{m}_0^3}\right]\frac{\delta\mathbf{m}^3}{3!} + \ldots \tag{4}$$

Ignoring all terms of order 2 and greater and substituting the remainder into Equation 3 yields

$$\left[\frac{\partial \mathbf{F}(\mathbf{m}_0)}{\partial \mathbf{m}_0}\right]\delta\mathbf{m} \approx \mathbf{d} - \mathbf{F}(\mathbf{m}_0) \tag{5}$$

At this point we want to consider our *a priori* uncertainty information. Associated with each observation d_i and prediction F_i are uncertainty estimates $\sigma_{d,i}$ and $\sigma_{F,i}$, respectively, which combine to yield an uncertainty associated with each residual $\sigma_{r,i}$ given by

$$\sigma_{r,i} = \sqrt{\sigma_{d,i}^2 + \sigma_{F,i}^2} \tag{6}$$

This *a priori* uncertainty information is introduced into the analysis by creating an $N \times N$ diagonal matrix $\boldsymbol{\sigma}$, the diagonal elements of which contain the values $\sigma_{r,i}$ as defined in Equation 6. We multiply both sides of Equation 5 by $\boldsymbol{\sigma}^{-1}$, which becomes

$$\boldsymbol{\sigma}^{-1} \left[\frac{\partial \mathbf{F}(\mathbf{m}_0)}{\partial \mathbf{m}_0} \right] \delta\mathbf{m} \cong \boldsymbol{\sigma}^{-1} \left[\mathbf{d} - \mathbf{F}(\mathbf{m}_0) \right] \tag{7}$$

Let us examine the terms of this equation. The right hand side is a vector of N weighted residuals, defined as the differences between the observations, **d**, and the predictions of those observations derived from the Earth model, **F**, applied to the estimate of the event location, $\mathbf{m}_0$. The weighting factors are the combined measurement and model uncertainties. Their inclusion gives greater weight in the analysis to residuals that have smaller uncertainties, and it renders all of the residuals unitless. The left hand side consists of three terms. The first is an $N \times M$ matrix of weighted partial derivatives of the N model predictions with respect to the M components of the estimated event location. Each element of this matrix describes the amount by which one of the predictions will increase as a result of a positive change in one of the M components of the estimated event location. When the predictions increase, the residuals decrease so the left hand side is a recipe for decreasing the residuals. The second term on the left side of Equation 7, $\delta\mathbf{m}$, is a vector of length M containing finite changes in each of the M components of the event location.

Note that the right and left hand sides of Equation 7 are related by an "approximately equal" symbol. This indicates that Equation 7 is only an approximation since the high order terms in Equation 4 were omitted. Equation 7 will be correct only to the extent that, in regions of the model parameter space near $\mathbf{m}_0$, changes in weighted residuals are directly proportional to weighted changes in model parameters. In this context, "near" means within a distance characterized by $\delta\mathbf{m}$.

For convenience of notation in all that follows, let us define a matrix **A** of weighted partial derivatives

$$\mathbf{A} = \boldsymbol{\sigma}^{-1} \frac{\partial \mathbf{F}(\mathbf{m}_0)}{\partial \mathbf{m}_0} \tag{8}$$

and a vector **r** of weighted residuals

$$\mathbf{r} = \boldsymbol{\sigma}^{-1} \left[\mathbf{d} - \mathbf{F}(\mathbf{m}_0) \right] \tag{9}$$

so that Equation 7 becomes

$$\mathbf{A}\, \delta\mathbf{m} \cong \mathbf{r} \tag{10}$$

Note that Equation 10 does not lead directly to a solution to our original problem, i.e., it does not yield an estimate of the value of $\delta\mathbf{m}$ that leads to **m**. Rather, it tells us only how small changes in a given event location will affect residuals between observed and predicted seismic quantities. What we seek is the particular value of $\delta\mathbf{m}$ which, when added to $\mathbf{m}_0$, **will** lead to the minimum of the sum squared weighted residuals, $\chi^2_{\min}$, where the sum squared weighted residuals, χ^2, is defined as

$$\chi^2 = \sum_{i=1}^{N} \left[r_i - \sum_{j=1}^{M} A_{ij} \delta m_j \right]^2 \tag{11}$$

$\chi^2_{\min}$ is found by taking the derivative of χ^2 with respect to each of the model parameters and setting them equal to 0:

$$\frac{\partial c^2}{\partial(dm_k)} = -2\sum_{i=1}^{N}\left[r_i - \sum_{j=1}^{M} A_{ij}\,dm_j\right]\tilde{A}_{ik} = 0\,; \quad k = 1, M \tag{12}$$

Reorganizing terms, this becomes

$$\sum_{i=1}^{N}\left[\sum_{j=1}^{M} A_{ij}\,dm_j\right]\tilde{A}_{ik} = \sum_{i=1}^{N} r_i A_{ik}\,; \quad k = 1, M \tag{13}$$

or equivalently

$$\mathbf{A}^T\ \mathbf{A}\ d\mathbf{m} = \mathbf{A}^T\ \mathbf{r} \tag{14}$$

Now, $\mathbf{A}^T\ \mathbf{A}$ is an $M \times M$ symmetric matrix so, if it is not singular, it will have an inverse and we can write

$$d\mathbf{m} = \left[\mathbf{A}^T\ \mathbf{A}\right]^{-1}\ \mathbf{A}^T\ \mathbf{r} \tag{15}$$

It remains to actually solve Equation 15. Menke (1989) and Lay and Wallace (1995) show that singular value decomposition (SVD) of **A** produces exactly the same least squares solution as Equation 15. SVD decomposes **A** into a set of matrices **U**, **W** and $\mathbf{V}^{\mathbf{T}}$ where **U** is an $N \times M$ column-orthogonal matrix and $\mathbf{V}^{\mathbf{T}}$ is the transpose of an $M \times M$ orthogonal matrix. **U** and **V** are orthogonal in the sense that their columns are orthonormal. The columns of **V** are M-dimensional vectors that describe the principal axes of the error ellipsoid of the solution vector $d\mathbf{m}$. **W** is an $M \times M$ diagonal matrix containing the so-called singular values of matrix **A**. The diagonal elements of **W** are all zero or positive (Press et al., 2002).

Replacing **A** by its decomposition we obtain

$$\mathbf{U}\ \ \mathbf{W}\ \ \mathbf{V}^{\mathrm{T}}\ \ d\mathbf{m} = \mathbf{r} \tag{16}$$

Now, since **U** and $\mathbf{V}^{\mathrm{T}}$ are orthogonal, their inverses are equal to their transposes. And since **W** is diagonal, its inverse is equal to the diagonal matrix whose elements are the reciprocals of the elements **W**. This allows us to write the solution to Equation 16 as

$$d\mathbf{m} = \mathbf{V}\ \ \mathbf{W}^{-1}\ \ \mathbf{U}^{\mathrm{T}}\ \ \mathbf{r} \tag{17}$$

or equivalently

$$dm_k = \sum_{i=1}^{M}\frac{\mathbf{U}_i\ \ \mathbf{r}}{w_i}\tilde{\mathbf{V}}_{k,i}\ ;\ k = 1, M \tag{18}$$

where the subscripts i on matrices **U** and **V** indicate column numbers and w_i indicates the i'th diagonal element of **W**. Equations 17 and 18 say that each element of $d\mathbf{m}$ is a linear combination of the columns of **V**, with coefficients obtained by forming the dot products of the columns of **U** with the vector of residuals, **r**, scaled by the singular values.

We have, finally, the solution that we are after: the value of $d\mathbf{m}$ which, when added to the initial event location estimate $\mathbf{m}_0$, produces **m**. When **m** is operated on by our earth model, **F**, (Equation 3), a set of predictions is produced that agrees as well as possible with the observations, in a least squares sense.

Alas, the last statement is almost, but not quite, true. It would be true if Equation 5 were exactly equivalent to Equation 3, which it is not because we linearized Equation 3 by ignoring all high order terms in Equation 4. However, if the conditions outlined in the second paragraph following Equation 5 are approximately satisfied, then $\delta\mathbf{m}$ will lead to a solution $\mathbf{m}$, which is closer to $c^2_{\min}$ than was $\mathbf{m}_0$. If Equation 3 is nearly linear in the model parameters, then $\mathbf{m}$ will be much closer than $\mathbf{m}_0$. If we accept the improved location as the initial estimate for another application of Equations 2-18, then the solution will be improved further still. If we continue to iteratively apply Equations 2-18 in this manner, we will ultimately reach a situation where the residuals are very close to the minimum we seek and the solution ceases to change significantly. At that point we can conclude that we have reached convergence and accept the solution as the final solution.

Poorly Constrained Events

Up to this point we have assumed that the solution to our problem was well constrained by the available data. What if that is not the case? For example, if the data set $\mathbf{d}$ consists only of azimuth observations from a large number of widely distributed seismic stations, it will be possible to accurately constrain the latitude and longitude of the event but it will not be possible to resolve the depth or the origin time. In matrix $\mathbf{A}$, all of the elements in the columns corresponding to the derivatives with respect to depth and origin time will contain zeroes. In this case, $\mathbf{A}$ is singular and the singular values that correspond to depth and origin time will be equal to zero.

Another situation in which problems can arise is when travel time observations are available from a cluster of stations, but all the stations are far from the event. In this case, there will be a trade off between the depth of the event and the origin time. Increasing the origin time of the event, without significantly impacting the residuals, can compensate for an increase in the estimated depth of the event. In this case, $\mathbf{A}$ is not singular but rather ill-conditioned. The singular values corresponding to depth and/or origin time will be much smaller than those corresponding to latitude and longitude. The degree to which $\mathbf{A}$ is ill-conditioned is characterized by the ratio of the largest to the smallest singular values, a quantity that is referred to as the condition number.

One of the significant advantages of the SVD algorithm is that after computing the SVD of $\mathbf{A}$, we can examine $\mathbf{W}$ to assess potential difficulties and take steps to alleviate them before finally computing $\delta\mathbf{m}$ using Equation 18 (Press et al., 2002).

If $\mathbf{A}$ is singular, then one or more of the singular values will be equal to zero and the condition number will be infinite. The difficulty will be encountered when we attempt to compute Equation 18 since we will be attempting to divide by zero. In this case we must take action before computing Equation 18 or our algorithm will generate an exception and fail.

In cases where the condition number is extremely large, round off errors in the computer may come in to play, yielding a solution with wildly large components that send our event location off into regions that make no physical sense. Fortunately, this situation appears to be rare in overdetermined seismic event location problems. More common is for the condition number to be moderately large, in which case it is possible to solve for all of the location parameters, but it may not be particularly useful to do so. In the second example described above where a trade-off between depth and origin time exists, the uncertainties on the depth and origin time of the event may be extremely large (larger than the dimensions of the Earth, for example) rendering the results meaningless.

When we encounter a situation with a large condition number our best option is to change the smallest singular value to infinity. This causes the algorithm to simply not solve for the parameter that corresponds to the manipulated singular value. In the two examples above, if we set the singular value corresponding to depth to infinity, we would simply give up trying to solve for depth. In Equation 18, where w_i appears in the denominator, this means that the element of $\delta\mathbf{m}$ corresponding to depth will be zero and depth will not deviate from its initial estimate.

Oscillating Solutions

Another difficulty that is frequently encountered when implementing the iterative linear least squares seismic event location algorithm described above is for the solution vector $\delta\mathbf{m}$ to oscillate, resulting in seismic event locations $\mathbf{m}$ that alternate between two or more significantly different locations. A set of seismic observations that generates this behavior is presented in Table 1 and the resulting oscillatory behavior is illustrated by the green curves in Figure 1. These six observations were drawn randomly from a global set of hand-picked travel time observations recorded for the May 1998 India nuclear test. Note that not only do all four components of the event location oscillate, but so does c^2. This fact indicates that our algorithm has failed since the solution is not moving in the direction of c^2_{min}.

To understand this behavior, we first seek the "best" solution, defined as the solution with the lowest c^2. To accomplish this we ran a series of locations with depth fixed at different levels from –24 km to 216 km. Since only 3 location parameters were being solved for, the algorithm behaved quietly, producing stable estimates of the latitude, longitude, origin time and c^2_{min}, with the event location fixed at each different depth. Figure 2a illustrates c^2_{min} as a function of depth with the blue curve representing the results of the experiment just described. c^2_{min} occurs near a depth of 30 km, which corresponds to the depth of the base of the crust in the IASPEI travel time model. Figure 2b illustrates the "best-fit" latitude and longitude as a function of depth with the blue curve representing the results of the experiment just described. The sharp kink in the curve corresponds to the latitude and longitude of the event location obtained with the event depth fixed at 30 km.

Table 1

Station	Latitude (degrees)	Longitude (degrees)	Phase	Observed Travel Time (seconds)	Distance (degrees)	Event-to-Station Azimuth (degrees)
UCH	42.2	74.5	Sn	379.1	14.9	7.9
PDY	59.6	112.7	PcS	825.5	42.6	29.5
HIA	49.3	119.7	P	483.0	42.6	46.0
KS31	37.4	127.9	P	522.6	47.8	63.2
EIL	29.7	35.0	P	395.1	32.3	282.8
OBN	55.1	36.6	P	441.4	37.6	327.1

The kink in the blue curve in Figure 2b suggests that a plausible cause of the failure of the location algorithm is that the assumption of linear behavior has been violated. Recall that in the derivation of the location algorithm we assumed that the derivative of the predicted seismic observations with respect to event location was approximately linear (Equations 4 and 5). The kink in Figure 2b indicates quite clearly that this is not the case and that the particular combination of observations that we have available in this location problem has led to a situation in which the combined derivatives of travel time with respect to latitude are highly non-linear at the crust-mantle boundary. When our location $\mathbf{m}_0$ is below the crust-mantle boundary, the derivatives and residuals combine to produce a change in location $\delta\mathbf{m}$ that moves the event location far above the crust-mantle boundary to a location where, due to non-linearity, c^2 is actually larger than it was at the previous location. At this new location, the derivatives and residuals combine to produce a change in location $\delta\mathbf{m}$ that moves the event location back to where it was before the most recent change in location was imposed.

In the particular example we are considering, the problem seems to be related to the inclusion of an observation of an Sn phase at station UCH. If this observation is omitted the situation is ameliorated

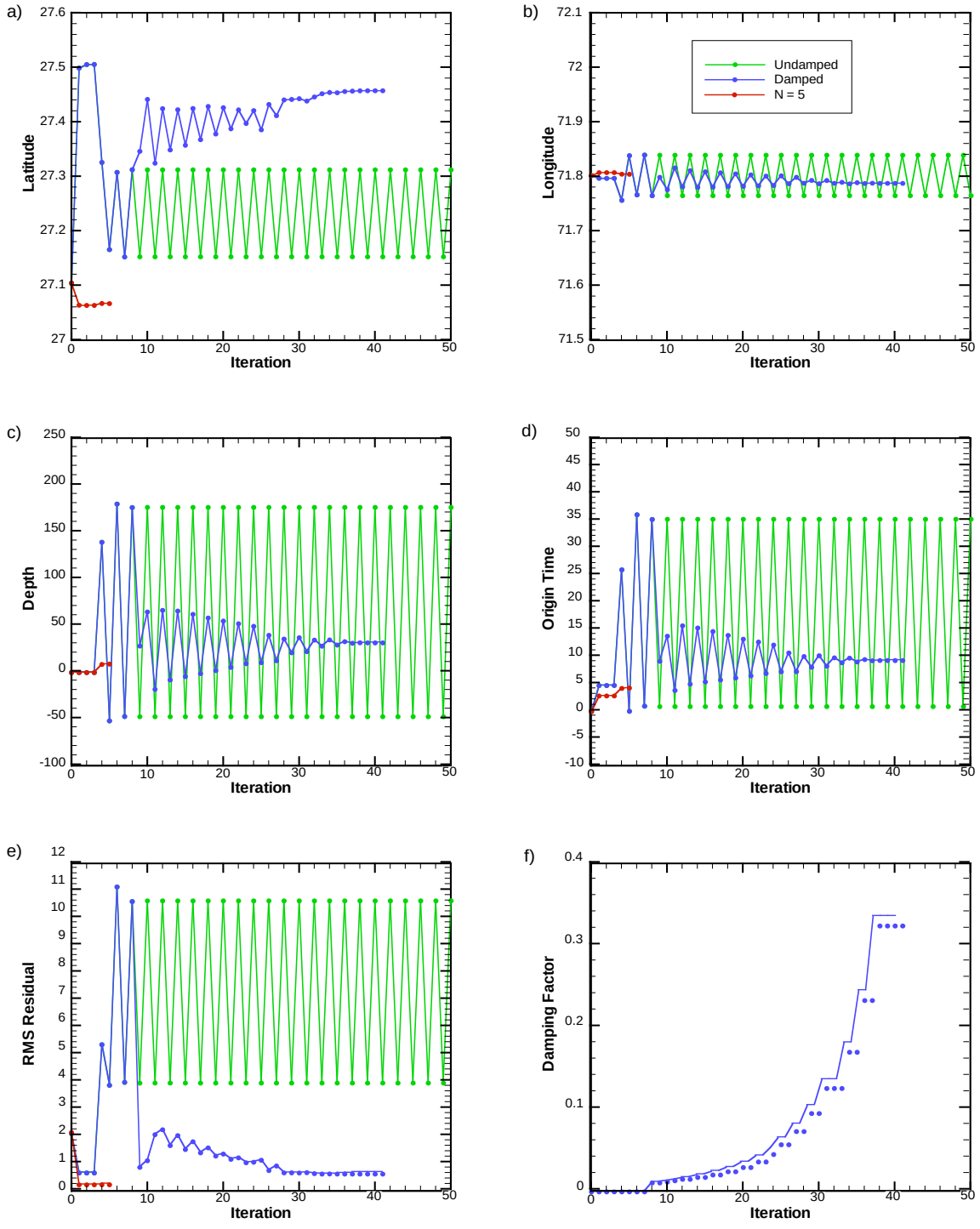

Figure 1 – The seismic event location, root mean square weighted residual and applied damping factor as a function of iteration number. The green curve illustrates the evolution of the undamped solution, which never converged, while the blue curve illustrates the damped solution. The red curve portrays the evolution of the solution obtained when the Sn phase was omitted from the data set.

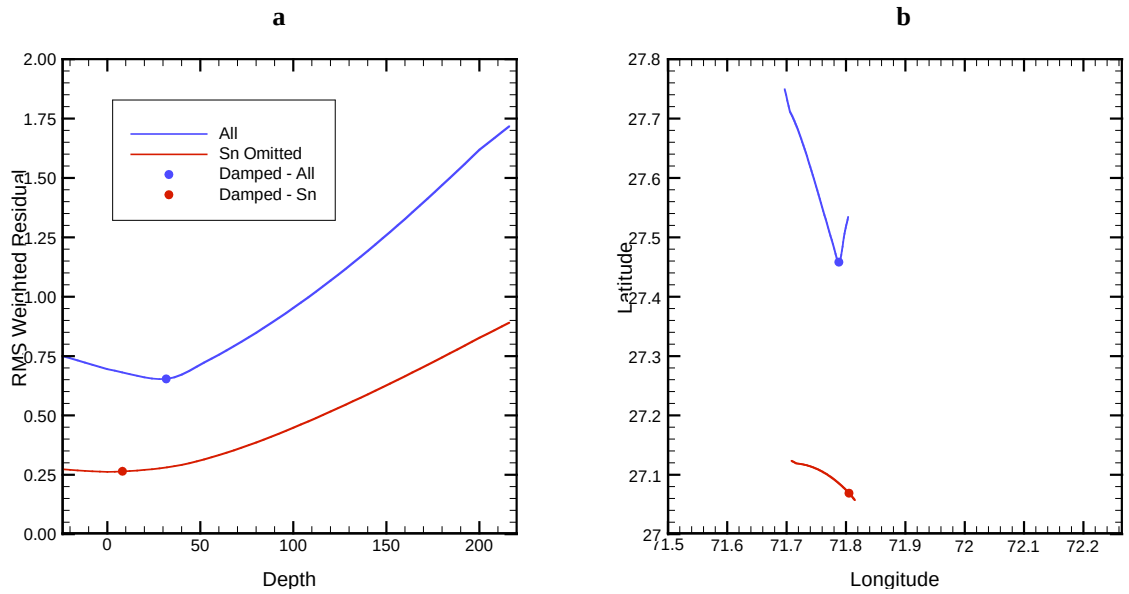

Figure 2 – a) Curves illustrate the root mean square weighted residual as a function of depth with depth held fixed at different levels. b) The curves illustrate the projection of the best-fit latitude and longitude onto a common horizontal plane when the depth was held fixed at different levels. In both figures, the symbols represent the position of the best-fit damped solution when depth was not held fixed. Blue curves and symbols represent solutions when all 6 observations were included, Red curves and symbols represent solutions when the Sn observation was omitted from the analysis.

substantially, as illustrated by the red curves in Figures 1 and 2. In Figure 2b, the kink in the latitude-longitude curve has disappeared indicating that the severe non-linearity, which was apparently introduced by the Sn observation, has disappeared. In Figure 1, the solution moves very quickly to convergence without exhibiting any oscillatory behavior.

While the problem can be resolved by discarding observations, that is a highly undesirable solution to the problem. A better alternative is to damp the solution vector such that the location changes by smaller amounts at each iteration, ultimately converging on the best-fit solution. This damping must be properly imposed however, such that the solution continues to move toward c^2_{min}. The appropriate course is to impose an additional constraint on the system, over and above the constraint that we seek to minimize c^2.

The additional constraint is that we wish to also minimize the length of the solution vector (Menke, 1989). These two constraints compete with other so by adding the minimum length constraint, we weaken the c^2_{min} constraint. Total minimization of the solution length alone would be accomplished by setting all the singular values to infinity, in which case the solution vector would consist of all zeroes and its length would be zero. We combine the c^2_{min} and minimum length constraints by adding a constant damping factor, ε, to each element of **W**. Equation 17 and 18 become

$$\delta\mathbf{m} = \mathbf{V}\,(\mathbf{W} + \varepsilon\mathbf{I})^{-1}\,\mathbf{U}^{T}\,\mathbf{r} \tag{19}$$

and

$$\delta\mathbf{m} = \sum_{i=1}^{M} \frac{\mathbf{U}_i\,\mathbf{r}}{w_i + \varepsilon}\,\mathbf{V}_i \tag{20}$$

Since ε appears in the denominator of Equation 20, it acts to reduce the magnitude of the changes in the location parameters in each iteration. So long as ε is not too large, the minimum c^2 constraint will dominate and the solution

will continue to move toward $c^2_{\min}$. This is precisely the behavior needed to overcome the oscillations induced by non-linearity. The trick is to impose sufficient damping to overcome the oscillations but not to impose so much that the solution stops moving before it reaches $c^2_{\min}$.

The algorithm we have implemented to accomplish this begins by initializing the applied damping factor, ε, to zero at the start of the location algorithm. If, after some minimum number of iterations, c^2 is observed to increase over its value at the conclusion of the previous iteration, the applied damping factor is set to some small initial damping factor, ε_0, which is typically some small fraction of the largest singular value. After each successive iteration, if c^2 is observed to increase over its value at the conclusion of the previous iteration, then the applied damping factor is multiplied by an additional factor, h, which consists of two components, h_{const} and h_{factor}, with

$$h = h_{const} + h_{factor} \frac{iteration}{\max iterations} \tag{21}$$

where *iteration* is the current iteration number and *maxiteration* is the user-specified maximum number of iterations that the algorithm is allowed to implement before aborting. Typically, both h_{const} and h_{factor} are set to equal 1. In this case, ε grows very slowly early during a run but then grows very rapidly as the maximum number of allowed iterations is approached. Experience indicates that this algorithm allows the solution to reach convergence before the damping factor gets to be so large that the solution no longer moves.

Application of this algorithm to the example problem is illustrated by the blue curve in Figure 1. The damping factors imposed as a function of iteration number are illustrated in Figure 1f. The maximum number of iterations allowed was set at 100. Oscillations are detected after just a few iterations and the damping factor begins to increase. After about 36 iterations, the solution has stabilized and oscillations, while still occurring with very small amplitude, are no longer discernible at the scale of the illustration in Figure 1. Finally, after 42 iterations, the algorithm converges. The fact that the algorithm converged on the "correct" solution is illustrated in Figure 2b, where the small symbols represent the solutions obtained with the damped algorithm just described. In all cases, the damped algorithm achieved solutions characterized by the minimum of c^2 as determined by the multiple fixed depth runs.

It is interesting to note that the $c^2_{\min}$ solution occurs very near the base of the crust at 30 km depth even though the event that produced the observations is known to have occurred at the earth's surface. Note also that the solutions obtained when the observation that induced the non-linearity was omitted occur at a much shallower depth than the non-linear solutions. One might speculate that the non-linearity induced by the particular combination of observations used in the analysis somehow pulled $c^2_{\min}$ to the point in the model space where the non-linearity was most pronounced. If this is the case, then the minimum sum squared weighted residual solution, whether obtained by the damped linear least squares algorithm or by any other solution algorithm that seeks to minimize c^2, might be misleading. The importance of this hypothesis must be kept in perspective, however, given that the uncertainty on the depth in the example presented is large (± 550 km), even compared to the amplitude of the oscillations encountered. This issue is the subject of continuing investigation.

CONCLUSION AND RECOMMENDATION

In this paper, we have reviewed the mathematical basis of the linear least squares inversion algorithm, which is the most widely used algorithm for estimating seismic event hypocenters and origin times. We have placed particular attention on the assumption of linearity of the predictions of the observations with respect to the seismic event location, showing how the assumption arises in the derivation and discussing the implications of the assumption. Finally, using a sample data set drawn from the full set of observations generated by the May 1998 India nuclear test, we explored the benefits of using damping in the linear least squares inversion technique to improve its performance in situations where the linearity assumption is violated.

REFERENCES

Lay, T. and T. C. Wallace (1995), *Modern Global Seismology*, Academic Press.

Menke, W. (1989), *Geophysical Data Analysis: Discrete Inverse Theory*, Academic Press.

Press, W. H., S. A. Teukolsky, W. T. Vetterling and B. P. Flannery (2002), *Numerical Recipes in C++, The Art of Scientific Computing*, 2nd Edition, Cambridge University Press.

PROBABILITY DENSITY FUNCTIONS FOR SECONDARY SEISMIC PHASE ARRIVALS

Eric A. Bergman[1] and E. R. Engdahl[2]

Global Seismological Services[1] and University of Colorado[2]

Sponsored by Defense Threat Reduction Agency

Contract No. DTRA01-02-P-0168

ABSTRACT

Seismic sources can be easily located with high confidence using only first-arriving P phases when there are large numbers of recording stations, well distributed in azimuth and distance. This is seldom the case, however, for seismic sources of interest to the nuclear explosion monitoring community. In cases of poor azimuthal distribution or small numbers of recording stations, improved accuracy may be gained by incorporating arrival times of secondary phases, but only if phase associations and weighting can be done in a statistically-valid manner. Under this project, we are developing a methodology to use probability density functions (PDFs) for this purpose, with the ultimate goal of making the use of secondary phases a standard part of routine earthquake location procedures. Following Buland (1986) we model the PDFs as a combination of Gaussian and Cauchy distributions, and we explore the usefulness of allowing the relative proportions of these parent distributions to vary for different phases. Sets of PDFs (for secondary phases of interest) are closely tied to the data sets from which they are derived, because the observability of different phases depends on the instrumentation, processing, and analysis procedures employed by contributing stations. A standard methodology for deriving estimates of PDF sets from different data sets is presented, with preliminary results of the analysis of two important arrival time data sets: a subset of ~17,000 well-located seismic sources from the International Seismic Centre (ISC) catalog, processed according to the methodology developed by Engdahl, van der Hilst, and Buland (the EHB standard, Engdahl *et al*, 1998), and an equivalent data set of arrival times from the Center for Monitoring Research. We propose an algorithm for phase association and weighting, based on these PDF sets, and compare locations of test data sets using traditional and PDF-based location methods.

OBJECTIVE

The objective of this research is to develop methodologies to characterize the distributions of secondary seismic phase arrival times in ways that facilitate their use in earthquake location algorithms. The statistical properties of these distributions should be used both in the association (phase identification) process and in weighting of data for inversion.

RESEARCH ACCOMPLISHED

Introduction

Very little research has been accomplished as of the date of submission of this paper, which is only two weeks after the start date of this contract. We have begun assembling the first data set for this study, and this is described below. The remainder of this section provides an introduction and motivation for this research.

This project focuses on several aspects of the earthquake location problem related to the use of secondary phases. These issues are related to the statistical properties of secondary phase arrivals and the optimal handling of those properties in a location program. We are developing methodologies by which these statistical properties can be utilized to give more accurate hypocenters with more accurate uncertainties. Failure to address these problems, while adding secondary phase data to the routine processing pipeline, may well lead to poorer estimates of seismic source parameters than if first-arriving phases alone were used.

Because of the differences in their missions, there are some important differences between the approaches of the earthquake and nuclear explosion monitoring communities in regard to location methodologies. The nuclear explosion monitoring community typically prefers to work with small networks of well-characterized, very high quality seismic stations, especially seismic arrays, while the earthquake community prefers to work with the largest possible set of data, regardless of instrumentation or quality. The nuclear explosion monitoring community is most concerned with location of seismic sources at regional distances, up to about 2000 km, whereas the earthquake community operates at every scale up to global. Earthquake data centers still depend heavily on reported "picks" from cooperating seismic stations, while nuclear explosion monitoring is done with highly trained analysts making the picks of arrival times from waveform data with standardized software and procedures. This additional (and substantial) effort is justified by the need to obtain the highest possible accuracy for small seismic events observed by small numbers of stations.

Despite these differences, the computer algorithms used for this purpose at organizations engaged in monitoring research (Center for Monitoring Research, CMR) or operational monitoring (International Date Centre [IDC], Vienna) are little different from those in use at major earthquake data centers such as the US Geological Survey's National Earthquake Information Center (NEIC), or the International Seismological Centre (ISC) in England. All these programs place more or less severe restrictions on which phases may be utilized other than first-arriving P phases. Other features in common among these programs are a rather crude treatment of phase association, reading errors, and weighting; although these problems exist even for the first-arriving P phase, they are especially severe for secondary phases. In fact, the limited use of secondary phases is, to a large extent, the result of concerns about how to handle these issues.

Use of Secondary Phases

For a number of years the preferred travel-time tables for nuclear monitoring only listed P waves (Herrin *et al*., 1968). The advantage, of course, is that, being the first arriving phase, it is relatively easy to select an onset time and associate it correctly as the P (or Pn, or PKP, depending on epicentral distance). An advantage of using only P waves is that this method more easily satisfies the requirement of the least squares regression used to solve the location problem, that all data (arrival time picks) are samples of the same random variable. However, even this useful simplification is invalidated when arrival times are selected from different instruments (one of the reasons for the WWSSN).

The use of S waves has now become quite common in local seismic network operations, especially since the ready availability of 3-component instruments. It is feasible because reasonably compatible P and S velocities can be

specified for small regions. Use of S and other secondary phases in location work at regional and global scales has been inhibited by concerns about baseline differences between different phases in the Jeffreys-Bullen (1940) Tables (a particular problem for S waves). This problem is partly resolved by IASPEI91 (Kennett and Engdahl, 1991) and related travel-time models that specifically seek the best *average* one-dimensional (1-D) global travel-time model for all main phases. Still, there are significant baseline offsets observable between different phases along particular source-station paths, reflecting lateral heterogeneity. This problem is worst at regional distances.

Use of secondary phases in the earthquake location algorithm is an obvious and extremely attractive way to increase the amount of data available to locate small seismic events that are observed by small numbers of stations—the most interesting situation in nuclear explosion monitoring. There are several obstacles to be overcome if secondary phases are to be incorporated successfully into routine monitoring work. By "success" we mean that the statistical properties of secondary phase readings are properly carried through the location algorithm. If this is achieved, use of secondary phase data cannot degrade the solution (although it may not improve the solution much). If statistical properties are not properly incorporated, there is a significant chance that the solution will be biased.

First of all, the arrival time of the phase must be picked in a consistent manner. Secondly it must be associated with a phase in order to calculate theoretical travel times. Then, a weight must be assigned. It is tempting to think that the first step is the most important, but in fact there has been little if any research to support that belief. This project deals with the latter two steps. Before we discuss them, however, it is necessary to say something about the characterization of probability density functions for seismic phases.

Probability Density Functions for Seismic Phases

It is well known that the probability density functions (PDFs) of seismic phase arrival time residuals can be adequately described by a Gaussian only in the near vicinity of the mean. A full description requires the superposition of a second distribution to account for the “long-tailed-ness” of real seismic residuals. Buland (1986) has shown that P residuals can be well modeled with a combination of a Gaussian and a Cauchy distribution (Evans *et al*., 2000). We will use this approach to describe the PDFs of secondary phases from selected data sets, but we will not assume that the relative proportions of Gaussian and Cauchy are constant among all phases, nor at all distances and depths. In doing this, we must recognize that allowing this variability violates the assumption of least squares concerning a common random variable and must investigate the consequences.

Phase Association

Driven by the need to monitor nuclear tests by other countries, earthquake location programs were among the first applications of computers in science, in the early 1960s (Engdahl and Gunst, 1966). These algorithms have changed remarkably little in 40 years. Perhaps the biggest change has been the widespread adoption of the IASPEI91 travel times and associated "tau-p" method of generating travel times (Buland and Chapman, 1983; Kennett and Engdahl, 1991) to replace the Jeffreys-Bullen Tables (Jeffreys and Bullen, 1940). The IASPEI91 model has been superseded by AK135 (Kennett *et al*., 1995) for standard global earthquake location work. The changes in AK135 were adopted to improve agreement between all secondary phases and primary phases. One important consequence of this change is that phase association has been made easier, by making it possible to easily compare theoretical travel times of many candidate phases with an unidentified reading. From a statistical point of view, however, this is far from an adequate solution.

Travel-time "curves", such as those generated using IASPEI91 and the tau-p software, have no reality, being simple representations of complex distributions of reported phase arrival times, with variability arising from mislocation of sources and stations, errors in time-keeping and reporting, uncertainties in picking, instrumentation differences, and—most importantly—lateral variations in Earth's structure. Phase association is a statistical process: regardless of how carefully a pick is made and how well a pick fits a travel-time curve, some doubt must remain. If the statistical nature of phase association is disregarded, the uncertainties of the calculated hypocenter must surely be biased.

The traditional statistic (truncation approach) used for phase association is simply the offset from a baseline, or residual against a travel-time curve. A fuller representation includes a measure of the spread of the distribution, as a function of epicentral distance and source depth, and a measure of the number of hits in the sample from which the

statistics are estimated, also as a function of distance and depth. It is extremely important to choose carefully the dataset from which the statistics are estimated, to reduce the effect of uncontrolled factors. For example, if one wished to determine statistical properties of secondary phase readings for use by the IDC in Vienna, it would be best to work with the dataset of readings in the Reviewed Event Bulletin (REB), and perhaps only a recent subset of the REB if there have been significant changes in procedures or data sources.

As first discussed in Engdahl *et al*. (1998) there is a serious negative consequence of the traditional method of phase association, in which the arrival is assigned to the most likely phase, i.e., the one whose travel-time curve is closest. It is common that two phases will be close to each other, such that their PDFs overlap significantly over a certain distance range. Then the standard procedure is equivalent to truncating each distribution at the point where their probabilities are equal, leaving a longer tail on the other side. The distributions are strongly distance-dependent, becoming more asymmetric as the phases converge. Then, if one were to use these data to estimate a revised "best" (mean) travel time of the phases, the estimate would be biased for both phases, such that they would diverge.

Engdahl *et al*. (1998) developed a solution to this problem for a limited application -- a suite of depth phases (pP, sP, pwP, and PcP) that frequently occur in close proximity. Having estimated the PDFs of these phases, including their relative amplitudes ("observability"), they devised an algorithm to "roll the dice" and assign an arrival to a phase based on the PDFs (Figure 1). Thus, an arrival might be assigned to a phase whose probability is not the highest at that point. Although the location of the earthquake that generated these arrivals will be similarly biased, the greatest concern may be the threat to the statistical integrity of the larger dataset. Because progress in seismology builds on previous work, it is extremely important to avoid introducing systematic biases into the database as a whole.

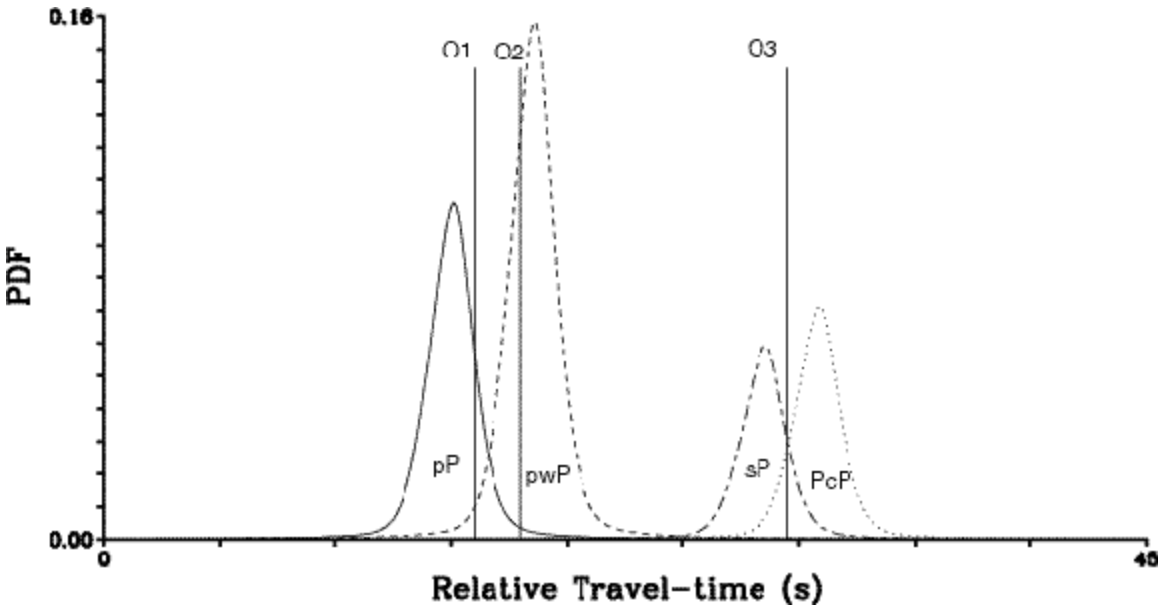

Figure 1. Probability density functions (PDFs) for four phases (pP, pwP, sP, and PcP) centered at their theoretical relative travel times from a hypothetical deep event and hypothetical observed phases (O1, O2, and O3) with unknown identifications (from Engdahl *et al*. 1998).

Like Engdahl *et al*. (1998), we will design the association algorithm to simultaneously associate all readings from a given station, forbidding more than one reading to be associated with any given phase. It is also possible for an arrival to be unassociated in this algorithm. In a statistical sense, this is required, as it is entirely possible for a reading to be made from a pulse of energy on a seismogram that has no relationship to the earthquake of interest.

Weighting of Secondary Phases

The uncertainty of derived hypocentral parameters is completely controlled by the weights assigned to the data. Computationally, the weights can be anything. Given the formulation of the location problem as a minimization of

the sum of squared errors, and the need to normalize the equation, the only sensible interpretation of weights is in terms of the uncertainty of the readings. In some circumstances it can be acceptable to assign a standard weight to all data; the location itself will not be effected by error in the assigned weight, but the size of the confidence ellipse will be scaled inversely to the weight.

In discussing weights (uncertainties) in location programs, it is important to retain the distinction between uncertainties arising from the picking of the reading from a seismogram and the uncertainty in the theoretical travel time used to calculate the residual. In the nuclear monitoring case (unlike the case of bulletin data), where analysts pick the readings, a direct measure of reading error is possible. Even in the case of bulletin data, it is possible to estimate reading error by multiple event location of clusters of events, because the contribution of the travel-time error is largely removed.

Using this information, it is possible to remove the contribution of reading errors from the PDFs of phases and reveal the PDF associated with lateral heterogeneity in the corresponding dataset. Then this PDF can be properly combined with the actual reading error of individual readings, which will constitute a far more rigorous statistical model than is currently used.

Secondary phase residuals at regional distances exhibit quite large scatter, such that if these readings are weighted inversely to variance, they may contribute almost nothing to the solution. It has been suggested that these phases are simply too difficult to pick. Multiple-event relocation studies (Engdahl and Bergman, 2001) reveal, however, that much of the scatter arises from lateral heterogeneity and from misassociation of phases. Many stations at regional distances consistently pick Pn arrivals from a given cluster (thus minimizing the effect of lateral heterogeneity) with a scatter of no more than a few tenths of seconds, comparable to the scatter of teleseismic arrivals (Figure 2). Remaining large residuals are often attributable to misassociation. The large effects of lateral heterogeneity also have important consequences for the phase association problem, in that arrivals may be far from their "correct" association.

Therefore, to use secondary arrivals in a statistically meaningful way at regional distances, it is essential to begin to unravel the effects of lateral heterogeneity. Major research efforts (e.g., Levshin *et al*, 2001) are addressing the problem of modeling lateral heterogeneity in the crust and upper mantle over large regions, but location algorithms need to be modified to incorporate statistical representations of that heterogeneity. To that end, we propose to investigate the signature of lateral heterogeneity in selected datasets of secondary phase data.

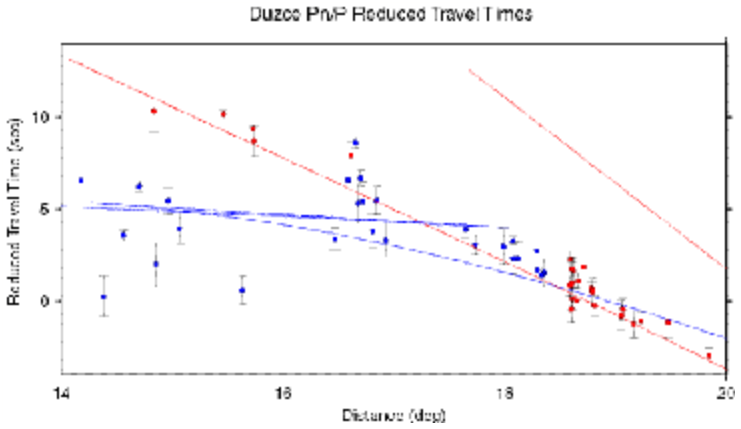

Figure 2. Path corrections at regional distance from the 1999 Duzce, Turkey, earthquake, estimated from multiple-event re-location and co-location with known ground truth events (located by a high-density aftershock network). Arrivals were re-associated. Path corrections are plotted against reduced P and Pn travel times for the distance range 14 to 20 degrees. Phases identified in this study as Pn arrivals are plotted in blue and as P arrivals in red. Phase identification in this distance range is complicated by the Pn triplication and by the arrival of a P phase bottoming in the transition zone. In particular, near 18 degrees (keeping in mind the +1 sec bias) phases identified as first arriving Pn could just as easily be associated with phase branches corresponding to P or the Pn cusp. From Engdahl and Bergman (2001).

A Global Dataset of Secondary Phase Arrivals

Our first dataset for secondary phase arrivals is derived from the EHB catalog of earthquakes (Engdahl *et al*, 1998). We chose not to use the entire EHB catalog, for three reasons. First, our primary goal of developing new methodologies for analysis of secondary phases would be hindered by the sheer size of the dataset. Second, the quality of the locations of the EHB events is quite variable, leading to excessive scatter in residuals. Finally, the natural distribution of seismic sources in the EHB catalog is quite unbalanced; interaction between the concentration of seismicity and stations in certain regions of the world with the lateral heterogeneity of the Earth will introduce undesirable correlations in the dataset of travel-time residuals.

We addressed all three problems by filtering the catalog with several criteria designed to produce a smaller, but higher quality, dataset of secondary phase arrival times from a set of events that is more evenly distributed around the globe than the raw EHB catalog. A "desirability" index D was calculated for each event, as the product of three terms:

$$\max[(1-(5.6-mag)^2),0]\times\frac{\sqrt{nlat}}{10}\times\max[\frac{(180-sazgap)}{180},0]$$

where *mag* is magnitude, ***nlat*** is the number of secondary phase readings, and ***sazgap*** is the secondary azimuth gap. With these values, events with magnitude less than 4.7 or greater than 6.5 will always have D=0, as will events with no later phase readings and events with a secondary azimuth gap of more than 180 degrees.

Our strategy for choosing a set of optimally distributed events is to divide the Earth into bins approximately 100 km on a side and 75 km in thickness (10 layers in depth). The events in each bin are ranked according to their desirability index D (with a minimum acceptable value of 0.1) and the five highest ranked events are retained for analysis.

The input dataset was a recent update of the EHB catalog, complete from 1964-1999, and pre-screened to remove events with obvious problems. The resulting dataset contained 315,595 events. The selection algorithm reduced this to 17,609 events sampling 6069 bins. There are 5.5 million phase readings associated with these events, an average of 315 per event, but the majority of these are first-arriving P phases.

We have further reduced the size (to 8663 events) of this dataset for our initial analysis, by selecting events with source depths less than 35 km and keeping only readings at epicentral distances less than 20° (Figure 3). The case of regional arrivals from shallow sources is, of course, of greatest relevance to the nuclear explosion monitoring community. We will eventually examine readings from other depth and distance ranges to build a complete picture of the statistical properties of secondary phases.

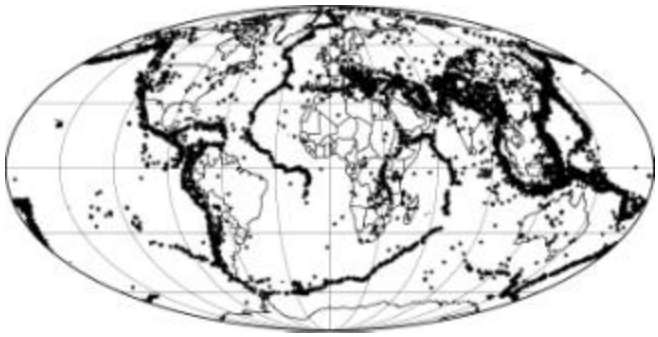

Figure 3. More than eight thousand (8,663) events selected for analysis of secondary phases at regional distances from shallow sources. Events shown have depths of less than 35 km and have readings at less than 20° epicentral distance. Most major seismic zones are represented, but a few portions of the mid-ocean ridge system are lost by these criteria.

The nearly-400,000 phase readings in this dataset are shown in Figure 4. The main features of the plot are the combined Pn and Sn arrivals. This kind of display tends to hide the complexities of back branches and triplications, although one can see signs of such features in the P data beyond about 12°.

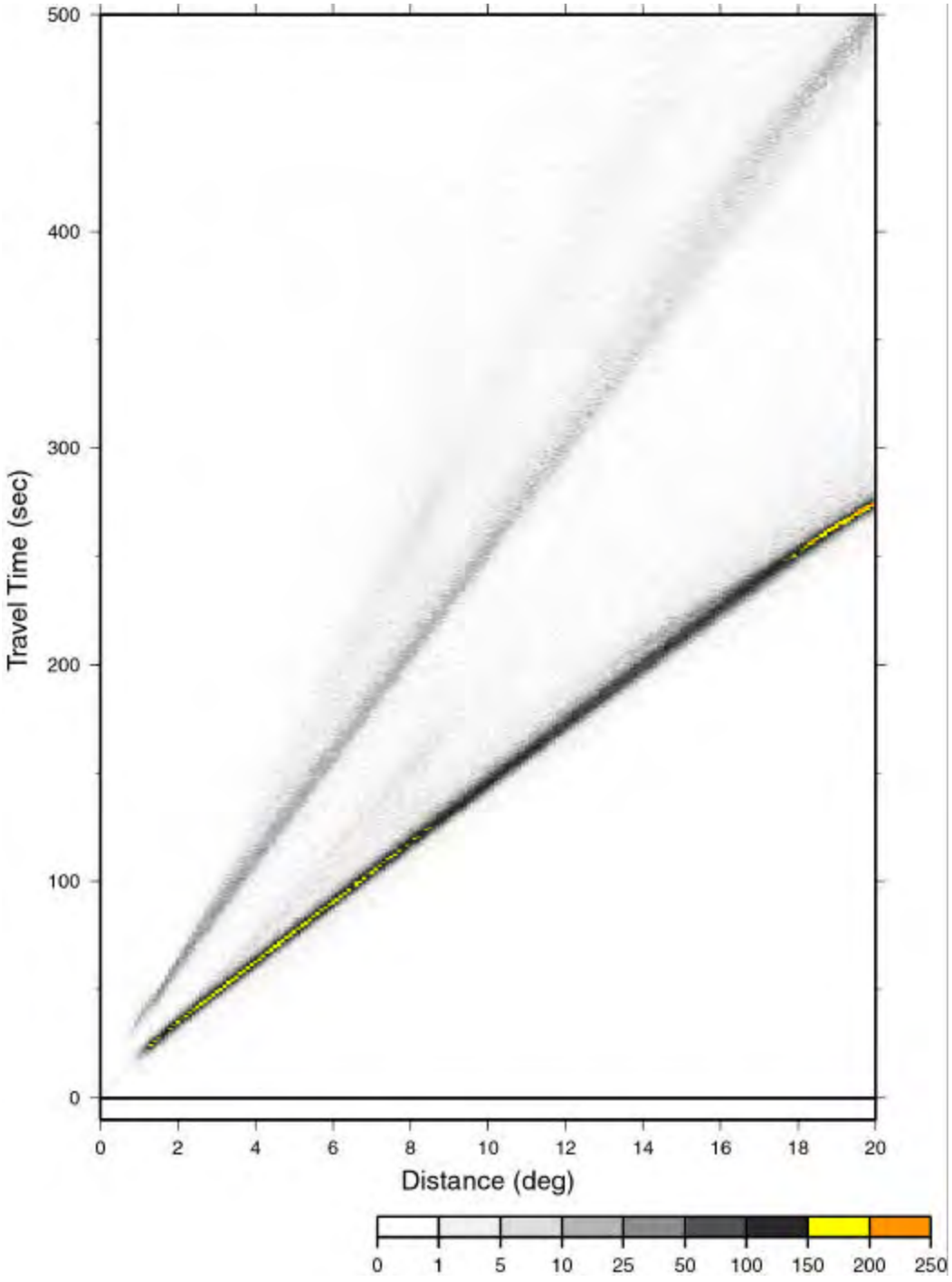

Figure 4. Density plot of all phase readings at distances less than 20° for the 8663 shallow (h<35 km) events in Figure 3.

The complexities of these distributions are revealed by density plots over smaller distance ranges, with a reduced time base, such as shown in Figure 5. Note that there appear to be very few observations associated with the back branch of P between 18 and 20°, nor with the cusp of Pn near 18°. However, the back branch of P extending to 14° is relatively well recorded.

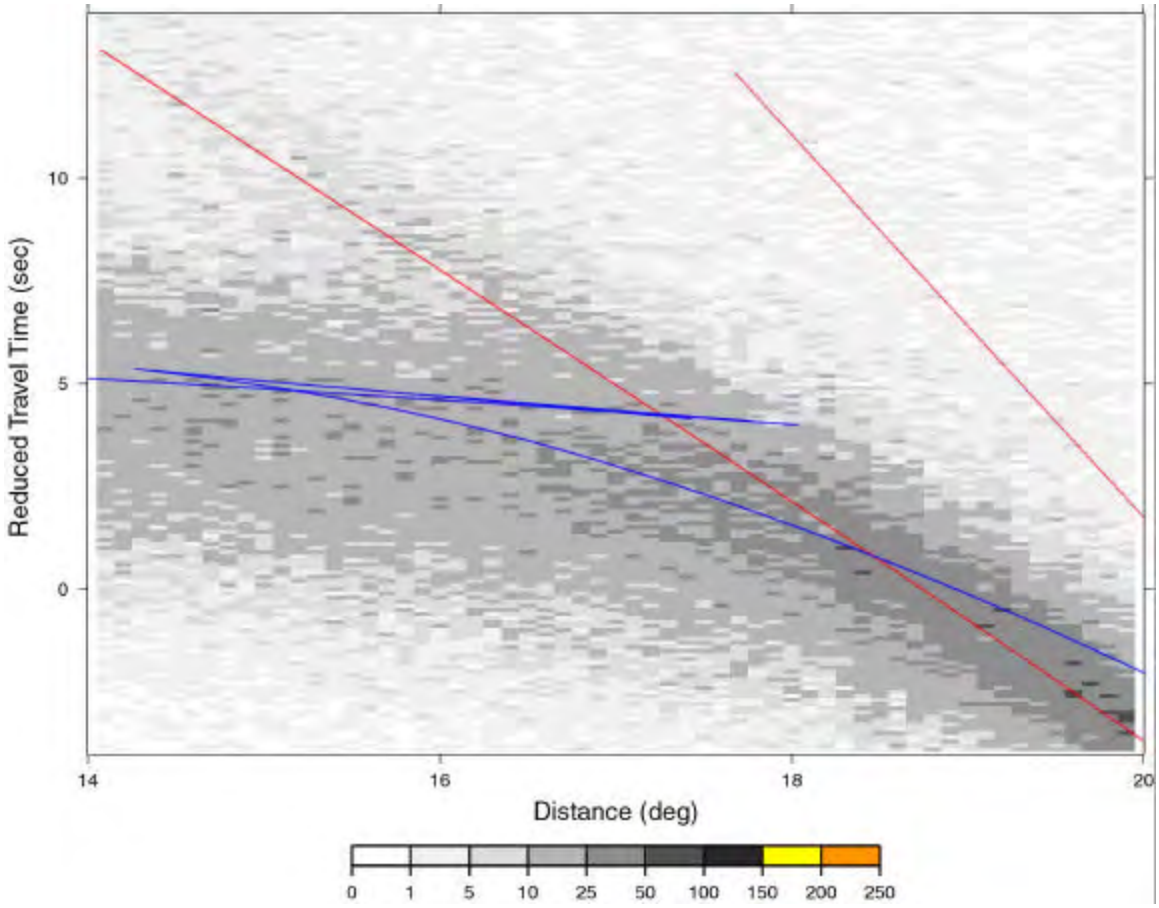

Figure 5. Density plot of phase readings near the Pn/P cross-over. Theoretical travel times (AK135) of Pn branches are shown in blue. Theoretical travel times of P branches are shown in red; travel times reduced with a velocity of 8 km/s.

Our analysis of such data will attempt to define PDFs for each significant branch in the data, including the regions where branches cross each other. Other investigations (Figure 2) indicate that much of the scatter observed in Figure 5 is caused by lateral heterogeneity (model error), not the inherent errors in reading these phases. Therefore, the PDFs determined will be strongly influenced by the particular dataset being analyzed. A subset of station-event pairs that sample a common path should display considerably tighter distributions than Figure 5. This will be tested. We should expect that different sets of PDFs will be preferred for different purposes (e.g., global monitoring vs. focused regional monitoring), which highlights the need for standard methodologies for determining PDFs from whatever dataset is of interest.

CONCLUSIONS AND RECOMMENDATIONS

No conclusions are reached at this preliminary stage of the investigation, except that it would be much more satisfying to be doing the research than writing about the results we hope to achieve.

REFERENCES

Buland, R. (1986). Uniform reduction error analysis, *Bull. Seism. Soc. Am.* **76**, 217-230.

Buland, R. and C. Chapman (1983). The computation of seismic travel times, *Bull. Seism. Soc. Am.* **73**, 1271-1302.

Engdahl, E. R. and R. H. Gunst (1966). Use of a high-speed computer for the preliminary determination of earthquake hypocenters, *Bull. Seism. Soc. Am.* **56**, 325-336.

Engdahl, E. R., R.D. Van der Hilst and R.P. Buland, Global teleseismic earthquake relocation with improved travel times and procedures for depth determination, *Bull. Seism. Soc. Amer*., **88**, 722-743, 1998.

Engdahl, E. R. and E. A. Bergman, Validation and Generation of Reference by Cluster Analysis, Location Workshop (oral presentation) and 23rd Seismic Research Review (poster presentation), Jackson Hole, WY, 1-5 October 2001.

Evans, M., N. Hastings, and B. Peacock (2000), *Statistical Distributions*, 3rd Ed., Wiley & Sons, New York, 221 pp.

Herrin, E., W. Tucker, J. Taggart, D. W. Gordon, and J. L. Lobdell (1968), Estimation of surface focus P travel times, *Bull. Seism. Soc. Am.*, **58**, 1273-1291.

Jeffreys, H. and K. E. Bullen (1940). *Seismological Tables*, British Association for the Advancement of Science, London.

Kennett, B. L. N. and E. R. Engdahl (1991). Travel times for global earthquake location and phase identification, *Geophys. J. Int.* **105**, 429-465.

Kennett, B. L. N., E. R. Engdahl, and R. Buland (1995). Constraints on seismic velocities in the Earth from travel times, *Geophys. J. Int.* **122**, 108-124.

Levshin, A. L., M. H. Ritzwoller, N. M. Shapiro, E. R. Engdahl, M. P. Barmin, and E. A. Bergman (2001), The use of a 3-D model to improve regional event locations (abstract), *Eos Trans. AGU*, **82***(47)*, Fall Meet. Suppl., Abstract S12A-0582, 2001.

A REFERENCE DATA SET FOR VALIDATING 3-D MODELS

E. R. Engdahl, Eric A. Bergman, Michael H. Ritzwoller, Nikolai M. Shapiro and Anatoli L. Levshin

University of Colorado, Boulder

Sponsored by Defense Threat Reduction Agency

Contracts No. DTRA01-00-C-0032 and DTRA01-99-C-0019

ABSTRACT

High-resolution cluster analysis (multiple-event relocation) of earthquakes and other seismic sources has been developed as a tool for assembling catalogs of reference events, especially those whose locations can be determined with an accuracy of 5 km or better (ground truth [GT] 5). We use the Hypocentroidal Decomposition (HDC) method of Jordan and Sverdrup (1981), which is well suited to the rigorous statistical analysis required for this task. An ongoing task is the identification and collection of potential reference events monitored by local seismic networks or recorded during temporary aftershock deployments. Cluster analysis is used with arrival-time data reported to the International Seismological Centre (ISC) and United States Geological Survey National Earthquake Information Center (USGS/NEIC) at regional and teleseismic distances to validate these reference events and to generate new GT5 reference events. The resulting catalog and derived parameters, such as empirical estimates of source-station path anomalies, provide a reference data set that can be used in experiments designed to validate three-dimensional (3-D) models of the region of interest.

To date HDC analyses have been performed on 26 earthquake and explosion sequences across Eurasia and North Africa. We examine the characteristics of our cluster data using, for example, plots of combined Pn/P residuals (corrected for origin time offset) at regional distances. For residuals in the range +/-15 sec, both raw and trimmed data show similar variations of median and spread as a function of distance, with a maximum spread near 12-13 degrees. Similar plots of empirical source-station path anomalies show a range of -7.5 sec to +5.0 sec, with maximum differences occurring at distances of 11 to 18 degrees where the influence of interfering travel-time branches makes phase identification difficult.

The University of Colorado (CUB) group has constructed from surface wave dispersion data a global 3-D S-wave velocity model of the crust and the upper mantle. S-wave speeds were converted into P-wave speeds based on laboratory-measured properties of mantle minerals and an average compositional model of the upper mantle. Regional path anomalies predicted by the CUB 3-D model are in much better agreement with empirical path anomalies derived by cluster analysis than with predictions made using a 1-D reference model (AK135). Moreover, agreement with the 3-D model predictions is significantly improved by re-identification of Pn and P phases (set during cluster analysis) based on the insights gained by ray tracing through the CUB model.

The CUB 3-D model is also used to relocate reference events either known exactly or validated by cluster analysis as GT5 or better. Culled Pn/P arrival-time data at regional distances are used with a grid search technique and with Source-Specific Station Corrections (SSSC's) derived from the CUB model to relocate the events. In a preliminary validation test, we find that the 3-D model improves locations relative to locations based on the 1-D model AK135 in 70-85% of all cases, with details depending on the number of reported phases used for relocation. Typically, the 3-D model reduces the location errors to about half the values attained with the 1-D model.

OBJECTIVE

The primary objective of this research effort is to develop a comprehensive reference event database with validated travel-time information for regional seismic phases recorded by International Monitoring System (IMS) and surrogate stations in Asia and North Africa. This database can be used to support the calculation of regional travel-time curves and source-specific station corrections (SSSC's).

RESEARCH ACCOMPLISHED

Introduction

There is a fundamental need for a validating data set of seismic events above the International Data Centre (IDC) event definition threshold (currently mb~3.75) with minimal systematic error of event location and from which reliable empirical estimates of source-station path anomalies with respect to a reference model can be determined. In this report, we first discuss the development of such a database by cluster analyses of earthquake and explosion sequences in Eurasia and northern Africa. We use primarily phase arrival-time data reported to the International Seismological Centre (ISC) and to the U.S. Geological Survey's National Earthquake Information Center (NEIC), or made available by other sources, that have been *groomed* using a procedure described by Engdahl et al., (EHB; 1998). The resulting catalog and derived parameters in this database provide a reference data set that can be used in experiments designed to validate three-dimensional (3-D) models of the region of interest. Such a 3-D model has been developed by the University of Colorado (CUB) group and is used in a validation test that compares model-predicted regional path anomalies with empirical path anomalies derived by cluster analysis. As an additional independent validation test, selected events derived by cluster analysis are relocated using only regional data in the 3-D model and compared to similar locations based on the 1-D model AK135 (Kennett et al., 1995).

Methodology

The cluster analysis used in this study is based on the Hypocentroidal Decomposition (HDC) method (Jordan and Sverdrup, 1981) for multiple event relocation. We seek situations where a number of moderate-size earthquakes are clustered (within about 50-100 km of each other) and where at least one of the events has been very well located by a local network. The events in the cluster may be widely distributed in time, as long as arrival-time data are available. This approach is fundamentally a high-resolution cluster analysis for relative event location, forming event clusters that contain one or more candidate reference events. In most cases, reference event data are available from short-term portable seismograph deployments following the initiation of seismic activity. The clusters typically are 50-100 km across and comprise up to 100 events of magnitude 3.5 or greater that have occurred since 1964 and that are well recorded at regional and teleseismic distances. The cluster is located in an absolute sense, as if all the data were from a single event, using the 1-D model AK135. The HDC analyses produce new locations that are defined by "cluster vectors" in space and origin time relative to the hypocentroid, which is then located in the traditional manner to yield absolute locations and origin times. Obviously, this process is subject to bias. To remove the bias, we shift the hypocentroid in space and time to provide an optimal match to one or more reference events that are included in the cluster. This brings all events in the cluster into close alignment with "ground truth". In addition, since the absolute locations and times of all the events in the cluster are now estimated with increased accuracy, many of the events in the cluster may now be "promoted" to reference event status at an appropriate GT level.

The degree of consistency between the relative locations as determined by global arrival-time data and the relative locations specified by the reference event data is one of the tests we use to validate candidate reference events. Shifts in epicenter and origin time (to best match the reference event locations) are typically in the range of 5-15 km and ± 2 seconds, respectively. We validate candidate reference events by requiring that the relative shift patterns of candidate reference events be consistent with the pattern of the corresponding cluster vectors from the HDC analysis. Discrepancies may be resolved by determining that the cluster vector is biased for some reason, or by rejecting the candidate reference event. For this reason, most clusters contributing to the database for this study are calibrated by several reference events.

Engdahl and Bergman (2001) have recently compiled a comprehensive database of well-located earthquakes and explosions that have been validated by cluster analysis. There are currently 23 clusters in this database: 6 explosion

clusters, most with source locations known to 2 km or better; 17 earthquake clusters, 12 that are believed to be accurate to 5 km or better; and the remainder 10 km or better. For each event, the database contains associated phase arrival times that were either reported to the ISC or NEIC or contributed by other sources. Hypocentroids for the clusters studied are plotted in Figure 1.

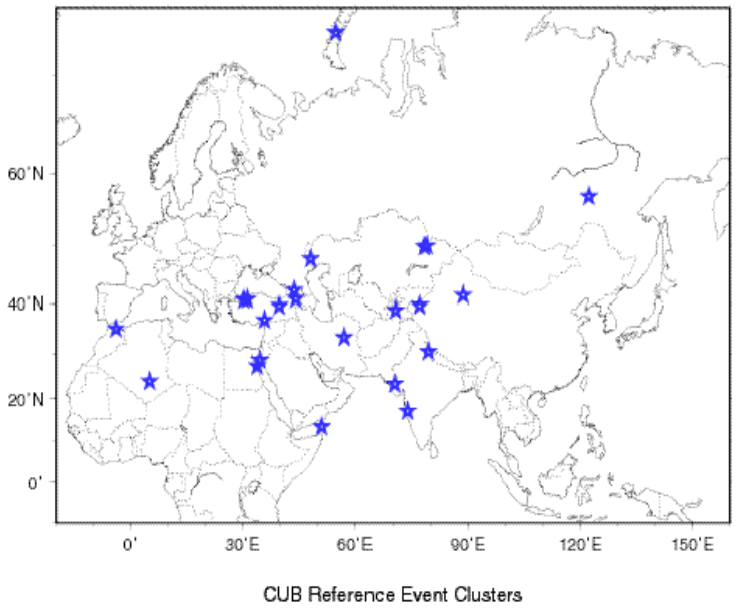

Figure 1. Locations of the explosion and earthquake clusters studied indicated by stars.

Parameters

Relevant parameters for all clusters studied are listed in Table 1. The location and depth given is for the *shifted* hypocentroid, representing the best fit to reference event locations. The origin time offset is the average difference between the reference event origin times and the origin times obtained by cluster analysis for those same events. Cluster origin times are basically set by the mean of station residuals at all distances. This is perhaps not the best way to make this estimate, as station coverage by distance range can vary (e.g., regional versus teleseismic), and we are considering alternative approaches. Nevertheless, those offsets are indicative of the differences between the crust and upper mantle of the real earth and that of the 1-D model AK135. Relative to AK135, positive offsets would indicate slower velocities and negative offsets faster velocities. On the other hand, the origin time offsets may also indicate errors in the reference event origin times that are normally fitted to within about +/-1 sec. These origin-time offsets can be quite large and, when plotted at their hypocentroid locations, (Figure 2) do seem to show a correlation with tectonic region.

Data

Another feature of our cluster analysis is that we use cluster residuals to estimate station-specific reading errors for each cluster. Use of these derived reading errors, as opposed to assuming standard fixed reading errors (which typically also include the effect of model error) for all arrivals, redistributes the data importance in the inverse problem, which changes the cluster vectors and the hypocentroid. Because of the way in which the HDC method decouples the problems of estimating cluster vectors and the hypocentroid, it is easy to use the derived reading error alone for the cluster vectors, and the reading error plus a separate estimate of model error for the hypocentroid. In the most common case, in which derived reading errors are—on average—smaller than what is usually assumed, the confidence ellipses of the cluster vectors are reduced in size.

Table 1. Cluster Parameters.

Table 1. Cluster Parameters

No.	Lat	Lon	Dep	dOT	nevt	nref	GTx	Name
1	36.938	35.825	33.6	-2.89	24	4	GT5	ADANA
2	13.513	51.069	10.0	-0.45	55	5	GT10	ADEN
3	28.754	34.608	14.0	-1.94	36	1	GT5	AQABA
4	47.875	48.139	0.1	0.53	7	7	GT1	AZGIR
5	49.954	78.871	0.0	0.81	100	100	GT1-2	BALAPAN
6	23.486	70.265	19.6	0.36	107	6	GT5	BHUJ
7	30.590	79.124	12.1	-0.18	86	8	GT5	CHAMOLI
8	49.784	78.072	0.0	0.66	151	146	GT1-2	DEGELEN
9	40.798	31.219	9.1	-0.64	41	2	GT5	DUZCE
10	39.588	39.805	6.4	-1.73	9	3	GT5	ERZIN
11	38.822	70.560	7.5	-1.55	28	4	GT5	GARM
12	27.482	33.864	12.8	-1.49	27	1	GT10	GUBAL
13	35.235	-3.930	6.2	-0.91	38	3	GT5	HOCEIMA
14	40.740	30.223	10.4	-0.51	34	5	GT5	IZMIT
15	39.660	76.988	19.6	-2.75	72	1	GT10	JIASHI
16	17.236	73.748	8.2	-0.29	31	10	GT5	KOYNA
17	41.580	88.605	0.0	0.43	20	13	GT1-2	LOPNOR
18	73.350	54.820	0.0	-1.65	29	28	GT1-2	NOVAYA
19	42.475	43.737	7.0	-1.28	35	5	GT5	RACHA
20	24.049	5.040	0.0	-0.08	5	5	GT0	SAHARA
21	57.092	122.276	31.5	-1.53	8	3	GT5	SIBERIA
22	40.957	44.215	5.6	-1.60	11	2	GT10	SPITAK
23	33.479	57.111	14.6	-1.95	35	2	GT10	TABAS

In columns left to right are listed: cluster number (No.); latitude, longitude and depth of cluster hypocentroid (Lat, Lon and Dep); origin-time offset (dOT), number of events forming each cluster (nevt); number of reference events used (nref); cluster GT level (GTx); and cluster name (Name).

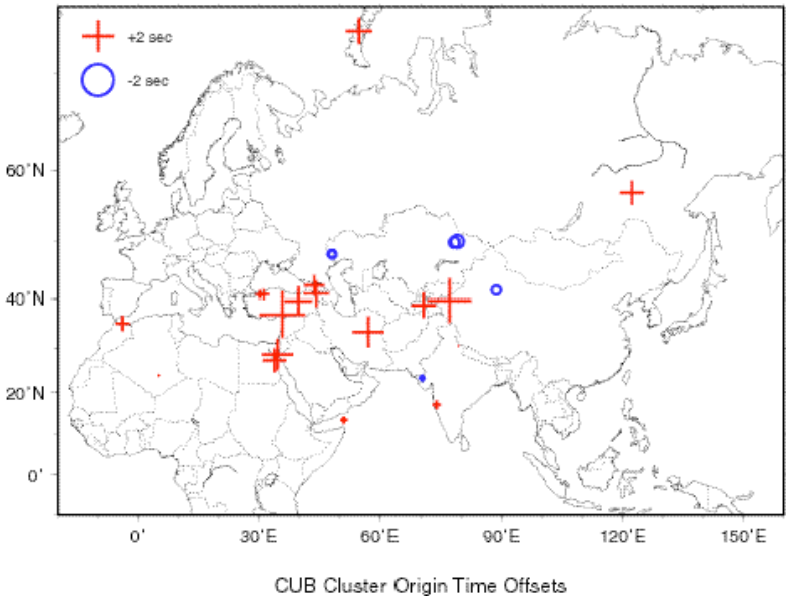

Figure 2. Cluster origin-time offsets. Scaling is given in upper left-hand corner. Earthquake clusters originating in tectonic regions of Eurasia generally have positive offsets, suggesting crust and upper mantle velocities slower than the reference model AK135.

In addition to obtaining more accurate locations, cluster analysis is useful in grooming the arrival-time data to identify and remove outliers. This is possible because cluster analysis estimates the average path anomaly for each seismic station that observes more than one of the events in the cluster. The residuals from this path anomaly are dominated by reading error as described above. Very large cluster residuals can be rejected as spurious readings, even if their absolute travel-time residual is small. Removing outliers in this way improves the resolution of relative locations and reduces the size of confidence ellipses. Figure 3 shows a plot of Pn and P residuals for all arrival times included in the cluster event database with outliers removed and with each cluster adjusted by its origin time offset. The plot is presented in this way so that the effects of anomalous path structure and station reading errors at regional distances are not confused with the effect of the average offset in residuals due to differences in upper mantle structure (relative to AK135). Not unexpectedly, estimates of the residual median and spread over one-degree distance bins show considerable variation over the regional distance range. In particular, residuals for Pn arrivals between about 9 and 17 degrees, corresponding to ray paths bottoming in the lithosphere well below the crust and perhaps encountering low-velocity zones, are more dispersed, with a maximum spread at distances of 12-13 degrees. A contributing factor to this dispersion at larger regional distances also could be the difficulty of phase identification between Pn and P in regions of highly complex structure where the cross-over distance between the first arriving branches of these phases can vary considerably.

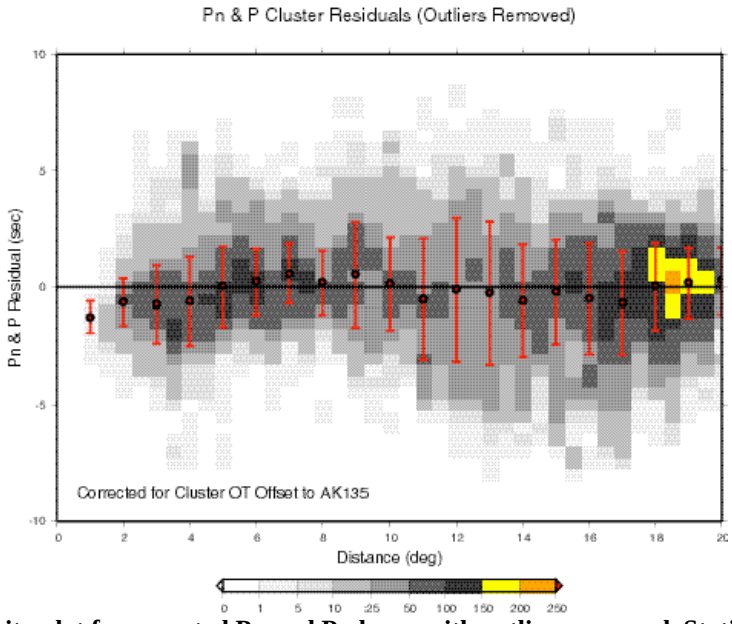

Figure 3. Residual density plot for reported Pn and P phases with outliers removed. Station cluster residuals corrected for cluster origin-time offset are binned at 0.5 degrees in distance and 0.5 sec in time. Bin hit counts are plotted according to the scale for number of hits at the bottom. Estimates of the residual median and spread at one-degree intervals are also over plotted as circles and vertical lines, respectively.

Path Anomalies

The expanded set of groomed residuals, relative to *shifted* hypocenters derived by cluster analysis, are now available to calculate source-station path anomalies. These anomalies are estimated relative to the 1-D reference model AK135 for regional seismic phases reported by IMS primary and surrogate seismic stations, and other seismic stations in the region of interest. This is a rather straightforward process by which, for each cluster, all groomed residuals are examined for phases of interest (Pg, Pn, P, Sg, Sn and S) at each of the reporting stations in that cluster. Medians and spreads are calculated for all these phases and the resulting source-station phase path anomalies accepted when minimum requirements of five observations and a spread of less than 1.40 sec and 2.8 sec is met for P-type and S-type phases, respectively. Ordinarily, there are too few Pg phases in the database and the S-type phase residuals are too noisy to obtain any useful results for those phases. For the Pn and P phase path anomalies at all distances, however, there were 848 and 5176 successful estimates of source-station path anomalies, respectively. The results are plotted for the regional distance range in Figure 4. These empirical estimates range from about -7.5

sec to +5.0 sec, with maximum differences occurring at distances of 11 to 18 degrees (similar to Figure 3) where the influence of interfering travel-time branches makes phase identification difficult.

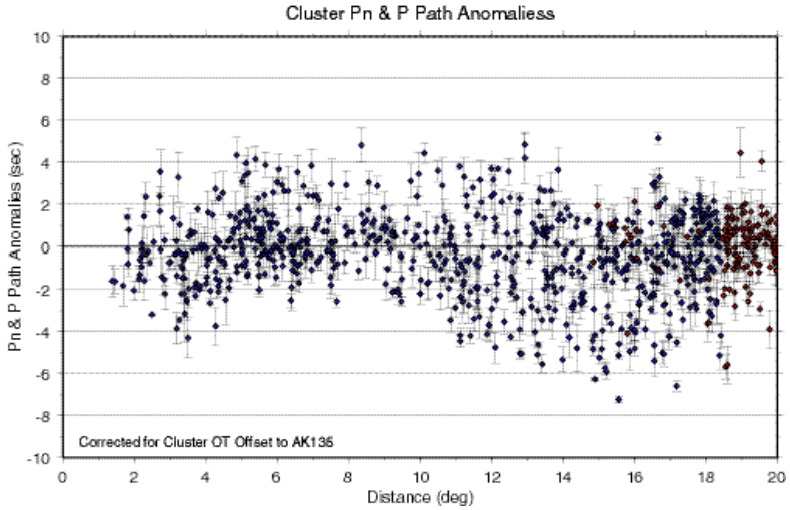

Figure 4. Cluster Pn (blue) and Pn (red) path anomalies (corrected for origin-time offsets) plotted as median and spread estimates with respect to distance.

3-D Model

The CUB 3-D model is created on a 2 deg x 2 deg grid to a depth of 400 km. Below 400 km the model reverts to the Harvard 3-D model S20a (Ekstrom and Dziewonski, 1998). The model is constructed using a Monte-Carlo inversion method (Shapiro and Ritzwoller, 2002a) applied to group (e.g., Ritzwoller and Levshin, 1998) and phase velocity dispersion curves (Trampert and Woodhouse, 1995; Ekstrom and Dziewonski, 1998). The crustal reference model used is CRUST2.0, which is an update of CRUST5.1 (Mooney et al., 1998). The surface wave tomography method used to develop the model is based on diffraction tomography (Ritzwoller et al, 2002), which uses a simplified version of the scattering sensitivity kernels that emerge from the Born or Rytov approximations. Diffraction tomography accounts for path-length dependent sensitivity, wave-front healing and associated diffraction effects, and provides a more accurate assessment of spatially variable resolution than traditional tomographic methods. Velocity vp is computed from vs using a theoretical conversion based on mineralogical partial derivatives for a hypothetical composition of the upper mantle. The method is based on the work of Goes et al. (2000) and is described in detail by Shapiro and Ritzwoller (2002b). In essence, given the mineralogical composition, partial derivatives of the elastic moduli with respect to the independent variables at infinite frequency, a mixing law, and a relation between temperature and shear Q which is the basis for the anelastic correction; the vs model is converted to temperature which is then converted to vp. In CUB2.0 this transformation has not been regionally tuned. Mineralogical composition is homogeneous across the region of study, there has been no account for the possible effects of fluids in the mantle beneath tectonically deformed regions, and shear Q is purely a function of temperature.

Validation - Station Path Anomalies

Pn and P rays were traced through the 3-D CUB model described to determine predicted travel times. These times were used to construct travel-time correction surfaces for the two phases. Empirically determined station path anomalies are plotted on these surfaces in Figure 5 for the Lop Nor and Racha clusters. In general, the more robust features of the predicted correction surface match the empirical anomalies. However, in detail there are some differences that may be the result of fine scale deviations of the real earth from the CUB model (i.e., at the edges of its resolution) and/or shallow crustal structures.

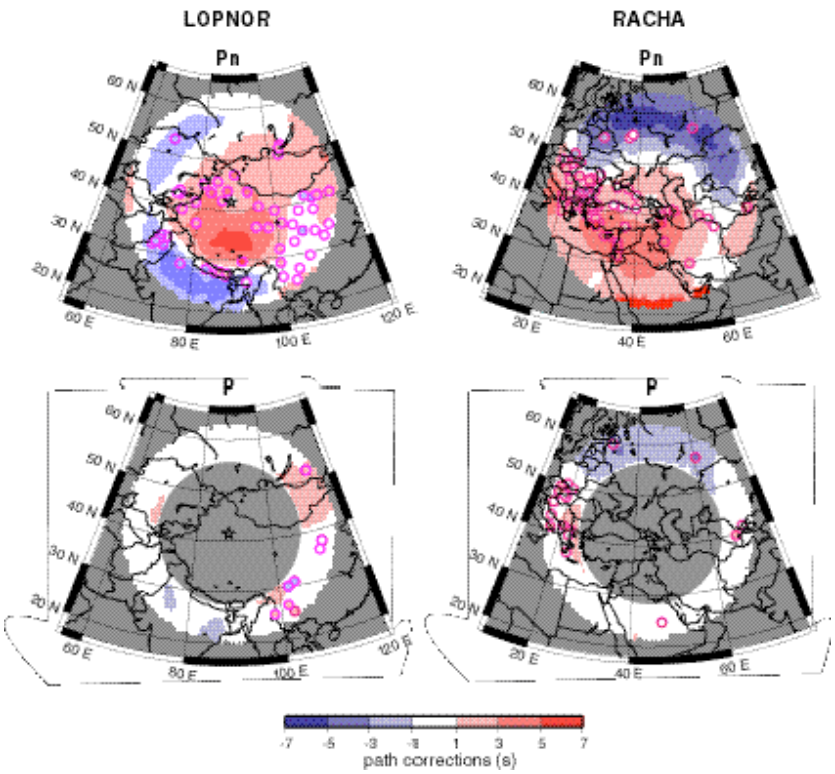

Figure 5. Event-centered Pn and P phase travel-time correction surfaces (relative to AK135) for the Lop Nor and Racha clusters compared with the empirical station path anomalies. The colored contours are the predictions from the CUB model referenced to the travel time from the 1-D model AK135.

An overall comparison between the P and Pn travel times predicted by the CUB model and the empirical station path anomalies for all GT5 or better clusters listed in Table 1 are plotted in Figure 6a. The correlation (0.84) is quite good, largely the result of using an improved model, but also a result of implementing an automated phase re-identification procedure. Basically, the phase identification (Pn or P), which provides the best fit in travel time to an empirically determined path anomaly, is adopted. A summary of the RMS-misfit with respect to the 1-D model AK135 shown in Figure 6b suggests significant improvement by using the 3-D CUB model to re-identify phases at distances where the first arriving Pn and P branches are predicted by the CUB model to cross. Proper phase identifications would not otherwise have been possible using a 1-D model alone and a fixed cross-over distance.

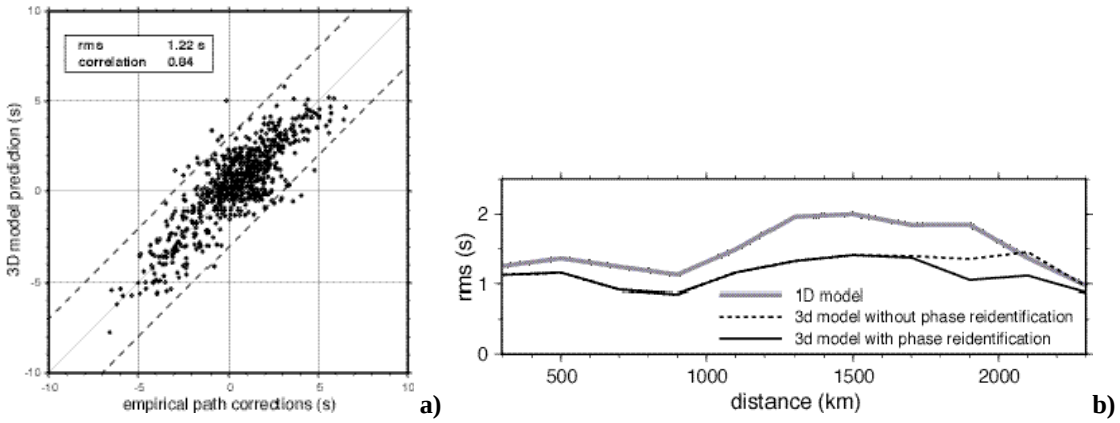

Figure 6. Overall comparison between the P and Pn travel times predicted by the CUB model and the empirical station path anomalies for all GT5 or better clusters listed in Table 1. Results are presented only for regional phase data (epicentral distance less than 20 degrees). (a) The empirical station path anomalies are on the horizontal axis and the 3-D model predictions on the vertical axis. (b) RMS-misfit between the empirical station path anomalies and the travel times predicted from three models plotted versus epicentral distance computed in a 200-km moving window (thick solid blue - AK135, solid black - CUB model with phase re-identification, and dashed black - CUB model without phase re-identification).

Validation - Relocation

The location procedure is based on a grid search, in which the rms misfit of predicted-to-observed travel times is the functional minimized (Levshin and Ritzwoller, 2002). Epicentral latitude and longitude are the two unknowns searched across a spatial grid. The third unknown, origin time, is found for each trial location by minimizing the rms residual. Event depth is fixed to the ground truth value because it trades off strongly with origin time and to first-order is independent of the epicentral location for shallow crustal events. Fixing event depth, therefore, has little effect on the error in the epicentral location in most cases. The grid is centered at a starting location (usually the teleseismic PDE location). Only first arriving mantle P phases at epicentral distances less than 20 degrees are used. The spatial grid is usually 1 x 1 km and covers 2500 square km. For each grid point, the difference between the observed and predicted time for each observation is found. Observations with residuals having absolute values above a certain threshold (3 s) relative to the starting location are discarded. The distance between the best spatial node (with minimal rms) and the ground truth location for a given event is considered as the relocation error. Examples of the rms misfit grid for a nuclear test at Lop Nor on 5/15/1995 using different models are shown in Figure 7.

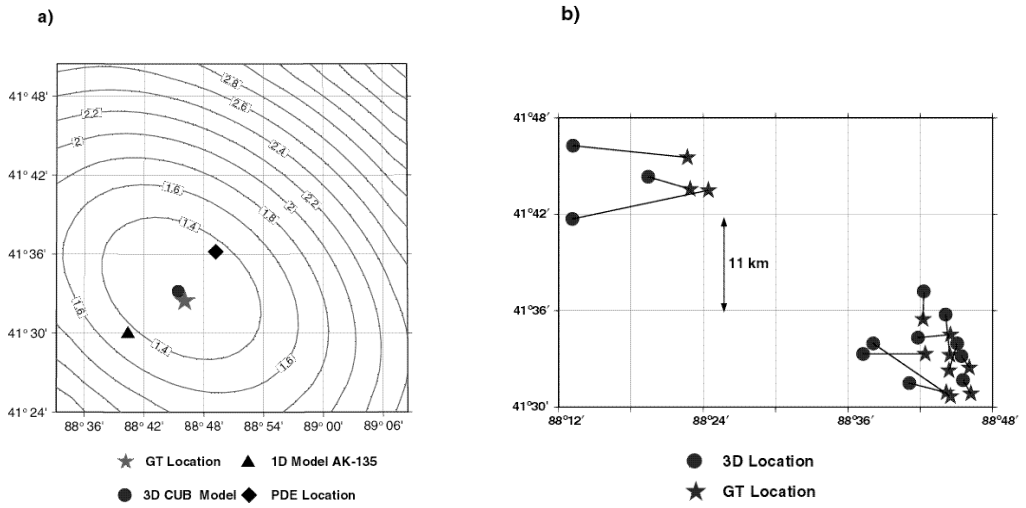

Figure 7. Grid-search method and location results for Lop Nor. (a) Misfit contours for one event at Lop Nor using the CUB 3-D model. The PDE location, the regional locations from the CUB 3-D model and from the 1-D model AK135 are also shown. (b) Mislocation vectors for locations based on the CUB 3-D model with respect to ground truth locations. This example is for events at the Lop Nor test site.

Table 2 summarizes the relocation results for all clusters studied. Typically, when only regional arrival-time data are used, the CUB 3-D model reduces location errors to about half the values obtained with the AK135 1-D model.

Table 2. Comparison of Relocations Using 3-D Model (CUB) and 1-D Model (AK135)

Table 2. Comparison of Relocations Using 3-D Model (CUB) and 1-D Model (AK135)

			3D model	1D model
	Cluster	#events	Error (km)	Error (km)
1	Adana	20	11.4	13.5
2	Aqaba	25	14.7	22.4
3	Azgir	7	6.1	29.2
4	Balapan	11	5.1	17.5
5	Chamoli	10	6.0	10.8
6	Degelen	8	8.5	27.7
7	Duzce	16	6.5	13.7
8	Erzin	6	8.1	14.4
9	Gazli	16	9.3	12.8
10	Hoceima	22	9.9	19.3
11	Izmit	8	8.4	11.7
12	Koyna	8	10.5	16.1
13	Lop Nor	13	8.3	18.8
14	Nov. Zemlya	2	3.7	20.7
15	Racha	11	5.3	25.2
16	Siberia	7	4.6	10.1
17	Tabas	12	9.8	19.2
	All clusters	202	8.0	17.8

CONCLUSIONS AND RECOMMENDATIONS

The Hypocentroidal Decomposition method of cluster analysis has proven to be very well suited to the requirements of ground truth validation exercises. Cluster analysis has been applied to 23 earthquake and explosion sequences in Asia and north Africa for which one or more of the associated reference events is known to an accuracy of 10 km or better (GT10). After removing bias in the relative locations by shifting the hypcentroid to best match reference event locations, these analyses produce new absolute origin times and locations for all the events in each cluster that can be used to determine source-station phase path anomalies across the region.

Estimates of empirical station path anomalies derived by cluster analysis provide a valuable independent validation tool for assessing 3-D models of the region of interest. Moreover, cluster hypocenters that have had systematic bias removed can also be used as a validation tool by demonstrating that locations based only on regional arrival times using a 3-D model can significantly improve locations using a 1-D model. The CUB 3-D model appears to perform quite well under these evaluation metrics.

REFERENCES

Ekstrom, G. and A.M. Dziewonski, The unique anisotropy of the Pacific upper mantle, *Nature*, 394, 168-172, 1998.

Engdahl, E.R., R.D. Van der Hilst and R.P. Buland, Global teleseismic earthquake relocation with improved travel times and procedures for depth determination, *Bull. Seism. Soc. Amer*., 88, 722-743, 1998.

Engdahl, E.R. and E.A. Bergman, Validation and generation of reference events by cluster analysis, *Proceedings of the 23rd Seismic Research Review, Jackson Hole,* 1-5 October, 2001, Vol. 1, 205-214.

Goes, S., R. Govers and R. Vacher, Shallow mantle temperatures under Europe from P and S wave tomography, *J. Geophys. Res*., 105, 11,153-11,169, 2000.

Jordan, T.H. and K.A. Sverdrup, Teleseismic location techniques and their application to earthquake clusters in the south-central Pacific, *Bull. Seis. Soc. Amer*., 71, 1105-1130, 1981.

Kennett, B.L.N., E.R. Engdahl and R.P. Buland, Constraints on seismic velocities in the Earth from travel times, *Geophys. J. Int.*, 122, 108-124, 1995.

Levshin, A.L., and M.H. Ritzwoller, Application of a global-scale 3D model to improve regional locations, *Studia Geoph. et Geod*., 46, 289-292, 2002.

Mooney, W.D., G. Laske and G. Masters, CRUST5.1: A global model at 5 degrees by 5 degrees, *J. Geophys. Res.* 102, 727-748, 1998.

Ritzwoller, M.H. and A.L. Levshin, Eurasian surface wave tomography: Group velocities, *J. Geophys. Res*., 103, 4839-4878 1998.

Ritzwoller, M.H., N.M. Shapiro, M.P. Barmin and A.L. Levshin, Global surface wave diffraction tomography, *J. Geophys. Res*., in press, 2002.

Shapiro, N.M. and M.H. Ritzwoller, Monte-Carlo inversion for a global shear velocity model of the crust and upper mantle, *Geophys. J. Int*., in press, 2002a.

Shapiro, N.M. and M.H. Ritzwoller, Thermodynamic constraints on seismic inversions, *Geophys. J. Int.*, submitted, 2002b.

Trampert, J., and J. Woodhouse, Global phase velocity maps of Love and Rayleigh waves between 40 and 150 seconds, *Geophys. J. Int*., 122, 675-690, 1995.

IMPROVEMENT IN DETECTION, LOCATION, AND IDENTIFICATION OF SMALL EVENTS THROUGH JOINT DATA ANALYSIS BY SEISMIC STATIONS IN THE MIDDLE EAST/EASTERN MEDITERRANEAN REGION

Yefim Gitterman,[1] Vladimir Pinsky,[1] Avi Shapira,[1] Mehmet Ergin,[2]
Dogan Kalafat,[3] G. Gurbuz,[3] Kyriakos Solomi[4]

Geophysical Institute of Israel (GII);[1] TUBITAK Marmara Research Center,
Earth and Marine Sciences Research Institute, Turkey;[2] Bogazici University,
Kandilli Observatory and Earthquake Research Institute, Istanbul, Turkey;[3]
Geological Survey Department of Cyprus[4]

Sponsored by Defense Threat Reduction Agency

Contract No. DTRA01-00-C-0119

ABSTRACT

The joint project of Israel, Cyprus, and Turkey is devoted to the collection of the Ground Truth (GT) data for calibration of the regional International Monitor ting System (IMS) stations, characterization of the national regional networks, and development of the data-processing software. During the second year of the project activity, we have extended the GT database and checked (by a relocation experiment) 70 collected calibration GT events in the East Mediterranean region. These included 19 explosions within the footprint of the ISN (13 GT0 explosions and six GT2 quarry blasts), and 51 GT5 earthquakes from Israel, Cyprus, and three seismic provinces - Izmit, Duzce and Adana - in Turkey.

For each of the calibration events, a computational relocation experiment was performed to make a quality tuning of the obtained source parameter estimates: coordinates (X, Y, Z) and origin time T0, and ensure that these estimates are reliable and accurate enough. For this experiment we have elaborated special software "RELOC," including the "SEIS" hypocenter search program, and new codes for estimation of the 90% hypocenter error ellipsoid. For EIL, MRNI and BRAR IMS stations, station-specific source corrections (SSSC) have been computed using GT coordinates and origin times, obtained through the relocation experiment. Most deviations of the observed P, S travel times from the IASPEI91 velocity model for Israel GT events were compensated by application of the local 1-D model. However, the similar attempt on regional scale to explain deviations from the 1-D model by the 3-D model CUB of the Colorado University did not provide the expected improvement.

Errors observed in SSSCs, constructed directly from empirical travel times, can be reduced by using more accurate velocity model. For updating the 1-D velocity models in the GT events, the VELEST joint epicenter solution program was applied in the area of Adana Basin (Cilician network, TUBITAK) and ISN region (GII). The data set contained 244 reliable Adana events and 170 ISN events of ML > 2.5 with good P and S readings. Initial RMS was 0.5 and 0.67 sec for each of the networks respectively and after a number of iterations, new 1-D velocity models have been achieved with RMS value of 0.3 sec for both of the networks.

In order to extend the Middle East GT0 database, GII conducts a series of large (20-25 tons) inland blasts, using the facilities of Israeli quarries. These explosions will provide data complementary to the Dead Sea underwater calibration shots of November 1999. A 25-ton single-fired calibration explosion of special experimental design was conducted at Rotem phosphate quarry in Negev, Southern Israel, on May 21, 2002. It was preceded by smaller trial shots, for estimating safety conditions and seismic efficiency of the large shot. Obtained results confirmed the estimations. The expected magnitude 3.0 was achieved. Records were obtained at numerous permanent and portable short-period (SP) and broadband (BB) seismometers as well as accelerographs, in the distance range 0.3 – 450 km, in Israel, Jordan and Cyprus. Compared to other calibration shots, the Rotem 25-ton blast showed seismic strength similar to the same size Balapan (STS, Kazakhstan) explosion, and 0.5-ton Dead Sea shot. For all controlled quarry blasts, a detailed GTI was collected. The recorded explosions and earthquakes provided data for corrections of regional travel times for regional networks and IMS stations EIL and the new array AS049 at Mt. Meron, verification and improvement of velocity models, attenuation (amplitude-distance) and magnitude-yield relations, characterization of new seismic sources and local mining practices, and multi-station discrimination analysis.

OBJECTIVE

The main objective of the project is to characterize and enhance the Comprehensive Nuclear-Test-Ban Treaty (CTBT) monitoring potential of small events in the eastern Mediterranean area, based on a jointly collected GT0-GT5 database of earthquakes and chemical explosions and on development and implementation of improved signal processing techniques.

RESEARCH ACCOMPLISHED

For this second stage of the project, the main effort was to evaluate travel times from GT sources of the events, jointly collected by the GII (Israel), the KOERI/TUBITAK (Turkey), and the GSDC (Cyprus) and provide direct station-specific source corrections (SSSCs) for the IMS stations EIL, MRNI (Israel) and BRAR (Turkey). For this purpose we needed to relocate and verify GT sources and fulfill quality measurement of arrival times to the IMS stations. Additional GT earthquakes, quarry blasts and calibration explosions were introduced in the database with corresponding assessment of yield magnitude and distance-time relationships. New 1-D velocity models for the area covered by the Israel Seismic Network (ISN) and Cilician network (Turkey) were obtained via application of the VELEST joint hypocenter inversion module.

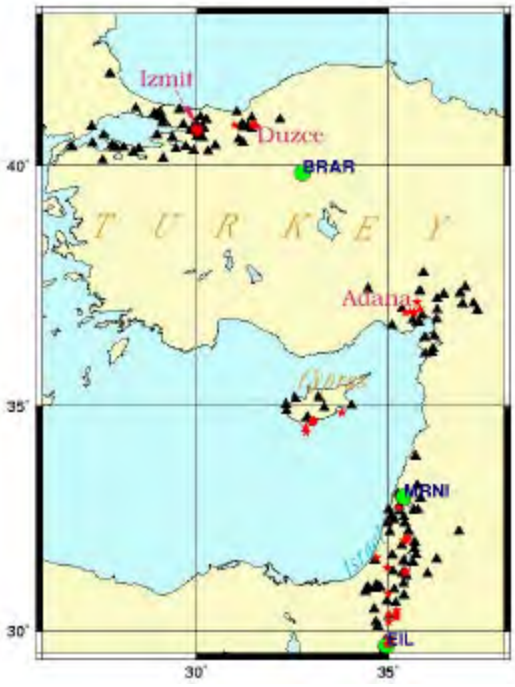

Figure 1. Location of the GT events. and Networks used for the location.

GT events database. The GT database, collected mostly at the project first stage (Shapira et al., 2001), consists of bulletin information and waveforms of around 70 events from five regions (see Fig.1): (1) Israel-Jordan events: GT0 explosions (13), GT2 explosions, GT2-GT5 earthquakes (all these data are recorded by the ISN); (2) Cyprus earthquakes; and three regions of Turkey recently stricken by the destructive earthquakes and the series of strong aftershocks: (3) Adana, (4) Izmit, and (5) Duzce.

Relocation experiment. Each of the selected GT events has been relocated on the basis of the corresponding local 1-D model and P,S readings with optimal weights (RW) (see Table 1), eliminating influence of the outliers and poor signal-to-noise ration (SNR) data. In addition, a computational experiment was completed with each event for verification and quality tuning of the obtained source parameter estimates: coordinates (X,Y,Z) and origin time OT. For this experiment we have designed special software "RELOC," using the "SEIS" hypocenter search program by A. Shapira, and a new hypocenter error estimation program. The program conducts a series of relocation tests, creating for each event a separate bulletin file and finally the characteristic table compiling results of all the relocations (see Table 1): (a)- with different fixed depths (RH), (b) with stations within 100-km radius only (RL); (c) based on P readings only (RP); (d) – relocation, with Gaussian random noise (σ=0.5 sec) added to the P, S readings (RN). The output parameters are: (a) coordinates, time and depth and their deviations dX, dY, dH and dT from the original bulletin, (b) minimum R_{min} and maximum R_{max} station distance from the source, (c) the total number of stations N used in the location procedure and those within 100 km - N100, (d) RMS – standard deviation of observed minus calculated arrival time, the 90% errors for the corresponding eT, eY, eX, eH parameters. In addition to the table we supply each of the experiments with three figures: (a) configuration of the recording network within ±50 km of the epicenter; (b) 90% error epicenter ellipse with major (Lmax) and minor semi-axes (Lmin) and the major axes azimuth (AZ), spotted by the 100 Monte-Carlo test epicenters; (c) the levels of the RMS. The estimated source coordinates and origin time were used for the travel-time calculations and derivation of the SSSCs.

Table 1. Example of relocation experiment.

TYPE	Lat	Long	H km	HH:MM:SEC	RMS sec	dY, km	dX, km	dH km	dT, sec	N, N100	Rmin, Rmax	gap deg	eY km	eX km	eH km	eT, sec
RW	30.399	34.994	9.	15:39:15.40	.2	-0.1	1.2	0.	-0.1	32, 16	5. 325.	79.	0.7	0.8	0.4	0.3
RH	30.404	34.985	12.	15:39:15.00	.2	0.4	0.2	2.	-0.5	32, 16	5. 325.	79.	0.9	1.9	0.9	0.1
RL100	30.403	34.989	8.	15:39:15.40	.2	0.3	0.7	0.	-0.1	19, 16	5. 292.	79.	0.8	1.6	0.5	0.1
RP	30.402	34.990	9.	15:39:15.40	.2	0.2	0.8	0.	-0.1	32, 16	5. 325.	79.	1.0	1.8	0.8	0.4
RN	30.398	35.002	10.	15:39:14.90	.5	-		1.	-0.6	32, 16	5. 325.	79.	2.0	3.9	2.1	0.3

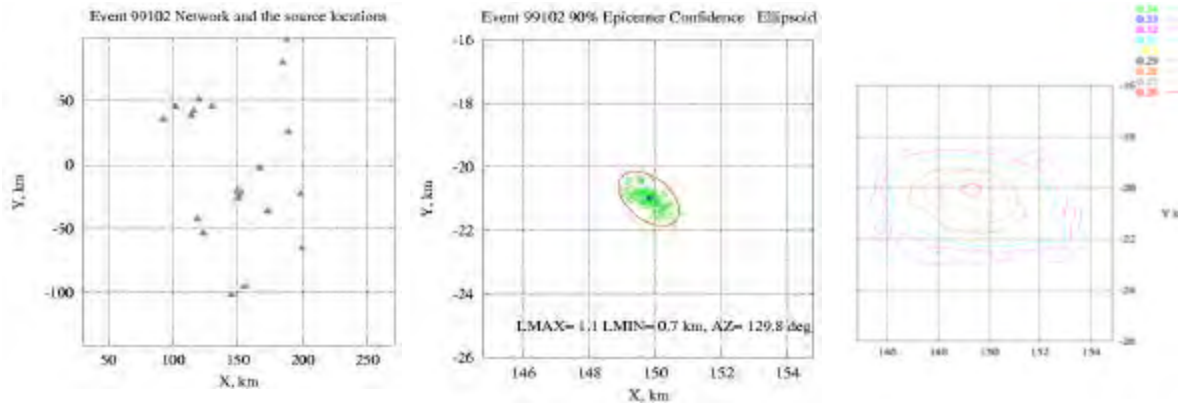

Figure 2. Example of the relocation experiment for the ISN event.(a) station configuration, (b) epicenter 90% error ellipsoid; (c) RMS contour graph.

Travel-time corrections for IMS stations EIL, MRNI relative local GT events. For calculation of the theoretical travel time *Tcalc* ($T_{IASPEI91}$) to the EIL and MRNI stations from Israel GT0, GT2, GT5 events, and earthquakes from Cyprus, we used both standard local T_{GII}, and Earth average $T_{IAPEI91}$ velocity models. In all other cases for calculation of the theoretical travel times from the GT events to the IMS stations, the IASPEI91 model was used. The results of comparison of experimental and model travel-time calculations are shown in Figs. 3 and 4. For the GT0 events, source coordinates and origin time were known exactly. We have taken EIL recordings with good SNR and measured travel times *Tobs* of the first P arrivals from the GT0 events to the EIL station, presented in Fig 3.

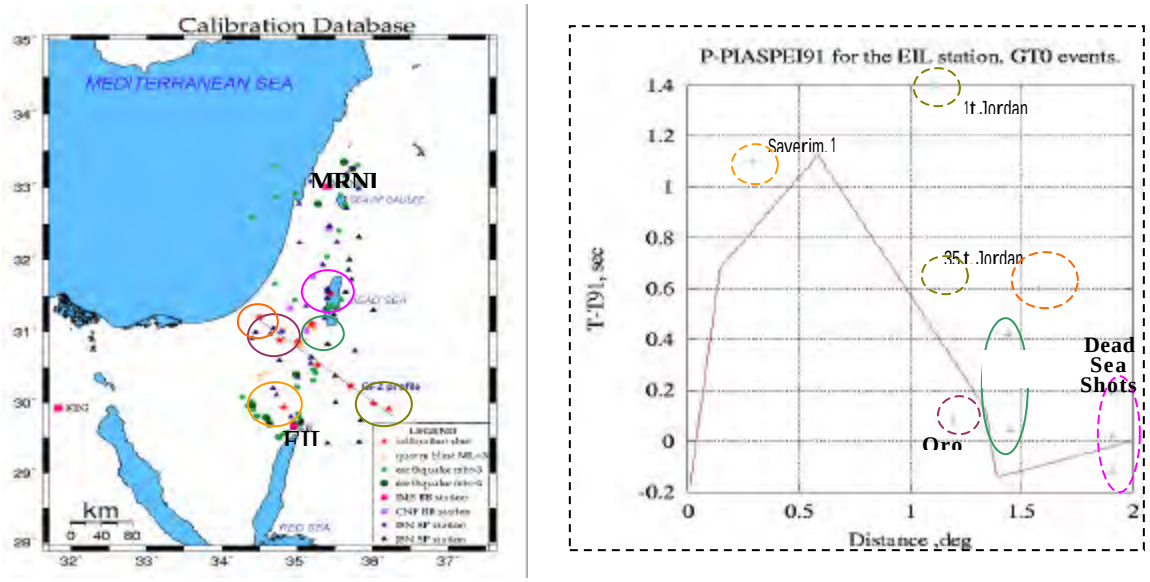

Figure 3. GT0 events and observed minus calculated time at station EIL using IASPEI91 velocity model. The curve shows T_{GII}-$T_{IASPEI91}$ dependency for the P (Pn, Pg) first arrivals.

Comparison of the *Tobs–Tcalc* for the two velocity models: GII and IASPEI91 shows that an essential difference (more than 1 sec) is observed for the Jordan 1-ton calibration explosion (DESERT2000 Group, 2000) and the close Sayerim shot. For the rest of the GT0 events, both models show good agreement with observations. For the MRNI station GT0 travel-time measurements are available now only for the Dead Sea shots of 1999, presented in Table 2 and showing ~0.3 sec early arrivals relative to both 1-D models.

Chosen GT5 events are shown in Fig. 4 (a). Figures 4 and 5 show T-$T_{IASPEI91}$ for the P and S first arrivals respectively for different distances from stations EIL and MRNI. Comparison of the measurements with the T_{GII}-$T_{IASPEI91}$ curves (calculated for the three depths: 4, 12 and 20 km), show that much of the travel-time error is explained by the difference between the IASPEI91

model (used for location by the International Data Centre), and the GII local model. Most of the measurements fit to the GII model better. Thus, in general, we prefer using the GII model instead of the IASPEI91 for the EIL in the (0 –3.5^o) distance range.

Table 2. P arrivals from the Dead Sea shots to MRNI.

N	Distance, deg	Azimuth	Phase	Date	Tobs-T_{GII}, sec	Tobs-$T_{IASPEI91}$, sec
Ex1	1.4740	358	Pn	1999/11/08	-0.33	-0.31
Ex2	1.4740	358	Pn	1999/11/10	-0.35	-0.29
Ex3	1.4740	358	Pn	1999/11/11	-0.30	-0.31

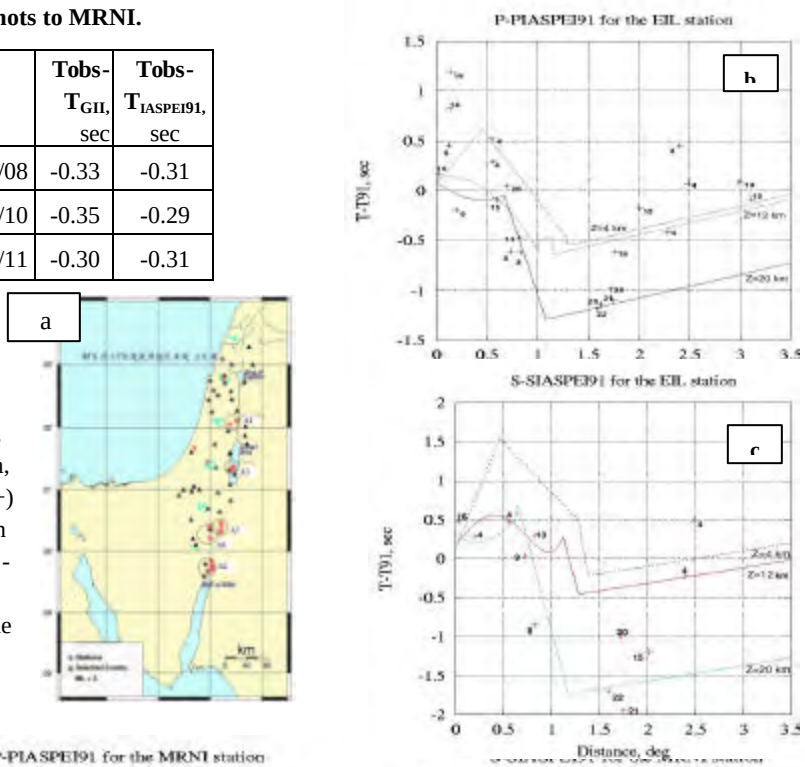

Figure 4. ISN GT5 earthquakes of ML>3, grouped in circles A1-A5 of R = 10 km, (a) and corresponding T_{obs}- $T_{IASPEI91}$ (+) for the EIL observed first arrivals P, Pn (b) and S, Sn (c), compared to the T_{GII} - $T_{IASPEI91}$ TT curves for the three depths: Z=4 km, 12 km and 20 km. The numbers, close to + show estimated source depth.

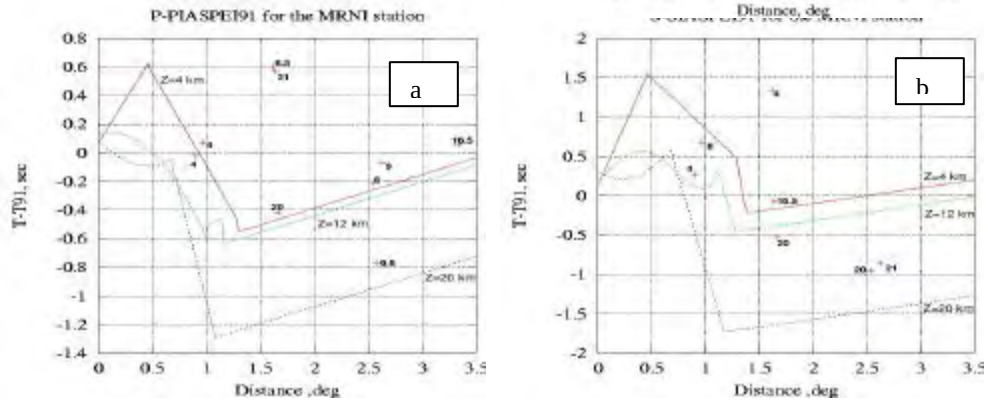

Figure 5. T_{obs}- $T_{IASPEI91}$ (+) from the ISN GT5 Israel earthquakes for the MRNI first arrivals of P, Pn (a) and S, Sn (b) compared to the (T_{GII} - $T_{IASPEI91}$) curves for the three depths: Z=4, 12 and 20 km.

However, there are a few remaining outliers with dt>0.5 sec that don't fit well with any model. For example, at small distances R<0.4^o (area A2), the measurements exhibit positive delay relative to both models. For most other events application of the local model provides a reasonable travel-time correction. For the IMS station MRNI, we notice two suspicious outliers at a distance of ~1.6^o, prompting correction of 0.6–1 sec for events from the area. It is interesting that these relatively deep (H > 16 km) events are almost at the same distance from EIL, but EIL arrivals from the same area show very good fit to the local model curves. For other MRNI arrival time measurements, shown on Figure 5, none of the models is preferable.

Travel-time corrections for IMS stations EIL, MRNI and BRAR relative to Izmit, Duzce, Adana, and Cyprus events. Empirical T_{obs}-$T_{IASPEI91}$ (for Pn first arrivals) for the given GT5 events from the collected database have been compared with T_{CUB}- $T_{IAPEI91}$, where T_{CUB} is the Pn travel time calculated using the D2tracerdn software by M. Barmin and the Colorado University (Boulder) 3-D global velocity model (2^o step) based on surface wave dispersion analysis (Ritzwoller and Levshin, 1998). The T_{CUB} curves are shown on Figure 6 together with Pn readings at the IMS stations from the corresponding GT regions.

Unfortunately, many of the Pn readings are not reliable enough due to low SNR. Those are marked with "?" sign. The numbers close to the points denote source depth estimated in the relocation analysis.

Figure 6 shows that travel times from Cyprus have early arrivals (relative to IASPEI91) at the three IMS stations and fit well with the CUB for EIL and MRNI. The TT correction at the stations is about -0.5 sec. Pn travel times at EIL and BRAR from Adana are close to the IASPEI91 model. Large systematic positive deviations (1 – 1.8) sec of TT from Duzce are observed at EIL and not explained by the CUB model. Present Izmit TT observations look close to the IASPEI91 for EIL and BRAR, but at MRNI they are large positive: 2-3 sec. Thus, unfortunately, there are no observations in our database even with clear onsets (except Cyprus events at EIL) that could explain discrepancies between observations for the 1-D IASPEI91 model and the CUB 3-D model.

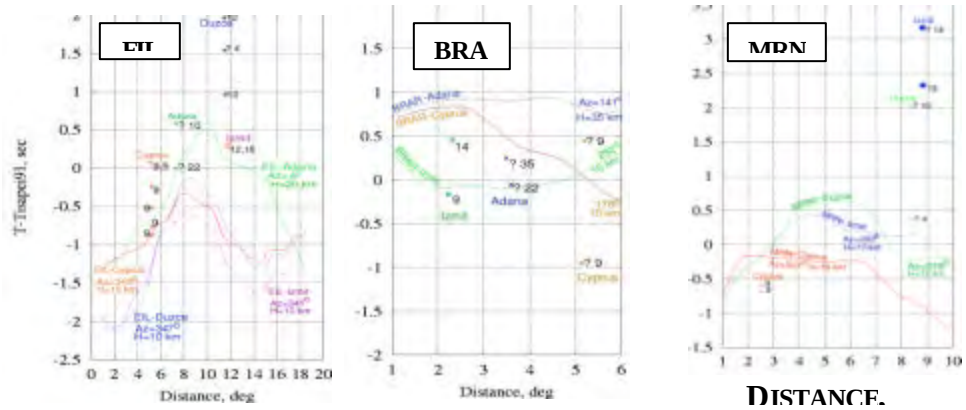

Figure 6. T_{obs}-$T_{IASPEI91}$, at the IMS stations EIL, BRAR and MRNI, from the Cyprus, Adana, Izmit and Duzce earthquakes, compared to the T_{CUB}-$T_{IASPEI91}$, calculated for the CUB10 model in the given directions from the IMS stations and at given source depth.

Calibration of the inland 25-ton explosion in the Negev desert, southern Israel.

Estimation of safety conditions and conducting preliminary test blasts. Blasts of this size without delays were never conducted at the quarry; therefore, the Rotem quarry managers requested from GII an estimation of safety ground motion conditions near the structures, located at ~ 4km, and for a high quarry wall located very close to the blast site (~ 220 m). To estimate ground motions (Peak Ground Velocity – PGV) for the planned explosion, we used an empirical relationship for single-fired blasts (Pergament et al., 1998):

$$-2.21*R^{-0.05}$$

$$PGV_{(mm/sec)} = 1000* Kv*\mathbf{R} \qquad (1)$$

where the scaled distance $R = r_{(m)}/W_{(kg)}^{1/3}$, r is epicentral distance, m, W – is charge weight, kg, rock condition coefficient Kv = 8.5, with variation ~ 30% (V. Pergament, e-mail communication).

For verification of safety analysis estimations, we conducted a test single-fired blast on 12/05/2002 (see Table 3 and Fig. 9), located close to the planned calibration shot. The blast ground motions were measured at several sites near the specified objects. The charge design (see below) was the same as for the calibration blast.

Table 3. Parameters of controlled ripple-fired and instantaneous quarry blasts at the Rotem quarry. Hole diameter $7^{7/8}$ inch, hole depth 13-14 m, exploded soft rocks - kaolins.

#	Date	Origin time (O.T.), GMT	M_L [x]	Measured coordin. X, Y, km		Charge tons	Delay msec	No. of delays	No. of holes
				X, km	Y, km				
1	08.05.2002	12:19:48.4[x]	2.5	167.86	57.33	~7.0	0	0	7
2	12.05.2002	10:33:57.46[*]	2.5	167.89	57.33	6.64**	0	0	7 (+20)
3	19.05.2002	12:05:10.8[x]	2.8	167.95	57.38	20	30	1	23
4	21.05.2002	13:00:05.554*	3.0	167.976	57.427	25	0	0	29

[x] - Local duration magnitude M_L, and origin time from ISN records.
* - Location and origin time provided by GPS.
** - This blast included 20 small charges for preparation of "onion" cavities (see Fig. 9).

Ground motions were measured by the Instantel BlastMate III equipment that provided 3-C records of ground velocity and calculated PGV vector and dominant frequencies. PGV values calculated by (1) fit well the measurements (Table 5). For the two closer sites the estimation errors are less than 10%, for the distant point the error is higher, but the PGV value is overestimated, thus providing more safety.

Table 4. Measurements and estimations for a test single-fired blast on 12/05/2002

Station	Distance km	Measurement site	Dominant frequency f_0, Hz	Vector PGV, mm/sec		Error %
				measured	estimated by Eq.(1)	
BM11	0.22	~5m from quarry wall	7.1-18.0	75.0	***69.4***	7.5
BM13	1.33	a middle point	6.9-10.0	3.88	***4.22***	8.8
BM15	3.69	near the structure	6.0-7.9	0.833	***1.09***	30.9

According to the most severe German code DIN 4150, used in Israel for safety estimations for quarry blasts, the threshold safety ground motions value for buildings PGV_{build} = 5 mm/sec (for frequencies f < 10 Hz), yielding a safe distance estimation for the planned 25-ton blast of 2.55 km (based on $+2\sigma$ level), i.e. less than the closest structure distance. Considering a threshold safety PGV value for the quarry wall of 400 mm/sec, we obtained from Eq. 1 that the maximal possible PGV near the wall is much lower.

During preparation of the calibration explosion, we collected data for two additional quarry blasts located at the same site. Blast design parameters, measured and estimated coordinates, and origin time are presented in Table 3 (including data for the test blast mentioned above). These preceding smaller blasts were used for a preliminary feasibility analysis of the planned experiment, and obtained results confirmed that the expected magnitude 3.0 can be achieved.

Blast design parameters, preparation and conducting the 25-ton calibration explosion. A special experimental design of a buried (contained) single-fired explosion (the "onion" method) was implemented by an Israel company. In this method a small initial charge (10-12 kg) is detonated on the bottom of a small diameter borehole, creating a near-spherical cavity with volume sufficient in which to place 1-2 tons of explosives (Fig. 7). The inner walls and space of created cavities are monitored by a special computerized video camera (Fig. 8), measuring cavity dimensions and checking for the presence of large cracks and voids. Then the boreholes are filled by a specified amount of explosives, forming near-spherical charges. The rest of the borehole volume is stemmed, providing a contained (or almost-contained) source with full coupling. Basic parameters of the 25-ton experimental explosion are presented in Table 5.

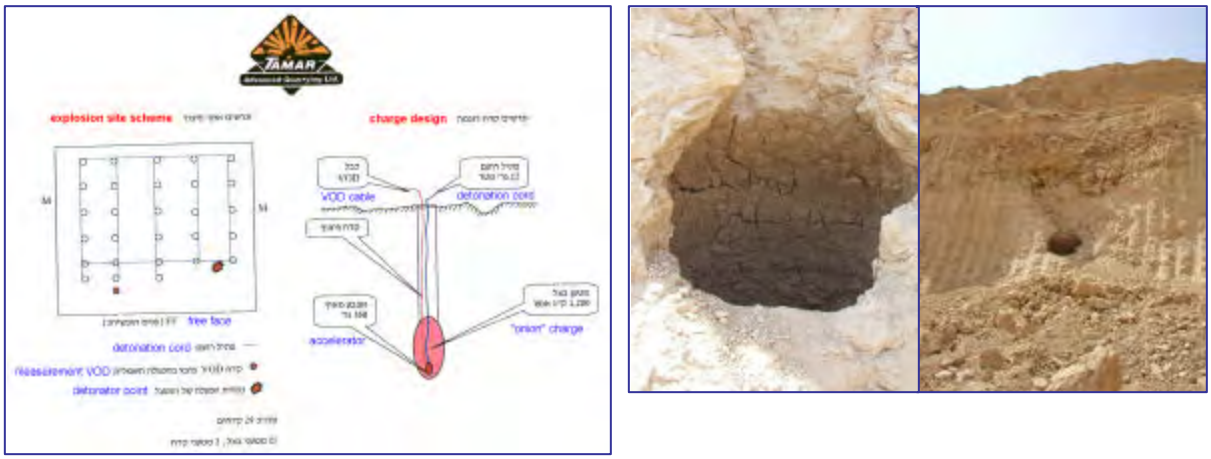

Figure 7. The "onion" charge design of the 25-ton blast. Photos show a cavity sample created during preparation for the blast and uncovered by an excavator.

Figure 8. Created borehole cavities are monitored by a special computerized video camera to measure cavity dimensions and check for the presence of large cracks and voids.

Table 5. Details of the calibration explosion design.

Borehole depth	13-14 m
Borehole diameter	$7^{7/8}$ in.
Number of boreholes	29 (27 "onions")
Distance between hole rows	17 m
Distance between holes in rows	17 m
Ammonium Nitrate	25000 kg
Main explosive - ANFO	26600 kg (incl.~8% Fuel Oil)
In-situ measured detonation velocity of ANFO (VOD)	3977 m/s
Explosive accelerator-Magnum X3	25 kg
Type of charge	concentrated – "onion"
Borehole predominant charge	1000 – 1200 kg
Stemming	12 m
Exploded rocks	kaolin (soft rocks)

Figure 9. Experimental blasts by the "onion" method at Rotem quarry (Negev). Upper photo shows initial small shots, to create near-spherical cavities ("onions"), used for the 25-ton calibration shot on 12/5/2002 (down photo).

A snapshot from the GII video-clip presented in Fig. 9 shows that the calibration explosion was almost contained. The "onion" charge design provided a small energy loss into the air. Only two holes of 29 were of usual (not "onion") design with a cylinder charge and a short (3-4 m) stemming. A rock outburst (on the left) corresponds to the location of these boreholes.

Near-source observations. For studying source function parameters and waveforms, three accelerographs K2-Etna (Kinemetrics) and two BlastMateIII seismometers, were placed in a close vicinity of the explosion on the basement layer of the exploded bench (Fig. 10). For verification of ground motion safety conditions, we installed also two BlastMateIII stations near the closest quarry structures at about 4 km.

Fig. 10. Location of the calibration explosion ( ), accelerograph sites ( ) and BlastMate stations ( ).

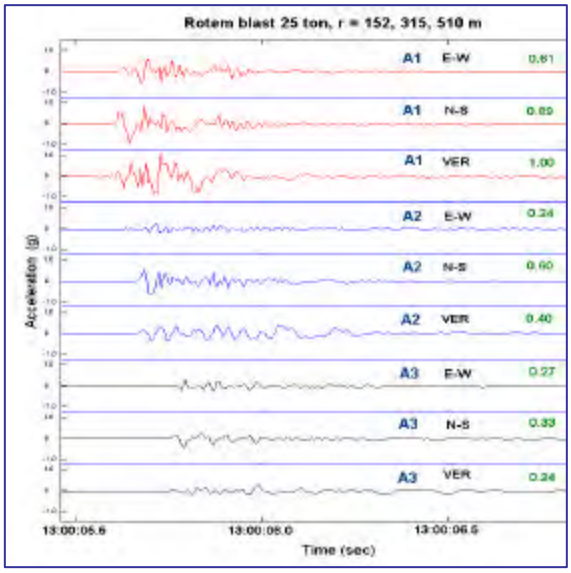

Figure 11. (Right) Recording acceleration ground motion at near-source distances by K2-Etna stations. Plots are in the absolute scale, numbers on the right show channel gain-factors relative to the closest A1 station.

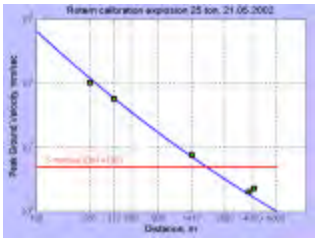

Figure 12. Estimated by Eq.1 (?) and measured (¦) ground velocity.

K2-Etna accelerographs are equipped by a GPS system and enabled estimating first arrival times and P-velocity of subsurface rocks (~ 2600 m/s). Recorded accelerograms are shown in Fig. 11. The closest accelerograph (r = 152 m) registered vertical acceleration more than 1g (1.234 g).

Like the case of the test blast on 12/05/02, PGV estimations correspond very well to the measurements (Fig. 12). For four sites estimation errors < 10%, for the station, located near the quarry structure, the measured value is significantly higher than the prediction, but it is still much lower than the safety threshold 5 mm/sec. No damage to the quarry walls or work structures was observed or reported after the 25-ton explosion.

Local and regional recordings. The four blasts (Table 3) were recorded at many ISN SP and BB stations and microarray EILESA (Fig. 13). The 25-ton calibration explosion was also well observed at many Jordanian stations, including IMS BB station AS056 (ASF) (Fig. 14). We revealed a weak signal after a heavy filtration at Cyprus BB station CSS (Fig. 14) at r=460 km, but failed to find a reliable signal at the closest Turkish station SMD (r=558 km). Several temporary seismometers were deployed during the calibration shot including surrogate stations at the site of a new IMS AS049 at Mt. Meron (under construction), providing GT0 data for the station calibration.

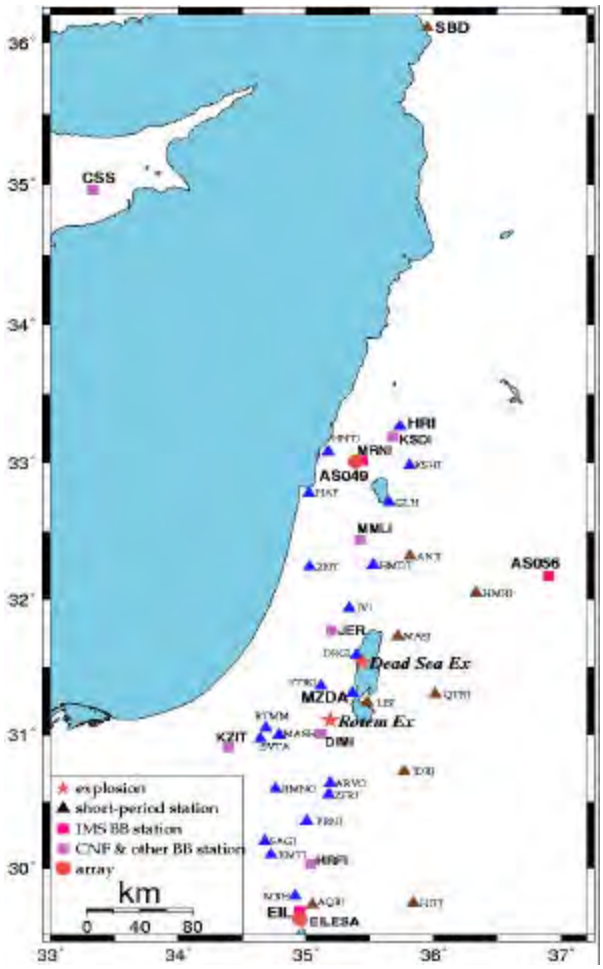

Figure 13. Explosion location and recording stations**.**

Comparing to other calibration explosions. The same specific charge design and source location for the series of blasts provide a basis for comparative analysis of amplitudes and waveforms for different source parameters, and estimating amplitude-distance and charge-magnitude relationships. We found that local magnitudes (for the Rotem blasts in soft rocks) estimated from the ISN records fit roughly the equation for single-fired quarry blasts in Israel (Gitterman, 1998) (Fig. 15). A small magnitude deficit ~0.5 unit relative to the upper limit for hard rock explosions (Khalturin, 1998) is observed.

Naturally, the Rotem blasts have much lower seismic efficiency than the Dead Sea calibration explosions (Gitterman and Shapira, 2001). However, the 25-ton Rotem ANFO blast, having a little smaller magnitude than the 0.5-ton Dead Sea shot (M_L=3.1), shows little bit stronger P-waves at different distances, and more important – demonstrates a better quality of first arrivals (Fig. 16).

Figure 14. (below) Recordings of the calibration shot at regional stations AS056 (Jordan) and CSS (Cyprus).

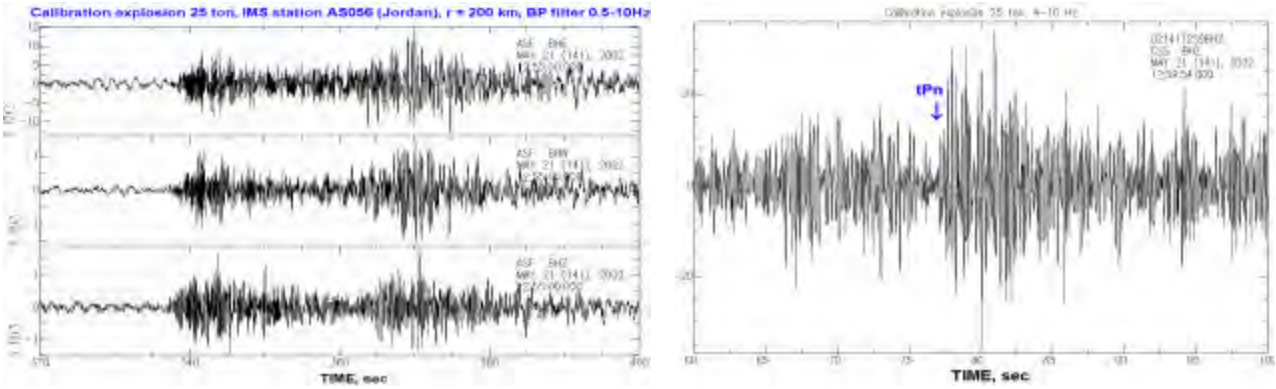

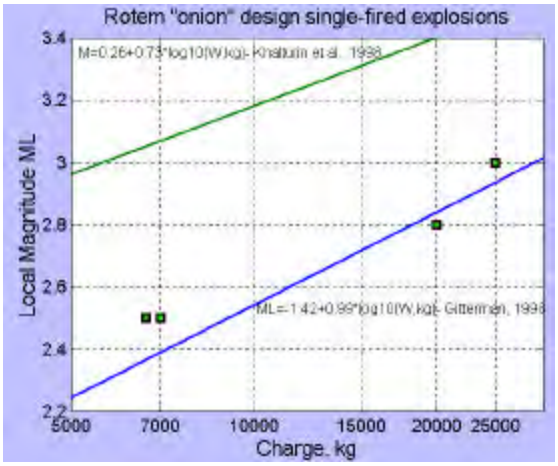

Figure 15. Local magnitudes for the Rotem blasts.

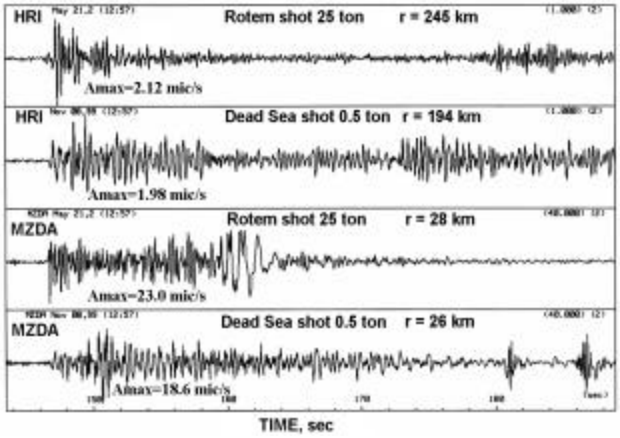

Figure 16. Comparison of amplitudes and waveforms for two Israel shots at close and remotest ISN stations.

We also compared the Rotem blast (in soft rocks - kaolin) with the same size Balapan (Kazakhstan STS) calibration explosion on Sept. 17, 1997, at 30-m depth (Kim, 1998). The Kazakh explosion was conducted under experimental conditions most favorable for generating seismic signals: more concentrated charge in one borehole, placed in crystalline rocks, high Q crust for the Kazakhstan platform. However, we found a rather similar average seismic strength for both explosions (Fig. 17), though the Balapan shot was observed at larger distances (~ 800 km), than the Israel blast (~450 km) in a different regional geology (thick upper crust sediments). The Rotem explosion shows obvious larger peak amplitudes compared to the empirical curve for the Israel single-fired multi-hole quarry blasts (Gitterman, 1998), probably due to the special charge design. It is interesting that the 0.5-ton Dead Sea shot has similar average seismic efficiency to both inland 25-ton shots.

Data for the 25-ton calibration explosion are presented at the GII Website: http://www.gii.co.il.

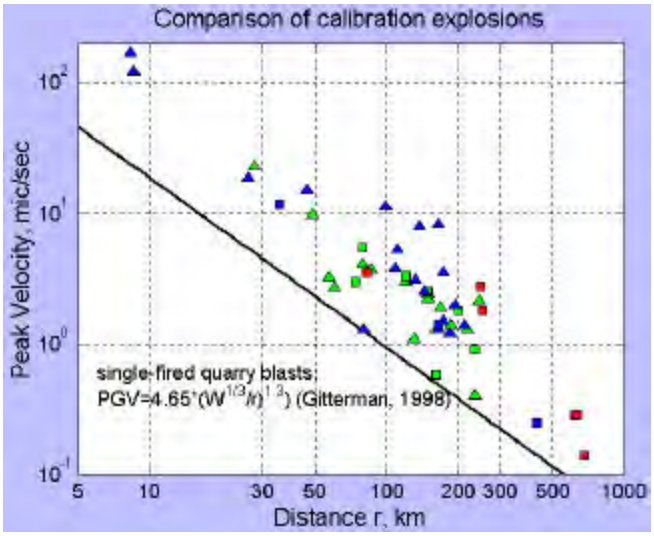

Figure 17. Comparison of peak amplitudes versus distance for three calibration shots: 25-ton Rotem (green), 0.5-ton Dead Sea (blue) and 25-ton Balapan (red) (triangles – SP stations, squares – BB stations).

Improvements of local 1-D velocity models. Errors in SSSCs constructed directly from empirical travel times can be caused by the origin time and hypocenter location error. The error may be reduced by using a more accurate velocity model. For improving the 1-D velocity models in the GT events area, we used the VELEST joint epicenter solution program (Kissling *et al*., 1994). The software was applied to the Adana Basin area (Cilician network, TUBITAK) and ISN region (GII). The data set contained 244 reliable Adana events and 170 ISN events of ML > 2.5 with good P and S readings. Initial RMS was 0.5 and 0.67 sec for each of the networks respectively and after 149 iterations of the VELEST for the Cilician and 67 for the ISN network, we achieved the RMS value 0.3 sec for both (see Fig. 18). As the result the existing regional 1-D models for the Cilician network (Ergin, 1999) and ISN (see Tables 6, 7) have been improved and used for relocation of the GT earthquakes. The new Adana model was constructed for the smaller area covered by the aftershocks of the June 27, 1998, earthquake.

Table 6. Crustal models for the Adana Basin

Regional (previous)		Local (new)	
Depth (km)	Vp km/sec	Depth (km)	Vp km/sec
0	4.5	0	2.5
2	5.0	2	4.5
4	6	4	4.9
12	6.15	6	5.8
28	6.6	12	6.5
32	7.8	24	7.2
		36	7.6
		40	8.8

Table 7. Crustal models for the ISN

Previous model		New model	
Depth, km	Vp, km/sec	Depth, km	Vp, km/sec
0	4.36	0	4.78
2.56	5.51	2	5.72
9.76	6.23	9.76	6.27
31.4	7.95	16	6.53
		28	6.97
		32	7.64
		40	

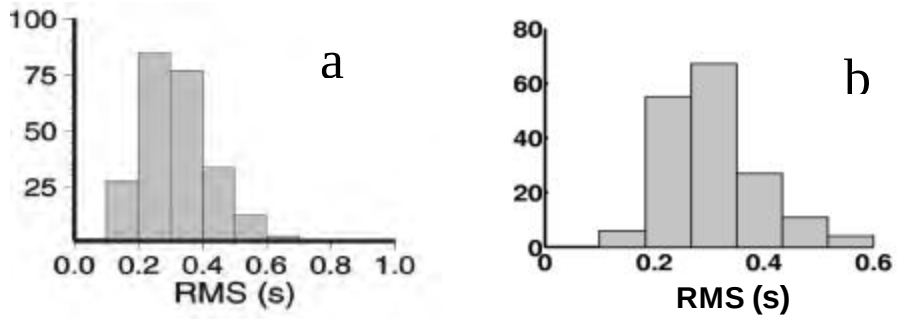

Figure 18. Distribution of event number versus residual Tobs-Tcalc (RMS) after application of VELEST software for the Adanda basin (Turkey) and Israel

CONCLUSIONS AND RECOMMENDATIONS

The newly developed RELOC tools helped to choose, relocate, and verify a number of GT events from Turkey, Cyprus and Israel, reducing travel-time deviation due to the origin time and hypocenter error to a fraction of a second. The GT0, GT2 and GT5 events, collected within ISN, provided SSSC estimation for the IMS stations EIL and MRNI in the distance range of 0 - 400 km and showed that the best travel-time correction in most cases can be obtained due to the local velocity model. However, there are several outliers and suspicious events requiring additional consideration.

GT earthquakes useful to compute direct SSSCs are rare because most of them are too weak to provide reliable first P and especially first S arrivals at the IMS stations. This is a reason for a large scatter in the estimated travel times from a small area, as for example, observed Cyprus readings at BRAR. However, even for good readings, such as Duzce and Cyprus events at EIL the scatter is about 1 sec. Moreover, even for high-quality P, S arrivals, (like Izmit events at MRNI and Duzce events at EIL), we got too large a deviation (2-3 sec) of the TT from the CUB. Thus, we need additional testing and verification of unreliable GT events and travel-time models.

The GII successfully conducted a series of explosions in the Rotem Phosphate quarry (Negev desert, 31.109°N, 35.189°E), including an inland seismic calibration explosion of 25 tons of ANFO on May 21, 2002, at 13:00:05.55 GMT. Magnitude 3.0 was reached owing to a special experimental charge design (the “onion” technique). Records were obtained at numerous permanent and portable SP and BB seismometers as well as accelerographs, in the distance range 0.3–450 km, in Israel, Jordan and Cyprus, with good quality first arrivals. Compared to other calibration shots, the Rotem 25-ton blast showed seismic efficiency similar to the

same size Balapan (STS, Kazakhstan) explosion, and 0.5-ton Dead Sea shot. The Rotem series (6.6- to 25-ton) enriched the regional GT0 database of different seismic sources for following discrimination analysis, provided new data for calculating accurate travel times of seismic waves to local and regional seismic stations and thus improved velocity models.

REFERENCES

Desert 2000 Group (2000). Multinational Geoscientific Research Effort Kicks Off in the Middle East, *Eos*, **81**, Num. 50, Dec. 12, 2000.

Ergin, M. (1999), Present day seismicity and seismotectonic characteristics of the Cilician region, Ph. D. Thesis, Istanbul Technical University, pp.312.

Gitterman, Y. (1998), Magnitude-yield correlation and amplitude attenuation of chemical explosions in the Middle East, *Proc. 20th Annual Seismic Research Symposium on Monitoring a Comprehensive Nuclear Test Ban Treaty*, Santa Fe, Sept.21-23, 1998, 302-311.

Gitterman, Y. and A. Shapira (2001), Dead Sea Seismic Calibration Experiment Contributes to CTBT Monitoring, *Seism. Res. Lett.*, **72**, No.2, 159-170.

Khalturin, V.I., T.G. Rautian, and P.G Richards (1998), The seismic signal strength of chemical explosions, *Bull. Seism. Soc. Am.*, **88**, 1511-1524.

Kim, W.-Y. (1998). Waveform data information product: calibration explosions at Semipalatinsk Test Site, Kazakhstan, during August and September, 1998. Lamont Doherty Earth Observatory Report, 9 pp.

Kissling, E., W.L. Ellsworth, D. Eberhart, and U. Kradolfer (1994), Initial reference models in local earthquake tomography, *J. Geophys Res*., **99**, 19,635-19,646.

Pergament, V., I. Malarov, P. Firstov, and Y. Gitterman (1998). Experimental evaluation of near-source seismic effects of quarry blasts. *Abstracts of the XXVI General Assembly of the European Seismological Commission*, Tel Aviv, August 23-28, 1998.

Ritzwoller, M.H. and A.L. Levshin (1998), Eurasian surface wave tomography: Group velocities, *J. Geophys. Res*., **103**, 4839-4878.

THE GNEM R&E PARAMETRIC GRID SOFTWARE SUITE: TOOLS FOR DATA CREATION, ACCESS, MANAGEMENT, VIEWING, AND EXPORT

James R. Hipp, Randall W. Simons, Lee Jensen, Lucinda A. Lindsey, and Mathew N. Chown

Sandia National Laboratories

Sponsored by National Nuclear Security Administration
Office of Nonproliferation Research and Engineering
Office of Defense Nuclear Nonproliferation

Contract No. DE-AC04-94AL85000

ABSTRACT

One of most important types of data in the National Nuclear Security Administration (NNSA) Ground-Based Nuclear Explosion Monitoring Research and Engineering (GNEM R&E) Knowledge Base (KB) is Parametric Grid (PG) data. PG data can be used to improve signal detection, signal association, and event discrimination, but so far its greatest use has been for improving event location by providing ground-truth-based corrections to travel-time base models. In this presentation we will discuss the Parametric Grid Software Suite (PGSS), which is the complete suite of GNEM R&E software developed by NNSA to create, access, manage, and view PG data. The PGSS consists of 4 main components, which are described below.

The primary PG population tool is the Knowledge Base Calibration Integration Tool (KBCIT). KBCIT is an interactive computer application whose goal is to produce interpolated calibration-based information that can be used to improve monitoring performance by improving precision of model predictions and by providing proper characterizations of uncertainty. It is used to analyze raw data and produce kriged corrections surfaces that can be included in the Knowledge Base. KBCIT not only produces the surfaces but also records all steps in the analysis for later review and possible revision.

The Parametric Grid Library (PGL) provides the interface to access the data and models stored in a PGL file database. The PGL represents the core software library used by all GNEM R&E tools that read or write PGL data (e.g. KBCIT). The PGL also provides a common access interface [the Common Grid Interface (CGI)] for many event monitoring pipeline codes. The library provides data representations and software models to support accurate and efficient seismic phase association and event location. The PGL currently provides direct support for travel-time, slowness, and azimuth data, as well as for generalized geophysical model data. PGL stores all of its data and model representations as Serialized Binary Stream Objects (SBSOs) that can be conveniently accessed using a set of database key objects. The key objects contain the SBSOs' descriptive meta-data information.

The Data Management Tool (DMT) provides access to PG data for purposes of managing the organization of the generated PGL file database, or for perusing the data for visualization and informational purposes. It is written as a GUI that can access the key file associated with any PGL file database and display it in an easily interpreted visual format. The format allows a user to view the entire object reference and dependency hierarchy, to remove objects from a database, copy objects from one database to another, or create new minimal PGL file databases that use a subset of one or more existing PGL file databases. The DMT also provides a mechanism to textually or visually display the content of any SBSO in a PGL file database. It will provide a means to locate and remove redundancy and to evaluate the overall storage efficiency of each type of supported SBSO.

The Viewing and Extraction Tool (VEXTool) provides a viewing and export capability for geophysical model data stored in the PGL database. VEXTool has four main displays providing different views of the geophysical data: the layer display, the volume display, the cross-section display, and the borehole display. Data from any of the displays can be exported for use by other analysis tools.

OBJECTIVE

Monitoring sensor data for possible nuclear explosions involves four fundamental tasks: signal detection, signal association, event location, and event identification. For all but the first of these, the task is accomplished by minimizing the misfit between observations and theoretical predictions, which in turn are dependent on the model of the Earth used. Thus, improving the quality of the Earth models used for monitoring is of critical importance and this is why it is a primary focus of the GNEM R&E efforts.

Having better Earth models is not enough, however; if the models are to be maintained and used for operational monitoring, we need a cohesive set of software tools to leverage the improved models' benefits. Population tools are needed to make it easy to process the data into the proper format, and to update the models when new data becomes available. The Earth models must be designed and defined into an integrated and extensible software system. An interface is needed around the models to serve predictions to various applications. An efficient, extensible storage format is needed to archive the models on disk. Finally, some sort of data management and viewing utility is needed to easily allow users to browse through the models to better understand them, and to make simple edits (deletions, insertions) as needed.

Researchers at Sandia Labs have been working to meet these needs by developing an integrated suite of tools collectively expressed as the Parametric Grid Software Suite.

RESEARCH ACCOMPLISHED

The PGSS consists of the primary data population tool, KBCIT, the low level storage, representation, and model library, PGL, the database management tool, DMT, and the viewing and export tool, VEXTool. We describe each below.

Knowledge Base Calibration Integration Tool (KBCIT)

The Knowledge Base Calibration Integration Tool (KBCIT) is an interactive computer application whose goal is to produce interpolated calibration based information that can be used to improve monitoring performance by improving precision of model predictions and by providing proper characterizations of uncertainty. It is used to analyze raw data and produce kriged correction surfaces, which can be included in the Knowledge Base. KBCIT not only produces the surfaces, but also records all steps in the analysis for later review and possible revision.

KBCIT allows the user to define the boundaries of regions, where the data in each region can be treated differently, including using different base models, trend removals, outlier limits and variograms in each region. (See Figure 1.) KBCIT allows the user to set parameters for blending functions to apply across region boundaries to avoid discontinuities. A declustering operation is available to reduce data set size by removing redundancy, and stabilize kriging by averaging values close to one another.

KBCIT uses the Parametric Grid Library, described below, to implement both stationary and non-stationary Bayesian kriging for interpolation of empirical data with uncertainties. (See Figure 2.) The results of kriging can be cross-validated by comparing empirical values with interpolated predictions based on a kriged surface formed using all but the values to be compared.

To provide a faster alternative to interpolating a kriged surface, the user can specify a tessellation on which KBCIT will pre-compute kriged values. Any combination of kriged and tessellated surfaces can be summed or differenced and viewed with an interactive 3D viewer. (See Figure 3.) Kriged and tessellated surfaces can be saved in a Parametric Grid database for use by other programs such as those doing event location.

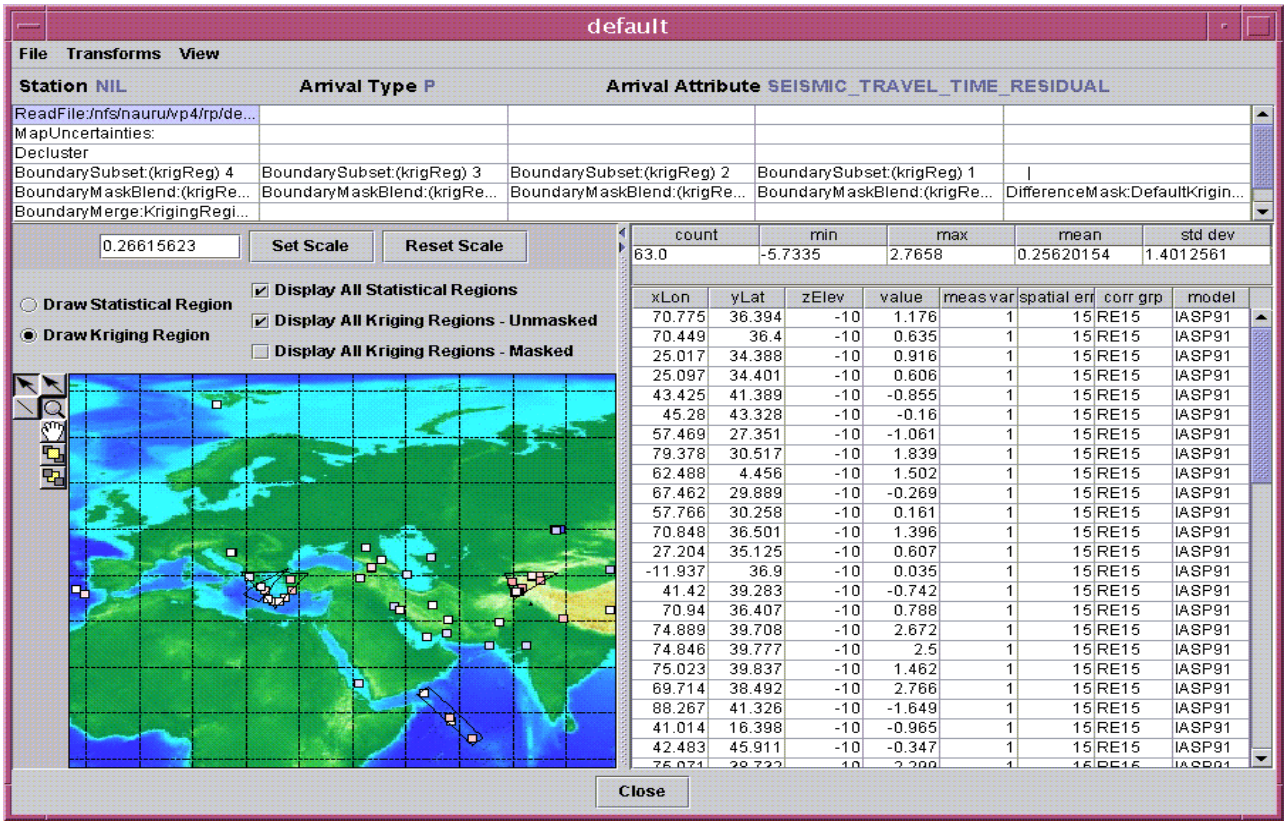

Figure 1. Kriging Set Window

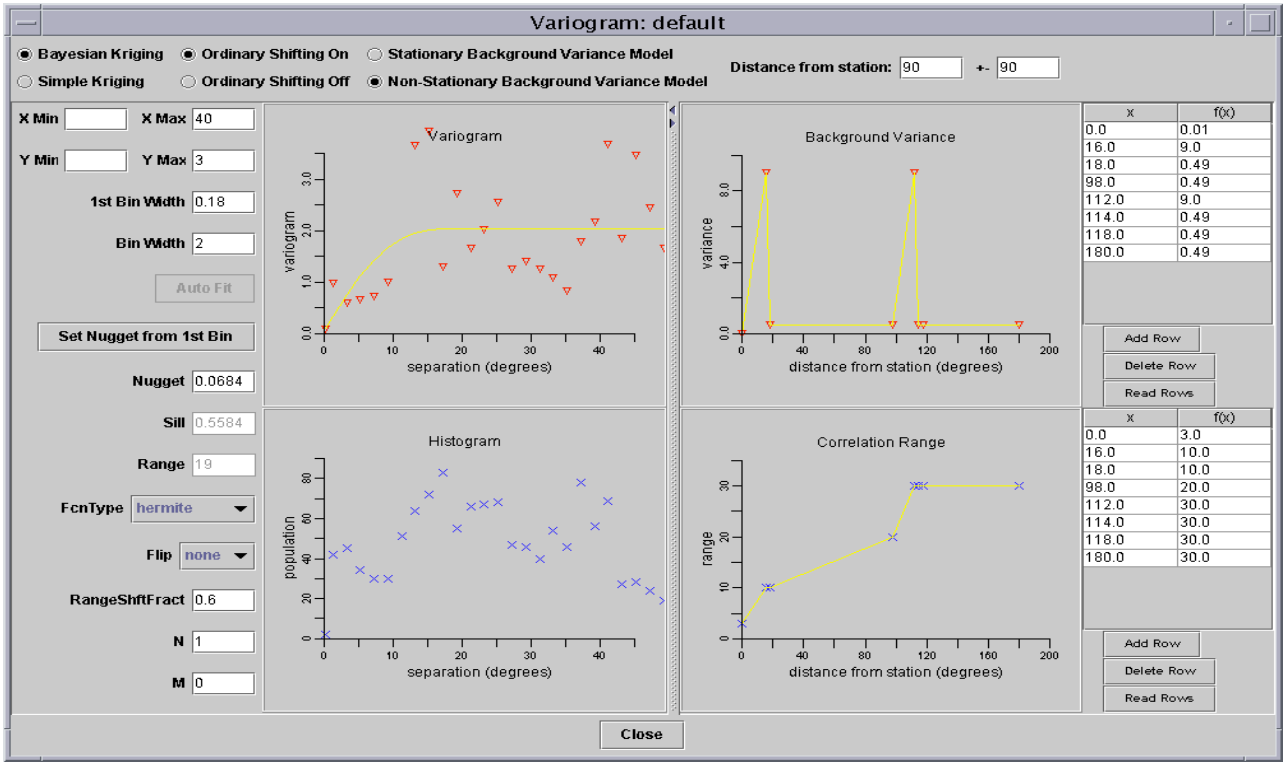

Figure 2. Variogram Window

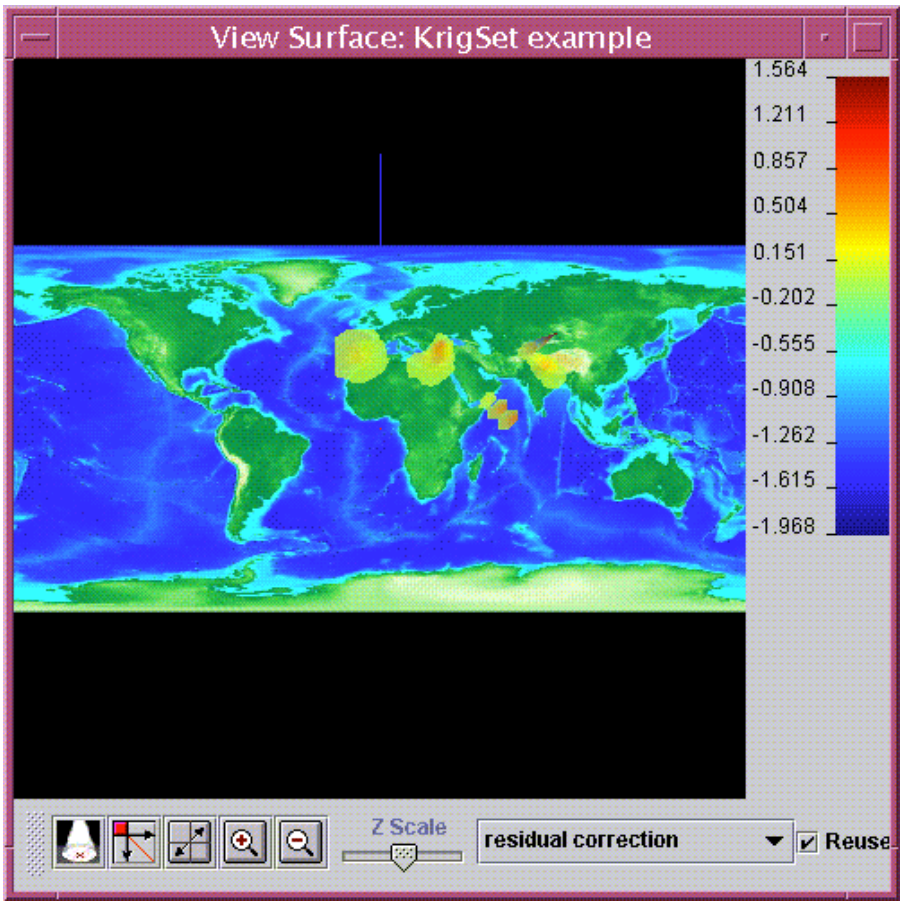

Figure 3. View Surface Window

Parametric Grid Library (PGL)

The Parametric Grid Library (PGL) provides the internal representation and client interfaces to access the data and models utilized by all GNEM R&E tools. This includes tools that provide a means of populating the PGL (e.g. KBCIT described above) and those that require access to its data or models (e.g. U.S. National Data Center (USNDC) codes). The library can be divided into several distinct functional groups that provide all necessary library capability. These groups include:

1) A physical models group that supports all basic and complex seismic modeling, Bayesian kriging for providing enhanced path corrections to the seismic models, and multi-region polygonal representations to provide a means for smoothly transitioning from discrete models defined in different tectonic regions;
2) A geometry group that provides the interface and representation functionality to support a variety of 1, 2, and 3 dimensional representation schemes. These include parametric and tessellated curve, surface, and volume representations, and a 2D point location facility;
3) A tessellation group that provides a means of generating and subsequently representing tessellated data for purposes of data interpolation and spatial searching;
4) A database group that defines the means to store and access arbitrary object data in a rapid manner;
5) An interfaces group that provides a Run-Time Type Identification (RTTI) facility for creating, managing, and destroying all database object types, and various client Application Programming Interfaces (APIs) for interfacing directly with the PGL functionality; and finally
6) A general utility group for providing other types of PGL requirements such as geometric vector support, memory management, and core level base class definitions.

Figure 4, below, depicts the structure of the various PGL groups outlined above.

The supported physical models provided by the PGL include travel-time, slowness, and azimuth. Each model consists of one or more discrete seismic regions. The specific characteristics of each of the regions are collected into a single object called a Reference object. Each Reference object is comprised of a base model definition and an optional 3D regional model. The 3D regional model can be incorporated as a residual model that increments, or improves, the values in the base model object, or as a standalone base model. In the case of travel-time, the Reference object can also contain an ellipticity correction model.

The collection of regional Reference objects is associated within a neighborhood of adjacent polygons. Each polygon defines the boundaries of a unique seismic region. Each edge of each polygon in the neighborhood can be modeled as a transition zone with an inner and outer boundary. The transition zone definition provides a means of smoothly varying both statistical and physical properties from one seismic region to the next. In addition to the one or more Reference objects, which are associated in a polygon neighborhood, the standard physical model will also contain a Station object that defines the station location for which the model was created.

Finally, a model can contain a path correction surface, which improves the accuracy and/or error definition of the physical properties for which the model was constructed. Although the surface is general in structure, it is usually created as a statistical surface representation using the PGL Bayesian kriging model. The Bayesian kriging model (Schultz, et. al., 1998) provides a means of utilizing correlation characteristics of known seismic ground-truth events to interpolate and improve the model values. This method produces the correction while minimizing the variance of the predicted error and provides an estimate of the error associated with the interpolated (or kriged) value. The job of defining the correlation characteristics and related kriging parameters that are used by the Bayesian kriging technique is the primary function of the KBCIT population tool described in the previous section.

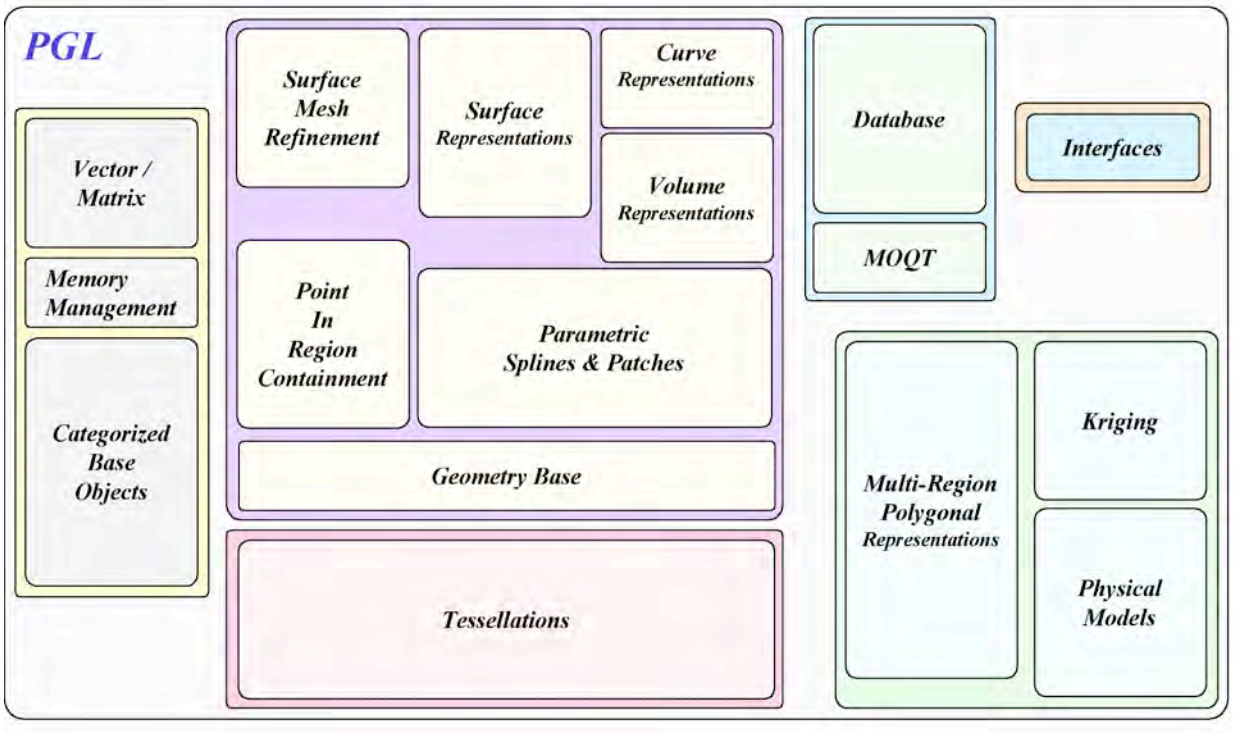

Figure 4 This Figure illustrates the six major components of the PG software library and various subcomponents of each group.

The PG Geometry group provides a means of representing data-centric curves, surfaces, and volumes. The primary means for representing geometric entities include parametrics and tessellations, and less often, a layered volume. Parametric representations can be defined when gridded data are available. A parametric representation can be formulated into linear, cubic, or quintic order polynomials in 1, 2, or 3 dimensions. A single parametric object can support multiple value definitions on the same grid. This provides an efficient means for storing multiple curves, surfaces, and volumes on a single unique grid. Full 1^{st} and 2^{nd} order derivative support is provided for all polynomial orders and spatial dimensions described above.

Unlike the parametric representation, the tessellated surface is used in cases where only unstructured 2 dimensional data are provided. The tessellated surface can also be used when high resolution is required in limited areas throughout a broader domain. Under these circumstances a tessellated surface can coarsen the unstructured mesh spacing in regions where low resolution is sufficient; and refine, or densify, the mesh spacing in regions where higher resolution is required. All PGL tessellations are Delaunay triangular (maximum angle minimized) tessellations. They can support constrained boundaries, which are guaranteed boundary representations, while maintaining the Delaunay criteria. This is important when exact representations of arbitrary boundaries (e.g. tectonic province boundaries) are required. Parametric representations are only capable of approximating unstructured boundaries.

Another major geometric object is the layered volume. This object utilizes a series of surfaces (parametric or tessellated) to represent a set of arbitrary layers. A typical use for a layered volume is to represent different stratified layers within the Earth. Layered volume objects are convenient when an independent parameters data cannot be easily or accurately represented in a rectilinear fashion (e.g. depth for the example above).

The PG tessellation group provides the functionality to construct, interpolate, and search tessellation objects. The interpolation aspects of tessellations are used to support geometric tessellated surfaces described in a previous paragraph. All tessellation interpolations utilize the gradient-based Natural Neighbor Interpolation (NNI) technique (Watson, 1992). Gradient-based NNI provides a continuous and smooth interpolation over any arbitrary unstructured Delaunay mesh.

The searching characteristics of the tessellation are utilized throughout the PGL hierarchy. Searching is used by the multi-region polygon neighborhood, described above, to locate all polygon transition boundaries that influence an arbitrary point location. The influencing point transitions are used to calculate a blending weight for each of the properties that are being interpolated in a physical model. Searching is used by the NNI interpolation technique to locate all triangles whose circum-circles contain the interpolation location. The surrounding set of triangle nodes are used to calculate NNI weights, which multiply the node values, whose summation produce the desired interpolant. Tessellated surface mesh refinement uses searching to locate new node insertion locations. The new nodes are added during mesh densification and mesh refinement operations. The Bayesian kriging algorithm uses tessellation searching to locate nearest neighbor ground-truth observations relative to a kriging interpolation location. The nearest neighbor observations are used in a “shifting” algorithm to transition between simple and neighborhood based kriging results depending on the proximity and spatial distributions of the observations about the interpolation location.

The PG database group provides the functionality to store and retrieve PGL objects from a flat-file or database in a generalized manner. Each object stored in the database is decomposed into a Meta-Data Key (MDK) and a Serialized Binary Stream (SBS). The MDK is used to contain summary information about the object including it’s object type (class name), date of creation, location in the database of the associated SBS, pertinent attributes (station, phase, base model, frequency, etc.), a description string, and a unique 16 byte (128 bit) hash string, called the Key String Identifier (KSI). The KSI uniquely identifies an object’s MDK for which it was created. Additionally, the MDK contains all dependency KSIs that are required to build the object associated with the MDK. All MDK objects are loaded from the database immediately after connecting to a database platform.

The SBS contains the actual concrete data necessary to construct the object. This data is stored separately in the database as a single binary blob. It is not accessed until the object is requested for creation from a client. The SBS is provided to the client (or the PG CGI object described below) to perform the instantiation.

The PGL interfaces group supports all current interfaces to PGL. These include the Common Grid Interface (CGI), a U.S. National Data Center (USNDC) code interface into the libloc library, an interface for the KBCIT population tool, and an interface for the Sandia seismic location code, LOCOO. Interfaces for the Data Management Tool (DMT) and the Viewing and Extraction Tool (VEXTool) are defined using the Java Native Interface (JNI) that connects directly into the PGL library. DMT and VEXTool are described below in the next two sections.

The CGI is used by all interfaces to create, evaluate, interpolate, and destroy all PGL maintained objects. Object instantiation requests are processed through CGI by providing CGI with the object's KSI. CGI will attempt to create the object associated with the KSI by first creating any of its dependent objects and ultimately by instantiating the requested object. The object can be evaluated or interpolated directly through the CGI generic interface, supported for all geometric objects, or by accessing the actual object using the Run-Time Type Identification (RTTI) facility provided by the CGI.

The last primary PG functionality group provides common utilitarian services to the all PG resources. This functionality includes a set of base classes used to divide the functionality into the groups defined here. The services also include a memory management object that allows pool allocation and destruction for small objects. This service is useful for efficiency reasons when many (near millions) small objects are repeatedly allocated and destroyed. Finally, the utility group provides a set of geometric vector classes for performing vector algebra in planar, spherical, and ellipsoidal surface geometries. These have proven to be useful and efficient constructs and are used throughout the entire PGL.

Data Management Tool (DMT)

The Data Management Tool (DMT) provides access to the PG data for purposes of managing the organization of the generated PG database, and for perusing the data for visualization and information purposes. The tool is written in Java providing a GUI front end and a JNI interface into PGL. The visualization component is primarily handled by the VEXTool application, which is the topic of the next section.

The database management facilities of the DMT include a means for inspecting the entire object reference and dependency hierarchy for any object in multiple databases simultaneously. These facilities provide mechanisms to copy or move objects and their dependents from one database to another or to simply remove them from their containing database entirely. These services allow a user to construct new databases from existing databases that use a subset of the objects contained in any of the existing databases. This provides a means for users to build databases that are tailored for spatially interesting regions or that contain objects that are specific for certain types of problems (e.g. seismic location). Figure 5, below illustrates a typical hierarchical dependency view of a database including object MDK listings and their dependents.

In addition to database object construction, the DMT also provides services for managing MDK modifications. These services permit a database administrator to correct errors or deficiencies in an MDK object in the database. Obviously, some of the MDK data cannot be changed such as object type, location of the SBS binary in the database, dependent object KSIs, etc. However, attribute and descriptive data can by modified and replaced back into the database without harming the overall database structure. This service is a key feature for performing routine maintenance on existing PG databases.

Another maintenance service involves generic searching facilities. Searching allows a user to discover specific patterns of data within the database. Search requests are formulated by supplying a generic search MDK object with the attributes of interest filled with desired patterns, and unimportant or irrelevant patterns left blank. All matches are returned to the user for inspection.

Finally, the database can be inspected for duplicate binaries. These are objects that have two or more MDKs that all point to SBSs that are duplicates of one-another. This can happened when identical objects are created at different times producing new MDKs with a different KSIs. These duplicates can be discovered and all but one may be removed. The DMT automatically updates the database dependency hierarchy to reflect the changes.

Aside from these features the DMT can also load individual SBSs for examining the contents of the serialized object in a textual format. This data is not available for change, as only a population tool is capable of modifying the data,

but it does provide a means for a researcher or analyst to examine the defining data from which the object is composed. Also, as mentioned above, the DMT can request a visual inspection of an SBS by calling the primary VEXTool visualization service. This is described in more detail in the next section.

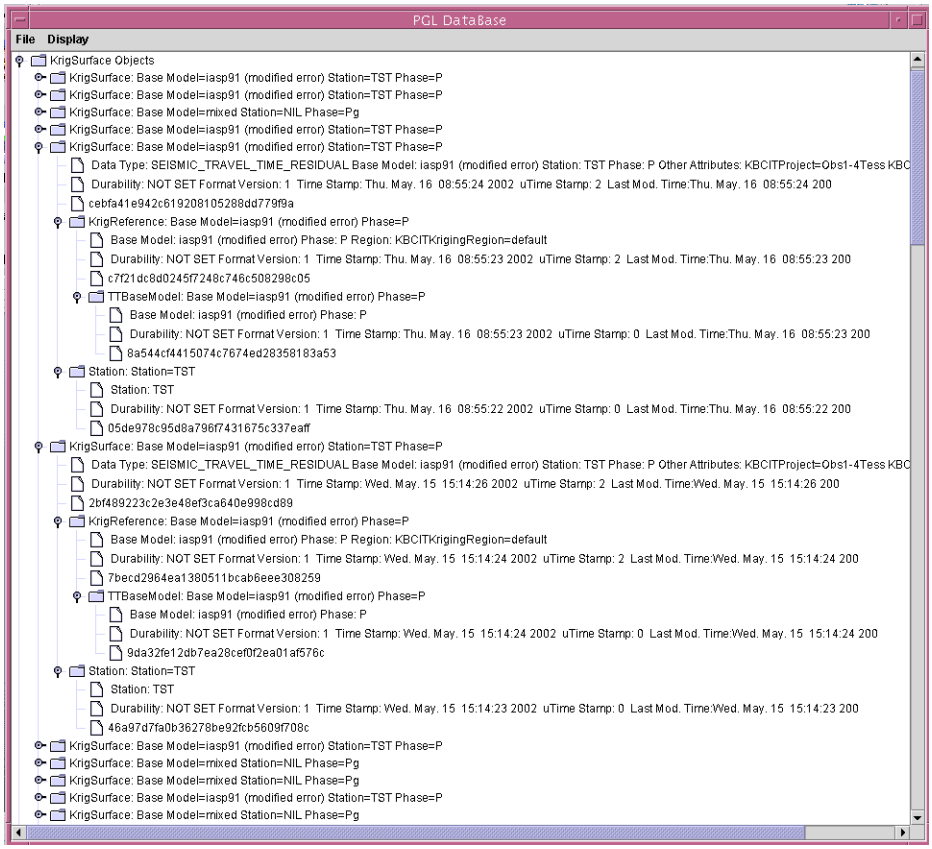

Figure 5. This Figure shows a typical screen shot of the DMT GUI displaying a hierarchical view of the database objects and their dependents.

Viewing And Extraction Tool (VEXTool)

The primary role of the VEXTool is to visualize the properties of any geometric object in a PG database, regardless of the objects type or dimension. It is also used to export interpolated model data to a number of third party tools utilized by GNEM researchers. The VEXTool interface was written in Java and provides a user friendly GUI for manipulating complex objects graphically. The tool utilizes a JNI interface for accessing the PG data and models directly through the PGL CGI object described above.

VEXTool can display an individual property of an object in 1, 2, or 3 dimensions or a range of properties as a set of curves or surfaces. Additionally, VEXTool can display multiple views of the same object simultaneously. Figure 6, illustrates a typical VEXTool screen dump where a property of a layered volume object is displayed simultaneously with a two dimensional cross-section and a 1-dimensional positional bore-hole.

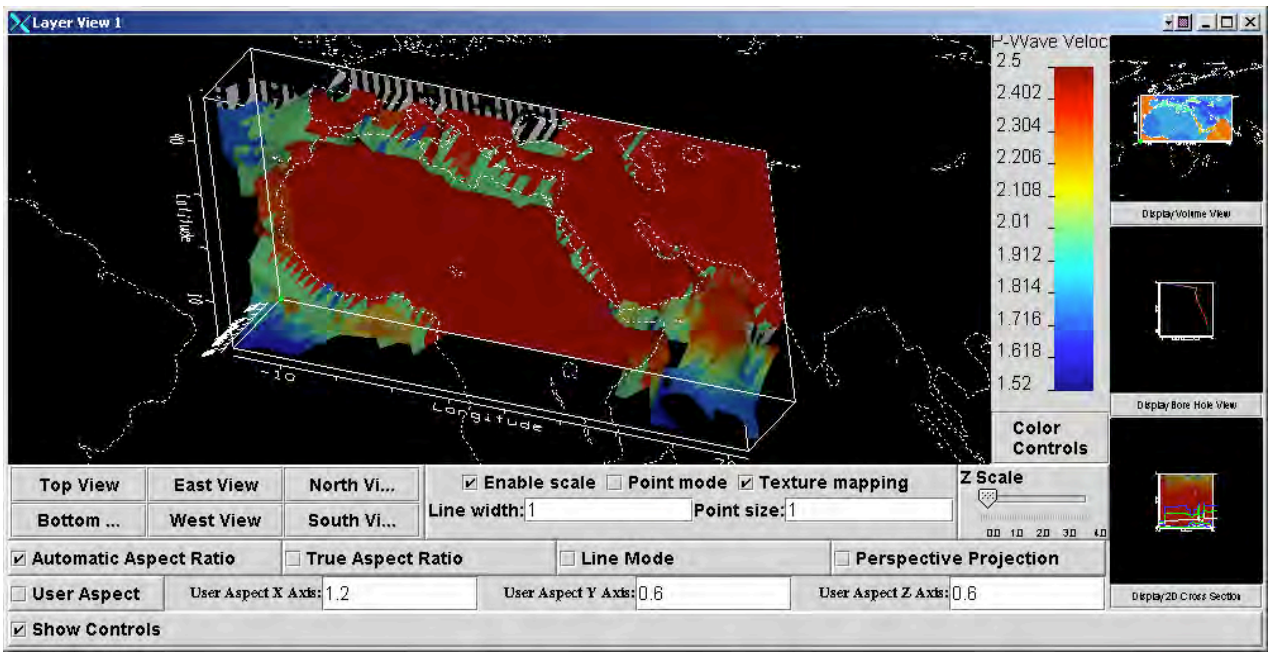

Figure 6. This Figure illustrates a typical VEXTool screen shot where a 3 dimensional layered volume object is shown displaying various geophysical properties in 3D, 2D cross-section, and 1D bore hole depictions.

CONCLUSIONS AND RECOMMENDATIONS

In this paper, researchers at Sandia Labs have defined a set of integrated software tools developed to take advantage of the improvements in Earth models available for seismic event monitoring. This integrated set of software, known as the Parametric Grid Software Suite, consists of data population, storage, modeling, and data management and viewing tools.

The population tool, KBCIT, provides interpolated calibration based information that can be used to improve monitoring performance by improving precision of model predictions and by providing proper characterizations of uncertainty. The underlying software representation of the Earth model is provided by the PGL. The PGL also provides a generalized object database for storing model data and a set of API interfaces utilized by the population, data management, and viewing tools. The PG data management facilities are handled by the DMT. The DMT is primarily responsible for maintaining and validating PG databases and for creating subset databases from existing ones. Finally, the VEXTool provides all model object viewing and data export facilities.

Future versions of the Parametric Grid Software Suite will continue to track with new enhancements in Earth models available for event monitoring. The rapid commitment of these new developments to software will ensure that the Earth model improvements are immediately available for use by GNEM researchers and analysts.

REFERENCES

Schultz, C., S. Myers, J. Hipp, and C. Young (1998), Nonstationary Bayesian Kriging: Application of Spatial Corrections to Improve Seismic Detection, Location and Identification, *Bull. Seism. Soc. Am.*, 1275-1288.

Watson, D. F., (1992), Contouring: A Guide To The Analysis and Display of Spatial Data, *Pergamon*, 321pp.

ENHANCED CTBT MONITORING THROUGH MODELING, PROCESSING AND EXTRACTION OF SECONDARY PHASE INFORMATION AT HIGH SIGNAL FREQUENCIES

Eystein S. Husebye,[1] Yuri V. Fedorenko,[1] and Elena B. Beketova[2]

University of Bergen, Norway;[1] Institute of Geology, KRC RAS, Petrozavodsk, Russia[2]

Sponsored by Defense Threat Reduction Agency

Contract No. DSWA 01-98-C-0159

ABSTRACT

The outstanding problem in seismogram analysis is that of extracting more information on secondary phases at high signal frequencies. We need pP- and sP-phases for improved focal depth estimates while Sn and Lg can significantly improve epicenter determinations. But why are these phases so difficult to pick even by experienced analysts? Also, theoretical considerations imply that, for example, pP and sP should be far easier to observe than obviously is the case. One reason may be scattering in the lithosphere causing relatively strong P-coda that tend to mask secondary arrivals. However, the major problem is not only phase picking *per se* but also validation as genuine pP, sP and Sn-phase arrivals. Our preference here is for a probabilistic approach that is unsupervised Bayesian classification (preferable) or maximum likelihood solution for probability density functions that provide with basis in time tables (velocity model) and hypocenter (likely focal sphere orientation) the probabilities of observing these phases across a network of stations -a truly complex task. The first step in any event analysis is to ensure a reasonable epicenter location estimate, which are not always available from an international data center. We have developed simple, efficient methods for doing so given a single 3-component station or a small network of stations. In the latter case we a fit plane to P-arrival times and in this manner obtain bearing (azimuth), which, in combination with distance estimated from $t_S - t_P$ time, provides an accurate epicenter location. The next step is to record preprocessing in order to enhance pickings of secondary phases like pP, sP etc. and our set-up includes bandpass (Bessel type), wavelet denoising and polarization filtering. The Lg-phase is prominent at local distances but its onset is not clear so analysts often fail in feature extractions of these phases. Introducing the Hilbert transform in combination with Savitzky - Golay filtering, the corresponding envelope is smooth and exhibits a relatively consistent waveform. The aim of any processing scheme is to extract useful phase information from event recordings and here a major problem is phase validation. Except for Lg, there is a unique solution to this problem. Hence we tested the deformable template (DT) concept on local SeisSchool records from North Sea earthquakes. The goal is extraction of consistent Lg onset times and amplitudes for many combinations of events-stations and with excellent results. We have not explored the DT-potential for discrimination. In contrast to Lg waves, validation is a most severe problem in picking pP-, sP- and Sn-phases since there are no clear diagnostics for identifying these arrivals in the P-coda. To check for pP- and sP-phases we are using data mining techniques for converting seismograms into features like ragged peaks. Each peak is then a potential pP-, and/or sP-phase candidate or a noise wavelet. These peaks are subjects for simplified maximum likelihood classification as our first tool for phase validation. Ground truth (GT) information is a must in this context, but so far we use synthetics for simulating real seismograms at local distances including focal sphere sweeps of fault plane orientations that influence amplitude ratios like pP/P. Results so far imply that for a network of three stations there is a 50% probability of finding a focal depth diagnostic phase like pP or sP.

OBJECTIVE

A long-standing problem in observational seismology and in a nuclear-explosion or treaty monitoring context is that of accurately locating small events at local and regional distances. In particular, the focal depth parameter has proved troublesome because those phases most sensitive to depth, namely pP, sP, Sn and possibly Rg, are observationally elusive. The latter statement is somewhat ambiguous since there are many secondary phase candidates between the first arriving Pn or Pg and the dominant Lg or Sg. With the modern Comprehensive Nuclear-Test-Ban Treaty International Monitoring System (CTBT/IMS) seismic recording systems, phase picking *per se* is not much of a problem but the challenge is that of phase validation. Simply, how do we know that a secondary arrival in fact is pP? An analyst is severely handicapped here because the numbers of phase and candidate combinations for network recordings are truly large. There is no obvious criterion here for phase identification as the k-space location of pP is similar to that of the first arriving P-phase, and even expert analyst phase definition is seldom very helpful. However, secondary phases would be helpful in obtaining refined hypocenter estimates so our research objective is therefore phase validation of secondary phase arrivals in local recordings. Since traditional approaches to this apparently simple problem -- like analyst trace inspections, cepstrum analysis and fault space screening -- are not providing consistent and robust results, our preference here is for a probabilistic approach. A more comprehensive strategy is that of unsupervised Bayesian classification, but for now we test the concept using the simpler maximum likelihood solution for a probability density function that provides a basis in time tables and hypocenter (focal sphere) with the probabilities of observing these phases across a network of stations. The realization of this objective entails completion of several subtasks namely 1) access to good database(s) including some reliable ground truth events, 2) flexible signal processing schemes (beyond that of simple bandpass filtering and stacking of array records), 3) automatic extraction of secondary phase parameters and 4) natural expectations of time domain arrival intervals and strengths of pP, sP, Sn etc.

RESEARCH ACCOMPLISHED

Rome was not build in one day nor is validation of secondary phases accomplished in a year. The status of our research efforts here and associated accomplishments are listed below:

Databases for Research

With all the seismometers deployed at present, establishing proper databases should apparently not be much of a problem. Firstly, secondary phases are a mix of deterministic and random origins so an obvious advantage in the initial research stage is the ability to use the records from station clusters that are small networks. Station separations in the CTBT/IMS network are large so not so convenient when comparison and consistency of secondary phases are the issue. Anyway, we have asked several colleagues for access to their databases preferably including GT information for a few earthquakes but so far with little success. The only positive response we have received is from SAIC (Murphy pers. com.) from whom we have received some 10 Hindu Kush events. A minor problem here is that the crustal structure in this area is not accurately known. In other cases, the data set(s) available do not contain waveforms and even S-phase observations are lacking. We are continuing our efforts to find suitable waveform data bases for validation research.

SeisSchool Digital Seismograph Network

The initiation of these instrumentation efforts commenced roughly two years ago and the status now is that of seven operational stations (see our web page http://pcg1.ifjf.uib.no for details). There are no operational costs as data transfer is via Internet but of course the SP seismometers used, the Cossack Ranger, cost some $ 2000 each. Most stations are deployed in the Bergen area and local recordings provide data of uniform and high quality (Figure 1) that is most important for basic seismological research.

A prominent feature of our SeisSchool network is an advanced database structure allowing data storage and organizing in a manner similar to those at NMR and CTBTO and with advanced software schemes integrated in the database structure. Data analysis for school network recordings does not require special copyrighted software nor scientific/seismological backgrounds aiming at broad user segments -- try for yourself here.

The first step in any seismic data-related research is to obtain location and magnitude parameters for the event in question. For local networks, use of these data is an advantage only in case such information is not available from regional centers, NEIC etc. We have considered several approaches and our preference is for the one where

Table 1. Location experiment for North Sea earthquake 01/06/02/ at 06/18/10.0.[1]

Agency	Longitude	Latitude	Focal depth (km)
NORSAR	3.057 E	61.7902 N	15.9
NSN (Bergen)	3.124 E	61.7350 N	4.0
Our Network (manual)	3.433 E	61.9034 N	3.72
Our Network (envelop)	3.441 E	61.9028 N	3.61
Our Network (piecewise)	3.469 E	61.9445 N	3.70

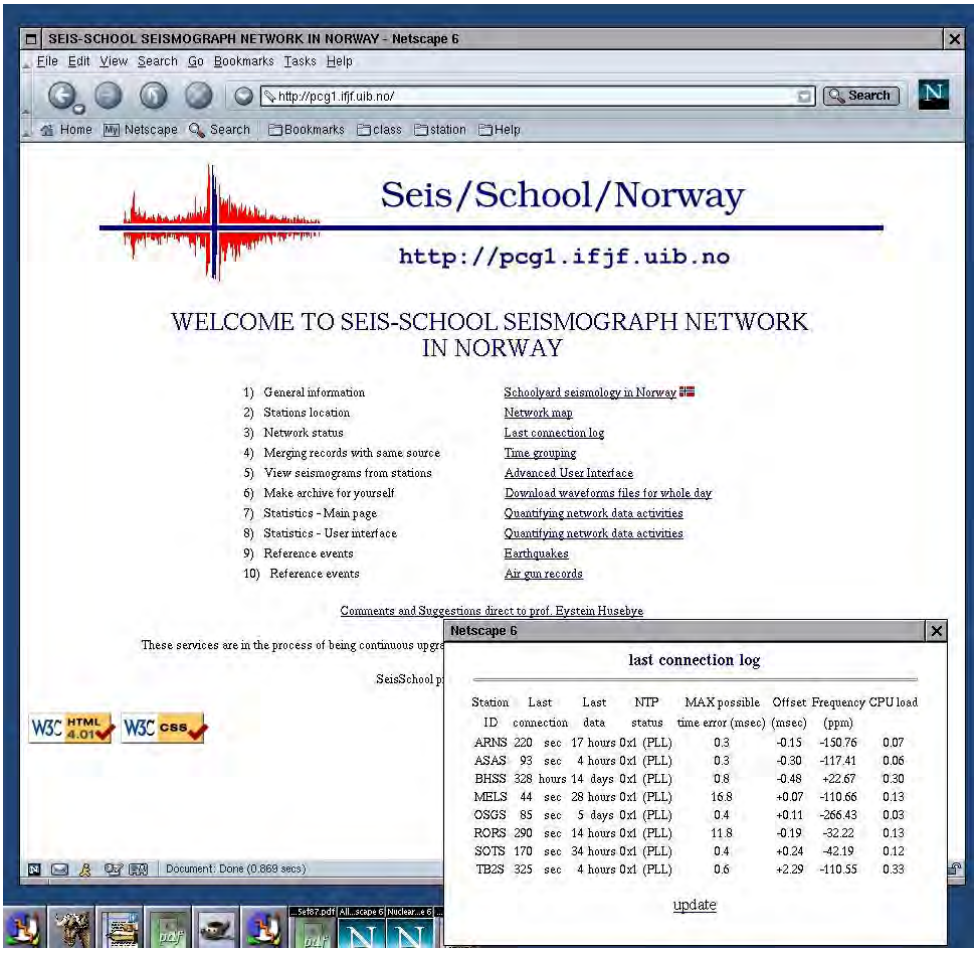

Figure 1. Web-page presentation of our Seis/School/Norway network with insert showing operational status of network stations. Just click on 5) for inspection of network recordings including several filtering and trace zooming options. The first version of epicenter location for any network event can be tested on 9) Reference events -> Earthquakes.

[1] Our solution is based on four school stations of aperture ca 30 km and is close to those from NORSAR and NSN (Bergen) having many observational phases. Our phase picking was as described in the text; using original records and also feature extractions from envelopes. The focal depth estimate was critically dependent on picked Sn-phases.

also model parameters like Pg- and Pn-velocities are subject to estimation. The reason is simple; for 4 - 6 stations each providing 2-3 phase picks, we have enough observations for estimating more than the three standard hypocenter parameters. An example of locating a local earthquake is given in Table 1 with epicenter solutions from NORSAR and Bergen (national network) given as references.

Deformable Template Analysis - Envelope Waveform Matching

There are various 'joint epicenter location' schemes for improved source locations. A variant hereof would be to use deformable template techniques for matching envelope waveforms between different events in a given area or comparing waveforms between network stations. The idea is simple albeit computational complex, namely that for the jth event the recording at station X is a linear deformation (stretching) of that at station Y. Alternatively, we may have a cluster of events or aftershocks but with recordings from only one station but still undertake deformable template analysis with good results. Preliminary testing of this concept on records from our school network produced close similarity between reference and deformed station recordings as illustrated in Figure 2 by Husebye and Fedorenko (2001). Here we discuss its practical usage in terms of signal feature extraction. Firstly, the linear shift between the envelope traces X and Y can be converted to a relative distance estimate since the Lg-group velocity is well known. Alternatively, we use the reference station as a master station and read arrival time of Lg-max amplitude at a corresponding position on the other station traces. It is also feasible to compare in this manner records from different events and then Master Event location techniques may be introduced for very accurate epicenter determination.

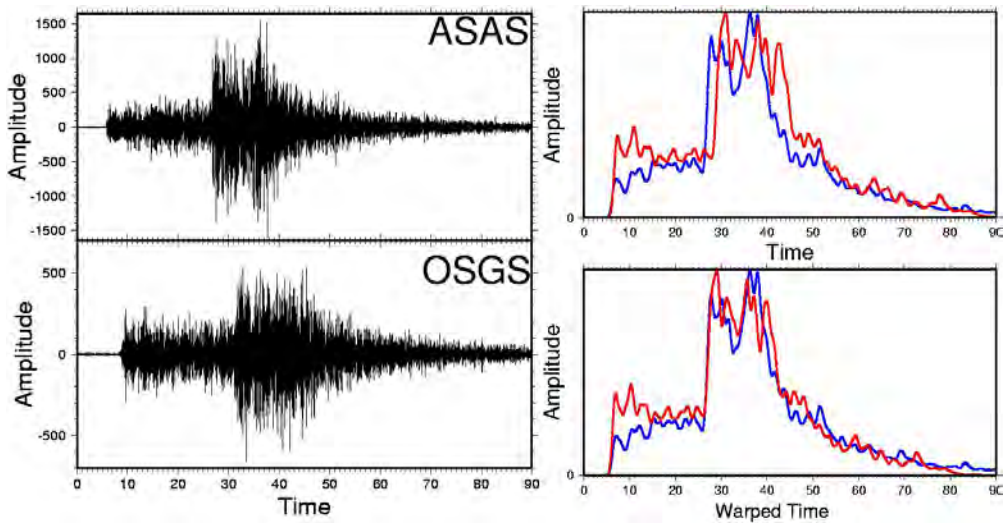

Figure 2. Linear time warping applied to envelopes of two Seis/School/Norway stations recordings.

An interesting research problem here is whether the deformable templates technique may be used for matching P-P-coda segments of records and thus improving secondary phase pickings and their subsequent validations.

Preprocessing Schemes

We pay much attention to the preprocessing scheme, because it produces phase candidates and implicitly defines resulting accuracy of the hypocenter location. We hope that automatic classification allows us to apply different signal processing procedures more freely because the probabilistic formulation of phase picking and hypocenter location would lead to automatic suppression of erroneous outliers. Filtering of initial waveforms in time domain is generally used to suppress that part of the spectra where the signal-to-noise ratio (SNR) is small, while in envelope processing, it is applied to smooth Hilbert transform output to suppress unimportant high-frequency noise and give extra weight to seismic phase arrivals. The same problem arises in polarization analysis where the phase is expected to be polarized but short in time; therefore the choice of a proper type of smoothing filter is essential. There is no general rule how to choose the best filter type and the optimal sequence of operations for an arbitrary signal. We discuss briefly our ongoing filtering tools preparations.

The most important part in building a preprocessing scheme is to understand how the information is contained in seismic signals. Regarding the problem of picking secondary phases, we concentrate on time domain processing and will select the filters by their pulse response, which describes how the information represented in the time domain is modified by filtering. We will consider Infinite Impulse Response (IIR) causal filters because of a previous bad experience with non-causal filters, which produced false ripples occasionally erroneously taken as phase arrivals.

Bessel, Butterworth and Chebyshev IIR Filter Types

There are many types of response approximation; we restrict ourselves to three commonly used filters: Bessel, Butterworth and Chebyshev. Bessel and Chebyshev types are two extremes; first is optimal for time domain and produces small artifacts (ripples) but is inefficient in frequency domain. The Chebyshev filter is "ringing" long after phase arrival thus producing a sort of artificial coda that may tend to obscure weak secondary phases. For this reason it is unacceptable for phase picking. The Butterworth type is an intermediate type, but it often produces ripples that can be taken as phase arrival, so we do not recommend it. As a rule, we are using the Bessel-type pulse optimal filter in view of its property of "preserving" signal energy within the first arriving cycles. Although Bessel-type filters are highly suitable for envelope smoothing, there is one interesting time-domain method of smoothing often named the "Savitzky-Golay filter". It is based on least squares polynomial fitting across a moving window within the data. A higher order polynomial makes it possible to achieve a high level of smoothing without attenuating the extremes in the data, which is essential for reliable secondary phase picking.

Raw Traces and Pre-whitening

Pre-whitening has a dual purpose of removing the low-frequency part of ambient noise and producing an approximate white noise spectrum as desired for the subsequent wavelet transform. Based on many spectral studies, we use a simple linear noise spectrum representation that is inversely proportional to frequency ω. Ambient noise exhibits, at least in coastal areas, strong seasonal variations in levels but not in form for $f > 1$ Hz, so the shape provides a robust and versatile spectrum representation. Using this noise feature we can easily transform initial seismic traces into traces with "white" seismic noise simply by differentiation preferably made through the Fast Fourier Transform (FFT). Stations in the SeisSchool network have a flat acceleration response; hence, pre-whitening is not used for our data, but it may be necessary to apply it to conventional sensors.

Wavelet Transform and Denoising

Like the Fourier transform, the wavelet transform (WT) is a linear operation on a data vector whose length usually is an integer power of 2, transforming it into a numerically different vector of the same length. In the wavelet domain basis functions $\psi(\tau, s; t)$ are somewhat complicated and have fanciful names like 'mother functions' and 'wavelets'. WT can be thought of as $X(\tau, s) = \int x(t)\psi_{\tau,s}(t)dt$ where $\psi_{\tau,s}(t) = (1/\sqrt{s})\psi[(t-\tau)/s]$. In the WT domain the axes are scale *s* or inverse frequency and τ, which is the time shift as the wavelet slides through the signal window. Physically this means that low scales, which is the high-frequency part of the signal, has good time resolution while high scales are low frequencies with good frequency resolution. Hence, most of the usefulness of wavelet operation rests on the fact that $X(\tau, s)$ can be severely truncated as shown in Press *et al*. (1992), thus removing weakly represented scattering and noise contributions. This operation is especially useful for denoising non-stationary seismic waveform data. The choice and corresponding length of the wavelet function may not be overly critical; so far we have some experience with wavelets of the types Daubechies 4, 12 and 20 as shown in Daubechies (1988) and Press *et al*. (1992). In practical seismogram analysis we expect that in the case of pure noise with approximately flat spectra after pre-whitening, the wavelet transform will also be flat so wavelet coefficients for different s and τ will possess similar amplitudes, which may be removed without substantial distortion of the original signals. The ongoing experiments with sequential filter operations are encouraging; we clearly obtain better results than conventional bandpass Butterworth filtering. The above 'filter package' would be incorporated in the SeisSchool database to ensure much practical experimenting.

Secondary Phase Picking, Parameterization and Feature Analysis

Above we have outlined a number of signal processing schemes currently being tested for relative suitability on our SeisSchool recordings. Naturally, we consider these schemes well suited for preparing initial seismic traces for detecting weak secondary phases like pP, sP and Sn. To do so in practice, we have to quantify what we mean with signal features and naturally how to extract them from which type of records. Initially, we start with manual pickings of the arrival times of presumed secondary phases and then adapt the proper automated signal feature extraction scheme. In practice we do both in parallel as we need a data set of secondary phases for testing on maximum likelihood concepts of phase validations (next section) while here we briefly outline automated picking schemes. Firstly, at local distances, high-frequency signals dominate the seismogram but the recordings are complex and not well suited for automatic and flexible phase pickings. In our processing schemes the final trace output is, with few exceptions, the envelope trace and not the original waveform trace. Also, there are no clear wave theory anchored criteria for separating wavelets of respectively random and deterministic origins during the phase picking process. Since we cannot invert high-frequency signal waveforms, our feature extraction is tied to kinematical signal parameters like arrival time and amplitude in envelope traces.

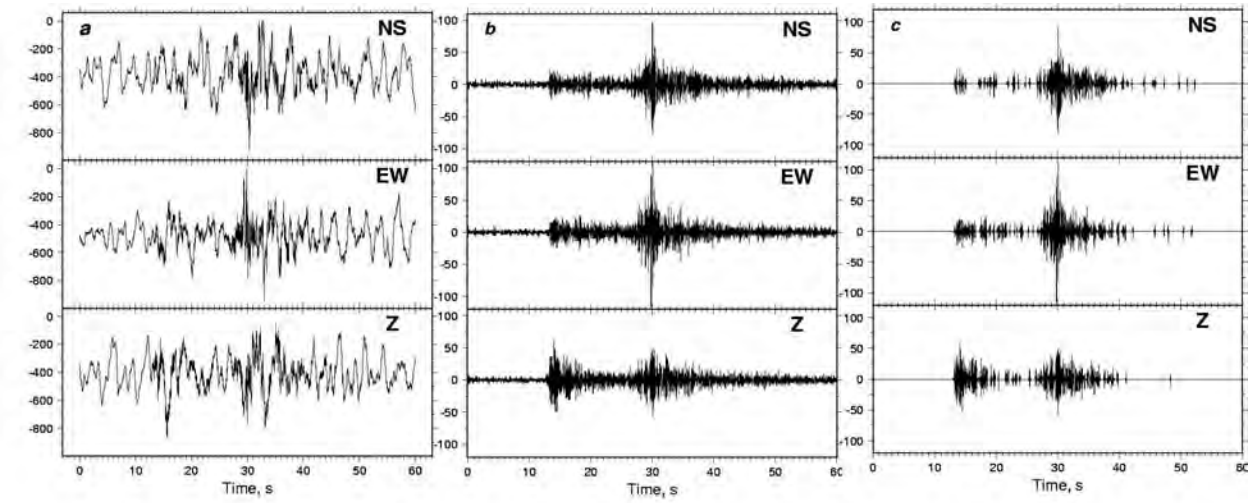

Figure 3. Original waveform processing. (a): Raw waveforms that are unfiltered Hoyanger (HYA) 3-component recordings of an arbitrarily chosen event; (b): Same event as in (a) but after pre-whitening; noise suppression is significant; (c): Same event as in (a) but after wavelet transform operation; preceding noise has been wiped out while the signal segments remains largely untouched.

Envelope Trace Segmentation

There are numerous techniques for economical time series representations as discussed by Pavlidis and Horowitz (1974) and Keogh and Smyth (1997) and methods for sequence recognizing and retrieval, where the features extracted are characteristic parts of the time series, so-called "feature shapes". Such methods do the same things as deformable template methods are supposed to do, that is time warping, shifting and uniform and non-uniform scaling of features. The latter is computationally much faster, partially due to economical representation of time series, partially because of simplicity of features. The economical representation critically impacts the sensitivity of the distance measure to various distortions and also can substantially determine the efficiency of the matching process. Thus, one seeks robust representation that are computationally efficient to work with. We are interested here in pursuing a representational language that can directly capture the notion of secondary phases shape. Piece-wise linear segmentations provide both an intuitive and practical method for representing curves in a simple parametric form (generalizations to low-order polynomial and spline representations are straightforward). There are a large number of different algorithms for segmenting a curve into the "best" piece-wise linear segments. Although appearing under different names and with slightly different implementation details, most of them can be grouped into one of the following three categories as shown by Keogh *et.al* (2001).

1. **Sliding Windows:** A segment is grown until it exceeds some error bound. The process repeats with the next data point not included in the newly approximated segment.
2. **Top-Down:** The time series is recursively partitioned until some stopping criterion is met.
3. **Bottom-Up:** Starting from the finest possible approximation, segments are merged until some stopping criterion is met.

Extracting of features from segmented envelopes is an easy and fast process. For example, we consider searching for the segments of the exact "inverted V" shape and/or rapidly ascending segments (Figure 4), using the angle between the adjacent segment as selector. We also extract the parameters of a segments constructing feature. The final choice of which shape "best" represents secondary phases is a major problem that must be resolved using simulated traces, real recordings from our network and GT recordings at local distances.

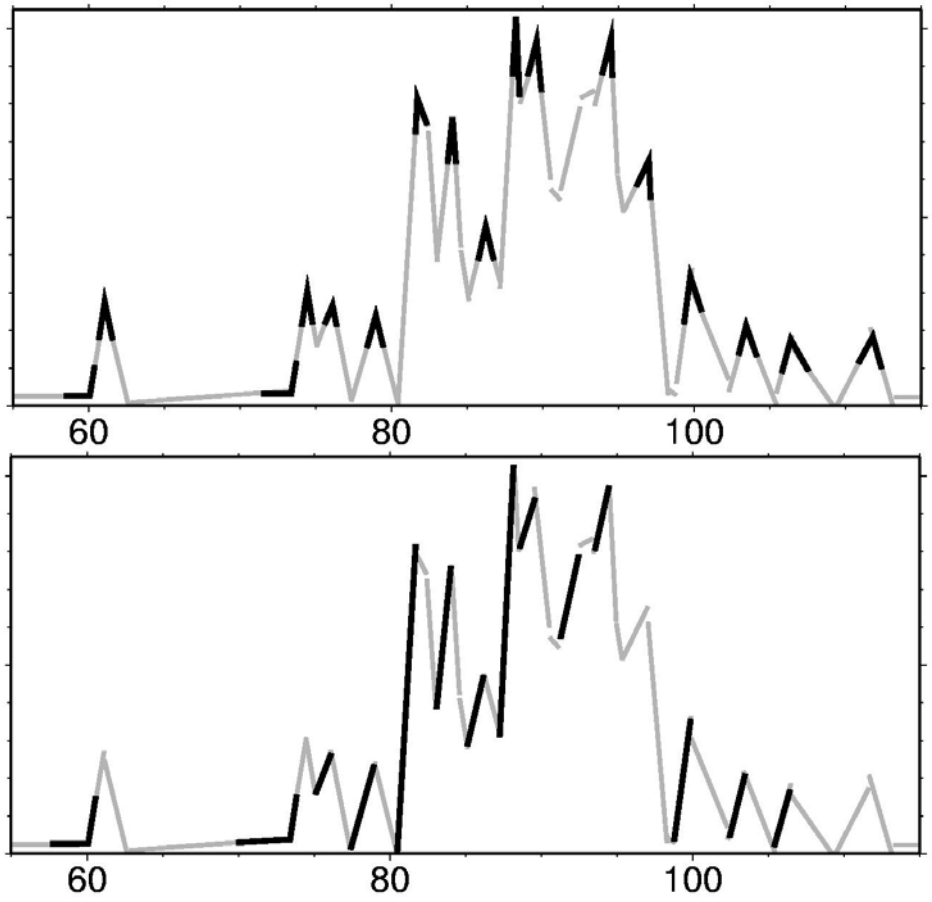

Figure 4. Extracting of features from envelope traces; upper triangle shapes and lower steep lines are used in our data mining experiments on trace segment representations. Both of these schemes give largely similar feature representations. Horizontal axis: time in seconds.

Needless to say, much experimenting is needed in determining which trace segmentation scheme is adequate for extracting phase information in an automatic manner from the seismic record.

Statistical Approach to Phase Validation

The problem of properly picking secondary phase arrivals is encountered in many seismological disciplines, perhaps foremost in long-range seismic profiling investigations. It appears that many of our colleagues by definition presume that any secondary arrival stems from a clearly defined crustal discontinuity stretching laterally for hundreds of kilometers -- both from a physical point of view, as this is not likely due to small impedance contrasts that can be accommodated in the crustal wave guide, but also from a geological point of view due to many tectonic deformations in the past. Also, seismic analysts are occasionally eager to report many (presumed) prominent phases,

which regrettably do not comply with travel-time expectations from standard Earth models. Hence, for a start, we may assume that the wavelet signal amplitudes are large relative to ambient noise and the P-coda so major problems in phase picking and phase identification originate from random layer reflections and complex topography. In other words we have more phase candidates than the obvious three classical ones -- pP, sP and Sn -- arriving between Pn or Pg and Lg or Sg. The phase readings stem from a network of five to ten stations so we are faced with a formidable multi-dimensional data space of observations to analyze with respect to arrival times (velocity model) and source radiation pattern (amplitude ratios).

Intuitively, we may wonder if the size of this data space can be reduced by more optimal processing schemes and/or by a trained analyst to identify false phase wavelets. With all combinations at hand such an approach would be futile in our opinion. However, a more general mathematical approach is to formulate the above validation problem as a classification or 'clustering' problem. A deterministic, brute force solution would be to search the whole model space, thus assigning the detected phase candidates to separate classes that conform to expected arrival times and amplitude ratios for pP and sP. Again, we are not convinced that this strategy really would provide a good solution to our validation problem. Below, we outline our approach to the phase validation problem using a maximum likelihood formulation and classic statistical mixture model for clustering. Although ML clustering is less general than Bayesian unsupervised classification, we sacrifice generality for the sake of simplicity. Mixture modeling concerns modeling a statistical distribution by a weighted sum of other distributions.

Let the input vectors $\mathbf{x}_1$, $\mathbf{x}_2$, …, $\mathbf{x}_n$ be observations from a set of unknown distributions E_1, E_2, …, E_k. Suppose that the probability density of the observation $\mathbf{x}_r$ with respect to E_i is given by $f_i(\mathbf{x}_r \mid \theta)$ for some unknown set of parameters θ. Also, suppose for each $\mathbf{x}_r$ and distribution E_i τ_r^i represents the probability that $\mathbf{x}_r$ belongs to E_i. Each input is constrained to belong to some distribution, so $\sum_{i=1}^{k} \tau_r^i = 1$. Given these definitions, the goal of the scheme is to find the parameters θ and τ_r^i that maximize the likelihood

$$L(\theta, \tau) = \prod_{r=1}^{n} \sum_{i=1}^{k} \tau_r^i f_i(\mathbf{x}_r \mid \theta)$$

Following Banfield and Raftery (1993), we simplify this equation even more by assuming that each input must belong to exactly one distribution. It discards the probabilities τ_r^i and introduces the vector $\boldsymbol{\gamma} = (\gamma_1, \gamma_2, ..., \gamma_n)$ to represent the identifying label for observations, so $\gamma_r = i$ if $\mathbf{x}_r$ comes from E_i. The goal is then to find the parameters θ and γ that maximize the likelihood

$$L(\theta, \gamma) = \prod_{r=1}^{n} f_{\gamma r}(\mathbf{x}_r \mid \theta) \tag{1}$$

Now the problem is to define $f_{\gamma r}(\mathbf{x}_r \mid \theta)$ for each possible distribution E_i using our knowledge about velocity model, hypocenter and stations locations, fault plane orientation, lithosphere scattering properties and surface and Moho reflectors that define P-coda duration, variance of ambient seismic noise and seismic signal amplitude.
As a practical example; we consider the simple case of the p.d.f. in $f_r(\mathbf{x}_r \mid \theta)$ only relating to wavelet arrival time. We further assume that all possible hypocenters are located within an elliptically shaped cylinder with discrete hypocenter positions O_i. Let the number of stations be Q and these stations record all M seismic phases. For each O_i and station S_q we calculate arrival time for M phases $\mathbf{T}_q = T_{iq}^m$, $m = 1,...,M$. The measured arrivals from O_i to station S_q are $\mathbf{t}_q = t_{iq}^m$ are presumed normally distributed with mean t_{iq}^m and variance σ_{iq}^m. Then, at each station we compose $\mathbf{t}_q$ choosing M phases from K candidates, $K \geq M$. Finally, we find γ which maximizes (2); it would be the set of secondary seismic phases expected from the model.

Naturally, it may be argued that this example is too simplified. Firstly, it is not likely that all phases appear between candidate wavelets at each station. Some phases obviously will be missed at some stations so we need to define the probability or compose our cases with missed arrivals. On the other hand, the unsupervised Bayesian learning approach is able to treat such cases and thus is superior to the simpler likelihood formulation on this account. Secondly, information about relative phase amplitudes, which really controls accuracy of measurements and defines

how likely it is to miss a phase, was not included in the above model as illustrated below. Still, the above example could be instructive. For example, we desire to estimate the probability that the power ratio $R = P_{\text{depth}} / P_{\text{Pg}}$ is greater than, for example, 10 at focal sphere; P_{depth} is a power of a depth phase leaving the focal sphere along the ray connecting source and station. In this case we presume that the Pg coda will not mask depth phases and that the fault plane orientation has a uniform angular distribution. The three recording stations are 130 km away from the epicenter with azimuths 0, 30 and 60 degrees respectively. Table 2 summarizes results of evaluating secondary phase power relative Pg obtained by a Monte-Carlo test. *N* is the number of stations involved; "Any phase" column shows the probability that *R*>10 for at least one secondary phase at focal sphere for any station.

Table 2. Probabilities for finding secondary phases pP, sP and Pmp in the earthquake records assuming uniformly distributed fault plane orientation.

N	$P(R_{\text{Pn}} > 10)$	$P(R_{\text{pP}} > 10)$	$P(R_{\text{sP}} > 10)$	$P(R_{\text{PmP}} > 10)$	**Any phase**
1	0.14	0.13	0.10	0.14	0.37
2	0.28	0.27	0.20	0.27	0.50
3	0.43	0.39	0.30	0.41	0.61

Table 2 implies that by using three stations, we may expect to pick at least one of the secondary phases masked by a strong Pg-coda with a probability about 60%. These results are also incomplete because the positions of secondary phase arrivals relative to the strong Pg phase are also important.

CONCLUSIONS AND RECOMMENDATIONS

Seismology provides a unique, observational platform to the dynamic Earth by recording elastic waves generated by small and large earthquakes any place in the world. As a science, seismology is exclusive since instrumentation is very expensive and subsequent data accesses are problematic for non-seismologists as well as many other geoscientists. We have here demonstrated that design and construction of inexpensive but high-quality SP seismometers are feasible and that easy, cost-free data access via the internet is now feasible (Figure 1).
Our end product will be a comprehensive phase picking and phase validation scheme. This would imply that analyst participation in routine record analysis and bulletin preparation work will be significantly reduced. In our opinion the initial waveforms are too complex for automated phase picking so we start analysis with simplifying waveforms and enhancing phase arrivals. These preprocessing steps include waveform bandpass filtering, then constructing rectilinearity and planarity envelopes using eigenvalues of polarization matrix and finally making a piece-wise envelope approximation. In order to estimate how much these transformations affect the final location, we compare the hypocenter position obtained from a) phases picked manually from original waveforms; b) phases picked manually from envelope maximum and c) obtained from "inverted V" features (Figure 4) of piece-wise approximations.

The results are slightly different, but the maximum distance between various epicenter locations for an off-shore earthquake in western Norway was less than 8 km and focal depth differences were within 2 km. To us, these results are encouraging at this initial step of concept development and the applicability of our preprocessing scheme. Step by step we proceed in the following manner:

1. We automatically obtain a first approximate epicenter location from first arriving phases through 'wavefront fitting'. Using the shape "like _/" we obtain first arrivals from piece-wise envelopes for all stations. At this stage we need to test whether these first arrivals are Pg or Pn or a Pg and Pn mixture across the network. We relocate and compare the residuals; if residuals are large, we rename Pn <-> Pg until location converges. Then we add one clearly seen phase Sn, Sg or Lg type and obtain an improved epicenter location.
2. We set the uncertainty of phase arrival time, say 0.3-0.5 sec; surround the epicenter by a mesh and use a grid search method to obtain the maximal value of the likelihood function. Then we add one of phase candidates for, to say, Sn, and recalculate likelihood. The candidate that adds most to the likelihood function is chosen as this stage.

3. Recalculate the hypocenter and repeat step 2 until we have a stable solution for hypocenter. We are now in the process of analyzing many local events -- not all from our own network -- and a particular interesting aspect here is whether we could estimate realistic probabilities of observing and picking secondary onsets bearing on focal depths.

Future Research: Locating accurately small seismic events recorded at local and regional distances, and particularly improving focal depth estimates, remains an outstanding problem. Our own research strategy and hence recommendations are:

1. More reference data sets stemming from dense networks and some events must comply with Ground Truth requirement for GT5 at least.
2. More attention must be given to the way records are analyzed; secondary phases like pP, sP and Sn are not obviously identified after simple bandpass filtering. Polarization filters may suppress random wavelets. Such phase observations are important for improved focal depth estimates.
3. Since secondary phases are not easily picked, probabilistic phase validation schemes are important as demonstrated here. We need far more observations in order to explore the most advanced strategies.
4. Learning aspects: deformable wavelet matching. In this way source location distortions are easily demonstrated but whether the technique is useful for validating deterministic secondary phase pickings remains to be seen.

Final remark: improved feature extractions from local recordings and hence improved CTBT monitoring capabilities dictate non-conventional approaches in both recording analysis and probabilistic interpretational tools in view of modest research progresses in this field over the last decades.

REFERENCES

Daubechies, I., (1988). Orthonormal bases of compactly supported wavelets. *Communications on Pure and Applied Mathematics,* **41**, pp. 909-996.

Fedorenko, Yu. V., E. S. Husebye and B. O. Ruud, (1999). Explosion Site Recognition: Neural Net Discriminator Using Three-Component Stations, *Phys. Earth Planet. Int.*, **113**, 131-142.

Husebye, E. S. and Y. V. Fedorenko, 2001. Seismic regionalization, signal detector and source locator. Proceedings of the 23rd DOD/DOE Seismic Research Review: Worldwide monitoring of Nuclear Explosions. Rep. no. LA-UR-01-4454. Vol. 1, 242 - 251. Oct 2-5/01, Jackson Hole; WY, USA.

Fedorenko, Yu. V. and E. S. Husebye, (1999). First Breaks - Automatic Phase Picking of P- and S- onsets in Seismic Records. *Geophys. Res. Lett.*, **26**, 3249-3253.

Keogh, Chu, Hart, and Pazzani, (2001). An Online Algorithm for Segmenting Time Series. IEEE International Conference on Data Mining.

Keogh, E. and P. Smyth, (1997). A probabilistic approach to fast pattern matching in time series databases. In Proceedings of the 3rd Conference on Knowledge Discovery in Databases and Data Mining, Newport Beach, VA, USA.

Pavlidis, T. and S. Horowitz, Segmentation of Plane Curves, IEEE Transactions on Computers, vol. c-23, no. 8, August 1974.

Press, W. H., S. A. Teukolsky, W. T. Vetterling and B. P. Flannery, (1992). Numerical Recipes in C: The Art of Scientific Computing, Chap. 13, 2nd Edition, Cambridge University Press.

DEMONSTRATION OF ADVANCED CONCEPTS FOR NUCLEAR TEST MONITORING APPLIED TO THE NUCLEAR TEST SITE AT LOP NOR, CHINA

Benjamin Kohl,[1] Robert North,[1] John R. Murphy,[1] Mark Fisk,[2] and Gregory Beall[1]

Science Applications International Corporation,[1] Mission Research Corporation[2]

Sponsored by Defense Threat Reduction Agency

Contract No. DTRA01-99-C-0025

ABSTRACT

Starting in October 2001 the Center for Monitoring Research (CMR) engaged in an advanced concept demonstration (ACD) to improve nuclear-explosion monitoring capability, focused on the Chinese test site at Lop Nor. A demonstration prototype system was developed by integrating innovative techniques gleaned from recent research and development advances. Emphasis was in the areas of detection, location and identification of underground nuclear explosions with particular attention to techniques applicable to regional seismology in and around the Chinese test site.

The demonstration prototype system was tested against a very large uniform and calibrated database of seismic recordings from over 200 explosions and earthquakes in the vicinity of Lop Nor. The data set, which was assembled from approximately 100,000 event recordings (~ 100 GB) from some 60 different seismic stations sampling the near-regional to teleseismic distance range, provides an unprecedented data resource that can be used to conduct appropriate and meaningful scale tests to quantitatively assess new monitoring techniques for this region.

The above referenced data were supplemented by theoretically scaling selected event recordings of historical nuclear explosions and earthquakes down to levels of $m_b = 3.5$, $m_b = 3.0$ and $m_b = 2.5$. This permitted, for the first time, realistic assessments of frequency dependent event detection and identification capability at low thresholds. The scaled waveforms were embedded in actual background noise and integrated into a database specifically designed for processing with a standard automated and interactive analysis pipeline compatible with those currently employed by the International Data Centre (IDC) and the United States National Data Center.

With respect to the final version of the processing and analysis tools delivered to the IDC by CMR, innovations in the ACD demonstration prototype system include site-specific threshold monitoring and the F-statistic detector to facilitate automated detection. Origin information and waveform data from the underground nuclear explosions historically conducted at Lop Nor were assembled and used to facilitate improved location, including:

- Development of static travel-time test-site corrections
- Calibration of regional travel times, i.e. Site-Specific Stations Correction (SSSCs) developed by the Defense Threat Reduction Agency (DTRA) Group 1 and Group 2 calibration consortia and integrated into the ACD
- Development of a waveform cross-correlation tool, used for making very accurate arrival picks
- Master event and joint hypocenter determination (JHD) relocation algorithms
- Non-gaussian confidence area visualization

To extend the applicability of the mb:Ms discriminant to low thresholds, phase-matched filtered-surface wave detection was integrated into the ACD demonstration prototype system. In the area of depth phase utilization, a number of innovations were integrated, including depth phase stacking and the use of F-statistic and probability traces. Regional 3-component amplitude ratios were calibrated specifically for the Lop Nor area and fused with other discriminants (depth, mb:Ms) to form event identifications based on multivariate syntheses.

The tuned ACD demonstration prototype system was applied to the systematic analysis of the events in the Lop Nor data sets. The results have confirmed that significant improvements in detection, location and identification capability in this region are achievable as a result of this effort.

OBJECTIVES

General Approach

To assess the potential applicability of recent research results to the overall objective of improving nuclear test monitoring capability, the Center for Monitoring Research (CMR) has been developing a test environment and approach, within which promising results and developments can be evaluated in the context of a broader nuclear test data processing and analysis system. Promising advanced concepts such as site-specific threshold monitoring (Kværna *et al*, 2001), high precision location through waveform cross-correlation and master event location (Fisk, 2002) and regional surface wave detection through phase matched filtering (Stevens *et al*, 2001) have shown great potential for improving detection, location and identification capabilities. These and many other similarly promising advanced concepts have been demonstrated within the realm of the individual research projects, limited in terms of the scope and resources of a basic research and development (R&D) project.

The CMR offers an open and flexible environment that is ideally suited to perform intensive, broadly scoped projects on short time scales specifically geared to assessing improvements to nuclear test monitoring capabilities. We have developed an approach termed an Advanced Concept Demonstration (ACD) that facilitates the rapid assessment and demonstration of realizable capability gains through appropriate scale testing, focused on a specific nuclear test monitoring problem. The approach we have developed leverages a wide range of resources that are not typically available to individual researchers, that are on the other hand available at the CMR. These include

- Database and extensive archive of International Monitoring System (IMS) waveform data
- Numerous specialized data sets (e.g. explosion and ground truth databases)
- System software i.e. the core of the data processing and analysis system used by both the International Data Centre (IDC) and the United States National Data Center (USNDC)
- Computer infrastructure, in particular numerous data processing servers and analysis workstations
- Software development team, well suited to rapid prototyping and integrating tools based on R&D efforts
- Operational test and evaluation experience; in particular, scientists and analysts familiar with the real-world challenges of processing and analyzing large volumes of data

As mentioned above, an ACD facilitates appropriate scale testing within the context of a broader nuclear test data processing and analysis system. We integrate and apply new prototype tools and R&D results at the appropriate point within the full range of processing and analysis steps going from signal detection, all the way through event identification. This has the benefit of assessing the performance of the advanced concepts under realistic conditions.

Aside from slight variations in approach due to the specifics of a particular focus area, all ACDs invoke a common process and summarized in the following six steps:

1. Use customer focus and technical challenges to define scope of the specific monitoring problem being addressed by the ACD
2. Identify relevant R&D results
3. Rapid prototype new tools based on research results
4. Integrate prototype tools and/or research contributions into a prototype demonstration system compatible with the core system software of the IDC and USNDC
5. Apply core system and ACD tools and against a variety of very large data sets
    a. Historical data for validation of techniques
    b. Scaled or synthetic data to allow testing at thresholds of interest for US monitoring objectives
6. Conduct performance evaluation

While the content and structure of the data sets are motivated by the specific requirements of the ACDs, it is recognized that these may have significant value to the R&D community at large. As a result the data sets are transitioned to the Research and Development Support System (RDSS) function of the CMR (Woodward and North, 2002), through which the data and some portion of processing and analysis results are made available to researchers.

In this paper we present the results of having conducted an ACD focused on assessing potential improvements to the capability to detect, locate and identify events in and around the nuclear test site at Lop Nor, China.

Lop Nor ACD Goals

The Chinese nuclear test site at Lop Nor (alternately referred to as Lop Nur in some publications) is of considerable interest and is a particularly attractive ACD focus area for a number of reasons. Commercial satellite imagery obtained by the CMR (Skov *et al*, 2002) shows evidence of continued activity of unknown purpose at the test site. The 45 historical nuclear explosions of which 23 were underground detonations (Yang *et al*, 2000) provide an excellent source of data for calibration and evaluation purposes, particularly since high quality ground truth locations are now available from Fisk (2002) for the most recent explosions with extensive waveform recordings. Finally capability for monitoring of Lop Nor has dramatically improved with the deployment of the seismic array at Makanchi, Kazakhstan.

A potential technical challenge to monitoring of the Lop Nor site is posed by the fact that the area is seismically active. Since 1964 the ISC reported some 370 earthquakes within the geographical area of 37° – 44° north latitude, 84° – 94° east longitude, most of which are at m_b 4 or larger. Figure 1 shows the ISC locations of earthquakes (orange circles) and underground nuclear explosions (red stars). The Harvard CMT solutions are also shown (beach balls) when available. It is clear that earthquakes occur within the test site area itself. In fact two moderate earthquakes (January 27 and 30, 1999) occurred within about 15 km of historical nuclear tests. As detection capability improves it can be expected that the number of small events detected within the historical test site will significantly increase. The challenge will be to supplement the capabilities of the Makanchi array and accurately locate and identify numerous small ($< m_b$ 3.0) events using regional seismic data.

Our baseline for assessing improvements obtained through the execution of the ACD was derived from the performance of the GSETT-3 and IMS network. This is embodied in the reviewed event bulletin (REB) of the Prototype International Data Center (PIDC) from 1995 – 2000, followed by the REB produced by the IDC after Feb. 20, 2000. An analysis of these bulletins reveals historical capability at Lop Nor as follows:

- Three-station 90% confidence detection threshold: m_b 3.6
- Location – 90% confidence coverage ellipse area: 3000 km^2 for m_b 3.5 events
- Event identification threshold: m_b 4.5

RESEARCH ACCOMPLISHED

The main effort of the Lop Nor ACD took place in the seven months between October 2001 and April 2002 involving numerous scientists and engineers. Rather than present the full scope of the accomplishments, in this paper we present a high-level summary of the results, and overviews of the data sets and integration activities.

Using metrics analogous to those presented in the "Objectives" section of this report, we summarize the accomplishments of the ACD as follows: it was demonstrated that by integrating a number of advanced concepts gleaned from recent research endeavors, significant improvements in detection, location and identification capability were achieved. As specifically applied to the Lop Nor test site, these improvements are:

- Detection – three-station 90% confidence detection threshold:
  - m_b 2.8, as validated through a combination of real and scaled explosion waveform data sets
  - m_b 2.5, expected as more experience is obtained with the Makanchi array (MKAR) allowing a robust single or two-station event definition criteria
- Location – 90% confidence coverage ellipse area:
  - 1200 km^2 for m_b 3.5 events, based on individual event locations using calibrated travel times
  - 40 km^2 for m_b 3.5 events that are within 20 km of historical explosions and exhibiting a high degree of waveform cross-correlation, based on a master event and/or JHD algorithms
- Location – mislocation of explosions:
  - Application of the waveform cross-correlation/master event location technique to explosions since 1990 and to the scaled explosion data showed that the median mislocation was reduced from 7.6 km to 0.4 km. For the same set of explosions, the median error ellipse area was reduced from 700 km^2 to 11 km^2. This indicates that with the ACD station set and tools, we can locate explosions at the test site to within 2 km of ground truth, even events as small as m_b 3 – 3.5.
- Event identification threshold: m_b 3.0, based on application to 162 earthquakes, actual nuclear explosions, and the scaled explosion waveform data sets

It should be noted that these improvements are based on the processing and analysis using a demonstration prototype system. It would take additional engineering effort to promote this functionality to the point where it could be integrated into the system of a monitoring agency such as the USNDC or the IDC. Further, capabilities are highly dependent on the particulars of the sensor network providing data. It is therefore expected that upon implementation of these advanced concepts in an actual monitoring environment, the capabilities could well be better than those listed above, depending on particular contributions of additional stations not considered in this ACD.

Development of Data Sets

A key element of the Lop Nor ACD was the assembly of data sets for the purpose of developing, testing, calibrating and ultimately validating the advanced concepts.

Station Set
In selecting the stations contributing to the data sets, we first chose to include all stations at regional distances to Lop Nor for which an appreciable amount of historical waveform data were available. Second we chose to include those teleseismic stations from either the GSETT-3 or IMS station networks that had excellent signal detection characteristics as determined from the recordings of historical Lop Nor explosions. This resulted in a network of approximately 60 stations as shown in Figure 2. It should be noted that the stations of the Chinese Digital Seismic Network (CDSN) were included in the ACD station set despite the fact that only one waveform record of a Lop Nor explosion is available from those stations. Because our capability assessments were largely based on the processing of scaled nuclear explosion data, our overall conclusions implicitly exclude the CDSN stations.

Figure 3 shows the relative performance of all the stations in the set. It clearly shows how the Makanchi array (MKAR) is the most important station for detection of events in and around Lop Nor. Other key sites are the regional three-component stations TKM2 and ULHL that are part of the Kirghiz network. The best performing teleseismic arrays are CMAR, NORES, ILAR and YKA.

Reference Data Set
The event based reference data set was assembled by first pulling together bulletin information from available open sources (ISC, PIDC, IDC) and then supplementing that with the Annual Bulletin of Chinese Earthquakes (ABCE) (Richards et. al, 2002). This produced the master list of events used to obtain waveform data from a variety of sources including the CMR archive, AFTAC, NORSAR, Blacknest, and the data management center at IRIS. The data set included 21 underground nuclear explosions and 51 events published in the PIDC or IDC REB since 1995 and 101 events published only in the ABCE during 1995 - 1999, all within the study area of 39° - 44° north latitude, 86° - 92° east longitude. More information about the reference data set is reported by Woodward and North (2002).

Fixed Data Set
To supplement the event based reference data set, we assembled a fixed data set consisting of 10 days of continuous waveform data for the period August 2 – 11, 2001. This data set was used for a variety of assessments, including determining background noise levels and false alarm rates. Further the fixed data set was processed with an objective of detecting and locating events not published in any bulletin. Three small events within the Lop Nor study area of 39° - 44° north latitude, 86° - 92° east longitude were detected and located by multiple stations using the ACD demonstration prototype system. Additionally several dozen small events from within the study area were detected by the Makanchi array only, however without further constraints they were not well located.

Scaled explosion waveforms
In order to assess monitoring capability with respect to the smallest explosions of current interest at Lop Nor, it is necessary to have access to broadband regional waveforms corresponding to explosions associated with the magnitude range from about $m_b = 2.5$ to $m_b = 3.5$, which encompasses the values expected from very small subkiloton tamped explosions, as well as from fully decoupled cavity explosions with yields greater than about 1 kt. However, at the present time, we have no observations available from Lop Nor explosions in this magnitude range, so it was necessary to theoretically scale data observed from larger explosions to obtain approximations to the signals expected from the smaller or decoupled explosions in order to quantitatively evaluate the applicability of various proposed monitoring strategies and algorithms. In the past, for applications to traditional short-period teleseismic data, such scaling has generally been accomplished by simply multiplying the observed narrowband waveforms by a frequency independent constant factor taken to be consistent with the difference in m_b values

between the observed and hypothetical explosions. However, this approach is not appropriate for broadband regional data and, consequently, in the present study we have employed the more sophisticated frequency dependent scaling methodology which is summarized as follows.

The expected ground motion time history for a small explosion can be determined from the observed ground motion from a large explosion at the same station if the spectral ratio of the two seismic source functions can be estimated. For the present application, we have approximated this source spectral ratio using the well-documented Mueller/Murphy explosion source model (Mueller and Murphy, 1971). In this case the scaled seismogram $Z_2(t)$ of a particular component of motion recorded at a fixed station can be derived from the recorded waveform by

$$Z_2(t) = \int Z_1(t)\, S(t - \tau)\, d\tau$$

Where $Z_1(t)$ is the original seismogram and S(t) is the explosion source scaling operator (i.e. the inverse transform of spectral ratio from the Mueller/Murphy explosion source model).

The procedure described above has been used to scale seismic data from the Lop Nor reference explosions of May 15, 1995 and July 29, 1996 down to the lower equivalent explosion yields of interest in the assessment of monitoring capability at that test site. As a test of the applicability of this methodology to Lop Nor explosions, we first theoretically scaled selected observed regional data from the larger of the two reference explosions (i.e. May 15, 1995, m_b(REB) = 5.73) to the source conditions of the smaller reference explosion (i.e. July 29, 1996, m_b(REB) = 4.71) and compared the resulting synthetics with the corresponding observed data from the smaller explosion. The results for station MAK ($\Delta \approx 7°$) are shown in Figure 4, where it can be seen that the theoretical scaling very accurately accounts for the observed frequency dependent changes in waveform characteristics, as evidenced by the pronounced change in the L_g/P amplitude ratio between the larger and smaller explosions. In this case, because the two explosions are not collocated, some differences are evident in detailed waveform characteristics and amplitude level between the scaled and observed data, with the theoretically scaled having a broadband peak amplitude level which is about a factor of 2 smaller than the observed at this station.

Integration of R&D elements and prototype into a demonstration system

Table 1 presents a listing of the key R&D elements, rapid prototyped tools, calibration and tuning results synthesized into a demonstration prototype system as part of this ACD. Our approach to integrating these elements was to use as a baseline, the monitoring system software that defines the core of both the IDC Release 3 upgrade delivery and the USNDC Phase 2 system.

We made numerous significant upgrades to many of the key elements of the core system, including the detection and feature extraction software (DFX) and the interactive analysis suite (ARS). When R&D elements or advanced concepts were implemented through direct changes to the core part of the system software they are categorized in Table 1 as “Software”. Some of the advanced concepts required implementation in the form of a new tool or component. In that case they are flagged in Table 1 as “Prototype software”. Finally a number of the changes were the result of tuning, calibration or reconfiguration. There were typically implemented by updates to existing parameter or configuration files, for example, detection recipes, SSSCs and magnitude correction files.

Table 1: R&D elements, prototype tools, calibration and tuning results integrated into a demonstration prototype system as part of the Lop Nor Advanced Concept Demonstration (ACD)

Monitoring Category	Element Type	Description
Detection	Tuning	Tuned recipes for sta/lta detector for the Makanchi array (MKAR)
	Software + Tuning	Implemented and integrated the F-statistic detector, developed and tuned recipes for regional and teleseismic arrays
	Software + Tuning	Implemented and integrated site-specific threshold monitoring (SSTM) focused on Lop Nor, using MKAR, key teleseismic arrays + selected regional 3-C stations, derived from Kværna *et al* (2001).
	Prototype software	Implemented event detection by triggering off of deviations of SSTM trace
	Tuning	Adapted global association algorithm (GA) to regional association, using fine regional grid and tuned phase association rules
	Prototype software	Developed and integrated a tool to facilitate tip-off based review of scrolling real-time waveform data, including beams, SNR and other traces
Location	Software	Upgraded system software to allow user selection between SSSCs
	Software	Upgraded system software to support a variety of location algorithms: single event technique (LocSAT), master event location or JHD
	Software	Upgraded system software to allow simultaneous analysis of numerous association, phase picking and location hypothesis of the same event
	Calibration	Incorporated SSSCs based on CUB1.0 model (McLaughlin et. al, 2002)
	Calibration	Incorporated kriged SSSCs based empirical data (Richards et. al, 2002)
	Calibration	Developed test site corrections based on ground truth (Fisk, 2002)
	Prototype software	Developed tool to allow phase retiming and master event locations based on waveform cross-correlation
	Prototype software	Developed tool to allow visualization of confidence regions based on non-gaussian error models (based on Rodi and Toksoz, 2001)
	Software	Upgraded system map display capability and incorporated commercial satellite imagery (including 1 meter IKONOS imagery)
Identification: depth	Prototype software	Developed and integrated depth phase stacking tool (Murphy *et al*, 2000)
	Prototype software	Developed and integrated display to facilitate interactive review of depth phase move-out
	Software	Upgraded interactive analysis suite to facilitate use of F-statistic and probability traces in picking and timing of depth phases
Identification mb:Ms	Prototype software	Integrated software (MaxPMF) to perform low threshold regional surface wave detection using phase matched filtering (Stevens *et al*, 2001)
	Software	Upgraded analysis suite to support interactive review of phase matched filtering results, including noise amplitude measurements
	Prototype software	Developed and integrated display to facilitate interactive review of mb:Ms discrimination results
	Prototype software	Developed and integrated software to compute and display RAMP results (Pearce *et al* 1988)
	Calibration	Recalibrated test site m_b, and Ms station magnitude corrections
Identification: regional amplitude ratios	Software	Upgraded system software to compute regional amplitudes using 3-component broad-band channels
	Calibration	Recalibrated regional amplitude ratio discriminant based on historical Lop Nor explosions and earthquakes
	Prototype software	Developed and integrated tools to facilitate interactive review and display of regional amplitude ratios and discriminant
Identification: summary	Prototype software	Developed and integrated tools to compute and display multi-variate event identification, combining depth, mb:Ms, and regional amplitude ratios

CONCLUSIONS AND RECOMMENDATIONS

During the Lop Nor ACD a very wide variety of techniques contributed at various levels. The following conclusions can be drawn as to the relative contributions of various tested concepts. With regard to detection capability, a number of conclusions are as follows:

- The main driver for improving detection at Lop Nor was clearly the tuned sta/lta detector running against the Makanchi array. To support a three station event definition criteria using stations outside China, the stations of the Kirghiz network (KNET), in particular TKM2 and ULHL were critical.
- The tuned F-statistic detector was a major element in increasing the teleseismic association rate particularly for events in the magnitude range 3.0 – 3.5.
- Site-specific threshold monitoring (SSTM) provided a robust method for assessing that no significant events had escaped detection. As an event detector, SSTM was robust with an extremely low false alarm rate, however it did not offer the low threshold capability of the tuned regional association (regional GA).

With regard to location, the conclusions are:

- Some improvements in location capability were obtained though calibration, specifically the use of SSSCs or test site corrections. The improvements were primarily in the form of better confidence area estimates. However the large measurement errors associated with small events will be the major driver.
- The most striking improvements came from the joint use of waveform cross-correlations to retime arrivals, coupled with master event location algorithms illustrated in Figures 5 and 6. The waveform cross-correlation method was applicable to events within about 20 km of one another, including in some cases the cross-correlations between the P arrivals of earthquakes and historical explosions, even for small events.

Finally with regard to identification,

- Some improvements were made in the identification of depth phases recorded teleseismically from moderate sized earthquakes. In particular 30 of 162 events (18.5%) were determined to be confidently deeper than 10 km using the new ACD depth tools. Teleseismic depth determination does contribute significantly as a robust discriminant for small events ($< m_b$ 3.5) occurring around Lop Nor. Research into regional depth determination will be required if depth is to be a robust discriminant at low thresholds.
- The detection of surface waves using phase matched filtering shows some promise in facilitating the extension of the mb:Ms discriminant down to events that are only recorded regionally.
- By far the most robust discrimination method for events around Lop Nor is through the use of regional 3-component amplitude ratios. It has been demonstrated for a very large variety of events including numerous small earthquakes and the scaled nuclear explosions indicating applicability to small events just above the detection threshold.

REFERENCES

Fisk, M. D. (2002), Accurate locations of nuclear explosions at the Lop Nor test site using alignment of seismograms and IKONOS satellite imagery, in press, *Bull. Seism. Soc. Am.*

Kværna, T., S. Mykkeltveit, E. Hicks, F. Ringdal and J. Schweitzer (2001), Regional seismic threshold monitoring, *23rd Seismic Research Review*, October 2-5.

McLaughlin, K., I. Bondár, X. Yang, J. Bhattacharyya, H. Israelsson, R. North, V. Kirichenko, E.R. Engdahl, M. Ritzwoller, A. Levshin, N. Shapiro, M. Antolik, A. Dziewonski, G. Ekström, H. Ghalib, I. Gupta, R. Wagner, W. Chan, W. Rivers, A. Hofstetter, A. Shapira, and G. Laske (2002), Seismic Location Calibration in the Mediterranean, North Africa, Middle East and Western Eurasia, *24th Seismic Research Review*, September 17-19.

Mueller, R. A. and J. R. Murphy (1971), Seismic characteristics of underground nuclear detonations. Part I. Seismic spectral scaling, *Bull. Seism. Soc. Am.* **61**, 1975.

Murphy, J. R., R. W. Cook and W. L. Rodi (2000), Improved focal depth determination for use in seismic monitoring of underground nuclear explosions, *Maxwell Technologies final report MSD-DFR-00-16621*.

Pearce, R. G., J. A Judson and A. Douglas (1988), On the use of P-wave seismograms to identify a double-couple source, *Bull. Seism. Soc. Am.*, 78, 561-671.

Richards, P.G, V.I. Khalturin, W.-Y. Kim, J. Armbruster, M. Fisk, V. Burlacu, C. Saikia, G. Ichinose, I. Morozov, E. Morozova, V. Cormier and A. Stroujkova (2002), Progress in location calibration for 30 IMS stations in East Asia, *Fourth Location Calibration Workshop*, Oslo, 22-26 April.

Rodi, W. and M. Toksoz (2001), Uncertainty analysis in seismic event location, *23rd Seismic Research Review*, October 2-5.

Skov, M., B. Kohl and R. L. Woodward (2002), Imagery assets for supporting nuclear explosion monitoring research and development, *24th Seismic Research Review*, September 17-19.

Stevens, J., D. Adams and G. Baker (2001), Improved surface wave detection and measurement using phase-matched filtering with a global one-degree dispersion model, *23rd Seismic Research Review*, October 2-5.

Woodward, R. L. and R. G. North (2002), A support system for nuclear explosion monitoring research and development, *24th Seismic Research Review*, September 17-19

.

Yang, X., R. L. North and C. Romney (2000), CMR nuclear explosion database (revision 3), *CMR Technical Report CMR-00/16*, August.

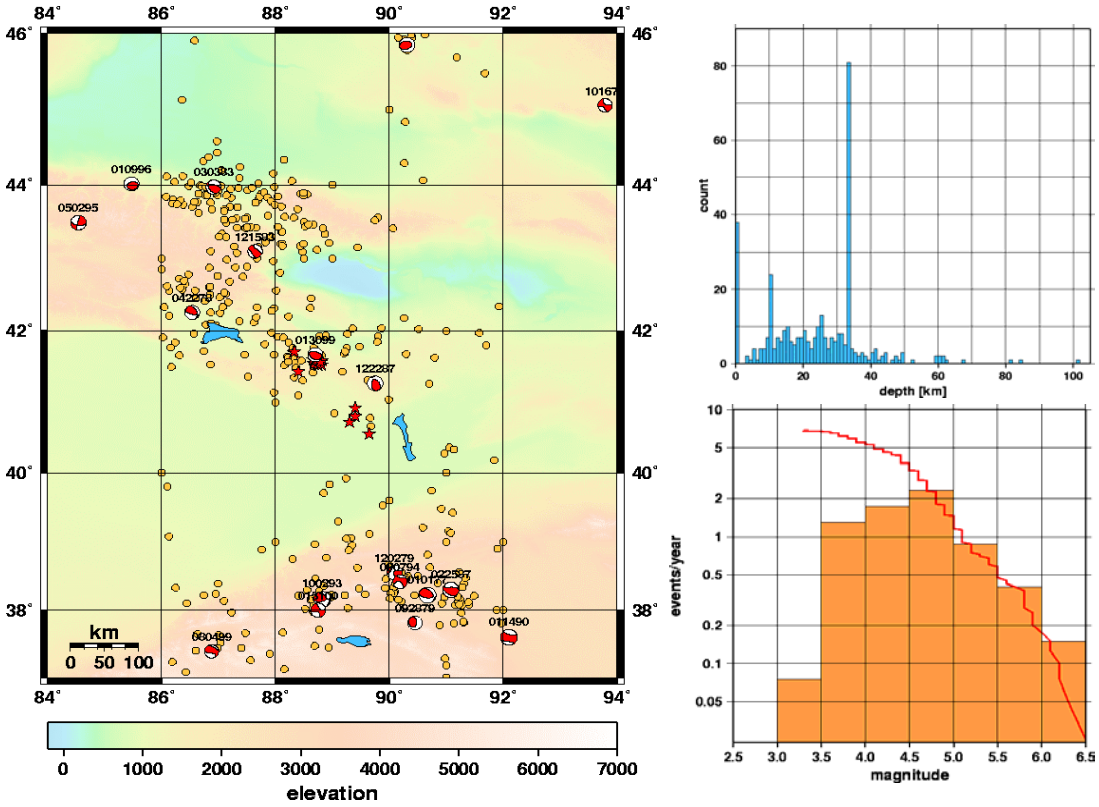

Figure 1: Left: seismicity of the Lop Nor region based on the ISC bulletin. Nuclear explosions are shown as red stars and the Harvard CMT solutions are shown as beach balls. Upper right: earthquake depth distribution in the ISC bulletin. Lower right: m_b recurrence distribution derived from the ISC bulletin.

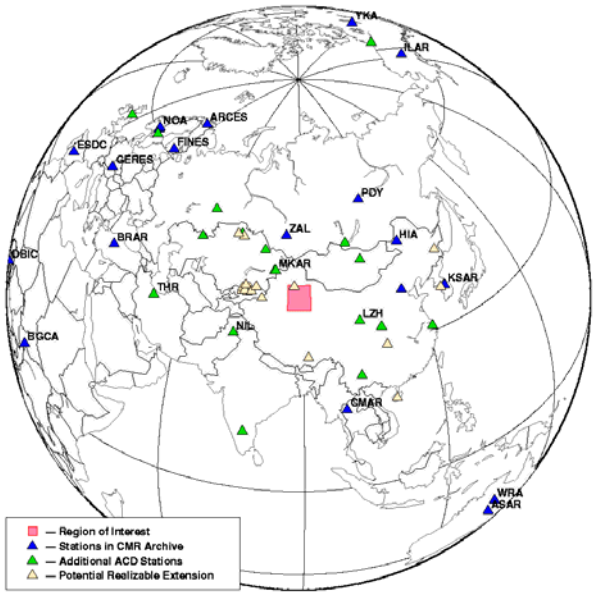

Figure 2: Stations contributing to the ACD data sets. Stations in blue are actual or surrogate IMS primary seismic stations as of June 2001. The green triangles are actual or future IMS auxiliary sites, while the tan symbols are non-IMS sites.

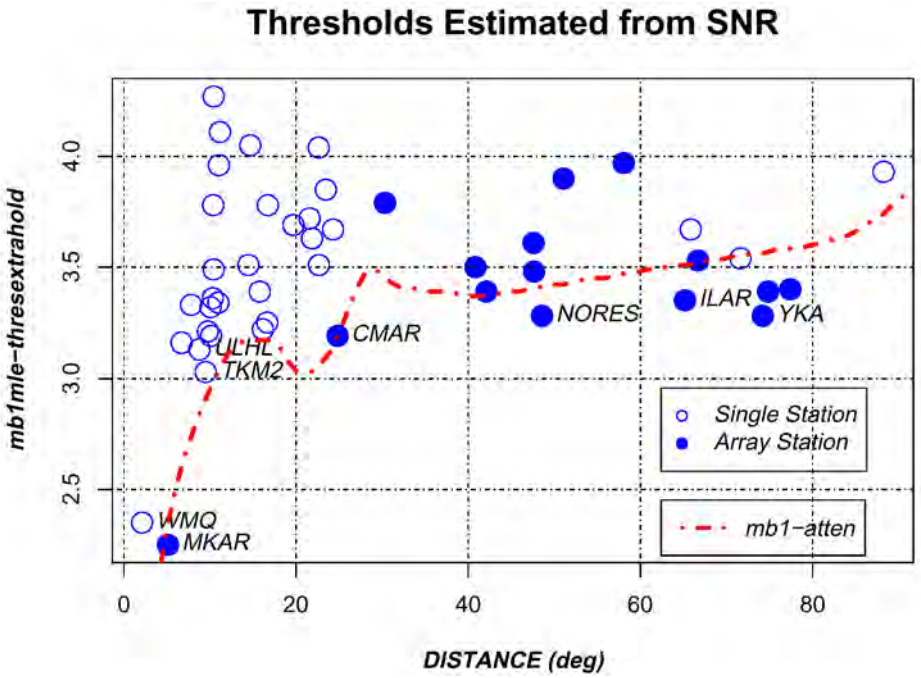

Figure 3: mb1mle station thresholds as a function of distance.

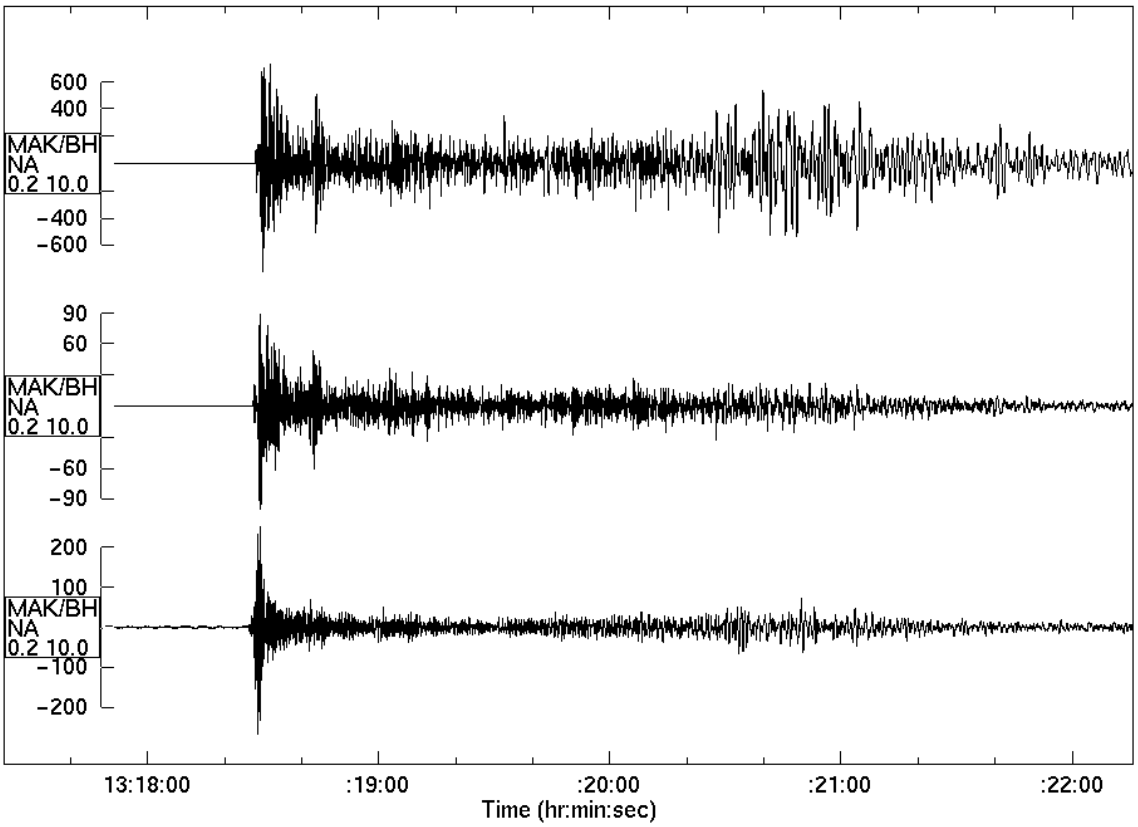

Figure 4: Comparison of the station MAK seismogram obtained by scaling the observed data from the larger May 15, 1995, (m_b = 5.73) reference Lop Nor explosion (top) to the source conditions of the smaller July 29, 1996, (m_b = 4.71) reference Lop Nor explosion (center) with the corresponding observed July 29, 1996, data (bottom).

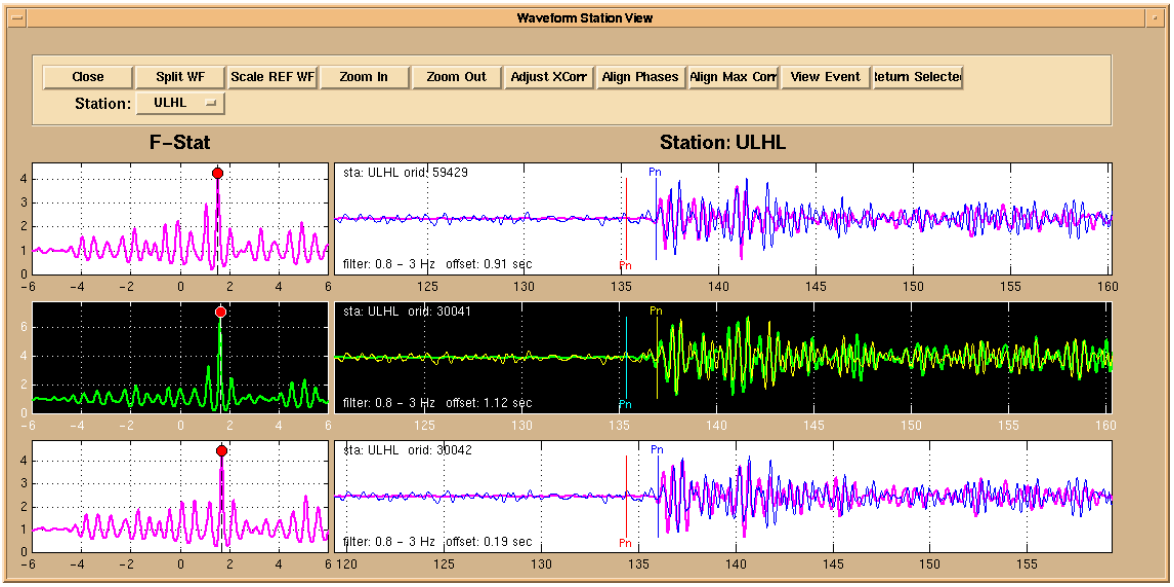

Figure 5: Illustration of the prototype waveform cross-correlation tool developed for the ACD to facilitate consistent arrival time picks. The right three panels show the waveforms scaled to the level of an m_b 3.0 nuclear explosion overlain on the records from historical explosions. The left three panels show the level of correlation displayed as an F-statistic. The analyst has the option to retime according to the maximum correlation and feed the resulting picks to a master event location (see Figure 6).

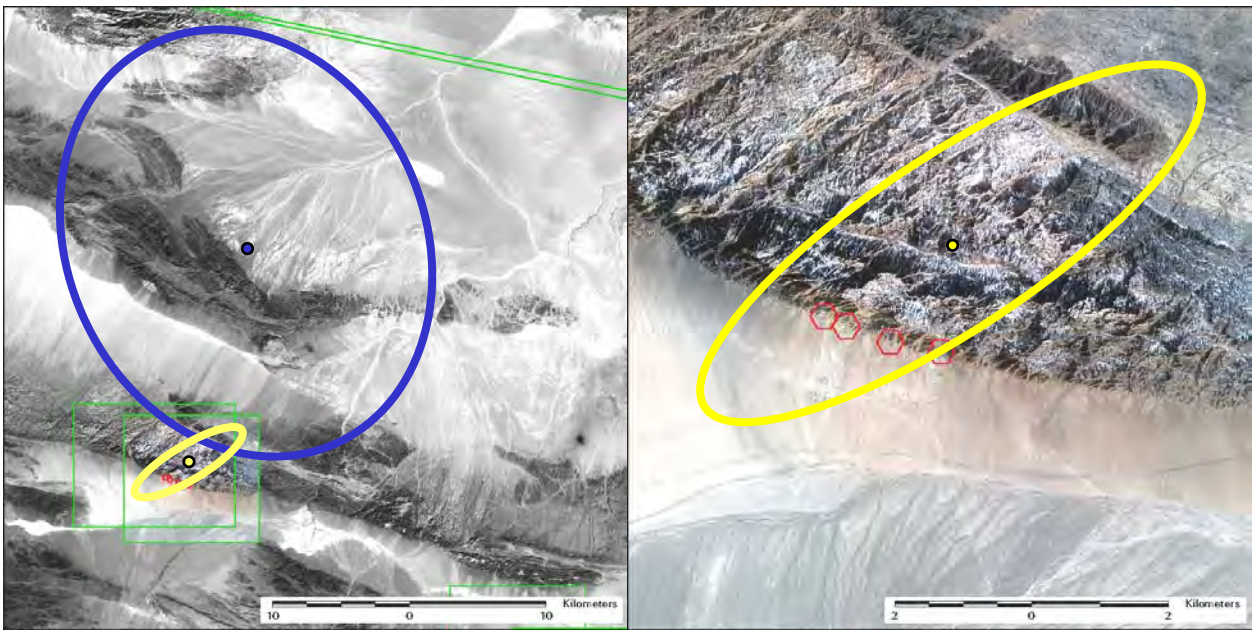

Figure 6: Comparison of locations obtained by processing and analyzing the waveforms from a known nuclear explosion scaled to m_b 3.0. The location depicted in blue in the left panel was obtained by using the calibrated travel times and a traditional single event location algorithm (LocSAT). The solution depicted in yellow was obtained by using the very consistent arrival picks that were made using the ACD waveform cross-correlation tool (Figure 5). Those picks were used in master event location algorithm and resulted in a mislocation of less than 1 km from ground truth. The panel on the left shows 5-m SPOT imagery as the background, while the zoomed view in the right panel displays 1-m IKONOS multi-spectral imagery. The red hexagons outline the known locations of adits in the northwestern part of the Lop Nor test site.

PERMISSIBLE SPATIO-TEMPORAL ERRORS OF SEISMIC EVENT LOCATION ACCURACY IN THE CONTEXT OF NUCLEAR-EXPLOSION-MONITORING REQUIREMENTS

Vladimir V. Kovalenko and Marat S. Mamsurov

Research Institute of Pulse Technique

Sponsored by the Comprehensive Nuclear-Test-Ban Treaty Organization

Contract No. 00/20/5020

ABSTRACT

Permissible ranges of distance-dependent modeling errors for the travel time of regional seismic waves and a new inter-epicenter criterion for estimation of the accuracy of seismic event location are considered. Together they provide a spatio-temporal range of values to meet the requirements of the Comprehensive Nuclear-Test-Ban Treaty (CTBT) for seismic event location accuracy.

OBJECTIVE

The objective is consideration of permissible ranges of distance-dependent modeling errors for the travel time of regional seismic waves and a new inter-epicenter criterion for estimation of the accuracy of seismic event location. Together they provide a spatio-temporal range of values to meet the requirements of the Comprehensive Nuclear-Test-Ban Treaty (CTBT) for seismic event location accuracy.

RESEARCH ACCOMPLISHED

The accuracy of seismic event location is ordinarily characterized by error ellipse sizes and the confidence level of the placement of the event epicenter into a given ellipse. In accordance with the Protocol to the CTBT (par. 3, p. II A) the error ellipse sizes must not exceed certain maximums. Studies by Mamsurov (2001) and Kovalenko and Mamsurov (2001, 2002) evaluated these restrictions and showed that for implementation of the CTBT requirements the root-mean-square (RMS) errors for travel time (σ_{tr}) of regional seismic phases must not exceed the values presented in Table 1 at a confidence level 0.9 for the error ellipse.

Table1. Permissible RMS deviations of travel times for regional seismic phases

Regional phases	**Phase velocities, km/sec**	**Permissible RMS deviations of travel-times, $\sigma_{tr.per}$, sec**
Pn	8.00	1.46
Pg	6.00	1.94
Sn	4.62	2.52
Lg	3.50	3.33

The estimates were made for typical phase velocities of seismic waves but can be made, as was shown in the cited works, for weighted averages of these velocities to match a given seismic wave velocity model. Thus, for any velocity of regional seismic wave (V, km/s) it is possible to find the maximum permissible travel-time error ($\sigma_{tr.per}$), which provides the required CTBT accuracy of seismic event location. This error for an uncertainty ellipse at 90 % confidence level depends on the wave velocity and the nature of the4 error ellipse. For example, $\sigma_{tr.per} = 11.65/V$ for an "elliptical" error ellipse and 8.39/V for a circular error ellipse (Figure 1**)**, where σ_x=11.65 km (semi-major axis) and σ_r = 8.39 km, respectively (Kovalenko and Mamsurov, 2001, 2002). Figure 1 presents these relations as two isosceles hyperbolas, whose asymptotes are coordinate axes; by means of this Figure it is possible to estimate the value of maximum permissible travel time error for any regional phase.

Following Beall *et al*. (1997) σ_{tr} can be presented as:

$$\sigma_{tr}^2 = \sigma_{md}^2 + \sigma_{ms}^2 \qquad (1)$$

Where: σ_{md} – modeling error, characterizing the error of the velocity model or hodograph with respect to the actual properties of the medium of seismic wave propagation;

σ_{ms} –error of measuring of the seismic waves arrivals.

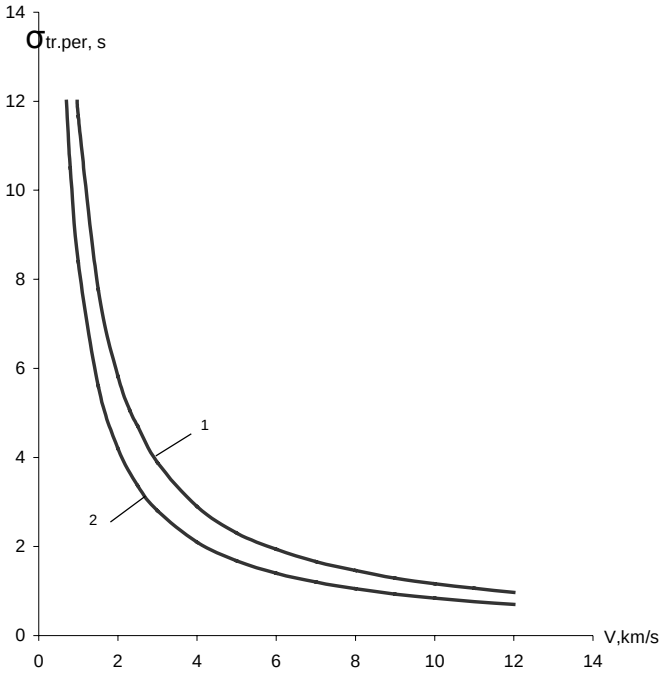

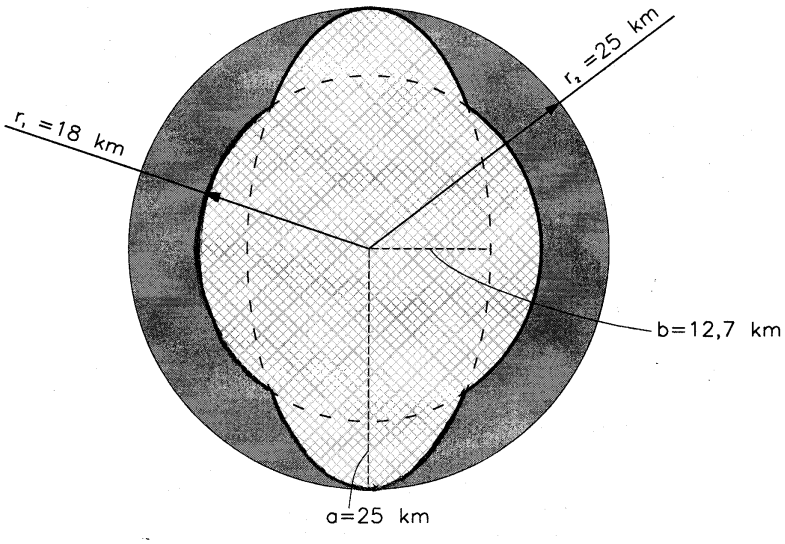

Figure 2. The field of permissible Inter-epicenter distances

Since σ_{ms} can be reduced by increasing signal/noise ratio (for example, to 0.5 sec and less for Pn waves), the dominating contribution to travel-time RMS error is the modeling error.

The simplest way of estimating modeling errors and their dependence on distance is from a typical hodograph:

$$T - R/V_{red} = (A \pm \sigma_A) - (B \pm \sigma_B)\, R \qquad (2)$$

Where: T – travel-time, R – distance, V_{red} – reduction velocity, A and B – regression constants, σ_A and σ_B – RMS errors for these constants.

As an example consider hodographs and their modeling errors for the East-European platform (Starovoit, *et al.* 2000). The regional hodograph parameters are given in Table 2, where r – correlation coefficient, RMS – travel-time deviation from averaged hodograph, N – number of observations. Data have been grouped so that the best approximation of the hodograph to observed data in the sense of minimum RMS deviation was provided. Modeling errors, calculated for these hodographs, and presented as RMS deviations of experimental data from the hodograph for sliding two degree windows with 50% overlap are shown in Table 3.

Table 2. Parameters of regional hodographs

Phases	Distance, km	Vred, km/s	A	σ_A	B	σ_B	N	R	RMS, sec
Pn	250-1150 1151-2500	8.00 8.00	7.867 13.806	0.351 0.402	0.0040 0.0094	0.0005 0.0002	51 218	0.78 0.94	0.8 1.3
Pg	250-1300	6.00	1.012	0.096	0.0075	0.0012	67	0.63	2.6
Sn	250-2500	4.62	15.640	1.420	0.0055	0.0008	138	0.52	4.1
Lg	250-2500	3.50	0.286	1.644	0.0063	0.0014	81	0.46	5.5

Table 3. Modeling errors for regional hodographs (sec).

Phases	Distance, degrees																	
	3	4	5	6	7	8	9	10	11	12	13	14	15	16	17	18	19	20
Pn	0.5	0.4	0.9	0.9	0.6	0.7	0.8	1.2	1.2	1.4	1.6	1.0	1.3	1.5	1.3	1.2	1.5	1.5
Pg	0.9	1.0	1.7	1.6	1.3	1.0	1.4	1.7	1.7									
Sn	3.8	3.9	2.9	2.6	2.9	3.4	3.3	3.9	3.4	2.9	3.5	3.8	3.7	3.0	3.0	3.5	2.7	3.2
Lg	4.5	4.7	6.7	7.0	5.7	2.6	3.8	4.4	5.1	5.7	4.5	4.7	5.5	5.8	6.3	7.1	7.1	3.7

Taking into account σ_{ms}= 0.5 sec for Pn and Pg waves and using modeling errors from Table 3 we see that for this case in all distance ranges $\sigma_{tr} < \sigma_{tr.per}$ in accordance with Table 1. However, modeling errors are too big for Sn and

Lg waves and the requirements on location accuracy are not satisfied, indicating the necessity of improvement of the model

Modeling errors play an important role in calculation of Station-Specific Source Corrections (SSSCs) for heterogeneous tectonic regions (Xiaoping *et al.*, 1998, Firbas, 1999).

Besides modeling error, an additional criterion is needed for reliable estimation of seismic event location. At present a criterion is used based on covering the true coordinates of the event epicenter by the error ellipse (Bondar, 1998). This criterion is contradictory, because reduction of accuracy and increasing error ellipse size enables coverage of the event epicenter, while for a high-accuracy system with a small error ellipse, this in many cases becomes impossible, although this does not indicate low quality for such a system.

An error ellipse may not cover the true epicenter, or may have an area exceeding 1,000 sq. km, but CTBT requirements can still be executed, since in most practical cases we are interested in how closely the extent epicenter determined by the observing system approaches the true location or to a GT event epicenter, chosen as standard. A less contradictory and more sensitive criterion of seismic event location accuracy is the estimation of inter-epicenter distance:

$$\Delta = \sqrt{(\lambda_2 - \lambda_1)^2 + (\varphi_2 - \varphi_1)^2} \qquad (3)$$

where Δ - distance between the true epicenter with coordinates (φ_1, λ_1) and the epicenter determined by the observing system with coordinates (φ_2, λ_2). It is necessary to also take into account RMS deviations of coordinates $\sigma_{\lambda 1}, \sigma_{\lambda 2}, \sigma_{\varphi 1}, \sigma_{\varphi 2}$ if they are accessible.

In accordance with CTBT requirements the inter-epicenter distance must not exceed 50 km in any direction, while the epicenter must be inside or at the boundaries of an error ellipse, whose area is less than or equal to 1,000 sq. km with a given level of confidence.

Criterion (3) consists of two zones (Figure 2). The first zone is a circle, with radius $\mathbf{r}_1$= 18 km and area 1,000 sq. km; in any direction the inter-epicenter distance does not exceed 36 km:

$$\Delta \leq 36 \text{ km} \qquad (4)$$

The boundary of the second zone is a circle of $\mathbf{r}_2$ = 25 km radius; in any direction the inter-epicenter distance does not exceed 50 km:

$$\Delta \leq 50 \text{ km} \qquad (5)$$

However, the area of the second circle (1963 sq. km) is almost twice as large as the CTBT value. Therefore, for implementation of the CTBT requirements, both epicenters, true and determined, must be inside or at the boundaries of an ellipse, whose area is 1,000 sq. km and semi-axes are: a= 25 km and b = 12.7 km, inscribed in the second circle. The conditions of getting of both epicenters inside and at the boundary of such ellipse leads to two inequalities:

$$\begin{aligned} (\lambda_1/25)^2 + (\varphi_1/12.7)^2 &\leq 1 \\ (\lambda_2/25)^2 + (\varphi_2/12.7) &\leq 1 \end{aligned} \qquad (6)$$

Thus the application of the proposed criterion consists of calculation of Δ, checking inequality (4) and, if $\Delta > 36$ km, testing of inequalities (5) and (6).

If $\Delta > 50$ km we overrun the permissible zone and it is necessary to take measures on reduce the modeling errors and increase the trustworthiness of the model.

Results of application of the proposed criterion are presented in Table 4, which confirms the effectiveness of estimating the seismic event location accuracy by the inter-epicenter distance Δ. The CTBT requirements for seismic event location accuracy are satisfied for all events of the Table 4, even though the simplest form of criterion ($\Delta \leq 36$ km) is used. In no case was a transition necessary to the second zone of the criterion (inequalities 5 and 6). We note that IASPEI-91 tables were used in this case in spite of the resulting problems: for all events the area of the error ellipse noticeably exceeded the permissible value, and for the event on 21.05.97 the error ellipse did not cover the true epicenter). Use of SSSCs (3-D) (Ryaboy *et al*. 2001) improved the accuracy of epicenter coordinate estimation, but for three events the area of the error ellipse still exceeded the permissible norm. Thus, as Table 4 shows, using only IASPEI-91 tables and the criterion of inter-epicenter distance it is possible to solve the problem without resorting to even 1-D regional models.

Of course, in a case when $\Delta > 50$ km, it is necessary for satisfaction of the CTBT requirements on location accuracy to use the newest geological and geophysical methods for construction of 1-D regional hodographs and models and for transition to 2-D and 3-D regional models if more simple methods do not give the required result. But at every stage it is reasonable to make sure that the possibility of simpler approaches was really exhausted.

Table 4. The estimation of seismic event location accuracy with the use of the criterion of the inter-epicenter distance

Event	IASPEI-91			Criterion of the Inter-epicenter distances			SSSCs (3-D)		
	Error of epic.loc., km	Square of err. ell., sq.km	Err.ell. covers of epic.	Distance between epic., km	Square of circle/ell., sq.km	Err.ell. covers of epic.	Error of epic.loc., km	Square of err. ell., sq.km	Err.ell. covers of epic.
333140, 17.04.95	22.4	2,399	+	23.0	415	+	7.2	478	+
Chem.Exp., 03.04.66	20.7	3,386	+	20.0	314	+	9.0	471	+
PNE, 10.12.61	28.3	3,281	+	27.0	572	+	4.5	479	+
PNE, 24.09.83	28.6	3,902	+	27.3	585	+	8.8	2,780	+
313623, 11.03.95	8.9	3,855	+	8.0	50.2	+	7.4	2,634	+
20307517, 27.01.99	11.5	3,012	+	10.7	89.2	+	2.2	773	+
1004498, 12.04.97	13.8	1,430	+	10.0	78.5	+	2.6	300	+
1108893, 16.08.97	17.8	2,278	+	11.3	101	+	6.2	528	+
271133, 5.01.95	28.3	4,113	+	29.0	660	+	7.0	873	+
1043706, 21.05.97	17.3	3,171	-	17.0	227	+	5.3	640	+
Ev73Sep19	18.9	4,830	+	19.0	283	+	6.7	1,078	+
Ev85Jul 18	24.2	5,507	+	24.0	452	+	9.9	843	+

CONCLUSIONS AND RECOMMENDATIONS

A simple method is provided of assessment of maximum permissible travel-time errors for regional seismic phases that provide implementation of the CTBT requirements on accuracy of seismic event location.

For regional hodographs a simple method is recommended of estimating modeling errors, the dominant constituent of total travel-time errors.

The limitations of the presently used criterion of seismic event location accuracy by error ellipse size and coverage of the true epicenter coordinates for a given event are noted.

A less contradictory and more effective criterion of estimation of seismic event location accuracy is offered based on assessment of the distance between the epicenter determined by the observing system and the true, given or GT location for the same event.

REFERENCES

Beall, G. *et al*. (1997), New style measurement and model errors, Center for Monitoring Research, CCB Memo CMR-97, Arlington, Virginia.

Bondar, I. (1998), Evaluation of PIDC Error Ellipses, Technical Report CMR-98/23, Arlington, Virginia.

Firbas, P. (1999), Calibration Based on Ground Truth Data and 3-D Modeling: Framework and Feasibility Study for Western Europe, Workshop on IMS Location Calibration, Oslo, Norway.

Kovalenko, V. and M. Mamsurov (2001), The Potentialities of Regional Seismic Monitoring, Proceedings of the 23rd annual DTRA/NNSA Seismic Research Review, Jackson Hole, Wyoming.

Kovalenko, V. and M. Mamsurov (2002), About Estimation of the Seismic Event Location Accuracy, Fourth Workshop on IMS Location Calibration, Oslo, Norway.

Mamsurov, M. (2001), Threshold Possibilities of the International Seismic Monitoring System, Third Workshop on IMS Location Calibration, Oslo, Norway.

Starovoit, O. *et al.* (2000), Regional Travel Time Curves at East-European Platform for Improved Location of the Seismic Events, Second Workshop on IMS Location Calibration, Oslo, Norway.

Xiaoping, Y. *et al.* (1998), SSSCs for Regional Phases at IMS Stations in North America and Fennoscandia, Technical Report CMR-98/46, Arlington, Virginia.

Ryaboy, V. *et al.* (2001), SSSCs Based on 3-D Modeling for Pn, Sn, and Pg Phases at IMS Stations in Northern America, Third Workshop on IMS Location Calibration, Oslo, Norway.

SEISMIC LOCATION CALIBRATION IN THE MEDITERRANEAN, NORTH AFRICA, MIDDLE EAST AND WESTER EURASIA

K. McLaughlin,[1] I. Bondár,[1] X. Yang,[1] J. Bhattacharyya,[1] H. Israelsson,[1] R. North,[1] V. Kirichenko,[2] E.R. Engdahl,[3] M. Ritzwoller,[3] A.Levshin,[3] N. Shapiro,[3] E. Bergman,[3] M. Antolik,[4] A. Dziewonski,[4] G. Ekström,[4] H. Ghalib,[5] I. Gupta,[5] R. Wagner,[5] W. Chan,[5] W. Rivers,[5] A. Hofstetter,[6] A. Shapira,[6] and G. Laske[7]

Science Applications International Corporation, [1] Western Services, Inc., [2] University of Colorado at Boulder, [3] Harvard University, [4] Multimax, Inc., [5] Geophysical Institute of Israel, [6] University of California at San Diego[7]

Sponsored by Defense Threat Reduction Agency

Contract No. DTRA01-00-C-0013

ABSTRACT

The objective of the Group 2 Consortium, which comprises the authors of this paper, is to improve seismic event locations and reduce bias and uncertainties in the Mediterranean, Middle East, North Africa and Western Eurasia by providing calibrated travel times for stations in the region. To achieve this goal we follow a model-based approach. High-quality reference events (ground truth or GT 0-5) are collected and validated to facilitate the validation of the global three-dimensional (3-D) models and travel-time correction surfaces.

The project is in its second and final phase. In Phase 1 we demonstrated that significant improvements are achieved by using travel-time correction surfaces generated from global 3-D models. Improved velocity models have reduced *a priori* travel-time variances by 50% while maintaining 90% coverage.

In Phase 2 improved 3D global models, such as the CUB2.0 (Shapiro *et al*, 2002) and the PS362 (Antolik *et al*, 2002) are employed to generate travel-time correction surfaces via ray-tracing. The CUB2.0 model, a global upper mantle model combined with the CRUST2.0 crustal model (Bassin *et al*, 2000), is used to generate correction surfaces for regional phases. For teleseismic travel-time correction surfaces, we employ the PS362 global whole mantle model where the crust is taken into account as a crustal correction derived from CRUST2.0.

A substantially larger set of GT0-5 reference events collected as part of the Consortium effort allows a thorough validation of the models and predicted travel times. Event cluster analysis (Engdahl and Bergman, 2002; Israelsson *et al*, 2002) plays an important role in validating reference events, predicted travel times and error models.

Preliminary results show that further improvements are achieved relative to our Phase 1 results. The comparison of the CUB2.0 travel-time predictions with empirical path corrections obtained from cluster analysis indicates significant improvements in model-based predictions. The potential of using calibrated teleseismic phases in conjunction with calibrated regional travel-times is demonstrated.

OBJECTIVES

The objective of the Group 2 Consortium is to improve seismic event locations and reduce bias and uncertainties in the Mediterranean, North Africa, Middle East and Western Eurasia using calibrated travel-times. We develop, test and validate model-based path-dependent travel-time corrections for stations in the study region.

RESEARCH ACCOMPLISHED

The Group 2 Consortium carries out the location calibration for seismic stations in the Mediterranean, North Africa, Middle East and Western Eurasia. We follow a model-based approach to develop path-dependent travel-time corrections. The project is divided into two phases. In Phase 1, which ended in Spring 2002, we developed preliminary corrections and demonstrated improvements due to calibration. The results are summarized below. Currently we are in the development stage of Phase 2. We spend considerable effort on improving our models and collecting, vetting and validating reference events. Preparations for a comprehensive relocation study are underway.

Summary of Phase 1 Results

McLaughlin *et al* (2002) have demonstrated that seismic event locations in Western Eurasia, the Middle East, Northern Africa, and Europe were improved using calibrated Pn and Sn travel-times at International Monitoring System (IMS) stations (Fig. 1a). Source-Specific Station Corrections (SSSC) were generated via ray-tracing through the CUB1.0 (Shapiro and Ritzwoller, 2002) global upper mantle velocity model. Modeling errors were estimated from residuals using the EHB catalog (Engdahl *et al*, 1998) w.r.t. CUB1.0 (Fig. 1b). Direct comparisons between the model-based corrections and empirical path corrections obtained from cluster analysis indicate that the modeling errors are conservative and capture 44% of the variance of the empirical path corrections.

To validate calibrated travel times, model errors and demonstrate location improvements, 571 GT0-10 reference events were relocated with and without SSSCs. Tests were conducted with calibrated regional phases alone. The results demonstrated statistically significant reduction in both mislocation and uncertainty (McLaughlin *et al*, 2002). The median area of error ellipses was reduced by 50% while the conservative modeling errors assured 90% coverage. The majority of the events were improved, while degradation was less than expected (Fig. 2), accounting for uncertainties in GT data, model and measurement errors. Calibration resulted in reduced Pn and Sn misfits and origin time errors. Finally, a network of IMS and IMS surrogate stations was used to demonstrate expected improvements in the future IMS network. The relocation results with the calibrated regional travel times met or exceeded the metrics recommended by the 1999 Oslo Location Workshop. The SSSCs for IMS stations in the Group 2 region have been approved by the Center for Monitoring Research Configuration Control Board (CCB) for automatic and interactive event location processing.

We recognize that the IMS network is primarily a sparse, teleseismic network. The location error due to a 1-s error in teleseismic travel times is more severe than that caused by a similar error in regional travel times (Fig. 3a). Therefore, the calibration of teleseismic travel times is the next logical step to further improve locations, especially of moderate to large sized events. Antolik *et al* (2001) have shown that spherical harmonic mantle models, such as SP12 (Su *et al*, 1994) can considerably improve teleseismic locations and perform better than high-resolution block models. We further investigate the performance of the SP12 model by relocating 1,700 GT0-10 events. Results show that teleseismic calibration yields statistically significant improvement in event locations and error ellipses while maintaining 90% coverage. Comparisons with empirical path corrections obtained from cluster analysis indicate that a significant part of the 3-D variability in the empirical data is explained by SP12. Fig. 3b shows the relocation of events in the Bhuj, India, aftershock sequence using teleseismic P SSSCs.

Several lessons have been learned from Phase 1, which provide guidance to our effort in Phase 2. A carefully vetted and validated reference event set with a good geographical coverage is essential for model-based location calibration. However, it is extremely difficult to identify and validate candidate ground truth events in regions with poor station coverage. Better estimates of model and measurement errors may further improve location performance. Besides Pn and Sn SSSCs, Pg and Lg corrections are also necessary for regional calibration. This requires an improved model of the crust and sediments. Depth-dependent SSSCs will face challenges in validation testing due to the lack of ground truth. Teleseismic SSSCs can provide the next level of significant improvement.

Model development

In Phase 2 we use improved global 3-D models to calculate travel-time correction surfaces. We employ the CUB2.0 and PS362 models to generate regional and teleseismic SSSCs, respectively.

The 3-D model CUB1.0 and its update CUB2.0 are created on a 2x2 degree grid to a depth of 400 km. Below 400 km both models revert to the Harvard 3-D model S20a (Ekström and Dziewonski, 1998). Both models were constructed using a Monte-Carlo inversion method (Shapiro and Ritzwoller, 2002a) applied to group (e.g., Ritzwoller and Levshin, 1998) and phase velocity dispersion curves (Trampert and Woodhouse, 1995; Ekström and Dziewonski, 1998).

There are three principal differences between CUB1.0 and CUB2.0. First, the models differ in the crustal reference model used. The crustal reference for CUB1.0 is CRUST5.1 of Mooney *et al* (1998), whereas CUB2.0 uses CRUST2.0 (Bassin *et al*, 2000). Second, the models are based on different surface wave tomography methods. CUB1.0 uses Gaussian tomography, which is based on geometrical ray-theory with intuitive Gaussian smoothing constraints to simulate surface wave sensitivities (Barmin *et al*, 2001). CUB2.0 is based on diffraction tomography (Ritzwoller *et al*, 2002), which uses a simplified version of the scattering sensitivity kernels that emerge from the Born or Rytov approximations. Diffraction tomography accounts for path-length dependent sensitivity, wave-front healing and associated diffraction effects, and provides a more accurate assessment of spatially variable resolution than traditional tomographic methods. Third, the models differ in the way in which Vp is computed from Vs. CUB1.0 uses a simple empirical logarithmic scaling relation $d\ln(Vp)/d\ln(Vs) \sim 0.5$, in which perturbations are taken relative to the Vs and Vp velocities in ak135 (Kennett *et al*, 1995). CUB2.0 uses a theoretical conversion based on mineralogical partial derivatives for a hypothetical composition of the upper mantle. The method is based on the work of Goes *et al* (2000) and is described in detail by Shapiro and Ritzwoller (2002b). In essence, given the mineralogical composition, partial derivatives of the elastic moduli with respect to the independent variables at infinite frequency, a mixing law, and a relation between temperature and shear Q which is the basis for the anelastic correction; the Vs model is converted to temperature, which is then converted to Vp. In CUB2.0 this transformation has not yet been regionally tuned. Mineralogical composition is homogeneous across the region of study; there has been no account for the possible effects of fluids in the mantle beneath tectonically deformed regions, and shear Q is purely a function of temperature.

Empirical station-path corrections provide invaluable validation of the travel times predicted from the 3-D models. Fig. 4 shows Pn and P travel times predicted by CUB2.0 compared with empirical station-path corrections for an explosion and an earthquake. The general distribution of anomalies is similar. Fig. 5 shows that CUB2.0 fits the empirical station-path corrections better than CUB1.0 in an overall sense. CUB2.0 provides both a lower root-mean-square (rms)-misfit and a better correlation coefficient than CUB1.0. Fig. 6 breaks the misfit into a function of distance. Both CUB1.0 and CUB2.0 provide improved fits to the station-path corrections, but CUB2.0 out performs CUB1.0 at all distances.

Recently, Antolik *et al* (2002) have developed a joint compressional and shear velocity model of the Earth's mantle. PS362 is a spherical harmonic degree-18 model with a horizontal length scale of 1000 km. Absolute and differential body-wave travel times as well as surface wave dispersion measurements have been used to develop PS362. Using a data set of GT0-10 earthquakes and explosions, Antolik *et al* (2002) have shown that PS362 achieves an improvement of about 10% in rms mislocation for explosions, relative to SP12. PS362 also decreases the origin time error by an average of 0.05 s over model SP12.

Teleseismic P- and S-wave SSSCs are computed with a perturbation theory based ray-tracer in the distance range 25º to 97º, in order to diminish the biasing effects of upper mantle triplications and the core-diffracted phases on the travel times. We estimate that the numerical noise in the SSSCs can be up to 0.15 s. For shear waves we use SV to compute the travel times. This is because teleseismic rays traveling through regions of strong shear wave anisotropy (above 220 km) are primarily sensitive to SV as their ray paths are nearly vertical, and many station operators pick the shear phases on the vertical channel only. We use the International Data Centre (IDC) model error, scaled by 0.5, for our SSSCs, the scaling factor being based on our experience with regional Pn and Sn modeling errors. Following an analysis of travel-time corrections for stations in the GSETT-3 network, we note that the average correction for

the P-waves is close to zero suggesting that the radially averaged part of the model may be similar to the IASPEI[1]-91 model. On the contrary, the average S-wave correction is -0.44 s, suggesting that the IASPEI-91 model is slower than the PS362 model. The P-corrections range between ±2 s, while the range for the S-corrections is ±7 s. We note that the spread of S-wave residuals is about four times larger than that of P. Fig. 7 shows a comparison between the PS362-predicted P travel-time correction surface relative to IASPEI-91 and the empirical path corrections obtained from HDC analysis (Engdahl and Bergman, 2001) for the Bhuj, India, aftershock sequence.

Reference Events

With the recognition that a high-quality set of reference events is crucial for validating models and travel-time correction surfaces, the Group 2 Consortium invests considerable effort in collecting and validating reference events. Due to this effort, the number of reference events has been doubled during Phase 2 (Fig. 8a). However, collecting reference events has proven to be more difficult than anticipated, especially in regions with sparse network coverage. We have established contacts in the Middle East and North Africa and acquired national bulletins that are normally not publicly available (e.g. Yemen, Kuwait, Saudi Arabia). Phases for identified reference events are being picked from the waveforms of existing and future IMS stations that infrequently report to organizations such as the ISC, NEIC or EMSC.

Improved selection criteria for candidate GT5 events at the 95% confidence level have been established and validated using GT0 explosions (Bondár *et al*, 2002a; Bondár *et al*, 2002b). These require that an event be located with

- at least 10 stations within 250 km with an azimuthal gap less than 110° and a secondary azimuthal gap less than 160°
- at least one station within 30 km from the epicenter

The latter constraint gives some confidence in depth. For the sake of regional studies we also require that events be recorded beyond 250 km.

To validate candidate reference events we employ multiple event location techniques, such as Joint Hypocenter Determination (JHD) (Douglas, 1967; Dewey, 1991) and Hypocentroidal Decomposition (HDC) (Jordan and Sverdrup, 1981; Engdahl and Bergman, 2001). The two methods were cross-validated (Israelsson *et al*, 2001) to ensure that they can be used interchangeably. Candidate events are accepted if multiple event location results, using phases from regional and teleseismic distance ranges, are consistent with the local network solution. Events, originally not identified as GT5 candidates in the clusters, may be promoted to GT5 level if the semi-major axis of their 90% confidence ellipse is less than 5 km.

Event cluster analysis also provides path-dependent station corrections (Engdahl and Bergman, 2001). These empirical path corrections have been proven to be an invaluable tool in the validation of model-based travel-time predictions and model errors. Fig 8b shows the regional paths of empirical path corrections in the Group 2 region.

Novel Approaches for the Validation of Calibrated Travel Times

In addition to the proven techniques such as comparing model-based SSSCs to empirical path corrections obtained from cluster analysis and relocating reference events with and without SSSCs, we explore new ways of validating travel-time correction surfaces.

Many of the reference events are recorded by several hundreds of stations with excellent azimuthal coverage. These events are located so well, that no matter whether calibrated travel times are applied or not, the locations will not change. Therefore, simply relocating these events has no statistical power to demonstrate improvements. We generate bulletins from the well-recorded events by taking random sparse subsets of stations that satisfy predefined constraints on the number of stations, primary and secondary azimuthal gaps. These bulletins simulate sparse networks and allow better estimations of location bias, mislocation and uncertainties. Fig. 9 shows the relocations of a GT5 earthquake, originally recorded by 195 regional stations, from the Hoceima, Morocco, cluster with unique

[1] International Association of Seismology and Physics of the Earth's Interior.

station configurations of 6-10 stations with an azimuthal gap less than 130° and a secondary gap less than 160°. The sparse network simulation indicates that calibrated travel times yield more than 50% reduction in location bias.

Despite the Consortium effort, vast areas are still not covered by reference events. We relocate the entire GSETT-3 bulletin in the study region to test the hypothesis that the scatter in seismicity decreases due to calibrated travel times. We quantify the scatter in seismicity via metrics such as entropy (Nicholson *et al*, 2000) and the ratio of the distance of nearest natural neighbors of calibrated and uncalibrated locations (Bondár *et al*, 2002c). Fig. 10a shows that the entropy decreases; i.e., the seismicity gets tighter, in most regions when regional SSSCs are applied. Fig. 10b shows the locations of mid-Atlantic ridge events without (left) and with (right) SSSCs. Although there is no ground truth available in this region, we may conclude that events align better on the ridge when calibrated travel-times are employed.

CONCLUSIONS AND RECOMMENDATIONS

In the first phase of the Consortium effort we have achieved statistically significant improvements in location and reduction of bias and uncertainties with respect to IASPEI-91 when using calibrated regional travel times calculated from the CUB1.0 model. We demonstrated that the next significant step to improve locations can be obtained by integrating calibrated regional and teleseismic travel times; that is, the calibration of travel times over the entire distance range.

In Phase 2 we employ improved 3-D models, such as the CUB2.0 and PS362, to calculate travel-time correction surfaces for regional and teleseismic phases. Both models show improvements relative to their predecessors, CUB1.0 and SP12; therefore, we anticipate that Phase 2 relocation results will be superior to those of Phase 1. In order to increase the statistical power of the relocation tests, we explore new approaches to validate calibrated travel times.

We continue our effort in collecting, validating and vetting reference events. Multiple event location of event clusters plays an important role in the validation of reference events as well as in the validation of model predictions through the empirical path corrections. The reference event list can be browsed at the Consortium's web site, http://g2calibration.cmr.gov, where each reference event is documented with metadata.

REFERENCES

Antolik, M., G. Ekström and A.M. Dziewonski (2001), Global Event Location with Full and Sparse Data Sets Using Three-dimensional Models of Mantle P-wave velocity, *Pure Appl. Geophys.*, **158**, 291-317.

Antolik, M., Y. J. Gu, A.M. Dziewonski and G. Ekström (2002), A new joint model of compressional and shear velocity in the mantle, submitted to *Geophys. J. Intl*.

Barmin, M.P., M.H. Ritzwoller, and A.L. Levshin (2001), A fast and reliable method for surface wave tomography, *Pure Appl. Geophys*., **158**, 1351 - 1375.

Bassin, C., G. Laske and G. Masters (2000), The Current Limits of Resolution for Surface Wave Tomography in North America, *EOS Trans AGU*, **81**.

Bondár, I., E.R. Engdahl, H. Israelsson, X. Yang, A. Hofstetter, H. Ghalib, I. Gupta, R. Wagner, V. Kirichenko and K. McLaughlin, Status of Reference Event Collection for Western Eurasia, the Middle East, Northern Africa and Europe - The Group 2 Location Calibration Consortium Reference Event List 2.0 Delivery (2002a), 4th Location Calibration Workshop, Oslo, 22-26 April.

Bondár, I., S.C Myers, E.R. Engdahl and E.A. Bergman (2002b), Epicenter accuracy based on seismic network criteria, submitted to *Geophys. J. Int*.

Bondár, I., K. McLaughlin, X. Yang and J. Bhattacharyya (2002c), Assessing Location Improvements without Ground Truth Data, *Seism. Res. Let*., **73**, 227.

Dewey, J.W., Joint epicenter determination for earthquakes occurring over several decades: a case history from Northern Algeria (1991), in: Seismicity, Seismotectonics and Seismic Risk of the Ibero-Maghreb Region, eds.: J. Mezcua and A. Udias, *Instituto Geografico Nacional, Monografia No. 8*, Madrid, Spain, 51-63.

Douglas, A. (1967), Joint Epicentre determination, *Nature*, **215**, 47-48.

Ekström, G. and A.M. Dziewonski (1998), The unique anisotropy of the Pacific upper mantle, *Nature*, **394**, 168-172.

Engdahl, E.R., R. van der Hilst and R. Buland (1998), Global Teleseismic Earthquake Relocation with improved Travel Times and Procedures for Depth Determination, *Bull. Seism. Soc. Am.*, **88**, 722-743.

Engdahl, E.R. and E.A. Bergman (2001), Validation and generation of reference events by cluster analysis, 23rd Seismic Research Review, Jackson Hole, 1-5 October.

Goes, S., R. Govers, and R. Vacher, (2000), Shallow mantle temperatures under Europe from P and S wave tomography, *J. Geophys. Res.*, **105**, 11,153-11,169.

Israelsson, H., E.R Engdahl and E.A. Bergman (2001), Cross validation of two methods for event cluster analysis, Group 2 Phase 1 Delivery Document, http://g2calibration.cmr.gov/calibration/files/hjd-hdc-validation.pdf

Jordan, T.H. and K.A. Sverdrup (1981), Teleseismic location techniques and their application to earthquake clusters in the South-central Pacific, *Bull. Seism. Soc. Am.*, **71**, 1105-1130.

Kennett, B. and E.R. Engdahl (1991), Travel Times for Global Earthquake Location and Phase Identification, *Geophys. J. Int.*, **105**, 429-465.

Kennett, B.L.N., E.R. Engdahl, and R. Buland (1995), Constraints on seismic velocities in the Earth from travel times, *Geophys. J. Int.*, **122**, 108-124.

McLaughlin, K., X. Yang, I. Bondár, J. Bhattacharyya, H. Israelsson, V. Kirichenko, Y. Kraev, E.R. Engdahl, M.H. Ritzwoller, A. Levshin, N.M. Shapiro, M. Barmin, M. Antolik, A. Dziewonski, G. Ekström, I. Gupta, R. Wagner, A. Hofstetter, A. Shapira and G. Laske (2002), Improved seismic event location in Europe, Middle East, North Africa and Western Asia using 3D model-based regional travel times, *Seism. Res. Let.*, **73**, 216.

Mooney, W.D., G. Laske, and G. Masters (1998), CRUST5.1: A global model at 5 degrees by 5 degrees. *J. Geophys. Res.*, **102**, 727-748.

Nicholson, T., M. Sambridge and Ó. Gudmundsson (2000), On entropy and clustering in earthquake hypocenter distributions, *Geophys. J. Int.*, **142**, 37-51.

Ritzwoller, M.H. and A.L. Levshin (1998), Eurasian surface wave tomography: Group velocities, *J. Geophys. Res.*, **103**, 4839 – 4878.

Ritzwoller, M.H., N.M. Shapiro, M.P. Barmin, and A.L. Levshin (2002), Global surface wave diffraction tomography, *J. Geophys. Res.*, in press.

Shapiro, N.M. and M.H. Ritzwoller (2002a), Monte-Carlo inversion for a global shear velocity model of the crust and upper mantle, *Geophys. J. Int.*, in press.

Shapiro, N.M. and M.H. Ritzwoller (2002b), Thermodynamic constraints on seismic inversions, submitted to *Geophys. J. Int.*

Su, W., R.L. Woodward and A.M. Dziewonski (1994), Degree-12 Model of Shear Velocity Heterogeneity in the Mantle, *J. Geophys. Res.*, **99**, 6945-6980.

Trampert, J., and J. Woodhouse (1995), Global phase velocity maps of Love and Rayleigh waves between 40 and 150 seconds, Geophys. J. Int., 122, 675-690.

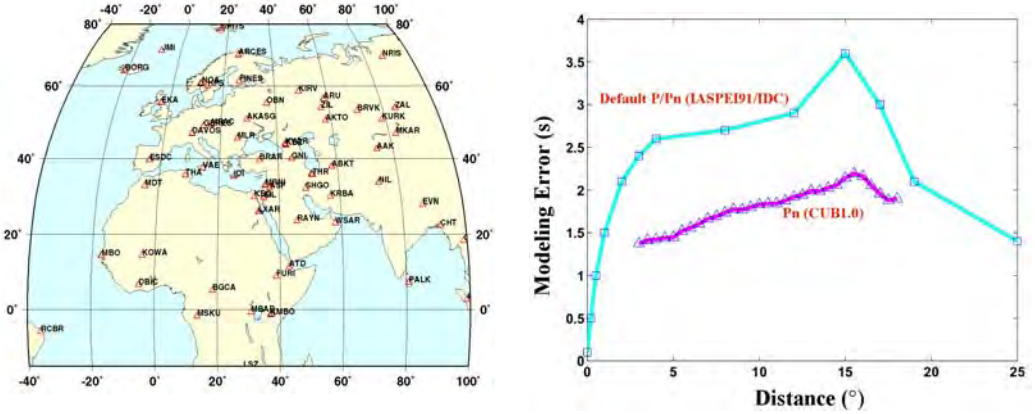

Figure 1. (a) IMS stations in the Group 2 region. (b) Distance-dependent Pn modeling errors used for CUB1.0 as compared to the IDC model errors.

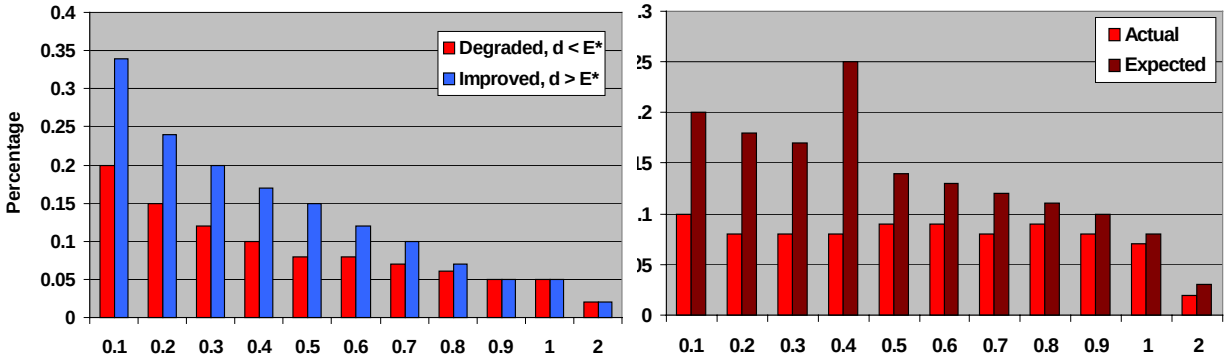

Figure 2. Normalized location improvement of 571 GT0-GT10 events using all Pn & Sn. (a) Improvement is larger than degradation for all values of the coverage test statistic, E*. (b) Degradation is less than predicted by random chance for all E* values.

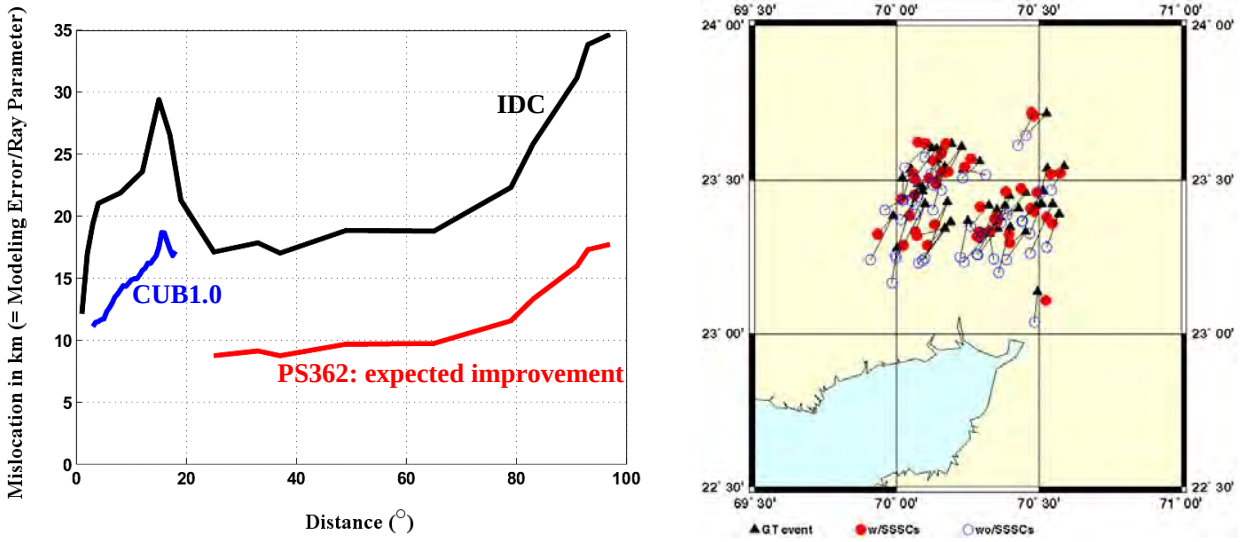

Figure 3. (a) Location error caused by 1-s error. The CUB1.0 model has significantly reduced Pn modeling errors. We expect similar reduction for teleseismic phases using the PS362 model. (b) Event relocation of 45 Bhuj, India, GT5 events using teleseismic P arrivals. The median mislocation is 12.8 km without SSSCs and 4.2 km with SSSCs.

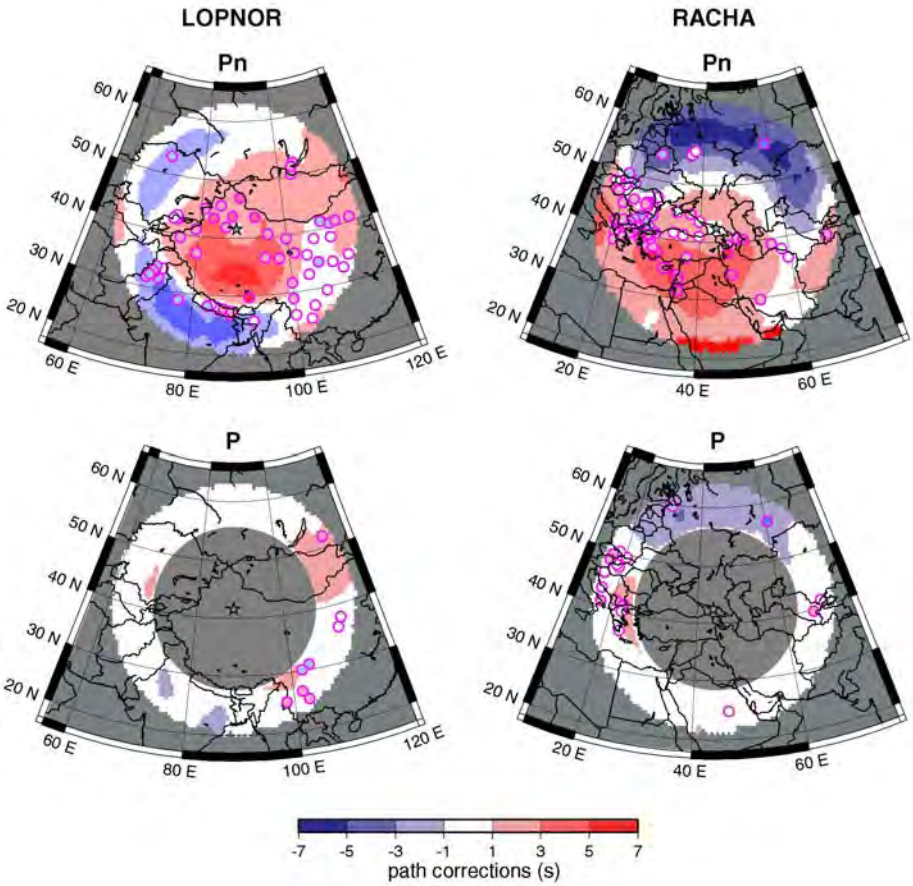

Figure 4. Comparison of empirical station-path corrections to the CUB2.0 predictions for two event clusters. The colored contours are the predictions from the model referenced to the travel time from the 1-D model ak135. The symbols are the empirical station-path corrections, color-coded similarly to the model predictions. Results are shown for two cluster regions: explosions at Lop Nor Test Site and earthquakes at Racha, Georgia.

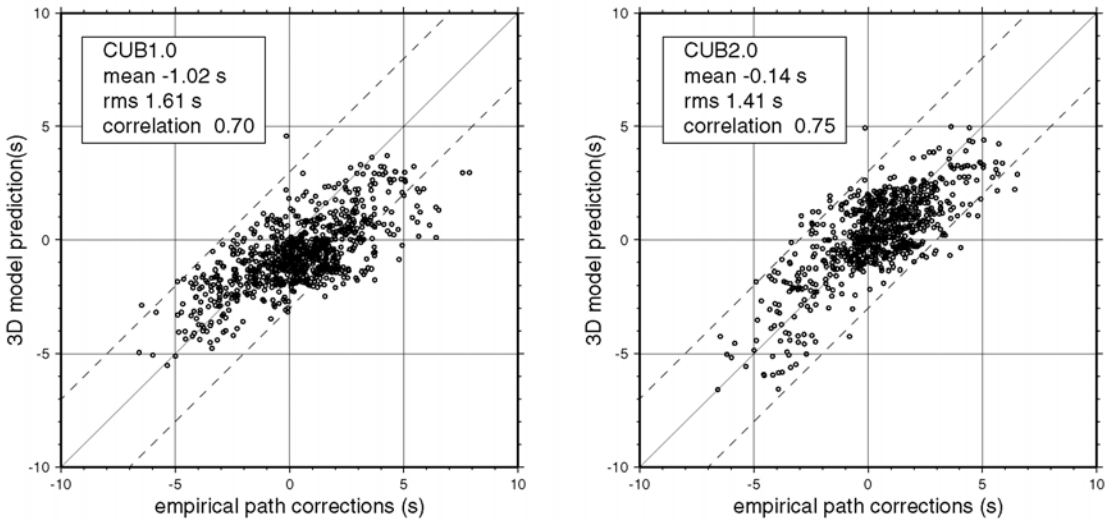

Figure 5. Fit of CUB1.0 and CUB2.0 predicted P and Pn travel times to the empirical station-path corrections. Results are presented only for regional phase data (epicentral distance less than 20 degrees). (a) The CUB1.0 travel times for P and Pn plotted versus the empirical station-path corrections. (b) Same as (a), but for CUB2.0.

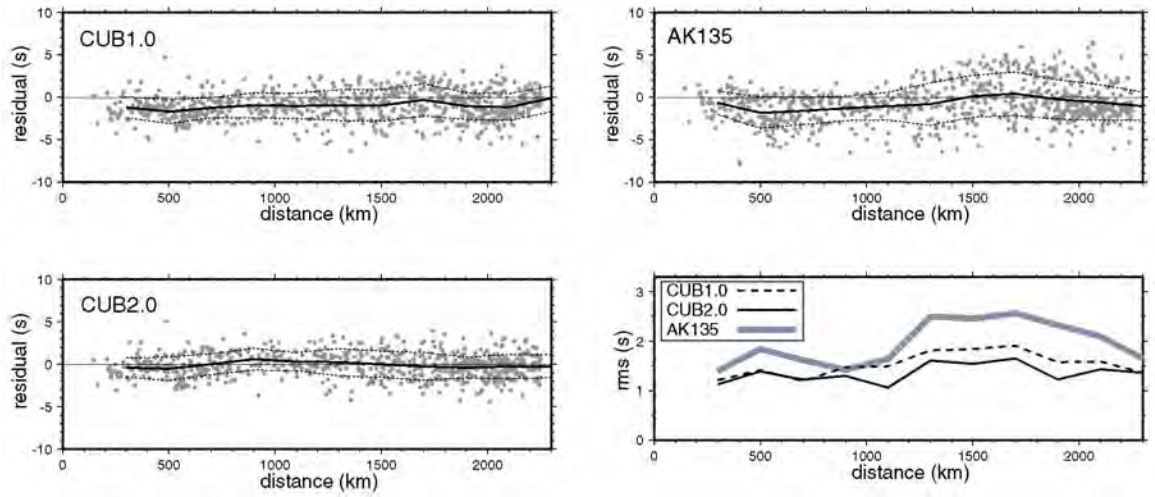

Figure 6. Residual between the travel times predicted from three models (CUB1.0, CUB2.0, ak135) and the empirical station-path corrections plotted versus epicentral distance. Distance dependent rms relative to the local mean is shown. Lower right: rms plotted versus distance for the three models.

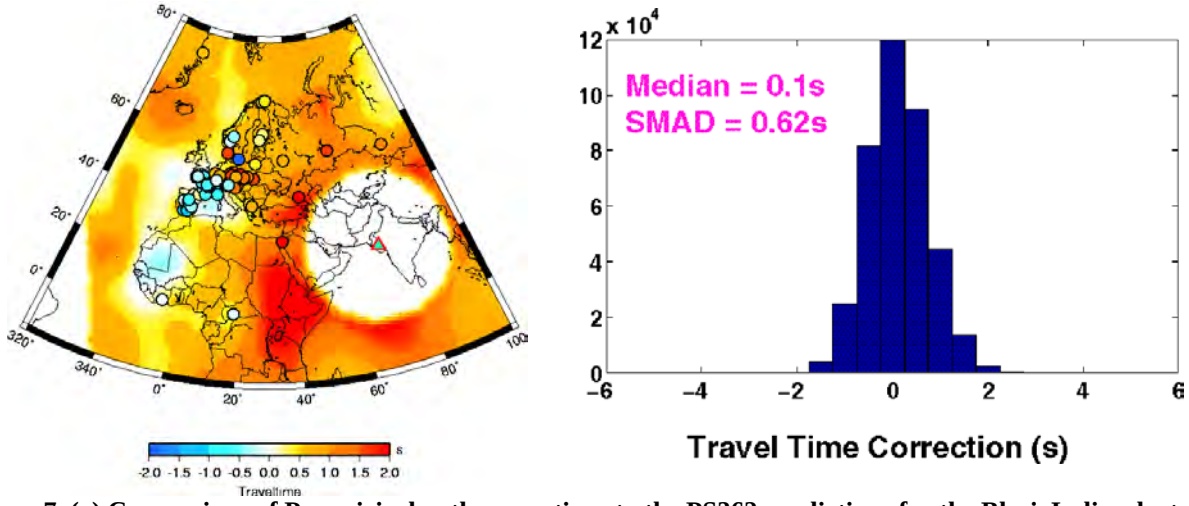

Figure 7. (a) Comparison of P empirical path corrections to the PS362 predictions for the Bhuj, India, cluster. Color contours are the model predictions, symbols, following the same color scale, are the empirical path corrections. (b) Distribution of P travel-time corrections for GSETT-3 stations using PS362.

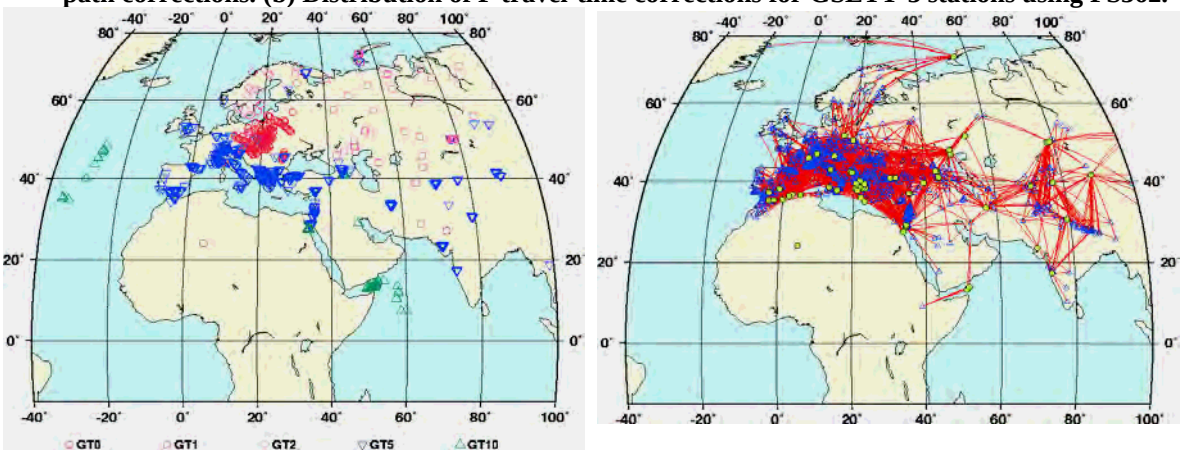

Figure 8. (a) 1,860 validated GT0-10 events in the Consortium's Reference Event List 2.0. (b) Event-station paths for which regional empirical path corrections, obtained from event cluster analysis, are available.

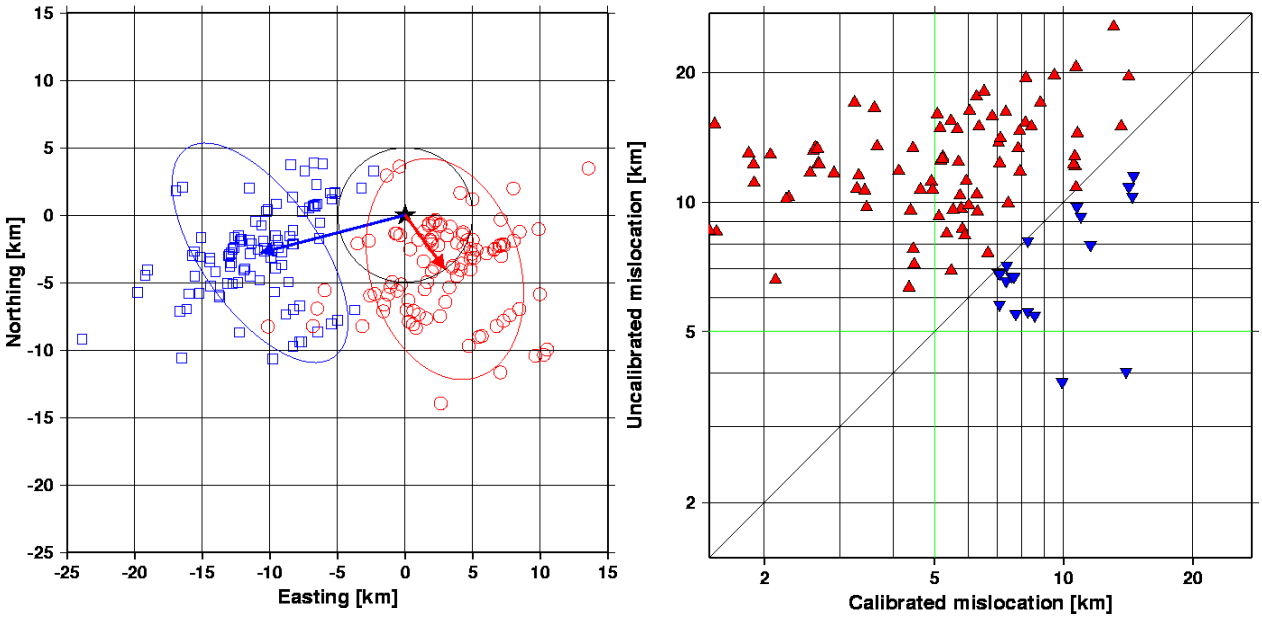

Figure 9. Relocation study of a GT5 event from the Hoceima, Morocco, cluster with sparse, random subsets of stations. Each random subnetwork is unique and has 6-10 stations with an azimuthal gap less than 130° and a secondary gap less than 160°. (a) Calibrated (circles) and uncalibrated (squares) locations relative to GT. The mean bias vectors together with their error ellipse are also shown. (b) Scatter plot of mislocations, points above the diagonal indicate improvements. Eighty per cent of the events were improved due to calibrated travel times, resulting in a 55% reduction in bias.

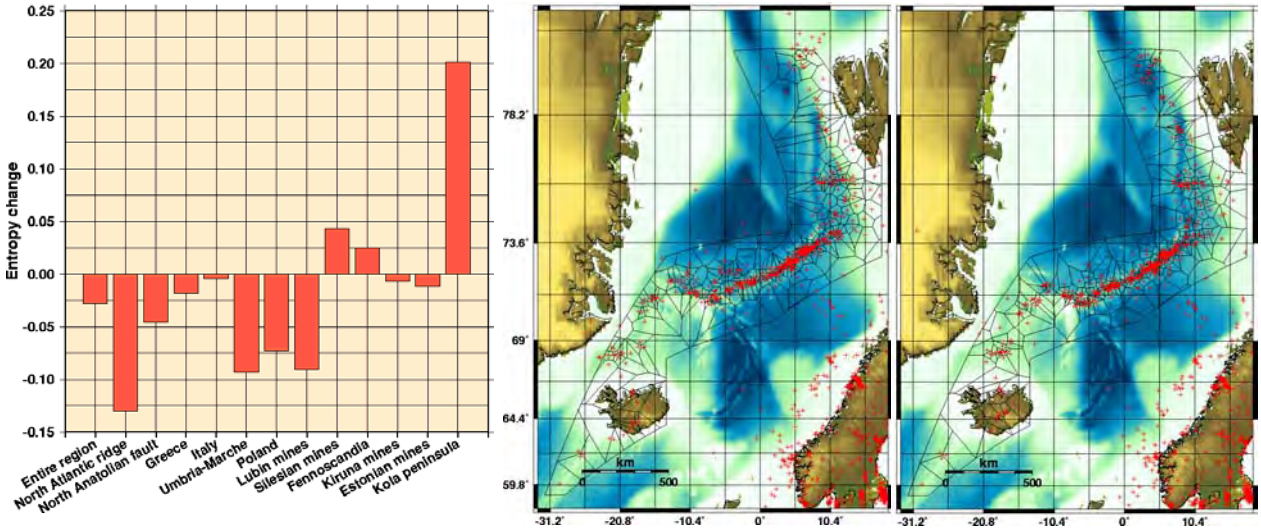

Figure 10. (a) Change in entropy in selected regions due to SSSCs when relocating the entire GSETT-3 Reviewed Event Bulletin using Pn and Sn phases only. Decreasing entropy indicates tighter seismicity. (b) mid-Atlantic ridge events located without (left) and with (right) calibrated regional travel times.

MULTIPLE ALGORITHM SIGNAL DETECTION USING NEURAL NETWORKS

Bion J. Merchant, [1] Jeffery T. Drake, [2] Darren Hart, [1] and Christopher J. Young[1]

Sandia National Laboratories[1], NASA Fellow, New Mexico State University[2]

Sponsored by National Nuclear Security Administration
Office of Nonproliferation Research and Engineering
Office of Defense Nuclear Nonproliferation

Contract No. DE-AC04-94AL85000

ABSTRACT

Nuclear explosion and non-proliferation monitoring require the processing of huge amounts of seismic sensor data, and the amount of data is increasing due to the continual, global expansion of monitoring stations. This overwhelming amount of data presents a great challenge to monitoring organizations that must detect and characterize seismic events. Given the limited number of analysts, detection is generally performed using automated techniques, freeing analysts to focus on other, more complex, problems. In this paper we evaluate the automated detection performance of a wide variety of algorithms and present results of fusing the best of these algorithms with a supervised neural network, forming a hybrid detector designed to take advantage of the "best" attributes of many algorithms.

Many different algorithms have been proposed for use in detecting seismic events. However, each algorithm has its own set of strengths and weaknesses. There is no single detection method that is guaranteed to work in all cases. Some researchers have begun simultaneously applying several different algorithms that complement one another. This is the approach that we take in this paper. We evaluate multiple detection algorithms to determine which are best suited for use together in automated detection.

We evaluate and present detection performance, using several detection algorithms as inputs, to a supervised neural network "trained" to predict the detection of an event. A neural network consists of multiple levels of input weights and non-linear functions that can be optimized to minimize the error between the output of the network and some ground-truth training data. Such neural networks can be designed and "trained" to detect events for a geographic region and optimized for any geological peculiarities of the region. The performance of the neural network is then compared to the results obtained by an analyst reviewing the same data. The data we use consists of events recorded by the New Mexico Institute of Mining and Technology network. These events include mining explosions from mines in New Mexico and eastern Arizona as well as earthquake activity throughout the region.

OBJECTIVE

The objective of this study is to investigate the use of neural networks for detecting seismic events. Our eventual intent is to develop neural network detectors for use in an automated processing pipeline for nuclear explosion and nonproliferation monitoring. In this paper, we will be investigating the process involved in preparing and training neural networks for use in seismic event detection.

Currently most automated processing pipelines detect seismic events through the use of a single algorithm that is computed from the incoming seismic waveform. One such commonly used algorithm is the STA/LTA. In order to detect an event, the real-time process looks for some change in the detection algorithm. This change can be defined in several ways, such as the slope of the algorithm output or the algorithms current level. The triggering method requires that an arbitrary threshold level be defined. If the threshold is too high, then events will go undetected and if the threshold is too low, the system will be overwhelmed by false-alarms. The optimal threshold level depends not only on the algorithm being used but also the seismicity of the particular geographic region that is being monitored.

A neural network can be trained to identify seismic events by distinguishing between the algorithm output from signal and noise waveforms. Rather than simply looking at the level of the detection algorithm, a neural network is trained to look for particular patterns in the algorithm. In the training process, a newly initialized neural network is presented with input patterns from both signal and the noise segments from the detection algorithms. The network parameters can then be optimized to best predict the source type for each of those input patterns.

We will be evaluating neural network detection using seismic data recorded by the New Mexico Tech Seismic Network (NMTSN). The data we will be using consists of mining explosions from a mine near Santa Rita in southern New Mexico during August 1997. There are 29 seismic events available from that time period. We will use a subset of those events to train a neural network and then run the network on the remaining events to evaluate the performance of the neural network.

Neural Networks

The type of neural network that we will be making use of in this study is called a feedforward, multi-layer network. The network consists of an arbitrary number of inputs nodes, a single output node, and one or more hidden layers. Each of the hidden layers contains a pre-defined number of nodes. Weighted links connect each node within a layer to all of the nodes within the next layer. The neural network also contains transfer functions between the layers to scale the outputs of each layer to a pre-defined range. The transfer function that we will be using is called a tansig function, which is similar to the hyperbolic tangent. This transfer function has the effect of scaling the outputs from -1 to 1, which simplifies the process of interpreting the output of the network.

The weighted links between the nodes can be adjusted to produce some desired output for a given set of inputs. This adjustment procedure is called the training of the neural network. So, a neural network can be thought of as a functional mapping between a domain of inputs and a range of outputs. In our case, the set of inputs consist of the outputs from several algorithms. We take a short window of the algorithm output for both a section of noisy waveform data and the initial onset of the seismic event signal. The noise inputs are mapped to a zero on the output of the neural network and the signal inputs are mapped to a one. The neural network is then trained to minimize the mean-squared error between its predicted outputs and our defined training outputs. This choice of a zero output for noise and a one output for signal allows for the neural network output to be interpreted as a probability of an event detection. The output of the neural network still requires some threshold level to trigger a detection, however selecting an appropriate probability level is simpler than selecting such a level on an STA/LTA where the values can range from 0 to infinite.

Determining the optimal size, the number of layers and the number of nodes in each layer, of a neural network is a difficult problem. There are many heuristics that have been suggested that relate the amount of training data to the number of weighted links or relate the number of inputs to the number of nodes in each layer. A suitable solution is to simply start with a small network and gradually increase the size until there is no further improvement in performance. However, this is generally a lengthy process involving trial and error.

Once a neural network has been initialized and trained, data can be run through the network a window length at a time. So, at each time step, a window of data will be loaded into the inputs of the neural network. The neural network will then output a single detection probability value. The process will then move over one time step and load the next window of data into the network. This continues indefinitely with the neural network producing a series of detection probabilities. For a given set of input algorithms, a neural network will generate an output sequence in which a value of one indicates the presence of an event and a value of zero indicates the absence of an event.

RESEARCH ACCOMPLISHED

The data that we will be using from the NMTSN is sampled at 100 Hz, however we have found that the usable frequency content is typically much less. So, the data is down-sampled to 25 Hz to reduce the amount of data that needs to be processed. In addition, the data is bandpass filtered from 2 to 8 Hz with a third-order Butterworth filter. For training the neural network, we are using a 0.5 second (13 sample) window of data centered on the Pg arrival for the signal window and starting 5 seconds in advance of the Pg arrival for the noise window. The Pg arrival is not necessarily the first arrival for these events, however for this dataset it has a much higher energy content than either the P or the Pn arrivals. So, we chose to window around this arrival because the algorithms appear to exhibit their desired responses during the Pg arrival. A different set of data might have a more appropriate arrival to use. By selecting the noise window 5 seconds in advance of the Pg, we ensure that the noise used in training the network is free from any portion of the signal.

Since the window length of the data is 13 samples long, any neural network that we construct will have 13 input nodes for each algorithm that is to be loaded into the network. If we were using two algorithms, the network would have 26 inputs. If there were 3 algorithms in use, the network would have 39 inputs, and so on.

The 29 events that we are using have been divided into 4 groups: training, testing, validation, and running. The training group contains 14 events and is used in the training process to evaluate how to adjust the network link weights so as to minimize the prediction error. The testing and validation groups each contain 5 events and are used during the training process to ensure that the network does not become overly trained for the set of training data. Finally, the running group contains the remaining 5 events, which are run concurrently through the neural network to determine the output sequence of the network for those events. This division of the data into groups allows us to evaluate the performance of the neural network independently of the data on which the network is being trained. Otherwise, any network that is created runs the risk of being overly trained for a specific set of data.

Below, in Figure 1, is a typical plot of the performance of a neural network as it is being trained. After several training epochs (an epoch being a single iteration in the optimization process) the performance of the training and validation datasets begins to level off while the training dataset is demonstrating further improvement. This would tend to indicate that the neural network is beginning to become overly optimized for the particular training set. At this point, further training provides little benefit.

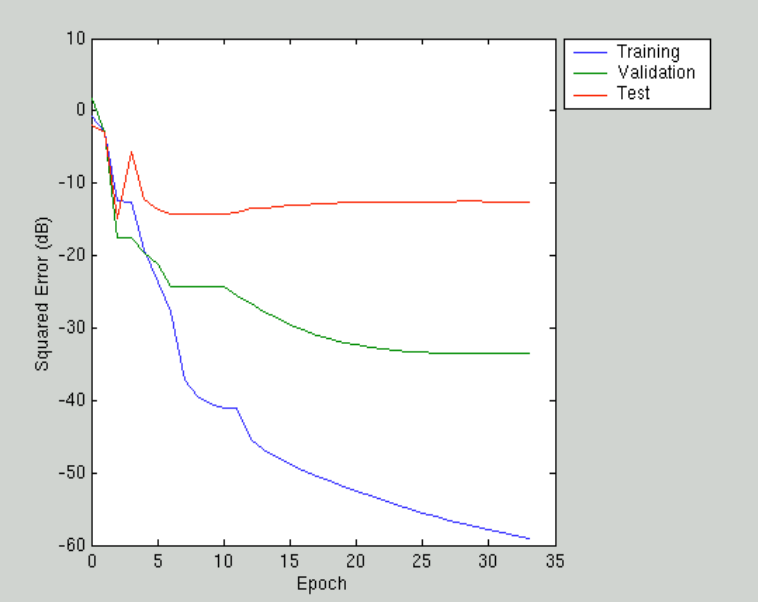

Figure 1. Typical performance of a neural network over time as it is being trained.

In order to form a neural network, there are several steps that must first be taken in preparation: select the algorithms to use as inputs to the neural network, piece out the section of data to use for training, and appropriately scale the inputs to normalize out differences in magnitude between events.

Selection of algorithms

We first had to select the algorithms that we wanted to use as inputs to the neural network. We have initially arbitrarily chosen several algorithms that exhibit significant changes in the presence of signal versus noise. The algorithms that we chose to examine for this study were the change in autoregressive coefficients (ARC) (Wang, 1997), kurtosis (Savvaidis, 2002), and STA/LTA.

Autoregressive coefficients are calculated by modeling the waveform as an autoregressive process. We chose to make use of a fourth-order AR model. At each time-step the AR coefficients are determined from the four previous samples. The ARC is then calculated to be the normalized difference between this time-steps AR coefficients and the previous time-steps AR coefficients. So, the ARC indicates how much the signal model changes between time-steps.

$$ARC = \frac{\left| \sum_{k=1}^{4} w_k(i) - \sum_{k=1}^{4} w_k(i-1) \right|}{\left| \sum_{k=1}^{4} w_k(i) \right|},$$

where $w_k(i)$ for k = 1..4 are the fourth-order AR coefficients at time i.

Kurtosis is measured as the ratio between the fourth-order central moment and the second-order central moment. It is typically interpreted as a measure of how gaussian a signal is. Kurtosis has a value of 0 for a gaussian signal and it increases as the signal becomes increasingly non-gaussian. This algorithm is included to take advantage of the tendency for noise to be gaussian and seismic events to be strongly non-gaussian.

An STA/LTA is the ratio between the short-term average energy and the long-term average energy and is the most commonly used method of detecting seismic events. Spikes within an STA/LTA indicate an abrupt increase in the

level of short-term energy. We make use of a 10 second long-term window and a 1 second short-term window. Examples of these three algorithm outputs are shown in Figure 2.

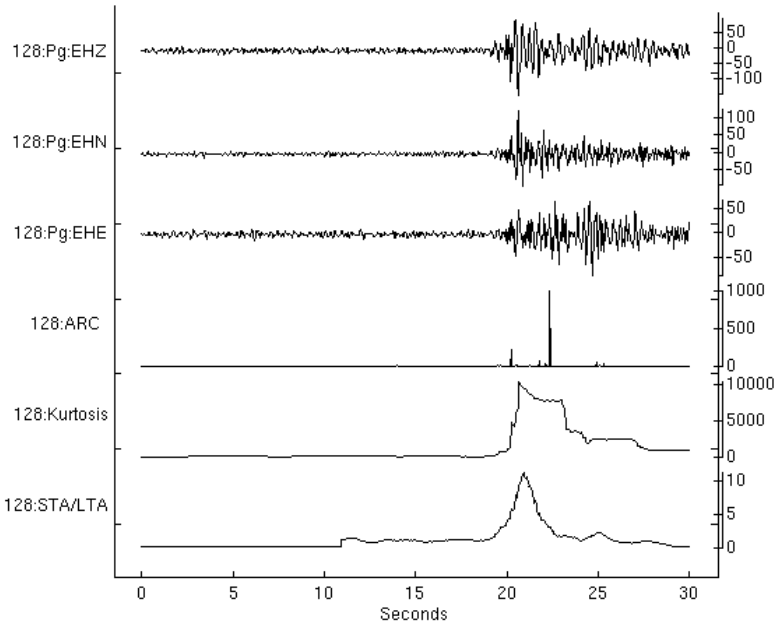

Figure 2. Waveforms and algorithms for one of the events. Three component waveform data is show, however only the z-component is used in computing the algorithms.

Time alignment of training data

A crucial step in the training of a neural network is selecting a portion of the waveform as training data and designating that window as being either signal or noise. If the training windows are poorly chosen, then they might not capture the feature of interest within the detection algorithm. This would inhibit the neural network from being able to properly identify the key features of the algorithm that indicate the presence of a signal. An example of a misaligned training window can be seen in Figure 3. One of the signal patterns was not lined up properly and so appears to be similar to the noise patterns.

To help facilitate the training window selection, we needed to have very precise arrival picks to identify the signal onset. To assist in the selection of the training windows, these events were hand picked and relocated by a seismic analyst familiar with the NMTSN. In addition, the training process requires some operator-assisted evaluation to verify that the training sets are consistent.

Neural network input scaling

A second key issue when preparing data for a neural network is how to scale the input patterns prior to loading them into the network. This issue applies to both training data and to data that is being run through the neural network. For many applications using neural networks, directly scaling the set of inputs is strongly discouraged. This makes sense when the inputs have some physical meaning such as distance or temperature. However, for the algorithms that we are using, the particular values of the detection algorithms have no meaning in and of themselves. Instead, the values are only meaningful in relationship to the values of the adjacent algorithm time-samples. The intent in applying some type of scaling to each window of data that is loaded into the network is to normalize for any differences in the relative magnitudes of the algorithms. This should help to make the neural networks detection capability invariant to differences in signal-to-noise ratios (SNR) between events.

For example, if we were examining an STA/LTA for two events, one of which has an SNR of 10 and the other has an SNR of 100, the smaller event would appear nearly flat relative to the much larger event. However, we desire to be able to detect either event equally well, regardless of the difference in SNR between them. So, we have chosen to scale the neural network inputs to eliminate variations in the level of the algorithms. This allows us to focus solely on relative changes in the algorithms.

Figure 3. Overlayed Kurtosis training patterns for signal (left) and noise (right) for the 14 training events.

In order to determine the method of scaling that achieves the best results, we built neural networks using several different methods of scaling: no scaling, normalize by the maximum, normalize to between zero and 1, and normalize to a mean of zero and a standard deviation of one. For each algorithm we will be presenting the scaling method that achieved that best results.

What we found was that, in general, the kurtosis and STA/LTA algorithms performed best when each window of data to be fed into the neural network was normalized by its maximum value. This normalization resulted in the neural networks being trained to detect transitions within the algorithm regardless of the particular value of the algorithm. The ARC algorithm had the best output when no scaling was applied to the input algorithm. However, as will be seen later, the ARC algorithm did not perform as well as kurtosis and STA/LTA.

Single algorithm neural networks

Initially, we began investigating the use of neural networks by evaluating the performance of neural networks that employ only a single input algorithm. We will be able to determine the optimal parameters for each algorithm individually as well as providing a basis for comparing the results from multiple algorithm neural networks. For each of the test runs, we formed a fairly simple neural network with 2 layers and 13 nodes within each layer. Determining the size of the neural network was a fairly arbitrary process. We ran simulations using different numbers of layers and nodes per layer and typically found only minor variations between the outputs of the networks. The size we chose was one that appeared to work well for all of the algorithms that we were using.

However, it is important to stress that there is no single optimal network configuration. The inputs algorithms and neural network outputs for each of the 5 events that were run through the network are shown in Figures 4-7.

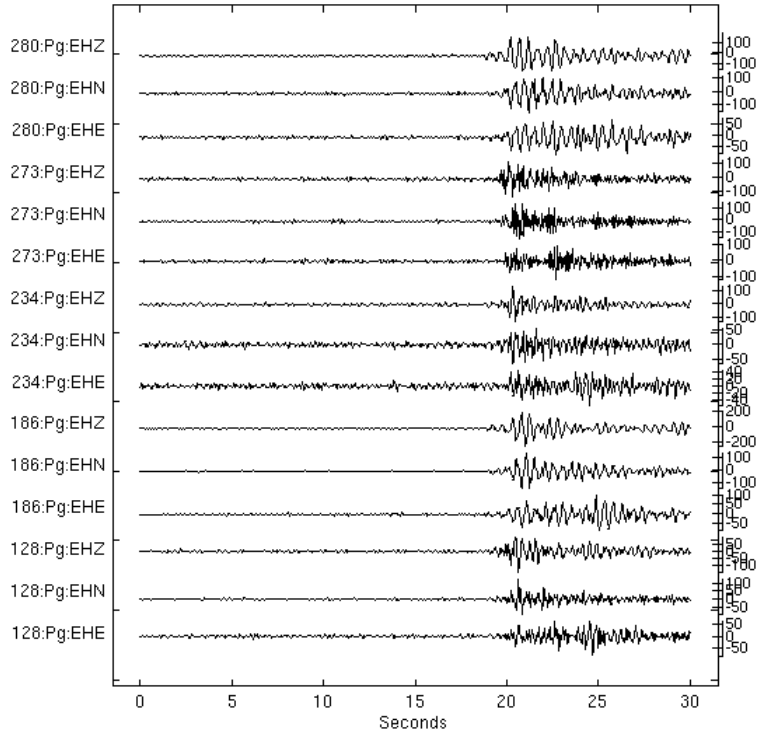

Figure 4. Seismic waveform data for the 5 events to be run in a neural network.

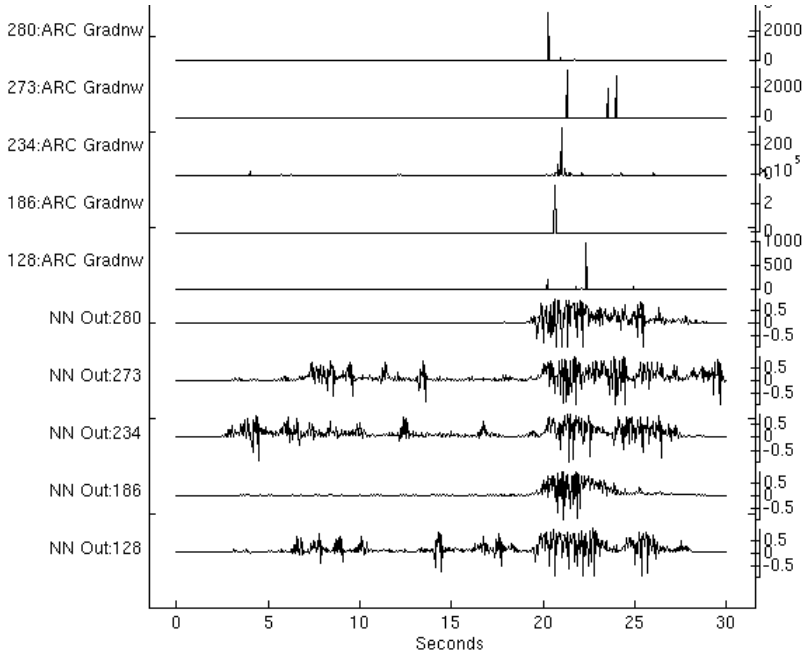

Figure 5. ARC processed data and neural network outputs for the data shown in Figure 4.

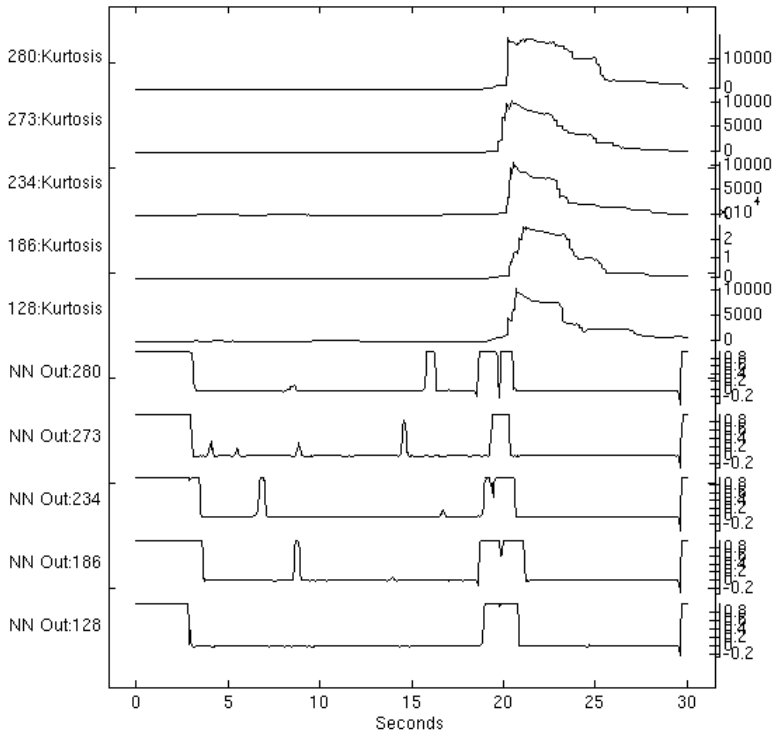

Figure 6. Kurtosis processed data and neural network outputs for the data shown in Figure 4.

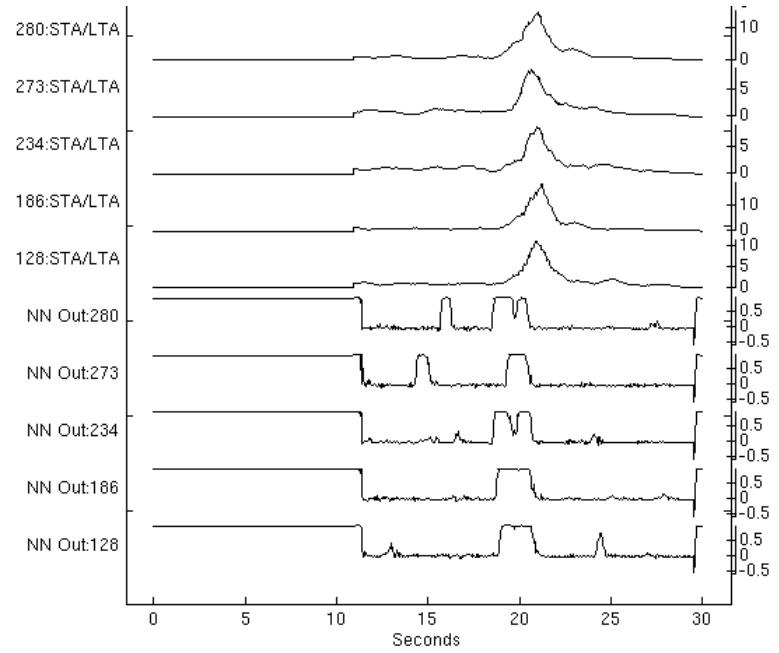

Figure 7. STA/LTA processed data and neural network outputs for the data shown in Figure 4.

Ideally, what we would expect to see in Figures 5, 6, and 7 above, would be for the neural network output to be zero prior to the arrival, one during the arrival, and then return to zero after the arrival. In each of the test runs, the data window was chosen such that the Pg arrival is located at the 20-second mark. This appears to be consistent with the algorithm output for each of the events. It is important to note in the figures above that there is a certain amount of startup time for each of the algorithms. The kurtosis algorithm has a startup time of 2.56 seconds, which corresponds to the window of data that is used to calculate each kurtosis value. Similarly, the STA/LTA algorithm has a startup time of 11 seconds (10 seconds for the LTA and 1 second for the STA) and ARC has a startup time of only 4 seconds. The effect of the algorithm startup is visible in the initial outputs of the neural networks.

The kurtosis and STA/LTA algorithms both appear to have clean outputs with fairly obvious indicators about the Pg arrival at 20 seconds. They each exhibit a few additional spikes in the neural network output. The ARC output, however, is very poor in comparison. Although the ARC algorithm appears to present strong indicators of the presence of a signal, it is very impulse throughout the signal. These other impulses are simply not visible due to the relative waveform scaling.

Multiple algorithm neural networks

We next formed a neural network using multiple algorithms as inputs. Based upon the test results from the single algorithm networks, we used both the kurtosis and STA/LTA, but not ARC, algorithms. The network configuration is the same 2 layers and 13 nodes per layer as in the previous section. The only change from before is that the multiple algorithm network will have 13 inputs per algorithm for a total of 26 input nodes. The input sequences and their corresponding outputs are shown in Figure 8.

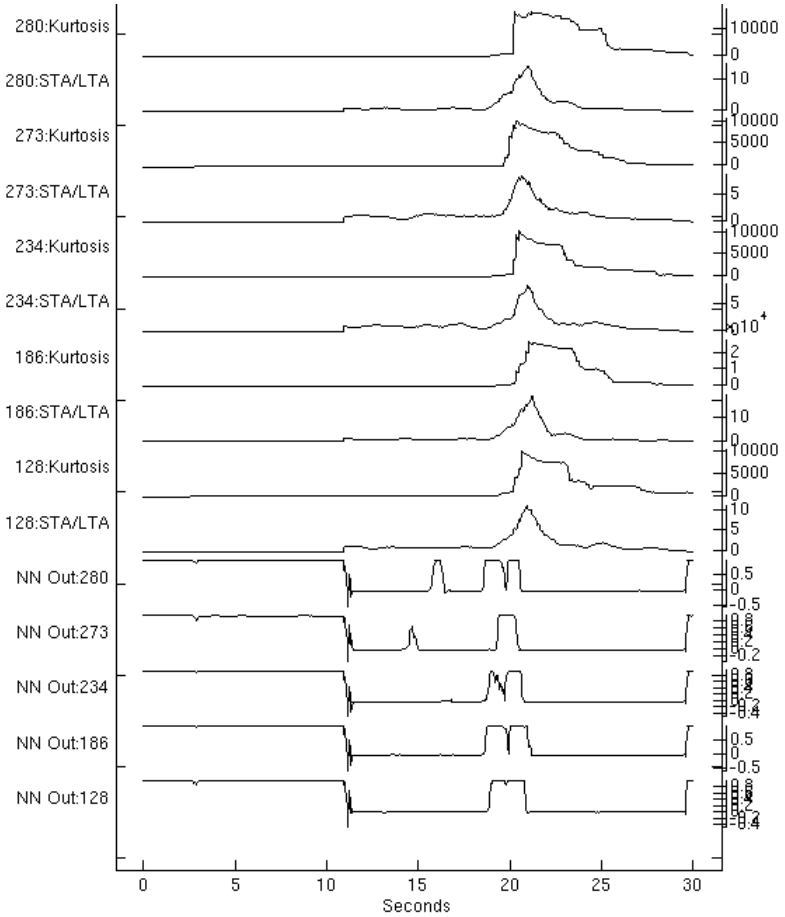

Figure 8. Kurtosis and STA/LTA processed data and neural network outputs for the data shown in Figure 4 using a multiple algorithm neural network.

Disregarding the algorithm startup, the combination of the two algorithms appears to have eliminated several of the false alarms that each of the single algorithm neural networks were exhibiting. Those output spikes that remain are the ones that were shared between the kurtosis and STA/LTA neural networks. This would tend to confirm that using multiple algorithms yields an improvement in the ability of a neural network to detect seismic events.

CONCLUSIONS AND RECOMMENDATIONS

In the course of evaluating the use of neural networks for use in seismic event detection, we have found that there are several key issues that need to be addressed prior to obtaining meaningful results. First, it is important to properly identify the features to be detected. We were able to largely resolve this problem by repicking the data. However, this issue could also be addressed by increasing the window of data that is fed into the neural network or by providing some means of manually adjusting the window for each training event. The second issue is the scaling of the window of data to be inputted to the neural network. Depending upon the algorithm, each window of data will need to be scaled independently to normalize for variation in SNR between events.

Using multiple algorithms in combination with a neural network should help to improve the performance of seismic event detection. We will be continuing in our study of this topic to further develop the ability to provide detection triggers from the neural network as well as examining additional algorithms for use in event detection.

REFERENCES

Jurkevics, A. (1988), Polarization Analysis of Three-Component Array Data, *Bull. Seism. Soc. Am.*, 78, 1725-1743.

Savvaidis, A., C. Papazachos, P. Soupios, O. Galanis, N. Grammalidis, Ch. Saragiotis, L, Hadjileontiadis, and S. Panas (2002), Implementation of Additional Seismological Software for the Determination of Earthquake Parameters Based on MatSeis and an Automatic Phase-detector Algorithm, *Seism. Res. Lett.*, 73, 56-69.

Wang, J. and T. Teng (1997), Identification and Picking of S Phase Using an Artificial Neural Network, *Bull. Seism. Soc. Am.*, 87, 1140 -1149.

Withers, M., R. Aster, C. Young, J. Beiriger, M. Harris, S. Moore, and J. Trujillo (1998), A Comparison of Select Trigger Algorithms for Automated Global Seismic Phase and Event Detection, *Bull. Seis. Soc. Am.*, 88, 95-106.

Zhao, Y. and K. Takano (1999), An Artificial Neural Network Approach for Broadband Seismic Phase Picking, *Bull. Seism. Soc. Am.*, 89, 670-680.

SEISMIC CALIBRATION OF GROUP 1 INTERNATIONAL MONITORING SYSTEM (IMS) STATIONS IN EASTERN ASIA FOR IMPROVED EVENT LOCATION

John R. Murphy,[1] William L. Rodi,[2] Michelle Johnson,[3] Jamil D. Sultanov,[4] Theron J. Bennett,[1]
M. Nafi Toksoz,[2] Carolynn E. Vincent,[3] Vladimir Ovtchinnikov,[4] Brian W. Barker,[1]
Anca M. Rosca,[3] and Yuri Shchukin[4]

Science Applications International Corporation,[1] Massachusetts Institute of Technology,[2]
Weston Geophysical Corporation,[3] Institute for Dynamics of the Geospheres[4]

Sponsored by Defense Threat Reduction Agency

Contract No. DTRA01-00-C-0024

ABSTRACT

A consortium of institutions that includes SAIC, Massachusetts Institute of Technology's (MIT's) Earth Resources Laboratory (ERL), Weston Geophysical Corporation and the Russian Institute for Dynamics of the Geospheres (IDG) is engaged in a research program directed toward the seismic travel-time calibration of the 30 Group 1 International Monitoring System (IMS) stations of eastern Asia. During the second year of this program, we have refined our preliminary 3-D velocity model of the region to incorporate a 1°-x-1° background model based on the surface wave inversion studies of Stevens and Adams (2001), as well as new submodels of the China, southeast Asia, and Korean peninsula regions. In addition, we have formulated and implemented a sophisticated, fully nonlinear tomographic inversion algorithm and applied it to the refinement of our velocity models of the Former Soviet Union (FSU) DSS region and the India/Pakistan region (WINPAK3D). Regional travel times through these revised 3-D velocity models have been computed using the Podvin/Lecomte finite difference algorithm and employed for purposes of model validation and the determination of Site-Specific Station Correction (SSSC) estimates for the IMS stations in this region. Validation studies of the DSS model have focused on comparisons with data from our Soviet explosion ground truth database, which currently consists of over 1000 carefully validated, regional P wave arrival time observations from distinct Soviet peaceful nuclear explosions (PNEs) and weapons tests. Results of these tests have confirmed that our tomographically refined DSS velocity model is highly accurate, with total root-mean-square (RMS) errors of less than 1 second for this dataset. In particular, we have demonstrated that this model predicts the observed ground truth travel times at locations near the IMS stations BRVK, NRI, TIK, YAK, PDY, TLY, ZAL, AAK and OBN with a degree of accuracy consistent with the regional seismic location goals of the project. For example, data recorded from a sample of 14 Soviet PNE events on a sparse network of 4-6 surrogate IMS stations were used to locate these explosions with and without the travel-time corrections predicted by our tomographically refined DSS 3-D velocity model, and it was found that the refined DSS model provides significantly more accurate seismic locations for these ground truth explosions than does the default IASPEI[1]-91 model (i.e. an average mislocation of 6.9 km as compared with 20.4 km). Similar validation studies of the tomographically refined WINPAK3D velocity model, conducted using ground truth earthquake data, have confirmed that this model is also quite accurate and that it provides significantly better seismic locations than other velocity models that have been proposed for this region. On the basis of these results, we have concluded that our current DSS and WINPAK3D velocity models are essentially final. P wave SSSC estimates, based on our revised velocity model of the Group 1 region, have now been estimated for all 30 Group 1 station locations; and we are in the process of delivering them to the Center for Monitoring Research for further independent evaluation. Finally, empirical correction surfaces that account for remaining unmodeled travel-time anomalies are also being estimated at a number of the Group 1 station locations using standard kriging algorithms. While these corrections appear to be quite precise, we are also investigating the potential utility of more sophisticated multi-station kriging algorithms that will satisfy seismic reciprocity constraints.

[1] International Association for Seismology and Physics of the Earth's Interior.

OBJECTIVES

The purpose of this effort is to develop improved 3-D velocity models, Site-Specific Station Corrections (SSSCs), and Slowness-Azimuth Station Corrections (SASCs) for eastern Asia, to demonstrate the effectiveness of these models and corrections in improving locations of seismic events, to evaluate the uncertainties associated with these improved models and corrections, and to install these models and corrections at the Center for Monitoring Research (CMR) and evaluate their performance. This calibration is focused on the 30 Group 1 IMS stations of eastern Asia shown in Figure 1. Our approach is based on a carefully crafted scientific approach, which effectively merges the limited observed calibration data with rigorous seismological and statistical modeling procedures. In our analysis the travel time for each station is represented as the sum of a model-based travel time and an empirical correction. The model-based component is obtained by raytracing through a 3-D velocity model of the crust and upper mantle regions surrounding each station, and the empirical correction is derived from calibration events observed at each IMS station where ground truth data are available.

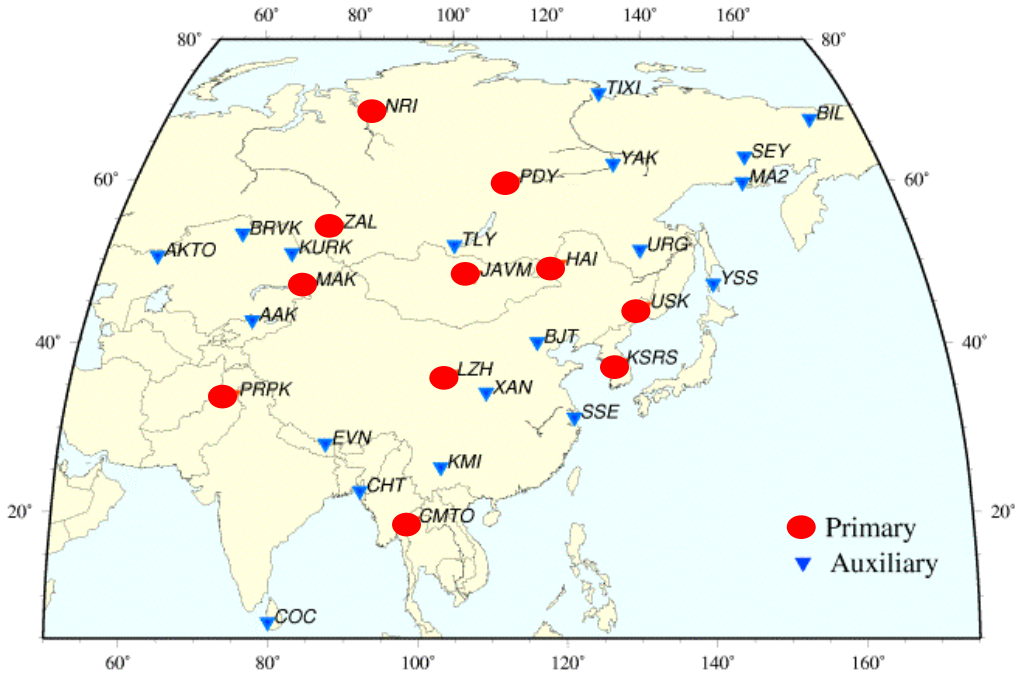

Figure 1. Locations of the 30 Group 1 IMS stations in eastern Asia.

RESEARCH ACCOMPLISHED

As noted above, we believe that a model-based approach to calculate travel-time corrections for Group 1 IMS stations in eastern Asia provides the best utilization of available knowledge for use in regions where the calibration data are sparse or non-existent, such as the many regions in Group 1, which are essentially aseismic. Therefore, the determination of travel-time tables and ultimately SSSCs is dependent on the identification of accurate velocity models to represent the crust and upper mantle in the regions surrounding each station. In defining these velocity models, we have drawn upon different knowledge bases depending on the levels of information available from the different areas and utilizing calibration data to update the model, in areas where the appropriate ground truth exists. The initial 3-D model (cf. Murphy *et al*, 2001) was composed of a hierarchy of models having different spatial resolutions; and this base model has continued to evolve during the past year, as more complete information has become available for different parts of the Group 1 region. Our general model for eastern Asia includes a new 1°-x-1° background model based on surface wave studies of Stevens *et al* (2001), a new China model developed at MIT by inverting travel-time data from Chinese earthquakes (see below), a new southeast Asia model compiled by Weston based on procedures similar to those used to define the WINPAK3D model, models for Thailand and the Korean peninsula based on surface wave studies modified by regional P-wave travel-time observations, and tomographically refined models covering much of the DSS and WINPAK3D areas where calibration event data were available.

One focus of the research efforts over the past year was to obtain a preliminary 3-D velocity model for China and the surrounding areas. To accomplish this objective, we have used the earthquake phase data from January 1990 to December 2001 from the Annual Bulletin of Chinese Earthquakes (cf. Chen, 1990-1998), which includes 16,642 earthquakes, recorded at 220 stations over 345,520 ray paths in China and surrounding areas (cf. Figure 2). These

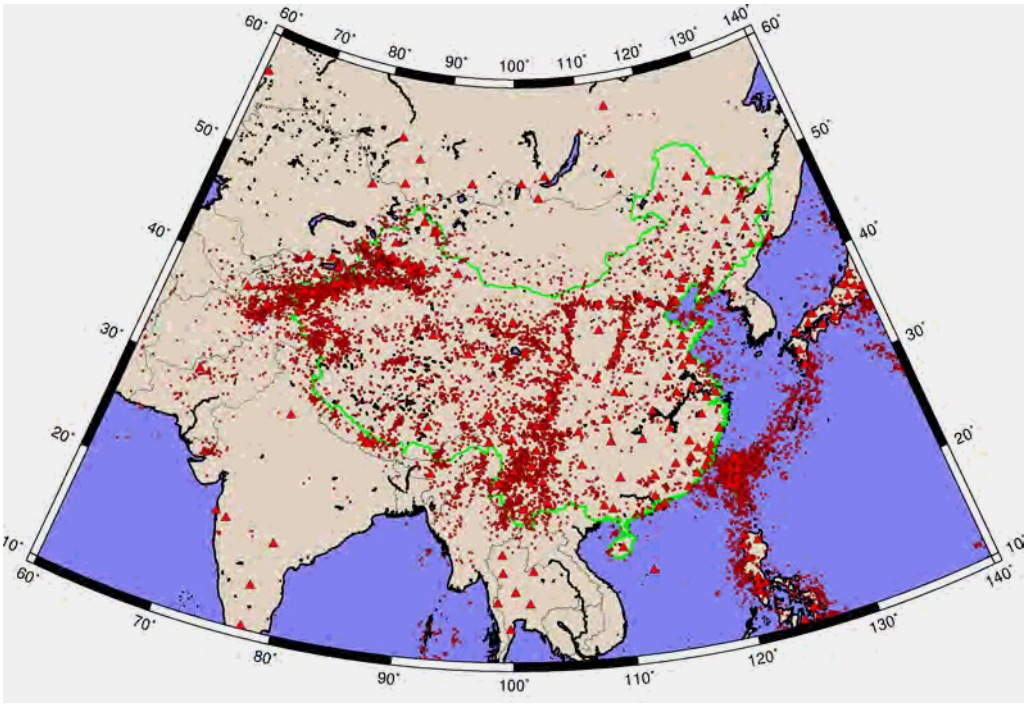

Figure 2. Locations of Chinese Bulletin events (circles) and stations (triangles) used to develop the velocity model for China.

data were analyzed by dividing the region into 1,312 1°-x-1° blocks covering China and Mongolia. In each block a 1-D velocity model was obtained by inverting the regional P-wave travel times over a 10°-x-10° region surrounding each block using a Monte Carlo algorithm to minimize the root-mean-square (RMS) travel-time residuals and invert for the optimal velocity models. Within each block the velocity structure is represented by a four-layer crust over one layer of upper mantle. The thickness of the top layer in each block was constrained to the values published by Laske *et al* (2001), and the Pn velocities were constrained to be within ± 0.1 km/sec of the values reported by Hearn and Ni (2001) for this region. The Monte Carlo inversion was then used to determine the thicknesses of the three other crustal layers, the four crustal P-wave velocities, and the Pn velocity in each block. The composite of the 1,312 1-D block models then gives the 3-D P-velocity model for the China/Mongolia region in the final model for eastern Asia. We illustrate the results of this model in Figure 3, showing the Pn velocity across the region.

Although there are some significant differences in detail, the Moho depths show the same general trends as reported in other models for the region (e.g. Laske *et al*, 2001; Stevens *et al*, 2001; Shapiro and Ritzwoller, 2001). There are some rather large differences in Pn velocities in specific areas from our model and those based on prior surface-wave inversion, and these will be investigated more closely. We have also compared the P-wave crustal velocity profiles as a function of depth for our model with the surface wave models and with those reported by other authors (viz. Mangino *et al*, 1999; Wu *et al*, 1997) at several specific locations within the China/Mongolia region and found that our P-wave velocity profiles fall nicely within the bounds of the other models in most areas.

It should be noted that the 3-D velocity model described above for China/Mongolia is viewed as preliminary and was not based on formal tomographic inversion of the available travel-time data; that remains to be done. However, we have made significant advances over the past year in tomographically refining the velocity models for two other areas (viz. the DSS region of the FSU and the WINPAK region of India/Pakistan) within our eastern Asia Group 1 study region. The state-of-the-art joint velocity tomography and event relocation algorithm, which we have

developed, uses the data set of regional seismic events to iteratively update the velocity model following a conjugate gradients technique that adjusts the velocity model to minimize the misfit between the calculated and observed

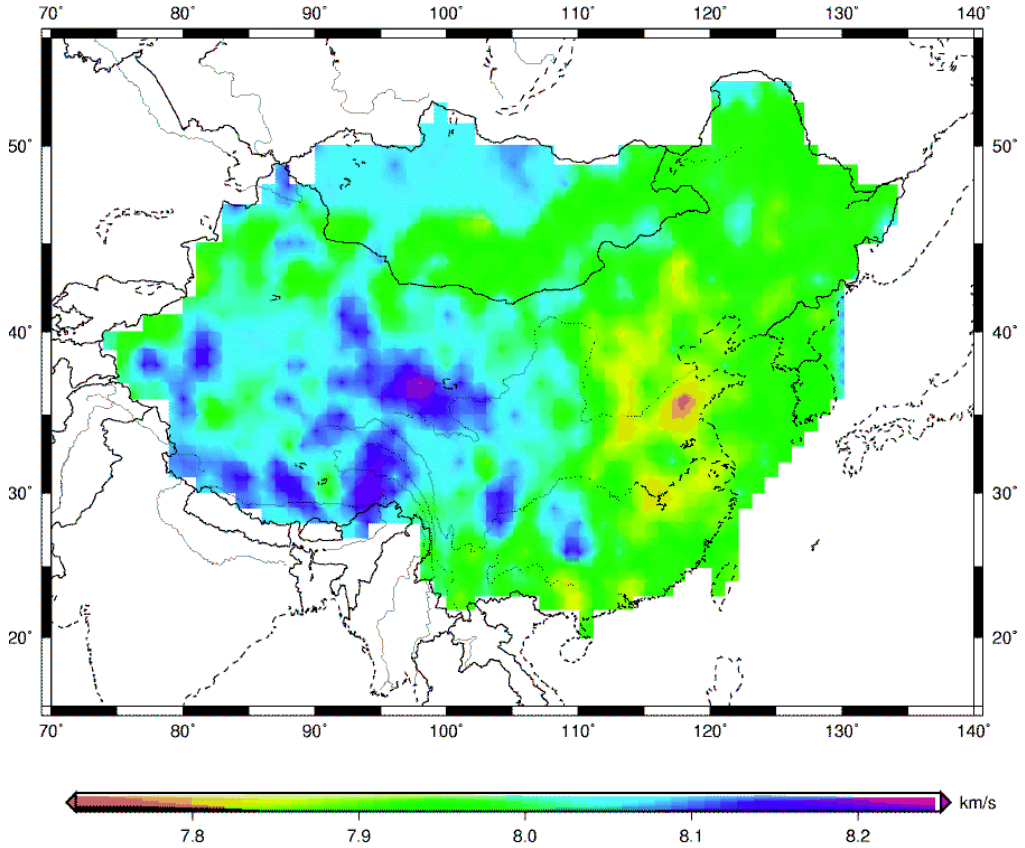

Figure 3. Pn upper mantle velocities for China/Mongolia derived from inversion of Chinese Bulletin earthquake data.

travel times from multiple stations and events, subject to smoothness constraints. The three major components of this algorithm are: (1) 3-D raytracing to predict first arrival times using a version of the Podvin/Lecomte (PL) method (cf. Podvin and Lecomte, 1991); (2) a 3-D grid search location algorithm to relocate events inside the appropriate velocity model; and (3) a linear conjugate gradient inversion algorithm to produce the updated velocity model inside each iteration of the process. Although we are currently only solving for Pn velocity in the inversion, model updates extend beyond Pn velocity. Based on the updated Pn velocity, velocities from the Moho down to 410 km are refined in a smooth manner, with a constant shift in velocity applied from the Moho extending to 210-km depth followed by a tapering between depths of 210 km and 410 km to provide a smooth transition to the 410-km discontinuity. This algorithm has been thoroughly tested and found to produce results that are reasonable and effective for adjusting velocity models to better represent the available calibration data. We have applied the tomography algorithm to two areas, where more abundant calibration data have been collected, using data from nuclear explosions at Semipalatinsk and Novaya Zemlya test sites and PNEs throughout the FSU, supplemented with some earthquake data, recorded at several current and historical stations in the DSS region and using data from a large sample of earthquakes in the WINPAK region recorded again at numerous regional stations. The results of these tomographic analyses are shown in Figure 4, where we have plotted the Pn velocities for the tomographically refined models covering the DSS and WINPAK3D areas. Focusing on the FSU region, there appears to be a definite correlation of the model results, derived from the tomography refinements, with published crust and upper mantle characteristics in the region. Examples are the two lower velocity features in the platform region to the north of BRVK which correlate remarkably well with regions of crustal thinning associated with the northeastern part of the Volga-Ural Uplift (northwest of BRVK) and with the crest of the West Siberian Platform (northeast of BRVK). The lower velocity region southeast of BRVK also correlates very well with the mapped northwestern part of the Kazakh foldbelt. So, the tomographic analyses produce velocity model refinements, which appear to be in reasonable agreement with geologic and tectonic features. Additional demonstration of the validity of these tomographic

refinements to the velocity models is provided by the resulting reduction in the travel-time residuals, as described below.

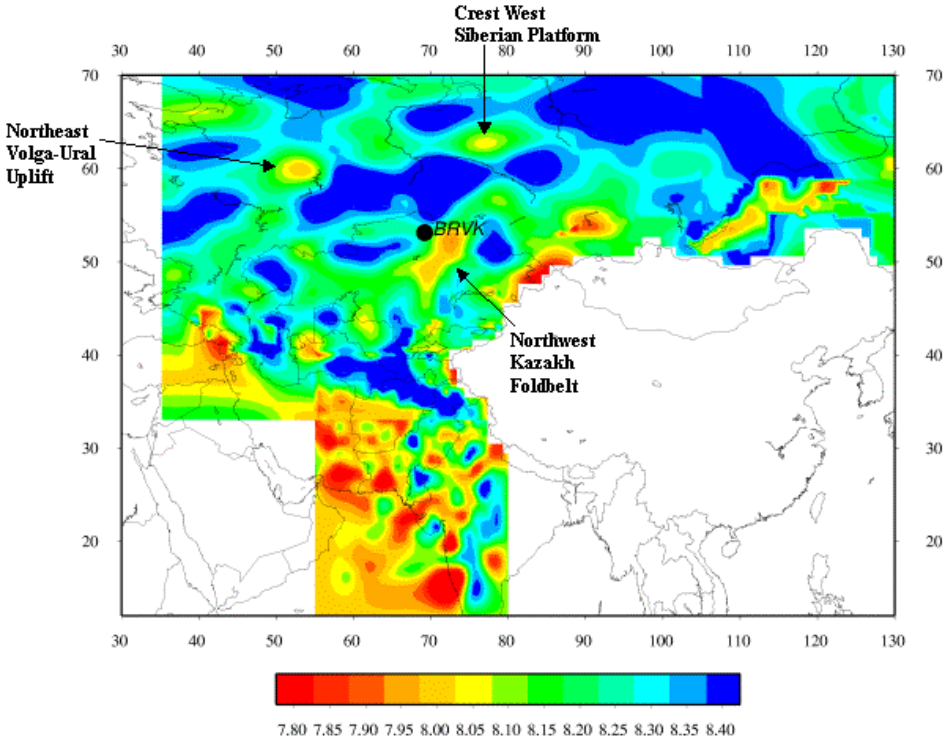

Figure 4. Tomographically refined Pn upper mantle velocities for the DSS and WINPAK regions.

We use a program module called QUILT to organize and assemble the models from the different regions covered by the Group 1 IMS stations into a composite 3-D model, which provides the basis for the SSSC calculations. The QUILT module allows us to integrate models with differing parameterizations and spatial resolutions from the different regions into a unified model that specifies the velocity profile at each geographic grid point as velocity/depth pairs from the earth's surface to a depth of 760 km, with velocity discontinuities at the ocean bottom, Moho, and the major mantle discontinuities at 410-km and 660-km depths. Grid spacing in the unified model is 0.5° in latitude, and longitude spacing is varied (with latitude) to be equal to latitude spacing, so as to preserve the grid aspect ratio. A second software module has been implemented to map the unified model from geographic to Cartesian coordinates that can be used by the Podvin/Lecomte raytracing algorithm and enable travel-time calculations at the resolution level required for the tomographic inversions and SSSC computations.

At the conclusion of the first year of this research program, we prepared estimates of the preliminary P-wave SSSCs for 20 Group 1 IMS stations, which were subsequently delivered to DTRA and CMR. As part of our program efforts over the past year, we have now computed the SSSCs for all 30 IMS station locations from the Group 1 region based on the revised velocity model described above. As an example we show in Figure 5 the P-wave surface-focus SSSCs for the area around station AAK. The values vary from –4.9 seconds to +7.0 seconds across the area. Largest negative values of the corrections occur on the far western and northern extremes, while greatest positive values occur to the southeast in China. Where the SSSCs are negative, the 3-D model travel times are shorter than those of IASPEI-91, indicating relatively higher velocities in the model; and, where the SSSCs are positive, they indicate model velocities are relatively lower than IASPEI-91. Digital versions of the SSSCs for surface focus plus 10 other focal depths (viz. 5, 10, 20, 30, 40, 50, 70, 100, 150, and 200 km) have been determined for each of the 30 Group 1 IMS station locations, and these have been delivered to the CMR for further testing and evaluation.

The ultimate test of the SSSCs derived from our 3-D velocity model is whether they enable more accurate event locations for the Group 1 region. To check this we made a number of P-wave travel-time comparisons for several individual IMS, or surrogate IMS stations, from our Group 1 region using explosion data from the FSU for ground

truth. As an example, Figure 6 shows observed P-wave travel-time residuals with respect to predictions based on the IASPEI-91 model and our refined 3-D velocity model for 55 Soviet PNEs observed at station BRVK. It is clear from the figure that the observed travel times are generally much faster than IASPEI-91 over most of the region. On the other hand, the size of the symbols is much smaller and more balanced, between positive and negative values,

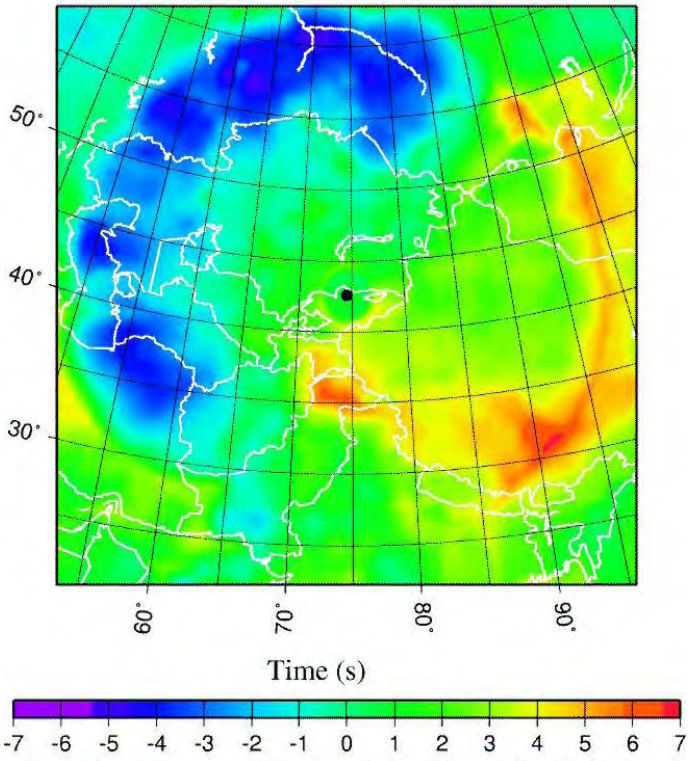

Figure 5. Surface-focus P-wave SSSCs for the region surrounding station AAK.

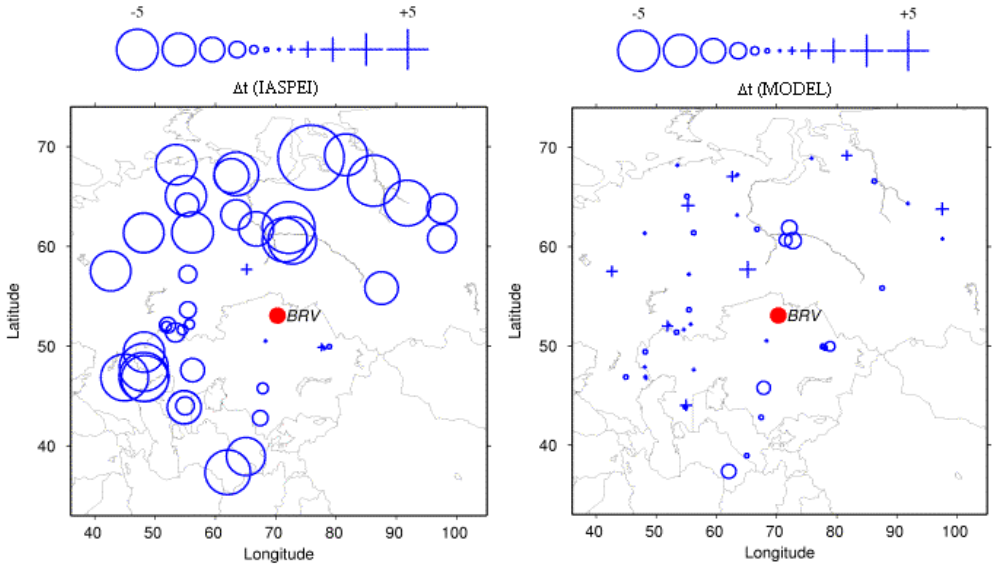

Figure 6. Comparison of observed BRVK P-wave residuals at calibration explosion locations for the IASPEI-91 model (left) and for our "final" 3-D velocity model (right).

for our 3-D velocity model. An even more dramatic example is shown in Figure 7 for station ELT. The large observed residuals for the PNEs with respect to the IASPEI-91 travel-time predictions are nearly completely accounted for in our final 3-D velocity model. There are significant reductions in both bias and scatter for the 3-D

model-based residuals over the IASPEI-91 results. Table 1 shows a more complete comparison between the IASPEI-91 and final 3-D velocity model for the average P-wave travel-time residuals for nine IMS or surrogate IMS stations from the Group 1 region determined from the PNE observations. It is noteworthy that at all stations, the

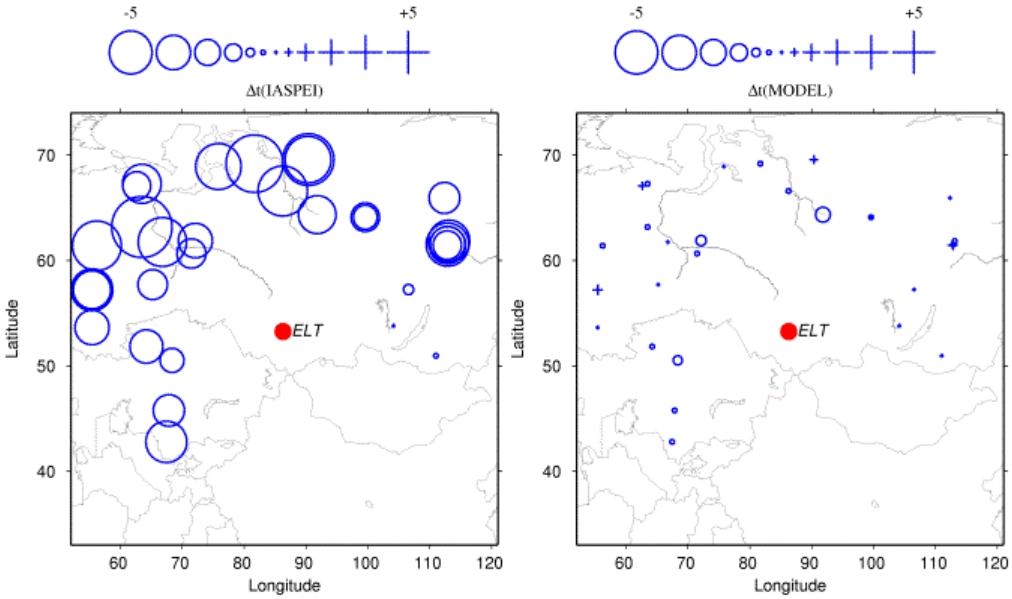

Figure 7. Comparison of observed ELT P-wave residuals at calibration explosion locations for IASPEI-91 model (left) and for our "final" 3-D velocity model (right).

Table 1. Summary of Soviet PNE statistics for IASPEI-91 and tomographically refined velocity model

	IASPEI-91		3-D Model	
Station	Δt, seconds	σ, seconds	Δt, seconds	σ, seconds
BRVK	-3.50	2.26	0.06	0.96
NRI	-3.34	2.93	-0.12	0.98
TIK	-4.33	1.38	0.27	0.90
YAK	-3.80	2.43	0.38	1.23
BOD (PDY)	-4.26	2.52	-0.56	0.93
IRK (TLY)	-3.46	2.67	-0.48	0.85
ELT (ZAL)	-4.10	1.66	-0.03	0.74
FRU (AAK)	-2.06	1.36	-0.07	1.14
M11 (OBN)	-4.01	1.83	-0.31	0.77

average travel-time residuals and their scatter are significantly reduced for our 3-D velocity model. As a further test, we used the data from 14 PNEs in the FSU, which were recorded at from four to six regional IMS or surrogate IMS stations. The events were relocated with our tomographically refined 3-D model as well as the IASPEI-91 model, and the locations were compared to the ground truth for the explosions. The mislocation measures are compared in Figure 8, where we see that the average error of 6.9 km for the 3-D model is much smaller than the average error of 20.4 km for the IASPEI-91 model.

By using calibration event data to enable tomographic refinement of the 3-D velocity model, we have designated a preference to account for travel-time residuals to the maximum extent possible as model adjustments, and then to estimate empirical station corrections to represent only any remaining unmodeled error. Kriging has been proposed as a method of representing the spatial dependence of empirical station corrections; and, to test this approach at selected stations, we have applied a simple kriging method to the travel-time residuals remaining after our

tomographic refinement of the 3-D velocity model of the DSS region. We applied the method to the stations with the most residual observations using primarily observations from PNEs in the FSU, except for station BRV where we had supplemental earthquake data. The derived empirical corrections, based on kriging, were found to further

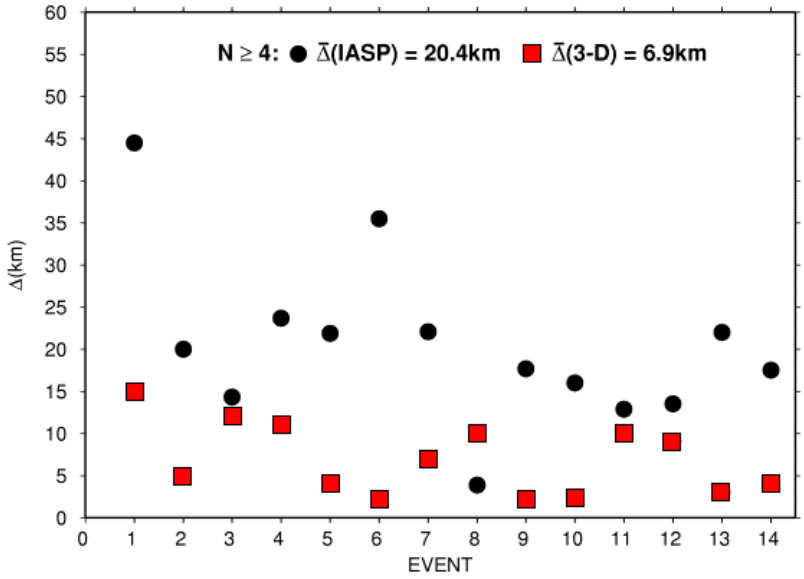

Figure 8. Comparison of regional seismic event location accuracies obtained for 14 selected Soviet PNE explosions with (3-D) and without (IASPEI) travel-time corrections predicted by the tomographically refined 3-D velocity model.

reduce the travel-time residual errors, as illustrated in Figure 9 for station BRVK. In this case the corrections were defined using the "leave one out" procedure, in which the correction surface was re-estimated for each explosion by leaving out the data point for that explosion. Application of the kriging correction further reduces the σ value from 0.92 seconds to 0.74 seconds, which we consider to be close to the lower bound on the resolution of the calibration process.

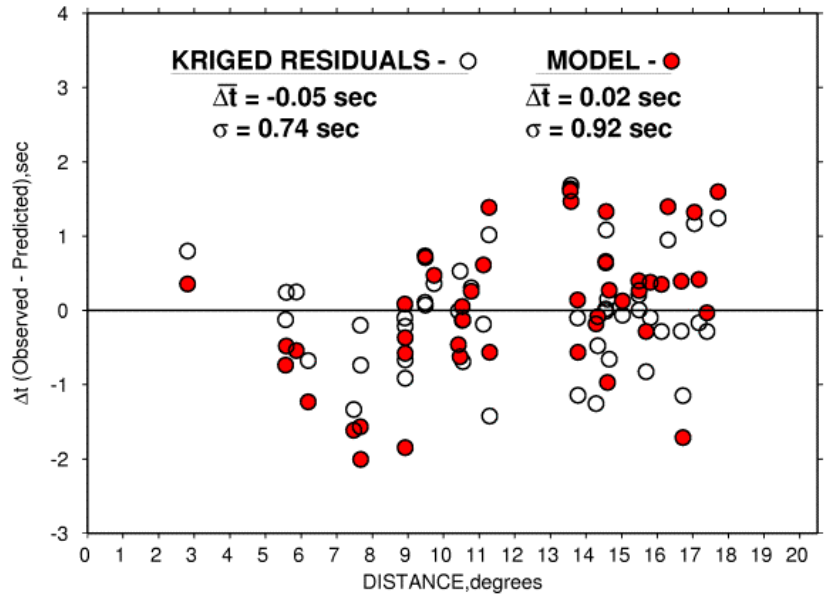

Figure 9. Comparison of PNE explosion travel-time residuals as a function of distance from station BRVK computed with respect to the kriged and to the refined 3-D velocity model.

Slowness and azimuth measurements are incorporated in routine locations at the IDC to improve location accuracy and decrease the size of error ellipses for small, poorly recorded events (Bondar *et al*, 1999). Azimuth and slowness estimates, however, can be biased, resulting in the need for SASCs. SASCs developed at the IDC are determined empirically using existing slowness and azimuth measurements at IMS stations; however, data at some IMS stations are insufficient to determine any corrections (Bondar *et al*, 1999). We have developed a preliminary technique to derive model-based SASCs that provide corrections at every point on a 3-D grid. This approach allows us to develop SASCs in regions where there are no previous data and for stations that have yet to be installed. Observed data can then be used to develop empirical corrections to the model-based SASCs.

Our technique for deriving SASCs is again based on the PL finite difference method, which we use for our travel-time calculations. Using reciprocity, travel times are calculated between a particular station location and all points in a 3-D grid of event locations. The slowness and azimuth observed at a station from a given event are the length and direction of the slowness vector defined by taking the gradient of travel time with respect to the station location. Our approach is to approximate this gradient by subtracting travel times computed for the actual station location from travel times calculated for perturbed station locations. Specifically, we compute travel times to each point in a 3-D grid, using the PL algorithm, from three different "station" locations: (1) at the proper station location, (2) displaced from the station by one node to the north, and (3) displaced from the station by one node to the east. We have chosen one-node displacement (5 km) for initial testing of this technique, but we are exploring varying the displacement amount for accuracy. The resulting travel-time grids are referred to as $T0_{ijk}$, $T1_{ijk}$ and $T2_{ijk}$, where *i, j,* and *k* index the 3-D grid. The north and east components of the horizontal slowness vector that would be observed at the station from an event at node *ijk* are then determined by taking the derivative of the travel time with respect to the Podvin/Lecomte grid spacing (*h*) as follows:

$$p^N_{ijk} = (T1_{ijk} - T0_{ijk})/h \qquad \text{and} \qquad p^E_{ijk} = (T2_{ijk} - T0_{ijk})/h \qquad (1)$$

We convert to azimuth and scalar horizontal slowness by

$$\alpha_{ijk} = \arctan\,(p^E_{ijk} / p^N_{ijk}) \qquad \text{and} \qquad p_{ijk} = \sqrt{(p^N_{ijk})^2 + (p^E_{ijk})^2} \qquad (2)$$

where α_{ijk} is the azimuth and p_{ijk} is the horizontal slowness observed at the station from an event at node *ijk*. Azimuth is clockwise from north. Slowness is calculated in seconds/km and then converted to seconds/degree. Note that with this approach we obtain the slowness vector for each point in the 3-D grid. To determine SASCs at each node relative to the IASPEI-91 model (Kennett and Engdahl, 1991), we subtract slowness and azimuth values based on the IASPEI-91 model from those predicted for the 3-D model. Commonly, slowness-azimuth corrections are depicted as vectors in slowness space. With the model-based approach, this method of plotting is inappropriate because there would be a vector for every point on a fine grid. Therefore, we present our corrections as separate azimuth and scalar slowness maps. Figure 10 shows preliminary azimuth and slowness corrections for station BRVK relative to IASPEI-91. We will continue to extend and evaluate this SASC estimation capability.

CONCLUSIONS AND RECOMMENDATIONS

The results of this project to date demonstrate the value and effectiveness of our model-based approach to determine regional SSSCs for use in improving seismic event location. Our approach utilizes a fully 3-D velocity model, which we supplement with empirical corrections to take account of all the calibration data that are available for the region. We expect this approach to be more reliable for use in many areas, which are essentially aseismic, and to account for source depth dependence, which is beyond the capabilities of purely statistical approaches for most parts of the world. During the past year the 3-D velocity model, which forms the basis for our SSSC estimates, has been supplemented and revised to include new information from several parts of the Group 1 region as well as tomographic adjustments to some areas based on available calibration data. Calibration data have also been used to test and validate SSSC computational procedures and to demonstrate the effectiveness of the calibration corrections in improving locations and reducing uncertainties. We find that use of P-wave SSSCs derived from our 3-D velocity model for regional travel-time corrections can produce average σ uncertainty levels on the order of 1 second or less, which is better than nominal teleseismic uncertainty. Such corrections produce significant reductions in event location errors.

Over the remaining year of this project, there are a number of tasks that remain to be addressed. In addition to model refinements and supplementation of the database, we will be developing calibration corrections for alternative

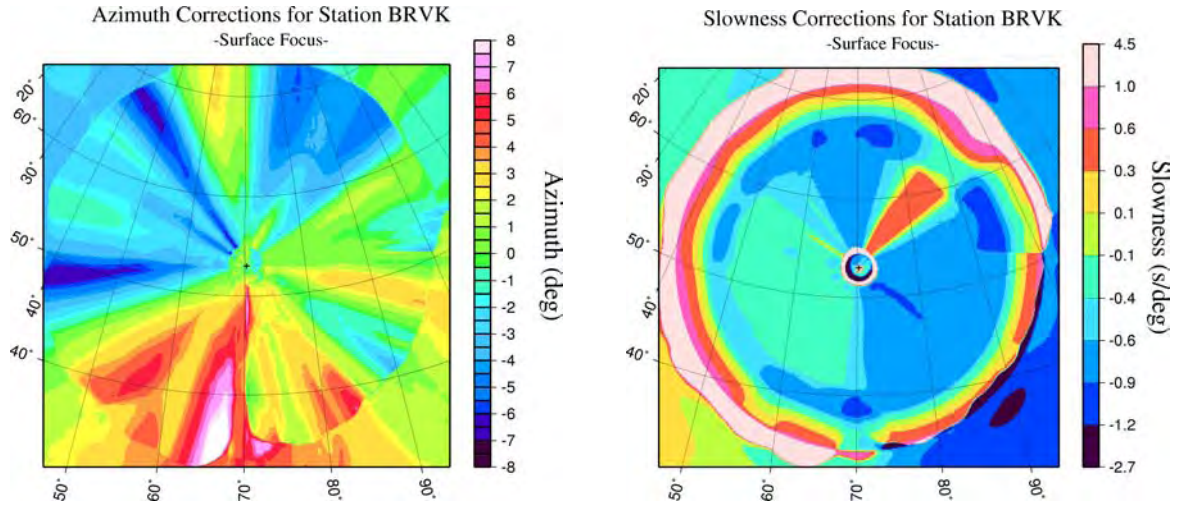

Figure 10. SASC corrections as derived from our 3-D tomographically updated model for station BRVK, relative to IASPEI-91, for a surface-focus source. Azimuth corrections are on the left. Scalar horizontal slowness corrections are in the figure to the right. Note that the color scale for slowness is not regularly spaced in order to better display the range of values.

regional phase types, refining procedures for predicting slowness-azimuth station corrections, and looking more closely at uncertainties and prediction errors. Specific areas of investigation include tomographic refinement and validation testing of China and other submodel areas, augmentation of the travel-time database for calibration events with other regional phases, including Pg, Sn, and Lg arrival times, improved empirical corrections to include improved kriging procedures which satisfy seismic reciprocity constraints, and estimation of prediction errors for the station corrections at the 30 Group 1 IMS station locations.

REFERENCES

Bondar, I., R. G. North, and G. Beall (1999), Teleseismic Slowness-Azimuth Station Corrections for the International Monitoring System Seismic Network, *Bull. Seism. Soc. Am.* **89**, 989-1003.

Chen, P. *et al* (1990-1998), *Annual Bulletin of Chinese Earthquakes* (ABCE), Chinese Seismology Bureau.

Hearn, T. M., and J. F. Ni (2001), Tomography and Location Problems in China Using Regional Travel-Time Data, *Proceedings of the 23rd Seismic Research Review: Worldwide Monitoring of Nuclear Explosions*, 155-160.

Kennett, B. L. N. and E. R. Engdahl (1991), Travel times for global earthquake location and phase identification, *Geophys. J. Int.* **105**, 429-465.

Laske, G., G. Masters, and C. Reif (2001), CRUST 2.0: A New Global Crustal Model at 2x2 Degrees, http://mahi.ucsd.edu/Gabi/rem.html.

Mangino, S., K. Priestley, and J. Ebel (1999), The Receiver Structure Beneath the China Digital Seismograph Network Stations, *Bull. Seism. Soc. Am.* **89**, 1053-1076.

Murphy, J., W. Rodi, M. Johnson, I. Kitov, D. Sultanov, B. Barker, C. Vincent, V. Ovtchinnikov, and Y Shchukin (2001), Seismic Calibration of Group 1 IMS Stations in Eastern Asia for Improved IDC Event Location, *Interim Technical Report* SAIC-01/1021, SAIC, San Diego, CA.

Podvin, P., and I. Lecomte (1991), Finite Difference Computation of Travel Times in Very Contrasted Velocity Models: A Massively Parallel Approach and Its Associated Tools, *Geophys. J. Int.* **105**, 271-284.

Shapiro, N. M., and M. H. Ritzwoller (2001), Monte-Carlo Inversion of Broadband Surface Wave Dispersion for a Global Shear Velocity Model of the Crust and Upper Mantle, *Geophys. J. Int.* **142**.

Stevens, J. L., D. A. Adams, and G. E. Baker (2001), Improved Surface Wave Detection and Measurement Using Phase-Matched Filtering with a Global One-Degree Dispersion Model, *Proceedings of the 23rd Seismic Research Review: Worldwide Monitoring of Nuclear Explosions*, 420-430.

Wu, F. T., A. L. Levshin, and V. M. Kozhevnikov (1997), Rayleigh Wave Group Velocity Tomography of Siberia, China and Vicinity, *Pure Appl. Geophys.* **149**, 447-473.

LOCATION CALIBRATION IN WESTERN EURASIA AND NORTH AFRICA: GROUND TRUTH, IMPROVED EARTH MODELS, BAYESIAN KRIGING, REGIONAL ANALYSIS, LOCATION ALGORITHMS, ARRAY CALIBRATION, AND VALIDATION

Stephen C. Myers, Megan Flanagan, Michael Pasyanos, William Walter, Paul Vincent, and Craig Schultz

Lawrence Livermore National Laboratory

Sponsored by National Nuclear Security Administration
Office of Nonproliferation Research and Engineering
Office of Defense Nuclear Nonproliferation

Contract No. W-7405-ENG-48

ABSTRACT

Improved seismic location is traditionally accomplished by better predicting arrival times for seismic phases. The National Nuclear Security Administration (NNSA) Ground-Based Nuclear-Explosion-Monitoring Research and Engineering (GNEM R&E) calibration effort at Lawrence Livermore National Laboratory (LLNL) begins with an extensive ground truth integration effort. Accurate locations, arrival picks, and waveforms are continuously added to the LLNL database, where they are cross-referenced with existing holdings and characterized for accuracy. The ground truth (GT) database is used to assess travel-time prediction accuracy for both Earth models that are developed here and models brought in through the integration process. When possible, we use data-driven techniques, such as tomography, to improve Earth models, and in aseismic regions, we build models through geophysical analogy. Regardless of the base model, we use empirical corrections (Bayesian Kriging) where GT events are available to ensure the most accurate travel-time prediction. Component validation is used to assess the importance of each calibration activity, and end-to-end validation of seismic event locations allows us to assess overall progress.

New techniques and approaches are aiding the calibration effort. 1) Earthquake location accuracy is improved by combining seismic and InSAR signals. The addition of InSAR data sets may allow us to reduce the uncertainty of uncalibrated global locations from 15 km to 5 km. 2) Region-specific wave field characterization extracts additional information from each seismic trace, bringing more information to bear on location. 3) We are developing new methods to assess travel-time prediction uncertainty from models, particularly in aseismic areas. Using Bayesian methodologies we assess uncertainty using limited ground-truth data sets. 4) Array calibration improves azimuth and slowness prediction and will help to better identify seismic phases and improve sparse-network location. 5) Lastly, in collaborative efforts, we are working to implement multiple-event grid search locations to improve both event precision and uncertainty propagation.

OBJECTIVE

Improvement in seismic location is accomplished by combining model-based and empirical travel-time and azimuth-slowness corrections. Model-based approaches are aimed at improving travel-time prediction at regional distance (between approximately 1.5° and 13°) and at upper-mantle triplication distances (between approximately 13° and 25°). Beyond upper mantle distance (between 25° and 90°) the IASPEI91 global earth model with a static station correction provides excellent travel-time prediction. Therefore, only the highest quality reference events are useful at teleseismic distances. After a calibration model is applied, empirical corrections are calculated using the Modified Bayesian Kriging algorithm (Schultz *et al*., 1998) with travel-time residuals for suitably well located calibration events. Our approach combines the extrapolative advantages of model-based corrections and the interpolative/geostatistical advantages of Kriging to produce hybrid travel-time predictions and uncertainty models. For ease of use, model-based and empirical corrections are combined to produce one travel-time correction and uncertainty model that is applied to the IASPEI91 global earth model. Validation of improvement and proper error characterization are performed at each step of the calibration process. Therefore, the importance of each calibration component is assessed and representative uncertainty estimates are assured. Final calibrations are tested in an end-to-end relocation of test data sets, providing a final validation of uncertainty estimates and improvement in location accuracy.

Overviews of the calibration process we employ can be found in previous Seismic Research Review proceedings. This year we provide more detailed discussion on selected aspects of the calibration process. The topics covered are 1) collection and characterization of calibration events, 2) assessment of model-based uncertainty, and 3) accounting for calibration events with a range in location accuracy.

RESEARCH ACCOMPLISHED

Calibration-Events

The accuracy of earth model and empirical travel-time predictions is limited to the accuracy of calibration events that are used to develop them. Therefore, collection and validation of a geographically distributed set of calibration events is critical to the success of any travel-time calibration effort. The GNEM R&E program integrates calibration events from a diverse set of sources, including dedicated scientific explosions; nuclear explosions; events with InSAR locations; global, regional, and local seismicity catalogs; mine explosions and collapses; and military activity. The database of calibration events includes not only numerous source types but also a range in location accuracy. Although events with perfectly known locations are most preferable, improvement in travel-time prediction is often achieved using calibration events with non-zero location uncertainty. Further, the goal of covering a wide geographic area requires inclusion of events that are not perfectly located.

Categorization of location accuracy is accomplished using the "GTX" system of Bondár (1998), where X is location accuracy. We modify this nomenclature by defining X as the 95% confidence that an epicenter is within X kilometers of the true location.

The vast majority of calibration event locations is determined seismically. For a minority of events, satellite information (photography or InSAR) can add independent constraints on location, and for a select few events (dedicated explosions) the Global Positioning System (GPS) can provide working level GT0. For events that are determined seismically, however, formal error ellipses are not a reliable metric of location accuracy. Analysis of seismic location accuracy is traditionally based on formal uncertainty. Most location algorithms rely on one of two methods to determine uncertainty. The first is based on the F-statistic, where the *a posteriori* residual distribution is mapped to a location confidence ellipsoid (Flinn, 1965). The second is based on the chi-square statistic, where *a priori* uncertainty for phase picking and travel-time prediction are mapped though the location algorithm to produce a coverage ellipsoid (Evernden, 1969). Proper application of either technique requires compliance with basic statistical assumptions. Both methods require Gaussian, zero mean, uncorrelated error processes. A number of studies suggest that these assumptions are violated in most seismic locations. Picking error tends to have "heavy" tails (Buland, 1986) and may be multimodal (Ryall and Schultz, 2002). The mean path-specific, travel-time prediction error is typically not zero, and travel-time prediction errors are typically correlated for similar ray paths (e.g. Myers and Schultz, 2000a).

Because formal error ellipses cannot be used to assess location accuracy, we are forced to use other information to assess location accuracy for potential calibration events.

Network configuration is a good indicator of seismic location accuracy. Events that are located within the footprint of a seismic network tend to be accurately located because sensitivity to travel-time prediction errors are minimized (see Myers and Schultz, 2000a for discussion). It is, therefore, useful to develop metrics for network coverage that are 1) easily derived from seismic catalogs and 2) empirically correlated to location accuracy. In particular, the maximum azimuthal gap (Sweeney, 1998) in station coverage and the secondary gap (maximum gap when any given station is removed from the network) (Bondár *et al*., 2002) are easy to calculate and are found to be indicative of location accuracy. Here we focus on the results of a collaborative effort among LLNL, the Center for Monitoring Research, and the University of Colorado that are reported in Bondár et al. (2002). Local network locations with at least 10 stations within 250 km, an azimuthal gap less than 110° and a secondary azimuthal gap less than 160° and at least one station within 30 km from the epicenter produce GT5 epicenters (Figure 1) are used. Regional networks between 2.5° and 10° with secondary azimuthal gap less than 120° produce GT20 epicenters, but only at the 90% confidence level. Lastly, teleseismic networks with secondary azimuthal gap less than 120° produce GT25, again at the 90% confidence level. These criteria are conservative and may be improved by using enhanced phase identification or simple travel-time corrections; this is the case for Engdahl *et al*. (1998). Myers and Schultz (2000a) find that when these additional measures are taken, teleseismic locations improve to GT15 (Figure 2). We note, however, that subduction zones are not sampled in the GT15 test data set, and locations in these regions are probably not GT15.

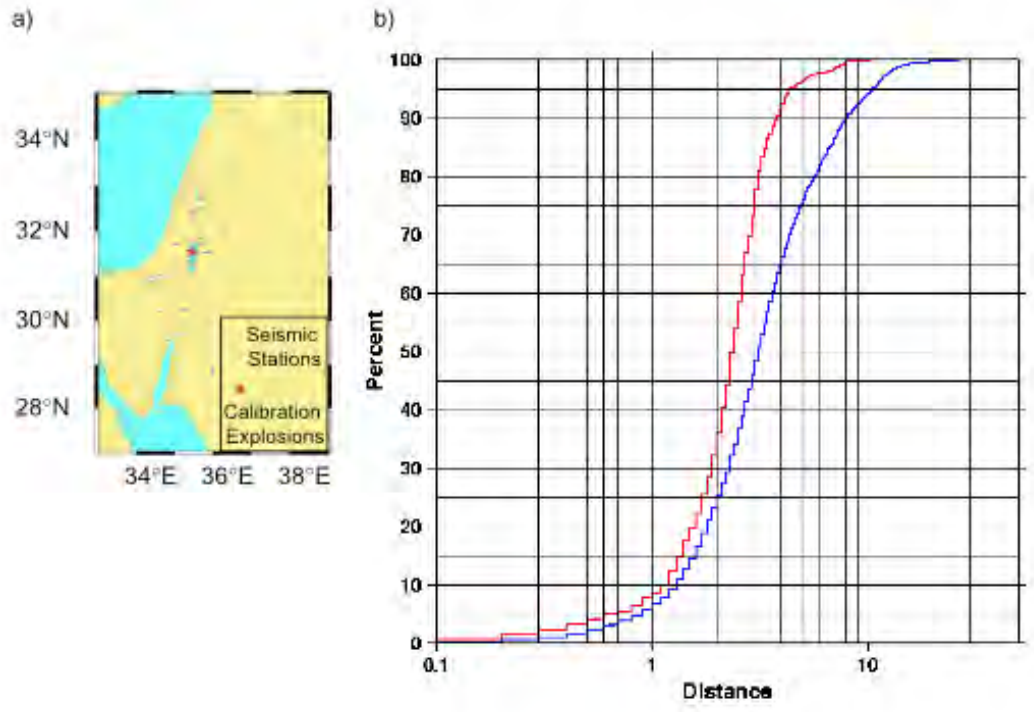

Figure 1. The 1999 Dead Sea calibration explosions and a Swiss munitions explosion are used to validate GT5 network criteria. The explosions are repeatedly located using 10 randomly selected stations from the dense local network. A) Dead Sea network configuration. B) Cumulative distribution of event mislocations: red is the curve for networks meeting the GT5 criteria, and blue is the curve for all network configurations (From of Bondar *et al*., 2002).

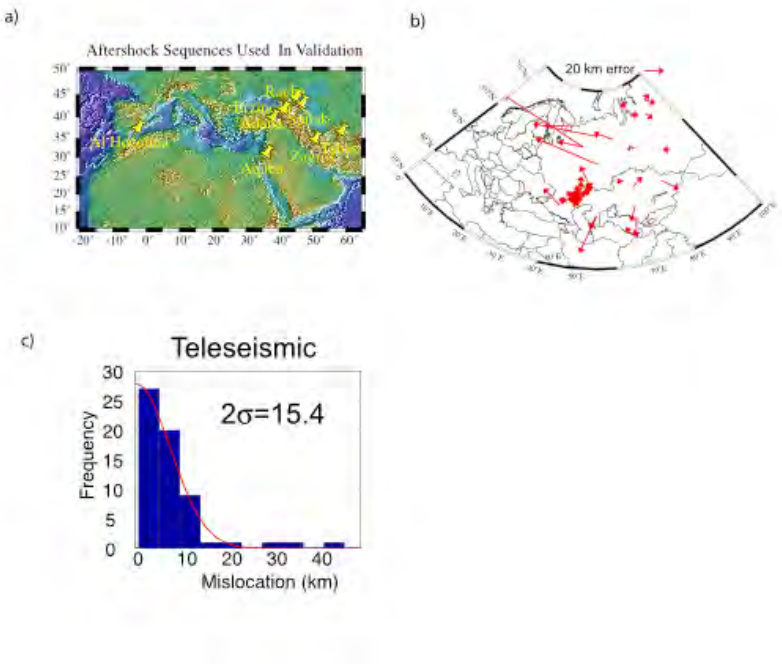

Figure 2. Validation GT15 for teleseismic locations of Engdahl *et al*. (1998) using local-network locations and peaceful nuclear explosions (PNEs). These locations are improved over routine global network locations by reassociating phases and use of regional travel-time corrections. A) Aftershock sequence locations used to validate teleseismic GT15. B) GT1 locations of Sultanov *et al*. (1999) with mislocation vectors of teleseismic locations. C) Distribution of teleseismic mislocation confirms that 95% of teleseismic locations are within 15 km of local-network or GT1 locations.

Location accuracy can be improved by using data complementary to seismic observations. InSAR data are particularly useful for constraining earthquake and mine activity that results in static surface deformation of more then a few centimeters. We have a cross-disciplinary effort to use InSAR for seismic calibration purposes. This effort includes expertise in processing interferometric data, allowing us the flexibility to combine satellite and seismic data into a joint location estimate. Figure 3 shows seismic and InSAR locations for the mb=5.3, April 10, 1998, earthquake in eastern Iran. In this example seismic locations are systematically offset to the north by approximately 20 km, compared to the InSAR location. Each of the seismic locations relies heavily on stations at teleseismic distance and, in this case, the locations meet the GT25 criteria outlined above (locations do not include additional processing). Based on modeling of the InSAR-constrained static displacement field, the source dimension of this earthquake is probably on the order of 5 km. Because we do not have sufficient resolution to attribute teleseismic first arrivals to moment release on a sub-portion of the fault, the InSAR epicenter is estimated to be GT5.

Cross-referencing all sources of calibration-event information is an important check on our database. In many instances several location estimates may be available for a single event. These sources of information may or may not make use of similar data sets, so estimated GT level for each catalog/study may be different. As part of the validation process, we cross-reference epicenters for each event to test the consistency predicted by the assigned GT level. This procedure is used not only to validate the GT level of events, but we have frequently found outlier data that may otherwise go unnoticed (Figure 4). In this example, satellite locations of Novaya Zemlya nuclear explosions (Skorve and Skogan, 1992) are compared to seismic locations determined relative to one satellite location (Marshall, 1994). Location differences for all but two of the events are consistent with GT1 for satellite locations and GT5 for teleseismic relative locations. We find, however, two events with anomalously large location differences. Although we are not completely certain about the origin of the differences, we note that subtraction of one integer degree from the satellite locations makes the location differences comparable to location differences for other events. It is important to note that the purpose of cross-referencing is not to identify preferred calibration-

event contributors, because each source of calibration information may have some outliers. The purpose is to check our GT assignments and flag suspect locations.

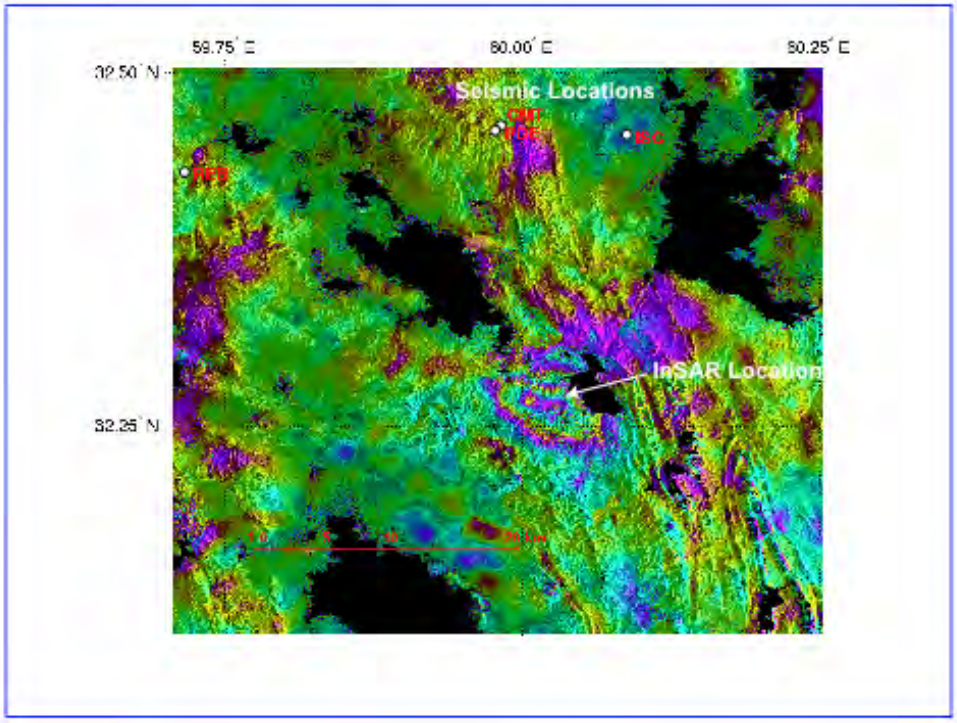

Figure 3. InSAR location of the mb=5.3, April 10, 1998, earthquake in eastern Iran. Global seismic estimates (red text) are biased by approximately 20 km to the north. (InSAR processing by Vincent, 2002)

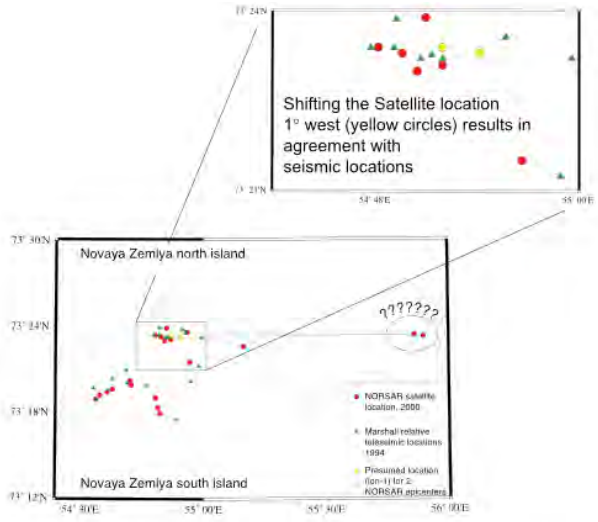

Figure 4. Cross-referencing can flag outlier data that may otherwise be used in calibration. In this example satellite locations of Skorve and Skogan (1992) are generally in good agreement with relative seismic location of Marshal, 1994. However, two satellite locations are outliers. Subtracting one integer degree of longitude brings the locations into agreement. These events are discarded in our calibration procedure.

Model Uncertainty Estimation

Geophysical models improve location performance in areas of limited empirical calibration. Similar to calibration-event collection, efforts begin with a survey of existing models. Each model is evaluated first and foremost using a travel-time prediction metric, which is more directly related to location improvement than metrics involving model velocities or discontinuities. Travel-time prediction accuracy is assessed in a non-stationary framework. Figure 5 shows an example of stationary and non-stationary uncertainty models. Although stationary (scalar) uncertainty is most desirable, we find that uncertainty for most models is dependent on event-station distance. For simple models, even distance-dependant uncertainty models do not capture the complexity of travel-time uncertainty. In these cases uncertainty must be assessed by geographic region, as show in Figure 5c.

Travel-time prediction uncertainty is most directly assessed by comparing model predictions with observations from calibration events. However, proper application of empirically determined error distributions requires representative geographic sampling. In areas with sparse data coverage, especially when non-stationary status requires higher-dimensional error models, representative data sampling is not achieved. In these cases we use a Bayesian approach that takes advantage of prior travel-time distribution information. With the Bayesian approach, we begin with a conservative, global estimate of travel-time uncertainty and reduce the distribution as data coverage improves.

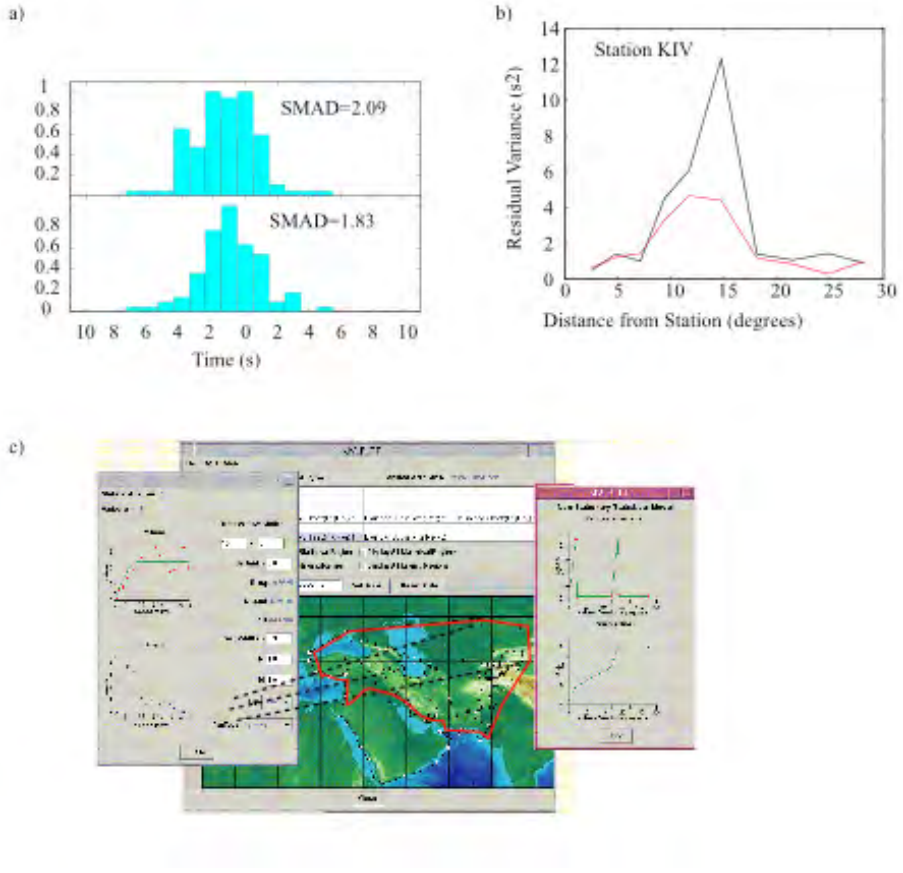

Figure 5. Example of a stationary and non-stationary travel-time residual characterization. a) All travel-time residuals are used to build one distribution. Improved prediction is suggested in the lower panel. b) Distance-dependent analysis shows that, in this instance, the improvement in prediction comes from events between about 7° and 18°. c) For simple models uncertainty must be assessed in distinct geographic regions. Simple distance dependence is not sufficient.

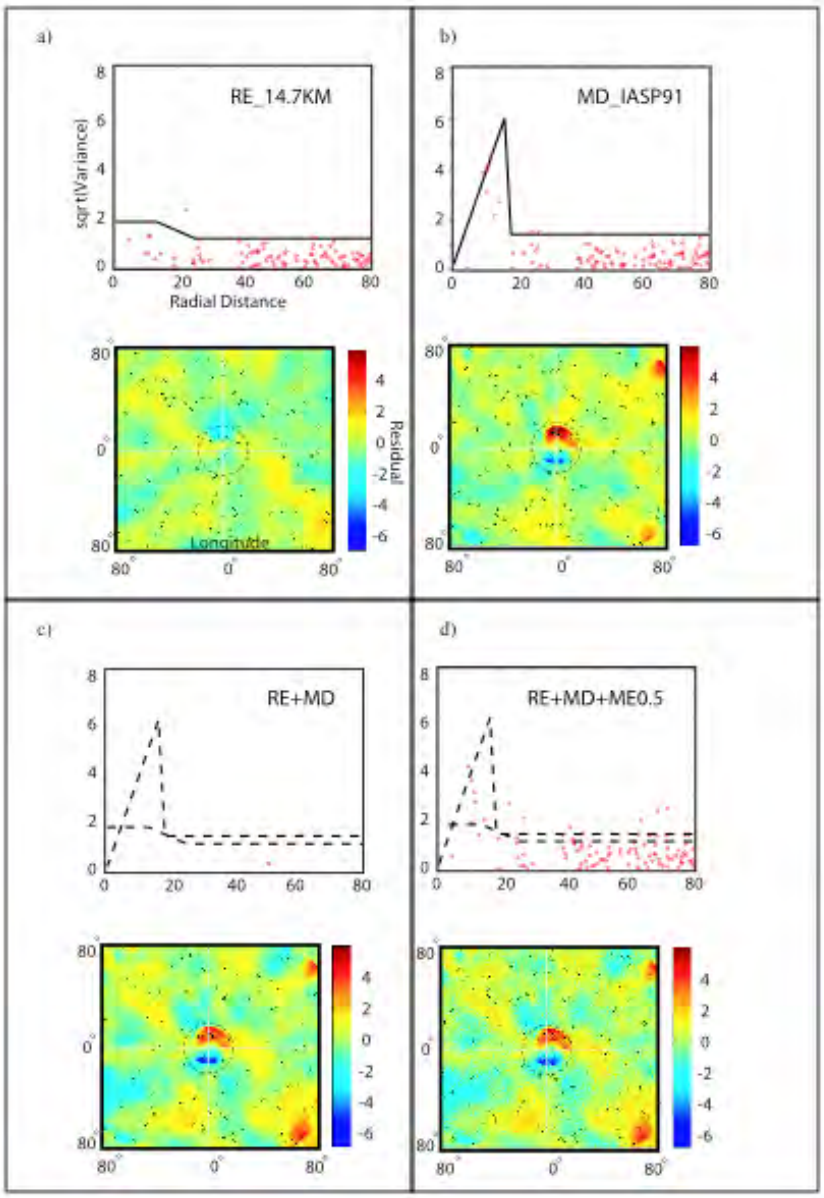

Figure 6. Synthetic generation of non-stationary travel-time residuals are used to test new techniques for assessing model uncertainty. a) Non-stationary travel-time residuals caused by calibration-event error. b) Non-stationary travel-time residuals caused by model error. c) Stationary residuals cause by picking error. d) The result of adding error process from a) b) and c).

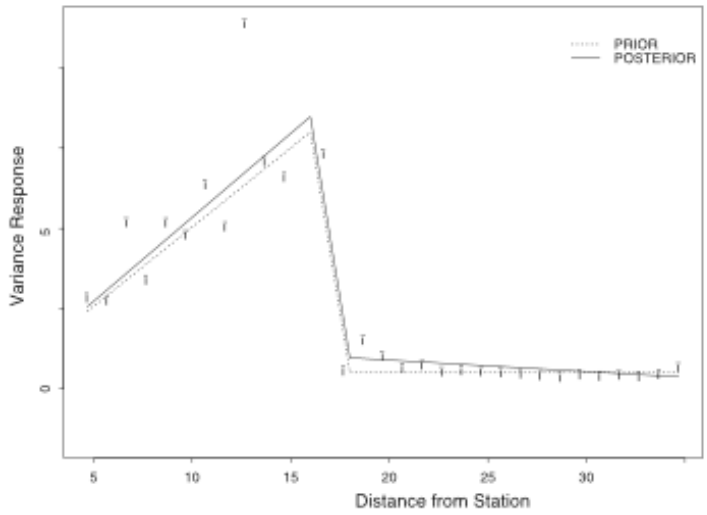

Figure 7. Example of Bayesian regression to determine model error. The *a priori* uncertainty (dotted line) is modified by observations to produce *a posteriori* estimate of uncertainty (solid line).

The Bayesian model estimator is currently tested using synthetic data sets. The synthetic data sets include additional error processes that complicate estimation of the desired model error. Inclusion of additional error processes make the synthetic tests as realistic as possible. Figure 6 is an example of a synthetic travel-time residual surface constructed using model, calibration event, and picking error. Panel a) shows non-stationary travel-time errors attributed to calibration-event location error (discussed below). Panel b) is the non-stationary model error, which is the error process we hope to extract from the data, and c) shows a stationary measurement error. All three of these error processes are combined to produce a synthetic error distribution from which example instances are constructed. An example of the Bayesian regression is shown in Figure 7. The prior estimate is the dotted line and the posterior estimate is the solid line. Although one outlier at a distance of approximately 13° suggests substantially increased uncertainty, the Bayesian prior tempers the posterior estimate.

Calibration-Event Error Propagation

Combining events with variable location accuracy is accomplished in a rigorous statistical framework. Travel-time measurement derived from more accurately located events should receive more weight than corrections from events with poorer location accuracy. Likewise, the uncertainty of travel-time corrections derived from more accurately located events should be reduced. Mapping location uncertainty to travel-time uncertainty is the first step in assessing the appropriate weights. This relationship is established by Myers (2001).

$$\sigma_{tt}^2 = \left(\frac{\partial t}{\partial \Delta} \sigma_{dist} \right)^2 \qquad [1]$$

where σ^2_{tt} is travel-time variance, $dt/d\Delta$ is the derivative of the travel-time curve, and σ^-_{dist} is the variance of the epicenter accuracy. Figure 8 shows the mapping of several GT levels into travel-time error as a function of distance. Therefore, the stationary calibration-event uncertainty maps to a non-stationary travel-time uncertainty, and proper propagation of errors requires application of Equation [1].

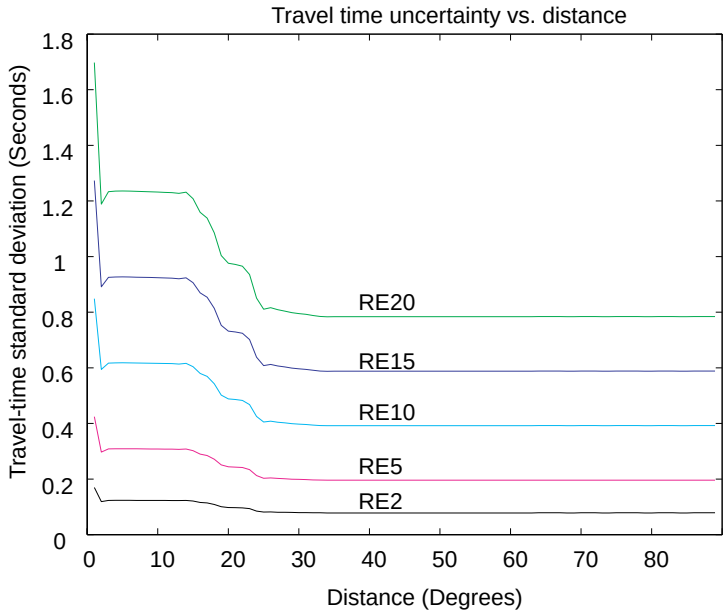

Figure 8. Travel-time uncertainty resulting from epicenter uncertainty as a function of distance for IASPEI91 P-waves is shown. The epicenter uncertainty is a worst-case scenario, where the error occurs along the great-circle path. Each curve is labeled by reference event (RE) level, where the number is the 95% confidence in the location accuracy (km). Note that overshoot at changes in gradient of the curves is the result of errant spline interpolation and should be ignored (From Myers, 2001)

Accounting for calibration-event bias

In some instances reference-event error contains a biased component. The GNEM R&E processing accounts for this through a declustering algorithm (Myers, 2001). Declustering combines events that are close to one another – events that may have similar vector mislocation – into one observation. Within each decluster bin, locations derived from the same source (e.g. teleseismic or local-network locations) are grouped and averaged separately. Then each of the groups are combined using a weighted average. Uncertainty for the group average is given by:

$$\tau_{re_i}^2 = \frac{1}{N^2} \sum_{j=1}^{N} \sum_{k=1}^{N} C_{jk} \qquad [2]$$

where τ^2 is the variance of the mean, N is the number of events, C_{jk} is the covariance, j and k count the events in the group.

After averaging the events belonging to individual groups, we combine the groups into a single decluster value via a weighted sum.

$$t_{decluster} = \sum_{i=1}^{M} w_i \bar{t}_{res_i} \qquad [3]$$

where $t_{decluster}$ is the declustered value, w_i is the weight of the i_{th} group, and t_{res} is the group average. The weights are a normalized inverse of the decluster uncertainty.

$$w_i = \frac{N_o}{\tau_i} \qquad [4]$$

where N_o is a normalizing factor.

The variance of the declustered point is then:

$$\tau_{decluster}^2 = \sum_{i=1}^{M} (w_i \tau_i)^2 \qquad [5]$$

CONCLUSIONS AND RECOMMENDATIONS

The LLNL location program encompasses each aspect of seismic calibration. Only a few of the components are highlighted here. In this paper we focus on collection, database building, validation, and cross-referencing of calibration events, as well as model error assessment and rigorous propagation calibration event location uncertainty to travel-time uncertainty.

In summary:
Collection of a diverse set of calibration events is critical to broad area calibration. LLNL combines seismic and satellite methods to obtain the most accurate source locations for calibration events. Cross-referencing calibration-event locations validates GT assignments and flags outliers. Models are judged on travel-time prediction. Assessment of model error using empirical observations is complicated by calibration-event and phase picking uncertainty. The LLNL Bayesian regression tool addresses GT and picking uncertainties and provides a quantitative means to account for data coverage during model uncertainty estimation. Stationary calibration event epicenter errors map to non-stationary travel-time uncertainties. Differing levels of GT are combined through a weighting system that is related to epicenter accuracy.

ACKNOWLEDGEMENTS

We thank Dave Harris, Bill Rodi, Istvan Bondar, Bob Engdahl, Eric Bergman, and Keith Koper for discussions and collaborations.

REFERENCES

Bondár, I., S.C. Myers, E.R. Engdahl, and E.A. Bergman (2002), Epicenter accuracy based on seismic network criteria, in preparation.

Buland, R. (1986), Uniform reduction error analysis, *Bull. Seismol. Soc. Am.*, **76**, 217-230.

Engdahl, E.R., R. van der Hilst and R. Buland (1998), Global Teleseismic Earthquake Relocation with improved Travel Times and Procedures for Depth Determination, *Bull. Seism. Soc. Am.*, **88**, 722-743.

Evernden, J. (1969), Precision of epicenters obtained by small numbers of world-wide stations, *Bull. Seism. Soc. Am.*, **59**, 1365-1398.

Flinn, E. (1965), Confidence regions and error determinations for seismic event location, *Rev. Geophys.*, **3**, 157-185.

Myers, S.C. and C.A. Schultz (2000a), Calibration of seismic travel time using events with seismically determined locations and origin times, *EOS Trans. AGU*, **81**, F845.

Myers, S. and C. Schultz (2000), Improving Sparse-Network Seismic Location with Bayesian Kriging and Teleseismically Constrained Calibration Events, *Bull. Seism. Soc. Am.*, **90**, 199-211.

Myers, S.C., Methods of travel-time residual declustering for the Knowledge Base Calibration and Integration Tool (KBCIT), UCRL-ID-142521, 2001.

Ryall, F. and C.A. Schultz (2001), Seismic waveform characterization at LLNL: analyst procedures and issues, Lawrence Livermore National Laboratory, UCRL-ID-146229.

Schultz, C., S. Myers, J. Hipp, and C. Young (1998), Nonstationary Bayesian Kriging: Application of Spatial Corrections to Improve Seismic Detection, Location and Identification, *Bull. Seism. Soc. Am.*, 1275-1288.

Skorve, J. and J. Skogan, The NUPI satellite study of the northern underground nuclear test area on Novaya Zemlya, NUPI Report No. 164, Oslo, Norway, 1992.

Sultanov, D.D., J.R. Murphy and Kh. D. Rubinstein, A seismic source summary for Soviet peaceful nuclear explosions, *Bull. Seism. Soc. Am.*, **89**, 640-647, 1999.

Sweeney, J. (1998), Criteria for Selecting Accurate Event Locations from NEIC and ISC Bulletins, Lawrence Livermore National Laboratory report UCRL-JC-130655.

GROUND TRUTH EVENTS FROM REGIONAL SEISMIC NETWORKS IN NORTHEASTERN AFRICA

Andrew A. Nyblade,[1] Richard A. Brazier,[1] Craig Schultz,[2] and Michael Pasyanos[2]

Penn State University,[1] Lawrence Livermore National Laboratory[2]

Sponsored by National Nuclear Security Administration
Office of Nonproliferation Research and Engineering
Office of Defense Nuclear Nonproliferation

Contract No. DE-FC03-02SF22500[1] and W-7405-ENG-48[2]

ABSTRACT

Determining accurate seismic locations with representative uncertainty estimates is of fundamental importance to ground-based nuclear explosion monitoring. In this project, we are developing a catalog of reference events (ground truth) in the northeast African area of interest where reference event coverage is exceptionally poor due to the limited station coverage by historic networks. We will provide accurately defined hypocenters within a range of ground truth (GT) levels (i.e., GT2, GT5, GT10), origin times, and focal mechanisms for several tens of earthquakes with magnitudes > 3 in northeastern Africa. The catalog will enable the seismic monitoring community to enhance their operational capability to monitor for nuclear tests in North Africa and the Middle East by increasing their ability to accurately locate and identify seismic events in these regions.

The ground truth events for northeastern Africa are being collected using state-of-the-art event location methods applied to broadband seismic data from regional networks in Ethiopia, Kenya, and Tanzania, as well as to broadband data from primary and auxiliary International Monitoring System (IMS) stations in the region. The ground truth catalog is being assembled by (1) determining origin time, focal mechanism and hypocenters with accuracies of 10 km or better (GT 10) for many events that lie within close proximity of recording stations or else are well recorded teleseismically; (2) using these events to construct regional travel-time correction surfaces using a Bayesian kriging technique, and (3) using the travel-time correction surfaces to obtain origin times and epicenters for numerous other events. Robust estimates of the uncertainties in the locations and origin times will also be determined.

Preliminary event locations for many M>4 events in East Africa have been obtained using P and S arrival times recorded by the Tanzania Broadband Seismic Experiment. This experiment consisted of 20 broadband seismic stations deployed across Tanzania in 1994 and 1995. From P and S arrival times, epicentral locations can be constrained to within 2-3 km and focal depths to within 5 km at the 1-sigma error level. Focal mechanisms for these events will be obtained using regional and teleseismic data from permanent stations, and the hypocentral locations will be refined by modeling local/regional waveforms from the Tanzania Broadband Seismic Experiment.

OBJECTIVE

In this project, our purpose is to develop a catalog of reference events (ground truth) in the northeast African area of interest where reference event coverage is exceptionally poor due to the limited station coverage in the past.

Introduction

Earthquakes in northeastern Africa provide a principal source of ground truth for North Africa and the Middle East. The earthquakes of interest are associated with the northern and central portions of the East African Rift System (Figure 1). Since there are very few earthquakes within North Africa proper or within large parts of the Middle East that can be used to develop a set of ground truth, naturally occurring events in northeastern Africa take on an added importance for improving nuclear explosion monitoring capabilities in the region.

The development of ground truth for North Africa and the Middle East has in the past been limited not only by the lack of appreciable seismicity within North Africa and parts of the Middle East but also by a dearth of seismic stations throughout most of Africa. This situation is now changing. We operated regional seismic networks in Ethiopia and Kenya comprised of 27 and 11 broadband stations, respectively, between 2000 and 2002, and several years ago (1994-1995) we operated a similar network of 20 broadband seismic stations in Tanzania. The broadband waveforms recorded by these networks, together with waveforms from primary and auxiliary IMS stations in the region, provide a rich data set that can be used to accurately locate earthquakes and determine their origin times and source mechanisms.

The ground truth catalog is being assembled by (1) determining origin time, focal mechanism and hypocenters with accuracies of 10 km or better (GT 10) for many events that lie within close proximity of recording stations or else are well recorded teleseismically; (2) using these events to construct regional travel-time correction surfaces using a Bayesian kriging technique, and (3) using the travel-time correction surfaces to obtain origin times and epicenters for numerous other events. Robust estimates of the uncertainties in the locations and origin times will also be determined.

Here we present preliminary locations for several events with M>4 in East Africa constrained by P and S arrival times recorded by the regional broadband network in Tanzania. We begin by providing background information about the geology of the region and on the broadband seismic experiments. This is followed by a discussion of our event locations and uncertainties, and we conclude with a brief description of future work.

RESEARCH ACCOMPLISHED

Background Information

The locations of the broadband seismic experiments, together with the geology and topography of East Africa, are shown in Figure 1. The geology of the region comprises an Archean craton (the Tanzania Craton, Figure 1) surrounded by Proterozoic mobile belts. The rift faults of the Cenozoic East African rift system have developed mainly within the Proterozoic mobile belts, forming a rift system with two branches (Western rift and Eastern rift).

The broadband seismic experiment in Tanzania was conducted in 1994 and 1995 and consisted of 20 seismic stations deployed for a year in two skewed arrays, one oriented more or less east-west, and the other northeast-southwest. The experiment was designed so that structure beneath the Archean Tanzania Craton and the terminus of the Eastern Rift in northern Tanzania could be imaged with seismic data from local, regional and teleseismic earthquakes. Information about the station configuration, recording parameters and other details of the field deployment have been reported by Nyblade *et al*. (1996).

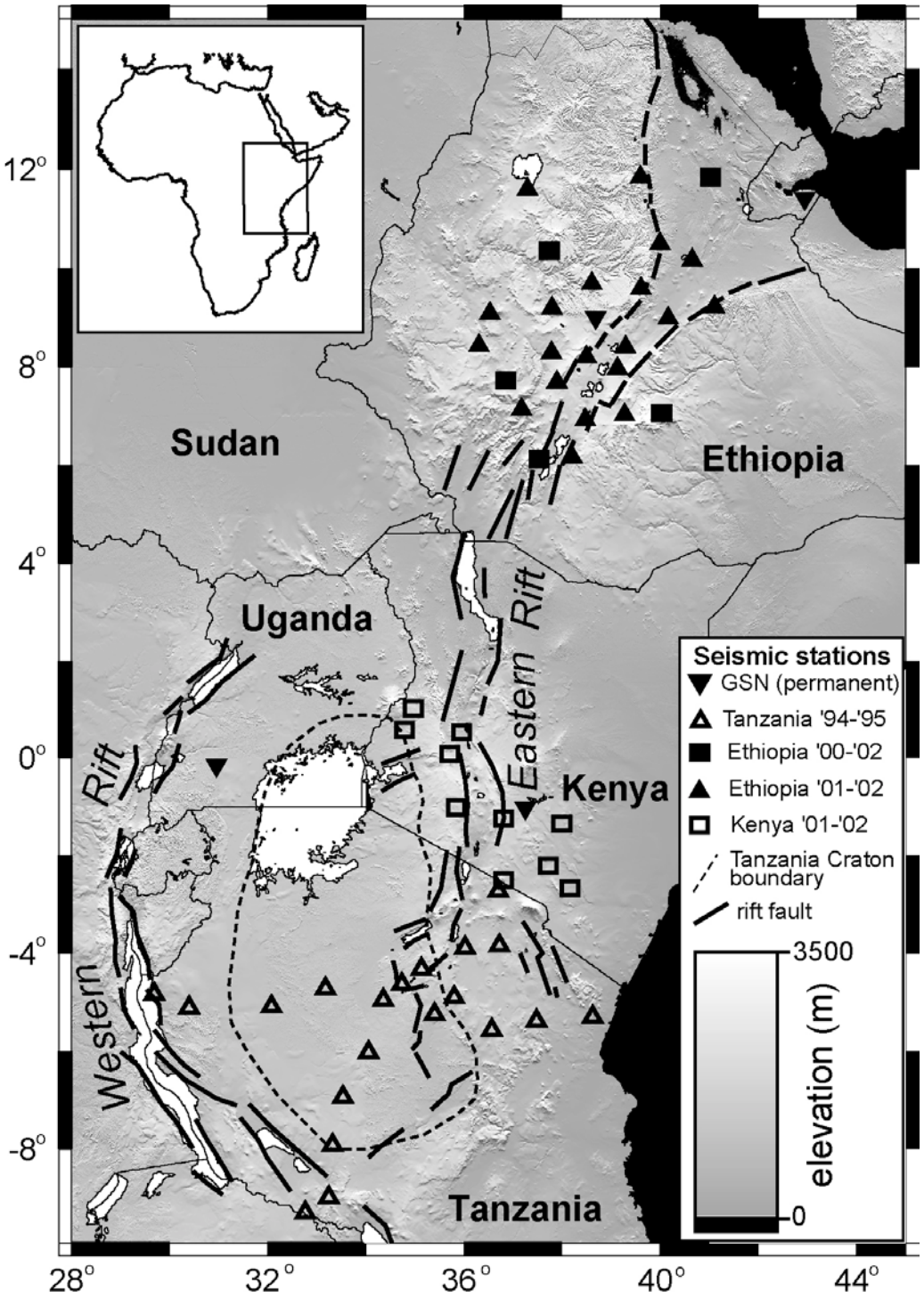

Figure 1. Topographic map of East Africa showing the Ethiopian and East African plateaus (regions with > 1000 m elevation), the outline of the Archean Tanzania craton, the major rift faults of the East African rift system, and the location of broadband seismic stations.

In the other broadband seismic experiments, seismic stations consisting of broadband sensors, 24-bit data loggers, 4-Gbyte hard disks, and Global Positioning System (GPS) clocks were deployed in regions of Ethiopia and Kenya safe for traveling (Figure 1). The stations were spaced 50 to 200 km apart and were located to optimize the recording of teleseismic body and surface waves that sample upper mantle structure beneath the Eastern Rift. For East Africa, the major source regions for teleseismic earthquakes are the Hindu Kush/Pamir region to the northeast and the Fiji/Tonga subduction zones to the east. Additional criteria used for site selection included access to bedrock, security, and year-round road conditions.

Installation of the Ethiopian stations was completed in two phases. During March 2000, five stations were installed around the periphery of the network, and then one year later (March 2001), an additional 20 stations were installed to make the network denser (Figure 1). All 25 stations were removed from the field in March 2002. Installation of the Kenyan stations took place during July and August 2001, and all 10 of the stations were removed in July 2002. Two data streams were recorded, a one sample/sec continuous stream and a twenty sample/sec continuous stream, yielding a data volume of 21 Mbytes per station per day. Data recovery for the Ethiopian stations was nearly 90%, and it was about 70% for the Kenyan stations.

Preliminary Event Locations

Preliminary event locations have been obtained for several events in East Africa with magnitudes $\geq$ 4 that were well recorded by the Tanzania Broadband Seismic Experiment. The preliminary locations were obtained using P and S arrival times, a regional velocity model for the crust and upper mantle constrained by a number of previous studies, and the event location code HYPOELLIPSE (Lahr, 1993). The P and S onset times were individually hand picked to within 0.1 seconds. A single velocity model representative of the entire area within the seismic network was used in the event location code and is shown in Table 1. Crust and uppermost mantle in East Africa has been studied in detail by many authors using refraction surveys, receiver functions, surface waves, regional waveforms and Pn tomography. From these studies, it is clear that crustal and uppermost mantle structure is fairly uniform in the Precambrian terrains away from the rift valleys proper (Last *et al*., 1997; Brazier *et al*., 2000; Nyblade, 2002; Langston *et al*., 2002; Fuchs *et al.* 1997 and references therein). Only minor differences in crustal thickness (2-5 km), mean crustal velocity (0.1-0.2 km/s), and uppermost mantle P velocities (0.1 – 0.2 km/s) are found between the various stations of the Tanzania network, and these differences introduce very small uncertainties in the event locations.

Table 1. Crust and uppermost mantle seismic structure for East Africa.

V1 (km/s)	V2 (km/s)	Poisson's Ratio	Moho Depth (km)	Mean crustal Vp (km/s)	Pn (km/s)
5.84	7.09	0.25	38	6.5	8.3

V1= uppermost crustal velocity; V2=lowermost crustal velocity

Table 2 summarizes the preliminary event origin times and locations, and the uncertainties associated with the locations. All of the events are well recorded on at least 11 stations over an azimuthal range of 130 or more degrees. A number of the events are within a few tens of kilometers of a station and none are more than a few hundred kilometers from a station. The magnitude estimates for these events come from using the maximum P wave amplitude within the first 5 seconds and the local magnitude scale for East Africa determined by Langston *et al*. (1998). Standard statistical measures at the 68% confidence interval in the error ellipse indicate that the hypocenters appear to be constrained to within a few kilometers. However, a detailed study of several of these events using regional waveform modeling (Langston *et al*., 2002) indicates that while the P and S arrival times do a fairly good job at constraining epicentral location, they do not provide tight constraints on source depth. Source depth for the events studied by Langston *et al*. (2002) are shown in Table 2. The source depth obtained from the P and S arrival times for these events differed from the source depths in Table 2 by 10 or more km.

For comparison, we also show in Table 2 the locations and origin times for several of the events taken from the International Seismic Centre (ISC) catalog. The comparison shows discrepancies in origin times of several seconds in most cases, and differences in event location of many tens of kilometers for some events. In addition, no catalog listings were found for two of the events.

CONCLUSIONS AND RECOMMENDATIONS

Future work will focus on obtaining accurate hypocenters for the regionally recorded events in Table 2 and many other events recorded on the Ethiopia and Kenya stations using a combination of proven modeling techniques. To improve upon the preliminary locations obtained from P and S arrival times, data from the closest stations will be used to determine incidence angles and ray parameters. By comparing them to theoretical values, source depth, epicentral distance, and back azimuth will be constrained. To refine the source depth estimate, depth phases recorded on nearby stations will be modeled assuming point dislocation sources. With source depths tightly constrained, the P and S arrival times can then be used to relocate epicenters. Finally, focal mechanisms will be determined using polarities and amplitudes of local and regional P and S phases in a grid-search technique, and the focal mechanisms will then be used with a wave number integration algorithm to compute full synthetic seismograms for several stations as a final check on the accuracy of the hypocenters.

In all of these steps it is crucial to have good velocity models for the crust and upper mantle. We will use analyses of receiver functions, surface waves and seismic refraction profiles to provide independent estimates of crustal and mantle velocities. In addition, we will make surface wave dispersion measurements of data from the three regional networks in the area. We will measure both Love and Rayleigh surface wave group velocities using a multiple narrow-band filter technique. Combined with thousands of other measurement made in the broader regional area (Pasyanos *et al*., 2001), we will conduct a high-resolution group velocity tomography of northeastern Africa. Using near-regional data will enable us to make more accurate short-period (5-15 seconds) measurements, which will allow us to constrain velocities in the uppermost crust. We will use the surface wave work, along with receiver functions and other data, to improve the velocity model of the crust and upper mantle, which will in turn improve the event locations.

To expand the catalog of events in northeastern Africa meeting the GT 10 specifications, we will take the events located using the approach described above and use them as calibration events to construct travel-time correction surfaces using the kriging method of Schultz *et al*., (1998, 1999) and Myers and Schultz (2000). The travel-time correction surfaces will then be used together with local and regional P arrivals to determine epicenters and origin times for numerous other events in the Ethiopia, Kenya and Tanzania data sets. Based on the expected proximity of many of these events to recording stations, we anticipate that there will be several tens of events whose epicenters will be determined to within 10 km.

The travel-time correction surfaces will be constructed following the approach outlined by Myers and Schultz (2000). For the regional networks, we will calculate travel-time residuals for the calibration events relative to a regional velocity model. The travel-time residuals will be assigned to the respective calibration epicenter, forming a set of spatially varying travel-time correction points. This set of points will then be declustered to reduce the dimensions of the observations, and this refined set of calibration points will be used with Bayesian kriging to form continuous travel-time surfaces that will provide source-specific corrections for each station in the regional networks. In locating epicenters, a standard location algorithm will be used with the kriging corrections applied. A conservative uncertainty estimate for the kriging correction will be used to characterize the travel-time-predication error, according to the procedure followed by Myers and Schultz (2000). This conservative estimate will be developed using rigorous statistical modeling with available seismic data. Cross-validations will be provided to ensure that the estimates are accurate. In general, these statistics will be used as input to generate chi-squared for robustly determining the final reference event error ellipses.

Table 2. Preliminary locations for earthquakes in East Africa with M > 4 from July 1994 – June 1995 recorded by the Tanzania Broadband Seismic Experiment.

Event: source	Yr:mo:day:hr:min:sec	Lat.	Lon.	D	M	N	Gap	RMS	Smaj	Az	Smin	Sez
1:This paper	94:07:20:11:32:04.30	-4.080	35.440	42	4.5	19	141	0.44	0.25	-106	0.45	1.7
1:ISC	94:07:20:11:31:58.49	-4.171	35.185	0	3.8			1.26	10.4	90	6.6	
2: This paper	94:08:18:00:45:48.80	-7.440	31.770	25*	5.9	17	167	1.77	0.35	-34	0.48	2*
2: ISC	94:08:18:00:45:52.70	-7.650	31.830	25	5.9			0.69	2.20	90	2.20	
3: This paper	94:09:05:04:08:56.04	-7.508	31.700	?	4.1	15	174	0.43	0.41	-59	0.70	?
3: ISC	94:09:05:04:08:50.41	-7.738	30.882	4	4.6			1.38	10.9	90	6.3	
4: This paper	94:09:30:01:36:53.14	-5.920	29.890	26	4.5	16	229	1.13	0.55	-40	1.18	1.4
4: ISC	94:09:30:01:36:47.62	-8.426	37.261	0	4.4			1.78	15.6	90	8.6	
5: This paper	94:11:12:12:18:00.00	-6.950	29.920	30*	5.3	16	221	0.55	0.42	-24	0.89	2*
5: ISC	94:11:12:12:18:01.33	-6.777	29.821	22	4.6			1.05	6.3	90	4.5	
6: This paper	94:11:12:20:16:59.37	-6.617	30.016	?	4.7	17	223	0.88	0.45	-33	0.96	?
6: ISC	94:11:12:20:16:49.66	-6.834	29.946	0	4.6			1.15	8.4	90	5.5	
7: This paper	94:11:16:01:08:11.20	-9.070	33.330	8*	4.5	17	193	0.80	0.48	-129	0.66	2*
7: ISC	94:11:16:01:08:09.07	-9.179	33.273	10	5.0			1.64	7.8	90	6.8	
8: This paper	94:11:27:04:20:51.65	-3.568	35.827	30	4.0	15	213	0.51	0.36	-93	0.95	0.7
8: ISC	94:11:27:04:20:44.27	-3.954	35.722	10	4.0			0.12	22.4	90	10.1	
9: This paper	94:12:25:04:25:27.44	-5.113	29.752	21	4.2	11	301	0.59	0.81	19	6.42	1.9
9: ISC	No listing											
10: This paper	95:01:29:00:23:35.02	-5.419	35.909	13	4.1	11	128	0.37	0.34	-107	0.51	1.0
10: ISC	No listing											

D = depth in km. * = depth was determined from regional depth phases (Langston *et al*., 2002). Otherwise depths were determined from only P and S arrival times.

M = magnitude. Magnitudes in this study are based on the ML scale from Langston *et al*. (1998). ISC magnitudes are a mixture of different types.

N = number of stations used in the event location.

Gap = azimuth range in stations.

RMS = Rms error in arrival times.

Smaj, Smin, Sez, Az = dimensions (in km) and orientation of the error ellipse. For this study, the numbers in the table are for a 68% confidence level. * on Sez numbers indicates that the depth uncertainty was obtained from modeling regional depth phases (Langston et al., 2002).

REFERENCES

Brazier, R., A.A. Nyblade, C. A. Langston, and T.J. Owens (2000), Pn velocities beneath the Tanzania Craton and adjacent rifted mobile belts, East Africa, *Geophys. Res. Lett.*, **27**, 2365-2368.

Fuchs, K., B. Altherr, B. Muller, and C. Prodehl (1997), Structure and dynamic processes in the lithosphere of the Afro-Arabian rift system: *Tectonophysics*, **278**, 1-352.

Lahr, J.C. (1993), Hypoellipse, a computer program for determining local earthquake hypocentral parameters, magnitude and first motion pattern, U.S. Geological Survey Open File Report 89-116.

Langston, C.A., R. Brazier, A.A. Nyblade and T. J. Owens (1998), Local magnitude scale and seismicity rate for Tanzania, East Africa, *Bull. Seis. Soc. Am.*, **88**, 712-721.

Langston, C.A., A.A. Nyblade, and T.J. Owens (2002), Regional wave propagation in Tanzania, East Africa, *J. Geophys. Res.*, **107**, 10.1029.

Last, R., A.A. Nyblade, C.A. Langston, and T.J. Owens (1997), Crustal structure of the East African plateau from receiver functions and Rayleigh wave phase velocities, *J. Geophys. Res., 102,* 24469-24483.

Myers, S., and C. Schultz (2000), Improving sparse network seismic location with Bayesian kriging and teleseismically constrained calibration events, *Bull. Seis. Soc. Am.*, **90**, 199-211.

Nyblade, A.A., C. Birt, C. A. Langston, T.J. Owens, and R. J. Last (1996), Seismic experiment reveals rifting of craton in Tanzania, *Eos Trans. AGU, 77*, 517-521.

Nyblade, A.A. (2002), Crust and upper mantle structure in East Africa and the origin of Cenozoic extension, magmatism and plateau uplift, in *Magmatic Rifted Margins*, edited by M. Menzies, C. Ebinger and S. Klemperer, Geological Society of America special paper 362-0, in press.

Pasyanos, M.E., W.R. Walter, and S.E. Hazler (2001), A surface wave dispersion study of the Middle East and North for monitoring the Comprehensive Nuclear-Test-Ban Treaty, *Pure and Applied Geophysics*.

Schultz, C., S. Myers, J. Hipp, and C. Young (1999), Nonstationary Bayesian kriging: a predictive technique to generate spatial corrections for seismic detection, location and identification, *Phys. Earth. Planet. Int.*, **113**, 321-338, 1999.

Schultz, C., S. Myers, J. Hipp, and C. Young (1998), Nonstationary Bayesian kriging: a predictive technique to generate spatial corrections for seismic detection, location and identification, *Bull. Seis. Soc. Am.*, **88**, 1275-1288.

ATTEMPTS TO ENHANCE ARRAY DETECTION CAPABILITY: A SEARCH FOR SYSTEMATIC ARRAY RESIDUALS

George E. Randall, Hans E. Hartse, and Lee K. Steck

Los Alamos National Laboratory

Sponsored by National Nuclear Security Administration
Office of Nonproliferation Research and Engineering
Office of Defense Nuclear Nonproliferation

Contract No. W-7405-ENG-36

ABSTRACT

We investigate the performance of array beams formed using the observed slowness and azimuth of arrival for large, well located events. For this study, we use event locations from the United States Geological Survey (USGS) Earthquake Data Reports (EDR). The deviations of the observed azimuths of arrival from the predicted azimuths of arrival based on a suite of events are used to estimate correction surfaces to be applied for improved azimuth estimation for phase association and event location. We have begun an exploratory effort to study the residual waveforms for seismic array elements. The individual seismic traces from array elements are shifted to a common geographic reference point using delays based on the observed slowness and azimuth of arrival, and then averaged to form the array beam. We then compute the residual seismograms by subtracting the beam from the time shifted traces for each element and study the residual traces for systematic effects. Any systematic effects in the residuals point to deviations from the assumed ideal array behavior. If we can identify and correct for systematic array deviations, we hope to improve array detection capability, as well as array estimates of azimuth and slowness.

OBJECTIVE

We evaluate and attempt to improve the performance of array beams formed using the observed slowness and azimuth of arrival for large, well located events. The deviations of the observed azimuths of arrival from the predicted azimuths of arrival based on a suite of events will be used to estimate correction surfaces to be applied for improved azimuth estimation for phase association and event location. Similarly, deviations in predicted and observed slowness of phases across the array are tabulated for correction surfaces. In addition to these efforts aimed at location and association, we are also closely examining the residuals of the beam forming process looking for systematic errors. Any systematic errors that can be explained and corrected (such as static delays or other variations from a simple plane wave propagation across the array) may improve the performance of the array for all events. If we can improve the array beam or FK performance for large well located events, we hope to lower the detection threshold for smaller events where the array enhancement of the signal to noise will be far more important.

RESEARCH ACCOMPLISHED

Seismic arrays have a long history in seismic verification and monitoring (Blandford 1974, Capon 1969, Capon 1970, Capon et. al. 1969, Capon et. al. 1968, Capon et. al. 1969, Green et. al. 1966, Mykkeltveit et. al. 1990). Techniques for processing array data are based on the assumption that the seismic wave field propagates as a plane wave across the array, allowing a simple prediction of the time of arrival of a wave front at each station for a given azimuth of arrival and phase velocity of propagation (or the reciprocal of phase velocity typically called slowness). For body waves, non-dispersive propagation is also assumed, so a seismic phase propagates without dispersive distortion. For typical arrays, this means the seismic phase is virtually unchanged as it propagates from element to element. In addition, arrays are designed with an element spacing that tries to preserve the correlation of the signal and exploit a lack of correlation of noise at frequencies of interest so that simple time shifting and summation will cause the signal to add constructively and the decorrelated noise to add destructively, increasing the signal-to-noise ratio (SNR). Deviations from the assumed model will cause degradation of performance of the array beam forming and estimation of azimuth of arrival and slowness. We are conducting an exploratory effort to evaluate seismic arrays for systematic deviations from the assumed model and are searching for possible simple corrections that may be applied to improve array performance.

Our initial efforts are applied to the Makanchi array, which is expected to be typical of future monitoring arrays. We have acquired data for the Makanchi array in Kazakhstan and extracted waveforms for events listed in the USGS

Figure 1. Map of Makanchi Array showing array geometry and scale.

EDR seismic event catalog.We have chosen large well located events so that we can expect clear arrivals with good signal to noise. These larger events should produce the best possible results from the array, and we hope any systematic residuals will lead us to correction terms that can be applied for smaller events. For the purpose of illustration in the paper, we are using a single event 361 km from the array at an azimuth of 149 degrees. The event has a USGS body wave magnitude of 4.8 and is recorded with good SNR. It has clear Pn, Pg, and Lg arrivals. We begin with simple linear delay and sum beam forming, evaluating both time domain and frequency domain beam forming. The slowness, or PseudoFK spectrum, based on simple delay and sum beam forming for a two-dimensional (2-D) grid of horizontal slownesses, defines the distribution of beam formed energy as a function of horizontal slowness. Each 2-D slowness point can be interpreted as a slowness and azimuth of arrival, and we evaluate the region of maximum beamed energy to estimate the slowness and azimuth. We scale the energy of the region vs. slowness for energy less than a simple fraction of the maximum energy to unit volume, and compute the first and second central moments. This gives us a useful estimate of the observed slowness and azimuth of approach as well as an analog to covariance describing the width of the peak and a measure of the uncertainty of the estimates of the arrival.

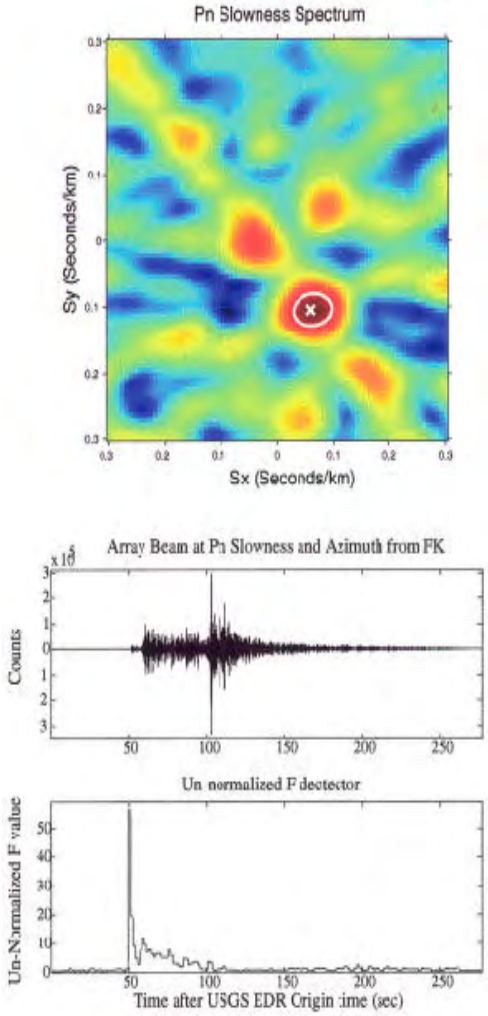

Figure 2. Slowness Spectrum of Pn arrival (at approximately 50 seconds) shown in upper colored panel. The cross represents the peak amplitude measured. The white oval is the 70% of peak amplitude contour bounding the region used to estimate averaged slowness and azimuth as well as confidence bounds. The lower panel shows the entire waveform beamed at the estimated Pn arrival parameters and the unscaled F detector.

The slowness spectrum is computed for a time window that is presumed to contain a seismic phase. The seismic traces for the time window for each of the nine short period vertical array elements have the mean removed and are tapered prior to Fourier transforming. The transforms are then phase shifted with delays that correspond to the travel time predicted by a plane wave propagation across the array to a reference point for a suite of horizontal slownesses in the North-South and East-West directions. At each two dimensional slowness point the energy of the summation of the phase shifted transforms is computed and plotted (Figure 2a) as a surface. The peak of the surface is found, and a region that is greater than 70% of the peak is identified as the main lobe of the array response for the arrival. The volume of the region is normalized to unity, so that it can be treated as a density function. The mean and covariance are computed as a measure of the interpolated peak arrival and an estimate of the elliptical shape and orientation of the peak as a function of slowness. The peak is converted from 2-D slowness to a polar vector of slowness for the arrival and the azimuth of approach to the array. The slowness is useful for phase identification based on the characteristic slowness values of regional phases. The azimuth is useful for associating phases into events and location. The deviations of observed slowness from travel-time model predictions, and azimuth from great circle arc propagation are used along with the estimates of the width of the slowness spectrum peak in slowness and azimuth about the arrival, to build correction surfaces for location.

Once a slowness and azimuth of arrival are estimated, a beam is formed using those parameters. A beam computed by phase shifting in the frequency domain and inverse transforming to the time domain is shown (Figure 2b) along with a trace that is the F detector (Blandford 1974). In the beam forming process, the individual station traces are shifted into the alignment predicted by the estimate based on peak energy of the slowness spectrum, and then averaged in the frequency domain. This frequency domain beam is then subtracted from the shifted station spectra to compute the residual spectra. The beam and residual spectra are all inverse Fourier transformed to the time domain. The F detector is computed by using a sliding 3-sec. window, shifted by 1.5 seconds. The ratio of the energy in the beam is divided by the energy in the residual waveforms, which, when properly normalized, is Blandford's F detector. The F detector grows as the coherent beam grows, and also grows as the energy in the residuals is minimized. In the example, the data are already of ample signal to noise to permit an analyst to pick the arrival. The F detector has been very useful in this study for finding coherent phases, but only when the data are high pass filtered prior to the process of beam forming and computation of the F detector. The coherence of the microseismic noise across the array at frequencies near 0.2 Hz seems to be the most likely problem for the degraded performance of the F detector on raw array data.

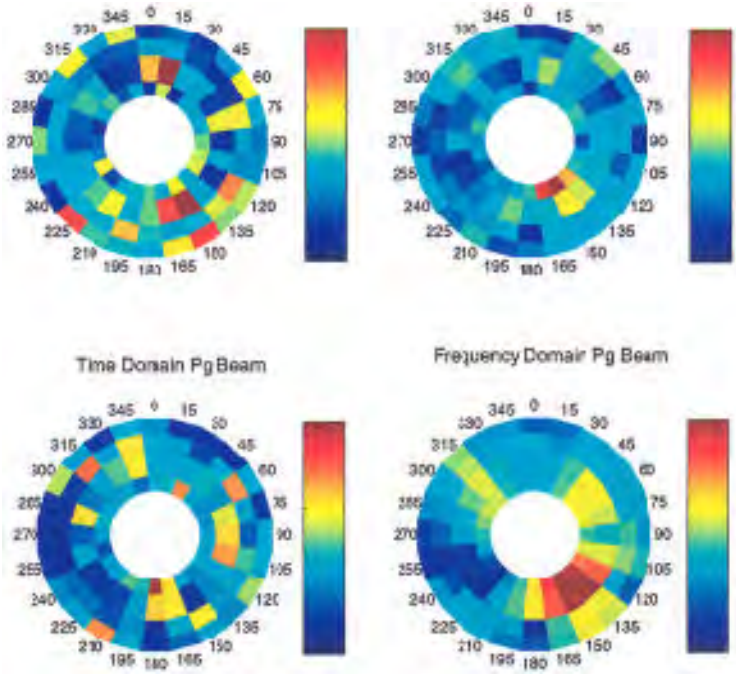

Figure 3. Comparison of time domain beams in the left column and frequency domain beams in the right column for Pn arrivals in the top row and Pg arrival in the bottom row.

Attempts at simple time domain beam forming as used in MatSeis proved to be a failure. The time domain beam forming uses a quantized time shifting process that computed the nearest array index offset to the predicted time shift and retrieves the time domain samples, then averaging as in the spectral technique. No attempt was made to compute the residuals or the F detector. The frequency and time domain beam formers were computed for Pn and Pg arrivals for azimuths in steps of 15 degrees, and the expected slownesses for Pn, Pg, Sn, and Lg starting with Pn as the inner ring and stepping outward one phase at a time. The rose plots are shown in Figure 3. The color bars indicate the energy color coding with the reds largest and the blues smallest. The frequency domain beams show peak energy near the 150 degree azimuth as predicted by the slowness spectrum and show a distribution of energy that falls away smoothly from the peak. The time domain beam former shows a poor distribution of false peaks and erratic energy distribution. We conclude that the time domain beam forming process is not reliable although it may be worth investigating linear interpolation to estimate the time shifted amplitude for the time domain beam forming.

After gaining confidence in the frequency domain beam forming, we started to look for systematic problems in the array residuals with the hope of interpreting any deviations from the plane wave propagation model. We beamed the entire waveform for the event at the estimated Pn slowness and arrival from the slowness spectrum. The results in Figure 4 show a number of features. The top panel shows the entire waveform for the beam and the individual station residual traces show large residuals in the Lg phase compared to the beamed Lg. The beam for Pn arrival parameters is far from the correct slowness for Lg, so the Lg phase is not reinforced by beam forming, and the averaging process then reduces the beamed amplitude of Lg, and the energy is captured by the residuals, which show the poor fit of the Lg beam using Pn arrival parameters. In the lower panel, we show an expanded version of the Pn portion of the beam. Several interesting features are visible. First, the residuals start with low amplitude at the Pn arrival but grow fairly rapidly to become larger than the beam. Second, the amplitudes of the residual tend to stay larger than the beam, which shows a general diminishing amplitude with time. Third, the residuals show what appears to be a slightly higher frequency content than the beam. Fourth, the residuals show a range of amplitudes; some are significantly large and some smaller. This leads us to conclude that only the initial Pn arrival appears coherent across the array, and the rapid growth in the residuals indicates a higher fraction of scattered energy at slightly higher frequencies relative to the Pn arrival. This Pn coda may be a candidate of coda analysis, comparing average of the coda analyses of the individual elements to the coda of the beam. More scrutiny of the residuals is required to determine the effective coherent bandwidth of the signal and what frequency bands are dominated by scattered energy. We also need to try a slowness spectrum analysis of the residuals in an attempt to identify any systematic errors from local heterogeneity or perhaps static delays.

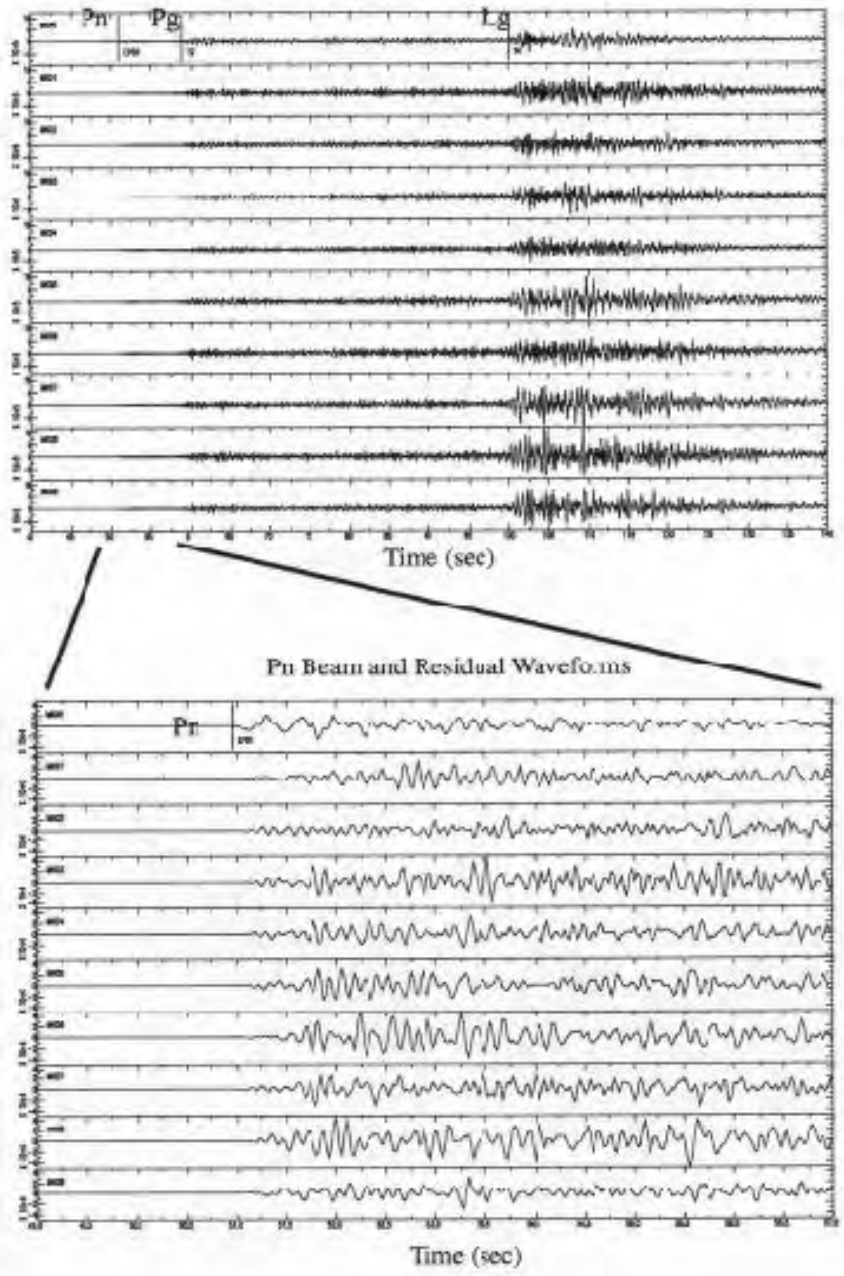

Figure 4. Comparison of the Pn beam and the residuals for each short period vertical array element. The entire trace is shown in the top panel and the Pn phase is shown in the lower panel.

CONCLUSIONS AND RECOMMENDATIONS

Our initial attempts to use time domain beam forming were deemed a failure as the distribution of energy as a function of slowness and azimuth was disturbingly poorly correlated to the azimuth and slowness for event with good signal-to-noise ratio and clear arrivals. We implemented a frequency domain beam former, using complex exponential terms to phase shift in the frequency domain, and found the results produced a distribution of energy as a function of slowness and azimuth consistent with other techniques, and basically consistent with the expected values. Time domain beam forming may need to be upgraded to use interpolation to shift between samples of the waveforms, but

frequency domain beam forming appears to be simple, straightforward and accurate. While we were developing the frequency domain beam forming routines, we added additional capability to generate residual seismograms and Blandford's (1974) F detector. The residual seismograms are simply the difference between the beam (computed by shifting all the seismograms for the individual arrays elements to a common location and averaging) and the shifted seismograms. The residual seismograms are potentially useful for analyzing the deviations from simple plane wave propagation. The F detector has potential as a phase detector, but at least for this dataset, we found that the detector had to be run on high-passed data even for events with good signal to noise. We suspect that the microseismic noise is still correlated across the array, and the high pass filter helps to further suppress the microseismic correlated noise, allowing the F detector to primarily respond to the arriving seismic phase and the higher frequency noise.

REFERENCES

Blandford,R.R. (1974), An Automatic Event Detector at the Tonto Forest Seismic Observatory, *Geophysics*, *39*, 633-643.

Capon, R. (1969), High-Resolution Frequency-Wavenumber Spectrum Analysis, *Proc. of the IEEE*, *57*, 1408-1418.

Capon, R. (1970), Applications of detection and estimation theory to large array, *Proc. of the IEEE*, *58*, 760-770.

Capon, R., R.J. Greenfield, and R.J. Kolker (1969), Multidimensional Maximum-Likelihood Processing of a Large Aperture Seismic Array, *Proc. of the IEEE*, *55*, 192-211.

Capon, R., R.J. Greenfield, R.J. Kolker, and R.T. Lacoss (1968), Short-period Signal Processing Results for the Large Aperture Seismic Array, *Geophysics*, *33*, 452-472.

Capon, R., R.J. Greenfield, and R.T. Lacoss (1969), Long-period Signal Processing Results for the Large Aperture Seismic Array, *Geophysics*, *34*, 305,329.

Green,P.E., E.J. Kelly, and M.J. Levin (1966), A Comparison of Array Processing Methods, *Geophys. J. Roy. Astron. Soc.*, *11*, 67-84.

Mykkeltveit, S, F. Ringdal, T. Kvaerna, and R.W. Alewine (1990), Application of regional arrays in seismic verification research, *Bull. Seim. Soc. Am.*, *80*, 1777-1800.

INCORPORATING SECONDARY PHASES IN 3D REGIONAL SEISMIC EVENT LOCATION: APPLICATION TO THE SPARSE NETWORK PROBLEM

Delaine Reiter, Jessie L. Bonner, Carolynn Vincent, and James Britton

Weston Geophysical Corporation

Sponsored by Defense Threat Reduction Agency

Contract No. DTRA01-00-C-0098

ABSTRACT

One of the most important issues in nuclear explosion monitoring is the accurate location of small seismic events that may only be recorded on a sparse, regional network. To address this problem, we have developed a method of regional seismic event location that fully incorporates 3D velocity models and travel-time prediction for multiple phase arrivals. To estimate event hypocenters, we utilize the 3D grid search location algorithm of Rodi and Toksöz (2001). This location method generates 3D Monte Carlo confidence regions in addition to the hypocentral parameters. We calculate station-centered travel- time grids for use in the location estimates via the 3D Podvin-Lecomte (1991) finite-difference method. We have extended the Podvin-Lecomte method to generate travel times for secondary regional phases such as *Pg*, *Sn* and depth phases (*pPn*, *sPn*, etc.). The resulting algorithm is unique in its ability to locate events using fully 3D models and all regional primary and secondary body-wave phase arrivals.

To demonstrate the technique, we have applied it to events recorded in Pakistan and the surrounding region. We identified events in the EHB bulletin (Engdahl *et al.*, 1998) that were well-recorded teleseismically (mb ≥ 4.1) and had recorded multiple teleseismic depth phase picks and at least one regional depth phase pick. We relocated these events using the phase arrival data from four International Monitoring System (IMS or IMS surrogate) stations in the Pakistan region and our tomographically derived, 3D *P*-wave velocity model (WINPAK3D) for the area (Reiter *et al.*, 2001). Using various combinations of regional *P*, *S*, and *pP* phase picks from this sparse network configuration, we have calculated hypocentral estimates and their associated Monte Carlo confidence regions. The results of these tests clearly indicate that even one regional depth phase pick can significantly improve depth accuracy and decrease the size of the hypocentral confidence regions. This improvement is particularly pronounced for events occurring at crustal and upper mantle depths that are of interest to nuclear monitoring agencies. The addition of shear phases can also improve the location estimates but is dependent on the accuracy of the *S* wave picks, which typically have more error than *P* wave picks.

OBJECTIVE

The overall objective of this research program is to produce a fully 3D grid-search location algorithm that can more accurately locate seismic events using the International Monitoring System (IMS) network. Within this framework we are investigating a number of extensions and applications of our basic algorithm, which is a regional event location method that incorporates 3D velocity models and travel-time predictions into a nested grid-search location technique. In this paper we investigate the improvements in the hypocentral and confidence region estimates that occur when we utilize both primary and secondary phases, and apply the resulting algorithm to the uncertainties associated with sparse regional network locations. Specifically, we apply our 3D model-based, grid-search location algorithm to five- and four-station network locations for events from southern Asia to examine how well we can determine event depths using various combinations of regional arrivals. The goal of our study is to show that the addition of secondary phases, in particular depth phases, can significantly increase the accuracy and confidence of sparse network depth estimates.

RESEARCH ACCOMPLISHED

Regional Event Location in 3D Models using Secondary Phases

One of the most important nuclear test-monitoring problems facing seismologists is the accurate location and identification of small seismic events that may not be recorded at teleseismic distances. In cases where the events are only recorded at regional distances on what will likely be a sparse network, with five or fewer stations and a large azimuthal gap, the accuracy of the velocity model and the incorporation of secondary phase arrivals are critically important to obtaining a valid location.

We have been developing a network location algorithm that incorporates 3D regional travel-time prediction with a Grid-search Multiple Event Location algorithm (GMEL) developed at M.I.T. (Rodi and Toksöz, 2000, 2001). The algorithm employs a recursive grid-search technique to find the best-fitting location parameters (origin time and hypocenter) of an event, and a Monte Carlo technique to obtain confidence regions on the location parameters. These numerical techniques avoid many of the restrictive assumptions and approximations used in conventional location algorithms (e.g., Geiger's method (Geiger, 1912)), but they are more computationally intensive.

To generate the synthetic travel times for GMEL, we use the Podvin and Lecomte (1991) method, which solves the travel time problem in a 3D medium using a finite difference approximation of Huygens' principle. The Podvin-Lecomte (P-L) method is capable of accurately modeling different propagation modes, such as transmitted and diffracted body waves or head waves. This method can provide accurate travel times in the presence of extremely severe, arbitrarily shaped velocity contrasts. Podvin-Lecomte travel-time prediction is an improvement over other similar methods (Vidale, 1990; Moser, 1991), which can encounter serious difficulties in the presence of sharp first-order contrasts. The velocity model is set up as a uniform grid in three dimensions, and first arrival travel times from each station are computed to each point within the grid. This method of travel time computation is considerably faster than two-point ray tracing in a 3D model, and the sources and receivers can be located anywhere within the model.

The grid-search location method (GMEL) has been modified to utilize any phase arrivals for which there are travel-time tables. To exploit this functionality with 3D velocity models, we have extended the method of P-L to allow us to predict travel times for regional secondary phases such as *Pg, pPn, sPn* and *Sn.* For the most prominent regional shear wave phase, *Sn*, there are no modifications necessary in the P-L code. All that is required is to input the appropriate shear wave velocity model and run the P-L code in its original mode.

Secondary regional phases such as *Pg* and *Sg* (or *Pb* and *Sb*) require a modification of the input velocity models prior to running the P-L code. For *Pg* and *Sg* phases, we ensure that the travel times are either that of an upgoing wave from a source in the upper crust or a wave bottoming in the upper crust. Therefore, for *Pg* or *Sg* phases we 'mask' the 3D velocity model below the uppermost crustal layer, provided there is such a demarcation in a given model. For *Pb* or *Sb* phases, the model 'masking' begins below the Moho to ensure that the waves are either originating in the lower crust or bottoming in the lower crust. Our modification entails replacing the velocity models below the appropriate layer with a very slow constant velocity and running the P-L code in its original format. For demonstration purposes, we show travel time calculation results in Figure 1 for the 1-D IASPEI model

(Kennett and Engdahl, 1991) that has both upper and lower crustal layers. The reduced travel times generated by P-L for *Pg*, *Pb*, and *Pn* are shown as a function of epicentral distance for a surface focus event (squares for *Pn*, triangles for *Pb* and diamonds for *Pg*). These travel times are compared to the analytical times (the lines underlying the respective markers) expected from the IASP91 model (Buland and Chapman, 1983). The fit is excellent for all phases, demonstrating that the P-L method can accurately produce secondary phase arrivals for use in a location routine. However, in the EHB (Engdahl *et al*., 1998) event bulletin, there are very few travel time picks for *Pg*, *Pb*, *Sg* or *Sb* designated as secondary phases, and none of these picks were utilized in producing event locations in the EHB database. Therefore, we currently do not produce independent secondary phase *Pg*, *Pb*, *Sg* or *Sb* tables for use in our location routine.

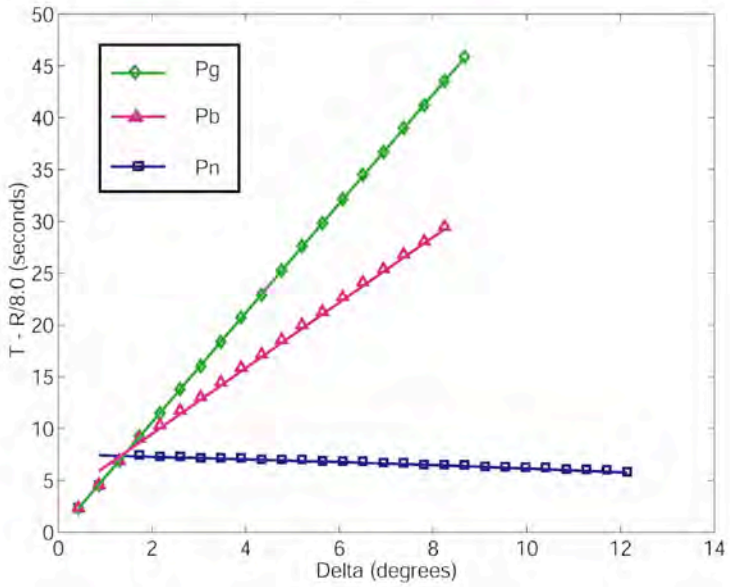

Figure 1. Reduced travel times from the IASP91 model as a function of epicentral distance for a surface focus event. The analytical times are plotted as lines, and the overlying markers are the travel times predicted by the P-L finite difference method for phases *Pn*, *Pb*, and *Pg*. The numerical technique accurately predicts the arrival times of the secondary phases.

The most extensive modification of the 3D travel-time prediction software is required to predict the arrival times for the depth phases such as *pPn* and *sPn*. For these phases, a two-part calculation is necessary to predict travel times from a particular station to points throughout the model. The first part of the calculation generates travel times from the station to every point in the travel time grid (corresponding to the "*P*" leg of a "*pP*" depth phase, for example). In the second part of the calculation, the travel time grid is reinitialized to contain only travel times from the surface of the first grid, and the P-L code is run again to generate the total depth phase travel times and complete the surface-to-event bounce portion of the path (the "*p*" leg of the "*pP*" depth phase) to all remaining points in the grid. Figure 2 shows a simplified schematic of the two-part process that generates depth phase arrival times using the 3D Podvin-Lecomte finite difference algorithm.

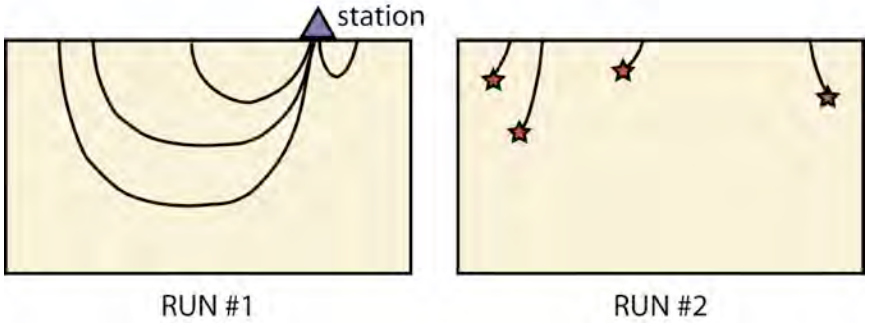

Figure 2. Simplified 2D schematic of method used to generate depth phase arrival times using the 3D Podvin-Lecomte finite difference method. The first run (on the left) generates times from the station to every point on the surface of the travel time grid. The second leg is initialized with the times from the first run, and the code is then used to generate the complete depth phase arrival times to all possible event points in the grid.

With the modifications to the P-L and GMEL codes to predict the travel times of depth phases and shear phases completed, we have the ability to include the secondary phase picks in regional location estimates. In the next section we first examine the accuracy of using only primary arrivals to estimate depth accuracy from sparse regional networks for a subset of events with well-constrained focal depths. Then we investigate how we can improve the depths by including the secondary phase arrivals in the location estimation.

Application to Depth Estimation Using a Sparse Network in Southern Asia

Successful monitoring of nuclear testing activity requires the accurate characterization of all recorded signals and the identification of any suspicious events that may be clandestine nuclear explosions. A definitive way to rule out a majority of seismic events as possible nuclear tests is to accurately determine that the source depth is greater than 15 km, as the practical limit of drilling and explosion emplacement is on the order of a few kilometers. However, depth determination still remains one of the most challenging problems for seismic monitoring, because variations in the depth of a seismic event can cause travel time differences that are indistinguishable from changes in the event's origin time. The problem is made more difficult for small events ($m_b < 4$) that are only recorded at regional distances on sparse networks. A regional location method that can more accurately determine depths for these small events would be a valuable resource for nuclear monitoring agencies. For that reason, we have applied our new 3D regional location technique that can incorporate secondary phases to the sparse network problem in Southern Asia.

Our first goal was to determine the depth location capabilities of a pseudo-IMS network in Southern Asia using only *P*-wave arrivals from four- and five-station networks. To complete this objective, we first compiled a test dataset of seismic events with accurate focal depths determined from multiple teleseismic depth phases. We examined the Center for Monitoring Research's (CMR) Reference Event Database (REDB) for events between 1995 and 2000 that occurred within the bounds of WINPAK3D, the Weston INdia and PAKistan regional 3D velocity model (Reiter *et al.*, 2001) that is bounded by 12° and 43° north latitudes and 55° and 80° east longitudes. Of the resulting 108 events, only 38 events had five or more teleseismic depth phases and were not used in the tomographic update of the WINPAK3D model (Reiter *et al*., 2001). We then cross-referenced the remaining candidate events with the EHB bulletin (Engdahl *et al*., 1998) and searched for events with at least five regional *P* arrivals. The resulting test dataset (Figure 3 and Table 1) includes 23 events with accurate focal depths that were used for our sparse network locations.

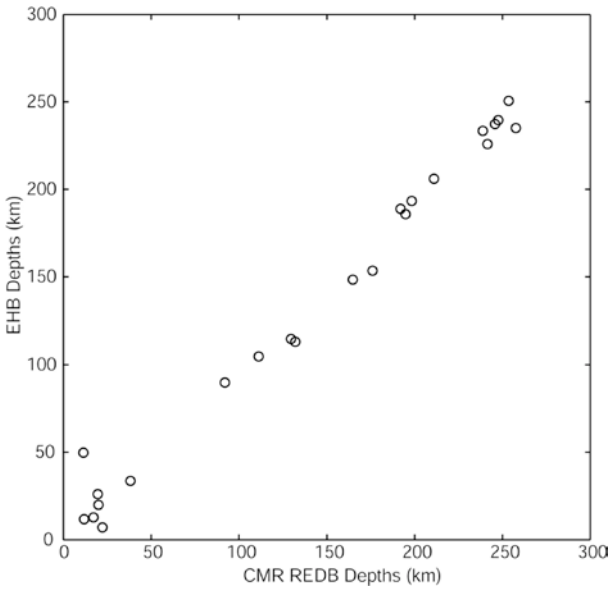

Figure 3. Depth comparison for the CMR REDB and EHB published depths for the 23 test events. The CMR REDB depth is based on five or more teleseismic depth phases and was chosen for the reference depth in this study.

Table 1. CMR REDB and EHB origin parameters for the test dataset.

CMR REDB								EHB			
Date	OT	Lat	Long	Z	mb	Depth Phases	EVID	OT	Lat	Long	Z
1/29/1995	1:20:13	36.84N	71.51E	111.1	4.9	7	303866	1:20:13	36.9367	71.532	104.8
5/16/1995	3:35:04	36.44N	70.95E	192	5.3	28	321673	3:35:04	36.4507	70.909	188.8
6/25/1995	6:38:33	37.91N	72.92E	164.8	4.7	5	328713	6:38:32	37.9485	72.984	148.4
8/17/1995	23:14:21	36.35N	71.14E	245.8	5.3	13	337013	23:14:21	36.4357	71.122	237.3
10/8/1995	8:55:48	40.93N	72.03E	22.2	5.7	29	345874	8:55:46	41.0025	72.155	7
10/18/1995	9:30:41	36.35N	70.39E	241.4	5.7	69	348234	9:30:40	36.4317	70.389	225.8
7/24/1996	17:23:54	35.91N	68.50E	11.5	5	21	402331	17:24:00	35.9838	68.61	49.8
9/14/1996	8:01:06	35.93N	70.66E	132.1	5.4	15	411509	8:01:05	36.0088	70.701	113.1
11/30/1996	11:02:50	36.30N	71.00E	253.6	4.6	30	424565	11:02:50	36.3636	71.036	250.6
3/19/1997	11:15:49	30.23N	67.93E	17.1	4.2	19	441655	11:15:50	30.3104	67.991	12.7
4/21/1997	9:16:24	36.93N	71.78E	176	4.8	5	447150	9:16:23	37.0359	71.835	153.4
5/15/1997	18:30:27	36.40N	70.85E	194.9	5.1	14	451554	18:30:26	36.4537	70.884	185.7
5/17/1997	3:07:30	29.65N	68.20E	11.8	4.4	8	451765	3:07:31	29.7014	68.179	11.8
5/17/1997	3:58:24	39.57N	76.92E	19.5	4.6	17	451769	3:58:25	39.5178	76.936	26
8/6/1997	15:00:12	36.43N	70.85E	198.4	4.7	22	464332	15:00:12	36.4668	70.873	193.4
8/9/1997	17:05:29	36.54N	60.38E	38.1	4.1	6	464801	17:05:28	36.5509	60.362	33.7
9/7/1997	10:15:25	29.96N	67.76E	20	5	27	469157	10:15:25	29.9813	67.771	20
11/1/1997	3:46:36	36.38N	70.74E	211.1	5.1	15	478539	3:46:35	36.4257	70.695	206.1
2/20/1998	12:18:10	36.54N	71.07E	257.6	5.8	22	249066	12:18:08	36.4537	71.074	235
3/6/1998	10:51:11	38.30N	73.35E	129.6	4.1	8	251346	10:51:09	38.293	73.383	114.8
3/9/1998	23:21:37	36.60N	71.08E	238.8	4.3	21	251914	23:21:36	36.4758	71.082	233.5
3/21/1998	18:22:32	36.37N	70.18E	247.7	5.9	16	253834	18:22:31	36.4157	70.136	239.5
6/10/1998	8:30:16	28.14N	58.46E	92	4.7	21	269821	8:30:15	28.1578	58.48	89.8

The first goal of this study was to empirically determine the depth estimation capabilities of a sparse network in southern Asia using only the first-arriving *P*-wave travel times. Thus, we relocated the events in Table 1 using only P-wave arrivals from four- and five-IMS stations in the region (Figure 4) including NIL (or nearby station CHCP), ABKT (previously ASH), and AAK (previously FRU). Two other IMS stations in the region are COC and KRM; however, data from these stations are not yet available, and thus surrogates were used for the relocations. For the station COC, the Indian stations HYB, POO, or NDI were used as directional surrogates, and QUE was used for the Iranian station KRM. Note that the results presented in this paper do not represent the final capabilities of the IMS network in this region; however, they do provide initial insight into the depth estimation capabilities of this sparse network. We relocated our database of 23 events using the GMEL algorithm with WINPAK3D as the velocity model.

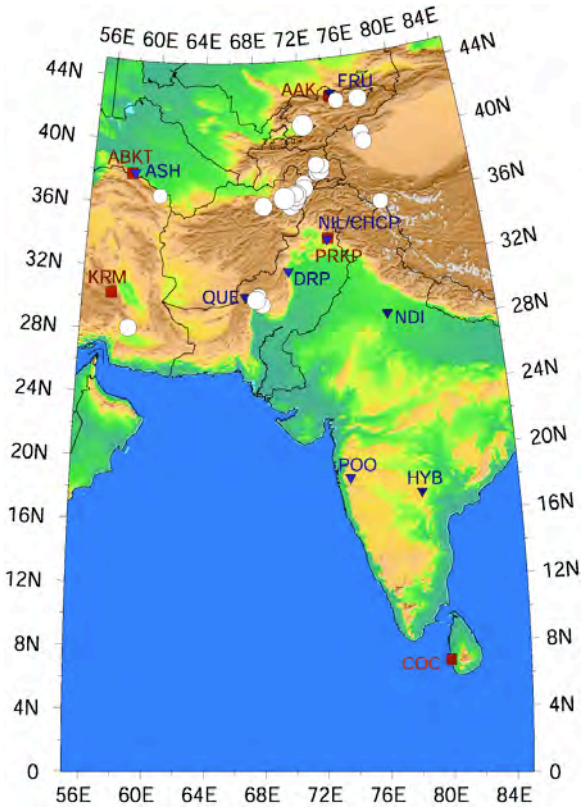

Figure 4. Locations of the test events (white circles), IMS stations (red squares) and surrogates (blue triangles) used in the four- and five-station 3D regional location study.

The results of the five IMS station locations are shown on the left side of Figure 5. The depth mislocation, determined as the difference between the maximum likelihood depth found by GMEL and the CMR REDB depth (Table 1), was less than 35 km for 21 out of the 23 events. Four of the 23 events (22%) had depth mislocation less than 10 km, while eight events had mislocation between 10 and 20 km. The mean depth mislocation was 27 km, and is only 18 km if the two outlier events are eliminated from the calculation. We also note that all CMR REDB depths fell within the 95% confidence interval determined from Monte Carlo simulations inherent in the grid-search algorithm. These results suggest that depths for events recorded on at least five regional stations in southern Asia will be very reliable.

The results for the four IMS station locations (Figure 5, right side) are not as promising. Only one of the 23 events had a depth mislocation less than 10 km and more than 75% of the events (18) had mislocation greater than 35 km. The mean depth mislocation increased to 88 km, and several of the CMR GTDB depths fell outside of the 95% confidence intervals determined from the grid-search algorithm. These results suggest that depths calculated for small events recorded only on four IMS stations in southern Asia will not be reliable. This implies that secondary

phases, and in particular depth phases, will be necessary to resolve the depths for many small events in southern Asia recorded by 4 or fewer stations.

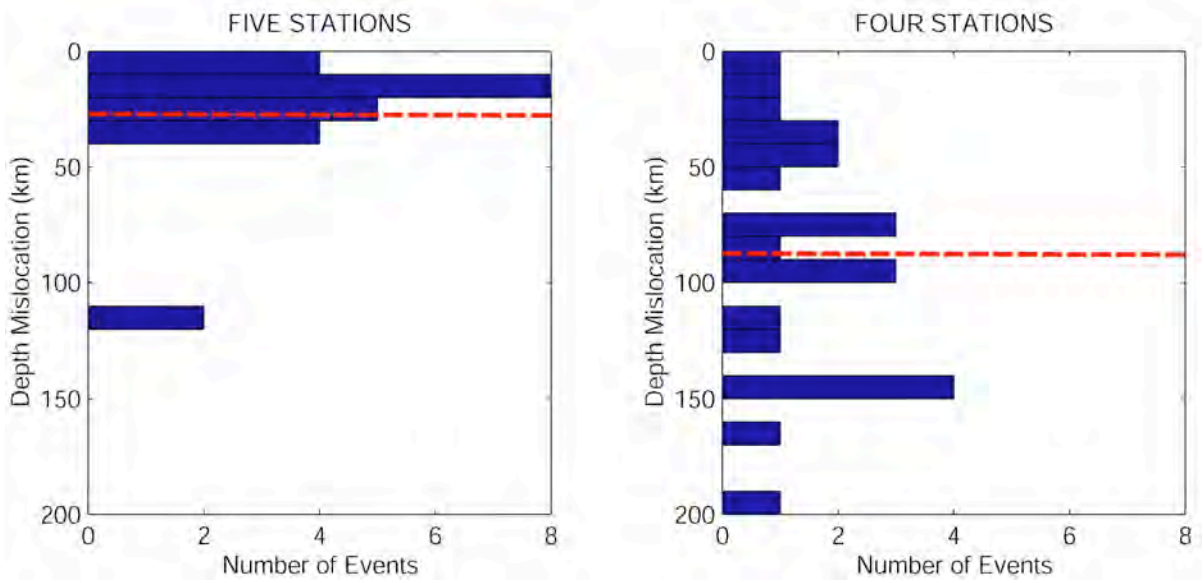

Figure 5. Histograms showing the depth mislocation for five (left) and four (right) station locations. The mean mislocation error is shown as the dashed red line.

To illustrate the effect of adding reliable depth phase picks on the hypocenter and confidence region estimates, we relocated the 23 events in Table 1 using the modified version of GMEL and any available secondary phases. However, of the 23 events in our database, none had regional depth phase picks (distances less than 15°) in the EHB database, although 15 of the 23 events have *pP* picks, nearly all of them at station HYB at epicentral distances between 16 – 22°. We note that this absence of regional depth phases (less than 15°) is by design for the EHB database. We then used cepstral techniques (Bonner *et al*., 2002a) in an attempt to detect and pick regional depth phases from the events listed in Table 1 as recorded at ABKT/ASH, AAK/FRU, NIL, and HYB. For example, Figure 6 shows the 4-station network geometry for an event from Table 1 (EHB database EVID 469157). This event was located at 20 km depth by both the CMR REDB and EHB bulletins, and neither bulletin had regional distance depth phase picks. Using the cepstral technique, we were able to pick *pPn* at stations ABKT/ASH and AAK/FRU (Bonner *et al*., 2002b). *Sn* picks were also available at stations AAK, NIL and NDI, giving a total of nine primary and secondary phase arrival times to utilize in relocating the event.

The hypocenters and Monte Carlo confidence regions found by GMEL using two subsets of the 4-station regional dataset for EVID 469157 are shown in Figure 7. The results from locating with the four *Pn* arrivals from each station are shown in the top row, and the bottom row shows the results found by including the two *pPn* arrivals at FRU and ASH with the four *Pn* arrivals at all stations. The left-hand columns are projections of the epicentral confidence region, while the right two columns are depth slices of the confidence regions through the best-fitting hypocenter. The CMR REDB "ground-truth" location is shown on each subplot as a white-filled circle that has an estimated accuracy of ± 15 km (shown as dashed green circles surrounding the CMR REDB location), and the minimum rms hypocenter from GMEL is shown as a white cross. We do not show the other two subsets of results (locations done with the *Pn* and *Sn* or with all of the *Pn*, *pPn* and *Sn* arrivals), because adding the *Sn* arrivals does not substantially affect the results in this case.

The results indicate that adding the two depth phase arrivals significantly improves the depth estimates for this event. The minimum-rms depth estimate from GMEL using only the four *Pn* arrivals is 163 km, giving a depth mislocation error of 143 km from the CMR REDB and EHB estimates, and the confidence regions indicate that the event depth could range anywhere from the surface to greater than 200 km. However, the addition of two depth phase picks at FRU and ASH produces a GMEL depth estimate of 13 km (i.e. a depth mislocation error of 7 km), and the confidence intervals tightly constrain the depth of the event to be between approximately 0-30 km.

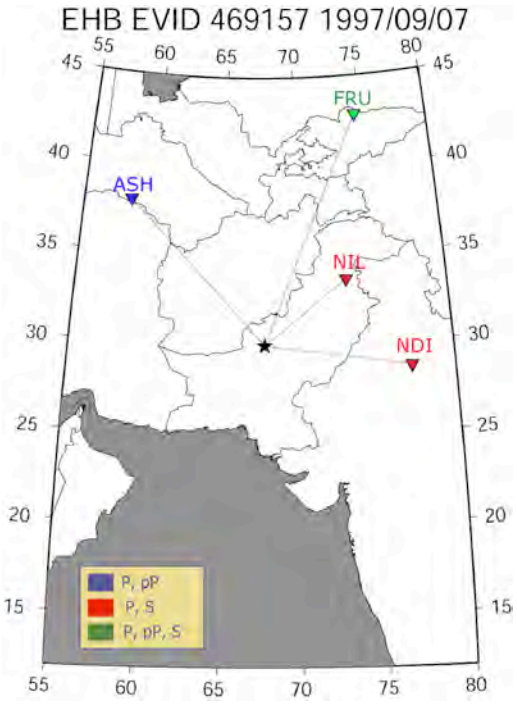

Figure 6. Four station regional network used to relocate Event No. 469157 from Table 1. The legend indicates which phase picks were available at a given station. Regional distance depth phases at stations ASH and FRU were picked using the cepstral F- statistic method of Bonner *et al.* (2002a).

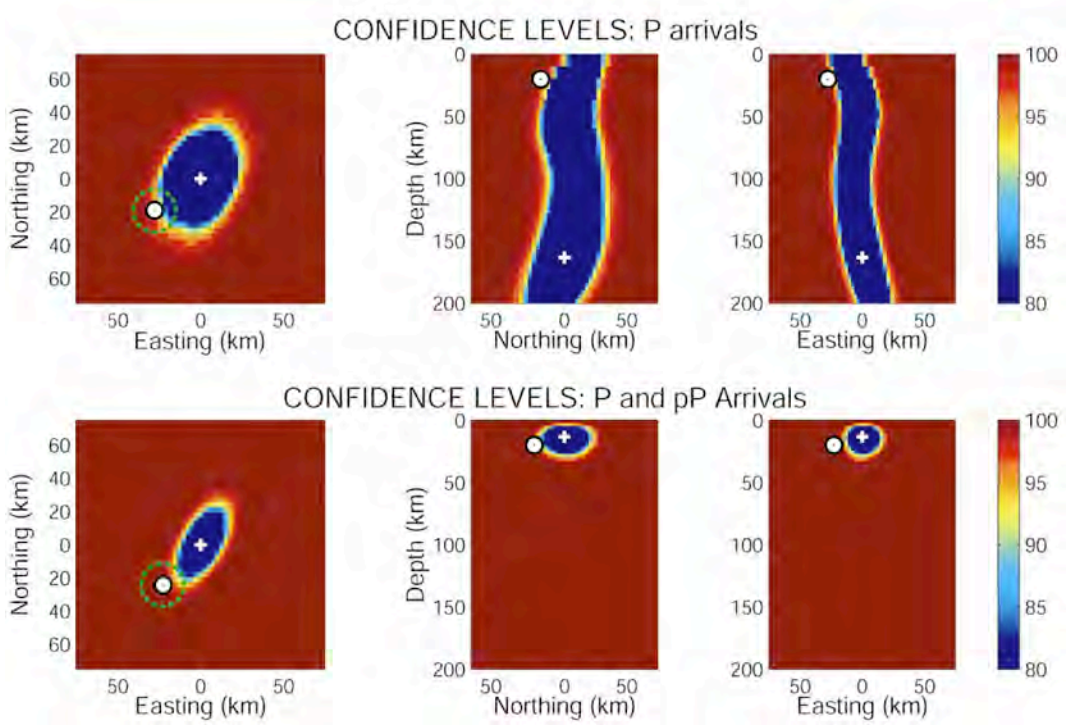

Figure 7. Hypocenter and confidence level estimates for two different sets of arrival picks from Event 469157. Top row: the event location using four *Pn* phase picks. Bottom row: the event location using four *Pn* picks and two *pPn* picks. The left-hand columns show the projections of the epicentral confidence regions, and the middle and right columns show depth slices through the minimum-rms hypocentral confidence regions. The white circles represent the CMR REDB "ground-truth" location (with the dashed green outer circles indicating the ±15 km accuracy of the published epicenter), and the white crosses are the minimum-rms locations found using GMEL.

CONCLUSIONS AND RECOMMENDATIONS

We have developed a fully 3D regional location algorithm that can utilize secondary phases such as *Pg*, *Sn* and depth phases (such as *pP*, *sP*) to better constrain network-derived hypocenter estimates. This location method is unique in that it utilizes grid search techniques, 3D velocity models and fully 3D travel-time prediction for primary and secondary phases to find the event hypocenters, and the method also produces Monte Carlo confidence regions on the location parameters. While the method of using 3D travel-time tables for secondary phases is currently developed using the location program GMEL, it can easily be integrated with routine location algorithms at the IDC by converting travel-time prediction tables to Source Specific Station Corrections (SSSCs) for each regional phase (*Sn, pPn, pSn*, etc). In this paper we applied the new location method to the problem of accurately determining the depth of events recorded regionally on a sparse network. To accomplish this objective, we investigated the depth estimation capability of four- and five-station regional network configurations using a subset of events from southern Asia with pre-existing, accurate focal depths.

Our location results suggest that regional depth phases will be necessary to resolve the depths for many small events in southern Asia and elsewhere when four or fewer stations record the event. Identification of depth phases, such as *pP* and *sP*, is dependent upon the amplitude of the arrival at a recording station. Source mechanism, path effects and reflection coefficients at the earth's surface control the depth phase amplitude as well as the amplitude of the *P* wave coda within which the depth phase will appear. When depth phases from an event are detected, an accurate source depth can be found by using the delay times of the depth phases relative to the *P* wave and the velocity profile near the source. Regional depth phase detection is extremely difficult because of the complexity of the regional seismogram and *P*-wave coda. Figure 8 verifies this fact by showing the depth phase detections listed in the Prototype International Data Center's (PIDC) Reviewed Event Bulletin (REB) for 1999. Less than 1% (45) of the 8072 *pP* picks were for stations at regional (less than 20°) distances.

Some of the currently available techniques to determine source depth from available depth phase data include body wave modeling (Goldstein and Dodge, 1998; Saikia and Helmberger, 1997), beamforming (Woodgold, 1999; Murphy *et al*., 1999), and relative amplitude techniques (Pearce, 1977). The cepstrum is another method that has been used in the past (Alexander, 1996 and Kemerait and Sutton, 1982) to detect depth phases in seismic data. We have used a cepstral F-statistic technique (Bonner *et al*., 2002b) in an attempt to detect regional depth phases from the events listed in Table 1 as recorded at ABKT/ASH, AAK/FRU, NIL, and HYB. Our results indicated that the

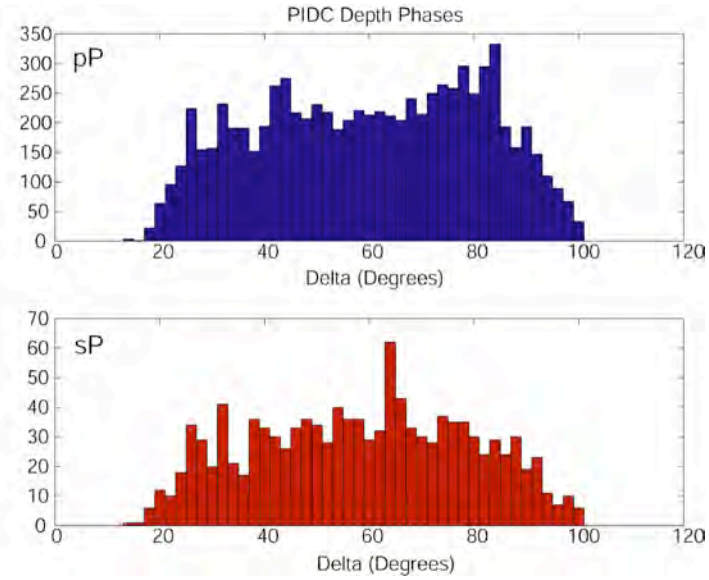

Figure 8. Depth phase (*pP*-top and *sP*-bottom) detections as a function of epicentral distance for the 1999 PIDC REB.

method was very successful at detecting regional depth phases at the stations HYB and ABKT/ASH. The method was less successful at AAK/FRU and NIL, because both stations were often located at near-regional distances to the events where the depth phases were masked by large secondary arrivals, or because the events were too deep to record regional depth phases. The results from this limited study suggest that regional depth phase arrivals are present in the data and a more concentrated effort is needed by analysts to pick these important phases. If the regional depth phases can be found with reliable accuracy, our location results indicate that they can be extremely helpful in improving the depth estimates from sparse network locations of regional events.

ACKNOWLEDGEMENTS

We are indebted to Bill Rodi for his GMEL program and helpful advice on this project. Bob Engdahl provided the latest version of the EHB bulletin, which we have used extensively in this study and others. We thank Xiaoping Yang for help in acquiring the statistics on depth phase detections at the pIDC. We also thank Anca Rosca for programming support and Shelly Johnson for help with the manuscript.

REFERENCES

Alexander, S. S. (1996), A new method for determining source depth from a single regional station, *Seismic Res. Letts*, 67, 63.

Bonner, J.L., D. T. Reiter, and R. H. Shumway (2002a), Application of a cepstral F statistic for improved depth determination, accepted to the *Bull. Seism. Soc. Am.*

Bonner, J. L., D. R. Reiter, and C. Vincent (2002b), Depth determination using sparse networks in southern Asia, in the *Conference Proceedings of 4th Annual Conference on Location Calibration and Event Screening*, 22-26 April 2002, Oslo, Norway.

Buland and Chapman (1983), The Computation of Seismic Travel Times, *Bull. Seism. Soc. Am*, 73, 1271-1302.

Engdahl, E. R., R. van der Hilst, and R. Buland (1998), Global teleseismic earthquake relocation with improved travel times and procedures for depth determination, *Bull. Seism. Soc. Am.*, 88, 722-743.

Geiger, L. (1912), Probability method for the determination of earthquake epicenters from the arrival time only, (translated from Geiger's 1910 German article), *Bulletin of St. Louis University*, 8 (1), 56-71.

Goldstein, P. and D. Dodge (1998), Depth and mechanism estimation using waveform modeling, in *Proceedings of the 20th Annual Seismic Research Symposium on Monitoring a Comprehensive Test Ban Treaty (CTBT)*, 238-247 (September 1998).

Kemerait, R. C. and A. F. Sutton (1982), A multidimensional approach to seismic event depth estimation, in *Geoexploration*, 20, 113-130.

Kennett, B.L.N. and E.R. Engdahl (1991), Traveltimes for global earthquake location and phase identification, *Geophys. J. Int.* 105, 429-465.

Moser, T.J. (1991), Shortest path calculation of seismic rays, *Geophysics*, 56, 59-67.

Murphy, J. R., R. W. Cook, and W.L. Rodi (1999), Improved focal depth determination for use in CTBT monitoring, *Proceedings of the 21st Annual Seismic Research Symposium: Technologies for Monitoring the Comprehensive Nuclear-Test-Ban Treaty (1999).*

Pearce, R.G. (1977), Fault plane solutions using relative amplitudes of *P* and *pP*, *Geophys. J. R. astr. Soc*., 50, 381-394.

Podvin, P. and I. Lecomte (1991), Finite difference computation of travel times in very contrasted velocity models: a massively parallel approach and its associated tools, *Geophys. J. Int*., 105, 271-284.

Reiter, D., W. Rodi, M. Johnson, C. Vincent, and A. Rosca (2001), A new regional velocity model of the India-Pakistan region,*Proceedings of the 23rd Seismic Research Review: Worldwide Monitoring of Nuclear Explosions*-October 2-5 2001, 305-314.

Rodi, W. and M. N. Toksöz (2000), Grid-search techniques for seismic event locations, *Proceedings, 22nd Annual DoD/DOE Seismic Research Symposium*, New Orleans, Louisiana (September 2000).

Rodi, W., and M.N. Toksöz (2001), Uncertainty analysis in seismic event location, *Proceedings, 23rd Seismic Research Review: Worldwide Monitoring of Nuclear Explosions*, Jackson Hole, Wyoming (October 2001).

Saikia, C.K. and D. V. Helmberger (1997), Approximation of rupture directivity in regional phases using upgoing and downgoing wave fields, *Bull. Seism. Soc. Am.*, 87, 987-998.

Vidale, J. (1990), Finite-difference calculation of traveltimes in three dimensions, *Geophys.*, 55, 521-526.

Woodgold, C. R. D. (1999), Wide-aperture beamforming of depth phases by timescale contraction, *Bull. Seis. Soc. Am*., 89, 165-177.

RESEARCH IN REGIONAL SEISMIC MONITORING

F. Ringdal,[1] T. Kværna,[1] E. Kremenetskaya,[2] V. Asming,[2] S. Mykkeltveit,[1]
C. Lindholm,[1] and J. Schweitzer[1]

NORSAR,[1] Kola Regional Seismological Centre[2]

Sponsored by Defense Threat Reduction Agency

Contract No. F08650-01-C-0055

ABSTRACT

This project represents a continuing effort aiming at three main topics: (a) to carry out research in regional monitoring of the European Arctic, (b) to apply experimental methods such as site-specific threshold monitoring to target areas of interest and assess the results and (c) to contribute to the global location calibration effort currently being undertaken by the Preparatory Commission (PrepCom) of the Comprehensive Nuclear Test-Ban-Treaty Organization's Working Group B in Vienna, Austria.

We have used data from the regional networks operated by NORSAR and the Kola Regional Seismological Centre (KRSC) to assess the seismicity and characteristics of regional phases of the European Arctic. An especially interesting recent seismic event, which has been analyzed in detail, occurred on Novaya Zemlya on 23 February 2002. This small event (magnitude about 3.0) is the first seismic event detected in or near Novaya Zemlya since the two Kara Sea events of 16 August 1997. The event was recorded with particularly high signal-to-noise ratio (SNR) by the International Monitoring System (IMS) arrays Spitsbergen and ARCES, and by the Amderma station (operated by KRSC) south of Novaya Zemlya. We have located the event at the eastern coast of Novaya Zemlya, approximately 100 km NE of the former nuclear test site. Our attempts to estimate the depth of this event proved inconclusive, and a depth of 0 could not be ruled out. We present comparisons of the recordings of this event to recordings of previous small events in the Novaya Zemlya region.

We have begun an effort to develop an optimized site-specific threshold monitoring system for the Lop Nor test site in China. Our aim is to calibrate all available high-quality seismic stations within regional distances and the best IMS arrays at teleseismic distances. As a calibration database, we have used several past nuclear explosions at the test site, combined with nearby, well-recorded earthquakes. Even though most events were recorded by only a few stations, this data set was sufficient to obtain a reasonable amplitude calibration for the purposes of this study.

Initial results show that, among the available stations, the IMS Makanchi array in Kazakhstan (at an epicentral distance of 6 degrees) is the most sensitive station for detecting events at Lop Nor, followed by some of the best teleseismic arrays, for example the NORES array in Norway. Combining the data by using the threshold monitoring technique, we have found that the Lop Nor site can be monitored down to a threshold close to m_b 3.2. This threshold is about 0.8 magnitude unit higher than the corresponding capability for the Novaya Zemlya test site, for which the highly sensitive arrays ARCES and Spitsbergen are both at a distance of only 10 degrees. We note that no stations inside China were selected for the Lop Nor study.

A workshop was held in Oslo, Norway, during 22-26 April 2002 in support of the global seismic event location calibration effort currently being undertaken by PrepCom's Working Group B in Vienna. The workshop, which was chaired by Dr. Frode Ringdal, was attended by 66 scientists from 12 countries and the Provisional Technical Secretariat of the CTBTO. The workshop was held jointly by the International Data Centre (IDC) Experts Groups on location calibration and event screening, and the results and recommendations were reported to Working Group B.

OBJECTIVE

This work represents a continued effort in seismic monitoring, with emphasis on studying earthquakes and explosions in the Barents/Kara Sea region, which includes the Russian nuclear test site at Novaya Zemlya. The overall objective is to characterize the seismicity of this region, to investigate the detection and location capability of regional seismic networks, and to study various methods for screening and identifying seismic events in order to improve monitoring of the Comprehensive Nuclear-Test-Ban Treaty. Another objective is to apply advanced site-specific seismic monitoring methods to other sites of special interest, in particular known nuclear test sites. A third objective is to support the international effort to provide regional location calibration of the International Monitoring System (IMS).

RESEARCH ACCOMPLISHED

Introduction

NORSAR and Kola Regional Seismological Centre (KRSC) of the Russian Academy of Sciences have for many years cooperated in the continuous monitoring of seismic events in northwest Russia and adjacent sea areas. The research has been based on data from a network of sensitive regional arrays that has been installed in northern Europe during the last decade in preparation for the CTBT International Monitoring System. This regional network, which comprises stations in Fennoscandia, Spitsbergen and NW Russia, provides a detection capability for the Barents/Kara Sea region that is close to m_b = 2.5 (Ringdal, 1997).

The research carried out during this effort is documented in detail in several contributions contained in the NORSAR Semiannual Technical Summaries. In the present paper we will limit the discussions to some recent results of interest in the general context of regional monitoring of seismic events in the European Arctic, a presentation of an initial threshold monitoring study for the Lop Nor test site in China and a brief review the location calibration effort currently underway for the IMS.

Low-magnitude seismic events in or near Novaya Zemlya

We have updated our previous studies of low-magnitude events in the Novaya Zemlya region recorded by the NORSAR regional seismic network. Table 1 and Figure 1 summarize the information on such events detected since 1980. In spite of the low threshold for detection, only eight seismic events with estimated location outside the test site have been recorded during these more than 20 years. Furthermore, we have since 1992 applied the site-specific threshold monitoring network to the test site, and have thereby been able to confirm that no other seismic event of magnitude 2.5 or greater has occurred in this region since then.

An especially interesting recent seismic event, which has been analyzed in detail, occurred on Novaya Zemlya on 23 February 2002. This small event (magnitude about 3.0) is the first seismic event detected in or near Novaya Zemlya since the two Kara Sea events of 16 August 1997. The event was recorded with particularly high SNR by the IMS arrays Spitsbergen (SPITS) and ARCES, and by the Amderma station (AMD), operated by KRSC, south of Novaya Zemlya. We have located the event at the eastern coast of Novaya Zemlya, approximately 100 km northeast of the former nuclear test site.

For this recent event, as well as other events recorded by the regional network, we have frequently noted uncertainties in onset measurements amounting to 1-2 seconds. This is, in fact, a general problem, and is due partly to the low SNR for some phases, partly to the emergent nature of some signal recordings. We have conducted a study to assess the effects of such uncertainty on location and depth estimates, using a number of seismic events in the European Arctic (Novaya Zemlya, Kara Sea, northern Norway, Kola Peninsula). For each event, and each detected phase, we selected up to three onset time picks, spanning the estimated uncertainty (typically +/- 1-2 seconds). We then relocated each event using all possible combinations of such time picks, and compiled all solutions except those which showed clear inconsistencies. In this way, we obtained a large number of locations and depths for each event, and made plots to indicate the distribution of both the epicenters and the estimated depths.

The results for the 23 February 2002 event near Novaya Zemlya are illustrated in Figure 2. We note that the epicentral error area is similar to the 90% confidence ellipse in Figure 1. The depth distribution is inconclusive, although most solutions have an estimated depth near 0. From the general study, we note that for all the analyzed events, except for one known earthquake in northern Norway, a depth of zero cannot be ruled out. We consider that this should serve as a caution against using estimated depth as a screening criterion in this region. In particular, we note that depth estimation using regional velocity models depend very strongly on the assumed Vp/Vs ratio.

Waveforms for the 23 February 2002 event from a number of seismic stations at regional distances from Novaya Zemlya are shown in Figure 3. The high SNRs indicate that this event is well above the detection threshold, especially for the Amderma, SPITS and ARCES stations. Note that by array beam forming, the SNR at ARCES and SPITS could be improved by more than 0.5 magnitude units. This again reconfirms the capability of this regional network to monitor seismic events at Novaya Zemlya down to a magnitude level of 2.0-2.5, depending on the actual background noise levels.

In the context of event screening, which is an important topic for the IDC, it is clear from these results that no screening should take place for a region with seismic activity as low as Novaya Zemlya. In fact, any seismic event in this region is of potential monitoring interest, and with a frequency of occurrence of magnitude 2.5 or larger at less than one event per year, the actual analysis work would be quite modest. Similarly, as noted by Ringdal *et. al*. (2000), the much larger geographical area of western Russia and the Barents Sea is also characterized by modest natural seismic activity, and could be exempted from event screening, at least at the current magnitude threshold of 3.5 for screening purposes.

Table 1: List of seismic events in or near Novaya Zemlya (1980-2002) located outside the test site

Date/time	Location	m_b	Comment
01.08.86/ 13.56.38	72.945 N, 56.549 E	4.3	Located by Marshall *et.al.* (1989)
31.12.92/ 09.29.24	73.600 N 55.200 E	2.7	Located by NORSAR
23.02.95/ 21.50.00	71.856 N, 55.685 E	2.5	Located by NORSAR
13.06.95/ 19.22.38	75.170 N, 56.740 E	3.5	Located by NORSAR
13.01.96/ 17.17.23	75.240 N, 56.660 E	2.4	Approximately co-located with preceding event
16.08.97/ 02.11.00	72.510 N, 57.550 E	3.5	Located by NORSAR
16.08.97/ 06.19.10	72.510 N, 57.550 E	2.6	Co-located with preceding event
23.02.02/ 01.21.14	74.047 N, 57.671 E	3.0	Located by NORSAR

Figure 1. Seismic events detected by the NORSAR regional array system in or near Novaya Zemlya during 1980-2002. Only events with estimated location outside the former nuclear test site are included. Estimated 90% error ellipses are indicated for each event.

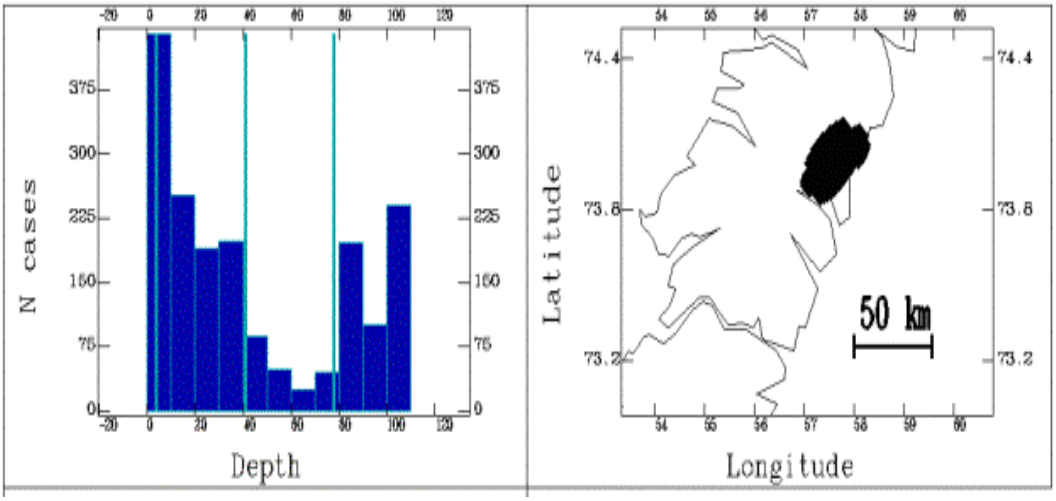

Figure 2. Estimates of the location of the 23.02.2002 seismic event, as explained in the text. Note that the epicenters correspond well with the estimated uncertainty ellipse of Figure 1, and that the depth of the event cannot be conclusively determined.

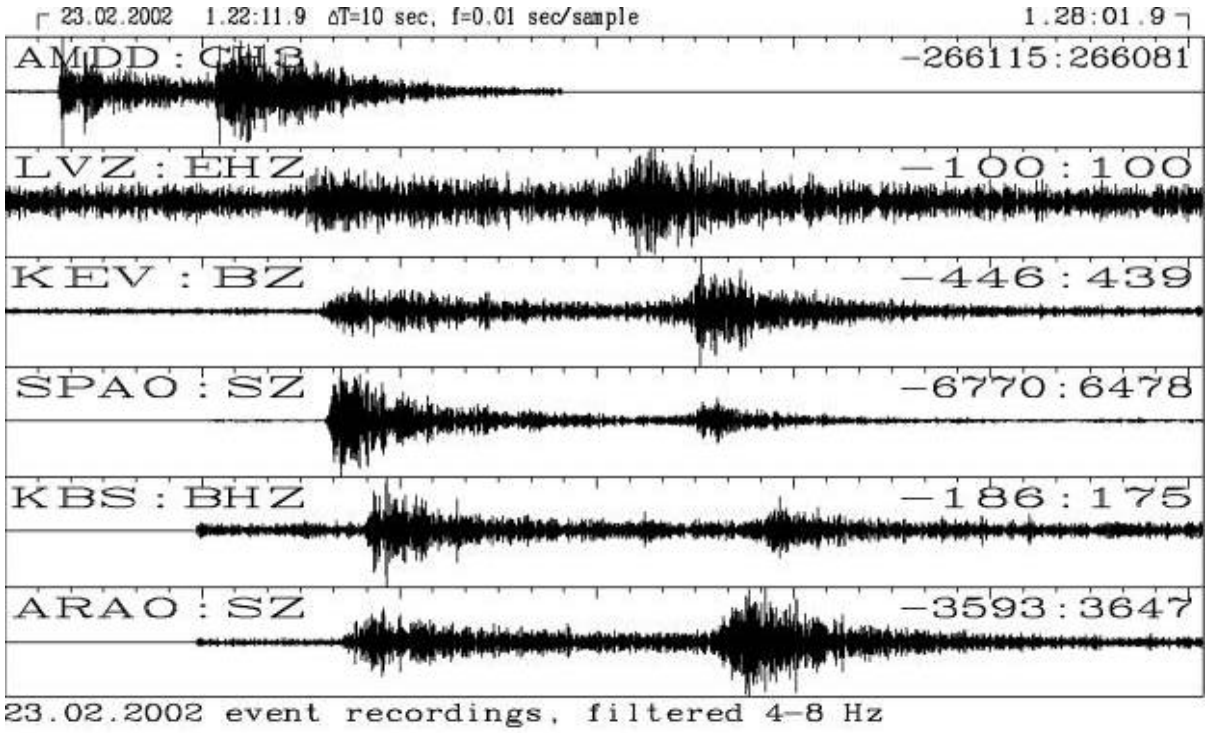

Figure 3. Recorded SPZ waveforms for the 23.02.2002 seismic event. The data are filtered in the 4- to 8-Hz band. Note the high P-phase SNR in particular at the Spitsbergen array (sensor SPA0) and the Amderma station (AMDD). Note also the relatively weak S-phase for the two stations at Spitsbergen (SPA0 and KBS).

Khibiny mines

We have continued our research on rockbursts and mining explosions in the mining areas of NW Russia, in particular the Khibiny Massif. Recently, seismic instrumentation has been installed inside the mines in the Khibiny Massif of the Kola Peninsula in order to provide origin times of the seismic events as well as to contribute to additional validation of the location accuracy. Figure 4 shows an example of recordings for a mining explosion of about magnitude 2.0.

We are also cooperating with Lawrence Livermore National Laboratory in a project funded by the National Nuclear Security Administration to carry out more detailed studies of the characteristics of recordings from mining events in northern Fennoscandia and Western Russia. That project includes the installation of additional seismometers along profiles in Norway, Finland, and the Kola Peninsula, for recording over a period of one year.

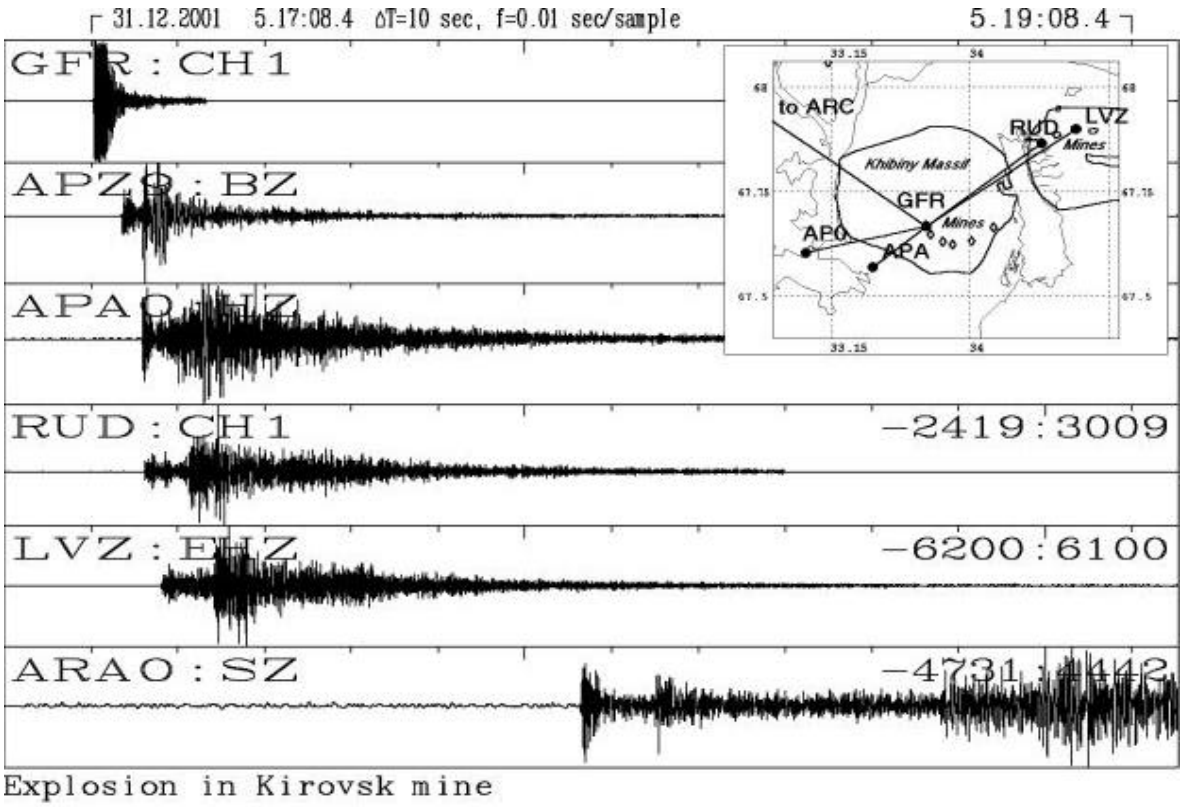

Figure 4. Example of recordings of a mining explosion in the Khibiny Massif, Kola Peninsula, using a network of recently installed local stations as well as stations at regional distances.

Threshold monitoring of the Lop Nor, China, test site

As part of the US Department of Defense Advanced Concept Demonstration (see Kohl, *et al*, this Proceedings), we have applied the Site-Specific Threshold Monitoring (SSTM) technique to the Lop Nor test site in China (Lindholm *et. al*., 2002). The emphasis has been on detection (and location) of small seismic events with mb < 4.0, and the purpose is to evaluate the SSTM method as a potential monitoring tool for this site. In contrast to most previous case studies, which have been based on recordings by seismic arrays at regional distances, we have in this study applied a combination of three-component stations and arrays, at both regional and teleseismic ranges.

Our efforts so far, as reported in this contribution, comprise mainly a study of available seismic stations, selection of those stations that are most sensitive to seismic events in the Lop Nor general area, and tuning of the signal parameters of these stations so as to prepare processing recipes for the application of the threshold monitoring tool.

Development of processing recipes

For the successful implementation of SSTM, beams filtered in optimal frequency bands must be steered from the individual arrays towards the Lop Nor test site, and amplitude calibration constants developed from

older events are applied to facilitate the calculation of continuous magnitude thresholds for the site. For single (or three-component) stations, the vertical component is filtered in the optimal frequency band.

For the purposes of this study, 23 single stations and arrays were initially chosen as shown in Figure 5. For each of the stations, data were collected from known nuclear tests at Lop Nor, and supplemented with data for low-magnitude earthquakes near the test site. We note that for most stations only a few data sets with explosions were available for the calibration.

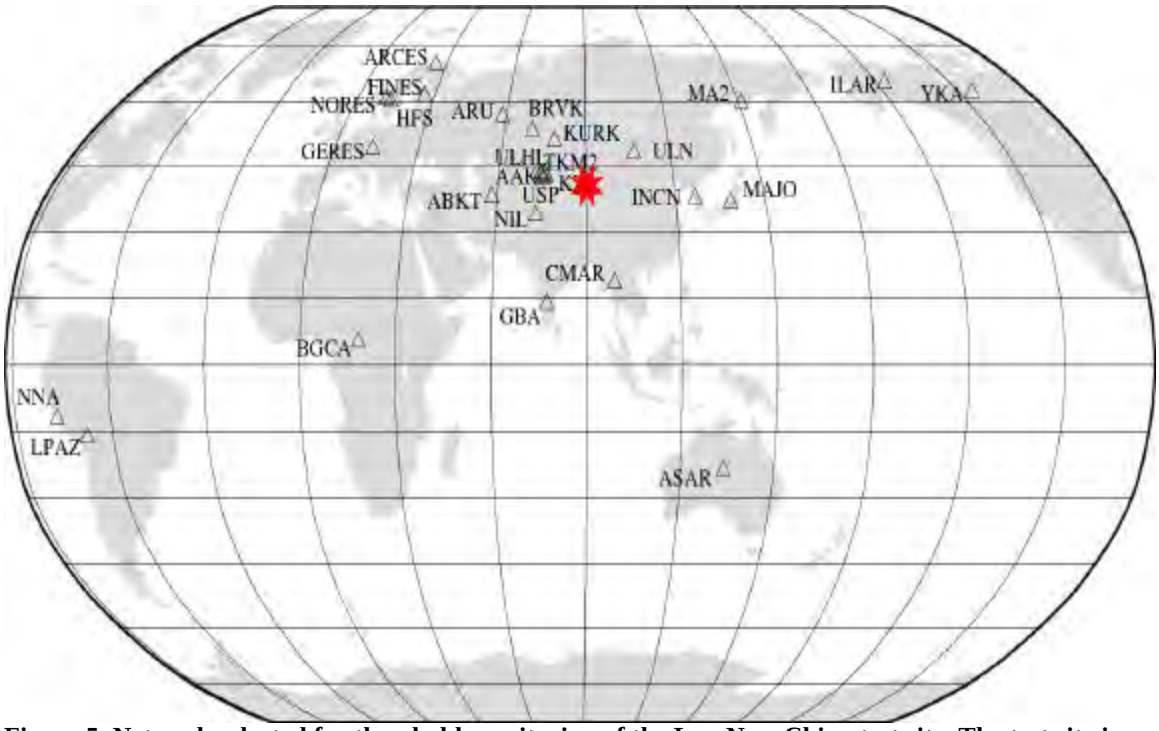

Figure 5. Network selected for threshold monitoring of the Lop Nor, China test site. The test site is marked with a star symbol.

Preliminary Results

Two performance tests were carried out. First, data for one day (September 10, 2001) were collected, and in these data the recordings of four explosions were scaled and embedded at some (but not all of the) stations. The explosions were scaled to magnitude 3.5 and 3.0, so that a total of eight embedded explosions were included. Secondly, a 10-day test period with data from August 2 through 11, 2001, was selected and data were collected for all available stations in our network. Figure 6 shows examples of network results of these two performance tests.

From these tests the following preliminary observations can be stated:

- Out of the eight embedded explosions on day 253, six were detected automatically on the threshold trace, and the remaining two could be clearly seen on the trace, even if the automatic detector did not trigger.
- The quiet day (214) did not have any events flagged.
- On day 217 the SSTM method triggered on two large teleseismic events.
- The network threshold is close to or better than 3.0 (based on both arrays and single stations). The “trigger level” (shown as a continuous, smooth line in Figure 6) is at magnitude 3.2 or lower.
- In a monitoring situation, all peaks exceeding the threshold could be analyzed. The maximum number of such peaks during one day was 10-15 for the days processed. If such peaks were analyzed, all of the scaled events on day 2001-253 would have been found.

The above observations should be evaluated under the perspective that the calibration is a preliminary one, where the majority of the stations could only be calibrated with one or two events/explosions, and where only some of the calibrated stations were included in the performance test. Furthermore, the day with embedded events did not include embedded data for all the stations, and this did reduce the performance of the threshold monitoring.

In the paper by Lindholm *et. al*. (2002), there is also some discussion of the relative performance of individual stations in the network. The SSTM threshold traces for single stations and arrays can in fact be used to assess this performance. We have observed that the arrays generally have thresholds between magnitude 3.2 and 3.8, and that the single stations vary considerably, from about 3.5 for the best (closest) stations to almost 4.5 for some of the lower performing stations. Some stations in the data set feature frequent data problems.

As the IMS is further developed, there is a clear potential for improvement in the performance illustrated above. For example, the sensitive array in Makanchi, Kazakhstan, was not available to us for the test period in August/September 2001. Studies of the performance of this array have indicated that it has a superior capability for detecting events at Lop Nor compared to the other stations in the network, and therefore would contribute to significantly improved thresholds, once included.

We also note that the current study has been done without including any Chinese IMS stations in our experimental network. Including such stations would no doubt contribute to improved thresholds, but there are other considerations that may make it useful to evaluate how the test site can be monitored using only stations outside the country.

Location Calibration

Oslo Workshop on location calibration

A workshop was held in Oslo, Norway, during 22-26 April 2002 in support of the global seismic event location calibration effort currently being undertaken by Working Group B of the CTBTO Preparatory Commission in Vienna, Austria. Dr. Frode Ringdal chaired the meeting, which was attended by 66 experts from 12 countries and the Provisional Technical Secretariat of the CTBTO The recommendations from this workshop have been provided in the paper CTBT/WGB/TL-2/70, issued by Working Group B of the CTBTO Preparatory Commission.

CONCLUSIONS AND RECOMMENDATIONS

The analysis of the 23 February 2002 Novaya Zemlya seismic event has reconfirmed our previous estimates of the detection and location capability of the regional network in northern Europe. This experimental network operation will continue, and will be used to evaluate and supplement the IMS network in this region. Further research is required in regional event identification criteria, especially depth estimation. In the case of depth estimates, a detailed study of the Vp/Vs ratio, as well as its uncertainty limits, should be undertaken.

Our initial performance tests of Site-Specific Threshold Monitoring for the Lop Nor test site were successful. We recommend that these initial tests be followed by more detailed studies, where, in particular, the calibration parameters should be more firmly established. It is also of interest to include additional sensitive IMS arrays in the monitoring network, and evaluate the ensuing improvement in capability.

The location calibration effort will continue to be an important part of our work. The recommendations provided in the paper CTBT/WGB/TL-2/70 should be followed up by the international community, and the progress of this work will be reviewed in a planned workshop in Oslo during 4-9 May 2003.

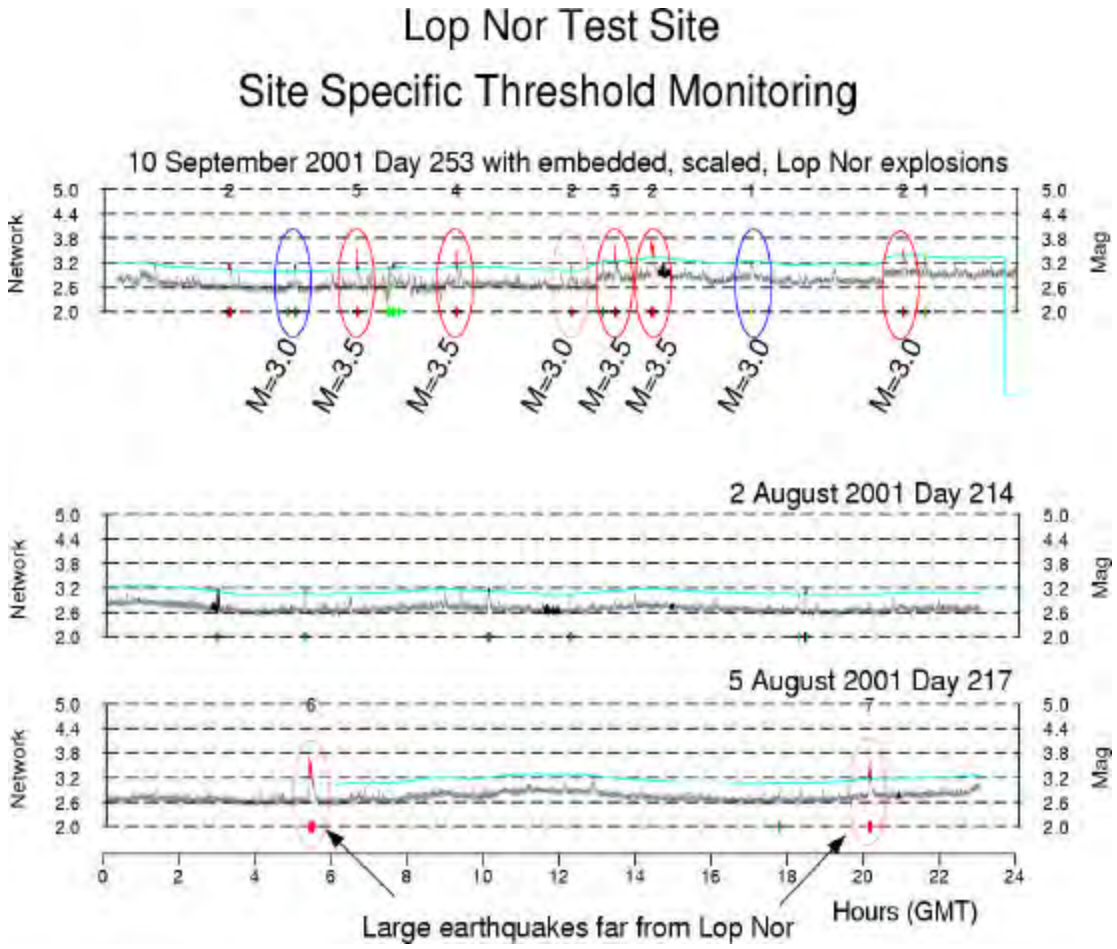

Figure 6. Threshold monitoring network traces from three different days. The upper trace is from day 253 with eight embedded Lop Nor explosion recordings scaled to magnitudes 3.0 and 3.5. The ellipses indicate the times of the embedded explosions. For six of the eight embedded explosions, the SSTM automatic analysis picked the events, while two events (No. 1 and No. 7) were not picked. The lower traces are from days 214 and 217. Day 214 is quiet with no detections, while day 217 shows two detections resulting from "interference" by large earthquakes (located far from Lop Nor). The continuous, smooth line above each threshold trace is an estimated "trigger level" for identifying significant peaks on the threshold trace.

REFERENCES

Lindholm, C., T. Kvœrna and J. Schweitzer (2002): Site-Specific Threshold Monitoring (SSTM) applied to the Lop Nor test site, *Semiannual Technical Summary, 1 July 2001 - 31 December 2001*, NORSAR Sci. Rep. 1-2002, Norway.

Marshall, P.D., R.C. Stewart and R.C. Lilwall (1989). The seismic disturbance on 1986 August 1 near Novaya Zemlya: a source of concern?, *Geophys. J*. **98**, 565-573.

Ringdal, F. (1997): Study of low-magnitude seismic events near the Novaya Zemlya nuclear test site, *Bull. Seism. Soc. Am.* **87** *No. 6*, 1563-1575.

Ringdal, F., E.O. Kremenetskaya, V.E. Asming, T. Kvœrna and J. Schweitzer (2000): Research in Regional Seismic Monitoring, *Paper presented at the 22nd Annual Seismic Research Symposium*, New Orleans.

GRID-SEARCH LOCATION METHODS FOR GROUND-TRUTH COLLECTION FROM LOCAL AND REGIONAL SEISMIC NETWORKS

William Rodi,[1] Craig A. Schultz,[2] William G. Hanley,[2]
Sudipta Sarkar,[1] and H. Sadi Kuleli[1]

Massachusetts Institute of Technology,[1] Lawrence Livermore National Laboratory[2]

Sponsored by National Nuclear Security Administration
Office of Nonproliferation Research and Engineering
Office of Defense Nuclear Nonproliferation

Contract No. DE-FC03-01SF22397[1] and W-7405-ENG-48[2]

ABSTRACT

This paper reports on preliminary efforts to develop improved seismic event location techniques that can be used to generate more and better quality reference events using data from local and regional seismic networks. Our approach builds on earlier and concurrent work on the development of grid-search-based algorithms for single-event location and multiple-event location (known as GSEL and GMEL, respectively). Owing to the flexibility of the grid-search approach, we are now able to address certain additional complexities that we expect to yield improved reference event locations. These are (1) allowing spatially variable (source-dependent) station travel-time corrections in a multiple-event location analysis, and (2) extending the statistical model of observational errors beyond the simple class of Gaussian and non-Gaussian models now used.

On the first topic, we have formulated an extension of the multiple-event location algorithm GMEL to be a joint location and kriging method. The purpose of this is to allow the simultaneous processing of non-clustered, spatially well-distributed events. The kriging paradigm is extended such that a universal function, or set of functions, generates travel-time corrections at all stations. This allows the incorporation of important physical constraints such as source-receiver reciprocity. On the second topic, we are developing a new probabilistic error model in terms of mixture-of-Gaussians (MOG) distributions. Such distributions can describe multiple error processes that are not adequately described with unimodal, symmetric distributions.

OBJECTIVE

The objective of this work is to develop improved earthquake location techniques that can be used to increase the number and accuracy of reference events obtained from local and regional seismic networks. Our approach is to extend existing multiple-event location methods to incorporate improved statistical models of the observational errors in the arrival times measured from low-magnitude events, and spatially variable path corrections that allow the processing of non-clustered events.

RESEARCH ACCOMPLISHED

The approach of multiple-event location has been successfully applied as a tool for expanding the set of well-located earthquakes that can be used as reference events for the calibration of seismic monitoring stations (Engdahl and Bergman, 2000; 2001). The key feature of this approach is that it pools information from several events recorded at various subsets of a seismic network, together with ground-truth (GT) constraints on one or more of the events (e.g. from a dense local network), with the result that the location accuracy of the events is improved over that obtained by locating them independently. When the location error is reduced sufficiently (e.g. <5 km), an event becomes a useful reference event for calibration.

In conjunction with another project, we have extended an earlier grid-search event location algorithm for locating single events (Rodi and Toksöz, 2000) to a basic multiple-event location algorithm applicable to small event clusters. The algorithm performs the same basic task as the hypocentral decomposition (HDC) method of Engdahl and Bergman (2000, 2001) and as several other multiple-event location algorithms (see Rodi *et al*., 2002), except that it accommodates a certain class of non-Gaussian models of observational errors. Our algorithm for multiple-event location, known as GMEL, is described in Rodi *et al*. (2002). Here, we summarize what GMEL does and our progress in designing the extensions to this algorithm needed for this project.

Grid-Search Multiple Event Location

GMEL simultaneously processes seismic arrival time, azimuth and slowness data observed for multiple events, stations and phases. For simplicity, we consider here the special case in which the data set comprises only arrival times and assume that at most one arrival (P) per event has been observed at a station. Let d_{ij} denote the arrival time observation for the ith station and jth event, where $i = 1, \ldots, n$, and $j = 1, \ldots, m$. The multiple-event location problem addressed by this project can be written

$$d_{ij} = t_j + T_i(\mathbf{x}_j) + c_{ij} + e_{ij} \,, \tag{1}$$

where t_j and $\mathbf{x}_j$, respectively, are the origin time and hypocenter of the jth event; T_i is the travel-time function for the ith station, obtained from an assumed Earth model; c_{ij} is an unknown path correction; and e_{ij} is an observational ("picking") error. Equation (1) applies only to the i, j pairs for which arrival times have been observed.

GMEL currently assumes that the data errors are random and independent, and that each has a generalized Gaussian distribution of order p, whose probability density function (p.d.f.) is given by

$$f(e_{ij}) = \frac{1}{K(p)\,\sigma_{ij}} \exp\left\{ -\frac{1}{p} \left| \frac{e_{ij} - \mu_{ij}}{\sigma_{ij}} \right|^p \right\} \tag{2}$$

(see Billings *et al*., 1994). In this formula, μ_{ij} is the mean of the p.d.f., σ_{ij} is its standard error, and $K(p)$ is a constant depending on p. The order p can be any number greater than or equal to one. For $p = 1$, the p.d.f. is a Laplace distribution (two-sided exponential) and for $p = 2$, it is Gaussian. GMEL currently assumes that the μ_{ij} are known (usually zero) and that the σ_{ij} are known in a relative sense, whereby

$$\sigma_{ij} = \sigma_i \, \nu_{ij} \tag{3}$$

with the ν_{ij} being known but the station-dependent scale parameters, σ_i, being unknown.

Regarding the path corrections, GMEL currently assumes that they are event-independent, implying

$$c_{ij} = c_i \tag{4}$$

where the c_i are station-dependent travel-time corrections. This assumes, in effect, that the events are in a small cluster.

GMEL jointly solves for the problem unknowns: t_j, $\mathbf{x}_j$, c_i and σ_i. It solves a maximum-likelihood criterion, i.e. it maximizes the likelihood function determined by the assumed error p.d.f.'s. Its algorithm for maximizing likelihood combines grid-search (for the $\mathbf{x}_j$), root-finding (for t_j and c_i) and analytical (for σ_i) techniques. (Root-finding to obtain t_j and c_i is used when $p \neq 2$.) The likelihood function is maximized subject to specified upper and lower bounds on each parameter, which in the case of the event parameters allows the incorporation of GT information.

We point out that with the generalized Gaussian error model, maximizing likelihood with respect to the event locations and station corrections, with the σ_i fixed, is equivalent to minimizing the data misfit function given in terms of the L_p norm of the data residuals (see Rodi *et al*., 2002).

Examples of Multiple-Event Location

We applied GMEL and our single-event grid-search location algorithm (GSEL) to events from the Izmit/Duzce earthquake sequence reported in the International Data Centre (IDC) Reviewed Event Bulletin. The data set comprised 205 events in the area of the North Anatolian Fault (NAF) within the time period 17 August 1999 (Izmit main shock) through 26 February 2000. Only P, Pg and Pn arrivals were used, which numbered 2471 at 44 International Monitoring System (IMS) stations. First, we applied GSEL to locate each event independently. Then we applied GMEL to locate the events jointly with the determination of station corrections. The corrections were bounded between -10 and 10 seconds (essentially unconstrained) and the station-dependent standard errors (σ_i) were bounded between 0.5 and 1.5. GMEL was run with both a Gaussian error model and Laplace error model ($p = 1$). Event depths were bounded between 0 and 300 km.

The results are shown in Figures 1 and 2. The improvement between single and multiple event location is most evident for events recorded at more than a few stations. To show this, the first figure displays only the 114 events with 10 or more arrivals, and the second one displays the 60 events with 15 or more arrivals. Both figures show that, compared to GSEL (top panels), the locations determined with GMEL exhibit a much more linear pattern that roughly parallels the surface expression of the North Anatolian Fault. Further, the spatial pattern of epicenters is slightly better when a Laplace error model (bottom panel in each figure) is used instead of a Gaussian error model (center panel).

We point out that, in this application, the assumption of event-independent station corrections is probably not very accurate since the event cluster has an east-west aperture of about 250 km while the closest station is within this distance of most of the events. However, the value of the multiple-event approach is still apparent; below we will discuss our efforts to relax the small-cluster restriction.

Extended Error Model

Measurements of the onset time, azimuth and slowness of seismic arrivals are subject to a number of different error processes, and often result in heavy-tailed and asymmetric residual distributions. Numerous studies of arrival times, going back to Jeffreys (1932), have tried to understand and remedy the impact these complex error processes have on the event locations. Buland (1986) and Engdahl *et al*. (1998), for example, used heavy tailed Cauchy distributions to remap phases and improve phase picks in global catalogs. However, only limited efforts have been made to incorporate distributions other than Gaussian into event location procedures, e.g. Billings *et al*. (1994), Dreger *et al*. (1998) and our current efforts with GSEL/GMEL. These efforts have all adopted the generalized Gaussian distribution, defined in equation (2), in their location procedures. While the generalized Gaussian can capture some of the complexities in picking error processes by allowing increasingly heavy tails for smaller p, it is still a symmetric, unimodal distribution that fails to capture problems of identifying the onset of low signal-to-noise signals and misidentifying secondary phases as the first arrival. Unless such phenomena are properly accounted for

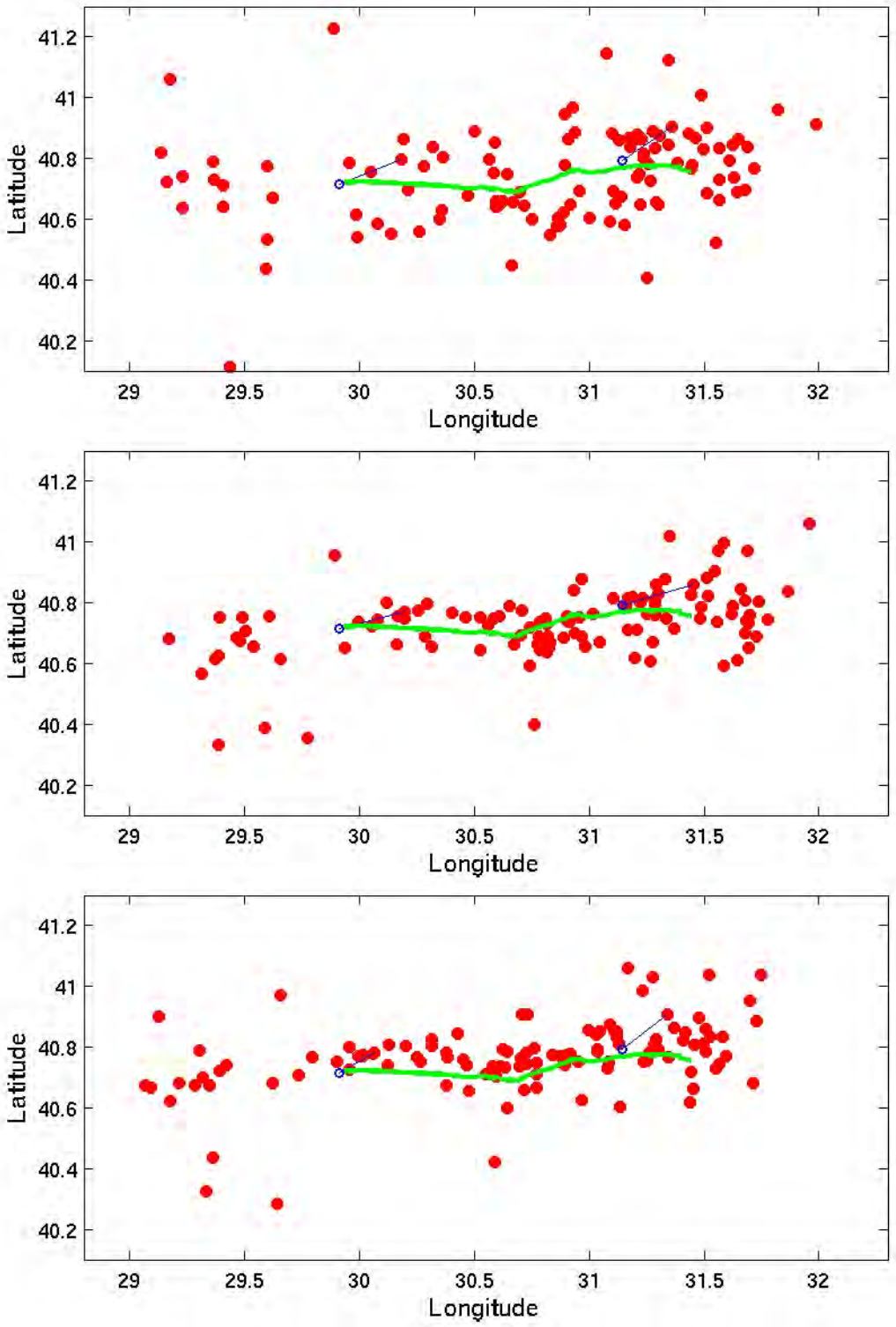

Figure 1: Locations of events from the Izmit/Duzce earthquake sequence, determined three ways. *Top*: Events located individually (GSEL). *Middle*: Multiple-event location (GMEL) with Gaussian (p = 2) error model. *Bottom*: Multiple-event location (GMEL) with Laplace (p = 1) error model. Only the events with 10 or more arrivals are shown. The continuous line is the surface expression of the North Anatolian Fault. The Izmit and Duzce mainshocks are connected to local network solutions (open circles) for these two events.

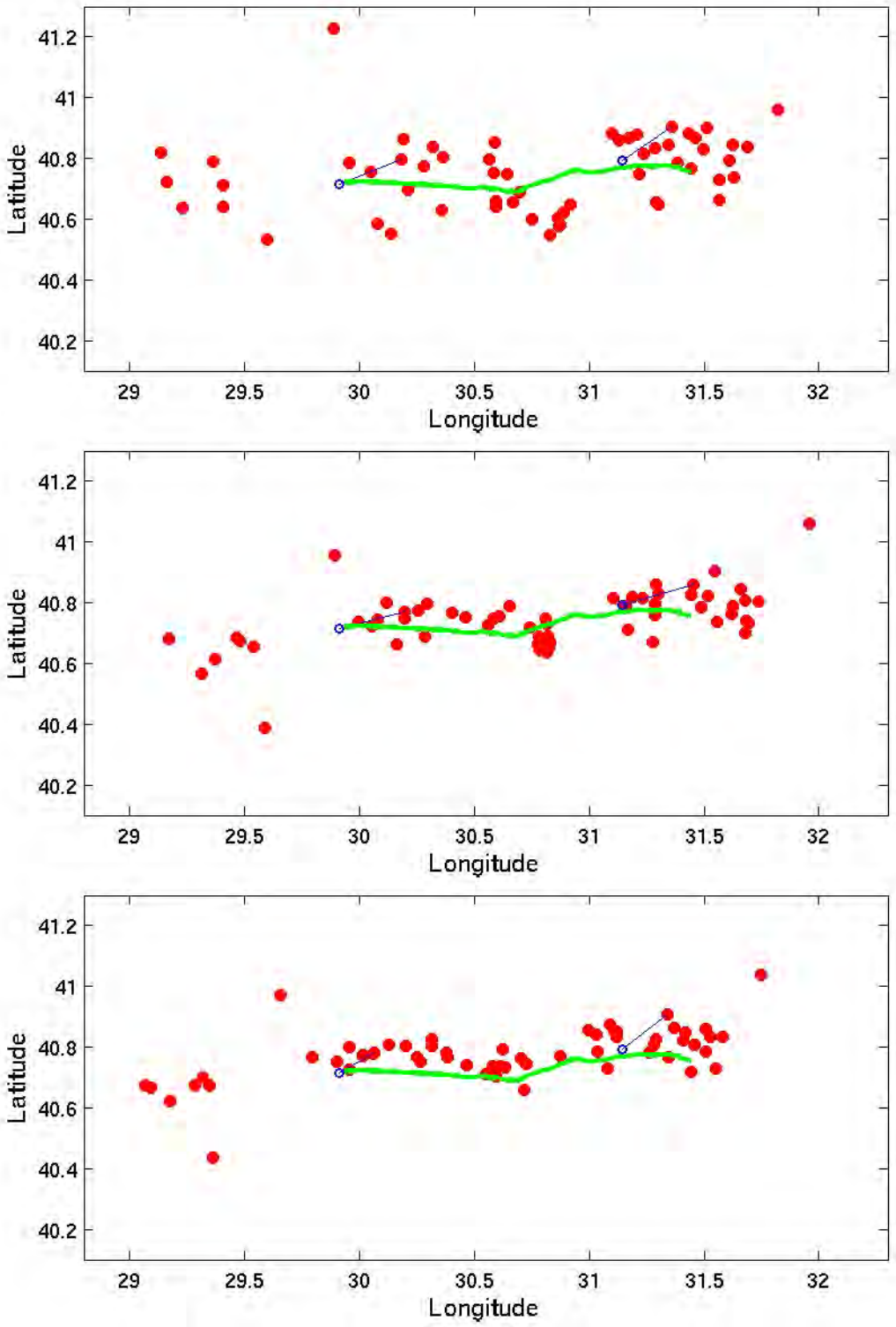

Figure 2: Locations of Izmit/Duzce earthquakes, determined three ways. This figure is the same as the preceding one except that only the events with 15 or more arrivals are shown.

in the location process, the errors in event locations obtained with sparse networks can be grossly underestimated. Figure 3 illustrates these difficulties with data from the 1991 Racha, Georgia, earthquake sequence.

In this project we are pursuing an alternative class of error distributions, first proposed by Jeffreys (1932), in which the error distribution is represented as a "mixture," or weighted sum, of Gaussian distributions having different means and variances. For K terms in the mixture, the p.d.f. of an observational error e is given by

$$f(e) = \sum_{k=1}^{K} a_k \frac{1}{\sqrt{2\pi}\sigma_k} \exp\left\{-\frac{1}{2}\left(\frac{e-\mu_k}{\sigma_k}\right)^2\right\} \qquad (5)$$

where the weights, a_k, sum to one. When the means, μ_k, differ, the distribution will be asymmetrical and allow, for example, a longer tail for positive errors (late picks) than for negative. Also, if the means differ sufficiently compared to the standard deviations, the distribution can be multi-modal.

We are currently pursuing the following tasks involved in implementing the mixture-of-Gaussians (MOG) error distribution in seismic event location. The first is the estimation of MOG distributions from observed travel-time residuals from regional and teleseismic stations. There are a variety of estimation methods that can be used for this purpose, but the most promising approaches we have identified are a variant of the expectation/maximization (EM) method (see McLachlan and Peel, 2000) and a Bayesian approach effected via a Gibbs or, more generally, Monte Carlo Markov Chain simulation (Gelman *et al*., 1995; Stephens, 1997). We are investigating these two approaches with respect to such issues as the need for good starting points, convergence rates and computational efficiency, divergence characterization (i.e., robustness of the process), and estimation error.

The second task we are pursuing is the modification of our grid-search multiple-event location algorithm (GMEL) to accept MOG error distributions. The use of MOG in place of generalized Gaussian p.d.f.s modifies the functional form of the likelihood function. While this poses no difficulty for a grid-search method, there are two issues we must deal with. One is that the root-finding procedure now used to maximize likelihood with respect to event origin times (t_j) and station corrections (c_i) must now deal with the fact that the likelihood may now be a multi-modal function of these parameters (not just the hypocenters). The second is that, while grid search already handles the multi-modality with respect to the $\mathbf{x}_j$, the possibility of local maxima will increase and the grid search may have to be that much more thorough.

Multiple-Event Location With Kriging

The assumption of source-independent station corrections restricts our multiple-event location method to events in clusters that are small compared to the distances to stations. This imposes a severe restriction on the event-station geometries that can be used in the multiple-event analysis. For example, stations too close to the cluster must be excluded and then processed separately to extract GT constraints, if an adequate local network exists for this purpose. A further restriction is that different clusters, even if they are reasonably near one another, must be processed separately, which makes it difficult to impose constraints on the spatial variability of path corrections as a function of source location.

To address these difficulties, we have formulated a generalization of the multiple-event location problem in which the path corrections are spatially variable. For example, if we replace the source-independent constraint in (4) with

$$c_{ij} = c_i(\mathbf{x}_j)\,, \qquad (6)$$

the problem then becomes a joint inverse problem of finding the m event locations and n station correction *functions* (or "surfaces"), $c_i(\mathbf{x})$. The problem of estimating station correction functions has been addressed by Schultz *et al.* (1998) with the geostatistical interpolation method known as *kriging*. However, this procedure is currently applied with the event locations fixed, and then independently for each station.

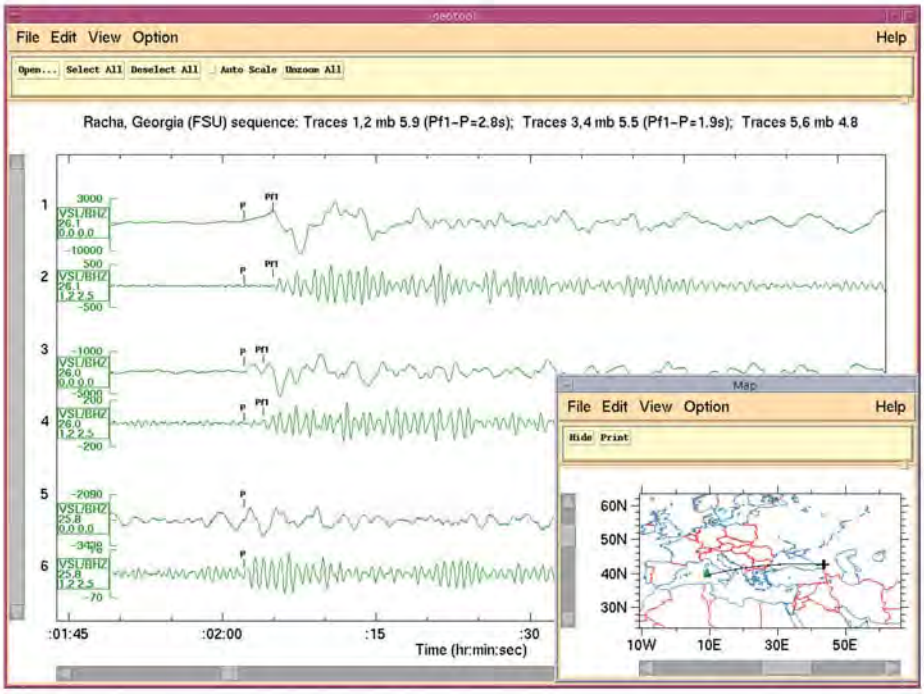

Figure 3. The Racha earthquake sequence exhibits the complex error processes in traveltime picks. This figure shows events of different magnitude filtered in different filter bands. The first two seismograms show the effect of magnitude on traveltime picks provided by a Livermore analyst. A large emergent first arrival causes about a 3 second shift from the pick on a regional event with less bandwidth. The second and third set of figures shows the misidentification of phases as the signal to noise decreases. The first smaller P phase (identified correctly for a large event) is missed on a regional event from the same source region. A secondary phase is misidentified and picked. This can lead to strong multi-modal behavior in the picking distribution and will be modeled with our technique.

Our formulation departs from the conventional kriging paradigm in the following ways. First, we define path corrections in terms of a universal correction function, or set of correction functions, which determine the path corrections for all events and stations. We also require the path corrections to obey source-receiver reciprocity. A simple example, which illustrates the concept but which may be too restrictive in practice, is to set

$$c_{ij} = c(\mathbf{y}_i) + c(\mathbf{x}_j) \qquad (7)$$

where $\mathbf{y}_i$ is the location of the ith station. The second departure from conventional kriging is to replace the minimum-variance criterion with a maximum-likelihood one. That is, we can jointly find event locations and, in the example of equation (7), a correction function $c(\mathbf{x})$, by maximizing the likelihood function already defined in our maximum-likelihood formulation. However, since the likelihood depends on only samples of $c(\mathbf{x})$, at station and event locations, it is necessary to add a term that regularizes the problem. If this term penalizes the spatial derivatives of $c(\mathbf{x})$, it imposes the equivalent constraint as the correlation function used in conventional kriging. We are currently developing the numerical techniques to perform the likelihood maximization with respect to correction functions.

CONCLUSIONS AND RECOMMENDATIONS

While we are clearly in the algorithm development stage at this point of our project, we believe we have formulated appropriate extensions of the multiple-event location method that will allow the method to be applied to less restrictive source-receiver geometries and with more realistic models of the errors in seismic arrival time data. Therefore, our approach will potentially be able to obtain references events, suitable for calibration studies, of smaller magnitude and in new source areas. We are actively developing the techniques to implement these extensions.

REFERENCES

Billings, S.D., M.S. Sambridge and B.L.N. Kennett (1994), Errors in hypocenter location: picking, model and magnitude dependence, *Bull. Seism. Soc. Am.* **84**, 1978-1990.

Buland, R. (1986), Uniform reduction error analysis, *Bull. Seism. Soc. Am.* **76**, 217-230.

Dreger, D., R. Uhrhammer, M. Pasyanos, J. Franck and V. Romanowicz (1998), Regional and far-regional earthquake locations and source parameters using sparse broadband networks: a test on the Ridgecrest sequence, *Bull. Seism. Soc. Am.* **88**, 1353-1362.

Engdahl, E.R. and E.A. Bergman (2000), Identification and validation of reference events within the area being regionally monitored by IMS stations in Asia and North Africa, *Proceedings*, 22nd Annual DoD/DOE Seismic Research Symposium, New Orleans.

Engdahl, E.R. and E.A. Bergman (2001), Validation and generation of reference events by cluster analysis, *Proceedings*, 23rd Annual DoD/DOE Seismic Research Review, Jackson Hole, Wyoming.

Engdahl, E.R., R. van der Hilst and R. Buland (1998), Global teleseismic earthquake relocation with improved travel times and procedures for depth determination, *Bull. Seism. Soc. Am.* **88**, 722-743.

Gelman, A., J. Carlin, H. Stern and D. Rubin (1995), *Bayesian Data Analysis*, Chapman and Hall, 420-438.

Jeffreys, H. (1932), An alternative to the rejection of observations, *Mon. Not. R. Astr. Soc, Geophys. Suppl.* **2**, 78-87.

McLachlan, G. and D. Peel (2000), *Finite Mixture Models*, Wiley Series in Probability and Statistics, 81--116.

Rodi, W. and M.N. Toksöz (2000), Grid-search techniques for seismic event location, *Proceedings*, 22nd Annual DoD/DOE Seismic Research Symposium, New Orleans.

Rodi, W., E.R. Engdahl, E.A. Bergman, F. Waldhauser, G.L. Pavlis, H. Israelsson and M.N. Toksöz (2002), A new grid-search multiple-event location algorithm and a comparison of methods, this volume.

Schultz, C.A., S.C. Myers, J. Hipp and C.J. Young (1998), Nonstationary Bayesian kriging: a predictive technique to generate spatial corrections for seismic detection, location, and identification, *Bull. Seism. Soc. Am.* **88**, 1275-1288.

Stephens, M. (1997), Bayesian methods for mixtures of normal distributions, Ph.D. Thesis, Mathematical Sciences, University of Oxford.

A NEW GRID-SEARCH MULTIPLE-EVENT LOCATION ALGORITHM AND A COMPARISON OF METHODS

William Rodi,[1] E. Robert Engdahl,[2] Eric A. Bergman,[2] Felix Waldhauser,[3]
Gary L. Pavlis,[4] Hans Israelsson,[5] James W. Dewey,[6] and M. Nafi Toksöz[1]

Massachusetts Institute of Technology,[1] University of Colorado at Boulder;[2]
Lamont-Doherty Earth Observatory;[3] Indiana University;[4]
Center for Monitoring Research;[5] U.S. Geological Survey[6]

Sponsored by Defense Threat Reduction Agency

Contract No. DTRA01-00-C-0102

ABSTRACT

Multiple-event location methods solve jointly for the location parameters (hypocenters and origin times) of seismic events in a cluster and travel-time corrections at the stations recording the events. This paper describes a new such method based on a grid-search approach. The algorithm (called GMEL) is an extension of an earlier single-event location algorithm (GSEL) and is based on a maximum-likelihood formulation of the location problem. By employing grid-search and root-finding techniques in lieu of a linearized inversion (Geiger's) method, GMEL accommodates non-Gaussian as well as Gaussian models of picking error and handles prior constraints such as the ground truth (GT) level of previously well-located events. We describe the algorithm and report on our efforts to extend our Monte Carlo technique for computing confidence regions on event locations, currently implemented in GSEL, to the multiple-event location problem. This extension will yield confidence regions that quantify the effects on location error of both picking errors and the uncertainty in estimated station corrections, i.e. calibration (or modeling) errors.

We report preliminary results of a test that compares GMEL and four other multiple-event location techniques: hypocentral decomposition (HDC), double differencing (DD), progressive multiple-event location (PMEL), and joint hypocenter determination (JHD). The test is being performed on two adjacent event clusters from the 1999 Izmit/Duzce earthquake sequence, previously analyzed by Engdahl and Bergman (2001) with the HDC method. We are independently applying the other methods to the data they used in an attempt to improve our understanding of the similarities and differences among these techniques and the effectiveness of the multiple-event location approach in general.

OBJECTIVE

Under the contract referenced above, we are developing a methodology for seismic event location that provides improved estimates of location uncertainty that can be used more reliably in the monitoring of small events using sparse seismic arrays. Our approach is based on a general, maximum-likelihood formulation of the location problem and implemented with computational tools such as grid-search and Monte Carlo simulation. With this approach we have been able to address such complexities as nonlinearity of the forward problem and non-Gaussian data errors.

A major objective of our project is to incorporate a more rigorous treatment of the errors in travel-time models (modeling errors) into our uncertainty analysis. Towards this goal we are attempting to link our uncertainty analysis to the calibration process, as performed with data from multiple events. Our first step has been to extend our single-event grid-search algorithm (GSEL) to a multiple-event one (GMEL). The basic task of GMEL is performed, in the Gaussian error case, by several other multiple-event location methods stemming back to the early work of Douglas (1967), Lilwall and Douglas (1970) and Dewey (1971). One part of this paper reports some collaborative work we are doing to compare these other methods and GMEL theoretically and in practice. The remainder of the paper describes GMEL itself and the approach we are developing to use it as a means of including the effects of modeling errors in location confidence regions.

RESEARCH ACCOMPLISHED

Multiple Event Location Problem

GMEL processes arbitrary data sets of seismic arrival times, azimuths and slownesses observed from multiple events for multiple stations and phases. To simplify the discussion here, we consider data sets comprising only arrival times.

We consider arrival times from m seismic events and n seismic stations. We denote the origin time and hypocenter of the jth event as t_j and $\mathbf{x}_j$, respectively. As a further simplification for this write-up, we assume there is at most one arrival time observed for each event-station pair, and denote this time as d_{ij} for the ith station and jth event. It is understood that d_{ij} exists only for a subset of the mn possibilities. The multiple-event location problem can then be written as

$$d_{ij} = t_j + T_i(\mathbf{x}_j) + c_{ij} + e_{ij} \; . \qquad (1)$$

Here, T_i is a known travel-time function for the ith station, obtained from an assumed Earth model; c_{ij} is an unknown correction to this function that accounts for differences between the real Earth and the assumed model; and e_{ij} is an observational ("picking") error.

The multiple-event location problem is to solve equation (1) for the location parameters ($\mathbf{x}_j$, t_j) of the m events jointly with the path corrections (c_{ij}). However, with no constraints on the path corrections, this problem is hopelessly ill posed. Therefore, GMEL and many previous methods assume that the path corrections at a given station are the same for all events, which is tantamount to assuming that the events are in a small cluster. In this case, we can replace c_{ij} with c_i and re-write (1) as

$$d_{ij} = t_j + T_i(\mathbf{x}_j) + c_i + e_{ij} \; . \qquad (2)$$

The problem unknowns are now the $\mathbf{x}_j$, t_j and c_i. The c_i are sometimes referred to as station corrections instead of path corrections, but it is important to realize they are dependent on the location of the event cluster.

GMEL

GMEL addresses the problem stated in equation (2) (with event-independent travel-time corrections) and solves jointly for the corrections and event location parameters. The error assumptions used are identical to those in GSEL (see Rodi and Toksöz, 2001), whereby each e_{ij} has a generalized Gaussian distribution of order p ($p = 2$ for Gaussian). In GMEL, the data standard errors, s_{ij}, are assumed known in a relative sense, such that

$$s_{ij} = s_i n_{ij} \tag{3}$$

where the n_{ij} are known, but the station-dependent scale parameter, s_i are not. The error model implies a likelihood function, L, given by

$$-\log L \;=\; \text{const} \;+\; \sum_i n_i \log s_i + \Psi(\mathbf{x}_1, t_1, \mathbf{x}_2, t_2, \ldots, c_1, c_2, \ldots) \tag{4}$$

where n_i is the number of events recorded at the ith station, and Ψ is a data misfit function. We can write Ψ as either a sum of station-specific or event-specific misfit functions, i.e.

$$\Psi = \sum_j \Psi_j^{\text{ev}}(\mathbf{x}_j, t_j, c_1, c_2, \ldots) = \sum_i \frac{1}{(s_i)^p} \Psi_i^{\text{st}}(\mathbf{x}_1, t_1, \mathbf{x}_2 t_2, \ldots, c_i) \tag{5}$$

with

$$\Psi_j^{\text{ev}}(\mathbf{x}_j, t_j, c_1, c_2, \ldots) = \sum_i \frac{1}{(s_i)^p} |\, d_{ij} - t_j - T_i(\mathbf{x}_j) - c_i|^p / (n_{ij})^p \tag{6}$$

$$\Psi_i^{\text{st}}(\mathbf{x}_1, t_1, \mathbf{x}_1, t_1, \ldots, c_i) = \sum_j |\, d_{ij} - t_j - T_i(\mathbf{x}_j) - c_i|^p / (n_{ij})^p . \tag{7}$$

GMEL maximizes the likelihood with respect to the event parameters ($\mathbf{x}_j$, t_j) and station parameters (c_i and s_i), subject to a prior upper and lower bound on each parameter. The constraints on $\mathbf{x}_j$ comprise bounds on depth and a maximum epicentral distance from some specified geographic point.

We point out that with the generalized Gaussian error model, maximizing likelihood with respect to the event locations and station corrections, with the s_i fixed, is equivalent to minimizing the data misfit, Ψ, and in the Gaussian case (p = 2) this is a nonlinear least-squares problem.

The scheme GMEL currently uses for maximizing likelihood is an iteration of a two-step process. First, fixing the station corrections and standard errors to their initial values (the average of their upper and lower bounds), each event is located in turn. This is performed by applying the single-event grid-search algorithm (GSEL) separately to each event. The second step is a loop over stations to estimate the station parameters (c_i and s_i) with the event locations fixed. As in the event loop, the stations can be treated individually. In the Gaussian case with unrestrictive prior bounds, each station correction is simply the weighted mean residual at the station, but in general GMEL uses a root-finding procedure to find the correction that minimizes Ψ_i^{st}, the data misfit function for the station. The event loops and station loops are repeated until the likelihood function stops achieving significant gains. We can summarize the GMEL algorithm as an iteration of the following:

1. For each j: minimize Ψ_j^{ev} with respect to $\mathbf{x}_j$ and t_j (with the c_i and s_i fixed)
2. For each i: minimize Ψ_i^{st} with respect to c_i (with the $\mathbf{x}_j$ and t_j fixed)
3. For each i: maximize L with respect to s_I:

$$s_i = (\Psi_i^{\text{st}} / n_i)^{1/p}.$$

Theoretical Comparison of Methods

The multiple-event location methods we compare here are

- JHD: joint hypocenter determination, version JHD89 (Dewey, 1971).
- HDC: hypocentral decomposition (Engdahl and Bergman, 2000; Jordan and Sverdrup, 1981).
- PMEL: progressive multiple-event location (Pavlis and Booker, 1983).
- DD: double-differencing (Waldhauser and Ellsworth, 2000).
- GMEL: grid-search multiple-event location.

We briefly describe the other methods in relation to GMEL. First, we note that PMEL, HDC and JHD all perform a joint least-squares inversion for event location parameters and event-independent station corrections; i.e. they minimize Ψ, defined in equations (5) through (7), with $p = 2$. DD does the same in a special case, which we will explain below. Second, we note that all of the methods except GMEL employ some sort of iterated linearized inversion algorithm for minimizing Ψ with respect to location parameters, as opposed to grid-search in the case of GMEL. The essential differences between the algorithms have to do with the order in which the unknown parameters are solved for. This potentially makes a significant difference between algorithms because of the trade-offs among the unknown parameters in the multiple-event location problem. Jordan and Sverdrup (1981) showed that, under some simplifying approximations, the inverse problem (2) does not have a unique solution in that there is a perfect trade-off between a four-dimensional projection of the station corrections and the mean hypocenter and origin time of the events. However, the relative locations amongst events and the complementary projection of the corrections can be determined uniquely, disallowing the effects of the data errors. However, relaxing their assumptions and allowing for data errors as well as possible deficiencies in the completeness of the data, the trade-offs between station corrections and event locations might be more complex.

We explained that GMEL minimizes the data misfit function with respect to the location of each event and the correction at each station in alternating loops over events and stations. JHD solves for all the parameters of all events and stations simultaneously in a linear inverse problem in which the travel-time functions, $T_i(\mathbf{x}_j)$, have been linearized about the current event locations. (The dependence on the t_j and c_i is exactly linear.) The solution of the linearized problem yields updates to event and station parameters that are added to their current values. The process is iterated, thus solving the nonlinear least-squares problem.

PMEL resembles GMEL in iterating over a two-step process, with one step updating the event locations and the other updating the station corrections. The events are relocated individually as in GMEL, but PMEL uses a conventional single-event location algorithm instead of grid search. The updating of station corrections is quite different from GMEL. PMEL solves for the c_i simultaneously in a linear system which has been pre-conditioned with an "annulling" or "projection" operator (Pavlis and Booker, 1980) that prevents the station corrections from fitting components of the travel-time residuals that can be fit with hypocenter changes on subsequent iterations. Thus, PMEL resolves trade-offs between station and event parameters in favor of the events. Since GMEL updates event locations prior to station corrections on each pass of its iteration, it also gives some preference to fitting the data with event parameters, but not as faithfully as PMEL.

HDC solves separately for the centroid location of the event cluster and the relative locations of the individual events with respect to this centroid ("cluster vectors"). It too repeats a two-step process, but again the steps are different from GMEL. The first step solves simultaneously for all the cluster vectors (relative locations) in the linear inverse problem resulting from linearizing the travel-time functions about the current absolute event locations. HDC pre-conditions this linear inverse problem in the opposite sense of PMEL; i.e., it projects out the sensitivity to station corrections, which couples the problem across events (instead of stations as in PMEL) and which gives preference to the station corrections in fitting the travel-time residuals. (Under the Jordan-Sverdrup assumptions, this preference amounts to the constraint that the cluster vectors sum to zero.) In the second step of the HDC process, the updated cluster vectors are added to the current cluster centroid to get updated absolute locations, and then updated data residuals are computed. The station averages of these residuals are used to update the cluster centroid, and any remaining average residual at each station is its station correction. These two steps are repeated in an iteration.

Of the algorithms discussed thus far, DD follows the HDC paradigm most closely, but the step of finding relative locations is quite different. It solves for the relative locations in a linearized inverse problem obtained by forming arrival time differences, at each station, between pairs of close-by events recorded by the station. Wolfe (in press) has shown that in a simple case (uniform data weighting and all possible event pairs used in the inversion) this differencing procedure is equivalent to the HDC projection technique but with an implicit station-dependent re-weighting of the data (i.e., $s_i^2 = 1/n_i$). In addition to omitting time differences for certain event pairs, another distinguishing feature of DD is that it can weight each difference in accordance with the distance between the two events. As a result of these features (omitting and distance-weighting of time differences), DD relaxes the assumption that path corrections (c_{ij}) are event-independent and, accordingly, does not precisely minimize the data misfit function, Ψ, defined above in equations (5) through (7).

The various algorithms compared here also differ with regard to two other issues: how they re-weight data during the inversion process, and how they incorporate ground truth information. It is much more difficult to compare these aspects of the algorithms, and we defer a discussion of them until a later paper. In the tests shown below, we have attempted to equalize their re-weighting schemes, and we compare only the *relative* event locations each method obtained.

Comparison of Methods Applied to the Izmit/Duzce Clusters

Engdahl and Bergman (2001) applied HDC to two adjacent event clusters comprising 34 events from the 17 August 1999 Izmit earthquake sequence and 41 events from the 12 November 1999 Duzce sequence. They used Pn and P arrival times from the US Geological Survey National Earthquake Information Center (USGS/NEIC), and ground-truth (local network) locations for a few of the events to constrain the centroid of each cluster. The HDC analysis resulted in approximately 3500 defining phases at 650 stations for the Izmit cluster, and 3200 phases at 600 stations for Duzce. The defining phases covered an epicentral distance range of 3 to 100 degrees in each case.

We have independently applied the other methods to the same arrival time data and GT information. The rules under which these tests were conducted are as follows:

- Each method must be applied to the same set of defining phases used by HDC, using the same phase associations (P vs. Pn).
- Outlier rejection cannot be used.
- Event depths must be fixed to the same depths fixed in the HDC analysis.

Here we show a subset of the results we have obtained thus far and offer a limited interpretation of these results. We show only the Duzce clusters and, with one exception, results which did not incorporate local-network (GT) constraints on the locations. The exception is JHD, which was not run without the GT constraints, but we note that the relative locations are unlikely affected since only two of the Duzce events had GT information. We will focus on relative locations and, to facilitate this, we display each solution registered to the HDC result by shifting it to have the same cluster centroid.

Figure 1 compares two GMEL solutions to the HDC solution. In one case (top panel) the data were weighted equally and the weights were not changed in the inversion. In the second case, GMEL adjusted the data variances in a station-dependent manner by setting the standard error for each station (s_I) to its r.m.s. residual, as described in the GMEL algorithm above. (However, each s_i was bounded between 0.5 and 2.0.) It is immediately noticeable from Figure 1 that the GMEL relative locations obtained with this station-dependent weighting are much closer to the HDC locations. In the bottom panel (station-dependent weighting) the GMEL and HDC relative locations differ more than 2 km for only a few events and never more than 5 km, unlike the top panel. This is because HDC used a similar method of station-dependent weighting of the data and because, apparently, how the data are weighted is an important aspect of multiple-event location in this instance.

Figure 2 compares the DD, PMEL and JHD results to the HDC result for the Duzce cluster. In these other methods, the data weighting is not the same as in HDC. Fixed, uniform weighting was used in PMEL and DD. In DD, however, some possible time differences between events were omitted (when the events were separated by more than 30 km), although the retained pairs were not distance-weighted. The JHD algorithm has a complex weighting scheme, but in this example the weights depend mainly on event-station distance and the effect of this might be roughly comparable to station-dependent weighting.

We see from Figure 2 that the other methods also produce relative locations for the Duzce events much like HDC. However, since the data weighting differs from HDC, the agreement is not as close as the second GMEL case. The JHD results (Figure 2, top) match the HDC ones quite well. The DD epicenters are not quite as close and the PMEL result shows the greatest differences from HDC. A possible reason for this is that PMEL used uniform weighting, which we saw caused significant differences from HDC in the first GMEL case. A second possible reason is that PMEL attempts to fit as much of the data as possible with event location differences. Repeating from above, this would not affect the relative locations in an ideal, noise-free case but the PMEL result suggests that it might affect them in practice. Of particular relevance to this is the fact that this test uses a very large number of stations. For the

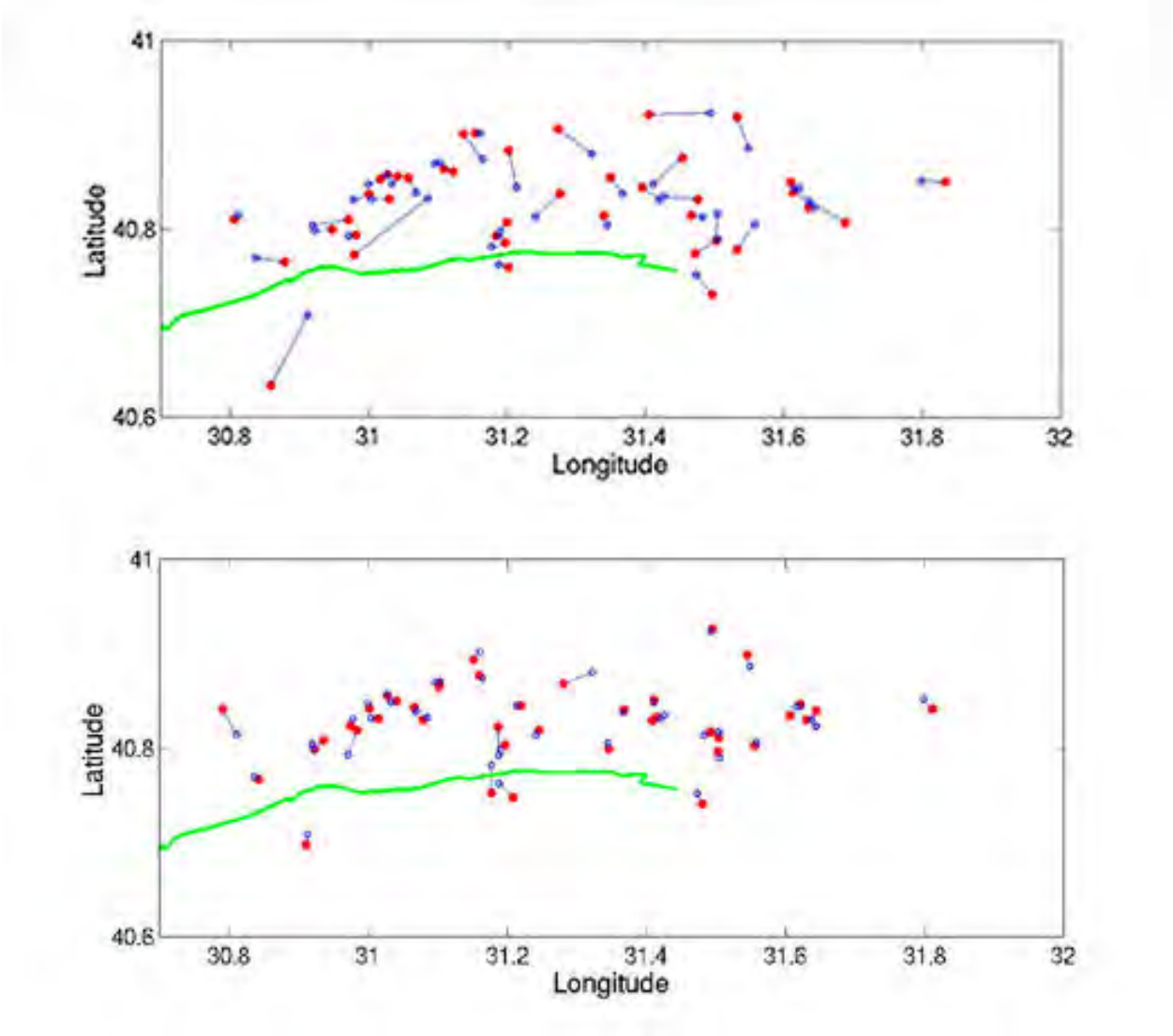

Figure 1: GMEL relative locations (filled circles) vs. HDC relative locations (unfilled) for the Duzce cluster. Two GMEL results are shown. *Top*: using fixed, uniform weighting of the data. *Bottom*: allowing a station-dependent weighting derived from the r.m.s. residual at each station. A line connects the HDC location of each event to the GMEL location of the same event. The surface trace of the North Anatolian Fault is shown for reference.

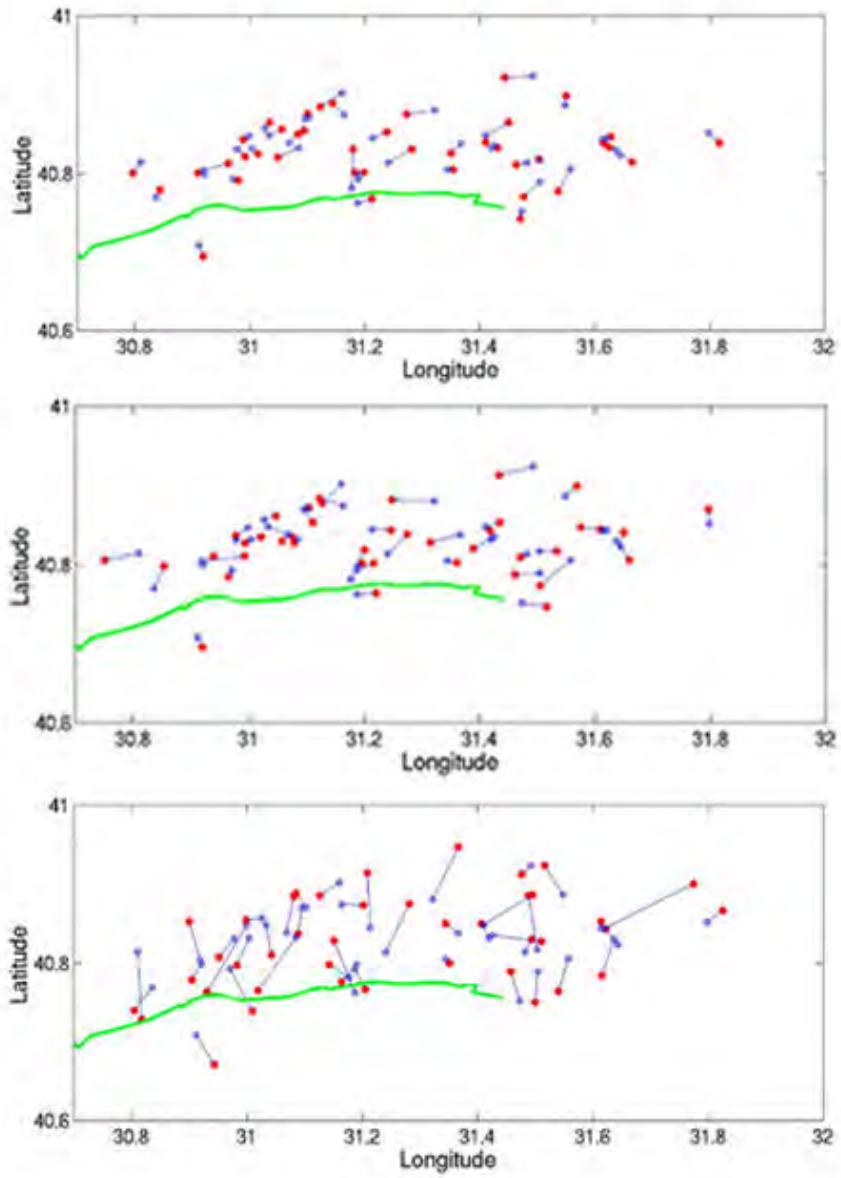

Figure 2: JHD, DD, and PMEL relative locations (filled circles) vs. HDC relative locations (unfilled) for the Duzce cluster. *Top*: JHD results, run with variable data weights. *Middle*: DD results, run with fixed, uniform data weights but with some differences omitted (see text). *Bottom*: PMEL results, run with fixed, uniform data weights.

Duzce cluster, the average number of arrivals per event is high (95) but the number of arrivals per station averages only 5.4. (The situation for Izmit is similar.) This provides the potential for trade-offs between the relative locations and station corrections.

This analysis and its conclusions must be considered preliminary since the comparisons made to date have not considered the errors (confidence regions) in the locations, which might explain some of the larger differences between methods. Since we have limited the comparisons to relative locations, we also have not considered the agreement of each method with available ground-truth locations, which is ultimately a more important test than the agreement between methods.

Confidence Regions and Modeling Errors

In Rodi and Toksöz (2000, 2001) we described a new approach to computing event location confidence regions for the single-event location problem. In the approach, the confidence region on an event hypocenter is defined as the locus of hypocenters which cannot be rejected based on a hypothesis test that compares the likelihood (L) achieved by any given hypocenter to the maximum likelihood achieved by the best hypocenter. The probability distribution of the test statistic, needed to associate a confidence level with the test, is inferred by Monte-Carlo simulation of the test statistic.

In the multiple-event problem, we seek to obtain a confidence region on an event hypocenter, say $\mathbf{x}_1$, allowing for the fact that the data depend also on the origin time of the event, the location parameters of the other $m - 1$ events, and the travel-time corrections at the n stations. All these parameters are not uniquely determined by the data, and our uncertainty approach applied to the full multiple-event system will, in principle, automatically account for trade-offs between $\mathbf{x}_1$ and these other parameters. In doing so, the confidence region on $\mathbf{x}_1$ will implicitly account for modeling errors (in this case, uncertainty in the station corrections).

To do this, we must consider two values of the likelihood function, L, given in equation (4). The first, $L_{\max}$, is the value achieved by the maximum-likelihood estimates of the parameters; i.e., L is maximized over all the station and event parameters. The second, which we define as a function of the hypocenter $\mathbf{x}_1$ and denote as $L_{\mathbf{x}_1}$, is the value achieved by maximizing L with respect to all the parameters except the hypocenter of event 1, which is fixed at $\mathbf{x}_1$. The test statistic for defining the confidence region on $\mathbf{x}_1$ is then

$$t(\mathbf{x}_1) = \log L_{\max} - \log L_{\mathbf{x}_1} \quad . \tag{8}$$

This statistic essentially compares how well the data can be fit with $\mathbf{x}_1$ fixed vs. free, with all the other parameters free to fit the data. The confidence region on $\mathbf{x}_1$ at confidence level b (e.g. b = 90%) is then given by the locus of hypocenters $\mathbf{x}_1$ satisfying

$$F[t(\mathbf{x}_1)] = b \; . \tag{9}$$

$F[\,]$ denotes the cumulative distribution function (c.d.f.) of a random variable.

The c.d.f. of t is determined by the assumed distribution of the data errors, e_{ij}. We are currently developing a Monte Carlo scheme for estimating the distribution of t. The scheme computes $\tau(\mathbf{x}_1)$ from many realizations of synthetic data generated using some assumed true parameters (event locations and station corrections) and varying samples of pseudo-random errors. Applying this approach in the multiple-event case is very computationally intensive since it involves the computation of many multiple-event inversions, one for each point $\mathbf{x}_1$ on a hypocenter grid, using the real data, and two for each realization of synthetic data. We have implemented a basic algorithm and are using it to perform a proof-of-concept of the approach while investigating computational shortcuts and approximations to make it more practical.

CONCLUSIONS AND RECOMMENDATIONS

We have developed a general theoretical and computational framework for characterizing the uncertainty in seismic event locations. At present, we are extending this framework to the multiple-event location problem in an attempt to determine event location confidence regions that rigorously account for the effects of errors in the travel-time forward model (modeling errors) in addition to observational (picking) errors. We extended our single-event grid-search location algorithm (GSEL) to a basic multiple-event algorithm (GMEL) for this purpose, and are now developing a Monte-Carlo technique for computing non-elliptical location confidence regions in the multiple-event problem.

Our comparison of GMEL to other multiple-event location methods (HDC, DD, JHD and PMEL) has helped to understand the similarities and differences among these methods, in theory and in practice. This is an important step in the development of GMEL and its new approach to location uncertainty. The initial comparison tests indicate that the different methods produce quite similar results when applied with the same data and assumptions. However, different manners of weighting the data and resolving parameter trade-offs appear to have a significant effect on the event locations determined by multiple-event location. We recommend more experiments of the type performed here, on other event clusters and data sets, to better understand these effects.

REFERENCES

Dewey, J.W. (1971), Seismicity studies with the method of joint hypocenter determination, Ph.D. Thesis, University of California, Berkeley.

Douglas, A. (1967), Joint epicentre determination, *Nature* **215**, 47-48.

Engdahl, E.R. and E.A. Bergman (2000), Identification and validation of reference events within the area being regionally monitored by IMS stations in Asia and North Africa, *Proceedings*, 22nd Annual DoD/DOE Seismic Research Symposium, New Orleans.

Engdahl, E.R. and E.A. Bergman (2001), Validation and generation of reference events by cluster analysis, *Proceedings*, 23rd Annual DoD/DOE Seismic Research Review, Jackson Hole, Wyoming.

Jordan, T.H. and K.A. Sverdrup (1981), Teleseismic location techniques and their application to earthquake clusters in the south-central Pacific, *Bull. Seism. Soc. Am.* **71**, 1105-1130.

Lilwall, R.C. and A. Douglas (1970), Estimation of P-wave travel-times using the joint epicentre method, *Geophys. J. R. Astr. Soc.* **19**, 165-181.

Pavlis, G.L and J.R. Booker (1980), The mixed discrete continuous inverse problem: application to the simultaneous determination of earthquake hypocenters and velocity structure, *J. Geophys. Res.* **85**, 4801-4810.

Pavlis, G.L, and J.R. Booker (1983), Progressive multiple event location (PMEL), *Bull. Seism. Soc. Am.* **73**, 1753-1777.

Rodi, W. and M.N. Toksöz (2000), Grid-search techniques for seismic event location, *Proceedings*, 22nd Annual DoD/DOE Seismic Research Symposium, New Orleans.

Rodi, W. and M.N. Toksöz (2001), Uncertainty analysis in seismic event location, *Proceedings*, 23rd Annual DoD/DOE Seismic Research Review, Jackson Hole, Wyoming.

Waldhauser, F. and W.L. Ellsworth (2000), A double-difference earthquake location algorithm: method and application to the northern Hayward fault, California, *Bull. Seism. Soc. Am.* **90**, 1353-1368.

Wolfe, C.J. (2002), On the mathematics of using difference operators to relocate earthquakes, *Bull. Seism. Soc. Am.*, in press.

REGIONAL WAVE PROPAGATION AND INFLUENCE OF MODEL-BASED AND EMPIRICAL SSSCs ON LOCATIONS IN AND AROUND THE INDIAN SUBCONTINENT

Chandan K. Saikia, Hong K. Thio, Gene Ichinose, and Bradley B. Woods

URS Group, Inc.

Sponsored by Defense Threat Reduction Agency

DTRA01-00-C-0033 and DSWA01-98-C-0146

ABSTRACT

The primary objective of this study was to obtain reliable locations for earthquakes occurring in and around the Indian subcontinent to provide calibration parameters for the region. To this end, we compiled regional seismic bulletins from various seismic networks that operate in the region. We used P- and S-wave travel times contained therein to relocate events that satisfy the ground truth (GT) 10 event location criterion; thereby producing a set of good quality ground truth locations. Furthermore, we have reviewed the crustal structure models published by various authors based on the P-wave travel times from earthquakes and shots, and the surface-wave dispersion. Based on this review, we were able to identify ten distinct regions representing the study area. For each region, we have also developed one-dimensional (1-D) crustal models. For many events we also compiled regional short-period and broadband waveforms from stations in India as well as the Incorporated Research Institutes for Seismology (IRIS) broadband stations outside India, for example NIL, LSA, and KMI. The broadband data were primarily used to calibrate crustal structure and develop a 1-D model. We found that the model developed this way has the ability to generate P_{nl} and surface-wave synthetic seismograms that are consistent with the recorded seismograms. Suitability of this model was examined by generating the Lg waves up to 2000-km distance and comparing them with those recorded by the broadband stations in the Indian subcontinent.

To further investigate the influence of 3-D crustal models on the locations, we have combined Laske and Mooney's crustal model of the region separately with the regionalized upper mantle (RUM) and van der Hilst tomographic models for the mantle and computed travel times for all stations that lie within 20^o of the central India, Jabalpur, earthquake of May 21, 1997, the Chamoli earthquake of March 28, 1999, the Bhuj earthquake of January 26, 2001, and a few GT10 events from northeast India. We applied the finite-difference code of Podvin and Lecomte (1991) to calculate travel times through a full 3D model with a cell size of 1.5 km on each side, thus yielding accuracy up to 0.1 sec. To accommodate a large model (consisting of an area within 20^o of a target station), we divided the model into four quadrants and ran the calculations for each quadrant separately. We also developed a quasi 3-D scheme (Saikia *et al.*, 2001) in which we calculate travel times at many receivers using 2-D cross-sections constructed from the 3-D model. We use a total of 36 cross-sections (2-D) centered on a target station or an event to represent the entire model. This quasi 3-D calculation uses 1 km x 1 km cells and runs at least seven times faster than the full 3-D model and requires 200 Mbyte of memory compared to the 3.2 Gbyte memory required by the full 3-D calculation. Both yield the same level of accuracy. The quasi-3D algorithm is more efficient than the dynamic ray tracing code currently being applied to similar problems, in run time, and also avoids the problem of rays encountering shadow zones. Analysis of the travel-time residuals between 3-D and 1-D International Association of Seismology and Physics of the Earth's Interior (IASPEI) -91 calculations and empirical residuals relative to the IASPEI-91 model compare well within several degrees, but difference are as large as -3 to +2 seconds at larger distances in some areas. Our next goal is to estimate the improvements in locations of the earthquakes by using both model-based and empirical station-specific source corrections (SSSCs). This will be examined using the criterion that error ellipses reduce significantly without the loss of 90% coverage.

OBJECTIVE

Regional path calibration is primarily dependent upon the accuracy of hypocentral locations of seismic events. An objective is to obtain regional seismic bulletins from various seismic networks that operate in and around the Indian subcontinent, augment the International Seismic Centre (ISC) database of P- and S-wave travel times, and relocate events that satisfy the GT10 event-location criterion. In this report, we shall also present results of different models developed for various regions of the Indian subcontinent. In addition, we also demonstrate a numerical approach that is useful in generating Lg waves up to 2000-km distance. Another objective of our continuing study is to investigate the influence of 3-D models on the locations of seismic events. In this regard, we will present results of travel-time differences of two models, namely CRUST2.0+RUM and CRUST2.0+van der Hilst topographic models, relative to the 1-D IASPEI-91 model. The finite-difference code of Podvin and Lecomte (1991) is used to calculate travel times through a full 3-D model. Since the desired area around the selected International Monitoring System (IMS) stations is large (up to 20^o from the station), the model is large. Therefore, the cell size becomes crucial to accurately estimate the travel times to different stations.

RESEARCH ACCOMPLISHED

Figure 1 shows GT 5-10 locations of seismic events compiled for the geographical regions in and around the Indian subcontinent. This was done by locating seismic events using P- and S-wave travel-time data available from all sources. For many events we were able to estimate depths independently of the travel-time data. That is, depths were obtained by identifying and modeling depth-related pP and sP phases in the teleseismic waveforms and broadband P_{nl} and surface waves in the regional broadband waveforms. In the process, we were also able to develop localized crustal models. The origin time and location were then estimated with a fixed depth relocation using the depths established by the above procedure. The majority of the events shown in Figure 1 are of the GT 10 quality from the aftershock sequences of the Chamoli earthquake of March 28, 1999, and the Bhuj earthquake of January 26, 2001, which have ground truth accuracy of 5 km. Some of these high-quality ground truth locations are presented in Table 1.

We developed local crustal models for several regions by inverting travel-time data from local networks. These regions include the northeastern and northwestern regions of India and the Tibetan Plateau. Figure 1 shows the locations of many aftershocks following the 28 March, Chamoli earthquake (M_w 6.8). We merged the local and regional data with the phase data collected from the portable stations deployed following the main shock (Saikia *et al*., 2001). We started with the local models and locations and iteratively inverted for a 1-D model; this was done for both with a low-velocity zone (LVZ) and one without. The model with the LVZ resulted in smaller P-wave residuals than the residuals obtained using the local model and fixed locations (Figure 2). The greatest improvement is with the crustal P arrivals within 150 km. We found that local models require only a minor adjustment in fitting the time-domain data (Figure 3).

The model developed in this manner may not fit the high-frequency Lg waves, often lacking the characteristic features, such as the duration of coda waves, of the recorded data. However, it is possible to randomize the model around an average crustal model of a given region in order to generate the synthetic Lg waves consistent with data. In a recent study, Krishna (2002) investigated the propagational characteristics of regional seismic phases in the Indian shield and used a profile of broadband waveforms recorded from the May 21, 1997, Jabalpur earthquake by the stations of the India Meteorological Department. We used the same profile and investigated if the Lg waves can be generated by implementing the random velocity model using the source parameters developed in Saikia (2000). Figure 4 shows the waveform agreement of the simulated Lg waves with those recorded at the broadband stations installed in the Indian subcontinent.

We were able to identify many crustal models in the region from other published studies (Bhattacharya, 1974; Arora and Mannekar, 1969; Chaudhury, 1976; Chun, 1986; and others). Every model published was assessed for the geographical area that were covered by the data, including redundant ones. Based on the literature review, we were able to divide the Indian subcontinent into eight regions, namely the Himalaya, Gangetic Plains, west Gangetic basin, western India, central shield, peninsular shield, northeast India and Myanmar (formerly Burma) (Figure 4). The details of these crustal models will be presented at the Seismic Research Review.

We are also developing a capability to be able to compute travel times through 3-D crustal models. Earlier we applied the finite-difference code of Podvin and Lecomte (1991) to calculate travel times through a full 3-D model with a cell size of 1.5 km on each side yielding accuracy up to 0.1sec (Saikia *et al*., 2000). In this investigation, we are applying an additional method, which is called the quasi 3-D finite-difference scheme, to estimate the effect of 3-D structure on regional travel times using the extended graph based on the shortest path algorithm (Moser, 1998). The quasi 3-D is a calculation of travel times at many receivers through 2-D cross-sections constructed from a full 3-D model, centered on the target station. We use a total of 36 2-D cross-sections at an interval of 10^o in azimuth. Each 2-D cross-section uses 1-km x 1-km cells and the entire calculation is at least seven times faster than the full 3-D calculations. To evaluate travel time at a location, the 2-D travel times of the nearest two locations are linearly interpolated. Figure 5a shows an example of travel-time (TT) residuals between the full 3-D and the IASPEI-91 1-D model. These TT residuals were computed for all stations (circles) that recorded the Jabalpur earthquake (M_w 5.7) of May 21, 1997, in central India. The calculation used the full 3-D model, which consists of Laske, and Mooney's 1998; http://mahi.ucsd.edu/Gabi/rem/html crust model on top of the van der Hilst upper-mantle tomographic model (van der Hilst *et al.*, 1997). The circles are the locations of stations for which travel times of P waves were reported in the ISC and local bulletins. Each circle is filled with color indicating the TT residuals between the recorded arrival times and travel times computed for the IASPEI-91 model. Any similarity in color-coding within the circle to its background indicated that the 3-D structure model is adequate for explaining the recorded travel times.

Also, note that the area encompassed in our calculation is large and was not practical to fit in the entire model in a single 3-D run with a cell size of 1.5 km on each side of the cube. A larger cell size will allow the incorporation of the entire model, but with increasing travel-time error. To keep the accuracy within 0.1sec, we therefore computed travel times for four sub-models, thus one model for each quadrant. This calculation required a memory of 3.2 Gbyte for each model and run time was about 180 minutes. Figure 5b shows the same TT residuals computed using the quasi 3-D method rather than the full 3-D model. In this calculation we used a curved grid that required only 200 Mbyte of memory. Each run required about three minutes and the entire calculation required about 108 minutes. These requirements make this quasi 3-D method very useful in computing travel times up to a large epicentral distance. In run time, the quasi 3-D algorithm is more efficient than the dynamic ray tracing code currently being applied to similar problems and also avoids the problems associated with the rays encountering the shadow zones.

We have also implemented the RUM model (Gudmundsson and Sambridge, 1998) by replacing the upper mantle tomographic model of van der Hilst. The RUM model has additional complexity introduced for the dipping slab structures. The RUM model parameterization is different from the tomographic model and warranted additional effort.

Figure 6a shows the quasi 3-D model residual variation with distance from the IASPEI-91 model. Figure 6 (b, c) shows two cross-sections showing the travel-time residuals of the RUM and van der Hilst models relative to the IASPEI-91 model. The short-wavelength variations seen in these calculations are primarily due to the crustal corrections from the CRUST2.0 models, whereas the longer wavelength anomalies (at great distances) are the results of both the crust as well as the mantle models.

Our main goal is to estimate the improvements in locations of the earthquakes by using both model-based and empirical SSSCs based on the principle that error ellipses reduce significantly without the loss of 90% coverage.

CONCLUSIONS AND RECOMMENDATIONS

We have completed development of regionalized crustal models in various regions of the Indian sub continent. These models can be used to compute travel times from different earthquake sources in the region using the technique presented by Bondar (Group B Oslo Workshop). We have also developed a list of ground truth events that will be useful for the calibration of the velocity model of the region. In Figure 1, we have shown locations of events that are of GT10 quality, or better. Many other events satisfy the criterion of GT25 events. The goal should be to refine locations of these GT25 events to the location accuracy of GT10 events. We expect the quasi 3-D approach will permit computing SSSCs reliably up to large epicentral distances (90^o) for the GT10 events in the region, and SSSCs so constructed will permit improvements to the location quality of the GT25 events.

ACKNOWLEDGEMENTS

We acknowledge many scientists from the Indian subcontinent and its neighboring regions, who shared their scientific knowledge.

REFERENCES

Arora, S. K. and A. M. Mannekar (1969). Precise determination of epicenters and origin times of surface focus seismic events, *Bull. Seis. Soc. Am*., **69**, 777-788.

Bhattacharya, S. N. (1974). The crust-mantle structure of the Indian peninsula from surface wave dispersion, *Geophy. J. Royal Astr. Soc*., **36**, 273- 283.

Chaudhury, H. M. (1969). Dispersion of short-range surface waves and the surficial layer in the region west of Delhi, *Indian J. Meteorological Geophy*., **17**, 385-394.

Chun, K-Y. (1986). Crustal block of western Ganga basin: A fragment of ocean affinity? *Bull. Seis. Soc. Am*., **76**, 1687-1698.

Gudmundsson, O. and M. Sambridge (1998). A regionalized upper-mantle (RUM) seismic model, *J. Geophys., Res*. **103**, No. B4, 7121-7136.

Krishna, V. G. (2002). Propagation of regional seismic phases in the Indian shield: Modeling for crustal and upper mantle velocity structure, *Bull. Seis. Soc. Am.*, (in review).

Mooney, W., G. Laske, and G. Master (1998). A global crustal model at 5x5^{o}, *J. Geophys. Res*., **103**, 727-747.

Moser, T. J. (1989), Efficient seismic ray tracing using graph theory, Soc. Exploration Geophys., 1990 Meeting, Expanded abstract, pp1106-1108, SEG, Tulsa, OK.

Podvin, P. and I. Lecomte (1991). Finite-difference computation of travel times in very contrasted velocity models: a massively parallel approach and its associated tools, *Geophys. J. Int*., **105**, 271-284.

Saikia, C. K. (2000). A method for path calibration using regional and teleseismic broadband seismograms: Application to the May 21, 1997 Jabalpur India earthquake (Mw 5.8), *Current Science*, Vol 79, No. 9, 1301-1315.

Saikia, C. K., H.-K. Thio and B. B. Woods (2000). Path calibration studies in and around the Indian subcontinent, Proceed. 22nd Seismic Research Symposium, 135-143.

van der Hilst, R. D., S. Widyantoro, and E. R. Engdahl (1997). Evidence for deep mantle circulation from global tomography, *Nature*, **386**, 578-584.

Table 1. Ground Truth Locations for Earthquakes in and around India

Date	hr:mn:ss	latitude	longitude	depth	mag	Region	
02/11/2001	02:33:20.6	23.366	70.576	19.9	4.0	Bhuj	GT5
02/11/2001	15:29:44.8	23.357	70.325	15.0	4.4	Bhuj	GT5
02/15/2001	10:04:42.4	23.371	70.362	15.0	4.8	Bhuj	GT5
02/19/2001	02:11:15.8	23.574	70.164	15.0	-.-	Bhuj	GT5
02/19/2001	08:24:19.7	23.597	70.229	1.0	5.1	Bhuj	GT5
05/21/1997	22:51:31.0	23.040	80.153	35.0	5.8	Jabalpur	GT10
06/04/1997	19:29:43.6	23.0283	80.1826	22.4	4.2	Jabalpur	GT10
03/28/1999	19:47:08.10	30.299	79.333	18.9	4.7	Chamoli	GT10
03/29/1999	08:49:47.00	30.301	79.302	9.8	4.3	Chamoli	GT10
04/06/1999	19:37:26.10	30.409	79.394	9.6	5.1	Chamoli	GT10
04/06/1999	20:46:42.10	30.413	79.406	7.3	4.6	Chamoli	GT10
04/07/1999	15:49:15.6	30.396	79.394	12.0	4.8	Chamoli	GT10
04/07/1999	16:23:30.0	30.471	79.319	11.0	4.4	Chamoli	GT10
08/29/1990	20:41:34.33	27.1763	92.7354	25.4	4.7	NE India	GT10
09/02/1990	06:29:26.05	26.5819	92.6700	57.3	4.6	NE India	GT10
06/23/1991	10:04:01.72	26.5883	93.1862	45.6	4.5	NE India	GT10
03/05/1996	09:27:37.30	26.434	92.935	49.6	4.0	NE India	GT10
05/14/1996	19:05:32.00	26.502	92.148	32.8	4.5	NE India	GT10
08/04/1996	13:51:32.6	26.452	93.186	43.4	4.3	NE India	GT10
11/19/1996	10:37:52.2	26.478	93.292	46.1	4.0	NE India	GT10
11/24/1996	00:52:11.80	26.859	92.685	43.1	4.2	NE India	GT10

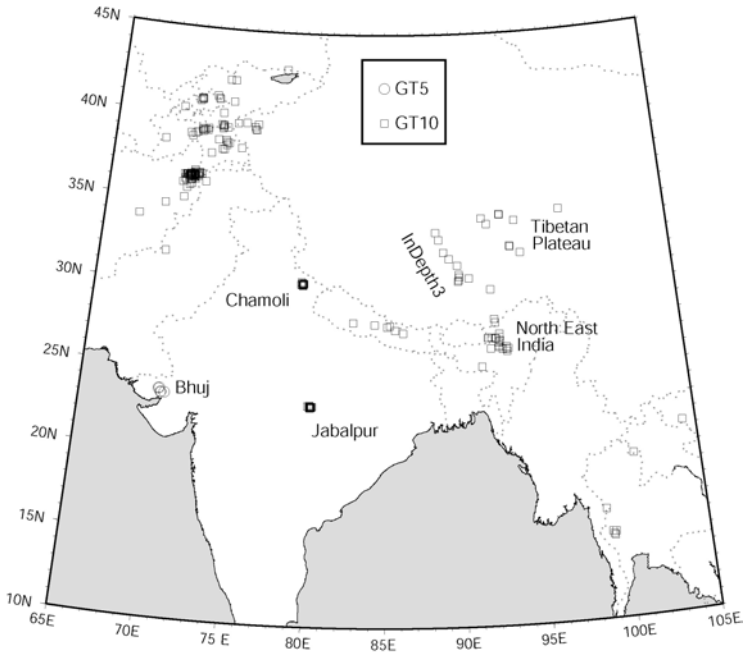

Figure 1. Map showing locations of a subset of ground truth events in and around the Indian subcontinent. The events shown by the boxes correspond to (GT)10 accuracy level and those by circles to (GT)5 accuracy level. The earthquakes were relocted using travel-time data from the local networks operating in the regions. The (GT)5 events were recorded by more than 15 stations surrounding the events within 50 km.

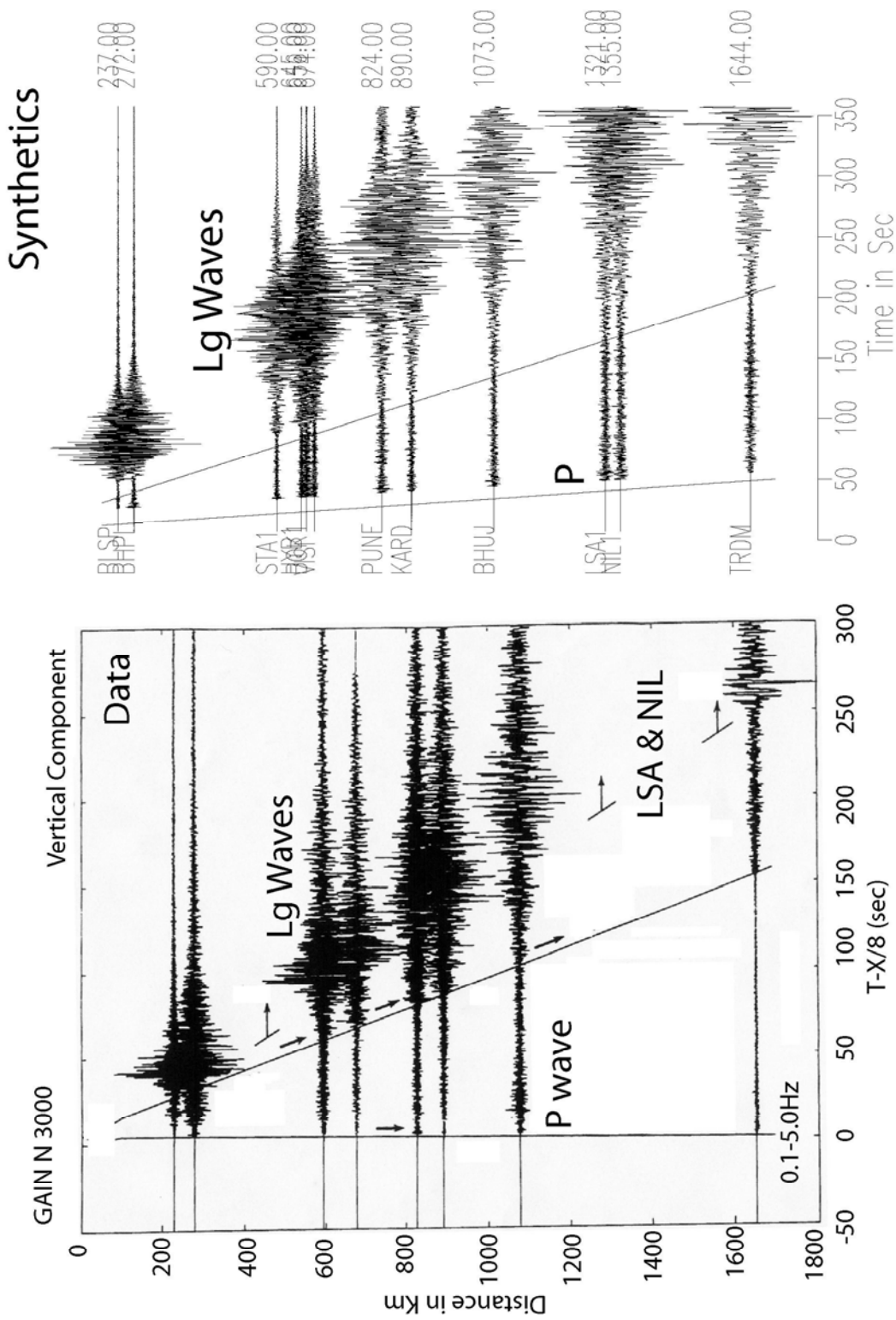

Figure 4. Lg waves as recorded by the broadband stations operated in the Indian Peninsula by India Meteorological Department (IMD). Left panel shows the data profile and on right is displayed the simulated Lg waves using laminar crustal model as discussed in Saikia (1994), a technique which was used successfully to model Lg waves recorded by the ECTN stations in eastern North America.

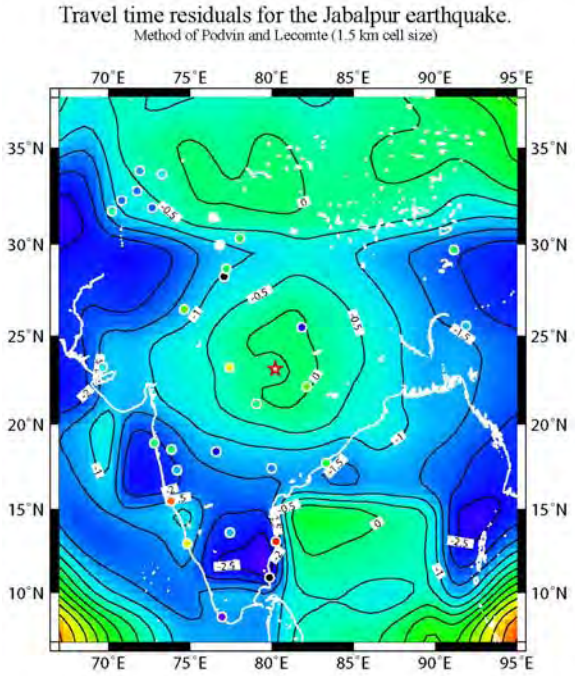

Figure 5a Theoretical travel time residuals computed for the Jabalpur earthquake based on the tomographic model of van der Hilst overlain by the crustal model of Laske and Mooney. The circles represent observed travel-time residuals, with the same color coding as the theoretical residuals. All residuals with respect to the Iaspei model. The theoretical residuals were computed using the method of Podvin and Lecomte (1991).

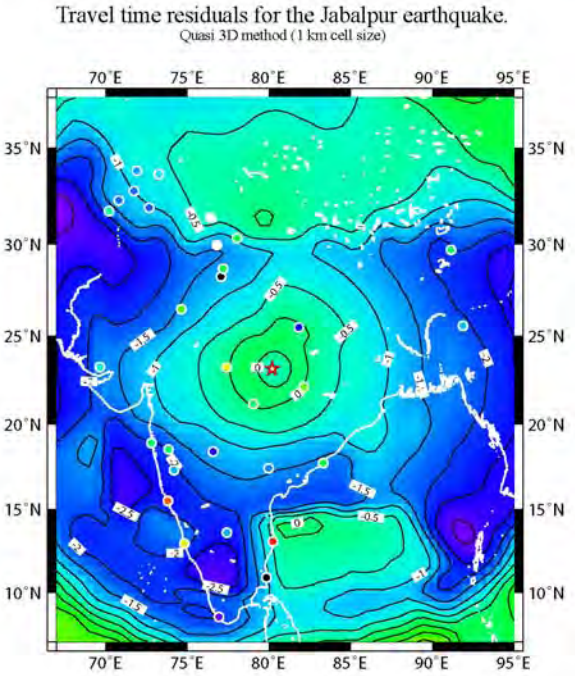

Figure 5b Theoretical travel time residuals computed for the Jabalpur earthquake based on the tomographic model of van der Hilst overlain by the crustal model of Laske and Mooney. The circles represent observed travel-time residuals, with the same color coding as the theoretical residuals. All residuals with respect to the Iaspei model. The theoretical residuals were computed by interpolating 36 2D residuals sections radiating out from the epicenter.

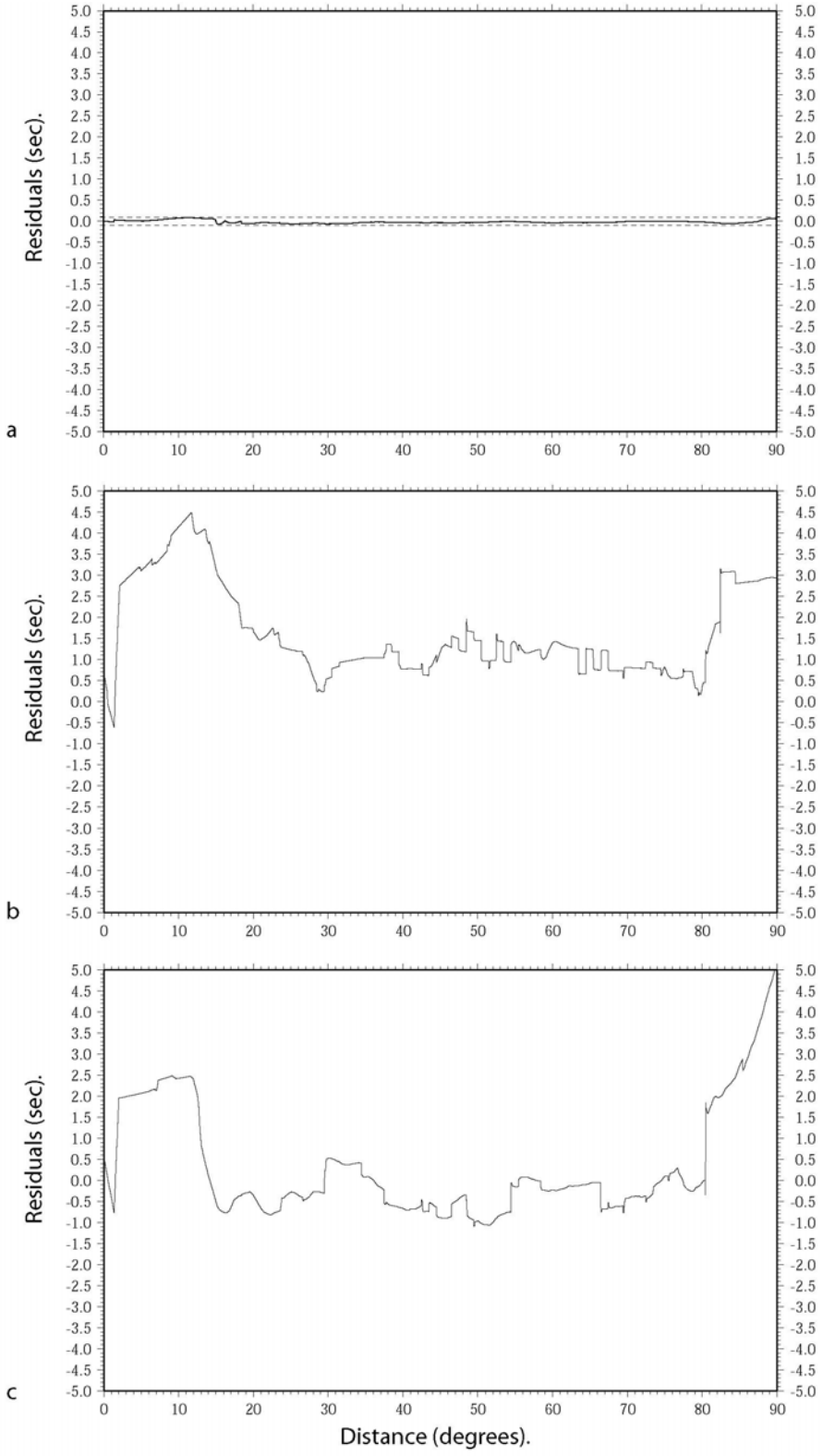

Figure 6. Traveltime residuals with respepct to tabulated IASP91 times as a function of distance from NIL at an azimuth of 20¡ for a - 1D model (IASP91 computed using the sortest-path algorithm), showing the ±.1 sec. interval with dashed lines, b - RUM/Crust2.0 and c - Vanderhilst/Crust5.1.

GROUND TRUTH LOCATIONS - A SYNERGY OF SEISMIC AND SYNTHETIC APERTURE RADAR INTERFEROMETRIC METHODS

C. K. Saikia,[1] R. Lohman,[2] G. Ichinose,[1] D. V. Helmberger,[2] M. Simons[2]and P. Rosen[3]

URS Group, [1] California Institute of Technology, [2] and Jet Propulsion Laboratory[3]

Sponsored by Defense Threat Reduction Agency

Contract Number DTRA01-00-C-0072

ABSTRACT

The primary objective of this study is to obtain reliable locations of moderate-sized ($4<M_w<6$) earthquakes in parts of Asia and the Middle East. The study is aimed at delivering a ground truth (GT) database consisting of locations, processed InSAR (Satellite Synthetic Aperture Radar Interferometry) phase and ground deformation maps for the general seismological community. We have developed combination of effective approaches to invert global travel-time phase data to obtain accurate locations. To this end, we have selected all events from the International Seismic Centre (ISC) bulletin that satisfy both GT10 and GT25 criteria and collected their phase data. From this entire event population, we selected a small set of events, estimated hypocentral depths by modeling the teleseismic depth phases and computed maps of surface deformation using software developed at USGS (United States Geological Survey) based on the equations of Okada (1992), which assumes an elastic half-space model. We are currently developing a code to include layered crustal model based on the frequency-wave number algorithm (Saikia, 1994). Surface deformation was computed to determine whether moderate-sized events that have larger depths (>10 km) would be resolvable in the processed InSAR interferograms, thus reducing the cost of radar data. We are currently processing the InSAR raw images obtained from EURIAMGE.

We present results obtained for one Southern Iran event (99/04/30, origin time:04h:20m:22.8s, 27.837^{o}N and 53.588^{o}E, 36km, M_w 4.9). We constructed two geocoded interferograms using images for track 20, frame 3051 (99/04/21-99/05/26) and for track 249, frame 3051 (99/04/02-99/06/11), respectively, by removing the topography (using a digital elevation model), filtering and unwrapping the phase. Note that these tracks include time period for at least three events occurring on the 28th and the 30th April and the 6th May of 1999 in Southern Iran. Of these, the third event is actually at more than a hundred miles from the track locations and is the largest (m_b~5.3). It is unlikely that the 05/06/99 event contributed to the interferograms because of its distance from the track. The remaining events are deep (h>30 km), and the 30th April event is larger. The geocoded interferogram show some earthquake deformation at 27.87^{o}N and 53.61^{o}E as a bulls eye of around two interferometric fringes. Both images have many elongated patterns throughout, but they correlate with the topography and have a much lower contribution to the interferograms than does the earthquake signal. The InSAR location is further away from the Harvard (27.74^{o}N, 52.96^{o}E), ISC and USGS (27.837^{o}N, 53.538^{o}E) locations and all have estimated depths that cannot lead to surface deformation to be discernable in the interferograms. This indicates that the contributing event is shallower (about 4 km) than the reported depths. To further ascertain the depth, we collected seismograms from all available stations. It was recorded at many stations, including those from temporary PASSCAL experiments. Of these, we compared seismograms from stations RAYN and ATD against a large shallow Southern Iran event (98/11/13, h=9 km, M_w=5.3). By analyzing seismograms from the April 30, 1999, and November 13, 1998, events we noted a high correlation in the different seismic wave groups, namely the P_{nl}, surface and high frequency Lg coda (>1Hz) waves. In addition to the amplitude, there is a good correlation in the travel times of these phases relative to their onset for the two events, indicating that the April 30 event (or the 28th event) is indeed shallow. We are now extending this analysis to other events in our study area and since many of the events are from the mountain regions, our analyses would also require high-resolution digital terrain elevation data.

OBJECTIVE

The goal of this ongoing study is to obtain reliable locations for moderate-sized ($4<M_w<6$) earthquakes in parts of Asia and the Middle East. This study will deliver a ground truth database consisting of locations, location errors, source parameters, associated waveform data, raw satellite synthetic aperture radar interferometry (InSAR) images, processed InSAR phase maps and ground deformation maps to the Center for Monitoring Research and the national laboratories. We will also provide these products to the general seismological community as well.

The basic goal of this study is improving of event locations that apparently satisfy the criterion of (GT)25 (e.g., Yang *et al*., 2000) for earthquakes which occurred in this study region to within an accuracy of (GT)10. To accomplish this goal, we developed a combination of approaches to invert global travel-time phase data to obtain accurate locations that prove effective (Saikia and Ichinose, 2001). This study also utilizes InSAR to locate shallow ($h<10$ km) and moderate-sized earthquakes for validating ground truth locations to within the level of 5 km location accuracy. We intend to determine the ground truth locations and fault parameters by modeling co seismic deformation observed from the processed InSAR images for comparison with prediction from seismology, which is an emerging technique. The final task is to combine the seismic and geodetic results to validate the GT locations. GT locations determined from InSAR will be used to develop station corrections for upper-mantle phase arrivals which in turn will be useful for relocating earthquakes within the magnitude range of ($4<M_w<5$) that are often recorded in this region by more than 30 stations within a distance of 20^o and with a maximum azimuthal gap of 90^o.

RESEARCH ACCOMPLISHED

The combination of InSAR and seismic data has a potential that remains relatively unexploited. Synthetic aperture radar interferometry developments have recently found applications to providing independent and ground-truth information based on ground surface deformation (e.g., Peltzer and Rosen, 1995; Feigl *et al.*, 1995; Massonnet, D., and K. L. Feigl, 1998; Lohman and Simons, 2000). Steck *et al*. (2000) used InSAR data to remove a location bias of 20 km for the relocation of the 1997 Tibetan mainshock (M_w 7.5). Correlating the co seismic fringe pattern derived from the InSAR data with hypocenter locations can be tricky because the centroid location may not necessarily coincide with the rupture initiation location for large earthquakes. Therefore, it is essential to concentrate on moderate-sized events (M_w~5) in order to reduce uncertainty in location due to the fault size. Earlier we investigated locations established through several InSAR analyses for earthquakes in various tectonic environments and compared with the locations determined by seismic methods using various strategic approaches (Saikia and Ichinose, 2001). In a continuing effort, we found that for earthquakes of Dec 12, 1992, Lander aftershock (M_w 5.4), June 29, 1992, Little Skull Mountain (M_w 5.6), Sept 07, 1999, Athens (M_w 5.9) and May 7, 1993, Eureka (M_w 6.1) it was possible to recover the seismic location within 10 km of the InSAR location. However, there is uncertainty in the location of the rupture initiation relative to the location proposed from the InSAR analysis for the two larger earthquakes. To this end, we have examined geodetic deformation and complexities in the teleseismic waveforms of a large earthquake (M_w 6.4) to check viability of a procedure that may be able to overcome this problem. In the following, we shall present preliminary results from this procedure.

To reduce the cost of radar data, we selected a small set of (GT)10 events spanning over the entire study region and depths down to 18 km. For each of these events, depths were estimated by modeling the pP and sP depth phases (Figure 1). We also computed the associated coseismic deformation using software developed at USGS (United States of Geological Survey) to ensure that the earthquakes are likely to cause some seismic deformation that will be recorded in the radar data. Next, we looked for tracks and frames for the radar data with small baseline (B). It is essential that B is small; otherwise there may be a lot of unwanted distortion in the phase interferogram, especially in a young tectonic regions (Rosen *et al*., 2000).

We studied a small event occurred in southern Iran on April 30, 1999 (see Table 1). Two geocoded interferograms were constructed using images for track 20, frame 3051 (99/04/21-99/05/26) and for track 249, frame 3051 (99/04/02-99/06/11), respectively, by removing the topography (using a digital elevation model, DEM), filtering and unwrapping the phase. Figure 2 shows the final phase interferogram where the earthquake can be seen to the upper right of the image at 27.89^oN and 53.62^oE as a bulls eye of around two interferometric fringes. The elongated pattern throughout these images correlates with the topography of the region of higher resolution. A further modeling of the InSAR amplitude indicated a shallow depth of 4 km for this event. The time between the first track

and last track included at least two other events occurring on the 28th April (18h:18m:18.8s, h=77km, m_b=4.5) and 6th May of 1999 (23h:00m:53.1s, 33km, m_b=5.9) in the vicinity of the 30th April event. The later event is too far away from the track locations to have contributed to the geodetic signal. Figure 3 shows a comparison of the uncorrected waveforms of events on the 28th and 30th recorded at a station RAYN in Saudi Arabia. The waveforms of the two events are remarkably similar indicating that the source mechanisms of the two events are similar. The peak amplitude is somewhat smaller for the 28th event. All reporting agencies indicated that these events are deep. Therefore, we compared its waveform with another event that occurred on 11/13/98 at the same location and depth of about 9 km (Figure 4). Figure 5 shows a comparison of waveforms between the events of 11/13/98 and 04/30/99 at RAYN at two frequency bands. The broadband displacement comparison shows strong Rayleigh waves on the 04/30/1999 event indicating that this event is shallower than event of 11/13/98. The longer duration of the high-frequency Lg waves for the 04/30/99 event also suggests that the event is more shallower than the 11/13/98 event.

Table 1 shows that the HRV location is the worst as it is about 65 km away from the InSAR location. We have also relocated this event using travel-time data and the constraints that depth is either free or fixed at 4 km. The location determined for the case when the depth is free, is about 3 km from the InSAR location. The location deteriorated when the depth was fixed by a mislocation of about 14 km. The USGS location remains within 10 km from the InSAR location. Finally, the event was fixed at the InSAR location and depth, and the best origin time was estimated (Table 1).

We finally present an indirect procedure which may be useful in recovering the hypocenter of a large magnitude earthquakes (M_w~6.5). The panel (b) of Figure 6 shows the slip model established for the Chi-Chi aftershock (Mw 6.4) by putting the hypocenter (shown by the star) in the upper left. We calculated theoretical InSAR data along the line of sight (panel c) using this slip model and hypocenter. Next, we reversed the problem and used this InSAR data shown in panel (c) and the teleseismic waveform as only the known data to invert for the hypocentral location. We divided the fault surface into many subfaults and varied the hypocenter location on the fault surface. For each hypocenter location, we estimated the misfit in teleseismic waveforms and the InSAR deformation (panel a). This misfit information was used to recover the original hypocenter location which is the star in panel (c). Our next step is to apply this approach to the some large earthquakes, such as the Eureka Valley earthquake of 05/17/1993 (Mw 6.0).

CONCLUSIONS AND RECOMMENDATION

Finding accurate ground-truth locations for earthquakes in areas where seismic network stations are sparse is often difficult because of the poor azimuthal station coverage. There may often be other logistical difficulties in accessing the local earthquake catalog. The InSAR analysis allows avoiding this shortcoming. The success with the 04/30/99 southern Iran earthquake demonstrates that seismic events can be located with a high level of accuracy through a synergy of InSAR and seismological methods that was illustrated by Saikia and Ichinose (2001). The only requirements are that the selected events are preferably shallow (say, h<10km) and have low magnitudes (M_w < 5.5). The low magnitude is preferred to minimize any uncertainty that may otherwise exist in case of the large magnitude earthquakes due to their large fault dimensions.

When the depth was known, the Iranian event was mislocated by 14.6 km relative to InSAR location, assumed as the ground truth location. On the other hand, when the depth was free, its location was off only by 3 km, suggesting that the earthquake location using the travel-time data alone is a highly non-linear process. Even the relative errors in the locations of the reference events can propagate systematic errors into the locations of other events. Therefore, ground truth locations based on the InSAR analysis are needed to evaluate the performance of any location scheme.

We have acquired SAR data of other earthquakes and the processing of data. In our continuing investigation to identify ground deformation in the InSAR images suggests that a high-resolution DEM model is essential for the SAR analysis to be successful in the area of our interest, especially in regions where ground surface topography is strong.

Large earthquakes often occur at shallow depth (h<15 km) and some leave extensive ground deformation. So far, they are not considered suitable for the purpose of ground truth locations because of the large extent of the fault dimensions and variability of the hypocenter location on the fault surface. Our on-going work on the Chi-Chi

aftershock and future plans to apply the approach to known large events for which geodetic signals have already been processed are aimed at avoiding these drawbacks.

ACKNOWLEDGEMENT

We thank our colleagues in EURIMAGE for making the radar data available to us urgently for this study.

REFERENCES

Feigl, K. L., A. Sergent, and D. Jack (1995). Estimation of an earthquake focal mechanism from a satellite radar interferogram: Application to the Dec 4, 1992 Landers aftershock, *Geophys. Res. Lett.*, **22**, No. 9, 1037-1040.

Lohman, M., and M. Simons (2000). Interferometric synthetic aperture radar imagery of the June 29, 1992, Little Skull Mountain earthquake, *EOS Trans. AGU,* **90** *Fall Meeting Suppl.*

Massonnet, D., and K. L. Feigl (1998). Radar Interferometry and its application to changes in the Earth's surface, *Rev. Geophys.* **36**. No. 4, 441-500.

Peltzer, G., and P. A. Rosen (1995). Surface displacement of the 17 May, 1993 Eureka Valley, California, earthquake observed by SAR Interferometry, *Science*, **268**, 1333-1336.

Rosen, P. A., S. Hensley, I. R. Joughin, F.K.Li., S. N. Madsen, E. Rodriguez, R. M. Goldstein (2000). Synthetic Aperture Radar Interferometry, *Proceed. of the IEEE*, **88**, No. 3, March.

Saikia, C. K., and G. Ichinose, and C. Ji (2001). Seismic event location strategy and path calibration in and around Indian subcontinent, Proceed. 23rd Seism. Res. Rev., Worlwide Monitoring of Nuclear Explosions , October 2-5, 2001, Jackson Hole, Wyoming

Steck., L. K., A. A. Velasco, A. H. Cogbill, and H. J. Patton (2000). Improving regional seismic event location in China, *Pure and Applied Geophysics* (in press).

Yang, X., I. Bondár, and C. Romney (2000). PIDC ground-truth event (GT) database (revision 1). CMR Technical Report CMR-00/15.

Table 1. Location Parameters for April 30, 1999 Southern Iran Earthquake

Date d/m/y	**Origin Time Hr:mn:ss**	**Latitude (N deg)**	**Longitude (E deg)**	**H (km)**	**ΔR (km)**	**Agency**
04/30/99		27.870	53.610			INSAR
04/30/99	04:20:02.0	27.765	53.519	33.1	14.68	ISC (MOS)
04/30/99	04:20:22.5	27.837	53.538	35.0	7.0	USGS
04/30/99	04:19:59.6	27.748	53.553	4.0 (F)	14.6	URS
04/30/99	04:20:05.4	27.866	53.576	45.0	3.04	URS
04/30/99	04:20:12.5	27.74	52.960	44.9	65.65	HRV
04/30/99	**04:20:0.1**	**27.870 (F)**	**53.610 (F)**	**4.0 (F)**		**Seis+INSAR**

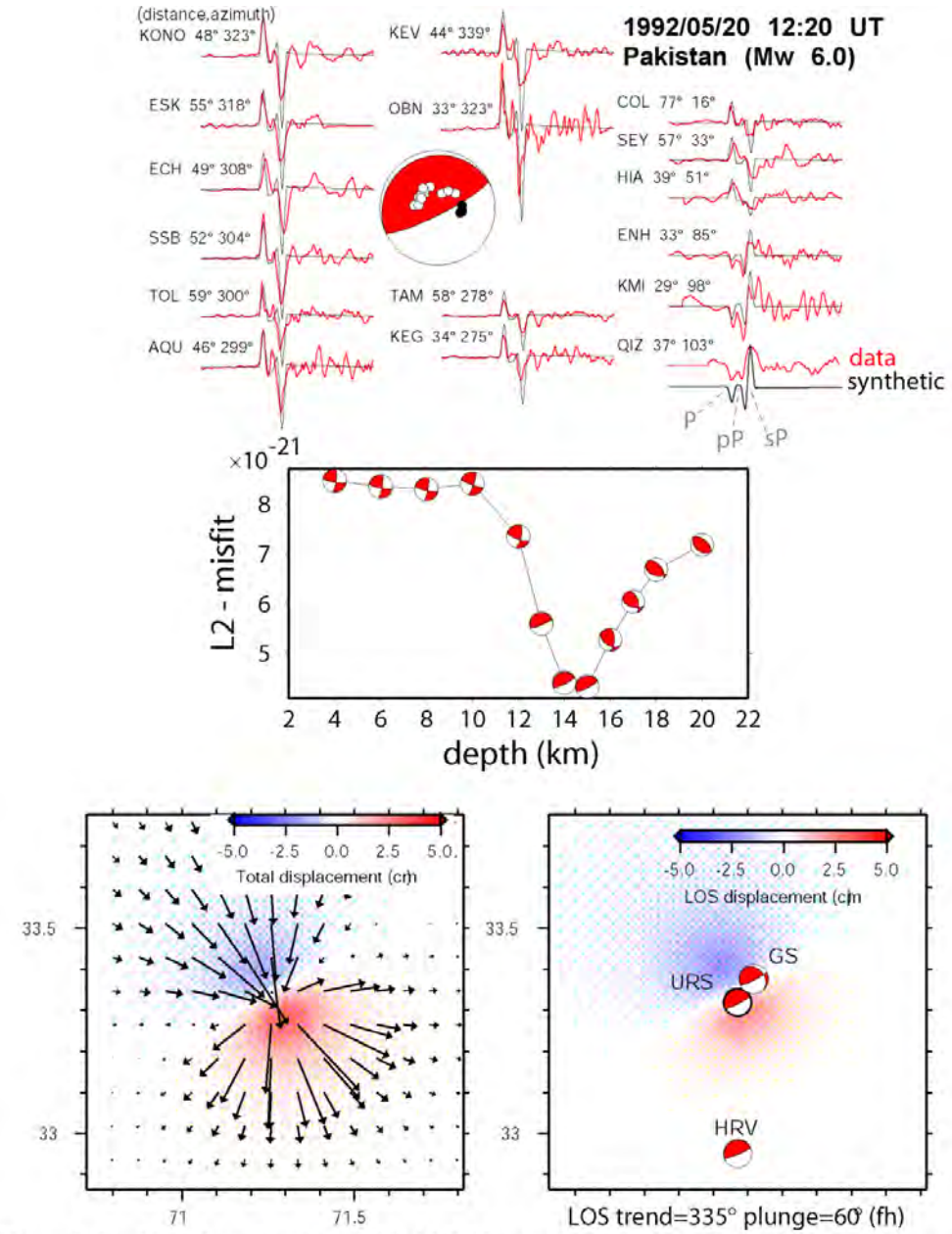

Figure 1. (top) Focal mechanism and (middle) hypocenter depth estimated from the inversion o teleseismic P-wave and depth phases. We determine these source parameters using a grid sear scheme. The resulting source parameters are then used to predict the coseismic deformation at the surface assuming an elastic halfspace. We do this for both nodal planes but since this event was relativly small and deep, there was no difference in deformation (not shown). See text for more details.

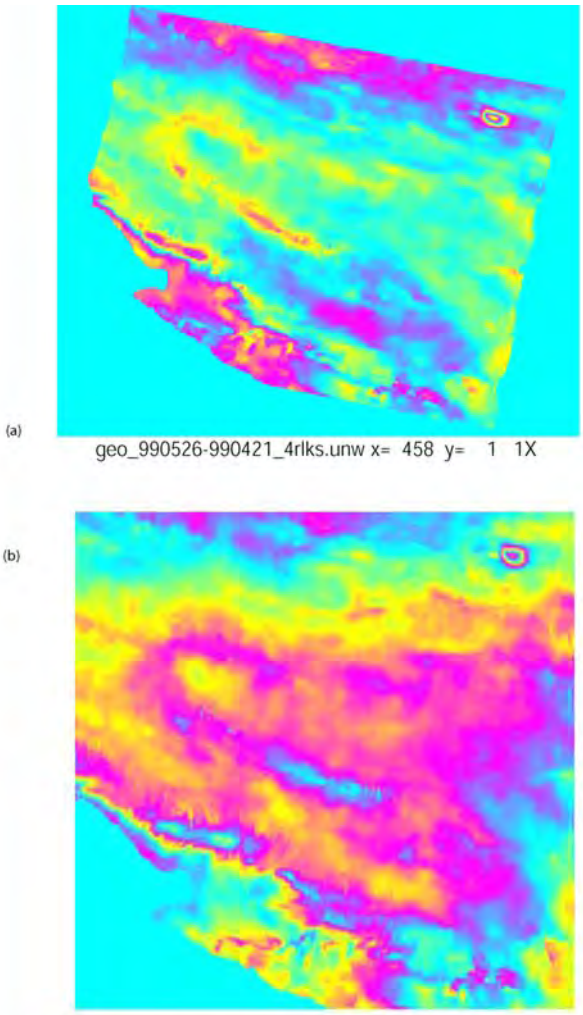

Figure 2. (a) Geocoded interferogram (99/04/21-99/05/26) for track 20 and frame 3051 (approximate geographic extents : 28.12N 52.70E; 27.94N 53.69E; (27.05E 53.48E and 27.23N, 52.50E. Topography is removed using DEM, filtered and unwrapped. The earthquake appears to the upper right of the image at 27.89N 53.61E as a bulleye of around 2 interferometric fringes. The other elongated patterns throughout the image correlate with topography and have much lower contribution to the interferogram than the earthquake signal. (b) This is a similar processing using low resolution topography removed

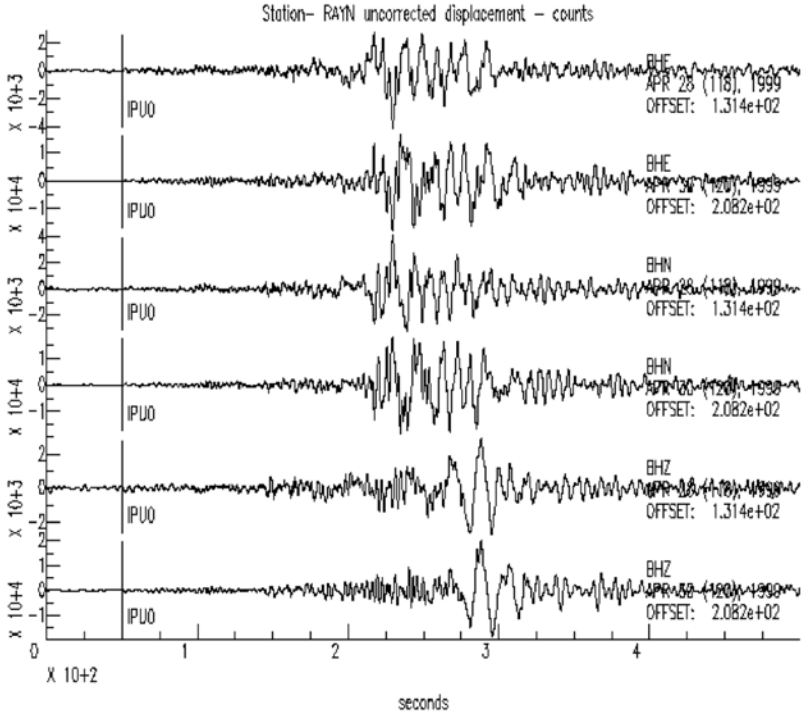

Figure 3. Comparison of broadband waveforms from two earthquakes in southern Iran. Note the similarities in waveforms. The events occurred only two days apart; the event of April 28 is smaller in magnitude. Although the both events may have contributed to the bulleye fringes in Figure 2, the event of the 30th April must have contibuted significantly.

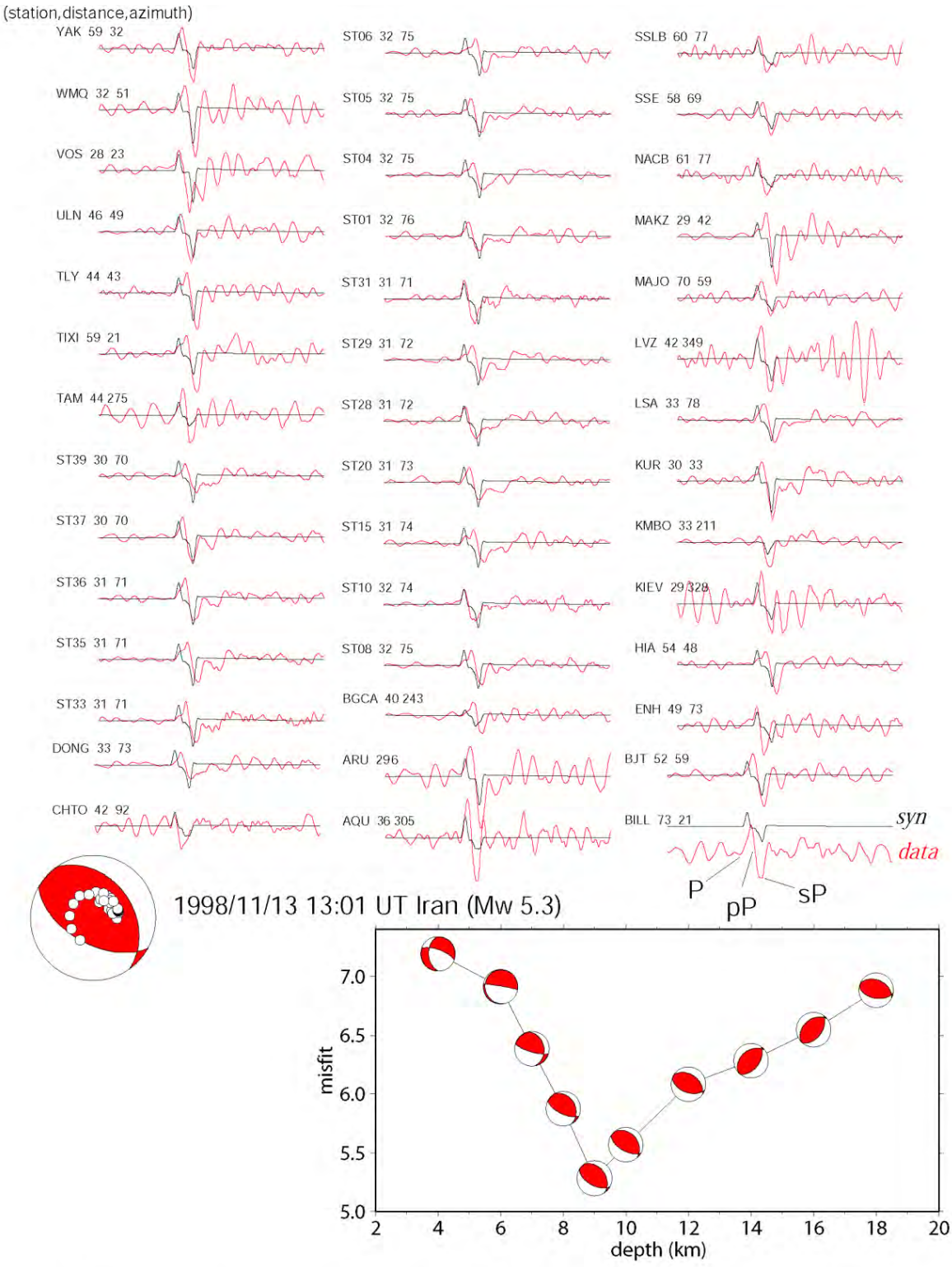

Figure 4. Focal Mechanism and hypocenter depth are estimated from the inversion of teleseismic P and depth phases using a grid search scheme. Note that the best depth for this event is 9 km.

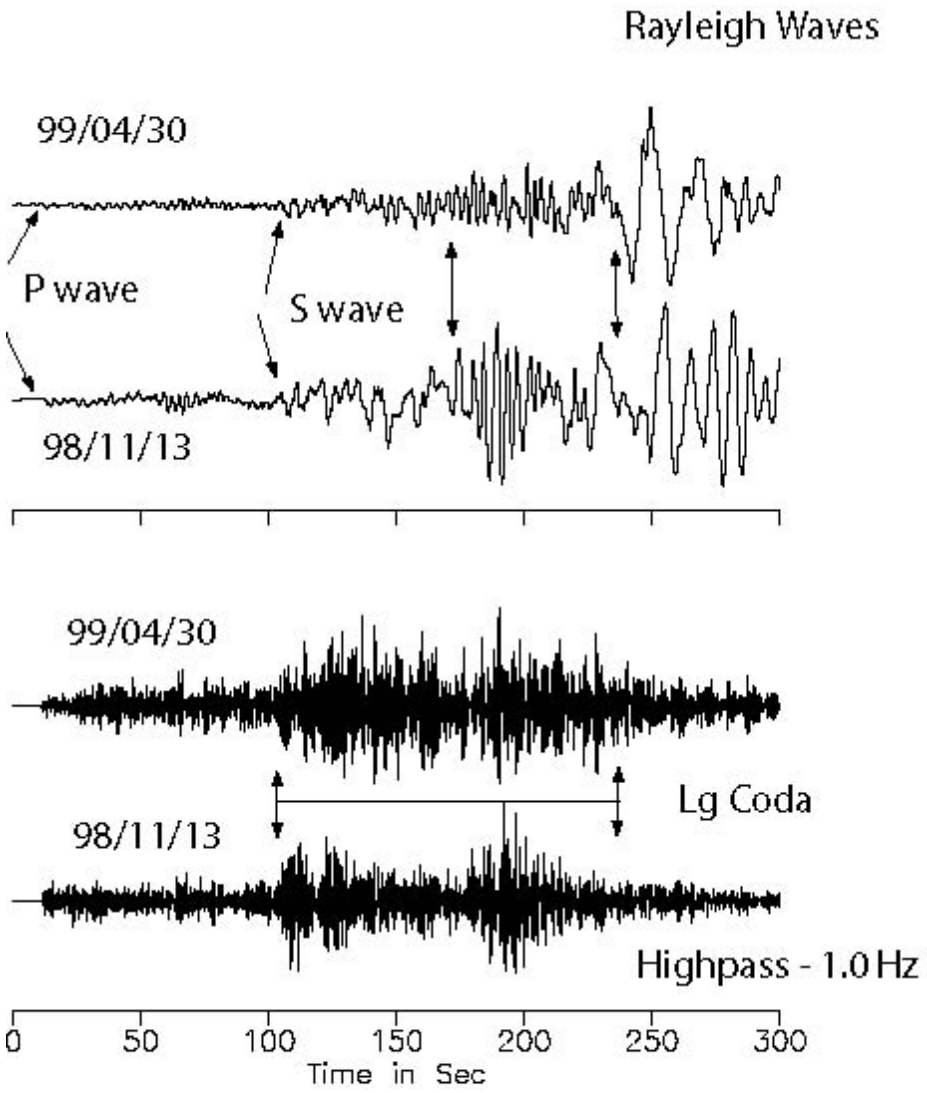

Figure 5. Comparison of seismograms recorded at RAYN (Saudi Arabia ~ 980 km) from the 04/30/99 earthquake with the seismograms recorded from the 11/13/98 (M_w 5.3) at two frequency bands. The top seismograms are the broadband displacements and the bottom seismograms are filtered versions at high frequency (>1Hz). Note the extension of Lg coda on the seismogram of 04/30/99 event suggesting that this earthquake must have occurred at shallow depth. The depth of the November event is about 9 km

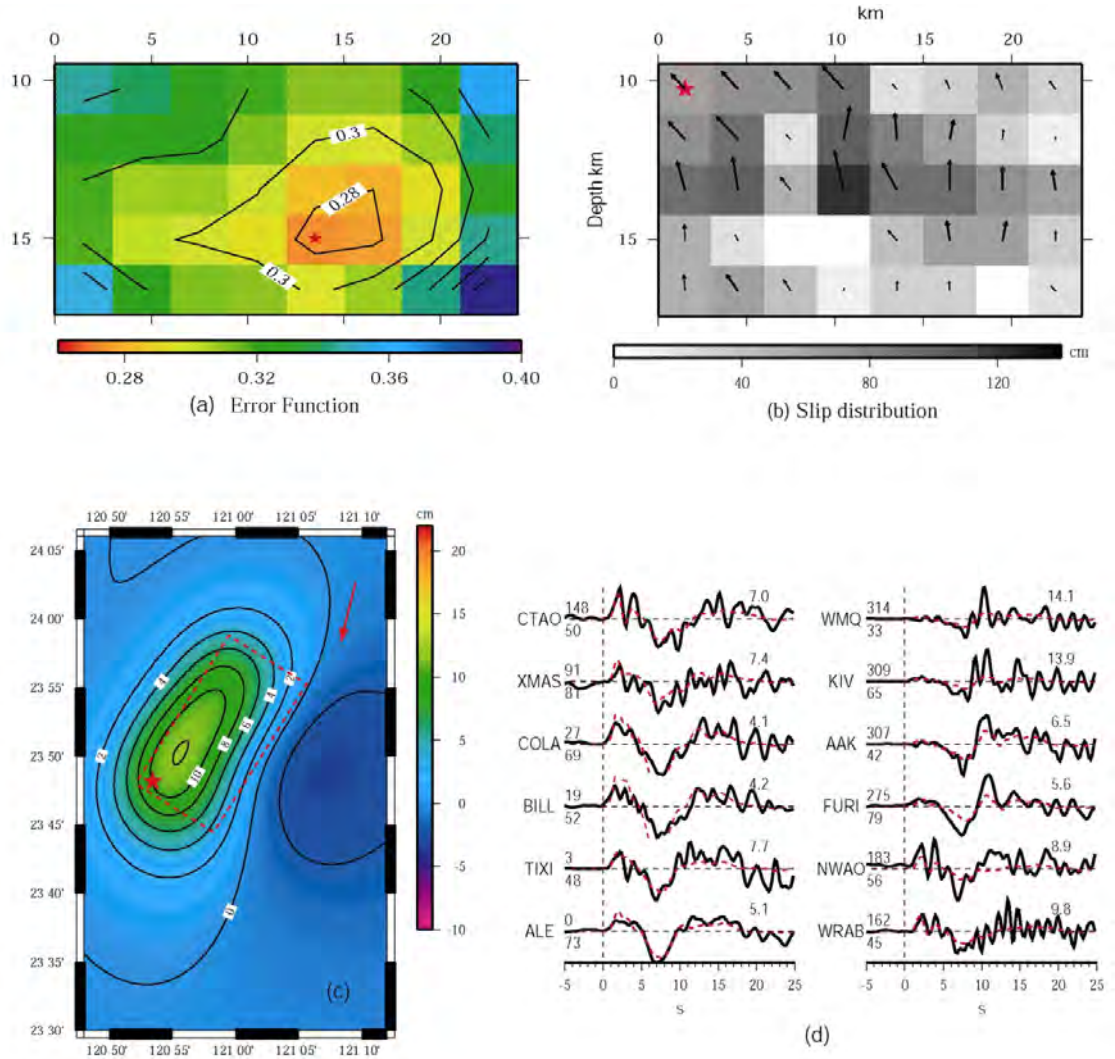

Figure 6. Determining hypocentral position by combined inverting teleseismic and Insar data. (a) Error function values when we put the hypocenter in the center of different subfaults. Star shows the target postion of hypocenter. (b) Inverted slip distribution when we put hypocenter at the upper-left corner. Star shows the position of hypocenter. Corresponding synthetics of InSar and seismic waves are shown in (c) and (d), respectively.

REGIONAL LOCATION CALIBRATION IN ASIA

Lee Steck, Hans Hartse, Chris Bradley, Claudia Aprea, Aaron Velasco, George Randall, and Jill Franks

Los Alamos National Laboratory

Sponsored by National Nuclear Security Administration
Office of Nonproliferation Research and Engineering
Office of Defense Nuclear Nonproliferation

Contract No. W-7405-ENG-36

ABSTRACT

Seismic event location for global nuclear explosion monitoring is a multi-faceted problem. This paper presents a spectrum of issues and efforts involved in improving location performance worldwide. Our efforts are largely designed around providing validated, rigorously calibrated travel times, azimuths, and slownesses along with accurate error estimates. To do so entails a significant effort that includes data mining, data integration, database management, developing optimal 1-, 2-, and 3-D Earth models, using the Earth models to predict wave propagation, developing corrections and errors for travel times, azimuths, and slownesses, and validation of all products. Results presented here will focus on Asia.

Previous work has shown that non-stationary modified Bayesian kriging of travel-time residuals successfully improves regional seismic event location, and this method is being extended to calculate corrections for azimuth and slowness. The ability to krige over 3-D Earth models is also being implemented. In order to produce the most useful corrections, we require accurate ground truth. For this we are continuing efforts to create a location database consisting of the best available seismic event locations and the most accurate and precise travel times. Building this database relies on participation from universities, other National Nuclear Security Administration (NNSA) laboratories, and contacts in private industry. Through the kriging procedure we are able to stabilize location algorithms, but the ultimate usefulness of the corrections themselves is directly related to the quality of the ground truth from which the corrections are derived. Indeed, epicentral mislocations from location algorithms (EvLoc) using travel-time correction surfaces are directly proportional to the location errors of the ground truth used to generate the corrections.

In aseismic regions, corrections for travel time, azimuth, and slowness are predicted from optimal Earth models using one of the following methods, depending on application: TauP, ray bending, reflectivity, or finite difference. We have developed a model-building tool that can incorporate many different types of data, from surfaces (Moho, bathymetry, topography), to local or regional 1-, 2-, and 3-D models, to reflection profiles, to point data. Numbers of layers are defined within prominent sections of the lithosphere, and interpolation between data points is used to create a smooth, self-consistent 3-D Earth model.

OBJECTIVE

The objective of this work is to improve seismic event location in Asia. We achieve our objective through a multi-faceted approach encompassing database development, data integration, geophysical model building, numerical simulation of wave propagation, travel-time kriging, location algorithm development, and validation.

RESEARCH ACCOMPLISHED

A new location database is being compiled to provide a preferred origin and a superset of arrivals compiled from all available global and regional catalogs. The effort has focused on merging global and regional seismic event bulletin information with Los Alamos National Laboratory (LANL)-generated phase arrival and waveform data using a combination of PERL scripts and the ORLoader codes. The result is a set of database tables that contain integrated seismic event data from many sources. These tables are the foundation for the creation of CSS3.0 ***assoc*** and ***arrival*** tables that will be used specifically for event relocations. Merging event bulletins and renaming of seismic phases follow separate pre-determined ranking schemes. As of this writing, we have about 600,000 preferred origins and 14,000,000 arrivals (excluding ISC and LANL picks). Of these arrivals, 8,500,000 are either P or Pn. About 150,000 waveforms have been tied to the database (748 from chemical explosions; 1086 from nuclear explosions) and 45,000 picks are being incorporated from LANL (see also Begnaud *et al*, this volume).

The InSAR component of our ground truth acquisition effort has produced some interesting global and regional results. Figure 1 shows theoretical predictions of ground displacement for several different fault orientations and depths. These results are used along with statistical seismicity patterns derived from the PDE catalog to predict the number of InSAR-observable earthquakes per year on a 2.5^{o} grid around the globe (Figure 2) (Earle and Cogbill, submitted manuscript). These results seem encouraging on the whole, but in a follow-on study in China, a number of problems were encountered that illustrate the difficulties in applying InSAR to smaller events (see Peltzer *et al*., 2001). A major difficulty with the area around China is the limited number of satellite download stations. Other problems arise from the high mountainous terrain and associated precipitation that can produce undesired signals. Figure 3 illustrates an InSAR result for a moderate-sized event in China.

We have completely revised and extended our regionalization of Asia to include southern Asia, northeast Russia, the Aleutian Islands, and Alaska (Figure 4). The principal changes in China were to combine some of the smaller and/or irregular provinces into more geophysically useful regions. The digitized provinces were defined based on the Exxon geologic maps. Our 3-D Asia model will be updated with these provinces using Litho3D and Model3D. Appropriate regional crustal models are inserted into the provinces and the 3SMAC model is used for the mantle.

Our modeling tool has been adapted to allow computation of 3-D travel times from any event to any station with no need to convert the output model to any other format. We have been using a 3-D bending method for computing minimum travel times, based on Steck and Prothero (1991). This code has been modified to perform in a 3-D spherical model, with topography. We have been exploring the validation of one of our *a-priori* models using this technique. The results allow us to explore which parts of any *a priori* model perform better (or worse) than IASPEI91 (or any other model). We have also included a new visualization tool: we can define a great circle transect from one station to any part of the model, and the code generates a 2-D cross-section. An additional, more qualitative assessment tool for validating models is developed using a wave front construction code (Hildebrand *et al*, 1999). This code has been also modified to perform in a 3-D spherical Earth. The wave front is constructed from interpolation of rays calculated via the shooting method.

As part of our regionalization effort, we have performed a literature search to gather velocity models from regional distances around MAKZ, a seismic array near Makanchi. As of this writing, we have compiled roughly 30 velocity models for the Tien Shan, Kazakhstan, and Siberian shield regions. These are being tested against data to determine the best fitting 1-D models. Eight Vp/Vs models have been gathered for eastern Kazakhstan, and these are shown in Figure 5.

To aid in our Asia calibration efforts, we are analyzing Makanchi and Karatau array data for FK performance and azimuth corrections. With only a handful of events analyzed, no major azimuthal perturbations are observed. Figure 6 shows an example of azimuth and slowness determined for an event recorded at MKAR. We have coded up the

pseudo-FK method, and have implemented improvements in both the error calculation as well as the peak energy calculation.

While correction surfaces are being compiled for stations of interest in Asia using NMBK (Schultz *et al*, 1999), we are also looking towards implementing new methods for locating events. Figure 7 shows a comparison between double-difference relocations and EvLoc relocations for an earthquake sequence in Tibet. Methods of optimizing the double difference and related correlation methods for seismic event relocation are being sought.

CONCLUSIONS AND RECOMMENDATIONS

We are making headway in solving the location problem in Asia. The task is a vast one, and a successful program requires the mutual cooperation of the Department of Energy/NNSA and Department of Defense efforts and the Air Force Technical Applications Center, along with universities and private companies. Results presented in this paper are a snapshot of recent progress in some of our research areas and further work will be presented at the 24th Seismic Research Review.

REFERENCES

Belyashova, N.N., V.I. Shacilov, N.N. Mikhailova, I.I. Komarov, Z.I. Sinyova, A.V. Belyashov, and M.N. Malakhova, On the Use of Calibration Explosions at the Former Semipalatinsk Test Site for Compiling a Travel-time Model of the Crust and Upper Mantle, *Pure Appl. Geophys.*, **158**, 193-209, 2001.

Egorkin, A.V., Velocity structure, composition and discrimination of crustal provinces in the former Soviet Union, *Tectonophysics*, **298**, 395-404, 1998.

Ghose, S., M.W. Hamburger, and J. Virieux, Three-dimensional velocity structure and earthquake Locations beneath the northern Tien Shan of Kyrgyzstan, central Asia, *J. Geophys. Res.*, **103**, 2725-2748, 1998.

Hildebrand S, M. Fehler, and C. Aprea (1999), Wavefront Construction: A Differential Geometry Approach, *SGI*, **70** , 199-206.

Jih, R.S., Location Calibration efforts in China, in Proceedings of the 20th Annual Seismic Research Symposium in Monitoring a Comprehensive Test Ban Treaty, 21-23 Sept 1998.

Kosarev, G.L., N.V. Petersen, L.P. Vinnik, and S.W. Roecker, Receiver functions for the Tien Shan analog broadband network: contrasts in the evolution of structures across the Talasso- Fergana Fault, *J. Geophys. Res.*, **98**, 4437-4448, 1993.

Mangino, S., K. Priestley, and J. Ebel, The receiver structure beneath the China Digital Seismograph Network Stations, *Bull. Seismol. Soc. Am.,* **89**, 1053-1076, 1999.

Morozova, E.A., I.B. Morozov, S.B. Smithson, and L.N. Solodilov, Heterogeneity of the uppermost mantle beneath Russian Eurasia from the ultra-long-range profile QUARTZ, *J. Geophys. Res.*, **104**, 20329-20348, 1999.

Petit, C., and J. Deverchere, Velocity structure of the northern Baikal rift, Siberia, from local and regional earthquake travel times, *Geophys. Res. Lett*., **22**, 1677-1680, 1995.

Priestley, K.F., G. Zandt, and G.E. Randall, Crustal structure in eastern Kazakh, USSR from teleseismic receiver functions, *Geophys. Res. Lett*., **15**, 613-616, 1988.

Priestley, K., J. Cipar, A. Egorkin, and N. Pavlenkova, Upper-mantle velocity structure beneath the Siberian platform, *Geophys. J. Int*., **118**, 369-378, 1994.

Roecker, S.W., T.M. Sabitova, L.P. Vinnik, Y.A. Burmakov, M.I. Golvanov, R. Mamatkanova, and L. Munirova, Three-Dimensional Elastic Wave Velocity Structure of the Western and Central Tien Shan, *J. Geophys. Res.*, **98**, 15779-15795, 1993.

Schultz, C., S. Myers, J. Hipp, and C. Young (1998), Nonstationary Bayesian Kriging: Application of Spatial Corrections to Improve Seismic Detection, Location and Identification, *Bull. Seism. Soc. Am*., 1275-1288.

Steck, L. and W. A. Prothero, 1991. A 3-D raytracer for teleseismic body-wave arrival times, *Bull. Seis. Soc. Am.*, **81**, 1332-1339**.**

Thurber, C., H. Given, and J. Berger, Regional seismic event location with a sparse network: application to eastern Kazakhstan, USSR, *J. Geophys Res.*, **94**, 17767-17780, 1989.

Thurber, C., C. Trabant, F. Haslinger, and R. Hartog, Nuclear explosion locations at the Balapan, Kazakhstan, nuclear test site: the effects of high-precision arrival times and three-dimensional structure, *phys. Earth Planet. Inter.*, **123**, 283-301, 2001.

Whitted, C.A., S.R. Taylor, A.A. Velasco, H.E. Hartse, and G. Zandt, A path specific study in central Asia from group velocity inversions and full waveform modeling, Los Alamos National Laboratory, LAUR-99-3040, 19 pp.

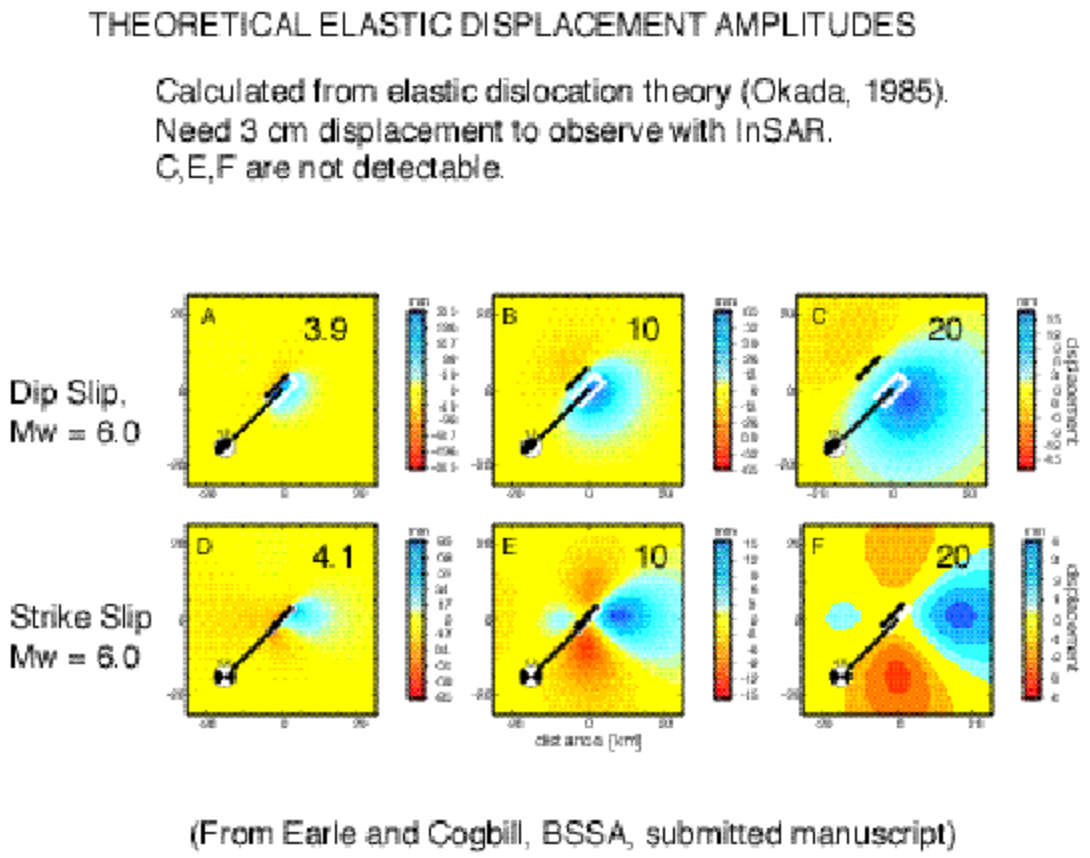

Figure 1. Plot showing theoretical line-of-sight co-seismic surface displacement in millimeters for dip-slip and strike-slip events. The white lines show the surface projection of the square fault planes, and the black lines show the surface trace of the fault. All displacements were calculated for M = 6.0. The centroid depths are A) 3.9 km, B) 10 km, C) 20 km, D) 4.3 km, E) 10 km, and F) 20 km. The dip-slip events (A, B, and C) all have a dip of 67^{o} and the strike-slip events (D, E, and F) have a dip of 85^{o}. The events C, E, and F lie outside the detection threshold.

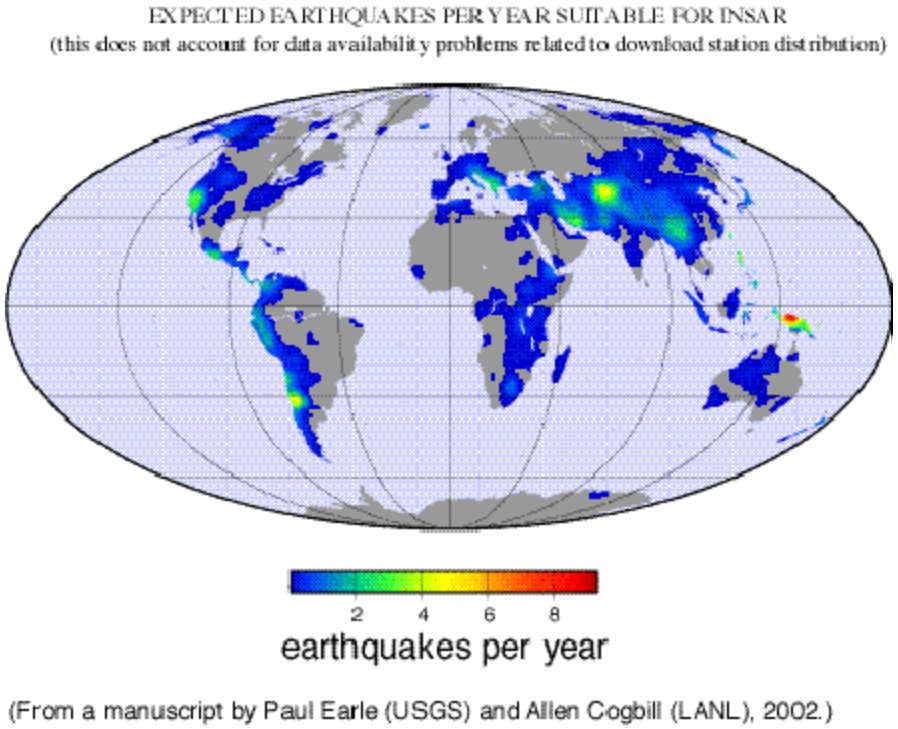

Figure 2. The number of magnitude 5.0 and greater shallow earthquakes occurring per year in a circle of radius 2.5°. The map was generated by calculating earthquake frequency within overlapping 2.5° radius caps and then smoothing the result. The frequency was obtained from 27 years of PDE data.

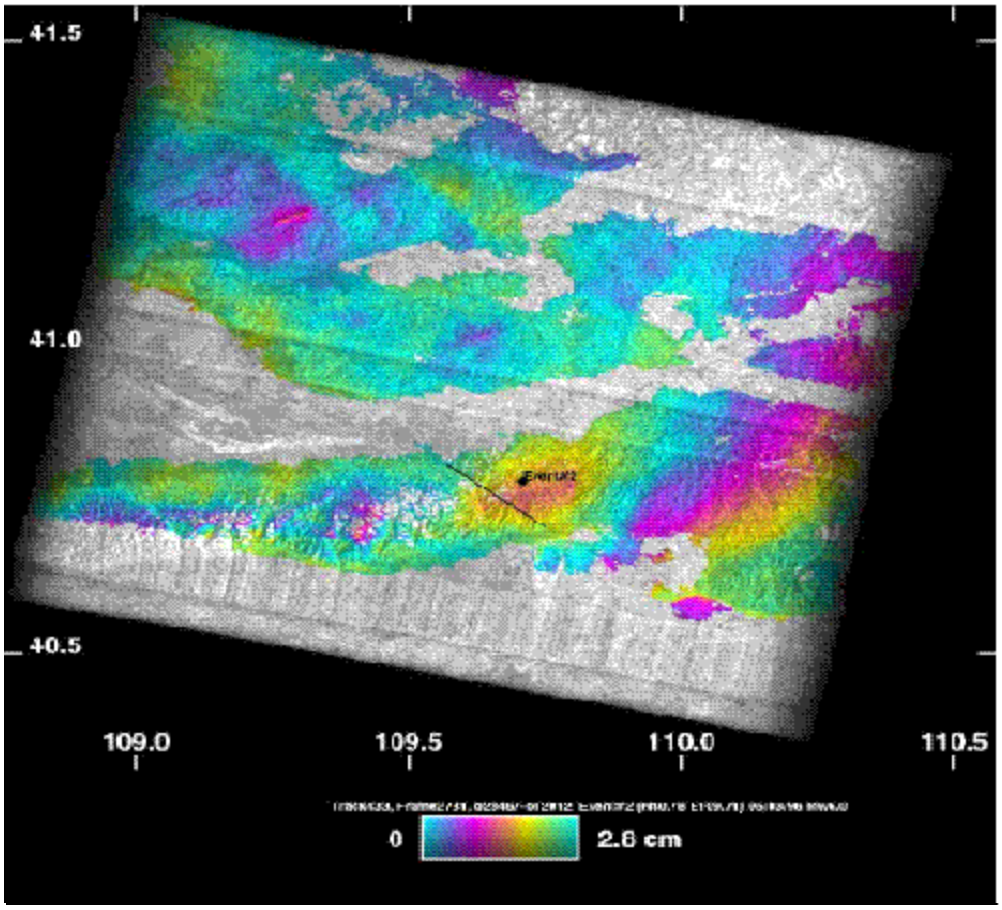

Figure 3. InSAR results for a moderate sized event in China, Mw 6.0. This was deemed a successful result, the only success in attempting to look at three Mw 5-6 events in China.

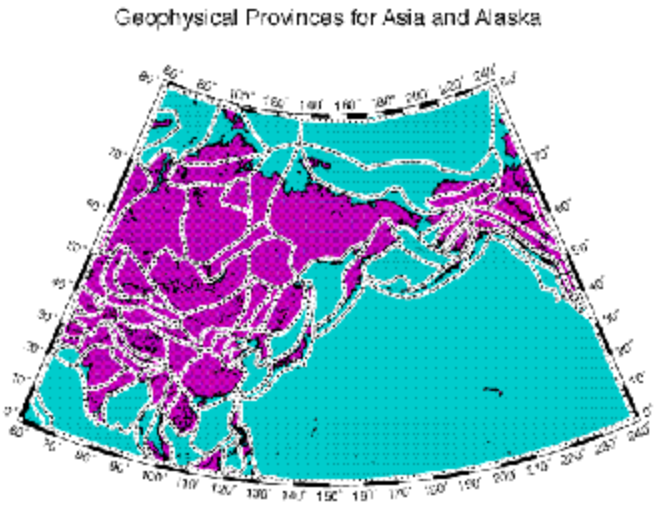

Figure 4. Our newly updated geophysical provinces for Asia and environs.

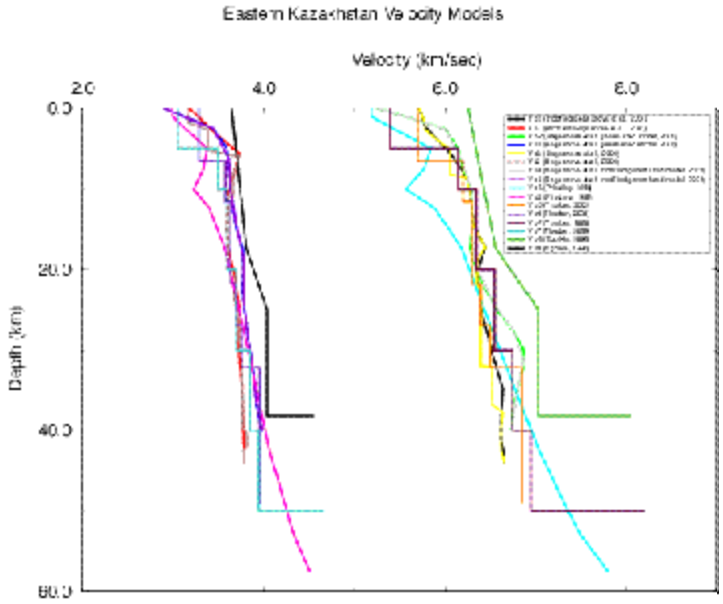

Figure 5. Sample velocity models for eastern Kazakhstan.

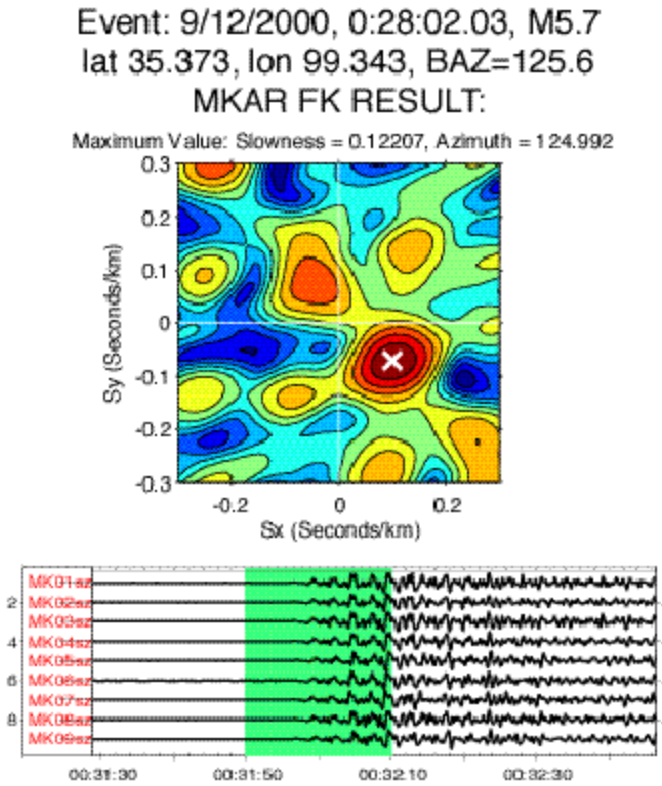

Figure 6. Pseudo FK result for station MKAR.

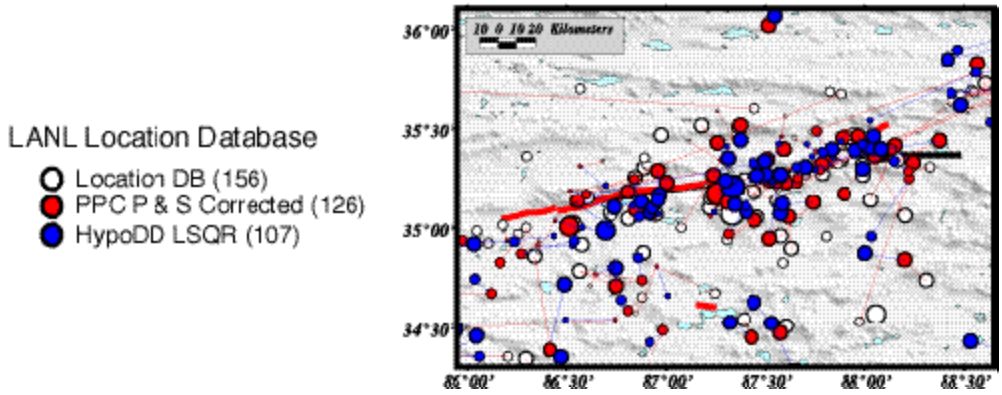

Figure 7. Comparison of EvLoc, EvLoc plus P and S corrections, and Double Difference locations.

METHODS FOR IMPROVING SEISMIC EVENT LOCATION PROCESSING

Clifford H. Thurber, Haijiang Zhang, Charlotte A. Rowe, and William J. Lutter

University of Wisconsin-Madison

Sponsored by Defense Threat Reduction Agency

Contract No. DTRA01-01-C-0085

ABSTRACT

Our research program consists of four components, each involving some aspect of multiple-event analysis: (1) high-precision waveform cross-correlation (WCC) for arrival time estimation, (2) robust event clustering, (3) waveform decomposition and source wavelet deconvolution reshaping, (4) double-difference (DD) multiple-event location and tomography. Our research is focusing initially on the development and testing of these seismic analysis methods using "ground-truth" datasets at different scales (local and regional), and will be followed by the application of these methods to "test-bed" seismic datasets, including tests on real-time data streams.

We are constructing two regional ground-truth datasets, one for New Mexico and one for California. The former dataset is from the New Mexico Tech short-period network and is dominated by small explosions, whereas the latter is from the UC-Berkeley broadband network and contains relatively large earthquakes (about 260 events of magnitude 4.3 and above). In each case, the ground-truth dataset will be used initially for algorithm assessment purposes and later as a "reference event" dataset for clustering and locating new events. The New Mexico "training" dataset is undergoing final grooming. For the California dataset, we have affirmed the quality of the ground-truth location information by carrying out a DD location analysis using catalog time-difference data. We also present initial results of hierarchical cross-correlation analysis applied to the California dataset.

We have completed the modifications to the integer portion of the cross-correlation software, adding the multiple eigentaper approach to provide improved integer correlation statistics. The modifications to the program logic provide the initial step for subsequent adaptation towards multiple frequency-scale correlations. In addition, modifications have been completed to interface the WCC software with our new DD tomography code (discussed below). We are preparing the California dataset for further DD location analysis and for processing with the regional-scale tomography code under development. At the same time, we will experiment with clustering and waveform decomposition and reshaping techniques to expand the ability to use WCC on large datasets. Efforts have also begun on an Earthworm-MatSeis real-time interface, including the generation of CSS database files from Earthworm.

We have developed a new DD tomography method that uses high-precision WCC relative arrival time picks as well as differential and absolute catalog arrival-time picks. "Double-difference" refers to the residual between the observed differential arrival-time picks and the predicted differential arrival-times. If two sources have almost identical source mechanisms and the differential signal scattering due to velocity heterogeneity along the ray path is minor, they will produce similar waveforms at the same station, allowing for the use of WCC to determine precise differential times. Compared to absolute travel-time picks, relative arrival-time picks obtained using WCC methods have a precision to the sub-sample level. When two sources are far away from each other so that their waveforms are not similar, we just use the relative catalog arrival-time pick differences. We also use the absolute travel-time picks to constrain the absolute event locations.

Our new DD tomography method has been applied to the Hayward fault, California, as an initial test to compare to previously published location results. In comparison to the standard seismic tomography method, the double-difference tomography method results in a sharper-featured velocity structure that is consistent with the geologic setting. At the same time, it produces absolute and relative event locations accurately, similar to the results obtained by the DD location method developed by Waldhauser and Ellsworth (2000). Our next steps are to apply this algorithm to another test dataset, from Parkfield, California, and then to develop the regional-scale version and apply it to our regional California ground-truth dataset.

OBJECTIVES

The standard processing approach for the determination of seismic event hypocentral locations involves a single-event procedure. Phase arrivals are timed and associated to define an event, and the associated phases are used (potentially along with arrival azimuths and slownesses) to compute a best-fitting location. It has been shown that order-of-magnitude reductions in event location errors and uncertainties are possible if multiple-event techniques are utilized. Recent studies of earthquakes in Hawaii (Rubin et al., 1998), California (Waldhauser et al., 1999), and at the Soultz geothermal area (Rowe et al., 2002), and of explosions at the Balapan test site (Phillips et al., 2001; Thurber et al., 2001), and others, have demonstrated in a dramatic fashion the substantial improvement in the definition of seismogenic features or in the accuracy of relative locations of ground-truth events that is possible with multiple-event methods utilizing high-precision arrival-time estimation.

Our research program consists of four components, each involving some aspect of multiple-event analysis: (1) high-precision WCC for relative arrival time estimation; (2) robust event clustering; (3) waveform decomposition and source wavelet deconvolution reshaping; (4) double-difference (DD) multiple-event location and tomography. In this paper, we will focus on our accomplishments under components 1, 2, and 4, plus our work on ground-truth datasets used for testing our analysis methods.

RESEARCH ACCOMPLISHED

Ground-Truth Datasets

We are constructing two regional ground-truth datasets, one for New Mexico and one for California. The former dataset is from the New Mexico Tech short-period network and is dominated by small explosions, whereas the latter is from the UC-Berkeley broadband network and contains relatively large earthquakes. The New Mexico dataset consists of two parts, one spanning July 1997-February 1998 that has undergone a complete repicking, relocation, WCC, and clustering analysis, and the other spanning January 2001-present that is being prepared for real-time testing. The California dataset was extracted from the Northern California Earthquake Data Center (NCEDC). We first affirmed the quality of the NCEDC catalog location information by carrying out a DD location analysis using catalog time-difference data for 130 events and 23 stations. We found that the DD locations reproduced those in the catalog within 2 to 3 km (in epicenter and depth) on average. We then used a combination of automatic and manual picking to augment and improve the available P arrival picks, and to provide analyst pick weights.

Waveform Cross-Correlation

WCC can be a powerful tool for improving earthquake phase identification and subsequent hypocenter locations. Our software is being built upon an initial package that was designed to retroactively process large catalogues having existing phase picks (P and S). This package compares similar waveforms and identifies families of events meeting specified cross-correlation thresholds, based on a master station or suite of stations. Within families of similar earthquakes, waveforms are compared on a station-by-station basis and their picks are adjusted by applying an L1-norm based conjugate gradient technique to the matrix of first differences. Consistent, mean-adjusted picks are re-entered into trace headers for other uses such as waveform stacking, hypocenter location or seismic tomography.

The WCC program has some features, which help it to perform in an auto-adaptive manner. These include: adaptive, full-spectrum cross-coherency-based prefiltering; a multi-component signal covariance estimator that provides automatic, adaptive polarization filtering to optimize signal linearity; and the use of multiple eigentapers in the subsample cross-spectral correlation step to reduce signal leakage and variance when estimating the signal cross-spectra. We have adapted the cross-correlation program with the addition of eigentapers in the coarse (integer-sample) cross-correlation step, and we are in the process of comparing this approach to coarse lag estimation with the previous method of applying multiple narrow-band filtering. Both approaches provide a means of estimating linearly independent realizations of the time series and therefore permitting quantitative error estimates for the integer correlation step; in future work we will combine the two strategies via application of multiple eigenwavelet methods.

The correlator has also been adapted so that its output may optionally be generated in a format that is compatible with the hypoDD program, so that joint location may be performed using the cross-correlation comparisons without actually solving for consistent pick lags and correcting the picks themselves. Further, the correlator now has an option of generating only one set of first-differences, for applications in which it is only desired to compare a set of "reference events" to the trace of a single ("test") event. This option is being tested in our hierarchical approach described in the next section.

Event Clustering

Waveform clustering, used to segregate signals in to families of similar events, has been tested with a variety of approaches. One successful approach has been to identify clusters based on very high standards of cross-correlation (0.8 or 0.85), resulting in many small multiplets of highly similar events. These are then cross-correlated and consistent pick adjustments are determined via a conjugate gradient solver. Waveforms are aligned on their new picks and stacked to provide a composite waveform representation for the cluster. These stacks are then cross-correlated among the multiplets and inconsistencies in the mean adjusted picks can be corrected by finding consistent adjustments among the stacks. The resulting stack pick lags are propagated to the parent traces. This has been shown to reduce the inter-cluster inconsistencies that result in cluster centroid biases when earthquakes are located using the new picks (these biases existed in the initial catalogue as well). Another related approach that has shown good success is application of the clustering program to the waveform stacks. Those traces whose stacks cluster together based on a high similarity coefficient are joined into larger, second order families. Their member traces are cross-correlated and adjusted for consistency within this larger group. The second-order clusters, following pick adjustment, are stacked yet again and their stacks are compared for similarity. This process may be performed in a hierarchical manner until stacks fail to cluster. Final adjustment of mean centroid picks on the ultimate stacks has been tested using an autopicker; this works well when many traces contribute to the stack but we are still testing different methods of estimating pick uncertainty from the autopicker functions. Phase-weighted stacking, jackknifing methods or multiple-frequency-band approaches may provide the best uncertainty estimates.

Most seismic stations exhibit signal quality problems to some extent or another. When analyzing datasets that cover a wide geographic expanse and a wide magnitude range, any master station may at times have poorer signal quality than other sensors in a network, either because of clipping for a large, nearby event, or poor signal/noise for smaller, more distant ones. Reliance on a single station to perform all similarity choices is therefore not generally the best approach, and we are testing the success of a more adaptive technique where two or more stations may have their waveform similarity matrices compared for consistency, particularly among events that have been orphaned in the clustering step for one of the stations.

Often the first arrival is very emergent and only later portions of the signal can be compared. In these cases, it is useful to have a sliding correlation window to search for similarity later in the event coda. We have modified the correlator to permit this, and have performed interactive testing to demonstrate that sometimes highly similar events, whose first arrivals were uncorrelatable, can be well aligned using the secondary phases. One does not generally expect even among similar events that alignment of later phases will necessarily optimally align the first arrivals; however, among events whose similarity has been established at several correlation lengths for several stations, this provides a means of identifying arrivals at noisier stations and improving the ability to estimate hypocenters for these events. We see this approach as a potential tool in generating autopicks at stations with poorer S/N; if a new event has been identified as belonging to a family of highly similar events, the pick for the poor station may be predicted based on its picks for better-recorded events in the same family, then the validity of the autopick may be verified (and its time adjusted) through comparing later, stronger portions of the waveforms.

WCC analysis of P wave data has shown the ability to identify event clusters based on the cross-correlation information. In a small study region, P wave data might suffice for identifying clusters and hence the source position. However, the smaller window lengths and high-frequency data used in WCC P-wave analysis limits the ability to construct unique location information in a larger study region. Shearer (1994) has demonstrated the use of low-frequency data (3 mHz to 0 0.1 Hz) for global event location and Withers et al. (1999) have successfully applied a similar method to local and regional data utilizing coarse and fine spatial grids. A hierarchical clustering analysis incorporating both the statistical advantages of cluster analysis with adaptive use of grid size and frequency content of the data set offers an alternate means to locate earthquakes. The order of magnitude reductions in location errors found with the use of WCC analysis for event clusters suggest a similar improvement can result from our

hierarchical clustering analysis, with location accuracy limited mainly by the distribution of the ground truth (reference event) locations, binning interval, and the clustering statistics.

We present the initial results on hierarchical WCC/clustering analysis on the California GT dataset, based on WCC analysis of P through surface waves in a first step and the P phase in a second step. We binned the events in 0.1° latitude and longitude bins and in 2.5 km depth bins. The largest magnitude events per bin comprise our 162 reference events, and the next largest 24 events are used for the test dataset. The reference events are displayed in Figure 1a, and the test events and stations used for the preliminary hierarchical analysis are shown in Figure 1b. The WCC analyses for the two steps were accomplished in a similar manner. Waveform data from each test event were cross-correlated against the reference event waveforms to determine the maximum value, in the whole region using low-frequency data in step one, and in a 2° region about the step-one location estimate using high-frequency data in step two. The maximum cross-correlation value per bin from the 7 stations was contoured as an indicator of test event location. Figures 2a and b display the results for a test event located near Los Angeles. For this example, the WCC analysis is performed on the vertical component data for both steps. The estimated location for this event falls with 25 km of the catalog location using the low-frequency data, and improves to 7.5 km using high-frequency data. The next step is to use WCC on the test event and nearby reference events followed by DD location of the event group.

Double-Difference Location and Tomography

The accuracy of event hypocenters is determined by several factors, including the network geometry, available phases, and arrival time accuracies (Pavlis, 1986). If more phases are available, the event hypocenters may be more stable. For example, S-wave phases will be very useful in constraining event depths and providing information that helps to decouple the hypocenters from the structure in the inversion (Gomberg et al., 1990). Due to the presence of noise, the arrival times picked either manually or automatically generally have errors. Recent studies have shown spectacular improvements in location precision for earthquakes and explosions when WCC and event clustering techniques are used to improve arrival time estimates or determine high-precision relative arrival times (VanDecar and Crosson, 1990). Such studies are based on the assumption that waves generated by two similar sources, propagating along similar paths, will generate similar waveforms, and WCC can then be used to determine precise relative arrival times. These studies have demonstrated substantial improvement in the definition of seismogenic features and in the accuracy of relative locations of ground-truth events that is possible using multiple-event methods with high-precision absolute or relative arrival-time data.

We can make an important distinction between the two fundamentally different ways WCC data has been used: (1) by directly using relative arrival times to determine relative event locations (e.g., Got et al., 1994; Waldhauser and Ellsworth, 2000), and (2) by adjusting absolute arrival time picks to minimize discrepancies among relative arrival times (Dodge et al., 1995; Rowe et al., 2002). The advantage of the former approach is that it incorporates all the available information contained within the multitude of relative arrival time differences with a direct measure of quality (the correlation value) associated explicitly with each datum. A disadvantage is that some simplifying assumption needs to be made to derive the locations from the arrival time differences. For example, in the method of Got et al. (1994), the events in a cluster have precisely the same take-off angle and azimuth to each station. As a result, the derived locations are ultimately relative, not absolute, so that some assumption must be made to end up with useful event coordinates (e.g., final locations are computed relative to a catalog-based cluster centroid). Waldhauser and Ellsworth (2000) proposed a different location algorithm, in which the spatial partial derivatives for the set of events are evaluated at different reference points. Thus the absolute event locations are obtained, rather than the relative locations. It is assumed, however, that the path anomalies from velocity heterogeneity are location independent. This assumption is valid for closely spaced events, but is not true for far apart events. As a result, the event locations are biased due to velocity heterogeneity (Wolfe, 2002). In contrast, the latter approach uses the relative arrival times to determine a much smaller number of adjusted arrival time picks, but these picks are absolute arrival times and so can be used to determine absolute locations (in an existing velocity model).

We have developed a new algorithm that combines the advantages and avoid the disadvantages of the above approaches. It is based on the code hypoDD of Waldhauser and Ellsworth (2001), and makes use of both absolute and relative arrival time data. The method determines a three-dimensional (3D) velocity model jointly with the absolute and relative event locations. This approach has the advantage of including relative arrival times with their quality values along with absolute arrival times, thereby not discarding valuable information by only using adjusted

picks, and at the same time dispensing with simplifying assumptions about ray path geometries or path anomalies and producing absolute locations, not just relative locations. To demonstrate the effectiveness of the method, we have applied this method to the Hayward fault dataset of Waldhauser and Ellsworth (2002) to show the fine scale structure of seismicity and to study the local three-dimensional seismic velocity structure.

The body wave arrival time T from an earthquake i to a seismic station k is expressed using ray theory as a path integral

$$T_k^i = t^i + \int_i^k u\,ds \tag{1}$$

where t_i is the origin time of event i, u is the slowness field and ds is an element of path length. The source coordinates (x_1, x_2, x_3), origin times, ray-paths, and the slowness field are unknown model parameters. The relationship between the arrival time and the event location is nonlinear, so a truncated Taylor series expansion is generally used to linearize Equation (1). The misfit between the observed and the predicted arrival times can be linearly related to the perturbations to the hypocenter and velocity structure parameters

$$r_k^i = \sum_{l=1}^{3} \frac{\partial T_k^i}{\partial x_l^i} \Delta x_l^i + \Delta t_k^i + \int_i^k \Delta u\,ds \tag{2}$$

If we subtract from Equation (2) an equivalent equation for event j, we have

$$r_k^i - r_k^j = \sum_{l=1}^{3} \frac{\partial T_k^i}{\partial x_l^i} \Delta x_l^i + \Delta t_k^i + \int_i^k \Delta u\,ds - \sum_{l=1}^{3} \frac{\partial T_k^j}{\partial x_l^j} \Delta x_l^j - \Delta t_k^j - \int_j^k \Delta u\,ds \tag{3}$$

Assuming that these two events are near each other so that the paths from these two events to the common station are almost identical and the velocity structure is known, then Equation (3) can be simplified as

$$r_k^i - r_k^j = \sum_{l=1}^{3} \frac{\partial T_k^i}{\partial x_l^i} \Delta x_l^i + \Delta t_k^i - \sum_{l=1}^{3} \frac{\partial T_k^j}{\partial x_l^j} \Delta x_l^j - \Delta t_k^j \tag{4}$$

Use of Equation (4) is known as the "double-difference" (DD) earthquake location algorithm (Waldhauser and Ellsworth, 2000). Wolfe (2002) has carried out an elegant comparison of this method to those of Jordan and Sverdrup (1981) and Got et al. (1994), pointing out the general similarities and subtle differences, and discussing the advantages and limitations of each method. Her most important conclusion is "that when the path anomalies from velocity heterogeneity change strongly with earthquake position, the bias effects can be reduced in the relative locations between closely spaced earthquakes, but the effects cannot be reduced in the relative locations between earthquakes spaced far apart." Two assumptions in the Waldhauser and Ellsworth (2000) method are key: an *a priori* layered velocity model is assumed, and they add a constraint equation forcing the mean shift of all earthquakes to be (approximately) zero.

We can generalize the 3D DD location method to jointly determine the 3D velocity structure and the (absolute) event locations. The equations for the DD tomography algorithm, hypo3VDD, are:

$$\begin{cases} r_k^i - r_k^j = \sum_{l=1}^{3} \frac{\partial T_k^i}{\partial x_l^i} \Delta x_l^i + \Delta t_k^i + \int_i^k \Delta u\,ds - \sum_{l=1}^{3} \frac{\partial T_k^j}{\partial x_l^j} \Delta x_l^j - \Delta t_k^j - \int_j^k \Delta u\,ds \\ r_k^i = \sum_{l=1}^{3} \frac{\partial T_k^i}{\partial x_l^i} \Delta x_l^i + \Delta t_k^i + \int_i^k \Delta u\,ds \end{cases} \tag{5}$$

Our tomography algorithm incorporates first-difference smoothing constraints, with a greater smoothing constraint weight applied to horizontal direction than the vertical (since vertical velocity changes are generally expected to be greater).

Figure 3a shows the location results from the application of hypo3VDD to the Hayward dataset. The earthquake locations are quite consistent with those from hypoDD (Figure 3b), but with a systematic SW shift. For comparison, we also relocate the events by using the standard tomography method with only the absolute catalog data (Figure 3c). We see that the event locations are still scattered, comparable to the catalog locations (Figure 3d). The velocity model shows a clear contrast across the fault, with the SW side faster, as expected. Figure 4a shows across-strike vertical sections through the velocity model resulting from the DD tomography method. We see that the Hayward fault is marked by a strong velocity contrast, similar to the results shown in Hole et al. (2000). This contrast persists vertically beneath the surface trace of the fault to the maximum depths constrained by the model. Higher velocity rocks are located to the west, consistent with the local geological setting. The strong velocity contrast near the surface is due to the boundary between the Franciscan terrane and the Great Valley Sequence. Figure 4b shows across-strike vertical sections through the velocity model from the standard tomography method with only absolute catalog data. Comparing Figures 4a and b, we note that the velocity contrast boundary is more consistent with the event locations and the velocity contrast is sharper in the model from the DD tomography method. DD tomography yields event locations that are more linear and concentrated (less "fuzzy") than those from the standard tomography method. Consequently, this makes the velocity contrast sharper and more consistent with the event locations. Our next step is to extend this method to regional scales.

CONCLUSIONS AND RECOMMENDATIONS

We have assembled the initial set of components and tools for our integrated multiple-event analysis process. These components include (1) regional ground truth datasets, (2) an improved and more versatile WCC algorithm, (3) a more sophisticated event clustering scheme, including the use of multiple waveform windows, and stacking and automatic stack pick readjustment, (4) a preliminary hierarchical process for WCC/clustering/location analysis using a set of reference events, and (5) a new DD tomography algorithm. Our recommendations for further work include (1) finalizing the ground truth datasets and submitting them to the knowledge base system, (2) adding a more user-friendly front end to the WCC software, (3) adding more sophisticated processing elements to the hierarchical WCC/clustering/location processing, including the testing of schemes for determining and/or correcting for event depths and creating generalized reference waveforms, (4) adding DD location capability to the MatSeis location software and/or LocSAT, and (5) creating a regional-scale version of our new DD tomography algorithm.

REFERENCES

Dodge D. A., G. C. Beroza, and W.L. Ellsworth (1995), Foreshock sequence of the 1992 Landers, California, earthquake and its implications for earthquake nucleation, *J. Geophys. Res.*, 100, 9865-9880.

Gomberg, J. S., K. M. Shedlock, and S. W. Roecker (1990), The effect of S-wave arrival times on the accuracy of hypocenter estimation, Bull. *Seism. Soc. Am.*, 80, 1605-1628.

Got, J.-L., J. Frechet, and F. W. Klein (1994), Deep fault plane geometry inferred from multiplet relative relocation beneath the south flank of Kilauea, *J. Geophy. Res.*, 99**,** 15,375-15,386.

Hole, J. A., T.M. Brocher, S. L. Klemperer, T. Parsons, H. M. Benz, and K.P. Furlong (2000), Three-dimensional seismic velocity structure of the San Francisco Bay area, *J. Geophys. Res.*, 105**,** 13,859-13,874.

Jordan, T. H. and K. A. Sverdrup, (1981) Teleseismic location techniques and their application to earthquake clusters in the south-central pacific, *Bull. Seism. Soc. Am.*, 71, 1105-1130.

Pavlis, G. L. (1986), Appraising earthquake hypocenter location errors: a complete practical approach for single-event locations, *Bull. Seism. Soc. Am.*, 76**,** 1699-1717.

Phillips, W.S., Hartse, H. E., and Steck, L. K. (2001), Precise relative location of 25 ton chemical explosions at Balapan using IMS stations, *Pure Appl. Geophys.*, 158, 173-192.

Rowe, C. A., R. C. Aster, W. S. Phillips, R. H. Jones, B. Borchers, and M. C. Fehler (2002), Using automated, high-precision repicking to improve delineation of microseismic structures at the Soultz geothermal reservoir, *Pure Appl. Geophys.*, 159, 563-596.

Rubin, A., D. Gillard, and J.-L. Got (1998), A re-examination of seismicity associated with the January 1983 dike intrusion at Kilauea volcano, Hawaii, *J. Geophys, Res.* 103, 10,003-10,015.

Shearer, P.M. (1994), Global seismic event detection using a matched filter on long-period seismograms, *J. Geophys. Res.*, 99, 13,713-13,725.

Thurber, C., C. Trabant, F. Haslinger, and R. Hartog (2001), Nuclear explosion locations at the Balapan, Kazakhstan, nuclear test site: the effects of high-precision arrival times and three-dimensional structure, *Phys. Earth Planet. Int.*, 123, 283-301.

VanDecar, J.C. and R. S. Crosson (1990), Determination of teleseismic relative phase arrival times using multi-channel cross-correlation and least squares, *Bull. Seism. Soc. Am.*, 80, 1548-1560.

Waldhauser, F., and W. L. Ellsworth, A double-difference earthquake location algorithm: Method and application to the Northern Hayward Fault, California, *Bull. Seism. Soc. Am.*, 90, 1353-1368, 2000.

Waldhauser, F., and W. L. Ellsworth, Fault structure and mechanics of the Hayward Fault, California, from double-difference earthquake locations, *J. Geophys. Res.*, 107, ESE 3, 1-13, 2002.

Waldhauser, F., W.L. Ellsworth, and A. Cole (1999), Slip-parallel seismic lineations on the northern Hayward Fault, California, *Geophys. Res. Lett.*, 26, 3525-3528.

Withers, M., R. Aster, and C. Young (1999), An automated local and regional seismic event detection and location system using waveform correlation, *Bull. Seism. Soc. Am.*, 89, 657-669.

Wolfe, C. J. (2002), On the mathematics of using difference operators to relocate earthquakes, *Bull. Seism. Soc. Am.*, in press.

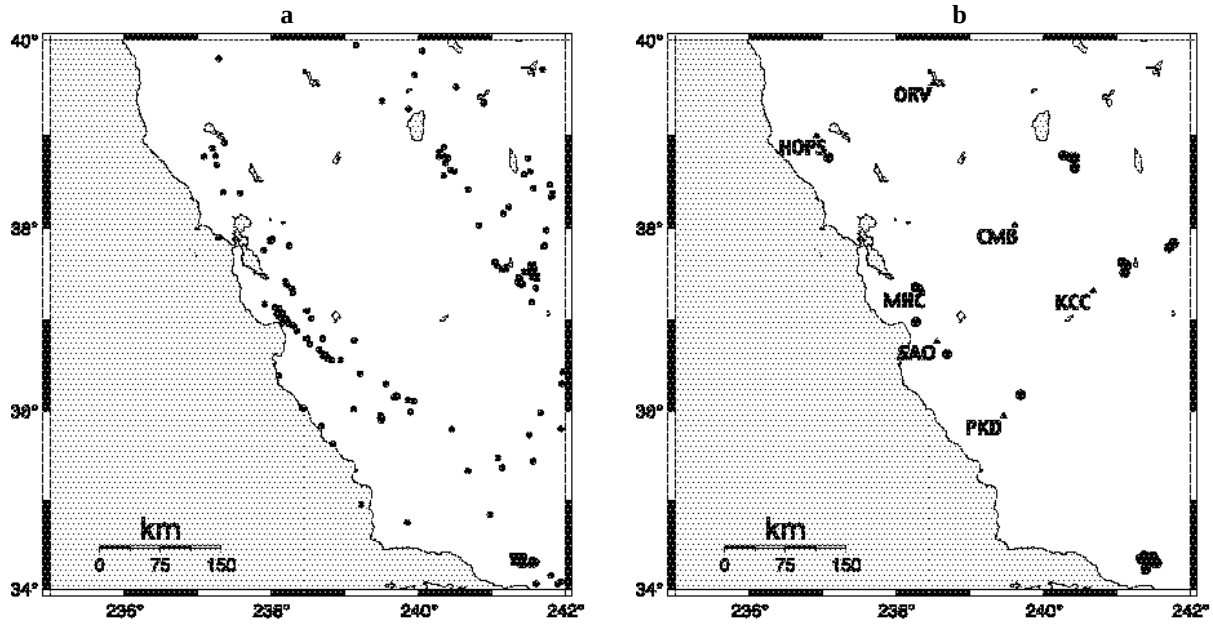

Figure 1. Maps of (a) reference events and (b) test events and test stations from our California ground-truth dataset.

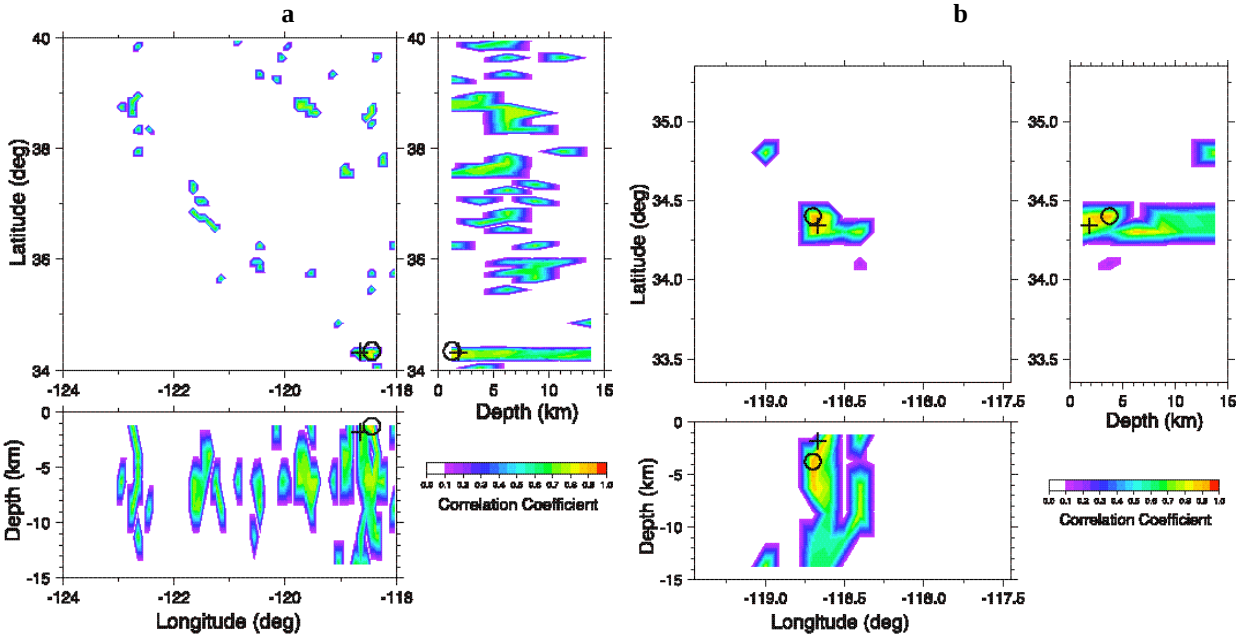

Figure 2. Contour plots (map view and depth sections) of the maximum cross-correlation value per bin for the 7 stations for a test event (located at lat. 34.3°, lon. -118.58°, and depth 1.8 km, cross) correlated against the set of reference events in the (a) low-frequency band (step one) and (b) high-frequency band (step two). Note the good low-resolution location estimate on the left (circle) and the improved high-resolution location estimate (circle) on the right.

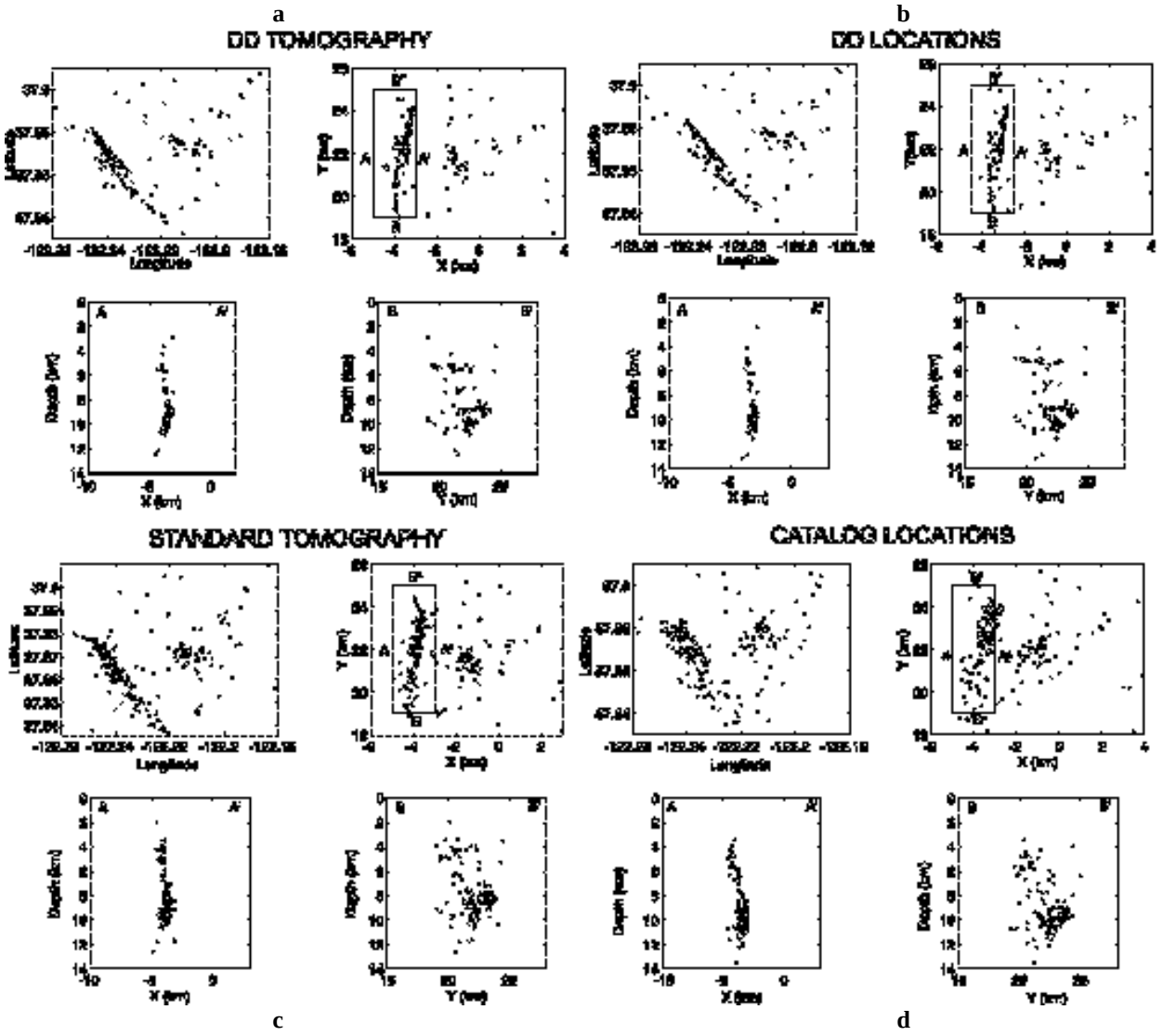

Figure 3. Comparison of earthquake locations along the Hayward fault determined using (a) DD tomography, (b) DD location, (c) standard tomography, and (d) catalog data (no DD data). Each part shows a lat-lon plot (upper left) and zoomed-in plots (rotated to fault-parallel/fault-normal) of epicenters (upper right) and fault-normal (lower left) and fault-parallel (lower right) depth sections. Note how closely the hypocenters in panels a and b resemble each other, but with a systematic SW shift. The tight clustering is not evident in either the standard tomography solution (c) or the catalog locations using absolute picks only (d).

a **b**

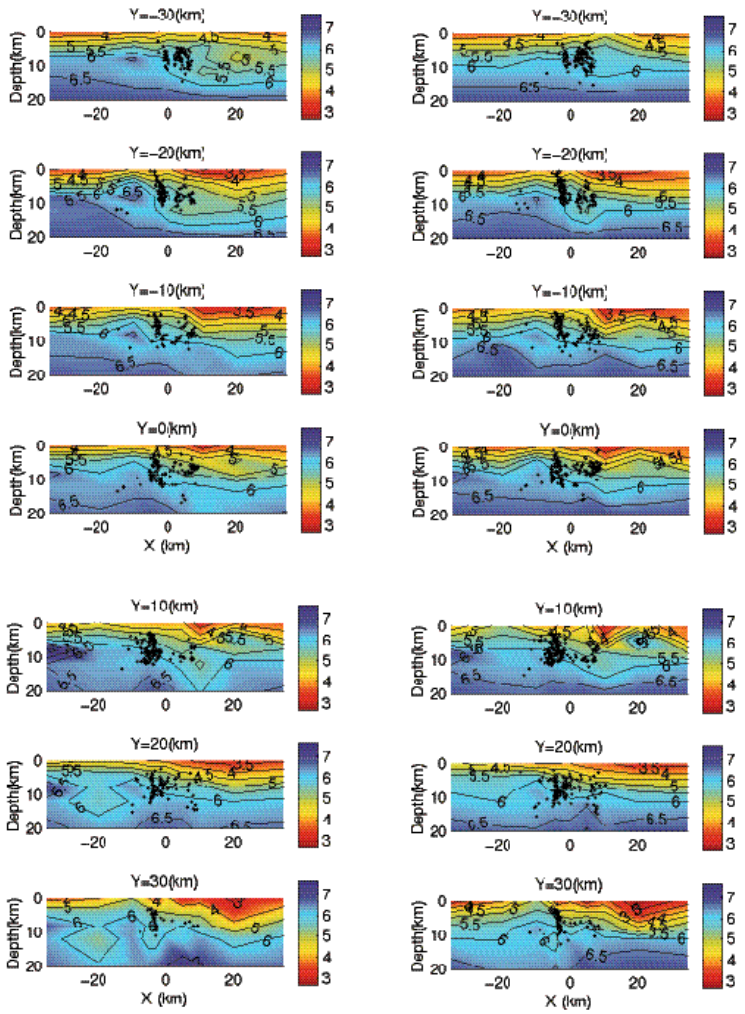

Figure 4. (a) The left-hand panels show fault-normal slices through the DD tomography model. The model has sharper features and a better correspondence between the main region of seismicity and the position of the sharp velocity contrast compared to the standard results (Figure 4b). (b) The right-hand panels show fault-normal slices through the standard tomography model. The model has features that are less sharp and a poorer correspondence between the main region of seismicity and the position of the velocity contrast than the DD results

COLLABORATIVE RESEARCH: SEISMIC CATALOGUE COMPLETENESS AND ACCURACY

Terry C. Wallace,[1] Frank Vernon,[2] and Gary Pavlis[3]

University of Arizona, [1] University of California San Diego,[2] Indiana University[3]

Sponsored by Defense Threat Reduction Agency

Contract No. DTRA01-00-C-0069,[1] Contract No. DTRA01-00-C-0062,[2]
and Contract No. DTRA01-00-C-0095[3]

ABSTRACT

The basic problem in assessing catalogues is assigning errors to locations and separating errors introduced by Earth structure versus the ensemble of stations chosen for the location. We are constructing a catalogue for the region stretching from Saudi Arabia to western China for 1995 to the present. We will use all available data sources, including several temporary, portable seismic experiments and private or national seismic networks that are not easily available to the researcher. The data sources include GSN, KNET, Geoscope, and Kaznet permanent networks; PASSCAL deployments in the Tien Shan, Pakistan, India, Saudi Arabia; and national networks from Oman, Jordan and Iran. The total number of stations with continuous broadband data in the area bounded by 10^o to 60^o N and 30^o to 110^o E is in excess of 130. Although some of the data streams are intermittent, or only deployed for part of the window of time in which we wish to develop the catalogue, we can estimate the number of events expected on the basis of the performance of KNET and the Saudi experiment is in excess of 25,000. The fact that high-quality seismic stations are located near the seismic activity makes the catalogue superior to any other product for the same region.

We have developed a new set of computer codes to process a database of arrival time data to produce improved estimates of two fundamentally different entities: (1) a set of three-dimensional (3-D) grids of travel-time corrections for each seismic station defined in the database, and (2) a set of improved location estimates for each seismic event that is consistent with the 3-D travel-time surfaces computed in the same procedure. The procedure we use has three steps: (1) cluster association, (2) location and simultaneous estimation of travel-time surfaces, and (3) error estimation.

We have looked at events of special interest. In central Asia a perfect set of test events is the “Omega” explosions conducted as part of the Kazakhstan-American calibration experiment. In addition to the International Monitoring System (IMS) stations, at least some of the Omega events were recorded by 19 additional stations at regional distances. We have conducted a series of experiments to (a) determine optimal station coverage to produce ground truth GT-5, (b) develop empirical procedures for optimizing the phase information from regional records, and (3) test several joint hypocenter determination scenarios. Our tests highlight the importance of calibrated stations and the benefits of using all available data.

OBJECTIVE

Seismic event detection and location are the single most important research issues for adequately monitoring a Comprehensive Nuclear-Test-Ban Treaty (CTBT). Confidence in a CTBT relies on the assumption that any underground nuclear weapons test will be detected at an adequate number of seismic stations such that it can be located with sufficient accuracy that the test could be confirmed with an on-sight inspection. Another way to put this is that confidence in seismically monitoring a CTBT is equivalent to confidence in the *seismic catalogue* that is produced by the monitoring system. There are two principle components of a catalogue: (1) completeness in terms of representing all the seismicity within the region of monitoring interest (referred to here as *detection*), and (2) the accuracy of the source parameters for the events within the catalogue.

The present IMS has a low detection threshold and presumably high location accuracy in the Baltic shield region of Europe. This is due to the presence of various NORSAR arrays, which dramatically enhance the regional detection level. Other areas, in particular the southern hemisphere and Asia, have much higher detection thresholds. The quality of the locations produced by the prototype IMS has been assessed by comparing it to other catalogs of seismicity, in particular the NEIC's PDE. However, this comparison can be problematic because the PDE is not complete and suffers from sparse station distribution. Further, the locations in the PDE are not vetted against ground truth nor corrected for known heterogeneity in earth structure. A better gauge of the quality of the IMS catalogue is to measure it against a detailed local catalogue. However, this is a difficult task because individual catalogues are constructed with unique methodology, and thus are of uneven quality.

We are constructing a catalogue for the region stretching from Saudi Arabia to western China for 1995 to the present. We will use all available data sources which includes several temporary, portable seismic experiments and private or national seismic networks which are not easily available to the researcher. The catalogue construction will have two principle tasks: detecting and associating seismic phase information (the number of expected events within the time frame is in excess of 25,000), and locating these events and assigning realistic location errors. There are several fundamental research tasks that need to be performed before the catalogue can be completed. These include research on locating events which are primarily recorded at regional distances, evaluating both formal and systematic errors, and assessing "true" detection capabilities. Once the catalogue is constructed, it will provide an excellent test bed for research on strategies for spotlighting regions of enhanced monitoring interest, provide the data base for detailed regional velocity models (which can be incorporated into a general location scheme), and most importantly, assess the quality of catalogues routinely produced for monitoring purposes.

RESEARCH ACCOMPLISHED

Catalogue Construction and Accuracy

Overview. The geographic region which stretches from the Middle East to central Asia is an area of monitoring interest. It is also a region in which there have been a number of portable seismic experiments mounted in the last few years due to the interest in the structure and dynamics of the India-Asia collision. The total number of stations with continuous broadband data in the area bounded by 10^o to 60^o N and 30^o to 110^o E is in excess of 130. Although some of the data streams are intermittent or only deployed for part of the window of time in which we wish to develop the catalogue, we can estimate the number of events expected on the basis of the performance of KNET and the Saudi experiment is in excess of 25,000. The fact that high quality seismic stations are located near the seisimicity will make the catalogue superior to any other product for the same region.

Comparisons with other catalogues. The most rigorous test of catalogue completeness is to compare a local or regional earthquake list with a global catalogue that is produced with a standard technique. We have constructed a catalogue using KNET, KZNET, and the PASSCAL experiment GHENGIS, for a three year period and compared that to the PDE. There are nearly an order of magnitude more events in the local/regional catalogue, and the magnitude range is extended nearly 2 full unites (magnitude 4.0 for PDE compared to 2.0 for the regional/local catalogue).

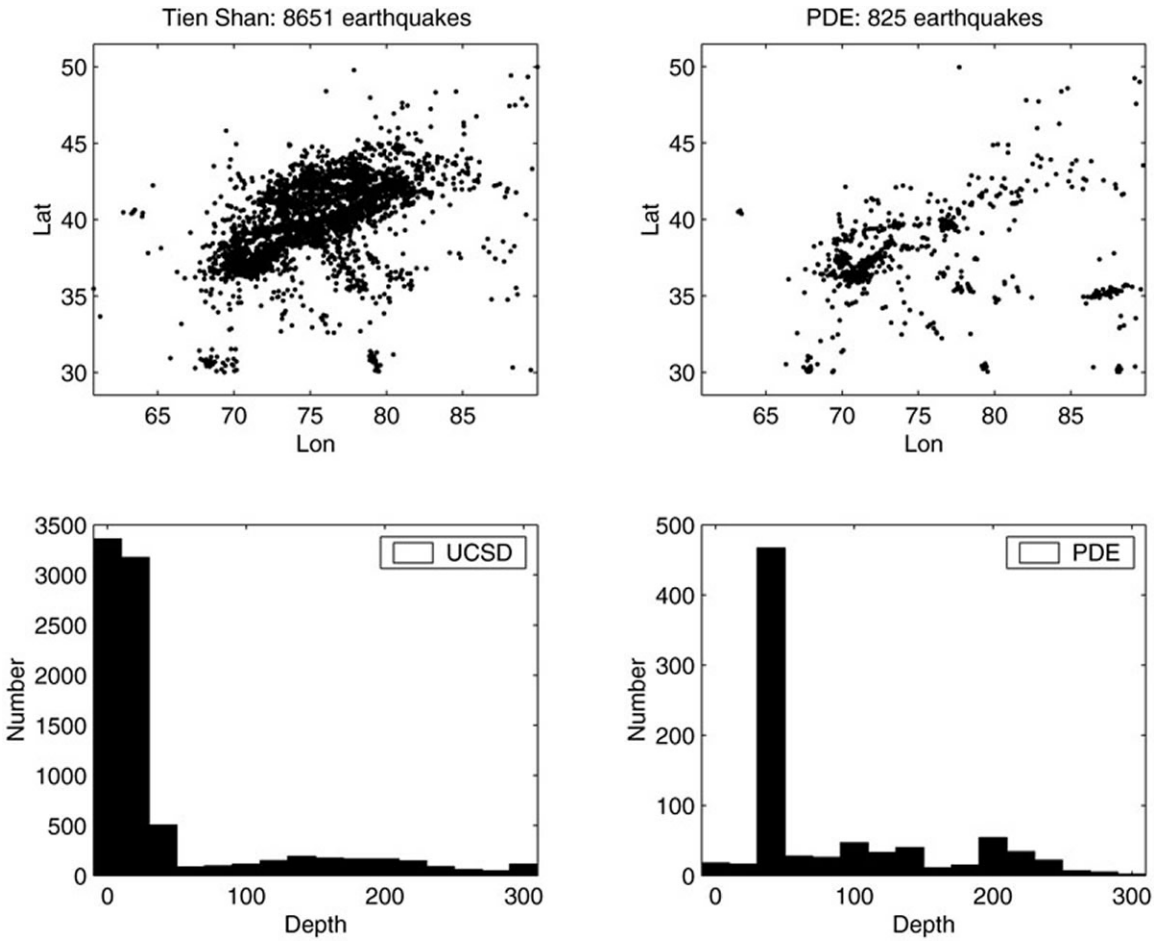

Figure 1: Comparison of regional/local catalogue to PDE

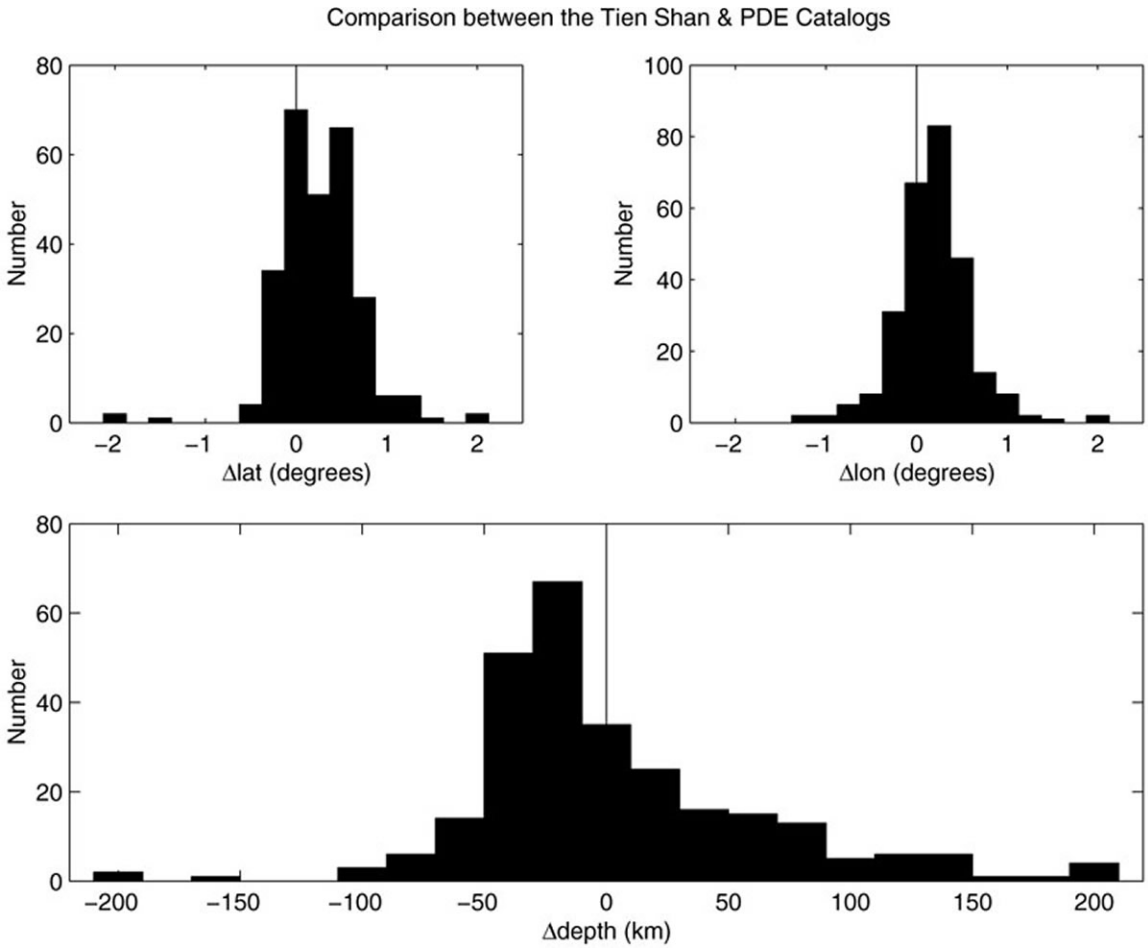

Figure 2: The differences between the local/regional catalogue parametrics and the PDE. If the locations are identidcal, then it will plot as a zero. The depth histogram has a large spike at –33 km associated subcrustal depth assigned to poorly located events in the PDE.

Event Location Methodology Development

Overview. We have developed a new set of computer codes to process a database of arrival time data to produce improved estimates of two fundamentally different entities: (1) a set of 3D grids of travel time corrections for each seismic station defined in the database, and (2) a set of improved location estimates for each seismic event that are consistent with the 3D travel time surfaces computed in the same procedure. In this section we describe this new algorithm and how it compares to other strategies that have been suggested for precision earthquake relocation.

Event cluster association. Our objective is to estimate a set of travel time corrections relative to a radially symmetric, reference earth model and to compute these corrections empirically in a 3D volume within the earth. The data we use for this purpose is arrival times of N_p seismic phases recorded at the set of N_s stations for which we have data. Consequently, the complete set of data objects we aim to produce is a set of N_s estimates of a 3D vector field (N_p travel time corrections per grid point) defined on some type of discrete grid. We chose to use a natural grid scheme for regional scale earth science applications that we will refer to as a geographical curvilinear grid (GCLgrid). A GCLgrid is a simple extension of what is commonly called a uniform field in the scientific visualization world. A uniform grid divides a box shaped region into a set of constant sized boxes. A GCLgrid makes the closest equivalent approximation in a spherical earth. That is, we divide a region of the earth into a series of spherical shells of equal thickness and then subdivide the shells into sub areas of approximately equal solid angles. To improve the uniformity of the grid at regional scales we translate the intersection of the prime meridian and equator to a specified origin, define a baseline using a great circle path at a specified azimuth, and then define an

equal angle grid of latitude and longitudes relative to this baseline and origin. This produces continent scale grids that have properties that do not depend upon the actual location of the grid. Simpler schemes based on the normal geographic reference, for example, commonly have serious distortions at high latitudes that are avoided by this method.

Once we define the geometry of a reference GCLgrid we process a list of associated events within a CSS3.0 database and link each event to one or more grid points using a database relation that is an extension of CSS3.0. The best recipe for assigning an event to a given point in space is an open question, but in the current implementation we use a simple set of rules based on distance. That is, we define a cylindrical region around each target grid point. The radius of this cylinder is initially set to a specified minimum size. We count the number of events within the specified volume. If a specified minimum number of events are not present within this volume the sphere is expanded incrementally until either the hit count exceeds the minimum or the radius exceeds a specified maximum. In the later case no links to the grid point are stored in the database. Otherwise we compute the hypocentroid (center of mass) of the ensemble of events and store the hypocentroid and indices that connect it to all events that form that ensemble.

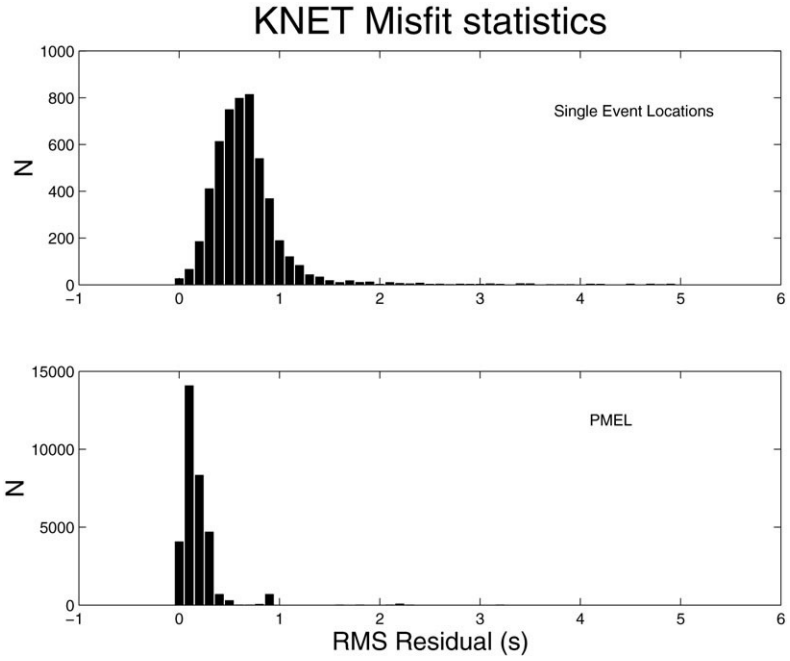

Figure 3: Misfits using PMEL vs. single event locations.

This simple approach is most appropriate for processing of existing catalog data for which waveforms may not be readily available. Current work is focused on utilizing waveform data as part of the clustering problem. That is, it is now widely known that sources that are closely located in space produce similar waveforms at common stations (reciprocal arrays). We are working on correlation methods based on a form of wavelet processing that builds on recent papers by Lilly and Park (1995), Bear and Pavlis (1997, 1999), and Bear et al. (1999). We use a set of special functions that Lilly and Park (1995) termed multiwavelets due to their close kinship to the Slepian tapers used in multitaper spectral analysis (Thomson, 1982). Multiwavelets provide a mechanism to produce a cross-correlation method that is a hybrid of Fourier and time-domain methods. We have successfully developed a computer program to use this technique for phased array processing of data from three-component broadband arrays with apertures of greater than 100 km. This program allows us to simultaneously estimate the following observables and to place objective error estimates on each measurement: (1) slowness vector of best fit plane wave, (2) travel time residuals at each station relative to the best fit plane wave, (3) particle motion estimates for each station, and (4) average particle motions for the entire array. These parameters are measured in multiple frequency bands and can averaged or examined independently to study their frequency dependence.

We are in the process of applying this technique to teleseismic and near-regional events recorded by the Kyrghyz network (KNET). We have found that with this approach we are able to measure P wave arrival times to subsample accuracy (timing uncertainty of the order of 0.01 s for teleseismic P waves recorded at 40 sps) and array slowness vectors to better than 1 part in 10^4. This may provide a superior way to utilize earthquake monitoring networks like KNET for regional location estimation. That is, it may be preferable to treat dense collections of broadband stations as phased arrays instead of utilizing individual arrival times in location estimation.

We are in the process of adapting the receiver array processing program to source arrays. That is, an ensemble of events located closely together in space observed at a single station commonly have coherent waveforms that can be processed by the same waveform multiwavelet correlation methods. There are two primary differences from receiver array processing and source array processing: (1) the key observables are different, we do not have to deal with slowness vectors but focus strictly on estimating precision time differences; and (2) the amplitudes from different sources can vary by orders of magnitude. The former makes the processing simpler than receiver array processing and the later is a major complication. For the later we are experimenting with a weighting scheme that measures coherence of each seismogram relative to the stack and downweights incoherent traces in an iterative procedure.

Location methodology. The approach we use for simultaneous estimation of improved earthquake locations and the ensemble of path corrections is the Separated Earthquake Location Method (SELM) described originally by Pavlis and Hokanson (1985). SELM is an extension of the Progressive Multiple Event Location (PMEL) method of Pavlis and Booker (1983). PMEL/SELM are multiple event location methods that are extensions of the classical Joint Hypocentral Determination (JHD) techniques (Douglas, 1967). The primary distinction between PMEL and JHD is that JHD solves the system of equations for an ensemble as a single, large matrix while PMEL separates the nonlinear location parameters from the linear, station correction terms. In our experience PMEL improves stability through iterative updates of earthquake hypocenter coordinates and through robustness introduced by automated deletions of events that have statistically significant differences in rms misfit compared to the ensemble average. This is not possible with JHD where the whole system of equations is inverted simultaneously.

SELM adds an important second feature that we exploit. Pavlis and Hokanson (1985) show how to construct a pair of complementary, orthogonal projectors, which we will refer to as $\boldsymbol{P}_R$ and $\boldsymbol{P}_N$. We apply these projectors using the relation

$$\boldsymbol{s} = \boldsymbol{P}_R \, \boldsymbol{s}_{3d} + \boldsymbol{P}_N \, \boldsymbol{s}_{data}$$

where $\boldsymbol{s}$ denotes a $N_s N_p$ vector of "path anomalies. That is, each component of $\boldsymbol{s}$, is a difference, $s_i=(t_{3d})_i - (t_{ref})_i$, between the travel time based on three-dimensional earth model and some 1-D reference model.

In the current implementation, which we will henceforth refer to as *dbpmel*, an ensemble of events and their related arrival times are associated with target points in space (GCLgrid structure) using the clustering algorithm described above. The actual algorithm uses a relational database table analogous to assoc that links event ids to grid points. The generalized PMEL/SELM program is then applied to the ensemble of events assigned to each target point in space. For points with sufficient data we compute the solution as described above. For points with insufficient data our method guarantees that our estimate of $\boldsymbol{s}=\boldsymbol{s}_{3d}$. That is, the computed path anomalies automatically revert to those computed from the reference 3D model when no data is available, but otherwise use all available data to refine the estimated path anomalies. The end result is a set of path anomaly estimates (defined on a GCLgrid in space) derived empirically as a best fit to all the available data.

The vectors we call $\boldsymbol{s}_{3d}$ and $\boldsymbol{s}_{data}$ use a different realization of 3D earth structure. Jordan and Sverdrup (1981) introduced the concept called the "hypocentroidal decomposition theorem. That is, for an ensemble of events that are localized in space the absolute location of the group is fundamentally indeterminate but precise estimates of $\boldsymbol{s}$ can dramatically reduce the scatter in the relative location of events within the group. The J&S method resolves this ambiguity by constructing a projector that annihilates the dependency of the solution on $\boldsymbol{s}$. Furthermore, recent work by Wolfe (2002) shows that the double difference technique (Waldhauser and Ellsworth, 2000) is actually equivalent to applying the J&S method to a weighted set of equations with the weights dependent on the number of pairs of events differenced. That is, both double difference and the J&S method explicitly or implicitly use projectors designed to annihilate the dependence upon s. The projectors we construct take the opposite approach. In *dbpmel* the projectors are constructed to annihilate the dependence of residuals on the hypocentral parameters

instead of $\boldsymbol{s}$. This allows us to utilize the term $\boldsymbol{P_R}\, \boldsymbol{s}_{3d}$ to add ancillary information to resolve the absolute location ambiguity. That is, we utilize a 3D model as a secondary reference model. The 3D model is used only to resolve the absolute location ambiguity. The data are used directly to estimate the term $\boldsymbol{P}_N\, \boldsymbol{s}_{data}$ using the PMEL algorithm. Because the $\boldsymbol{P}_R$ and $\boldsymbol{P}_N$ projectors are orthogonal the two procedures are decoupled within the limits of linearization. The method described in Jordan and Sverdrup's 1984 paper shares this decoupling feature but is incapable of applying the equivalent of $\boldsymbol{P_R}\, \boldsymbol{s}_{3d}$ exactly because it forces the solution to be independent of s. Double difference solutions can accomplish almost the same thing by computing all theoretical travel times in a 3D reference model. We would argue, however, that our approach has two advantages over a 3D implementation of double differencing. First, 3D travel time computation remains a major computing problem. In our implementation 3D model estimates need to only be computed once per grid point instead of for all travel time calculations. Given that results presented here on regional catalogs with the order of 10^4 events have run times of the order of cpu days, this is not a factor that can be dismissed. Secondly, Wolfe (2002) shows that a problem with applying double differences to regional catalogs is that the entire catalog gets linked together in a complex way that depends on the distribution of events and stations. This means that if new data become available a relocation with double differences would have to always start from all the available data to keep results internally consistent. Our PME/SELM implementation, in contrast, is localized through the gridding scheme. It could, in principle, be automated to update each grid point as a each new event is recorded. Such an approach would allow a scheme for continuous updates of empirical, 3D travel time grids as new data are acquired.

Improving Locations and Errors

A problem-free seismic network with excellent azimuthal coverage of the seismic area of interest and an accurate model of the velocity structure does not guarantee precise earthquake locations. This is because location errors can result from uncertainties in the time of the seismic wave's arrival or misidentification of the seismic phases. New algorithms, based on seismic waveform cross-correlation, can account for uncertainties in arrival times and in some cases correct for misidentified phases (e.g., Jordan & Sverdrup 1981; Pavlis, 1986; Got et al., 1994). These methods make use of the fact that earthquakes from the same region (< 3 km) who's seismic waves travel the same path from source-to-station have similar waveforms. By correlating similar waveforms, we can often obtain sub-sample accuracy of seismic wave arrival times. This, in turn, can reduce the relative errors in earthquake locations to tens or hundreds of meters, values that are often an order of magnitude smaller than the errors in the original catalogues (Kilb & Rubin, 2002).

We demonstrate the power of these relocation methods with a simple example using Tien Shan catalogue data of aftershocks from the August 27, 1998 M6.1 earthquake in the Xinjiang province of China. Here, we correlate a master event with all other events (Figure 4). A more sophisticated approach, such as that of Got et al. (1994), compares each event to every other event. Using Got's method we can identify clusters of similar waveforms from events that may be ~co-located but have different focal mechanisms. We are currently streamlining and updating the algorithms and computer codes of Got et al. 1994 to interface with our ANTELOPE formatted databases. Our aim is to confirm the accuracy of the final locations by comparing results derived from the PMEL algorithm with the results derived from the Got algorithms.

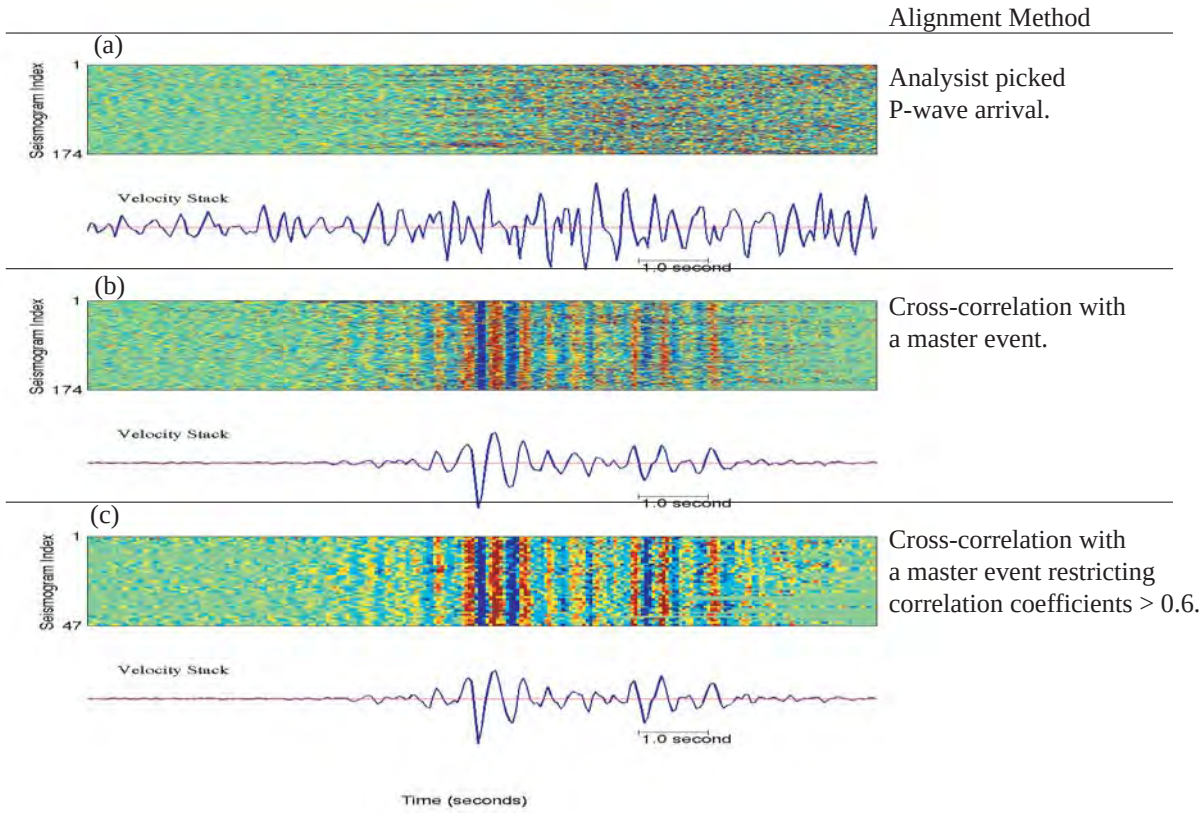

Figure 4: Simple example of waveform cross-correlation with a master event. (a) Vertical seismic waveforms from 174 earthquakes aligned on the analysts picked P-wave arrival (upward motion is red; downward motion is blue). As the noisy data stack shows, this alignment is not optimal. (b) After cross-correlation with a master event, the stack has a clear S-wave signature, and as many as 12-20 fringes are identifiable in the color map, indicating similarity in the seismic waveforms. (c) As in (b) but restricting all pair-wise correlation coefficients to be above 0.6. This limits the dataset to 47 earthquakes.

CONCLUSIONS AND RECOMMENDATIONS

We have constructed a catalogue for central Asia using regional networks and temporary PASSCAL deployments. The catalogue has 10 times as many events as the PDE for the same spatio-temporal footprint, and the difference in location scales with event size. Further, our catalogue is rich in small events that do not appear in other global catalogues such as the REB and ISC, and represents the power of regional monitoring with national resources or portable experiments. At present, the locations are from automated processing; in the next year we will relocate these events using the progressive multiple event methodology, which was also developed and enhanced during this contract year.

ACKNOWLEDGEMENTS

Although the Authors are the Principal Investigators on the project, a number of others are working on the various tasks. Deborah Kilb has been working on the catalogue completeness analysis and is using her experience on waveform cross-correlation to help with the travel errors. Tammy Baldwin has been working on the use of PMEL with sparse stations. Marie Renwald helped with the production of this paper.

REFERENCES

Bear, L. K., G. L. Pavlis, and G. H. R. Bokelmann (1999). Multiwavelet analysis of three-component seismic arrays: Application to measure effective anisotropy at Pinon Flats, California, *Bull. Seism. Soc. Amer.*, **89**, 693-705.

Bear, L. K. and G. L. Pavlis (1999). Multichannel estimation of time residuals from seismic data using multiwavelets, *Bull. Seism. Soc. Amer.*, **89,** 681-692.

Bear, L.K. and G.L. Pavlis (1997) Estimation of slowness vectors and their uncertainties using multiwavelet seismic array processing, *Bull. Seism. Soc. Amer*., **87**, 755-769.

Douglas, A. (1967). Joint epicentre location, *Nature*, **215**, 45-48.

Jordan, T. H. and K. S. Sverdrup (1981). Teleseismic location techniques and their application to earthquake clusters in the south-central Pacific, *Bull. Seism. Soc. Amer.*, **71**, 1105-1130.

Lilly, J. M. and J. Park (1995). Multiwavelet spectral and polarization analyses of seismic records, *Geophys. J. Int.*, **122**, 1001-1021.

Pavlis, G. L. (1992). Appraising relative earthquake location errors, *Bull. Seism. Soc. Amer.,* **82**, 836-859.

Pavlis, G. L. (1986). Appraising earthquake hypocenter location errors: a complete, practical approach for single event locations, *Bull. Seis. Soc. Amer.*, *76*, 1699-1717.

Pavlis, G. L. and J. R. Booker (1983). Progressive multiple event location (PMEL), *Bull. Seis. Soc. Amer.*, **73**, 1753-1777.

Pavlis, G. L. and N. B. Hokanson (1985). Separated earthquake location, *J. Geophys. Res.*, **90**, 12,777 12,789.

Thomson, D. J. (1982). Spectrum estimation and harmonic analysis, *Proc. IEEE*, **70**, 1055-1096.

Waldhauser, F. and W. L. Ellsworth (2001). A double-difference earthquake location algorithm; method and application to the northern Hayward fault, California, *Bull. Seism. Soc. Amer.*, **90**, 1353-1368.

Wolfe, C. J. (2002). A note on earthquake relocation using difference operators, *Bull. Seism. Soc. Amer.*, in press.

Seismic Identification and Source Characterization

IMPROVING ESTIMATES OF DEPTH, MAGNITUDE, AND FAULTING PARAMETERS OF EARTHQUAKES IN CENTRAL ASIA

Charles J. Ammon,[1] George E. Randall,[2] Jordi Julia,[1] Eliana Arias[1]

Penn State University,[1] Los Alamos National Laboratory[2]

Sponsored by National Nuclear Security Administration
Office of Nonproliferation Research and Engineering
Office of Defense Nuclear Nonproliferation

Contract No. DE-FC04-02AL67668[1] and W-7405-ENG-36[2]

ABSTRACT

Accurate and stable seismic source parameters for small-to-moderate size events are essential for many aspects of regional nuclear-explosion monitoring. For example, magnitude and distance amplitude corrections (MDAC) have been developed for regional discrimination, but they rely on stable moment estimates. We develop a catalog of regional earthquakes in eastern Asia with estimated seismic moments, source mechanisms, and depths using regional seismic data. A significant challenge of modeling small-to-moderate-size seismic sources is the necessity of relying on short-period signals with long travel paths that have substantial sensitivity to earth structure along the path. When the path effects are unknown or difficult to account for, we must rely on components of seismic signals that are minimally dependent on the structure. Although regional surface-wave phases are strongly influenced by structure, surface-wave amplitude spectra can be modeled adequately with relatively simple earth models, and these spectra carry valuable information on source character. Our efforts build on existing seismic source analysis techniques. We directly model regional seismograms where possible but combine those with surface-wave amplitude spectra observed at more distant regional stations. The inversion is performed using a grid search for strike, dip, rake, moment, and depth. Choosing suitable weights for the different data sets remains a challenge that will only be overcome with experience. Initially, all data are weighted equally by normalizing seismograms and spectra by their uncertainty and the number of observations in each data set. For larger events (MW > 5) we can also include long-period (approximately 40-s period) body-wave trains, which can be modeled reliably using simple stratified earth models. The use of spectra and long-period signals is ideal for estimating the moment and faulting geometry of signals but simple least-squares norms based on these signals do not often provide satisfactory resolution of source depth (when the source is shallow). However, in cases where the long-period mechanism is relatively stable as a function of depth, we can overcome this limitation by exploiting signals more diagnostic of source depth such as teleseismic body-waveforms, broadband Pn waveforms, or select short-period Rayleigh wave spectra. Our recent focus has been on the inclusion of signal-to-noise estimates into the inversion norms, tracking separate norms for time and frequency-domain signals, separate norms for P-SV-Rayleigh and SH-Love wave signals, and the use of more statistically robust amplitude spectral measures. Our preliminary results suggest that Harvard CMT moments may be biased slightly high for events near the low end of their threshold. We have not modeled enough events to explore potential regional variations in the bias. Moments from the inversion can be used to help calibrate coda-based magnitude scales for the region.

coverage of radiation patterns is improved and second, Rayleigh wave amplitude spectra contain valuable information on the source depth. For shallow events, improved resolution of the depth requires short-period information because the information on shallow depths is contained in the short-period signals. Herrmann (1979) exploited information in intermediate-period surface waves to estimate the faulting geometry and depth of earthquakes in east and central North America from old analog records. He observed signals out to distances of thousands of kilometers and extracted spectral amplitudes suitable for constraining the earthquake parameters. Our experience suggests that observations from such large distances in central Asia are not as simple or robust as those in the stable part of North America (*e.g.* Levshin *et al.*,1990). The signal amplitudes are complicated due to scattering and intrinsic attenuation, but generally well observed for larger events (Mw ~ 5). However, signals from small events may be isolated from background noise and extracted using phase-match filtering exploiting dispersion observations from larger events.

OBJECTIVE

Estimating the source type or faulting geometry of small seismic events located hundreds of kilometers from the nearest seismometer can be difficult. Typically one of two classes of modeling approaches is adopted: spectral or time-domain. Spectral techniques use the observed variation in surface-wave spectra as a function of azimuth to match the radiation pattern of the source (*e.g.* Patton, 1976, 1980, 1998; Herrmann, 1976, 1979; Romanowicz, 1982; Patton and Zandt, 1992; Herrmann and Ammon, 1997, and many others). Time-domain methods are straightforward matches to the observed seismograms and include both amplitude and phase information (*e.g.* Langston, 1981; Dreger and Helmberger, 1991, 1992, 1993; Lay *et al.*, 1994; Randall *et al*., 1995; Ghose *et al*, 1998; Ammon *et al*., 1998, and others). Spectral methods can be designed to include amplitude only, or amplitude and phase information, while time-domain methods include both. Phase information provides valuable constraints on the source mechanism and depth, but the observed phase is often sensitive to details in Earth structure along the propagation path. Time-domain source inversion methods are usually applied to large events with good long-period signals or short-period signals of small events that have minimal distortion from Earth structure (such as teleseismic P and SH waves) or local and close-regional (less than a few hundred *km*) signals. To use phase in surface-wave spectral analyses, a good estimate of the surface-wave phase velocity variations between the source and receiver is needed.

In the case of nuclear-explosion monitoring, the best signals from a shallow small event are most likely to be short-period surface waves. But directly fitting the phase of short-period Rayleigh waves (probably the best regionally observed, deterministic signal from a small, shallow event) is challenging because these waves are sensitive to shallow, variable structure along the propagation path. Rayleigh-wave spectral amplitudes are less sensitive to structure variations than the corresponding signal phase, and contain valuable information on the source depth. Thus, it is desirable to combine the part of distant signals that is less sensitive to structure with the amplitude and phase information from the closer stations.

Simultaneous spectral and time-domain seismic source modeling

To achieve this, we combine surface-wave spectral amplitude modeling and time-domain waveform fitting in a grid-search algorithm to estimate the source mechanism (systematically check strike, dip, rake, and depth, and include an isotropic source for comparison). The procedure includes surface-wave amplitude information for stations distant from the source and includes both amplitude and phase information from the closer observations and teleseismic body waves if the event is large enough for these to be observed (Figure 1). Incorporating observations from more distant stations makes a significant contribution to seismic source studies in two important ways: First, the azimuthal coverage of radiation patterns is improved and second, Rayleigh wave amplitude spectra contain valuable information on the source depth. For shallow events, improved resolution of the depth requires short-period information because the information on shallow depths is contained in the short-period signals. Herrmann (1979) exploited information in intermediate-period surface waves to estimate the faulting geometry and depth of earthquakes in east and central North America from old analog records. He observed signals out to distances of thousands of kilometers and extracted spectral amplitudes suitable for constraining the earthquake parameters. Our experience suggests that observations from such large distances in central Asia are not as simple or robust as those in the stable part of North America (*e.g.* Levshin *et al.*,1990). The signal amplitudes are complicated due to scattering and intrinsic attenuation, but generally well observed for larger events (Mw ~ 5). However, signals from small events may be isolated from background noise and extracted using phase-match filtering exploiting dispersion observations from larger events.

RESEARCH ACCOMPLISHED

The goal of estimating source depth with some precision requires a combination of observations. Particularly valuable in constraining earthquake depth are short-period Rayleigh waves, which may contain a spectral notch indicative of source depth (e.g. Herrmann, 1979) but often show systematic amplitude variations that vary with depth. Short-period surface waves can be tricky and when analyzing the signals some form of mode isolation can help simplify their interpretation. For now we have used group velocity windows with spectral smoothing to simplify the seismic signals, but our spot checking the impact of mode isolation indicates that it is often not necessary for larger events - or

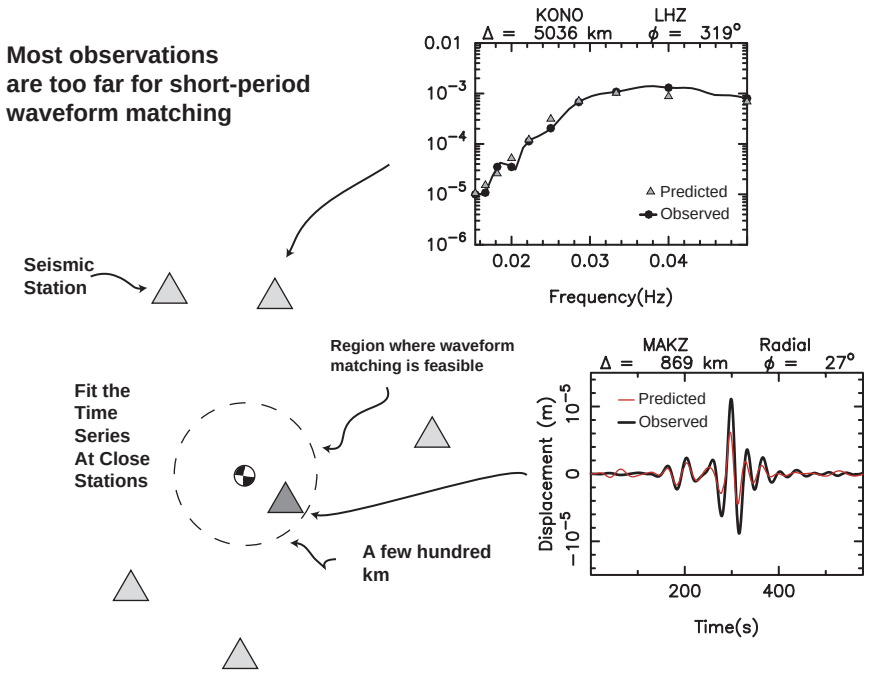

Figure 1. Schematic illustration of the joint source parameter inversion scheme. The triangles represent seismic stations, the focal mechanism represents the source location. The basic idea is to combine observations with a minimal sensitivity to earth structure to produce more accurate estimates of the event mechanism and depth. Since most observations are too far for direct short-period waveform modeling, we sacrifice the phase information and use only the more robust spectral amplitudes at those sites. Phase information is included from seismograms recorded at nearby stations, teleseismic P-waves, or regional *Pnl* arrivals. Sample observations and predictions are shown to the right of the cartoon.

at best it adds little improvement. Such may not be the case for small events with low signal-to-noise where some form of signal enhancement is needed.

Our primary control on the source mechanism arises from the azimuthal variation of Rayleigh and Love wave spectra. Nearby time-domain signals provide the required phase information as well as additional information on the mechanism and often the most sensitivity to depth. All spectra are estimated using a windowed auto-correlation function which produces smoother and statistically more reliable spectral amplitudes. This procedure requires substantially more time than simply using the FFT amplitude spectrum since the smoothing requires that we incorporate periods adjacent to those used in the misfit norm. However, the smooth, statistically better measures will undoubtedly be more valuable for analyses of path effects and systematic variations in signals at particular stations. The seismic moment for each mechanism tested in the grid search is estimated using an L1 fit to the logarithm of spectral amplitudes of all the signals. Green's functions are computed using a generic model of a slightly thicker than average (46 km) continent resting on and earth-flattening transformed version of the isotropic PREM model.

Our early inversions revealed that many of the data available from the global seismic networks are noisy or contain other problems that render them unsuitable for use in an inversion. To identify such problems we visually inspect all the data in the bandwidth from 100 to 20 seconds period to identify signals with grossly inadequate signal-to-noise ratios. To insure that we rely more heavily on the best observations, we weight each spectral observation by the inverse of the ambient seismic noise at the same period. The ambient noise is estimated using the pre-P-wave signal. Each signal's spectrum is also weighted relative to all other spectra using the mean of spectral amplitude of the noise in the period range of interest. Distant stations are down-weighted using a simple one-over-distance measure - this is strictly a pragmatic approach designed to include our *a priori* assumption that the model we are using is probably best suited for short paths. Interestingly, we have found little correlation of misfits with distance, suggesting that we are able to fit the most distant observations with the same fidelity with which we can fit the intermediate distance obser-

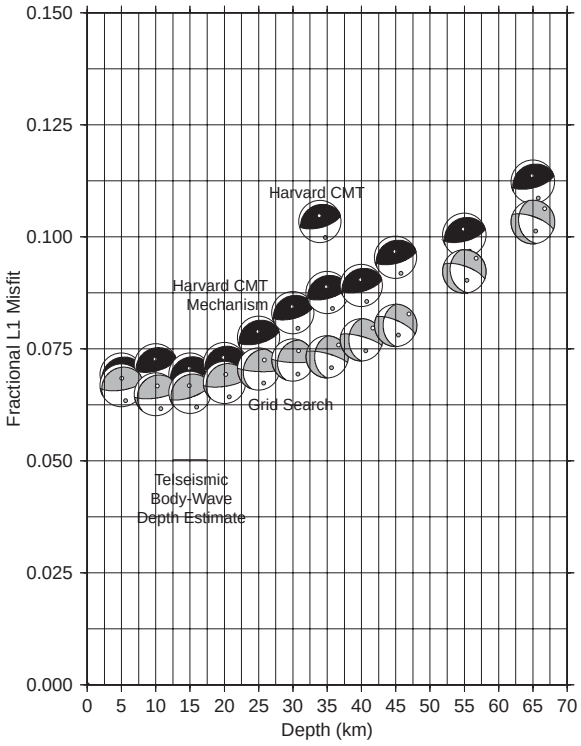

Figure 2. Misfit versus depth variation (along with mechanism variations) for a fixed mechanism (moment, depth) and full grid searches (mechanism, moment, depth).

vations. Azimuthal bias in station coverage is moderated by weighting observations by the number of other signals within 15° azimuthal range of the particular observation. In other words, a signal separated from all others by a gap of more than 15° has an azimuthal weight of 1.0, a signal with four other signals within 15° has an azimuthal weight of 0.2 (1/5, including the observation). Automating the weights reduces substantially the time needed to adjust the parameters during an inversion. Observation weights reflect our attempts to cope with the problems of driving an inversion with a single-number norm.

Although each event is different, the combination of these observations can produce good depth, mechanism, and seismic moment constraints. An example depth-misfit curve is shown in Figure 2. The shallow nature of this reverse faulting event is very nicely constrained by the short-period surface waves, as well as nearby time-domain signals. The mechanism near the top-center of the plot (33 km, 0.1 misfit) identifies the misfit of the Harvard CMT solution to our observations using the Harvard best double couple, the Harvard seismic moment, and the assumed source depth of 33 km. The other dark shaded mechanisms identify grid-search results assuming the Harvard CMT best double-couple mechanism with a seismic moment optimized to fit our data using Green's functions for our model. The optimal moment for the assumed Harvard mechanism is about 20% lower than that reported in the CMT catalog. The lightly shaded mechanisms are the results of a full grid search with a free mechanism and seismic moment. The best fitting solutions from both the constrained and unconstrained grid searches agree well in both mechanism and depth (near 10 km). The unconstrained mechanism is slightly rotated relative to the Harvard solution, but the agreement is certainly within uncertainties of either technique. The abrupt change in focal mechanism in the full grid search results near 25 km does not correspond to a change in the velocity model but is a depth at which the fit to the time domain signals degrades quickly. The variation in the complete norm shown in Figure 2 does not necessarily reflect the variation in fit to just the time-domain signals. To identify such instances we track five norms, 1. vertical-radial time-domain and 2. spectral misfits, 3. transverse time-domain and 4. spectral misfit, and the 5. combination of all misfits (which we used in Figure 2).

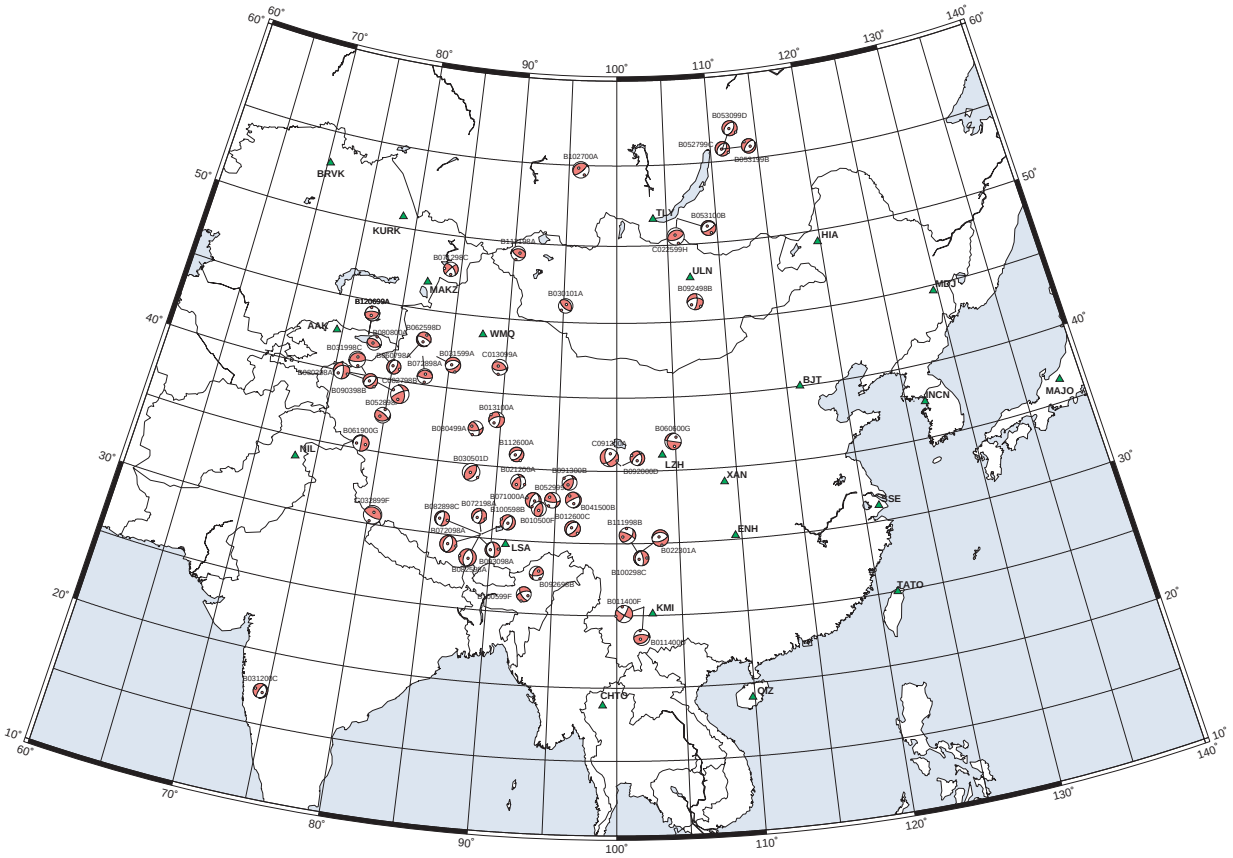

Figure 3. The map above shows the results of inversions using the waveforms and spectra for 30 events in the Harvard CMT Catalog. The results are generally consistent although some of our mechanisms have significant rotations relative to the CMT solutions (and what you might expect from tectonics). We believe that part of the problem with our preliminary results lies in the use of small-amplitude signals. Our seismic moments (or Mw) are less sensitive to variations in structure and noisy traces (for these inversions we used the L1 norm and the median values to compute an optimal moment in the period range from 65 to 20 s). For some events, no nearby waveforms are available and the results are ambiguous (but constrained) - for example, the rake can be changed by $-\pi$.

Joint Amplitude-Spectra/Seismogram Grid-Search Inversion Results

Preliminary grid-search results are shown in Figure 3. In general our results agree with the Harvard mechanisms, although often some rotation of the mechanisms is required by our data and occasionally we appear to have less control on the mechanism. Perhaps the most interesting difference is the dependence of the seismic moment difference between Harvard and our analyses on seismic moment. For moderate-size events (Mw > 5.5) our moments agree well with Harvard's, for events near the threshold of the CMT method, more often than not the Harvard CMT moment is larger than the moments derived by us (Figure 4). No doubt some of the difference arises from the different models used in each method and our moment is really a fit of the spectrum from 80 to 20 seconds, for the smaller events, Harvard's moment is generally more appropriate near 40 seconds period (when only body waves are used). Most interesting is the character of the discrepancy, which suggests a systematic difference as a function of moment. For the smaller magnitude events, the misfit is substantial when inspecting the time-domain signals. All events with a grid-search moment magnitude less than 5.0 produce positive residual magnitudes (which indicates overestimation by Harvard or underestimation by us). Such differences may reflect the excitation functions for the different velocity structures assumed in each method, and while they cannot be resolved completely (moment depends on the assumed structure), the differences can be important and are worth noting.

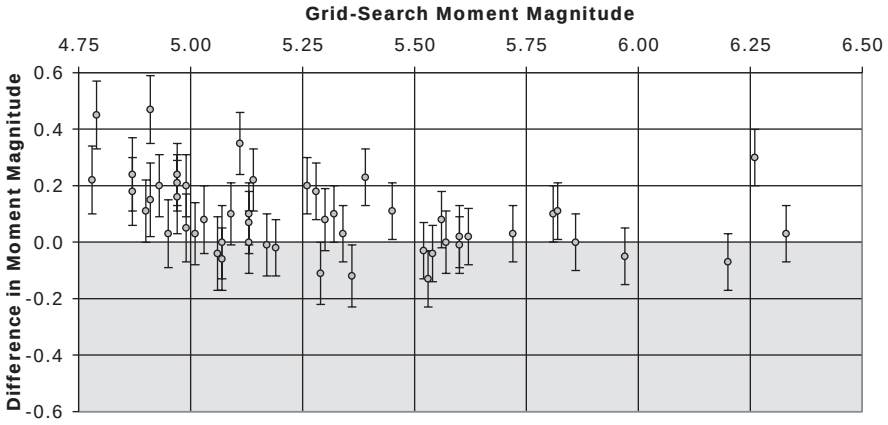

Figure 4. Comparison of the moment from grid searches and the Harvard CMT moment. Vertical axis shows the (Harvard Mw) — (Grid-Search Mw). Since the two approaches use different velocity structures and fit the data over different, finite bandwidths, the agreement should not be perfect. The CMT method tends to over-predict (or our method under-predicts) the moment for small events. Uncertainties were computed for the Harvard CMT using a Monte-Carlo method. The outlier at Mw 6.25 is a result of our failure to incorporate a time function for this larger event (Mw > 6.5).

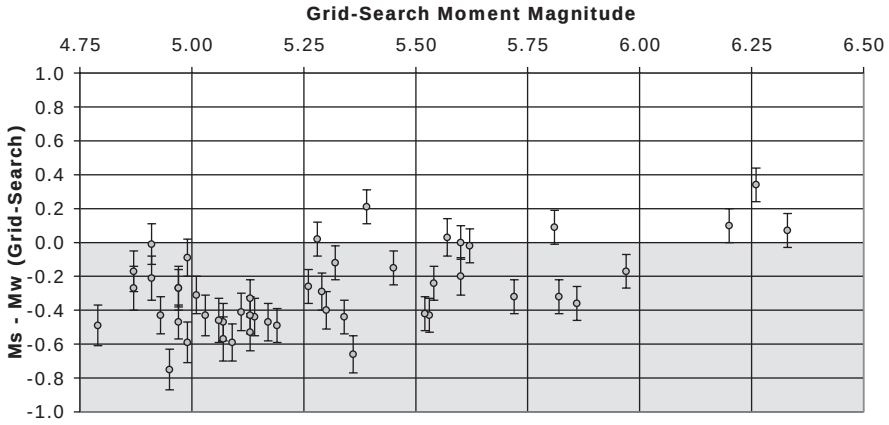

Figure 5. Comparison of the moment magnitude from grid searches and the USGS Ms estimate. Vertical axis shows the (Ms) — (Grid-Search Mw). Uncertainties were computed for the grid-search were computed using a Monte-Carlo method on the CMT moments (an approximation).

The moment-magnitudes obtained from the two waveform modeling techniques agree better than either does with Ms. A comparison of the grid-search M_W and the USGS Ms is shown in Figure 5. For simplicity, we've assumed the same uncertainty in grid search M_W as exists in the Harvard CMT solution. Here the trend is the opposite with M_S for smaller events under-predicting their size. The trend is unchanged if you use the Harvard CMT moments - the differences are larger.

CONCLUSIONS AND RECOMMENDATIONS

The addition of teleseismic body waves directly into the inversion will also help refine the depths of the larger events for which the body-wave signals are adequate. It may be possible to simply use the teleseismic body waves to estimate depth, fixing the moment and mechanism from the spectra and regional seismograms. Then a relatively easy-to-implement cross-correlation misfit norm, which requires little effort on aligning the signals, could be used to estimate

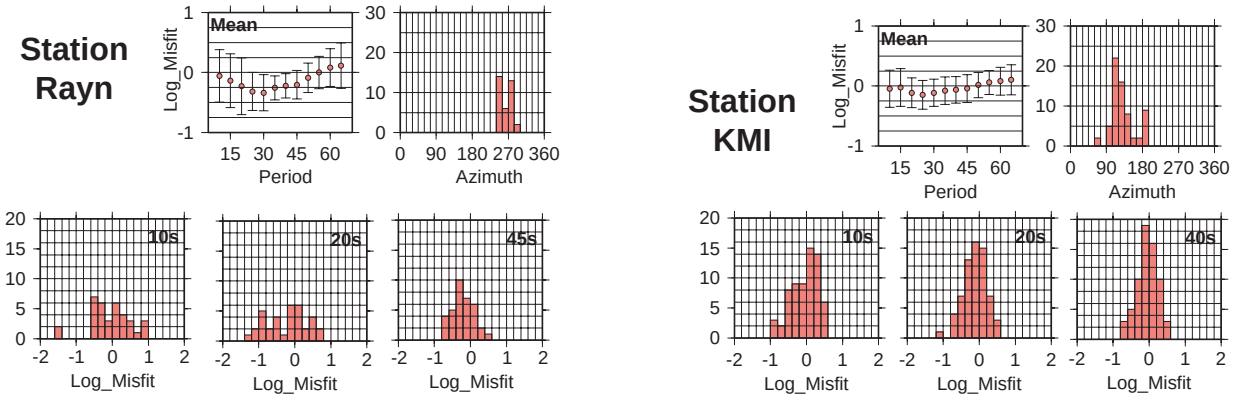

Figure 6. Comparison of path complexity issues in modeling. The panel on the left shows the performance of station RAYN (Saudi Arabia) in the inversion of events in Asia compared with station KMI located in south-central Asia. As expected KMI performs much better. We recommend that information based on the actual fits of the data of large events signals can be used to construct a table of station weights for events in different locations (eventually). Note the variation in performance with period. These weights should perform better than simple distance-dependent weights.

the depth. For the shallowest events, inspection of short-period surface waves from nearby stations may help confirm source depth and add important confidence to the grid-search results. Such additional information is subjective but there may be no likely way to avoid classifying solution quality without some fuzziness. Seismic signals are complex, and their sensitivity to different aspects of the source are difficult to quantify with easily computed misfit norms.

The key to producing a reliable system for inverting spectra and seismograms is the assignment of appropriate weights to the observations. Weighting by signal-to-noise is a straightforward decision. Other weights require more expertise and experience to assign. In particular, we have computed misfits for a set of events throughout central Asia. We recommend that any system designed to invert for moment, mechanism, and depth be adaptable and updated to include new information on station performance (e.g. Figure 6). These station experience-based weights are not so much a statement on station quality, but on path complexity. This information could, for example, be used to replace our simple distance-dependent weight using information on path complexity and length, which is reflected in the station misfits. These weights would also naturally be period-dependent, and we expect that the longer periods may be less corrupted by geologic complexity.

ACKNOWLEDGEMENTS

We thank P. Wessel and W. H. F. Smith, the authors of GMT for producing easy-to-use, quality software for making maps and charts and T. J. Pearson, author of the PGPLOT library, for producing a robust, flexible, well-documented graphics library.

REFERENCES

Ammon, C. J., R. B. Herrmann, C. A. Langston and H. Benz (1996), Source parameters of the January 16, 1994 Wyomissing Hills, Pennsylvania earthquakes, *Seism. Res. Letters*, **69,** 261-269.

Dreger, D. S., and D. V. Helmberger (1990), Complex faulting deduced from broadband modeling of the 28 February 1990 Upland Earthquake, *Bull. Seism. Soc. Am.*, **81**, 1129-1144.

Dreger, D. S., and D. V. Helmberger (1991), Source Parameters of the Sierra Madre earthquake from regional and local body waves, *Geophys. Res. Letters*, **18**, 2015-2018.

Dreger, D. S., and D. V. Helmberger (1993), Determination of source parameters at regional distances with three-component sparse network data, *J. Geophys. Res.*, **98**, 8107-8125.

Ghose, S., M. W. Hamburger and C. J. Ammon (1998), Source parameters of moderate-size earthquakes in the Tien Shan, central Asia from regional moment tensor inversion, *Geophys. Res. Letters*, **25**, 3181-3184.

Herrmann, R. B. (1979), Surface wave focal mechanisms for eastern North American Earthquakes with tectonic implications, *J. Geophys. Res*., **84**, 3543-3552.

Herrmann, R. B. (1986), Surface-Wave studies of some South Carolina earthquakes, *Bull. Seism. Soc. Am*., **76,** 111-121.

Langston, C. A. (1981), Source inversion of seismic waveforms: the Koyna, India, Earthquakes of 13 September, 1967, *Bull. Seism. Soc. Am*., **71**, 1-24.

Lay, T., C. J. Ammon, A. A. Velasco, J. Ritsema, T. C. Wallace and H. J. Patton (1994), Near-real time seismology: Rapid analysis of earthquake faulting, GSA Today, 4, 129,132-134.

Levshin, A., L. Ratnikova and J. Berger (1992), Peculiarities of surface-wave propagation across central Asia, *Bull. Seism. Soc. Am*., **82**, 2464-2493.

Patton, H. (1976), A note on the source mechanism of the southeastern Missouri earthquake of October 21, 1965, *J. Geophys. Res*., **81**, 1483-1486.

Patton, H. (1980), Reference point equalization method for determining the source and path effects of surface waves, *J. Geophys. Res*., **85**, 821-848.

Patton, H. J. (1998), Bias in the centroid moment tensor for central Asian earthquakes: Evidence from regional surface wave data, *J. Geophys. Res.*, **103**, 26,963-26,974.

Patton, H. J., and G. Zandt (1992), Seismic moment tensors for western U. S. earthquakes and implications for the tectonic stress field, J. Geophys. Res., 96, 18,245-18,259.

Randall, G. R., C. J. Ammon and T. J. Owens (1995), Moment-tensor estimation using regional seismograms from a Tibetan Plateau portable network deployment, *Geophys. Res. Letters*, **22**, 1665-1668.

Romanowicz, B. A. (1982), Moment tensor inversion of long-period Rayleigh Waves: A new approach, *J. Geophys. Res.*, **87**, 5395-5407.

DEVELOPMENT AND INVESTIGATION OF TRANSPORTABLE REGIONAL DISCRIMINANTS

Douglas R. Baumgardt, Zoltan Der, Meghan Keohane, and Angelina Freeman

ENSCO, Inc.

Sponsored by Defense Threat Reduction Agency

Contract No. DTRA01-00-C-0043

ABSTRACT

In this project, we are investigating problems associated with the transportability of regional phase amplitude ratios, such as *Pn/Sn* or *Pn/Lg* ratios, for discrimination of explosions and earthquakes for nuclear-explosion and treaty monitoring in different tectonic regions. In one study, we have improved our algorithm, developed last year, for identifying and quantifying the causes of the variance of regional *P/S* ratios using analysis of variance. We have developed an expectation maximization (EM) algorithm for two-way or three-way analysis of variance (ANOVA2-ANOVA3) for partitioning the variance of *P/S* ratio measurements into source, site, and path effects. The EM algorithm can be applied to combinations of data sets where there may be missing data. The algorithm is being tested on Scandinavian array recordings of earthquakes, nuclear explosions and mine blasts. Also, a user interface has been developed in Matlab© for applying the EM ANOVA2-ANOVA3 algorithm to array data. We have initiated an investigation of a new regional magnitude scale, similar to the *mb(Lg)* magnitude, called *mb(Sn+Lg)* magnitude based on the sum total of the regional shear energy contained in the regional *Sn* and *Lg* phases. This study is motivated by previous observations of *Lg* blockage that might limit the use of *mb(Lg)* for discrimination. Because the *Sn* and *Lg* phases have sometimes been observed to trade off in amplitude in regions of blockage, the *mb(Sn+Lg)* scale may be more stable than a magnitude scale based on either phase individually. Initially, we have developed a magnitude scale based on measurements of the total energy in the *Sn* and *Lg* wavetrain, corrected for distance attenuation, and calibrated to teleseismic *mb*. We have tested the *mb(Sn+Lg)* scale with earthquake data recorded by the old ILPA array in northern Iran, Zagros events recorded at regional seismic stations in the Middle East, and earthquakes and explosions in China and Russia recorded at CDSN stations. Finally, we began statistical study of the transportability of *P/S* ratio discriminants using separability measures and optimum transformations in order to reduce dimensionality of multiple frequency *P/S* ratios. These transformations consist of calculating the intra-class and inter-class scatter matrices for *P/S* ratio discriminants and using the eigenvectors, corresponding to the largest eigenvalues, of the inter-class matrix to compute optimum transformation of discriminants that provide best separation. We are applying this analysis to distance-corrected discriminants in different regions (e.g., China, Eurasia, North America) in order to compare discriminant effectiveness for different regions and to evaluate the transportability of optimum discriminant decision surfaces.

OBJECTIVE

Introduction

We are investigating issues concerned with the transportability of regional discriminants developed in a region of a distinct tectonic type and applied to another region of different tectonic type. The best definition of a region must be based on homogeneous propagation characteristics for the seismic phases involved and not on political or geographical subdivision. This implies some commonality in the crustal and upper-mantle structures with regards to tectonic origin. It is rather pointless, for instance, to compare the performance of a *Pg/Lg* discriminant in Scandinavia and western North America. The '*Pg* phase' in these two regions is obviously not the same. In Scandinavia, the Pg is relatively small in amplitude compared to *Pn* and *Lg*, whereas in western North America, the *Pg* is the largest regional compressional phase. Thus, it is likely that the two do not represent the same 'phase' propagating in the similar waveguides.

A totally different issue is how to handle regions with notably anomalous propagation characteristics. It has been noted earlier (Baumgardt, 2001) that certain crustal discontinuities, such as sedimentary basins, are associated with blockages or high attenuation of various regional seismic phases, primarily *Lg*. Since such regions may be relatively small in dimensions, it may be difficult to predict their effect on the spectra and amplitudes of seismic phases with paths crossing them and correct for them. Nevertheless, many such regions have been identified. Examples of these are the southern end of the Caspian Sea, Tibet, some regions of Iran, and the Andes Mountain regions. Typically, these regions are often areas that have been subjected to recent tectonic deformation and occupy narrow bands. If appropriate corrections have not been made for such regions of blockage, it may be the best to avoid applying seismic phase measurements involving these in routine discrimination.

In this paper, we discuss research efforts conducted to investigate factors that affect discriminant transportability and to investigate possible seismic discrimination approaches that are more robust for transportability. As a follow-on to our previous study of single array variances (Baumgardt *et al*, 2001), we have continued to examine, by means of analysis of variance (ANOVA), the contribution of site effects on the variance of regional *P/S* amplitude. In this paper, we have applied our ANOVA approach to multiple arrays. The goal of this work is to quantify the residual variance of regional *P/S* amplitude ratios after correction for attenuation. In the second study, we have investigated the problem of dimensionality reduction for multi-band regional *P/S* ratios and the combination of features that produce the optimal discrimination. In the third study, we have investigated the utility of a new regional magnitude based on the sum total of the energy in the *Sn* and *Lg* wavetrain, which we call *mb(Sn+Lg)*, that may be more stable than *mb(Lg)* in regions of strong Lg blockage.

RESEARCH ACCOMPLISHED

Multi-Array Analysis of the Site Variance of Regional P/S Ratios

In our initial study (Baumgardt *et al*, 2001), we studied the variations in the Pn, Lg, and Pn/Lg amplitude ratios recorded at Scandinavian events from underwater explosions. A two-way analysis of variance method (ANOVA2) was applied to study the partitioning of the amplitude and ratio fluctuations between site and source effects. As a follow-up to this study, we have begun a study of multi-array ANOVA2. In ANOVA2, we fit the following model to the amplitudes and amplitude ratios:

$$y_{ijk} = m + a_{,j} + b_{i,} + e_{ijk}$$

where y_{ijk} are the array element amplitudes or amplitude ratios, m is the mean of all the data, $a_{,j}$ is the source term, $b_{i,}$ is the site term, and e_{ijk} is the error term. This model is fit to the logarithms of amplitudes and amplitude ratios where it is assumed that the amplitudes and ratios are log-normal and dependent on both the additive event and the site effects, both of which are specified to have a zero sum. The errors are assumed to be normally distributed. ANOVA2, in essence, tests the hypothesis that the data come from the same population with a common mean (Johnson and Wichern, 1988). In this study, we focus on the variations in the site terms and ignore for the time being the significance tests on the commonality of the mean.

As an example of this analysis for multiple arrays, we applied it to the Pn, Lg, and Pn/Lg amplitude ratios measured for three seismic arrays. The data for this study came from a set of underwater explosions in the Baltic that were

recorded at three Scandinavian high-frequency seismic arrays, NORESS, FINES, and HFS, originally studied by Baumgardt and Der (1998). Our approach was to measure the amplitudes and their ratios, after correcting the amplitudes for distance. The results of the analysis in two frequency bands, 2-4 Hz and 4.5-9 Hz, are shown in Figure 1.

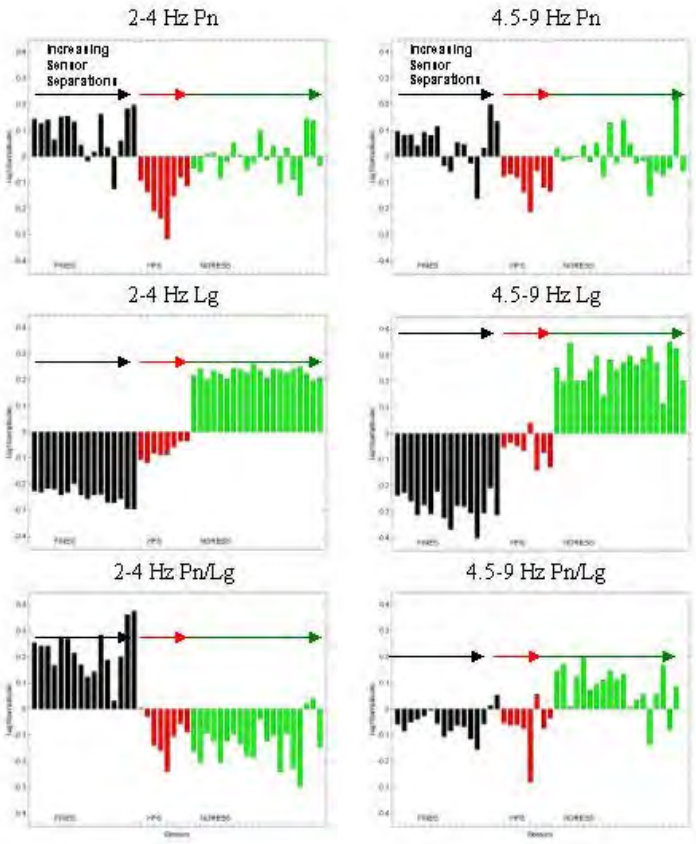

Figure 1. Examples of the effects of the arrays and sites in two frequency bands within arrays on the Pn/Lg ratio in two frequency bands obtained from ANOVA2. A generalized version of the EM algorithm was used to fill in a small number of missing observations. The site terms for each array are designated by different colors

Figure 1 shows that there are strong biases due to each array and site effects within each array. The ANOVA analysis of single arrays, described by Baumgardt *et al* (2001) gave Pn amplitude variations that controlled the variations in Pn/Lg site terms and the Lg site terms were more stable across the arrays. This is clearly evident in Figure 1 for the ANOVA applied to three arrays in combination, where the Pn site corrections have somewhat random variations of positive and negative values, with the exception of HFS in the 2- to 4-Hz band. The Lg variations, however, all have the same sign for each array. Thus, the random variations in the Pn site terms map into the Pn/Lg corrections.

The results of this study indicate that the principle site effect contribution to Pn/Lg variations is coming from the Pn site effects. However, when examining the variations between sites, the Lg variations are larger in magnitude than the Pn variations. Note that these amplitudes have been corrected for distance, so that these variations appear to be coming primarily from the site effects. Thus, when using the Pn/Lg ratio to identify seismic events, this variance needs to be factored into the estimates of the measurement precision for Pn/Lg ratios.

Transportability Issues

Assuming the existence of geophysically well-defined regions, the term *transportability* may mean the following different things:

1. Applicability of the same discriminant with statistics adapted to the specific region using available learning data sets and applying a consistent methodology to classify events (e.g. Fisk *et al*, 1996).
2. Applicability of a discriminant to various regions without any modifications, i.e. using statistics from other similar regions.
3. Application of the same discriminant with some adaptation of parameters but using assumed statistics for certain types of events (such as nuclear explosions) if learning sets for these are not available in the region.

In this paper, we prefer definition 1 while reconciling ourselves with the occasional necessity of applying definition 3. Option 2 is not likely to work because of the variability in the definition and physical nature of regional 'phases' from region to region. We shall also adapt the usual definitions of regional phases as they are commonly picked in the seismic bulletins from various regions, even though their excitation and propagation may be different from region to region. Given this regional variability, it seems certain the efficiency of discrimination will vary from region to region in a way that can be described in quantitative terms if sufficiently large learning data sets are available. In this paper we have not achieved this as yet, but we are attempting to set up a framework for worldwide transportability studies.

At regional distances, the most common discriminants used are distance-corrected spectral ratios of various wave groups. These constitute multi-dimensional discriminants because spectral ratio measurements are performed over numerous frequency bands and for multiple combinations of regional arrivals. Inspecting a typical plot of such data for a group of explosions and earthquakes, it is obvious that the distributions of the spectral ratios tend to be similar in various neighboring frequency bands, thus providing redundant information because of the strong correlation among the measurements in various bands and phase combinations. Typically, the separation between explosion and earthquake populations is poor at low frequencies (1-2 Hz) and improves with increasing frequency. Classification of a new event is commonly based on the positions of its many data points in such a graph relative to known earthquake and explosion data plotted in the same graph (e.g. Ryall *et al*, 1995).

Obviously, we do not need all the measurements in all spectral bands because some measurements may be more important than the others. Likewise, we may not need all the spectral ratios either. The question of how to combine such multiple measurements in the most effective way has not been studied extensively in regional seismology. Thus, the dimensionality of the data could be reduced considerably with appropriate data manipulation. Metrics of discrimination effectiveness are also needed to be able to compare various regions with regards to discrimination efficiency and transportability. What follows is a brief description of algorithms used in this study.

Handling of Missing Data-Generalized EM algorithm

In our data sets of spectral ratios, ratios in some bands may be missing. This may result from censoring of data because of low signal-to-noise ratios in either the numerator or denominator phases or other data problems. In order to utilize the available data fully, it is desirable to substitute estimated values into the slots of missing data and thus make the rest of the good data available to improve the correlation matrices used in discrimination.

We use the technique of expectation maximization (EM) to interpolate missing data using the available data values. We apply the following iterative procedure to compute the extrapolated data matrix:

a. Compute the first 'current' correlation coefficient matrix from the events that have complete sets of values in all frequency bands
b. Extrapolate the missing data points for all events that need them employing the 'current' correlation coefficient matrix using the formula below.
c. Compute the 'current' correlation coefficient matrix from the extrapolated data set; if the preset iteration number is reached go to d; otherwise, remove the extrapolated values and go to b.
d. Compute the correlation (not correlation coefficient) matrix for the reconstructed data set. These will be used in the separability analyses. Output the completed data matrix.

The extrapolated missing values a_i are computed as

$$a_i = \frac{\sum_k |C_{ik}| (a_k + m_i - m_k)}{\sum_k |C_{ik}|},$$

where the C_{ik} are the 'current' correlation coefficients, the summation over k occurs over the existing data values, and i is the index of the missing value. We are essentially correcting for the differences in means (m) between the existing and missing components and weight these according to the absolute values of the average correlations between them. As the iteration progresses, the values of the means, correlations, and extrapolated values will be optimized in some sense.

This completes the EM process. Typically a few iterations are quite sufficient. The approach described above is not the rigorous EM algorithm described in Duda *et al* (2001) but the one termed *generalized EM* algorithm by the same source, which includes a number of *ad hoc* methods for data extrapolation. The exact algorithm involves the iterative estimation of the population parameters from the existing data points without extrapolation of the missing values. It is cumbersome and slow computationally because numerous probabilities, usually assumed to be Gaussian, need to be computed. We feel that such complexity is not justified in this application. We go through this procedure in order to exploit the correlation information contained in the incomplete events and set up extrapolated data matrices that can be used in the handling of dimension reduction and separability issues.

Separability Measures and Optimum Transformations

Since spectral ratios of multiple regional phases in multiple frequency bands constitute discriminants with high dimensionality, dimensionality reduction is a desirable goal. Moreover, discrimination analysis will define the most efficient way to combine data and eliminate the measurements that contribute little to the solution.

Given the distributions of empirical data containing known event types, one can utilize several measures to examine how well a given category separates from others. The measures listed are based on the comparisons of the within-class scatter matrices $\boldsymbol{S}_W$ to the between-class scatter matrix $\boldsymbol{S}_B$. Different definitions of scatter matrices are given by Fukunaga (1990), Duda *et al* (2001), and Tou and Gonzalez (1974). The definition given to $\boldsymbol{S}_W$ by Duda *et al* (2001) for the two-class case is

$$\mathbf{S}_W = \mathbf{S}_1 + \mathbf{S}_2$$

and where

$$\mathbf{S}_i = \sum_{x \in D_i} (\mathbf{x} - \mathbf{m}_i)(\mathbf{x} - \mathbf{m}_i)^t,$$

where $\mathbf{m}_i$ is the mean vector of population i and the sum is over elements of class i . The between class scatter matrices $\boldsymbol{S}_B$ can be defined as

$$\mathbf{S}_B = (\mathbf{m}_1 - \mathbf{m}_2)(\mathbf{m}_1 - \mathbf{m}_2)^t$$

The solutions to the eigenvalue problem

$$\mathbf{S}_W^{-1}\ \mathbf{S}_B\ \mathbf{w} = l\ \mathbf{w}$$

from the equation above can be used to determine an optimum transformation for reducing the dimensionality of the problem (Duda *et al* 2001). The eigenvector associated with the largest eigenvalue, λ, gives an indication of the relative importance of the various orthogonal eigenvector components of the problem. The simplest transformation is the linear combination comprising the Fisher linear discriminant, expressed as,

$$\mathbf{w} = \mathbf{S}_W^{-1}(\mathbf{m}_1 - \mathbf{m}_2).$$

Thus, the optimum direction for best linear separation of the two populations is a projection of the vector connecting the means transformed by the matrix $\mathbf{S}_W^{-1}$. If this matrix is close to diagonal, the results should be similar to intuitive expectation based on the scatter diagrams. If not, the results may be hard to explain intuitively. Since we are striving for a simple optimum linear transformation, we shall use this transformation in our study. We have found that a simple linear discriminant derived from the transformation above works well for multi-band regional phase spectral ratios for both a single pair of phases or combinations of several of these. Fukunaga (1990) recommends that several eigenvectors associated with the largest m eigenvalues be used for discrimination in a lower dimensional subspace. He used scatter matrices different from those given above.

A number of separability measures are listed by Fukunaga (1990). A measure often used is the Bhattacharayya distance, expressed as,

$$B = 1/8(\mathbf{m}_1 - \mathbf{m}_2)^t \left[\frac{\mathbf{S}_1 + \mathbf{S}_2}{2}\right]^{-1} (\mathbf{m}_1 - \mathbf{m}_2) + \ln \frac{\left|\frac{\mathbf{S}_1 + \mathbf{S}_2}{2}\right|}{\sqrt{|\mathbf{S}_1||\mathbf{S}_2|}},$$

where S_1 and S_2 are the multivariate covariance matrices of the two populations and $\mathbf{m_1}$ and $\mathbf{m_2}$ are the means. Since the Bhattacharayya distance applies strictly to Gaussian populations, it may not be informative if the distributions are much different from the normal distributions (Duda *et al* 2001). The larger this measure, the better is the separability. Such measures are being used in this study to evaluate relative effectiveness of dicriminants in various regions.

Discrimination Results

We applied the above algorithms to two data sets. In both cases, the best known distance corrections were used (Jenkins *et al* 1998). The only exception is China where we have modified the Pg distance correction to correct for visible mismatches with our data.

China Data Set

The first data set, from China, contains both nuclear explosions and earthquakes. The data set consists of earthquakes around the WMQ region, Kazakh nuclear explosions, and one nuclear explosion at the Chinese test site, Lop Nor. The scatter plot of Pn/Lg ratios in four frequency bands is shown in Figure 2.

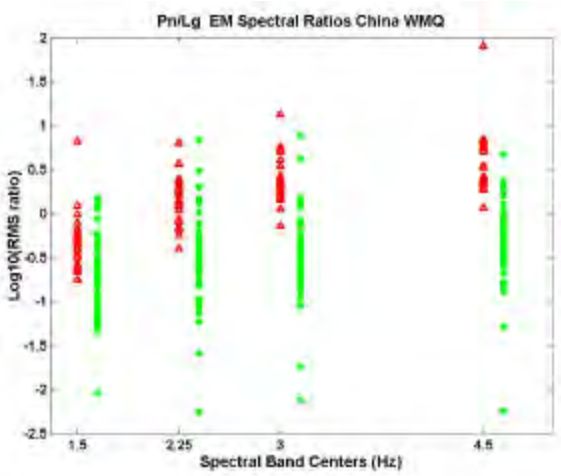

Figure 2. Scatter plot of the Pn/Lg spectral ratio data or four frequency bands from China. Red triangles denote explosions and green dots indicate earthquakes.

These data show poor separation generally, but the separation between explosion and earthquake populations improves with increasing filter band center frequency. After computing the various scatter matrices and subjecting the results to the eigenvalue-eigenvector analysis, the eigenvalues (Figure 3) show that we have at most two components, associated with the largest eigenvalues that can be used for effective discrimination.

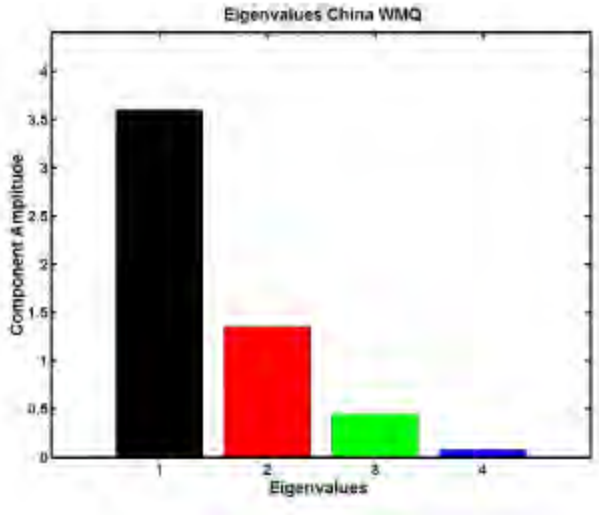

Figure 3. Eigenvalue spread derived from the analysis of Pn/Lg amplitude ratios for the Chinese station WMQ.

Plots of the eigenvectors in Figure 4 show how the Pn/Lg spectral ratio values in various bands can be combined to provide the discriminants in decreasing order of importance.

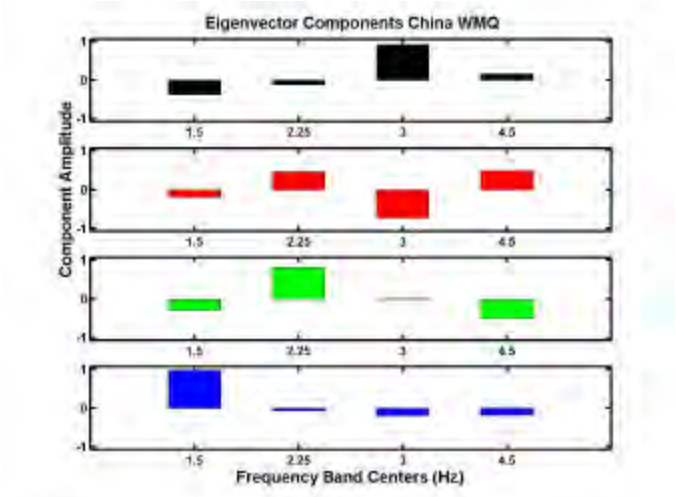

Figure 4. Plots of eigenvectors from the analysis of the China data. The first eigenvector has a dominant component for the 3-Hz band where the best separation exists. The last gives the largest weight to the first frequency band, the least effective discrimination.

Figure 5 shows plots of the ratios transformed with the eigenvectors shown in Figure 4. That is, linear combinations of original Pn/Lg ratios were computed using the weights shown in Figure 4, and these combinations are plotted versus eigenvector in Figure 5. The first eigenvector clearly produces the greatest separation. Explaining the details of the rest would be hard. Nevertheless, the first two combinations will give the best separation. There is a definite shift between the means of the projection on the second eigenvector that could also be used to complement the results from the first. The rest of the transformed ratios in Figure 5 clearly overlap completely.

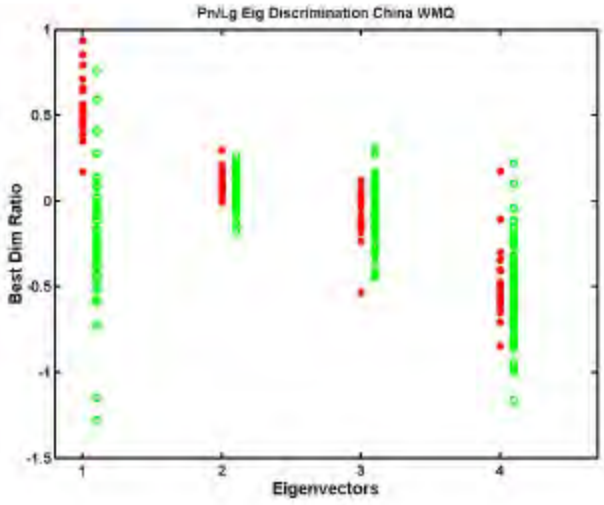

Figure 5. Discrimination plots for the China data set. Obviously, the best separation between the explosions (red dots) and the earthquakes (green dots) is achieved by the eigenvector #1 associated with the largest eigenvalue. The second eigenvector gives a small shift in means but large overlap. The remaining two overlap completely.

Nevada Test Site (NTS) Explosion vs. Skull Mountain Data Set

To compare this analysis with another region, we show the results of the analysis of Pn/Lg and Pg/Lg ratio data from the NTS and Skull Mountain earthquake data sets, originally studied by Walter *et al* (1995). These data sets consist of Skull Mountain earthquakes and NTS nuclear explosions as recorded at the Lawrence Livermore National Laboratory stations in Kanab, Utah, (KNB) and Mina Nevada (MNA). In this analysis, we combine Pn/Lg and Pg/Lg measurements into a 14-dimensional scheme.

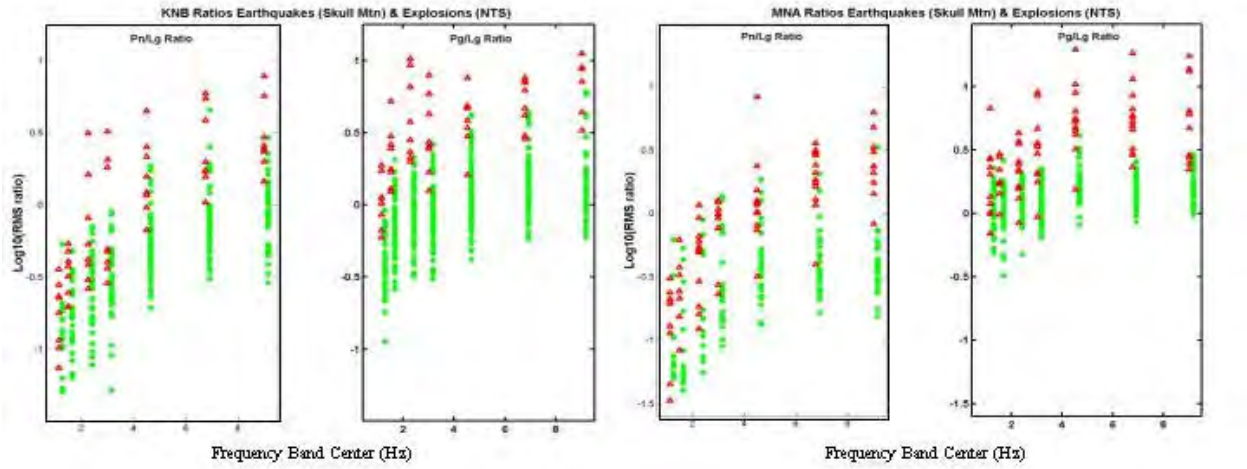

(a) (b)

Figure 6. Scatter plots of Pn/Lg and Pg/Lg ratios for Skull Mountain earthquakes and NTS nuclear explosions at stations Kanab, Utah, (KNB) (a) and Mina, Nevada, (MNA) (b).

The evident improved scatter in both ratios at both stations with frequency has been pointed out by Walter *et al* (1995). It has been a generally accepted tenet of discrimination that the earthquake/explosion separation increases

with frequency (e.g., Goldstein, 1995). The eigenanalysis was applied to the combination of Pn/Lg and Pg/Lg ratios, and the resultant eigenvector weights are shown in Figure 7.

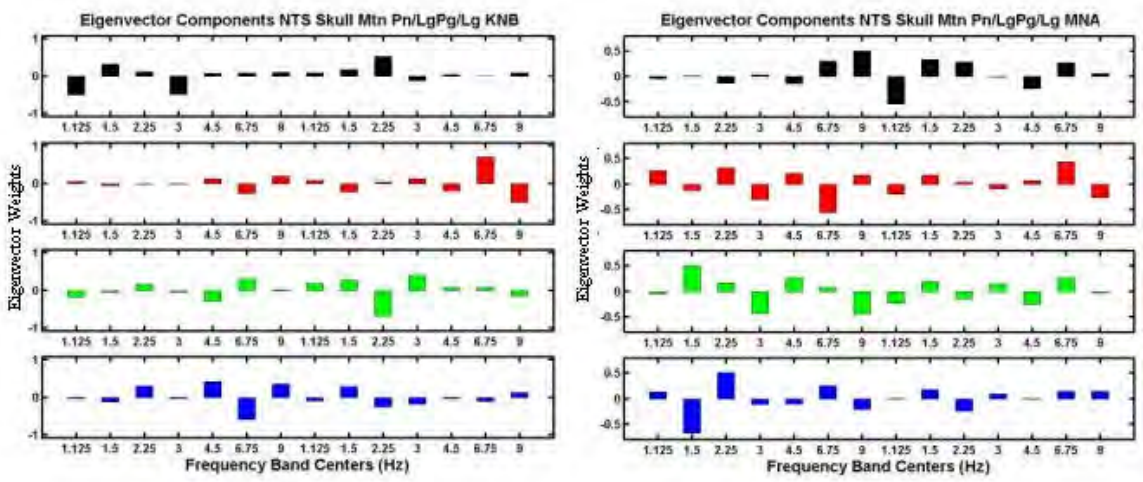

(a) (b)

Figure 7. Eigenvectors for KNB (a) and MNA (b) computed from the amplitude ratios of earthquakes and explosions in Figure 6.

The weights for the principal eigenvalue, which are the first rows in Figure 7, to do not seem to be much larger for the high-frequency ratios. In fact, for KNB in Figure 7 (a), the weights seems strongest for lower frequency Pn/Lg amplitude ratios. Finally, Figure 9 shows the resultant transformed discriminants.

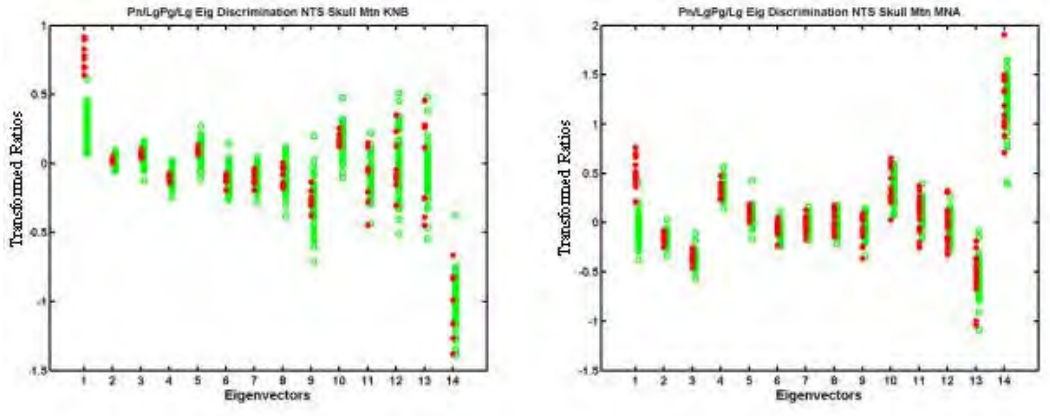

(a) (b)

Figure 8. Resultant transformed amplitude ratios after applying the weights in Figure 7 to the amplitude ratios in Figure 6.

The transformations clearly show the best separation on the first eigenvalue, although the separation is better for KNB than for MNA. Why the eigenanalysis seems to weight lower frequencies more than higher at KNB is not clear. Perhaps the actual means of the explosion and earthquake populations are separated more at low frequency than at high, even though there appears to be more overlap in the low-frequency bands.

Regional Magnitude Analysis

This study has been motivated by recent work of Patton (2001), who has argued that the regional mb magnitude scaled based on Lg, mb(Lg) originally developed by Nuttli (1973), is transportable between different tectonic

regions. However, Baumgardt (2001) has shown many instances when Lg is blocked and thus mb(Lg) could not be used. Further, Baumgardt (2001) suggested that Lg and Sn amplitude blockages may trade off, that is, when Lg is blocked, Sn waves have stronger amplitudes. Discrimination studies in regions of Lg blockages, such as Novaya Zemlya, frequently use Sn in place of Lg in spectral amplitude ratios (e.g., Ryall *et al*, 1995). This suggest that perhaps Sn may be used in regions where Lg is blocked and visa versa.

In this study, we have investigated the relative stability of regional magnitudes based in Sn and Lg amplitudes and on the sum of the amplitudes. We have extended the method of Nuttli (1973) to develop mb(Sn) and mb (Sn+Lg) magnitudes. First, the Sn and Lg amplitudes are measured in various frequency bands. To correspond to standard practice for mb (Lg), the band from 0.5 to 1 Hz is measured but other higher frequencies have also been studied. We have applied this method on earthquakes in the Zagros Mountains of Western Iran recorded at surrounding regional stations that record both Sn and Lg. An example of this analysis is shown in Figure 9 for the station RAYN in Saudi Arabia. The plots show comparison of mb(Lg), mb(Sn), and mb(Sn+Lg) compared with the standard NEIS mb.

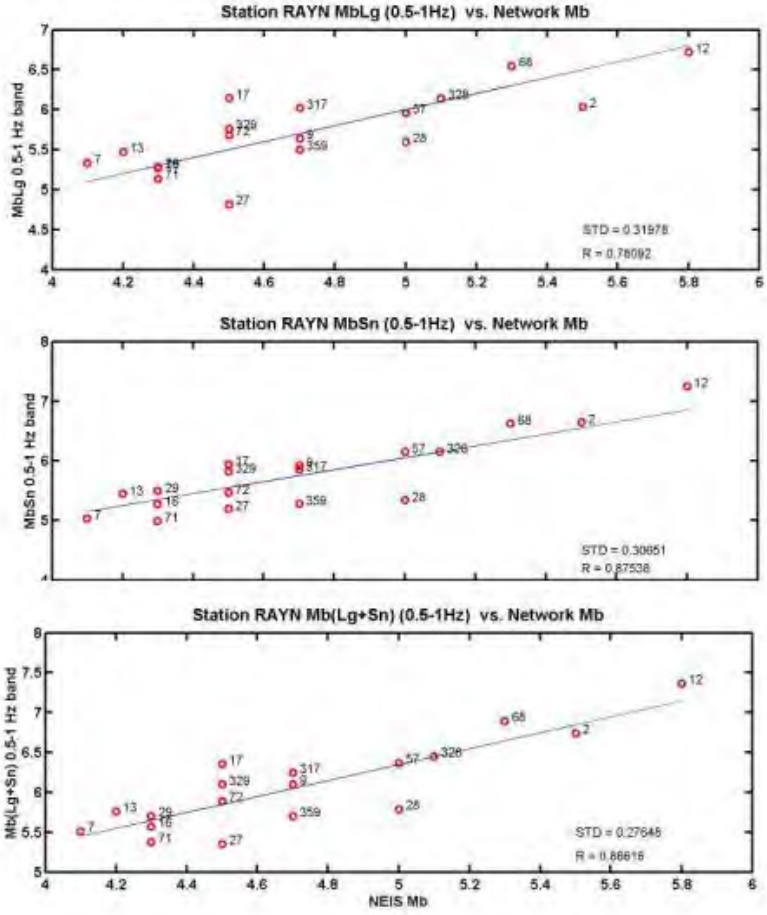

Figure 9: Plots of mb(Lg), mb(Sn), and mb(Lg+Sn) computed for earthquakes in the Zagros Mountains of western Iran recorded at the station RAYN against NEIS mb.

The line fitted to the data in Figure 9 has slope 1. These plots show that all three of these magnitudes scale well with NEIS mb. The scatter for the mb(Lg+Sn) was less than that of either mb(Lg) or mb(Sn). We are continuing to investigate these magnitudes in other regions where we have observed partial or complete Lg blockage.

CONCLUSIONS AND RECOMMENDATIONS

Multi-array analysis of site effects on regional phase spectral ratios for a close group of underwater explosions in the Baltic Sea show prominent biases apparently associated with each particular array. These biases are likely due to

propagation and source radiation directionality effects. In addition, there are site-related variations within each array, which are likely to be associated with local geology. Such estimates of site effects may be used as corrections in discrimination work. We have investigated the problem of dimensionality reduction for multi-band spectral ratio data. We have found that a simple Fisher discriminant applied to multi-band regional spectral ratio data gives a good separation between earthquake and explosion populations comparable to or better than the best visible separation on scatter plots. We have initiated an investigation of a new regional magnitude scale, similar to the *mb(Lg)* magnitude, called *mb(Sn+Lg)* magnitude based on the sum total of the regional shear energy contained in the regional *Sn* and *Lg* phases. This study is motivated by previous observations of *Lg* blockage that might limit the use of *mb(Lg)* for discrimination. Because the *Sn* and *Lg* phases have sometimes been observed to trade off in amplitude in regions of blockage, the *mb(Sn+Lg)* scale may be more stable than a magnitude scale based on either phase individually.

REFERENCES

Baumgardt, D. R. (2001). Sedimentary basins and the blockage of Lg wave propagation in the continents, *Pure Appl. Geophys*., **158**, 1207-1250.

Baumgardt, D.R. and Z. Der (1998). Identification of presumed shallow underwater chemical explosions using land-based regional arrays, *Bull. Seism. Soc. Am*., **88**, 581-595.

Baumgardt, D. R., Z. Der, and A. Freeman (2001). Investigation of the partitioning of source and receiver-site factors on the variance of regional P/S amplitude ratio discriminants, *Proceedings of the 23rd Seismic Research Review: Worldwide Monitoring of Nuclear Explosions – October 2-5, 2001*, Jackson Hole, Wyoming.

Duda, R.O., P.E. Hart, and D.G. Stork (2001), *Pattern Classification*. Wiley-Interscience.

Fisk, M.D., H.L. Gray, and G.D. McCartor (1996), Regional event discrimination without transporting thresholds. *Bull. Seism. Soc. Am*., **86**, 1545-1558.

Fukunaga, K. (1990), *Introduction to Statistical Pattern Recognition*, Academic Press.

Goldstein, P., Slopes of P- to S-Wave Spectral Ratios-a Broadband Regional Seismic Discriminant and a Physical Model, *Geophys. Res. Lett.* **22**, 3147-3150 1995.

Jenkins, R. D., T.J. Sereno, and D.A. Brumbaugh (1998), Regional attenuation at PIDC stations and the transportability of the S/P discriminant. Final Report, *SAIC-98/3012/AFRL-VS-HA-TR-98-0046*, Science Application International, Inc., La Jolla, CA.

Johnson, A. and D.W. Wichern (1988*). Applied Multivariate Statistical Analysis*, Prentice Hall, Englewood Cliffs, New Jersey.

Nuttli, O.W. (1973). Seismic wave attenuation and magnitude relations for eastern North America, *J. Geophys. Res*., **78**, 876-885.

Patton, H. (2001). Regional magnitude scaling, transportability, and Ms:mb discrimination at small magnitudes, *Pure Appl. Geophys*, **158**.

Ryall, A.S., D.R. Baumgardt, M.D. Fisk, and F. Riviere-Barbier (1995), Resolving regional discrimination problems: some case stories, in *Monitoring a Comprehensive Test Ban Treaty*, E.S. Husebye and A.M. Dainty eds. 721-742.

Tou, J. T., and R.C. Gonzalez (1974*), Pattern Recognition Principles*, Addison-Wesley.

Walter, W.R., K. Mayeda, and H.J. Patton (1995). Phase and spectra ratio discrimination between NTS earthquakes and explosions Part 1: Empirical observations, *Bull. Seism. Soc. Am*., **85**, 1050-1067.

DEVELOPMENT OF A MINING EXPLOSION DATABASE FOR SOUTHERN ASIA

Jessie L. Bonner,[1] David B. Harris,[2] Shirley Rieven,[3] Ileana M. Tibuleac,[1] and James M. Britton[1]

Weston Geophysical Corporation,[1] Lawrence Livermore National Laboratory,[2] and
Obsidian Scientific, Inc.[3]

Sponsored by the National Nuclear Security Administration
Office of Nonproliferation Research and Engineering
Office of Defense Nuclear Nonproliferation

Contract No. DE-FG02-01ER83341[1] and W-7405-ENG-48[2]

ABSTRACT

We have recently initiated the development of a high-quality mining explosion database for southern Asia consisting of detailed mining information together with seismograms recorded from mine blasts in India, Pakistan, and the surrounding regions. The database will be used to support the location, detection, and discrimination of mining explosions from earthquakes and nuclear explosions in this region. The preliminary development of the database has been completed in three research tasks: (1) collection and integration of mining data, (2) acquisition and analyses of seismic data, and (3) location, ground truth classification, and characterization of the mine blasts.

The mining database developed for this study currently contains over 240 mines and mineral deposits in southern Asia. These data include information on location, geology, commodities, production, mineralogy, references, operator, mining explosion resources, and additional parameters that were integrated into a single, digital database. The current focus of the database is on the Indian states of Andhra Pradesh and Rajasthan, and during the next phase of the project, we plan to expand the focus to other Indian states as well as Pakistan, Iran, and other regions.

We collected waveform data from several stations in southern Asia including HYB, GBA, NIL, and other proprietary data sources. We applied the waveform correlation method (Harris, 1991) on data collected from these stations during two months. For example, at HYB, the GEOSCOPE station in central India, a simple STA/LTA detector determined 413 detections, of which over 96% of the events occurred within daytime hours, for data acquired between 1 November and 31 December 1999. The detected events were then correlated down to a threshold of 0.7 resulting in several small clusters and one very large one. We have also developed and employed a detector to highlight events with short-period Rayleigh waves (*Rg*), which are often visible on mine blast seismograms in central and southern India.

Using single-station/array location techniques, we found several mines with blasts that contribute to the regional seismicity. In southern India, we located events in the Bellary-Hospet and Kudremukh iron-ore districts. In central India, we located events, with m_b magnitudes ranging from 1.6 to 2.6, originating from different mines in the extensive Godavari Valley Coal Field. Finally, in the northeastern Indian state of Rajasthan, we determined locations for events with $m_b \sim 3$ at the Rampura Agucha open pit zinc mine. These locations, waveforms, overhead imagery, and other information have all been incorporated into the mining explosion database. This resource may be of increasing importance now that stringent regulations on foreign mining interests in southern Asia have been relaxed, paving the way for larger mines in the region.

OBJECTIVE

The objective of our project is to develop a research database for southern Asia that will consist of detailed mining information together with seismograms recorded from mine blasts in India, Pakistan, and the surrounding regions. The database will be used to support the location and detection of mining explosions in this region and to increase opportunities for high-quality ground truth data. The preliminary development of the database has been completed in three research tasks:

- Collection and integration of data for mining districts and mine operations within southern Asia including location, geology, commodities, production, mineralogy, references, operator, mining explosion resources, and additional parameters into a single, digital database,
- Collection of seismic waveforms from mining explosions for inclusion in the database, and
- Analysis of these data for ground truth classification and mining statistics.

The results of the initial phase of this research are described in the following sections of this paper. Our results show that ground truth information, essential for monitoring efforts in southern Asia, can be compiled from these and additional data into a single comprehensive mining explosion database.

RESEARCH ACCOMPLISHED

Mining Database Development

Dr. Tom Weaver of Los Alamos National Laboratory previously compiled an extensive unpublished database of over 18000 mines and mineral deposits (henceforth called the Weaver database) from around the world. The Weaver database has information on 132 mines and districts in our study region. We used this database as an initial reference in our development of a mining explosion database for southern Asia. The information in the Weaver database includes mine location, geology, commodities, production, mineralogy, references, operator, opening, and closing dates. For some mines, he had compiled all of the above-mentioned data, while in other cases he had determined only an approximate location and mine name.

We have determined additional sources of information from within the international and local mining community to update and complete the Weaver database, as needed. Reviews of historical literature on economic geology and resources in India, Pakistan and Burma (Mehdiratta, 1962) were conducted together with web- and paper-based literature searches for information on mineral resources, production and exports for the following countries: Afghanistan, Bangladesh, Bhutan, China (western section), India (all states), Iran (eastern section), Myanmar (Burma), Pakistan, Sri Lanka, Tajikistan, Turkmenistan, Uzbekistan, and Nepal. The amount of readily available information for mineral resources in each of these countries and their states varied considerably. For instance, a number of Indian states had active and well-maintained web sites that summarized natural resources and identified specific commodities. Other countries, such as Afghanistan, had little representation except for reviews available in the journal *Annual Mining Review* (1996-1999). Lists of commodities and resources for each state were compiled and used to search for journal articles pertaining to mining activities in the countries of interest. Several hundred-journal articles were researched and used to identify mine names, mine districts, commodities, states and countries. On this basis, an updated mines database was developed containing the fields shown in Figure 1.

The updated mines database contains information on over 230 mines and mineral deposits in southern Asia and is a deliverable for this project in various formats. For some mining localities, geographic coordinates were available, while the coordinates (Figure 2) for approximately 50 of the mines were identified by cross-referencing the local municipality names with the name of the mine or district. The locations of the mines from the original Weaver database are shown as red diamonds, while updates to the database completed during the initial stages of this research project are presented as white diamonds.

Due to the very large number of references, mines and mineral deposits in the region (there are over 5000 active mines in the Indian state of Andhra Pradesh alone (http://www.andhrapradesh.com)), we determined that the scope of the initial research phase should be limited to populating the database for regions where we have access to seismic data. For example, Andhra Pradesh, India was a primary focus of the research as station HYB often records

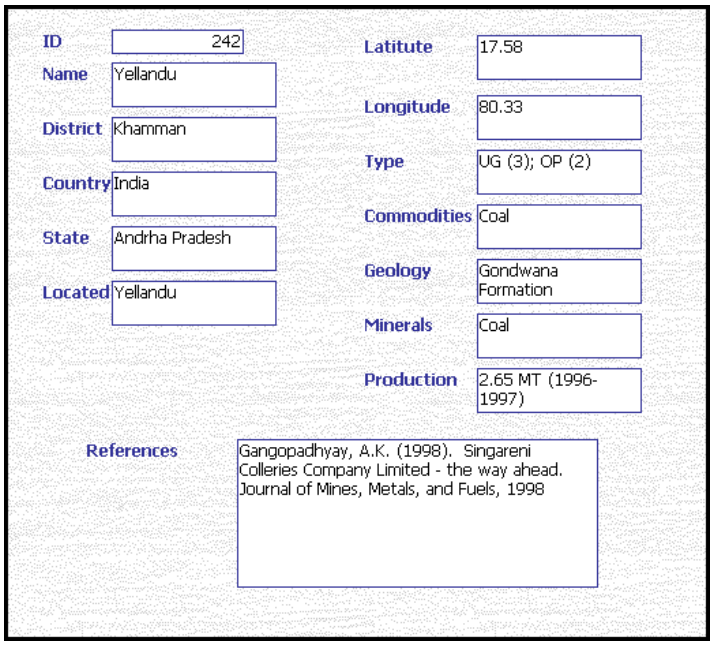

Figure 1. Example of an entry in our southern Asia mining database for a coalmine in Andhra Pradesh. The fields in the database include mine and district name, country, state, nearest town, latitude, longitude, type of mining, commodities, geology, extracted minerals and resources, production values, and references. The Yellandu mine is part of the Godavari Valley coal field in western Andhra Pradesh. The mine consists of three underground inclines and 2 open pit cast mines.

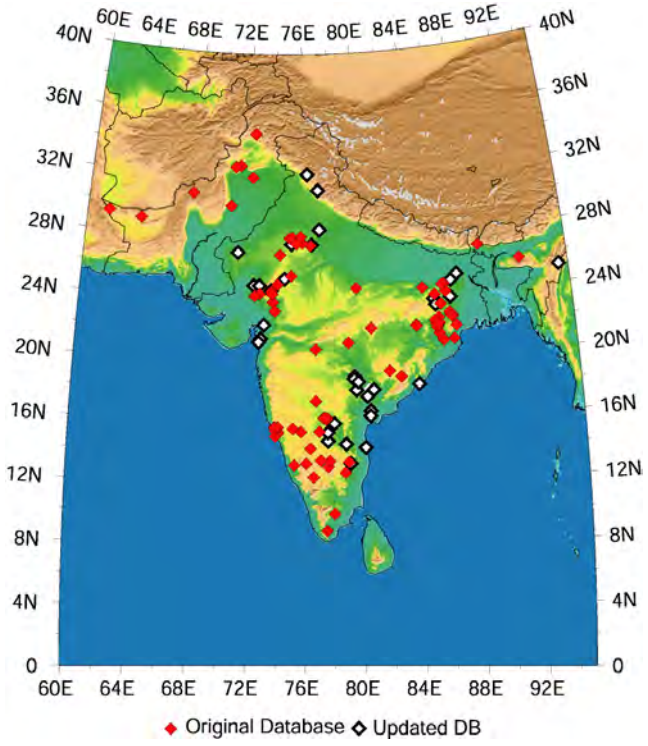

Figure 2. Locations of mines and mineral deposits in southern Asia as listed in the original Weaver database (red diamonds) and with the recent update (white diamonds) performed during the current research project.

mining explosions, some of which are presented in subsequent sections of this report. The current version of the database includes all mines and mining districts identified in Andhra Pradesh and Rajasthan using the method described above. All reference citations used to identify the mine/district have been entered in the appropriate record in the "reference" field of the database. In addition to the Andhra Pradesh and Rajasthan mines, the new version of the updated database also includes the identifications of mines in the Indian states of Assam, Manipur, Bihar (Jharkhand), Goa, Gujarat, Haryana, Himachal Pradesh, and Jammu & Kashmir. All remaining Indian states,

and all other countries have had mines identified, but neither their identities nor their supporting references have been entered into the current database. We will complete the development of this database during the next stage of the project.

Data Sources for Mine Blast Waveforms

We have collected waveform data from stations in southern Asia in order to determine the contribution of mining explosions to regional seismograms. Table I shows the stations for which data have been collected to populate the database. We examined data from HYB (Table 1), a three-component station in central India that is part of the GEOSCOPE network. We have also compiled seismic data for the Gauribidanur Seismic Array (GBA) in central India. This medium aperture seismic array has twenty short-period seismometers arranged as two perpendicular arms (i.e., a cross array) and was operated by the Atomic Weapons Research Establishment (AWRE) of the United Kingdom between 04 March 1979 and 27 July 1996. Finally, we have permitted access to additional proprietary data sources in southern Asia for which we have examined the waveform data for mine blasts. During the next research stage, we will seek additional stations and sources of seismic waveform data.

Table 1. Stations in southern Asia for which waveforms were processed for mine blast detection.

STATION	LOCATION	TYPE	NETWORK	LATITUDE	LONGITUDE	OPERATION DATES
HYB	Hyderabad, India	3C	GEOSCOPE	17.417	78.553	15 Jan 1989 - present
GBA	Gauribidanur, India	Array	AWRE	13.6042	77.4361	04 Mar 1979- 27 July 1996

.

Location Methodology

In regions with few seismic stations and small ($m_b < 4$) sized events, traditional location methods cannot always satisfy the location accuracy requirements for monitoring. This leads to location algorithms based on observations made at single stations and/or arrays. To locate an event with a single station, the slowness vector for the various seismic phases recorded (e.g., *Pn*, *Pg*) must be estimated. For a single three-component (3-C) station, the horizontal projection of the slowness vector is the backazimuth, and the vertical projection gives the angle of incidence that can be converted to an apparent phase given a known receiver crustal structure. In contrast to typical location routines for moderate-sized events that use a single scalar observable for one component of ground motion, this method incorporates the important information from all three components of the ground motion. For arrays, the backazimuth is derived from estimates of the slowness vector determined by fitting a plane to many sensor arrival times with the array using a correlation technique (Tibuleac and Herrin, 1997) or by beamforming (Ruud *et al*., 1998). The epicentral distance is calculated from the differences in travel times between secondary and primary phases (e.g., *Lg-Pn* or *Lg-Pg*). Given the station-to-source azimuth (backazimuth) and the epicentral distance, the epicenter location can be determined using standard geometric formulae.

The mining explosions in India are, in fact, small-sized events, and few seismic stations are available. We developed a single-station location technique capable of locating such events. Our method begins with adopting a model for the region surrounding the station. Reiter *et al*. (2001) developed a *P*-wave velocity model for India and Pakistan (called WINPAK3D), which was used to obtain velocity profiles near each station. The velocity profile was then used to estimate the *Pn* and *Pg* travel times as a function of distance from each station. We assumed a constant velocity of 3.5 km/s to calculate the *Lg* travel times as a function of distance, and note that this velocity will be refined as more data are analyzed in this region. The epicentral distance was then calculated by equating the observed difference between the *Lg* and *Pn/Pg* arrival times to the predicted travel time difference. Once the backazimuth is estimated, either for 3-C stations or the GBA array (using the f-k routines of Matseis (Young, 1997)), the source is located and compared to known locations from the mining database.

For example, stations HYB and GBA are located in the shield region of India where WINPAK3D velocity structure is based upon previous studies (Priestley *et al.*, 2001). These researchers have shown the crustal structure in this region is relatively simple and can be approximated by two layers over a mantle half space (Figure 3). Using the standard refraction equation for a three-layer model (Burger, 1992), we derived an equation for epicentral distance (x) as a function of the *Lg-Pn* travel time distance ($\Delta_{Lg\text{-}Pn}$):

$$x = 6.25\ (\Delta_{Lg\text{-}Pn}) + 53 \quad \text{for } 1.7° < x < \sim 5° \qquad (1)$$

Using standard group velocities for *Pg* and *Lg* of 6.0 km/s and 3.5 km/s, respectively, we determined the equation for epicentral distance as:

$$x = 8.4\ (\Delta_{Lg\text{-}Pg}) \qquad (2)$$

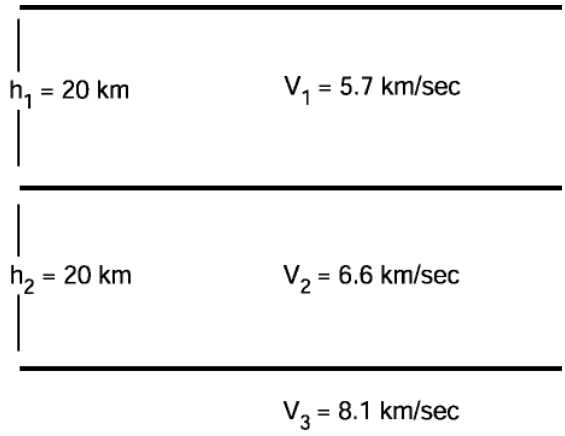

Figure 3. Average WINPAK3D P-wave velocity structure of west-central India.

Regional Mine Blast Seismicity at GBA

GBA data are an excellent source of regional mining explosions as documented by Krishna and Ramesh (2000). They compiled explosion seismograms recorded at GBA from various mines (Figure 4) in India to provide evidence for an upper crustal waveguide for *Pg* with a scattering zone in the upper 15 km of crust. In the upper plots of Figure 5, we provide example seismograms recorded at GBA from the Bellary-Hospet iron-ore region and the Kalyadi copper districts in Karnataka, India. We determined backazimuths for these seismograms by bandpass filtering between 0.8 and 2 Hz (lower plots) and performing *f-k* analyses on the *Rg* arrivals. Locations were determined by converting the *Lg-Pn/Pg* travel time differences to epicentral distances using formulae developed from regional models (Eqs. 1 and 2).

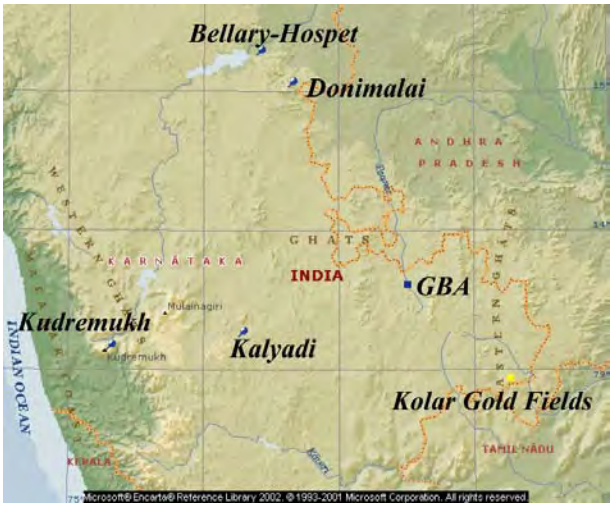

Figure 4. Location of the GBA cross array (star) in the state of Karnataka, India. Also shown are the locations of the Bellary-Hospet, Donimalai, and Kudremukh iron-ore districts and the Kalyadi copper district. The Kolar Gold Field is a deep underground mine complex located near Bangalore, India.

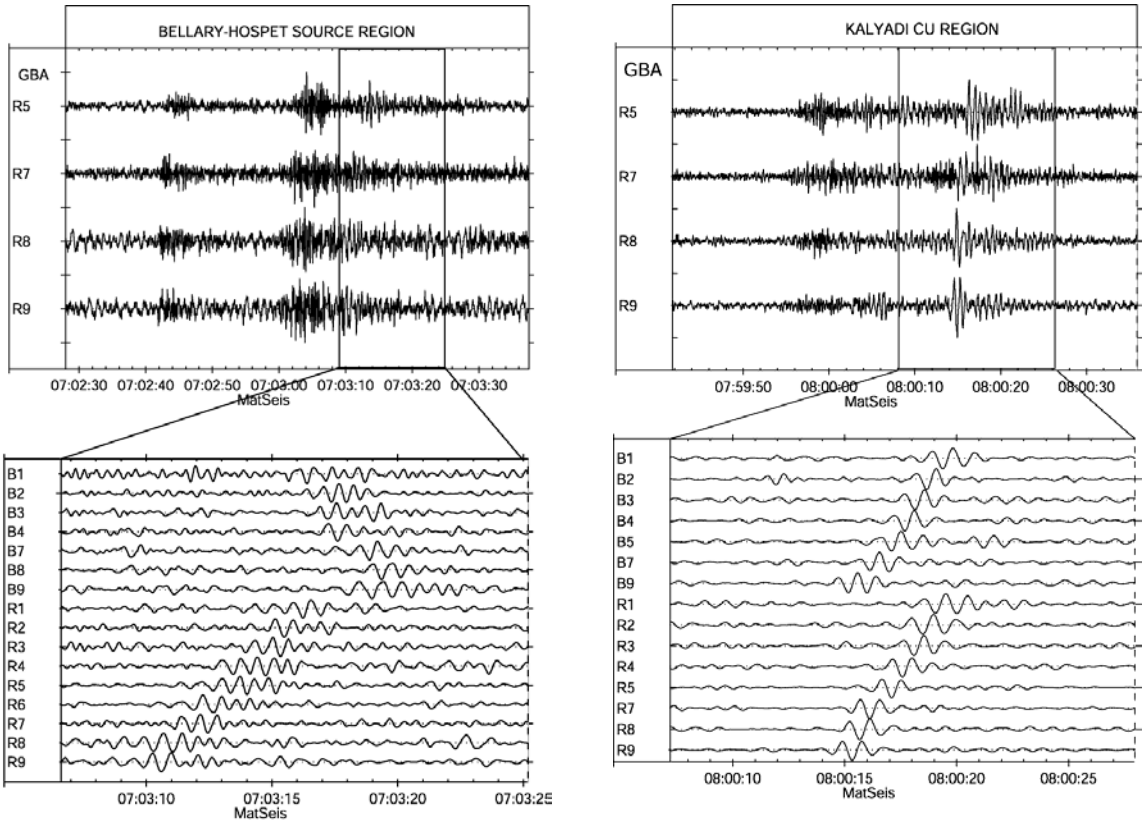

Figure 5. (Upper Left) Seismograms from a mine blast in the Bellary-Hospet iron-ore district recorded on four elements at GBA. (LowerLeft). Bandpass filtered *Rg* arrivals are presented all available seismic elements at GBA. We completed an f-k analysis on the *Rg* to determine a backazimuth of 332° for the explosion. (Upper Right) Seismograms from a suspected mine blast in the region of the Kalyadi copper mines recorded on 4 elements at GBA. (Lower Right). Bandpass filtered *Rg* arrivals are presented for all elements of GBA. The *Rg* signals were processed using f-k techniques to determine a back azimuth of 252° for the explosion.

Regional Mine Blast Seismicity at HYB

We performed the waveform correlation method (Harris, 1991) on two months of data (1 November to 31 December 1999) recorded at station HYB. First, a simple STA/LTA detector performed on the filtered (bandpassed between 1 and 4 Hz) seismic data determined 413 detections for the two months. These were then correlated down to a threshold of 0.7 resulting in several small clusters and one very large cluster. Figure 6 shows the time of day and day of week when the detections occurred. The majority of the detections occured between 04:00 and 11:00 UTC (9:30 AM to 4:30 PM local time) suggesting that most detections at HYB are from mining explosions or daytime construction explosions in the region.

The largest cluster resulted from correlation of simple *Rg* signals from a small mine near station HYB. Four additional clusters were chosen for a more detailed study. Example waveforms for these clusters are shown in Figure 7. The three-component records consist of a small *Pg* signal and large *Lg* and *Rg* arrivals. The seismograms were bandpass filtered between 0.8 and 6 Hz to increase the signal-to-noise ratio (SNR).

For each event in clusters 2, 9, 10, and 12, we measured the *Pg* and *Lg* arrival times, amplitudes, and periods, and determined the backazimuths using the 3-C waveforms. For several of the events, the *Pg* SNR was too low (< 1.5 – 2) for analysis, and thus the event was not analyzed. We used Equation 2 to estimate the epicentral distance based

upon the observed *Lg-Pg* travel times, and then converted distance and backazimuth to the source latitude and longitude. The locations are plotted in Figure 8.

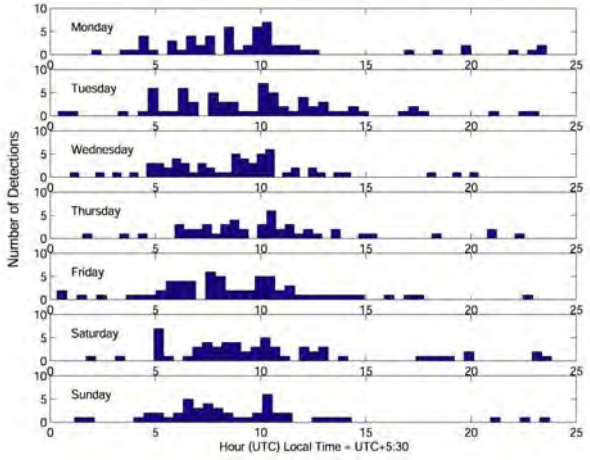

Figure 6. Occurrence times for the 413 detections from the waveform correlation technique performed on 2 months of continuous HYB data.

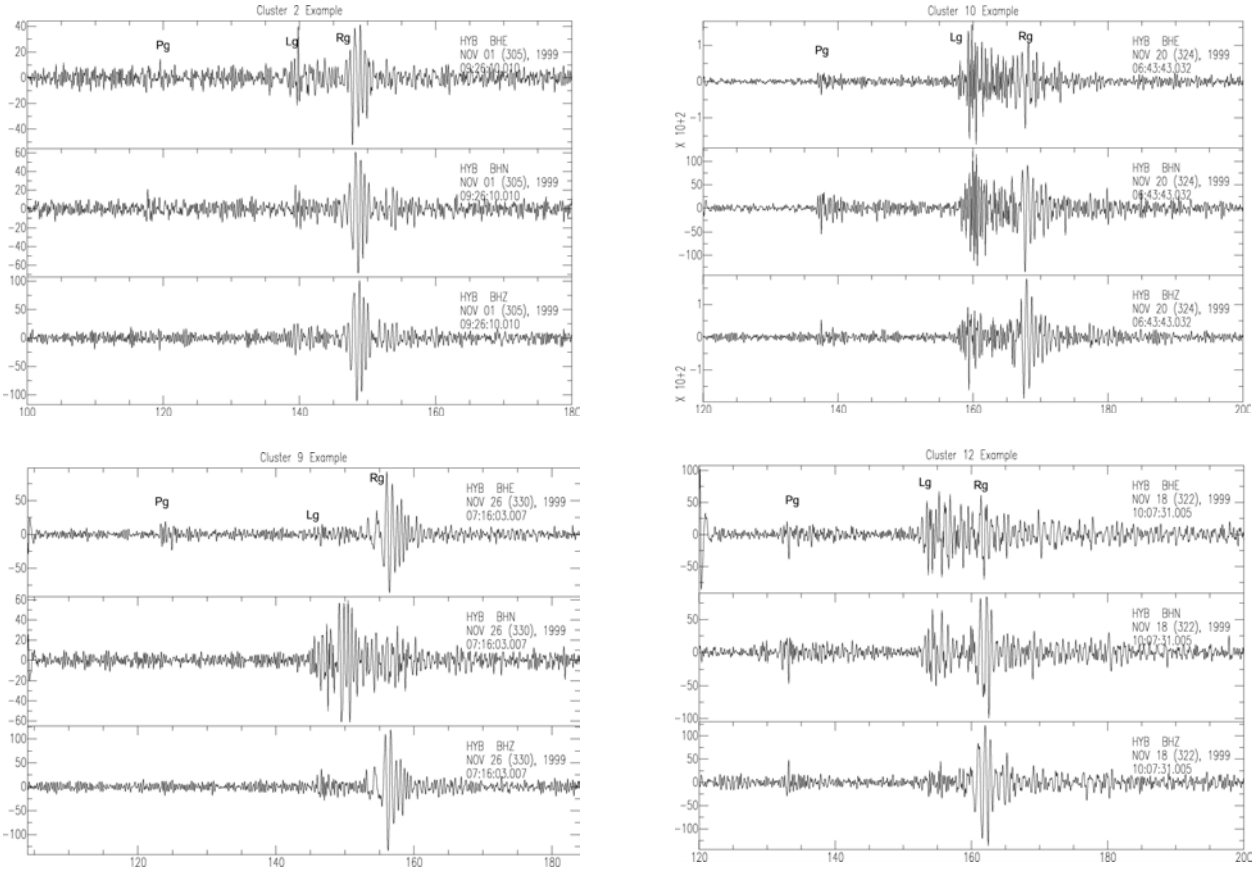

Figure 7. (Upper Left) Three-component seismograms for an event from cluster 2. The traces were bandpass filtered between 0.8 and 4 Hz. (Lower Left) Event from cluster 9. (Upper Right) Event from cluster 10. (Lower Right) Event from cluster 12.

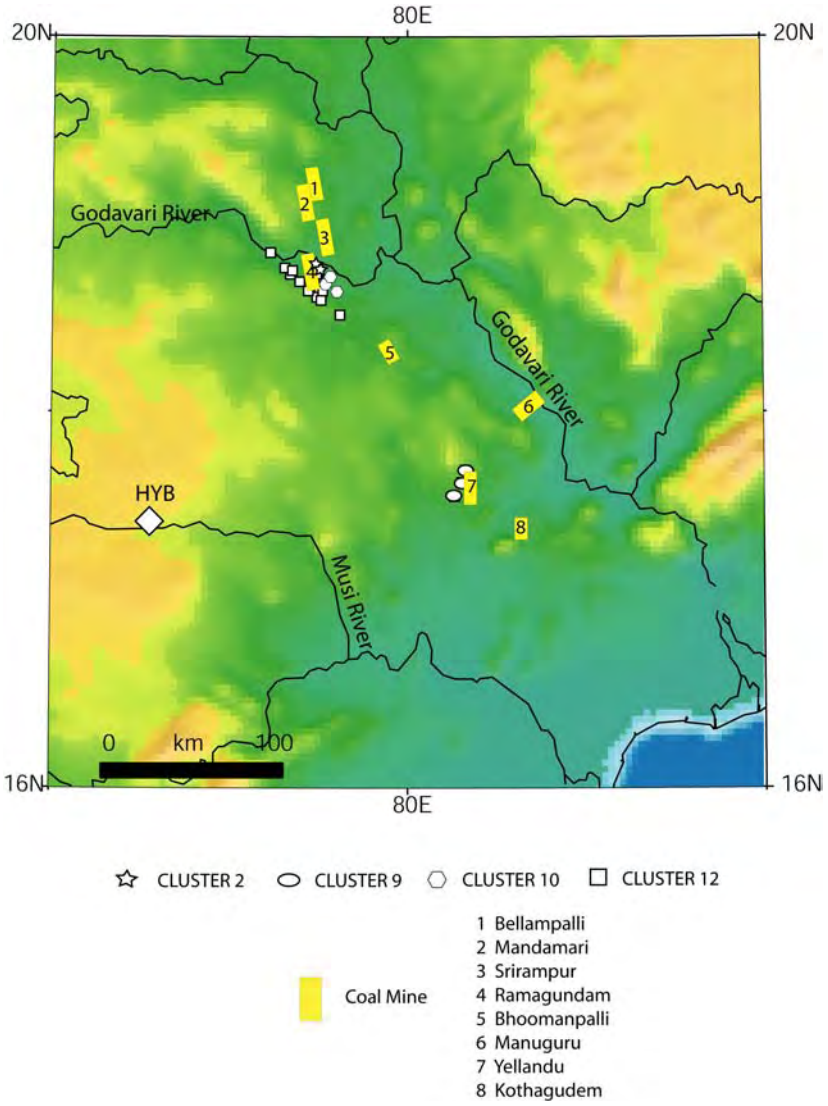

Figure 8. Single-station (HYB) locations for the events in clusters 2, 9, 10, and 12. Also shown are the known locations of mines in the Godavari Valley Coalfield.

The locations of coal mines in the Godavari Valley Coal Field (GVCF) are presented in Figure 8 in relation to the event cluster locations. Coal was first discovered in the GCVF in 1871 near the village of Yellandu, in the state of Andhra Pradesh. The coal is found in the northwest-southeast trending, fault-bounded Gondwana basin in Carbonaceous-aged sediments, and the Godavari River cuts across these sediments in a northwest to southeast direction as seen in Figure 8. The mines and processing infrastructure in the coal fields are presently operated by the state-owned Singareni Collieries Company Limited (SCCL), and the coal bearing strata are located in 3 districts of Andhra Pradesh: Adilabad, Karminagar, and Khamman. Mines in the region consist of both underground and opencast surface operations. In total, there are 62 underground mines and 11 open-pit mines in GVCF (Gangopadhyay, 1998).

The Yellandu mine of the GCVF is the source of the cluster 9 mining explosions as seen in Figure 8. Because of low SNR for the Pg arrivals, only 3 of the 6 events from the cluster could be located. We used 25-meter resolution satellite imagery to identify the opencast pits at Yellandu. We do not have blaster confirmation of the individual pit for the cluster 9 events; however, our event locations and the center of the mine differ on average by less than 10 km. The range of $m_b(Pg)$ magnitudes for the explosions in cluster 9 was 1.5 to 2.4.

The locations for clusters 2, 10, and 12 are near the Ramagundam mines of the Karminagar district as seen on the 25-meter resolution satellite imagery (Figure 9). The scatter in the locations is oriented along a NW-SE arc projected from HYB and is caused by uncertainties in backazimuth projection (±6°). The Ramagundam mine is the most productive mining region of the GVCF, with four opencast mines. Given the scatter in the azimuth data, it is difficult to pinpoint the individual pits responsible for the clusters. The m_b (*Lg*) magnitudes for clusters 2, 10, and 12 ranged from 1.5 to 2.0, 1.6 to 2.6, and 1.7 to 2.6, respectively.

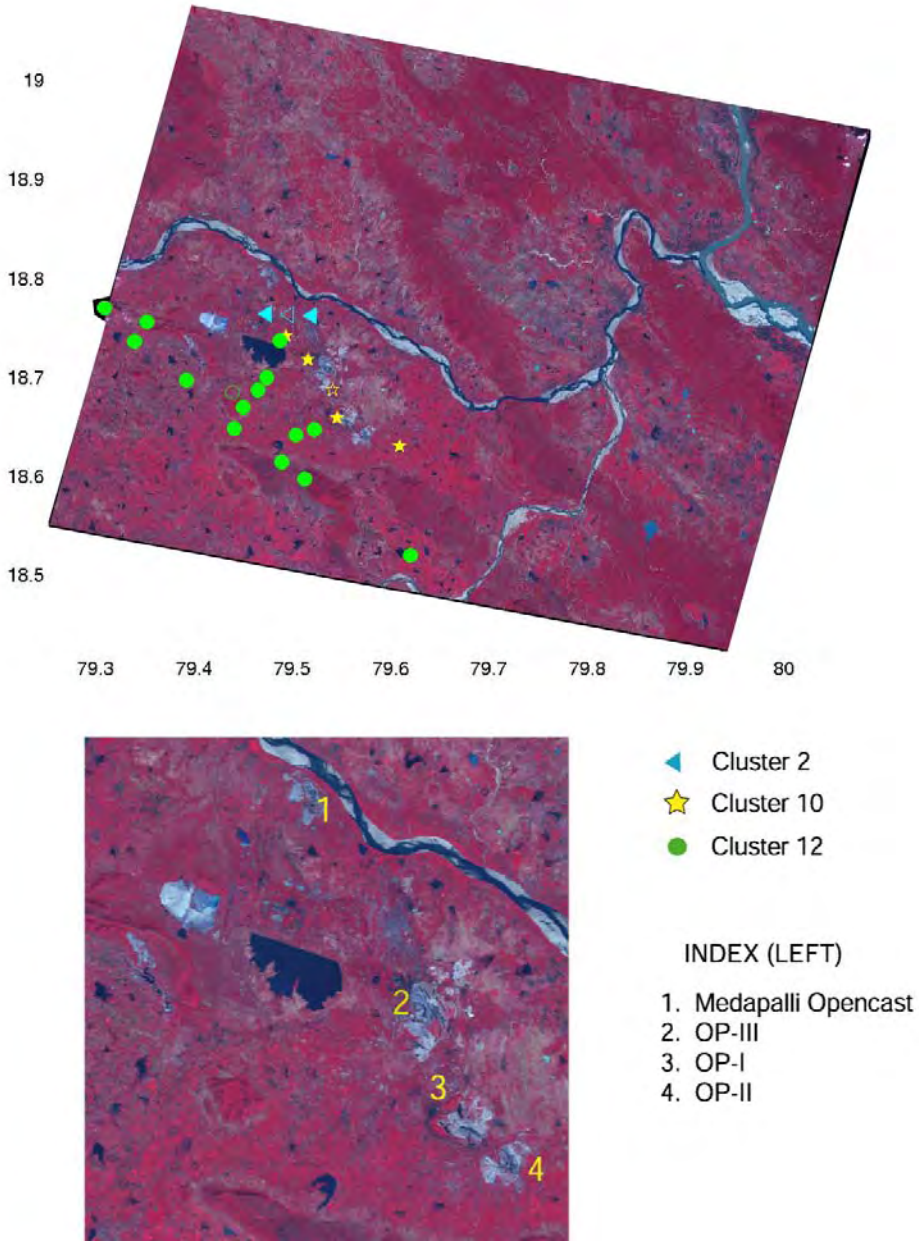

Figure 9. (Top) Locations for events in clusters 2, 10, and 12 shown as closed triangles, stars, and circles, respectively, overlain on a 25-meter resolution Spot photo. The average location for each cluster is shown as the open symbol. (Bottom) Inset from top figure showing locations of the open pits of the Ramagundam mine.

CONCLUSIONS AND RECOMMENDATIONS

Our research has uncovered new sources of mining information for southern Asia, allowing us to update the Weaver mining database. We have separated mining explosions from the background seismicity in India using the waveform correlation technique (Harris, 1991) and identified iron ore, copper and coal mining blasts in southern India and production shots in zinc mines in northwestern India. Our single-station event characterization method has the capability to locate mine blasts and other near-regional events in India to within 10-15 km of the ground truth locations. This level of accuracy allows us to determine the mine conducting the blasting, but does not allow us to pinpoint the actual pit with certainty. We recognize the mining explosions recorded thus far are small events ($1.5 < m_b < 2.9$) and do not offer optimal examples of ground truth data. However, the mining explosion database will be expanded significantly during the next phase of the project to include more recent sources of data that could reveal larger mining explosions in the region.

ACKNOWLEDGEMENTS

We wish to thank Tom Weaver for allowing us access to his mining database in southern Asia. We also thank Supriyo Mitra for help on various aspects of this project. We thank James Lewkowicz, Anca Rosca, Delaine Reiter and Jim Britton for helpful comments on the manuscript.

REFERENCES

Burger, H.R. (1992), Exploration geophysics of the shallow subsurface. Prentice Hall, Englewood Cliffs, NJ. 489p.

Gangopadhyay, A. K., (1998). Singareni Collieries Company Limited – the way ahead, in the *Journal of Mines, Metals, and Fuels Special Issue on the Singareni Collieries Company Limited*, 46, No. 2, 38-44.

Harris, D.B. (1991), A waveform correlation method for identifying quarry explosions, *Bull. Seism. Soc. Am.,* 81, 2395.

Krishna, V. G. and D. S. Ramesh (2000), Propagation of crustal waveguide trapped Pg and seismic velocity structure in the south Indian shield, *Bull. Seism. Soc. Am.,* 90, 1281-1294.

Mehdiratta, R.C. (1962). Geology of India, Pakistan, and Burma, Second Edition. ATMA RAM and Sons, Delhi, India.

Priestley, K., V. Gaur, S. Rai, J. Bonner, and J. Lewkowicz (2001), Broadband seismic studies in southern Asia, *Proceedings of the 23rd Seismic Research Review on Worldwide Monitoring of Nuclear Explosions.* October 2-5, 2001, Vol. 1, 1-12 p.100-109.

Reiter, D. T., M. Johnson, A. Rosca, C. Vincent (2001), Development of a regional 3-D velocity model of the Pakistan region for improved seismic event location. Final Report, Weston Geophysical, 27 p.

Ruud, B. O., E. S. Husebye, S. F. Ingate, and A. Christoffersson (1998), Event location at any distance using seismic data and a single, three-component station, *Bull. Seism. Soc. Am.,* 78, 309-325.

Tibuleac, I.M. and E. T. Herrin (1997), Calibration studies at TXAR, *Seism. Res. Lets*., 68, 353-365.

Young, C., (1997), Matseis: a seismic toolbox for MATLAB, *Proceedings of the 18th Annual DoD/DOE Seismic Research Symposium.*

"Map of Central India" (2002), Microsoft Encarta Interactive World Atlas.

MODELING SHORT-PERIOD SURFACE WAVES FROM SMALL EXPLOSIONS AT THE SHAGAN TEST SITE

Jessie L. Bonner,[1] Jeffrey L. Orrey,[2] and Anca C. Rosca[1]

Weston Geophysical Corporation,[1] GeoVisual Technologies Inc.[2]

Sponsored by the National Nuclear Security Administration
Office of Nonproliferation Research and Engineering
Office of Defense Nuclear Nonproliferation

Contract No. DE-FG02-00ER83123

ABSTRACT

The objective of our research is to study the generation and propagation of short-period (0.2 to 12 secs) surface waves from a variety of different classifications of explosions. Thus, we have assembled a dataset of local and regional recordings of single-fired chemical explosions (Non-Proliferation Experiment and Balapan Depth of Burial shots), coal-mining explosions (including cast and coal shots from northern Arizona), rock fragmentation shots (Arizona), and quarry blasts (Central Texas). The dataset includes detailed source parameters including origin times, shot patterns, and additional information key to modeling the physics of the various explosions. In the upcoming year, we plan to supplement this dataset with additional close-in and regional recordings of hard-rock fragmentation blasts in Minnesota.

During the past year, our research has focused on the near-source modeling of twelve single-fired chemical explosions detonated in boreholes at the former Soviet nuclear test site near the Shagan River (STS) in Kazakhstan. The depths of these explosions ranged from 2.5 to 550 m, while the explosive yield varied from 2 to 25 tons. To quantify the generation and propagation of *Rg* from these explosions, we developed a shallow velocity model for STS by combining surficial and borehole geology with velocity profiles from Bonner *et al*. (2001). This model divides the region into several zones, including a fast southwestern (SW) section and a slow northeastern (NE) section separated by transitional regions. We then determined the attenuation quality factor for *Rg* (Q_{Rq}) at frequencies of 0.5, 1, 1.8, 3.5, and 5.5 Hz. In the slower NE section, *Rg* is strongly attenuated and has a Q_{Rq} value of approximately 10 at 1 Hz that increases with increasing frequency. However, for paths within the faster SW section, we observe Q_{Rq} values that are on average 5 times greater and as large as an order of magnitude greater. These differences in velocity and attenuation may be the source of spatial biases in regional and teleseismic waveform characteristics observed at STS (Ringdahl *et al*., 1992; Phillips *et al*., 2001). We have ported a numerical wave field modeling method, the Generalized Fourier Method (GFM) developed by Orrey *et al*. (2002), to a Linux computer cluster in order to generate Green's functions for the 3D STS model. Our preliminary results suggest that the modeling will provide accurate characterizations of propagation effects at STS. Strong lateral velocity and attenuation variations at STS affect the propagation of short period surface waves. We have also used the method to examine near-source conversion of *Rg* into *S* phases. For the next stage of this research, we propose to combine the MineSeis code of Yang (1998) with the GFM code to model delay-fired mining explosions in complex near-source and regional 3D media.

OBJECTIVES

The objectives of this research project are to create physically realistic models of short-period (0.2 to 12 seconds) surface wave generation from small chemical explosions and different classifications of mine blasts, and to understand the propagation characteristics of these surface waves, including the scattering of *Rg* into *Lg*, in complex tectonic regimes. To accomplish these objectives, we have:

- Collected local and regional seismic data sets with short-period (0.5 to 12 sec) surface waves generated from chemical and mining explosions in North America, India, and Kazakhstan,
- Initiated use of a numerical modeling package to generate short-period surface waves from different explosion sources and to propagate them through complex, 3D media, and
- Compared preliminary numerical results to empirical data to aid in development of regional explosion discriminants based upon surface waves.

The progress in the development of the 3D surface wave modeling program and the preliminary results of applying the technique to a model for the Shagan Test Site (STS) in Kazakhstan are discussed in this paper.

RESEARCH ACCOMPLISHED

Regional Wavefield Modeling in 3D Media Using the Generalized Fourier Method

We are applying a numerical wavefield modeling method to generate Green's functions for regional, 3D Earth models. Numerical methods allow the incorporation of realistic structural features such as strong lateral velocity variations, anelastic attenuation and surface topography, which affect the propagation of short period surface waves. However, numerical methods such as finite difference or pseudospectral are computationally very expensive in 3D, where doubling the frequency of a simulation requires eight times as many nodes for a fixed spatial sampling of the wave field. For a particular method, the overall computational effort increases by roughly an order of magnitude with a doubling of frequency (Orrey, 1995).

The numerical method we use is a generalization of the Fourier pseudospectral method. In the Fourier pseudospectral approximation, the spatial approximations of the field variables are truncated Fourier series. Derivatives in the equations of motion are computed by performing spatial FFTs, multiplying by wave numbers, and performing inverse FFTs. The overall efficiency of the Fourier method using second-order time integration is higher for 3D elastic applications compared to a fourth-order in space, second-order in time finite difference method when measured in terms of CPU and memory requirements (Fornberg, 1987). The principal disadvantage of the standard Fourier method, particularly for our applications to surface wave scattering mechanisms, is that boundary conditions at grid edges are intrinsically periodic due to the implementation with FFTs. Therefore, standard Fourier solutions involving interactions of the wave field with the traction-free surface of the earth are inherently flawed. In the Generalized Fourier Method (GFM) used for our simulations, this periodicity is removed for the free surface by supplementing the trigonometric basis functions of the standard method with additional, discontinuity functions that approximate the spatial discontinuities of the field variables at the free surface. For a detailed discussion of the GFM method, the reader is referred to Orrey *et al*. (2002).

An additional advantage of the Fourier method over finite differencing is that the FFT computations allow for efficient solution on parallel computer architectures (Orrey and Robinson, 2002; Furumura *et al.*, 1998), with individual processors computing FFTs for separate columns and rows in the 3D computational grid. In our present implementation of GFM on a nine-node Linux cluster, the computational grid is partitioned into planar sections and distributed among processors as shown in Figure 1, using the Message Passing Interface for parallelization. During each time iteration of wave field evolution, horizontal sections of the computational grid are initially distributed over the NP processing elements, with NZ/NP node planes passed to each processor. After computing the X and Y differentials of the equations of motion via FFTs along rows and columns of each plane, the data set is transposed to

the distribution shown on the right hand side of Figure 1 for computation of differentials in Z. This step requires significant interprocessor communication. The data set is then transposed back to the distribution on the left hand side of Figure 1 for the next time iteration. The code has been optimized for data transfer, interprocessor communication and processor latency, with profiling tools used to tune the parallel performance.

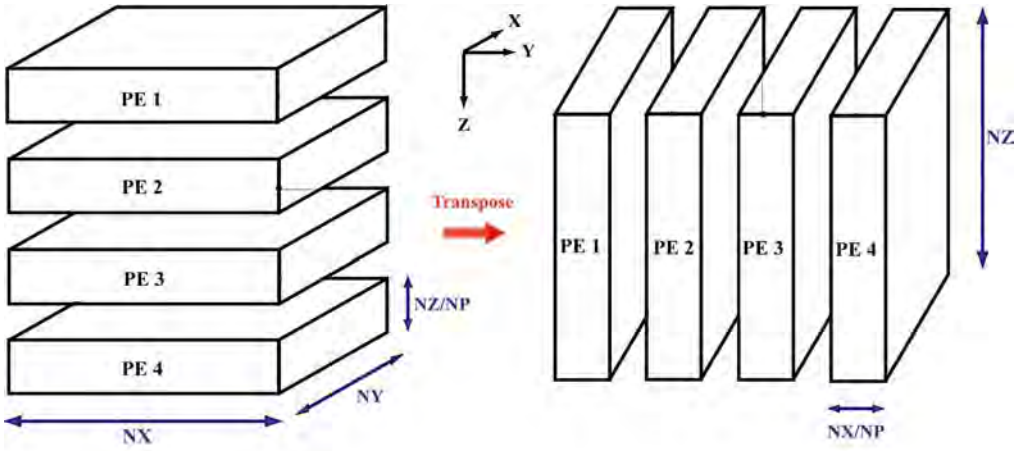

Figure 1. Schematic of domain partitioning for a four-processor distribution of the computational grid and the transpose operation requiring interprocessor communication.

Modeling *Rg* Generation and Propagation at the Shagan Test Site

We have modeled the *Rg* generation and propagation from single-fired explosions at the former Soviet Union Test Site near the Shagan River in Balapan, Kazakhstan. These explosions were conducted to destroy the unused boreholes as part of the decommissioning of the facility. The first set of explosions were conducted in boreholes 1071, 1311, 1381, and 1349 with explosive weights of 25 tons and emplacement depths of 28 m, 50 m, 300 m, and 550 m, respectively. The explosives were emplaced in neogenic clays (1311) and crystalline rock (1071, 1349 and 1381). The primary scientific objective of this series of explosions was to determine the effect of depth of burial (DOB) on the discrimination of nuclear explosions. In addition to the DOB study, six additional explosive borehole closures were recorded, and the depth of the explosives emplacement for these closures ranged from 2.5 to 46 meters with 2 ton yields. The charge in borehole 1381 was detonated in granoseyenites, while the charges in five other boreholes (1327, 1386, 1389, 1409 and 1419) were detonated in neogenic clays. In the following paragraphs, we describe the development of the velocity and attenuation models for STS and present the preliminary results of modeling the observed data with the GFM3D technique.

Variations in STS geology were first noted when we inverted the short-period Rayleigh waves for shallow velocity structure (Bonner *et al.*, 2001). We generated dispersion curves for the station-source pairs for all 10 explosions and found that the test site comprises several distinct regions separated by transitional zones. The group velocity tomography map for 1 Hz *Rg* showed a relatively high velocity region to the southwest (SW) and a low velocity region in the northeast (NE) separated by transition zones. These regions of the test site correlate with zones determined from differences in teleseismic magnitudes (Ringdal *et al.*, 1992). We suspect the faster velocities in the SW region are related to crystalline rocks at or near the surface. Cores for test hole 1383 show crystalline rocks within 5 m of the surface. The low velocities associated with the transition zone follow the Shagan River towards the southwest, and may be related to alluvium overlying the intrusive crystalline rocks near this section of the test site. Lithologic logs from boreholes in this region confirm that alluvium and weathered rock with thickness as great as 350 m overlie the crystalline rocks. In the NE region logs show thick sections of alluvium and unconsolidated tuffs that overlie the Paleozoic sedimentary section. We inverted the dispersion curves for the paths in the SW and

NE sections of STS and determined five distinct velocity profiles for this region (Figure 2). We then used these velocity profiles to develop an initial 3D *P*- and *S*-wave velocity model for STS (Figure 3). We note that over the coming months, we plan to increase the complexity of the 3D model, however the preliminary model is adequate for initial numerical simulations.

The model was developed using a 2 x 2 x 0.125 km spatial discretization (hence the blocky shape of the model as shown in Figure 3), and then resampled to 0.125 x 0.125 x 0.125 km. This discretization resulted in 243 grid points (30.4 km) in both the East-West and North-South directions and 63 grid points (7.8 km) in the vertical direction for a total of 3.7 million nodes. The discretization is designed so that the smallest wavelength (λ) surface wave (in our case, 4 Hz *Rg* with $\lambda \sim$ 0.5 km) is sampled by at least four grid nodes. The parameters for the GFM runs are listed in Table 1. The computer time necessary to run a model with these dimensions in order to synthesize 15 seconds of data is approximately 6 hours using a nine-node Linux cluster. This computational performance was obtained for models that do not incorporate anelasticity. Once we have incorporated anelasticity into the parallel implementation of the code, using the method of Emmerich and Korn (1987), the performance is expected to decrease by about 20% due to the additional computational requirements. However, we are working to implement additional optimization features and expect to keep the run times within a practical time frame for the frequency and distance ranges of interest.

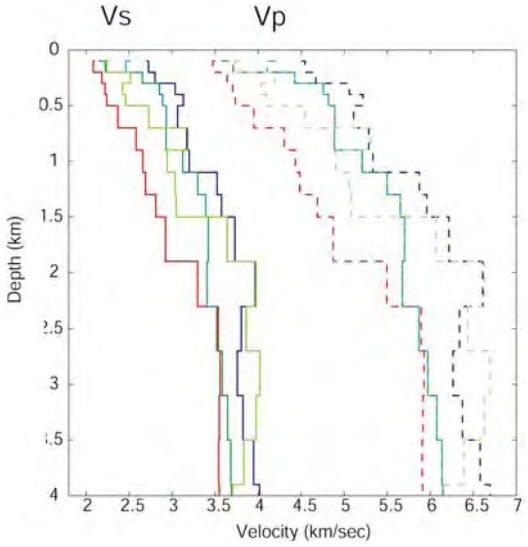

Figure 2. *P*- and *S*-wave velocity profiles used to develop a 3D model for the STS.

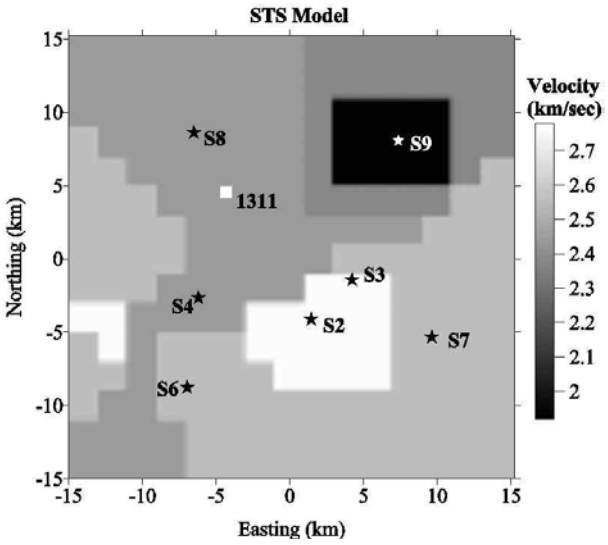

Figure 3. Shear-wave velocity at 0.2 km depth for the STS. Also shown are the location of borehole 1311 and stations that recorded this explosive borehole closure.

Table 1. STS 3D Modeling Parameters

Parameter	Value	Parameter	Value
Spatial discretization	0.125 km	E-W extent of model	30.4 km
Temporal discretization	0.0112 sec	N-S extent of model	30.4 km
Number of E-W grid points	243	Vertical extent of model	7.8 km
Number of N-S grid points	243	Number of time steps	4016
Numbr of Vertical grid points	63	Simulation time	15 sec

We modeled the local amplitude decay (Figure 4) for the explosions based upon the location of the travel paths relative to the SW and NE sections of STS. Our initial modeling of *Rg* attenuation considered all data and determined similar Q values (Q_{Rq} ~ 10 at 1 Hz) as Meyers *et al.*, (1999) who at that time were only able to examine the data from three explosions. We analyzed the data from all ten explosions conducted during these experiments. We searched for station pairs with similar source-to-station azimuths and found two such paths for the slow velocity NE section of the test site, 3 paths in the faster SW section, and one path that consisted of approximately 50% of each section. We computed the Q_{Rq} using the following equation (Aki and Richards, 1980) which includes geometric spreading and anelastic attenuation;

$$A_{Rg} \propto \frac{Ao}{\sqrt{r}} \exp\left(\frac{-wr}{2C_{Rg}(w)Q(w)}\right)$$

where A_{Rg} is the *Rg* amplitude at distance *r* and angular frequency w, C_{Rg} is the *Rg* velocity determined from dispersion curves, *Q* is the quality factor, and *Ao* controls the overall amplitude level. We calculated the Q_{Rq} at frequencies of 0.5, 1, 1.8, 3.5, and 5.5 Hz and the results are shown in Figure 4. *Rg* is strongly attenuated in the slower NE section and has a value of approximately 10 at 1 Hz that increases with increasing frequency. However, for paths within the faster SW section, we see Q values that are on average 5 times greater and are as large as an order of magnitude greater. For each section we incorporated the mean value at 1 Hz into a Q model for the upper crust of STS; however, the initial simulations presented in this paper were completed without anelasticity; anelasticity is currently being incorporated into the parallel version of the GFM3D code.

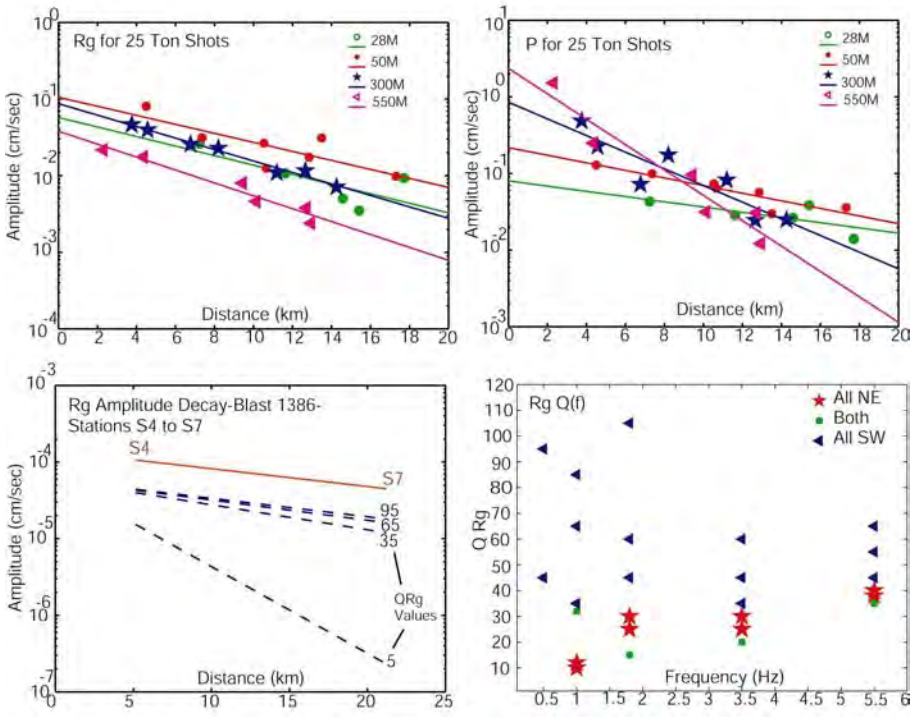

Figure 4. (Top Left) Amplitude decay of *Rg* for the 25 ton shots at STS approximated with a least squares line for each depth. Note that the shallowest explosion had reduced *Rg* amplitudes equivalent to the 300 m shot. Given that the P wave amplitudes are also smaller (Top Right), the explosives may have not detonated full yield, however, differences in source mechanics can not be ruled out. (Lower Left), 1 Hz Rg amplitude decay between stations S4 and S7 for the explosion at Hole 1386 (See Figure 5). The solid red line connects the observed data points, while the dashed lines are the calculated decay based upon Q values of 5, 35, 65, and 95. The scatter in the amplitude decay can be reduced by considering propagation in the NE and SW sections separately. We note very high attenuation (low Q; Lower Right) in the NE section with lower attenuation in the SW section.

The long-term goal of this modeling project is to quantify the near-source processes, such as secondary source effects (e.g., scattering, spall, block motions, tectonic release), that affect regional seismograms recorded in different tectonic regimes. The first steps of the project, completed for this paper, are 1) testing the accuracy of the GFM3D method in modeling local data that has traversed paths of simple and/or complex geologies and 2) performing initial analyses of the effects of small-scale heterogeneities on *Rg* generation and propagation. To accomplish the first goal, we completed GFM3D simulations for three different sources in the STS 3D velocity model. A point source explosion was considered for the source and placed at the locations and depths of three of the DOB experiment boreholes (Table 2). We have not modeled the data for a fourth DOB explosion detonated at 28 meters in borehole 1071; however, we plan to model this explosion together with six other explosions in the region during the upcoming year.

Table 2. Source Locations for GFM3D Simulations.

Borehole	Latitude	Longitude	Yield (tons)	Depth (m)	Model X	Model Y
1311	49.9412	78.7860	25	50	-4.58	4.53
1381	49.8837	78.8147	25	300	-2.53	-1.87
1349	49.8794	78.8493	25	550	-0.05	-2.35

The results of performing the GFM3D simulations on the preliminary STS model are shown in Figures 5-7. Figure 5 presents the comparison of the observed and modeled data in different bandwidths for station S2 from the 25-ton explosion detonated at 50 m depth in borehole 1311. The synthetic seismograms are shown as the first three traces (in order N, E, and Z) in Figures 6 and 7 and are compared with the three-component recordings (last three traces in order N, E, and Z) from a seven station local network deployed by Los Alamos National Laboratory. The observed and synthetic traces were converted to displacement, band-pass filtered between 0.5 and 4 Hz, plotted on equivalent time scales, and normalized to the maximum amplitude in each trace.

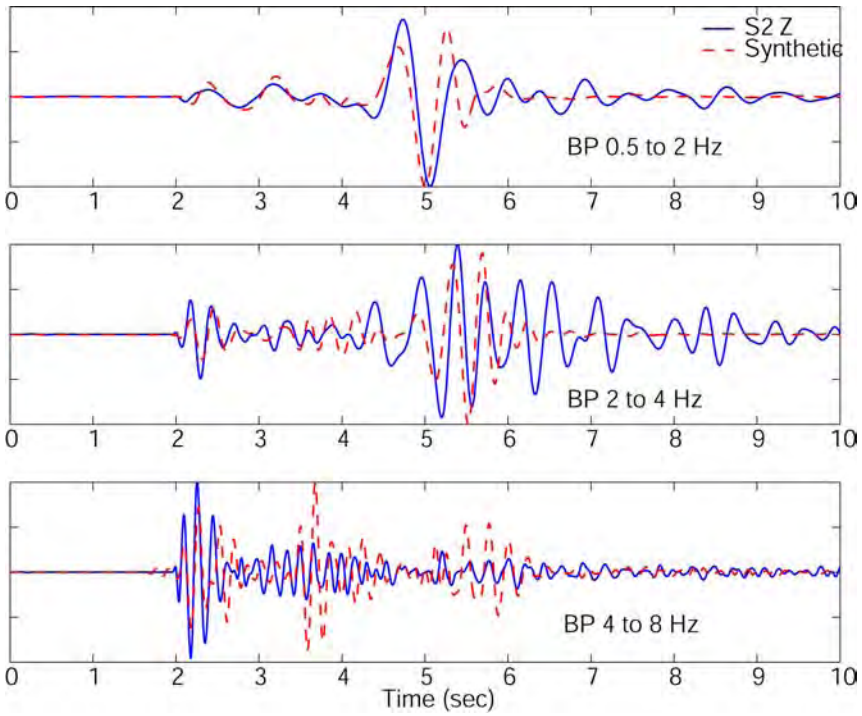

Figure 5. Comparison of station S2 data for the explosion at Borehole 1311 with GFM3D simulations band-passed at (top) 0.5 to 2 Hz, (middle) 2 to 4 Hz, and (bottom) 4 to 8 Hz.

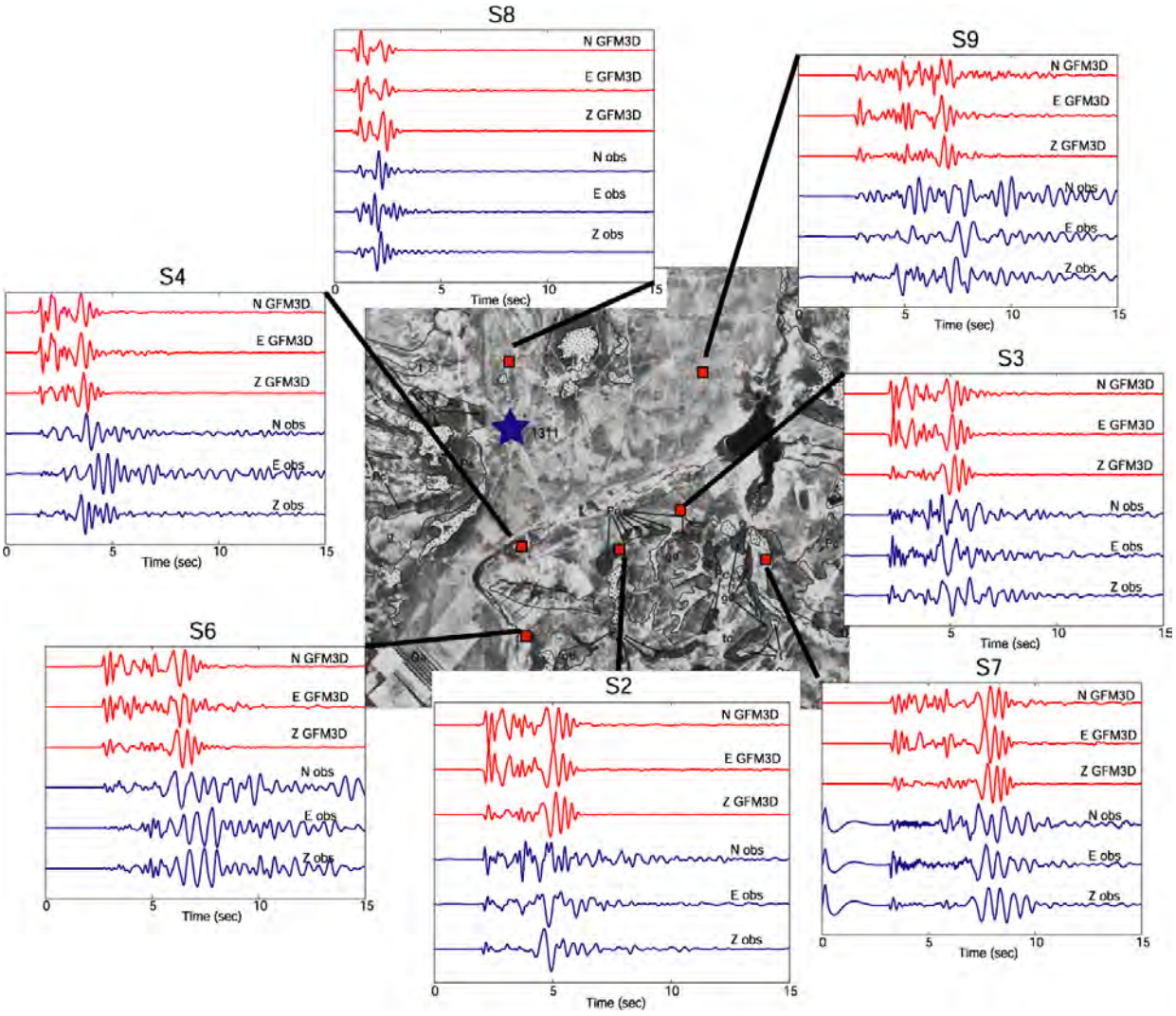

Figure 6. Comparison of observed local seismograms from the explosion at borehole 1311 with GFM3D synthetic traces. Each subplot corresponds to a station that recorded this 50-ton explosion at a depth of 50 m. The first three traces are the N, E, and Z traces synthesized using the STS velocity model and the GFM3D code followed by the observed N, E, and Z waveforms. All data were filtered between 0.5 and 4 Hz. The overhead imagery and interpreted geology is from Davis and Berlin (1992).

Based on the initial STS model, our results are very promising, as the simulated traces show good correlation (in both the arrival times and the waveform characteristics of the *P*, S, and *Rg* arrivals) to the observed data for most of the stations. The largest observed arrival at all seven stations is *Rg*, however, the complexity of the *Rg* packet varies significantly at each station. For example, the observed data at station S8 shows a high frequency, pulse-like Rayleigh wave with relatively no dispersion as compared to station S7 that shows longer period, dispersed *Rg*. We were able to simulate the approximate *Rg/P* ratios observed at 5 of 7 stations, with the modeled data for stations near the source (S4 and S8) predicting larger *P* wave arrivals than observed. For most of the stations, the modeling predicted short-period Rayleigh wave trains that replicated significant portions of the observed *Rg*. At stations S3, S4, and S7, the modeled *Rg* (Z components) and the observed data have high correlation throughout the entire wave packet. At other stations (S2, S6, and S8), the model traces only match the initial cycles of the *Rg* wave train.

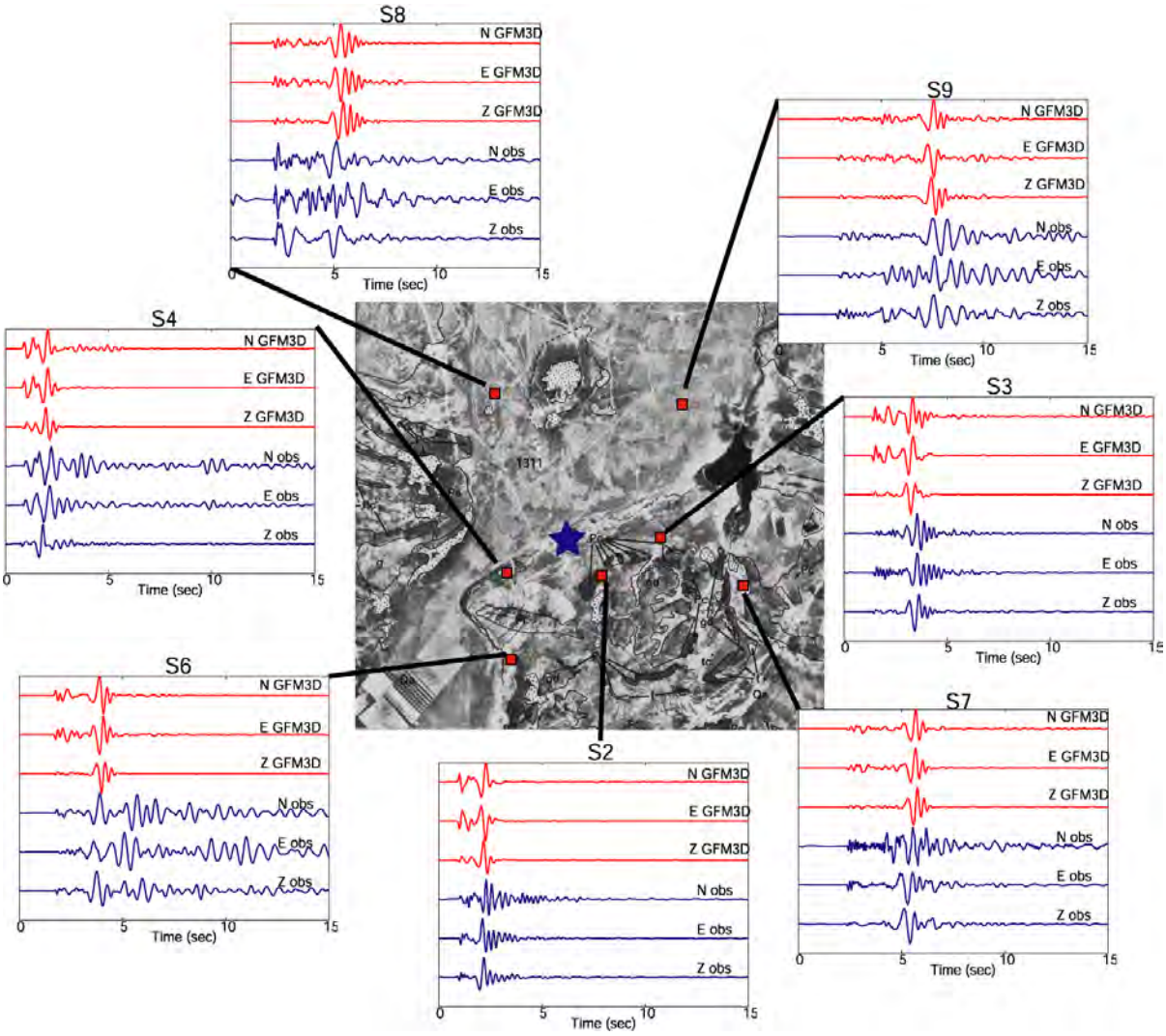

Figure 7. Comparison of observed local seismograms from the explosion at borehole 1381 with GFM3D synthetic traces. Each subplot corresponds to a station that recorded this 50-ton explosion at a depth of 300 m. The first three traces are the N, E, and Z traces synthesized using the STS velocity model and the GFM3D code followed by the observed N, E, and Z waveforms. All data were filtered between 0.5 and 4 Hz.

We had less success matching the waveforms at station S9 (Figure 6), which is located in the complex NE section of the STS. The observed data for this event shows the longest signal duration for the STS seismic network. One possible reason for the extended signal duration is reverberations in a near-surface low-velocity layer. The model in this region (Figures 2 and 3) does have a near-surface low-velocity layer. However, the relative amplitudes of these reverberations as compared to the data could not be matched. Also of interest at this station are the arrival times for *P*, *S*, and *Rg*. While the modeling predicts accurate arrival times for P and S (within 0.2 seconds of the observed data), the predicted *Rg* arrives 0.5 secs prior to the observed signal. As noted in Figure 3, the preliminary model in this complex region is essentially a 2D path with minimal 3D effects. It is possible that a more complex 3-D model in this region, possibly developed using borehole logs or laboratory *P*- and *S*-wave velocities from core samples, could improve the results for station S9.

We obtain similar success rates for modeling the explosion at 300 m depth in borehole 1381 (Figure 7). In these examples, we find a better fit to the S9 *P*, *S*, and *Rg* arrivals; however, we get poor matches with the data at stations S6 and S8. We also observe longer signal duration than modeled for the data at S6. Because of space limitations in

this paper, the results of the 550 m depth explosion at borehole 1349 are not presented but are available for review. These results, while preliminary, suggest the GFM3D method is an accurate technique to model the generation and propagation of short-period surface waves and body waves.

A second goal of the short-term modeling project at STS was to examine the addition of near-source random variations to the velocity values of the layered structure. In this regard, Figure 8 illustrates the effects of random spatial variations (max 10%) in the velocity values within 3 km of the source inside the STS model in both the vertical and lateral directions. Random variations in upper-crustal velocity structure measured in boreholes have often been found to be 25% and greater, thus a 10% fluctuation is not extreme and is probably conservative. We then modeled a point source explosion at 50 m depth and propagated the seismic energy to the stations shown in Figure 8. We then compared these data with random near-source heterogeneities to the GFM3D runs without the velocity variations (same data shown in Figure 6). The resulting seismograms and spectra for the modeling to station S7 are shown in Figure 9. The near-source scattering in the randomized model creates larger amplitudes for the entire *Rg* wave train; however, the most pronounced increase occurs in the 3 to 10 Hz frequency band. The increase in this frequency band may have very important ramifications in the generation of the regional distance *Lg* shear phase from explosions. In fact, Myers *et al.* (1999) examined the regional data from these explosions at STS and concluded that the dominant mechanism for enhanced regional *Lg* and *Sn* excitation for shallower 1311 explosion is local *Rg* scattering. Thus, to properly quantify the effect of this near source scattering at regional distances, we plan to develop a larger model for this region of Kazakhstan and model the regional seismograms for these explosions. We also plan to examine the effect of random variations along the entire path length in addition to the near-source regions.

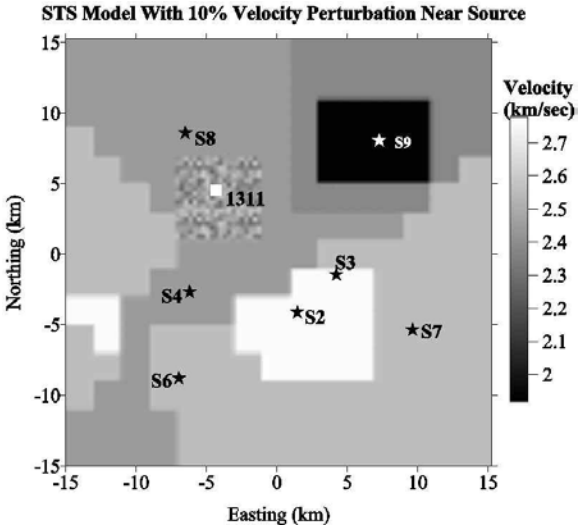

Figure 8. Shear-wave velocity at 0.2 km depth for a STS model with 10% near-soure velocity perturbations. Also shown are the location of borehole 1311 and stations that recorded this explosive borehole closure. The velocities have been randomized within 3 km of the source to examine the effects of near-source scattering on the *Rg* wave train.

CONCLUSIONS AND RECOMMENDATIONS

A parallelized version of the Generalized Fourier Method has been implemented on a nine-node Linux cluster system, and we have used the code to model the *Rg* generation and propagation from single-fired explosions at the former Soviet Union Test Site near the Shagan River (STS) in Balapan, Kazakhstan. The results using our initial 3D velocity models for STS are very encouraging and show the method is suitable to examine source characteristics such as radiation patterns and secondary effects (e.g. scattering). We will continue the modeling of these explosions at STS by refining the velocity models and by examining the effects of near-source scattering on regional data. In addition, we will incorporate our inferred Q models of the site into the GFM code, using the method of Emmerich and Korn (1987). Given the low inferred Q values in the NE section of the STS model, we expect the Q effects on the waveforms to be critical for an accurate characterization of the energy partitioning between body and surface wave phases. Also, we will work with David Yang of Los Alamos National Laboratory to combine his MineSeis1.1 (Yang, 1998) program with the GFM3D code. By combining realistic source effects from his code with the GFM3D wavefield synthesis, we expect to have a powerful and robust method for modeling the complexity of regional, explosion-generated surface waves propagated through various tectonic regimes.

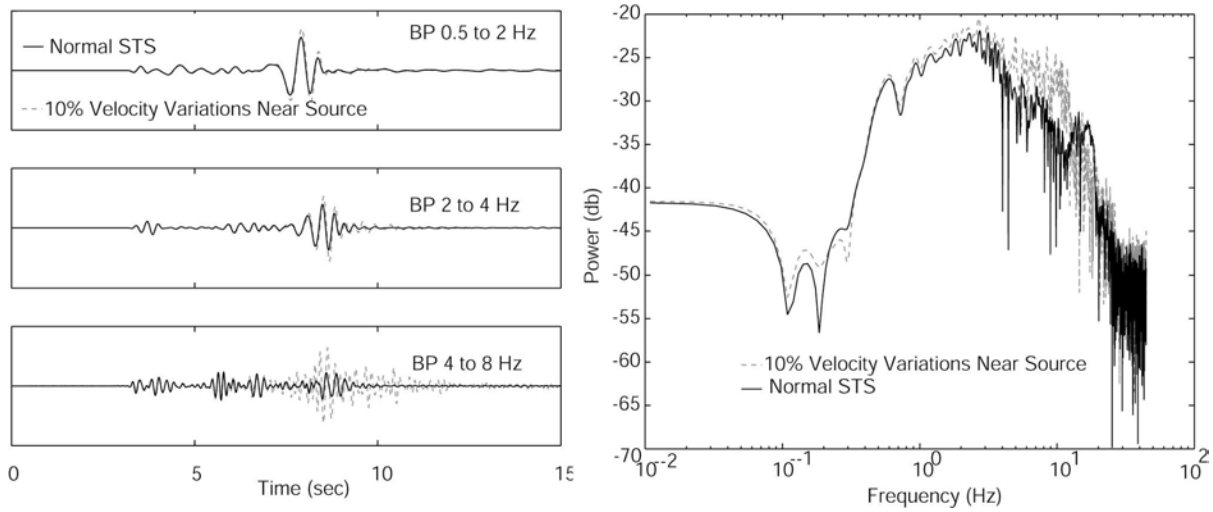

Figure 9. Seismograms and spectra for synthesized data at S7 showing the effects of applying 10% random velocity fluctuations to the near-source structure.

ACKNOWLEDGMENTS

We thank Howard Patton, David Yang, and Brian Stump for helpful comments on this research project. We also wish to thank D. Craig Pearson and Diane Baker for help acquiring the DOB data. Finally, we thank Delaine Reiter, Ileana Tibuleac, and Jim Lewkowicz for help with the manuscript and additional support with this project.

REFERENCES

Aki, K. and P.G. Richards (1980), Quantitative Seismology: Theory and Methods, W.H. Freeman, New York.

Bonner, J., D.C. Pearson, W.S. Phillips, and S.R. Taylor (2001), Shallow velocity structure of the Shagan River Test Site in eastern Kazakhstan, *Pure and Applied Geophysics*, 158, 2017-2039.

Davis, P. A., and G. L. Berlin (1992), Geologic mapping of the Semipalintisk region using Land Sat thematic mapper and spot panochromatic data, *LAUR-92-310*, 15 pp.

Emmerich, H. and M. Korn (1987), Incorporation of Attenuation into Time-Domain Computations of Seismic Wave fields, *Geophysics*, 52(9), 1252-1264.

Fornberg, B., (1987), The pseudospectral method: Comparisons with finite differences for the elastic wave equation, *Geophysics*, 52, 483—501.

Furumura, T., B. L. N. Kennett, and H. Takenaka (1998), Parallel 3-D pseudospectral simulation of seismic wave propagation, *Geophysics*, 63, 279—288.

Myers, S. C., W. R. Walter, K. M. Mayeda, and L. Glenn (1999), Observations in support of *Rg* scattering as a source for explosion S waves: regional and local recordings of the 1997 Kazakhstan depth of burial experiment, *Bull Seism. Soc. Am.*, 89, 544-549.

Orrey, J. L. and G. Robinson (2002), A Parallel Implementation of the Generalized Fourier Method for Elastic Wave Simulations, in preparation for submittal to *Geophysics*.

Orrey, J. L., C. B. Archambeau and G. A. Frazier (2002), Complete Seismic Wave Field Synthesis with a Pseudospectral Method: The Generalized Fourier Method, revised manuscript to be submitted to *Geophys. J. Int.*

Phillips, W.S., H. J. Patton, and H. E. Hartse (2001), Regional coda magnitudes in central Asia and m_b(*Lg*) transportability, Proceedings *of the 23rd Annual Seismic Review: Worldwide Monitoring of Nuclear Explosions-October 2-5, 2001*, 580-589.

Ringdal, F., P. D. Marshall, and R. W. Alewine (1992), Seismic yield determination of Soviet underground nuclear explosions at the Shagan River test site, *Geophys. J. Int.* 109, 65-77.

Yang, X. (1998), MineSeis – A MATLAB GUI program to calculate synthetic seismograms from a linear, multi-shot blast source model, in *Proceedings of the 20th Annual Seismic Research Symposium on Monitoring a Comprehensive Test Ban Treaty*, 21-23 September, 1998, Santa Fe, New Mexico, 755-764.

SEISMIC MONITORING OF BLASTING ACTIVITY IN RUSSIA

Michael A.H. Hedlin

University of California, San Diego

Sponsored by Defense Threat Reduction Agency

Contract No. DTRA01-00-C-0115

ABSTRACT

Two significant mining regions in Russia lie near Novosibirsk and at the Kursk Magnetic Anomaly. A small percentage of events from these areas trigger the International Monitoring System (IMS). We have studied IMS recordings of events from these areas with the main goal of better understanding how these blasts are detonated and how these events will be most effectively monitored using IMS data. We have collected ground-truth information on the mining blasts and crustal structure in the area to facilitate modeling of the events. We have focused on sifting out from further consideration routine mining events and identifying detonation anomalies. We define master traces to represent tight clusters of mining events and to be used to identify anomalous events. We have examined recordings of events from eight significant event clusters in the 500-km-long Kuzbass/Abakan mining trend near Novosibirsk. The recordings were made by the IMS station ZAL. We see significant variations in the P onset and early coda between different events in clusters. We have found strong evidence of a detonation anomaly in just one of the events (out of 178 examined). Differences in the onset wave trains are attributed largely to differences in the firing patterns.

Time independent spectral modulations have been observed in seismic signals produced by delay-fired mining events in mining regions throughout the world. The Novosibirsk trend is no exception to this rule. Delay-fired events in many mining regions, such as Kuzbass/Abakan, are also commonly associated with enhanced long-period (2- to 8-s) surface waves. The mine blasts in Russian mining regions appear, seismically, to resemble large blasts recorded in other regions (such as Wyoming). Techniques found to be effective in Wyoming, reviewed by Hedlin *et al*., 2002 and Stump *et al*., 2002, are expected to perform well when applied to recordings from the Novosibirsk and Kursk mining areas.

OBJECTIVE

Seismic recordings of mine blasts in the Kursk and Novosibirsk regions of Russia made by stations in the IMS hold a wealth of information about how these events were detonated. Our main objective is to use these data to learn how mining events can be successfully, and routinely, discriminated from single explosions and earthquakes. We seek evidence from the seismic recordings of anomalous, sympathetic detonations that might be confused with hidden nuclear tests. We use simulations of mine blasts, based on ground-truth data, to model the recorded waveforms and explore the utility of these events for obscuring instantaneous detonations.

RESEARCH ACCOMPLISHED

Briefly, our research has involved IMS recordings of mine blasts near Novosibirsk and near Kursk, Russia. We have obtained ground truth data for a small subset of blasts in the Novosibirsk area and have used this information for modeling seismic waves at regional distances from these events. In this section we present a brief overview of progress toward our main objectives.

IMS recordings of Novosibirsk region events

Dataset: Only one IMS seismic station lies within 500 km of the Novosibirsk mining trend (Figure 1). This station, ZAL, has provided, by far, the most informative recordings of events in this trend. Consequently, data from this station have played a central role in our analysis. We have collected ZAL recordings of events that span the entire 500-km mining trend. This trend comprises over 70 mines; however, it includes several very active clusters of mines (Figure 2). We have received *a priori* identifications of over 200 blasts in this trend and have collected recordings of 178 events. We also have *a priori* identifications of 58 earthquakes. Ground truth data on these events was provided by V. Khalturin (Lamont-Doherty Earth Observatory -- LDEO).

Routine Screening: We have found recordings made at more distant IMS stations, and the regional network KNET, have a more limited value for describing mining events in this region and screening them from further consideration. Routine screening of events from this trend involves quantification of spectral rugosity, such as that displayed in Figure 3. The screening also compares mid-period amplitudes with short-period amplitudes recorded at the nearby IMS station ZAL. A comparison of short- and mid-period wave amplitudes is shown in Figure 4.

Possible Detonation Anomaly: The amplitude screening software described above identified one event, recorded at a range of 103 km from ZAL, as an outlier with greater than expected P wave amplitudes when compared with the surface waves (Figure 4). The recordings of this event made at ZAL are shown in Figure 5. Ground truth data have been unavailable for this event although the seismic data suggests a detonation anomaly occurred ~ 3 seconds into the blast sequence.

Ground Truth

One explosion for which we have received ground truth information occurred at the Sibirginsky Open Pit Coal Mine on July 28, 2001 (Figures 2 and 6). This pit is located in the Kuzbass mining region near the center of the trend. The information was obtained by Vitaly Khalturin (LDEO), who also witnessed the blast. The blast was used to fracture the consolidated sediment layer above the coal seam and did not involve casting. The diagram in Figure 6 shows the complexity of this event. The shot sequence was initiated at the north end and included 57 rows ranging from 2 shots to 30 with a total of 666 shots involving 520,380 kg of explosives in the entire blast. Shots in most rows were detonated simultaneously with 50 msec delays between rows. The 50 msec delays in this figure are shown by the "X" marks. Some rows were split into two segments by a 20-msec delay in the middle. These shorter delays occurred at the "=" marks. The entire blast shot spanned 2.9 seconds. The event was assigned an energy class of 7.7 and a local magnitude of 2.8. Shot depths ranged from 16 to 28 meters. The salient features of this blast are that large numbers of shots are detonated simultaneously. Ground truth on other blasts indicates that this kind of blast is commonly used in this region.

Modeling

Routine Blast Following numerous authors, we model fracture and cast blasts in the Novosibirsk area assuming linear superimposition. The result of one simulation is shown in Figure 7. The shot grid used for this calculation

consists of 50 rows of 10 shots each. All shots in each row are detonated simultaneously with rows separated in time by 50 msec and in space by 5 m. The velocity model used in these simulations was based on the work of Solovyev, *et al*. (2000). The modeling indicates that events that do not involve casting will produce spectral modulations below 10 Hz substantial surface waves as observed in most recordings made at regional distances by the IMS station ZAL.

Although the ground truth information that prompted this calculation comes from the plans for the shot, and has not been verified through observation of the actual event, it has been useful in that it shows us how complicated these events are and gives us a physical explanation of the observed spectral modulations.

Anomalous Blasts: We have presented observational evidence for a significant near-simultaneous detonation anomaly in a mine blast near the IMS station ZAL. Events such as these have single-fire characteristics and might prove to be problematic in a discrimination analysis (Stump *et al*., 2002). In our study of anomalous events in this region, we look specifically at blast patterns that are known to be used in this area and estimate the yield that can be detonated simultaneously, and remain hidden, during the mine sequence. One example is based on the routine blast grid considered in Figure 6. In Figure 8 we show a suite of vertical component synthetics generated using this blast grid with instantaneous, over-buried, charges detonated immediately beneath. The charges vary from 100,000 to 500,000 kg. Further details on this calculation are provided in the figure caption.

Blasting at the Kursk Magnetic Anomaly

In 1987, mines at the Kursk Magnetic Anomaly (KMA) provided 10% of the world's iron from rich bands of ore. Prior to 1995, KMA was one of the most significant mining areas in Russia. The largest blasts (> 300 tons) were conducted in the surface mines at the Lebedinsky, Stoilensky and Mikhailovsky mining combines and are used for casting near-surface material. The ore is covered by sediment, which ranges in thickness from 37 to 500 m (Leith, 1995). Kursk "conventional" blasts, like many blasts in the Novosibirsk region, detonate entire rows of charges simultaneously. This type of blast has been used less frequently since the early 1990s as some blasts were detonated with delays within the rows. Mine blasts are also often detonated in blocks separated by ~ 1 second. Delays within the blocks range from 20 to 50 msec, again, as has been observed in the Novosibirsk region. The completed primary seismic network will place 13 stations within 2000 km of KMA (Figure 9).

Monitoring Priority: Our first objective in our study of Kursk mining activity was to assess the importance of this region to the nuclear explosion monitoring community given mining activity since January 1, 1995. In 1987, the region was responsible for up to half of the large (> 300 tons) non-coal mining blasts in the Former Soviet Union (FSU). As reviewed by Leith, the economic down-turn in the early 1990s led to fewer, and smaller, blasts in this region. A list of reviewed events from an area including the three mining combines from January 1, 1995, to the present returned just one event (Figure 10). The event occurred in 2001 on February 2 and was assigned a body wave magnitude of 3.2. We have no ground truth for this event. The location error suggests that the event likely occurred at the Mikhailovsky combine. It appears that presently the Kursk region lies a distant second to the Novosibirsk area in terms of significance for treaty monitoring.

Ground truth: Prof Spivak (IDG) has provided a catalog of blasts at the Lebedinsky, Stoilensky and Mikhailovsky combines in the Kursk region with yield above 100 tons and a list of underground events with yield above 10 tons.

Screening methods: Two permanent and six temporary seismic stations located at KMA recorded 12 blasts from August through September 1995 and recorded spectral modulations. Our analysis of IMS data to assess the utility of these modulations, and energy partitioning, for routine screening of events from this region is ongoing.

CONCLUSIONS AND RECOMMENDATIONS

Events in the Novosibirsk region do not commonly trigger IMS sensors. Events that do should be readily screened out using techniques developed for large mine blasts in Wyoming. These events routinely produce spectral modulations and long-period surface waves that are due to the long duration of the delay-fired shot sequence. We have found evidence for one detonation anomaly in this region based on the seismic data. Routine monitoring of this region will have to rely heavily on the IMS station ZAL.

Significant progress in the study of mining blasts in the Novosibirsk region will require more accurate ground truth data on the mine blasts as well as an improved velocity model of the region. A calibration experiment in this area would provide much-needed basic empirical data that could be used to further our understanding of single and delay-fired events in the mining trend. Such knowledge will be required to provide a physical basis for establishing a dividing line between normal and abnormal events of the sort considered in this paper.

Presently, the Kursk region does not appear to pose a significant concern for the monitoring community. A return to simultaneous detonation of large numbers of charges, or a return to higher yield and more frequent blasting, would raise the profile of this mining region considerably.

ACKNOWLEDGEMENTS

Vitaly Khalturin provided information on blasts and earthquakes in the vicinity of Novosibirsk. David Yang provided Green's functions for the simulations of blasts in the Novosibirsk region. We thank Bill Leith, who assisted by putting our group into contact with the IDG group, including Alexander Spivak, and for providing his report on mining in the Kursk region.

REFERENCES

Hedlin, M.A.H., B. Stump, D.C. Pearson, and X. Yang (2002), Identification of mining blasts at mid- to far-regional distances using low-frequency seismic signals, *Pure and Applied Geophysics*, **159** No. 4, 831-864.

Leith, B., 1995, Large Mining Blasts from the Kursk Mining Region, Russia, Final USGS/UC-LLL report B291532.

Solovyev, V.M., V.S. Seleznev, I.V. Zhemchugova, and A.V. Liseykin (2000), Deep Structure of Altai-Sayans region from the seismological systems of observations. Seismology in Siberia at the Millenium Boundary, The proceedings of International Conference, Novosibirsk, Nauka Publ. House, p222-228.

Stump, B., Hedlin, M.A.H., Pearson, D.C., Hsu, V., 2002, Characterization of Mining Explosions at Regional Distances – Implications with the International Monitoring System.

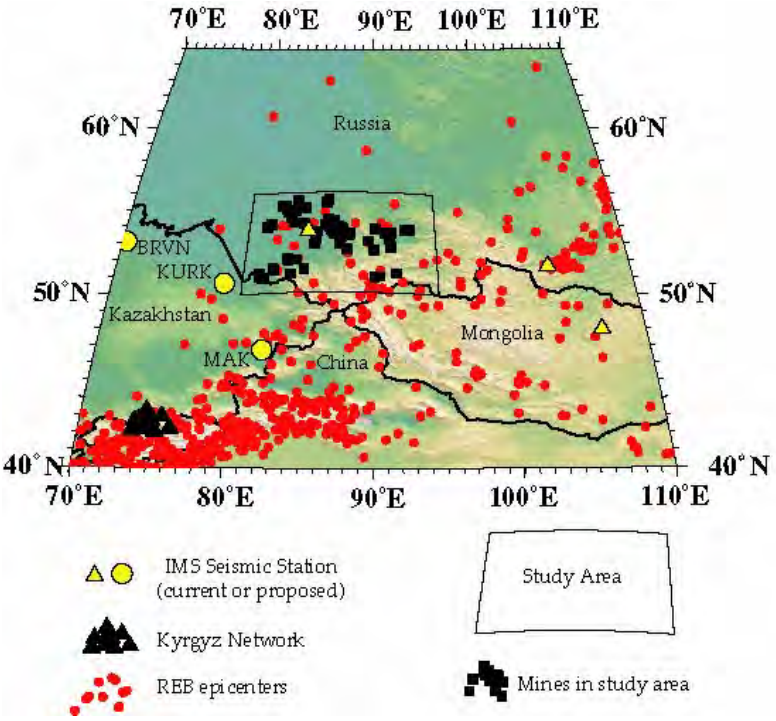

Figure 1. Seismic events reported in the reviewed event bulletin between 1/1/95 and 2/20/2000 are plotted with seismic stations in Central Asia near the study area. The study area includes 72+ surface and underground mines in the Altai-Sayan mining trend.

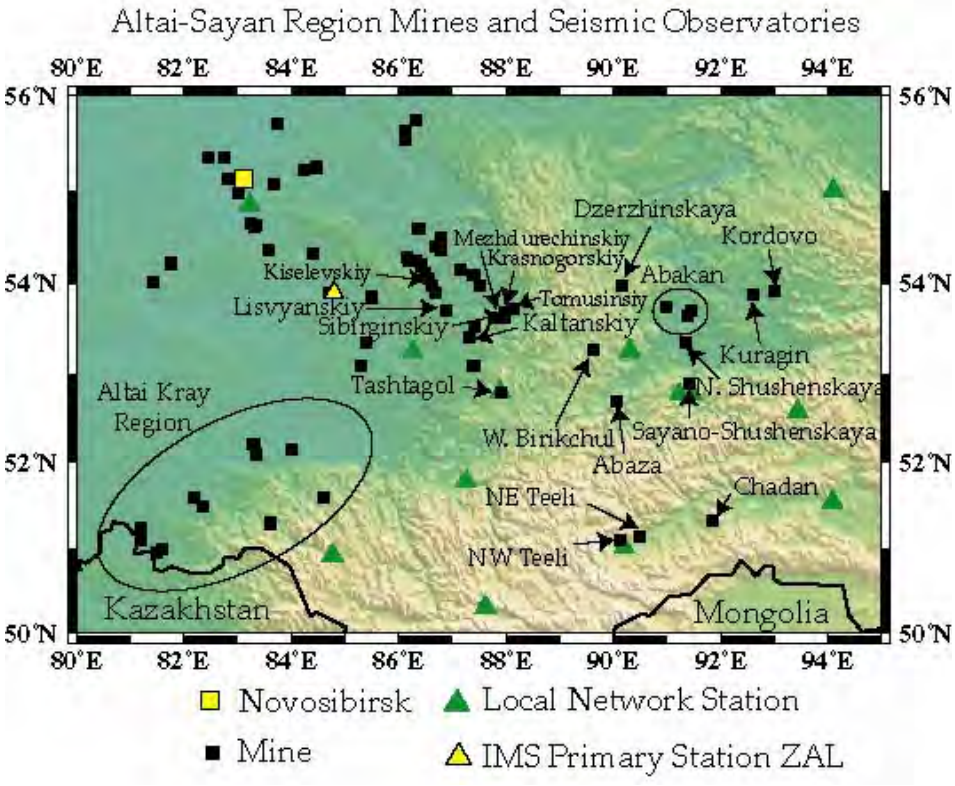

Figure 2. Mines located in the Altai-Sayan mining region. Most mines are located to the east of Novosibirsk, Russia, and are located less than 559 km from the IMS primary 3-component seismic station at Zalesovo. Blast yield and frequency are strongly dependent on the area of the mine. The Altai Kray mining region is responsible for relatively few number of small blasts. Significant blasting is common in the Kuzbass region near the center of the map. The mining region is monitored closely by stations in the Altai-Sayan Seismological Expedition regional network.

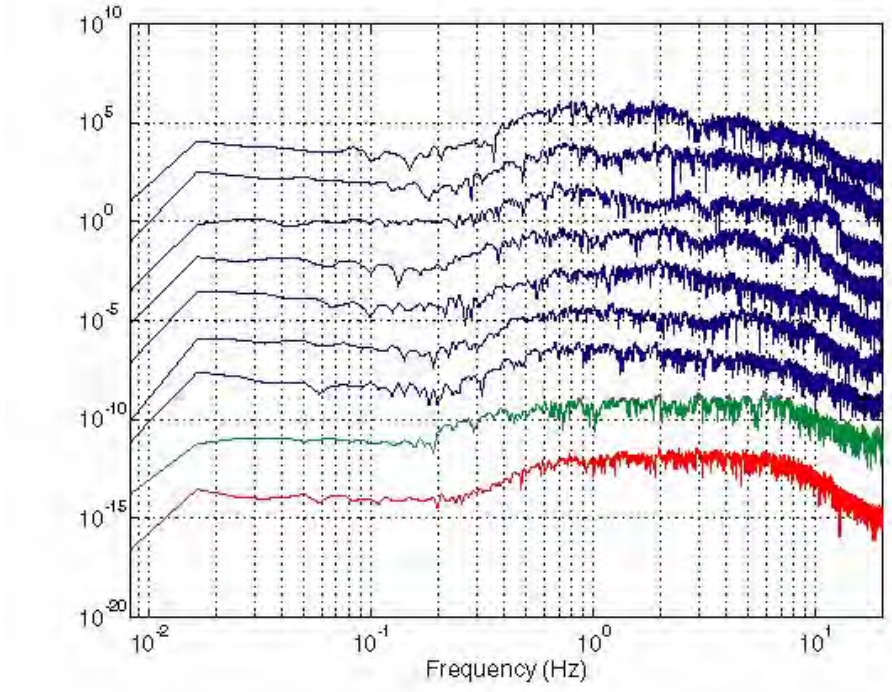

Figure 3. Vertical component spectra from events in the Sibirginsky cluster. Modeling indicates that the observed spectral modulations are due to shot finiteness in time and not directly due to inter-row or inter-shot delays. The lowest trace in this figure was taken from a recording of an earthquake located near the cluster. The second lowest spectrum is from the event shown in Figure 6.

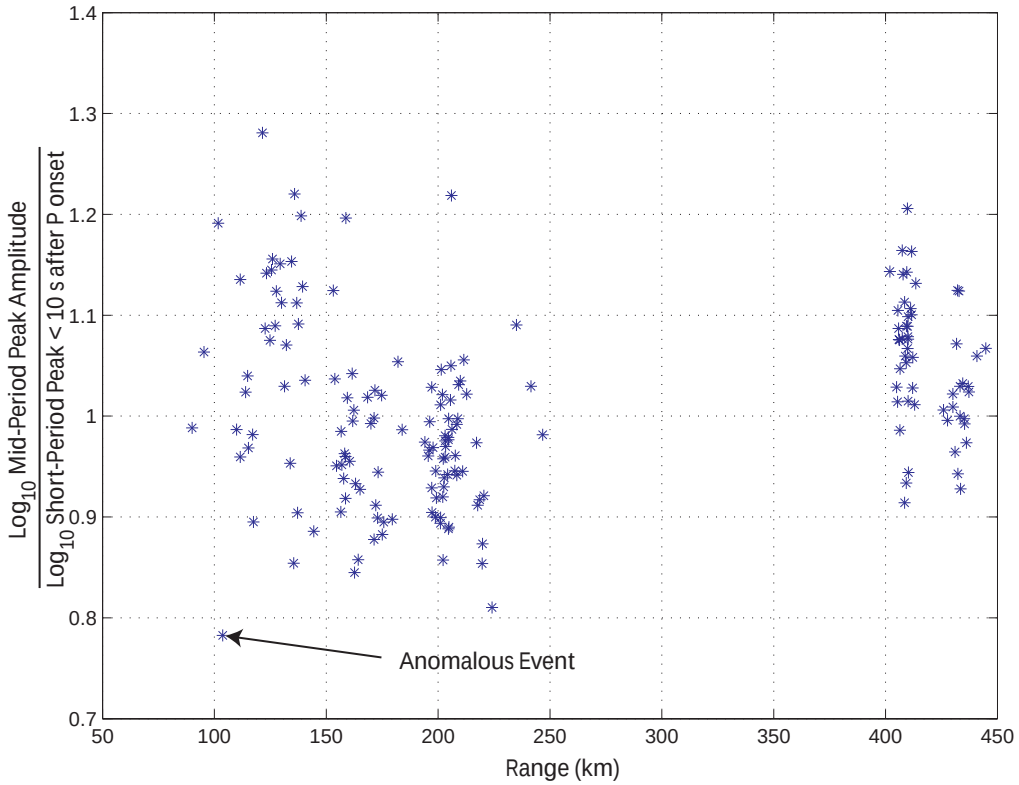

Figure 4. Of 178 mining events considered in the 500-km-long mining trend near Novosibirsk, one was automatically identified as anomalous by software that compares peak, high-frequency amplitudes recorded within 10 s of the P onset on the short-period channel at ZAL with mid-period peak amplitudes at times when the surface waves are expected.

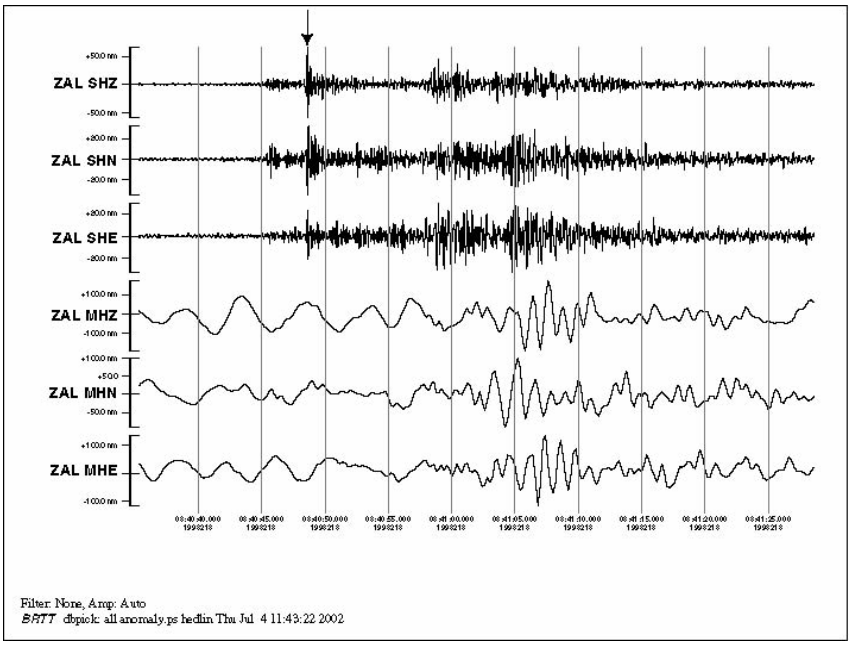

Figure 5. The short- and mid-period recordings made at ZAL of the event highlighted in Figure 4 are shown above. A possibl y is shown ~ 3 seconds after the P wave onset. Ground truth data

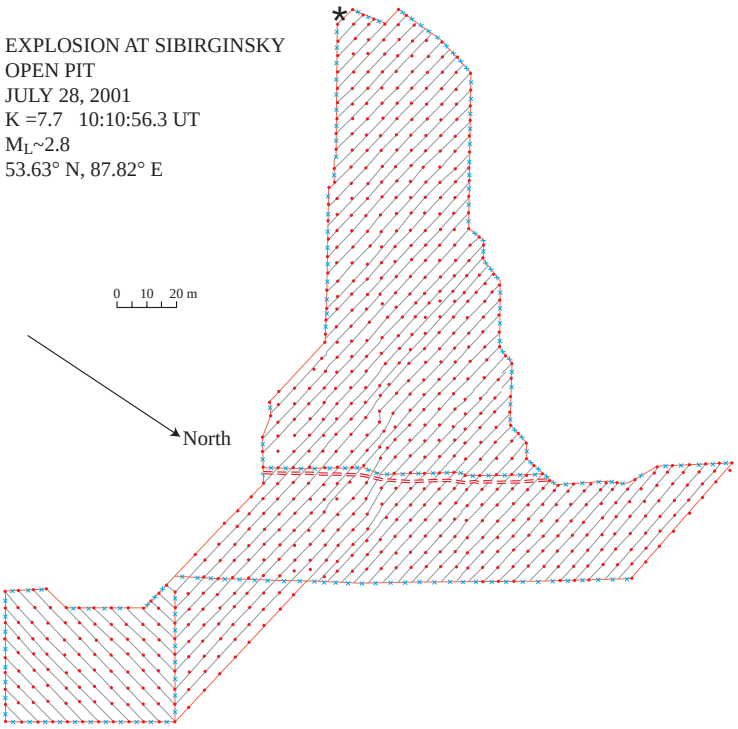

Figure 6. Blast grid for one event at the Sibirginsky open-pit coal mine. The blast was used to fracture the overburden. The blast sequence was initiated at the "*" at the upper limit of the grid. Inter-row delays were 50 msec and are represented by the "X" marks. Some rows were detonated with a single 20 msec delay ("=") sign.

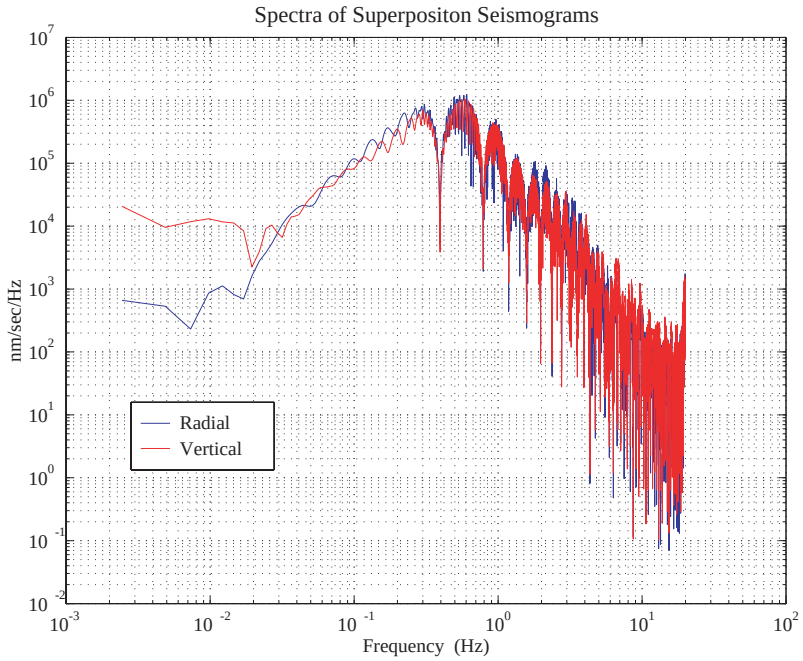

Figure 7. Vertical and radial component spectra from a simulated fracture shot at the Sibirginsky coal mine in the Kuzbass. The synthetics were calculated at a range of 200 km (the distance from the mine to ZAL). The generic event comprises 50 rows of 10 shots each. Time delays between rows are 50 msec, all shots in each row are detonated simultaneously. The inter-row delays produce spectral modulations starting at 20 Hz. Modulations seen at lower frequencies in this simulation are due to the duration of the shot. Similar modulations are commonly observed in recorded data at the IMS station ZAL. The superposition spectra shown above were calculated using the Mineseis package provided by David Yang (LANL).

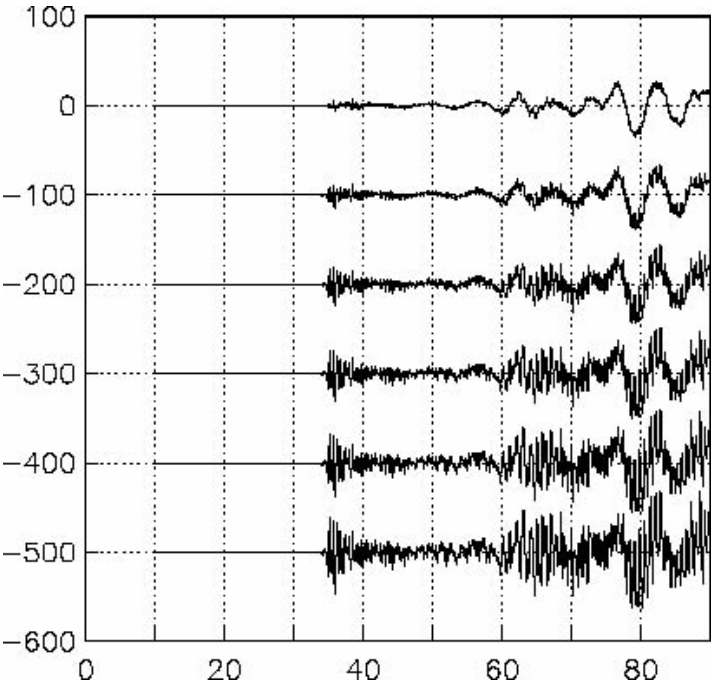

Figure 8. Vertical component synthetics from the generic blast shown in Figure 4 are shown in the upper trace. The delay-fired event is predicted to generate a substantial long-period surface wave. Surface waves are observed commonly at ZAL. The lower five traces are, from top to bottom, the blast detonated with single detonations of 100,000 (top) to 500,000 kg (bottom). The instantaneous charges are buried at depths ranging from 15 to 25 m. The ratio of peak amplitude at long-periods to short periods decreases with increasing yield of the instantaneous shot.

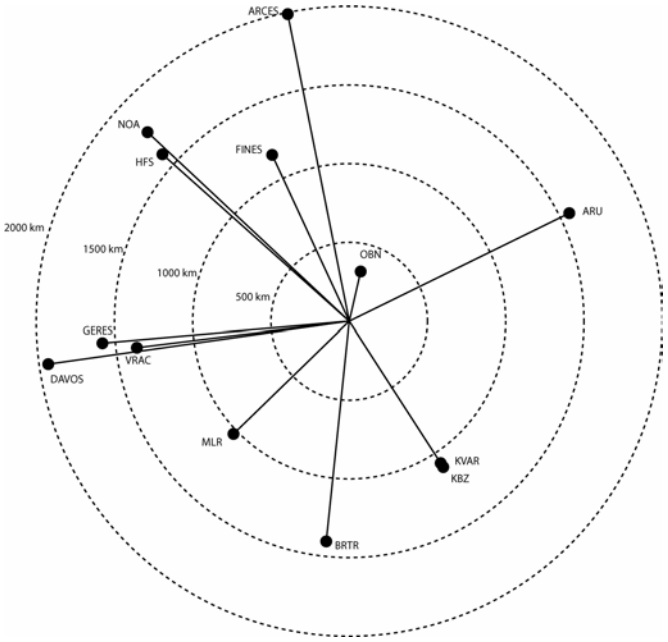

Figure 9. Coverage of the Kursk mining region by stations in the primary IMS seismic network. The closest station, OBN, is located 323 km to the north.

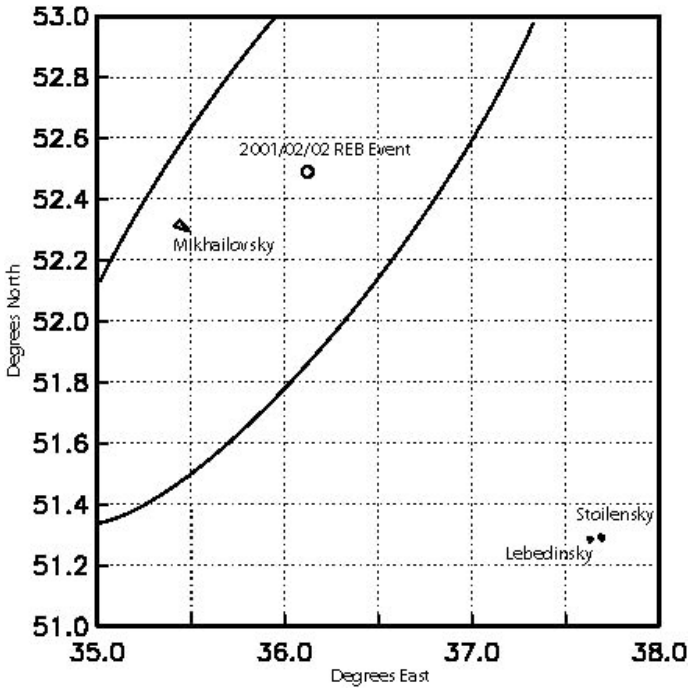

Figure 10. From 1/1/95 to present, a single event at the KMA was reported in the REB. The event location with error ellipse is shown with the mine locations.

DISCREPANCIES AMONG PIDC, ISC, AND USGS SEISMIC MAGNITUDES

Won-Young Kim, John Granville, and Paul G. Richards,

Lamont-Doherty Earth Observatory of Columbia University

Sponsored by Defense Threat Reduction Agency

Contract No. DTRA01-00-C-0074

ABSTRACT

We are working to document and then to explain the well-known systematic differences between magnitudes (mb) assigned by the prototype International Data Centre (PIDC), the International Seismological Centre (ISC), and the United States Geological Survey (USGS). To do this, we first obtain "classical magnitudes" that reproduce the instrumentation and procedures associated with the Veith-Clawson magnitude scale. Though others claim to assign such magnitudes using broadband data, current practice is notably different from the actual Veith-Clawson protocol, and uses measurements made from narrow-band filtered data derived from broadband instruments. We obtain classical magnitudes by making time-domain measurements using WWSSN seismograms simulated from digital waveforms, thus allowing us to maintain consistency with the original Veith-Clawson magnitude scale.

Our first project, now submitted for publication, describes the systematic differences between PIDC mb and USGS (PDE) mb for 13 underground nuclear explosions and 10 large earthquakes (PDE mb $\geq$ 6.4). We have now begun to study a larger group of seismic events, spread across different depths and magnitudes, that all have USGS (PDE) mb = 5.0. For these we have obtained the Veith-Clawson mb. For 50 events, the average VC mb is 4.7, and the average Reviewed Event Bulletin (REB) mb is 4.5. Thus, the VC mb values are generally lower that the PDE mb. Our VC mb values are greater than or equal to the REB mb for all 50 events. The average discrepancy (VC mb - REB mb) is 0.2 m.u., which is less than half the discrepancy for large events (PDE mb $\geq$ 6.4) we studied earlier. The discrepancy is the same (0.2 m.u.) for events in the REB assigned a default depth of zero as it is for events that are assigned an actual focal depth. However, this may not continue to be the case when more events are included. For the 50 events, the VC event mb's range from 4.0-5.2, while the REB event mb's range from 4.0-5.0. We have also attempted to assign a Veith-Clawson mb for a set of events for which the USGS (PDE) mb is 4.0. For these events, there are only a few stations reporting an mb, and these overwhelmingly are array stations, for which the SNR is typically too low to permit assigning a station mb from a single reference channel. These are preliminary results, to be re-evaluated when we have examined a larger number of events.

OBJECTIVE

Our first goal with this project has been to document differences among teleseismic body-wave magnitudes, m_b, published by three different organizations that monitor global seismicity. These are the Prototype International Data Centre (PIDC), the US Geological Survey's National Earthquake Information Center (USGS/NEIC) — which publishes the Preliminary Determination of Epicenters (PDE), and the International Seismological Centre (ISC). Our second goal is to reach a quantitative understanding of at least some of the contributing causes of the observed differences.

RESEARCH ACCOMPLISHED

Introduction

Although seismic magnitudes are intended to be a measure of source strength, it is well known that in practice they are influenced by numerous additional factors such as the particular set of stations reporting individual magnitudes, the instrument responses, and the details of how each station magnitude is assigned.

Because many problems in assigning magnitude can be avoided by use of a set of fixed stations and standardization of measurements, the PIDC m_b has the potential to achieve a more consistent set of short-period magnitudes, as well as one that is more promptly available after an event than magnitudes published by other organizations. It was therefore of concern that when the PIDC began publishing seismic event bulletins daily in January 1995, it was apparent that PIDC body-wave magnitudes (m_b) were systematically lower than PDE m_b values assigned by the USGS. The amount of this discrepancy is approximately 0.4 magnitude units (m.u.), although, as we have shown in Kim *et al.* (2001) and Granville *et al.* (2002), for large magnitude earthquakes the offset is even greater. These two papers, reporting earlier work on this project, were studies of magnitudes assigned for a set of 13 underground nuclear explosions and a set of 10 large earthquakes that all had PDE $m_b \geq 6.4$. The basic methodology was to compare the PIDC values of station m_b (sometimes referred to as the Reviewed Event Bulletin m_b, or REB m_b) with the Veith-Clawson (VC) m_b worked up from the same set of seismograms as those used by the PIDC. We have chosen the latter m_b scale as a reference, because it is a Richter-type m_b that follows a well-defined measurement protocol (Veith and Clawson, 1972), and is based on a specific instrument response — the WWSSN short-period seismometer — that was widely used for twenty years and that enabled the use of short-period magnitudes measured with greater precision than those of previous generations. Our previous work on this project concluded that the PIDC m_b and the VC m_b were in quite good agreement for the nuclear explosions; but that for large earthquakes, they gave significantly different magnitudes, due largely to choice of the time window in which maximum amplitude was measured, and to the differences in frequency band through which the broadband data were passed, prior to assigning these two magnitudes.

The present paper is in two parts. First, we document differences among PIDC, USGS, and ISC m_b values, noting that most previous studies of this general type have emphasized comparisons between just the PIDC and the USGS. The main issue here, is to see whether there is any common ground among these three m_b values, or whether they each have distinctive characteristics. Second, we extend our previous comparisons of PIDC m_b and Veith-Clawson m_b for large events, to a set of 100 earthquakes that all have PDE $m_b = 5.0$. Again we made measurements from the same seismograms (1521 of them) as were analyzed by the PIDC. The main issue in this latter study is whether the significant magnitude differences found for large earthquakes persist for moderate earthquakes.

Comparisons among PIDC, USGS, and ISC values of m_b

For each of the twelve quarters from 1997 to 1999, we have extracted from ISC databases the set of seismic events that were assigned m_b values by all three agencies that routinely publish bulletins of global seismicity — that is, by the PIDC, the USGS, and the ISC. Numbers ranged from a low of 2008 events in the fourth quarter of 1998, to a high of 2883 events in the fourth quarter of 1997. In this brief paper we focus on just the first quarter of 1997, for which there were exactly 2600 events assigned an m_b value by all three agencies.

Figure 1 shows four different ways to compare these magnitudes. As noted in the figure caption, there are significant differences between ISC and NEIC m_b values for magnitudes below about 5. And, these two magnitudes

have different behavior with respect to the PIDC m_b at the lower magnitudes. Presumably the differences here between ISC and NEIC are due to the fact that measurements of ground amplitude *A*, and period *T*, made by the PIDC, are accepted and used by the ISC; but the USGS does not use these measurements. (In making location estimates, the USGS uses arrival times reported by the PIDC for International Monitoring System (IMS) stations. But for *A* and *T* measurements at IMS stations, the USGS either makes the measurements in-house, or in some cases accepts them from station operators.) Figure 1 also shows, in the lower right panel, a tendency for ISC magnitudes to merge with NEIC m_b for the larger events, but to become smaller than NEIC values as magnitude decreases. The question here is how much the ISC values for the smaller magnitude events are dominated by *A* and *T* measurements made by the PIDC. It is a great benefit for the ISC to have information from the PIDC on events at smaller magnitude — detected principally by the IMS array stations — but does the ISC have additional contributed magnitudes at low magnitude? Note that the bottom left panel of Figure 1 appears to show on average about the same offset (between ISC and PIDC) at lower magnitudes, as the offset at higher magnitudes. But all these magnitudes are given to one decimal place, so each point at lower magnitudes can represent many events, and it is not possible to tell from this panel where the centroid of one set of magnitudes lies, corresponding to a constant magnitude on the other scale.

The bottom right panel of Figure 1 shows the cumulative magnitude distribution of the 2600 events, for each scale. This is the number of events greater than a given magnitude. The events have been sorted in descending order separately for each scale, so that a particular order number may be associated with different events on different scales. Nevertheless, since these are the same 2600 events, the comparison in this panel is a useful device to see how the magnitude discrepancy between different scales varies as a function of magnitude. The discrepancy between PIDC and NEIC magnitudes stays approximately constant at about 0.4 m. u. over a range of about 1.5 m.u., becoming larger for the largest five events and smaller for the smallest one thousand events. The ISC magnitude distribution moves between the other two scales, being close to NEIC at large magnitudes so that there is about 0.4 to 0.5 m. u. offset from the PIDC m_b, for the few largest events, with the ISC – PIDC offset diminishing quite steadily at lower magnitudes.

In assessing the degree of dependence of the ISC on the PIDC for reported magnitudes of small events, it should be noted that discussion here is limited only to events for which there are adequate teleseismic detections to permit measurement of *A* and *T* values by all three agencies. The ISC derives a Gutenberg-Richter m_b and the PIDC uses Veith-Clawson distance corrections so the actual station magnitudes will be slightly different for any seismogram used by both the ISC and PIDC. At low magnitude, the ISC reports very large numbers of additional events for which no teleseismic m_b is available.

Figure 2 shows, for each of the PIDC, NEIC and ISC m_b scales, the number of contributing stations as a function of m_b. Although as expected the NEIC and ISC have far more stations than the PIDC at magnitudes greater than about 5, it is still difficult to tell how many stations are contributing at lower magnitudes — though the figure caption attempts to make an estimate. However the differences and dependences between the three agencies become clearer in Figure 3, which shows comparisons similar to those of Figure 1, but using just the number of stations reporting, instead of the magnitude values directly.

It is remarkable in Figure 3, how different the three panels are. The line "$x = y$" is shown (for which the two numbers would be equal). Almost all the points in the two sub-figures on the left (top and bottom) lie to the right of this line, indicating that the ISC almost always uses more stations to determine m_b than does either the NEIC (top left) or the PIDC (bottom left). This is presumably because the ISC uses almost all the NEIC's and PIDC's magnitude readings, and can only add stations in each case. From the bottom left panel, we see from the significant number of points to the right if the "$x = y$" line that indeed the ISC uses significantly more stations for determining m_b than does the PIDC, for almost all events. However, it is also clear that the actual value of the ISC event m_b at low magnitude is likely to be strongly controlled by the PIDC values, whereas the NEIC magnitudes must be quite independent because there is such a lack of correlation (between NEIC and PIDC) on the number of stations used, for the smaller events (see upper right panel).

We have results corresponding to Figures 1, 2, 3 for each of the twelve quarters in 1997 to 1999. As noted in Granville *et al*. (2002), for these years the knowledge of instrument responses at IMS stations had improved enough to avoid some of the earlier problems apparent in certain PIDC station m_b values during 1995 and 1996.

Comparisons between PIDC magnitude and a classical (Veith-Clawson) magnitude

In this project, in seeking to assess m_b values published by the PIDC, we recognize that comparisons with NEIC and ISC values, while interesting, are difficult to interpret at a basic level. The difficulties stem from various changes in the way in which USGS and ISC magnitudes have been assigned over the last ten years, and also by the uses that the USGS and the ISC have themselves made of measurements of ground amplitude *A* and period *T* reported by the PIDC (though the USGS stopped using such measurements in August 1996). As a classical or traditional standard against which to compare the PIDC m_b values, we have instead chosen to use the Veith–Clawson m_b. Specifically we have simulated Worldwide Standard Seismographic Network short-period signals from broadband records and made the Veith-Clawson measurement (Veith and Clawson, 1972). We concentrated at first on some quite large seismic sources in order to avoid the problems of using a few sensitive arrays (which can dominate the characteristics of seismicity bulletins because most events are small and such events are detected mostly by arrays). Our results in these first studies (Granville *et al*., 2002) were based on several hundred simulated WWSSN seismograms (460 for 13 underground nuclear explosions, for which the PIDC called in auxiliary stations as well as primary stations; and 200 for 10 earthquakes, for which the PIDC had no great need for auxiliary station information so most of the data came from primary stations).

Here we present preliminary results from a new study of 100 earthquakes around the world that all had PDE m_b exactly equal to 5.0. We obtained broadband seismograms for all of the 3-component stations used by the PIDC to report station magnitudes for these events, and we also obtained an appropriate single digital channel (the reference channel) for each of the array stations used by the PIDC to assign station magnitudes for these events. This study required the simulation of 1521 WWSSN short-period seismograms, from each of which we made the classical measurements of *A* and *T* and converted to m_b by procedures described by Veith and Clawson (1972). The set of VC stations magnitudes for each event were then averaged arithmetically to obtain the classical VC event m_b. Figure 4 compares the PIDC (REB) event m_b vs. the VC m_b for the 100 events with PDE $m_b = 5.0$. We found that the average PIDC event m_b was 4.49, i.e. about 0.5 m.u. smaller than the PDE m_b value. The average VC m_b was 4.65 and thus closer to the PIDC than the PDE value. Thus, the average discrepancy (VC m_b – PIDC m_b) was 0.16 m.u. This is less than half the VC – PIDC discrepancy for large magnitude (PDE $m_b \geq 6.4$) events studied earlier. The average discrepancy between NEIC and VC was 0.35 m.u., somewhat larger than expected.

The station m_b values, both PIDC (from the REB) and VC, are shown in Figure 5. Again it is clear that in most cases, the VC station m_b exceeds the PIDC station m_b. It is of some interest that the distribution of differences between these m_b values, which has a mean of 0.16 m.u., is not symmetric. This preliminary result is shown in Figure 6. Finally in this section on VC magnitudes, we note a depth effect. For those PDE m_b 5.0 events assigned the default depth of zero in the REB (36 events), the average VC event m_b is 4.8, whereas the VC event m_b for events with a non-zero focal depth is 4.6 (64 events). VC magnitudes are significantly sensitive to event depth, even with measurements made on seismograms with the passband for which this scale was designed.

In order to understand even better how the PIDC procedure for assigning body-wave magnitudes differs from the classical method by which such short-period magnitudes are assigned, we must examine events with various depth ranges separately, to see the influence of attenuation in the upper mantle near subduction zones, and the influence of depth phases.

CONCLUSIONS AND RECOMMENDATIONS

As we near the end of this two-year project, we remain convinced of the potential for PIDC magnitudes (and by extension, IDC magnitudes from Vienna) to provide stable short-period teleseismic body-wave magnitudes. Problems with calibration (instrument responses) of some stations, apparent in the first two years of PIDC operation (only after many months of effort to resolve inconsistencies), are largely solved. And it is clear that PIDC m_b values for small events are having a significant effect on ISC m_b values. However, as shown by our comparisons of PIDC m_b values with the classical Veith-Clawson values obtained from the same seismograms used by the PIDC, it is also clear that the PIDC values depart significantly from the traditional short-period magnitude scales which were developed in the 1960s through the 1980s.

Such a discrepancy has the potential to generate a number of problems, because it fundamentally undercuts the concept of any absolute reference level for a short-period magnitude. (All empirical magnitude scales imply that magnitude zero, or some other fixed magnitude, corresponds to a particular amplitude of ground motion at some fixed distance. This amplitude can be taken as a reference level.) In order to establish continuity with earlier decades in which short-period magnitude scales where developed, and became the basis for numerous quite precise studies that quantified different types of seismic sources, we advocate continued assignment of m_b values by the international monitoring community, using a traditional instrument response. Equally if not more important, we advocate use of a time window for making the measurement of ground amplitude, that is larger than the 5.5-s window used by the PIDC. Such a change would likely reduce significantly the discrepancy between PIDC and other magnitude scales, for events above magnitude 5.

ACKNOWLEDGEMENTS

We appreciate extensive information, comments, encouragement, and advice throughout this project from Jim Dewey and Bruce Presgrave of the USGS/NEIC, and from Ray Willemann of the ISC.

REFERENCES

Granville, J., W.-Y. Kim, and P. Richards (2002), An Assessment of Seismic Body-Wave Magnitudes Published by the Prototype International Data Centre, ms. submitted to *Seismol. Res. Lett.*, 20 pages.

Kim, W.-Y., P. Richards, and J. Granville (2001), Discrepancies Between PIDC, IDC, and USGS Seismic Magnitudes, *Proceedings of the 23rd Seismic Research Review*, Jackson Hole, Wyoming.

Veith, K., and G. Clawson (1972), Magnitude from Short-Period P-Wave Data, *Bull. Seism. Soc. Am.*, **62**, 535-452.

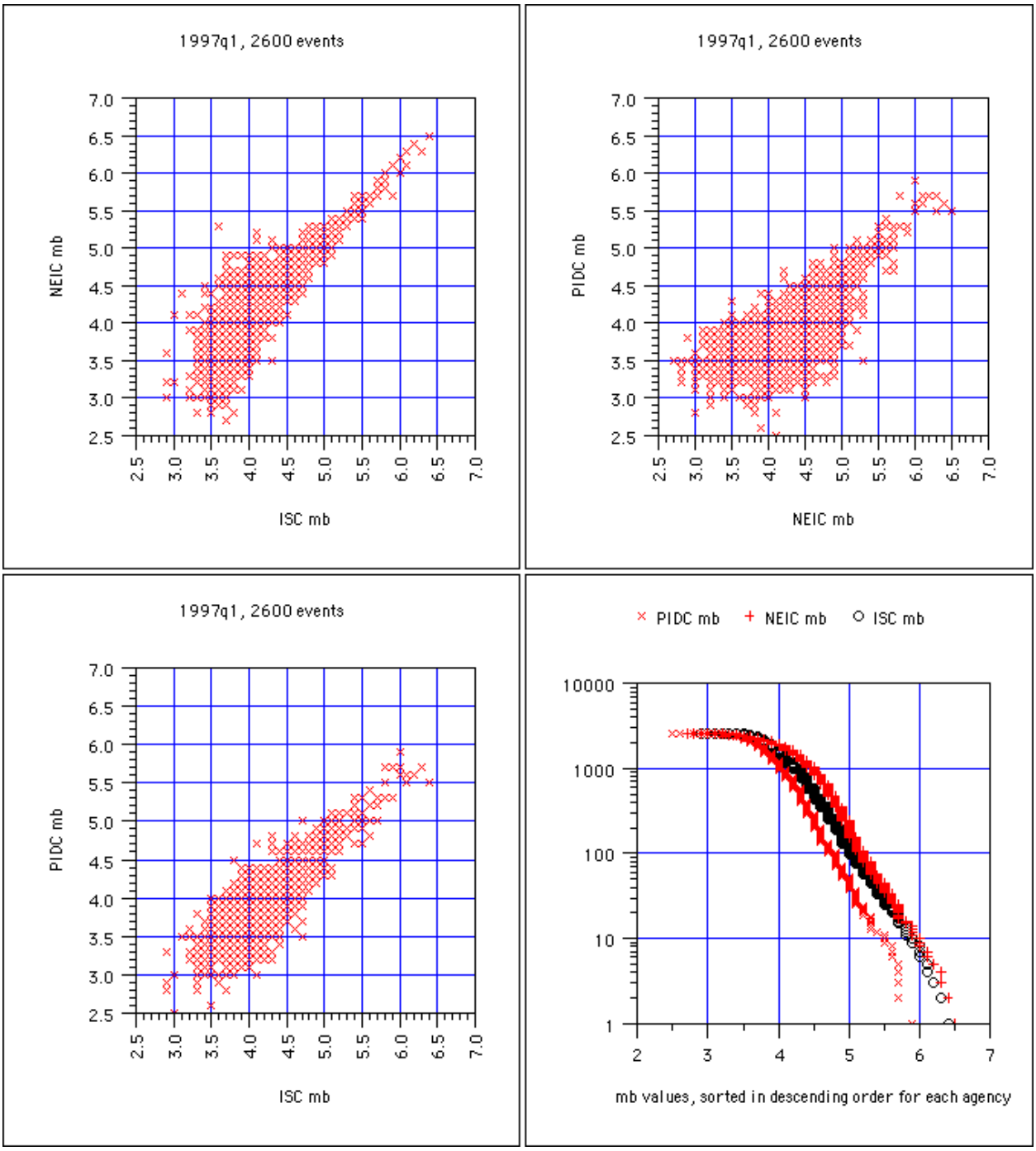

Figure 1. Four different comparisons among m_b values assigned by the PIDC, the NEIC (USGS) and the ISC, for the first quarter of 1997. The top right panel shows the familiar discrepancy, of NEIC values being typically larger than PIDC values, with considerable scatter at low magnitudes. But the upper left panel shows that NEIC and ISC values are quite poorly correlated, at least below magnitude 5. The lower left panel shows a discrepancy between ISC and PIDC, but with much less scatter than is the case between NEIC and ISC. On the bottom right, the 2600 magnitudes from each agency are sorted. Over about 1.5 m.u., there is a constant offset of about 0.4 units between PIDC and NEIC, but the ISC changes from NEIC values at high magnitude, almost to PIDC values at low magnitudes.

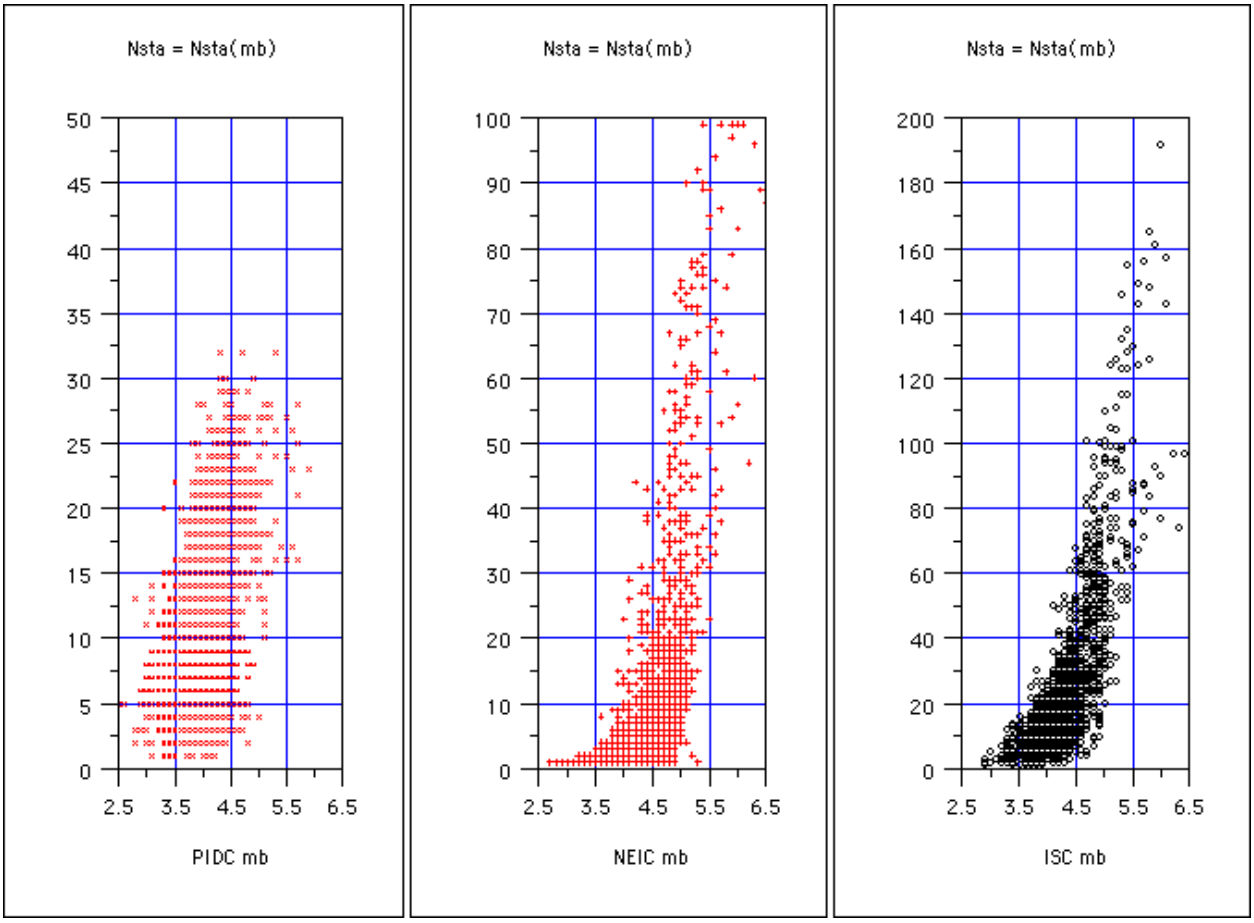

Figure 2. The number of stations contributing station magnitude values is shown for the same time period underlying Figure 1 (first quarter, 1997), and for the same set of 2600 events. Note that the scale for the number of stations doubles from PIDC to NEIC to ISC. The typical magnitude 4 event, as monitored by the USGS, has only about five station magnitudes (though considerably more for a limited number of events). But for the PIDC, as well as the ISC, the typical number is much greater.

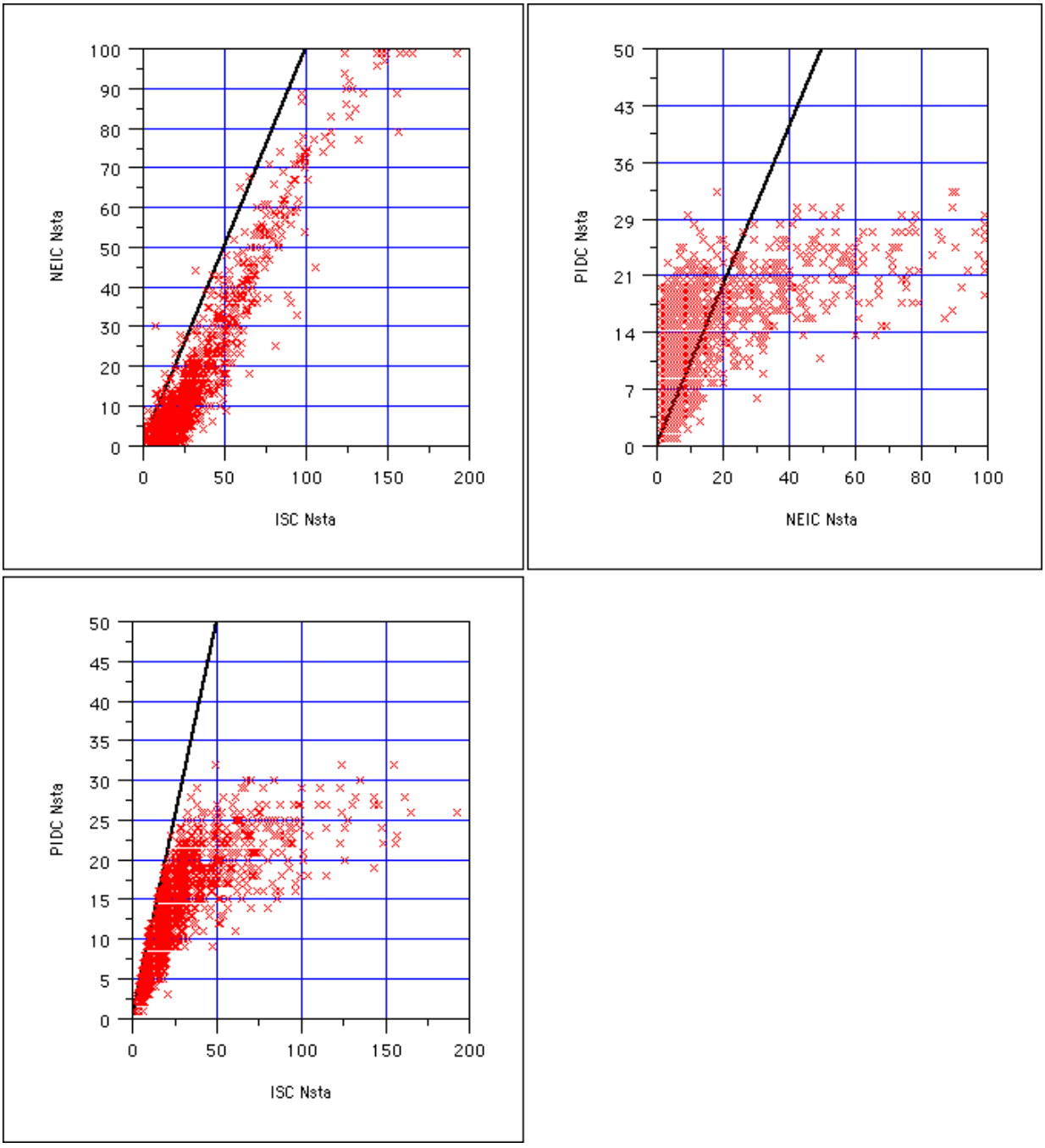

Figure 3. These three sub-figures show comparisons among the number of stations used to assign m_b values, just for the 2600 seismic events during the first quarter of 1997 that have m_b assigned by the PIDC, the USGS/NEIC, and the ISC. The comparisons are quite different in the three different panels. The upper left panel generally shows good correspondence between the number of stations used to assign m_b, by the NEIC and the ISC. The upper right panel shows much lower correspondence, in station numbers used by the PIDC and the NEIC. (Note that the NEIC does not use values of amplitude and period, needed to compute station magnitudes that are measured by the PIDC.) The lower left panel shows remarkably high correspondence between the number of stations used to assign m_b, by the PIDC and the ISC, when the number of stations is quite low. The ISC does use PIDC measurements of amplitude and period, which apparently, according to this sub-figure, typically provide about half the station m_b values used by the ISC at low magnitude.

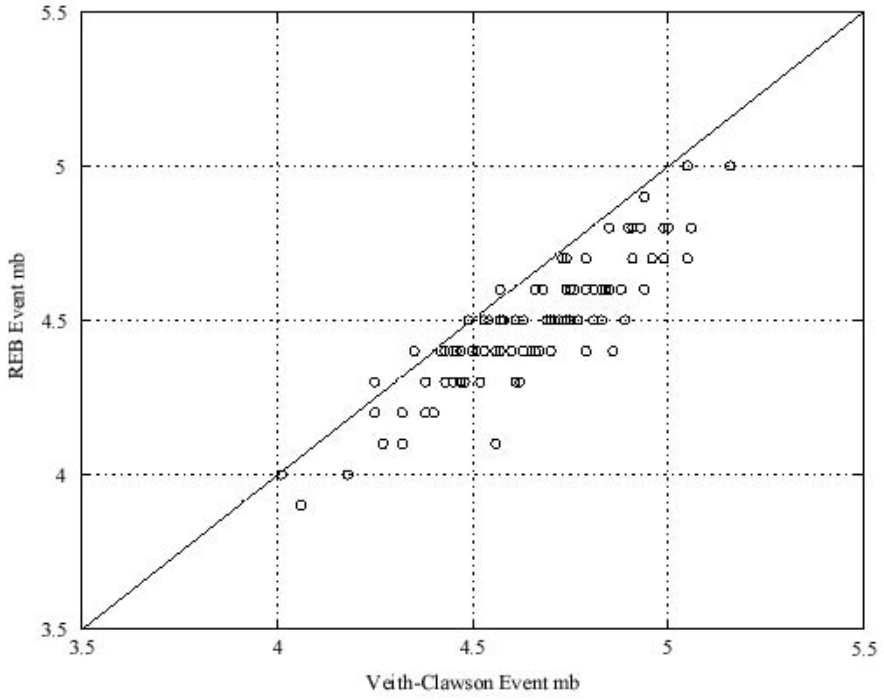

Figure 4. A comparison of mb(REB) against mb(VC), for 100 earthquakes during 1997–1998 that all had mb(PDE) = 5.

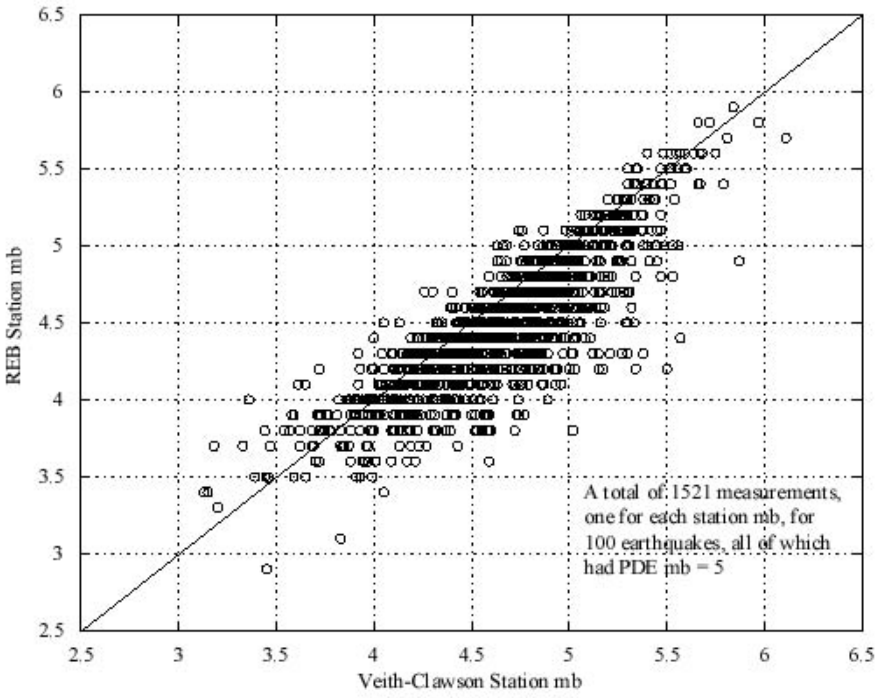

Figure 5. Similar to Figure 4, but now the individual station magnitude values are compared.

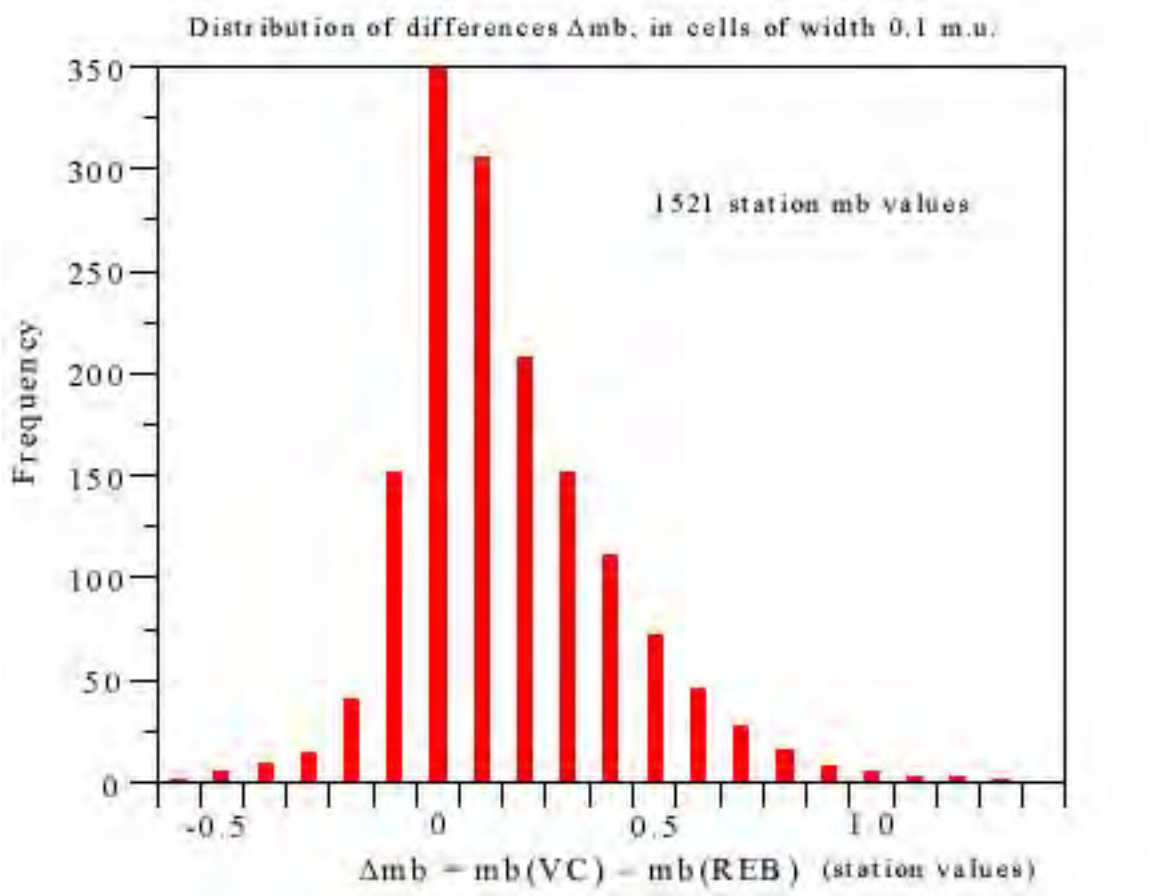

Figure 6. Histogram showing the distribution of differences between Veith–Clawson station mb and the REB station mb, for the individual station observations.

STABLE AND TRANSPORTABLE REGIONAL MAGNITUDES BASED ON CODA-DERIVED MOMENT-RATE SPECTRA

Kevin Mayeda,[1] Tuna Eken,[2] Abraham Hofstetter,[3] Jennifer L. O'Boyle,[1]
Niyazi Turkelli,[2] and William R. Walter[1]

Lawrence Livermore National Laboratory[1]
Kandilli Observatory and Earthquake Research Institute[2]
Geophysical Institute of Israel[3]

Sponsored by National Nuclear Security Administration
Office of Nonproliferation Research and Engineering
Office of Defense Nuclear Proliferation

Contract No. W7405-ENG-48,[1] DE-FC03-01SF22416,[2] and DE-FC03-01SF22417[3]

ABSTRACT

We describe an empirical method of calibrating stable seismic source moment-rate spectra derived from regional coda envelopes using broadband stations. The main goal is to develop a regional magnitude methodology that has the following properties: 1) it is tied to an absolute scale and is thus unbiased and transportable; 2) it can be tied seamlessly to the well-established teleseismic and regional catalogs; 3) it is applicable to small events using a sparse network of regional stations; 4) it is flexible enough to utilize S_n-coda, L_g-coda, or *P*-coda, whichever phase has the best signal-to-noise ratio. The results of this calibration will yield source spectra and derived magnitudes that are more stable than any other direct-phase measure to date. Our empirical procedure accounts for all propagation, site, and *S*-to-coda transfer function effects. The resultant coda-derived moment-rate spectra are then used to provide any traditional band-limited magnitude (e.g., M_L, m_b etc.) as well as an unbiased, unsaturated magnitude (moment magnitude, M_w) that is tied to a physical measure of earthquake size (i.e., seismic moment). We validate our results by comparing our coda-derived moment estimates with those obtained from long-period waveform modeling. In order to demonstrate the usefulness and transportability of our method, we chose the Eastern Mediterranean region as our study area in general, and Turkey and adjacent areas in particular. Most importantly, using those observations of broadband stations in Turkey we demonstrate that the inter-station magnitude scatter is significantly reduced when using the coda-based magnitudes (i.e., M_w(coda) and m_b(coda)). Once calibrated, the coda-derived source spectra provide stable, unbiased magnitude estimates for events that are too small either to be reliably waveform modeled or to be seen at far-regional and teleseismic distances. Using broadband observations of events in the Gulf of Aqaba we found that our source amplitude estimates were nearly insensitive to the source radiation pattern and exhibited roughly a factor of 4 to 5 less inter-station scatter when compared against coda duration and conventional direct-phase measurements (e.g., P_g, L_g).

OBJECTIVE

Magnitude estimation forms an integral part in any seismic monitoring endeavor. For sparse local and regional seismic networks a stable and unbiased magnitude is of utmost importance for establishing accurate seismicity catalogs and assessing seismic hazard potential. In the context of underground nuclear explosion monitoring, magnitudes are used to construct detection threshold curves, differentiate between earthquakes and explosions (e.g., seismic discriminants such as m_b:M_s, m_b:M_o), and estimate nuclear explosion yield. In addition to magnitude, regional short-period discriminants for small-to-moderate sized events using P_n, P_g, S_n, and L_g all suffer from source and path heterogeneity. The coda spectral ratio discriminant, however, which compares high frequencies (f ~ 6 Hz) with low frequencies (f ~ 1 Hz), has been shown to be a more stable discriminant than L_g spectral ratios (Walter *et al*., 1995, Hartse *et al*., 1995). As a consequence of the direct wave variability, multi-station averaging is necessary to reduce the amplitude scatter. If the average station spacing is large (~1500 km), such as the International Monitoring System (IMS) network, the ability to measure a stable magnitude and/or source amplitude for small-to-moderate sized events becomes difficult because of limited number of regional stations over which to average direct-phase variability. Since these events cannot be measured teleseismically we require a stable, regional measure of source size from as little as one station.

The theoretical background of coda generation and empirical observations has been the subject of extensive study during the last four decades (e.g., see a review by Sato and Fehler, 1998). The coda stability stems from a time-domain measurement made simultaneously over a large portion of the seismogram, thereby averaging over the scattered wavefield. Unlike conventional narrowband regional magnitudes, which are relative measurements that often have regional biases (e.g., $m_b(P_g)$, $m_b(P_n)$, $m_b(L_g)$, M_s, M_L, M_d), magnitudes formed from our coda-derived moment-rate spectra are unbiased and not as sensitive to the undesirable effects of source radiation pattern, 3-D path heterogeneity, constructive/destructive interference near the recording site, and phase blockage. Furthermore, unlike teleseismic *P*-based magnitudes, the regional coda-based M_w is absolute and will not suffer from biases introduced by upper mantle variations beneath the source region. These biases can cause source size and explosion yield estimation errors if they are not accounted for properly. The coda methodology can provide a universal and transportable magnitude based on source spectra derived from *P* and/or *S* coda envelopes. These source spectra can be used to estimate a stable single-station M_w from the long-period levels (which by definition is absolute and transportable). Alternatively, we can convolve our source spectra with a short-period instrument response and define a regional or local magnitude, which can be tied to already established local and teleseismic catalogs (e.g., M_L, m_b etc.). For small regions such as the Nevada Test Site (NTS) (see Mayeda, 1993) and aftershock zones we find that a single-station coda magnitude is equivalent to roughly a 16-station network average using direct waves (e.g., $m_b(P_n)$, $m_b(P_g)$ and $m_b(L_g)$). For larger regions (such as earthquakes distributed throughout the western U.S.) the crustal averaging properties of the coda are equivalent to a 64-station network (Mayeda and Walter, 1996). Another important advantage of the method is that we are not restricted to using one type of coda. For example, Mayeda (unpublished) has applied the approach to paths between Novaya Zemlya and Fennoscandia using *P*-codas, and S_n-codas because of L_g blockage.

This study differs in a number of ways from recent coda source studies (e.g., Mayeda, 1993; Hartse *et al*., 1995; Mayeda and Walter, 1996). First, Mayeda (1993) used the simple analytic scattering formulation of Aki (1969) to measure the late L_g coda (measured after twice the L_g travel time) for NTS explosions recorded at Lawrence Livermore Natioanl Laboratory's four regional broadband stations. This approach simply demonstrated that an m_b based on ~1 Hz regional coda envelopes were significantly more stable (factor of 3 to 5) than those based on P_n and L_g. There was no need to incorporate path corrections since all the events came from the small region of NTS. Hartse *et al*. (1995) stacked narrowband envelopes for small local earthquakes in and around the NTS region to construct 'type curves' which could be used to match subsequent events for source amplitude measurements. By assuming that the local coda was homogeneously distributed in the region they did not need to incorporate a distance correction. Both methods were perfectly adequate for these specific monitoring scenarios, but were not applicable to events that were widely distributed. To measure coda-derived source spectra over regional distances, Mayeda and Walter (1996) used a 2-D, distance-dependent multiple scattering model to generate synthetic envelopes for earthquakes distributed throughout the western United States. However, the use of the scattering model did not account for all the path effects and additional 'ad-hoc' path corrections had to be made. The approach described in the current study expands upon the previous studies described above. Our strictly empirical formulation accounts for distance-dependent changes in coda envelope shape, spanning both local and regional distances. In addition, our path corrections are empirically based, without assumption of any scattering model and applicable over a wide

distance range. We use the same approach of Mayeda and Walter (1996) in tying our coda amplitudes to an absolute scale.

RESEARCH ACCOMPLISHED

The first part of this project included refining the coda methodology using broadband data from events along the Dead Sea rift region. We found that our source amplitude estimates were nearly insensitive to the expected source radiation pattern and exhibited roughly a factor of 3 to 5 less inter-station scatter when compared against coda duration and conventional direct-phase measurements (e.g., P_g, L_g). We also found that the coda stability, as measured by the inter-station scatter for common events, reached a minimum value beyond a certain critical measurement window length. For example, at 6-8 Hz, the inter-station standard deviation was less than 0.08 provided the coda measurement was at least ~60 seconds in duration, whereas at 1.5-2.0 Hz the critical window length was 150 seconds. For all frequency bands, as the coda window becomes shorter the standard deviation increases, asymptotically approaching the direct wave scatter. The next phase of our project is still on-going, but has resulted in the collection of over 250 events from the NEIC catalog that were recorded by regional broadband stations ISP, ISK, MALT, and VANB in Turkey, as well as KIV and GNI in neighboring countries to the east (see Figure 1).

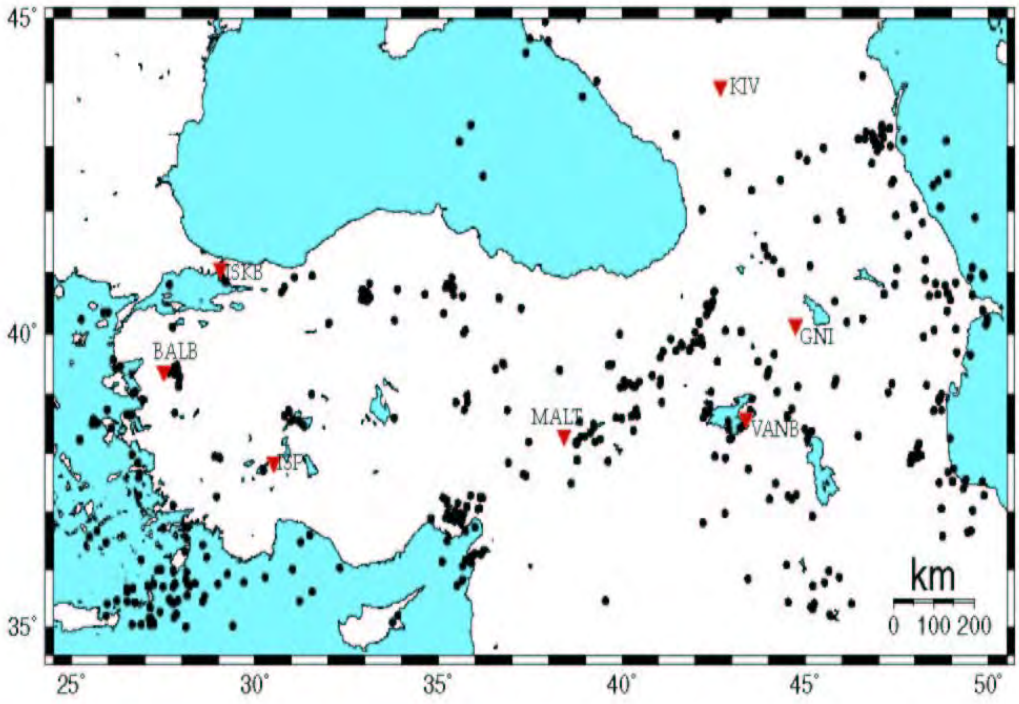

Figure 1. The collection of more than 250 events from the NEIC catalog. These events were recorded by regional broadband stations ISP, ISK, MALT and VANB in Turkey, as well as KIV and GNI in neighboring countries to the East.

Our preliminary results are very encouraging especially since this region is significantly larger and more tectonically complicated than the Dead Sea rift region.

Using common events recorded at two stations separated by roughly 800 km (MALT and ISP), we applied the coda methodology by forming narrowband envelopes using frequencies ranging between 0.02 and 1.0 Hz. We next formed velocity vs. distance curves for each frequency band, then found coda shape parameters as a function of distance. As a first attempt, we applied a grid-search approach to find the distance corrections that minimized the inter-station standard deviation. Figure 2 shows comparisons of distance-corrected coda amplitudes for two frequency bands as well as distance-corrected direct waves for comparison.

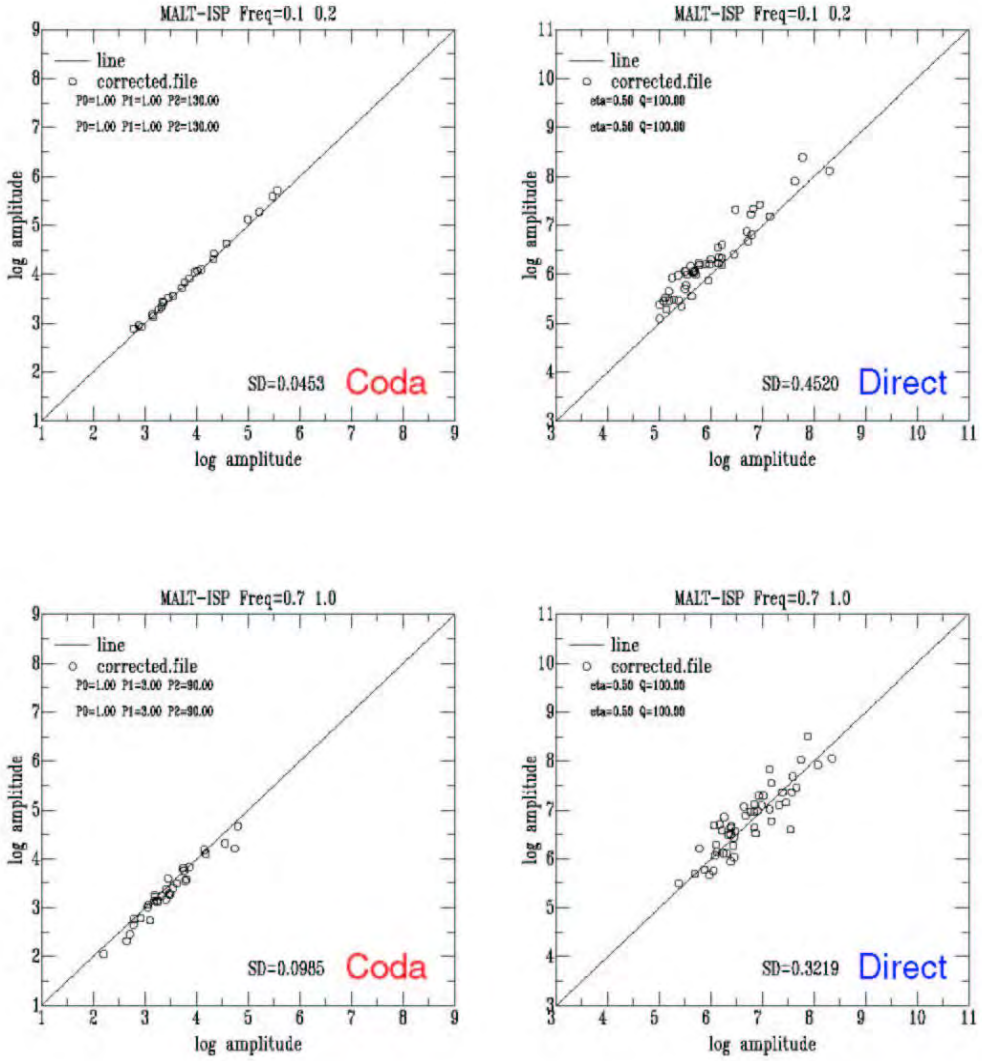

Figure 2. Comparisons of distance-corrected coda amplitudes for two frequency bands, as well as distance-corrected direct waves.

The coda results are surprisingly good for these wavelengths considering the lateral geologic complexity in Turkey. Our next steps will be to compute moment magnitude for selected earthquakes in the region and use them to tie our measurements to an absolute scale. We expect at the higher frequencies the complicated geologic structure may require us to use a 2-D distance correction rather than a simple homogeneous 1-D radially symmetric model.

CONCLUSIONS AND RECOMMENDATIONS

This paper describes an empirical methodology to transform non-dimensional coda amplitudes into stable moment-rate spectra. Once calibrated, the coda-derived spectra can provide unbiased, absolute magnitude estimates for events that are too small either to be waveform modeled or to be seen teleseismically. Our empirical path and site corrections were verified by comparing our seismic moment estimates against independent estimates from long-period waveform modeling. We found that source amplitude estimates were virtually insensitive to the source radiation pattern and exhibited roughly a factor of 3 to 5 less inter-station scatter when compared against conventional direct-phase measurements (e.g., P_g, L_g) as well as coda duration. We are now applying the same approach to the broader, more complicated region of Turkey.

REFERENCES

Aki, K., (1969). Analysis of the seismic coda of local earthquakes as scattered waves, *J. Geophys. Res*. **74**, 615-631.

Hartse, H. E., W. S. Phillips, M. C. Fehler, and L. S. House (1995). Single-station spectral discrimination using coda waves, *Bull. Seism. Soc. Am*. **85**, 1464-1474.

Mayeda, K. (1993). $m_b(L_g\text{Coda})$: A stable single station estimator of magnitude, *Bull. Seis. Soc. Amer*. **83**, 851-861.

Mayeda, K. and W. R. Walter (1996). Moment, energy, stress drop, and source spectra of western United States earthquakes from regional coda envelopes, *J. Geophys. Res*. **101**, 11195-11208.

Sato, H. and Fehler, M. (1998). Seismic wave propagation and scattering in the heterogeneous earth, AIP Press, Modern Acoustics and Signal Processing.

Walter, W. R., K. M. Mayeda, and H. J. Patton (1995). Phase and spectral ratio discrimination between NTS earthquakes and explosions. Part I: Empirical observations, *Bull. Seis. Soc. Am.* **85**, 1050-1067.

IMPROVED FOCAL DEPTH DETERMINATION FOR USE IN NUCLEAR-EXPLOSION MONITORING

John R. Murphy,[1] Brian W. Barker,[1] and William L. Rodi[2]

Science Applications International Corporation[1] and Massachusetts Institute of Technology[2]

Sponsored by Defense Threat Reduction Agency

Contract No. DTRA01-01-C-0056

ABSTRACT

Seismic event location remains as one of the important discriminants for separating natural tectonic and explosive events. However, in order to be useful for discrimination purposes, the uncertainties associated with seismic locations must be well defined, and this has proven to be difficult to accomplish to the required degree of accuracy. In particular, high-confidence estimation of focal depths remains as an outstanding monitoring problem. Over the past several years, we have been pursuing a research program that is directed toward the development of improved detection and identification procedures for the depth phases pP and sP, as well as formulation of a new algorithm for computing more reliable confidence intervals on focal depth estimates determined from P-wave first arrival times. With regard to depth phase identification, we have investigated the utility of a fully automatic network stacking algorithm that maps the International Data Centre (IDC) post-P detection times at a station into candidate depth phases using the pP - P and sP - P delay times predicted by the IASPEI-91 travel-time tables for that epicentral distance and then combines the individual station results as a function of candidate source depth. This automatic algorithm has now been applied to data from about 150 Reviewed Event Bulletin (REB) events in the Hindu Kush and in the Hokkaido and central Honshu regions of Japan, as well as the region surrounding the Chinese Lop Nor test site. Prominent candidate pP and sP peaks have been identified in the resulting network detection stacks for a majority of these events, including some with mb values as low as 3.7 and depths as shallow as 20 km.

This algorithm has now been implemented in a software module that interacts directly with the standard IDC analyst review station (ARS) and is currently being delivered to the RDSS at the Center for Monitoring Research (CMR) for full-scale evaluation and testing. We have also begun to investigate the applicability of calibrated regional S - P arrival-time information to the estimation of independent event origin times for use as constraints in the hypocenter location process. Although the detailed nature of the trade-off between focal depth and origin time can be complex in practical applications to small events for which few data of limited azimuthal distribution may be available, an ability to independently constrain origin time can often lead to significantly improved focal depth estimates. In particular, differences between origin times determined from regional S - P times and the corresponding origin times determined from standard hypocenter location codes with focal depths constrained to zero can be used to infer focal depth bounds that are useful for event screening purposes. For this reason, we have been collecting regional seismic data recorded at selected International Monitoring System stations from samples of earthquakes with well determined focal depths located in the Hindu Kush and in the Hokkaido and central Honshu regions of Japan and are developing calibrated S - P travel-time relations for use in the determination of independent origin times. Preliminary results suggest that this approach can consistently identify, with a high degree of confidence, subcrustal events as being too deep to be explosions.

OBJECTIVES

The objectives of this research program are to determine more reliable estimates of the uncertainties associated with the different focal depth estimation procedures and to increase the number of events that can be identified as earthquakes on the basis of focal depth through the implementation of new and improved analysis tools. This is being accomplished through the development of improved procedures for identifying and using the teleseismic depth phases pP and sP, the incorporation of regional S-P based origin time constraints into an improved depth estimation algorithm, and the development of more robust statistical hypothesis tests for use in event screening. This effort includes the implementation and large-scale testing of these new algorithms on the Research and Development Support System (RDSS) at the CMR.

RESEARCH ACCOMPLISHED

During this initial year of the contract, the effort has focused on the continuation of the development of improved tools for the detection and identification of the depth phases pP and sP and on the preliminary evaluation of the use of calibrated regional S-P time intervals to constrain event origin times for use in focal depth determination. With regard to depth phase identification, we have been attempting to improve the frequency and reliability of the identification of the depth phases pP and sP through the use of network beam forming (Murphy *et al*, 2000). In our approach, post-P arrivals observed at each station for a given event are mapped from functions of delay times with respect to P to functions of source depth using the pP-P and sP-P delay times predicted by the IASPEI-91 travel-time tables for the various station distances. These functions of depth for all the stations in the detecting network are then added together to identify arrivals consistent with the predicted depth phase move-outs over the entire range of potential source depths. That is, the observed delay times of all post-P arrivals with respect to P are translated into equivalent focal depths under the hypothesis that they are either pP or sP arrivals. Those arrivals that are consistent with such hypotheses should then show up as peaks on a stacked network depth function. In the present application, difficulties associated with the variability of observed short-period signals between widely separated stations are avoided by stacking unit amplitude boxcar functions centered on the post-P detection times, which are automatically determined at each station by front end signal processing procedures. One advantage of this approach is that not only is it fully automatic, but it includes only signals that have triggered a detection, which should help to minimize the inclusion of questionable arrivals in the analysis. Figure 1 shows an example of the application of this algorithm to the automatic post-P detection times for the Hindu Kush earthquake of 1998/02/14. It can be seen that the network detection stack in this case shows a pronounced peak at a depth corresponding to the published REB depth for this event, indicating the presence of a good candidate pP phase that should be further reviewed by the analyst. This automatic algorithm has now been applied to data from over 200 REB events located in the Hindu Kush, Lop Nor, Hokkaido and central Honshu regions identified on the map of Figure 2. Prominent candidate pP and sP peaks have been identified in the resulting network detection stacks for a majority of these events, including some with mb values as low as 3.7 and depths as shallow as 20 km, indicating that this algorithm can provide the analyst with information useful for the confident identification of additional pP and sP phases.

In order to make this depth phase stacking procedure available for large-scale testing and further evaluation on the RDSS at the CMR, the algorithm described above has now been formally integrated into the Analyst Review Station (ARS) software employed at the IDC and US NDC. In this implementation, the analyst initiates a fully automatic process from the ARS that causes all of the post-P detection times for the current event to be recovered from the automatic detection files and passed to the depth phase stacking module, where they are converted into their corresponding depth traces, stacked, and presented back to the analyst in an X-Window display. This interactive interface to ARS is illustrated in Figure 3, which shows the pP, sP, and pP + sP depth phase stacks for the Lop Nor region earthquake of 1999/01/27. Note that the sum of the pP and sP stacks shows a pronounced candidate depth phase peak near the published REB depth of about 18 km for this earthquake. In this implementation, by clicking on this or any other candidate peak with the mouse, the analyst initiates a process by which the corresponding waveforms are brought up in the standard ARS display with the data time aligned on the predicted pP times corresponding to the selected trial depth. These data can then be further processed using the bandpass filter routine or any of the other signal processing algorithms available in the ARS. A sample of the resulting ARS display for this selected Lop Nor region earthquake is shown in Figure 4, where it can be seen that there are multiple candidate pP and sP arrivals at the arrival times predicted for that selected trial depth. Moreover, in this case the strong variation of the pP/P amplitude ratios over wide ranges in distance and azimuth permit the analyst to identify pP and sP arrivals with high confidence, thereby enabling this event to be confidently screened out as a natural earthquake.

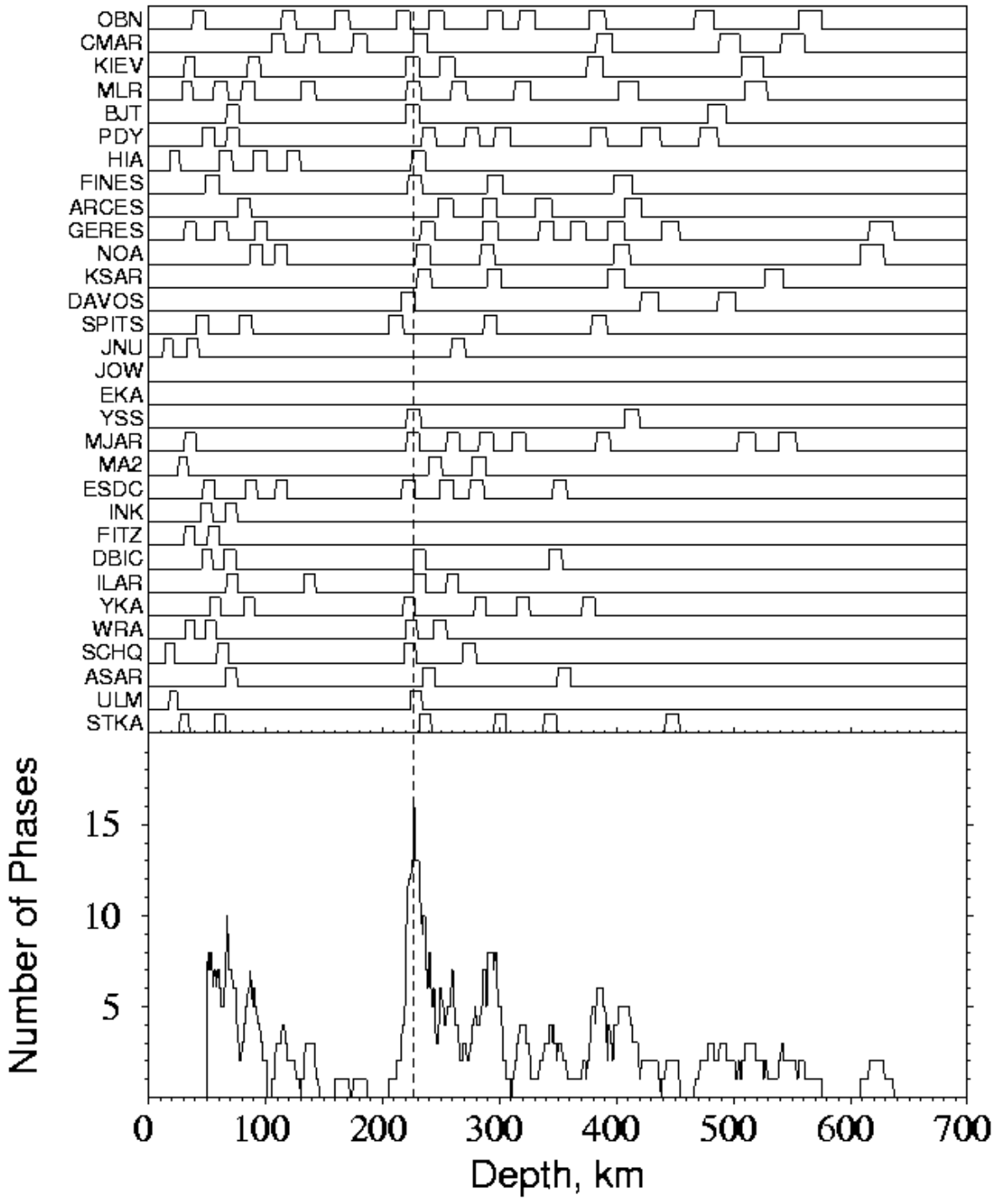

Figure 1. Network detection stack of pP for the Hindu Kush earthquake of 1998/02/14, m_b = 5.03. The dashed vertical line coincides with the REB depth estimate of 226 km.

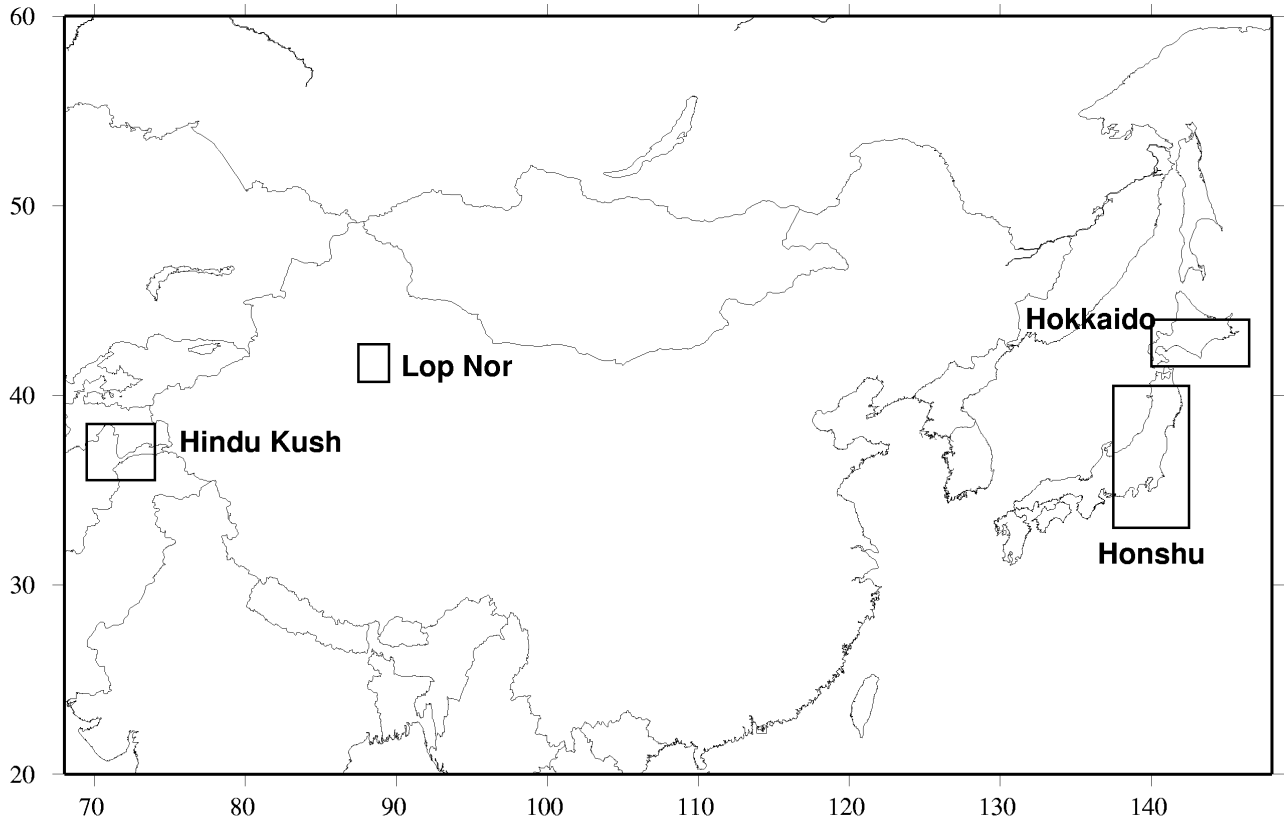

Figure 2. Map locations of the events in the Hindu Kush, Lop Nor, Hokkaido and central Honshu regions used in the evaluation of the depth phase stacking algorithm.

The utility of this RDSS implementation is currently being further tested in analyst review of data recorded from a large sample of Lop Nor region events.

We have also begun to investigate the applicability of calibrated regional S-P arrival time information to the estimation of independent event origin times for use as constraints in the hypocenter location process. It is well known that there exists a trade-off between focal depth and event origin time in the hypocenter location problem. Although the detailed nature of this trade-off can be complex in practical applications to small events for which few data of limited azimuthal distribution may be available, an ability to independently constrain the event origin time can nonetheless lead to significantly improved focal depth estimates. More specifically, if S-P differential time information is available from well-calibrated regional stations, it can be used to provide useful, independent estimates of the event origin time for use as constraints in the hypocenter location process. That is, if t_0 is the event origin time and t_P and t_S are the observed arrival times of P and S waves that have traveled essentially the same path to a station at distance Δ from the event, it follows that:

$$\begin{aligned} t_P &= t_0 + T_P(\Delta, h) \\ t_S &= t_0 + T_S(\Delta, h) \end{aligned} \qquad (1)$$

where h denotes the focal depth and T_P, T_S are the travel-time functions for P and S arrivals as a function of epicentral distance and focal depth. It follows that we can relate the origin time to the observed S-P time interval as

$$t_P - t_0 = \frac{1}{\left[\frac{T_S(\Delta,h)}{T_P(\Delta,h)} - 1\right]}(t_S - t_P) \qquad (2)$$

or

$$t_0 = t_P - \frac{1}{\left[\frac{T_S(\Delta,h)}{T_P(\Delta,h)} - 1\right]}(t_S - t_P) \qquad (3)$$

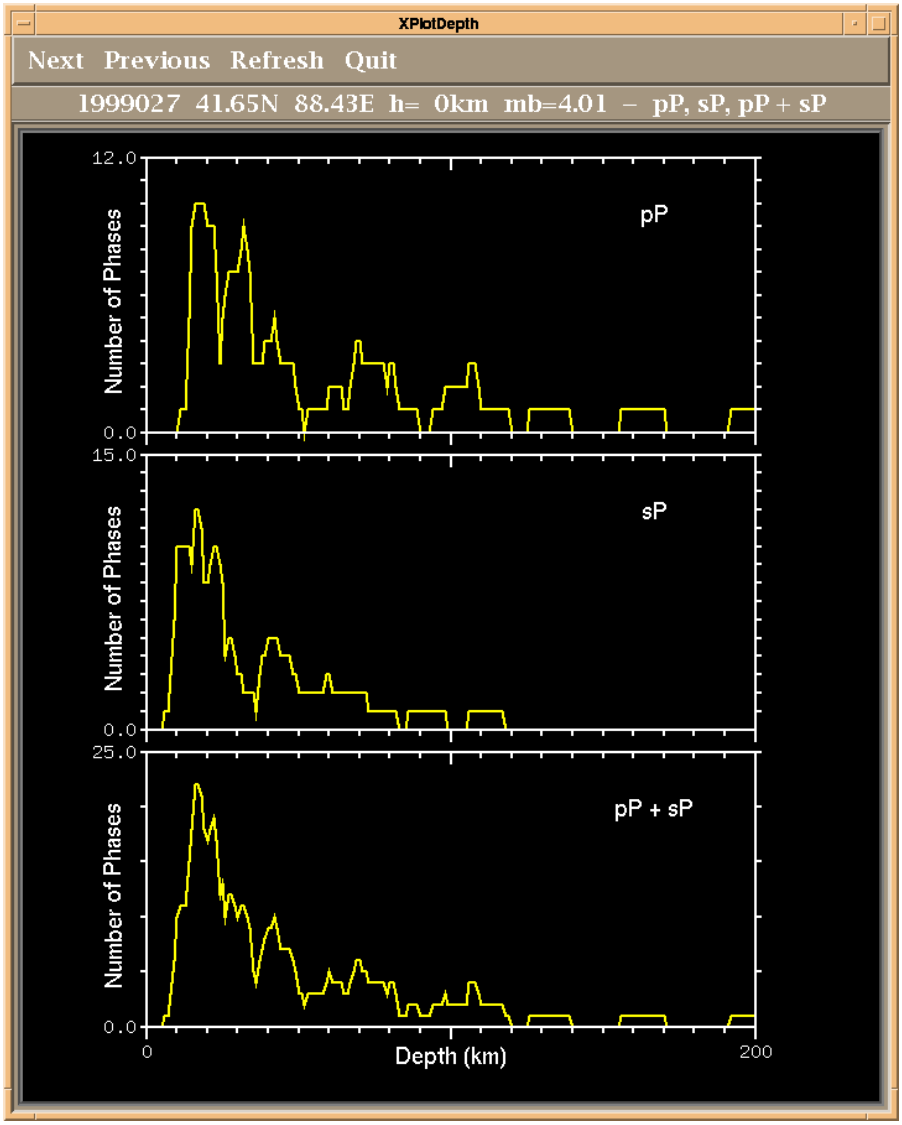

Figure 3. Network detection stacks of pP (top), sP(middle) and their sum (bottom) for the Lop Nor region earthquake of 1999/01/27.

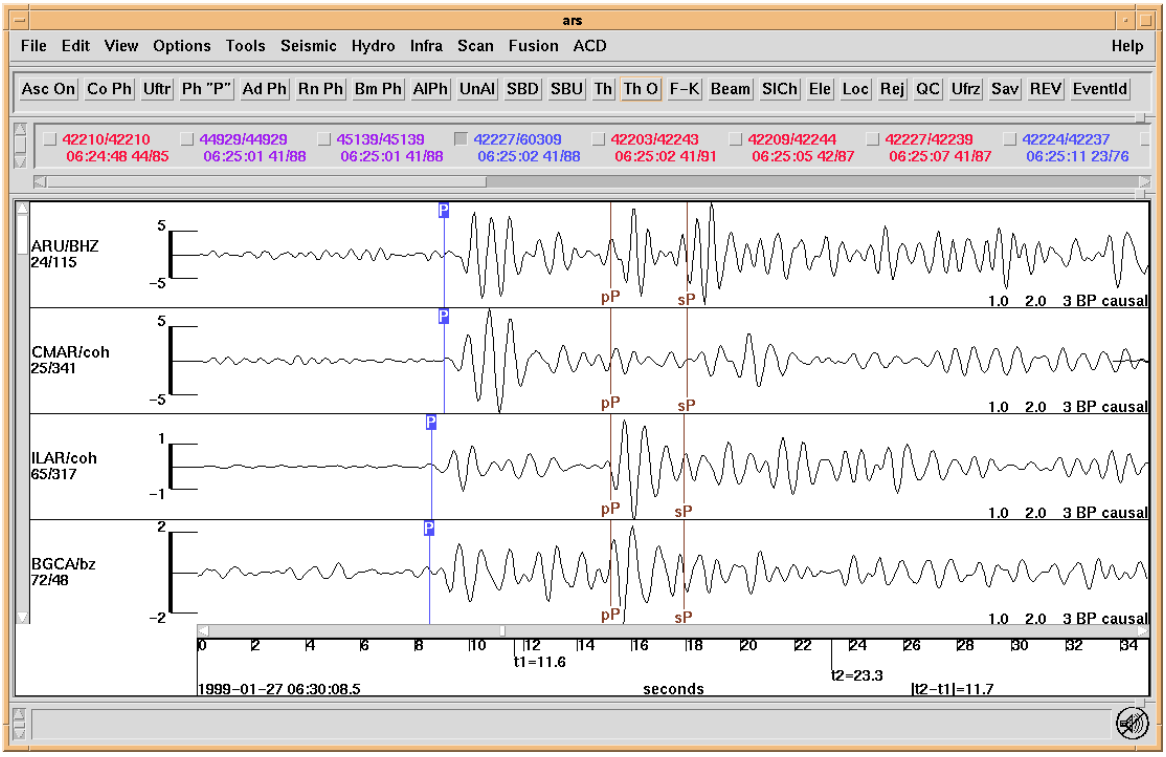

Figure 4. ARS Display of bandpass filtered waveforms for the Lop Nor region earthquake of 1999/01/27, shown time aligned on the predicted pP arrival times corresponding to the selected candidate depth (i.e. 18 km) from Figure 3.

Now, if the travel paths for the observed P and S arrivals are the same and the ratio of compressional (α) to shear (β) wave velocity along these paths is constant, independent of Δ and h, then (3) can be simplified to

$$t_0 \;=\; t_P - \frac{1}{\left[\frac{\alpha}{\beta} - 1\right]}\left(t_S - t_P\right) \qquad (4)$$

which is the relation originally proposed by Wadati some 75 years ago. It follows that if the average ratio α/β along paths to a selected regional station from events in a specified source region can be determined, then the event origin time can be estimated from observed P and S arrival times. Our focal depth hypothesis test is formulated by comparing this S-P-based origin time estimate, t_0(S-P), with the corresponding teleseismic-based origin time, $\tilde{t}_0\ (h = 0\ \text{km})$, determined with the depth constrained to zero. Substantial differences in these two estimates provide evidence of significant focal depth. In particular, since from the IASPEI-91 tables $\tilde{t}_0\ (h = 10\ \text{km}) - \tilde{t}_0\ (h = 0\ \text{km}) \approx$ 1.5 seconds and the measured variability of $t_0\ (\text{S} - \text{P}) - \tilde{t}_0\ (h = 0\ \text{km})$ for well-located events recorded at calibrated regional stations is on the order of ± 3.5 seconds, we have assumed for preliminary analysis purposes that differences of $t_0\ (\text{S} - \text{P}) - \tilde{t}_0\ (h = 0\ \text{km})$ greater than about 5 seconds provide high confidence that the event depth is greater than 10 km and, consequently, that the event can be confidently screened out as a natural earthquake source.

We are currently evaluating this hypothesis test using regional data recorded from events in the four source regions of Figure 2 for which the event depths have been well constrained by validated depth phase observations. For this application, P and S arrival times were determined at selected regional stations for well located events and the

resulting $t_P - t_0$ and $t_S - t_P$ time intervals were used to evaluate the calibration constant in equation (2), where t_0 denotes the origin time from the well constrained hypocenter solution. Origin times for events recorded at each calibrated station were then estimated from observed $t_S - t_P$ intervals and compared with corresponding constrained teleseismic origin time estimates, $\tilde{t}_0\,(h = 0 \text{ km})$, to test for significant focal depth. This process is illustrated for a sample of Honshu events recorded at station MJAR in Figure 5, where the determination of the calibration constant (left) and its application in a focal depth hypothesis test (right) are shown. It can be seen that, in this case, almost all the events with validated focal depths of greater than 50 km can be screened out as being too deep to be explosions with high confidence. The dashed line in the right-hand panel of this figure denotes the value of $\tilde{t}_0\,(h) - \tilde{t}_0\,(h = 0 \text{ km})$ predicted as a function of focal depth by the teleseismic IASPEI-91 travel-time values, and it can be seen that the observed data show some systematic deviations from this relation that may indicate variations in the regional station calibration constant as a function of epicentral distance and focal depth that will need to be further evaluated. In any case, this hypothesis test clearly shows promise for applications to event screening on the basis of focal depth.

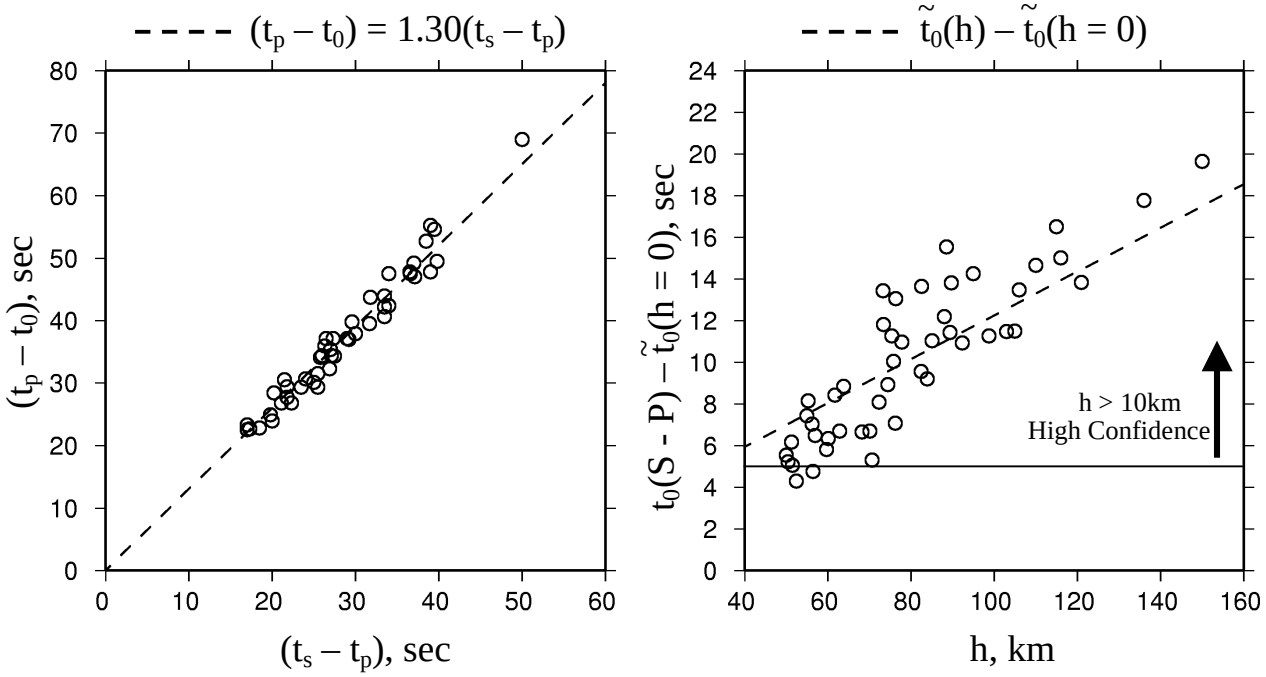

Figure 5. Application of the S-P origin time hypothesis test to data recorded at regional station MJAR from selected Honshu earthquakes. The left panel illustrates the estimation of the regional station calibration constant, while the right panel shows the results of the hypothesis test as a function of focal depth for a sample of well-located events.

CONCLUSIONS AND RECOMMENDATIONS

The first year of a three-year research investigation directed toward the development of improved focal depth estimates for use in event screening has now been completed. A principal result of this investigation has been the formulation and testing of an automated procedure for stacking raw P wave detection data to identify candidate pP and sP depth phases for further review by the analyst. This algorithm has now been formally integrated into the Analyst Review Station (ARS) software employed at the IDC and US NDC and delivered to the RDSS at the CMR for further evaluation and large-scale testing. Work was also initiated on the formulation of a depth hypothesis test based on the application of calibrated regional S-P time intervals to constrain event origin time. Preliminary

applications of this test to selected well located events in the Hindu Kush and Honshu source regions have indicated that it shows promise for use in event screening.

REFERENCE

Murphy, J. R., R. W. Cook, and W. L. Rodi (2000), Improved Focal Depth Determination for Use in Seismic Monitoring of Underground Nuclear Explosions, *Maxwell Technologies Final Report* MSD-DFR-00-16621.

REGIONAL MAGNITUDE STUDIES IN CHINA AND SURROUNDING AREAS

W. Scott Phillips, Howard J. Patton, Claudia Aprea, Hans E. Hartse, and Steven R. Taylor

Los Alamos National Laboratory

Sponsored by National Nuclear Security Administration
Office of Nonproliferation Research and Engineering
Office of Defense Nuclear Nonproliferation

Contract No. W-7405-ENG-36

ABSTRACT

Magnitude research at Los Alamos National Laboratory is focused on improving the transportability of mb(LgCoda) and mb(Lg) through the application of advanced calibration methods and better characterization of scaling relationships with respect to yield or a surrogate, such as mb(P). In addition, we are investigating the scaling behavior between regional magnitudes, motivated by the constraint that mb(LgCoda) should transition into mb(Lg) at small magnitudes as signal-to-noise limitations restrict the use of coda waves.

We investigate the use of regional coda for magnitude determination because scattered coda waves smooth over path effects and provide redundant, thus precise, measurements that can be tied to moment, magnitude or yield following calibration. In heterogeneous regions, such as China and central Asia, however, we find that path averaging is not complete and regionally varying corrections must be applied. We do this using tomographic imaging techniques, applied to amplitude differences in order to eliminate unknown source effects. Tomography gives RMS log10 amplitude residuals of 0.06-0.08 for coda and 0.10-0.14 for direct Lg in bands near 1 Hz. Results correlate well with regional geology, while coda images are smoother than those of direct Lg due to partial path averaging. After applying corrections that flatten earthquake spectra below estimated corners and shift results to match waveform modeled estimates of moment, we obtain precise moment rate spectra for earthquakes and apparent source spectra for explosions that include coupling and near source path effects. The regional calibration enables comparing spectra from widely spaced sources and results can be tied to estimates of magnitude and yield for monitoring purposes.

After regional corrections are applied and magnitudes computed, we investigate scaling relationships for explosions with plots of regional magnitude versus mb(P). Since material coupling variations should be common for all seismic radiation, regional and teleseismic, P and S waves alike, comparisons of the relationships between test sites can also be used to investigate differences in energy partitioning. The energy partitioning for the Nevada Test Site (NTS) is particularly anomalous on plots of mb(P) versus mb(Lg) for 1 Hz compared to nuclear tests in central Asia. Indeed, the anomaly is so great that it must be caused mainly by mis-calibration of Lg Q for NTS explosions. This is consistent with independent results that suggest that Nuttli (1986) and Patton (1988) under-estimated the Lg Q using the method of Herrmann (1980).

For explosions, regional magnitudes, mb(LgCoda) and mb(Lg), need not scale 1-to-1 with mb(P) due to effects of a near-source transfer function that converts the initial compressional wavefield into S waves making up Lg and coda waves. We show evidence for variability in the scaling with mb(P) for different test sites and even for different areas within test sites. But there is no consensus that the variations are significant, and some questions arise whether the results are consistent for mb(LgCoda) and for mb(Lg). This raises questions about the generation mechanisms of Lg and coda waves by explosions, which many argue should be tightly linked. We are investigating the issue of a common source for Lg and coda waves through the development of scaling relationships between mb(LgCoda) and mb(Lg).

OBJECTIVE

We calibrate regional phase amplitudes, both direct and coda, to understand source effects and to determine magnitude and yield. Our objective is to develop a transportable methodology that can be used to characterize small events over broad areas.

RESEARCH ACCOMPLISHED--CODA

We calibrated coda amplitudes for 26 stations and their surrogates in China and central Asia (Figure 1). These data include Borovoye explosion records obtained from the Lamont-Doherty Earth Observatory (LDEO) (Kim *et al*., 2001). Of the available Borovoye data, we used short-period (1.5-s) records from the KS (gain 4500, 164 events, 1974-), KSM (gain 1000, 38 events, 1985-) and KSVM (gain 50, 45 events, 1984-) instruments (Kim and Ekstrom, 1996). We manually repaired glitches in these records and marked saturated or otherwise poor data sections to avoid in later processing. Except for saturated and noisy intervals, envelopes from these records matched well between instruments and with BRVK envelopes in the few cases where common events could be found.

Following the regional coda methods of Mayeda (1993), we obtained coda amplitudes by fitting distance-calibrated peak amplitude and coda shape curves in a series of narrow bands, 0.03 – 8 Hz. Path corrections were then obtained using tomographic images based on coda amplitude differences for events recorded at multiple stations. We assumed isotropic source radiation to perform the tomography, with the advantage that source-scaling effects are removed by taking differences. The path corrections give precise relative amplitudes within each band, residual RMS 0.06-0.08 log10 units, covering the entire study area. Relative levels between bands were adjusted by inverting for corrections that flatten earthquake spectra below estimated corners, based on mb (Taylor and Hartse, 1998). This step was carried out using an L1 simplex method. Finally, the absolute spectral level was determined to match scalar moments from waveform modeling for a small number of events (Figure 1). The resulting scatter between coda and waveform moments was 0.18 Nm.

Our calibration strategy using earthquake data has corrected for deep path effects but cannot be expected to account for near-source effects such as coupling, Rg to Lg conversion, or shallow path effects on explosion data. Earthquake moment rate spectra are expected to be accurately characterized; however, because near source effects remain in the explosion results, we term these "apparent source spectra."

Apparent source spectra results show low levels of scatter for explosions recorded at multiple stations (Figure 2). This scatter has been minimized during tomographic inversion. Central Asia explosions show a marked peaked behavior that scales with size, as can be seen in the results from Degelen Mountain (Figure 3). Note that the Omega series, 100-T chemical shots continue this behavior. The peaks are similar to behavior observed at NTS, but occur in higher bands, which will cause transportability problems between these areas.

RESEARCH ACCOMPLISHED --Lg

Calibration of amplitude decay corrections is critical for the determination of regional magnitudes. A great deal of effort has been expended developing Q tomography for regional phases in central Asia. The results for areas that LANL is working on are relatively mature for Lg and coda waves, and we are reasonably sure that determinations of mb(Lg) and mb(LgCoda) have path effects removed to first order. This is an important milestone as we move ahead with studies of the scaling of regional magnitudes with respect to yield and teleseismic mb for explosions detonated in a variety of testing environments.

Coupling variations, as we know from experience at NTS, can introduce significant variations into magnitude-log yield relationships. In an absolute sense, coupling variations pose a major challenge for yield estimation. For our studies of transportability, we would like to mitigate the effects of coupling so that other transportability issues can be studied. These issues include: (1) whether or not 1-Hz mb(Lg) and mb(LgCoda) based mainly on shear-wave energy scale 1:1 with mb(P), (2) quantifying regional effects on mb(P) determinations, as well as (3) testing regional amplitude corrections for other areas of the world where nuclear explosions have been tested.

One way to mitigate the effects of coupling variations for explosions detonated in a variety of media is to plot magnitude versus magnitude. This is because the coupling efficiency is largely uniform for the entire elastic

wavefield, regional and teleseismic, P and S waves alike. For example, gas porosity of the emplacement media has virtually the same effect on teleseismic mb as it has on regional mb(Lg) for NTS explosions (e.g., Patton, 1988).

In our studies of regional mb(Lg) scaling with teleseismic mb, we have been careful to use as often as possible maximum-likelihood estimates of mb(P) to avoid problems with censoring bias at small magnitudes.

The graph in Figure 4 shows a summary of observations for explosions detonated at NTS and at test sites in central Asia (Balapan, Degelen, and Lop Nor; see figure caption for details). A line mb(Lg) = mb(P) is shown for reference. The population of NTS explosions as a whole is large enough to say unequivocally that mb(Lg) and mb(P) do not scale 1-to-1. There are scaling variations (not shown) between test areas at NTS. At this stage in our work, the numbers are too few to say anything definitive about non-unity scaling for explosions at test sites in central Asia. We are currently working on measuring mb(Lg) and mb(LgCoda) for a larger number of Soviet peaceful nuclear explosions (PNEs) and Semipalatinsk explosions to add to this plot.

Offsets between explosion populations detonated at different test sites are of interest in light of possible regional effects on teleseismic mb. This is referred to as test site bias, which has been attributed to upper mantle attenuation effects. There are no discernable offsets between central Asia explosions detonated at Balapan, Degelen, and Lop Nor. On the other hand, the offset between NTS and central Asia is large. Test biases were estimated for NTS, Balapan, and Degelen by Nuttli in the 1980s, but his estimates do not agree with the results in Figure 4. Independent of Nuttli's results, numerous studies using different methods have consistently shown that a regional magnitude bias is pervasive for areas of the western United States, and its effect is to reduce the mb(P) by about 0.3-0.4 mu. It is notable that correcting teleseismic mb of NTS explosions upward by 0.4 mu falls far short of closing the gap between NTS and central Asia populations in Figure 4.

Given our confidence in the path calibrations for Lg Q used to determine mb(Lg) for central Asia, the remaining offset must reflect either real differences in the energy partitioning between P and S waves for NTS explosions compared to three test sites in central Asia with uniform results, or a problem with the Lg path calibration for western United States. Recent evidence suggests a problem with the path calibration for western United States.

CONCLUSIONS AND RECOMMENDATIONS

Apparent source spectra of central Asia explosions have been estimated using coda techniques. These spectra feature peaks that scale with size and could result from overshoot in the time function of explosions or from Rg-to-Lg scattering in the source region. The peaks occur in higher bands than does similar behavior at NTS, which makes transportability of a single-band amplitude-magnitude formula difficult between all test sites. Other, multi-band formulae could show more transportable behavior. Otherwise better characterization and correction for the spectral peaks will be necessary.

It appears that Lg Q was underestimated by Nuttli (1986) and Patton (1988) using the coda-wave frequency dispersion method of Herrmann (1980). At the 2001 23rd Seismic Research Review, we presented results for central Asian explosions where Nuttli's magnitudes were found to be systematically large compared to mb(Lg) values determined from stations much closer to the source. As is the case for NTS, the Lg Q determined from coda-wave dispersion on paths to Scandinavian stations was underestimated. New estimates of Lg Q based on coda amplitude decay for NTS explosions are significantly larger compared to the Q determined by Nuttli and Patton. We are using the new Lg Q values to re-calibrate NTS.

ACKNOWLEDGMENTS

We are grateful to W.-Y. Kim, P.G. Richards and colleagues at LDEO for providing Borovoye data for this study.

REFERENCES

Herrmann, R. B. (1980) Q estimates using the coda of local earthquakes, *Bull. Seismol. Soc. Am*., **70**, 447-468.

Kim, W.-Y., P. G. Richards, V. Adushkin, and V. Ovtchinnikov (2001). Borovoye digital seismogram archive for underground nuclear tests during 1966-1996, Data report on the web at http://www.ldeo.columbia.edu/datarep/index.hmtl Borovoye Archive for UNT Information Product."

Kim, W.-Y. and G. Ekstrom (1996), Instrument responses of digital seismographs at Borovoye, Kazakhstan by inversion of transient calibration pulses, *Bull. Seism. Soc. Am*., **86**, 191-203.

Mayeda, K.M., mb(LgCoda): A stable single station estimator of magnitude, *Bull. Seism. Soc. Am*., **83**, 851-861.

Nuttli, O. W. (1986). Yield estimates of Nevada Test Site explosions obtained from seismic Lg waves, *J. Geophys. Res*., **91**, 2137-2151.

Patton, H. J. (1988). Application of Nuttli's method to estimate yield of Nevada Test Site explosions recorded on Lawrence Livermore National Laboratory's Digital Seismic System, *Bull. Seism. Soc. Am*., **78**, 1759-1772.

Taylor, S.R. and H.E. Hartse (1998), A procedure for estimation of source and propagation amplitude corrections for regional seismic discriminants, *J. Geophys. Res*., **103**, 2781-2789.

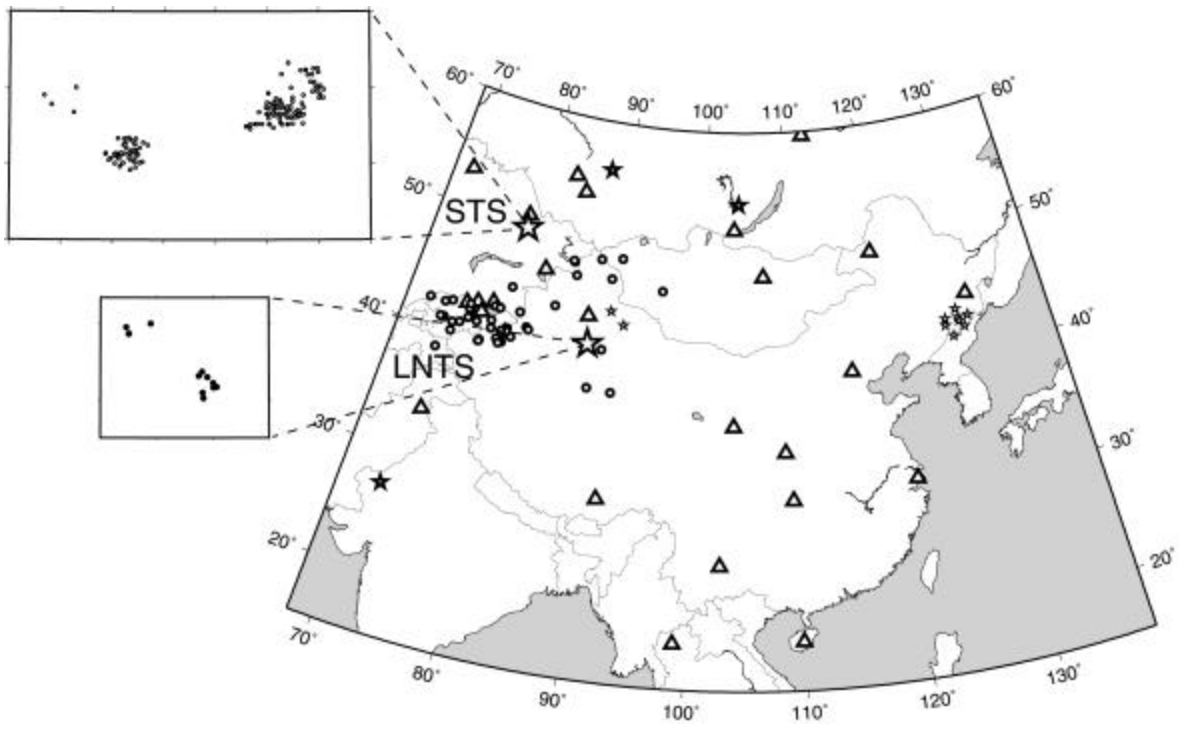

Figure 1. Stations and explosions used in the coda study. A 26-station network is shown (triangles); many stations include surrogates from multiple deployments. Test sites and isolated nuclear and single-shot chemical explosions are shown by stars, with insets giving event distributions at Semipalatinsk and Lop Nor. Earthquakes for which independently determined moments are available and were used to set absolute spectral levels are shown by circles.

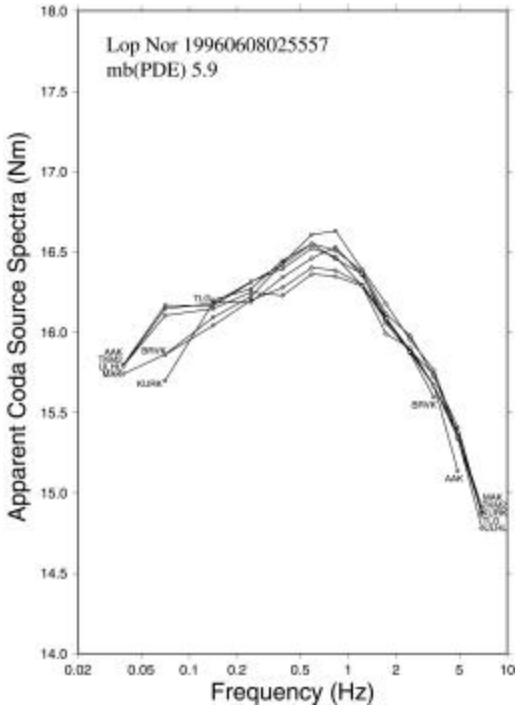

Figure 2. Apparent source spectra determined using coda wave data from seven stations, for a Lop Nor test. Stations are indicated at spectra endpoints. The inter-station consistency is especially good for bands above 1 Hz.

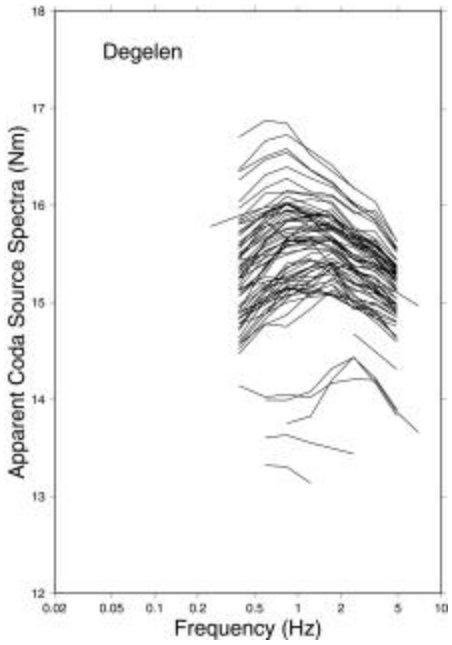

Figure 3. Apparent source spectra from coda for Degelen Mountain. events, including Omega series, 100T chemical explosions.

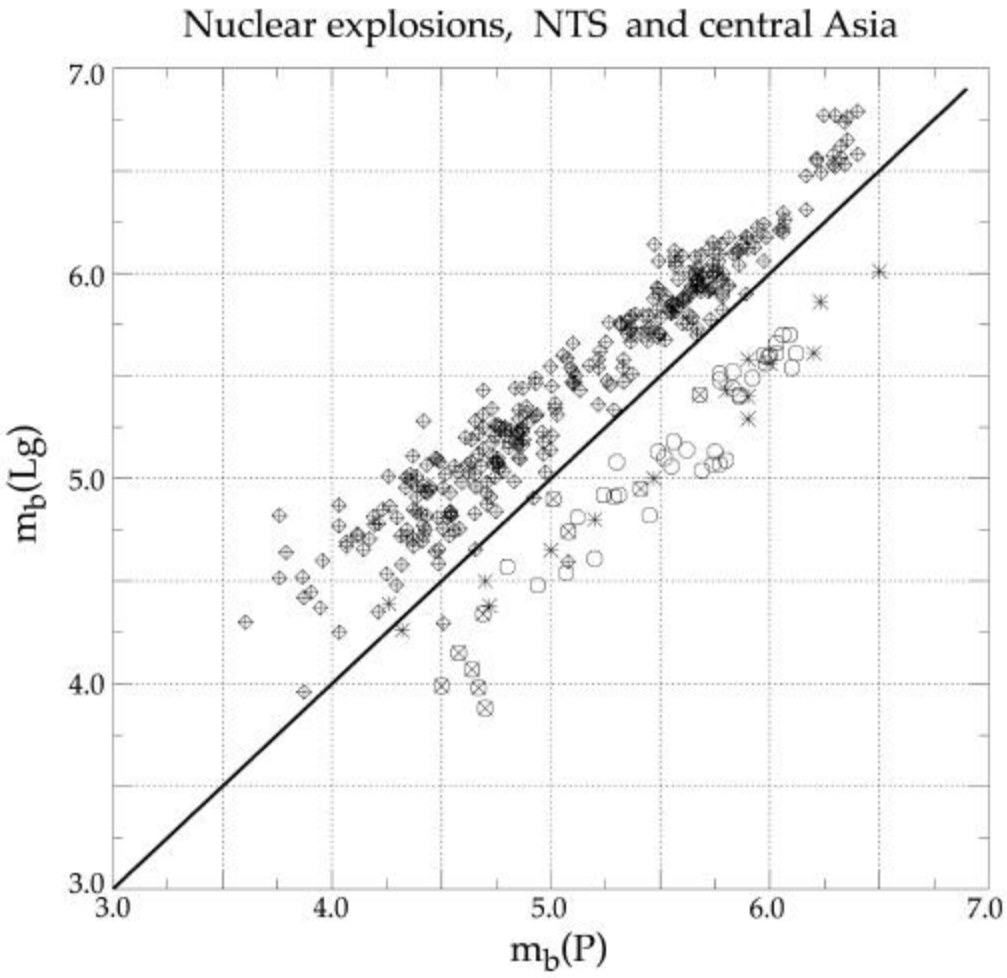

Figure 4. Measurements of mb(Lg) and teleseismic mb for over 325 nuclear explosions at the Nevada Test Site (grey diamonds) and at test sites in central Asia. Thirty-seven explosions at Balapan are plotted as open circles, 10 Degelen explosions as x's enclosed by circles, and 15 Lop Nor explosions as asterisks. All mb(P) values for NTS explosions are AWE (Atomic Weapons Establishment, Blacknest; Marshall and Lilwall, pers. comm.) determinations using maximum likelihood methods. A majority of the mb (P) measurements for central Asia explosions are also AWE determinations, although there are several Degelen shots for which mb(Pn) was substituted and about half of the mb(P) for Lop Nor shots are from the International Seismological Centre (ISC) catalog. mb(Lg) values for NTS explosions are from the work of Nuttli (1986) and Patton(1988), while mb(Lg) for central Asian explosions were determined in this study using waveform data from the Borovoye digital archive (Kim *et al*, 2001), and from stations AAK, MAK, NIL and WMQ.

TRANSFER FUNCTIONS AND SESIMIC DISCRIMINATION

Marie D. Renwald,[1] Terry C. Wallace,[1] and Steven R. Taylor[2]
University of Arizona,[1] Los Alamos National Laboratory[2]

Sponsored by National Nuclear Security Administration
Office of Nonproliferation Research and Engineering
Office of Defense Nuclear Nonproliferation

Contract No. DE-FG03-01SF22482[1] and W-7405-ENG-36[2]

ABSTRACT

Nuclear explosion monitoring requires both the detection and the identification of underground explosions. Although fundamental source physics can predict the basic character of a seismic recording from an explosion, experience indicates that discrimination between explosions and earthquakes is highly station centric. This is particularly true for recordings at regional distances where propagation and station site effects associated with a complex crustal waveguide can overprint source signature. As new stations are installed in official monitoring networks, the lack of recording history can dramatically affect confidence in discrimination. Though some monitoring stations have established recording histories, a significant portion has never recorded a nuclear explosion. To address this problem, we are investigating procedures to "map" the recording history of a station that has had a long period of operation onto a newly installed station. Our goal is to develop a transfer function to predict the recording at a given seismic station from the actual recording at a nearby station.

To accomplish this, we have used a data set consisting of waveforms from nuclear explosions detonated at the Lop Nor test site in western China as well as earthquakes within a 100-km radius of that site. The waveforms were recorded at the ten-station Kyrgyz [KNET] array located in Kyrgyzstan approximately 1100 km from Lop Nor. The data span from 1992 through 1999 and contain six known explosions and nine earthquakes. The KNET stations are all very broadband (STS-2 seismometers), and have station separations ranging from 30 km to 250 km. The KNET stations are located in a variety of geologic environments, making the assembled data set a good test bed for investigating both the variability of spectral measurements as well as the scale lengths for predicting station-to-station correlations.

OBJECTIVE

Seismic discrimination requires calibration. This is especially true at regional distances where the seismic wavefield has very strong signatures of the travel path, and empirical evidence suggests that even small variation in source-to-station paths can cause unexpected changes in energy partitioning between Pn, Pg, Sn, S and Lg. Although the general characteristics of seismic discriminants, such as high-frequency P-to-S amplitude ratios, can be used to qualitatively identify explosions, only a database with ground truth explosions will allow quantitative and statistical assessment of identification capabilities. However, many of the IMS and other monitoring stations have never recorded a nuclear event at regional distances. For this reason we are using *historical* recordings of nuclear explosions at stations near the locations of present monitoring seismic stations to devise a methodology to predict discrimination.

The basic problem of discrimination is to clearly determine whether an unknown seismic waveform was generated by an explosion or an earthquake. Various discriminants, such as the Pn/Lg show variability from event to event: in other words, the discriminants do not define a point but rather a population. Discrimination then becomes a problem of separating populations of measurements associated with explosions and earthquakes. For regional spectral discriminants there is no single measurement that separates populations for all regions, even after corrections for propagation and size (for example MDAC, or magnitude-distance amplitude corrections); thus, regional discrimination is largely an empirical technique in which spectral ratios from ground truth events are used to statistically assess the source character of an unknown event. If no ground truth events exist for nuclear explosions, then some technique must be used to simulate the expected seismic waveforms. This requires at least three transfer or filter functions: (1) a source excitation function that accounts for the explosion spectral effects, (2) a propagation filter that accounts for the effects of crustal and mantle structure on the partitioning of seismic energy as well as focusing and attenuation effects, and (3) a site response. There are several ways to develop these transfer functions or filters. Our objective in this research project is to develop techniques for transfer functions, and to develop understanding of transportability of regional discriminants.

RESEARCH ACCOMPLISHED

We have explored the possibility of generating transfer functions using ratios for various spectral bands for known events. The basic problem can be analyzed using the frequency-domain model for seismic-wave generation and propagation. Consider the observed amplitude spectrum between a given source, *i*, and receiver, *j*, to be given by:

$$A_{ij}(\omega) = S_i(\omega)E_{ij}(\omega)P_j(\omega) \tag{1}$$

where S is the source-excitation spectrum, E is the Earth response, and P is the site response. Letting $i = X,Q$ for explosion, earthquake, respectively and $j = S,O$ for surrogate and operational station, respectively, we can write three equations representing the data that will be available for calibrating a new station

$$\begin{aligned} A_{QS}(\omega) &= S_Q(\omega)E_{QS}(\omega)P_S(\omega) \\ A_{QO}(\omega) &= S_Q(\omega)E_{QO}(\omega)P_O(\omega) \\ A_{XS}(\omega) &= S_X(\omega)E_{XS}(\omega)P_S(\omega) \end{aligned} \tag{2}$$

and we wish to predict what the explosion spectra will look like at the operational station

$$A_{XO}(\omega) = S_X(\omega)E_{XO}(\omega)P_O(\omega) \tag{3}$$

For a common source (assume a well-recorded earthquake for this example) recorded at both S and O, we wish to predict the explosion characteristics at O. We note that it is necessary for the calibration earthquake to be in the vicinity of the region being monitored (*how close* is one of the questions we will consider in this study). Computing a spectral ratio for the calibration earthquake recorded at S and O (using equation 2)

$$\frac{A_{QO}(\omega)}{A_{QS}(\omega)} = \frac{E_{QO}(\omega)P_O(\omega)}{E_{QS}(\omega)P_S(\omega)} = T_Q(\omega) \tag{4}$$

so

$$A_{QO}(\omega) = T_Q(\omega)A_{QS}(\omega) \tag{5}$$

Similarly,

$$\frac{A_{XO}(\omega)}{A_{XS}(\omega)} = \frac{E_{XO}(\omega)P_O(\omega)}{E_{XS}(\omega)P_S(\omega)} = T_X(\omega) \tag{6}$$

and

$$A_{XO}(\omega) = T_X(\omega)A_{XS}(\omega) \tag{7}$$

Noting that we do not actually have $A_{XO}(\omega)$, we wish to study if we can predict it from

$$A_{XO}(\omega) = T_Q(\omega)A_{XS}(\omega) \tag{8}$$

The fundamental question that we wish to answer in this study is whether equation (8) is applicable to the problem of predicting explosion characteristics at a newly operational seismic station and, if so, what are the associated limitations and errors. This is equivalent to asking "is $T_X(\omega) = T_Q(\omega)$?". From equations (4) and (6) we have

$$\frac{E_{XO}(\omega)P_O(\omega)}{E_{XS}(\omega)P_S(\omega)} = \frac{E_{QO}(\omega)P_O(\omega)}{E_{QS}(\omega)P_S(\omega)} \tag{9}$$

Thus, we are assuming

$$\frac{E_{XO}(\omega)}{E_{XS}(\omega)} \approx \frac{E_{QO}(\omega)}{E_{QS}(\omega)} \tag{10}$$

Obviously, there are potentially many limitations to this assumption. Examples include depth effects (i.e. depth *Q* > depth *X*), source-mechanism effects, and differences in location. Keeping in mind that discriminants are typically computed by taking logarithms of spectral ratios, some of these effects may be reduced by analyzing a number of calibration events.

We have developed a test bed to examine the nature of the transfer functions. The test data consist of waveforms from nuclear explosions detonated at the Lop Nor test site in western China as well as earthquakes within a 100-km radius. The waveforms were recorded at the ten-station Kyrgyz [KNET] array located in Kyrgyzstan approximately 1100 km from Lop Nor. The data span from 1992 through 1999 and contains six known explosions and nine earthquakes. The KNET stations are all very broadband (STS-2 seismometers), and have station separations ranging from 30 km to 250 km. The KNET stations are located in a variety of geologic environments, making the assembled data set a good test bed for investigating both the variability of spectral measurements as well as the scale lengths for predicting station-to-station correlations. The data are presented in Table 1.

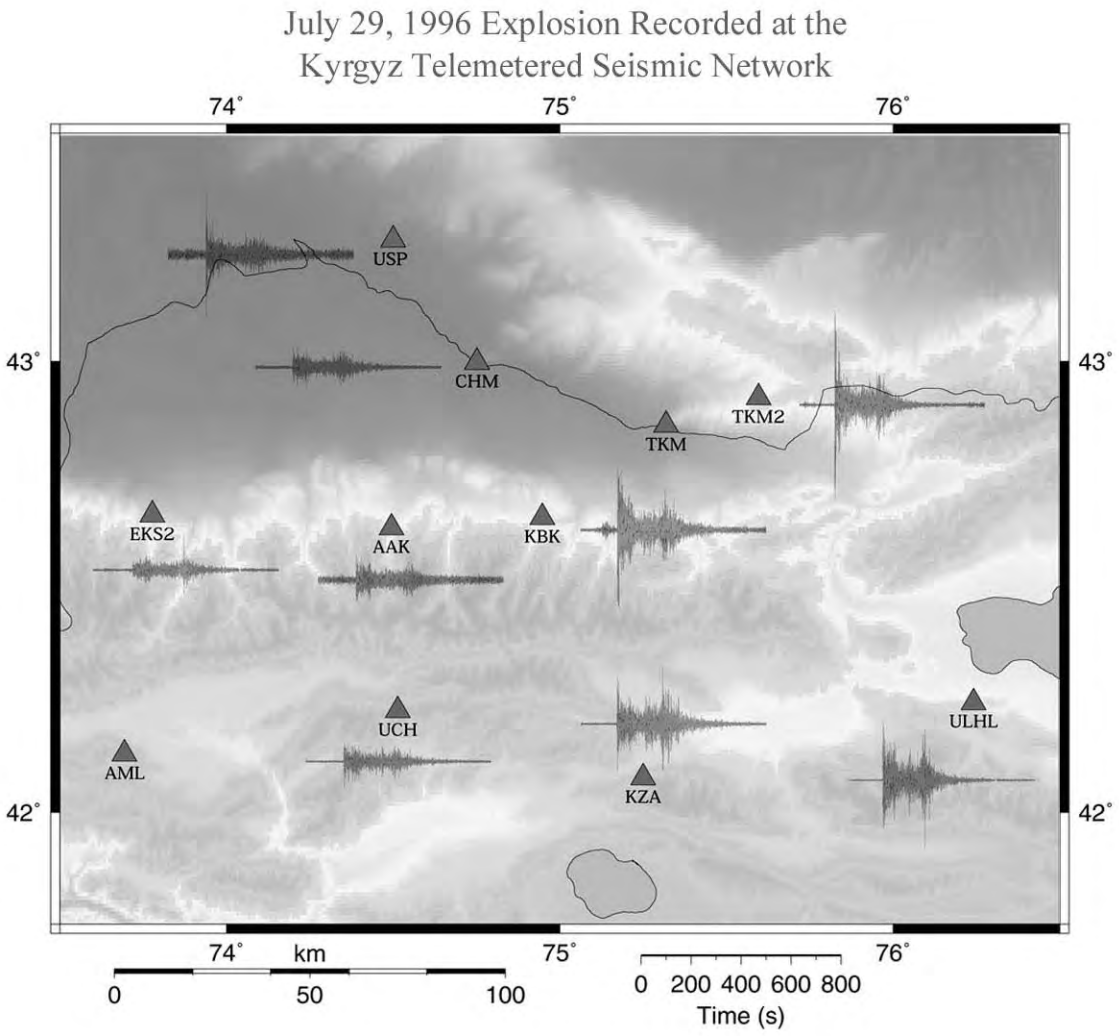

Figure 1: Waveform variability across KNET for the Lop Nor explosion of July 29,1996. Waveforms are on the same amplitude scale, and approximately 800 seconds of record are shown.

Figure 1 shows the waveforms from the former People's Republic of China (PRC) underground test on July 29, 1996; there is a remarkable change in waveform character across KNET. Stations east of KBK (and including KBK) have very large relative P wave amplitudes, whereas those to the west have smaller absolute amplitudes, and the P to S (or Lg) energy dramatically decreases. There is no surface geology that might explain this variation, although the trend is repeated for all Lop Nor explosions.

The challenge posed by what is shown in Figure 1 is basic to developing transfer functions.

- How does the transfer function developed for earthquakes distort the spectral signatures for explosions?
- Over what range of distances can sources be distributed and still yield reliable transfer spectra? A complementary question is
- Over what scale lengths can transfer functions be applied?

As a first test of a transfer function procedure, we have used measurements of various spectral discriminates made at KBK to "predict" the behavior of the discriminants at other stations. A value of the ratio pair for KBK – Station (where station is any of the KNET stations) for a calibration explosion is used to calculate an expected value of the spectral discriminant for all other explosions recorded. Figure 2 shows the results for four different spectral discriminants.

Table 1: Data used in the transfer function analysis. *EX* =explosion, *EQ*=earthquake. The x denotes whether the event was recorded by a given station.

Event ▼ Station ►	AAK	AML	CHM	EKS2	KBK	KZA	TKM	TKM2	UCH	ULHL	USP
1992-05-21 *EX*	x		x	x							
1993-10-05 *EX*	x	x	x	x	x		x				
1994-10-07 *EX*		x	x	x	x	x			x	x	x
1994-12-26 *EQ*	x			x				x		x	
1995-08-02 *EQ*	x			x	x	x		x		x	x
1995-08-17 *EX*			x	x	x	x		x		x	x
1996-03-20 *EQ*	x		x	x	x	x		x	x	x	x
1996-05-10 *EQ*	x				x	x		x			x
1996-06-08 *EX*	x		x		x				x		x
1996-07-29 *EX*	x		x	x	x	x		x	x	x	x
1999-01-27 *EQ*	x	x		x	x	x		x	x	x	x
1999-01-30 *EQ*	x	x	x	x	x	x		x	x	x	x
1999-05-01 *EQ*	x	x		x	x	x		x	x	x	x
1999-05-17 *EQ*	x	x		x	x	x		x	x	x	x
1999-10-18 *EQ*	x	x	x		x	x		x	x	x	x

CONCLUSIONS AND RECOMMENDATIONS

Preliminary tests on transporting spectral discriminants from a station being used for calibration to nearby stations show that simple procedures work even when stations are separated by more than 100 km. Further, although the signature of receiver geology and topography on the individual waveforms appears to be significant, the repeatability of the spectral ratios is robust. At present we have only tested explosion-to-explosion transfer functions, and the next step is to develop the statistical population of earthquake-to-earthquake transfer functions. Finally, we will explore the cross-source transfer functions (explosion-to-earthquakes).

ACKNOWLEDGEMENTS

The data were supplied by the Incorporated Research Institutes in Seismology (IRIS) Data Management Center (DMC).

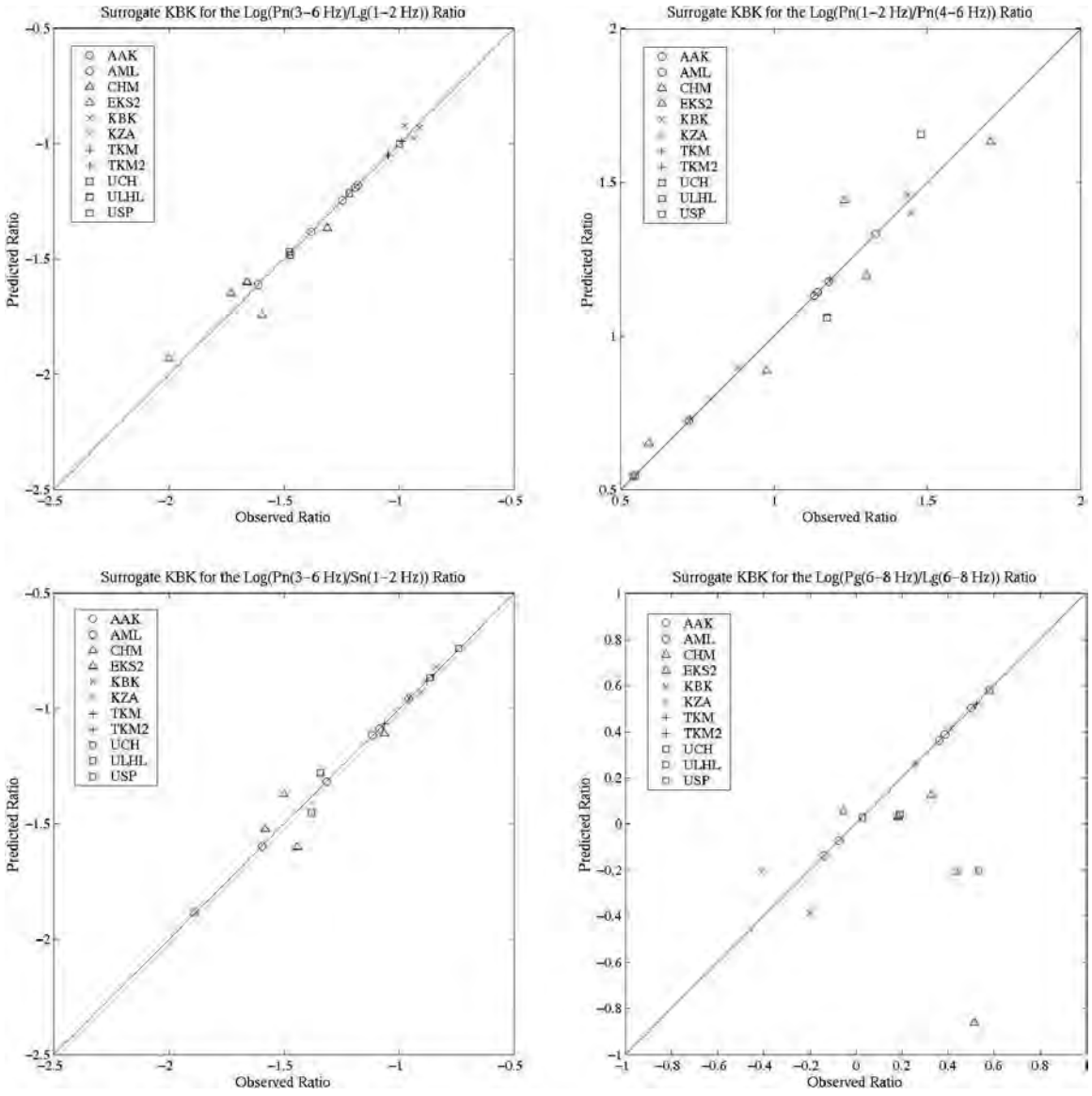

Figure 2: Performance of transfer functions for various spectral discriminates. KBK is the calibration station, and the "known" explosion is the average of the transfer function for five Lop Nor explosions. The predicted value gives the result from the transfer function.

GENERATION OF HIGH-FREQUENCY P AND S WAVE ENERGY BY ROCK FRACTURE DURING A BURIED EXPLOSION: ITS EFFECT ON P/S DISCRIMINANTS AT LOW MAGNITUDE

Charles Sammis

University of Southern California

Sponsored by Defense Threat Reduction Agency

Contract No. DTRA01-01-C-0086

ABSTRACT

The growth of pre-existing fractures is an important physical process that contributes to the generation of high-frequency seismic waves by explosions. Characterized as damage, this crack growth affects the seismic source in two important ways. First, increased damage weakens the rock by lowering its elastic modulus. Second, the growing fractures act as secondary sources of seismic energy. This secondary energy may further weaken crushed rock in the source region by "acoustic fluidization," and it may make a significant contribution to the far-field radiation. Secondary seismic radiation is investigated here using an equivalent elastic method to approximate the stress field surrounding an underground explosion and a micro-mechanical damage mechanics model to calculate the associated increase in damage. Because our damage mechanics calculates the nucleation and growth of individual fractures, a seismic moment tensor can be found for each. Integration over all such growing cracks yields secondary elastic waves that radiate into the far field. While the contribution from an individual crack is small, the combined effect of many cracks in a large region of increased damage can produce primary waves comparable in amplitude to those generated directly by the explosion. Any asymmetry in the growth of damage is very effective in generating S waves. Sources of asymmetry investigated here include a pre-existing tectonic shear stress or a preferred orientation of initial cracks. The effect of different lithologies is primarily reflected in the initial damage and size of the initial flaws. The amount of new damage is controlled primarily by the initial damage, while the size of the zone of new damage is controlled primarily by the size of the initial flaws.

OBJECTIVE

Introduction

Several different processes occur in the rock near a tamped underground explosion, as illustrated in Figure 1 (see, e.g., Rodean, 1971). The explosion is initially contained within a cavity of radius r_c, which has been excavated from the surrounding rock. At the time of detonation a hot pressurized gas is created within the cavity, which causes it to expand. Some of the surrounding rock may be vaporized and added to the cavity gas at this time. The sudden expansion of the cavity generates a shock wave that propagates outward causing major damage to the surrounding rock and producing the series of regimes summarized in Figure 1. Rock first flows plastically; then is stressed beyond its brittle failure limit and becomes granulated; then is stressed to the point where radial cracks grow but failure is not reached; then deforms anelastically where pre-existing cracks slide but do not grow; and finally deforms elastically. These regimes reflect the decrease in energy density in the shock with distance from the explosion caused partly by spherical spreading and partly by the fact that energy is being used to fracture and deform the rock. The shock wave gradually decays into an inelastic wave involving non-linear motions, which further decays with distance until a radius is reached where the motions are small enough to be described by the ordinary elastodynamic equations of linear elasticity. Beyond this elastic radius, r_e, the disturbance caused by the explosion can be modeled as linear elastic waves that propagate throughout the rest of the earth.

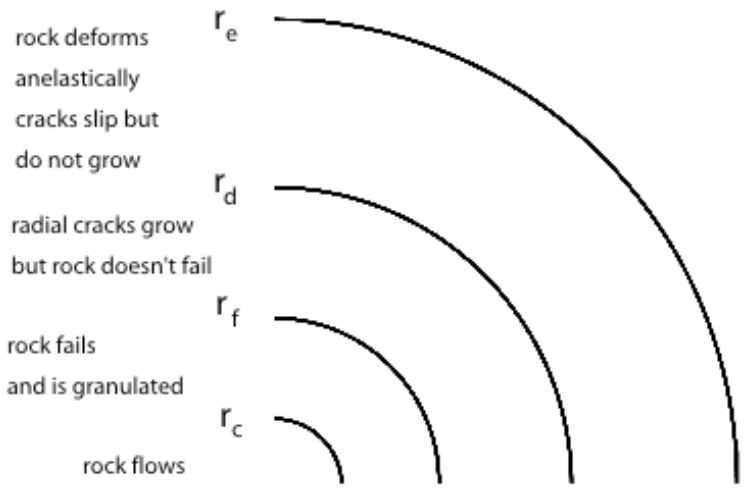

Figure 1. Schematic diagram of the region surrounding a contained explosion in rock: r_c is the cavity radius, r_f is the radius to which failure occurs, r_d is the radius to which new damage is created, and r_e is the elastic radius beyond which waves can be approximated as elastic.

These processes that occur around an explosion can have strong effects on the elastic waves that are radiated beyond the elastic radius r_e. In this report we concentrate on the growth of pre-existing cracks that can affect the radiated elastic waves in at least three different ways. First, intense cracking will significantly lower the bulk modulus and shear modulus near the source (O'Connell and Budianski, 1974; Rimer *et al*. 1998). Second, it has been speculated that when cracking extends into the failure regime, acoustic fluidization can lower the basic strength of the rock (Sammis, 1998). Third, motions on the cracks serve as secondary sources of elastic waves that can contribute to the net seismic radiation field. The primary objective of the work reported here is to provide a quantitative assessment of this third phenomenon. The intent is to determine how these secondary sources modify the P and S waves generated by the explosion and radiated to the far field.

We approach this problem by using the formulation of Ashby and Sammis (1990) to model the nucleation and growth of cracks in the source region, which is here referred to as damage. Calculation of this damage requires knowledge of the stress field in the region surrounding the source, which is approximated in this study by the equivalent elastic method. The micro-mechanical model of damage provides the parameters necessary to represent each crack as a seismic moment tensor that is then used to calculate the elastic waves radiated by the damage.

Finally, we consider the cumulative effect of all the cracks in the damage zone in order to estimate the contribution of damage to P and S waves in the far field.

RESEARCH ACCOMPLISHED

Damage Mechanics

The concept of damage used here is that developed by Ashby and Sammis (1990). In that paper, the conditions under which an initial crack can nucleate additional cracking are derived. Only the basic equations needed to calculate the increase in damage at the shock front will be repeated here. In 3-D, the initial damage is defined as

$$D_0 = \tfrac{4}{3}\pi\left(a\cos\chi\right)^3 N_V\,, \tag{1}$$

where a is the radius of penny-shaped cracks, χ is angle describing the orientation of the cracks (see Figure. 2) and N_V is the number of cracks per unit volume. In response to loading, wing cracks of length l grow at opposite edges of the initial crack thereby increasing the damage to

$$D = \tfrac{4}{3}\pi\left(l + a\cos\chi\right)^3 N_V\,. \tag{2}$$

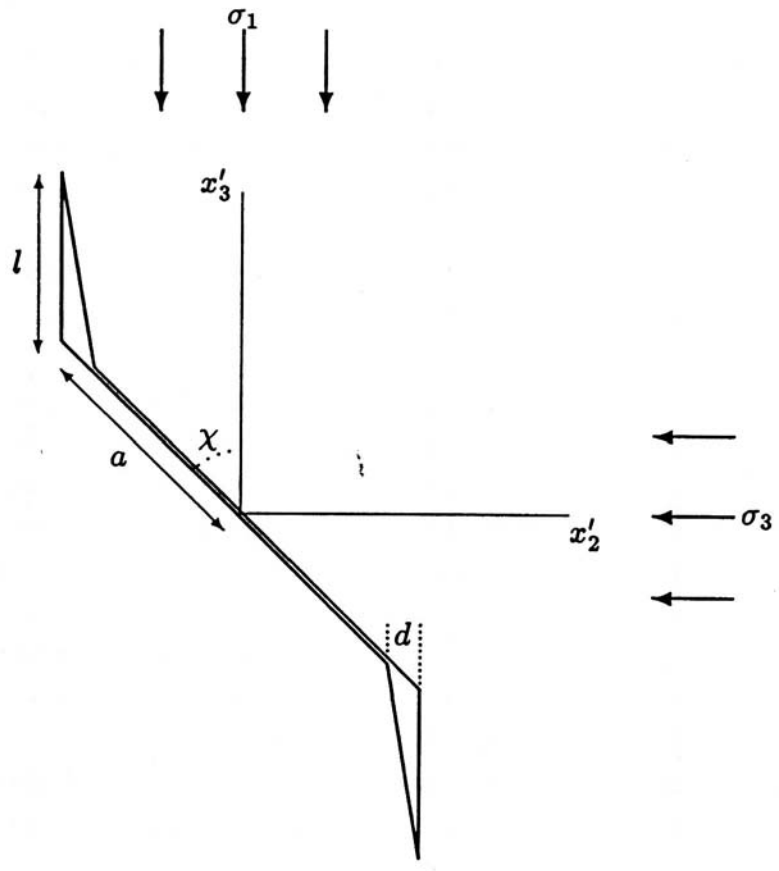

Figure 2. Geometry of a penny-shaped crack of radius *a,* which is extended by wing cracks of length *l*.

The value of l is determined by letting the wing cracks grow until the stress intensity factor at the tip decreases to the fracture toughness of the medium. The equation that must be solved to determine the final amount of damage is (Ashby and Sammis, 1990)

$$S_1 = -\frac{C_2\left(\left(\frac{D}{D_0}\right)^{1/3} - 1 + \frac{\beta}{\cos\chi}\right)^{2/3} - S_3\left[C_1\left(1 + \left(\frac{C_3 D_0^{2/3}}{1 - D^{2/3}}\right)\left(\left(\frac{D}{D_0}\right)^{1/3} - 1\right)^2\right) + C_4\left(\left(\frac{D}{D_0}\right)^{1/3} - 1\right)^2\right]}{1 + \frac{C_3 D_0^{2/3}}{1 - D^{2/3}}\left(\left(\frac{D}{D_0}\right)^{1/3} - 1\right)^2} \tag{3}$$

Here S_1 and S_3 are the maximum and minimum normalized principal compressive stresses given by

$$S_1 = \frac{\sigma_1}{K_{Ic}/\sqrt{\pi a}}, \qquad S_3 = \frac{\sigma_3}{K_{Ic}/\sqrt{\pi a}} \tag{4}$$

and K_{Ic} is the critical stress intensity for mode I cracks, a material property. The constants in (3) are

$$\begin{aligned} C_1 &= \frac{\left(1+\mu^2\right)^{1/2} + \mu}{\left(1+\mu^2\right)^{1/2} - \mu} \\ C_2 &= \pi\left(\cos\chi\right)^{3/2}\sqrt{3/\beta}\,\frac{1}{\left(1+\mu^2\right)^{1/2} - \mu} \\ C_3 &= 2 \\ C_4 &= 2\pi\left(\cos\chi\right)^{2}\sqrt{3/\beta}\,\frac{1}{\left(1+\mu^2\right)^{1/2} - \mu} \end{aligned} \tag{5}$$

In these last equations, μ is the coefficient of static friction and β is a correction factor for the effective length of the crack, typically 0.45 introduced by Ashby and Sammis (1990) to bring their approximate analytical model into agreement with numerical simulations in the limit of small *l*. Also, χ is assumed here to be 45°.

Given the initial damage D_0 and the principal stresses σ_1 and σ_3, equation (3) can be used to calculate the equilibrium state of damage. This is a cubic equation in the damage, which we solve numerically. There are three possible outcomes. At low stresses, wing cracks do not nucleate and we get no real solutions. At intermediate stresses we calculate a value of $D>D_0$ until a maximum is reached above which we again get no real solutions. Ashby and Sammis (1990) interpret this maximum as failure since, for additional loading, damage increases at decreasing stress, an unstable condition leading to shear localization. We do not attempt to model this post-failure regime beyond identifying it as the granulated region described in the introduction, and as a possible site for further weakening by acoustic fluidization.

Stress Field Surrounding an Explosion – The Effective Elastic Medium

In order to model the increase in damage, we require the principal stresses generated by the explosion as a function of distance and time. This is made difficult by the existence of the nonlinear processes between the cavity radius and the effective elastic radius, beyond which the assumptions of ordinary linear elasticity are valid. Sophisticated computer codes have been developed which include hydrodynamic effects, shock waves, and nonlinear equations of state (see, for example, Rodean, 1971; King *et al*., 1989; Glenn, 1993; Glenn and Goldstein, 1994, for discussion and further references). We use here an approximate method to calculate the stresses surrounding an explosion that is based on the equivalent elastic method developed by earthquake engineers to model the nonlinear behavior of soils that that occurs during strong ground motion. The central idea is to make the material properties a function of the stress in the outward propagating pressure pulse and then to adjust these material properties in an iterative process until the appropriate values are present at all distances from the source. In effect, the nonlinear stress-strain behavior is approximated by a series of linear relationships that change with the level of stress. The present

formulation, described by Johnson (1993), relates density and bulk elastic properties to the peak pressure and shear and anelastic properties to the maximum shear strain.

The details of this model are published in Johnson and Sammis (2001) and will not be repeated here. In that paper we modeled the 1 kt chemical explosion detonated in September 1993 as part of the Non-Proliferation Experiment (NPE) (see Denny, 1994). The results of this simulation and attendant damage calculations are summarized in the next section.

Simulation of the NPE Explosion

The first objective in modeling the 1993 NPE event was to check the ability of the equivalent elastic method to simulate the stress field around and explosion. As illustrated in Figure 3 the model gives reasonable values for the peak velocity as a function of distance out to about one kilometer beyond which the model predicts slightly higher velocities than those observed. The calculated waveforms (Figure 4) were also comparable to those observed except for a bit of excessive reverberation.

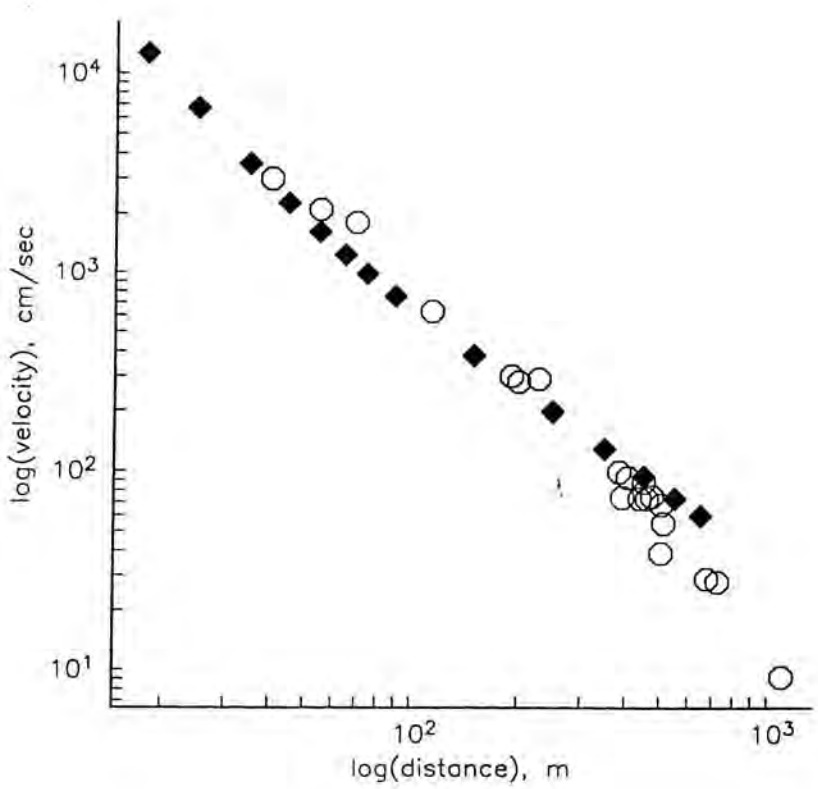

Figure 3. Measured and calculated peak velocities for the NPE explosion. The open symbols are observations taken from Smith (1994) and Olsen and Peratt (1994), while the filled symbols were calculated with the equivalent elastic method (from Johnson and Sammis, 2001).

Having established that the equivalent elastic method gives a good approximation to the observed motions close to the NPE explosion, we now asked whether stresses were sufficiently high to produce an increase in damage. As illustrated in Figure 5, the shock front does indeed produce an increase in damage at a distance of 35 m. Note that the damage does not increase during peak load, but during unloading when the tangential (hoop) stress decreases more rapidly than the radial stress.

Finally, we asked whether the seismic radiation generated by the increase in crack damage makes a significant contribution to the seismic signal in the far field. In order to do this we derived a moment tensor representation of the damage and then calculated the radiated elastic waves using a Green function approach.

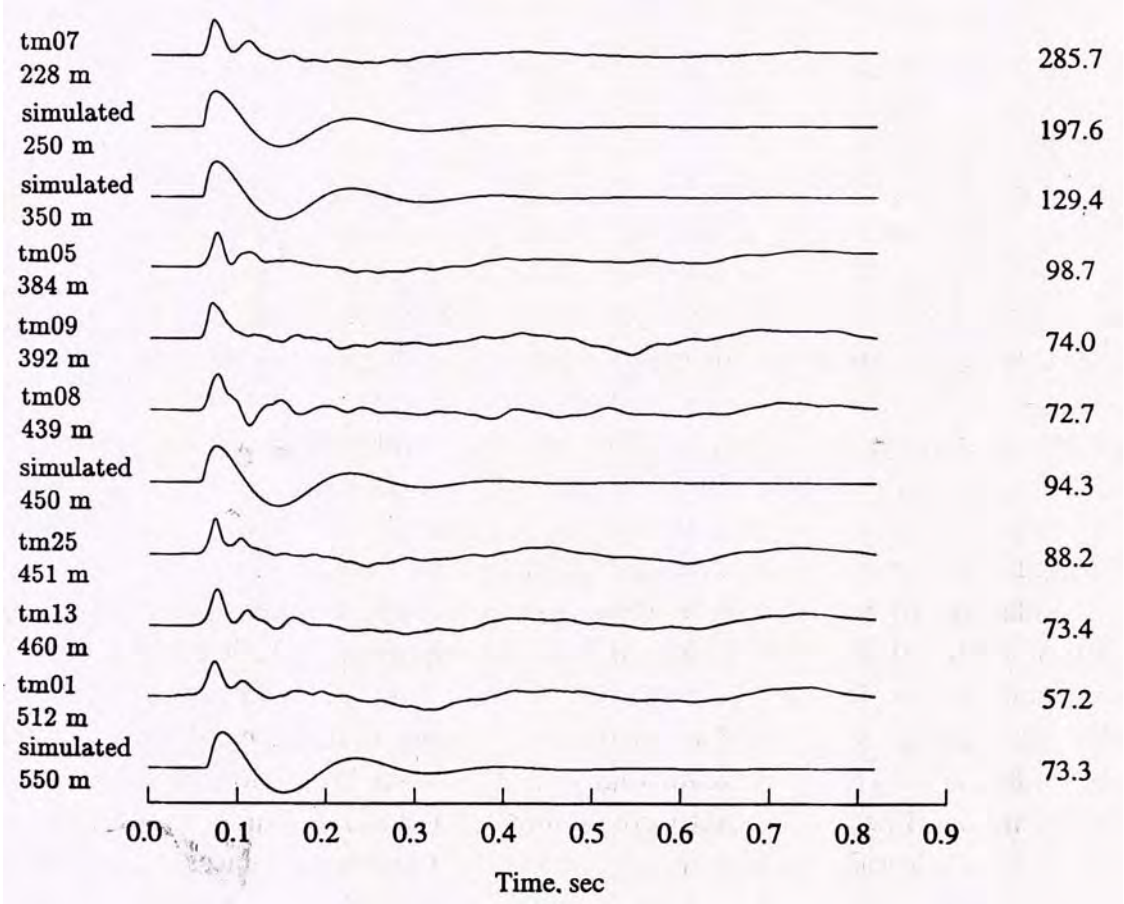

Figure 4. Comparison between measured and calculated waveforms for the NPE explosion. The traces labeled with tm are the radial velocities measured by Olsen and Peratt (1994) at the radial distances shown. The traces labeled with simulated are the radial velocities calculated with the equivalent elastic method at the radial distances shown. The numbers on the right are maximum velocities on the traces in units of cm/sec (from Johnson and Sammis, 2001).

The damage of Ashby and Sammis (1990) is modeled as an initial crack that is extended by wing cracks. Johnson and Sammis (2001) represented this as the combination of two separate source moment tensors: shear dislocation on the initial crack gives a scalar moment tensor per unit volume of

$$m_s = \frac{9}{2}\frac{\lambda+2\mu}{\lambda+\mu}\frac{K_{Ic}}{(\pi a\cos\chi)^{1/2}}\frac{D_0}{\sin\chi\cos^2\chi}\left[\left(\frac{D}{D_0}\right)^{1/3}-1\right]^{1/2} \tag{6}$$

while tensile opening of the wing cracks give

$$m_t = \frac{3(\lambda+2\mu)^2}{2\mu(\lambda+\mu)}\frac{K_{Ic}}{(\pi a\cos\chi)^{1/2}}D_0\left[\left(\frac{D}{D_0}\right)^{1/3}-1\right]^{5/2} \tag{7}$$

A complete specification of the moment tensor for the damage requires that the orientation of the cracks be considered. We did this by transforming the local coordinates of the initial cracks (which varied with position around the source) to a fixed coordinate system for wave propagation to a specified field point. These transformations are straightforward but messy and are given in Johnson and Sammis (2001).

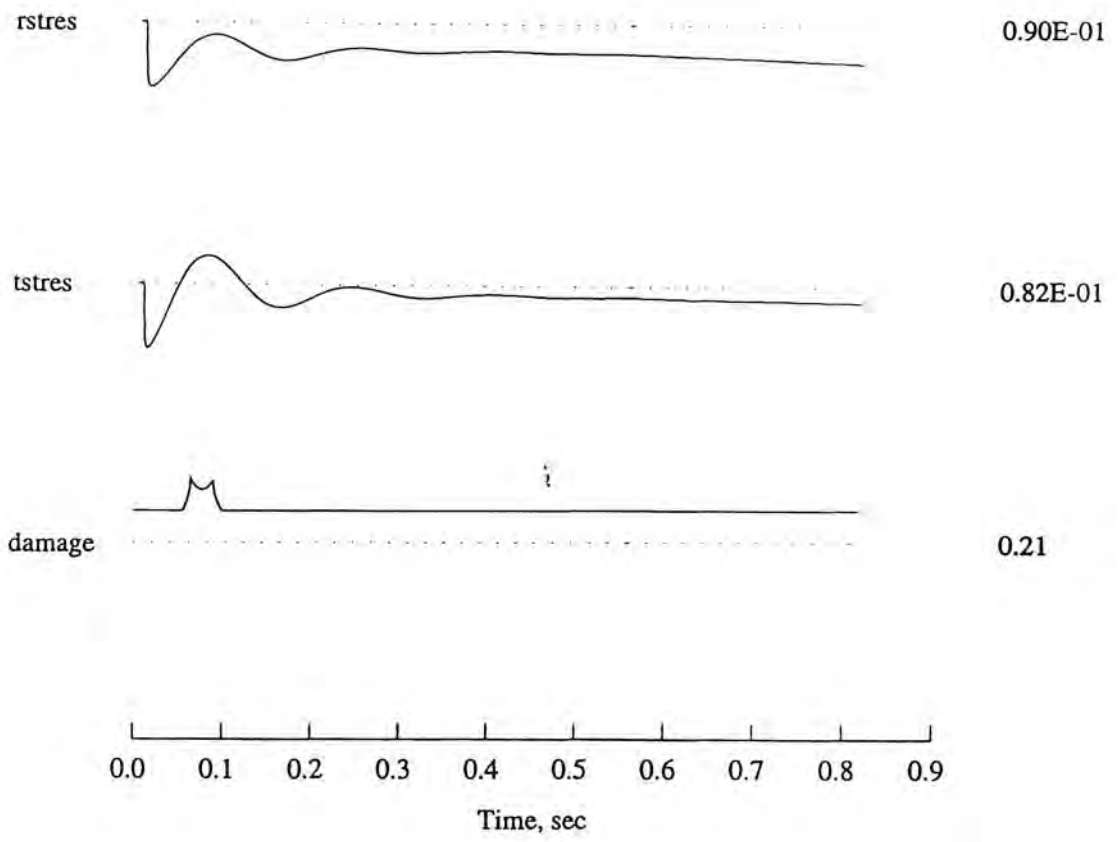

Figure 5. Calculated radial stress, tangential stress, and damage for a distance of 35 m from the NPE explosion. The numbers on the right are peak stress in units of GPa for the stresses. An initial damage of D_0=0.10 and an initial crack radius of a=0.10 cm were used in these calculations (from Johnson and Sammis, 2001).

The net contribution of the damage to the radiated signal is calculated as an integral over the entire damage zone, taking into account the amount of damage, the orientation of the cracks, and the time history of the motion on the cracks at each point in this zone. Such integrals were obtained by numerical methods using the following procedure:

- The region surrounding the source was divided into a large number of small volume elements.
- The equivalent elastic method was used to calculate the principal stresses within each volume element as a function of time.
- Equation (3) was used to determine if an increase in damage occurred within the volume element and, if so, the amount of increase ant the time at which it begins.
- The increase in damage was converted to a moment tensor.
- The displacements at the receiver location were calculated by using a Green function and integrating over every volume element where there was an increase in damage.
- The results of these calculations for the NPE explosion are summarized in Tables 1 and 2.

Table 1. Effect of Initial Damage

Initial Damage D_0	Failure Damage D_f	Failure radius r_f (m)	Damage radius r_d (m)	Maximum Velocity V_{max} (450 m), cm/sec
0.01	0.09	25	25	0.9
0.05	0.26	35	45	8.4
0.10	0.40	35	45	16.1
0.20	0.53	35	45	28.2
0.40	0.73	35	45	44.8
0.80	1.13	35	45	88.9

Crack radius a=0.1 cm in all cases

Table 2. Effect of Initial Crack Radius

Crack radius a	Failure Damage Df	Failure radius rf (m)	Damage radius rd (m)	Maximum Velocity Vmax (450 m) cm/sec
0.01	0.22	18	18	2.6
0.10	0.40	35	45	16.1
1.00	0.39	75	90	21.1
10.0	0.40	90	150	13.1

Initial damage D_0=0.1 in all cases.

Figure 6 shows the waveforms for a range of different initial crack sizes.

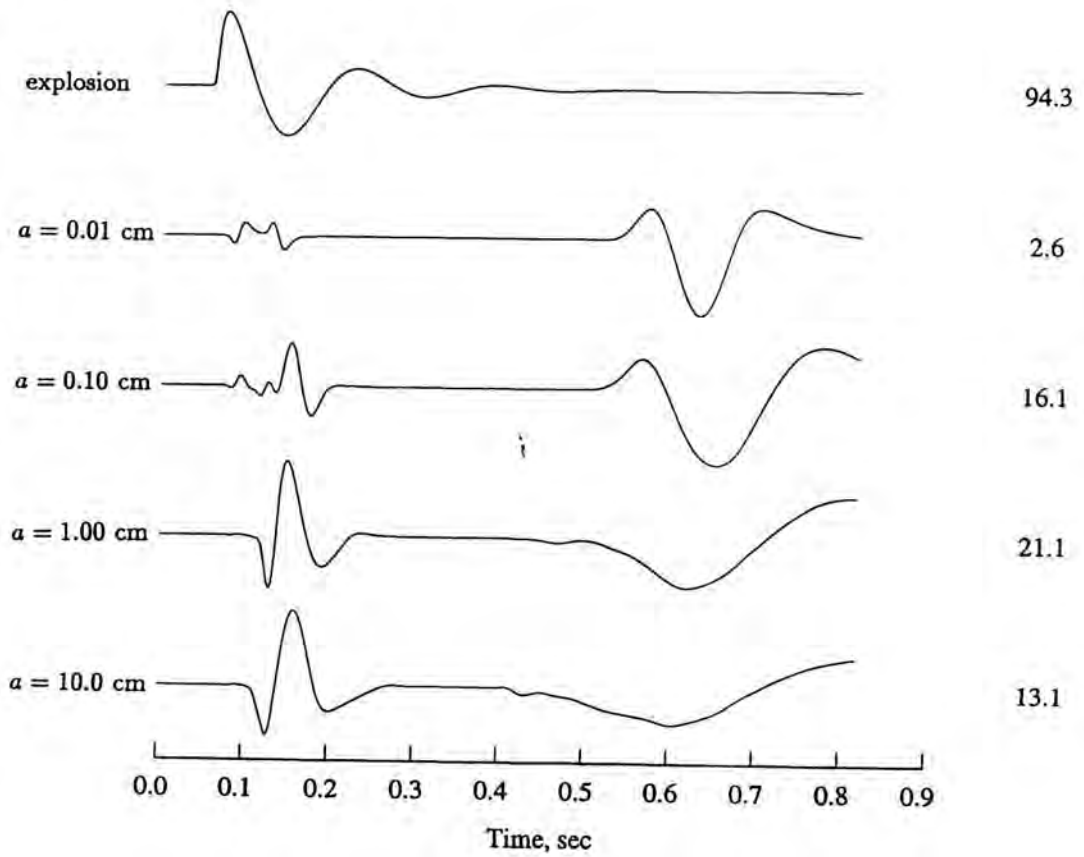

Figure 6. Effect of initial crack radius on the radiated secondary waves for an initial damage of D_0=0.10 (from Johnson and Sammis, 2001).

CONCLUSIONS AND RECOMMENDATIONS

This study has considered one of the processes that may occur in the region of high stresses immediately surrounding an explosion detonated in rock, the extension of pre-existing cracks. Using a combination of analytical and numerical methods, the physics of this crack extension process has been modeled. The results have interesting and significant implications with regard to the elastic waves that are radiated by explosive sources.

Combining the equivalent elastic method of calculating stresses in the near-source region of an explosion (Johnson, 1993) with a micro-mechanical damage model (Ashby and Sammis, 1990) leads to an approximate but efficient method of estimating the growth of pre-existing cracks. Sample calculations for the NPE chemical explosion revealed that the stress waves from the explosion were capable of generating significant amounts of crack growth in an extensive region surrounding the source, with the extent and shape of this region depending upon such parameters as the initial damage, the size of the cracks, the amount of pre-stress and orientation of the cracks. These calculations suggest that the extent of the damaged zone is most sensitive to the initial crack radius, varying from a radial distance of about 45 m for a crack radius of 0.1 cm to about 150 m for a crack radius of 10 cm for this 1 kt explosion. These numbers are consistent with the results reported by Rimer *et al*. (1998) for Russian explosions in hard rocks, which underwent intensive fracturing extending out to a scaled radius of 40 $m/kt^{1/3}$ and occasional fracturing observed out to about 200 $m/kt^{1/3}$.

These calculations also suggest that the growth of the cracks does not occur at the time of peak stress, but significantly later when the tangential stress is relaxing more rapidly than the radial stress. This leads to a damage front that follows behind the outward propagating stress wave with a velocity between those of P and S waves. In addition to calculating the time when the cracks begin to grow, it is also possible to calculate the amount of growth and the orientation of the cracks that are growing. This information is sufficient to calculate a seismic moment tensor for the crack growth, which in turn can be used to calculate the secondary elastic waves generated by the crack growth. Because two different processes accomplish crack growth, sliding on the pre-existing cracks and the extension of wing cracks, the moment tensor also consists of two different parts. Thus one of the contributions of this study is a procedure for estimating the secondary elastic waves that are generated when there is growth of cracks in a zone surrounding an explosion.

While the contribution from a single crack is small, the integration over the many cracks in a large zone of increased damage surrounding an explosion may lead to the generation of seismic waves that are comparable in amplitude to those of the explosion itself. For an isotropic homogeneous distribution of cracks, the composite moment tensor is isotropic and thus radiates only P waves into the far field. However, any departure from spherical symmetry in the problem leads to the generation of S waves. In this paper we investigated two types of asymmetry 1) a pre-stress in the vicinity of the explosion and 2) a preferred orientation of the cracks in the vicinity of the explosion. Both types of asymmetry have similar effects if the pre-stress and crack orientations are chosen in a consistent manner. Included in these effects are significant S waves that emerge from the region surrounding the explosion and thus appear to be generated by the explosion itself.

The effects of crack growth calculated in this paper should be regarded as minima because the increase in damage was stopped at the inception of failure. Damage is likely to continue beyond this point but we are not aware of a suitable method of calculating damage, along with stress and strain in the unstable post-failure regime. This is one aspect of the problem that definitely needs further research. Sammis (1998) has suggested acoustic fluidization (Melosh, 1979) as a possible method of modeling this type of behavior, and this aspect of the problem is currently being pursued.

Another area in which further research would be useful is a more complete connection between the equivalent elastic treatment and the damage mechanics. In the present study the shear modulus and energy loss are modeled using empirical relations borrowed from the soil mechanics. In principle, it should be possible to calculate the change in elastic moduli caused by a change in damage using a method such as that of O'Connell and Budiansky (1974) and to calculate the loss of energy due to the damage directly from fracture mechanics.

Finally, the method should be further tested against the recorded waveforms from the larger U.S. nuclear explosions in granite (Hardhat, Piledriver, and Shoal) and the Russian hard rock waveforms when they become available in digital form next year.

REFERENCES

Ashby, M.F., and C.G. Sammis (1990), The damage mechanics of brittle solids in compression, *PAGEOPH*, **133**, 489-521.

Denny, M. D., Introduction and highlights, in Proceedings of the Symposium on the Non-Proliferation Experiment (NPE): Results and Implications for Test Ban Treaties, M. D. Denny (editor), CONF-9404100, Department of Energy, 1994.

Glenn, L. A. (1993), Energy-density effects on seismic decoupling, *J. Geophys. Res*., **98**, 1933-1942.

Glenn, L. A., and P. Goldstein (1994), Seismic decoupling with chemical and nuclear explosions in salt, *J. Geophys. Res.*, **99**, 11,723-11,730.

Johnson, L. R., Wave propagation near explosive sources, PL-TR-93-2118, Phillips Laboratory, 22 pp., 1993.

Johnson, L.R. and C.G. Sammis (2001), Effects of rock damage on seismic waves generated by explosions, *Pure and Applied Geophysics*, **158**, 1869-1908.

King, D. S., B. E. Freeman, D. D. Eilers, and J. D. Johnson (1989), The effective yield of a nuclear explosion in a small cavity in geologic material: enhanced coupling revisited, *J. Geophys. Res*., **94**, 12,375-12,385.

Melosh, H. J. (1979), Acoustic fluidization: A new geologic process, *J. Geophys. Res*., **84**, 7513-7520.

O'Connell, R. J., and B. Budiansky (1974), Seismic velocities in dry and saturated cracked solids, *J. Geophys. Res*., **79**, 5412-5426.

Olsen, K. H., and A. L. Peratt, Free-field ground motion for the non-proliferation experiment: preliminary comparisons with nearby nuclear events, in Proceedings of the Symposium on the Non-Proliferation Experiment (NPE): Results and Implications for Test Ban Treaties, M. D. Denny (editor), CONF-9404100, Department of Energy, 1994.

Rimer, N., J. L. Stevens, J. R. Murphy, and G. G. Kocharyan, Estimating seismic characteristics of explosions in hard rock using a micro-mechanical damage model, p. 392-400 in Proceedings of the 20th Annual Seismic Research Symposium on Monitoring a Comprehensive Test Ban Treaty, J. Fantroy, D. Heatley, J. Warren, F. Chavez, and C. Meade (eds), Department of Defense and U.S. Department of Energy, 1998.

Rodean, H. C., Nuclear-Explosion Seismology, U. S. Atomic Energy Commission, TID-25572, 156 pp., 1971.

Sammis, C. G., Acoustic fluidization in the damage regime of explosions in crystalline rock, p. 417-421 in Proceedings of the 20th Annual Seismic Research Symposium on Monitoring a Comprehensive Test Ban Treaty, J. Fantroy, D. Heatley, J. Warren, F. Chavez, and C. Meade (eds), Department of Defense and U.S. Department of Energy, 1998.

Smith, C. W., NPE - close-in stress and motion measurements, in Proceedings of the Symposium on the Non-Proliferation Experiment (NPE): Results and Implications for Test Ban Treaties}, M. D. Denny (editor), CONF-9404100, Department of Energy, 1994.

IMPROVED SURFACE WAVE DISPERSION MODELS AND AZIMUTH ESTIMATION TECHNIQUES

Jeffry L. Stevens, David A. Adams, and G. Eli Baker

Science Applications International Corporation

Sponsored by Defense Threat Reduction Agency

Contract No. DTRA01-01-C-0082

ABSTRACT

Surface waves are of primary importance for nuclear monitoring because the Ms:mb discriminant and its regional variants are among the most reliable means of determining whether an event is an earthquake or an explosion. When surface waves can be measured, in most cases they unambiguously identify an event as an earthquake or an explosion. The goal of this project is to reduce the magnitude threshold for which surface waves can be identified and measured reliably, and to improve the accuracy of surface wave measurement, using phase-matched filtering, development of global regionalized earth and dispersion models, and other techniques.

Global regionalized earth and dispersion models are being developed by inversion of a very large data set of phase and group velocity dispersion measurements. Two new data sets have recently been received and incorporated: a new data set of about 9,000 measurements from SLU, and an expanded data set from the University of Colorado. The complete data set now contains 725,000 dispersion data points. We are reviewing the current data set to find areas where new data is required to fill gaps or resolve ambiguity, and to identify incorrect or anomalous data. Because of the very large size of the data set, we are developing new methods to review and manage the data.

The dispersion measurements are inverted for earth structure, and the earth structure is then used to generate dispersion predictions. This is accomplished in the following way. The inversion is performed for approximately 600 distinct base structures, which were originally derived from the Crust 2.0 models over the AK135 mantle model. The Moho depth, bathymetry, and sediment depths vary on a one-degree grid. Moho depths are derived from Crust 2.0, sediment depths from the Laske and Masters sediment maps, and bathymetry from ETOPO5. Moho depth, bathymetry and sediment properties are fixed in the inversion, while crust and upper mantle velocities are allowed to vary in the base models. Phase and group velocity dispersion curves are calculated for each of 64,800 models on the one-degree grid. The phase velocity dispersion curves are used to calculate phase-matched filters to improve detection.

Automatic processing of surface waves at the International Data Center calculates a station to event azimuth estimate based on polarization analysis, but the algorithm currently in use has been found to be unreliable for a large fraction of surface wave arrivals, particularly for lower amplitude arrivals. Selby (2000) suggested that a different azimuth estimation algorithm, based on a technique due to Chael (1997) would be more robust than the algorithm currently used in the automatic processing system. Part of the problem is due to high noise levels on the horizontal components, particularly at stations using tri-axial instruments. This problem can only be resolved with better instrumentation; however better analysis techniques could improve results on the rest of the data set. We have implemented Selby's method for azimuth estimation within the automatic surface wave processing program Maxpmf and compared the results with the existing method for estimating azimuth from 3-Component data on data with known surface wave arrivals. The results show a reduction in the standard deviation of the azimuth residuals from 72º to 33º with the new method. Work is continuing to optimize the performance of both azimuth estimation techniques.

OBJECTIVE

The goal of this project is to reduce the magnitude threshold for which surface waves can be identified and measured reliably, and to improve the accuracy of surface wave measurement, using phase-matched filtering, development of global regionalized earth and dispersion models, and other techniques.

RESEARCH ACCOMPLISHED

During the first year of this project, we have focused on two areas: improvements to global earth models and dispersion maps, and implementation and testing of azimuth estimation techniques at three component stations based on polarization analysis. This project continues some of the work done under an earlier project (Stevens *et al*, 2001b). In that project, we started with a set of ~150 earth models defined on a five degree grid originally derived from Crust 5.0 (Stevens and McLaughlin, 2001), replaced this with a starting model derived from Crust 2.0, and developed a set of dispersion curves and earth models defined on a one degree grid. The technique for doing this is described in the following section. In the current project, we are developing improvements to the data set and the inversion technique. We are performing a comprehensive review of the data set to identify anomalous data and to determine whether these data are inconsistent with the model because of inaccuracies in the model, errors in the data, or anomalous paths that cannot be modeled with the current procedure. Because of the complexity of working with this very large data set, we have developed some interactive tools to help with this task. We have also greatly improved the performance of the inversion scheme, so that the time required for an inversion has been reduced from over 24 hours to about 7 hours on a Compaq ES40 computer with three 667 MHz Alpha processors.

Surface Wave Dispersion Data Set

We have continued to add new dispersion data to our global data set. Two new data sets have been received and incorporated: a new data set of about 9,000 measurements from St. Louis University (Perez, 2001), and an expanded data set from the University of Colorado (Levshin *et al*, 2002). The complete data set now contains 725,761 dispersion data points. Other data in this data set is described in Stevens *et al* (2001a,b).

One-Degree Earth Model

We have developed a one-degree Earth model made up of layers of ice, water, sediments, crust and upper mantle. Currently this model depends on 8886 free parameters that are adjusted by least squares fitting to group and phase velocity dispersion data of Rayleigh waves. Most of the data set consists of group velocity measurements. The free parameters are the S-wave velocities of layers of 570 different model types. Other constrained parameters in the model are P wave velocities, densities and Q. P wave velocities are constrained via a constant Poisson's ratio of 0.27, and density via Birch's Law of $\rho = 0.65\beta + 400$ where ρ is density and β is shear velocity in MKS units. Q corresponds to PREM in the mantle, and is set according to Swanger's law Q=β/10 (in MKS units) in the crust and upper mantle unless other information is available. The model types are based on the Crust 2.0 2x2 degree crustal types (Bassin *et al.*, 2000 and Laske *et al.* 2001) and also on ocean ages (Stevens and Adams, 2000).

The procedure for constructing the inversion models is illustrated in Figure 1. The top few km of the model (consisting of water, ice and/or sediments) are fixed and match data from one degree bathymetry maps made by averaging Etopo5 five minute measurements of topography, and Laske and Masters (1997) 1 degree maps of sediments. There is an explicit discontinuity between the bottom of the sediments and the crust. There are three or more crustal layers. The Crust 2.0 models that were the starting point for these structures have three crustal layers, but we found it necessary to add more layers in regions of thick crust. There is another explicit discontinuity at the Crust/Mantle boundary. The Moho depth is derived from Crust 2.0 and varies on a 2-degree grid. The mantle starting model is derived from AK135 (Kennett, *et al*, 1995). With these constraints, the inversion is performed for the shear velocity of the crust and upper mantle to a depth of 300 km. Below 300 km the earth structure is fixed, and the inversion model is required to be continuous with the mantle structure at the base of the inversion.

In broad ocean areas, we replace the Crust 2.0 model with models distinct for each ocean and subdivided by ocean age. We also separate into distinct models Crust 2.0 models that are geographically separated. So, for example, if Crust 2.0 has the same model type in North America and in Asia, we use the same starting model for each, but treat them as separate models in the inversion. Figures 2 and 3 show the global distribution of starting model types.

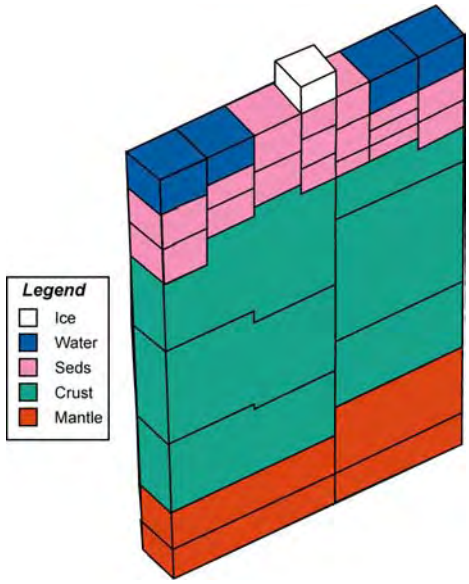

Figure 1. Surface wave inversions are performed for a set of earth models consisting of mantle, crust, sediments, and in some layers, water or ice. The properties of the ice and sediment layers are held fixed, as is the Moho depth, and inversion is performed for the shear velocity in the crust and upper mantle.

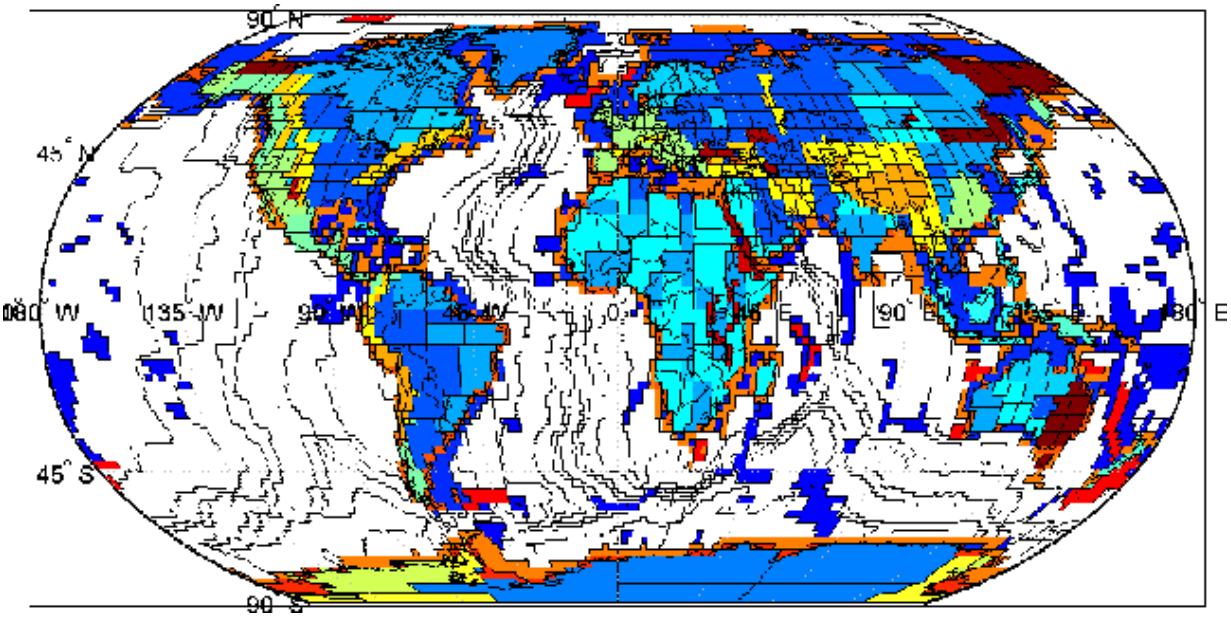

Figure 2. Starting models for inversion in continental areas. Each color is a different model type. The initial starting models for inversion are the Crust 2.0 model types. Separate models (with the same initial structure) are used for geographically separated Crust 2.0 models of the same type.

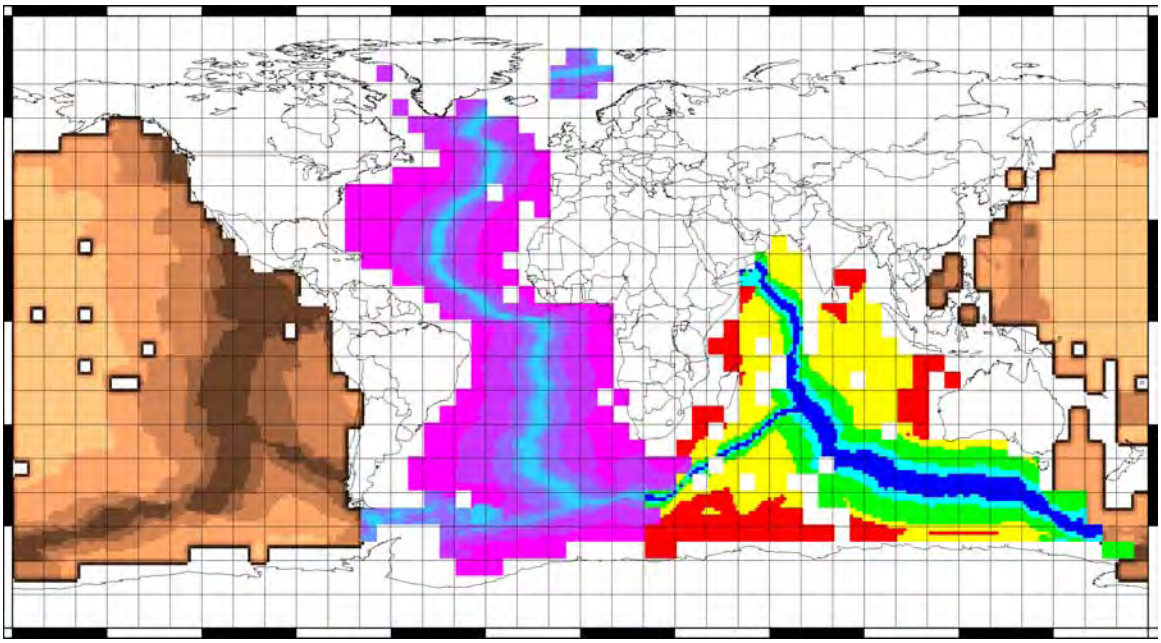

Figure 3. Starting models for broad ocean areas are separated by age. Distinct models are used for each ocean.

Tools for Model and Data Analysis

Because of the very large size of the data set, it has become increasingly difficult to evaluate the results, identify problem data, and determine where new models are needed. To assist with this effort, we have developed data and model analysis and visualization tools using Matlab and the Matlab Mapping Toolbox. These are interactive tools and include multiple ways of representing data and models with zoom adjustable scales. The tools are modular and can be easily modified and extended. These characteristics are important for finding quick answers to questions about the large and complex data set and model. The link between data appraisal and model parameter adjustment is strong, and the ability to examine data and model frequently and in different ways allows us to focus in on those aspects of the inversion that need to change. For example, we can examine spatial variations of data fit, find outliers, and find under or over regularized regions in the model. Such tasks can be very time consuming using non-interactive graphics tools.

Example of Interactive Tools Applied to Data Analysis

The following example demonstrates how the Matlab tools can be used to categorize data according to data fit and to find long wavelength variations in data misfit. We categorize all data into four sets.

1. Good data consistent or almost consistent with the model. These correspond to smooth dispersion curves with similar dispersion curves on neighboring paths.
2. Good data inconsistent with model. Typically these correspond to multiple dispersion curves along similar paths that consistently disagree with model predictions. These show that model improvement is needed.
3. Indeterminate data. These correspond to isolated paths where ray density is too low to determine whether differences are caused by data or model problems. In this case, more data along similar paths is needed.
4. Poor data points. These are identified by being inconsistent with dispersion curves of neighboring paths, and or with other frequencies in the same dispersion curve.

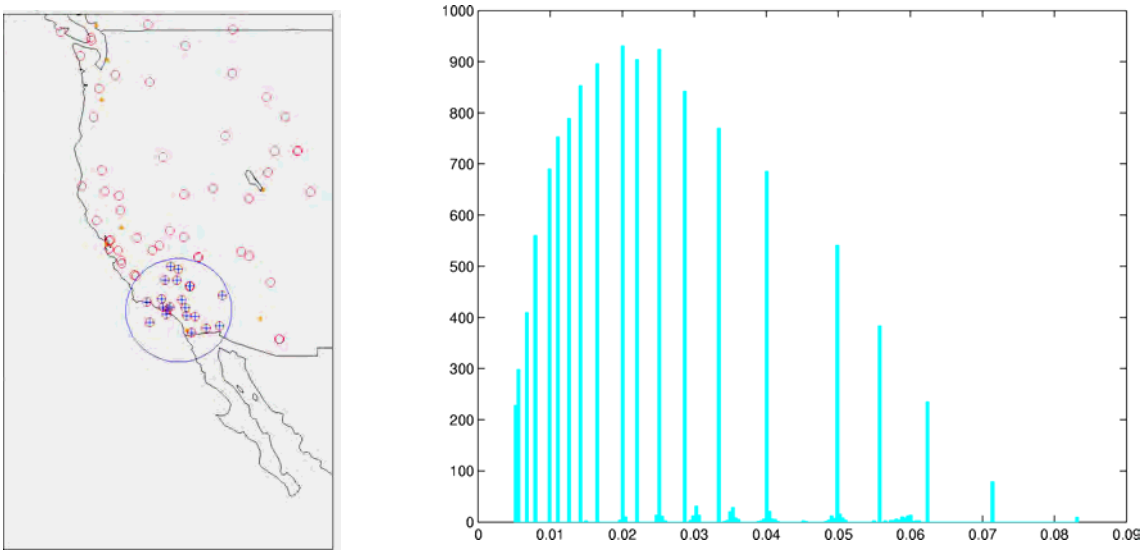

Figure 4. Locations of all stations in the western US appearing in our data set. The histogram to the right shows the distribution of group velocity measurements made at the stations in southern California marked with blue crosses.

Using the interactive tool, the user can select a region and find the characteristics of all rays starting or ending in the region. Figure 4 shows the locations of stations and sources selected within a circular region in and near Southern California appearing in the data set and a histogram of the distribution of corresponding group velocity measurements. The user can then select a subset of data, for example, by frequency band. Figure 5 shows all of the paths recorded at the Southern California stations at frequencies between .018 and .037 Hz. The paths are color coded according to the residual $1\text{-}s_o/s_{p,}$ where s_o and s_p are the observed and predicted group slownesses. Blue paths indicate paths where observations are slower than predicted, red faster than predicted. The scale is truncated to make colors more sensitive to variations nearer zero. Long wavelength variations in data fit appear as smooth color variations in Figure 5. These can be used in the future to build station dependent correction surfaces or tables, or to drive model improvements through reparameterization by densification of model types, or layers, or by localized relaxation of regularizing parameters (smoothing and damping parameters). Dark red and blue paths are mostly associated with poor data points (category 4), however there are several nearby paths that show consistent low velocities between Southern California and the South Atlantic Ocean.

Geographic and model information can be displayed together with the paths. Figure 6 shows sedimentary thicknesses together with paths starting in the blue circle shown in Figure 4. Figure 7 shows color-coded group velocity dispersion curves for the paths shown in Figure 6 with crosses for predicted and circles for observed velocities. The colors are used for cross-referencing between Figures 6 and 7. Interactively, the user can select a dispersion curve on Figure 7 and find the path on Figure 6, or vice-versa. Comparing Figures 5-7 it can seen that the anomalous data points discussed above pass close to or within the sediments off of the northern coast of South America. These therefore correspond to a geophysical effect rather than data error, and most likely will require the introduction of a new model type.

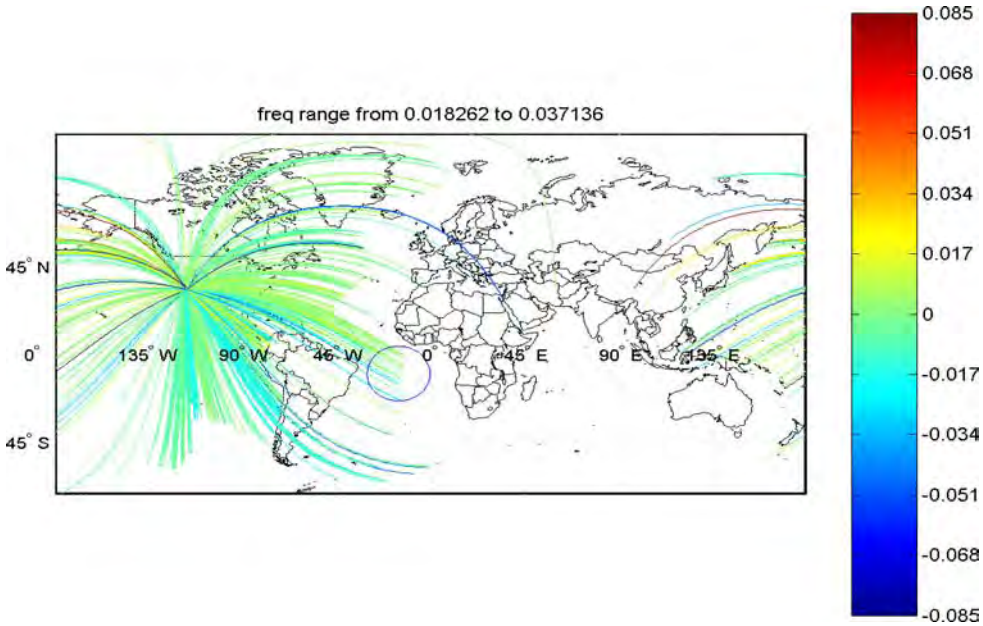

Figure 5. All ray paths for surface waves recorded at the southern California stations at frequencies between .018 and .037 Hz. The paths are color coded according to the residual $1\text{-}s_o/s_p$. Blue means the observations are slow relative to the model, red fast relative to the model.

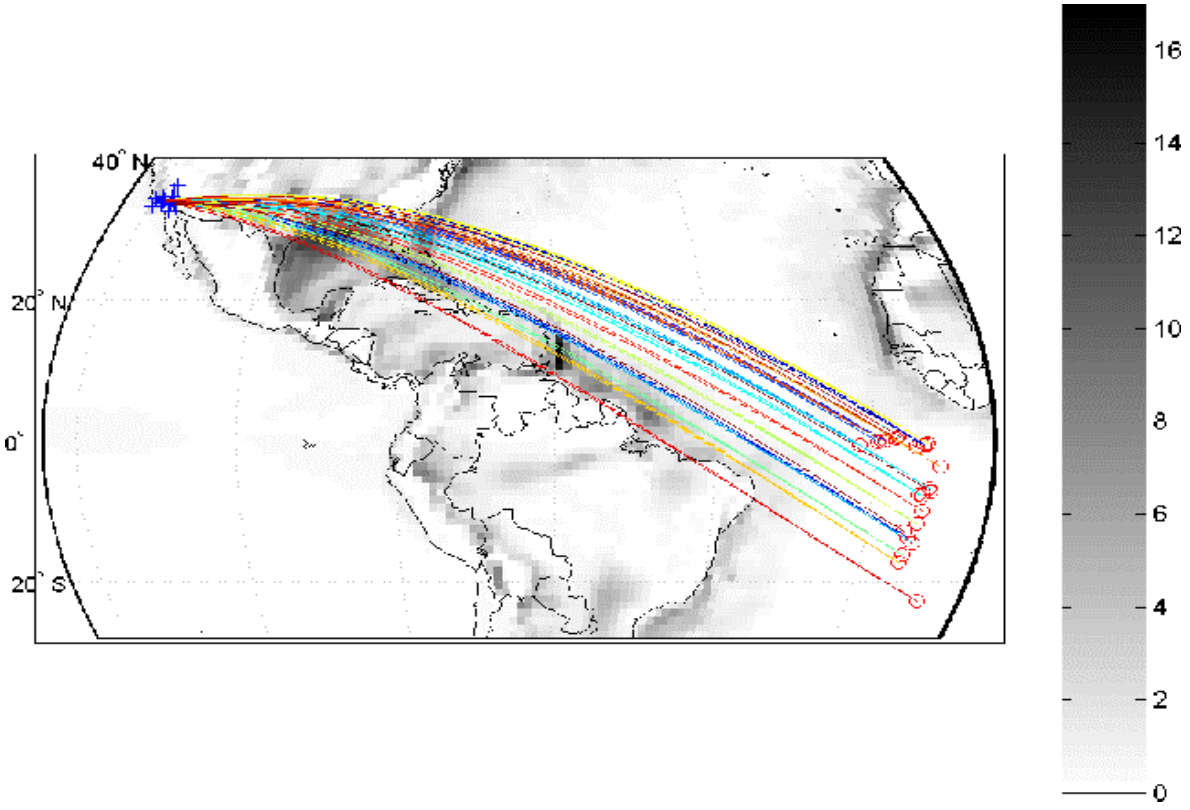

Figure 6. Sedimentary thickness in kilometers and all paths starting in the blue circle shown in Figure 5. The ray colors correspond to the dispersion curve colors in Figure 7.

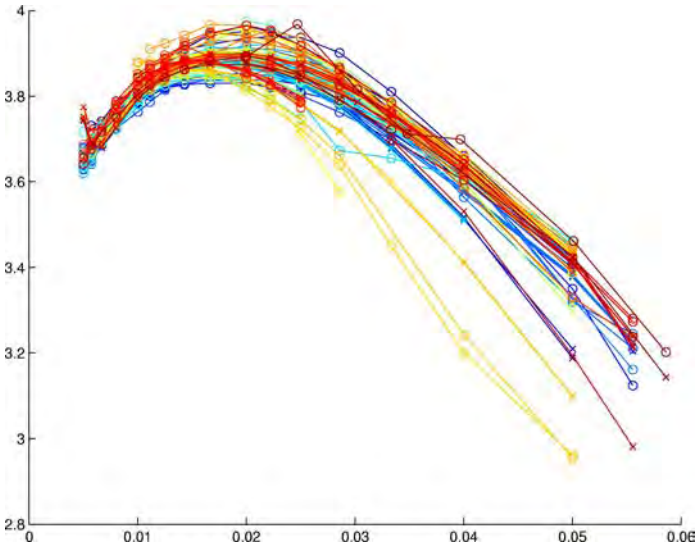

Figure 7. Color-coded group velocity dispersion curves for paths shown in Figure 6 with crosses for predicted and circles for observed velocities. The colors correspond to the path colors in Figure 6. The lowest velocity curves correspond to the anomalous curves discussed in reference to Figure 5.

The Selby/Chael Azimuth Estimation Algorithm

The azimuth estimation technique used by the automatic surface wave processing program Maxsurf at the IDC is based on an algorithm due to Smart (1977). When Maxsurf was first installed at the PIDC, it used this azimuth test in addition to a dispersion test to identify surface wave arrivals. That is, it used three-component or array data to estimate the azimuth to the source and compared this with the known azimuth. If it was not within a specified error, the arrival was rejected and not included in the database. However, review of processing results showed that a large number of arrivals, particularly at three component stations, were being rejected even though they showed a clear arrival on the vertical component. Further analysis showed that the azimuth errors were primarily due to high noise levels on the horizontal components. An example is shown in Figure 8, showing seismograms and spectra at ZAL from the Chinese nuclear test of July 28, 1996. Because of these problems, the azimuth test was removed and replaced with a post-processing algorithm to remove misassociated arrivals.

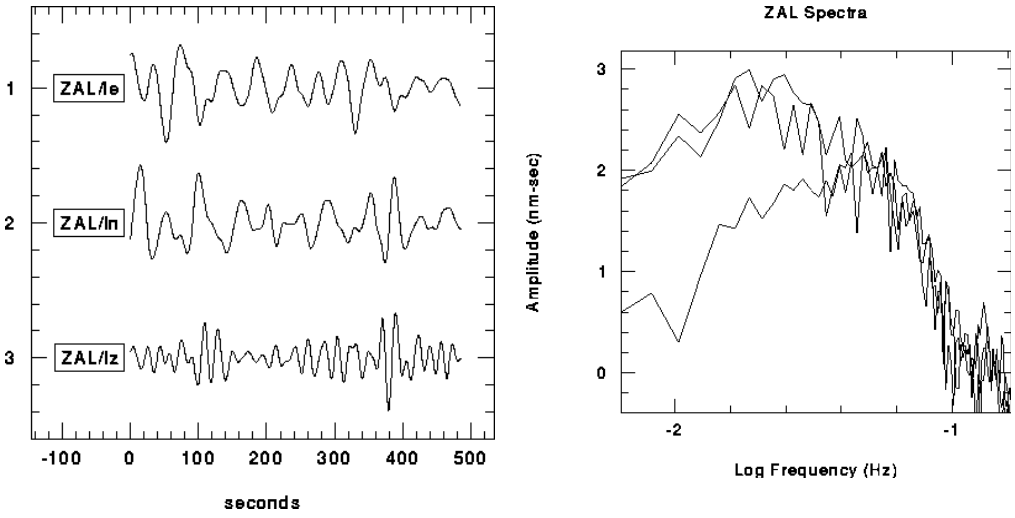

Figure 8. Seismograms (left) and corresponding spectra (right) from the Chinese nuclear test of July 28, 1996 recorded at ZAL at a distance of 12.7 degrees. Note the good signal on the vertical component, but high noise levels that obscure the signal on the horizontal components. This event had an M_s of 2.8 based on arrivals at ZAL and NRI.

Recently, Selby (2000) suggested that a different azimuth estimation algorithm, similar to that developed by Chael (1997) would be more robust that the algorithm currently used in Maxsurf. He processed a set of data using this algorithm and then compared it with the azimuth estimates in the Reviewed Event Bulletin (REB) and found significantly improved results. Although no algorithm is likely to work with very noisy data such as that shown in Figure 8, an improved algorithm could make the azimuth estimate more useful as a means of associating arrivals.

We have implemented Selby's method for azimuth estimation within Maxpmf and compared the results with the existing method for estimating azimuth from 3-component data. The algorithm takes advantage of the fact that the vertical and Hilbert transformed radial ground motion are highly correlated. Specifically, it finds the back-azimuth for which the correlation of the vertical and Hilbert transformed radial is a maximum. Selby presents the cross-correlation, normalized as follows,

$$C_{z\bar{r}} = \frac{S_{z\bar{r}}}{S_{zz} S_{\bar{r}\bar{r}}}, \tag{1}$$

where,

$$S_{jk} = \sum_{\tau=1}^{N} x_j(\tau) x_k(\tau). \tag{2}$$

The implementation uses the correlation of the Hilbert transformed vertical, as that only has to be calculated once, with the radial, for one degree increments of back-azimuth. While Selby uses the maximum positive correlation as the back-azimuth, Chael (1997) uses the central azimuth, determined by the circular mean.

Circular statistics are analogous, but not identical, to linear statistics. For example, while the mean of 359 and 1 is 180, the circular mean of 359° and 1° degree is 0°, which is the correct answer for averaging directions. We find the circular mean separately for the positive and negative values of the cross-correlation at each one-degree increment of back-azimuth, and average those results for greater accuracy. For synthetic Rayleigh waves with noise added, the circular mean provides more accurate estimates than does the maximum correlation. The poorer the S/N, the greater the advantage of using the circular mean. We have implemented both methods and are testing whether there is a significant difference for real data.

For noise-free data (i.e. synthetics), equation 1 will return a negative or positive constant. That is because cross-correlation of the Hilbert transformed vertical and radial and the autocorrelation of the radials change in synch as the algorithm steps through back-azimuths. Our implementation of the algorithm therefore provides two methods of estimating the similarity of the components. One uses the correlation coefficient, that is, nearly equation 1, but with the normalization using square root of the denominator, as follows,

$$C_{z\bar{r}} = \frac{S_{z\bar{r}}}{\sqrt{S_{zz} S_{\bar{r}\bar{r}}}}. \tag{3}$$

The second method is intended to avoid the problem described above when data are noise free. It does not normalize by $S_{\bar{r}\bar{r}}$, but instead uses,

$$C_{z\bar{r}} = \frac{S_{z\bar{r}}}{S_{zz}}. \tag{4}$$

The results of our initial test are shown in Figure 9. Work is continuing to determine the optimum time window, frequency bands, and other parameters for both methods, but at least this initial test shows a significant improvement, quantified by a reduction in standard deviation of the azimuth residual from 79 degrees to 45 degrees.

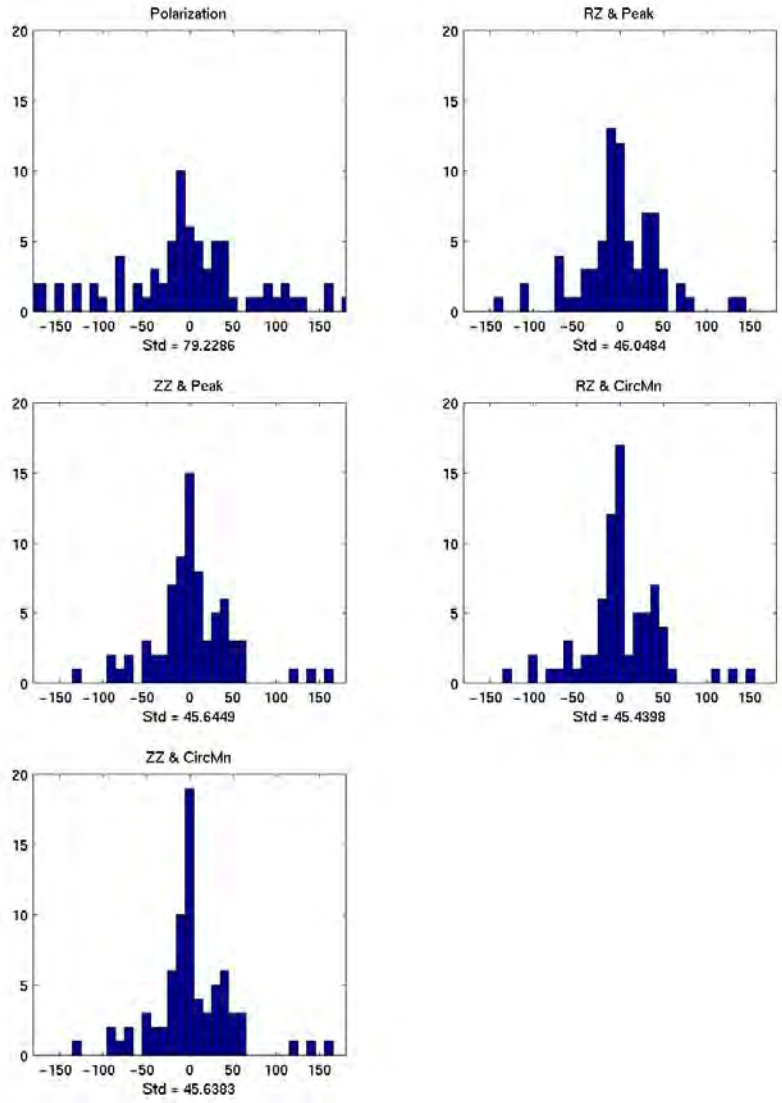

Figure 9. Distribution of azimuth residuals for known surface wave arrivals. Top left figure uses the algorithm that is currently implemented in Maxsurf. The other figures use the Selby/Chael method using different sets of parameters as discussed in the text. These preliminary results show that the error rate is reduced substantially by the new method.

CONCLUSIONS AND RECOMMENDATIONS

Surface wave research is continuing in the following areas:

- Surface wave dispersion models are being improved through:
  - A careful review of existing data, and continuing addition of new data.
  - Improvements to model types and constraints.
  - Development of interactive tools to improve speed and accuracy of analysis.
- An azimuth estimation technique for three-component data proposed by Selby is being implemented and tested. Initial results show substantial improvement.
- Surface wave measurement is being improved through
  - Phase-matched filtering enhanced by development of better dispersion models.
  - Development of path-corrected spectral magnitudes.
  - Development of methods to remove bad noise data.

ACKNOWLEDGEMENTS

We would like to thank Mike Ritzwoller, Anatoli Levshin and Nikolai Shapiro of the University of Colorado, Bob Herrmann of St. Louis University, and their coworkers for the use of their data in this project.

REFERENCES

Bassin, C., Laske, G. and Masters, G. (2000), The Current Limits of Resolution for Surface Wave Tomography in North America, *EOS Trans AGU*, **81**, F897.

Chael, E. P. (1997), "An automated Rayleigh wave detection algorithm," *Bull. Seism. Soc. Am.*, **87**, 157-163.

Kennett, B.L.N., E.R. Engdahl, and R. Buland (1995), Constraints on seismic velocities in the Earth from travel times, *Geophys J Int*, **122,** 108-124.

Laske G., and G. Masters (1997), A Global Digital Map of Sediment Thickness, *EOS Trans. AGU*, **78**.

Laske, G., G. Masters, and C. Reif, Crust 2.0 (2001), A new global crustal model at 2*2 degrees, http://mahi.ucsd.edu/Gabi/rem.html.

Levshin, A., J. L. Stevens, M. H. Ritzwoller, and D. A. Adams (2002), "Short Period (7s-15s) Group Velocity Measurements and Maps in Central Asia," Proceedings of the 24th Annual DOD/DOE Seismic Research Symposium, 17-19 September 2002 (this volume).

Perez, F. M., (2001), Surface wave dispersion about the New Madrid Region, MS thesis, Saint Louis University.

Selby, N.D. (2000), "Identification, Association, and Analysis of Rayleigh Waves in a CTBT Monitoring Context," Proceedings of the 22nd Annual DOD/DOE Seismic Research Symposium, 12-15 September 2000.

Smart, E. (1977), "A Three-Component, Single-Station Maximum-Likelihood Surface Wave Processor", SDAC-TR-77-14, Teledyne Geotech, Alexandria, VA.

Stevens, J. L., and D.A. Adams, (2000), Improved Surface Wave Detection and Measurement Using Phase-Matched Filtering and Improved Regionalized Models, Proceedings of the 22nd Annual DOD/DOE Seismic Research Symposium, 12-15 September 2000.

Stevens, J. L., D. A. Adams, and G. E. Baker, (2001a), "Phase-matched filtering with a one degree dispersion model" Proceedings of the 23rd Annual DOD/DOE Seismic Research Symposium, 1-5 October 2001.

Stevens, J. L., D. A. Adams and G. E. Baker (2001b), "Surface wave detection and measurement using a one degree global dispersion grid," SAIC Final Report to Defense Threat Reduction Agency, SAIC-01/1084, December.

Stevens, J. L. and K. L. McLaughlin (2001), "Optimization of surface wave identification and measurement," *Pure and Applied Geophysics*, **158**, no. 7, pp 1547-1582.

NEAR-FIELD AND REGIONAL MODELING OF EXPLOSIONS AT THE DEGELEN TEST SITE

Jeffry L. Stevens,[1] Norton Rimer,[1] Heming Xu,[1] G. Eli Baker,[1] John R. Murphy,[1]
Gevorg G. Kocharyan[2] and Boris A. Ivanov[2]

Science Applications International Corporation,[1] Institute for the Dynamics of the Geospheres[2]

Sponsored by Defense Threat Reduction Agency

Contract No. DTRA01-00-C-0050

ABSTRACT

The objective of this research program is to improve the capability to predict the seismic source characteristics of underground explosions in rock. This is being accomplished by development of improved dynamic failure models that are constrained by a large unique data set of near-field waveforms and parametric data from both US tests and historic Soviet explosions at the Degelen Test Site. In addition, we are analyzing regional seismic data along a seismic line located north of the Degelen Test Site that recorded data at nine stations spaced approximately evenly from the test site to a distance of about 100 km. This project is a collaborative effort between SAIC and the Russian Institute for the Dynamics of the Geospheres (IDG).

IDG is in the process of digitizing data from 25 nuclear tests at Degelen. The complete data set consists of 81 near-field waveforms recorded underground at shot depth and 124 near-regional seismic records. Most seismic records include both a vertical and radial waveform. This data set provides a rare opportunity to observe and model the seismic wavefield of the explosions as they evolve from the near field of the explosion out to regional distances. To date, IDG has digitized 75 near-field waveforms and 97 seismic waveforms from 16 events having explosive yields ranging from 0.3 kT up to 125 kT. We are in the process of defining the optimum procedures to model these data. The goal is to develop material models that are consistent with the data and have a realistic physical basis. Work to date at SAIC has focused on implementation and testing of improved numerical modeling procedures and simulation of near-regional data. We are testing acoustic fluidization as a physical mechanism for strength reduction in nonlinear explosion simulations. Near regional data is being modeled using wave number integration. We are also comparing the Degelen data with similar data from the Piledriver and Hardhat Nevada Test Site (NTS) explosions in granitic rocks.

To more easily compare these data, we scaled all of the Degelen and NTS near-field particle velocity records to the same explosive yield. These data were then organized based on yield-scaled pulse widths and pulse shapes. The NTS events, the seven Degelen explosions with yields greater than 18 kT, and some of the lower yield events, gave records with positive and negative pulse widths that strongly suggest free-field ground motion. The records from a few of the other, lowest yield explosions had unusual shapes that indicated probable contamination by nearby fault or block motion. There is considerable variation among the pulse amplitudes and shapes of the free-field data. Some of this variation, particularly the consistent differences in pulse width, indicates some interesting and potentially important differences in physical mechanisms operating for subsets of explosions. Peak velocities at a given scaled range from the free-field events vary by a factor of 4, while positive pulse widths from Degelen vary by a factor of 3. Even the widest pulses from Degelen explosions, however, with one exception, are narrower than the pulse widths from the NTS events. Three of the higher yield explosions from Degelen, with yields of 125, 100, and 23.7 kT, form a “narrow pulse set” that were numerically simulated without the use of any strength reduction mechanism. The other four higher yield Degelen explosions, with yields from 19 to 78 kT, and some of the lower yield events, form a “wide pulse set”, encompassing a gradation of pulse widths, that require the use of a gradation of strength reduction parameters in the numerical simulations. Simulation of the even wider pulses from the NTS explosions may be accomplished using different parameters in the same strength reduction model. The effects on pulse widths resulting from changes in Degelen site material properties due to earlier nearby explosions has yet to be quantified. The data set of near-field and regional waveforms will be delivered to the Center for Monitoring Research upon completion of this project.

OBJECTIVE

The main objective of this research program is to improve the capability to predict the seismic source characteristics of underground explosions in rock. This is being accomplished by development of improved dynamic failure models for hardrock that are constrained by a large unique data set of near-field waveforms and parametric data from both US tests and historic Soviet explosions at the Degelen Test Site. In addition, we are analyzing regional seismic data along a seismic line located north of the Degelen Test Site that recorded data at nine stations spaced approximately evenly from the test site to a distance of about 100 km. This project is a collaborative effort between SAIC and the Russian Institute for the Dynamics of the Geospheres (IDG).

RESEARCH ACCOMPLISHED

Introduction

Empirical and numerical models of explosion sources do a fairly good job of matching observed seismic signals, but the physical basis for the explosion source is still not well understood. In particular, numerical models of explosion sources developed using laboratory measurements of rock properties predict particle velocity pulse widths that are roughly a factor of 3-5 smaller than those observed near field in hardrock events such as Piledriver. The basic problem is that the strength of the rock measured in the laboratory is much larger than the apparent strength of the rock as determined from the near field ground motion.

A number of solutions to these problems have been proposed over the years, including the effective stress model (Rimer, *et al*, 1984), and various types of damage models. These models all have the characteristic that the material strength is reduced dynamically to a very low level when the rock fails. The effective stress model says that the weakness comes from water within the rock matrix, and that the broken rock in effect floats on water that is squeezed out of pores or fractures when the rock fails. Although there are questions about the realism of this physical model, it works fairly well to explain the near field waveforms. Figure 1 shows a comparison of the Piledriver waveforms with waveforms calculated using the effective stress model. The agreement is quite good, particularly at the closer two stations. Furthermore, when the Piledriver simulation was scaled to the appropriate yield and compared with other US explosions in granite (Hardhat and Shoal), agreement with the observed waveforms was also quite good (Stevens, *et al*, 1986).

Under a previous DTRA contract, SAIC worked together with the IDG and the University of Southern California (USC) to develop improved material models. IDG provided extensive pre- and post-shot measurements of material properties close to nuclear and chemical explosions. SAIC implemented the damage mechanics model for the growth and coalescence of cracks in brittle rocks under compressive loading which was developed by Prof. Charles Sammis of USC into our nonlinear finite difference codes and then used this model to simulate the observed explosion damage and a small set of near field waveforms provided by IDG. Since the Sammis damage model does not predict what happens to the rock after unstable brittle failure occurs, we introduced a friction law model post-failure. However, realistic values of friction did not provide enough strength reduction to match the near field data. To match the data, the coefficient of friction must be dropped to very low values (as low as 0.02) for rubbleized rock, but this again leaves the question of what physical mechanism could be responsible for these very low values and corresponding low strength. See Rimer *et al* (1999) for the results of this work.

A possible answer initially proposed by Melosh (1979) is “acoustic fluidization”. The physics behind this mechanism is that there is a complex dynamic acoustic wavefield that causes high frequency vibrations in the broken rock. These vibrations cause rapidly changing regions of high and low normal stress, and remove the frictional normal stress from parts of the rock as it moves. Consequently parts of the rock are not confined by the frictional stress and in effect have much lower strength. Acoustic fluidization has been used to explain other phenomena such as landslides and craters (Melosh and Ivanov, 1999), which have been similarly difficult to explain because of anomalously low apparent friction.

Analyses of Degelen Near Field and Near Regional Seismic Data

The numerical modeling component of this project is being constrained by a much better data set than has been available in the past, including near field waveforms from both US nuclear tests and the testing program of the

former Soviet Union. IDG has near field records from a number of nuclear explosions at the Degelen test site that are being digitized for this project. IDG will also be providing near source material properties measurements from these events. In addition, IDG has data from a seismic line located north of the Degelen test site that was maintained with consistent instrumentation for many years during the Soviet testing program. Figure 2 shows a map illustrating the location of the test sites and the seismic stations. The 9 seismic stations are spread out at approximately even intervals from the Degelen test site out to a distance of about 100 km. IDG is also digitizing seismic data from these stations for all of the events that have near field records. This provides a rare opportunity to observe and model the seismic wavefield of the explosions as they evolve from the near field of the explosion out to regional distances. The data that IDG has identified for digitization, and the data digitized as of this writing are listed in Table 1. Figure 3 shows waveforms from one of these explosions.

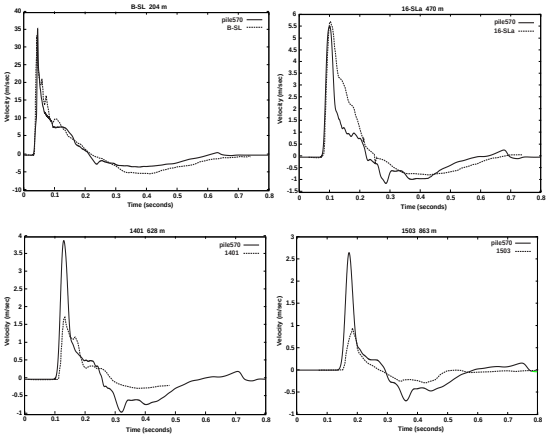

Figure 1. Particle velocity measurements at working point depth from Piledriver compared to numerical simulation pile570.

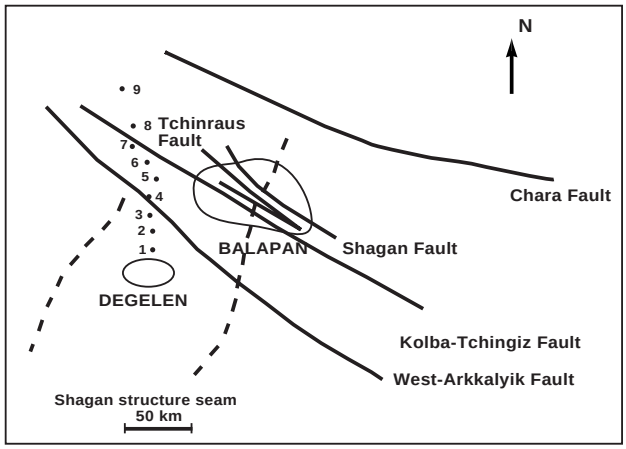

Figure 2. Map showing the locations of the former Soviet Degelen and Balapan test sites, faults, and seismic stations.

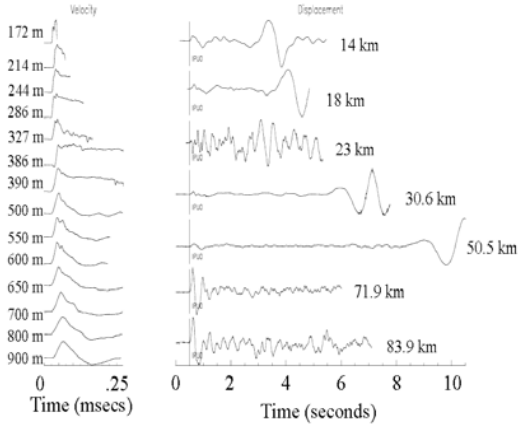

Figure 3. Near-field (left) and near regional seismic (right) waveforms from the 1987/07/17 event.

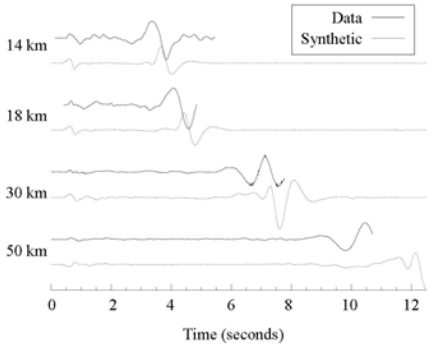

Figure 4. Synthetic and observed seismograms for the 1987/07/17 event. Synthetics were created using wavenumber integration and were low pass filtered at 2 Hz.

The near field records in Figure 3 show the evolution of the waveform from the nonlinear to linear regions. Unfortunately, the absolute times are not yet available for the records. The near regional records show the evolution of the waveform from 14 to 83 km. A strong Rg phase is present in several seismograms that persists to quite a long distance. Some of the records end before the start of the Rg phase and therefore do not show it. Figure 4 shows a comparison of synthetic and observed seismograms for three of the near regional waveforms from the 1987/07/17 event. The synthetic seismograms were constructed using wavenumber integration using the East Kazakh structure. The synthetic seismograms were low-pass filtered at 2 Hz. The persistence of Rg calls into question the explanation of Rg scattering as the source of Lg since that mechanism requires most of Rg to scatter into Lg within a few kilometers of the source.

Figure 5 shows a comparison between near-field peak particle velocity measurements from the Degelen explosions and from explosions at the US and French (Hoggar) granite sites. The solid curve gives peak velocities from the

Table 1. Degelen events with near field and/or seismic records and waveforms digitized. Total number of records including multiples are shown in parentheses. Explosion yield, m_b, and depth of burial are shown.

Date	Yield (kT)	m_b	Depth of Burial, (m)	No. of Near field records	Number Digitized	Distance Range, (m)	No. of Seismic Records	Number Digitized	Distance Range, (km)
1988/04/22	2.3	4.9	124	2	2	69-183	3	3 (11)	57-81
1988/11/23	19	5.4	204	4	3	280-475	9	9 (26)	14-83
1987/07/17	78	5.8	267	14	14	170-900	7	7 (23)	14.5-84
1987/10/16	1.1	4.6	82	4	4	55-132	8	8 (27)	4-64
1989/10/04	1.8	4.7	94	4	4 (5)	45-285	8	8 (25)	16-85
1981/07/17	9.3	5.16	146	3	3	115-310	8	8 (27)	15-80
1965/02/04	18/44	-	262	4	4	147-750	9	peaks	14-83
1964/05/16	23.7	5.6	253/ 262	4	4	150-600	9	peaks	13-79
1966/03/20	100	6.0	294/ 320	4	4	300-600	9	peaks	15-84
1966/02/13	125	6.1	297/ 343	4	4	350-600	9	peaks	14-79
1973/12/31	0.5	-	157	4	4(5)	110-230			
1974/12/16	3	4.8	126	4	2(5)	100-200			
1978/03/26	30	5.6	260	6	6	76-316			
1980/06/25	0.3	-	152	3	3	155-310			
1982/12/25	1.7	4.8	112	4	4	90-190			
1984/10/18	1.4	4.5	106	5	5	35-160			
1968/07/12		5.3	172	2		80-90			
1968/12/18		5.0	194	3		200-510			
1970/06/28		5.7	332	2		200-240			
1980/09/25		4.77		3		100-160			
1971/12/15		4.9	115				9		7.5-85
1987/05/06							9		13-83
1987/12/20							9		13-83
1988/10/18							9		11-77
1989/02/17							9		10-77

pile570 effective stress simulation. Almost all of the historic granite data, and the Degelen data received to date, lie on or below this prediction. The four shaded triangles in the left plot of Figure 5 are the peak velocities from the records shown in Figure 1, all from gauges emplaced at the Piledriver source depth of burial. The two gauges at larger ranges, that give relatively lower peak velocities, and most of the other gauges emplaced at depths above the explosion working point, were located on the opposite side of the source from the two closer-in gauges.

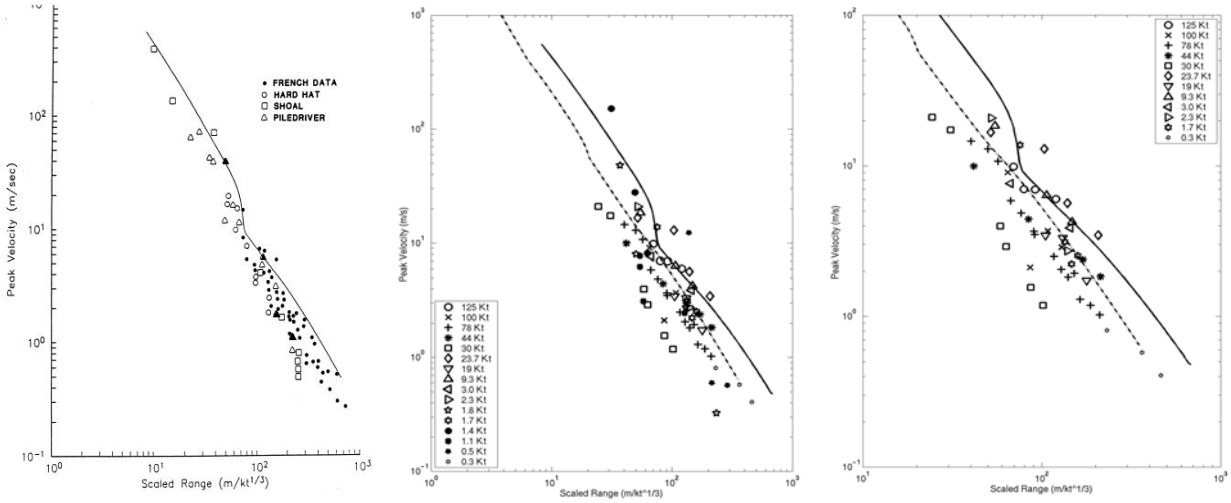

Figure 5. Peak particle velocity vs. scaled range for historic data from US and French explosions (left), for the 16 Degelen explosions digitized to date (center), and for the 12 Degelen events designated as showing free-field pulse shapes (right). The solid line is the prediction from the pile570 effective stress simulation shown earlier in Figure 1. The dashed line is the predicted peak velocity for the Degelen DE12 simulation.

The very first sets of digitized data received from IDG (plotted in Rimer, *et al*, 1999) did not include the Degelen explosions with relatively high peak velocities. Thus, these early Degelen peak velocities appeared at that time to be near the lower bound of the historic granite data. A Degelen simulation model, consisting of the Sammis failure model, followed by a large reduction in frictional strength for rubbleized rock elements, was developed to match the pulse widths from the first sets of digitized Degelen data. This model, labeled as DE12 in Rimer, el al (1999), is shown as a dashed curve in the two right plots of Figure 5. It provides a better fit on average to all of the Degelen particle velocity peaks than does the higher peak velocity pile570 simulation. However, this DE12 model, as will be shown below, is consistent with only a subset of the Degelen data received more recently from IDG.

We have carefully analyzed the near-field particle velocity pulses from the first 16 Degelen explosions of Table 1 and excluded the data from four of these events as more characteristic of localized fault or block motions than of free-field ground motion. Pulse widths from three of the four events in general show very wide positive velocity pulses with almost constant outward velocity plateaus extending from some point after peak velocity to the end of the digitized data. These excluded events have explosive yields of 1.1, 1.8, and 1.4 kT. The fourth event, having a yield of 0.5 kT, has two records that look like the block motions from the first three excluded events, and two at larger scaled ranges with very large positive pulses that do have more of a free-field shape, but have almost no negative velocities. Another event, with explosive yield of 0.3 kT, is borderline, with reasonable pulse shapes obtained at scaled ranges larger than any of the other Degelen data. These records, however, have scaled positive and negative pulse widths much larger than the rest of the data. We have included this event in the free-field data set shown on the right plot (with the enlarged scale) in Figure 5. This 12 event "free-field set" thus consists of the 8 explosions with yields greater than 9 kT and only 4 events with lower yields (3 kT or less). It is not surprising that a significant fraction of the data from the lower yield, and thus shorter wave length, explosions appear to be more contaminated by local block motion. This free-field set, apart from the data from the high velocity 23.7 kT explosion, and the very low velocity 30-kT explosion, shows considerably less scatter about the dashed DE12 prediction than did the full data set.

To more easily compare the individual Degelen "free-field" particle velocity pulses from explosions of different yields, we have cube-root-of-yield-scaled these data to the Piledriver yield of 62 kT. Since the quality of the particle velocity pulse data vary greatly between explosions and even between records from the same explosion, we reduced the data to be plotted from 56 particle velocity pulses to a somewhat more manageable best quality 34. These were further subdivided into a subset of 24 records from 8 explosions that have relatively wide positive pulses (shown in Figures 6) and a smaller subset of 10 records from 3 explosions that have narrower positive pulses (shown in Figure 7). In each Figure, the records have been ordered by increasing scaled range and have been plotted together with results at the same range from the DE12 simulation. Almost all of the omitted 18 records were from the larger wide pulse subset. Since the original digitized data did not contain the actual explosion zero times, the data in each plot has been time-shifted to correspond roughly to the arrival times of the numerical simulation. In the following discussions, individual particle velocity records will always be referenced by their scaled to 62-kT ranges and original explosive yields.

The DE12 model was designed to simulate the pulse widths from the first two explosions listed in Table 1 (2.3 and 19 kT) as well as a few of the records from the third (78-kT) explosion. All three of these free-field explosions were later categorized as belonging to the wide pulse subset. This simulation was also required to give a cavity radius and a Reduced Displacement Potential (RDP) consistent with general observations from the Degelen site. Agreement between simulated and measured positive and negative pulses was best at the 704 m range from the 19-kT explosion, but the measured positive pulse at the 741 m range (and other ranges) from the 78-kT explosion are somewhat narrower than those simulated. Only two partial records are available from the 2.3-kT explosion, with one of these, at 551 m, considerably wider than other explosion records at similar scaled ranges. As more digitized data were received from the 78-kT event, and still later from the other events of the data set, it became clear that there is a significant gradation of pulse widths within even the wide pulse subset.

Some of the wide pulse data exhibit a second positive pulse with either a second obvious peak or traces of a plateau similar to both the DE12 simulation and the data at 704 m from the 19-kT explosion, while others show no evidence of such a second pulse. As an example, for the 1.7-kT event, all four of the records shown in Figure 6 appear to give consistent shapes that include such a second pulse. The gauges from the closest-in and furthest-out of the four ranges, located near the emplacement tunnel, give positive pulse widths in good agreement with DE12, while the middle two gauges, at substantially different azimuths from the others, give narrower pulses. In contrast to these

data from the 1.7-kT event, most of the records from the 78-kT and 44-kT explosions exhibit little or no second pulse.

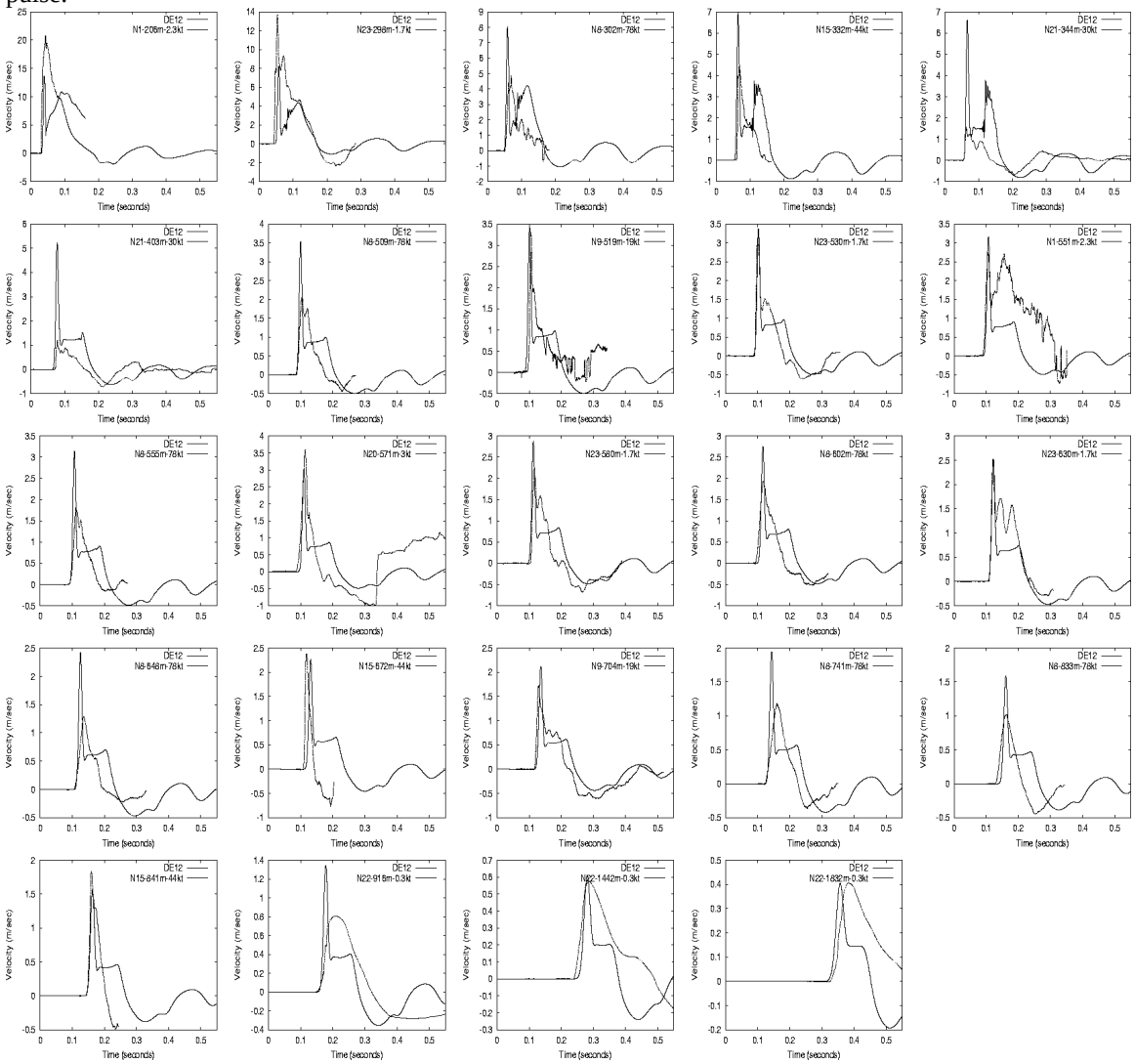

Figure 6. Particle velocity pulses (scaled to Piledriver yield) from the "wide pulse" Degelen data subset compared with the results of simulation DE12 (the solid curves).

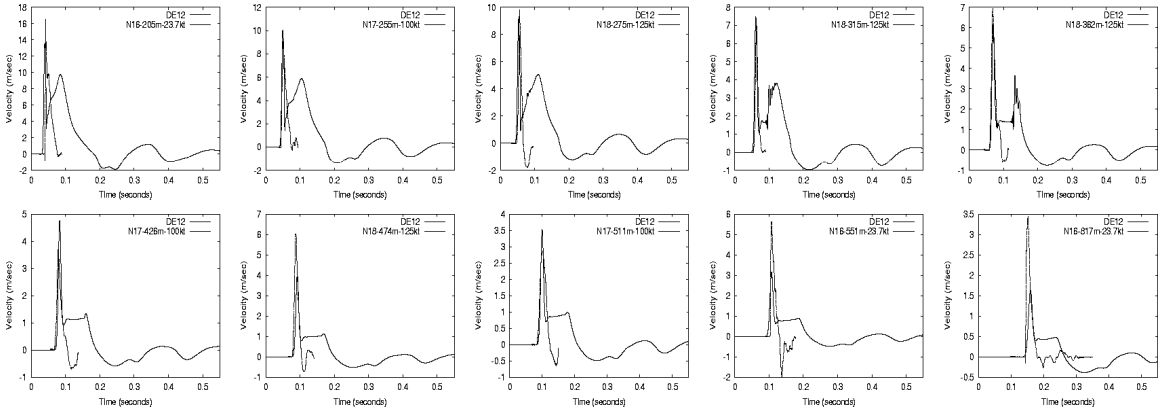

Figure 7. Particle velocity pulses from the "narrow pulse" data subset compared with the results of DE12.

It is of course possible that some or all of the recorded second pulses are either the result of some systematic errors in gauge response or perhaps indications of some non-free-field response of the rock at these sites. In the absence of convincing evidence, we are choosing to treat these records as free-field. This leads to the hypotheses that the material models required to simulate the records from even just the wide pulse subset, or more likely the material constants within any one particular set of material models, may be different for each explosion site.

The particle velocity records from the three "narrow pulse" explosions shown in Figure 7 give somewhat different peak amplitudes, but very similar positive pulse shapes. In general, these records do not exhibit the two pulse structure apparent in much of the wide pulse subset. The majority of these plots also show narrow negative pulses, although at least one record from each of the three explosions does not show such a negative.

With one exception, every positive pulse shown from the 8 explosions in Figure 6 is much wider than any of the pulses from the three explosion "narrow pulse" subset shown in Figure 7. This exception is the 44- (or 18-) kT explosion that does not fit very well in either the wide or narrow subsets. The 44-kT explosion has one wide pulse, at the smaller range of 332 m, one narrow pulse, at the middle range of 672 m, and a pulse slightly narrower than the wide pulse subset at the larger range of 841 m. We have chosen to place this explosion in the wide subset for two reasons. First, the narrow pulse explosions of Figure 7 also tend to show very narrow negative pulses, while the most complete negative pulse record from the 44-kT event, at 672 m, is wider than those of Figure 7. Second, if we use the smaller of the two explosive yields given to us for this event, and scale up to 62 kT, positive and negative pulse widths increase by about 35 percent from those shown in Figure 6.

The two very low amplitude records from the 30-kT explosion that are shown in Figure 6 (and those at smaller ranges that are not shown) have pulse shapes and pulse widths similar to others of the wide pulse subset. In the absence of specific site material properties for this and other explosion sites, we have no satisfactory explanation for the low peak amplitudes from this explosion. Depth of burial is consistent with those for the other large explosions of Table 1 that were at sites described as in granite. Only the narrow pulse 100- and 125-kT explosions, at sites described as in quartz porphoryte, were more deeply buried. The m_b values given in Table 1 also do not provide any confirmation of the low near-field particle velocity amplitudes from the 30-kT event.

Figure 8 shows comparisons between records at three of the four ranges shown earlier from Piledriver (the solid curves) and some of the records from similar scaled ranges from wide pulse Degelen explosions, scaled to 62 kT. Representative records from the wide pulse Degelen explosions are not available at scaled ranges approximating the 207 m range of the first (and widest) Piledriver particle velocity record. Near the 470 m range, the Piledriver positive and negative pulses are clearly much wider than those from Degelen explosions, although the general shapes of the Piledriver and Degelen positive pulses are quite similar.

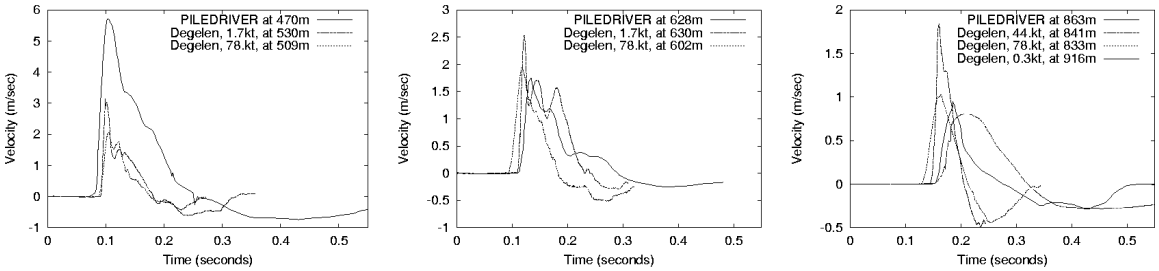

Figure 8. Comparisons between particle velocity pulses at three ranges from Piledriver and from Degelen wide pulse explosion records (scaled to 62 kT) at nearby scaled ranges.

Differences between the records from the US and Degelen granite sites are less obvious at the two larger ranges. We have seen earlier that the peak amplitudes from Piledriver are small at these two ranges relative to those that would be predicted from the two closer-in records. At 628 m, the Piledriver record looks very similar to the record from the 78-kT event out to a time of roughly 0.2 seconds (if the arrival time of the 78-kT record is shifted to coincide with the Piledriver arrival). Near 0.2 seconds, the Piledriver positive pulse at 628 m begins to stretch out in time, with an almost constant velocity plateau visible on this record, giving a much later time zero crossing and a wider negative pulse than both the Degelen records. At this range, the record from the 1.7-kT explosion shows a steeper rise to peak, multiple peaks, and a significantly wider positive pulse than the Piledriver record, at least until

that record begins to stretch out in time. The Piledriver record at 863 m also shows such a stretching, but not the constant velocity plateau recorded at 628 m. The record from the 78-kT event is in good agreement until this stretching begins.

The particle velocity comparisons made near the 863 m range illustrate the large gradation in pulse shapes and pulse widths recorded from Degelen "wide pulse" explosions, with the 44-kT record showing a steeper rise, a higher peak, a narrower pulse, than the 78-kT record, but a similar negative peak. The narrowest of the three very wide pulses obtained from the scaled 0.3-kT explosion is wider than the Piledriver record at a slightly smaller scaled range. When these particle velocity records are time-integrated, only the Piledriver records at the two closest-in ranges (207 and 470 m) give peak displacements significantly larger than all of the Degelen records at comparable scaled ranges. Peak displacement from the 1.7-kT explosion is similar in magnitude to that from Piledriver near 628 m.

We next examine the digitized near regional seismic records. The 8 explosions with digitized seismic data include all 3 of the narrow pulse subset. The primary purpose of this analysis of the 8 largest Degelen explosions for which we have such data is to determine whether or not the differences in pulse widths observed for the near-field data are observable at larger, seismic ranges. Based on the near-field observations, we would expect the seismograms at larger ranges from the "narrow pulse" subset of explosions to have relatively smaller amplitudes.

We first empirically determine a distance correction for the 8 explosions. We determine a slope of log(Amplitude) vs. distance for each event, and then find the average of the slopes, weighted by the number of points contributing to each curve. The distance correction is approximately -.014 of log(amplitude) in mm per km. The data for each explosion is then corrected to a 10 km distance. Assuming $\log_{10}(\text{amplitude})=B\cdot\log_{10}(\text{yield})+C$, these data are used to estimate a B of 0.76 and a C of -1.76. These values do not change significantly if we determine them separately from the narrow and wide pulse data subsets. From just the wide pulse data we obtain B=0.83 and C=-1.8, and from the narrow pulse data we obtain B=0.79 and C=-1.7. Figure 9 shows log amplitude versus distance, corrected for distance and yield using the values of B and C above obtained for all the seismic data. Figure 10 shows the mean values for each event, of the data in Figure 9. There is no apparent difference in near regional amplitude between the explosions with narrow and those with wide velocity pulses in the near field.

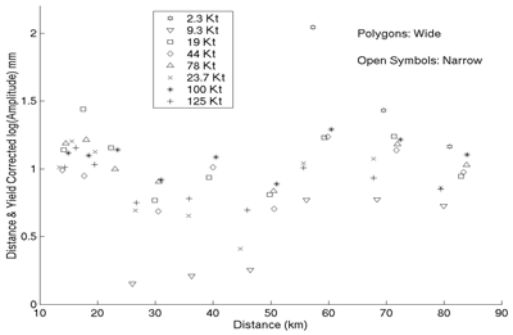

Figure 9. Distance and yield corrected log amplitudes of vertical seismograms recorded from 13 to 84 km. Open symbols (+, *, and x) are used for events that have narrow velocity pulses in the near field, and polygons are used for events that have wide pulses.

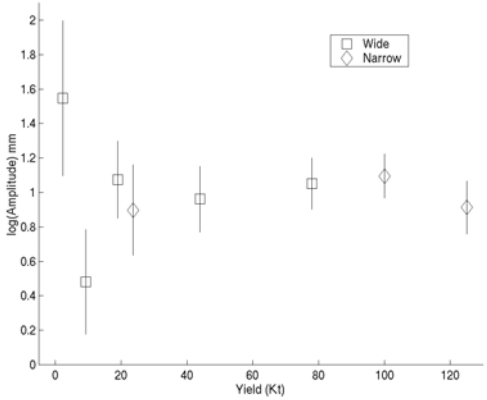

Figure 10. Mean values with one standard deviation confidence intervals for each event for the data shown in Figure 9.

Numerical Modeling of Explosions

The near and far field data from US and Degelen explosions have provided a set of constraints to test out several competing mechanisms for both the "failure/rubblization process" and the post-failure "strength reduction" process. The 3 strength reduction mechanisms and 2 rock failure mechanisms given in Table 2 have been emphasized, first for Piledriver, and then for the wide pulse Degelen events. Here, Yield/Failure (YF) refers to a model in which the yield and failure surfaces coincide, a no bulking flow rule, and a failure surface based on laboratory tests on fractured granite. Finite plastic work is required for rubblization and a standard friction law used for rubblized rock. In the Shock Damage (SS) model, strength reduction to a damaged friction law failure surface is based on the shear strain in the element, mimicking the lateral stretching of a rock element during the divergent outward motion. Parameter studies have been completed using both competing failure/rubblization processes together with each of

the strength reduction mechanisms that are appropriate. (Pore pressure buildup in the effective stress process is incompatible with the crack opening in the Sammis model.) Reasonable simulations of the Piledriver data (particle velocities, cavity radius, RDP) have been obtained for each combination denoted by the letter P in Table 2.

Table 2. **Combinations of failure/rubblization processes and strength reduction mechanisms for which simulations of Piledriver (P) and Degelen wide pulse explosions (D) have been accomplished.**

Strength Reduction Mechanisms/ Failure/Rubblization Processes	Shock Damage (SS)	Acoustic Fluidization (AF)	Effective Stress (EF)
Sammis Damage Mechanics (SA)	P, D	P, D	
Yield/Failure (YF)	P, D	P, D	P

Our goal was to use parametric simulations of the near and far field data from Degelen events to further evaluate and perhaps discriminate between these competing physical mechanisms. Our preliminary calculations of the 3 narrow pulse explosions to date show that the best fits to both the positive and negative pulses are obtained using the YF model and no strength reduction model. This best fit to date of the narrow pulse velocity data also gives a cavity radius of 29.0 m, just within the 28-36 m range of the Degelen observations. A static RDP of about 6,000 m^3 and a peak RDP of roughly 7500 m^3 were computed from this simulation. This computed peak RDP was only slightly larger than the peak RDPs that were obtained from the particle velocity data from narrow pulse explosions. All Degelen calculations were made using an overburden pressure of 50 bars, much smaller than the 120 bars for the deeper Piledriver event. Use of the larger overburden pressures consistent with the 35–75% larger depths of burial of the narrow pulse explosions would be expected to reduce the amplitudes of the simulated RDPs somewhat.

The parametric calculations made to date for the 9 wide pulse explosions indicate that each of the 4 model combinations in Table 2 can be made to fit some of the features of the Degelen data. We have ordered the best simulations with each of the four model combinations from best overall fit to worst fit as follows: 1) SA-SS, 2) YF-AF, 3) SA-AF, 4) YF-SS. Note that we have had more extensive experience with the effects of parametric changes in the SA-SS models dating back to Rimer, *et al* (1999) and the DE12 simulation. However, our best efforts so far have not resulted in simulations using the other model combinations that provide as good a fit to as many (but certainly not all) of the wide pulse records as did the SA-SS combination. Figure 11 shows comparisons between the simulated and measured particle velocity pulses from the SA-SS best fit. Note that in comparison with the DE12 results shown earlier in Figure 6, the peak velocities are smaller, and positive pulses are narrower, thus greatly increasing the quality of the match to much of the Degelen wide pulse data set. This was accomplished by a single, but significant, change in the DE12 parameter set (Table 6-1 of Rimer, *et al*, 1999), i.e., reduction of the slope in the linear shear modulus reduction vs. damage parameter relation from 400 to 300 kb. This parameter change results in less reduction in shear and bulk moduli near the cavity, less dilatant behavior near the cavity, less P-wave velocity reduction near the cavity, and thus a weaker (narrower), dilatant, second positive pulse, a smaller static RDP of 11,000 m^3, and about a 10% larger final cavity radius (34.5 m).

The model combinations made using an improved version of the acoustic fluidization model provide best fits that are clearly superior to the best fit we could get so far using the YF-SS model. This version incorporates the "block model" described in Melosh and Ivanov (1999) which represents the motion of a system of oscillating blocks as a viscous motion with an effective kinematic viscosity whenever shear stress is larger than the Bingham limit. This shear stress dependence replaces the dependence of the frictional strength upon kinetic energy in our earlier implementations of AF.

CONCLUSIONS AND RECOMMENDATIONS

IDG is in the process of digitizing data from 25 nuclear tests at the Degelen test site. The complete data set consists of 81 near field waveforms recorded underground at shot depth and 124 (unique) near regional seismic records. IDG has digitized 75 near field waveforms and 97 seismic waveforms (including multiple records of the same signal), and will complete digitization of the remainder over the duration of this project. The data set of near field and regional waveforms will be delivered to the Center for Monitoring Research upon completion of this project.

We are in the process of modeling this data. The goal is to develop material models that are consistent with the data and have a realistic physical basis. Work to date has focused on implementation and testing of improved numerical

modeling procedures and simulation of near regional data. We are testing acoustic fluidization as a physical mechanism for strength reduction in nonlinear explosion simulations. Preliminary results are promising, but additional work is required to improve the realism of the models. During the next year, we will continue this modeling effort. Near field data will be modeled with our nonlinear finite difference code as described in this report. Near regional data will be modeled using wave number integration. We plan to also look at observed teleseismic amplitudes from explosions with wide and narrow near field velocity pulses to see whether these correlate.

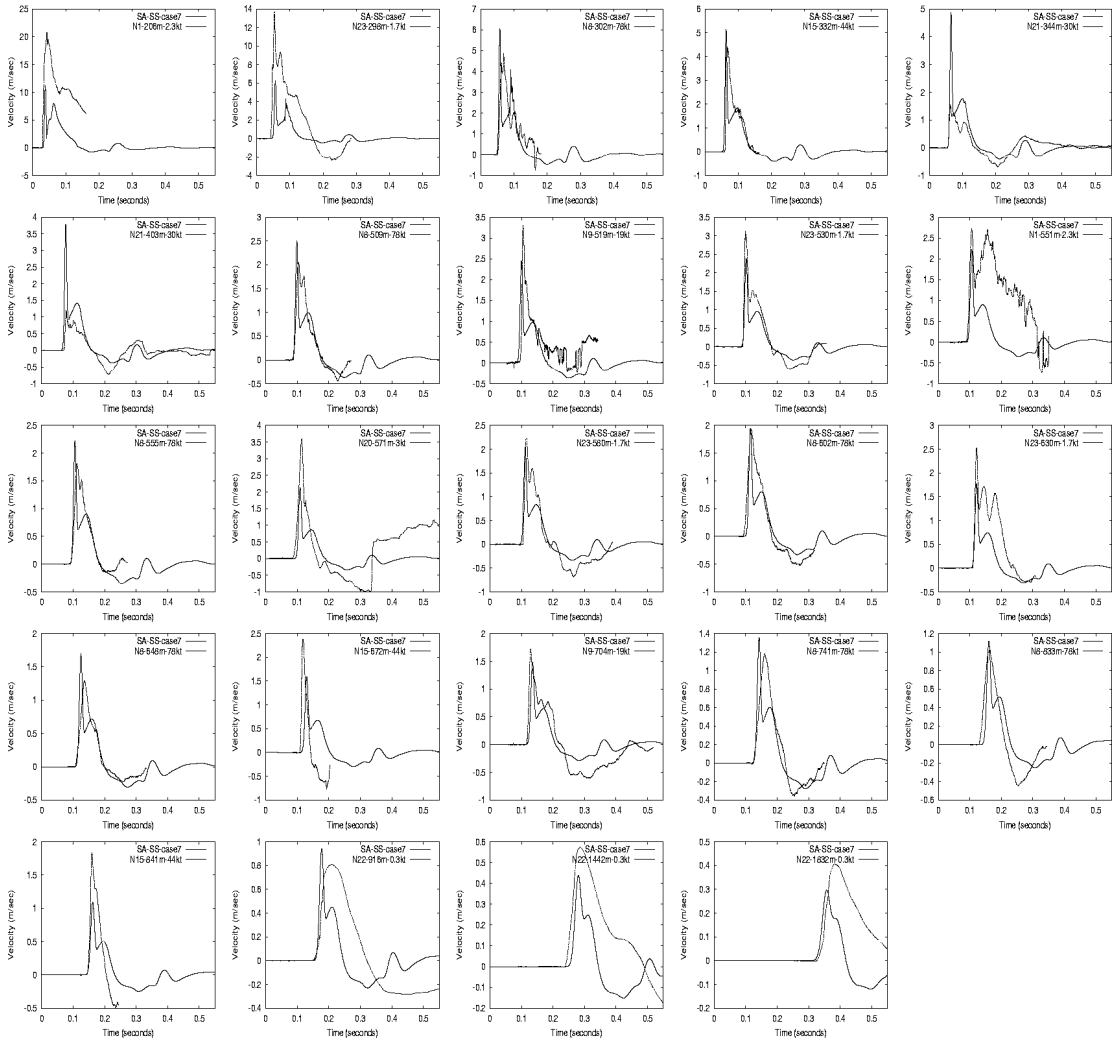

Figure 11. Comparison between particle velocity pulses from the wide pulse Degelen subset and the results of the best fit simulation using the SA-SS model combination (the solid curves).

REFERENCES

Melosh, H.J. (1979), "Acoustic Fluidization: A New Geologic Process?," *J. Geophys. Res*., **84**, 7513, December.

Melosh, H.J., and B.A. Ivanov (1999), "Impact Crater Collapse," *Annual Rev. Earth Planet Science*, **27**, pp385-415.

Rimer, N., S. M. Day, G. A. Hegemier, H. E. Read, S. K. Garg, and S. Peyton (1984), "Effect of Pore Fluid Pressure on Explosive Ground Motions in Low Porosity Brittle Rocks," DNA-TR-85-245, July.

Rimer, N., J.L. Stevens, J.R. Murphy, and G.G. Kocharyan (1999), "Estimating Seismic Source Characteristics of Explosions in Hardrock Using a Micro-Mechanical Damage Model," Maxwell Technologies Final Report MTSD-DTR-99-16423, July.

Stevens, J. L., N. Rimer, and S. M. Day (1986), "Constraints on modeling of underground explosions in granite," S-CUBED annual report, AFGL-TR-86-0264, SSS-R-87-8312, October.

SEISMIC AND INFRASOUND DATA AND MODELS AT NEAR-REGIONAL DISTANCES

Brian W. Stump, Sara Mihan McKenna, Christopher Hayward and Tae-Sung Kim

Southern Methodist University

Sponsored by Air Force Technical Applications Center

Contract No. DSWA01-98-C-0131

ABSTRACT

The Korean Peninsula provides a unique laboratory for studying regional seismic and infrasound wave propagation. Numerous broadband seismic stations in the region and a variety of natural and man-made sources provide opportunities for characterizing wave propagation and source effects. The region includes two arrays, KSAR and CHNAR (the seismo-acoustic array near Chulwon operated by Korea Institute of Geosciences and Mineral Resources and Southern Methodist University). The purpose of this research is to investigate how array and network data with ground truth can be used in characterizing source and propagation path effects for seismic and infrasonic waves. Ground truth information plays a critical role in the interpretation of signals and has included near-field observations from industrial blasts, newspaper accounts of accidental explosions, blast design information for mine explosions and near-field observations of earthquakes. Mining blasts in the Republic of Korea are constrained to about 2000 kg. Combining design pattern information and near-source observations illustrates that peak amplitudes of regional seismic phases are greatly reduced from those expected for a contained single-fired explosion. At CHNAR an average of three to four seismic events and one seismo-acoustic event are observed per day.

Analysis of the infrasound data suggests that there are many more infrasound signals than seismic. For example, during a one-week time period over 400 infrasound events were recorded. These data motivated an in-depth analysis of the lonesome infrasound signals. Based on infrasound signals that accompany seismic signals, we believe that many of the infrasound sources are within 200 km of the array (near regional). We have modeled these arrivals using an infrasonic modeling program (InfraMAP) employing three data sets: Horizontal Wind Model and Mass Spectrometer, Incoherent Scatter (HWM/MSIS) data, hourly meteorological data, and daily mean meteorological data. Hourly data were broken down into six hourly blocks at Hour 0, Hour 6, Hour 12 and Hour 18 and obtained by weather balloon from OSAN Air Force Base, 131 km to the south of CHNAR. MSIS/HWM models predict no arrivals closer than 250 km during this time period. Mean daily data predict arrivals at around 18-20 km and actual hourly data predict arrivals almost on top of the source, as close as 0.5 km away. Comparing back azimuths observed with back azimuths predicted by infrasonic ray path modeling, we note that the hourly data accurately predict the arrival back azimuths. This leads us to believe that hourly meteorological data are of immense importance when considering infrasonic arrival predictions for near-regional distance.

OBJECTIVE:

The seismo-acoustic array, CHNAR, in the Republic of Korea was installed in the far north of the Republic of Korea for the purposes of determining the numbers and types of signals that are observed on both seismic and infrasound sensors (Stump *et al.*, 2000). Southern Methodist University (SMU), in cooperation with Korea Institute of Geosciences and Mineral Resources (KIGAM), jointly operate the array and conduct research on the resulting data. This cooperative work began with a preliminary study of events (Figure 1a) that has been summarized by Stump *et al.*, 2001. This work suggested that the array recorded some three to five seismic and one seismo-acoustic event each day. As illustrated in Figure 1a, the events clustered into groups. Nearly all the seismo-acoustic events were found to occur during working hours indicative of man-made causes. Additionally, as Figure 1a suggests, many events in both North and South Korea were found to be within 200 km of the array. This range is not fully understood from theory as typical infrasound propagation models predict few if any arrivals in this distance range.

These early results motivated supporting work to gather ground truth information for sources that produced signals at CHNAR. A number of procedures were undertaken to establish the ground truth, including the acquisition of near-source ground motions from mining events, documentation of construction blasting through video records or engineer notes, press documentation of accidents, and near-source ground motion records of earthquakes. Figure 1b illustrates some of this ground truth information with its spatial distribution across the Korean Peninsula.

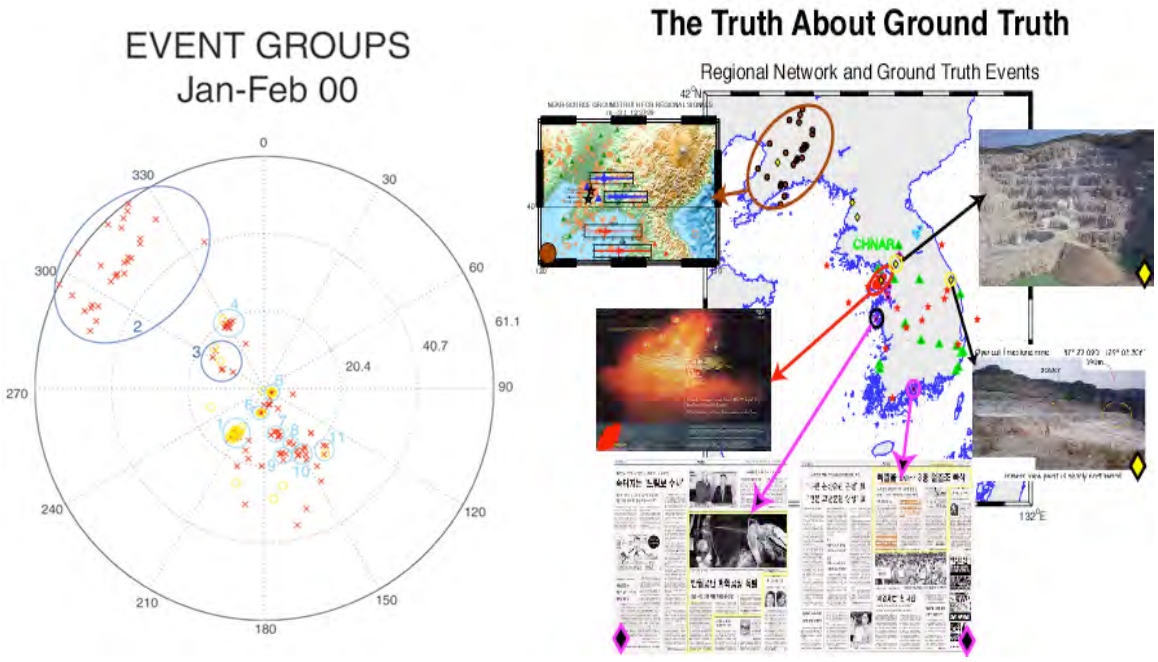

Figure 1a: Preliminary locations of seismic (red x) and seismo-acoustic (yellow o) events located using data from CHNAR (Stump *et al.*, 2001). The locations are plotted as a function of back azimuth and L_g-P time (s) that can be converted to range (km) by multiplying by 8. 1b: Examples of ground truth for events recorded at CHNAR. Earthquake – brown circles; Construction blasts – red squares; Accidental explosions – black and purple diamonds; Mining explosions – yellow and black diamonds.

Based upon these preliminary results, a comprehensive study of seismo-acoustic events has been undertaken by Il-Young Che at KIGAM. All the seismo-acoustic events from this study for the calendar years 2000 and 2001 are documented in Figure 2. In each year, the events in both the north and south cluster into groups as found in the preliminary two-month study. There is an apparent increase in the number of seismo-acoustic events in North Korea during 2001.

The event locations in Figure 2 are based upon the seismic arrival times and back azimuth estimates using the data from all the stations of the KIGAM network. Preliminary locations are completed automatically, but an analyst reviews all final locations. There are many times more seismic-only events that are not plotted in this figure. We also note that there are many more infrasound alone signals than seismo-acoustic signals.

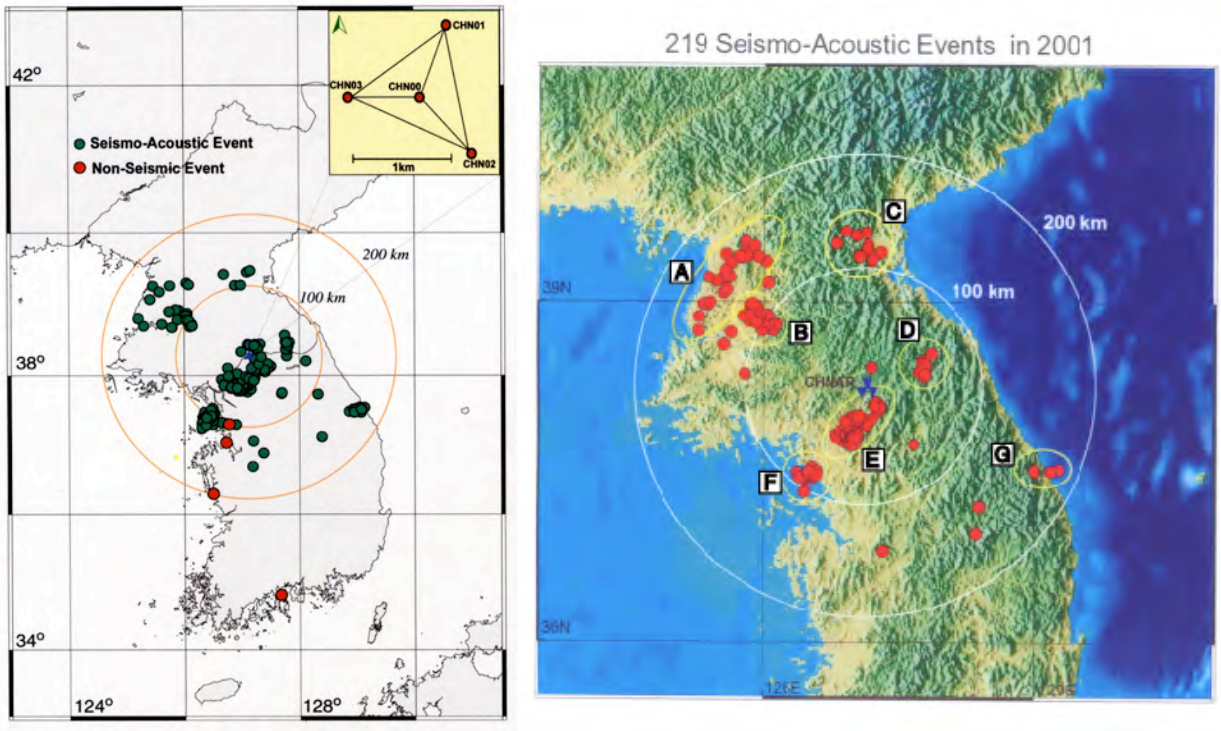

Figure 2a: Seismo-acoustic events for 2000. 2b: Seismo-acoustic events for 2001. Event location is based upon arrival times and back azimuth estimates using data from all the seismic stations in the KIGAM network. Based upon the location, a search is made for a complementary acoustic signal at CHNAR in order for the event to be designated as seismo-acoustic (Figures from I.-Y. Che, KIGAM).

The events plotted in Figures 2a and 2b are all within 200 km of CHNAR. The 2001 data are divided into seven groups for purposes of analysis and are designated Groups A-G in Figure 2a.

RESEARCH ACCOMPLISHED

Ground Truth

We illustrate ground truth information from some of the event groups in Figure 2b.

Seismo-acoustic events in Group E southwest of CHNAR represent a number of hard rock mines in South Korea. Ground truth information was acquired from several of the mining shots in this region. As noted earlier, most of these shots use modest amounts of explosives and are delay-fired. The blast design information and in-mine seismic measurements for one of these events are reproduced in Figure 3. In this shot, a total of 2980 kg of explosives was detonated using 17- and 42-ms delays.

We produced an impulse time series representative of this delay pattern. The spectrum from this model is compared to the double integrated near-source accelerogram indicating that the impulse time series is reflective of the source. The model and near-source displacement spectra indicate that the regional amplitudes from the delay-fired explosion are reduced in size by a factor of 10-100 from what would be expected from a 2980-kg single-fired explosion. The data at CHNAR from this explosion are also included in the figure illustrating that the signal is just above

background noise. Both the limited amount of explosives and the delay-fired pattern may be responsible for the small magnitudes of seismo-acoustic events observed in South Korea. This result suggests that unless the blasting practice is well understood, one should not use waveforms from delay-fired explosions to constrain the relationship between magnitude and amount of explosives.

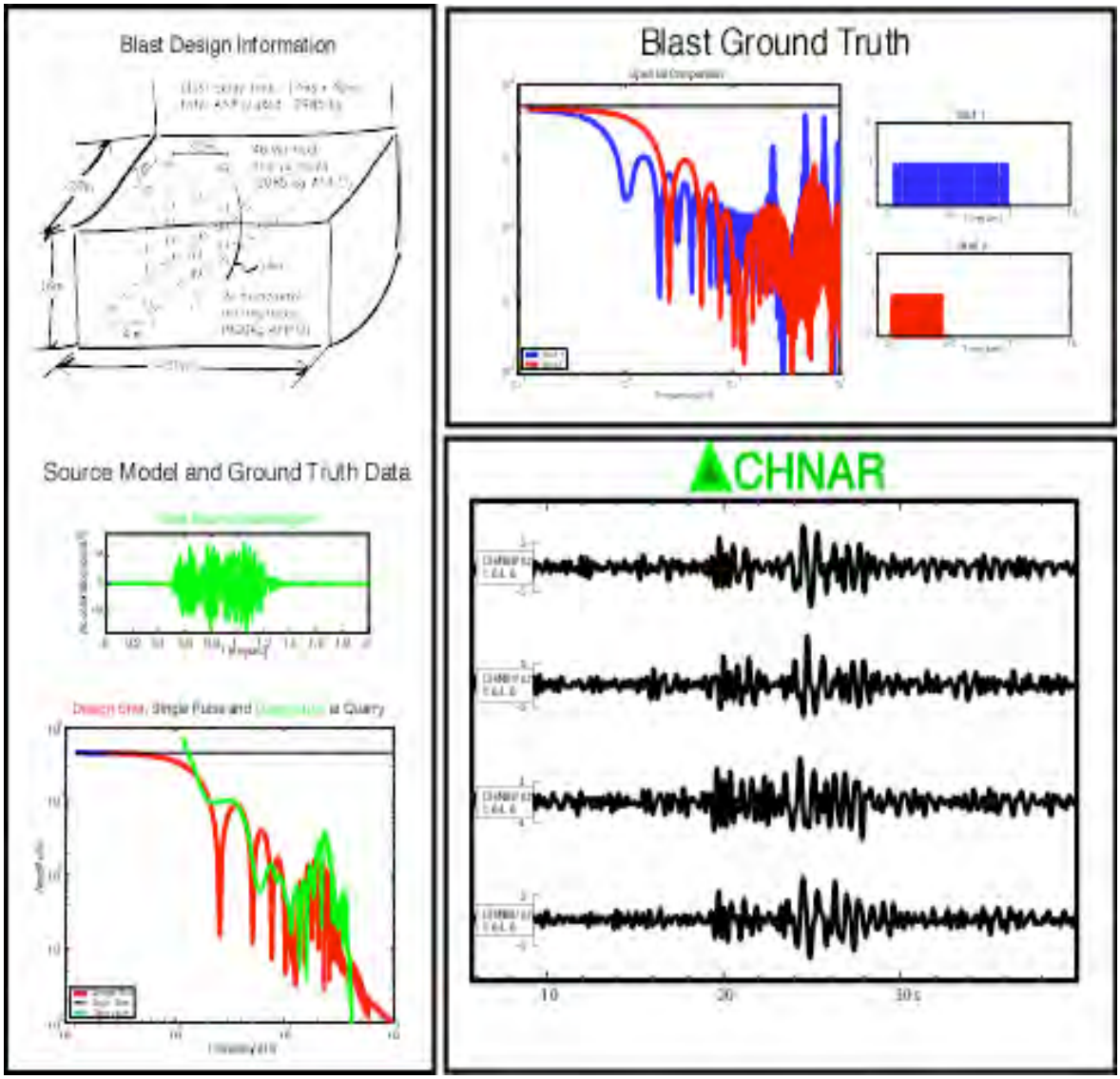

Figure 3: Ground truth from a mining explosion in Group E. The ground truth includes the amount of explosives, timing and near-source accelerogram records. The impulse time series is compared in the frequency domain to the double integrated accelerogram. The data recorded at CHNAR for this event are also included and indicate the relative small size of the seismic signals.

Group F events are associated with construction at the new international airport near Seoul. We conducted a limited study of a collection of seismo-acoustic events from the new airport. A comparative study of the waveforms from Group F was undertaken and provided precise L_g-P times that were used to estimate distance from CHNAR. This distance estimate was combined with seismic and infrasound back azimuth estimates to produce the event locations reproduced in Figure 4. Two event clusters were identified and the seismic waveforms were sorted into these two groups and compared. The similarity of high-frequency waveforms (8-16 Hz) in each group suggests that waveform coherence may be useful in comparing near-by events. These results also are suggestive of the importance of

infrasound back azimuth estimates for improved event location. The difference in waveforms between the two groups may be reflective of the different propagation path effects. Alternatively, the differences may reflect blasting practices in the two regions.

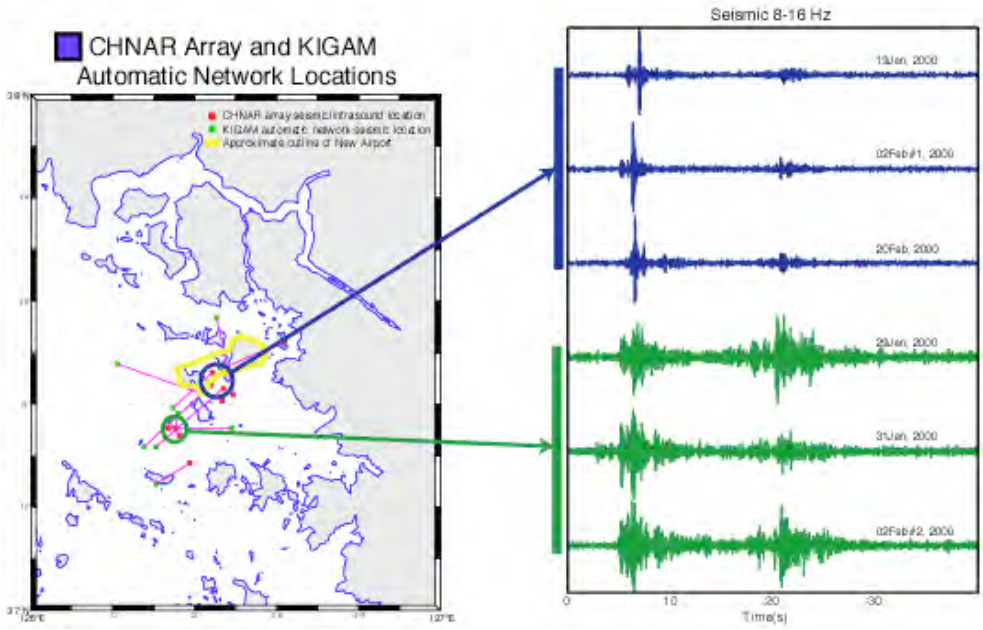

Figure 4: Seismo-acoustic event locations at the site of the new international airport near Seoul (Group F in Figure 2b). The events are divided into two groups (green and blue circles). The events from each group produce similar waveforms in the 8- to 16-Hz band.

Infrasound signals that accompany the seismic signals from the airport construction are illustrated in Figure 5. Two distinct source regions associated with the new construction were identified by the seismic data, and the accompanying infrasound signals are color coded to match. Infrasound signals from five events are shown in Figure 5. There is some indication that the infrasound waveform is characteristic of the source region as well. The infrasound signals for one event observed across CHNAR are plotted below right and illustrate high signal correlation in the 1- to 5-Hz band.

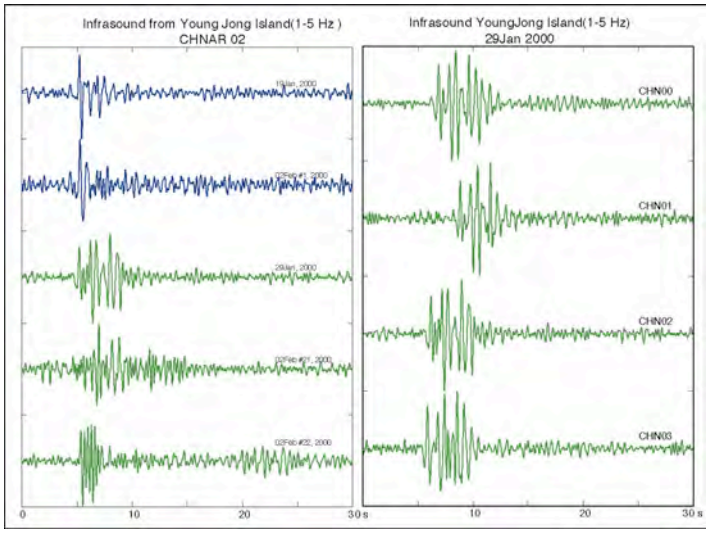

Figure 5: Single sensor infrasound signals from five of the seismo-acoustic events identified in Figure 4 are displayed in the left panel (Group F in Figure 2b). The color of the waveform corresponds to the event groups identified earlier. Signals recorded across the array for one of the events are reproduced in the right panel.

Infrasound Modeling

The seismo-acoustic array at CHNAR, South Korea, was used to evaluate all lone infrasonic arrivals for one week each in October and November 1999, and February, April, June, August 2000. Each infrasound arrival was processed for azimuth, time, phase velocity, and "type". Typically, there are one to two seismo-acoustic events per day observed. In contrast there are between 10 and 100 times more infrasound-only signals. The azimuth and time of arrival for these signals is summarized in Figure 6. The vast majority of events during the same 24-hour period occur during daylight hours suggesting man-made origin. The azimuths from which the signals propagate vary from month to month. The relatively high-frequency content (4-5 Hz and above) as well as the short signal duration and seismo-acoustic arrivals suggests short propagation path effects of less than 200 km.

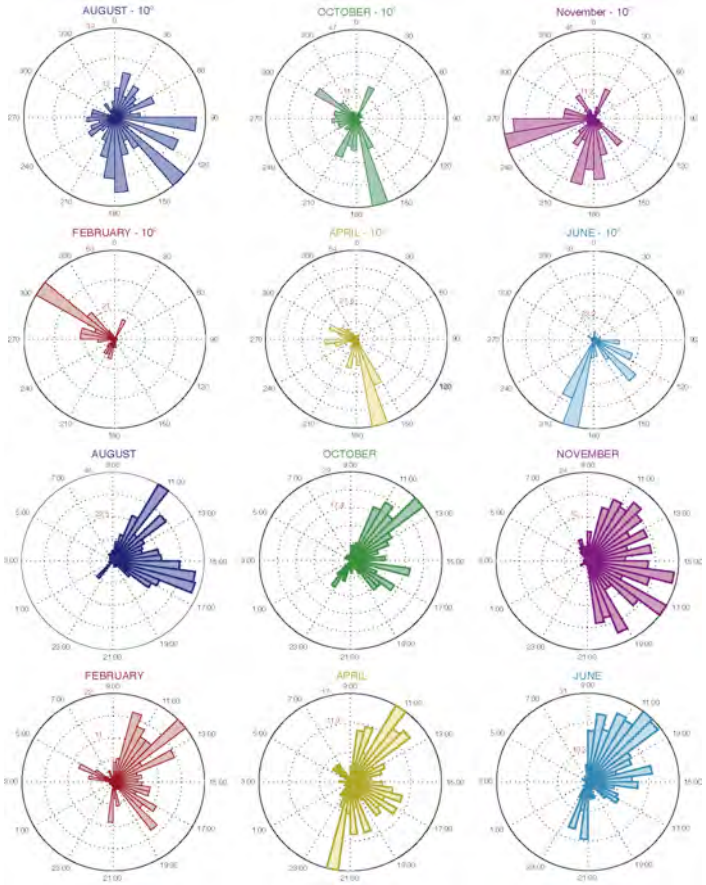

Figure 6: Summary of event back azimuth (top panel) and event arrival time (bottom panel) for the lonesome infrasound signals from August, October, November, February, April and June

An infrasonic modeling package, InfraMAP (Norris and Gibson, 2001), was used to model ray path arrivals with standard seasonally averaged atmospheric profiles. Most atmospheric modeling is done using HWM (Horizontal Wind Model) and MSIS (Mass Spectrometer, Incoherent Scatter) data sets. HWM and MSIS are comprehensive empirical global models of winds and temperatures averaged over each season for decades. Most often, the ray paths to be modeled are "tele"-infrasonic, rays that travel through and turn in the thermosphere, or the upper 20 km or so of the atmosphere. As the thermosphere is essentially stable over daily time periods, this assumption for propagation is valid. For this study, we are interested in the stratosphere and troposphere, essentially the area including and below the jet stream (40-50 km). To turn a ray, there must be an increase in velocity greater than the speed of sound near the surface to create ducts. Using these models, infrasonic ray tracing was completed for the Korean Peninsula. Figure 7 illustrates a typical result for HWM/MSIS ray tracing illustrating the first ground return at nearly 300 km.

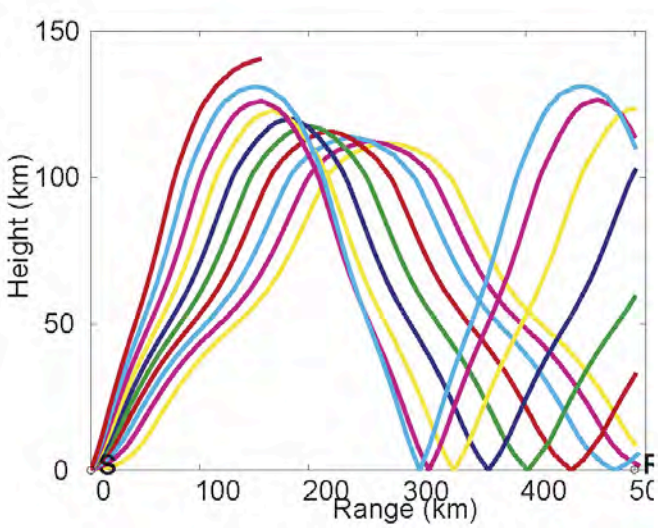

Figure 7: Ray tracing based upon average atmospheric models for the Korean Peninsula using the InfraMAP tool.

The lack of predicted returns within 300 km of the source motivated an exploration of the importance of actual meteorological data for the model troposphere. Such data were collected from OSAN, South Korea, the closest weather station to our array (Figure 8). InfraMAP calculates effective sound speed along a great circle path from source to receiver. Ray path calculations were completed along back azimuths spanning 360^{o} in order to quantify the azimuthal effects of the winds in troposphere.

The effective sound speed profiles were calculated using the following formula:

$C_{eff} = C_t + n \cdot v$ where

$C_t = ((a*R*T)/(m))^{0.5} = 20.07*(T)^{0.5}$ (Temperature contribution)

$n \cdot v$ = component of wind velocity in the direction of propagation (Wind contribution)

Monthly and daily averaged meteorological data from Osan are reproduced in Figure 9. These data were used in the ray tracing investigation of troposphere returns.

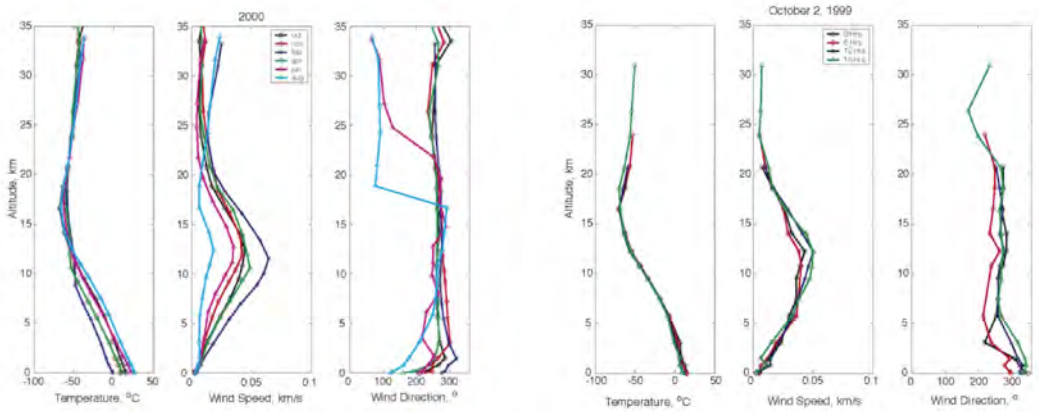

Figure 8a (left): Average monthly meteorological data including temperature, wind speed and direction as a function of altitude in the troposphere. 8b: Hourly meteorological data for 2 October 1999.

Ray paths created from using daily averaged meteorological data from August 4 are summarized in Figure 9. An example ray path is illustrated along with a pie chart illustrating the azimuths of predicted arrivals (red portions of the pie chart). The first arrival returns at about 18 km, much closer than the globally averaged data used in Figure 7, illustrating the possible importance of troposphere winds on short propagation distances.

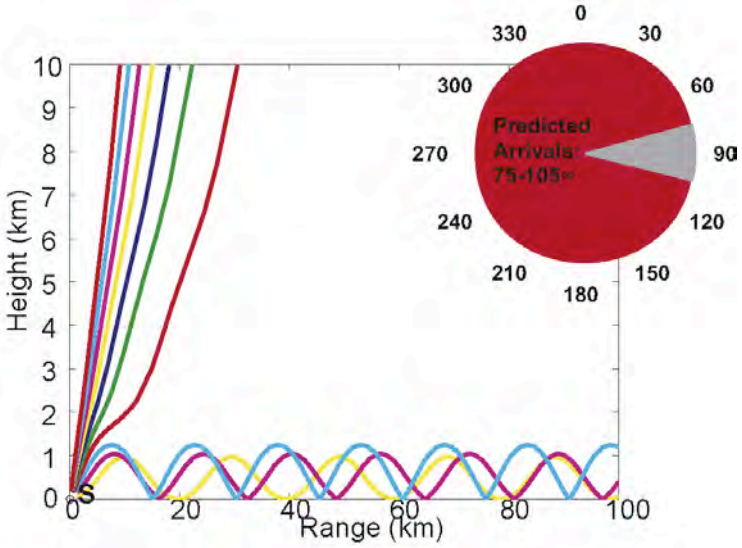

Figure 9: Ray tracing was conducted through a model in which the troposphere was replaced with a daily average wind data for August 4, 2000. The ray tracing produces arrivals that turn between 1 and 2 km and return energy to the ground a distances beyond 15 km for azimuths of 105-75° (red portion).

Figure 8b illustrates that winds at low altitude can change on time scales of hours. In order to investigate the possible importance of short term temporal variation in troposphere wind patterns on short propagation paths, ray tracing was completed using the observed winds at two time periods separated by six hours (Figure 10) for August 4, 2000. Arrivals are predicted along low altitude ducts for each data set but the changes in the winds over the six-hour time period produce significant variations in the azimuths along which the low-altitude energy will propagate. These hourly data predictions are also different from that predicted by the daily averaged winds used to produce Figure 9. These numerical models suggest that detailed meteorological data may be necessary for the interpretation of short distance infrasonic arrivals (10-300 km). These models also suggest that the azimuth of infrasound observations may change over short time periods. One might speculate that intermittent observations from sources could be expected as a result of these meteorological effects.

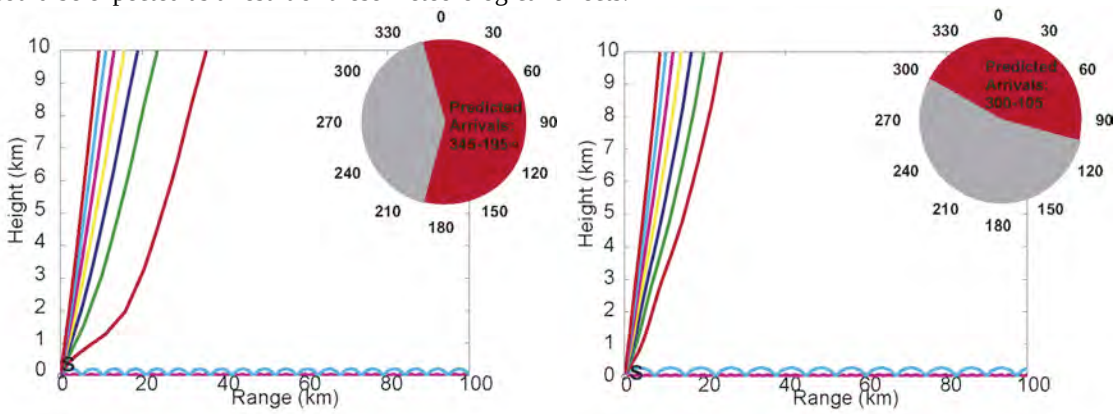

Figure 10a: Ray tracing for August 4, 2000, where the troposphere model is replaced with observed wind data for Hour 0. 10b: Ray tracing for August 4, 2000, where the troposphere model is replaced with observed wind data for Hour 6. There is a dramatic change in the azimuths that predict arrivals at short source-to-receiver distances.

CONCLUSIONS AND RECOMMENDATIONS

Ground Truth

Seismo-acoustic events are regularly observed at CHNAR. The seismo-acoustic array provides the opportunity to locate and characterize these events. Over two years, 2000 and 2001, a little less than one seismo-acoustic event per day was observed at the array. As illustrated in Figure 2, the vast majority of these events occurs within 200 km of the array. Additionally, the events are found to cluster into groups indicating that they are characteristic of man-made sources.

Several of the sources identified by the seismo-acoustic analysis were investigated as to generating mechanism. A ground truth database has been developed that indicates sources of seismo-acoustic energy include mining explosions and construction blasts. No acoustic signals have been associated with known small magnitude earthquakes.

Detailed ground truth on a number of mining explosions illustrates the dramatic effect that delay-firing has on peak amplitudes of the seismic phases. Synthetic models supported by close-in measurements suggest that delay-firing reduces the amplitudes of high-frequency regional phases by a factor of 10 to 100, thus explaining the small magnitudes for many of the Korean mining explosions.

A simple experiment was conducted in which seismic and infrasonic data were combined to produce a combined event location. The event distance was estimated using arrival time data at CHNAR. These events had accompanying infrasonic signals that were used to estimate the event back azimuth. This investigation focused on signals from construction blasts at the new airport near Seoul. The resulting event locations clustered into two relatively tight groups. The seismic waveforms for all events in each group were compared and produced strong correlation to frequencies in excess of 10 Hz. The seismic signals from the two groups, despite being relatively close to one another, were not correlated. These results suggest that infrasound data may be useful in refining event locations and may be combined with seismic signal coherence to further refine locations.

Infrasound Modeling

Many more infrasound signals are observed at CHNAR than seismic or seismo-acoustic signals. In order to assess the characteristics of these signals and investigate possible temporal variations in these signals, all acoustic signals occurring for one 7-day period in each of six months during the year spanning October 1999 to October 2000 were analyzed. The temporal occurrences of these signals suggest that they are man made as they only occur during daylight hours. The back azimuths for these signals show monthly, daily, and hourly variations as well.

The high-frequency nature of these signals (5 Hz and above) and the fact that seismo-acoustic signals with similar frequency content occur within 200 km of CHNAR suggest that the lonesome infrasound signals have propagated along relatively short paths. Ray tracing using the InfraMAP was undertaken in order to assess the possible paths these signals have taken. Average atmospheric models for the Korean Peninsula predict no arrivals within the 200-km range. The short paths suggested that variations in the temperature and winds in the troposphere might account for the arrivals, thus meteorological data was obtained and incorporated into the lower atmosphere model. Ray tracing through these models produces arrivals that return to the surface at close ranges (< 200 km). The meteorological data was taken on 6-hour intervals and further suggest that variations on these relatively short time scales may produce short distance propagation ducts that open and close. These numerical results are supported by hourly variations in observed azimuths for the lonesome acoustic waves. This suggests that the lack of an associated acoustic arrival with a seismic arrival cannot be used to rule out a surface explosion source.

REFERENCES

Norris, D. and R. Gibson, 2001. InfraMAP Propagation Modeling Enhancements and the Study of Recent Bolide Events, *Proceedings of the 23rd Seismic Research Review: Worldwide Monitoring of Nuclear Explosions,* October 2001, Jackson Hole, Wyoming.

Stump, B., C. Hayward, S.M. House, M.-S. Jun and J.-S. Jeon, 2000. A Small Aperture Seismo-Acoustic Array, Signal Assessment, in *Proceedings of the 22nd Annual Seismic Research Symposium: Planning for Verification of and Compliance with the Comprehensive Nuclear-Test-Ban Treaty (CTBT),* September 2000, New Orleans, Louisiana.

Stump, B., M.-S. Jun, C. Hayward, J.-S. Jeon, I.-Y. Che, S.M. House and T.-S. Kim, 2001. Assessment of Seismic and Infrasound Signals in Korea with Ground Truth, *Proceedings of the 23rd Seismic Research Review: Worldwide Monitoring of Nuclear Explosions,* October 2001, Jackson Hole, Wyoming.

CALIBRATION OF THE M_s:m_b DISCRIMINANT AT NVAR

Ileana M. Tibuleac,[1] Jessie L. Bonner,[1] Eugene T. Herrin,[2] and David G. Harkrider[3]

Weston Geophysical Corporation,[1] Southern Methodist University[2], Boston College[3]

Sponsored by Defense Threat Reduction Agency

Contract No. DTRA01-01-C-0080

ABSTRACT

The ability to accurately discriminate small magnitude events in areas of high monitoring concern may often rely on calibrated discriminants based upon measurements made at a single array. We are currently in the first year of a systematic evaluation of the M_s and m_b magnitude scales at NVAR (Mina, Nevada) where a broadband tripartite and short-period array will be used to help identify small amplitude Rayleigh- and P-wave motions. To date, we have initiated the data collection and NVAR m_b calibration phases of the project, and we have examined the characteristics of near-regional Rayleigh waves recorded at NVAR and MNV. Our data collection has focused on events within 20 degrees epicentral distance of NVAR that occurred between January 1999 and June 2002. We have collected waveform data from over 570 events recorded at NVAR and nearby stations, including 128 events that were only available from the archives at the Southern Methodist University Data Center. We are also analyzing the historic explosion and earthquake database for the MNV station (Denny, 1998), which is co-located with one of the broadband elements (NV31) of NVAR.

Reducing m_b bias is essential for successful application of the M_s:m_b discriminant, thus an initial research objective was to calibrate station corrections for the individual sites of the NVAR array to the body wave magnitude formula developed by Denny *et al.* (1987) at MNV. We used *Pn* and *Pg* phases from 7 events located within 13 degrees from NVAR and, using a regression of NV31 against MNV amplitudes, we estimated C=-0.01 for NV31. Using a different set of 17 earthquakes on or close to NTS we estimated C=-0.16 for NV08 and C=-1.29 for NV32. In an attempt to use the larger amplitudes of *Pg* arrivals in a formula calibrated against MNV values, we have also developed a m_b(*Pg*) formula for events near and on NTS.

As a result of NVAR's close proximity to the Nevada Test Site, the surface waves recorded at this station from events on or near the test site are dominated by short-period Rayleigh waves with a dominant period considerably less than 20 secs. We have used phase match filtering techniques to extract Rayleigh waves from several Yucca Flat explosions, and observed that the 20 second surface waves fall below detection thresholds near m_b=4.1; however, the short-period Rayleigh waves (< 12 sec) are still measurable at m_b=3.7 and lower for explosions. These results suggest that the surface wave magnitude scale for this region must be calibrated at these shorter-periods in order to examine the performance of the M_s:m_b discriminant at smaller magnitudes.

OBJECTIVES

The ability to accurately discriminate small magnitude events in areas of high monitoring concern may often rely on a discriminant that has been calibrated for a single array or station. The objectives of this research are two-fold: The first will be a systematic evaluation and calibration of the M_s and m_b magnitude scales at NVAR (Mina, Nevada) where a broadband tripartite will be used to help properly identify small Rayleigh- wave motion. One of these broadband sites is co-located with the longstanding seismic station, MNV thus making possible the comparison of the MNV extensive historical explosion database with regional earthquakes. The second objective is to determine whether surface waves in the period band of 4 to 15 seconds can be used to accurately characterize source size. This bandwidth is considerably less than the 17 to 22 second Rayleigh waves typically used in M_s formulae. By including shorter-period surface waves in the magnitude formulae, we may be able to calculate M_s for additional near-regional events with body-wave magnitudes below 4.0 thus allowing for a thorough examination of the M_s:m_b discriminant at smaller magnitudes.

Several new regional arrays are planned for deployment during the next decade to improve capabilities for the detection, location, and discrimination of small nuclear explosions. As a result, these arrays may be within near-regional distances of known or future test sites where the performance of the M_s:m_b discriminant is not well understood. We are attempting to quantify the performance of this discriminant using near-regional data recorded at the IMS array NVAR (Figure 1) located approximately 200 km northwest of the Nevada Test Site (NTS). The array, which has been online since December 1998, consists of 10 short-period elements centered in a three-component broadband tripartite (15, 25, and 25 km legs). The northeastern station of the tripartite is collocated with station MNV, which is one of four stations in the Lawrence Livermore seismic network that has recorded most of the NTS explosions. We are currently in the initial year of the project, and we have collected our initial explosion and earthquake datasets, calibrated body wave magnitude formulae for these events in a manner consistent with Denny *et al*. (1987), and initiated research on characterizing the short-period Rayleigh waves generated on or near NTS. In the upcoming year, we will formulate the M_s scale for NVAR using the method of Marshall and Basham (1972) by calibrating distance and path dependent terms for near-regional distances and paths in this region of the western United States. Eventually, our goal will be to test the results on data recorded in other regions of monitoring concerns.

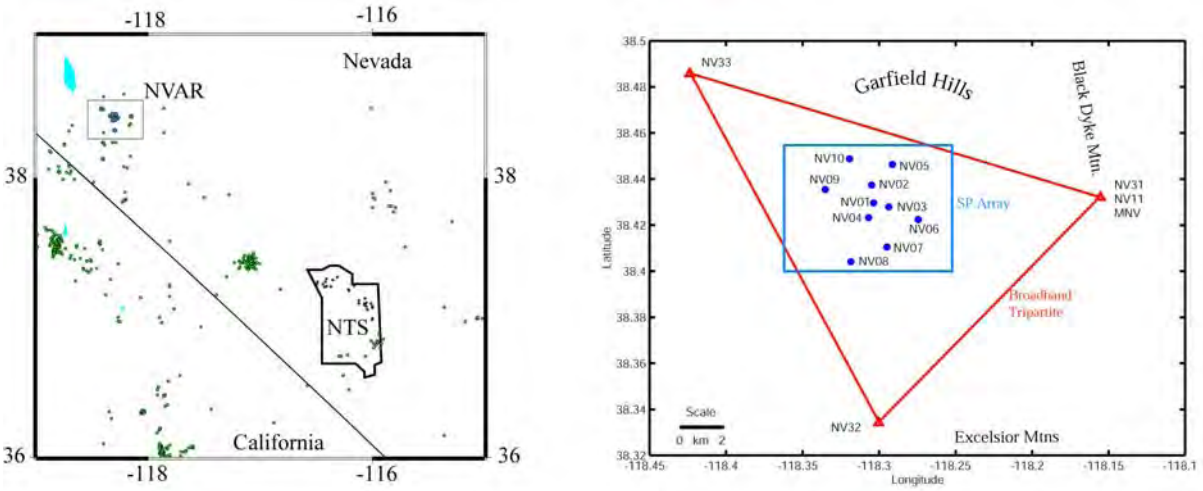

Figure 1. (Left) Map showing the location of NVAR relative to the Nevada Test Site (NTS). Also shown are the locations of regional earthquakes (green circles) recorded at NVAR since December 1998 and nuclear explosions (circles above the letters NTS) at NTS between November 1988 and September 1992. (Right) Geometry of the NVAR array including the short period (SP) elements (circles) and broadband tripartite (diamonds). The station MNV, which has recorded many of the NTS explosions, is collocated with the NV31 and NV11 stations of the NVAR array.

RESEARCH ACCOMPLISHED

Database Collection

Our data collection has focused on earthquakes within 20 degrees epicentral distance of NVAR that occurred between January 1999 and March 2002. We have collected waveform data from over 570 events recorded at NVAR and nearby stations, including 128 events that were only available from the archives at the Southern Methodist University Data Center. We have also acquired the historic explosion and earthquake database for the MNV station (Denny, 1998). Most of the events discussed in the following paper occurred on or near the Nevada Test Site (NTS) and are shown in Figure 1.

Calibration of a Regional m_b Scale at NVAR: *Pn*

The Denny *et al.* (1987) body wave magnitude formula (referred to henceforth at the DTV m_b) was specifically developed for western Unites States (US) using many events on or near NTS. They used the extensive database of earthquakes, explosions and nuclear explosions on NTS to establish a regional m_b formula at MNV, LAC, KNB, and ELK. MNV and the NVAR element NV31 are collocated (Figure 1) in the same mine and vault, thus in order to compare the historical explosions database to the new earthquake database, we calibrated the broadband elements NV31, NV32, NV33 and the short period element NV08 to the DTV m_b estimates at MNV for events on or near NTS.

We first calibrated the station dependent terms for the DTV m_b formula using the broadband and the NV08 short period elements at NVAR. The station correction, C, in their formula:

$$m_b = \log_{10}(A) + 2.4\log_{10}(\Delta) - 3.95 + C \quad (1)$$

where A is zero-to-peak amplitude in nm and Δ is the distance in km was determined to be +0.02 for MNV (Denny *et al*., 1987). We calibrated station NV31 to compare it with the value determined for MNV. For this task, we used *Pn* and *Pg* amplitudes from 7 earthquakes that occurred during the first 3 months of 1999 (Table 1) within 3 – 13 degrees from NVAR. The events were chosen with adequate signal-to-noise (SNR) ratios and data available from both MNV and NV31.

The logarithmic plot of *Pn* (stars) and *Pg* (circles) amplitudes in nm is presented in Figure 2 for MNV (abscissa) and NV31 (ordinate). We observe a linear dependence of NV31 and MNV amplitudes and from an L2 norm fit of the data (represented as the solid line in Figure 2), we developed the following relationship:

$$\log_{10}(A_{NV31}) = 1.004\log_{10}(A_{mnv}) + 0.035. \quad (2)$$

Thus, the constant for NV31 was determined to be C_{NV31}=-0.015 in order to have the same magnitude estimates as for the station MNV.

Table 1. Events recorded at both NVAR and MNV and reported by the prototype International Data Center (pIDC). Both *Pn* and *Pg* arrivals were analyzed for events marked with *. Locations and magnitudes are from the PIDC.

DATE	TIME	LATITUDE (DEG)	LONGITUDE (DEG)	M_B	DISTANCE (DEG)
1999/02/21*	16:50	30.93	-115.69	3.7	7.8
1999/02/24	10:02	41.30	-123.33	2.8	4.8
1999/03/09	17:48	43.32	-127.51	4.4	8.5
1999/03/13*	13:31	32.74	-116.02	3.3	6.0
1999/03/14	22:43	32.55	-104.20	3.5	12.9
1999/03/16	18:06	42.19	-125.42	4.0	6.6
1999/03/23*	18:36	36.60	-121.61	3.5	3.2

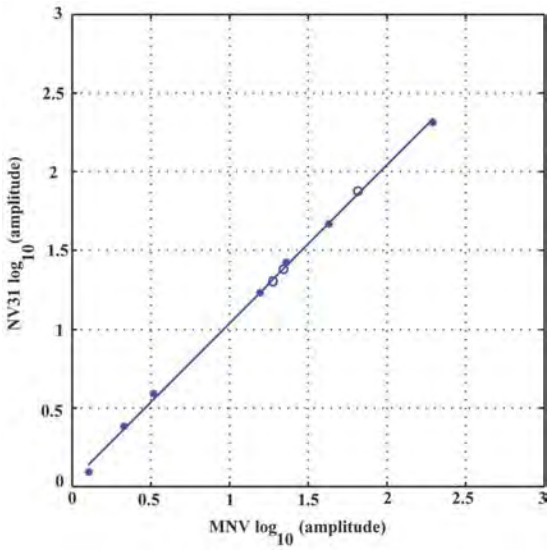

Figure 2. Amplitude estimates (nm) at NV31 as a function of MNV amplitudes (nm), for events in Table 1. Stars are first arrival measurements and open circles are *Pg* amplitude estimates.

To calculate the DTV m_b station corrections for the NV08, NV32 and NV33 stations relative to the NV31 DTV m_b, we used raw amplitude measurements from a data set of 17 events that occurred between May 1999 and June 2002 on or near NTS (Table 2). As noted from this table, we had a complete dataset for NV08, but the data availability for the broadband elements of the array is less complete. We note that NV33 was installed at a later date resulting in fewer numbers of events for analysis. For most events, the *Pn* the arrival was weak (e.g., events within 1.3 – 1.5 degrees epicentral distance, where *Pn* and *Pg* arrive within a one – two seconds time window) and in some cases only through array processing were we able to extract the *Pn* phase (Tibuleac and Herrin, 2001). Also, smaller amplitudes result in larger measurement error.

Table 2. Earthquakes near or on NTS used to calibrate Denny *et al.* (1987) magnitude formula at NV08, NV31, NV32, and NV33. Letter y shows events with *Pn* phase picks. Locations and magnitudes are by PIDC, except for events marked by stars, where locations were formed by the University of Nevada-Reno (UNR) network.

DATE	TIME	LATITUDE (DEG)	LONGITUDE (DEG)	PIDC M_B	DISTANCE (DEG)	NV08	NV31	NV32	NV33
1999/05/15	13:22	37.49	-118.62	4.7	0.97	y	y	y	
1999/05/15	13:28	37.53	-118.40	3.3	0.9	y	y	y	
1999/08/01	04:17	37.35	-117.06	3.2	1.46	y		y	
1999/08/01	16:06	37.34	-117.02	4.8	1.49	y		y	
1999/08/01	16:11	37.35	-116.91	4.2	1.54	y		y	
1999/08/01	16:26	37.40	-117.20	3.4	1.35	y		y	
1999/08/01	16:27	37.42	-116.88	4.1	1.51	y		y	
1999/08/02	05:40	37.36	-117.07	3.2	1.45	y		y	
1999/08/02	06:05	37.37	-117.02	4.5	1.47	y		y	
1999/09/26	20:11	37.36	-117.14	3.4	1.41	y	y	y	y
2000/02/28	23:08	36.00	-177.92	3.5	2.44	y	y	y	y
2000/03/02	15:00	36.08	-117.10	3.6	2.43	y	y	y	y
2002/02/19*	07:32	37.37	-117.10	3.3	1.41	y	y		
2002/03/03*	00:09	35.47	-116.48	3.0	3.29	y	y	y	y
2002/03/05*	22:23	37.37	-117.13	3.2	1.4	y	y		
2003/03/24*	10:44	37.00	-115.07	4.2	2.92	y	y		
2002/06/14*	12:40	36.71	-116.3	4.4	2.33	y	y		

In Figure 3a (upper left) we compared the corrected DTV m_b estimates at NV31 to estimates by PIDC (stars) and UNR (open circles). Observations at NV31 underestimate magnitudes for two events on NTS (distance 2.4 deg), one event at 3.2 degrees distance SE of NTS and one event near Scotty's Junction, 50 km west of NTS. However, the low magnitude estimates seem to be consistent and seen at both NV08 and NV31 (Figure 3 b) while NV32 and

NV33 do not seem to have the same behavior (Figure 3 c and d). These variations could also be the result of the complex nature of the geology of this array. The upper right and the bottom plots in Figure 3 (b,c,d) show the DTV m_b (with no station corrections) for NV08, NV32 and NV33, respectively, as a function of DTV corrected m_b at NV31 (equivalent to the MNV magnitude). L2 norm linear fits are calculated, represented by solid lines in the figures and the results are presented in Table 3. A slope close to 1 was observed between all DTV m_b values except the ones at NV33 versus NV31, possible due to the small number of estimates. Considering the value of the slopes, we calculated the DTV m_b constants for NV08 (C=-0.16) and for NV32 (C = -1.29). After applying these corrections, the L2 fits do not change, however, an L1 fit for NV08 and NV31 DTV m_b gives slopes of 0.98 (NV08 corrected DTV m_b versus NV31 corrected DTV m_b) respectively 0.97 for the same at NV32 versus NV31 The results presented in this section are preliminary as we continue to analyze events from near-regional distance to further improve the m_b calibration at NVAR.

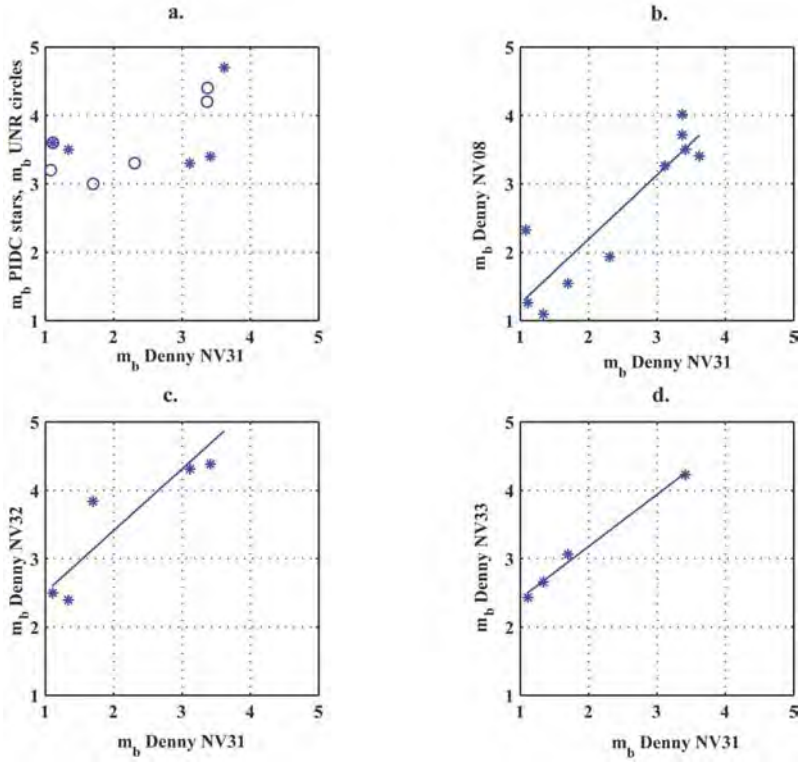

Figure 3. a) PIDC (stars) and UNR (open circles) m_b as a function of DTV m_b values, corrected to the MNV magnitude, at NV31. b) Uncorrected DTV m_b values at NV08 as a function of corrected DTV m_b at NV31 for events on or near NTS. c) Results for NV32. d) Results for NV33.

Table 3. L2 norm linear fit for NV08, NV32, NV33 (uncorrected) DTV m_b as a function of NV31 (corrected) DTV m_b and an L2 norm linear fit between NV08 and NV32

L2 NORM LINEAR FIT	FIGURE 3	NUMBER OF ESTIMATES
$m_{bNV08}(Pn) = 0.94 m_{bNV31} + 0.30$	b	10
$m_{bNV32}(Pn) = 0.90 m_{bNV31} + 1.59$	c	6
$m_{bNV33}(Pn) = 0.76 m_{bNV31} + 1.64$	d	4
$m_{bNV08}(Pn) = 0.98 m_{bNV32} - 1.18$	-	13

Calibration of a Regional m_b Scale at NVAR: *Pg*

For the events near and on the NTS that we studied, the largest arrival on the seismogram was *Pg*. In an attempt to use these larger arrivals, we have calibrated the DTV m_b for *Pg* as well, for NV08, NV31 and NV32. Figure 4a presents the values of m_b for DTV formula applied at NV31 on *Pg* the same way as on *Pn* as a function of PIDC (stars) and UNR (open circles) values. Surprisingly, these magnitudes values are closer for each event than the Pn magnitudes, even if applying the same magnitude formula for both *Pg* and *Pn* is erroneous. We have empirically calculated a formula for $m_b(Pg)$. To correct for the distance dependence, we performed a regression of the difference between the DTV magnitudes at NV31 and $\log_{10}$ of the *Pg* amplitude at all NV08, NV31, and NV32. The correction term to replace 2.44 in DTV formula was 2.72 for Pg. From *Pn* magnitude regressed against *Pg* magnitude values at NV31, we determined the following formula to obtain the equivalent of the DTV body wave magnitude using *Pg* arrivals:

$$m_b(Pg) = \log_{10}(A) + 2.72\log_{10}(\Delta) - C1 \qquad (3)$$

where A is the zero to peak Pg amplitude, Δ is the distance in km and C1 = 5.71 at NV31. The other subplots of Figure 4 present regressions of the magnitude values calculated with this formula at NV08, NV32 and NV31. The L1 norm solid lines equations are presented in Table 4. Our calculations show that C1 = 5.75 at NV08 and C1 = 6.68 at NV32. After applying the correction, the L1 fit gives a slope of 1.01 for NV32 as a function of NV31 magnitude values instead of a slope of 1.28 (see table 4).

Table 4. L1 norm linear fit for NV08, NV32, NV31 (*Pg* uncorrected) DTV m_b as a function of NV31 (*Pn* corrected) DTV m_b.

L1 NORM LINEAR FIT	FIGURE 5	NUMBER OF ESTIMATES
$m_{bNV08}(Pg) = 0.94m_{bNV31} + 0.09$	b	10
$m_{bNV32}(Pg) = 1.28m_{bNV31} + 0.23$	c	5
$m_{bNV31}(Pg) = 0.97m_{bNV31} + 0.07$	d	10

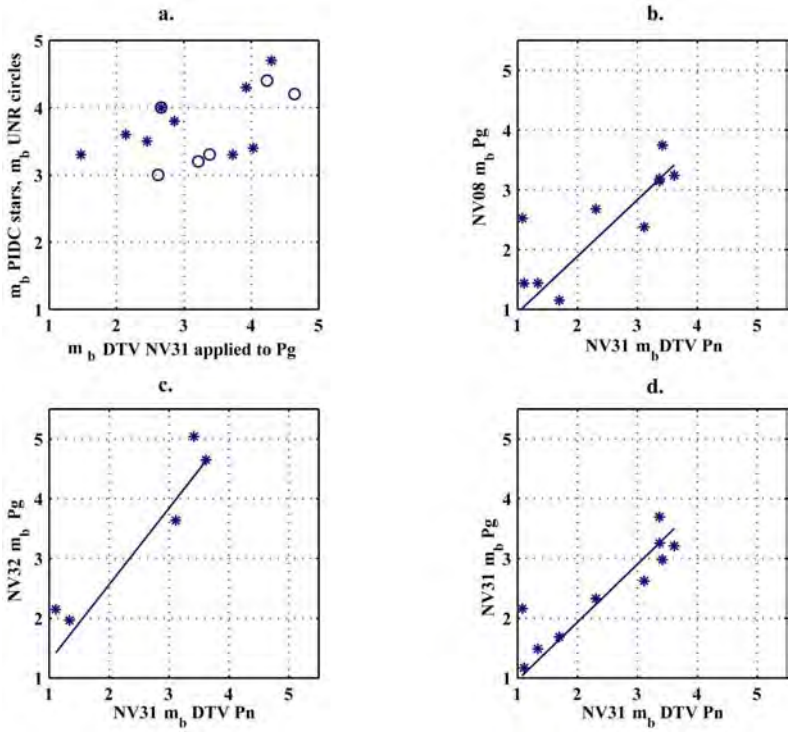

Figure 4. a) PIDC and UNR magnitudes represented as a function of the NV31 DTV magnitude formula, as applied to *Pg*. (b, c, d) Formula (3) and *Pg* amplitudes were used to calculate magnitude values for NV08, NV32 and NV31, respectively, then these values were regressed against the magnitude values calculated with DTV formula for *Pn* at NV31. The solid lines are L1 fits presented in Table 4.

Characterization of Short-Period Rayleigh Waves at Near-Regional Distances

Once the m_b calibration at NVAR is completed, our research focus will shift to the development and calibration of near-regional surface wave magnitude scales. The surface waves recorded at this station from events on or near NTS (about 200 km to the SE) are dominated by short-period (< 12 sec) energy. This fact makes measurement of a conventional and stable M_s difficult, as surface wave magnitudes (Marshall and Basham, 1972; von Seggern, 1977; Vanek *et al*., 1962) are defined in the 17 to 23 second band. For example, the data from the NTS explosion TEXARKANA (2/10/89) as recorded at MNV is shown in the upper plot of Figure 5. We performed a multiple filter analyses (Dziewonski *et al*., 1969) on the data and used the resulting group velocity dispersion curve to design a phase matched filter (PMF; Herrin and Goforth, 1977) to extract the fundamental mode Rayleigh waves (lower plot of Figure 5). We then performed a narrow band-pass filter (BP 17 – 23 seconds) on the PMF extracted Rayleigh waves and the results are overlain in the lower plot of Figure 4. These data show that the 20 second surface waves for this m_b=5.2 event have amplitudes that are 8-10 dB smaller than the 7-8 second Rayleigh waves. As event size is decreased, the 20-second surface waves will fall below the detection threshold prior to the 7-8 sec energy limiting the applicability of the typical M_s measurement.

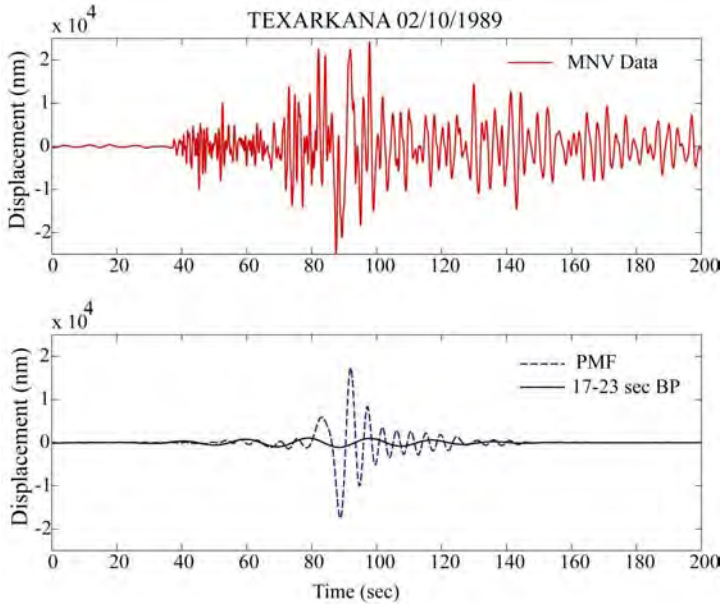

Figure 5. Waveforms from the NTS explosion TEXARKANA (Upper) recorded at station MNV. The phase match filtered Rayleigh waves (lower dashed lines) show the peak in the surface wave train corresponds to a period of 7.1 seconds and has an amplitude that is 8-10 dB larger than the surface waves in the 17 to 23 band (black line) that are typically used for measuring M_s.

These results suggest that the entire Rayleigh-wave train, not just 20-second period data, is needed for our study. Thus an initial stage of our research has been to perform the PMF technique on our explosion and earthquake datasets. For example, the PMF extracted surface waves for events from the Yucca Flats region of NTS between 1988 and 1992 are shown in Figure 6. The results show that 8 events with m_b > 4.1 had ~20 second surface waves; however, all of the events showed the 7-8 second Airy phase that dominates the propagation path from NTS to MNV (NVAR). For two events (m_b < 3.7), the largest period observed was 12.5 seconds. In addition to extracting the data, the PMF also offers enhanced signal-to-noise ratio (SNR) for dispersed Rayleigh waves as compared to routine bandpass filtering techniques. Thus, for small events in which a filter cannot be derived independently, we have derived the phase associated with a given path using the mainshock or large aftershock of an aftershock sequence. We have completed this for aftershocks from the Scotty's Junction aftershock sequence (50 km west of NTS) and extracted 5-8 second surface waves for events with m_b as small as 2.7. Cleary, developing and calibrating a M_s scale for surface wave periods less than 10 sec will allow us to characterize smaller events recorded only at near-regional distances.

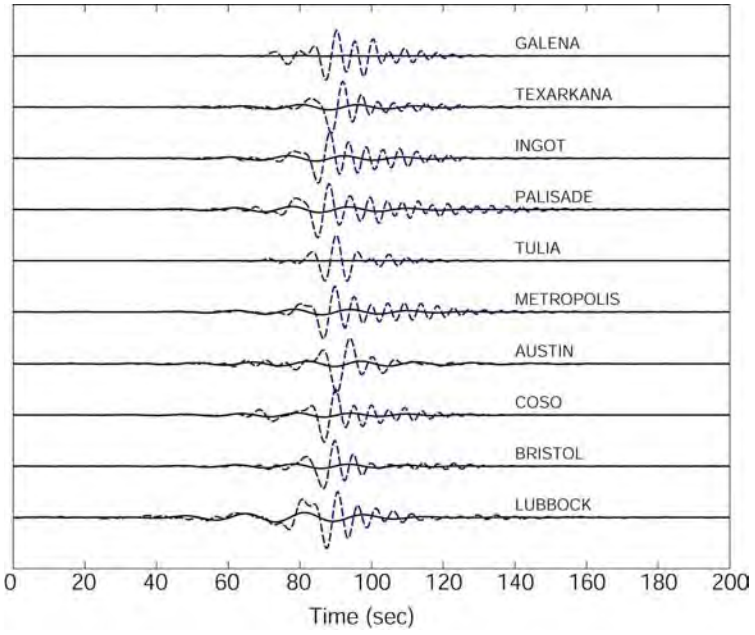

Figure 6. PMF (dashed) extracted Rayleigh waves from Yucca Flat explosions. The solid lines show the PMF data bandpass filtered between 17 and 23 seconds. The explosions TULIA (m_b=3.7) and GALENA (m_b=3.6) did not have measurable surface waves in the 17 to 23 second band at MNV. The data were scaled to the maximum amplitude of each PMF trace.

We will examine the performances of several M_s formulae at near-regional distances during this project, including the Rezapour and Pearce (1998) and Marshall and Basham (1972) equations. Marshall and Basham (1972) reformulated the Prague formula (Vanek *et al.*, 1962) as:

$$M_s = \log_{10}(A_{max}) + B'(\Delta) + P(T) + 0.008h \quad (4)$$

where A_{max} is the maximum Rayleigh wave amplitude (0 to Peak in nm), $B'(\Delta)$ is a distance correction, P(T) is a path correction as a function of period, T, and h is the depth of the event in kilometers. The distance correction (Marshall and Basham, 1972) approximated the 1.66 $\log_{10}(\Delta)$ term for distances at large teleseismic differences and was proportional to 0.8 $\log_{10}(\Delta)$ for regional distances (Basham, 1971). More recently, a study by Herak and Herak (1993) showed that surface wave amplitudes decrease as $\Delta^{+1.094}$. The path correction is determined from the amplitude of the group velocity (U) dispersion curve predicted by the method of stationary phase (Ewing *et al.*, 1957) with the following equation:

$$P(T) = \frac{U}{T^{3/2}\sqrt{\frac{dU}{dT}}}. \quad (5)$$

Marshall and Basham (1972) show P(T) corrections for varying lithospheric structures, however, the authors limited their analyses to periods greater than 10 seconds. We used the group velocity dispersion curves generated from the multiple filter analyses to obtain P(T) for periods between 4 and 10 seconds. For the dominant period (7 sec) of the Yucca Flat explosions shown in Figure 6, the P(T) correction is approximately -0.8 magnitude units (m.u) relative to measurements made at 20 seconds.

We used the Marshall and Basham (1972) formula (Equation 4) and dispersion-curve generated P(T) (equation 5) to calculate preliminary M_s values for both 20 second (Figure 7; circles) and 7 seconds (asterisks) Rayleigh wave data from the Yucca Flat events. Both the $M_s(20)$ and $M_s(7)$ values show similar trends; however, the $M_s(7)$ values are approximately 0.24 m.u. larger. We plan to examine the source of this discrepancy which could be associated with incorrect attenuation for the near-regional, short-period Rayleigh waves or the difficulties of measuring P(T) near an

Airy phase. We note that Denny *et al*. (1987) used the Marshall and Basham (1972) formula with regional NTS data to improve the separation of earthquake and explosion populations based on the M_s:m_b discriminant. However, they were only able to apply their method to a single explosion with $m_b < 3.8$. Our initial study of only 10 events from the Yucca Flats region have found surface waves for two events at these smaller magnitudes, and we will continue to use the phase match filtering, array processing methods, and other techniques to extract Rayleigh waves from small earthquakes and explosions. Another method of calculating regional M_s for data with periods less than 20 seconds was developed by Woods and Harkrider (1995). In their method, synthetic seismograms are used to establish a relationship between the amplitudes of the regional Rayleigh-wave pulse and associated Rayleigh waves that have propagated to distances of 40°. These methods allowed for the calculation of M_s values for nuclear explosions over a wider magnitude range than previously accomplished. We plan to use their method and compare the synthesized M_s values with ours calculated directly from near-regional measurements of short-period surface waves.

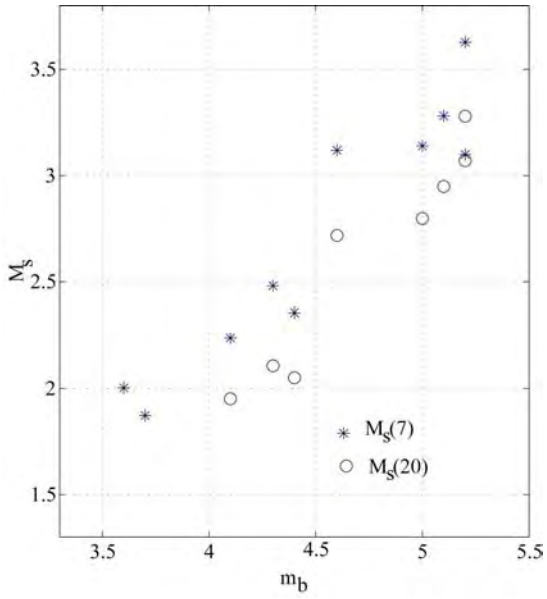

Figure 7. Comparison of M_s values calculated for Yucca Flat explosions using 7 second (asterisks) and 20 second (circles) Rayleigh wave data.

CONCLUSIONS AND RECOMMENDATIONS

Our preliminary dataset has allowed us to calibrate the DTV m_b (Denny *et al.*, 1987) formula for *Pn* arrivals recorded at element NV31, collocated with the historical station MNV. We have determined DTV m_b constants for NV08 and NV32 to calibrate them against corrected DTV m_b measured at element NV31, for events on or near NTS. We observed systematic and consistent underestimation of magnitudes for events on NTS at NV08 and NV31; however, we have not completed results at NV33 because of a limited database. Since, to this date, we found only a small number of suitable earthquakes on and around NTS, these observations remain to be confirmed by a larger collection of events, and thus the results presented within are preliminary and will be updated as more data become available. We have calibrated the *P*g magnitude values measured at NV08, NV31 and NV32 against corrected DTV m_b measured at element NV31. To obtain these magnitude values we found new corrections for distance and new constants.

As a result of NVAR's near-regional distance (less than 250 km) to the Nevada Test Site, the surface waves recorded at this station from events on or near the test site are dominated by an short-period Rayleigh wave with period considerably less than 20 secs. We have used phase match filtering techniques to extract Rayleigh waves from several Yucca Flat explosions, and observed that the 20 second surface waves fall below detection thresholds near m_b=4.1; however, the shorter-period Rayleigh waves are still measurable at m_b=3.7 and lower. These results suggest that the surface wave magnitude scale for this region must be calibrated at these shorter-periods in order to examine the performance of the M_s:m_b discriminant at smaller magnitudes. We plan to compare the direct

measurements to measurements made on synthesized 20 second period data using the technique of Woods and Harkrider (1995).

ACKNOWLEDGMENTS

We would like to thank Nancy Cunningham, Bill Walter, and Howard Patton for their help in acquiring the various datasets used for this project.

REFERENCES

Denny, M.D., S.R. Taylor, and E.S. Vergino (1987), Investigation of m_b and M_s formulas for the western United States and their impact on the M_s/m_b discriminant, *Bull. Seism. Soc. Am.* 77, 987.

Denny, M. D. (1998), Mina Seismic Data: Historic background for CTBT Monitoring, UCRL-MI-130657.

Dziewonski, A., S. Bloch, and M. Landisman (1969), A technique for the analysis of transient seismic signals, *Bull. Seism. Soc. Am.* 59, 427.

Evernden, J.F. (1971), Variation of Rayleigh wave amplitude with distance, *Bull. Seism. Soc. Am.* 61, 231.

Ewing, ,W. M., F., Press, and W. S. Jardetsky (1956), *Elastic waves in layered media*, McGraw Hill, New York.

Herak, M. and D. Herak (1993), Distance dependence of M_s and calibrating function for 20 second Rayleigh waves, *Bull. Seism. Soc. Am.* 83, 1681.

Herrin, E. and T. Goforth (1977), Phase-matched filters: application to the study of Rayleigh waves, *Bull. Seism. Soc. Am.* 67, 1259.

Marshall, P.D. and P.W. Basham (1972), Discrimination between earthquakes and underground explosions employing and improved M_s scale, *Geophys. J. R. astr. Soc.*, 28, 431.

Rezapour, M. and R. G. Pearce (1998), Bias in surface-wave magnitude doe to inadequate distance corrections, *Bull. Seism. Soc. Am.*, 88, *43-61.*

von Seggern, D. (1977), Amplitude distance relation for 20-Second Rayleigh waves, *Bull. Seism. Soc. Am.*, 67, 405-511.

Tibuleac, Ileana M. and E. T. Herrin (1997), Calibration studies at TXAR, *Seis. Res. Lett*, 68, 353.

Tibuleac, Ileana M. and E. T. Herrin (2001), Detection and Location Capability at NVAR for events on the Nevada Test Site, *Seis. Res. Lett.*, 72, 97.

Tibuleac, I.M., E. T. Herrin and P. Negraru (2001), Calibration studies at NVAR, *Seis. Res. Lett*,72, 754.

Vanek, J., A. Zatopek, V. Karnik, N.V. Kondorskaya, Y.V. Riznichenko, E.F. Savarensky, S.L. Solov'ev, N.V. Shebalin (1962), Standardization of magnitude scales, *Bull. (Izvest.)* Acad. Sci. U.S.S.R., Geophys. Ser., 2, 108.

Woods, B.B. and D.G. Harkrider (1995), Determining surface-wave magnitudes from regional Nevada Test Site data, Geophys. J. Int. 120, 474.

IDENTIFICATION IN WESTERN EURASIA: REGIONAL BODY-WAVE CORRECTIONS AND SURFACE-WAVE TOMOGRAPHY MODELS TO IMPROVE DISCRIMINATION

William R. Walter, Arthur J. Rodgers, Michael E. Pasyanos, Kevin M. Mayeda, and Alan Sicherman

Lawrence Livermore National Laboratory

Sponsored by National Nuclear Security Administration
Office of Nonproliferation Research and Engineering
Office of Defense Nuclear Nonproliferation

Contract No. W-7405-ENG-48

ABSTRACT

Our identification research is focused on the problem of correctly discriminating small magnitude explosions from a background of earthquakes, mining tremors, and other events. Small magnitude monitoring leads to an emphasis on regional waveforms. The goal is to reduce the variance within the population of each type of event, while increasing the separation between the explosions and the other event types. We address this problem for both broad categories of seismic waves, body waves, and surface waves. First, we map out the effects of propagation and source size in advance so that they can be accounted for and removed from observed events. This can dramatically reduce the population variance. Second, we try to optimize the measurement process to improve the separation between population types.

For body waves we focus on the identification power of the short-period regional phases Pn, Pg, Sn and Lg, and coda that can often be detected down to very small magnitudes. It is now well established that particular ratios of these phases, such as 6- to 8-Hz Pn/Lg, can effectively discriminate between closely located explosions and earthquakes. To extend this discrimination power over broad areas, we developed a revised Magnitude and Distance Amplitude Correction (MDAC2) procedure (Walter and Taylor, 2002). This joint source and path model fits the observed spectra and removes magnitude and distance trends from the data. The MDAC2 procedure makes use of the extremely stable coda estimates of Mw for source magnitude and can also use independent Q tomography to help reduce trade-offs in fitting spectra. We can then apply the Kriging operation (e.g. Schultz *et al*., 1998) to the MDAC2 residuals to provide full 2-D path corrections by phase and frequency band. These corrections allow the exploration of all possible ratios and multivariate combinations of ratios for their discrimination power. We also make use of the MDAC2 spectra and the noise spectra to determine the expected signal-to-noise value of each phase and use that to optimize the multivariate discriminants as a function of location. We quantify the discrimination power using the misidentified event trade-off curves and an equiprobable measure. In addition to the traditional phases, we are also exploring the application of coda amplitudes in discrimination. Coda-derived spectra can be peaked due to Rg-to-coda scattering, which can indicate an unusually shallow source.

For surface waves we continue to make improvements in our regional group velocity tomography models of Western Eurasia and North Africa. The tomography models provide high-resolution maps of group velocity from 10- to 100-s period. The maps also provide estimates of the expected phase spectra of new events that can be used in phase-match filters to compress the expected signals and improve the signal-to-noise ratio on surface wave magnitude (Ms) estimates. Phase match filters in combination with regional Ms formulas can significantly lower the threshold at which Ms can be measured, extending the M_s:m_b discriminant. We have measured Ms in western Eurasia for thousands of events at tens of stations, with and without phase match filtering, and found a marked improvement in discrimination. Here we start to quantify the improvement to both discrimination performance and the Ms threshold reduction.

OBJECTIVE

We continue developing, testing, and refining size-, distance-, and location-based regional seismic amplitude corrections to facilitate the comparison of all events that are recorded at a particular seismic station. These corrections, calibrated for each station, reduce amplitude measurement scatter and improve discrimination performance. We test the methods on well-known (ground truth) datasets in the U.S. and then apply them to the uncalibrated stations in Eurasia, Africa, and other regions of interest to improve underground nuclear test monitoring capability.

RESEARCH ACCOMPLISHED

As part of the overall National Nuclear Security Administration Ground-based Nuclear Explosion Monitoring (GNEM) Research and Engineering program, we continue to pursue a comprehensive research effort to improve our capabilities to seismically characterize and discriminate underground nuclear tests from other natural and man-made sources of seismicity. To reduce the monitoring magnitude threshold, we make use of regional body and surface wave data to calibrate each seismic station. Our goals are to reduce the variance and improve the separation between earthquakes and explosion populations by accounting for the effects of propagation and differential source size. Here, we briefly review three of these efforts: 1) MDAC2 - a revised spectral normalization technique to improve regional body-wave discrimination, 2) regional coda envelope based spectral peaking as an indicator of shallow depth events and 3) Improved M_s:m_b discrimination using high-resolution surface wave tomography.

MDAC2

Effective earthquake-explosion discrimination has been demonstrated in a broad variety of studies using ratios of regional amplitudes in high-frequency (primarily 1-to 20-Hz) bands (e.g. Walter *et al*., 1995; Taylor, 1996; Rodgers and Walter, 2002; Taylor *et al*., 2002; and many others). When similarly sized earthquakes and explosions are nearly co-located, we can understand the observed seismic contrasts, such as the relative P-to-S wave excitation, in terms of depth, material property, focal mechanism and source time function differences. For example, in Figure 1, we compare pairs of earthquakes and explosions of similar size and location and recorded at a common station. The traces have been high-frequency band passed at 6-8 Hz and show the characteristic discrimination difference, where in each case the explosion has larger P wave amplitudes relative to the S waves when compared to the earthquake.

The availability of such reference events, particularly nuclear tests, to compare to a new event in question is highly non-uniform and limited. Therefore, in real monitoring cases, we are often interested in comparing events that are not co-located, not recorded at the same station and may have quite different sizes. In order to make sure any observed differences between a new event in question and the reference events (or models) are not due to differences in path or magnitude, we must correct for these effects. For the past several years, we have been working with our colleagues at Los Alamos National Laboratory on the best ways to model and remove magnitude and distance trends from regional amplitudes. The original MDAC (Magnitude and Distance Amplitude Correction) procedure involved estimating and removing a simple theoretical earthquake spectrum from the data to remove any magnitude and distance trends in the regional phase amplitudes and any discriminants formed from those amplitudes (Taylor *et al*., 2002). We have just completed a refined and improved version of the procedure (MDAC2) by generalizing the source model, taking advantage of independent moment estimates and reducing some of the free parameters (Walter and Taylor, 2002).

The source spectrum depends upon the seismic moment and stress drop and can have additional complications due to non-constant stress drop scaling and differential P/S corner frequency effects. We require the different phases for the same event recorded at the same station to have the same moment and apparent stress (or stress drop) values and other source parameters, such as corner frequencies to be related to each other. This requirement effectively imposes some of the ratio constraints discussed in Rodgers and Walter (2002) on the amplitudes and improves discrimination performance. While such models of source spectra are certainly oversimplified, they have proven track records of providing good first-order fits to real earthquakes. In addition they also provide simple theoretical models to use in aseismic areas.

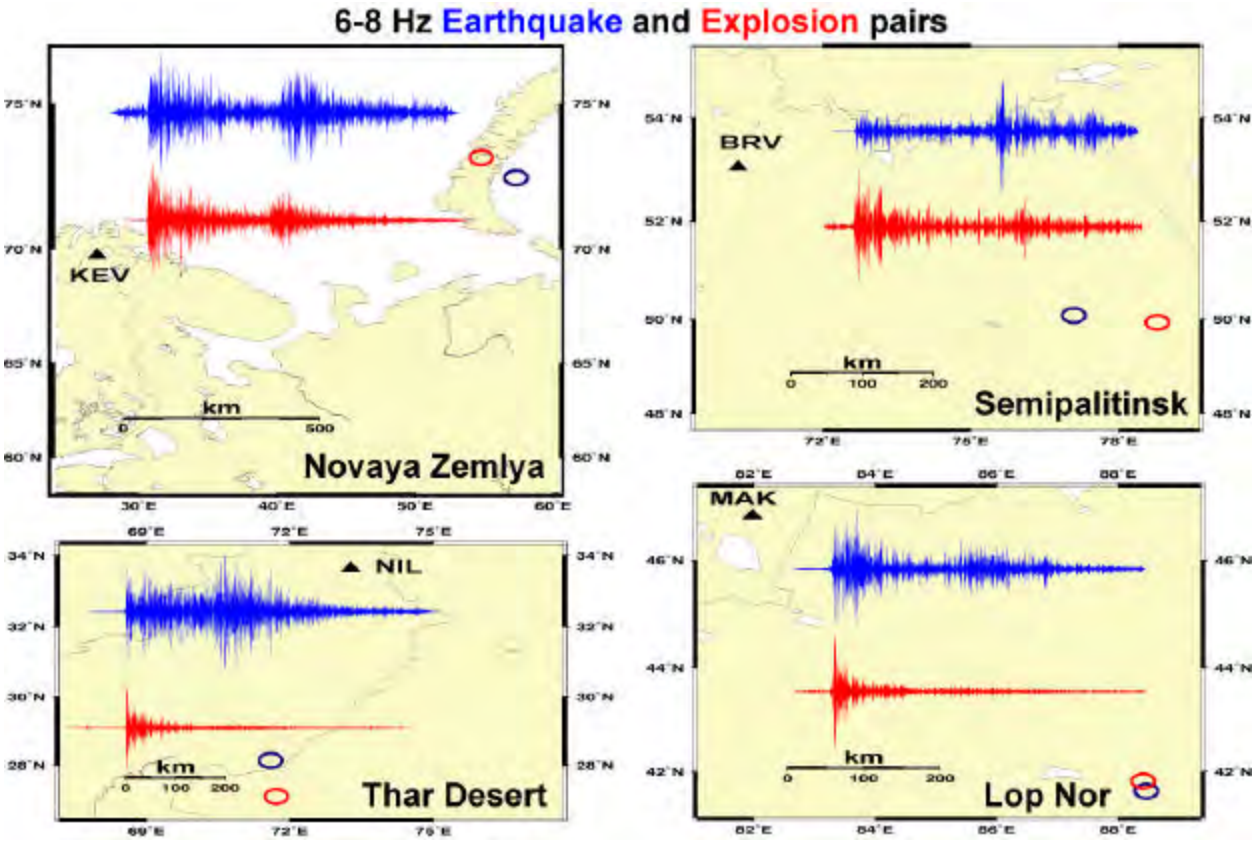

Figure 1. 6- to 8-Hz bandpass seismograms of earthquakes (blue) and explosions (red) show relative P to S wave amplitude differences that allow discrimination between the two source types.

The details of the MDAC2 formulation are given in Walter and Taylor (2002). The predicted spectrum is a convolution of the revised source terms and the previously used geometrical spreading, site, and apparent attenuation terms. We can write the log of the MDAC2 predicted spectrum as (Walter and Taylor, 2001):

$$\log P(f,R) = \log(S_o) - \log\left(1+\left(\frac{w}{w_c}\right)^2\right) + \log G(R) + Site(f) - \frac{pR}{Q_o c} f^{(1-g)} \log(e) \qquad (1)$$

for a regional phase with velocity c. Here S_o is the source low-frequency spectral level and w_c is the source corner frequency. These terms are set by the input moment (we use the stable coda measures, see Mayeda *et al*, this volume), the apparent stress scaling and material property terms. Apparent stress, geometrical spreading ($G(R)$), site effect, and attenuation (Q_o, g) terms are typically solved for using a grid search technique that simultaneously minimizes the spectral fit residual and residual magnitude and distance trends. In this way, *a priori* information such as previous studies on geometrical spreading or Q-tomography results can be easily incorporated.

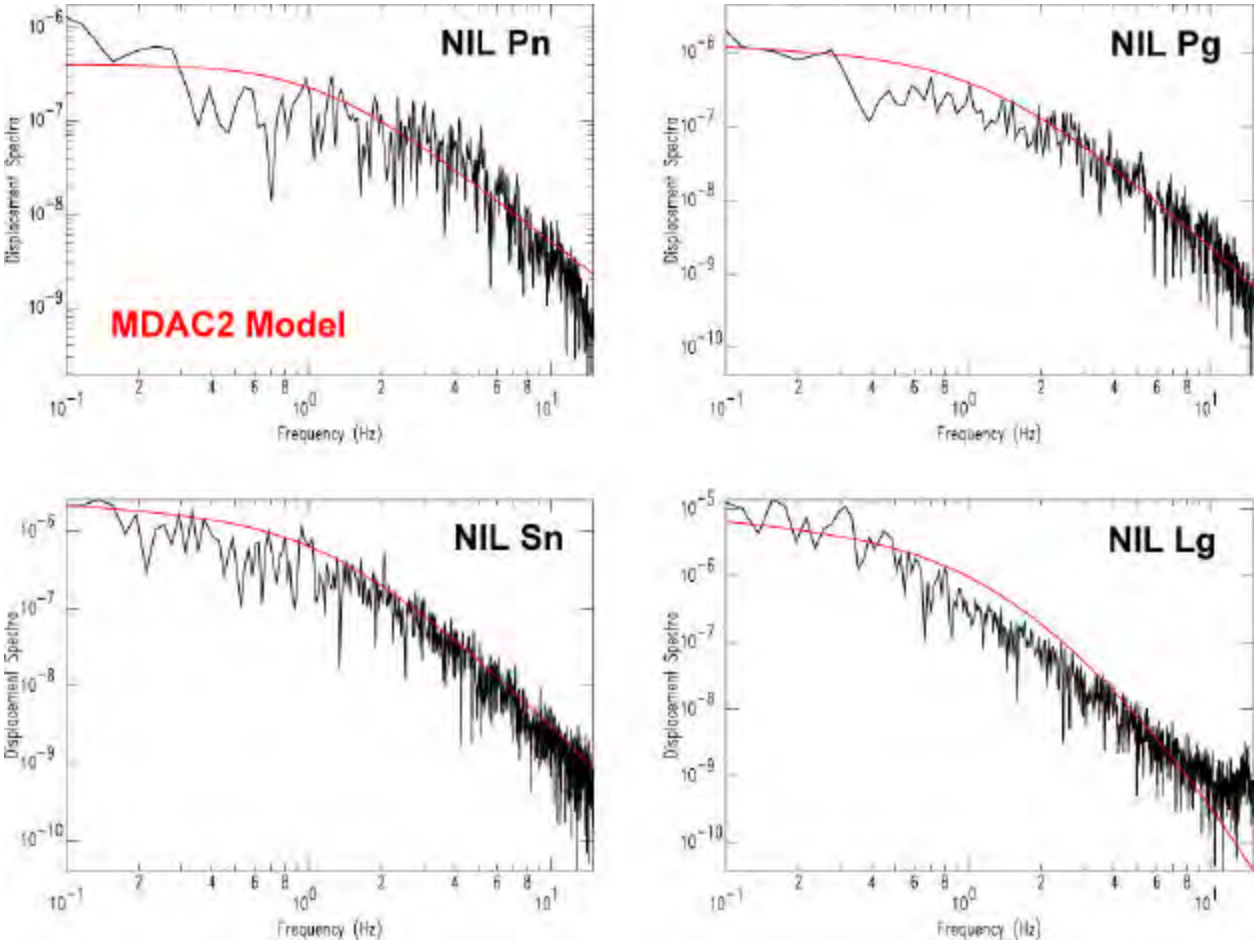

Figure 2. Comparison of observed (black) and MDAC2 model (red) spectra for a regional earthquake recorded at NIL.

In Figure 2 we show a comparison of the observed regional phase spectra (Pn, Pg, Sn and Lg) for a regional earthquake recorded at station NIL with the model spectra. Overall, the match is reasonable, though the Lg attenuation and site terms could use further refinement. By subtracting these model spectra, we essentially normalize the observations for effects of source, 1-D path, and site. However, 3-D path effects remain in the residuals. We can further reduce the MDAC2 residual amplitude variance by using the Bayesian kriging method of Schultz *et al* (1998) on the results. For each phase and frequency band we create kriged residual surfaces. These surfaces can then be used to create any discriminant measurement of choice. For example we can make phase, spectral and cross-spectral ratio measurements between any phase and frequency combination. In practice it is found that the best discriminant performance comes from combining several different ratio measurements (e.g. Taylor, 1996).

We test these ideas on a dataset of regional events with magnitude greater than 3.5 recorded at NIL (e.g., Rodgers and Walter, 2002). In Figure 3, we show the raw measurements, MDAC2 corrected measurements, and the kriged MDAC2 residual measurements as a function of the equiprobable measure. The equiprobable point provides a measure of the overlap of the earthquake and explosion populations. It is the point on a receiver-operator tradeoff curve of the error rates where the error rates are equal. For example an equiprobable measure of 0.1 implies that 10% of the earthquakes are misclassified as explosions and 10% of explosions are misclassified as earthquakes. In practice one might choose a decision line with unequal error rates, such as by picking a low probability of misclassifying an explosion. The equiprobable point provides a single numerical measure of performance that is much more intuitive than other measures such as Mahalanobis distance, though it can be related to that measure. We plot this against the number of optimal combinations of measurements, using the LDA (Linear Discriminant

Analysis) rule. For example the best single measurement, the best combination of two measurements and so forth. From this plot we can see at a glance that MDAC2, kriging, and multivariate combinations of measures each contribute to a significant improvement over the best single raw measure, and the overall result is an order of magnitude improvement in discrimination capability.

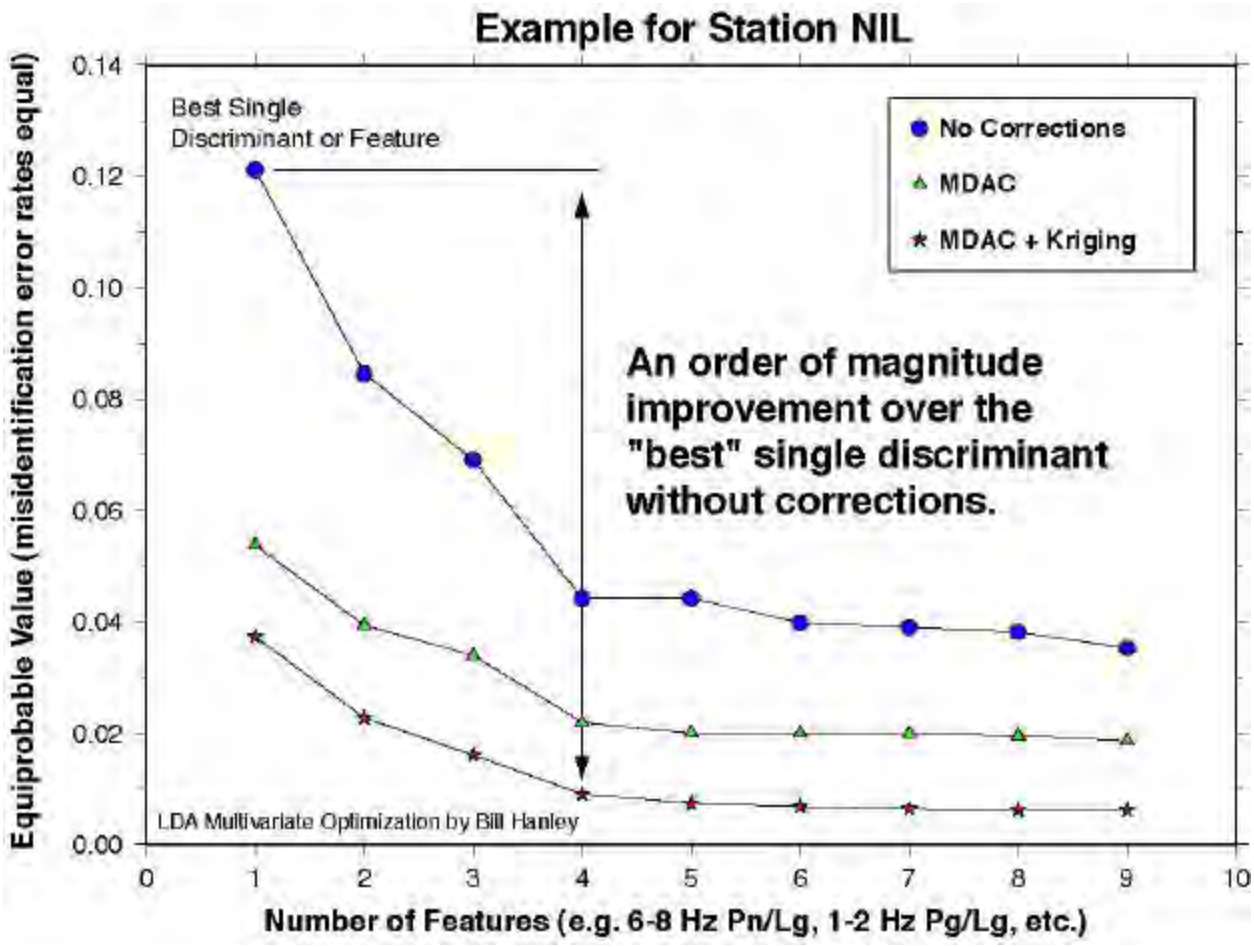

Figure 3. Plot of raw, MDAC corrected and kriged MDAC residual equiprobable values versus the number of feature measurements that go into an LDA discriminant. Feature measures are individual ratios such as 6- to 8-Hz Pn/Lg or 6- 8-Hz Pg / 1- to 2-Hz Sn (after Rodgers, Hanley, Sicherman and Walter, paper in preparation).

Coda Spectral Peaking as a Depth Indicator

In previous work we found that regional coda envelopes could be used to estimate source spectra and seismic moments from earthquakes down to very small sizes (Mayeda and Walter, 1996). These regional coda-derived spectra also show unusual peaking for very shallow events that we attribute to Rg-to-S coda scattering (Myers *et al*., 1999). We are continuing to explore this idea as a better way to identify very shallow events than by direct Rg identification. The Rg phase usually scatters and attenuates to the point at which it can no longer be identified within a few hundred kilometers of the source or less. However, its imprint remains on the coda spectra at much greater distances, and, by examining the size and frequency of the coda-based spectral peak, we hope to be able to use it as an indicator of very shallow events such as explosions. As an example we show in Figure 4 the coda

spectra of the May 11, 1998, Indian nuclear test compared with a number of nearby earthquakes. Note the strong spectral peak in the explosion spectra at about 1.5 Hz when compared with the earthquakes. We are also testing various ways to use this property and a depth discriminant. The left hand side of Figure 4 shows one such measure, moment versus m_b, both derived from the coda spectra, which appears to separate the explosion from the earthquakes.

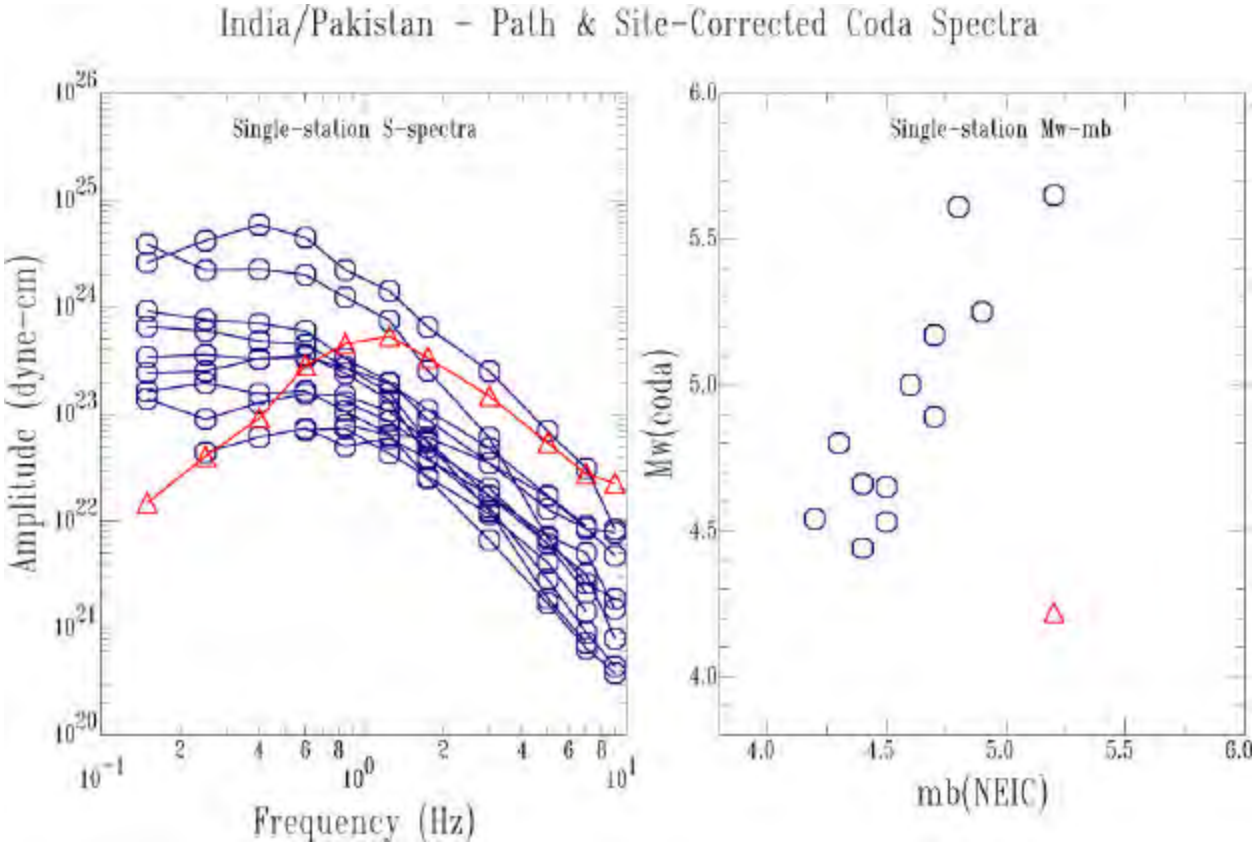

Figure 4. Regional coda envelope based spectra of regional events recorded at station NIL. The Indian test of May 11, 1998, is shown in red triangles. The right hand side shows discrimination on a moment-magnitude plot.

Phase-Matched M_S-m_b

The teleseismic magnitude ratio M_S:m_b is one of the best understood and most effective discriminants known (e.g. Stevens and Day, 1985). Several studies have also shown that it appears to be effective down to as small magnitudes as can be measured regionally (e.g., Denny *et al*., 1987). The problem is that the 20-s surface wave amplitude on which M_S is based can be below the noise even at regional distances. We are researching several ways to allow M_S measurements on smaller magnitude events to be made and used to improve discrimination. One way is to allow regional M_S measurements at periods between 10 and 20 s where the regional Airy phase produces the largest amplitudes (e.g., Denny *et al*., 1987). Additionally we can improve signal-to-noise by making use of phase-match filters (e.g. Herrin and Goforth, 1977). This is particularly attractive because in addition to reducing the noise level in the signal, it can provide an accurate maximum Ms estimate even on a very noisy trace. For small explosions that have reduced M_S excitation to start with and may not have observable surface waves, this method can still provide some discrimination power relative to earthquakes of the same mb that do have measurable M_S.

For the past several years, we have been carrying out systematic measurements of Rayleigh and Love wave group velocities in Western Eurasia with the goal of creating high-resolution tomography models (Pasyanos *et al*., 2001).

We follow the guidelines for measurements laid out in the 1998 surface wave workshop (Walter and Ritzwoller, 1998) and we have exchanged group velocity curves with groups at the University of Colorado and SAIC/Maxwell. The tomography maps that we have created are thus formed from both our own regional measurements and the broader measurements provided by those two groups. Overall, we have examined more than 20,000 seismograms and made more than 9,900 Rayleigh wave measurements and 5,400 Love wave measurements at periods from 10-100 seconds. These numbers apply to the middle period range and the number of good measurements decreases at the shorter and longer periods. In addition we have incorporated more than 3,000 path measurements from the University of Colorado (Ritzwoller, written communication) and SAIC/Maxwell (Stevens, written communication). We are currently using the surface wave tomography model in conjunction with receiver functions to estimate velocity structure in Western Eurasia (see Ammon *et al*., this volume).

The Rayleigh wave group velocity tomography described above can be used to provide predicted group velocity curves for input to a phase-match filtering routine. We can pre-calculate the expected group velocity at a station for any nearby event using the tomography model. In Figure 5, we show such a surface for station KEV in Norway. In addition we can use the measurements to provide an additional refinement to the model predictions using an intelligent interpolation technique. Here we use the Bayesian kriging technique of Schultz *et al*. (1998) on the measured residuals and add these back to the surface. Pasyanos (2000) previously demonstrated that this model plus a kriging approach provides better estimates of group velocity than either the model or kriging alone. Figure 5 shows an example of a PDE explosion and compares the raw data, a bandpass-filtered signal, and a re-dispersed seismogram from a phase-match filter. Note the improved signal-to noise ratio in the phase-match trace.

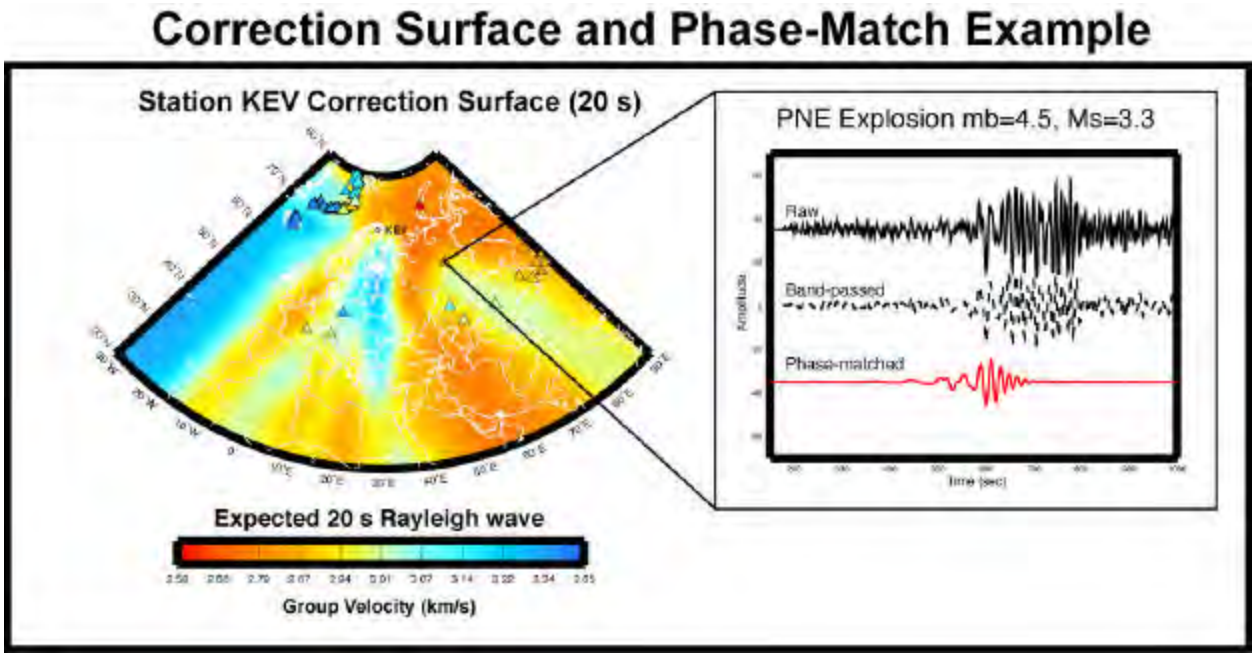

Figure 5. Correction surface for KEV showing predicted 20-s Rayleigh group velocities as a function of event location. The inset compares the results of three different sets of processing on a seismogram from a peaceful nuclear explosion. The phase-match re-dispersed seismogram result comes from using the correction surface.

To test the improvement provided by phase match filtering on M_s:m_b, we performed a test on a large dataset in Western Eurasia. We examine events with m_b from the National Earthquake Information Center larger than 3.5 where at least four stations record the event with a signal to pre-event noise ratio greater than 1.5. In the western Eurasia region covered by the tomography, this resulted in 1600 earthquakes and 11 explosions. Decreasing the number of stations or the signal-to-noise floor would allow more events. For these events we measured Ms using the formula of Rezapour and Pearce (1998). The maximum likelihood M_s was measured both by traditional band pass filtering and after phase matching filtering using the high-resolution tomography model. We tried a variety of tests in which we varied the SNR or number of stations we found that in almost all cases, phase match filtering improves the M_s:m_b discrimination. We show an example in Figure 6 below for the parameters discussed above.

The left hand side shows M_s versus m_b. We then remove the linear trend to form an M_s:m_b measure in the middle plot. From this scatter plot, we determine the receiver operator curve of the types of misidentification error. The phase match based M_s improves the overall discrimination performance by nearly a factor of two. Here we hold the dataset in common, but in further testing, we estimate that the phase match is able to lower the M_s detection measurement threshold by roughly 0.3 magnitude units or a factor of two. Both of these effects, improved discrimination performance and lower Ms measurement thresholds, indicate that using phase-match filtering for the M_s measurement can significantly improve discrimination performance.

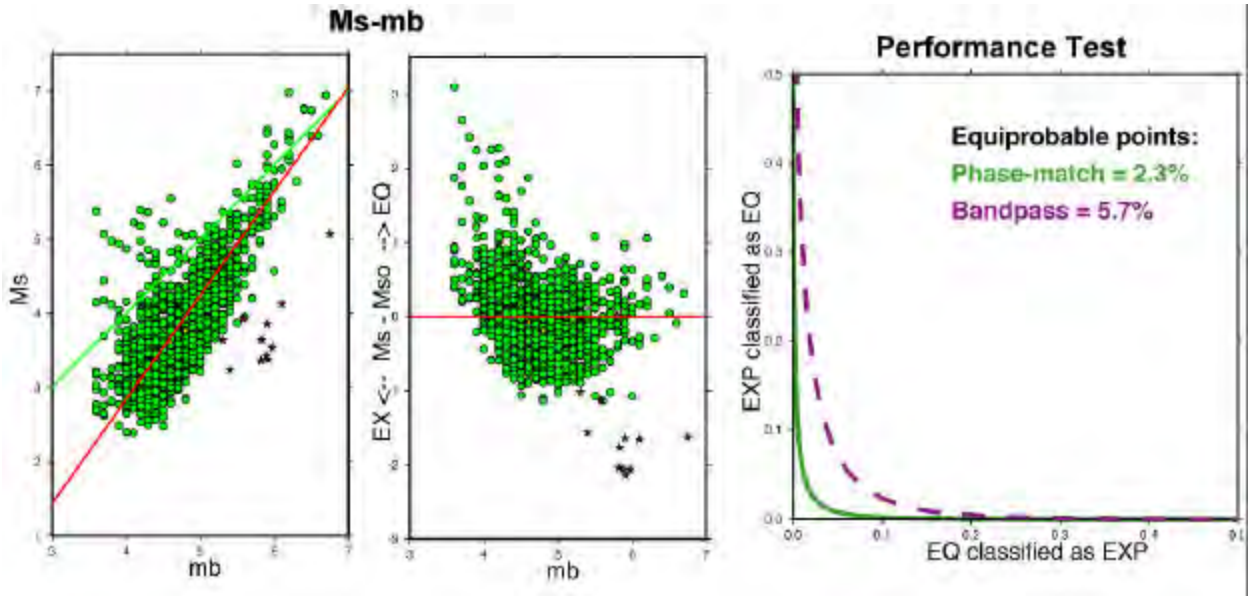

Figure 6. A Western Eurasia dataset test of M_s:m_b on left. Earthquakes are green circles and explosions are red stars. We remove the earthquake data trend from all data in the middle plot to form a magnitude independent measure of discrimination. The right hand plot shows the error rates from the de-trended data and the discrimination improvement provided by phase match filtering versus bandpass filtering.

CONCLUSIONS AND RECOMMENDATIONS

Regional discrimination algorithms require calibration at each seismic station to be used for nuclear explosion monitoring. We have developed a revised Magnitude and Distance Amplitude Correction procedure to remove source size and path effects from regional body-wave phases. This allows the comparison of any new regional events recorded at a calibrated station with all available reference data and models. This also facilitates the combination of individual measures to form multivariate discriminants that can have significantly better performance. We have also developed surface wave group velocity maps and correction surfaces for phase-match filtering to improve Ms:m_b discrimination and lower its effective threshold. Calibrating seismic stations to monitor for nuclear testing is a challenging task that will require processing large amounts of data, and collaboration with government, academic and industry researchers and incorporation of the extensive R&D results both within and outside of NNSA.

ACKNOWLEDGEMENTS

We thank Steve Taylor at LANL for many discussions on the topics of MDAC and regional discrimination as well as for supplying the MAK explosion and earthquake data pair in Figure 1. We thank Mike Ritzwoller and Jeff Stevens for sharing their group velocity measures.

REFERENCES

Denny, M. D., S. R. Taylor, and E. S. Vergino (1987). Investigation of mb and Ms formulas for the western United States and their impact on the Ms/mb discriminant, *Bull. Seism. Soc. Am*., **77**, 987-995.

Herrin, E. and T. Goforth (1977). Phase-matched filters: Applications to the study of Rayleigh waves, *Bull. Seism. Soc. Amer.*, **67**, 1259-1275.

Mayeda, K. M. and W. R. Walter, (1996). Moment, energy, stress drop and source spectra of Western U.S. earthquakes from regional coda envelopes, *J. Geophys. Res*., **101,** 11,195-11,208.

Myers, S. C, W. R. Walter, K. Mayeda, and L. Glenn (1999). Observations in support of Rg scattering as a source for explosions S waves: regional and local recordings of the 1997 Kazakhstan depth of burial experiment, *Bull. Seism. Soc. Am.*, **89**, 544-549.

Pasyanos, M. E. (2000). Predicting geophysical measurements: testing a combined empirical and model-based approach using surface waves, *Bull. Seism. Soc. Am.*, **90**, 790-796.

Pasyanos, M. E., W. R. Walter and S. E. Hazler (2001). A surface wave dis persion study of the Middle East and North Africa for monitoring the comprehensive nuclear-test-ban treaty, *Pure. Appl. Geophys*., **158**, 1145-1474.

Rezapour, M. and R. G. Pearce (1998). Bias in surface wave magnitude Ms due to inadequate distance corrections, *Bull. Seism. Soc. Am*., **88**, 43-61.

Rodgers, A. J. and W. R. Walter, (2002). Seismic Discrimination of the May 11, 1998 Indian Nuclear Test with Short-Period Regional Data From Station NIL (Nilore, Pakistan), *Pure Appl. Geophys.* **159**, 679-700.

Schultz, C., S. Myers, J. Hipp, and C. Young (1998). Nonstationary Bayesian kriging: a predictive technique to generate corrections for detection, location and discrimination, *Bull. Seism. Soc. Am.*, **88** 1275-1288.

Stevens, J. L. and S. M. Day (1985). The physical basis of mb:Ms and variable frequency magnitude methods for earthquakes and explosion discrimination, *J. Geophys. Res.*, **90**, 3009-3020.

Taylor, S., (1996). Analysis of high-frequency Pg/Lg ratios from NTS explosions and Western U.S. earthquakes, *Bull. Seism. Soc. Am.*, **86**, 1042-1053.

Taylor, S., A. Velasco, H. Hartse, W. S. Philips, W. R. Walter, and A. Rodgers, (2002). Amplitude corrections for regional discrimination, *Pure. App. Geophys*. **159**, 623-650.

Walter, W. R., K. Mayeda, and H. J. Patton, (1995). Phase and spectral ratio discrimination between NTS earthquakes and explosions Part 1: Empirical observations, *Bull. Seism. Soc. Am.*, **85**., 1050-1067.

Walter, W. R. and M. Ritzwoller, (1998). Summary report of the workshop on the U.S. use of surface waves for monitoring the CTBT, Lawrence Livermore National Laboratory *UCRL-ID-131835*, 16 pp.

Walter, W. R. and S. R. Taylor (2001), A revised Magnitude and Distance Amplitude Correction (MDAC2) procedure for regional seismic discriminants, Lawrence Livermore National Laboratory UCRL-ID-146882.

IMPROVING THE FUNDAMENTAL UNDERSTANDING OF REGIONAL SEISMIC SIGNAL PROCESSING WITH A UNIQUE WESTERN US DATASET

William R. Walter,[1] Kenneth D. Smith,[2] Stanley D. Ruppert,[1] Teresa F. Hauk,[1] Jennifer L. O'Boyle,[1] Flori Ryall,[1] Michael A. Firpo,[1] and Douglas A. Dodge[1]

Lawrence Livermore National Laboratory,[1] University of Nevada, Reno[2]

Sponsored by National Nuclear Security Administration
Office of Nonproliferation Research and Engineering
Office of Defense Nuclear Nonproliferation

Contract Nos. W-7405-ENG-48[1] and DE-FC03-01SF22419[2]

ABSTRACT

This project builds a unique historic database of regional distance nuclear explosion, earthquake, and mine-related digital broadband seismograms. The emphasis is on data from Lawrence Livermore National Laboratory (LLNL)-managed stations MNA, ELK, KNB and LAC that recorded many nuclear tests and nearby earthquakes in broadband digital form since 1980. We also include data from other open broadband stations in the western United States with long operating histories and/or ties to the International Monitoring System (IMS) (e.g. PFO, YKA, CMB, NEW, DUG, ANMO, TUC). These waveforms are associated with a reconciled catalog of events and station response information to facilitate analysis. The goal is to create a high-quality database that can be used in the future to analyze fundamental regional detection, location, magnitude, and discrimination issues.

In the initial stages of the project, we are collecting continuous data from open stations and recovering event data from the LLNL-managed stations from past nuclear tests and earthquakes that exist but have not been collected together into a coherent database. We have also collected six different regional network catalogs from the University of Nevada, Reno (UNR), to provide accurate independent location information for events on the Nevada Test Site (NTS) and in the surrounding region. We have used NNSA-developed software to reconcile these catalogs with each other and to incorporate them into a set of larger continental scale (CNSS, USGS mining catalog compiled by Jim Dewey) and global scale (PDE, REB, ISC) catalogs. Finally, we incorporate the best catalogs of NTS nuclear event locations (DOE Rev 15) and source properties (Springer *et al*. 2002). The result is a single catalog of preferred origins, source information, and station information from which regional waveforms can be extracted from continuous data and associated within the database.

Using the reconciled catalogs and databases, we are working with the UNR network data to determine a subset of about 100 events that are well located and cover a range of magnitudes, source types, and locations. An experienced analyst will then review this dataset during the summer/fall of 2002. She will pick all arrival onsets with quantitative uncertainties and make note of data problems (timing errors, glitches, dropouts) and issues. The resulting arrivals and comments will then be loaded into the database for future researcher use. It is anticipated that this set of consistently picked, independently located data will provide an effective test set for regional sparse station location algorithms. In addition because the set will include nuclear tests, earthquakes, and mine-related events, each with related source parameters, it will provide a valuable test set for regional discrimination and magnitude estimation as well.

We are concentrating on the subset of well-located events that have been picked by our analyst. A final CSS 3.0-format-compatible relational database of these approximately100 events will be put onto a CD-ROM and distributed for other researchers to use in benchmarking regional algorithms after the conclusion of the project.

OBJECTIVE

The objective of this project is to build a historic western U.S. database of regional distance nuclear explosion, earthquake, and mine-related digital broadband seismograms with their associated parameters (origins times and location, instrument response, etc.). Although the original title of the project remains unchanged, its scope has been reduced to match the level of funding. Therefore we focus on a subset of this data to undergo careful quality control, to provide independent regional network ground truth location, and to perform quantitative regional phase picking. This subset will be released as a CD-ROM at the conclusion of the project and provide source type and location ground truth data for monitoring researchers to make use of in benchmarking algorithms.

RESEARCH ACCOMPLISHED

Seismic nuclear monitoring research is data driven. The number of digital seismic records of underground nuclear tests at regional distances is quite restricted both in number and geographical location. Consequently the finite number of existing regional nuclear test records is a unique resource that needs to be thoroughly exploited to create the best verification system possible. We believe that this exploitation is incomplete for the extensive Nevada Test Site (NTS) nuclear explosion records. Therefore in this project our goal is to build the largest, most complete, and best-documented database of explosions, earthquakes, mine blasts and mine tremors in the western U.S. Once completed, this database, we believe, will provide a well-organized and highly efficient way to conduct fundamental monitoring research on regional seismic event detection, location, identification and characterization.

Building a Comprehensive Western U.S. Database

The process of building this new database involves a series of steps, which include:

1. Collecting local, regional and global seismicity catalogs around NTS and the western U.S.
2. Reconciling catalogs into a single table of events with preferred origin information
3. Compiling event parameter information (e.g. yield, material properties, focal mechanisms, etc.)
4. Collecting continuous data from selected stations
5. Compiling station site and instrument response information
6. Extracting event waveforms from continuous data and loading into database with ties to the reconciled catalog
7. Selecting a high quality data subset to analyze
8. Quantitatively analyzing the data subset and loading timing picks and uncertainties into database
9. Distributing data subset and maintaining a database for use in nuclear explosion monitoring research

At the time of this writing, we have completed steps 1-5 and are working on steps 6-9. Here we briefly describe the research accomplished on this project so far.

We have attempted to obtain as complete a list of catalogs in the vicinity of the NTS and the western U.S. as possible. A full list of the dates and locations of all U.S. nuclear explosions is available from DOE (US DOE 2000). Some of these events have announced yields. In addition Springer *et al.* (2002) have compiled the most complete listing of working point parameters (e.g. depth, working point density, velocity, gas porosity) for U.S. underground nuclear tests. These parameters affect seismic frequency content and discriminants (e.g. Walter *et al*., 1995). The University of Nevada Reno (UNR) runs regional seismic networks in southern and northern Nevada that provide the most complete and accurate lists of earthquakes for this region. We have worked with UNR to obtain as complete a set of catalogs for the state of Nevada as possible. We believe these local networks can be used to obtain independent high-quality ground truth location and depth information.

In addition to Nevada and NTS catalogs, we have also collected a number of regional and global scale catalogs. A very nice U. S. regional seismicity catalog is compiled regularly by the University of California at Berkeley from most of the regional seismic network operator's catalogs in this country as part of the Council of National Seismic Stations (see http://www.cnss.org). Although this catalog contains a very large number of events, it does not capture all the events in the local UNR catalogs listed above. We have also collected the USGS mine explosion listing that is compiled by Jim Dewey. Finally, we include the standard global catalogs from the USGS Preliminary Determination of Epicenters (PDE), the International Seismological Commission (ISC) and the International Monitoring System (IMS) Reviewed Event Bulletin (REB).

We have gained much experience in building large reconciled databases over the past several years (see O'Boyle *et al*, this volume) and we make full use of these tools and procedures in this project. We assign each of these catalogs a rank order for reconciliation. The catalogs are then parsed and locations and origin times are compared. Events in common are assigned to one unique event identification number and the highest ranking catalog's origin information then becomes the preferred one. The other origin information is retained as well. In this way we build up a single listing of events that can be used to extract waveforms from continuous data or tie to event segmented data. For a more complete discussion of the catalog reconciliation process see O'Boyle *et al*. (this volume).

Table 1. Seismicity Catalogs Collected, Parsed and Reconciled for this Project

Date Range	Source Types	Catalog Name	Comments and References
1945-1992	Nuclear tests	DOE U.S. Announced List	Revision 15 (USDOE, 2002)
1946-1992	Nuclear tests	Springer catalog	Below surface tests, Springer *et al* (2002)
1978-2000	Earthquakes	UNR_SGB_merged	Covers Southern Great Basin (SGB) only
1992-2000	Earthquakes	UNR_SGB_relocated	Covers Southern Great Basin (SGB) only. Smith *et al*. (2002)
1868-2000	Earthquakes	YMP_PSHA	Yucca Mountain Project (YMP) Probability of Seismic Hazard Assessment (contains a composite of many catalogs within 300 km of YM)
1978-1999	Earthquakes	UNR_NN_consolidated	Covers northern Nevada (NN) area only
2000-2001	Earthquakes	UNR_2000-2001	University of Nevada Reno networks catalog
1850-1998	Earthquakes	Nevada historic catalog	Compiled by Depolo and Depolo (1999)
1898-2002	Earthquakes	CNSS	Council of National Seismic Stations - a partially reconciled catalog of western US seismicity compiled by UC Berkeley
1920-2002	Earthquakes, explosion and mine tremors	USGS Monthly PDE	Preliminary Determination of Epicenters (PDE)
1964-1999	Earthquakes	ISC	International Seismological Commission (ISC)
1995-2000	Earthquakes	IMS REB	Comprehensive Nuclear-Test-Ban Treaty International Monitoring System (IMS) Reviewed Event Bulletin (REB)
1997-2002	Mine Blasts	USGS Dewey catalog	A catalog of mining explosions compiled by Jim Dewey at the U.S. Geological Survey

A major emphasis of this project is on regional seismic waveforms from the four seismic stations of the Lawrence Livermore National Laboratory (LLNL) operated Livermore NTS Network (LNN). These stations have been all digital since about 1980 and have recorded more than 120 underground nuclear tests in that time. In addition there are a number of waveforms that were digitized from analog records that are of more uncertain quality. We have identified LNN waveforms from approximately 320 nuclear tests to review for quality control and include in the database. Another large database of regional nuclear seismic waveforms was recorded on the Leo Brady Seismic Network (stations BMN, DAC, LDS, MVU, TPH), which is operated by Sandia National Laboratory (Lee, 2001). We are actively working with Sandia personnel to include this data set in the database as well. Both of these

networks have recorded hundreds of regional earthquakes, many in close proximity to prior nuclear tests, which make an excellent dataset for studying the physical basis of regional seismic discrimination.

In addition to the National Laboratory run networks, we have also collected data from other broadband open seismic stations that are archived by the IRIS DMC. We have selected just a subset of these stations with emphasis on stations that have long operating histories, stations that are part of the IMS network and stations that are spread throughout the western U.S. Table 2 below gives a list of the stations for which we have collected data to be included in the database.

Table 2. Seismic Station Data Retrieved for Event Waveform Extraction to Database

Data Type and Period	Station code	Location and comments
Continuous 1988-2001	PFO	Pinion Flat, California (IMS auxiliary station)
Continuous 1989-2001	COR	Corvallis, Oregon
Continuous 1989-2001	ANMO	Albuquerque, New Mexico (IMS auxiliary station)
Continuous 1992-2001	CMB	Columbia, California
Continuous 1992-2001	TUC	Tucson, Arizona
Continuous 1993-2001	YBH	Yreka, California (IMS auxiliary station)
Continuous 1997-2001	DUG	Dugway, Utah
Continuous 1997-2001	TPNV	Tonopah Springs, Nevada
Continuous 1997-2001	NEW	Newport, Washington (IMS auxiliary station)
Event segments	ELK	Elko, Nevada (IMS auxiliary station)
Event segments	KNB	Kanab, Utah
Event segments	MNV	Mina, Nevada (IMS primary array element)
Event segments	LAC	Landers, California (closed in 1999)
Event segments	BMN	Battle Mountain, Nevada
Event segments	DAC	Darwin, California
Event segments	LDS	Leeds, Utah
Event segments	TPH	Tonopah, Nevada
Event segments	MVU	Marysvale, Utah

In Figure 1 we show a map of the region covered by this project, with the locations of stations (Table 2) for which we are archiving seismic data and the locations of the reconciled events for the time period from 1997-present (July 2002). We have chosen 1997 as the starting point for this plot since that is when the Dewey catalog of mine seismicity starts. The reconciled catalog as a whole goes back to 1852. Figure 1 shows the more than 8000 earthquakes and 1600 mining events (mainly explosions) in our reconciled catalog with magnitudes (mb, Mw or ML) greater than or equal to 2.5. The catalog does include events of all magnitudes, and in some locations where the UNR network is dense; there are magnitudes of -1 or less. At the time this map was produced, the reconciliation was not quite finished and the final map shown at the meeting will include even more earthquakes.

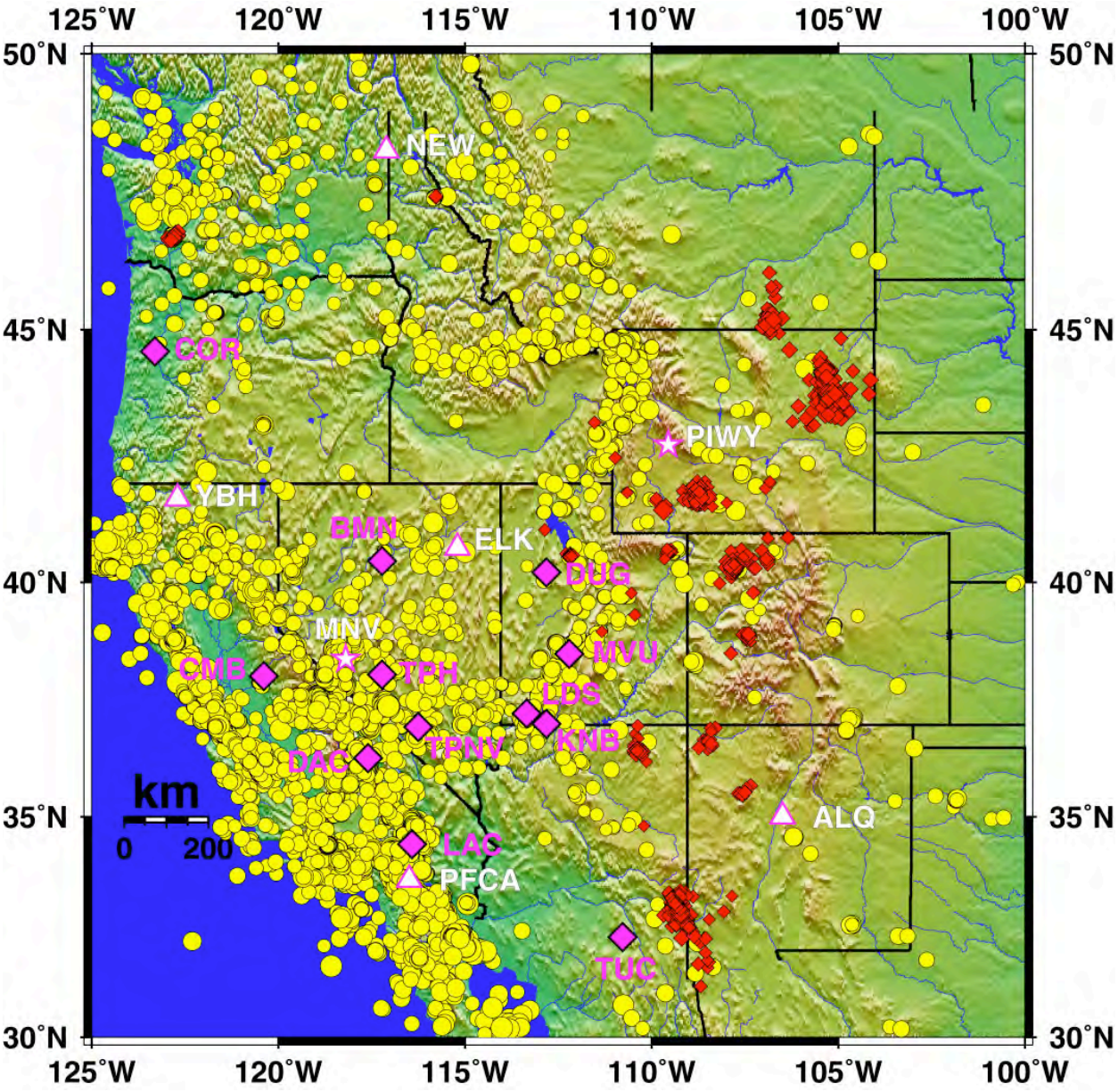

Figure 1. A shaded relief map showing the locations of seismic stations and select events in this project. Stations are listed in Table 2, and the events are drawn from a reconciled composite catalog created from the catalogs listed in Table 1. IMS primary stations are plotted as white stars. IMS auxiliary stations are plotted as white triangles, and other broadband stations are plotted as pink diamonds. Seismic stations are labeled by name. Earthquakes are plotted as yellow circles and mine seismicity as small red diamonds. Seismic event symbols are scaled by magnitude.

High-Quality Data Subset

Once we have completed the reconciled catalog of seismicity, extracted the available seismic waveforms for each event and organized the results into the western U.S. database, we want to select a high-quality subset for detailed analysis. We plan to comb through the thousands of events in the database with magnitudes greater than about 2 to find events recorded at many stations with good quality waveforms and well document locations and source properties.

One goal for this high-quality subset is to choose events with excellent ground truth hypocenters from the regional networks for use in location research. We will work with the UNR network locations and picks to determine the level of accuracy of the locations and will relocate some events to improve them. Once we have selected the high-quality subset, an experienced seismic analyst, will examine the data. She will pick all arrival onsets with quantitative uncertainties and make note of data problems (timing errors, glitches, dropouts) and other issues. Her arrivals and comments will then be loaded into the database for future researcher use. We believe her picks at local, near and far regional distances when combined with the independent ground truth will be useful in testing and benchmarking sparse station location algorithms.

We also want to select the high-quality data set with an eye towards discrimination research. Therefore, in addition to excellent ground truth locations, we also want to choose events that have well documented source properties. For explosions this means working point source medium properties such as density, P-velocity, and gas porosity. We plan to select explosions that span the full range of these properties. We want to include some of a small number of explosions with announced yields to facilitate yield estimation research. Finally, we want to span the full range of magnitudes and depths and will therefore include a few of the larger explosions that were conducted prior to the limit of 150-kT imposed by the Threshold Test Ban Treaty of 1974. For earthquakes we want to select events that cover a range of magnitudes, depths, and locations through the western U.S. We also want to provide focal mechanism information for as many of the events as possible. The impact of variations in focal mechanism and depth on regional discriminants are the subjects of current research (e.g. Zhang *et al*., 2002).

In Figure 2, we show an example of some candidate events we are examining around NTS for inclusion in the high-quality data subset. The high level of natural earthquake activity since the 1992 Landers earthquake provides a nice dataset to contrast with the nuclear tests that ended in 1992. Recently a number of studies have been done that investigate the details of this seismicity (e.g. Smith *et al*, 2002; Ichinose, 2002). We plan to review these studies and use them to provide additional ground truth about these events.

At the conclusion of this project, we plan to put the high-quality subset of approximately 100 events, along with associated parameters (time picks, focal mechanisms, source media properties, etc.) on a CD-ROM in CSS 3.0 compatible database format for release to interested monitoring researchers. We hope this well organized and compact set of data will prove useful in both researching and benchmarking seismic monitoring algorithms in detection, location, identification and magnitude yield estimation.

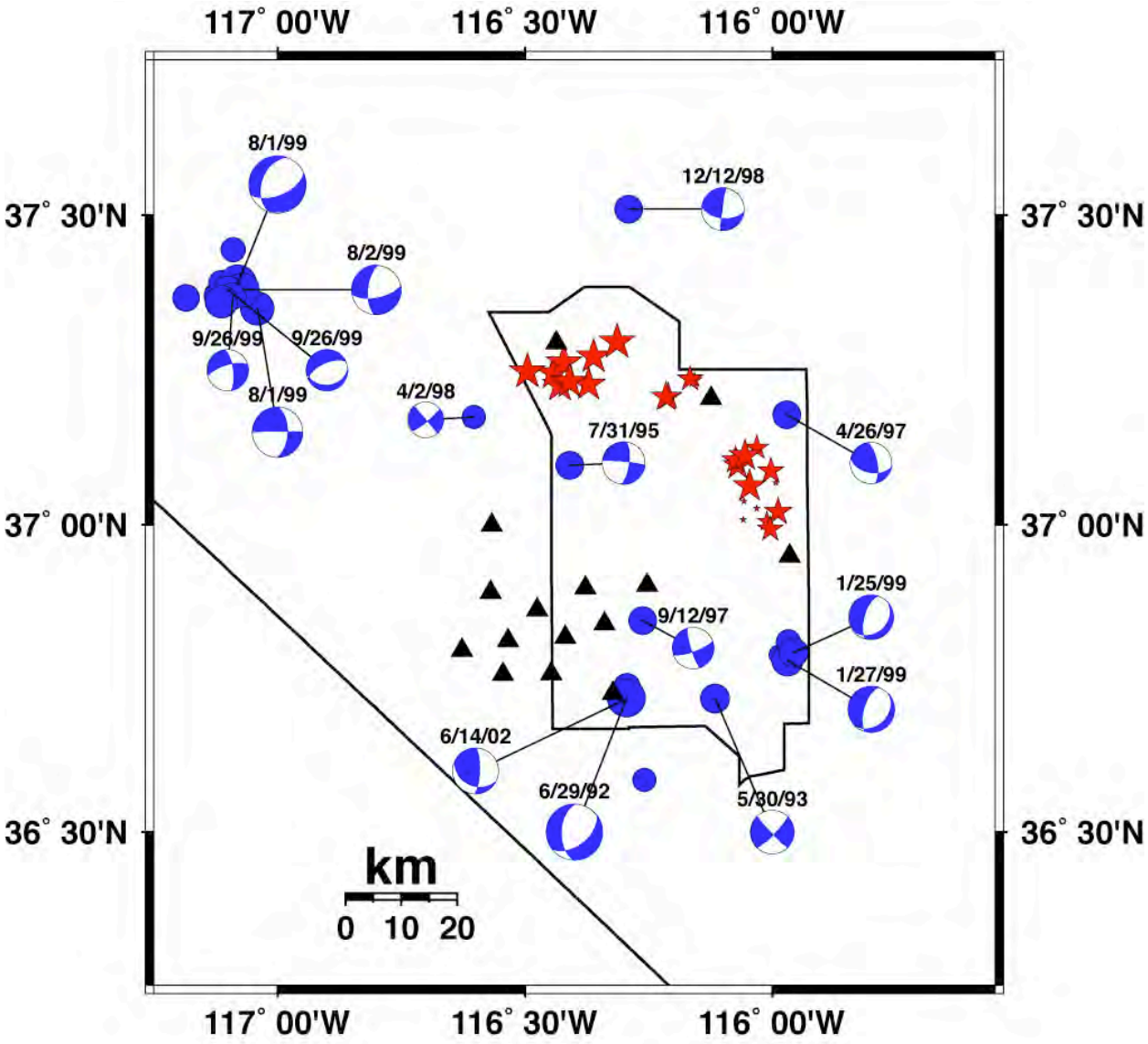

Figure 2. A map showing 25 earthquakes (blue circles) and 25 explosions (red stars) from 1989-2002 near NTS that are under consideration for inclusion in the high-quality data subset. The map shows the boundaries of NTS and the locations of some of the UNR-run Southern Great Basin network that can provide excellent ground truth hypocenter information for many of these events. Also shown are focal mechanisms for about 15 of these earthquakes drawn from regional studies by Smith *et al* (2002), Ichinose *et al* (2002) and the U. C. Berkeley moment tensor catalog. These earthquakes cover most of the seismicity in this region with magnitudes greater than about 3.5. The nuclear explosions cover the most recent 25 events when seismic network coverage is most complete and include all three main testing areas at NTS (Pahute Mesa, Rainier Mesa and Yucca Flat). The explosions also cover a fairly full range of magnitude, depths, and source material properties.

CONCLUSIONS AND RECOMMENDATIONS

We continue our project to build the most complete and best-documented database of regional distance nuclear explosion, earthquake, and mine-related digital broadband seismograms in the western U.S. We plan to select and mark phase onset times for a high-quality subset of these data, which will be distributed at the conclusion of this project. We believe this set of consistently picked, independently located data will provide an effective test set for regional sparse station location algorithms. In addition because the set will include nuclear tests, earthquakes, and mine-related events, each with related source parameters, it will provide a valuable test set for regional discrimination and magnitude/yield estimation as well.

REFERENCES

DePolo, D. M and C. M. DePolo, (1999). Earthquakes in Nevada, Nevada Bureau of Mines and Geology, Map 119.

Ichinose, G. A., J. G. Anderson, and K. D. Smith (2002). Source parameters of Eastern California and Western Nevada Earthquakes from regional moment tensor inversion, *Bull. Seism. Soc. Am*. (submitted) 2002.

Lee, J. W., (2001). A new seismic data system for determining nuclear test yields at the Nevada Test Site, Sandia National Laboratory Report, SAND2001-3373.

Smith, K. D., D. von Seggern, D. Depolo, (2002). Seismicity in the vicinity of Yucca Mountain 1992-2000 and regional tectonic process, *Bull. Seism. Soc. Am.* (submitted) 2002.

Springer, D. L., G. A. Pawloski, J. L. Ricca, R. F. Rohrer and D. K. Smith, (2002). Seismic source summary for all U. S. below surface nuclear explosions, *Bull. Seism. Soc. Am.* (in press) 2002.

United States Department of Energy, (2000). United States Nuclear Tests, July 1945 through September 1992, Technical Report DOE/NV-209-REV15.

Walter, W. R., K. Mayeda, and H. J. Patton (1995). Phase and spectral ratio discrimination between NTS earthquakes and explosions Part 1: Empirical observations, *Bull. Seism. Soc. Am.,* **85**., 1050-1067.

Zhang, J., T. Lay, J. Zaslow and W. R. Walter, Source effects on regional seismic discriminant measurements, *Bull. Seism. Soc. Am*. (in press) 2002.

EVALUATION OF INTERMEDIATE-PERIOD (10- TO 30-SEC) RAYLEIGH-WAVE GROUP-VELOCITY MAPS FOR CENTRAL ASIA

Xiaoning Yang,[1] Steven R. Taylor,[1] Howard J. Patton,[1] Monica Maceira,[1,2] and Aaron A. Velasco[1,3]

Los Alamos National Laboratory,[1] Penn State University,[2] University of Texas at El Paso[3]

Sponsored by National Nuclear Security Administration
Office of Nonproliferation Research and Engineering
Office of Defense Nuclear Nonproliferation

Contract No. W-7405-ENG-36

ABSTRACT

We are evaluating the 10- to 30-second Rayleigh-wave group-velocity maps for central Asia constructed from maps developed by Levshin *et al.* (2001), Ritzwoller and Levshin (1998) and Stevens *et al.* (2001) for predicting surface-wave arrival times. Currently, we are focusing on the region between 15 and 55 degrees north latitude and 70 and 120 degrees east longitude. A new set of group-velocity measurements not included in the development of the tomographic maps has been used in the evaluation. The overall arrival-time predictions at all periods from the maps are good with the best predictions at 15 seconds. The group-velocity prediction-error (prediction minus measurement) distribution at 15 seconds has a mean of –0.0125 km/sec and a standard deviation of 0.095 km/sec.

We have tested the effectiveness of the maps in extracting surface-wave signals through phase-match filtering. Phase-matched filters constructed from the group-velocity maps seem to be effective in isolating and enhancing surface wave signals. In general, phase-matched filters have similar or better performance compared with bandpass filters in extracting surface-wave signals in the 17- to 23-second period range. Phase-matched filters could be particularly useful in situations in which multi-pathing is significant, surface waves from multiple events arrive close in time or there exists 20-second noise. Using the group-velocity maps also improved the number of surface-wave detections by 23% over a one-dimensional (1-D) model detection. It illustrates the usefulness of developing accurate group-velocity maps in lowering the surface-wave detection threshold.

We will begin testing the applicability of shorter period amplitude measures for estimating group-velocity maps down to 5 seconds. We also plan to broaden our study area to include regions further to the north.

OBJECTIVE

The objective of this research is to develop methods for improvements to the regional m_b-M_s discriminant. The research currently focuses on the evaluation and refinement of existing Rayleigh-wave group-velocity tomographic maps. These maps are used to construct phase-matched filters in an effort to reduce surface-wave detection thresholds and to construct regional M_s scales. Our evaluation and refinement is part of the product integration process for US National Data Center monitoring operations.

RESEARCH ACCOMPLISHED

Study Region, Periods and the Group-Velocity Maps

Our current effort is focused on the central-Asia region between 15 and 55 degrees north latitude and between 70 and 120 degrees east longitude, and for periods between 10 and 30 seconds. There are a few group-velocity maps developed recently by different researchers that cover portions of the region and portions of the period range that we are studying. Ritzwoller and Levshin (1998) inverted group-velocity maps for the Eurasia continent that included our study area. The frequency range of their maps is from 20 to 200 seconds. Stevens *et al.* (2001) calculated global group-velocity maps for periods from 4 seconds up to 400 seconds from their global crust and upper-mantle structure model. Levshin *et al.* (2001) inverted a set of short- to intermediate-period (7 to 20 seconds) group-velocity measurements and obtained tomographic maps for the south Asia and east Africa region (10° ~ 50° N, 20° ~ 140° E). For the purpose of lowering surface-wave detection thresholds and developing regional M_s scales, these shorter period maps are important.

To construct group-velocity maps for our region and for the periods between 10 and 30 seconds, we requested group-velocity maps from the above mentioned authors. Figure 1 illustrates the coverage of these maps except that of Stevens *et al.*'s (2001) maps (which are global,) and our study area. Restricted by the periods that these maps cover, we selected periods of 10, 11, 12, 13, 14, 15, 16, 18, 20, 25 and 30 seconds for our composite maps. We used

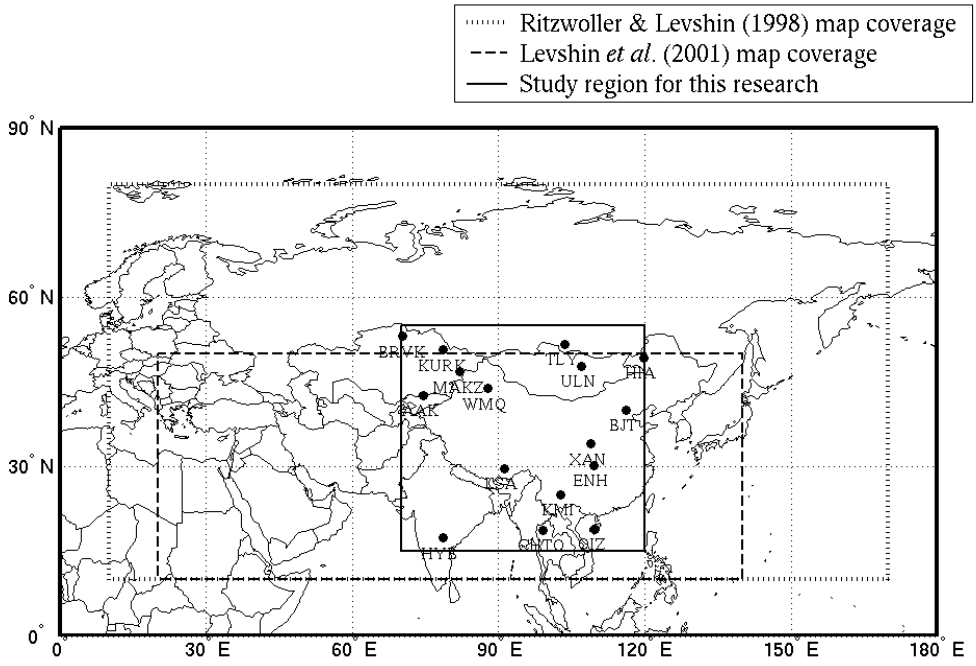

Figure 1. Geographic coverage of two of the group-velocity maps used in constructing the composite maps, and the study region. Data recorded at stations indicated in the figure were used in the analysis.

Levshin *et al.*'s (2001) maps for periods from 10 to 20 seconds and for the region south of 50° N in the composite maps. We used Stevens *et al.*'s (2001) maps for portions of the composite maps between 50° N and 55° N not covered by Levshin *et al.*'s (2001) maps from 10 to 18 seconds. For a 20-second map, we used Ritzwoller *et al.*'s (1998) map to fill in the area between 50° N and 55° N. We also used Ritzwoller *et al.*'s (1998) maps to construct the 25- and 30-second maps. The composite maps have a 1-degree spatial resolution. Figure 2 displays the 20-second composite group-velocity map for the study region. Major geographic features such as the Indian Subcontinent, the Himalaya Mountains, the Tarim Basin, the Junggar Basin, the Bay of Bengal and the South China

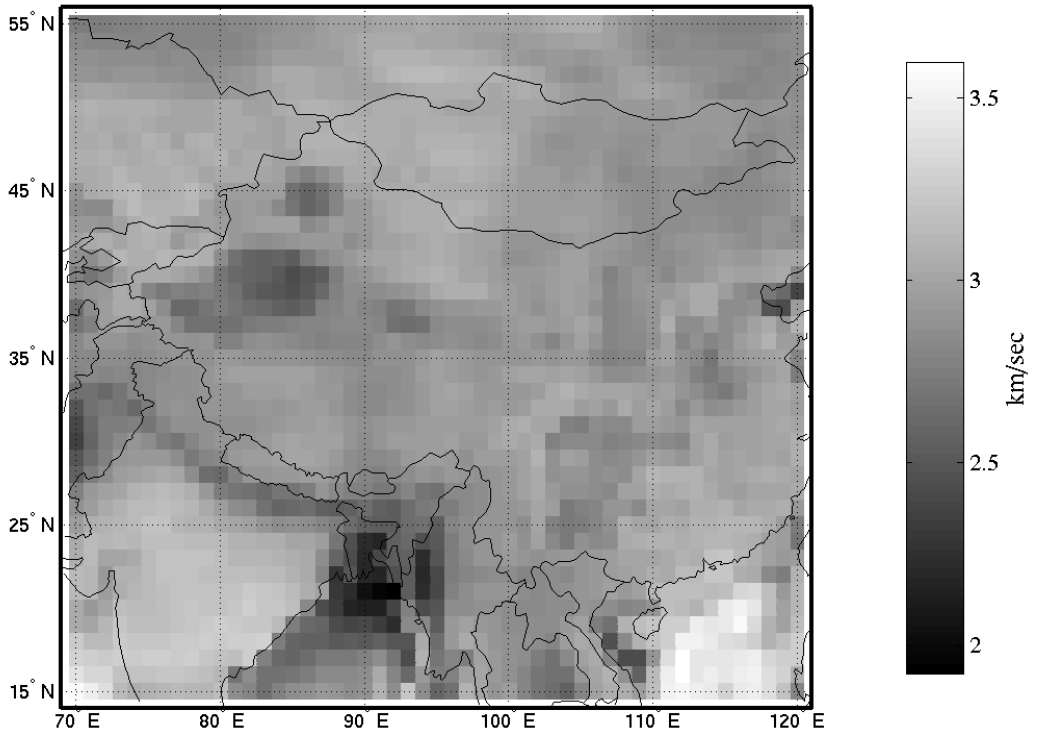

Figure 2. The composite, 20-second group-velocity map. The map has 1-degree resolution. Major geographic features are delineated by the variations of the group velocities.

Sea are characterized by deviations of surface-wave group velocities from the average. It suggests the consistency of the map with the tectonics of the region.

Group-Velocity Data

In order to evaluate the group-velocity maps, we collected a set of vertical, broadband seismogram data recorded at stations shown in Figure 1 to make group-velocity measurements. These data are for events with magnitudes equal to or larger than 4 that occurred in 2001 in the study region. The data set was not used in inverting for the group-velocity maps that we intended to evaluate. Figure 3 shows the distribution of these events along with the stations that provided the data. Also shown is the path coverage of the 20-second group-velocity measurements. The numbers of the group-velocity measurements that we made from this data set range from 1403 to 1860 for different periods. The total number of measurements is 18755 for 293 events.

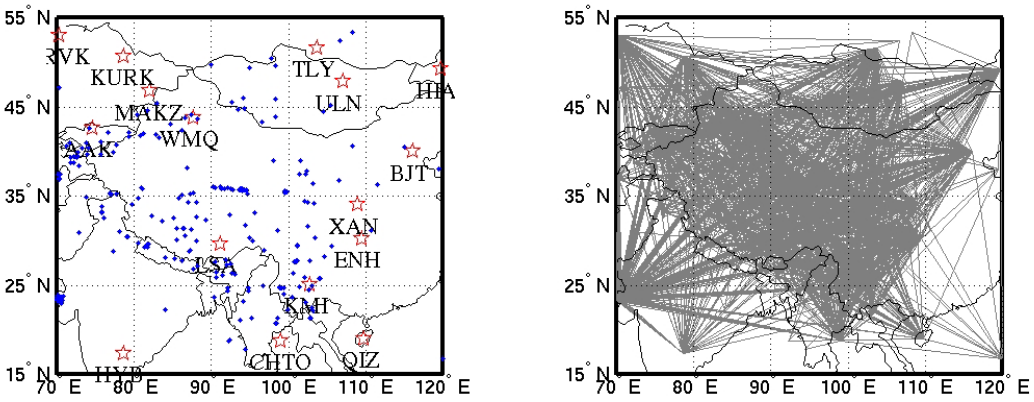

Figure 3. The event distribution for the data set that we collected (left) and the path distribution of 20-second group-velocity measurements that we made (right). The dots in the left plot are the events. The great-circle paths are shown as gray lines in the right plot.

Group-Velocity Map Evaluation

We took several approaches to evaluate the performance of the group-velocity maps in predicting measured data. We calculated the differences between measured group velocities and predicted values and analyzed the residua distribution. We also constructed phase-matched filters from the group-velocity maps and applied the filters to surface-wave seismograms to see the effectiveness of the filters in enhancing the surface-wave signal-to-noise (S/N) ratio. Finally, we used Stevens and McLaughlin's (2001) surface-wave detection method and tested the improvement of the 2-D group-velocity maps in surface-wave detection over a 1-D China model (Jih, 1998).

Residua analysis

Figure 4 plots the results of the residua analysis. Residua were obtained by subtracting the measurements from the predictions. They can be thought of as the prediction error with positive residua corresponding to faster group-velocity predictions. Plot b in the figure includes data for all periods. Analysis of data for individual period yielded similar distributions.

The overall map predictions are very good. Measured and predicted average group velocities follow each other closely. Most of the residua lie within the range between –0.5 and +0.5 km/sec. Their distribution is Gaussian-like with a mean close to zero. The standard deviations of the residua are in the similar range as those of the root-mean-square misfits of some surface-wave tomographic studies. For example, Ritzwoller and Levshin (1998) obtained a misfit of 0.09 km/sec for the 20-second Rayleigh wave. The misfit for 20-second Rayleigh wave was 0.127 km/sec in the surface-wave tomographic study of Pasyanos *et al.* (2001). The residua standard deviations of this analysis range from 0.095 to 0.138 km/sec with the minimum at 15 seconds. Whereas the map performance does not vary significantly across the period range of this analysis, best predictions occur near 15 seconds with the smallest residua standard deviations and smallest relative prediction errors.

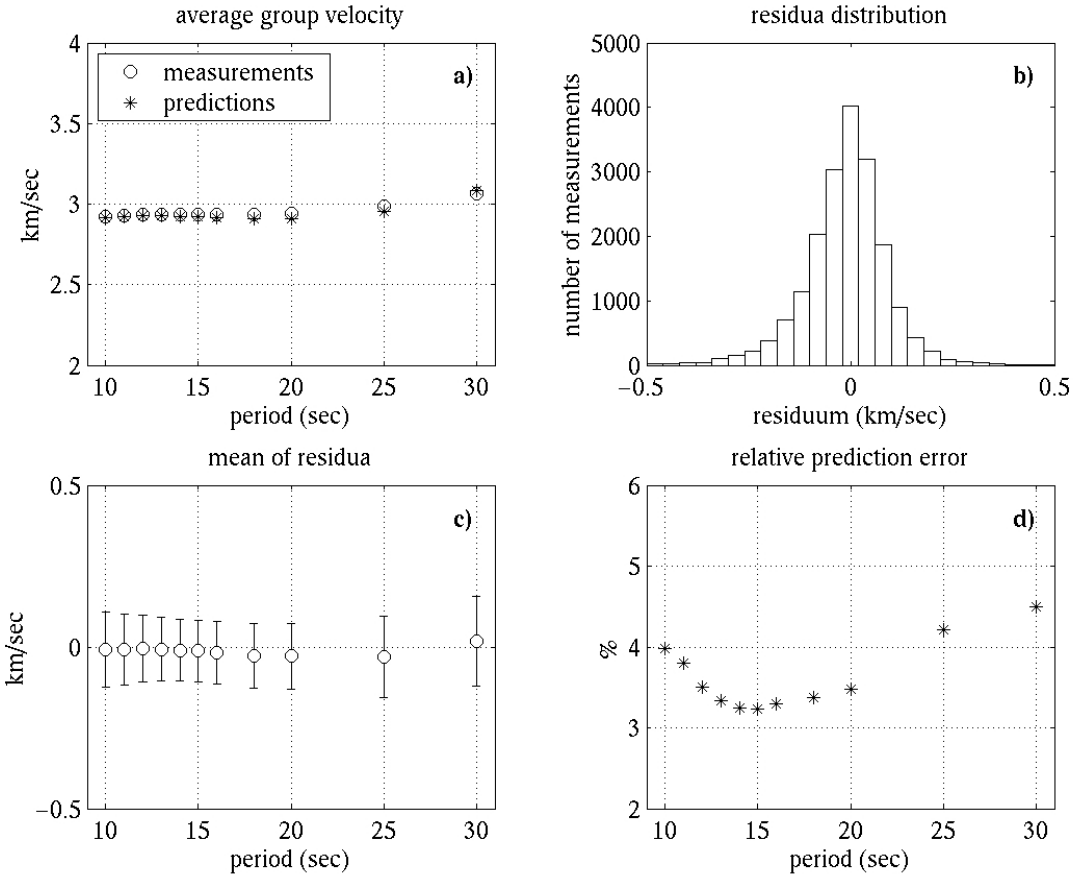

Figure 4. Residua analysis results. a) Average group velocities from the measurements and from the predictions. b) Distribution of residua obtained by subtracting the measurements from the predictions. Data for all periods are included. c) Mean of the residua as a function of period with one standard deviation of the residua as error bars. d) Relative prediction error obtained by dividing the residua standard deviation by the average measured group-velocities.

Phase-match filtering

Phase-matched filters (e.g., Herrin and Goforth, 1977) are used to enhance the S/N ratio of surface waves. The effectiveness of a phase-matched filter in extracting surface-wave signals depends on the accuracy of the group-velocities used to construct the filter. We constructed phase-matched filters with the group-velocity information from the maps and applied the filters to our data set. In general, the phase-matched filters are able to isolate the surface waves and suppress noise and other signals that do not arrive within the time window that the filters predict for the surface waves. Figure 5 gives such an example. If the event is well located, the group-velocity maps seem to be able to provide information accurate enough to construct an effective phase-matched filter.

In current practice, surface-wave magnitudes are calculated from amplitudes measured near 20 seconds. This is the reason that we focus our analysis around this period. One of the methods to improve the S/N ratio of a narrow-band surface-wave signal is to bandpass filter the data. We compared the methods of bandpass filtering and phase-match filtering by filtering both the original signal and the phase-match filtered signal between 17 and 23 seconds. For a large portion of the data tested, the two methods produced similar results to those shown in Figure 6. We did find situations where an additional phase-match filtering prior to bandpass filtering produced better results. An example is illustrated in Figure 7. We believe that phase-matched filters are useful particularly in situations in which multi-pathing is significant, surface waves from different events arrive close in time, or there is 20-second background noise in the data.

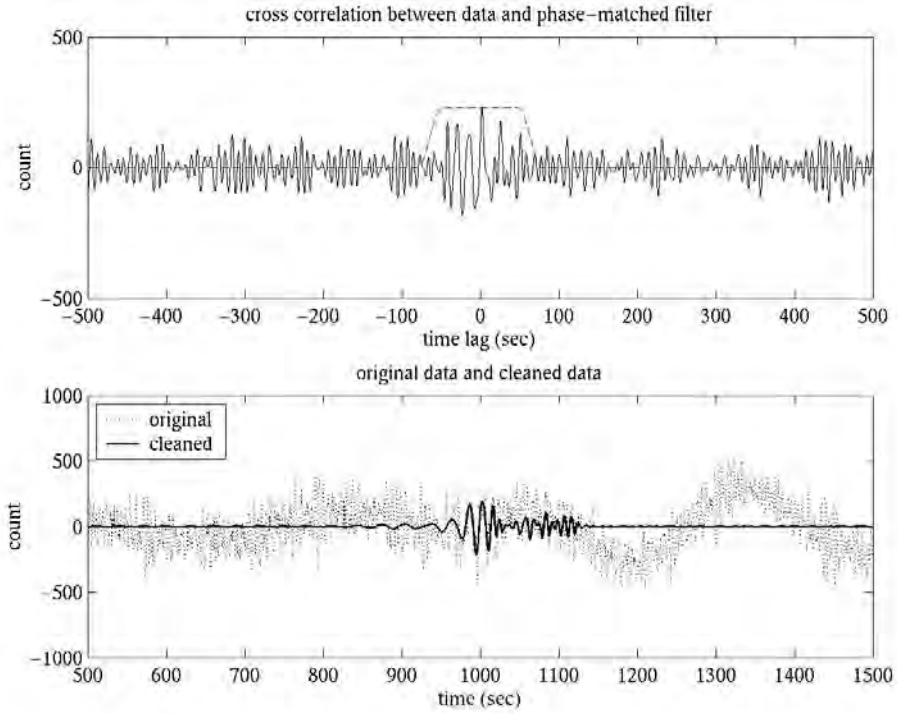

Figure 5. An example of phase-match filtering of the broadband data. The upper panel shows the cross-correlation between the data and the phase-matched filter constructed using group velocities from the maps. The event is an m_b 4.8 event and the epicentral distance is 2788 km. The cross-correlation is windowed (dashed line) and convolved with the filter to obtain the cleaned data (lower panel). The effect of the phase-matched filter in extracting the surface wave is apparent.

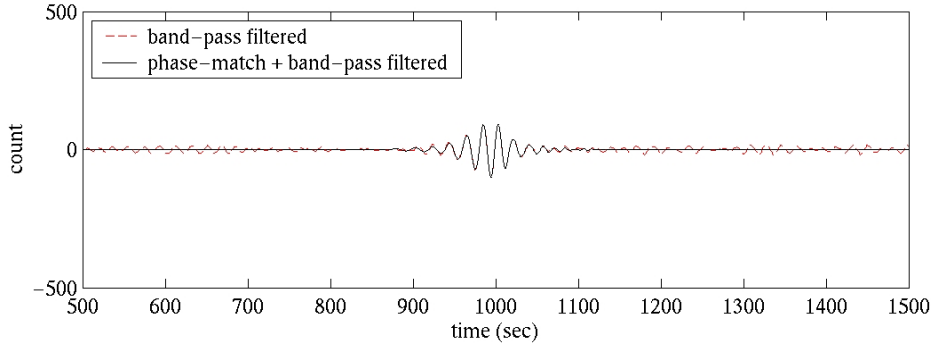

Figure 6. Comparison between the two filtering methods. Bandpass filter was applied to the data shown in the lower panel of Figure 5. In this case, simply bandpass filtering the broadband data has effects similar to phase-match plus band-pass filtering.

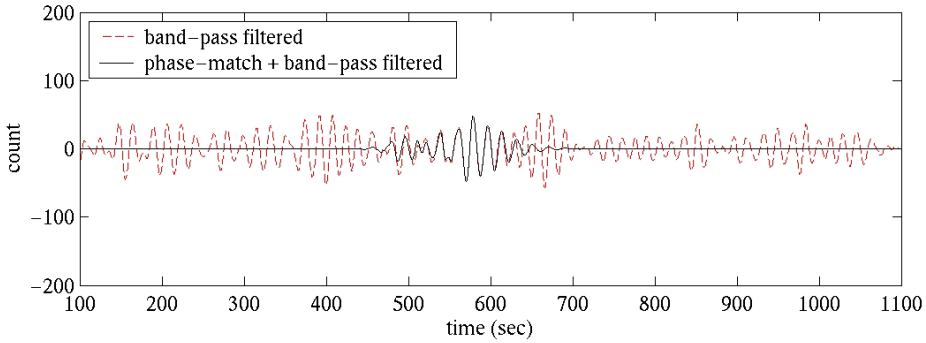

Figure 7. An example showing the difference between bandpass filtering method and phase-match plus bandpass filtering method. Due to the presence of 20-second noise resulting from a variety of possible sources, simple bandpass filtering cannot determine the surface wave unequivocally.

Surface-wave detection

Accurate group-velocity estimates can be used to improve the surface-wave detection. Stevens and McLaughlin (2001) described a method to detect surface waves with group-velocity information, which is used at the International Data Centre (IDC). The method uses multiple bandpass filters to filter the data and measures the arrival time of the peak amplitude at each period. If a certain percentage of the measurements fall within the range predicted by the group-velocity maps, the method declares a surface-wave detection.

We adopted Stevens and McLaughlin's (2001) method and tested the improvement of the group-velocity maps in detecting surface waves over some simplified 1-D models on our data set. In their practice, Stevens and McLaughlin (2001) made eight measurements within the period range between 17 and 50 seconds. To use our maps, we made measurements at each period between 10 and 30 seconds where we have a map. This period range covers shorter periods than Stevens and McLaughlin's (2001) period range. It should be more suitable for detecting smaller events at shorter epicentral distances. The equation used to define the arrival-time interval for a detection is (Stevens and McLaughlin, 2001):

$$\frac{r}{v_p + v_0} - p_0 T - t_0 < t < \frac{r}{v_p - v_0} + p_0 T + t_0 ,$$

where r is the epicentral distance, v_p is the predicted group velocity and T is the period; v_0, p_0 and t_0 are constants that the user can use to adjust the width of the arrival-time interval. We set these constants to 0.2 km/sec, 1 and 0 sec, respectively. If 70% of the measurements fall within this interval, the detection is deemed successful. These parameters are the same as those used by Stevens and McLaughlin (2001).

Figure 8 plots the number of surface-wave detections using different group-velocity models. PREM and China are group-velocity predictions calculated from the PREM model and a 1-D China crustal model from Jih (1998). The use of group-velocity maps increased the number of detections by 23% over that with the China model.

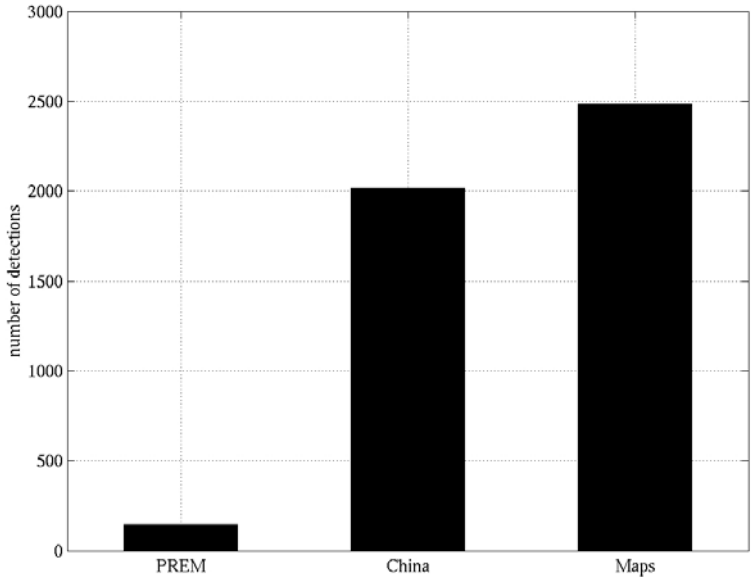

Figure 8. Number of surface-wave detections using different group-velocity models. PREM and China models are group-velocity predictions from the PREM earth model and a 1-D China crustal model (Jih, 1998). Maps are the composite group-velocity maps we evaluated.

CONCLUSIONS AND RECOMMENDATIONS

We have evaluated Rayleigh-wave group-velocity maps for the central Asia region constructed from results of previous studies (Ritzwoller and Levshin, 1998; Stevens *et al.*, 2001; Levshin *et al.*, 2001). We collected vertical broadband data not used by these studies for the evaluation. We compared our group-velocity measurements with the map predictions. We tested the ability of the maps in constructing effective phase-matched filters. We also examined the improvement that the maps can achieve in surface-wave detection.

In all our tests, the maps performed well. Residua between the predictions and the measurements made on data not used in the inversion of the maps are of the same order as the misfits of data that were used in certain surface-wave inversions (Ritzwoller and Levshin, 1998; Pasyanos *et al.*, 2001). Phase-matched filters constructed from the group-velocity maps seem to be effective in isolating surface waves and enhancing the S/N ratio. Surface-wave detections are increased by 23% by replacing a 1-D model with the 2-D group-velocity maps.

In order to lower the M_s detection threshold, surface waves with periods shorter than 20 seconds might need to be exploited. Enhancing the shorter period surface-wave signal requires accurate group-velocity maps at those periods. We are currently investigating the possibility of inverting for group-velocity maps down to 5 seconds at least for relatively small regions. We will make measurements at all periods below 200 seconds. New measurements at periods below 10 seconds can be used to improve the path density for certain regions that previous studies achieved. We also plan to broaden our region of evaluation to encompass the region further to the north. This will allow us to make use of new IMS stations in that region.

ACKNOWLEDGEMENTS

We thank Anatoli Levshin of the University of Colorado at Boulder (CUB) for providing their group-velocity maps. The Eurasia maps were downloaded from the CUB web site. The global maps were downloaded from Maxwell's (now SAIC) web site. We appreciate Michael Ritzwoller and Jeffry Stevens' efforts in making these maps available.

REFERENCES

Herrin, E. T. and T. T. Goforth (1977), Phase Matched Filters: Application to the Study of Rayleigh Waves, *Bull. Seism. Soc. Am.* **67**, 1259-1275.

Jih, R. S. (1998), Location Calibration Efforts in China, in *Proceedings of the 20th Annual Seismic Research Symposium on Monitoring a Comprehensive Test Ban Treaty*, 44-55.

Levshin, A. L., M. H. Ritzwoller, M. P. Barmin, and J. L. Stevens (2001), Short Period Group Velocity Measurements and Maps in Central Asia, in *Proceedings of the 23rd Seismic Research Review: Worldwide Monitoring of Nuclear Explosions*, Vol. I, 258-269.

Ritzwoller, M. H. and A. L. Levshin (1998), Eurasian Surface Wave Tomography: Group Velocities, *J. Geophys. Res.* **103**, 4839-4878.

Pasyanos, M. E., W. R. Walter, and S. E. Hazler (2001), A Surface Wave Dispersion Study of the Middle East and North Africa for Monitoring the Comprehensive Nuclear-Test-Ban Treaty, *Pure Appl. Geophys.* **158**, 1445-1474.

Stevens, J. L., D. A. Adams, and G. E. Baker (2001), Improved Surface Wave Detection and measurement Using Phase-Matched Filtering with a Global One-Degree Dispersion Model, in *Proceedings of the 23rd Seismic Research Review: Worldwide Monitoring of Nuclear Explosions*, 420-430.

Stevens, J. L. and K. L. McLaughlin (2001), Optimization of Surface Wave Identification and Measurement, *Pure Appl. Geophys.* **158,** 1547-1582.

Proceedings of the
24th Seismic Research Review --
Nuclear Explosion Monitoring:
Innovation and Integration

September 17-19, 2002

Ponte Vedra Beach, Florida

Volume II

Hydroacoustic Monitoring
Radionuclide Monitoring
Infrasound Monitoring
Data Processing and Analysis
Other Topics

Approved for Public Release; further dissemination unlimited.

LA-UR-02-5048

To view these Proceedings online, visit

http://www.nemre.nn.doe.gov/review2002

Vol. II

2002

Proceedings of the24th Seismic Research Review
Nuclear Explosion Monitoring: Innovation and Integration

Table of Contents - Volume II

4. Hydroacoustic Monitoring 619

4-01 **Castor, K., P. Gerstoft, W. Kuperman, G. D'Spain, and B. McDonald**
Nonlinear Effects in Long-Range Propagation 621

4-02 **Hanson, J., R. Bowman, and G. Beall**
An Advanced Concept Demonstration for Monitoring the Indian Ocean 632

4-03 **Harben, P., C. de Groot-Hedlin, and D. Blackman**
Acoustic Sources for Blockage Calibration of Ocean Basins: Results from the October 2001 Indian Ocean Cruise 643

4-04 **Okal, E., J. Talandier, and O. Hyvernaud**
Hydroacoustic T Phases from Large Icebergs Drifting in the Ross Sea 652

4-05 **Tolstoy, M. and D. Bohnenstiehl**
Analysis of Hydroacoustic Signals In The Indian Ocean 666

4-06 **Upton, Z. and J. Pulli**
Localization of Sub-Sea Earthquakes Using Hydroacoustic Reflections and Matched-Field Processing 676

5. Radionuclide Monitoring 687

5-01 **Arthur, R., H. Miley, and L. Todd**
Be-7 Cross-Talk in RASA Continuous Air Samplers 689

5-02 **Heimbigner, T., J. McIntyre, T. Bowyer, J. Hayes, and M. Panisko**
Environmental Monitoring of Radioxenon in Support of the Radionuclide Measurement System of the International Monitoring System 694

5-03 **Penn, D., S. Biegalski, and K. Biegalski**
Status of the Automated Radioxenon Sampler Analyzer and the International Monitoring System International Noble Gas Experiment 701

5-04 **Robbins, D., J. Rynes, and K. Foltz Biegalski**
Radionuclide Software Installation at the US National Data Center 711

5-05 **Robbins, D., J. Rynes, and M. Eisenbray**
Radionuclide Detection Threshold In The Lop Nor Region 721

6. Infrasound Monitoring 731

6-01 **Chael, E. and R. Whitaker**
Infrasound Signal Library 733

6-02 **D'Spain, G., M. Hedlin, J. Orcutt, W. Kuperman, C. de Groot-Hedlin, L. Berger, and G. Rovner**
Application of Physics-Based Underwater Acoustic Signal and Array-Processing Techniques to Infrasound-Source Localization 735

6-03 **Garces, M. and C. Hetzer**
Evaluation of Infrasonic Detection Algorithms 745

6-04 **Garces, M., C. Hetzer, K. Lindquist, and D. Drob**
Source Location Algorithm for Infrasonic Monitoring 755

6-05 **Garces, M., C. Hetzer, S. Businger, and M. Willis**
Modeling of Microbarom Signals in the Pacific 766

6-06 **Gibson, R. and D. Norris**
Integration of Near-Real-Time Atmospheric Models with InfraMAP and Applications to Modeling Infrasound from Rockets 775

6-07 **Hedlin, M. and J. Berger**
Experiments with Infrasonic Noise-Reducing Spatial Filters 783

6-08 **Krasnov, V. and Y. Drobzheva**
Optimum Filtration of Acoustic Pulses Caused by Underground Nuclear and Above-Ground Chemical Explosions 793

6-09 **Minaya, E., G. Avila, C. Condori, A. Córdova , and F. Vega**
The Bolivian Altiplano with the Infrasound Array IS08 799

6-10 **Norris, D. and R. Gibson**
InfraMAP Enhancements: Environmental/Propagation Variability and Localization Accuracy of Infrasonic Networks 809

6-11 **Sarker, G. and W. Kim**
Analysis of Infrasound Signals from Large Mining Blasts at Kurchatov and Borovoye, Kazakstan 814

6-12 **Shumway, R.**
Detection and Location Capabilities of Multiple Infrasound Arrays 823

6-13 **Whitaker, R., D. ReVelle, and T. Sandoval**
On Infrasound Detection and Location Strategies 830

7. Data Processing and Analysis 837

7-01 **Begnaud, M., J. Aguilar-Chang, A. Velasco, and L. Steck**
Developing Regional Seismic Databases for Improving Event Location and Ground Truth Data Sets in Asia 839

7-02 **Hellweg, M., D. Dreger, B. Romanowicz, and J. Stevens**
Development of Automated Moment Tensor Software at the Prototype International Data Centre 845

7-03 **Kvaerna, T., E. Hicks, J. Schweitzer, and F. Ringdal**
Regional Seismic Threshold Monitoring 859

7-04 **Mooney, W. and S. Detweiler**
Ground Truth Data in India and China from Dense Local Networks and Calibration Experiments 869

7-05 **Rivers, W., C. Schultz, and D. Dodge**
Efficient Integration of Old and New Research Tools for Automating the Identification and Analysis of Seismic Reference Events 882

7-06 **Skov, M., B. Kohl, and R. Woodward**
Imagery Assets for Supporting Nuclear Explosion Monitoring Research and Development 892

7-07 **Wilkening, L., M. Chown, and B. Merchant**
The GNEM R&E Spatial Data Interface 900

7-08 **Woodward, R. and R. North**
A Support System for Nuclear Explosion Monitoring Research and Development 906

7-09 **Young, C., E. Chael, and B. Merchant**
Version 1.7 of MatSeis and the GNEM R&E Regional Analysis Tools 915

8. Other Topics 925

8-01 **Hasting, M. and S. Barrientos**
The Upgrade of the International Monitoring System Primary Station at Sonseca, Spain, (PS-40): A Before and After Comparison of the Short-Period Array 927

8-02 **Herrin, E., P. Negraru, P. Golden, and C. Mulcahy**
Local Site Effects at the Nevada Seismic Array(NVAR) 940

8-03 **Kromer, R., J. Harris, and T. Townsend**
Seismic Data Acquisition System (SDAS) Component Evaluation 950

Hydroacoustic Monitoring

NONLINEAR EFFECTS IN LONG RANGE PROPAGATION

Kaëlig Castor,[1] Peter Gerstoft, W. A. Kuperman,[1] Gerald L. D'Spain,[1] and B. Edward McDonald[2]

Scripps Institution of Oceanography[1] and Naval Research Laboratory[2]

Sponsored by Defense Threat Reduction Agency

Contract No. DTRA01-00-C-0084

ABSTRACT

The Nonlinear Progressive Wave Equation (NPE) (McDonald and Kuperman, 1987) computer code was coupled with a linear normal mode code in order to study propagation from a high-intensity source in either shallow or deep water. Simulations using the coupled NPE/linear code are used to study both harmonic (high-frequency) and parametric (low-frequency) generation and propagation in shallow or deep water with long-range propagation paths. Included in the modeling are both shock dissipation and linear attenuation. The results of these studies are presented.

OBJECTIVE

Linear acoustic propagation in a waveguide has been studied extensively theoretically, numerically and experimentally. In case of a large underwater explosion, nonlinear processes affect the properties of the acoustic wave. One can expect to characterize and localize nuclear underwater explosions by examining spectrograms, which would show this specific nonlinear behavior (Kuperman et al, 2001; D'Spain et al 2000; Gerstoft, 1999).

The aim of this paper is to highlight the nonlinear phenomena of acoustical propagation such as the nonlinear steepening and shock dissipation. The nonlinear scar in a pulse propagated over long ranges is discussed. Work on this topic has also been carried out by B. Ed McDonald (2002).

Introduction

The nonlinear progressive wave equation (NPE) (McDonald *et al*, 1987; McDonald, 2000, 2002) has been developed to investigate nonlinear acoustic effects (including shocks) in an ocean waveguide. This model assumes propagation within a narrow angle and provides an alternative to the linear parabolic equation (PE) and normal mode (NM) approaches. The model is derived from the Euler equations of fluid dynamics retaining lowest order nonlinearity augmented by an adiabatic equation of state relating pressure and density. The NPE is cast in a wave-following coordinate system moving at a nominal average sound speed c_0 in a preferred propagation direction r. For azimuthally symmetric propagation, the NPE in cylindrical (r, z) coordinates is

$$\frac{\partial R}{\partial t} = -\frac{\partial}{\partial r}\left(c_1 R + \frac{b\, c_0}{2} R^2 \right) - \frac{c_0}{2}\frac{R}{r} - \frac{c_0}{2}\int_{rf}^{r} \frac{\partial^2 R}{\partial z^2} dr \,, \qquad (1)$$

where b is the nonlinear parameter (≈3.5 for the ocean), c_1 is the environmental sound speed fluctuation about c_0. $R = r'/r_0$ is the dimension-less density perturbation where r_0 is the unperturbed density and $r' = r - r_0$. The NPE can be also formulated in terms of a dimension-less pressure variable $Q = p'/r_0 c_0^2$ by substituting R with Q in Eq. (1) (Ambrosiano *et al*, 1990). The terms on the right hand side of Eq. (1) represent from left to right, refraction, nonlinear steepening, radial spreading, and diffraction. The quadratic nonlinearity in Eq.(1) implies that the nonlinear contribution to the local sound speed is $b\, c_0 R$. A linear propagation mode can be invoked in the code simply by setting $b = 0$. The water is assumed to be an inviscid fluid and linear attenuation in the sediment layer was included.

RESEARCH ACCOMPLISHED

The nonlinear propagation of an acoustic wave induces high frequency harmonics. Furthermore, the nonlinear interaction of two monochromatic waves at frequencies f_1 and f_2 propagating in the same direction leads to a secondary radiation at frequencies $f_2 \pm f_1$. This parametric interaction effect is commonly used in many applications such as transducer realization providing high focused underwater acoustic intensity for active sonar; this effect is also used for measurements of the nonlinear parameter in liquids or biologic environments and solids (Barriere, 2002; Marchal, 2002; Lee *et al*, 1995; Hamilton *et al*, 1998).

The work presented in this paper focuses on the physical phenomena that influence the spectral distribution of the energy during propagation in order to understand the characteristics of acoustic signals measured after long-range nonlinear propagation. For this purpose, acoustic propagation for different source waveforms is investigated.

Two narrowband sources in shallow water

All the results presented in this section are for a 200-m depth Pekeris waveguide (Fig. 1.a.). The sound speed in the water column is 1500 m/s and is 1550 m/s in the sediment. At a source depth of 100 m, the NPE code is initialized by a sum of two narrowband sources centered at frequencies f_1=275 Hz and f_2=425 Hz, respectively (Fig. 2.a and 2.d). The wave packet is modulated by two Gaussian envelopes in depth and range. This source allows the study of spectral evolution of the acoustic waves due to nonlinearity within the propagation. High-frequency sources are convenient to get narrow frequency bands and to observe both harmonic and parametric generation. The aim of this section is to evaluate the relative energy associated with both effects. Figures 2.c. and 2.d. represent the depth-

averaged spectrum for two narrow band sources at the initial range and at the 280-m range where secondary waves created by both parametric ($f_2 \pm f_1$) and harmonic ($2f_1$ & $2f_2$) effects appear clearly. Higher order radiation with low amplitudes at other different frequency combinations, $2(f_2 - f_1) = 300$ Hz, $3(f_2 - f_1) = 450$ Hz, $4(f_2 - f_1) = 600$ Hz, and $f_1+2(f_2 - f_1)=2f_2+f_1=575$ Hz are also distinguishable.

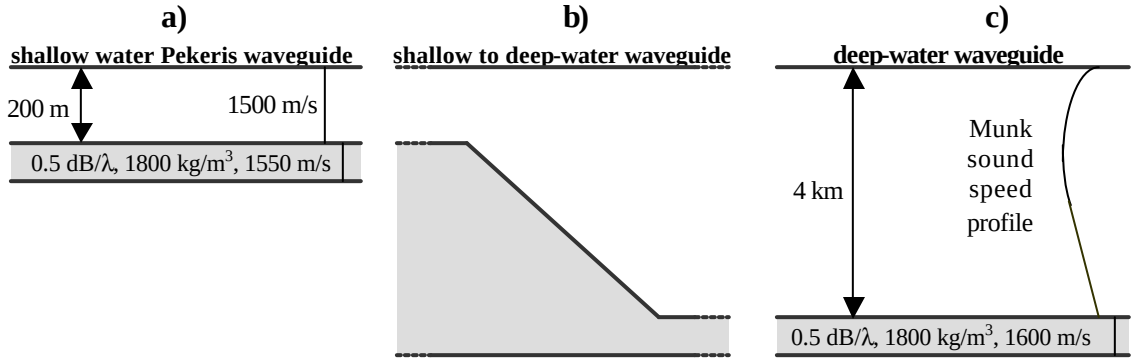

Figure 1. Representation of the environments used in the simulations.

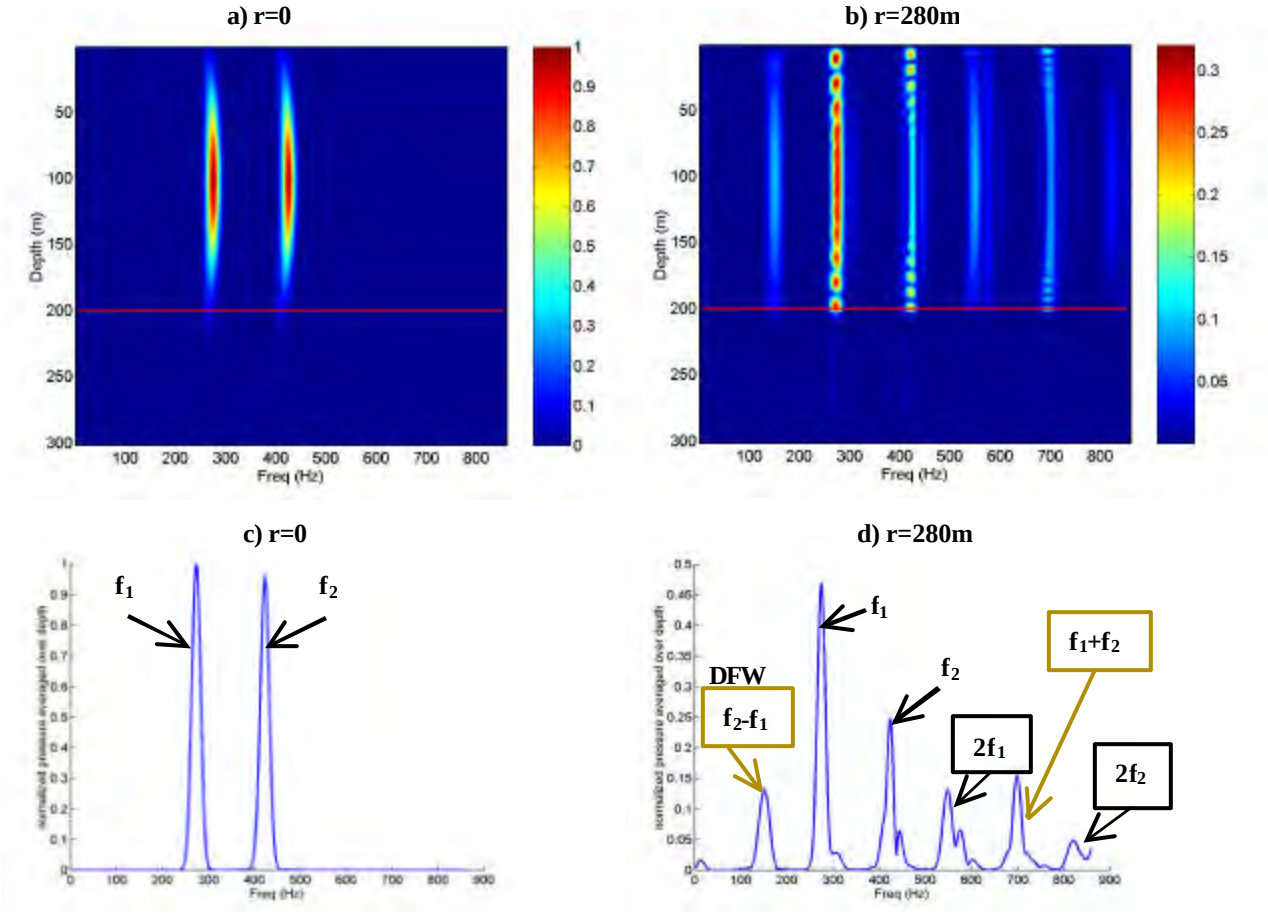

Figure 2: (a & b) Normalized spectrum for two narrow band sources (f_1=275 Hz, f_2=425 Hz) with a source overdensity $R_m=3.10^{-3}$. (c & d) Normalized depth-averaged spectrum. (a & c) range=0. (b & d) range=280m.

Figure 3.a. represents for different maximum overdensity levels R_m the normalized total energy defined by

$$E_T(r) = \sum_i \left| p(f_i, r) \right|^2 \Big/ \sum_i \left| p(f_i, r=0) \right|^2 , \qquad (2)$$

where $\left| p(f_i, r) \right|$ is the amplitude of the pressure at the frequency f_i and at the range *r*. Even if the total energy is higher for a high source level, Figure 3(a). shows that the relative losses are much larger for high initial amplitudes since nonlinear effects induce shock dissipation in addition to classical linear absorption.

The only parametric effect considered here is the difference frequency wave (DFW) generation, which is directly related to the low-frequency generation. Figures 3(b) and 3(c) show the energy ratios E_h and E_p, respectively, associated to harmonics and DFW, which are expressed as follows

$$E_h(r) = \left(\left| p(2f_1, r) \right|^2 + \left| p(2f_2, r) \right|^2 \right) \Big/ E_i \qquad (3)$$

$$\text{and } E_p(r) = \left| p(f_2 - f_1, r) \right|^2 \Big/ E_i , \qquad (4)$$

with the initial energy E_i calculated such that

$$E_i = \left| p(f_1, r=0) \right|^2 + \left| p(f_2, r=0) \right|^2 . \qquad (5)$$

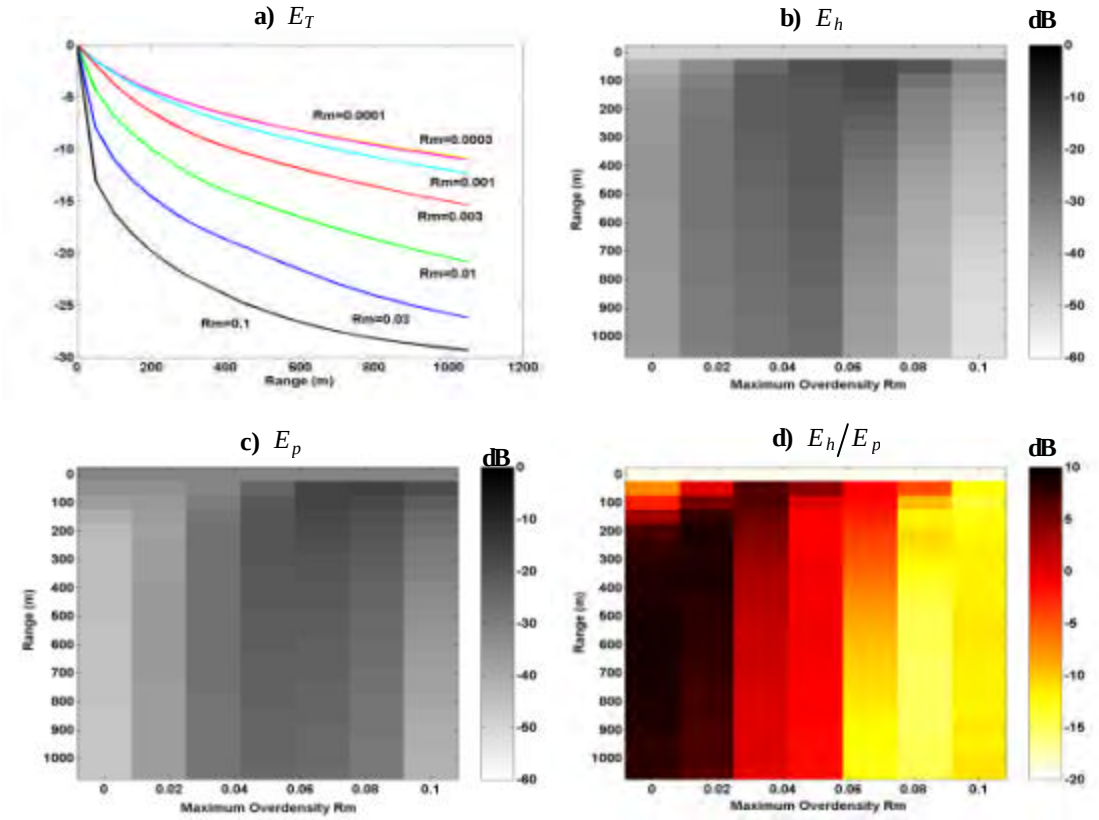

Figure 3: Energy ratios versus range and source overdensity R_m.: (a) Total energy E_T, Eq. (2). (b) Energy in the first harmonic components E_h, Eq. (3). (c) Energy in the parametric difference frequency component E_p, Eq. (4). (d) Energy ratio E_h / E_p.

Near the source, both parametric DFW (E_p) and harmonic (E_h) energy increase for larger source overdensity until an optimum is reached (Fig. 3(b) and 3(c). Both nonlinear effects are in competition with shock wave dissipation. The shock wave leads to an energy absorption process in addition to the intrinsic attenuation. When a discontinuity appears in the waveform profile, the shock wave formation distance is reached. For a shock wave, a cascade of higher frequencies is generated (Hamilton, 1998). This phenomenon increases entropy locally and constitutes a

mechanism of energy dissipation even in a perfect fluid. This shock wave formation distance decreases when the source level increases. Thus, for a strong explosion, nonlinearities are important and shock dissipation occurs at shorter ranges and leads to a high-energy decay.

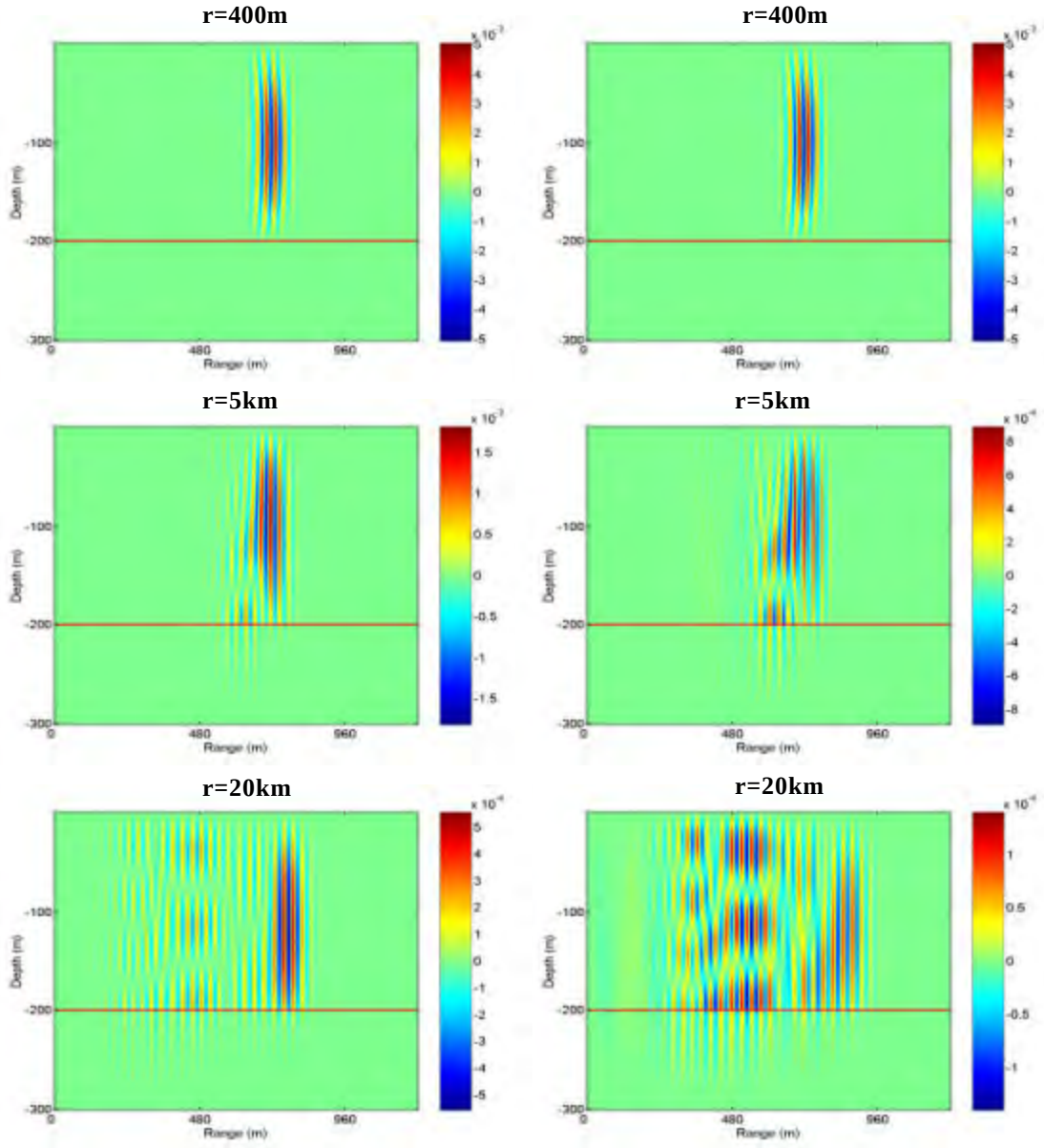

Figure 4: Snapshots at different ranges (400 m, 5 km, 20 km) for both linear (left) and nonlinear (right) shallow water cases with a single narrow band source centered at 50 Hz with a source overdensity $R_m = 3.5\ 10^{-3}$.

Finally, even if harmonic (Fig. 3[b]) and difference frequency (Fig. 3[c]) generation have almost the same behavior versus range, there is a weak shift between maximum overdensities for which respective normalized energies E_h and E_p are maximal. Since absorption is more important at higher frequencies, harmonics are damped faster during propagation than the DFW. These observations are also relevant for Figure 3(d), which shows the ratio E_h / E_p. In this figure, three parts can be distinguished: The first part is for low-source overdensities where the shock wave formation distance is large. The harmonic generation due to the nonlinear steepening is greater than the parametric DFW. In the second part, for intermediate levels, both nonlinear effects are of similar importance. In the third part, for high-amplitude source, the shock wave formation distance is shorter. Strong absorption occurs then at short

ranges and leads to harmonic dissipation. The low difference frequency wave is thus predominant.

Single narrowband source

In this section, the source conditions are a five-cycle sine-wave packet with a center frequency of 50 Hz, modulated by Gaussian envelopes in depth and range. Figure 4 shows snapshots at different ranges for linear and nonlinear propagation in the Pekeris shallow water waveguide defined in part A (Fig. 1[a]). Corresponding time series are represented in Figure 5 at the source depth (100 m).

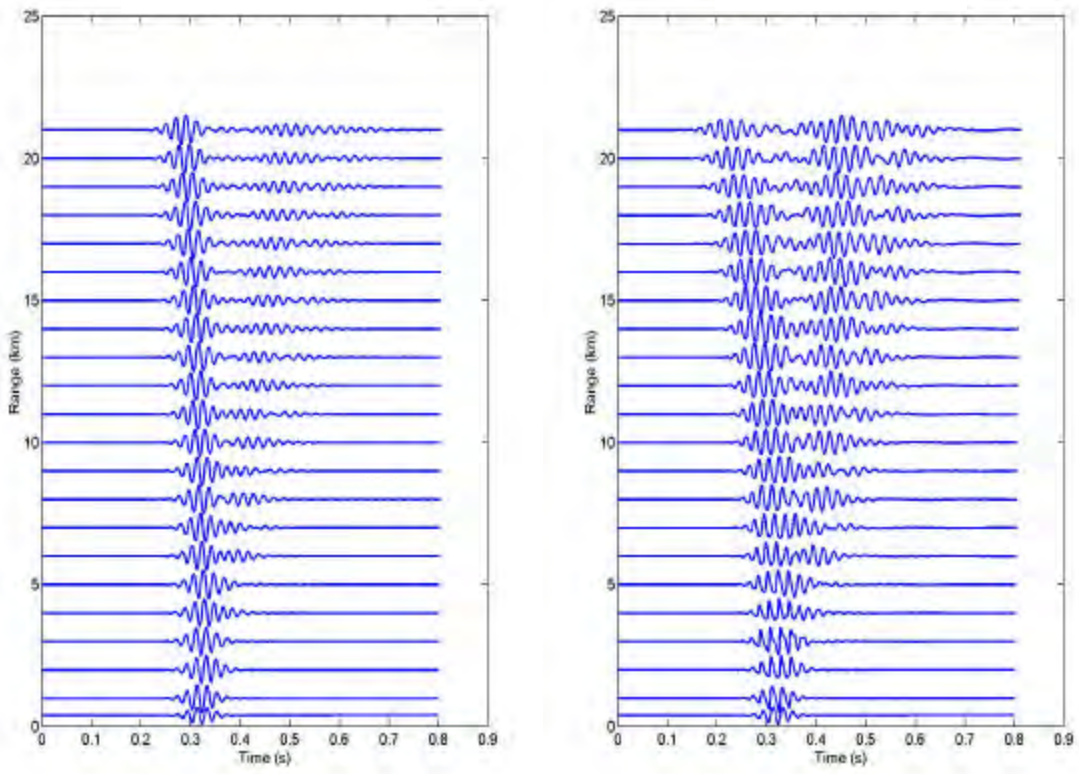

Figure 5: Time series at the source depth (100 m) for linear (left) and nonlinear (right) shallow water cases with a single narrowband source centered at 50 Hz with a source overdensity $R_m = 3.5\ 10^{-3}$.

Even though the presence of nonlinearity does not lend itself to straightforward representation in linear normal modes, similarities between the two cases are expected since the nonlinearities are weak. The modal dispersion can be seen in both cases (Fig. 4). At 20-km range, four modes can be distinguished, and one can observe that the lower order modes travel faster. Because nonlinear effects lead to low- and high-frequency generation, the spectral distribution of the energy is generally more complicated and spread over a broad frequency band. Consequently, in the nonlinear case there is an energy transfer toward higher modes and the excitation of each mode is more uniform than in the linear case as can be seen at 20-km range in Figure 4. Furthermore, an important difference is the wave steepening (Fig. 5). In the nonlinear case, the wave form starts out sinusoidal, develops a sawtooth profile (range 3-6 km), and ultimately falls victim to effects of dissipation and reverts to a waveform resembling the signal at the source, although much reduced in amplitude (this attenuation is not visible in the time series representation shown in Fig. 5 since all the signals are normalized by their maximum at each range for lisibility). After an initial phase in which the nonlinear wave loses energy to shock processes and increased bottom penetration, its interaction with the waveguide becomes essentially linear. Then, a linear adiabatic normal mode code can be used to propagate the field to much longer ranges (i.e. several hundred kilometers), using less CPU time.

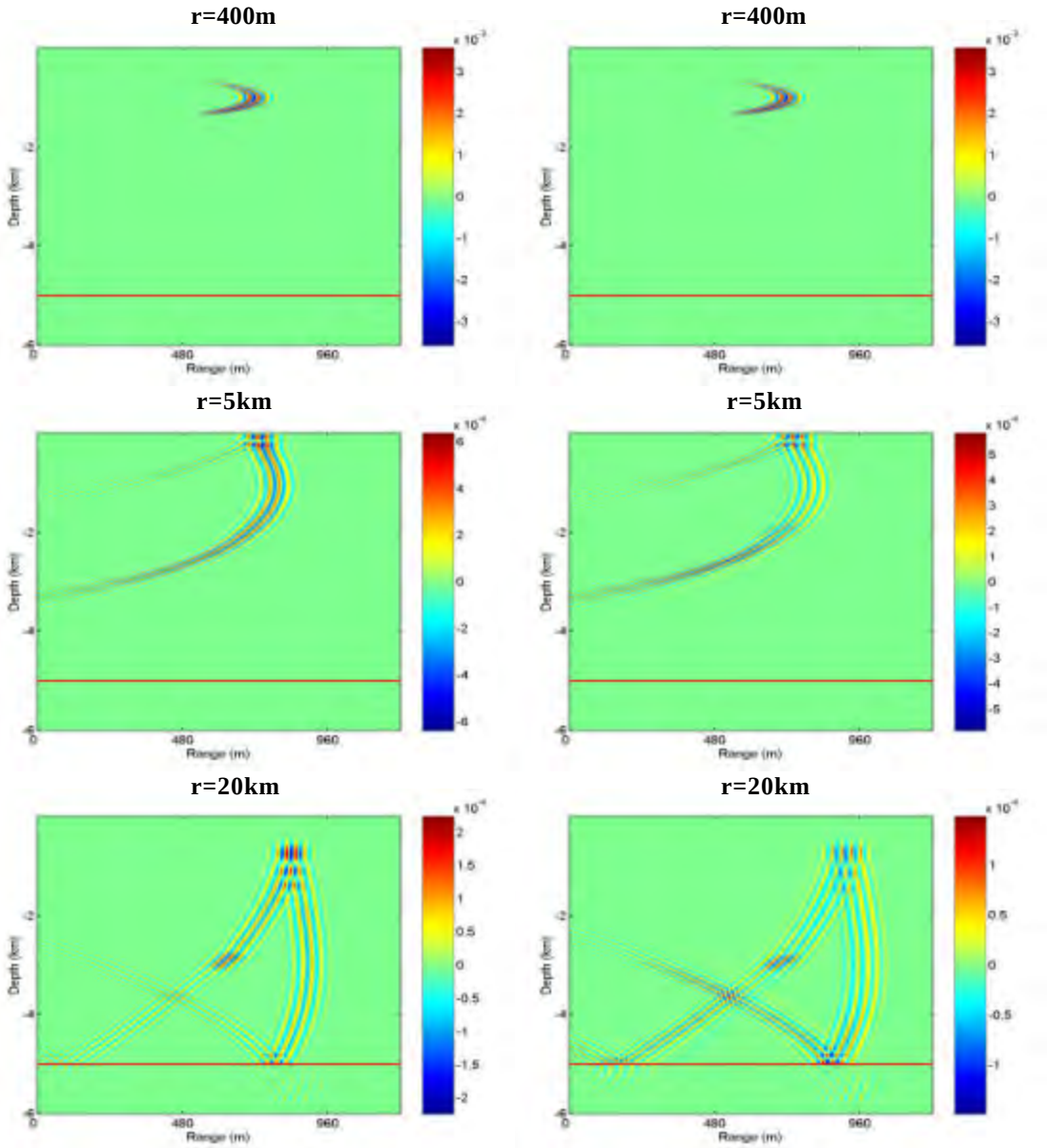

Figure 6: Snapshots at different ranges (400 m, 5 km, 20 km) for both linear (left) and nonlinear (right) deep water cases with a single narrow band source centered at 50 Hz with a source overdensity R_m=3.5 10^{-3}.

With the same source, Figures 6 and 7 show respectively snapshots and time series, at 1 km corresponding to the source depth, for linear and nonlinear cases within a 5-km deep water waveguide. The sound speed in the sediment layer is 1600 m/s and the absorption coefficient is 0.5 dB/λ (Fig. 1.c.). The results show a weak interaction with the sediments and a localization of the energy at a depth where the sound speed is minimum. In the nonlinear case, there is more energy in the tail of the signal and the pulse duration is longer than in the linear case (Fig. 6). For both cases the signal that appears, at about 4 km and 0.8 s in Figure 7, is due to the bottom bounce, and at about 10 km, this signal melts together with the direct arrival.

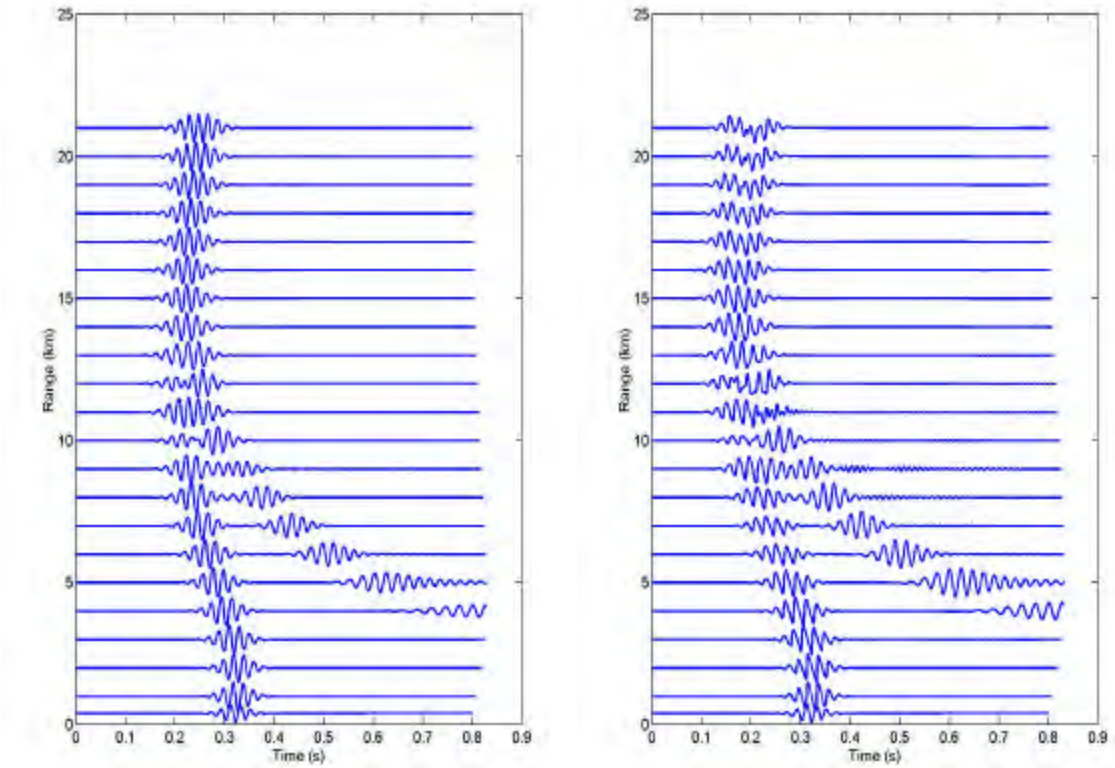

Figure 7: Time series at the source depth (1 km) for linear (left) and nonlinear (right) deep water cases with a single narrowband source centered at 50 Hz with a source overdensity R_m=3.5 10^{-3}.

Figures 8 and 9 compare the influence of the source frequency on the normalized depth averaged spectrum for nonlinear propagation at several ranges. For a 50-Hz source (Fig. 6), one can see both difference-frequency wave Δf (DFW) and harmonic generation. Because of the frequency dependence of the viscous absorption, the waves f, 2f, 3f are damped faster than the DFW. Therefore, only the difference frequency Δf exists at long ranges. There is a tendency for the spectrum to shift toward lower frequencies. However, in the shallow water, Figure 9 shows that the waveguide cut-off frequency (3.75 Hz in this example) limits this tendency for very low frequencies: for a 10-Hz source, the parametric difference frequency wave, related to the source broad frequency band, is not generated since it is below the waveguide cut-off frequency. Also, amplitudes for this 10-Hz source show a weaker dissipation than for the 50-Hz source case.

Below the waveguide cut-off frequency, no mode is generated; thus no modal energy propagates. An important difference between shallow and deep water is this waveguide cut-off frequency, which is greater in shallow water (f_c=3.75 Hz) and leads consequently to eliminate a part of the DFW energy, whereas, in deep water, the waveguide cut-off frequency is much smaller (f_c=0.15 Hz), so DFW generation is less affected in this case.

Long-range propagation

Since the nonlinear effects are important near the source, there is a range for which the amplitude is sufficiently low so that a linear normal mode code can be used to propagate the acoustic field further. The fields from the NPE code at 20 km for both shallow and deep water environments are used as a source in the Kraken normal mode code (Porter, 1991). For the shallow water case, the adiabatic approximation is used to propagate the field to deep water. The snapshots for linear and nonlinear cases are plotted respectively for this shallow-to-deep-water case (Figs. 1[b] and 10) and deep-water case (Fig. 1.c and 11). The results show that the influence of the nonlinear effects on acoustical propagation are greater if the explosion occurs in shallow water. In shallow water, the dispersion of mode-like arrival structures develops more rapidly for a nonlinear case (McDonald, 2002) than when the energy is

linearly propagated. When the energy is linearly propagated in deep water, the snapshots keep this different modal dispersion (Fig. 10). The nonlinear effects will cause the frequency spectrum to be broader and will usually excite a broader spectrum of modes, with more relative energy for the high-order modes. This causes a larger time spread. When the signal propagates to deep water, the signals keep this larger time spread (Fig. 10).

In contrast, for deep-water explosions, the nonlinearities do not generate a modal arrival structure, partly because of little interaction with the bottom. The typical modal arrival structure occurs at long ranges where the signals amplitudes are weak and nonlinear effects will not give a larger time spread (Fig. 11).

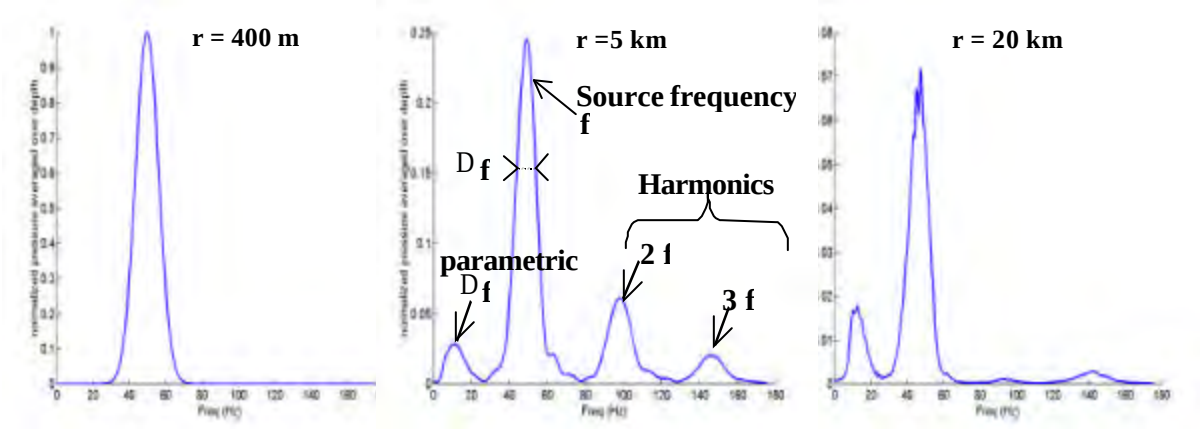

Figure 8: Depth-averaged spectrum at several ranges (r = 400 m, 5 km, and 20 km) for a nonlinear shallow water case with a single narrow frequency band source centered at f = 50 Hz with a source overdensity $R_m = 3.5\ 10^{-3}$.

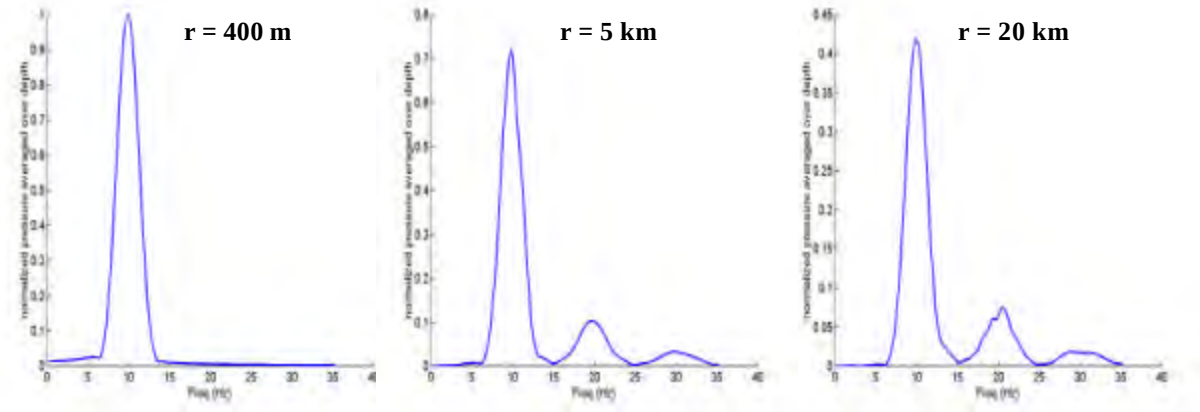

Figure 9: Depth-averaged spectrum at several ranges (r = 400 m, 5 km, and 20 km) for a nonlinear shallow water case with a single narrow frequency band source centered at f = 10 Hz with a source overdensity $R_m = 3.5\ 10^{-3}$. Due to the waveguide cut-off frequency, 3.75 Hz, there is no generation of the parametric difference frequencies.

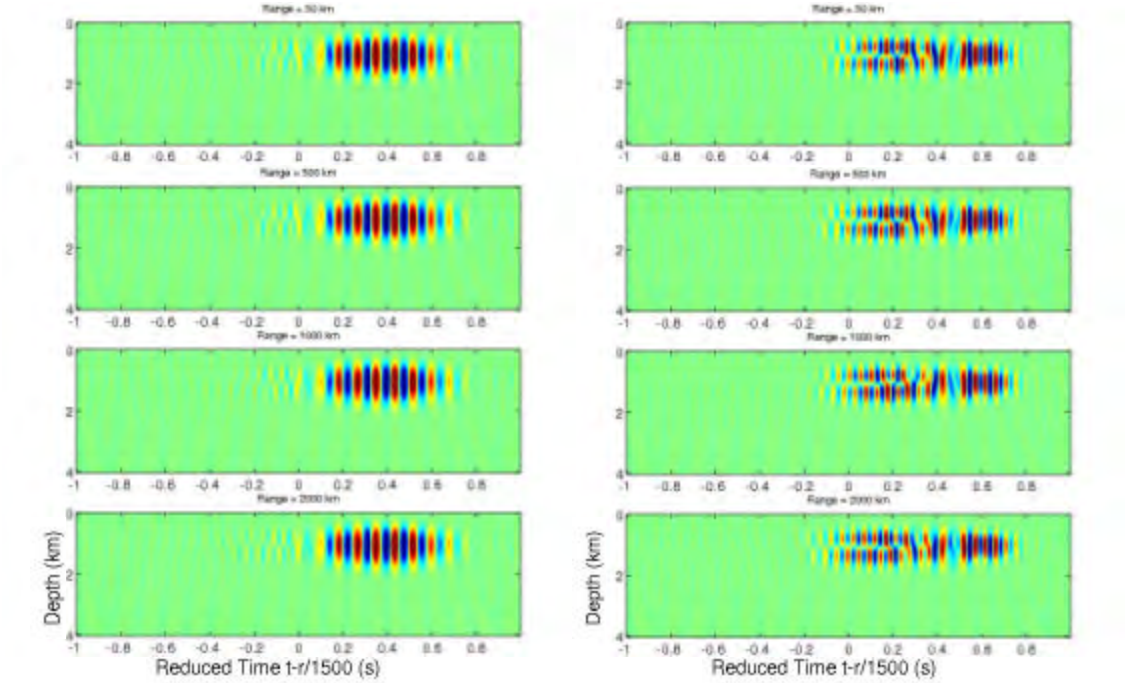

Figure 10: Time series for linear (left) and nonlinear (right) shallow-to-deep-water cases (f = 10 Hz, r = 50 km, 500 km, 1000 km, 2000 km).

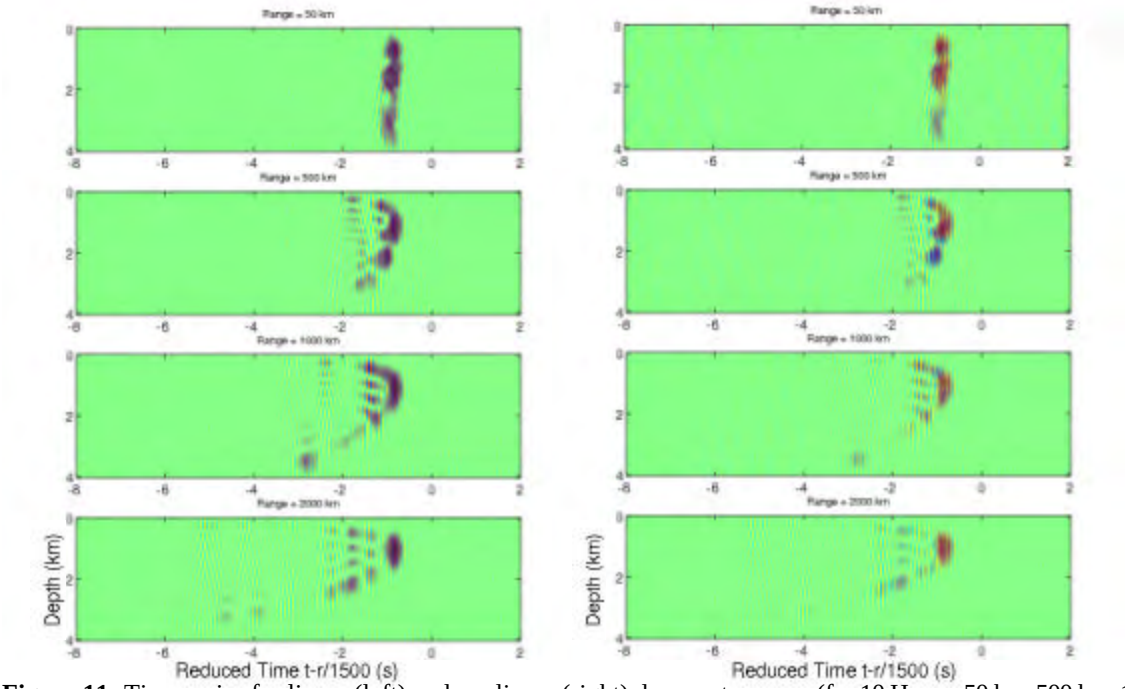

Figure 11: Time series for linear (left) and nonlinear (right) deep water cases (f = 10 Hz, r = 50 km, 500 km, 1000 km, 2000 km).

CONCLUSION AND RECOMMENDATIONS

Results presented here suggest that undersea explosions may be characterized by studying their spectral evolution over long-range nonlinear acoustical propagation. In shallow water, the signal interacts with the bottom earlier than in deep water, thus initially lower geometrical spreading is obtained (cylindrical versus geometric spreading). Therefore, signal amplitudes are initially higher than in the deep water case, causing stronger nonlinear effects. The

nonlinear effects will cause the frequency spectrum to be broader and will usually excite a broader spectrum of modes, with more relative energy for the high order modes. In shallow water, low order modes travel faster than high order modes and the nonlinearity will give a larger time spread of the received pulse.

Nonlinear effects on the modal dispersion are much more significant in shallow water than in deep water. Thus, if the event starts in shallow water, it would be easier to discriminate between signals that entered the ocean as linear waves (for example a seismic event or underground explosion) and those that began as nonlinear waves in the ocean itself. In this last case, after long-range propagation, the spectrum is strongly shifted toward low frequencies because of both difference frequency generation and shock dissipation processes. During propagation in shallow waveguide, the lowest frequencies might not be supported by the waveguide, due to modal cut-off. Thus, the low-frequency parametric wave might not always be observed.

ACKNOWLEDGMENTS

The authors are grateful to Philippe Roux for his support and helpful discussions.

REFERENCES

Ambrosiano J. J., D. Plante, B.E. McDonald, W.A. Kuperman (1990), Nonlinear propagation in an ocean acoustic waveguide, *J. Acoust. Soc. Amer.*, **87**, 1473-1481.

Barriere Ch. (2002), Effet de la diffraction sur l'interaction parametrique d'ondes acoustiques. Application a la mesure de parametres de non linearite et de champs acoustiques, PhD dissertation, Universite Denis Diderot-Paris 7.

D' Spain G. L., W.A. Kuperman, J. Orcutt J, and M. Hedlin (2000), Long Range Localization of impulsive sources in the Atmosphere and Ocean from Focus Regions in Single Element Spectrograms, Proc. of 22nd Annual Seismic Research Symposium.

Gerstoft P. (1999), Assessment of hydroacoustic processing in the CTBT release one monitoring software, Comprehensive Nuclear-Test-Ban-Treaty Organisation, Vienna, Austria.

Hamilton M. F. and D.T. Blackstock (1998), *Nonlinear acoustics*, Academic Press.

Kuperman W. A., B.E. McDonald, and G.L. D' Spain (2001), Arrival structure of long-range propagation excited by a finite amplitude source, Proc. of 23rd Annual Seismic Research Symposium.

Marchal J. (2002), Acoustique non lineaire: contribution theorique et experimentale a l'etude de l'emission parametrique, PhD dissertation, Universite Pierre et Marie Curie-Paris 6.

Lee Y. -S. and M.F. Hamilton (1995), Time-domain modeling of pulsed finite-amplitude sound beams, *J. Acoust. Soc. Amer.*, **97**, 906-917.

McDonald B. E. and W.A. Kuperman (1987), Time domain formulation for pulse propagation including nonlinear behavior at a caustic, *J. Acoust. Soc. Amer.*, **81**, 1406-1417.

McDonald B. E. (2000), High-angle formulation for the nonlinear progressive-wave equation model, *Wave Motion*, **31**, 165-171.

McDonald B. E. (2002), Nonlinear effects in source localization, in *Ocean Acoustic Interference Phenomena*, eds. W. A. Kuperman and G. L. D'Spain, AIP Press, NY.

Porter M. (1991), The Kraken normal mode program, SACLANTCEN SM—245.

AN ADVANCED CONCEPT DEMONSTRATION FOR MONITORING THE INDIAN OCEAN

Jeffrey A. Hanson, Roger Bowman, and Gregory Beall

Science Applications International Corporation

Sponsored by Defense Threat Reduction Agency

Contract No. DTRA01-99-C-0025

ABSTRACT

The Center for Monitoring Research (CMR) has embarked on an advanced concept demonstration (ACD) focused on improving nuclear explosion monitoring in the vicinity of the Indian Ocean. Central to the demonstration are the new hydrophone assets. These are the International Monitoring System's (IMS) hydrophone stations at Diego Garcia (part of the British Indian Ocean Territories) and Cape Leeuwin, Australia. The third Indian Ocean hydrophone station at Crozet Island will be simulated for purposes of this work because it is not currently operational.

The primary goal of the ACD is to demonstrate new approaches that improve the capability to detect, locate and characterize in-water sources in the context of an operational monitoring system. The advances that are being implemented include optimizing signal processing for the new tri-partite hydrophone array stations, improving acoustic propagation and attenuation models, making use of basin reflections, and creating visualization tools for more effective analysis.

A supporting effort for the ACD is to create realistic synthetic data for events of interest. Demonstrating the system improvement requires data representative of realistic scenarios that test the monitoring objectives. Large explosions are the primary events of interest. However there are no examples of large explosions since the new stations became operational. The few examples that are recorded in other ocean basins are of limited use because of the difference in instrumentation and basin characteristics, and therefore we require synthetic data. However, synthetics often contain many of the same assumptions that were used to create the operational system. The results from synthetics must be validated against real data to the extent possible. Thus, compilation of real data sets that can validate the synthetics and characterize the day-to-day system operation is also a major portion of the ACD.

OBJECTIVE

The CMR in Arlington, Virginia, has begun developing a series of Advanced Concept Demonstrations (ACD) that are designed to improve current operational nuclear-explosion monitoring systems by incorporating state-of-the-art research in a prototype operational system. The demonstrations concentrate on different regions that include test sites and geographic regions of interest. The demonstration described here focuses on the Indian Ocean, which is of particular interest because it is the first ocean basin covered by the new International Monitoring System's (IMS) hydrophone stations. The demonstration is currently under development with completion anticipated by the end of 2002.

The overall objective for the Indian Ocean ACD is to demonstrate new approaches that improve capability for monitoring in-water and sub-ocean sources in the Indian Ocean Basin with an emphasis on exploiting data from the new hydroacoustic stations. Our specific goal is to show improvement in detection, location, and characterization of events in the IOB compared to the current Nuclear Test Detection System (NTDS) at the CMR. The ACD will be assessed relative to the current baseline system. Some of the ACD components will provide new capability that does not exist in the current system while other parts will improve various aspects of the system's ability in detecting, locating, or characterizing an event.

RESEARCH ACCOMPLISHED

Hydrophone Array Processing

There are currently two new hydrophone stations operating in the Indian Ocean with a third scheduled to come on-line in spring of 2003. The operational systems are located off Cape Leeuwin, Australia, (HA01) and the island of Diego Garcia, British Indian Ocean Territories (HA08). The third station is located at Crozet Island in the southwest of the basin. These stations provide significantly higher quality data than the initial IMS hydrophone stations (e.g., Wake and Ascension Island).

The new stations consist of multiple hydrophones arranged as triads with inter-element spacing on the order of 2 km. The Cape Leeuwin station (HA01) is a single triad off the west coast of Australia. The Diego Garcia station (HA08) has two triads located northwest and southeast of the island to avoid blockage from the Chagos Archipelago. The station at Crozet (HA04) will also have two triads to the north and south of the island.

Figure 1. IMS Hydroacoustic Station Locations. Each triangle represents a triad of hydrophones. The current operational instruments are the two triads at Diego Garcia and the single triad at Cape Leeuwin. The two triads at Crozet are scheduled to come online in spring, 2003.

One of the efforts in this ACD is the implementation of coherent array processing of the triads in order to increase detection sensitivity. Current hydroacoustic station processing runs a detector on each individual hydrophone. Detections within a triad are then grouped, and azimuths are estimated by cross-correlating the waveforms. Although this method does produce accurate azimuths, it is not taking advantage of the possible signal gain using the triads as arrays. A 5-dB gain in the signal-to-noise ratio (SNR) is theoretically possible.

On initial examination, the triads appear inadequate to use as typical hydroacoustic arrays. The element spacing (~2000 m) is large relative to the typical signal wavelength (~200 m at 8 Hz), which results in severe spatial aliasing for narrow band signals (Figure 2). However, a signal with sufficient bandwidth removes much of degeneracy and allows the triads to be processed as coherent arrays (Figure 3).

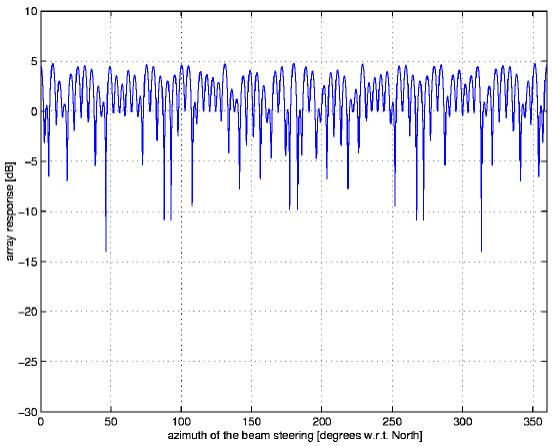

Figure 2 Array Beam Response for an Idealized Hydrophone Triad. The response is calculated for a monochromatic plane wave arriving from the south (8 Hz). The triad element spacing is much larger than the wavelength, which leads to the severe spatial aliasing.

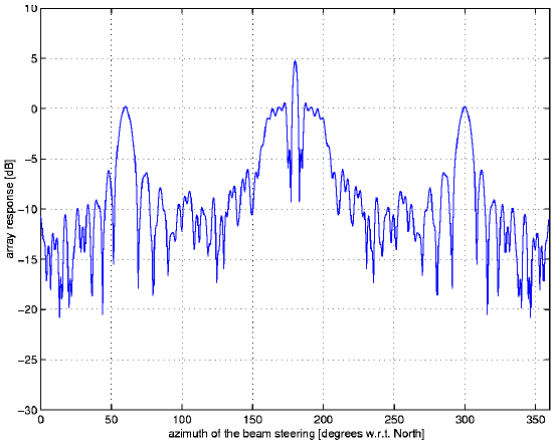

Figure 3 Array Beam Response for an Idealized Hydrophone Triad Using a Broadband signal. The response is calculated for a plane wave arriving from the south with energy between 6 to 10 Hz. The bandwidth of the signal reduces the side-lobes and produces a unique peak corresponding to the actual arrival azimuth.

The standard NTDS detection processing for coherent arrays uses what are known as beam recipes. The beam recipes specify a set of filter bands and steering angles that are used to compute beams. Each beam is fed into a signal detector that triggers on a preset SNR threshold. A suite of frequency bands is used because the band with highest SNR is not known a priori. The azimuthal spacing of the beam recipes depends on the width of the main lobe in the array's response function, which in turn depends on the center frequency of the signal. Table 1 specifies the number of beam recipes necessary for each frequency band necessary for coherent array detection processing. The total number of beams is 2690. This is significantly more than used for a typical seismic array that have on the order of a few hundred beams. This increase results in a considerably greater computational burden than current NTDS processing. However, initial results indicate that the system is capable of processing the typical hydroacoustic triad data.

Table 1. Predicted Main Lobe Width with Required Number of Beam Recipes

Frequency Band	Center Frequency (Hz)	Azimuth Main-Lobe Width (deg)	Number of Beam Recipes
1 - 2	1.5	19.02	20
1.5 - 3	2.25	12.66	30
2 - 4	3	9.49	40
3 - 6	4.5	6.32	60
4 -8	6	4.74	80
6 - 12	9	3.16	120
8 - 16	12	2.37	180
12 - 24	18	1.58	240
16 - 32	24	1.18	360
24 - 48	36	0.79	480
32 - 64	48	0.59	720
1 - 48	24.5	1.16	360
Total			2690

Capability Assessment

One technique for measuring the improvement of detecting and locating in-water events is to regionalize the basin into areas where some given criteria can or cannot be achieved. The variation in size of these areas between the current and ACD systems provides an intuitive quantification of the system's improvement. This analysis is in large part a predictive one because observational data do not exist to characterize the entire basin. These predictions will be validated using the available data.

We are dividing the basin into four main regions based on the ability to satisfy a set of criteria for an in-water explosion (an example of criteria set would be a detection threshold of mb=3.5 and 90% error ellipse area < 5000 km^2). The categories are:

1. Criteria achieved using the seismic network alone.
2. Criteria achieved using the hydrophone network alone.
3. Criteria achieved using some combination of the seismic and hydrophone networks together.
4. Criteria not achieved with the specified networks.

Because this particular ACD does not focus on enhancing seismic-only processing, the region covered by (1) should not change between the current and ACD systems and thus can be ignored for our purposes. It is useful to delineate area (2) because it should be relatively invariant to changes in a magnitude threshold criterion. This is due to the much lower detection threshold of the hydroacoustic network than the seismic network. The category (2) area established using an mb=3.5 threshold is nearly equivalent to the area found using mb=2.5 or even mb=1.5. It is the areas covered in (3) and (4) that we anticipate exhibiting the largest improvements (Figure 4). These areas also cover most of the ocean margins and are more relevant to security issues.

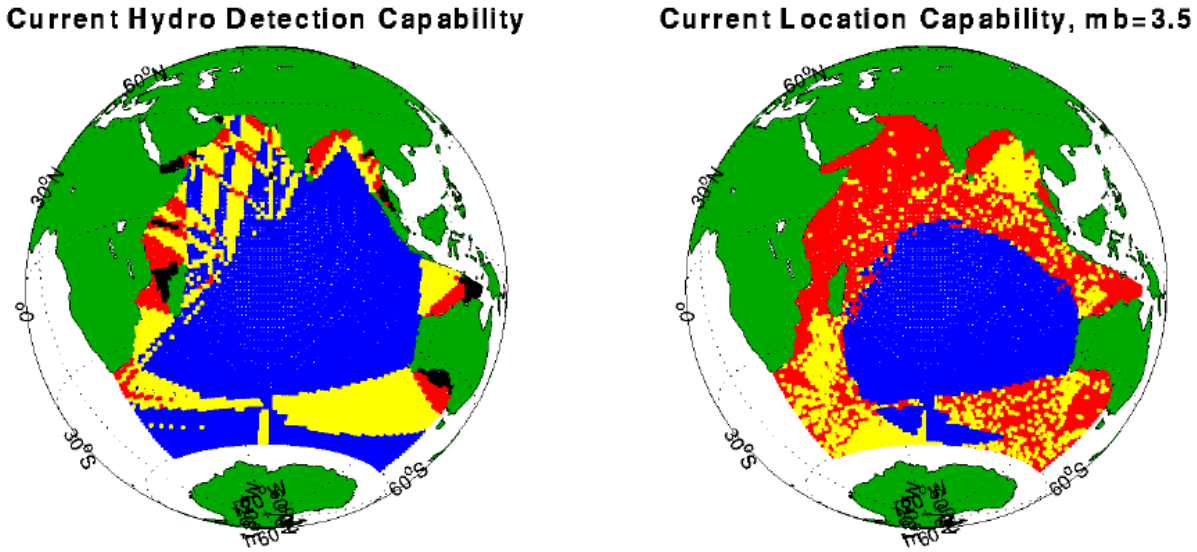

Figure 4. Example of Predicted Detection and Location Capability of the Current System. The left figure depicts hydroacoustic detection capability. The colors correspond to the number of detecting stations: 0-black, 1-red, 2-yellow, and 3-blue. The right figure depicts location capability using the criteria described in the text. The categorized regions are represented as different colors. Blue depicts the area that achieves the criteria using only the hydroacoustic network (category 2). Yellow depicts the area that achieves the criteria using both the hydroacoustic and the seismic network (category 3). Red depicts the area that does not meet the criteria (area 4). In this example the seismic-only processing (category 1) covers a minute region because of the low magnitude threshold. The ACD system is expected to reduce the area in red by improving measurements and models and by including new signal types such as reflected hydroacoustic signals.

Data Sets

Four sets of data will be used during this effort:

- The Calibration Data Set (CDS),
- The Fixed Data Set (FDS),
- Synthetic Data
- Live Data

The CDS will be a compilation of waveform data recorded during the calibration experiment conducted by Lawrence Livermore National Laboratory and Scripps Institution of Oceanography (Blackman *et al*., 2002) and data recorded during a seismic refraction experiment on the Southeast Indian Ridge (Cochran *et al*., 2002). These data contain the only real ground truth that we have for the new hydrophone stations. The sources that were used for both the calibration experiment and the refraction experiment were relatively small. The signals from these experiments will be primarily useful in validating travel-time modeling errors and possibly azimuthal measurement errors.

The FDS will provide a fixed set of hydroacoustic and seismic waveform data that can be used to assess and compare results of the different systems. The FDS contains a variety of signals from events throughout the IOB including mid-ocean ridge, trench, and inter-plate earthquakes. The variety of source locations will test the system's robustness and help validate our predicted assessments for monitoring signals of interest. In addition, the hydroacoustic waveform data cover a variety of noise conditions.

Because no large explosions have been recorded at the new hydrophone stations, synthetic waveforms are needed to characterize the system performance for a signal of interest. The synthetic waveforms will be generated by propagating an appropriate source function through range-dependent media extracted from oceanographic databases. The synthetics will be imbedded in typical background noise for the station.

The live data set consists of the waveform data from hydroacoustic and seismic stations that continuously arrive at the CMR. The ACD systems are intended to demonstrate prototype operational systems and as such are designed to process data in near real-time. The data include the hydrophone stations and primary IMS seismic stations.

Reflection Processing

The detection threshold of the hydroacoustic network for an in-water explosion is generally very low due to the efficient coupling of the source and the low attenuation within the ocean's sound channel. However, the geometry of the hydroacoustic network is not always sufficient to adequately constrain the event location. In these cases the current system relies on the seismic network. The ACD system will use hydroacoustic reflections in addition to the direct hydroacoustic and seismic signals to help constrain the location.

Reflections from earthquake-generated signals have been observed and identified at the hydrophone stations (e.g. Harben and Boro, 2001, Hanson, 2001). The azimuth estimates at the triads are generally accurate enough to identify the physical reflectors. Because the travel time between the reflector and the station can be computed, the reflector can be used as a synthetic omni-directional hydroacoustic station. These synthetic stations only provide an arrival time because it is not generally possible to determine the angle at which energy arrived at the reflector.

Hydroacoustic reflections can greatly improve the ability of the network to locate events. The reflections not only improve the geometrical coverage of an event, but they can also observe events where the direct path is completely blocked. Figures 5 and 6 show analysis of an event in the Mozambique Channel, which is one of the few areas in the Indian Ocean that have no direct path to any of the IMS hydrophone stations. This event would need additional information to constrain the location in the way that a regional seismic arrival would, but the reflections provide critical constraints for an event whose magnitude was near the seismic threshold.

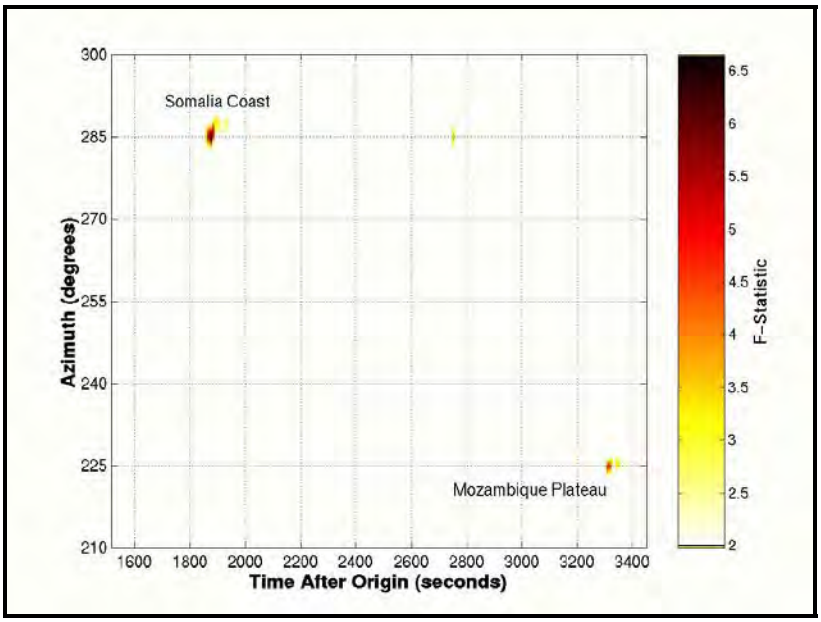

Figure 5. Time-bearing plot showing two reflections at the northern Diego Garcia triad for the event shown in Figure 6. The reflections are discrete arrivals that can be used to help constrain the event location. The azimuth estimates allow the physical reflector to be identified.

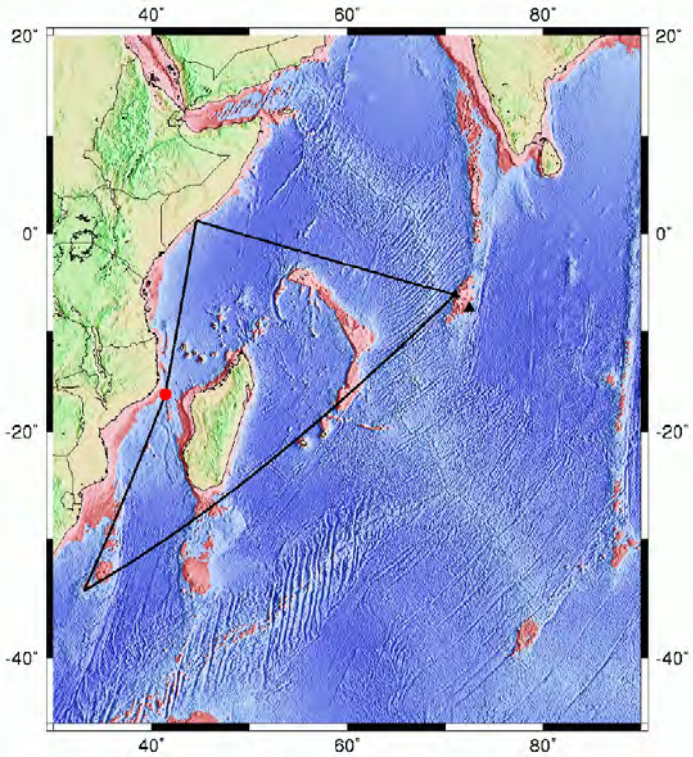

Figure 6. Example of reflections from a blocked event. The event occurred on April 2, 2002. The earthquake's epicenter is shown as the red dot in the Mozambique Channel. The black lines show the inferred path for the two reflectors seen in Figure 5. Bathymetry shallower than 2000 m is shaded pink to help identify potential reflectors. It is signals like these that will help improve the system's capabilities.

Visualization Tools

A large portion of the effort will be to provide an analyst with a set of tools that will enhance an analyst's ability to detect, locate and characterize an event. Some of these tools are standard applications that have been used by researchers for years, but have not been integrated into the NTDS operational environment for day-to-day operations. Other tools are implementations of novel methods that are relevant to the hydroacoustic monitoring problem. These components include a spectrogram tool, a cepstrum review tool, a blockage review tool, and an azimuth display tool. Figures 7 and 8 show examples of a spectrogram tool and a cepstrum review tool. Figure 5 shows an example of what the azimuth display tool will provide.

The spectrogram allows analysts to quickly identify signals and choose the frequency band that maximizes SNR. Small signals are observable that could be overlooked in a time series representation. The cepstrum tool allows the analyst to review results from automatic processing that are of critical importance in characterizing and identifying events. It can also be useful in associating arrivals to a single event because the cepstrum is relatively invariant to path effects. The blockage review tool will aid the analyst in associating arrivals and to look for evidence that contradicts a given location (such as no signal at an unblocked receiver). The azimuth display tool provides a detailed image of the coherent energy arriving at a hydrophone station. This is important for obtaining the best azimuth estimate for direct arrivals and for identifying potential reflections. All of these tools are intended for use in an operational system. They will be integrated into the analyst's environment to support routine analysis of events that are of potentially interest.

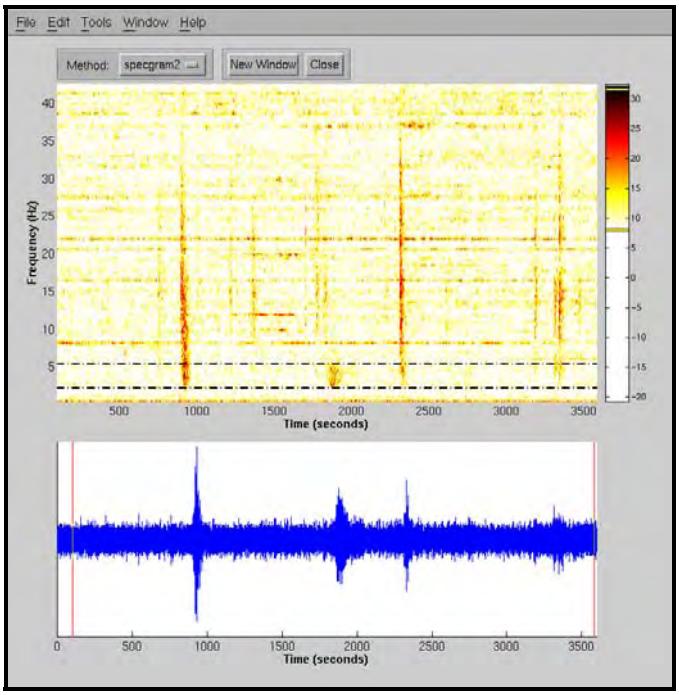

Figure 7. Example of a Spectrogram Tool. The spectrogram is the favored tool for analyzing hydroacoustic signals. The ACD is implementing an integrated spectrogram tool for analyst review. This particular spectrogram allows the analyst to simultaneously view the waveform and spectrogram, interactively choose filter bands, and adjust the color scale. The tool uses a sophisticated algorithm to enhance transient signals, which are the signals of greatest interest for test monitoring.

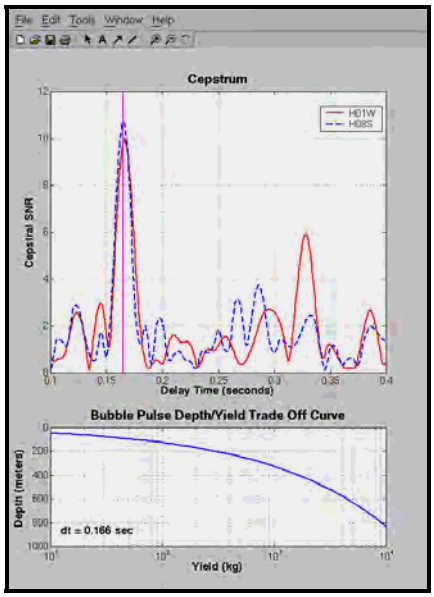

Figure 8. Example of a Cepstral Analysis Tool. The ability to review and modify cepstral results will be a new feature of this ACD. This tool allows the analyst to confirm the very important event characterization measurement. The estimated delay time (the first peak in the cepstrum) determines a depth/yield trade-off curve that will be used in determining a hydroacoustic magnitude. The automatic system picks the maximum peak that sometimes corresponds to the second bubble pulse and needs to be corrected by the analyst. The cepstra can also provide strong evidence for phase association as shown in this example with two signals measured at widely separated hydrophones that have nearly identical cepstral peaks.

Hydroacoustic Magnitudes

We are implementing a method for estimating a hydroacoustic station magnitude for in-water explosions. The energy measures extracted during processing (peak energy and total energy) provide some constraint on the magnitude of a particular event. However, it is difficult to directly determine quantities such as yield from these measures. The energy loss (transmission loss) due to propagation through the oceanic waveguide must be included in a yield determination.

Once a location for an event has been estimated, the transmission loss (TL) between the event location and a given hydroacoustic station can be calculated. TL is calculated for a number of potential source depths and across a wide frequency band. A standard model is used to calculate a set of candidate energy spectra as a function of charge weight and detonation depth consistent with the measured bubble pulse period. TL estimates and the source spectra are combined to predict a set of candidate energy spectra at the hydrophone station. The yield corresponding to the candidate spectra that best-matches the measured spectrum is used as the hydroacoustic magnitude estimate. This also provides an estimate of the source depth. An important feature of this approach is that it exploits the shape of the energy spectrum across the available frequency band. This shape provides critical information about the charge weight and detonation depth. Both the transmission loss and source spectra vary with frequency depending upon (among other factors) the source depth assumed.

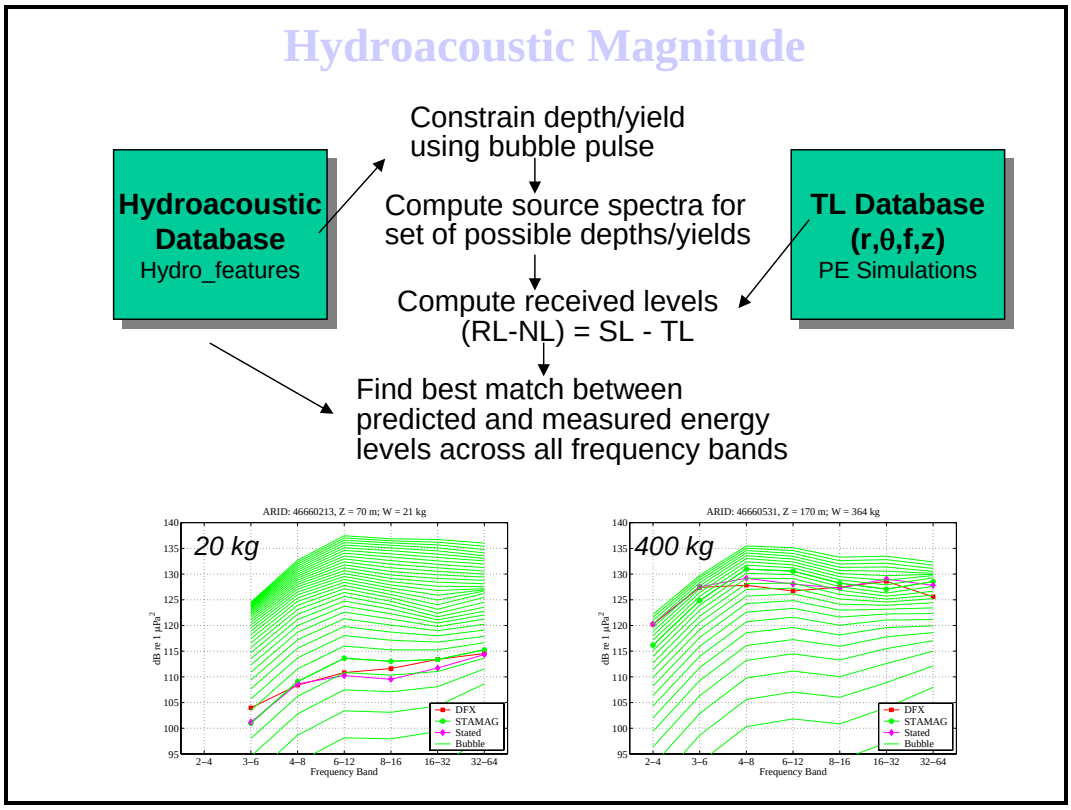

Figure 9. Estimation of hydroacoustic magnitudes. The received signal levels are matched to simulations based on source path and constrained using the bubble pulse depth/yield trade-off. The two examples use the actual measurements from explosions with nominal yields of 20-kg and 400-kg TNT equivalent.

Results using data from a well-documented seismic refraction survey show that accurate estimates of source yield and detonation depth are possible. This suggests that the measured spectral shapes and levels are sufficiently resolved in frequency, and that they can be predicted with sufficient fidelity using standard acoustic propagation codes and environmental databases.

CONCLUSIONS AND RECOMMENDATIONS

The new IMS hydrophone stations in the Indian Ocean provide a great opportunity to improve our hydroacoustic processing for detecting nuclear explosions in the region. This project will demonstrate enhancements in detection, localization and characterization of events occurring in the Indian Ocean Basin.

The Indian Ocean Advanced Concept Demonstration will improve detection by using coherent array processing and by providing analysts with visualization tools. The system's location capabilities increase by improving azimuth estimates, improving travel-time models, and incorporating hydroacoustic reflections into the location algorithm. The analyst will have significantly better resources to associate signals together including the spectrogram tool, the cepstral review tool, and the blockage review tool. New characterization abilities include the cepstral review tool and hydroacoustic magnitude estimation.

The data sets being compiled for the demonstration provide a unique resource that will be useful not only for evaluation of this project, but also for evaluating future enhancements to the system. There continues to be a need for definitive calibration data. This is especially true in regards to evaluating locations using reflected phases.

ACKNOWLEDGEMENTS

We would like to thank G. Eli Baker, Donna Blackman, Paul Dysart, Mariana Eneva, Charles N. Katz, and Brian Sperry for their contributions to this project.

REFERENCES

Blackman, D., C. de Groot-Hedlin, P. Harben, A. Sauter, and J. Orcutt (2002, submitted), Scattering and Propagation of Controlled Acoustic Signals Throughout the Indian Ocean Basin, *J. Acoust. Soc. Amer*.

Hanson, J.A. (2001), Initial Observations from the BIOT Hydroacoustic Station, *Proceedings from the CTBTO Hydroacoustic Workshop, October 8-11, 2001*.

Hanson, J.A., R. Le Bras, P. Dysart, D. Brumbaugh, A. Gault, and J. Guern (2001), Operational Processing of Hydroacoustics at the Prototype International Data Center, *Pure Appl. Geophys*., **158**, 425-456.

Harben, P.E. and C.O. Boro (2001), Implosion Source Development and Diego Garcia Reflections, *Proceedings 23rd Seismic Research Review*, 23-31.

Pulli, J.J. and Z.M. Upton (2001), Hydroacoustic Blockage at Diego Garcia: Models and Observations, *Proceedings 23rd Seismic Research Review,* 45-54.

Cochran, J.R. (2002), Cruise Report R/V Maurice Ewing, December 7, 2001 – January 25, 2002, Fremantle, Australia to Hobart, Australia, EW0114.

ACOUSTIC SOURCES FOR BLOCKAGE CALIBRATION OF OCEAN BASINS: RESULTS FROM THE OCTOBER 2001 INDIAN OCEAN CRUISE

Philip E. Harben,[1] Catherine de Groot-Hedlin,[2] and Donna Blackman[2]

Lawrence Livermore National Laboratory[1] and Scripps Institution of Oceanography[2]

Sponsored by Office of Nonproliferation Research and Engineering
Office of Defense Nuclear Nonproliferation
National Nuclear Security Administration

Contract No. W-7405-ENG-48[1] and DE-FC03-01SF22356[2]

ABSTRACT

Blockage and transmission loss calibration of hydroacoustic stations for explosion monitoring is important for assessing monitoring capability from new and existing stations. Unlike acoustic travel time, generally predicted with good accuracy by models, blockage and transmission loss predictions along many ray paths are poor. In large part, this is due to the relative coarseness of the global bathymetry databases for the acoustic frequency range of monitoring interest (1-100 Hz). When higher resolution bathymetry databases are integrated into models, blockage prediction accuracy improves; however, such high-resolution bathymetry databases are not available in large regions, such as the Indian Ocean, due to sparse coverage. A data-driven approach to the blockage and transmission loss prediction problem is an approach that sidesteps the bathymetry database problem as well as other difficulties such as modeling diffraction, higher modes, and providing predictions as a function of frequency. The data-driven approach requires a large number of ground truth events recorded at a specific station to calibrate it and allow prediction of blockage and transmission loss from a hypothetical source. Earthquakes can provide most of the calibration events but, with the exception of submarine volcanoes, there is no significant energy in the T-phase above about 15 Hz. To calibrate stations at higher frequencies, an artificial source is necessary. The purpose of the 2001 Indian Ocean cruise was to test three such sources at ocean basin scale.

Three sources were tested: an airgun array, a spherical implosion system, and a cylindrical implosion system. These sources were fired at numerous locations along a great circle ship-track between the Seychelles and Perth, Australia, and recorded at the Diego Garcia and Cape Leeuwin hydroacoustic stations. The airgun system was fired over shallow and/or sloping bathymetry along the track as much as possible to maximize coupling into the sound channel via bottom scattering. Although airgun signals were detected at Diego Garcia and at Cape Leeuwin, detections were not seen in several cases because the coupling was dependent on the complex process of bottom scattering into the SOFAR channel. The spherical implosion system was fired in two different configurations: 1-sphere and 5-sphere. The 22-liter single-sphere implosions were reliably detected at Diego Garcia for ranges from 800 km to 1200 km when fired at sound channel depths of 680 m. The 5-sphere shots were a cluster of 22-l spheres fired at 680 m. Both 5-sphere tests were reliably recorded at both Diego Garcia (4000- to 4500-km ranges) and Cape Leeuwin (1500- to 2000-km range). The sphere implosions produced useful signal from 40 Hz through 100 Hz. The sphere implosion systems also proved to be highly repeatable, especially the 1-sphere system. Tests with the cylindrical implosion system produced signal level too low to be detected at the International Monitoring System (IMS) hydroacoustic stations. A future cruise will test two additional sources: small explosives and a large continuous wave source previously employed in ATOC (Acoustic Thermometry of the Oceans Climate) experiments.

OBJECTIVE

The overall objective of this research is to assemble a database that provides accurate blockage prediction from any hypothetical oceanic source location to all hydroacoustic monitoring stations of interest. We know from experience that a model-based approach to this problem is not always accurate. The BBN Inc. code — HydroCAM — continues to be used at the National Data Center for model-based prediction of acoustic signal blockage. Model-based blockage predictions suffer, to first order, from the generally coarse bathymetry data available for the world's oceans. Less important, but significant, sources of model error are: ignoring scattering and diffraction, using only mode-1 propagation, and an inability to conveniently determine blockage as a function of source frequency.

The approach to improving blockage prediction in the world's oceans is to improve model capabilities by improving the resolution of the bathymetry databases and to assemble a database of ground truth events that define the blockage at any particular station. Emulating the regional seismic travel-time correction methodology, hydroacoustic ground truth data will trump any model prediction for locations close to where ground truth is available. The best prediction will transition to model-based when the location is far from any ground truth data. A critical issue in building the ground truth databases is understanding the suite of sources that will be needed and the limitations of each in providing the desired broadband blockage information. The nature of the source, accuracy of the source location, bandwidth of the source, and strength of the source will define the applicability of the source and the limitations for use in the database. For example, oceanic and near-coast earthquakes that generate large T-phases will certainly be a class of sources that make up a large part of a ground truth blockage prediction database. That they will not be the only class of sources is also clear since the bandwith is generally limited to 1-15 Hz (much lower than in-water explosions) and their location is difficult to accurately assess (DeGroot-Hedlin, 2001) because the T-phase is not necessarily generated at the earthquake epicenter. We seek to understand the sources we will need in a complete ground truth database. To this end we have completed a cruise that tests three sources: two implosion source systems and an airgun array. The man-made sources sought are those that complement the natural sources: energy in the higher frequencies of the monitoring band (15-100 Hz), accurate locations, and sufficient signal for ocean-basin propagation ranges. The research conducted and presented here has a focus on a sphere implosion system that appears to meet some of the criteria for a man-made source with blockage calibration utility, though other sources remain to be tested.

RESEARCH ACCOMPLISHED

The research accomplished falls under three headings: 1) Blockage Issues, 2) Implosion Source Studies, and 3) Cruise Results. Our discussion of blockage issues will map out some of the difficulties and concerns that must be at the forefront of any attempt to improve blockage prediction capabilities. The Implosion Source Studies section will document the progress made over the past year in understanding the glass sphere implosion source, its utility, and its limitation in controlled-source calibration. Finally, a summary of the Indian Ocean cruise results will be presented. This cruise took place in October 2001 and tested three different controlled sources for hydroacoustic monitoring station calibration at long ranges.

Blockage Issues

Acoustic blockage prediction in hydroacoustic monitoring has yet to be clearly defined by a concise set of measurements. Model predictions with HydroCAM, for example, can estimate if a particular source-receiver path is blocked or unblocked in accordance with a minimum-ocean-depth criterion along the path. When done for all source paths to a given receiver, a map of blockage for that ocean basin results. The maps generated are very different if the blockage criteria are 800 meters vs. 50 meters, and no single depth criterion produces a best or most accurate map. The reason the models are inadequate is that scattering, diffraction, and reflections - and their frequency dependence - is not accounted for. In addition, the bathymetry databases are inadequate for the acoustic frequencies of interest. Examples of model-predicted blockage at a 50-meter-depth criterion along a particular source-receiver path have been shown to have large amplitude signals from earthquake events that get through, although the coherency of the signals among the tri-partite sensors is significantly degraded (Harben, 2001). Completely blocked source-receiver paths have been shown to have consistent reflected phase arrivals from the same topographic feature.

Blockage prediction is needed to assess which hydroacoustic stations, for a particular source region, can be used in detection, location, and discrimination analysis. That assessment can be made, but it will not always be a simple *yes* or *no* answer for any particular station. A full assessment - which will be backed by a ground truth database - will need to have a set of measurements on direct path attenuation and scattering energy loss, loss in coherency due to scattering, and reflected phases that may be used in subsequent analyses, all with frequency dependence. The question of blockage along a particular path may have an answer like: full blockage at high frequency along the direct path, adequate signal-to-noise ratio (S/N) at low frequencies but with a complete loss of coherency between tripartite sensors (i.e. back azimuth estimation not possible), two consistent reflected phases for large source energy with unblocked paths. Deciding on the most appropriate measures and automating them in a ground truth database used for blockage prediction is an essential next step.

Implosion Source Studies

The development of an imploding glass sphere source has been documented in past reports (see Harben, 2000; Pulli, 2000; and Harben, 2001). Here we present new results from tests and models that improve our understanding of source phenomenology, repeatability, and utility in calibration.

The single-sphere implosion source signal has now been recorded four times under similar conditions, though in widely varying locations. The implosions were conducted at nominally 680-m depth and recorded with a hydrophone hung off the side of the ship, nominally 30-m deep. The recordings are all overplotted in Figure 1. The repeatability of the source is apparent. This is an important result for calibration purposes because it allows for accurate transmission loss and other amplitude-dependent measurements with this source.

We modeled the source (Tipton, 1991) using a C-language Arbitrary Lagrangian-Eulerian code (CALE). Although our results showed qualitative agreement, the modeled peak pressure was half that observed. In consultations with the glass manufacturer, we found that the glass spheres were sealed in a partial vacuum due to the high air temperatures in the vicinity of the molten glass. When we modeled partial vacuums within the glass sphere, we were able to resolve the inconsistency in peak pressure. The modeling predicts the glass sphere internal pressure as 1/6 to 1/8 atmosphere, consistent with air pressures at temperatures of molten glass.

The 5-sphere system had been tested once off the Pacific coast in 2001 at 137-m depth (see Figure 2, left panel). During this test, one of the spheres failed, and the resulting shock wave caused the other spheres to fail. This is evident in the recorded waveform. The beginning of the record has the characteristic signature of a single-sphere implosion -- the sphere that self-failed. The time between the first sphere shock wave and the larger grouping of impulses that follow is controlled not by the acoustic propagation time between spheres but by the collapse time. The implosions at 680 m (Figure 2, right panel) show a markedly different signature that can only be interpreted as a nearly simultaneous implosion of all five spheres due to the smashing cylinder. Apparently, the cracking propagates from sphere to sphere (which are touching) and hence the implosion timing of individual spheres is controlled by the acoustic propagation time. It is also evident that the 5-sphere system is not as repeatable as the 1-sphere source, though the waveforms are similar. This is consistent with expectations if the spheres are failing nearly simultaneously. Such a failure does not have spherical symmetry and will consequently have a complex radiation pattern.

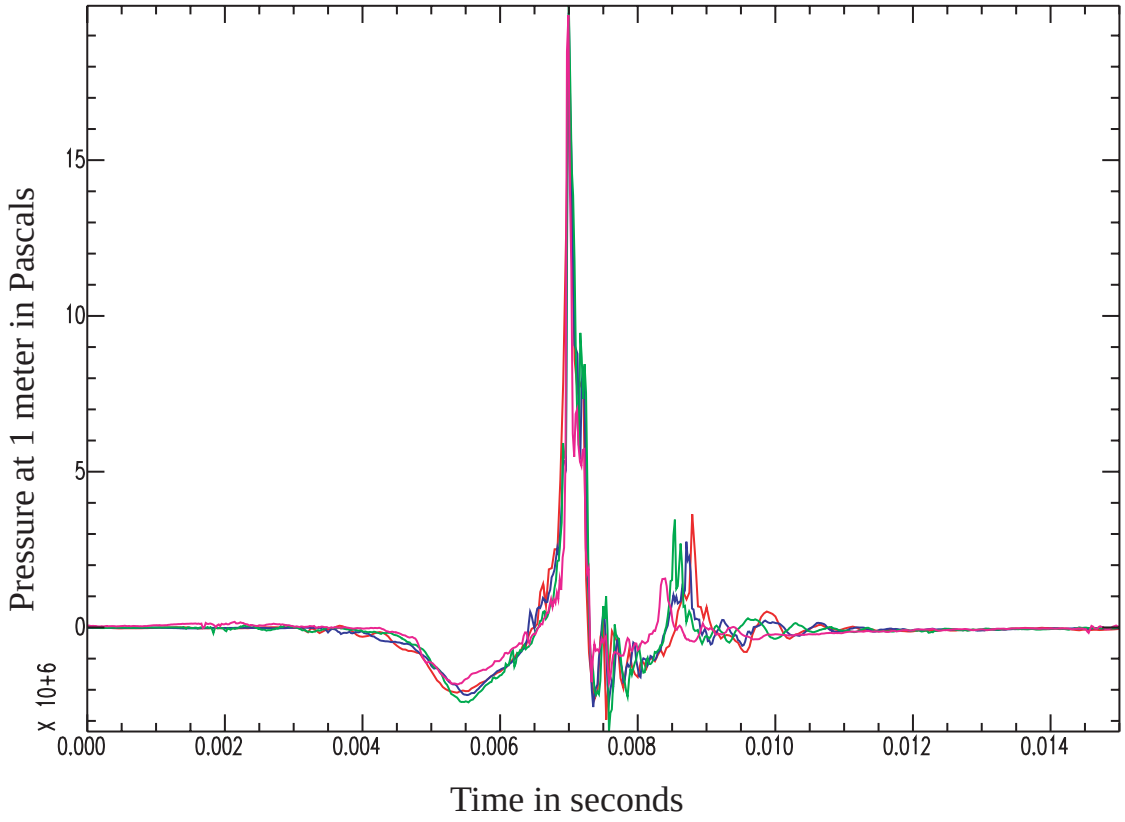

Figure 1. Repeated single-sphere implosions under similar conditions (680-m depth and projected to 1 m from the source). Note the good repeatability, especially for the implosion and main shock.

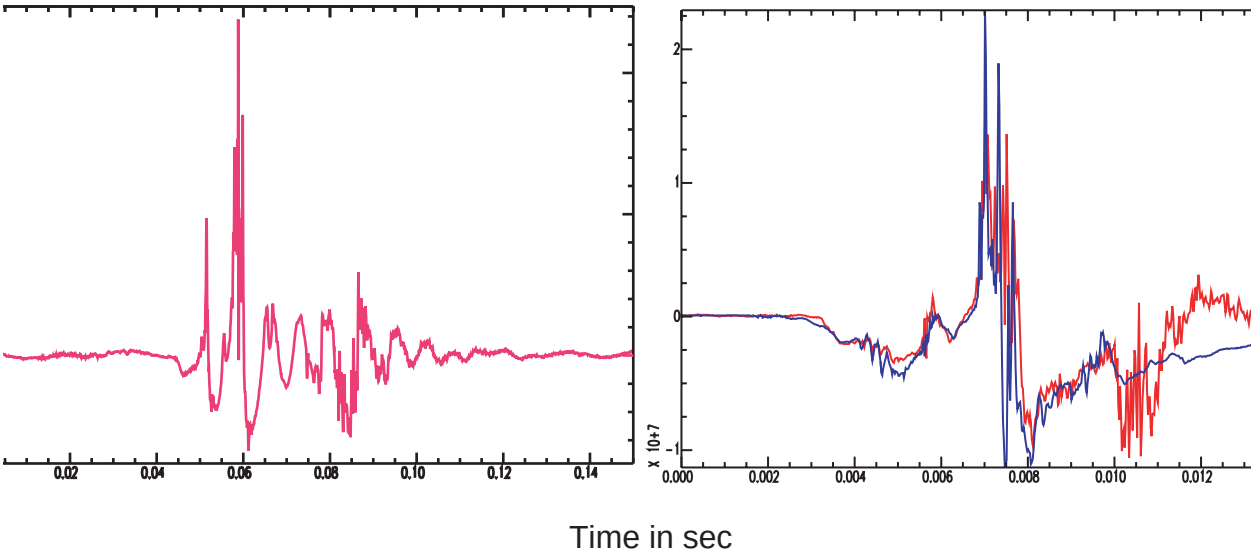

Figure 2. The 5-sphere implosion source waveforms are shown at 137 m (left) and for two tests at 680 m. Both plots are source strength at 1 m in Pascals. The horizontal axis is time in seconds. Note that the 137-m test was initiated by self-failure of a glass sphere. The 680-m tests were initiated properly by the cracking system.

Cruise Results

The purpose of the October 2001 Indian Ocean cruise aboard the Maurice Ewing was to produce acoustic signals at various locations in the Indian Ocean basin so that the nature of sound propagation, and losses, can be documented. One goal was to determine what types of topography are conducive to using large, shallow sources that require that energy be scattered off the seafloor into the SOFAR channel, for basin scale propagation. Another goal was to determine the range at which small, deep imploding sources can be detected at distant receivers. The acoustic sources consist of a large array of airguns, imploding glass spheres, and a triggered imploding cylinder. The receivers are permanently installed hydrophones that are part of the IMS that is overseen by the Comprehensive Nuclear-Test-Ban Treaty Organization. Each hydrophone station consists of three instruments. Two stations are deployed in the vicinity of Diego Garcia, on the east and west slopes of Chagos platform. One station is installed off Cape Leeuwin, southwestern Australia.

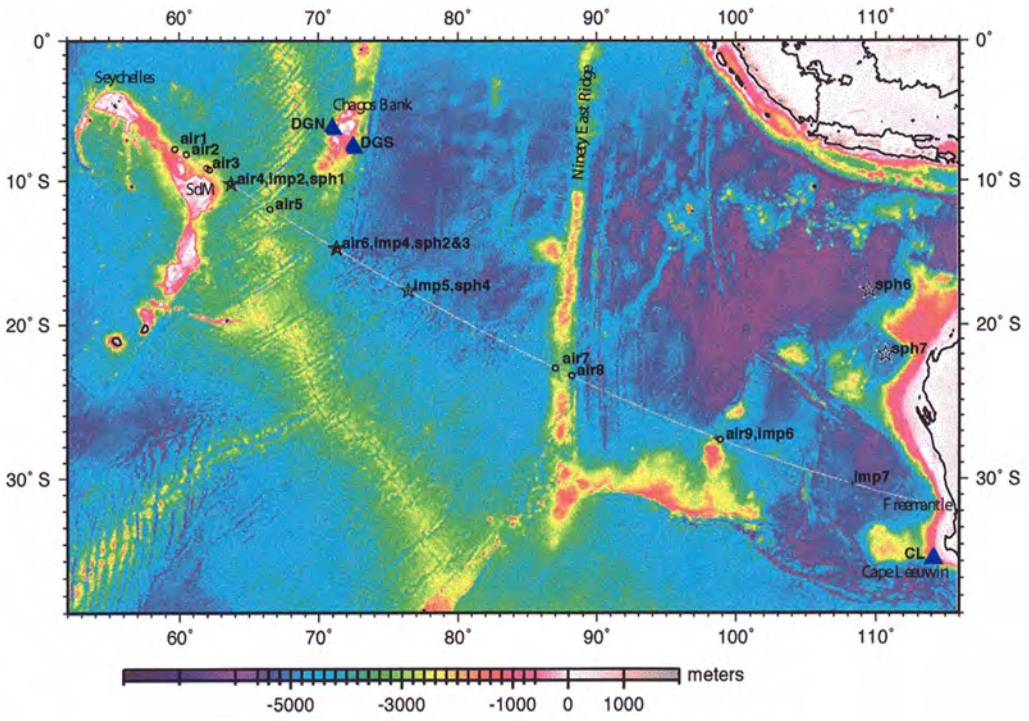

Figure 3. Topographic model of Smith and Sandwell (1997) in the Indian Ocean region is overlain by the 2001 R/V Ewing shiptrack (gray line) and the acoustic source locations for our experiment. IMS hydrophone stations are shown by blue triangles. Circles show where the airgun array shooting (air) was conducted. Stars show glass sphere (sph) implosion stations and 5-sphere implosions are highlighted in white. Crosses are where the MPL/SIO imploding cylinder (imp) was fired. SdM indicates Saya de Mahla bank.

The 'standard' Ewing array of 20 airguns was used. Total volume of the array was 8465 cubic inches. The shot interval was varied from 57 - 173 s. Each shooting period lasted about 30 min. The imploding glass spheres were those described above. Both 1-sphere and 5-sphere systems were tested. The triggered imploding cylinder was a 900-lb. reusable system which operates by using the available hydrostatic pressure at depth to mechanically open an empty 20-l cylinder upon electrical command. Displaced water fills the cylinder, generating an acoustical signal. We recorded all the implosion source waveform on a TEAC RD-145T 16-track using a calibrated (-194dB re 1V/uPa) Ball hydrophone. The hydrophone was deployed from the ship's deck. Shackles were attached to the cable to add weight, but at some stations the cable was not particularly vertical in the water. The sample rate was set to either 24000 or 48000 SPS for the stations.

The cruise track is shown in Figure 3 with the location of the IMS recording stations and the location of each source deployment. The cruise originated in the Seychelles and ended in Freeport, Australia, on the great circle path route between the two. Attempts were made to test airguns in areas of shallow and/or variable seafloor topography. The two 5-sphere shots, shown off the northwest coast of Australia, were conducted for us by researchers on a subsequent cruise.

Airguns: Near source recordings of the airgun array shots indicate very consistent source signatures. Shot durations are on the order of 40 ms, and most of the output energy is in the 6- to 110-Hz band, with peaks at 8 Hz and 14 Hz.

S/N for waveforms recorded at the IMS receivers in the Indian Ocean are shown as a function of frequency in Figure 4. Overall, S/Ns at Diego Garcia south (DGS) and Cape Leeuwin (CL) are much poorer than those at Diego Garcia north (DGN). In part, this is due to higher noise levels at these stations; noise levels at DGS and CL exceed those at DGN by about 6 dB and 12 dB, respectively. As expected, the S/N vary as a function of both source and receiver location mainly due to acoustic blockage. Propagation to DGS was blocked by the Chagos Bank for the first four airgun sites (the first 78 shots). Cape Leeuwin was expected to be blocked from the first site by the Saya de Malha bank and from some of the subsequent five sites by the Ninety East Ridge. Propagation to DGN was blocked by the Chagos Bank for all but the first four sites.

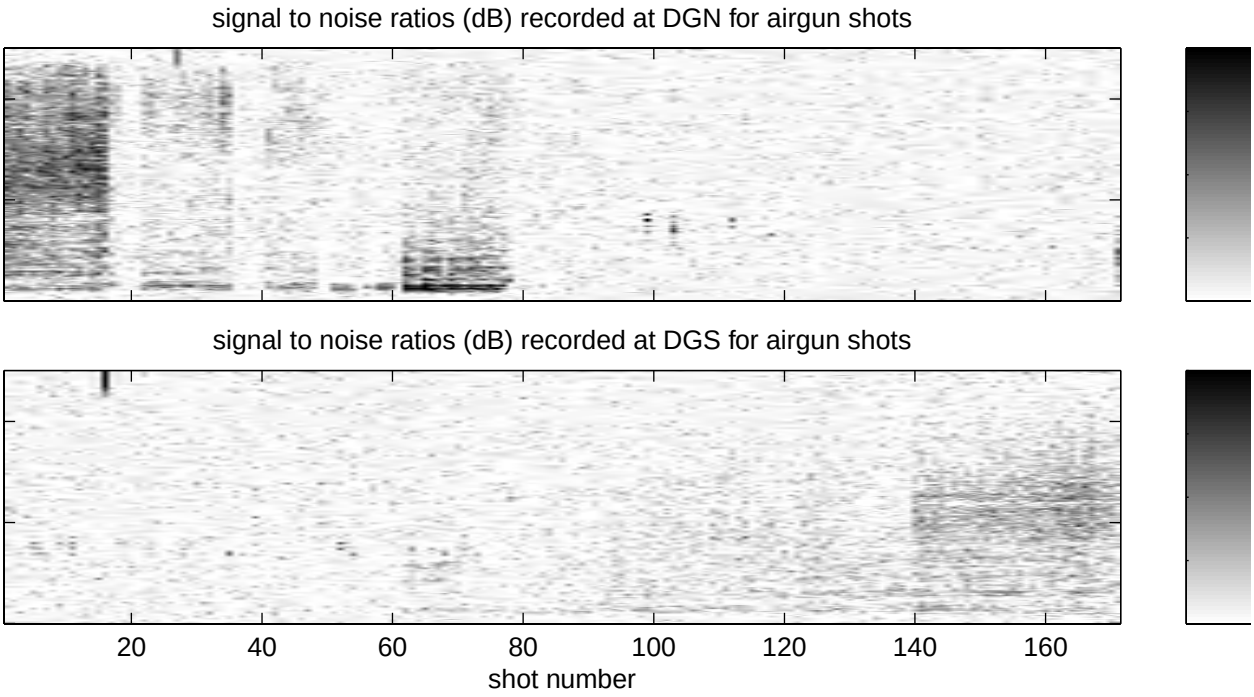

Figure 4. The S/N of the recorded waveforms are displayed in a shaded grey scale as a function of shot number and frequency. Note the recordings were at Diego Garcia north (top) and Diego Garcia south (bottom).

Bathymetry in the source region also affects the observed S/N. Waveforms were detected only when the airgun was shot over ridges, consistent with expectations. Shots 1-16 were located over shallow, sloping seafloor near the Mascarene Plateau just south of the Seychelles. Shots 62-78 were located over the Mid-Indian Ridge. Finally shots 141-178, detected at both DGS and Cape Leeuwin, were near the Ninety East Ridge. Modeling results indicate that energy from these shots couples to the SOFAR channel by downward propagation. However, several other sites were also located in shallow water, but coupled poorly to the SOFAR channel. Modeling is continuing to determine why.

Imploding Spheres: The imploding glass sphere tests showed that a single-glass-sphere system could be detected at unblocked ranges of at least 1200 km. The single-sphere spectra are shown in Figure 5 for three implosions

conducted south of Diego Garcia and recorded at the north Diego Garcia station (left panel) and at the south station (center and right panel). The signals were not observable in the time records unless high pass filtered. We determined a good corner for the high pass to be about 40 Hz. The S/N difference as a function of frequency clearly demonstrates that the imploding sphere will be limited as a calibration source to frequencies above about 40 Hz.

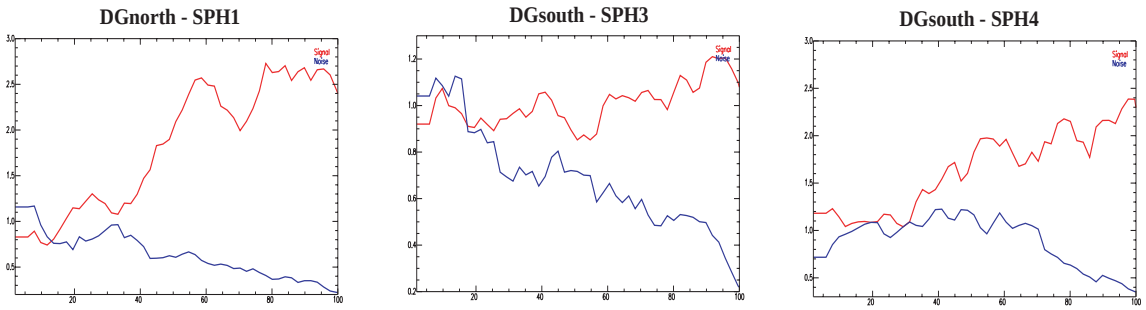

Figure 5. Spectra of the signal and pre-event noise levels for three single-sphere implosions as recorded at the Diego Garcia hydroacoustic monitoring stations. The horizontal scale is frequency in Hz. The vertical scale is normalized to 20-Hz noise levels in each case. The red curves are signal spectra, the blue are pre-event noise. A smoothed average of the three hydrophones at each station is shown.

The 5-sphere implosions were both conducted along the western Australia continental margin with ranges to Diego Garcia of 4168 km and 4397 km and ranges to Cape Leeuwin of 1960 km and 1465 km. The time waveform records are shown in Figure 6. The horizontal scale is in seconds with different time window lengths for the top panels compared to the bottom ones. The waveforms were 4-pole high passed at 40 Hz. Clearly, we are able to record a signal at both stations and hence have demonstrated the possibility of ocean basin scale calibration using the 5-sphere system. As with the single-sphere system, frequency content of the propagating signal is limited to 40 Hz and above. It is clear from the S/N of the recordings that the source strength is woefully inadequate for producing reflections off continental margins and islands that would be detectable. The relatively small amount of dispersion in the signal, after propagation over 4000-km ranges, indicated the implosion sources may be a good source for acoustic travel-time studies.

Imploding Cylinders: The cylindrical imploder (Sauter, 1996) was tested at six locations in the Indian Ocean. Although the imploding volume and test depth were similar, the imploding spheres had a peak pressure 20 times larger than the cylindrical imploder. This is due to the optimum convergent geometry of a sphere that gives rise to a larger shock wave. Because of the significantly lower peak pressures, the cylindrical imploder signals were not observed at the Diego Garcia and Cape Leeuwin stations.

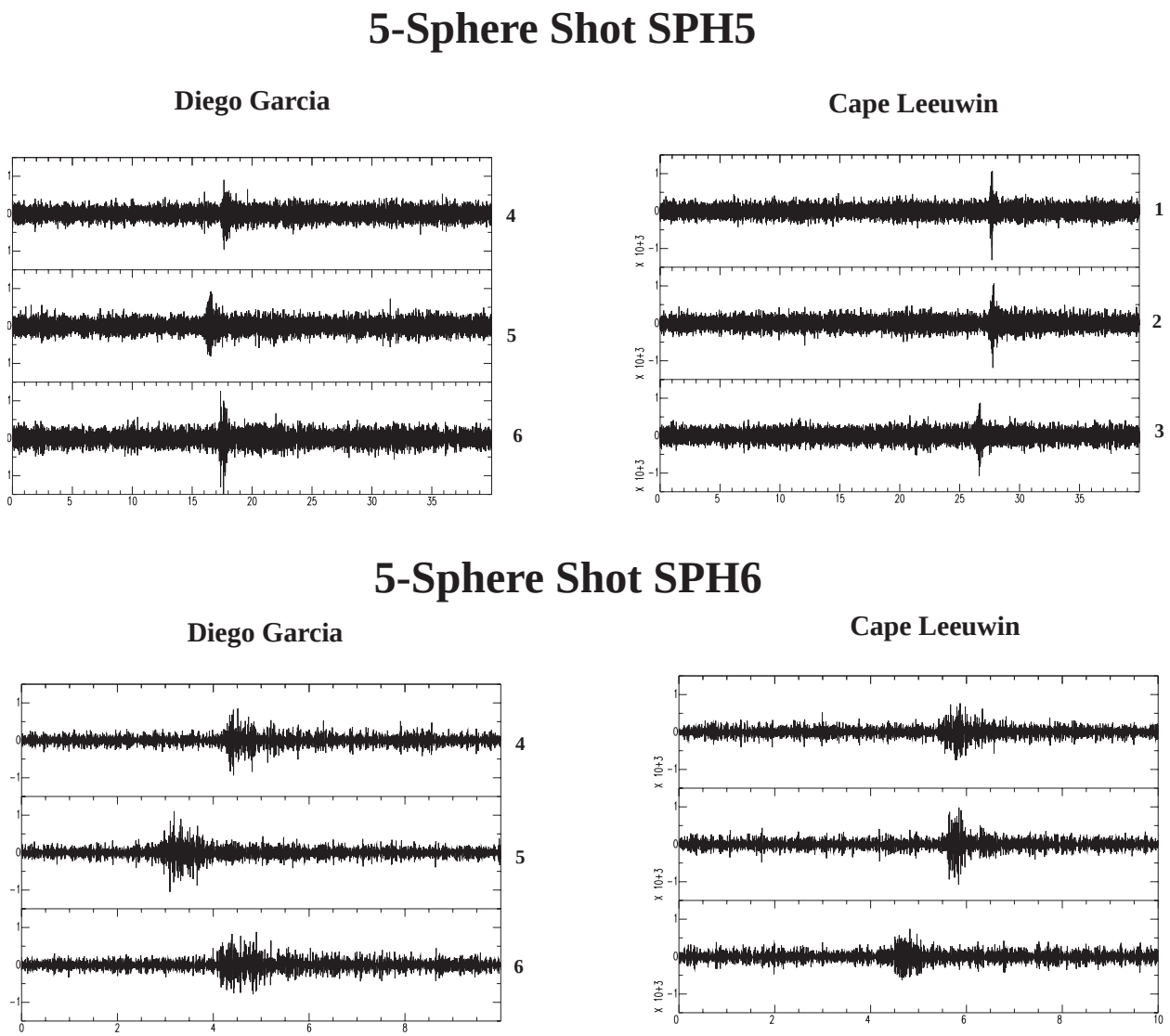

Figure 6. Recordings of the 5-sphere glass sphere implosions are shown with high-pass filtering at 40 Hz. The top two panels show the recording from shot SPH5 at both the Diego Garcia and Cape Leeuwin stations. The bottom panels shows the recordings for shot SPH6.

CONCLUSIONS AND RECOMMENDATIONS

The challenge of providing accurate assessments of acoustic signal blockage in the world's oceans is a large one. Purely model-based approaches fail because of inadequate bathymetric resolution in current databases and simplifying assumptions that make the calculations tractable. Establishing a database of ground-truth events is a strategy that is proving effective in regional travel-time calibration for seismic monitoring. Such an approach holds promise for acoustic signal blockage as well but has distinctly different technical issues that must be resolved. Unlike the solid earth, the acoustic medium is changing on a seasonal basis and hence a particular source-receiver path that is blocked in the summer could be open in the winter. Another issue is low-frequency (1- to 15-Hz) blockage vs. high-frequency blockage (15 to 100 Hz). Most earthquake sources are low frequency and hence can not be used to predict high-frequency blockage. Man-made sources can provide the high-frequency ground truth, and we are beginning to understand the utility of some types of man-made sources in providing ground truth for acoustic blockage prediction.

An Indian Ocean cruise conducted in October 2001 tested implosion and airgun sources at source-receiver distances up to 4400 km. The results show that the glass sphere implosion source has utility at long ranges but only in the frequency band of 40-100 Hz. The airgun sources, unfortunately, are not consistently useful because coupling into the SOFAR channel -- hence long-range propagation -- is controlled by bottom scattering, which is highly variable. A follow-on cruise scheduled for May 2003 in the Indian Ocean will test explosives, an ATOC-type fixed-frequency source, and glass sphere implosions. The results of this cruise should complete the ground work needed before planning a systematic man-made source calibration study of an ocean basin.

We have alluded to the importance of reflected acoustic phases for increasing monitoring capability of hydroacoustic networks without any hardware changes (see Pulli, 2000). The practical application of this will require ground-truth calibration of all the major reflectors in an ocean basin. To first order, we believe that earthquake sources will be the best way to accomplish this because the acoustic energy is great enough to generate reflected phases with adequate S/N at the receiver. It will be necessary to understand how the reflected phases are altered at higher frequency. For this, a man-made source will probably be used though we cannot say at this stage if anything other than a large explosion will be capable of generating the acoustic energy needed to provide adequate S/N on the reflected phases.

ACKNOWLEDGEMENTS

We thank Allen Sauter and the Ewing ship crew for helping with all aspects of the cruise logistics and source deployments. We are also grateful to Fiona Sutherland and the shipboard crew for conducting the two 5-sphere deployments during the subsequent cruise leg. We are indebted to the staff of the Air Force Technical Applications Center and the Center for Monitoring Research for supplying the recordings from Diego Garcia and Cape Leeuwin during the time period of the cruise. Thanks to Doug Clarke and Willy Moss for implosion source modeling with the CALE code.

REFERENCES

de Groot-Hedlin, C.D. and J.A. Orcutt (2001), Excitation of T-phases by Seafloor Scattering, *J. Acoust. Soc. Am.* 109, 1944-54.

Harben, P.E., C. Boro, L. Dorman, and J. Pulli (2000), Use of Imploding Spheres: An Alternative to Explosives As Acoustic Sources At Mid-Latitude SOFAR Channel Depths, UCRL-ID-139032.

Harben, P.E. and C. Boro (2001), Diego Garcia Reflections and Implosion Source Development, *Proceedings of 23rd DTRA/NNSA Seismic Research Review*, Jackson Hole, WY.

Pulli, J.J., Z. Upton, R. Gibson, J. Angell, T. Farrell, and R. Nadel (2000), Characterization of Reflected Arrivals and Implications for Hydroacoustic Test-Ban-Treaty Monitoring, *BBN Tech. Memor.* W1380.

Pulli J.J. and P.E. Harben (2000), Hydroacoustic Calibration with Imploding Glass Spheres, in *22nd DoD/DOE Seismic Research Proc*., Vol. III, pp. 65-74.

Sauter, A., L. Dorman, E. Canuteson (1996), Development of a Seismo/Acoustic Implosive Source, *EOS Trans.* AGU.

Smith, W.H.F. and D.T. Sandwell (1997), Global Seafloor Topography from Satellite Altimetry and Ship Soundings, Science **277**, 1956-1962.

Tipton, R. (1991), CALE User s Manual, Version 920701, Lawrence Livermore National Laboratory, Livermore, CA.

HYDROACOUSTIC T PHASES FROM LARGE ICEBERGS DRIFTING IN THE ROSS SEA

Emile A. Okal[1], Jacques Talandier[2], and Olivier Hyvernaud[2]

Northwestern University[1]; Laboratoire de Géophysique, Papeete, Tahiti[2]

Sponsored by Defense Threat Reduction Agency[1] and Commissariat à l'Energie Atomique[2]

[1]Contract Number DTRA01-00-C-0065

ABSTRACT

In Late 2000, numerous sequences of T phases were detected by seismic stations of the Polynesian network and in the Cook Islands, with an origin in the Ross Sea off the coast of Antarctica. This observation was corroborated by records at seismic stations, at permanent sites VNDA and SBA, and at the volcano monitoring network on Erebus. A combined location procedure using both seismic phases (presumed to be Lg) and T phases, narrowed down the source of the activity to huge icebergs which at the time were drifting in the Ross Sea after calving off the Ross Ice shelf. The signals present a broad variety of spectral characteristics, most of them featuring prominent eigenfrequencies in the 4-to-7 Hz range, often complemented by overtones. Most epicenters follow the spatio-temporal evolution of the drift of iceberg B15-B. The majority of the signals are generated during a 36-day time window when it is speculated that B15-B collided with smaller icebergs or was scraping the ocean floor on the shallow continental shelf. We speculate on the possible physical nature of the resonator generating the signals, which could correspond to an elastic mode of the iceberg, or to the oscillation of the fluid-filled crack in the ice. The signals differ from those previously recorded during volcanoseismic swarms in that the spectral lines have a much higher quality factor Q (in general found to be > 100). Such oscillations document a new source of acoustic energy in the ocean column, which is of general interest in the framework of the CTBT. The location procedure used in this context also underlines the powerful synergy which can be developed between various kinds of geophysical data. In 2002, more such signals are being recorded from various sites aound Antarctica, and we also report on these developments, following the break-up of a gigantic segment of the Ross Ice shelf on 2002 May 10.

OBJECTIVE

The objective of this research is the analysis of the source characteristics of hydroacoustics signals in the world's oceans, and in particular the discrimination between man-made explosions and natural sources, such as earthquakes, landslides and volcanoes. We report here on the identification of a new source capable of contributing significant hydroacoustic energy over extended periods of time.

RESEARCH ACCOMPLISHED

Starting in August 2000, seismic stations operating as *T* –phase stations in Polynesia detected irregular activity originating from the Southern Ocean. The activity was concentrated in a group of 13 sequences (hereafter the "Ross Events") whose principal characteristics are listed in Table 1, with representative spectrograms of signals shown on Figures 1a-d. At seismic stations located on atolls, such as Vaihoa (VAH), the acoustic-to-seismic conversion is particularly efficient, and the seismic signal at the *T* –phase station can be regarded as essentially equivalent to the acoustic one inside the SOFAR, within the frequency window of interest ($2 \leq f \leq 16$ Hz). In most instances, the energy of the Ross events is concentrated at one or several prominent frequencies, which suggests that its source must involve the oscillation of some kind of resonator, a model also supported by the often long duration of the signals, e.g., Event 4, which lasts for 3 hours. However, some sequences feature significantly broader spectra (e.g., Event 12), and some like Event 2 (Figure 1a) last no more than 2 minutes. In addition, the frequency of the largely monochromatic signals does fluctuate with time, a property already observed during the Hollister volcanic swarm (Talandier and Okal, 1996), with some of the Ross events featuring more substantial variations of frequency with time (e.g., Event 7), which give the spectrograms a contorted, "snake-shaped" aspect. Finally, several sequences end with singular signals exhibiting an increase of frequency with time (suggestive of the shrinking of the resonator), which can be slow and gradual (Event 4) or fast and abrupt (Event 3, Figure 1b). In the case of Event 13, the termination of the sequence involves a complex evolution of prominent frequencies with time, featuring several episodes of frequency decrease, a property termed "gliding" and identified during episodes of volcanic tremor (Hagerty et al., 1997) which in general terms would suggest a geometrical expansion of the resonator (Chouet, 1996).

A systematic effort was conducted to complement the Polynesian dataset with records at other Pacific seismic stations. When available, the IRIS station at Rarotonga (RAR) provided increased azimuthal aperture; the station was, however, inoperative from 04 to 18 December 2000. Unfortunately, no other seismic station could contribute *T* –phase signals, and this for a variety of reasons, including blockage at NOUC, JOHN, and at the ocean-bottom observatory H2O; unfavorable station locations involving long post-conversion seismic paths (TAU, KIP, XMAS); a probable combination of those two effects at VIB; and a high level of background noise at the small island of Pitcairn (PTCN). Finally, no signal was detected at Easter Island (RPN), where detection of *T* phases has been previously recognized as irregular (Okal and Talandier, 1997; Okal et al., 2001; Reymond et al., 2001).

The principal events in the sequence were first located using the techniques developed by Talandier and Okal (1996) during the Hollister volcanic swarm: using whenever possible impulsive arrival times of sharp sub-events, or in their absence, differential travel-times between stations by cross-correlating the fluctuations with time of the frequency of quasi-monochromatic *T* waves. After implementing station corrections to compensate for the post-conversion land path, the locations of the sources were inverted using the seasonally adjusted, laterally varying model of acoustic velocities of Levitus et al. (1994). The location procedure is enhanced by a Monte Carlo algorithm consisting of injecting Gaussian noise into the dataset of arrival times (Wysession et al., 1991); a best-fitting ellipse is then computed for the resulting cluster of epicenters.

In all cases, these preliminary epicenters locate in the general area of the Ross Sea, and of the Borchgrevink and George V coasts of Antarctica, but the limited azimuthal coverage provided by the band of available stations (at most 30°) results in weak resolution of epicentral distance. Nevertheless, several statistically distinct groups can be identified, with Events 2 and 13 along the coasts, while the remaining epicenters locate in the center of the Ross Sea.

In view of these preliminary results, we conducted a systematic search for additional records of conventional seismic waves at Antarctic stations. We were able to identify signals at the IRIS station at Scott Base (SBA), at the GTSN station Vanda (VNDA), and at several stations of the Mount Erebus Volcanic Observatory (MEVO), located on Ross Island (courtesy of Dr. Richard Aster).

In order to use the Antarctic seismic signals in a combined relocation with the Polynesian T phases, we need to know the velocity of seismic waves along the source-to-receiver path. For this purpose, we tested a series of relocations, for variable values of the velocity V to the Antarctic stations. In this experiment, we used a priori bounds of $V_{\min} = 1.3$ km/s, thus including the possibility of an acoustic velocity in the cold waters of the Southern sea, and $V_{\max} = 8.25$ km/s, corresponding to a P_n velocity under the continental shelf, and we varied V in increments of 0.05 km/s. For each value of V, we quantify the quality of the relocation through the root-means squares of the residuals, σ. We determined that the best-fitting value of V is consistently $V_{opt} = 3.7 \pm 0.2$ km/s.

The interpretation of V_{opt} is not straightforward, and remains somewhat unresolved. On the one hand, it matches well the velocity of P waves in recrystallized ice (Thiel, 1961). However, and even in the case of Event 1, which may have occurred on the Ross Ice Shelf or at its boundary (see below), this interpretation is improbable, since the ice shelf is only 300 m thick, i.e., less than 1/5 of the longest wavelengths recorded in Antarctica. For the other events located farther North, satellite imagery disproves the existence of a continuous layer of thick ice along the path to VNDA.

Rather, we propose to interpret the arrivals at $V_{opt} = 3.7$ km/s as L_g wavetrains, and interpreted as shear energy trapped in the continental crust (e.g., Knopoff, 1973). As documented, for example by Bouchon (1982) and Campillo et al. (1984), L_g can be the first prominent arrival at regional distances in conditions where P arrivals do not emerge from noise, in particular for shallow crustal dislocation sources. In addition, L_g energy can propagate efficiently at frequencies of a few Hz (Bouchon, 1982). Furthermore, the value of V_{opt} falls in the range of predicted and observed L_g velocities in the relevant frequency window (Cara and Minster, 1981). Finally, we will see that the epicentral locations of the Ross Sea events are on the continental shelf or at its boundaries, so that L_g wavetrains would not be blocked by transit over an oceanic path.

Notwithstanding our inability to definitely identify the nature of the seismic phases recorded at Antarctic stations, we will use the optimized velocity $V_{opt} = 3.7$ km/s for all seismic phases at Antarctic stations in order to locate the Ross events from a combined dataset of acoustic and seismic arrival times.

As discussed in Table 1, out of the 13 sequences investigated, we obtain seven very well constrained locations, with semi-major axes of ≈ 25 km for the Monte Carlo ellipses (Events 2, 3, 5, 8, 10, 11, 12), and two poorly resolved ones (Events 1 and 13). The remaining sequences (Events 4, 6, 7, 9) are given tentative locations based on their temporal association with well-located events. As shown on Figure 2, all epicenters, except Events 1, 2, and 13, fall in the center of the Ross Sea. The location of Event 13 (Figure 1d), which was recorded neither by the Antarctic stations nor by RKT, could not be improved beyond the estimate obtained from Polynesian T phases. Event 1 (15 August 2000) has a large uncertainty, but lies significantly South of the November-December group. As for Event 2 (08 November 2000), it has a well constrained epicenter just South of Cape Adare on the Borchgrevink Coast.

We reject volcanism as a possible origin of the Ross Sea events. First, an important aspect of our results is that all nine located events cannot share a common epicenter. This is well documented by the Monte Carlo ellipses on Figure 2, and was confirmed by a formal attempt at inverting the full dataset of arrival times for a common epicenter and distinct origin times, which resulted in unacceptable residuals of more than one minute. We conclude that the location of the Ross Sea events moved with time in a generally SE to NW direction (with the exception of Event 2). Their spatio-temporal evolution is in sharp contrast with our previous experience of long-range hydroacoustic detection at volcanic sites such as Macdonald Seamount and Hollister Ridge (Talandier and Okal, 1996). Second, we note the presence of three known sites of volcanic (or fumarolic) activity in the area: Erebus (77.6°S; 167.2°E), Melbourne (74.35°S; 164.70°E) and the Balleny Islands (66°S; 163°E). When tested as possible epicenters for our datasets, r.m.s. residuals exceeding several minutes made all of these locations unacceptable. In the case of Event 12, for example, Erebus was a legitimate epicenter on the basis of the RSP hydroacoustic data alone). However, the inclusion of the Antarctic dataset leads to a discrepancy of more than 9 minutes between Polynesian and Antarctic stations. We reject volcanism as a source of the Ross Sea events, since even an uncharted volcanic source would have had to move hundreds of km across the Ross Sea over a period of a few weeks.

Rather, we propose that the sources of the Ross Sea events lie within very large icebergs, documented to have calved off the Ross Ice Shelf in the [Northern] Spring of 2000, and which were drifting across the Ross Sea in a northwesterly direction during the later part of the year. We base our interpretation on the dataset of reported coordinates and infrared satellite photographs available from the web site of the University of Wisconsin's Antarctic Meteorological Research Center (Anonymous, 2002a).

Around March-April 2000, Iceberg B-15 (300 km by 40 km) and the smaller B-17 to the East calved off the shelf around 78°S, between 177 and 165°W. By 15 August 2000, the date of Event 1, B-15 had broken up into two principal pieces, B-15A and B-15B, and several smaller fragments. B-15B then takes a Northerly path towards the Center of the Ross Sea, at an average drift velocity of 4 km/day (or 5 cm/s). Figure 2 plots the positions of B-15B and B-17 at a number of dates between 09 November 2000 and 05 January 2001. During that time window, B-15B engages in a large rotation, collides with B-17 in Early November 2000, calves off a further small fragment, B-15F, on its West side, some time between 14 November and 29 November 2000, and frees itself from B-17 as the latter breaks into pieces around 30 December 2000. By 05 January 2001, B15-B has taken a Northwesterly direction, rounds Cape Adare about 03 May 2001 (it has then broken into two parts), and then progresses along the Oates Coast, where it currently (2002) lies around 155°E (Anonymous, 2002b).

As documented on Figure 2, there is a spectacular correlation between the epicenters of Events 3, 5, 8, 10, 11 and 12 (and hence presumably of the intervening Events 4, 6, 7, 9) and the location of the icebergs B15-B and B-17. In particular, the spatio-temporal evolution from the Southeastern group of epicenters (3, 5, 8) in November to the Northwestern one (10, 11, 12) in December mimics the drift and rotation of B-15B. In the case of the relatively poorly located Event 1 (on 15 August 2000), Figure 2 shows the Northern end of the large Monte Carlo ellipse similarly intersecting the position of B15-B on that same day.

On this basis, we propose that the source of the Ross Sea events consists of unidentified phenomena taking place inside large icebergs (principally B15-B) drifting in the Ross Sea.

As discussed below, we can offer only vague speculation as to the nature of the events taking place inside the icebergs and generating the hydroacoustic and seismic signals studied. Whatever these phenomena may be, it is remarkable that they take place only during a small part of the long drift of B-15B from the Ross Ice shelf to Cape Adare and beyond, namely during a 36-day window and over a distance of less than 200 km (with the exception of Event 1, farther South). In particular, B-15B becomes silent after 18 December 2000, and during its 4-month voyage to Cape Adare. We know of no prominent bathymetric feature which would explain this pattern through hydroacoustic blockage along the path to Polynesia. Rather, B-15B's silence must reflect the cessation of the physical source process.

Among possible mechanisms for the excitation of an oscillator, that would be geographically (or temporally) controlled, we envision collisions with other ice masses, and rubbing on the sea floor. A possible scenario would correlate the Ross Sea events with the collision between B-15B and B-17, which lasted at least one month, until B-17 breaks into pieces at the end of December. Another scenario would be to invoke friction on the floor of the Ross Sea. Bathymetric coverage of the Ross Sea is scarce, especially since the relevant area lies outside the Southern limit (72°S) of Smith and Sandwell's (1994) satellite altimetry database. However, the Northern portion of B-15B's path (traveled Westwards after 01 January 2001) most probably lies over deep water, whereas its Southern portion (traveled Northwards) is over the continental shelf. We can only speculate as to the presence of large seamounts or other underwater structures, against which the iceberg could have rubbed, but the spatio-temporal distribution of the Ross Sea events would be in very general agreement with this scenario. We also note that significant iceberg furrows have been documented on the sea floor, including around Antarctica, at depths as great as 400 to 500 m (Harris and Jollymore, 1974; Barnes and Lien, 1988), making it legitimate to assume that motion over the continental shelf at similar depths would occasionally involve scraping against bathymetric features. Finally, as shown by Campillo et al. (1984), a superficial source (such as an iceberg scraping the ocean floor) will excite L_g most efficiently, whereas the excitation of P_g would be relatively insensitive to depth; these properties would lead naturally to L_g being the prominent seismic phase for sources exciting the solid Earth at the water-crust interface.

Regarding the actual physical nature of the sources generating the Ross Sea signals, the prominence of distinctive frequencies (typically 4 Hz) in many spectra (occasionally with harmonics) suggests the oscillation of a resonator. In this respect, our sources differ significantly from the "icequakes" widely observed ever since seismic stations were installed on glaciers and large icecaps. Being essentially instantaneous sources, the latter are characterized by short durations and a broad spectrum featuring high frequencies (Sinadinovski et al., 1999). Even the so-called "low-frequency icequakes" attributed to calving of ice blocks from glaciers (Qamar, 1988) and occasionally featuring a monochromatic spectrum (VanWormer and Berg, 1973) are of much shorter duration than the Ross events.

In order to investigate more in detail the spectral characteristics (eigenfrequency and quality factor Q) of a representative signal, we selected the VAH record from Event 4 (on 12 November 2000) because of its exceptional duration (3 hours). For this purpose, we use a running window of 81.9 s duration (4096 samples), offset 10 s at a time. At

each step, we then identify the frequency f_0 at which the spectral amplitude $X(f)$ reaches its maximum, which we interpret as the eigenfrequency of the resonator, and we fit a resonance curve of the form

$$X_r(f) = \frac{A}{\sqrt{(f - f_0)^2 + \frac{\pi^2 f_0^2}{Q^2}}} \tag{1}$$

to the shape of the spectral amplitude $X(f)$ in the frequency interval $I\ \{f_0 - 0.125\,\text{Hz} \le f \le f_0 + 0.125\,\text{Hz}\}$. We retain only values of Q for those windows where $X(f_0)$ is at least 40% of its maximum value, and for which the spectral line is adequately modeled by (1), as defined its goodness of fit. The two frames on Figure 3 show the variation of f_0 and Q as a function of time t, taken at the center of the running window.

While f_0 can remain remarkably constant over intervals of time of a few minutes (see Figure 1), Figure 3a shows that it varies significantly on a time scale of tens of minutes. Changes in f_0 can be continuous (e.g., the "gliding" observed at the start of the record), or sharp and stepwise, the windows with stronger and cleaner signals being more stable in frequency. This would require the presence of several oscillators, some of which capable of an evolution with time of their eigenfrequency, which in turn most probably expresses an evolution of their dimension.

The quality factors Q of the resonators range between 100 and 650, with an inverse average value of 250, much greater than typically reported for volcanic tremor (Q = 5 to 10) or even during the Hollister swarms (Q = 20 to 50); this further argues strongly against a volcanic origin for the Ross Sea signals. The attenuation of seismic waves in ice has been reported in the Greenland icefield by Langleben (1969) who reported a fall-off coefficient $c_1 = 4.45 \times 10^{-2}$ dB m^{-1} kHz^{-1} equivalent to Q = 166, and in sea ice by Kohnen (1970), who gives a slope of attenuation with frequency $q = 0.56 \times 10^{-5}$ m^{-1} Hz^{-1}, equivalent to Q = 175. Note however that these values were measured at considerably higher frequencies in both studies, and on longitudinal waves in the latter.

Speculating further on the possible physical nature of the resonator, we note the approximate dimensions of B-15B, 135 km by 40 km, and we take its thickness as at least 300 m, based on an estimation of the emerged fraction from airborne photographs, and of the thickness of the Ross Ice shelf from seismic soundings. We can then eliminate gravitational oscillations as the source of the signals, since the bobbing frequency of the iceberg on the sea would be on the order of 30 mHz, rather than 4 Hz. Rolling and pitching eigenfrequencies would also be much lower than observed — on the order of 20 mHz.

Rather, the frequencies observed could represent various eigenmodes of oscillation of the iceberg. For example, for a 300-m thick ice layer, the eigenfrequency of a vertical shear mode would be 3.07 Hz (with $\beta = 1.84$ km/s, or a Poisson ratio of 0.34). The eigenfrequency of a fundamental "Crary" mode (Ewing and Crary, 1934; essentially a shear wave propagating horizontally with a phase velocity equal to the P –velocity α) would be 3.51 Hz for the ice sheet in a vacuum; it could be affected by the presence of water (Press and Ewing, 1951), but its order of magnitude would remain in general agreement with the resonance frequencies observed in our signals. This interpretation would be particularly likely under the assumption that the ice mass is set in resonance by scraping the ocean floor, or rubbing against another ice mass; it could also explain the presence of harmonics, or overtones, since several modes would be excited by a source essentially similar to hitting a bell, and resulting in musical "richness". However, under this scenario, the iceberg would be expected to resonate at a set of discrete, and well defined pitches, and the observed continuous fluctuation of eigenfrequency with time would be more difficult to explain.

Another scenario would involve the resonance of a fluid-filled cavity in a mode comparable to the oscillation of magma within a fissure in a volcanic system (Aki et al., 1977). As summarized by Chouet (1996), the eigenfrequencies of such as a resonator are complex functions of its size and shape, and of the impedance contrast between the fluid filling the crack and the surrounding medium. In the particular case of icebergs, the fluid would have to be water, but the almost certain presence of air bubbles could greatly reduce the sound speed in the fluid. Furthermore, this model could explain the observed fluctuations of frequency with time, as both the dimension of the resonator and the supply of air bubbles could be expected to vary with time continuously, for example during filling or emptying of the fluid in the crack. These interpretations remain of course highly speculative at this point.

CONCLUSIONS AND RECOMMENDATIONS

We have documented prolonged episodes of hydroacoustic activity in the Ross Sea during the months of August-December 2000. By combining datasets of T phases recorded in Polynesia with regional seismic phases recorded at

Antarctic stations, we obtain epicentral locations correlating systematically with the position of large icebergs, specifically B-15 B and B-17, which were drifting in the Ross Sea at that time, and thus we conclude that the signals originated at or inside the icebergs. This study illustrates the powerful synergy obtained by combining hydroacoustic and classical seismological datasets, and resulting in epicentral precision of a few tens of km in a very remote area of the world's oceans.

Despite a broad variability in the spectral characteristics of the Ross events, they cannot be compared to seismic sources previously identified and analyzed in the ice environment, such as icequakes and calving events. Rather, our observations define a new kind of source capable of contributing hydroacoustic energy to the SOFAR channel over extended periods of time. The presence of preferential frequencies in the 3 to 7 Hz range (often associated with overtones) clearly implicates the resonance of an oscillator, whose exact nature presently eludes us. In the context of the use of hydroacoustic waves for explosion monitoring, it is clear that a deeper investigation of the phenomena involved is warranted; a possible avenue would involve the direct deployment of portable seismic stations on massive icebergs known to be calving off the major Antarctic ice shelves (May 2002).

REFERENCES

Aki, K., M. Fehler, and S. Das (1977), Source mechanism of volcanic tremor; fluid-driven crack models and their application to the 1963 Kilauea eruption, *J. Volcanol. Geotherm. Res.*, 2, 259−287.

Anonymous (2002a), Antarctic Meteorological Research Center, http://amrc.ssec.wisc.edu, Univ. Wisconsin, Madison.

Anonymous (2002b), National Ocean and Atmospheric Administration, http://www.noaanews.noaa.gov/ stories/s862.htm, U.S. Dept. of Commerce.

Barnes, P.W., and R. Lien (1988), Icebergs rework shelf sediments to 500 m off Antarctica, *Geology*, 16, 1130−1133.

Bouchon, M. (1982), The complete synthesis of seismic crustal phases at regional distances, *J. Geophys. Res.*, 87, 1735−1741.

Campillo, M., M. Bouchon, and B. Massinon (1984), Theoretical study of the excitation, spectral characteristics, and geometrical attenuation of regional seismic phases, *Bull. Seismol. Soc. Amer.*, 74, 79−90.

Cara, M., and J.B. Minster (1981), Multi-mode analysis of Rayleigh-type L_g, *Bull. Seismol. Soc. Amer.*, 71, 973−984.

Chouet, B. (1996), New methods and future trends in seismological volcano monitoring, in: *Monitoring and mitigation of volcano hazards*, ed. by R. Scarpa, and R.I. Tilling, pp. 23−97, Springer, Berlin.

Ewing, M., and A.P. Crary (1934), Propagation of elastic waves in ice, II, *Physics*, 5, 181−184.

Hagerty, M.T., M.A. Garces, S.Y. Schwartz, and M. Protti (1997), Long-term broad-band observations of ground deformations at Arenal Volcano, Costa Rica, *Eos, Trans. Amer. Geophys. Un.*, 78, (46), F431 [abstract].

Harris, I.McK., and P.G. Jollymore (1974), Iceberg furrow marks on the continental shelf Northeast of Belle Isle, Newfoundland, *Can. J. Earth Sci.*, 11, 443−524.

Knopoff, L. (1973), Interpretation of L_g, *Geophys. J. Roy. astr. Soc.*, 33, 387−402.

Kohnen, H. (1970), Über die Absorption elastischer longitudinaler Wellen im Eis, *Polarforschung*, 39, 269−275.

Langleben, M.P. (1969), Attenuation of sound in sea ice, 10−500 kHz, *J. Glaciology*, 8, 399−406.

Levitus, S, T.P. Boyer, J. Antonov, R. Burgett, and M.E. Conkright (1994), *World Ocean Atlas 1994*, NOAA/NESDIS, Silver Springs, Maryland.

Neave, K.G., and J.C. Savage (1970), Icequakes on the Athabasca glacier, *J. Geophys. Res.* 75, 1351−1362.

Okal, E.A., and J. Talandier (1997), *T* waves from the great 1994 Bolivian deep earthquake in relation to channeling of *S* wave energy up the slab, *J. Geophys. Res.*, 102, 27421-27437.

Okal, E.A., P.-J. Alasset, O. Hyvernaud, and F. Schindelé (2001), The deficient *T* waves of tsunami earthquakes, *Geophys. J. Intl.*, submitted.

Press, F., and M. Ewing (1951), Propagation of elastic waves in a floating ice sheet, *Trans. Amer. Geophys Un.*, 32, 673−678.

Qamar, A. (1988), Calving: A source of low-frequency seismic signals from Columbia Glacier, Alaska, *J. Geophys. Res.*, 93, 6615−6623.

Reymond, D., O. Hyvernaud, J. Talandier, and E.A. Okal (2001), *T* –wave detection of two underwater explosions off Hawaii on April 13, 2000, *Bull. Seismol. Soc. Amer.*, submitted.

Sinadinovski, C., K. Muirhead, S, Spiliopoulos, and D. Jespen (1999), Effective discrimination of icequakes on seismic records from Mawson station, *Phys. Earth Planet. Inter.*, 113, 203−211,

Smith, W.H.F., and D.T. Sandwell (1994), Bathymetric prediction from dense satellite altimetry and sparse shipboard bathymetry, *J. Geophys. Res.,* 99, 21803−21824.

Talandier, J., and E.A. Okal (1996), Monochromatic *T* waves from underwater volcanoes in the Pacific Ocean: Ringing witnesses to geyser processes?, *Bull. Seismol. Soc. Amer.,* 86, 1529-1544.

Thiel, E., and N.A. Ostenso (1961), Seismic studies on Antarctic ice shelves, *Geophysics*, 26, 706−715.

VanWormer, D., and E. Berg (1973), Seismic evidence for glacier motion, *J. Glaciology,* 12, 259−265.

Wysession, M.E., E.A. Okal, and K.L. Miller (1991), Intraplate seismicity of the Pacific Basin, 1913−1988, *Pure Appl. Geophys.,* 135, 261-359.

Table 1. Principal characteristics of the 13 events studied

Number	Date and time D M (J)	Epicenter (°S)	Epicenter (°E)	Duration (mn)	Peak-to-peak velocity at VAH (μm/s)	Remarks
1	15 AUG (228) 22:28:18.6	78.21	-168.61	1.3	1.23	Edge of Ross Ice Shelf. No data at RAR, RKT. Monochromatic signal (3.5 Hz) with overtones; sharp impulsive beginning.
2	08 NOV (313) 22:18:31.3	72.10	170.16	2	2.18	Borchgrevink Land. Relatively monochromatic; frequency fluctuates; no overtones.
3	12 NOV (317) 01:13:26.6	75.76	-175.75	8	0.62	Central Ross Sea. Generally weak at Antarctic stns. Narrow spectrum centered around 4 Hz. Strong final puff with frequency increasing with time.
4	12 NOV (317) 06:00 — 09:00	75.8	-175.8	3 hr	0.24	Central Ross Sea. Only traces in Polynesia (except VAH); No signal at SBA and Erebus. Long signal, generally monochromatic (2.5 to 4 Hz), with frequency fluctuations but few overtones.
5	14 NOV (319) 01:01:56.6	75.92	-175.60	3	0.81	Central Ross Sea. No data: Erebus; No signal: SBA. Relatively broad spectrum on acoustic records. Dominant frequency 2.5 Hz at VNDA.
6	19 NOV (324) ~ 02:30	75.8	-175.8	10	0.42	No signal: RSP except VAH. No data: Erebus, SBA. Broad spectrum (2 − 16 Hz). Assumed in same area as Events 3−5, based on times at VNDA & VAH.
7	21 NOV (326) 15:22	75.8	-175.8	10	0.24	No signal: Polynesia except VAH. No data: Erebus, SBA. Fluctuation of dominant *f*, leading to "snake-shaped" spectrogram. Assumed at same location as Events 4−6, based on VNDA & VAH times.
8	22 NOV (327) 21:32:13.0	75.85	-176.28	10	0.34	Central Ross Sea. No data: Erebus, SBA. Same general characteristics as Event 7.
9	05 DEC (340) 03:21:19.8	75.08	-177.75	8	0.30	Central Ross Sea. No data: Erebus; No signal: SBA. Broad spectrum (2 − 10 Hz), with dominant f = 2.9 Hz. Final sequence with sharply increasing frequency.
10	05 DEC (340) ~ 20:46	75.1	-177.8	15	0.32	Noisy record; broad spectrum (2 - 10 Hz), with 2 sequences; assumed to share location of Event 9.
11	15 DEC (350) 03:16:14	74.4	-178.4	10	0.44	Central Ross Sea. No signal: SBA. Broad spectra (2 - 12 Hz); weak correlation of acoustic and seismic records.
12	18 DEC (353) 09:56:29.1	74.82	-178.68	8	0.42	Central Ross Sea. Two parts; 1st short (30 s) with impulsive start; 2nd emergent and long (150 s). Broad spectrum.
13	14 JAN (014) 2001 17:36:10	67.0	141.5	7	1.31	Off Oates or George V Coasts. No signal: RKT; all Antarctic stations. Relatively broad spectrum with dominant *f* at 4, 5.5 and 7 Hz; first sequence ends abruptly, followed by short (60 s) puff, with spectrogram showing several lines of strongly decreasing frequencies (gliding). Location only tentative.

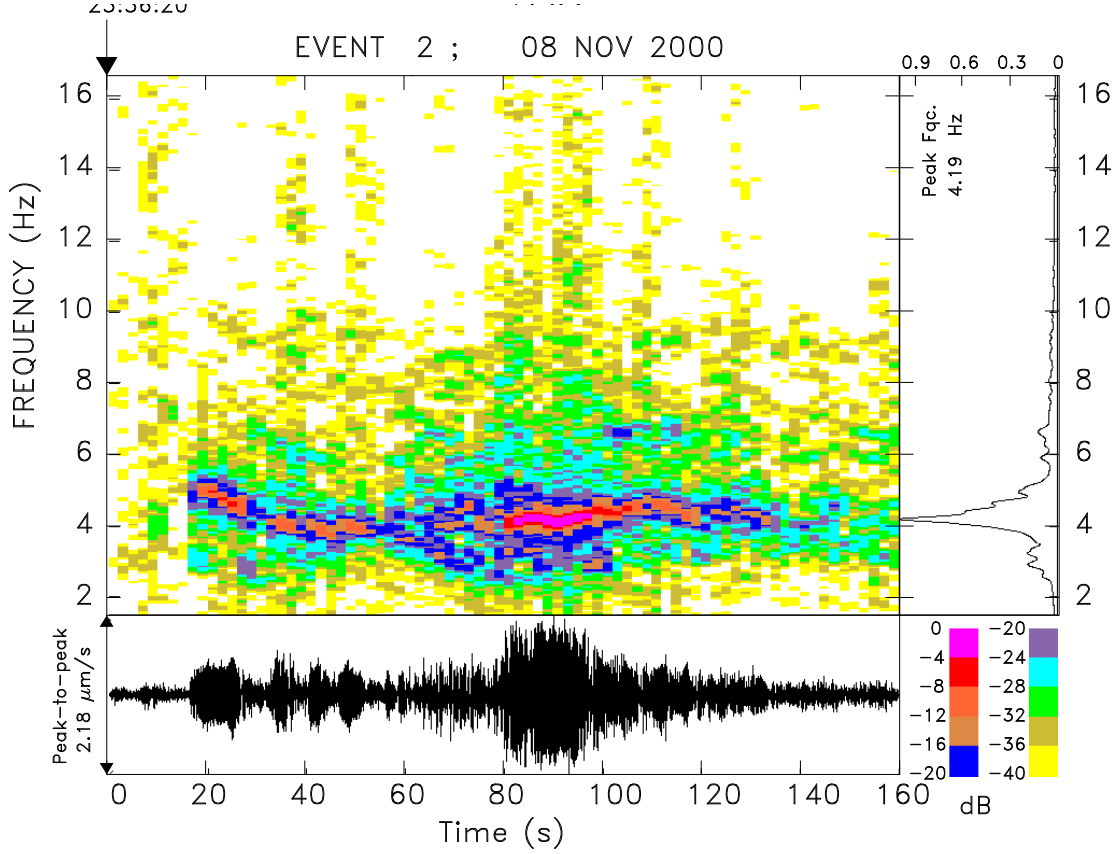

Figure 1a. T-phase record of Event 2 at Vaihoa. The figure is composed of three frames: The bottom one shows a 160-second time series of the ground velocity (in black), high-passed filtered for $f \geq 2$ Hz. The frame at right is a plot of the amplitude spectrum of the high-pass-filtered ground velocity record. The main color frame is a spectrogram representation of the distribution of spectral amplitude in the record, as a function of time and frequency. The color-coding is logarithmic, with the key (in dB relative to the most energetic pixel) given at bottom right. White pixels correspond to spectral amplitudes below −40 dB. Note the impulsive start of the signal, and the slow, contained, fluctuation of the prominent frequency with time.

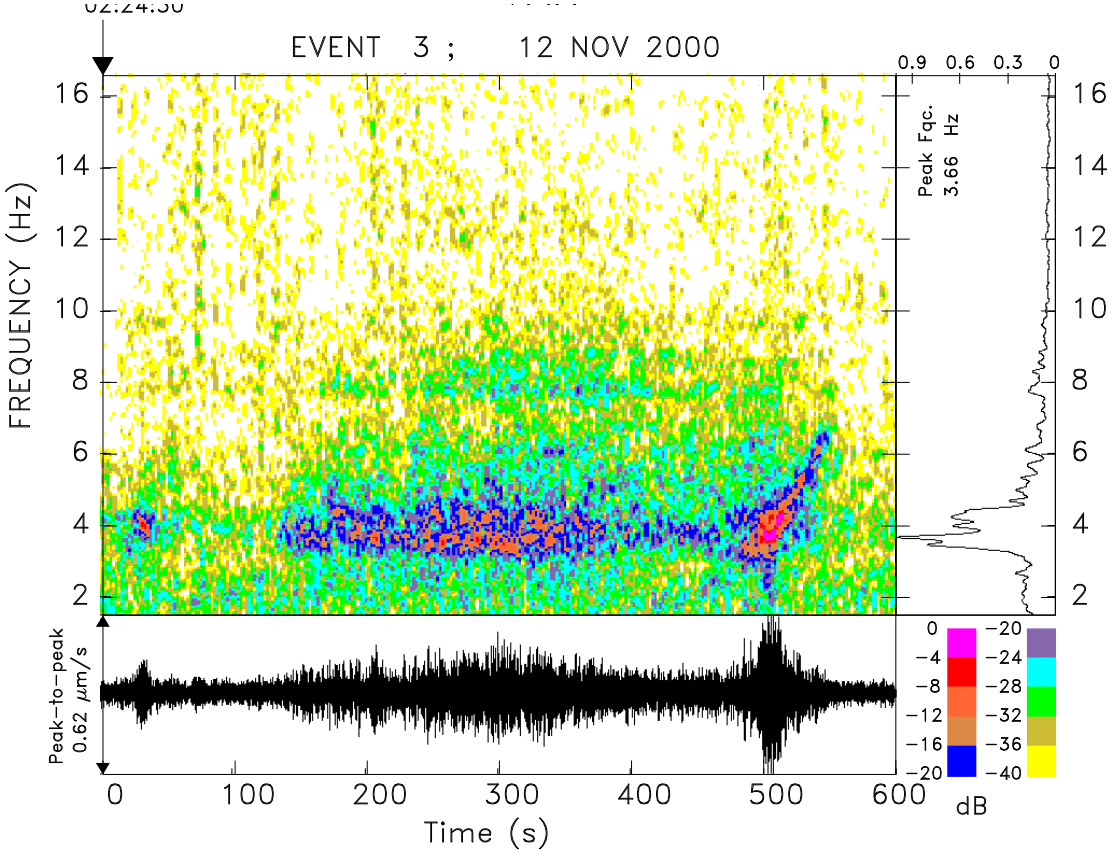

Figure 1b. Same as Figure 1a for Event 3. The time series is now 600−s long. Note the singular signal ending the sequence, featuring an increase of frequency with time.

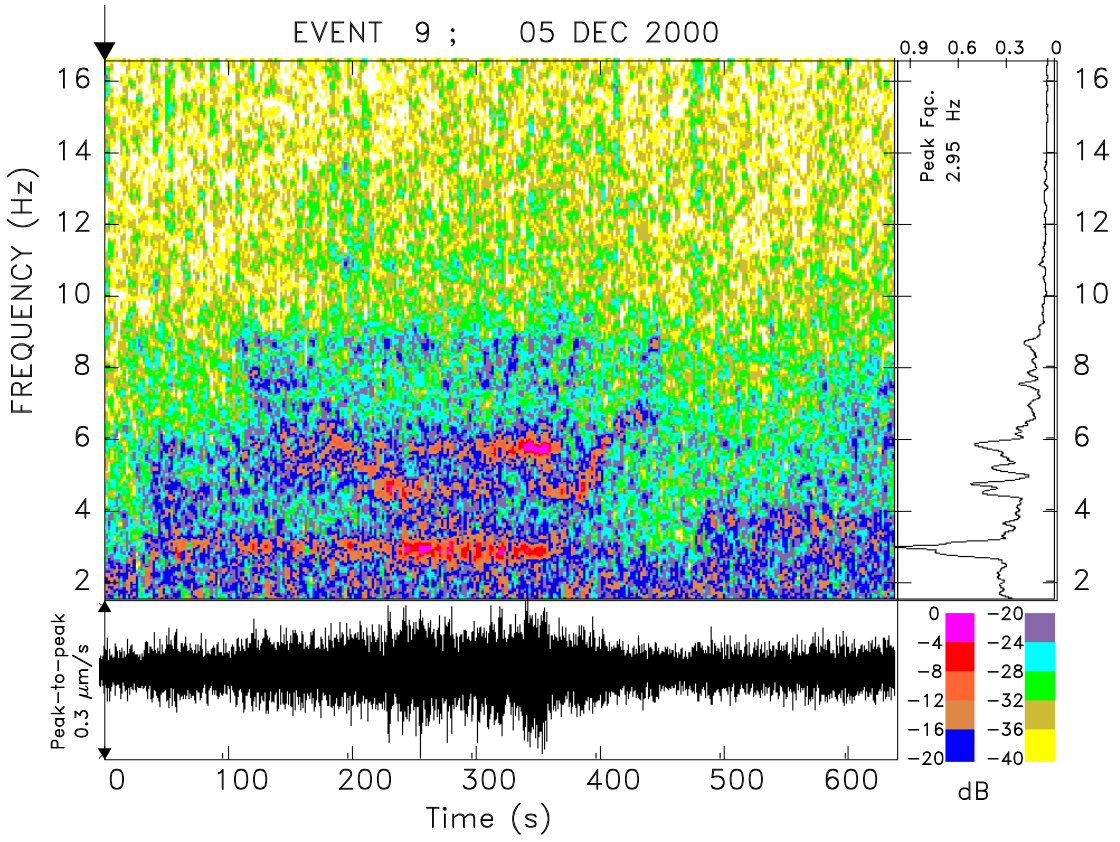

Figure 1c. Same as Figure 1a for Event 9. Note the relative complexity of the spectrum, and the trend towards an increase in frequency at the end of the main pulse (400 s into the signal).

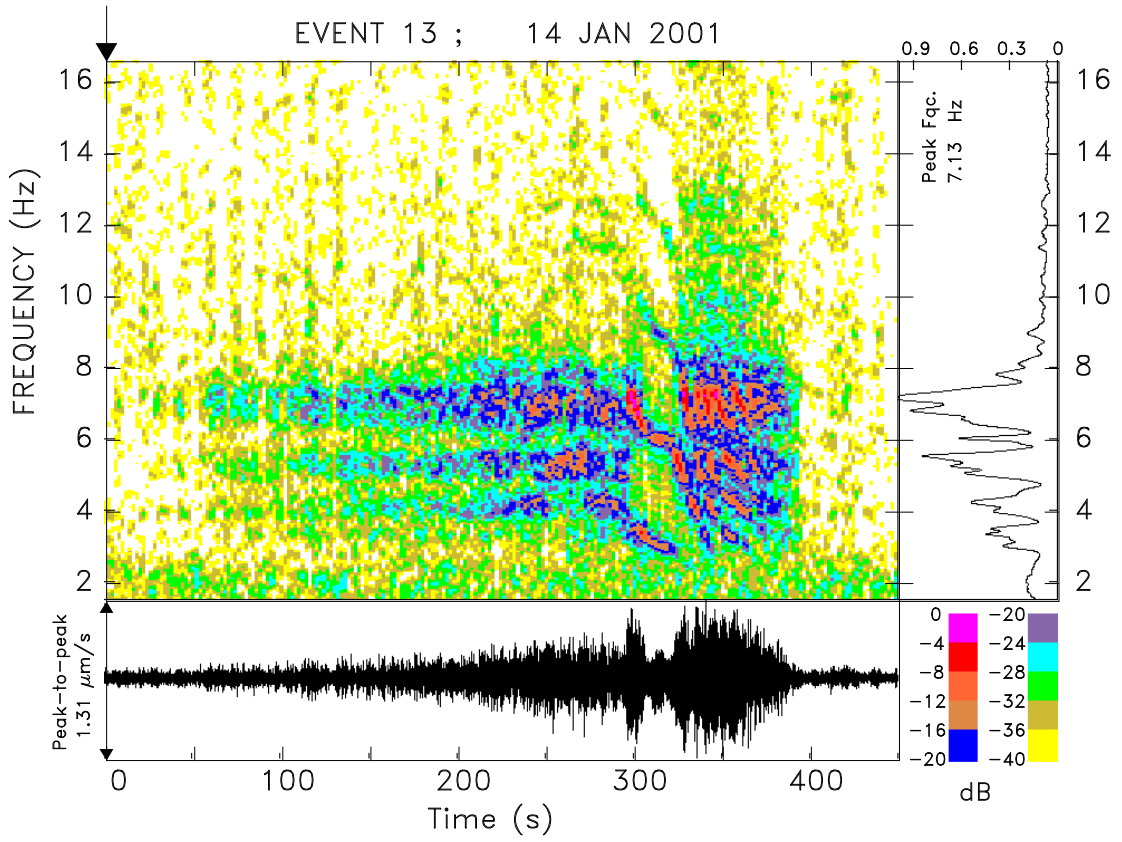

Figure 1d. Same as Figure 1a for Event 13. Note the complex character of the spectrogram, especially in the final phases of the pulse, where the eigenfrequency tends to decrease with time ("gliding").

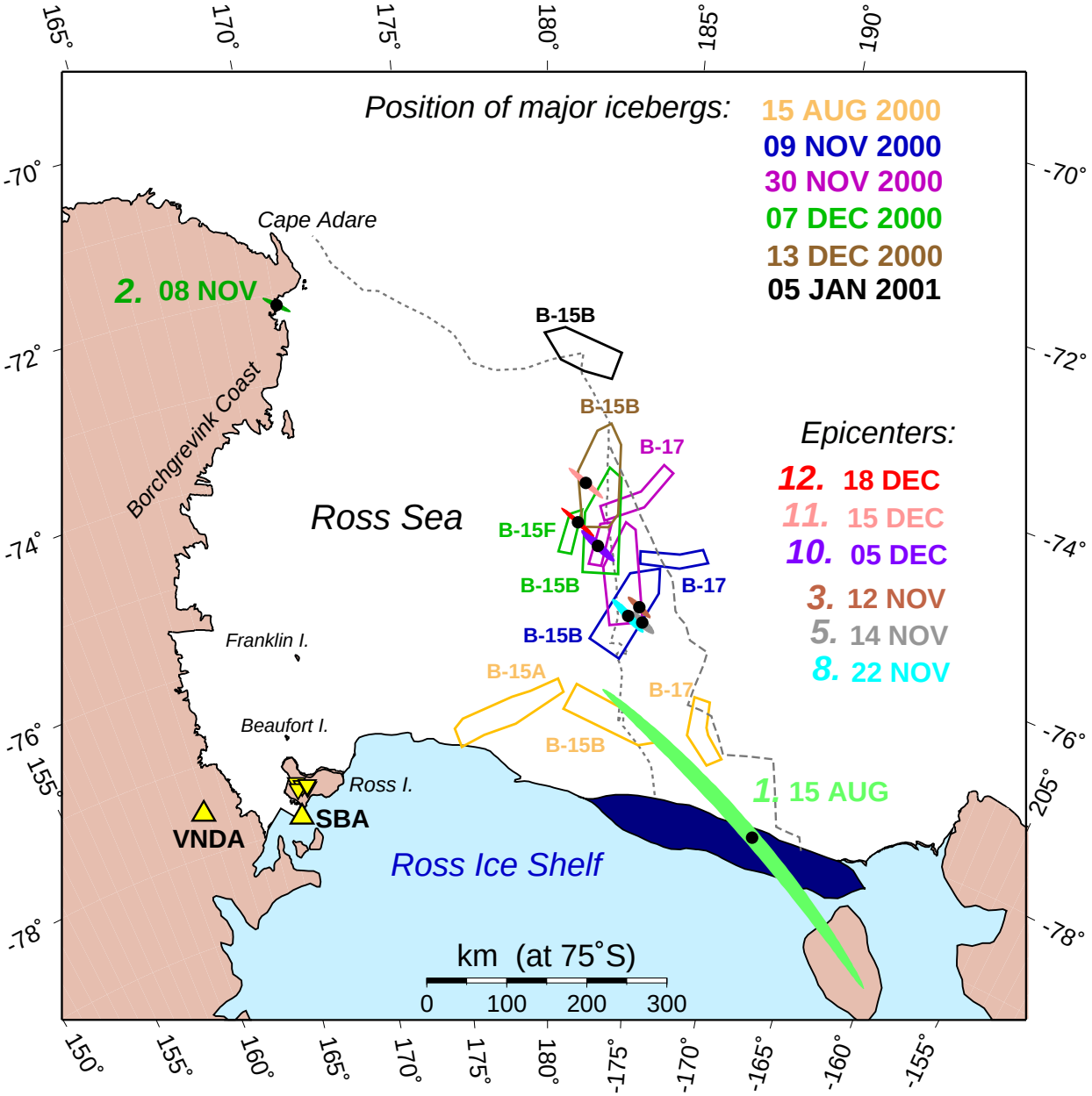

Figure 2. Final epicenters obtained by joint inversion of T-phase and seismic data. The individual epicenters are shown as black solid dots and the associated Monte Carlo ellipses are shaded (see color key at right; Event numbers in italics). The position of B-15 B is shown schematically at a number of dates from August 2000 to January 2001 (color-keyed; legend at top). Positions of the smaller iceberg B-17 are also shown at a few critical times until Late November 2000, when it breaks up into pieces following its collision with B-15 B. The paths of the two icebergs are also shown continuously by the dotted (B-15 B) and dashed (B-17) lines. The upward-pointing triangles show the global network seismic stations VNDA and SBA, the downward-pointing ones the MEVO network on Ross Island. The dark blue region schematizes the portion of the shelf which calved off and eventually gave rise to the B-15 and B-17 series. The projection is equidistant azimuthal centered at the South Pole.

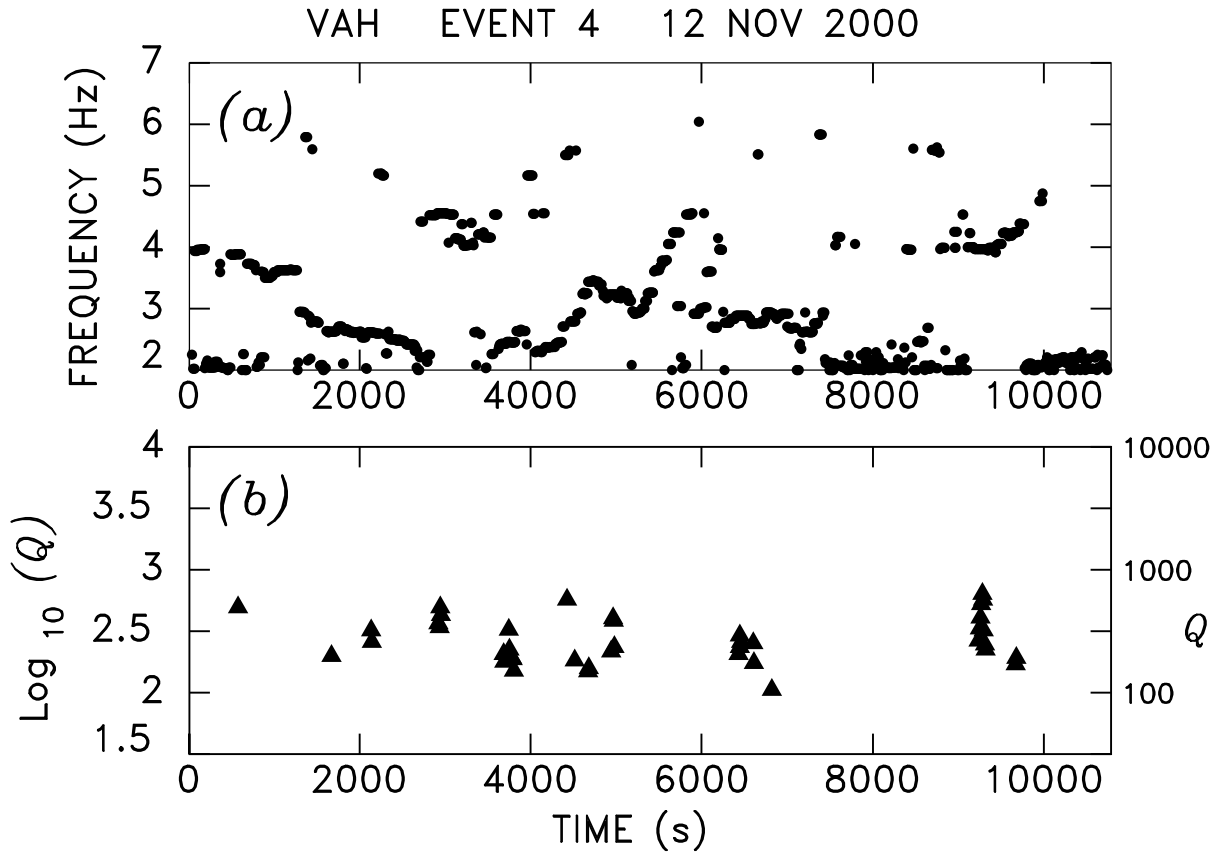

Figure 3. Evolution of spectral properties with time during Event 4. (a): Frequency f_0 at maximum of spectral amplitude. (b): Values of *Q* retained by application of quality thresholds.

ANALYSIS OF HYDROACOUSTIC SIGNALS IN THE INDIAN OCEAN

M. Tolstoy and D.R. Bohnenstiehl

Lamont-Doherty Earth Observatory, Columbia University

Sponsored by Defense Threat Reduction Agency

Contract No. DTRA01-01-C-0070

ABSTRACT

Hydroacoustic processing software developed over the past decade by National Oceanographic and Atmospheric Administration Pacific Marine Environmental Laboratory (NOAA/PMEL) has been modified to process CSS 3.0 format data from hydroacoustic stations within the Indian Ocean. This allows for the simultaneous inspection of multiple hydrophone channels, displaying trace amplitudes and spectrograms. When the hydroacoustic station at Crozet (H04) comes online in February 2003, this software package will allow events within the Indian Ocean Basin to be rapidly located solely on the basis of hydroacoustic arrivals, using a non-linear least squares algorithm that minimizes the differences between recorded and predicted T-wave arrives. Previous work in other ocean basins suggests that this approach will improve significantly our detection capability and location accuracy for Indian Ocean earthquakes. Given the final configuration of the Indian Ocean Hydroacoustic Network (stations H04, H08, H01), point-source simulations suggest location accuracy of ~2 km (68% level) within much of the array, assuming a random arrival error with normal distribution and standard deviation of 0.75 s for all channels. However, errors within the ocean sound velocity model and the width of the T-wave source region will decrease the accuracy of locations within the basin.

Commonly detected signals at the existing Diego Garcia (H08) and Cape Leeuwin (H01) hydrophones include a range of seismic phases (most commonly T, P and S), marine mammal vocalizations, ice-sheet movements, airguns and shipping noise, as well as other presently unidentified sounds that may be anthropogenic or natural in origin. Initial estimates of station noise levels indicate that Diego Garcia North is the quietest station, followed by Diego Garcia South and then Cape Leeuwin. When a full year's data have been analyzed, a catalog of annual noise variations will be merged with seismic and T-wave derived earthquake catalogs to examine the impact of noise on the hydrophones array's detection and location capabilities.

The natural seismicity within the ocean basin is used to map out areas of topographic blockage. The expected arrival time at individual hydrophones is calculated from Reviewed Event Bulletin (REB) events and each hydrophone is inspected for detectable T-waves. Based on the presence or absence of signals, regions of topographic blockage are mapped for the H01 and H08 hydrophones. Preliminary analysis of 2002 data indicates that >3.0 m_b events within the deep basin should be detectable on at least one hydrophone triad, given the final configuration of the network.

The incorporation of CSS 3.0 format data into the NOAA/PMEL processing suite improves synergy between hydroacoustic and seismic datasets. In the future, T-wave arrivals at island atoll stations (such as COCO, Keeling Island) could be used jointly with the hydrophone stations to locate events within an ocean sound velocity model.

OBJECTIVES

Hydroacoustic monitoring is a critical component of the Comprehensive Nuclear-Test-Ban Treaty (CTBT). It ensures that nuclear tests conducted in the ocean, or in the lower atmosphere directly above the ocean, do not go undetected. As such, it is essential that sub-oceanic earthquakes and other natural acoustic sources can be identified and subsequently ruled out as explosions. This requires a full characterization of the geological, biological and man-made noises generated within an ocean basin on a day-to-day basis. Characterizing the source and location of various signals provides an important framework by which to further improve our understanding of hydroacoustic wave propagation. Moreover, as the hydroacoustic network expands into new areas of geologic and anthropogenic complexity, prioritizing such work ensures the timely and efficient use of the network as a monitoring tool.

Given the limited number of hydroacoustic stations within the present International Monitoring System (IMS) that report to the International Data Centre (IDC), we also must assess the ability of land-based stations alone, or in conjunction with a limited number of hydrophones, to accurately detect and locate events within the oceans.

The research presented here represents a preliminary characterization and quantification of Indian Ocean acoustic sources, using existing IMS hydroacoustic stations (Figure 1). The routine location of events using hydroacoustic sensors alone will begin once the Crozet hydroacoustic station comes on line. Existing techniques for locating events using topographic reflections are too labor intensive to be used for all the many thousands of events occurring in the Indian Ocean basin each year. As part of this research we have adapted existing academic hydroacoustic analysis software to incorporate both hydroacoustic and seismic data from the IMS. This software will allow rapid location of small events when the Indian Ocean network is completed and currently provides an efficient platform for event characterization and quantification. This includes not only identifying the source origin and signal strength but also providing station specific topographic blockage and background noise information.

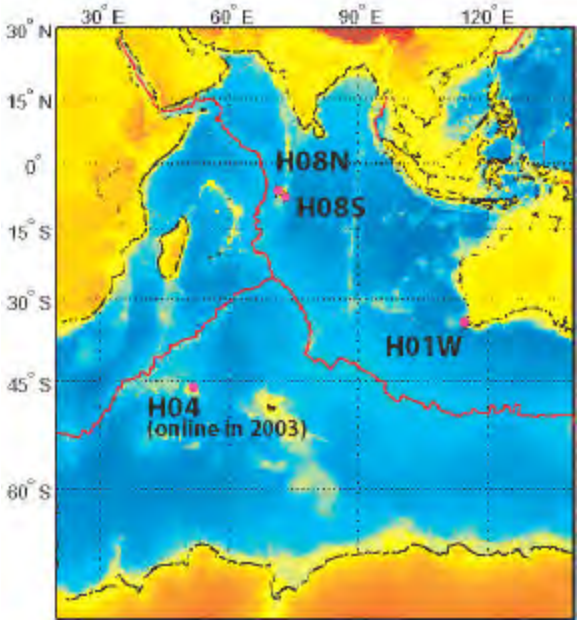

Figure 1. Location of IMS hydroacoustic stations in the Indian Ocean. Diego Garcia North & South (HO8N & HO8S) and Cape Leeuwin (HO1W) are currently operational. Crozet (H04) is expected to come on-line in February 2003. At each station there is a three-hydrophone array, or triad, with an instrument separation of ~2 km.

RESEARCH ACCOMPLISHED

Software

We have adapted the hydroacoustic analysis software developed at NOAA-PMEL (Fox et al., 2001) for use in the Indian Ocean. This work included the development of an Indian Ocean sound speed model (based on the Generalized Digital Environmental Model (GDEM) developed by the US Naval Oceanographic Office) and writing of conversion code to allow the CSS format data to be read directly into the software. The software allows data from different stations to be visually inspected, side by side, (Figure 2) and for events to be picked and located.

Based on the final configuration of the Indian Ocean Hydroacoustic Network (when the Crozet stations are operational), point-source simulations are used to predict the expected location errors. Figure 3 shows expected location error for events observed on at least three of the hydroacoustic stations (H-08S, H-01 & H04). The event location and magnitude is calculated based on an iterative, non-linear least squares method developed at NOAA-PMEL in which the sound is propagated through the ocean medium as represented by digital sound speed, in this case the GDEM model. A preliminary location and source time is used to predict arrival times at each sensor. The predicted time is compared to recorded arrival times, and the differences iteratively minimized using a Gradient-Expansion (Marquardt) algorithm, a least-squares method. Following the determination of the position and source time, statistics are calculated and a simple spherical and cylindrical propagation equation is used to estimate propagation loss for each path. This factor is applied to the peak recorded acoustic energy for each sensor and multiple independent estimates of the source strength calculated. The mean and variance of this estimate is saved (Fox *et al*. 2001). Based on the final configuration of the Indian Ocean Hydroacoustic Network (when the Crozet hydrophones are operational), point-source simulations are used to predict the expected location errors. Figure 3 shows expected location errors in kilometers for point-source events observed on at least three of the hydroacoustic stations (H-08S, H-01 & H04).

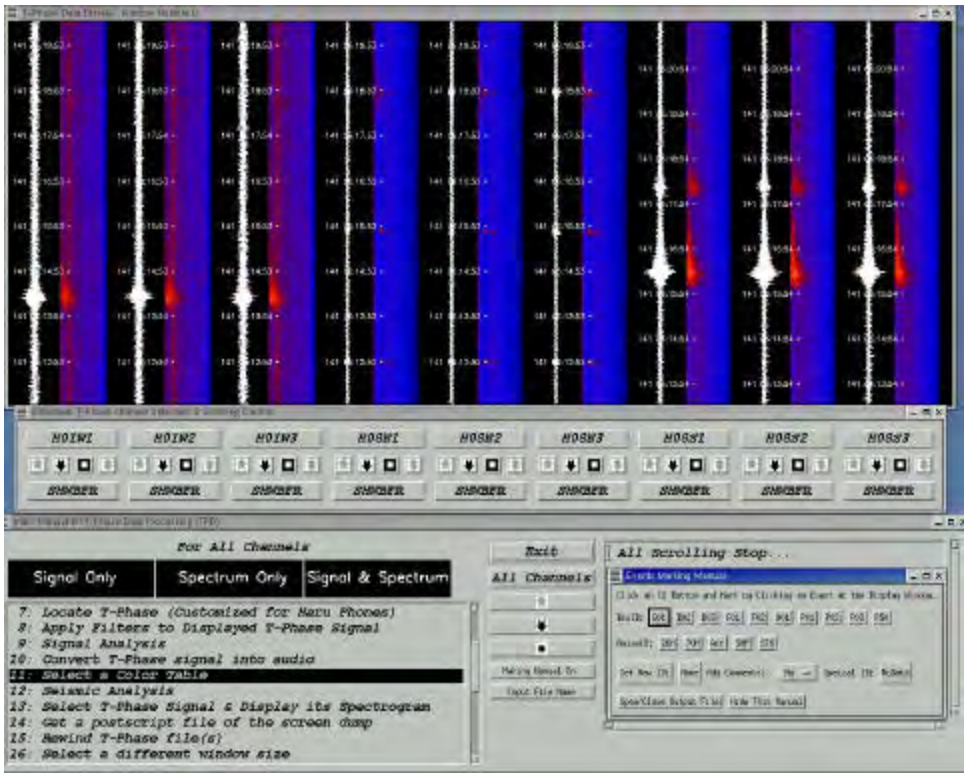

Figure 2. Example of software interface with data being simultaneously scrolled at all three hydroacoustic sites. Time increases on vertical axis, with trace amplitudes and 0-125 Hz spectrograms displayed.

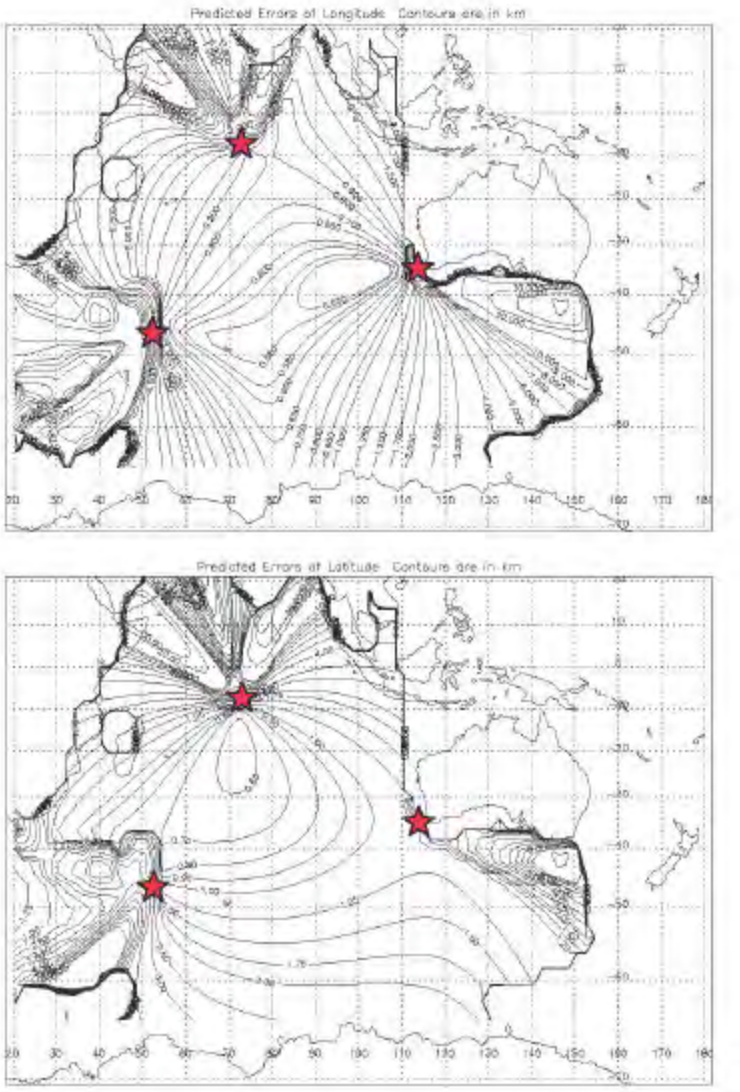

Figure 3. Predicted point-source location errors using an Indian Ocean sound speed model for the anticipated hydrophone configuration in February 2003 (see Figure 1). Location error estimates in latitude and longitude represent the 1σ (68%) confidence level and are given in kilometers. The error field was generated from Monte Carlo simulations of point sources and assumes arrival picks from six hydrophones (two at each triad, red stars). For each simulation the point-source location is prescribed and a random error with normal distribution and 0.75-s standard derivation is added to each arrival. The standard deviation of the picking error is based on calibrations within the Pacific (Fox *et al*., 2001). Location errors may be larger due to uncertainties in sound speeds along the path, which are not well known, and the width of the T-wave source region on the seafloor. However, similar to arrays in the Atlantic and Pacific Oceans, we expect to be able to calibrate the Indian Ocean array using known sources.

Synergy with land seismic data

The software development completed now allows data from land-based seismic stations to be scrolled simultaneously along side the hydroacoustic data (Figure 4). For stations near the coast, a simple time correction (to allow for the faster travel time of the crustal borne portion of the T-wave) would allow near shore stations to be used as additional T-wave monitoring sites, thus improving location accuracy.

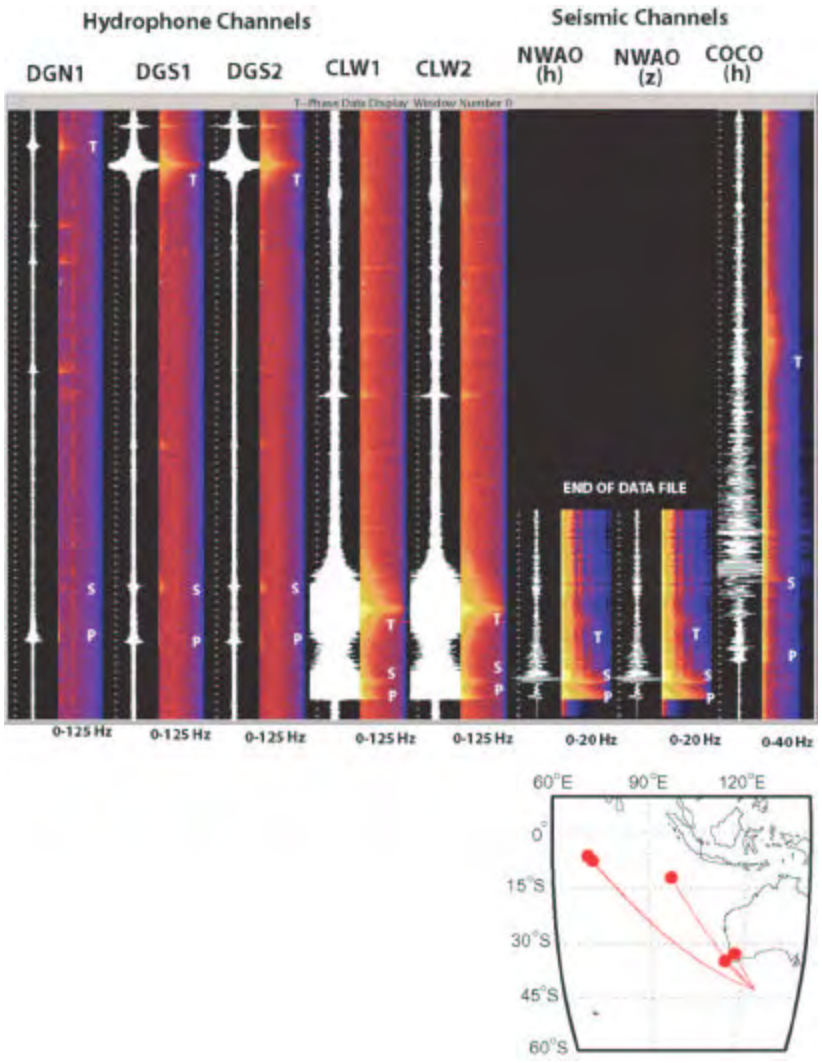

Figure 4. Example of arrivals from a large ocean basin event (7.1 Mw, JD 346, 2001) on hydrophones (HO8N, H08S & HO1W), and land seismic stations in southwestern Australia (NWAO) and Cocos/Keeling Island (COCO). Great circle paths are shown below. NWAO is ~200 km from the shelf where the T-wave would be converted into a crustal phase, so it is not ideal. However, the event was large enough that some T-wave related energy is still observed. Note it is about the same distance from the event as HOW1, and the P & S arrivals come in at the same time. The T-wave energy arrives earlier at NWAO, however, since it travels at faster crustal velocities for the last ~200 km of its path. The COCO station is located on a small island atoll, providing a short seismic path and excellent T-wave recording.

Event Characterization

Characterization of events is accomplished through visual inspection of the data, primarily in spectrogram form. Considerations in determining the event type include frequency content, duration, pattern through time, and relative amplitude if it is seen at both HO8 and HO1. While some signals are apparent in the waveform data, the spectrogram is much more informative, as seen in some of the examples below (Figure 5). Event characterization is important for a number of reasons. First, it is the initial step that must be taken before quantifying events and characterizing the 'typical' background signals in the Indian Ocean. Further, it will enable improved detection algorithms to be developed by establishing the amplitude and time/frequency range of various known signals.

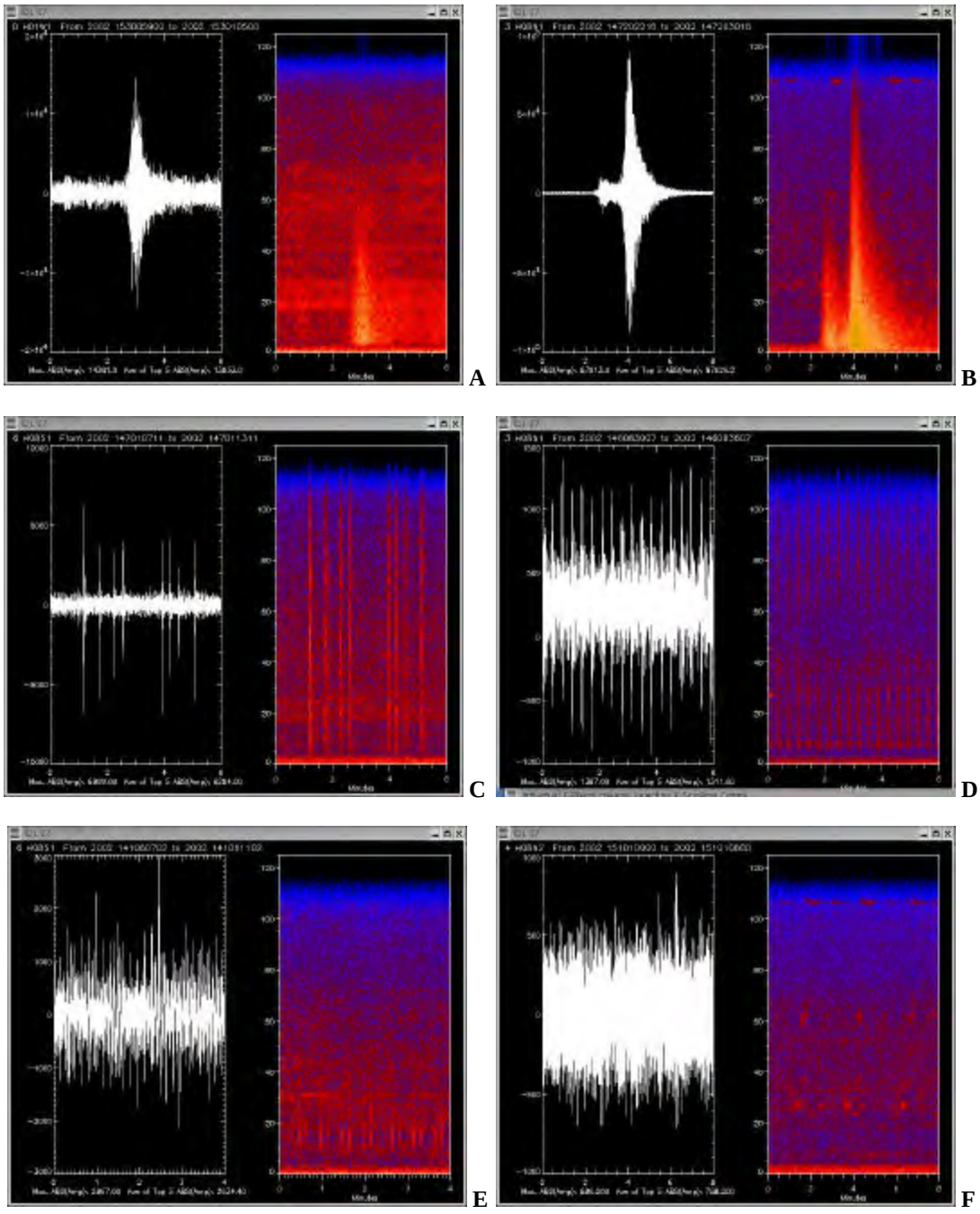

Figure 5: Examples of events observed regularly in the Indian Ocean. A) Typical T-wave arrival. B) P-wave arrival, followed by T-wave arrival. P-waves can be dis tinguished form T-waves by their more abrupt initiation. C) These 'spikes' look similar to airguns, but do not show the regular repeat intervals of airguns, and sometimes show up as individual spikes, without any indication of airgunning in the area before or after. These are of concern as possible explosive signals. D) Airgunning is frequently observed, but is easily distinguished from an explosion by its regular repeat interval (often 10 or 20 seconds). E) Fin Whale. F) Blue Whale.

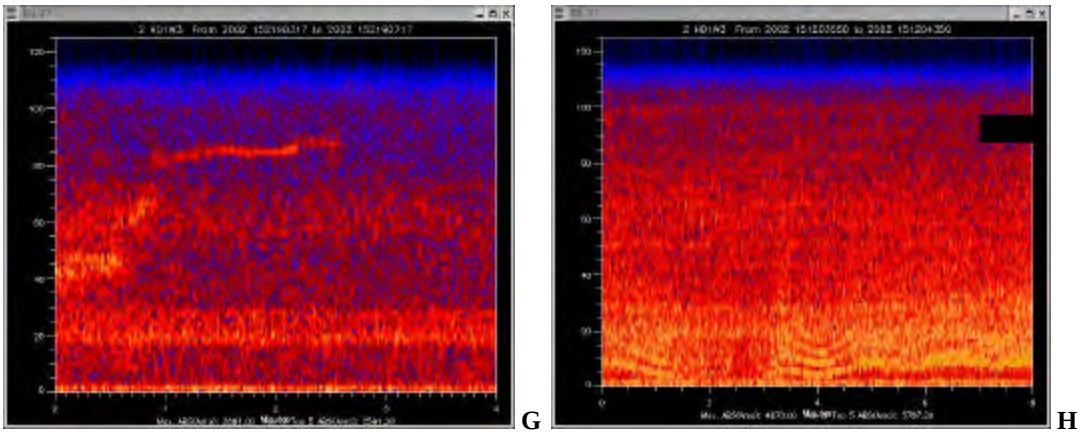

G **H**

Figure 5. (continued) Examples of events observed regularly in the Indian Ocean. G) This high-frequency 'screech' may be biological in origin (perhaps a whale call). H) These low-frequency signals consist of monochromatic bands that evolve, or undulate, through time. They are similar in nature to T-phase signals associated with the movement of icebergs off the Antarctic shelf, as described by Talandier et al. (2002) from island stations in Polynesia.

A quantification of some of these signals for one week can be found in Table 1. Note final column on Table 1 is described as 'sharp signals'. These refer to events similar to what is seen in Figure 5C, where there is a sharp signal that cannot be associated with airgunning or other obvious causes, and therefore may be explosive in origin. The number of events detected at any given station is likely to vary from week to week (or day to day as shown) depending on levels of local and regional seismicity, and seasonal variations in anthropogenic (shipping, airgunning) and natural (mammal vocalizations, ice movement) background noise sources. Such variation may impact our ability to detect and locate other signals.

This table represents the number of times each feature was identified in the hydrophone data. The P- and T-wave arrivals were marked every time an event was seen. The air guns were marked every hour making 24 the greatest number of events allowed in one day. The whale calls were marked each hour every time a unique signal was seen (i.e. one hour may be marked twice if different whale species were observed within that hour). Many individual whale calls lasts for over an hour and were marked for each hour in which they appeared.

Table 1. Event quantification for week of May 26th – June 1st 2002.

Day	T-Waves			P- and S-Waves			Air Guns (out of 24)			Whales			Sharp Signals		
	H01W	H08N	H08S	H01W	H08N	H08S	H01W	H08N	H08S	H01W	H08N	H08S	H01W	H08N	H08S
146	12	6	8	0	10	4	2	5	0	5	23	4	1	1	1
147	12	20	15	0	4	2	3	8	0	14	34	28	1	1	6
148	18	12	8	0	5	2	3	6	0	8	28	11	2	0	2
149	35	13	13	0	6	1	3	0	0	10	22	15	2	0	11
150	23	11	14	0	5	1	3	0	0	1	17	14	1	1	3
151	22	13	4	1	6	1	0	0	0	4	27	22	3	0	9
152	12	10	6	0	6	1	0	0	0	2	25	22	0	0	6
Total	135	85	68	1	42	12	14	19	0	44	176	116	10	3	38

Topographic Blockage

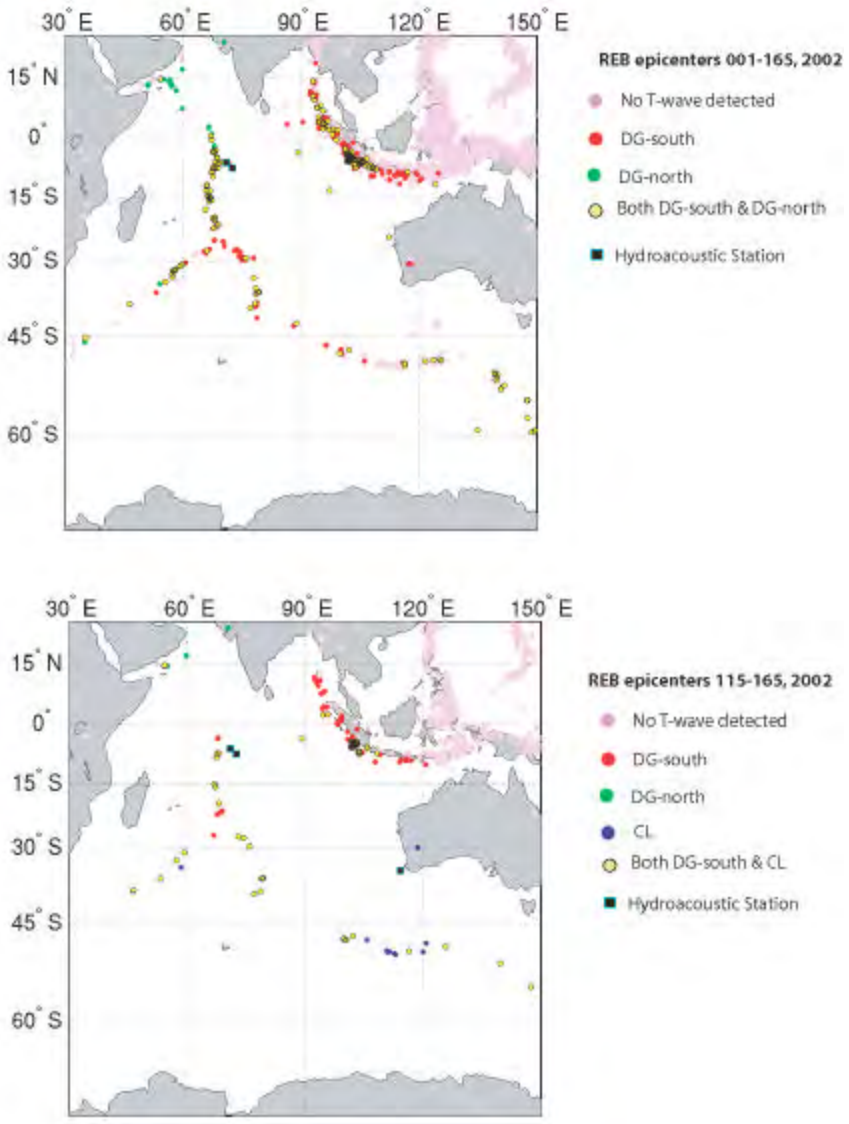

Figure 6. Locations of > 3.0 m_b events listed in the REB and observed at the Diego Garcia and Cape Leeuwin hydroacoustic stations. Top figure shows events for Julian days 1-165, 2002, for Diego Garcia stations only. Bottom figure shows events for Julian days 115-165, 2002, (CL arrival data become available through the REB on day 115) as observed on all three stations. Note that some events were observed at DG-North, as well as DG-South and CL, but are covered by the yellow symbols.

Predicted paths of topographic blockage can be modeled using seafloor bathymetry maps and station locations (e.g. Pulli and Upton, 2001); however, this is sometimes dependent on poorly known bathymetry and varies with event magnitude. Another approach is to examine the T-wave arrival records for known events, which were located using land station body wave arrivals (e.g. also Pulli and Upton, 2001). Below we present some initial results based on events observed in 2002. Figure 6 shows the events in the first 165 days of 2002 that were observed at Diego Garcia (HO8N & HO8S), as well as events that were observed at Cape Leeuwin (H01) and Diego Garcia from Julian days 115-165 (when Cape Leeuwin arrival data are available). These figures illustrate that there is reasonably good coverage to single stations within the Indian Ocean. Figure 7 indicates the raypaths for these hydroacoustically

detected events, and so provides a map of areas where complete blockage does not occur. However, there is also clear evidence that the magnitude of the event can impact degree of blockage. For example, in the top panel of Figure 5 there is a cluster of events at ~ 43S, 125E that are not observed at Diego Garcia South (HO8S). These events are aftershocks of a very large (Mw=7.1) earthquake in the same area in December 2001 that *was* observed at Diego Garcia South – (see Figure 4.). These much smaller magnitude events in early 2002 were not large enough to be detected above background noise at the H08, perhaps due in part to partial blockage associated with Broken Ridge (the elevated area running along ~32°S west of Cape Leeuwin).

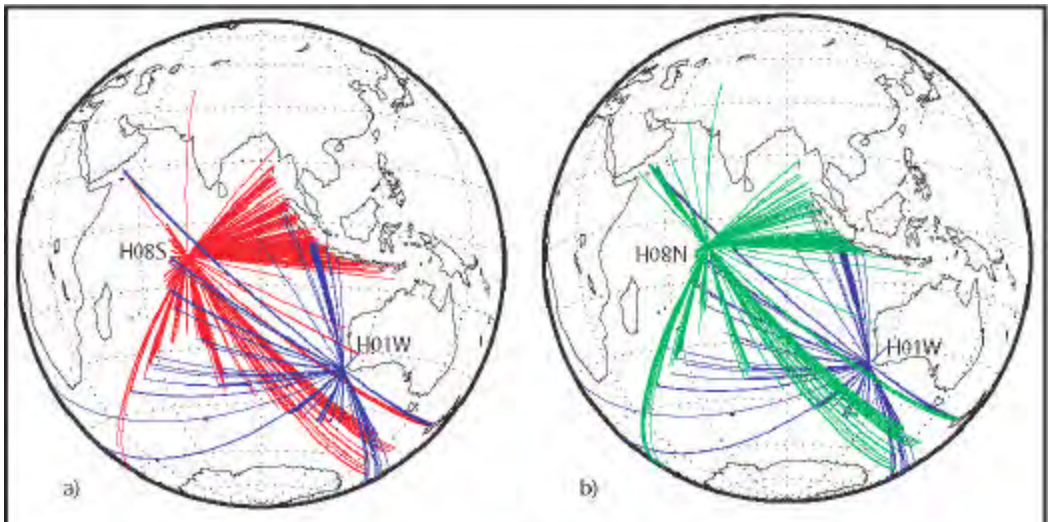

Figure 7. Epicenters (REB) to hydrophone paths for T-waves within the Indian Ocean Basin. a) Epicenter to H08S [Diego Garcia South] path in red and epicenter to H01W [Cape Leeuwin] path in blue. b) Epicenter to H08N [Diego Garcia North] path in green and epicenter to H01W [Cape Leeuwin] path in blue. H08N and H08S detects from 001-165, 2002. H01W detection from 115-165, 2002.

Background Noise

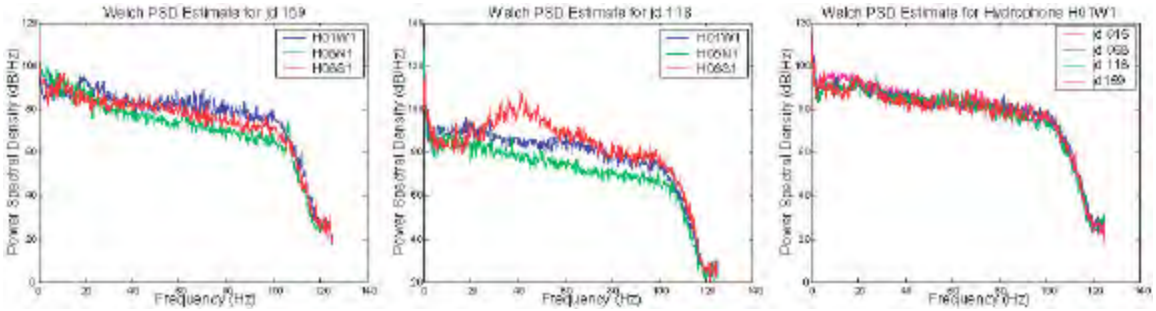

A **B** **C**

Figure 8. Daily noise spectra for HO8N, HO8S and HO1W. A) Spectra for Julian Day 159, 2002, at all three sites. B) Spectra for Julian Day 118, 2002, at all three sites. Note the influence of a particularly loud ship in HO8S (red). C) Spectra for various days from January 15th through June 8th at HO1W.

The background noise at hydrophone sites is controlled by a number of factors including proximity to shore (wave noise), weather variations and shipping in the area. The level of background noise is a critical factor in the ability of a station to observe specific events. As background noise increases, the detection sensitivity of the station decreases accordingly. Many noise sources are seasonal; therefore, it is important to characterize the noise for the full annual

spectrum. Previous work at Diego Garcia (Hanson, 2001) has shown that Diego Garcia North is quieter than Diego Garcia South, and that both sites show a slight decrease (~3db) in noise level between January and July. Figure 8a illustrates that in general Diego Garcia North is quieter than Diego Garcia South, and that both are quieter than Cape Leeuwin. However, Figure 8b shows that this can vary on a daily basis when unusual noise sources are present. Figure 8c shows a snapshot of Cape Leeuwin daily noise profiles at various dates from January through May 2002. No clear seasonal variation is apparent, but since daily noise variations are susceptible to local events, a more detailed look at more days is required before drawing any conclusions. Eventually daily, weekly and monthly averages will be provided when a full year's data has been delivered and analyzed.

CONCLUSIONS AND RECOMMENDATIONS

We have adapted existing hydroacoustic processing software to read the CSS 3.0 format. This allows hydroacoustic data from the presently available H08 (Diego Garcia) and H01 (Cape Leeuwin) stations to be examined by an analyst in an efficient manner, viewing both amplitude traces and spectrograms. These modifications also will facilitate increased synergy between seismic (island or near shore stations) and hydroacoustic data sets.

As data from the H04 (Crozet) hydrophones become available, earthquake events will be located solely on the basis of T-wave arrivals. Previous work and limited ground truth in other ocean basins suggests this approach will improve significantly our ability to detect and locate moderate size earthquakes and other hydroacoustic signals.

Using the data presently available from H08 and H01, we have begun an effort to characterize and catalog sound sources within the Indian Ocean Basin. These include seismic phases, marine mammal vocalizations, airguns and possible ice-sheet movements. Initial noise estimates indicate that Diego Garcia South appears to be the quietest triad, followed by Diego Garcia North and then Cape Leeuwin.

Initial blockage results indicate good spatial coverage of much of the Indian Ocean by at least one hydrophone.

ACKNOWLEDGEMENTS

We thank E. Chapp for assistance in figure preparation and the analysis of these data. The NOAA/PMEL hydroacoustic software was developed over the course of many years by C. Fox, A. Lau, A. Schreiner and R. Dziak, and funded through the NOAA vents program.

REFERENCES

Fox, C.G., H. Matsumoto, and T.-K. Lau (2001), Monitoring Pacific Ocean Seismicity from an Autonomous Hydrophone Array, *J. Geophys. Res.*, **106**, 4183-4206, 2001.

Pulli, J.J., and Z.M. Upton (2001), Hydroacoustic Blockage at Diego Garcia: Models and Observations, *Proceedings of the 23rd Seismic Research Review*, Vol. II, 45-54.

Hanson, J.A. (2001), Initial Analysis of Data from the New Diego Garcia Hydroacoustic Station, *Proceedings of the 23rd Seismic Research Review*, Vol. II, 12-22.

Talandier, J., P.-F. Piserchia and E.A. Okal (2002), Hydroacoustic signals detected in Polynesia from mega-iceberg drifting in the Ross Sea, Antarctica, *abstract, annual meeting SSA, Seismological Research Letters,* **73**, 217.

LOCALIZATION OF SUB-SEA EARTHQUAKES USING HYDROACOUSTIC REFLECTIONS AND MATCHED-FIELD PROCESSING

Zachary M. Upton and Jay J. Pulli

BBN Technologies

Sponsored by National Nuclear Security Administration
Office of Nonproliferation Research and Engineering
Office of Defense Nuclear Nonproliferation

Contract No. DE-AC03-02SF22560

ABSTRACT

The purpose of this study is to investigate the localization of long-range hydroacoustic events, such as sub-sea earthquakes and underwater explosions, received at a single monitoring station. A matched-field technique is used to predict synthetic waveforms that would be received at a hydroacoustic station for a given source location. A grid of potential source locations is selected based on the areas of natural seismicity defined by the mid-ocean ridges in the Indian Ocean and the subduction zones to the east (Carlsberg Ridge, Mid-Indian Ridge, Southeast & Southwest Indian Ocean Ridges, and Java Trench). This matched-field technique makes use of a previously designed propagation model (Pulli, *et al*, 2000) along with a detailed knowledge of bathymetry to predict arrivals at the receiver including reflections from bathymetric features. An earthquake detected at the Diego Garcia hydroacoustic station in the Indian Ocean, for which bathymetric reflectors have already been identified (Harben and Boro, 2001), is used to validate the synthetic waveform algorithm. Earthquakes in the Indian Ocean are then localized using the matched-field algorithm and signals recorded at Diego Garcia. These localizations are used to study the sensitivity of the matched-field algorithm. This research shows that hydroacoustic events can be localized using data from single stations if reflections from bathymetric features are included.

OBJECTIVE

The objective of this research is to assess the feasibility of using matched-field techniques to localize sub-sea earthquakes and underwater explosions using a single monitoring station and hydroacoustic reflections. Previous research has shown that reflected arrivals from an explosion or earthquake can be predicted for a given source-receiver pair. This study seeks to extend that work by creating a field of modeled waveforms and comparing them to the measured waveform using matched-field techniques.

The value of single station localization using hydroacoustic reflections is that it has the potential to extend the detection and localization coverage of the International Monitoring System (IMS) hydroacoustic network. Acoustic energy from a strategically placed explosion might have a direct acoustic path to only one IMS station. Worse, the energy might have no direct acoustic path. However, if reflections can be used as a basis for detection and/or localization, areas that were once not covered by the IMS hydroacoustic network could be considered within its coverage.

RESEARCH ACCOMPLISHED

Validation of reflector model in the Indian Ocean

The first step in this study was to validate past research on reflections for use in the Indian Ocean. Pulli, *et. al*. (2000) designed a model that, for a given source-receiver pair, calculated potential bathymetric reflectors in an ocean basin. The model used these potential reflectors to form the impulse response of the ocean basin. By convolving this impulse response with a synthetic source function, the model was able to predict a received waveform envelope based on the direct arrival and bathymetric reflections. Pulli *et. al*. (2000) then used this model to predict waveforms received at stations in the Atlantic and Pacific Oceans.

The Indian Ocean is chosen as the ocean basin for this study because of the IMS station HA08 located near Diego Garcia. This station not only provides a consistent, reliable source of hydroacoustic data, but it is the first IMS hydroacoustic station to begin to transmit data to the International Data Centre (Vienna, Austria) and Prototype International Data Center (Virginia, USA). Earthquakes regularly occur in the Indian Ocean and are a good source of acoustic information. Analyses of the signals from some of these earthquakes show what appear to be reflected arrivals (Harben and Boro, (2001); Hansen (2001).

In a paper written in 2001, Harben and Boro study a magnitude 6.8 earthquake that occurred January 18, 2000, near Jawa, Indonesia. Figure 1 is a map depicting the location of this earthquake, determined using seismic techniques, with respect to the Diego Garcia IMS station. The waveform envelope of this earthquake, recorded on the north array at Diego Garcia, is shown in the top graph of Figure 2. To validate the reflections model for use in the Indian Ocean, the model was run using the origin of the earthquake as the source location and a nominal, centralized location for the northern array of the Diego Garcia IMS station as the receiver position. The bottom graph in Figure 2 shows the synthetic waveform result of the model calculations.

Note that the major reflections at approximately 55 minutes and 59 minutes are identified by the synthetic waveform. Harben and Boro identify a reflector at the Seychelles/Mauritius Plateau that corresponds to the reflections at approximately 55 minutes. There is a peak in the envelope that is not in the replica waveform (at ~42 minutes). This peak could be the result of some non-reflected energy, like a low-level aftershock. It could also simply be a deficiency in the model that caused the discrepancy between the real and synthesized waveforms. These results are comparable to those in the Atlantic and Pacific Oceans, and therefore validate the use of the reflections model, and its resulting synthetic waveforms, in the Indian Ocean Basin.

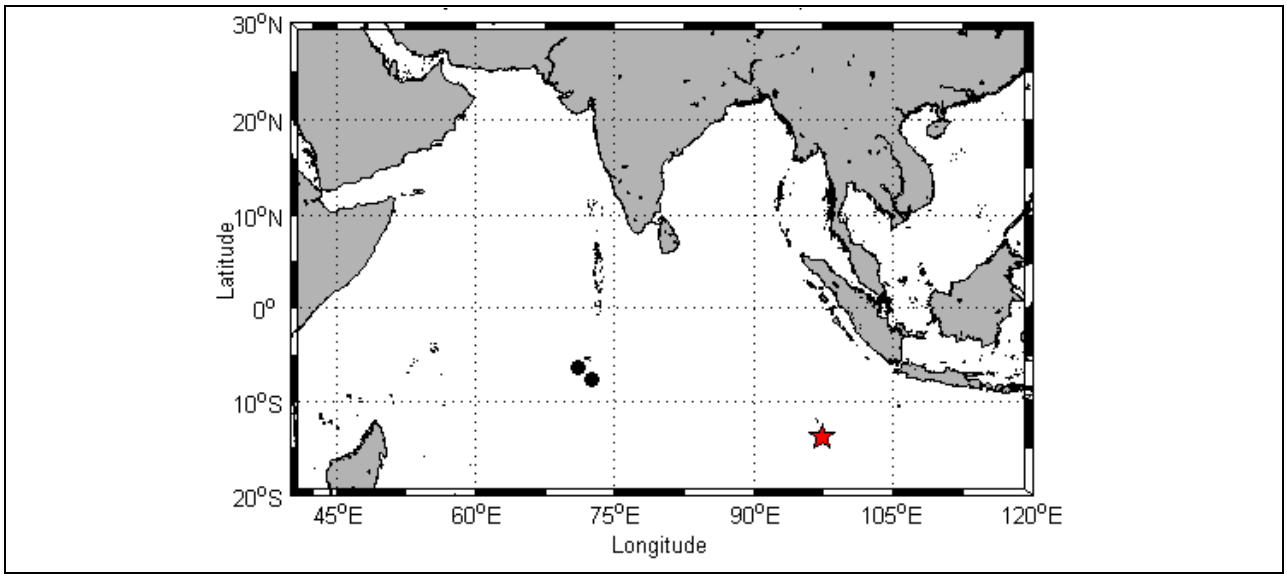

Figure 1. Location of the January 18, 2001, earthquake near Jawa, Indonesia (red star). The Diego Garcia IMS station is also shown in black circles.

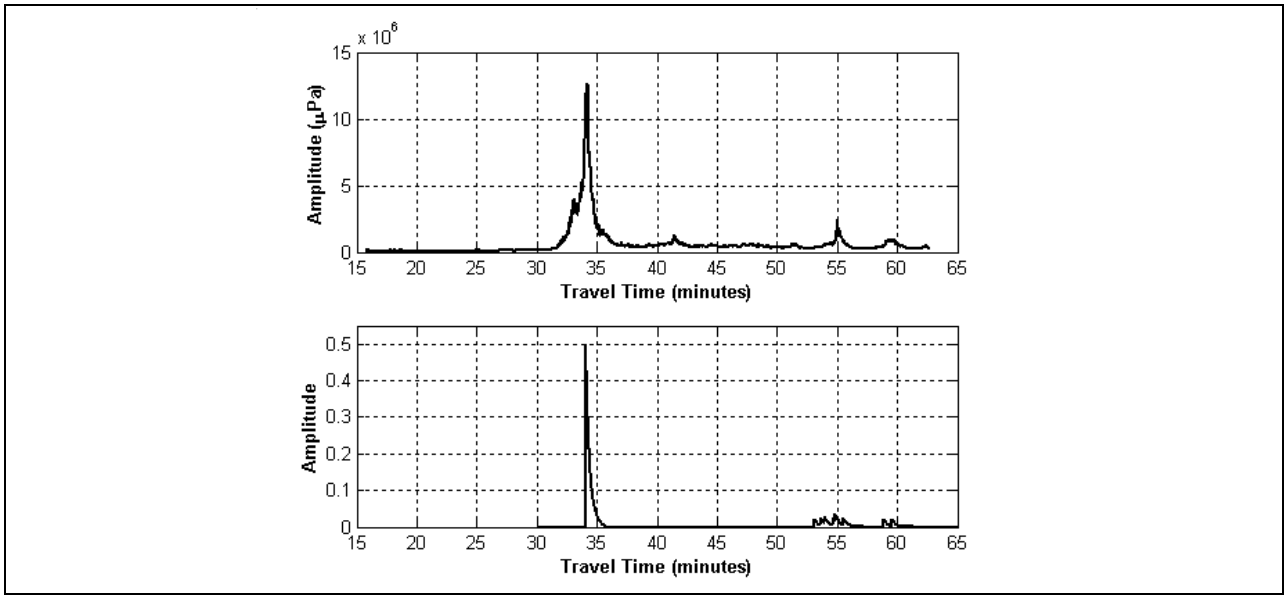

Figure 2. Real received waveform envelope from Diego Garcia North (top) and the output of the reflections model, the synthetic waveform (bottom).

Indian Ocean seismicity grid

The first step in the matched-field localization process was to generate a geographically disparate set of source locations. To attempt matched-field localization on an ocean-size scale, one might begin with a coarse grid of the entire ocean. However, time, measured data, and computer processing power were limiting factors in this research. There are no available recordings of explosions in the Indian Ocean. However, there are recordings of earthquakes. These earthquakes occur in a relatively limited number of geographic areas under the ocean (i.e. along mid-ocean ridges). Earthquakes, therefore, are an excellent source to test the methodology.

To minimize the time and processing power spent calculating synthetic waveforms, a series of source locations was selected that roughly matched the areas of peak seismic activity in the Indian Ocean. Figure 3 shows the map of

seismic activity in the Indian Ocean for 2000 and 2001 at left and the matched-field replica locations at right. The reflections model was used to create synthetic waveforms for each replica location.

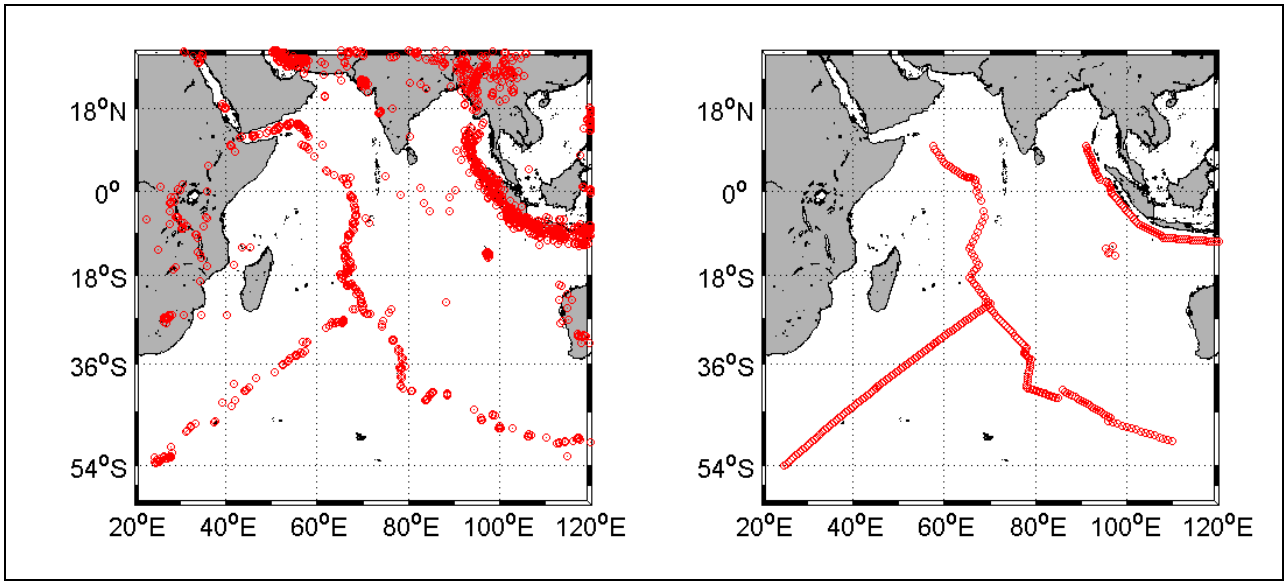

Figure 3. Map of seismic event locations for 2000-2001 (United States Geological Survey) at left, matched field replica locations at right.

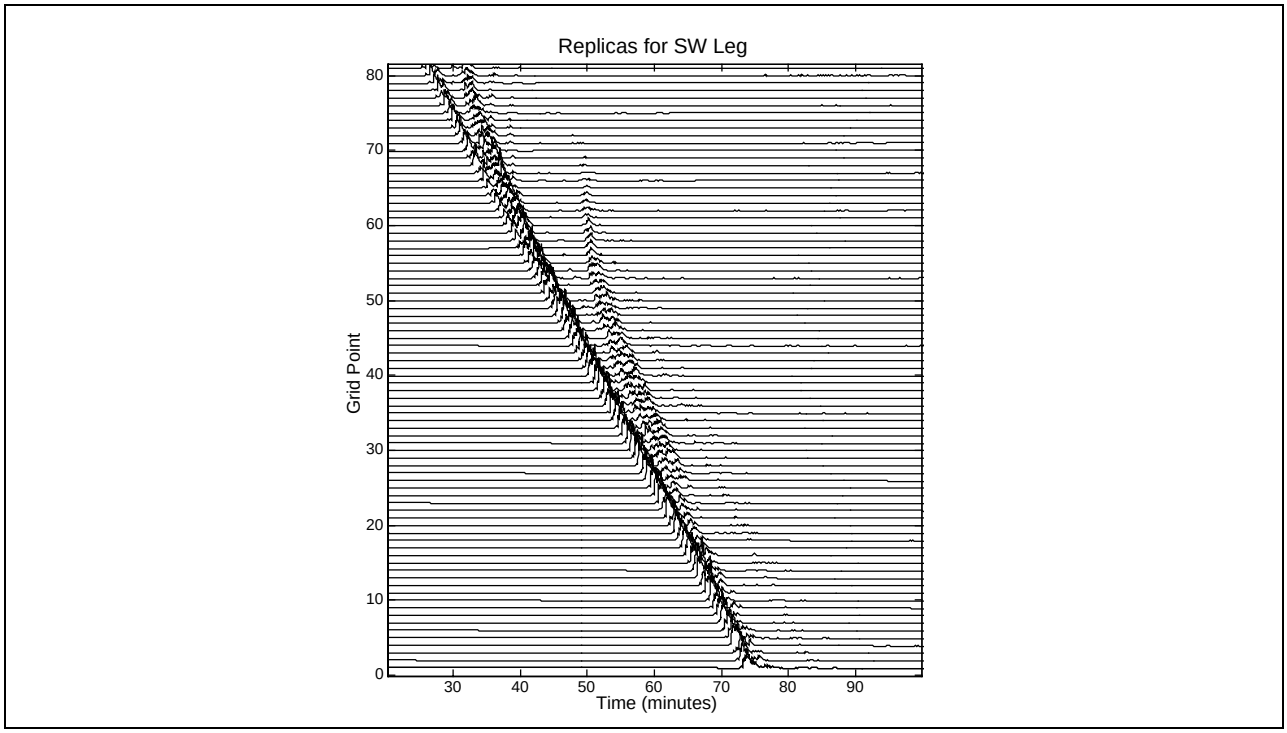

Figure 4. Synthetic waveforms for the Southwest leg of the source replica locations.

Localization Algorithm

A matched-field algorithm was developed to efficiently and effectively localize the earthquake signals and to display the results in a manner that was easily understood. Comparing 300+ replicas to over an hour of signal could be a very time consuming task. Since the only parts of the waveform that are of interest in the localization are the direct

and reflected arrivals, it makes sense to only correlate around them and not over the entire waveform. The real measured envelope is analyzed first. A noise estimate is calculated in 5-sec windows across the envelope. Since the noise estimate is only to be used as a basis for thresholding, it need not be terribly precise. Therefore, in each 5-sec window after the direct arrival time, the slope of the envelope is calculated using the beginning and end samples. Windows that have a slope greater than a prescribed maximum slope are considered signal. Windows with a slope less than a prescribed maximum slope are considered noise. An average value of noise is calculated within each of the noise windows. To detect the direct and reflected arrivals, a threshold is set above the calculated noise estimate. The points at which the waveform is above the threshold are considered direct or reflected arrivals and the rest of the waveform is set to zero. Figure 5 shows an example of the result of the noise estimate and detection. The top graph shows the original waveform. The bottom graph shows the detections in the thresholded waveform. These arrivals are found using a threshold of 6 dB above the noise estimate.

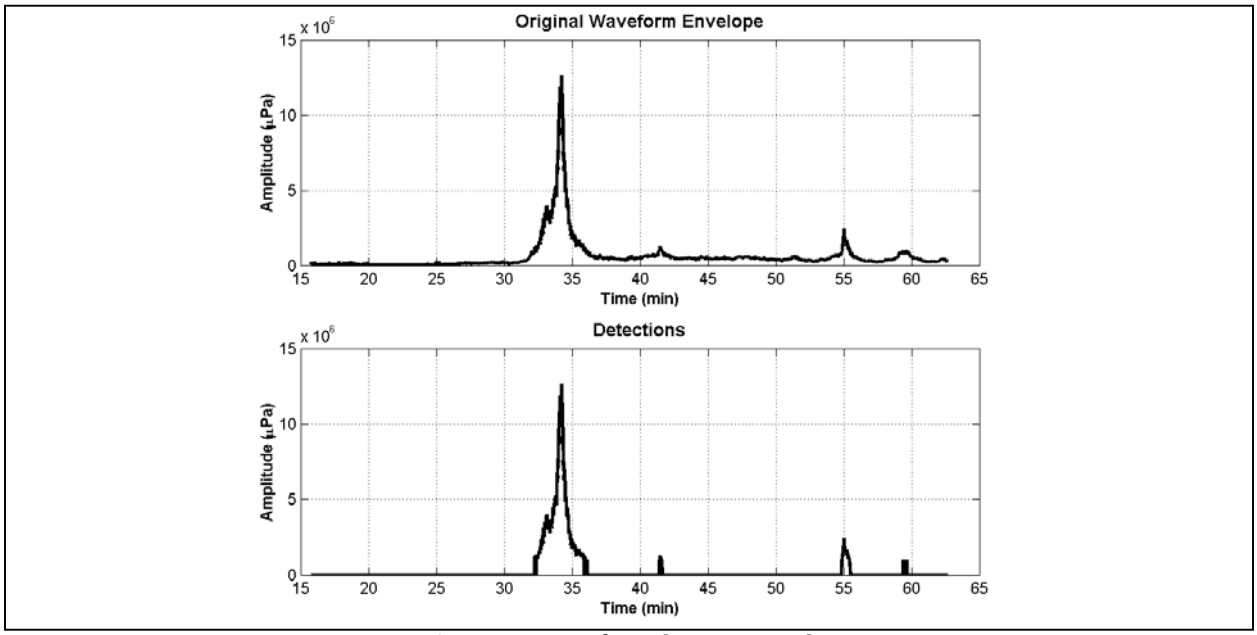

Figure 5. Waveform detection results.

To complete the matched-field localization, the replica waveforms are correlated with this thresholded waveform. However, in this instance and many others, the direct arrival is much stronger than the reflected ones. Each detection area (in time) is normalized by dividing by its maximum to consider the direct and reflected arrivals equally. This operation is performed on both the measured and the replica waveforms.

For the last piece of pre-processing before the actual localization, it is necessary to make sure that the direct arrival in the thresholded waveform would be correlated with the first arrival in the replica waveforms. This eliminates any large correlation between the direct arrival of the thresholded waveform and a reflected arrival in a replica. To achieve this goal, the replica is tested. If the time of the first arrival in the replica does not match the first arrival in the real waveform, the replica is set to zero around the time of the real direct arrival, thus eliminating the chance of any undesired high correlation. Reflected arrivals are correlated simply by their occurrence in time.

To correlate multiple replicas with the thresholded waveform, a loop is set up that cross-correlates the replica waveforms with the raw waveform during the detection time periods. Cross-correlations are performed in 5-sec windows. A replica waveform that is a strong match to the raw waveform in a particular time window has a high cross-correlation at the zero lag time. To determine the relative localization strength of a particular replica waveform, the zero-lag correlation is summed over the correlated waveform segments. Therefore, the replica with the highest summed zero-lag correlation over the direct and reflected arrivals is the strongest localization.

Display of results

Typically, matched-field localization results are displayed as ambiguity surfaces that allow the viewer to pick the most likely localization (for example, in range and azimuth). However, in this case, the potential source positions are located on an irregular grid over the areas of frequent seismicity in the Indian Ocean. The results of the localization are displayed on a map similar to that of Figure 3. However, in this case, the source locations are color-coded by their respective summed zero-lag correlation, with the blue end of the color spectrum being low correlation level and the red end being high correlation level. In this way an ambiguity 'line' is formed analogous to the traditional ambiguity surface. Jensen, *et al* (1994) provide more information on ambiguity surfaces.

Localization Case 1 – The January 18, 2000, Jawa, Indonesia, earthquake revisited

The localization algorithm was tested first using the Jawa, Indonesia, earthquake described in Harben and Boro, 2001. A map of the seismic (United States Geological Survey -- USGS) location of the earthquake was shown in Figure 1. The waveform envelope of this earthquake was shown in Figure 2. The detections have already been shown in Figure 2. The output of the localization algorithm is shown in Figure 6. The results displayed in Figure 6 show that the strongest localization strength, or the highest overall correlation occurred at the only red dot on the map. Table 1 is a comparison between the ground truth of the earthquake and the calculated location.

Table 1. Ground Truth Location vs. Calculated Location – Jawa, Indonesia, Earthquake

Location Type	Latitude	Longitude
Ground Truth Source Location (USGS)	13.802S	97.453E
Calculated Location	13.80S	97.45E

The results of this localization demonstrate that, when there is a grid point in close proximity to the event location, this algorithm can localize the event accurately. The distance between the ground truth location and the calculated location is 0.4 km. What is interesting in this result is that there is only one point in the area whose relative correlation level comes near that of the calculated location. Its correlation level, however, is only about two-thirds of that of the localization point. Therefore, based on only the initial test, the algorithm is fairly sensitive to location.

Figure 7 compares the replica waveform at the calculated location with the replica at the point that is nearest to it. These waveforms illustrate the difference in response that occurs with changes in location. The two points are 150 km apart.

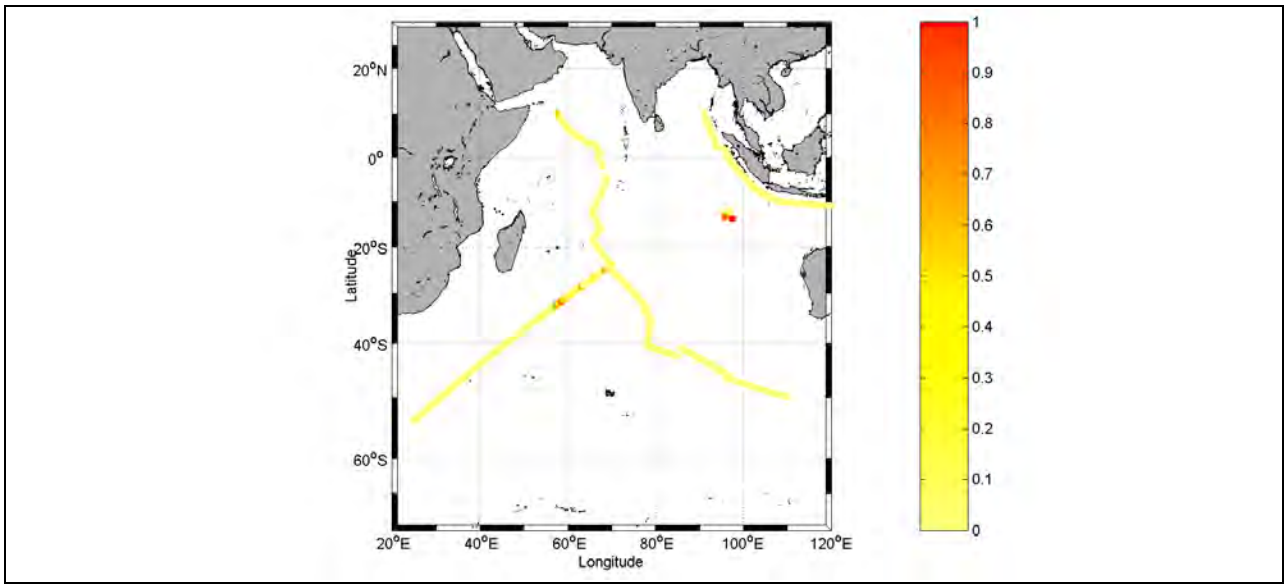

Figure 6. Visualization of the localization of the January 18, 2000, earthquake near Jawa, Indonesia.

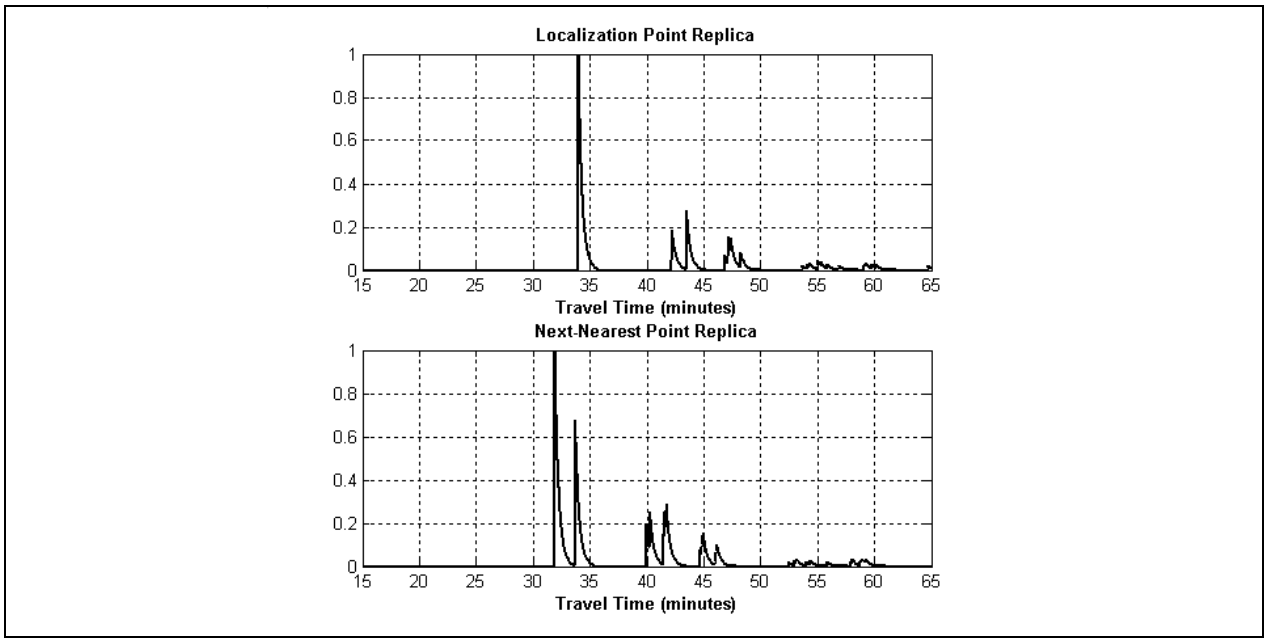

Figure 7. Comparison of the localization point replica with the next-nearest (geographically) replica.

Localization Case 2 – The April 19, 2001, Mid-Indian Ridge Earthquake

This 4.5-m_b earthquake is another event that exhibits direct and reflected arrivals suitable for study and attempted localization. The earthquake's ground-truth location and its relationship to Diego Garcia are shown in Figure 8. In contrast to the first case, there is not a replica source point within 50 km of the actual event location. The mid-ocean ridges are wide in comparison to the discrete grid of replica source locations, and this earthquake occurred away from the grid.

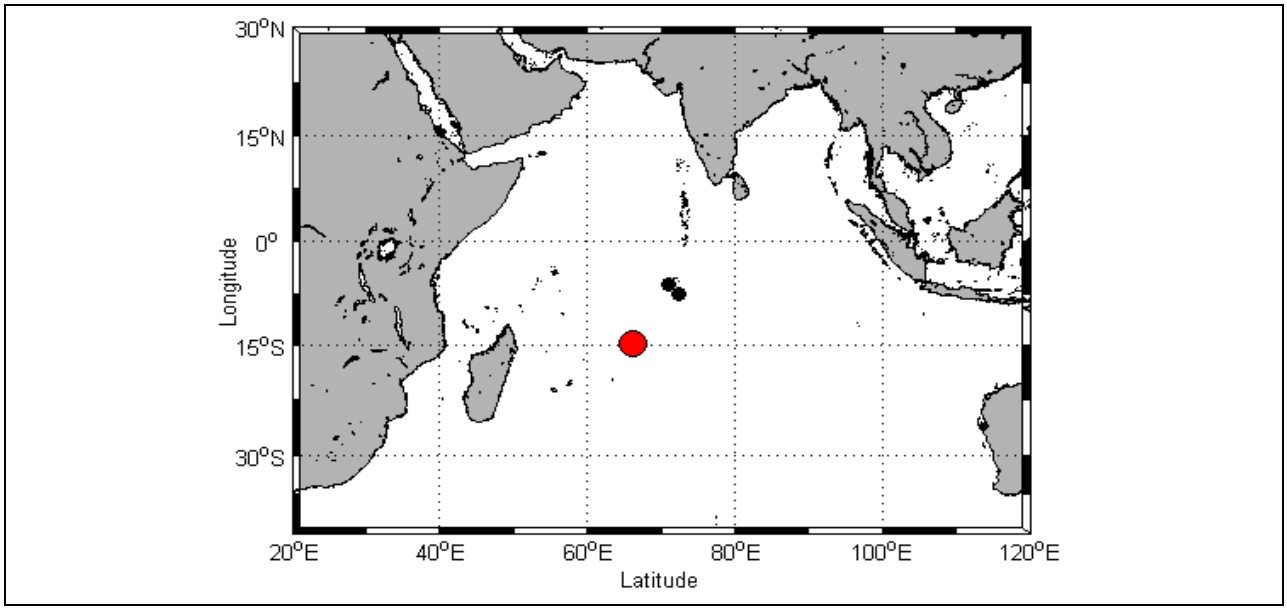

Figure 8. Location of the April 19, 2001, Mid-Indian Ridge Earthquake (red dot) and the Diego Garcia IMS Stations (black dots).

The earthquake's signal envelope, as recorded at the northern Diego Garcia array, is shown in Figure 9. The direct arrival (at ~12 minutes) and the reflected arrivals at 27 and 30 minutes, respectively, are immediately apparent. The localization algorithm output is shown in Figure 10. The comparison between the ground truth location and computed location is shown in Table 2.

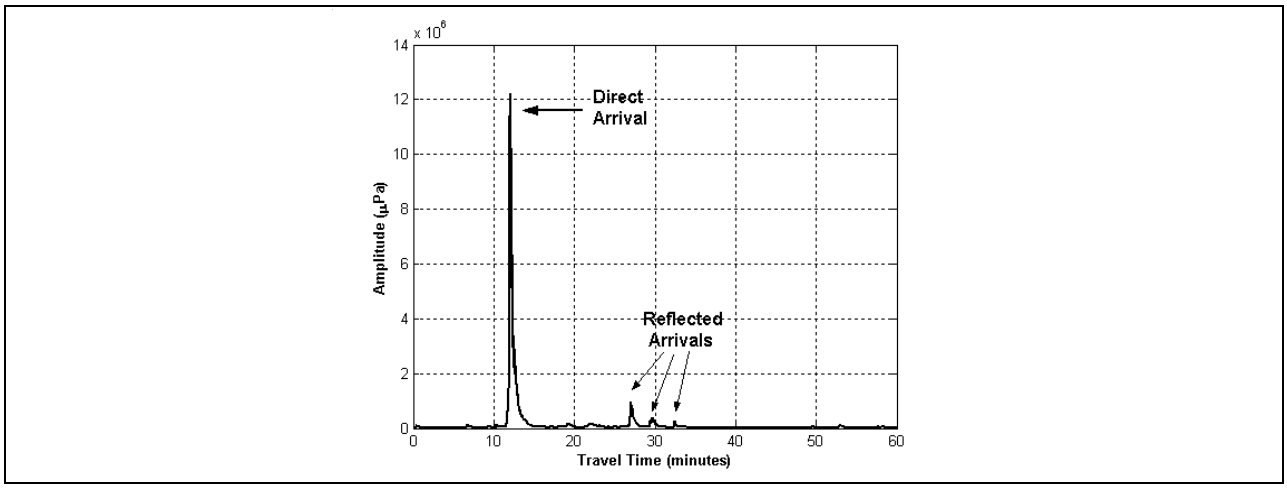

Figure 9. Waveform envelope of the April 19, 2001, Mid-Indian Ridge Earthquake as recorded at DGN.

Table 2. Ground truth location vs. localization location – Mid-Indian Ridge Earthquake

Location Type	Latitude	Longitude
Ground Truth Source Location (USGS)	14.63S	66.21E
Localization Location (Northernmost)	15.13S	67E
Localization Location (Southernmost)	23.67S	69.5E

The analysis of this localization is somewhat more difficult than the first event. The localization output shows two red boxes of nearly equal relative localization strength. The northernmost red box is near the earthquake location (101 km). The southern localization is much further from the earthquake location (1058 km).

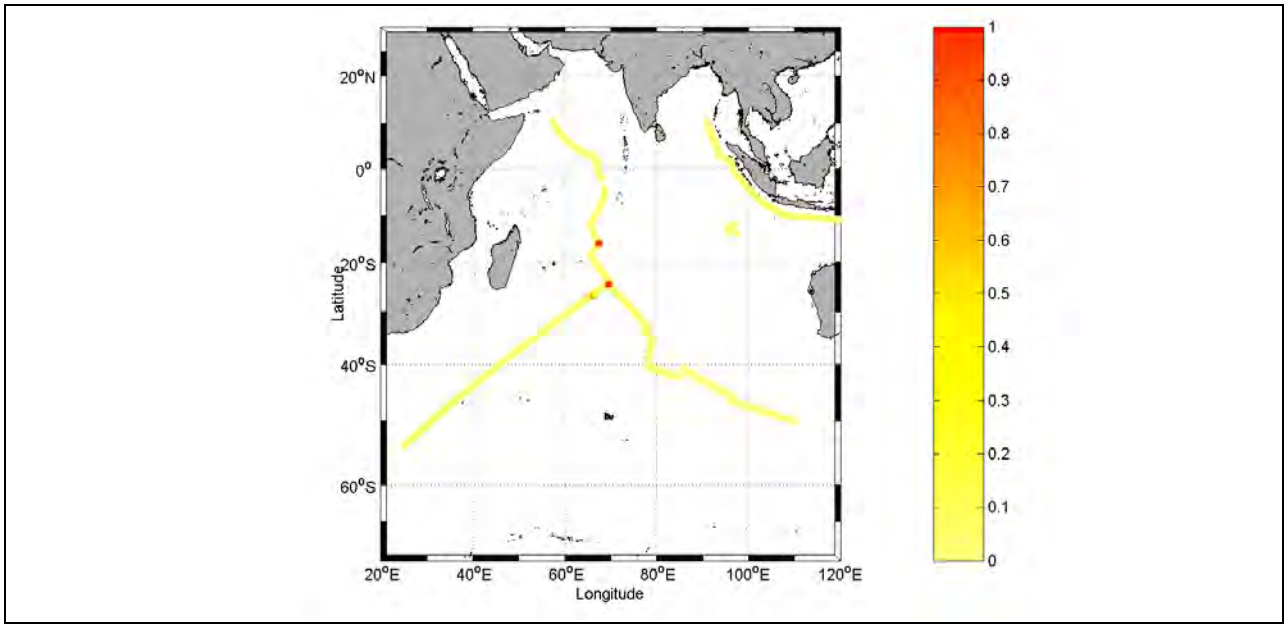

Figure 10 . Localization Algorithm Output.

Many factors could contribute to this result. First, there is not a grid point in close proximity to the earthquake. In the first example, it was shown that the algorithm is very sensitive to location. For an earthquake localization in which the event location does have a corresponding grid point, the surrounding points could be much weaker in correlation level. Therefore, the fact that the localization algorithm produced two localizations in this case is not a surprise. Second, the localization algorithm, as designed, eliminates the amplitude discrimination capability of the cross-correlation function. By normalizing all the arrivals (direct and reflected) by their respective maximum value, the direct and reflected arrivals were weighted equally in terms of the correlation. However, in doing so, the relative strength of the arrivals is masked, since each arrival will have a peak value of one.

CONCLUSIONS AND RECCOMENDATIONS

In this study, it has been shown that long-range hydroacoustic reflections can be used as a basis for the creation of replica waveforms, at a specific receiver location, for a geographically disparate set of source locations. It has also been shown that these replica waveforms can be used in a matched-field localization algorithm to determine the source location of an acoustic signal.

The localization algorithm exhibited sensitivity to the location of the replica positions. If there was a grid point near the event location, the event could be accurately localized. Also, nearby grid points did not exhibit spurious high localization strengths that might damage the accuracy of localization. However, in the case of an event that did not have a nearby replica grid point, the algorithm produced a dual localization. One of these localizations was a true localization, in that the grid point selected was near the event location. However, the other localization point was over 1000 km away from the event location. The two results, though very different, yield some similar conclusions. This algorithm is capable of localizing sources on an ocean-basin-sized scale. However, for the algorithm to make accurate localizations anywhere in the ocean, the grid of potential source locations would have to be fairly dense. The density of the grid, in fact, would probably have to be correlated to the desired localization accuracy.

Though the results of this study are very encouraging, there are many areas of research that could improve the capability of localizing events using long-range hydroacoustic reflections. The most obvious is to extend the calculations here to a grid of an entire ocean. A whole-ocean case would validate this method for use in the IMS. The localization algorithm and reflections models exhibit a few weaknesses that are worthy of further study. For instance, the localization algorithm deliberately eliminates the amplitude discrimination power of cross-correlation. A limited amount of change to the pre-correlation processing could allow the localization algorithm to take full advantage of this characteristic.

A brief list of other possible future study areas follows:

- A study of reflector strength calculations. In the current synthetic waveform model, the amplitudes of the arrivals do not match well to the data. Including a better calculation of reflector area or a better impulse response weighting function might improve the match between synthetic and reflected data.
- A study on the use of higher resolution bathymetry to develop a better measure of bathymetric slope in the reflections model. In what direction should slope be calculated? How can the directional gradient be determined? This study could be performed using higher resolution topographic databases to obtain an accurate, yet unclassified result.
- An investigation of the use of different source functions for convolution with the ocean basin impulse response model in the reflections model. Is there a better source function that is both more representative of the event in question and provides better synthetic replicas?
- An investigation of the use of more than zero-lag correlation. Is there a method that will yield better localizations?
- An investigation of the use of back-azimuth calculations in conjunction with travel time to improve the reflections model.

Finally, HydroCAM, the modeling software used to perform the travel-time calculations for this study, assumes a source in the water column when it makes its travel-time calculations. Earthquakes occur many kilometers below the ocean floor. For an earthquake that takes place 30 km under the ocean floor, seismic waves must travel in earth for about 30 km before their energy is converted to sound. Assuming a seismic velocity of approximately 6 km/sec, these waves will take about 5 sec to reach the earth/water interface. The best modeling of earthquakes that could be accomplished in this research was to set up the source on the bottom of the ocean. In the scope of calculations that span hours, the 5-sec bias does not seem to hamper localization, but a final topic of future study would be to analyze the benefit of adding a few seconds to the travel-time measurements to account for this bias.

ACKNOWLEDGEMENTS

The initial research and development of the reflections model for this study was performed under Defense Threat Reduction Agency (DTRA) contract number DSWA 01-97-C-0164. Additional support was provided through internal funding at BBN Technologies. We thank Phil Harben of Lawrence Livermore National Laboratory for providing data and insight during the course of this work. We also thank Dr. Anthony Lyons of Penn State University for useful discussions and suggestions.

REFERENCES

Angell, J., T. Farrell, and J. Pulli (1998), Characterization of reflected hydroacoustic signals, Proc. 20th Annual Seismic Research Symposium, 650-659.

Bendat, Julius S. and Allen G. Piersol. *Engineering Applications of Correlation and Spectral Analysis.* Second Edition, John Wiley and Sons, Inc. 1993.

Hanson, J. (2001), Initial Analysis of Data from the New Diego Garcia Hydroacoustic Station, 23rd Seismic Research Review, Jackson Hole, WY, LA-UR-01-4454.

Harben, P. and C. Boro. (2001), Implosion Source Development and Diego Garcia Reflections, Proc. 23rd Seismic Research Review, Jackson Hole, WY, LA-UR-01-4454.

Jensen, Finn B, W.A. Kuperman, M.B. Porter, and H. Schmidt. *Computational Ocean Acoustics*. American Institute of Physics. 1994

Pulli, J.J., Z. Upton, R. Gibson, T. Farrell (2000), Modeling Long-Range Hydroacoustic Reflections in the Atlantic and Pacific Oceans, Proceedings of the 22nd Seismic Research Symposium, New Orleans, LA, Defense Threat Reduction Agency, OMB No. 0704-0188.

Pulli, J.J., T. Farrell, and R. Gibson (1999), Characterization and utilization of hydroacoustic signals reflected from continents and bathymetric features, 21st Seismic Research Symposium, Las Vegas, NV, LA-UR-99-4700.

Radionuclide Monitoring

BE-7 CROSS-TALK IN RASA CONTINUOUS AIR SAMPLERS

Richard J. Arthur, Harry S. Miley, and Lindsay C. Todd

Pacific Northwest National Laboratory

Sponsored by National Nuclear Security Administration
Office of Nonproliferation Research and Engineering
Office of Defense Nuclear Nonproliferation

Contract No. DE-AC06-76RLO 1830

ABSTRACT

Several experiments were run to determine the extent of cross talk on existing RASA systems. The most definitive experiment consisted of shutting off power to the blower motor and advancing the filter media so that no exposed media was visible to the HPGe detector. The MDL for detecting Be-7 was thereby confirmed. A series of 5 blank filters were counted before power was restored to the blower motor.

Comparison of several spectra for the blank filters confirmed that levels of Be-7 were below detection levels. The blank filters were subsequently removed and counted on an ultra-low-background HPGe detector. The presence of Be-7 was clearly visible in several of the blank filters, but not in others.

Several theories are advanced to account for the presence of trace levels of Be-7 in the blank filters. Changes to the commercially available RASA are proposed based on the findings of this study. While these possibilities are put forward by the authors in the spirit of producing the best possible scientific data for atmospheric science research, the authors do not feel that cross talk or any other minor problems materially reduce the value of the RASA or any similar system for detecting and reasonably quantifying the size and nature of an atmospheric nuclear event.

OBJECTIVE

The Radionuclide Aerosol Sampler/Analyzer[1] (RASA) detects natural radionuclides in air samples by collecting a large volume sample (>15,000 m^3) through a high efficiency filter, decaying the sample to reduce radon daughters, then advancing the filter automatically into a lead shield containing a large germanium detector. This arrangement allows the RASA to monitor the air for anthropogenic or natural radioactive materials in an automatic, remote, and unattended way.

Considering the use of the RASA in monitoring for fission debris in the air from use of nuclear weapons or reactor accidents, certain fission products are considered key. The RASA was designed to achieve better than 10 µBq/m^3 of Ba-140, one such key fission isotope. In reality, however, RASA installations typically only detect primordial radionuclides (from potassium, uranium, or thorium present in the Earth's composition) such as K-40, Pb-212, Pb-214, Bi-212, Bi-214, and Tl-208 plus Be-7 that is produced in the upper atmosphere from cosmic ray proton reactions on Ar-40. A typical RASA gamma-ray spectrum is shown in Figure 1.

Be-7 is present in most RASA air samples, and with sufficient intensity to have very small statistical errors. Figure 2 shows the results of automated Be-7 analyses on a large number of RASA samples. The results have been histogrammed by the size of the statistical error bar on the Be-7 peak at 477 keV. Because most radon decay products have fairly short half lives (less that 11 hours), after a few days the only remaining material on a filter may likely be Be-7 (53 days) and low levels of the long-lived species K-40 (1.3 x 10^9 y). In addition, Be-7 contamination of surfaces tends to linger if caused by electrostatic precipitation from the atmosphere or contact with an unsealed filter.

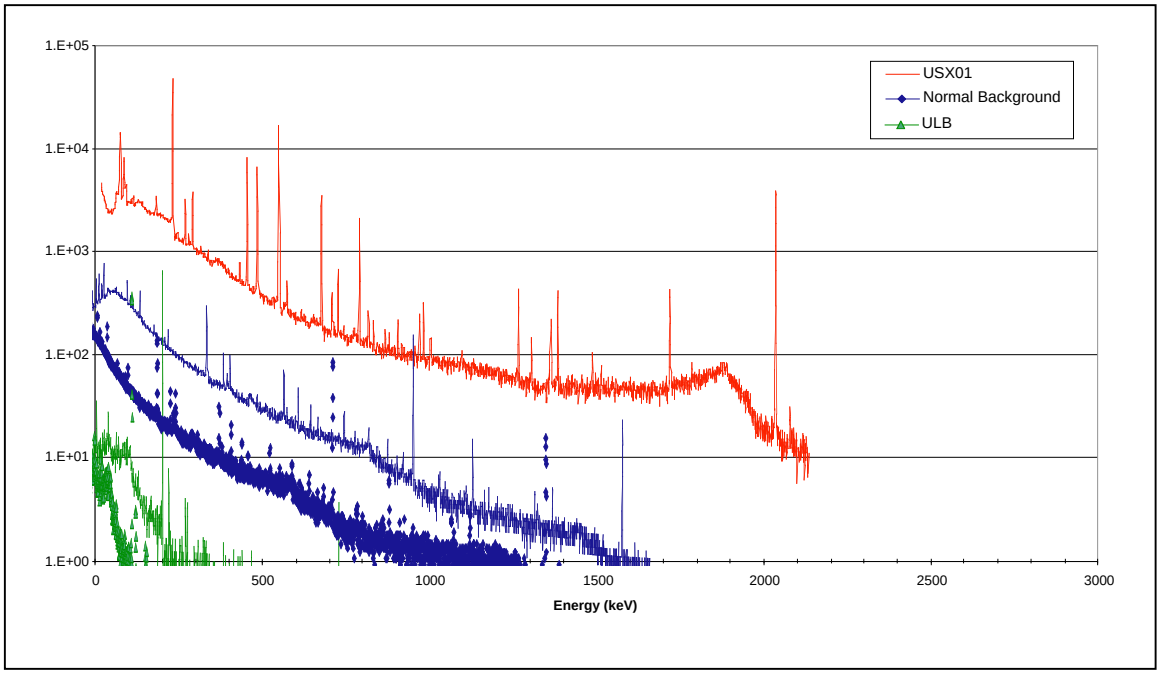

Figure 1. A typical RASA spectrum taken in Richland, Washington. Also shown is a system blank and a well decayed filter measured in an ultra-low background counter. Substantial radon daughters associated with aerosols are visible in the RASA spectrum.

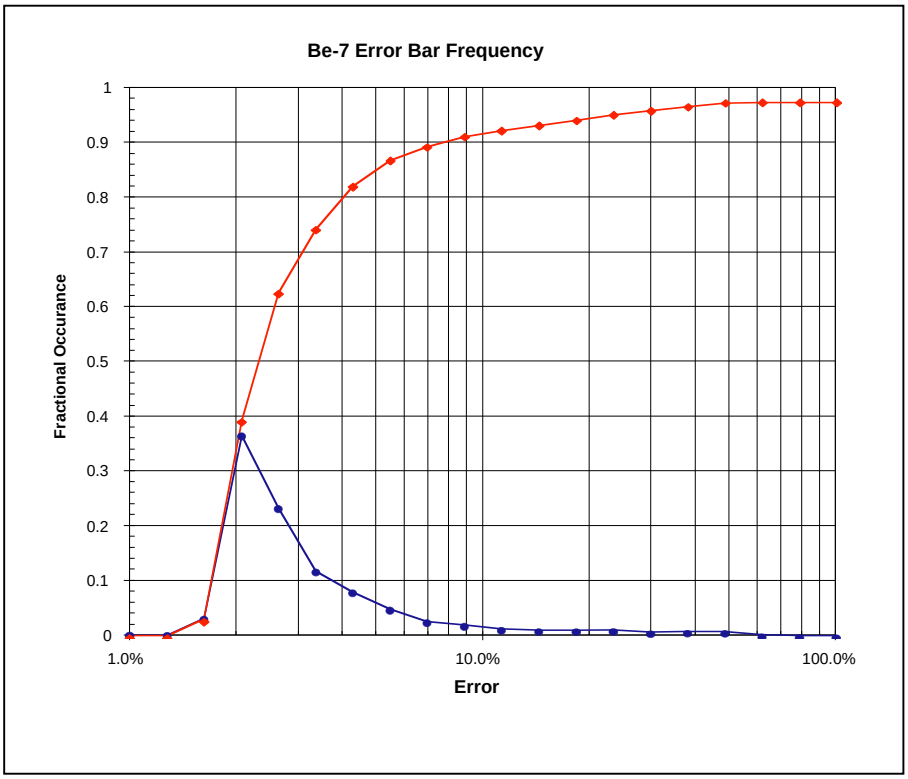

Figure 2. Plot is showing probability vs. size of statistical error bar.

The mechanics of the RASA are such that the filter area is large at the time of sampling and smaller during the radionuclide measurement. To accomplish this, the RASA employs six parallel continuous filter strips played off of long rolls, through the sample head, into a decay position, then wrapped around the germanium detector. The six strips are widely separated in the sample head, then brought together in a bundle and sealed as they advance into the decay position. In principle, then, the exposed filter samples have no opportunity to contaminate the detector area. A pair of motorized rollers advances the entire continuous filter bundle from the output side of the lead shield. Figure 3 shows a schematic layout of part of the RASA mechanical apparatus. It should be noted that substantial openings in the lead shield facilitate the entry and exit of the filter bundle.

Observation of the Cross Talk Effect

During normal operation of the RASA or any monitoring device it is occasionally required to perform a system blank. A system blank, in the case of the RASA, consists of measuring the background radiation recorded by the detector when a filter bundle is present in the shield that had zero accumulated air volume. In recent operations of this type, a slight Be-7 signal was detected. Several immediate possibilities presented themselves: that the volume of air within the shield contained that much Be-7, that Be-7 contamination within the sample head was becoming attached to blank filters, and that the substantial quantity of Be-7 on the filter before and after the blank were contributing to the blank spectrum, an effect casually labeled “cross-talk” for the purposes of this discussion.

A cursory examination of the position of the filters in the decay and output locations (labeled A and C in the diagram) shows that 7.5% and 20% of these filters, respectively, have a line-of-sight view of the detector, but at a substantially greater distance (about 5 times greater) than the filter under examination.

Original design estimates were that about 1% of the signals recorded for a given sample would come from the next sample, mostly due to short-lived radon daughters. No consideration of the contribution to a blank was made.

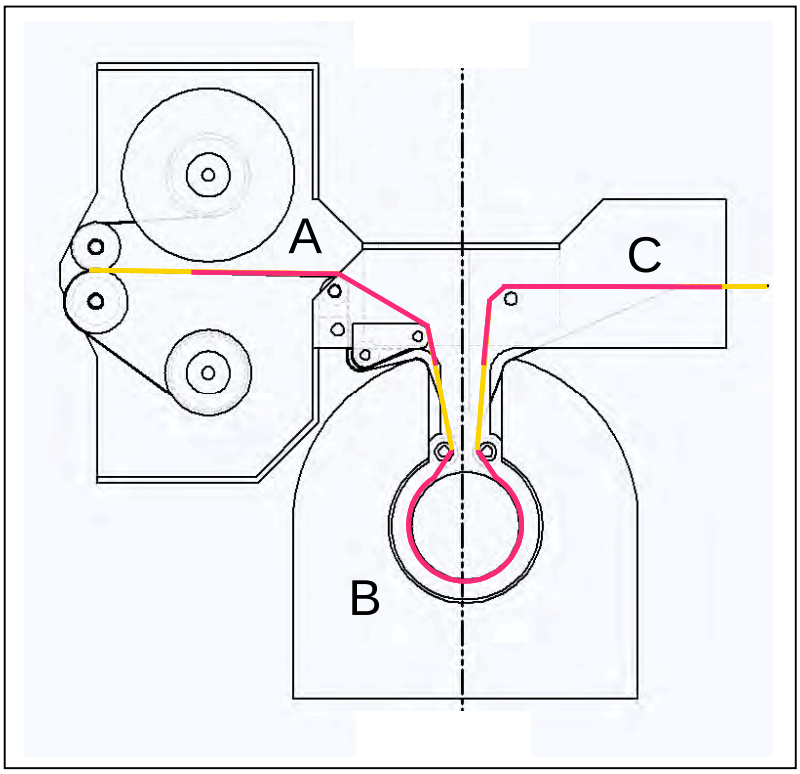

Figure 3. The basic layout of the RASA showing the decay position (A), the measurement location (B) and the output location (C). The rollers in the left hand portion of the diagram apply a polyester film to the filter to seal it.

The size of the cross talk from the decay position was estimated by comparing the integral of the Be-7 counts for a blank with a normal atmospheric sample in the decay position. The next day, the normal sample was in the shield. Only 320 net Be-7 counts were observed in the blank vs.170142 net counts when the normal sample was counted. This yields a 2.8% effect, but does not completely explain the Be-7 signals. In tests where blanks were advanced in the normal daily method into the decay, count, and output positions, some traces of Be-7 have been reported by RASA users. This seems to indicate that possibly more than one cross-talk effect is occurring.

A commercially produced RASA in operation in Richland, Washington was set to reproduce the results by disconnecting the blower, manually advancing filters until a blank was in each location, then 5 blanks were allowed to advance in the normal daily manner. After this, the blower was reconnected and the system ran in the usual manner. The samples were measured by the RASA itself, but to improve the sensitivity the samples were later counted on an ultra-low background spectrometer[2].

Table 1. Results of ultra-low background testing of RASA blanks. Note: No cross talk of gamma-rays from one sample to another is possible in this scenario since the samples were out of the RASA and in another counting system.

Filter ID	Comments	ULB Be-7 Rate	ULB Activity
02002 02704	Normal loading		
05	"		
06	"		
07	"		
08	Light loading		
09	Blank, blower off	12.5 cts/day	145 mBq
10	"	9.38 cts/day	109 mBq
11	"	<1 cts/day	<12 mBq
12	"	<1 cts/day	<12 mBq
13	"	<1 cts/day	<12 mBq
14	Blank, blower on	<1 cts/day	<12 mBq
15	"	24.6 cts/day	285 mBq
16	"	24.4 cts/day	282 mBq
17	Normal loading		
18	"		

The automated analysis of the blanks (09-16) showed either no Be-7 or a very questionable result consistent with no Be-7. The ultra-low level counting did yield interesting results, however.

CONCLUSIONS AND RECOMMENDATIONS

From the ultra-low level counting summarized in Table 1, we may conclude several facts.

First, contamination of blank filters while in the sample head, if it occurs, contributes less than 1 count per day of Be-7. Similarly, contamination from one filter to another via scraping or rubbing is limited to less than one count per day.

Second, the operation of the blower seems to cause a low level of contamination on adjacent blank filters. This contamination is 5%-10% the size of the original cross talk effect. Two theories are suggested as to the source of this contamination.

1. Be-7 on particulate adheres to the outside of the polypropylene envelope as it passes into a small leak in the sample head.

2. Be-7 in room air is filtered through a presumably blank filter between regular samples due to a leak in the sample head.

Remedies to the effects listed above include a redirected filter path to greatly reduce or eliminate the gross (~3%) effect of cross talk. This effect and remedy are rather certain. Another, so-far untested remedy would be to seal the known gaps in the commercial RASA sample head so no air is allowed to flow over or through media in or near the decay position.

REFERENCES

S.M. Bowyer, et al, *IEEE Transaction on Nuclear Science*, Vol. **44**, No. 3 (1997) 551-556.

H.S. Miley, et al, *J. of Radionanlytical and Nuclear Chemistry, Articles*, Vol. **160**, No. 2 (1992) 371-385;

R.J. Arthur, et al, *J. of Radionanlytical and Nuclear Chemistry, Articles*, Vol. **160**, No. 2 (1992) 297-304.

ENVIRONMENTAL MONITORING OF RADIOXENON IN SUPPORT OF THE RADIONUCLIDE MEASUREMENT SYSTEM OF THE INTERNATIONAL MONITORING SYSTEM

Tom R. Heimbigner, Justin I. McIntyre, Theodore W. Bowyer, James C. Hayes, and Mark E. Panisko

Pacific Northwest National Laboratory

Sponsored by National Nuclear Security Administration
Office of Nonproliferation Research and Engineering
Office of Defense Nuclear Nonproliferation

Contract No. DE-AC06-76RLO 1830

ABSTRACT

The Automated Radioxenon Analyzer/Sampler (ARSA) has been deployed at several locations throughout the world: Richland, WA; New York City, NY; Charlottesville, VA; Freiburg, Germany; and, most recently, Guangzhou, China. In each of these locations, the ARSA has measured varying concentrations of ^{131m}Xe, ^{133}Xe, ^{133m}Xe, and ^{135}Xe. These concentrations of radioxenon come from a variety of sources such as nuclear reactors, medical hospitals, and nuclear fuel reprocessing; the concentrations vary by location. This makes it necessary to utilize the isotope ratios as well as their concentrations to differentiate ambient radioxenon emissions from those released by clandestine underground nuclear explosions. High concentrations and multiple isotope identification within a single sample are good measures of potentially suspect radioxenon emissions. Utilizing the ratios of the concentrations of ^{135}Xe to ^{133}Xe and ^{133}Xe to ^{133m}Xe enhances the separation of the more mundane emissions from clandestine underground nuclear detonations. This paper presents concentration data collected from each of the sites and explores the ability of ratios to discriminate between reactor effluents and underground nuclear tests. Analyses to date indicate that concentration levels, multiple radioxenon isotopes in a single sample, the presence of ^{133m}Xe and several isotopic ratios will all be good indicators of clandestine underground nuclear explosions and the combination of two or more of these measures will provide strong evidence of such activities.

OBJECTIVE

Several versions of the ARSA, developed at the Pacific Northwest National Laboratory (PNNL), have been deployed at several locations throughout the world during the past five years. Deployments were first undertaken at the Environmental Monitoring Laboratory (EML) in New York City during 1997 (Bowyer 1997), second in Orlando, Florida in 1999, and third in Freiburg, Germany in 1999-2001 (Bowyer 2002). Additional systems were run in Orlando Florida and Charlottesville, VA in 2001-2002 with one of the units deployed in Guangzhou, China in late July 2002; a PNNL model has run continually in Richland, WA area since May of 2001. All systems have measured ^{133}Xe and ^{135}Xe, which represent two of the three most important radioxenon isotopes that are indicative of a nuclear explosion. In some locations, concentrations of ^{131m}Xe have been measured and less frequently ^{133m}Xe has been measured.

These measured radioxenon concentrations represent an ambient background that will be present at some of the planned deployment locations outlined by the Provisional Technical Secretariat (PTS). These emissions can be attributed to nuclear power reactor operations, hospital use of ^{133}Xe for medical testing, and fuel reprocessing activities to a lesser extent (Bowyer and Perkins 1998). In all instances the measured concentrations for ^{133}Xe have been well above the 1 mBq/m^3 minimum detectable concentration (MDC) requirement adopted by the Comprehensive Nuclear-Test-Ban-Treaty Organization (CTBTO) Preparatory Commission (Preparatory 1999). For several of the deployed locations (Florida, Charlottesville, Germany, and New York City) the ARSA, which has a ^{133}Xe MDC below 0.2 mBq/m^3, had a significant number of samples with ^{133}Xe concentrations above the 0.2 mBq/m^3 MDC level. For the samples collected and measured in the Freiburg, Germany location over 95% had a detection of ^{133}Xe, see Figure 1. Though no MDC's have been set for ^{131m}Xe and ^{133m}Xe the PTS required that any of the deployed system be capable of measuring them and the ARSA has achieved MDC's for the two metastable isotopes of less than 0.3 mBq/m^3 and for ^{135}Xe below 1.0 mBq/m^3.

The measured concentrations and the identification of multiple isotopes within a single sample at all of the sampling locations merited further analysis of the data to determine the isotopic ratios from non-nuclear detonation sources. In the cases of multiple isotopes, the ^{135}Xe/^{133}Xe ratio clearly indicated that the plumes were from a source other than a nuclear explosion. The further absence of statistically significant amounts of ^{133m}Xe also provided a key indication that the plumes were from background sources. The most recent set of data obtained in Richland, Washington illustrates the identification problem; through the use of isotope identification and the ^{135}Xe/^{133}Xe ratio, the collected sample in Richland has been unambiguously assigned to the local nuclear reactor.

The discussion here is centered on nuclear reactor emissions, but it is important to point out that the two other likely sources of radioxenon isotopes will have unique ratios as well. For both medical uses and fuel processing activities the ^{131m}Xe/^{133}Xe plays an important role. For medical uses, only ^{133}Xe is used and 20 mCi is the typical dose used. These samples also contain ~0.5% ^{131m}Xe concentrations upon arrival (within 5 days of generation). After several weeks the ratio of ^{131m}Xe/^{133}Xe becomes very large (>> 10:1) and samples that are not used will be released to the atmosphere as part of the disposal process. For nuclear fuel reprocessing the ^{131m}Xe/^{133}Xe ratio will also be high because it is stored for several months to allow the decay of short-lived radionuclides before it is processed. Both of these activities will not have significant ^{135}Xe or ^{133m}Xe concentrations.

RESEARCH ACCOMPLISHED

Monitoring ambient levels of some radioxenons has a long history and the introduction of the Comprehensive-Nuclear-Test-Ban-Treaty in 1996 increased the interest in measuring atmospheric concentrations of the four radioxenons that are most likely to escape from an underground nuclear explosion and last long enough to be measured by a world wide radioxenon network. Historically, both anthropogenic and cosmogenic sources of these radioxenon isotopes were investigated and initial work indicated that concentrations from even small (1kT) subsurface nuclear explosions would be much greater than those produced by other means (Bowyer and Perkins 1998). Figure 2 shows the ^{133}Xe/^{133m}Xe and ^{135}Xe/^{133}Xe ratios that are expected for an operating nuclear reactor in equilibrium and those expected for an underground nuclear explosion. It is clear that the ratios are several orders of magnitude higher for a nuclear detonation than they are for a nuclear reactor.

New York City 1997

The first reported environmental measurement of 135Xe concentration were taken by the first prototype ARSA unit at the Environmental Monitoring Laboratory in New York City during April of 1997(see Figure 3). The 135Xe/133Xe ratio for this sample was 0.13 and, along with the lack of any measurable 133mXe concentration, indicates that this plume was from a local reactor, Xe-133 concentrations were also seen during this field test.

Freiburg Germany (1999-2001)

The PTS Phase II testing was done at the Institute for Atmospheric Research (IAR) and included systems from Sweden (SAUNA), France (SPALAX), Russia (ARIX) and the ARSA system. IAR hosted the test and provided analysis of the archived samples that each of the systems collected. Comparisons of the concentration data from each of the systems were in good agreement with one another and will be detailed in a subsequent publication.

During this test the ambient concentrations of ^{133}Xe fluctuated between approximately 1.0 and 120 mBq/m^3 on a daily basis (see Figure 1). Xenon-135 was seen in several of the samples during the 15-month test and the other two isotopes of interest ^{131m}Xe and ^{133m}Xe were seen as well. For one of the samples collected during this time a ^{135}Xe/^{133}Xe ratio of 2.1 was measured, which is almost four times higher than that expected for a nuclear reactor operating in equilibrium. This was a clear indication that additional reactor operations analysis was required to account for a sample that was not from an underground nuclear detonation.

High ratios of ^{131m}Xe/^{133}Xe were seen on two occasions, which indicates either a release from a nuclear fuel reprocessing plant or a release of an old (>2 months) medical sample of ^{133}Xe by a nearby hospital.

Richland 2001

The running of the ARSA system in Richland has typically yielded radioxenon concentrations below the MDC levels of the system. Low radioxenon concentrations are expected in several of the PTS radionuclide station locations in the Southern Hemisphere due to the low numbers of nuclear reactors

The Richland location of the ARSA offers a unique test ground for ratios as it is in very close proximity of a nuclear reactor run by Columbia Generating Station (the WNP-II 2-GW BWR is less than 8 miles from the sampling station) with a prevailing wind direction blowing effluents away from the sampling site. During July of 2002, the reactor had a scheduled shutdown for biannual maintenance and refueling. A spike of ^{133}Xe and ^{135}Xe was seen at the sampling site within hours of reactor shutdown. The ^{133}Xe concentration was fairly low (0.74 mBq/m^3) and the ^{135}Xe concentration was (3.1 mBq/m^3), which was high for the Richland area, as ^{135}Xe had not been detected previously. This gave a ^{135}Xe/^{133}Xe ratio of ~4.2, which is the highest that has been measured by the ARSA. There were no measurable quantities of ^{133m}Xe or ^{131m}Xe found in the two samples that had the ^{133}Xe and ^{135}Xe. With the high ratio of ^{135}Xe/^{133}Xe and the lack of ^{133m}Xe, the samples indicate the source was a nuclear reactor that was not in equilibrium.

These results are consistent with results obtained by irradiation of 10.1 grams of HEU using a 9.0 x 10^8 neutron/sec PuBe source at PNNL. The HEU was sealed in a gastight container, irradiated for several days and, thus, provided ^{133}Xe and ^{135}Xe. The head gas was drawn off and directly injected into the ARSA beta cells to provide calibration data for the beta energies (see Figure 4). The ^{133}Xe/^{135}Xe ratio ranges between 6 and 10, and depends on how soon the sample is injected into the ARSA detector after irradiation and the length of the irradiation.

Nuclear Reactor Shutdown

During a reactor shutdown the rapid decrease in the neutron flux allows the buildup of ^{135}Xe within the fuel rods, i.e. the ^{135}Xe is no longer being burned. Thermal stresses related to the reactor cool down facilitate the release of the trapped radioxenons within the fuel rods. Figure 5 shows the increase in the ^{135}Xe after shutdown of the reactor. The concentration peaks after about 10 hours by a factor of approximately 20 from normal operations; thus the ^{135}Xe/^{133}Xe ratio will go from about 0.5 to 10 during the first day after shutdown. The July 28, 2001 release from WNP-II 2-GW BWR was 4.2, which is well matched to the expected results.

Nuclear Reactor Startup

During the startup of a nuclear reactor the ^{135}Xe builds quickly compared to ^{133}Xe because the shorter half-lives of the ^{135}Te and ^{133}Te grandparents and ^{135}I and ^{133}I parents that feed into their respective production. This coupled with an increase in gas leakage due to thermal stressing of the fuel rods leads to high ratios and high concentrations of both xenon isotopes. The reactor is slowly ramped up over a 10-day period in 10 daily steps of 10%. Figure 6 shows the various ratios determined for a pressurized water reactor. It takes approximately 3 weeks to be within 10% of equilibrium for the ^{135}Xe/^{133}Xe ratio, more than 4 weeks for the ^{133}Xe/^{131m}Xe ratio to be in equilibrium and the ^{133}Xe/^{133m}Xe ratio is stable shortly after startup.

As the reactor comes up to full power, the production of ^{135}Xe is suppressed because of its extremely high neutron capture cross-section (2.6×10^6 barns) and the ^{135}Xe/^{133}Xe ratio will drop to those levels indicated for a stable reactor in Figure 6. After the reactor has reached equilibrium the ^{135}Xe/^{133}Xe ratio is approximately 0.5 and the ^{135}Xe/^{133m}Xe ratio is approximately 11. The release of additional ^{131m}Xe, ^{133m}Xe and ^{133}Xe and ^{135}Xe is further suppressed because the reactor/fuel rods have reached thermal equilibrium.

CONCLUSIONS AND RECOMMENDATIONS

As more data are acquired from the several radioxenon monitoring stations currently operating analyses will be required to discriminate between reactor related radioxenon and that expected from possible underground nuclear detonations. Analyses to date indicate that concentration levels, multiple radioxenon isotopes in a single sample, the presence of ^{133m}Xe and several isotopic ratios will all be good indicators of clandestine underground nuclear explosions and the combination of two or more of these measures will provide strong evidence of such activities.

ACKNOWLEDGEMENTS

The authors would like to thank members of the International Noble Gas Experiment (INGE) for useful discussions and a successful noble gas experiment and the operators of the Columbia Generating Station WNP-II 2-GW BWR reactor for fruitful discussions on reactor operations.

REFERENCES

Bowyer, TW, C Schlosser, KH Abel, M Auer, JC Hayes, TR Heimbigner, JI McIntyre, ME Panisko, PL Reeder, H Satorius, J Schulze, and W Weiss, *Detection and analysis of xenon isotopes for the comprehensive nuclear-test-ban treaty international monitoring system, J. Envir. Radio.* 59, Issue: 2, pp. 139-151, 2002.

Bowyer, TW, K. H. Abel, C. W. Hubbard, M. E. Panisko, P. L. Reeder, R. C. Thompson, and R. A. Warner, *Field Testing of Collection and Measurement of Radioxenon for the Comprehensive Test Ban Treaty*, J. Radioanal. Nucl. Chem., 240, pp. 109, 1999.

Bowyer TW, KH Abel, ME Panisko, RC Thompson, and RA Warner, *Observation of ^{135}Xe with the PNNL ARSA System*. PNNL-11654, Pacific Northwest National Laboratory, Richland, WA, 1997.

Bowyer TW, KH Abel, WK Hensley, and RW Perkins, Ambient *^{133}Xe Levels in the Northeast United States.*" Journal of Environmental Radioactivity 37, No. 2, pp. 143-153, 1997

Preparatory Commission for Comprehensive Nuclear-Test-Ban-Treaty Organization, *Operational Manual for Radionuclide and the International Exchange of Radionuclide Data*, CTBT/WGB/TL-11/5/Rev. 4, 1999.

Bowyer TW, RW Perkins, KH Abel, WK Hensley, CW Hubbard, AD McKinnon, ME Panisko, PL Reeder, RC Thompson, and RA Warner, *Xenon Radionuclides, Atmospheric: Monitoring*, Encyclopedia of Environmental Analysis and Remediation, editor RA Meyers, publisher John Wiley & Sons, Inc., pp. 5299-5314, 1998.

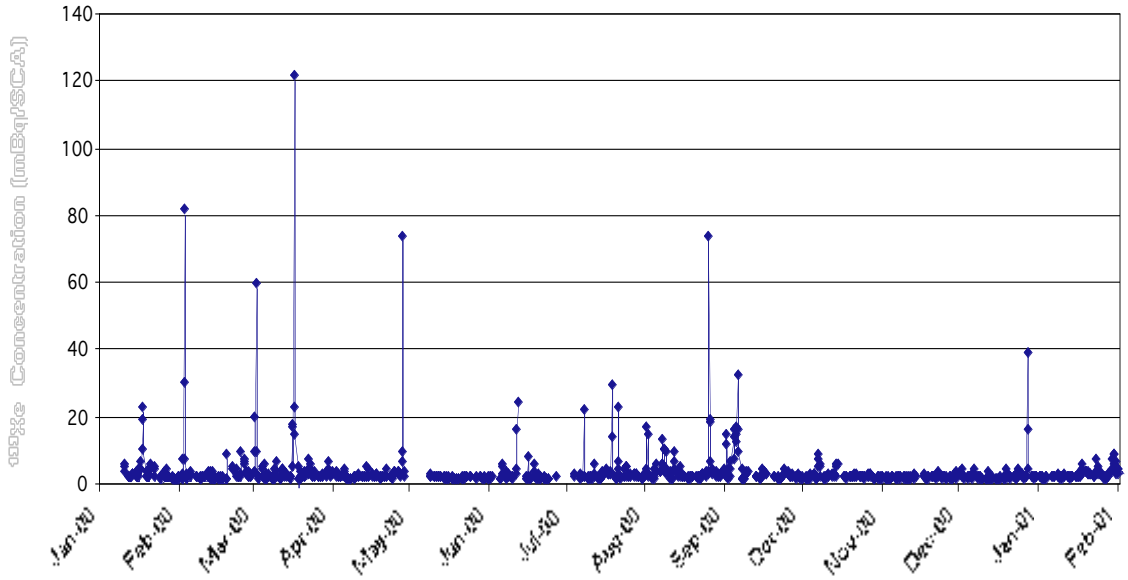

Figure 1. Freiburg ^{133}Xe concentration results for the period January 2000 to February 2001. Over 1100 samples were collected and measured during the test. The chart clearly indicates that for radioxenon measurement systems located in areas with large numbers of nuclear reactors high concentration of ^{133}Xe will be seen regularly.

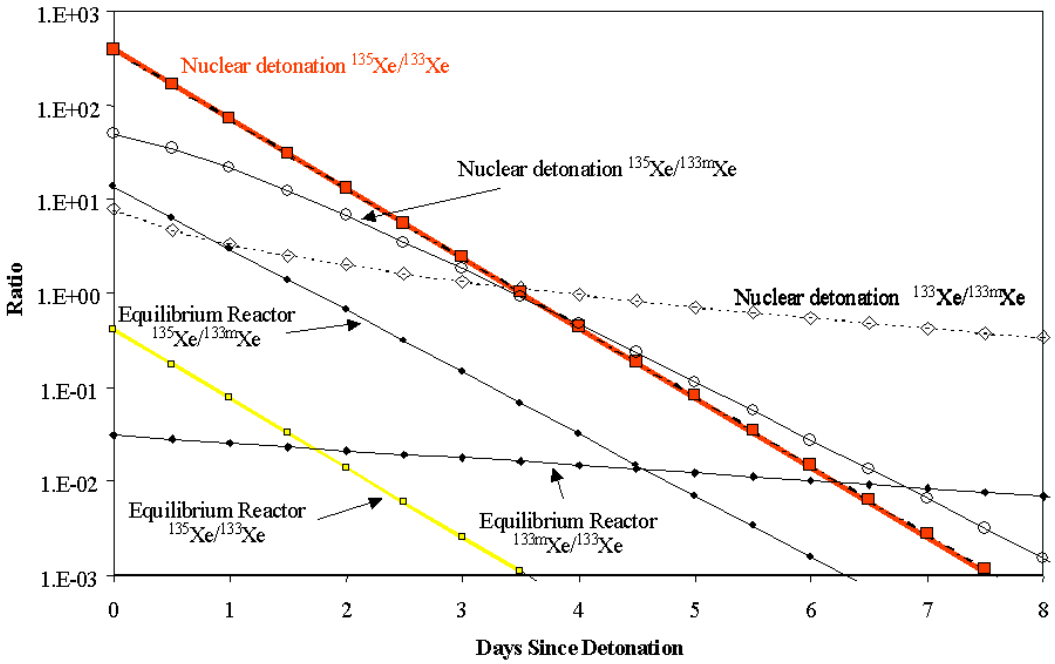

Figure 2. Expected activity ratios for ^{133}Xe/^{133}mXe, ^{133}Xe/^{133}mXe and ^{135}Xe/^{133}Xe with respect to release time from a subsurface nuclear detonation and from an operating reactor. All of the reactor ratios are lower than the nuclear detonation ratios, and in some cases by several orders of magnitude for several days.

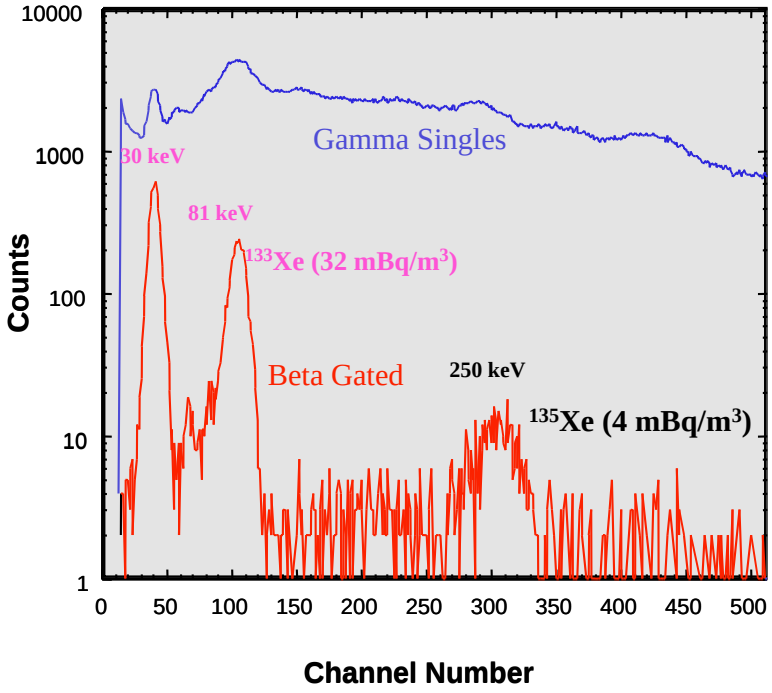

Figure 3. Gamma-ray spectrum of first reported environmental concentration measurement of ^{135}Xe along with ^{133}Xe. The lower red curve is the beta-gated gamma spectrum and the higher blue curve is the ungated gamma spectrum. This data was taken by the first prototype ARSA unit at the Environmental Monitoring Laboratory in New York City, 1997. The ^{135}Xe/^{133}Xe ratio for this sample was 0.13 that is indicative of a release from a stable reactor or a plume that has traveled large distances from either a reactor that was powering up or down.

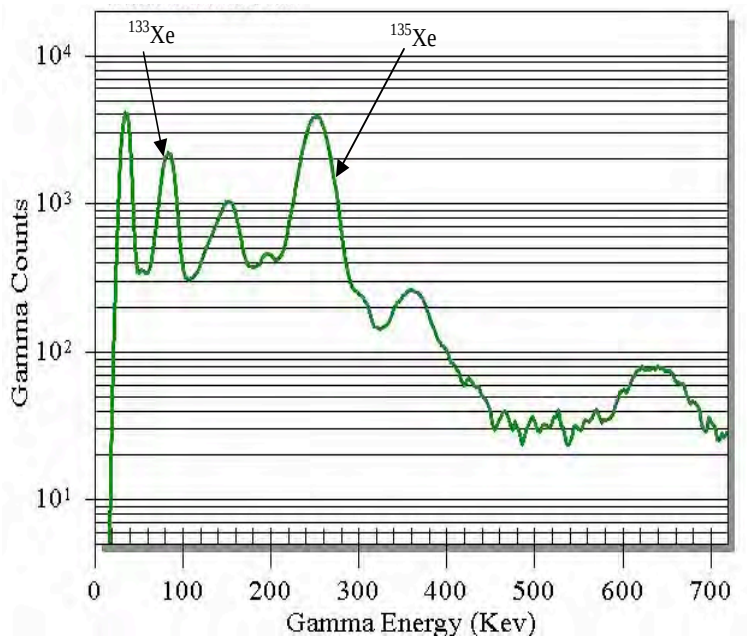

Figure 4. A beta-gated gamma spectrum from ARSA obtained using the fission product gases produced by irradiating HEU with a PuBe neutron source. The two radioxenon isotopes ^{133}Xe and ^{135}Xe are present at 30 and 81-keV and 250-keV respectively.

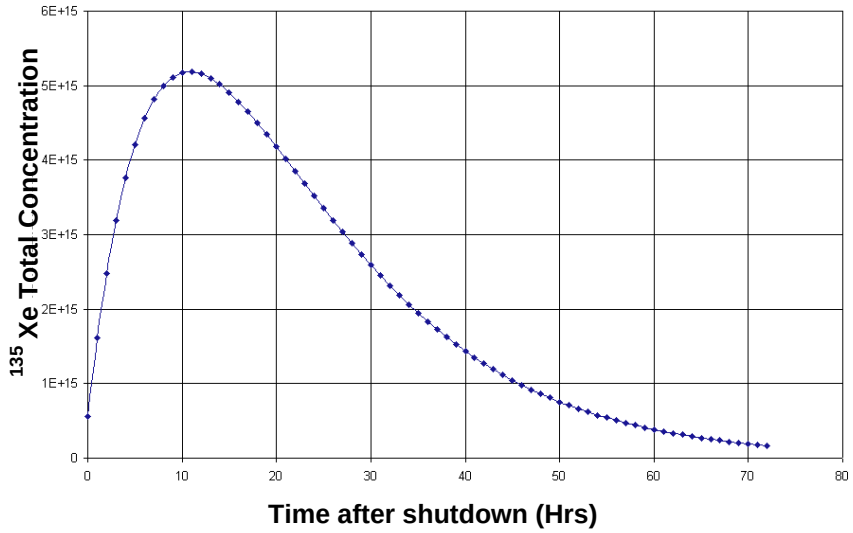

Figure 5. Xenon-135 concentration with respect to time after a full power shutdown of PWR reactor. The increase is due to the lack of burn up caused by neutrons in the reactor core.

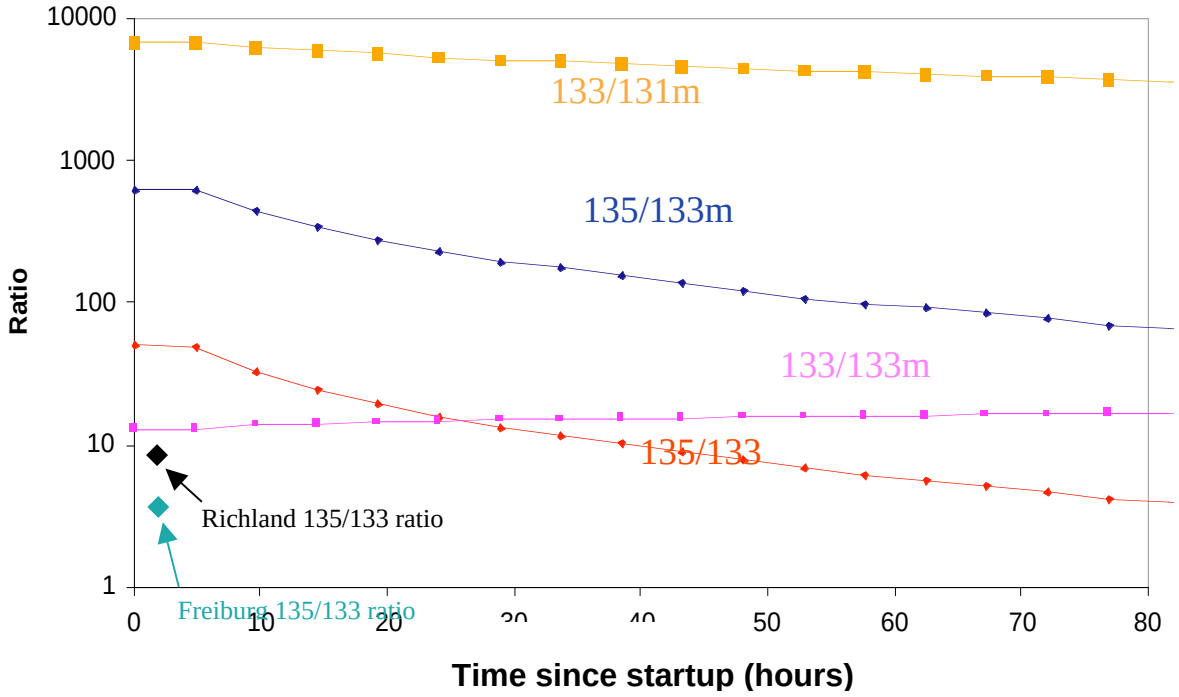

Figure 6. Radioxenon ratios during startup of a pressure-water reactor. The two data points represent the measured ratios for the Freiburg and Richland radioxenon samples.

STATUS OF THE AUTOMATED RADIOXENON SAMPLER ANALYZER, AND THE INTERNATIONAL MONITORING SYSTEM INTERNATIONAL NOBLE GAS EXPERIMENT

David Penn, Steven Biegalski, and Kendra Biegalski

Veridian Systems Division

Sponsored by Defense Threat Reduction Agency

Contract No. DTRA01-99-C-0031

ABSTRACT

As part of the US involvement in the development and deployment of an International Monitoring System (IMS) for monitoring nuclear explosions, the Automated Radioxenon Sampler Analyzer (ARSA) was developed. The ARSA system automatically and continuously samples the atmosphere to separate elemental xenon via selective adsorption. The collected xenon sample is transferred to a radiation counting device where the electron and photon radiation spectra are acquired. The radiation spectra data are then transmitted to the International Data Centre (IDC) in Vienna, Austria for archiving, analysis and distribution to state signatories. A combination of four radioactive xenon isotopes and isomers are of particular interest for nuclear explosion monitoring purposes: ^{131m}Xe, ^{133m}Xe, ^{133}Xe, and ^{135}Xe. Four xenon-sampling systems have been built to support the IMS and currently they are in a testing and validation program, the International Noble Gas Experiment (INGE). As part of the third Phase of the INGE, the ARSA will be installed in Guangzhou, China and operated by local technicians and scientists at the Guangdong Environmental Radiation Research and Monitoring Center (GERC). Veridian Systems Division is the prime contractor for the installation and maintenance for the ARSA with the support of the original developers, Pacific Northwest National Laboratory (PNNL). Once installed at the GERC, the ARSA is scheduled to remain in China for one year, with an option to extend the period for an additional year.

In the past year Veridian Systems Division, under contract with the Defense Threat Reduction Agency (DTRA), has been performing an independent operational test and evaluation of a commercially manufactured ARSA prototype. The manufactured prototype will be delivered to Guangzhou. The manufactured prototype operates in the same manner as the original ARSA, built by PNNL, but does have some mechanical differences. Therefore it was necessary to perform a month long performance test in Charlottesville, Virginia to provide evidence to the IDC that the prototype meets the minimum requirements for the IMS. Once the ARSA is installed at the GERC, the local operators will become responsible for the daily operation and maintenance of the system.

The data produced by the ARSA during Phase III includes the electron-photon coincidence spectra as well as various sensor and instrumentation signals that are used to determine the “State of Health” (SOH) of the system. The data is transmitted from the ARSA automatically at two-hour intervals and delivered via the Internet to the International Data Center (IDC). From the IDC, it is distributed to Phase III participants and state signatories.

OBJECTIVE

This paper discusses the performance of the ARSA prior to its installation in China, the challenges that arose during the site coordination meetings, and the issues observed during the operation to date.

RESEARCH AND ACCOMPLISHMENTS

The International Noble Gas Experiment (INGE), Phase III

The American Automated Radioxenon Sampler Analyzer (ARSA) is one of four devices participating in the INGE and will be installed at the GERC in Guangzhou, China during the summer of 2002. The other three systems, and their respective installation sites, are composed of the:

1. French SPALAX located in Papeete, Tahiti
2. Russian ARIX located in Rio de Janeiro, Brazil
3. Swedish SAUNA located in Spitsbergen, Norway

The ARSA is being installed by Veridian Systems Division (VSD) scientists with the support of scientists from the Pacific Northwest National Laboratory (PNNL). It is the responsibility of VSD to ensure the performance of the ARSA with respect to the IMS requirements both before and after the installation. It is also the responsibility of VSD to provide oversight to the Chinese operators regarding the infrastructure requirements of the ARSA. To facilitate the success of the ARSA in the INGE a site coordination meeting was held at the GERC to solidify the responsibilities for each of the parties involved. The site coordination meeting was held during April of 2002. During the site coordination meeting VSD was given the opportunity to inspect the site and provide the local operators with the infrastructure upgrade requirements for proper operation of the ARSA.

Site Coordination

Representatives attended the site coordination meeting from VSD, PNNL, GERC, and the IMS. The meeting itinerary included an in depth inspection of the facility where the ARSA will be installed, the method proposed to move it to its final location and the data and communications channels that will be required for operation of the system.

The GERC representatives were supplied with a list of infrastructure requirements, see Table 1, in advance of the meeting and many of the requirements had already been met.

Table 1. ARSA Facility Requirements for Guangzhou, China

Facility Area	Requirement	Comments
Building Structure	ARSA Size is 36”x72”x72”	The entryways at the site must allow for the ARSA to enter the building.
	Floor loading	The weight of the ARSA is 2000 lbs. This weight is distributed over eight 1-inch diameter feet.
	On-site receiving	The site must have a facility to receive the ARSA when it is shipped.
	On-site moving of ARSA	The site must have equipment to facilitate the movement of the ARSA from the receiving location to the ARSA lab.
Communications	Phone line or Network Drop	The facility must have a mechanism for ARSA communications. The specifics of the local communications must be conveyed to Veridian before installation so that the ARSA may be configured and so that the proper parts are brought to the installation.

Air intake/ventilation	Outside air is needed.	A 4" flex hose will run out the lab window to the roof of the building. A rain hood/cap/bend and screen will be placed at the end of the intake tube.
Noise	System noise is around 80 dB.	Noise abatement measures may be required.
Power	230 V, 50/60Hz, single phase	A 230 V line will need to be installed.
	25 Amps	The power for the ARSA will require at least a 40 Amp breaker.
Site Security	Lab window	Security will be placed on ARSA lab windows.
	Doors	Locks will be placed on ARSA lab doors and access limited to specified personnel.
Drainage	Drainage is required for ARSA (about one quart per day)	A line must be run to the nearest drain.
Air Conditioning	Power output of ARSA is about 5 kW.	A minimum of 2-tons of air conditions is required.
System Ground	ARSA should be grounded.	It is recommended that the ARSA have a specific ground.
Storage Space	Shipping containers need to be stored.	Additional space beyond the ARSA lab need for storage.
Tools	ARSA utilizes standard tools.	English based tools needed.
Support Gases	Nitrogen bottles needed for ARSA	The site should obtain 99.999% grade (or higher purity) nitrogen for the ARSA The ARSA consumes about 200 cubic feet of nitrogen each month under normal operations.

In general the facility was in good condition and the laboratory where the ARSA will be installed had been renovated recently. The laboratory is separated into three sections, one of which houses a particulate system, see Figure 1, which samples the atmosphere for aerosols as part of the IMS. In Figure 1 the particulate system is in the room on the left and the ARSA will be installed in the room on the right.

Figure 1 ARSA lab at CN22

Since much work had already been completed to the site, few upgrades were required; the most important of which are:

1. Converting the three phase 380 V power to single phase 220 V, 25 A
2. Increasing the air conditioning capacity from 4.2 kW to 7 kW
3. Changing the location of the air intake on the roof of the building.

The first two of the above upgrades are straightforward but the third was required because it was located approximately 1 meter downstream from a chemical lab fume hood exhaust system. (Figure 2) The air intake has been relocated upstream of the location approximately 10 meters from the vent.

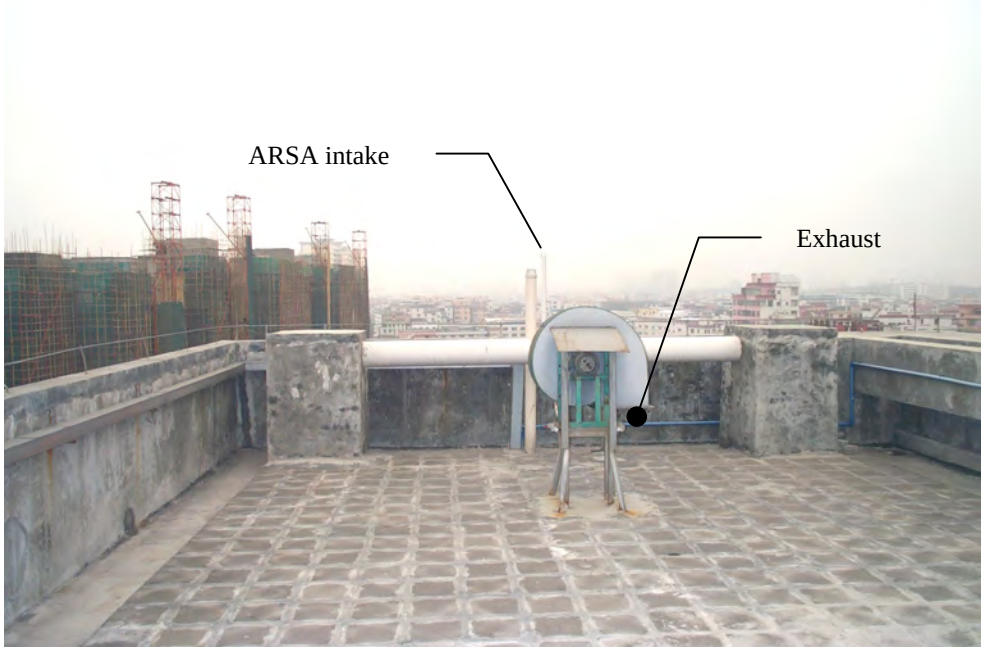

Figure 2. ARSA intake and fume hood vent location

The remainder of the coordination meeting involved discussions regarding the shipping procedures, customs, communications, and operation of the ARSA. The schedule put into place for the ARSA was to tune the system in the two to three weeks following the coordination meeting. Once the system was tuned it begin a pre-shipment performance testing period for one month in Charlottesville, Virginia. Once the baseline performance of the ARSA is determined and found acceptable by the IDC it would be ready for shipment. In parallel with the performance testing the Chinese were to complete the infrastructure upgrades and assist Veridian with determining the customs procedures. The ARSA was not to be shut down and disassembled until all of these issues were resolved. The customs issue was of particular importance because there is typically a deposit required for items temporarily imported into China. In the case of the ARSA, a representative from the Chinese Ministry of Defense was of great assistance and applied for the system to be brought in with no deposit required. At the time of writing this paper, the requirements for shipment were recently received and the ARSA is being prepared for shipment.

Once the ARSA is shipped, it will be stored temporarily by the shipping company in Guangzhou until the install team arrives. The ARSA will be tentatively scheduled for delivery at the site on the third day of the installation period. During the first two days of the installation period, the install team will perform a final inspection of the site and provide some limited training to the local operators so that they can assist with the installation. Since the lab is located on the 7th floor of the building and there is no elevator or external lifting mechanism, the GERC is responsible for coordinating with a local contractor to lift the ARSA from the ground floor to the laboratory on the 7th floor. Lifting the ARSA to the 7th floor will be accomplished through an open space in the stairwell, see Figures 3 and 4. The lifting will be done by constructing a frame above the 7th floor and using an electric winch to lift the

ARSA. A platform will be built at the 7th floor to extend under the ARSA and transfer it to the lab. Once the ARSA is in the lab, it will be installed on a vibration isolation pad to help decouple vibration from the compressor to the surrounding labs instrumentation, in particular the HPGe detector that is located approximately 2 meters away.

Figure 4. Stairwell at ground level

Figure 3. Stairwell opening

The last significant discussion during the site coordination meeting was electronic access to the machine and data transmission. At the time of the coordination meeting, the GERC did not have a LAN and connected to the Internet via an analog modem. It was originally agreed that the ARSA would be configured to do the same but after experiencing some difficulty with the analog service, it was agreed that an ADSL connection would be installed. Also, the ARSA will be configured to send data to the IDC at two-hour intervals that will then forward the data to Phase III participants and state signatories.

Pre-Shipment Testing

Since the ARSA being delivered for the INGE Phase III was not produced by PNNL, but by an independent manufacturer, the system was subjected to a month long pre-shipment test. This test was put into place to provide evidence to the IDC that the system complies with the minimum requirements for the IMS. Since the ARSA had been operating well and producing high quality data for some time before the site coordination meeting, there were few items that needed to be addressed before the test began.

The intrusion detection system on the ARSA was installed but needed to be configured for proper operation as well as two sensors for the room temperature and humidity needed to be integrated. The ARSA xenon quantification instrumentation (a cathetometer and infrared absorption meter) calibration was also checked and the format for transmitted data was modified to reflect the message format and protocols required by the International Data Center (IDC). The test was initiated on 13 May 2002 and ended on 10 June 2002. The data produced was transmitted to the Center for Basic and Applied Research and the IDC for analysis. The ARSA pre-shipment test report was generated based on this data and the performance was found to be acceptable by the IMS. The technical and data requirements for the period of performance are summarized in Tables 2 and 3. In addition to the technical requirements, it should be noted that the ARSA has provided a level of service where it was online for 97% of the test. It should also be noted that the time off-line was not due to a mechanical failure but was a safety mechanism protecting the machine during a severe weather condition.

Table 2. Data Requirements

Requirement	Type of Data	Recording and Saving	Transmission to IDC
1	Partial spectra	Every 2h	Every 2h
2	Full spectrum	Three times per day	Three times per day
3	State-of-Health data	Every 10 min and when it is switched on and off	Every 2h
4	UPS on/off	Every 10 min and when it is switched on and off	Every 2h
	Main power on/off	Every 10 min and when it is	Every 2h

5		switched on and off	
6	Auxiliary power	Every 10min and when it is switched on and off	Every 2 h
7	Meteorological data	Every 10min	Every 2 h
8	Indoor room temperature	Every 10min	Every 2 h
9	Indoor humidity	Every 10min	Every 2 h

Table 3. Technical Requirements

Requirement	Characteristics	Minimum requirements
1	Air flow	0.4 m^3 h^{-1}
2	Total volume of sample	10 m^3
3	Collection time	£ 24 h
4	Measurement time	£ 24 h
5	Time before reporting	£ 48 h
6	Reporting frequency	Daily
7	Isotopes measured	^{131m}Xe, ^{133m}Xe, ^{133}Xe, ^{135}Xe
8	Measurement mode	Beta-gamma coincidence or high resolution gamma spectroscopy
9	Minimum detectable concentration	1 mBq m^{-3} for ^{133}Xe

During the pre-shipment test the ARSA collected and measured atmospheric xenon continuously over the testing period with the exception of approximately 12 hours. This offline time was due to a severe storm (lightning, thunder, tornadoes) that tripped the manual main power circuit breaker. It was necessary to manually reset the breaker, located in the building fuse box, for the system to restart.

Data Performance

The data performance results are listed below and summarize the performance for the current configuration of the ARSA. The list numbers can be used as a reference to the requirements in Table 2. The data format for all transmitted messages is compliant with the specifications provided by the IDC in [IDC3.4.1r3] "Formats + Protocols for Messages".

1. The ARSA partial spectra functionality is provided on demand through a software menu item and when the system is stopped either manually or automatically.
2. Full spectra are recorded, saved, and transmitted by the ARSA three times per day. The data transmission frequency can be seen in Figure 1. Data was not sent on the 5th and 6th due to the power outage, partial spectra were recorded before the system automatically shut down on UPS power. Once the system is restarted, it must complete at least two collection cycles before a new sample is transferred to the radiation detector for counting. This produces a delay before new data is transmitted.
3. State-of-Health data were recorded at ten-minute intervals and transmitted to the IDC every two hours. The SOH refers to the readings from various sensors and systems on the ARSA that are used to monitor the performance and for diagnostics. The SOH data is structured as groups, or blocks, of data for organization. See [IDC 3.4.1r3] for more details.
4. The UPS status is recorded every ten minutes and is included in the #PowerSupply block of the State-of-Health messages.
5. The main power status is recorded at ten minute intervals and included in the #PowerSupply block of the State-of-Health messages.
6. Auxiliary power on the ARSA is only provided as battery power through the UPS. Once main power is lost, the system will operate for ten minutes before a command is sent to automatically shut the system down. The ARSA UPS battery is sufficient to power the system for three consecutive power losses without recharging, approximately 30 minutes.
7. Meteorological data is not provided by the ARSA system.

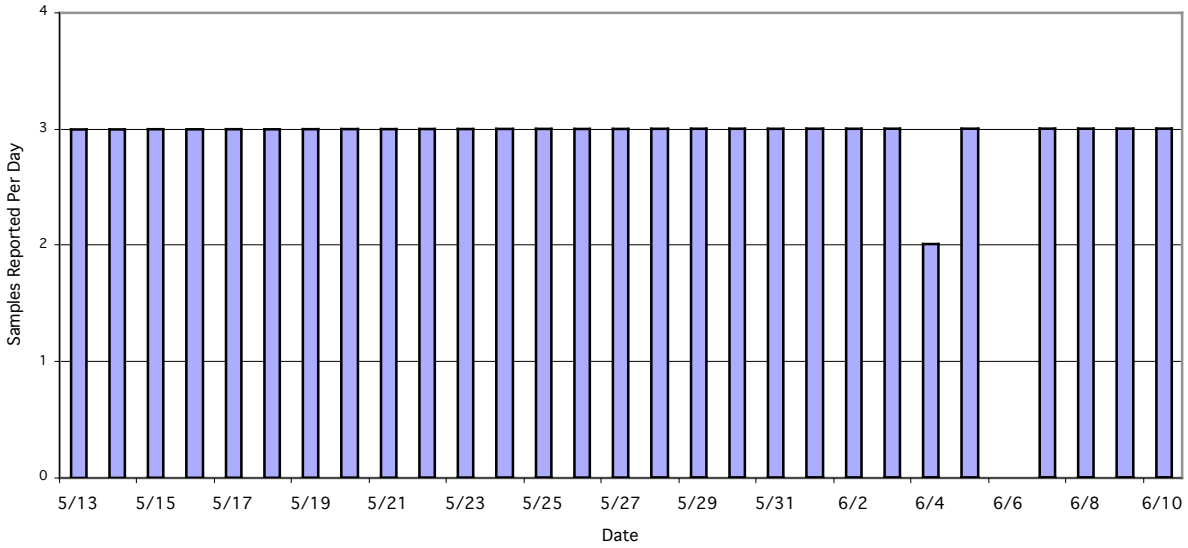

Figure 5 Complete sample measurement reporting frequency

8. The indoor room temperature sensor reading is recorded every ten minutes and reported every two hours in the #DetectorEnv block of the State-of-Health messages.
9. The indoor room humidity sensor reading is recorded every ten minutes and reported every two hours in the #DetectorEnv block of the State-of-Health messages.

Technical Performance

1. The total airflow produced by the system during the testing period can be seen in Figure 6. The mean value for the period is 5.94 $m^3 h^{-1}$ with a standard deviation of 0.004 $m^3 h^{-1}$.

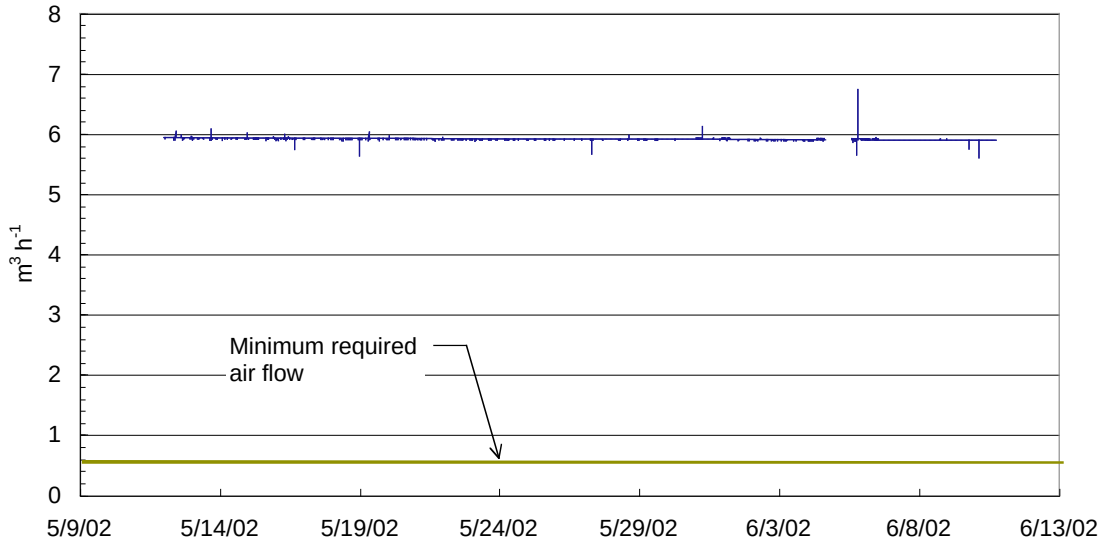

Figure 6. Total airflow through system

2. The total volume of each sample during the performance period is shown in Figure 7. The mean value is 17.63 m^3 with a standard deviation of 0.15 m^3.

3. The mean collection time for each sample is eight hours plus or minus ten minutes. The collection time was determined by calculating the amount of time a flow control valve was open for sample collection.
4. The mean measurement time for the gas samples during the performance test is 24.00 hours with a standard deviation of 0.01 hours. The mean measurement time for the gas background measurements is 7.36 hours with a standard deviation of 0.01 hours.
5. The time before reporting data was examined by comparing the dates a sample measurement acquisition stopped and the date the data was transmitted. In all cases the dates were the same indicating no more than 24 hours passed before the data was reported.
6. During the performance period, sample spectra were consistently reported three times per day with the exception of the 4th, 5th, and 6th of June. On the 4th of June two samples were reported before the system shut down. On the 5th of June the three samples being measured at the time the system was shutdown on the 5th were transmitted.
7. Figure 9 displays the spectra measured for a sample collected over the 7th and 8th of June. The abscissa and ordinate represent the beta and gamma measurement energy range that provides evidence of the beta-gamma coincidence measurement mode. The outlined boxes are indicative of the regions of interest for the four isotopes that are required to be measured (^{131m}Xe, ^{133m}Xe, ^{133}Xe, ^{135}Xe).
8. The minimum detectable concentration for the performance test period was consistently below the 1 mBq m^{-3} specification for ^{133}Xe. The mean values for each of the sample cells are reported in Table 4 with the data represented in Figure 8.

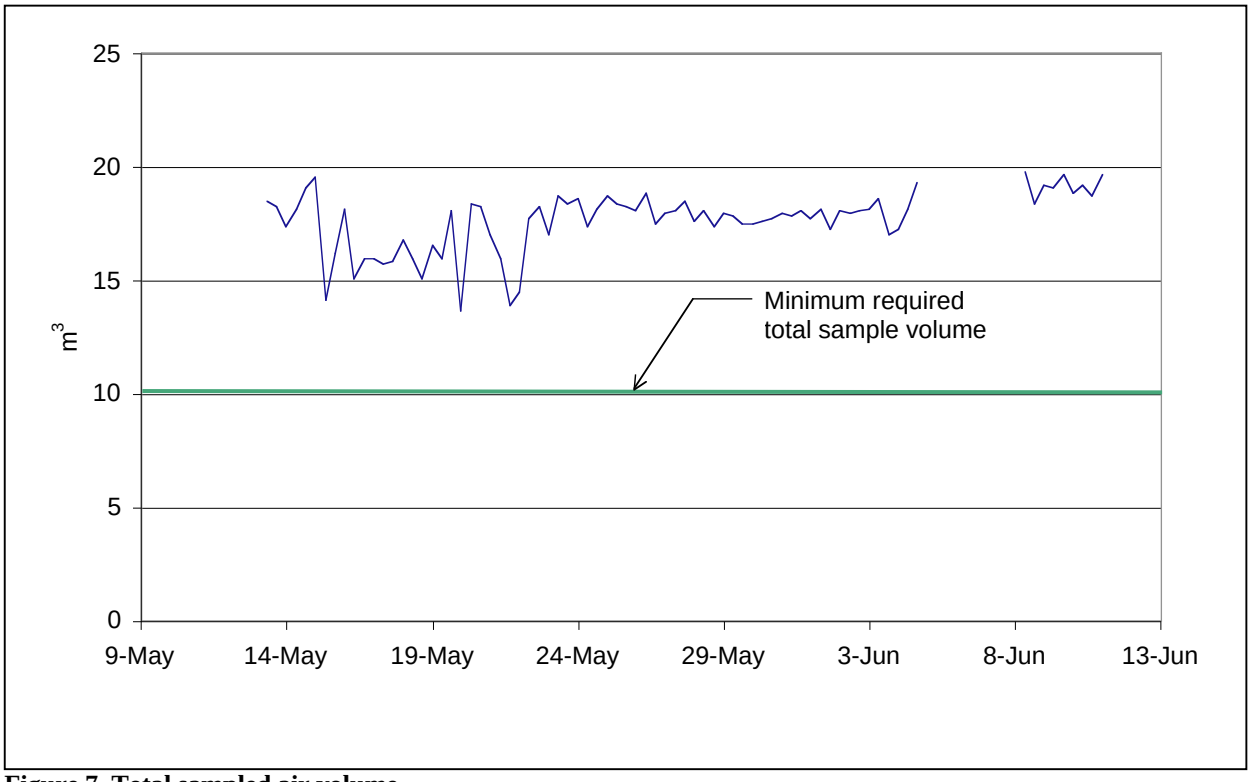

Figure 7. Total sampled air volume

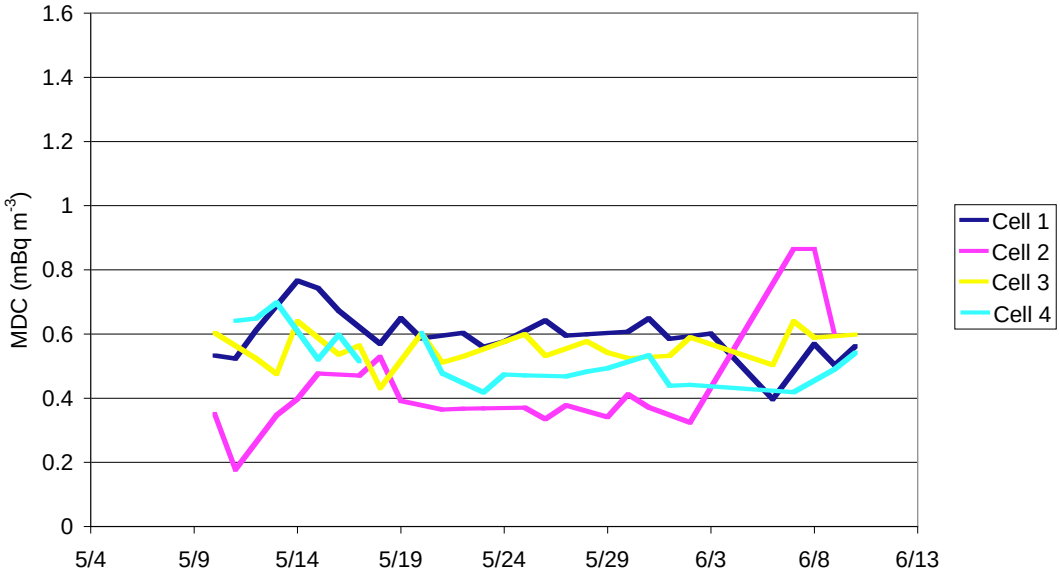

Figure 8. ^{133}**Xe MDC values for the individual detector cells**

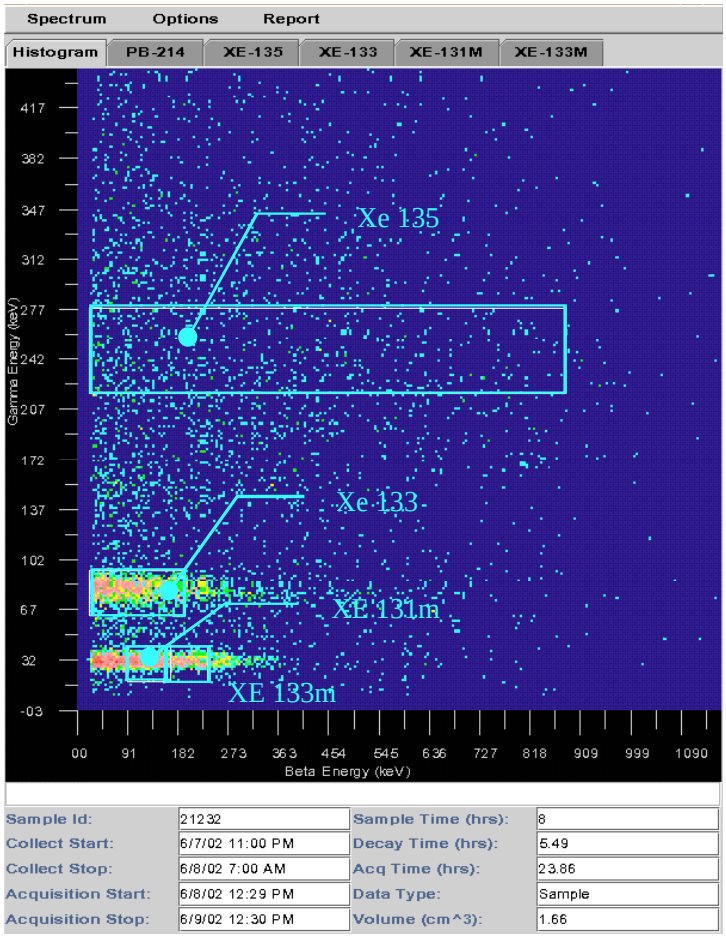

Figure 9. Sample beta-gamma coincidence data

Table 4. Mean MDC Values

Detector Cell	*Mean ^{133}Xe MDC mBq m^{-3}*	*Standard Deviation*
1	0.60	0.08
2	0.43	0.17
3	0.56	0.05
4	0.52	0.08

CONCLUSIONS AND RECOMENDATIONS

The status of the ARSA is that it is ready to be installed at the GERC; this should be accomplished by the end of the summer, 2002. At the time of writing this paper, a draft of the infrastructure upgrade report was received and the ARSA is being prepared for shipment to Guangzhou. Once the system arrives and is cleared by customs, the install team will leave for the site. The installation is scheduled for one month, which includes mechanically installing the system, setting up communications with the IDC, checking the calibration of the system, training the local operators, and preparing the system for a one month post installation performance test. After the post installation performance test is complete and the IDC approves the installation report, VSD will enter into a maintenance mode. The local operators will be required to perform the daily operation of the ARSA that includes inspection of the State-of-Health and spectral data as well as perform any required unscheduled maintenance. VSD will continue to support the ARSA by reviewing the data on an intermittent basis to ensure the proper performance of the machine and performing scheduled maintenance at six-month intervals.

RADIONUCLIDE SOFTWARE INSTALLATION AT THE US NATIONAL DATA CENTER

Daniel J. Robbins, Joel Rynes, and Kendra Foltz Biegalski

Veridian

Sponsored by Defense Threat Reduction Agency

Contract No. DTRA01-99-C-0031

ABSTRACT

Two recently developed radionuclide software systems developed through the US Defense Threat Reduction Agency will be installed at the US National Data Center. These are the Radionuclide Monitoring System (RMS) Release 3 Upgrade (R3U) software and the Forensic Event Tool (FET) application software. Development of the software, including the algorithms and the commercial off the shelf software (COTS) used are described.
The RMS software suite, which supports an automated data pipeline, has been developed by Veridian within the Center of Monitoring Research (CMR) for use the with International Monitoring System (IMS) data over the last five years. The most recent revision of the software suite, R3U, includes improvements and bug fixes to several tools to optimize high throughput radionuclide data management and analysis. The *rms_analyze* and *rms_xanalyze* tools automatically analyze gamma-ray spectra and three-dimensional (3-D) beta-gamma coincidence spectra, respectively. *Inspectra* provides the user the capability to interactively analyze spectra from gamma-ray detectors, while *Coriant* does the same with 3-D beta-gamma coincidence spectra. *Trendvue* provides graphical display of a detector's performance history, state of health, and station meteorology. The *Analyst Work Area* (AWA) displays station-operating conditions. *Multiple Analyst Review* (MAR) organizes the interactive review of data by a team of analysts and *Workflow* displays received data. The increase in functionality and other improvements made to each of these tools and the supporting database as part of the R3U is described in detail.

The RMS software suite was enhanced with Cascade Summing Correction (CSC) software. Multiple gamma-rays are sometimes emitted per decay and can be measured simultaneously in the detector. This effect can lead to inaccurate radionuclide activity concentrations (over a factor of two in some cases). The CSC software requires the detector to have a total efficiency calibration. Because this calibration is not typically performed at the radionuclide stations, the Monte Carlo N-Particle program was used to model the total efficiency of typical high-purity gamma-ray detectors.

The FET software suite includes the *Nuclear Sources and Assets Database – Geographical Information System* (NUSAD - GIS) as well as the *Radionuclide Ratio Analysis Tool* (RRAT). NUSAD is a special purpose database, which includes all known potential sources of fission products that might be detected by environmental atmospheric sampling along with the known monitoring assets that can detect fission products in the atmosphere. The NUSAD – GIS incorporates a geographical information display in which NUSAD spatial data are converted to "shapefiles" and are viewable by ESRI compatible products such as ArcView. The RRAT is an analytical tool used for evaluating the concentration ratios of radioactive fission products in environmental samples. Analysis of these ratios via the RRAT can be used to determine possible sources of the measured radionuclides.

OBJECTIVE

This paper describes Version 5 of the Radionuclide Monitoring System (RMS) software developed at the Center for Monitoring Research (CMR) and is scheduled to be installed at the United States National Data Center (NDC) in the summer of 2002. RMS 5.0 includes the RMS Release 3 Upgrade (R3U) software that was delivered to the International Data Centre (IDC) in December 2001 and is scheduled to be installed at the Russian Federation NDC during the summer of 2002; several significant enhancements to the baseline RMS software including the addition of Cascade Summing Correction (CSC) software; and the addition of Forensic Event Tools (FET) to the RMS suite. The FET software suite includes the *Radionuclide Ratio Analysis Tool* (RRAT) and the *Nuclear Sources and Assets Database* (NUSAD). The US NDC currently uses RMS Release 3 (R3) software. In the following sections the new components of the RMS software will be described and the differences between the R3U and R3 software will be summarized. To keep this paper at a reasonable length, the functions of the software will be discussed only at a high level.

RESEARCH ACCOMPLISHED

Forensic Event Toolbox

The Forensic Event Toolbox (FET) currently consists of two software applications, the *Radionuclide Ratio Analysis Tool* (RRAT) and the *Nuclear Sources and Assets Database* (NUSAD) *Geographic Information System* (GIS). Both applications continue to be developed. They are described in turn.

Radionuclide Ratio Analysis Tool

Background

It was plain several years ago that a decisive method for proving that radioactive debris emanates from a nuclear detonation was needed. Anthropogenic radionuclides in the atmosphere can originate from many sources including a controlled or accidental release at a nuclear reactor or a fuel reprocessing facility. The rate of production for various fission products is dependent on the fissioning species (either ^{235}U, ^{239}Pu or other fissionable isotope) and the energy of the neutron that initiates the fission. Nearly all nuclear reactors operate with neutron energies that follow a Maxwellian distribution having a mean at the energy corresponding to the operating temperature of the reactor, about 0.025 eV. They also produce fissions almost exclusively in ^{235}U. Nuclear weapons, on the other hand, rarely have any significant moderation so that the energy distribution of the neutrons is nearly the same as that for the energy distribution at the time of fission. This distribution is non-Maxwellian, has a mean energy of about 2 MeV and has peak energy of 6 MeV. The fissioning species may be either ^{235}U or ^{239}Pu. In addition, the fissions in a nuclear detonation all occur almost instantly, while a nuclear reactor produces fission products over a lengthy period up to over a year long. Many of the fission products decay away or are transfigured by the absorption of neutrons. The result of these processes is that the mix of fission products that come from a nuclear weapon are decidedly different from the mix that comes from a nuclear reactor.

Nuclear scientists working at the CMR looked for a way to use the difference in fission product inventories to distinguish between radioactive debris from a nuclear reactor and that from a nuclear detonation. The method they chose was to compare the ratios of concentration of several prominent fission product pairs. The ratios of these fission product pairs are strongly indicative of the source, reactor or bomb, of the fission products.

Analytical Approach

From the enormous list of fission products available, 25 were chosen as nuclides of interest (NOI) because they had moderate half-lives (several hours to several years), high specific activity and relatively large fission product yields. This set of attributes makes them the most likely fission products to be detected following an attempted clandestine nuclear test. From these fission products eight pairs were selected to ratio. The radio-xenon pairs were selected because they were made up of the three xenon isotopes more likely to be detected and measured. The particulate fission product pairs were selected following the suggestion of Doctor Yehuda Finkelstein[1]

Table 1 Nuclides of Interest and Default Ratios for the Radionuclide Ratio Analysis Tool.

Nuclides of Interest		Default Ratios
Sr-89	Xe-131	Xe-135/Xe-133
Y-91	Xe-133m	Xe-133m/Xe-133
Y-93	Xe-133	Mo-99/Nd-147
Zr-95	Xe-135	Ce-143/Zr-95
Zr-97	Cs-137	Nd-147/Ce-141
Mo-99	Ba-140	Nd-147/Zr-95
Ru-103	La-140	Ce-143/Nd-147
Rh-105	Ce-141	Mo-99/Ce-141
Sn-125m	Ce-143	
Te-127	Pr-143	
Sb-128	Nd-147	
Te-129	Pm-149	

The total activity of each nuclide of interest was calculated at the end of irradiation for a pressurized water reactor using ORIGEN/SCALE[2] for two operating scenarios, a normal run between refueling of 365 days and a run ended prematurely after 3 days at full power. The total activity of each nuclide was also calculated using the England and Rider Fission Product Tables[3] for each ^{235}U and ^{239}Pu exposed to fission spectrum neutrons. These values were taken to be representative of the relative production of fission products produced in basic nuclear weapons using each of the two species as fuel.

An algorithm, based on the Bateman decay equation, was written and encoded to decay each fission product species from the time of release, specified by the user, to a future collection time, also specified by the user. It is postulated that in use the time of release will come from SHI information or another source indicating that a suspect nuclear detonation has occurred. The collection time will come from the collection stop time in the Radionuclide Monitoring System database for samples that the user is trying to determine a source for.

Another algorithm was written to compare the activity ratios of the sample to the activity ratios of the possible sources: reactor long operation, reactor short operation, uranium fueled bomb and plutonium fueled bomb. The algorithm selects the scenario ratio set with greatest similarity to the sample ratio set and identifies that scenario as the most likely source of the debris in the sample. This algorithm takes the ratio of each selected pair of nuclides in each sample and divides it by the activity concentration ratio of the same pair of nuclides from each scenario, per Equation 1. It takes the absolute value of the natural log of this ratio. The result is called the Disparity. A perfect fit will result in a ratio of 1.0 and a natural log of zero, so the value closer to zero is chosen.

$$Disparity = \left|\ln\left(R_{sample} / R_{scenario}\right)\right| \qquad \textbf{Equation 1}$$

Data Entry

The user enters the initial information on the **Sample Id Tab**, shown in Figure 1. After selecting an Event Date and Hour and the number of days to extend the query, the user selects the station codes of the stations likely to have collected samples during the period of interest, then presses the "Query Samples" button. The tool populates the "Sample Ids of Interest" window with all samples collected at the selected stations during the period of interest. The user can then review the summary of radionuclides detected in the samples and decide which to keep for analysis.

Next the user selects the **NOI Tab**. The user must select one reactor scenario and one weapon scenario for the tool to compare the sample results to. The user may accept the default NOI Pair List or delete any or all of them. The user may also select any nuclide from the list of NOI to use as a numerator and any other nuclide from the list as a denominator in a custom ratio pair. The user then selects "Submit Config" to launch the analysis. The user will then select the **Reports Tab** or the **Plots Tab** to view the results

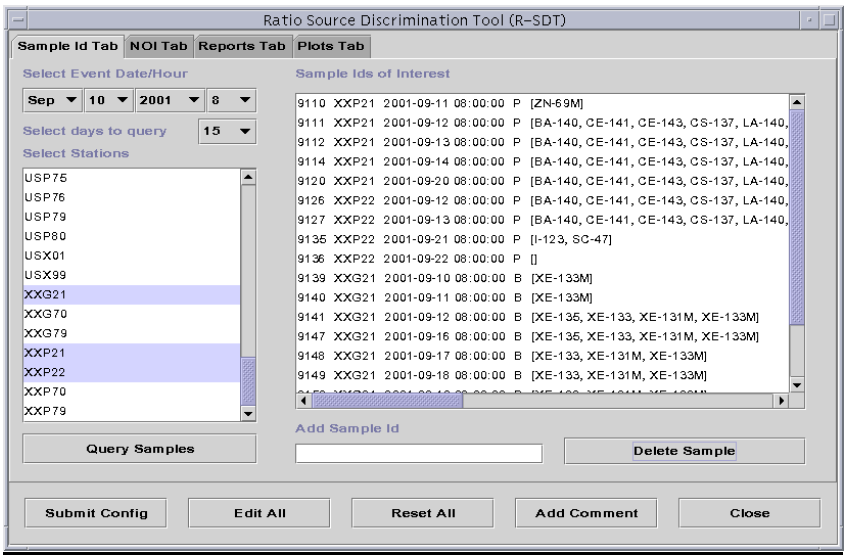

Figure 1 Sample Id Tab from the Radionuclide Ratio Analysis Tool.

Result Reporting

In the **Reports Tab**, the tool averages the results of Equation 1 over all values or separates the results by ratio pair, sample, or collection site at the user's discretion. The overall average minimizes the uncertainty in the results. Allowing the results to be viewed and averaged by ratio pair, sample and collection site give the user tools to identify the source of errant data and to selectively reject that data to improve the overall certainty of the results.
In addition to sorting and averaging the results, the tool permits plotting of the ratios by NOI pair in the **Plots Tab**, as shown in Figure 2. The user selects the NOI pair for plotting and then selects "Graph Pair." The tool will plot the ratio of the selected NOI pair over time for each of the scenarios selected on the **NOI Tab** and will plot the sample ratios for the same NOI pair. It will do a correlation of the sample ratios against each of the scenarios and will list the coefficient of determination, the square of the correlation coefficient, for each case. This provides additional analytical information to the user as well as a visual presentation of the analytical results.

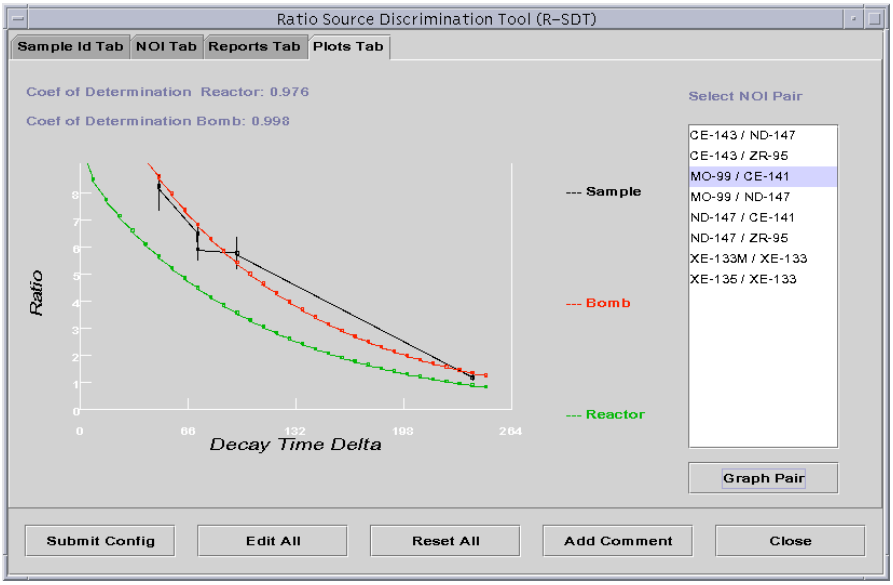

Figure 2 Plots Tab from the Radionuclide Ratio Analysis Tool.

Future Work

Two major efforts are needed to improve the capabilities of the RRAT, one in the baseline data and one in the analytical tools.

Currently there are only two reactor scenarios available, a normal duration run and a very short period of operation of a pressurized water reactor. Boiling water reactors would probably not produce significantly different results for the same length of operating period. However, some reactors, in particular the Canadian Deuterium Reactor or CANDU and the Russian designed RBMK, refuel online so that the period of irradiation for the fuel may be quite short and the initial fission product activity ratios may be quite different from light water reactors. Also, some reactors, in particular fast breeder reactors, have a much more energetic neutron spectrum than light water reactors and this probably results in initial fission product activity ratios that are significantly different. Both type of reactors need to be modeled using ORIGEN and the scenarios need to be added to the options in the RRAT.

Currently, the RRAT performs a crude averaging of the ratio of ratios of NOIs. This is augmented by correlation of selected ratios over time. However, improved analytical techniques are desired. One method that shows high promise is multi-variant analysis. This will entail expanding the correlation approach to comparing several NOI pair ratios to each other. This appears to be possible only by using a common denominator and an effort to develop an algorithm to perform this analysis should be a goal for the near future.

Nuclear Assets and Sources Database

Database

The *Nuclear Assets and Sources Database* (NUSAD) is an Oracle-based database that contains information on sources of nuclear debris in the environment and the assets that might detect that debris. It has been described in detail in a previous SRR[4]. A source is any facility that could potentially release radionuclides and an asset is any device that can detect radionuclides. These data can be used to help determine the source of radionuclides found in data at the NDC, or to identify additional assets that might provide data confirming or refuting data on file.

NUSAD contains three broad classes of data: assets, sources and geographical. Information on each reference is included in the database, including the title, publication details, author, and how the data were used in the NUSAD. The NUSAD database schema contains approximately 40 database tables and is available upon request. The NUSAD Geographical Display Tool has been upgraded to two new tools.

Data Entering Tool

NUSAD data are stored on an Oracle database. The *Data Entering Tool* (DET) was created to provide easy access to the NUSAD data, without requiring users to have substantial knowledge of SQL and the NUSAD schema. The DET includes a graphic user interface (GUI) written with Java. It provides an interface that permits authorized users to easily enter, delete, modify, and view data. The NUSAD DET allows data to be accessed either through a browser or editor window.

Geographical Information System

To aid in future visualization, the NUSAD – *Geographical Information System* (NUSAD – GIS) was provided to the NDC. Software has been installed that converts NUSAD spatial data to *shapefiles*. *Shapefiles* are the file format that can be viewed by commercial-off-the-shelf (COTS) software from the ESRI Corporation called ARCView, ARCIMS, and ARCExplorer. The NUSAD – GIS comprises two programs, the first collects data from a NUSAD table or view and writes these data to a text file stored on the file server. The second program reads this text file and creates the *shapefile.*

These additions to the NUSAD greatly enhance the potential to visualize, interpret and present analyses of data from environmental collection of fission and activation products. In addition, the visualization tools aid the analyses themselves.

Radionuclide Monitoring System, Release 3 Upgrade

The Radionuclide Monitoring System (RMS) Release 3 Upgrade (R3U) includes several software tools to aid analysts in processing the large throughput of data from global arrays of environmental radionuclide sensors and to aid managers in monitoring the performance of automated equipment. The software has been described elsewhere[5], so this paper will describe enhancements to the existing suite.

Rms_analyze

Rms_analyze launches automatically when the data import routine recognizes an incoming pulse-height data message, although it can be called to execute manually by a user. It uses the data in the Radionuclide Monitoring System (RMS) Database. After receiving spectral data, the program locates peaks, determines peak area, and updates the calibration metrics of the detector. Following the calibration update, it performs a second peak location and peak area measurement. *Rms_analyze* then identifies and quantifies radionuclide activity concentrations, calculates the minimum detectable concentrations (MDC) for nuclides of interest, calculates parent, daughter activity relationships and performs several quality control tests. The output can then be used by automated routines to prioritize the sample for analyst review, notify analysts, notify subscribers of unusual events and send out an Automated Radionuclide Report (ARR).

Two improvements have been made to *rms_analyze*:

- The warning and error messages have been enhanced.
- The on-line help manual has been enhanced.
- Bug fixes were carried out.
-

Rms_xanalyze

Rms_xanalyze[6] functions similarly to *rms_analyze*, except that it operates on 3-D beta-gamma coincidence spectral data from noble gas stations. *Rms_xanalyze* determines net counts in predefined regions of interest (it is consequently very dependent on reported calibration information), identifies the presence of ^{131m}Xe, ^{133}Xe, ^{133m}Xe, ^{135}Xe and radon daughters by comparing net counts to the counting limit, and calculates activity concentrations and MDCs for the identified radioxenon isotopes. The output is used the same way as the output from *rms_analyze*.
The following enhancements have been made to *rms_xanalyze*:

- A reanalysis capability has been added through the command line.
- An automatic control check on the xenon sample volume has been added.
- Linear and quadratic energy versus channel regressions (ECR) have been made available for analysis.
- The timing of reading from and writing to the database has been improved.
- The interference counts algorithm has been modified so that all nuclides with a potential to interfere with counting are now included, with their associated uncertainties, in calculating the corrected activity of the nuclide of interest.

Inspectra

Like the programs above, *Inspectra* has been described in detail previously[5]. It provides a means for the user to manually evaluate sample pulse-height spectra and override the automated decisions of *rms_analyze*.
The following enhancements were added to Inspectra for R3U:

- The ability to edit general comments and support for a predefined list of general comments were added.
- The capability to undo the remove nuclide command was provided.
- The “WP224” label was changed to NOI (Nuclide of Interest).
- Peak search sensitivity vs. peak significance scatter plot option was added.
- 3-D beta-gamma coincidence samples are now filtered from the **Open Sample Dialog**
- The Role indicator was added to the main *Inspectra* window
- The display of real half-lives and half-lives used by *rms_analyze* in the **Nuclide Library Dialog** was added so that the user is aware of artificialities created for processing some natural radionuclides. It was found to be necessary to create these artificial half-lives to avoid over-correction for decay and consequent over correction for background counts.

- The capability to perform sample reprocessing using resolution versus energy regression (RER) pair data was added.
- Cross-hairs on graphs to facilitate data interpretation were added to the display.
- New timeliness flags are displayed (particulate samples only).
- Several bugs were eliminated.
-

Coriant

Coriant[6] provides for the manual review of 3-D beta-gamma spectra from noble gas stations. The following enhancements have been added to *Coriant* in the Release 3 Upgrade:

- A new **Reanalysis Dialog** facilitates modification of:
  - Number of Compton background channels used in net region of interest (ROI) area determination.
  - ECR coefficients.
  - Turn on/off detector and gas background subtractions.
- Graph coordinates are now displayed in **Histogram Tab**.
- ROIs in 2-D beta-gamma spectra are now highlighted
- The *Multiple Analyst Review* (MAR) Tool has been linked to *Coriant*:
  - Release without categorization option has been added.
  - Permissions are now checked for adding comments and releasing spectra.
- General improvements in data display were made to the **Isotope Tab Dialog** and the **ROI Dialog**.
- Bugs were eliminated.
-

Trendvue

Trendvue has been described in detail in reference 5. The application allows the user to visualize various parameters of radionuclide sensors over time in order to recognize trend development. The following enhancements were added to Trendvue for the RMS R3U:

- The ability to create log plots was added.
- The ability to plot status of health (SOH) data was added.
- Swing COTS was added to provide a capability to create wind plots.
- The ability to plot larger number on xy-Graph was provided.
- Updated y-axis hash mark function was added.
- The ability to query on released samples only for some parameters was added.
-

Analyst Work Area

The *Analyst Work Area* (AWA) provides the user the ability to graphically view the status of reports from radionuclide sensors in the IMS. It has been described in reference 5. No changes were made to the AWA for RMS Release 3 upgrade.

Multiple Analyst Review

The *Multiple Analyst Review* (MAR) is described in reference 5. The tool permits a user to manage the assignment of data to analysts to review. The following enhancements have been added to the MAR for Release 3 Upgrade:

- The ability to add, delete, and modify users' default roles has been provided.
- The MAR was integrated into the database;
  - The assignment of permissions for the MAR and the database (controls database read and write access) were combined.
  - The creation of roles for the MAR and the database were combined.
- An Exit button was added.

Rms_categorize

Rms_categorize[5] is used to automatically prioritize both particulate and noble gas samples based on the amount and types of radionuclides identified. The results of the prioritization step are stored in the database and alert messages

are sent to subscribers based on the results. Previously, the Exponentially Weighted Moving Average (EWMA) method was the only prioritization algorithm available. In R3U two separate algorithms on a per station and a per nuclide basis can now be chosen to prioritize samples. These are the EWMA and the Recent Distribution Categorization (RDC) algorithms.

The RDC algorithm works by comparing the current activity measurement with the last ten activity measurements for that nuclide at that station. If the difference between the current measurement and the mean measurement is greater than a configurable number of standard deviations (default two), then the sample is anomalous. In addition, if there are not ten previous measurements or if the nuclide has not been detected at least three times in the past thirty days at that station, then the sample is anomalous. The RDC algorithm, unlike the EWMA algorithm, is not dependent on the order in which the samples are received. The RDC algorithm is typically better for radionuclides detected on an occasional basis whereas the EWMA algorithm typically is better for frequently detected radionuclides.

Baseline Software Enhancements

Cascade Summing Correction

One of the difficulties in measuring radioisotopes with gamma ray detection is cascade summing. Typically, nuclides of the isotope being counted decay to the excited state of another isotope. This excited state quickly decays to the ground state by the emission of gamma rays. Many of the radioisotopes that are measured emit multiple gamma rays of different energy. On occasion, two or more of these gamma rays enter the detector nearly simultaneously and are counted as one gamma ray having an energy equivalent to the sum of the energies of all the gamma rays.

A good example is ^{60}Co as shown in Figure 3. Cobalt-60 decays to ^{60}Ni by the emission of a beta particle. The excited ^{60}Ni nucleus emits two principle gamma rays to reach its ground state, one at 1.173 MeV and one at 1.332 MeV. Usually these gamma rays will be counted separately, but sometimes they are counted as one gamma ray with energy of 2.505 MeV resulting in an erroneously high count of photons at that energy and an erroneously low count of photons at the other two energies.

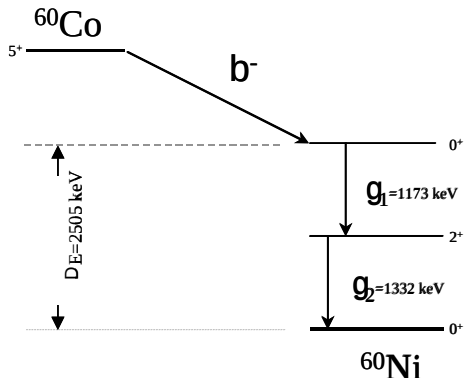

Figure 3 Decay scheme of ^{60}Co.

The inaccuracies introduced by coincidence summing, as much as a factor of two, carry over to cause inaccuracies in other tools such as the RRAT. It is important that corrections are calculated and a more accurate value for the activities of these radioisotopes be found. The cascade summing correction (CSC) was developed to do this.

The CSC was integrated into the radionuclide analysis software (*rms_analyze*) so that it executes after the nuclides are identified. It requires decay specific correction coefficients and both the peak and total detector efficiency. The decay specific coefficients were obtained from the Evaluated Nuclear Structure Data File (ENSDF). The RMS current formats and protocols allow the total efficiency to be stored in the sample data file. However, because this calibration is not typically performed at the stations, the Monte Carlo N-Particle (MCNP) code, developed by Oak Ridge National Laboratory, was used to model total efficiency for typical detector systems.

The activity correction factor is, therefore, both decay and detector specific. Table 2 below shows the activity correction factors for a typical HPGe detector for the key-line activity of all fission and activation products in the CMR radionuclide library that are subject to cascade summing effects. The isotopes with the largest and smallest correction coefficients are highlighted in the table. These correction coefficients do not include x-ray effects. Consideration should be given to researching the impact of x-rays on counting accuracy and entering correction factors for them in the analysis software if their impact is significant.

Table 2 CSC ratios for activation and fission products in R3U library.

Nuclide	Type	Halflife	Ratio	Nuclide	Type	Halflife	Ratio
AG-106M	activation	8.460 D	1.794	K-42	activation	12.360 H	1.004
AG-108M	activation	127.000 Y	1.507	LA-140	fission (p)	1.678 D	1.263
AG-110M	activation	249.760 D	1.521	MO-99	fission (p)	2.748 D	1.268
AG-111	fission (p)	7.450 D	0.994	NA-24	activation	14.959 H	1.123
AS-74	activation	17.770 D	1.000	ND-147	fission (p)	10.980 D	1.012
AS-76	activation	1.097 D	0.850	NP-239	activation	2.357 D	1.017
AU-196	activation	6.183 D	1.053	PB-203	activation	2.161 D	1.007
AU-196M	activation	9.700 H	1.663	PD-112	fission (p)	21.030 H	1.101
AU-198	activation	2.694 D	1.001	PM-149	fission (p)	2.212 D	1.000
BA-133	activation	10.520 Y	1.137	PM-151	fission (p)	1.183 D	0.866
BA-136M	fission (p)	0.308 S	1.533	PR-144	fission (p)	17.280 M	1.033
BA-140	fission (p)	12.752 D	1.073	RB-84	activation	32.770 D	1.001
BR-77	activation	2.377 D	1.018	RH-102	activation	207.000 D	1.072
CD-115M	fission (p)	44.600 D	0.996	RH-105	fission (p)	1.473 D	1.000
CE-143	fission (p)	1.377 D	1.147	RU-103	fission (p)	39.260 D	0.999
CE-144	fission (p)	284.894 D	0.941	RU-106	fission (p)	1.023 Y	1.208
CO-57	activation	271.800 D	1.025	SB-120	activation	5.760 D	2.077
CO-58	activation	70.820 D	1.216	SB-122	activation	2.700 D	1.009
CO-60	activation	5.271 Y	1.170	SB-124	activation	60.200 D	1.144
CR-51	activation	27.702 D	1.002	SB-125	fission (p)	2.730 Y	1.080
CS-132	activation	6.479 D	1.025	SB-126	fission (p)	12.400 D	2.161
CS-134	activation	2.062 Y	1.245	SB-127	fission (p)	3.850 D	1.005
CS-136	fission (p)	13.160 D	1.452	SB-128	fission (p)	9.010 H	2.631
EU-152	activation	13.542 Y	1.218	SC-46	activation	83.810 D	1.181
EU-152M	activation	9.274 H	1.236	SE-75	activation	119.779 D	1.228
EU-155	fission (p)	4.680 Y	0.981	SM-153	fission (p)	1.928 D	1.057
EU-156	fission (p)	15.190 D	1.175	SM-156	fission (p)	9.400 H	1.061
EU-157	fission (p)	15.180 H	1.112	SN-125	fission (p)	9.640 D	1.175
FE-59	activation	44.496 D	1.012	SR-91	fission (p)	9.630 H	0.996
GA-72	activation	14.100 H	1.210	TE-129	fission (p)	1.160 H	1.051
HG-203	activation	46.612 D	1.007	TE-129M	fission (p)	33.600 D	1.000
I-123	activation	13.200 H	1.003	TE-131M	fission (p)	1.250 D	1.388
I-130	fission (p)	12.360 H	1.617	TE-132	fission (p)	3.204 D	1.112
I-131	fission (p)	8.040 D	0.973	TM-168	activation	93.100 D	1.704
I-132	fission (p)	2.295 H	1.453	U-237	activation	6.750 D	1.241
I-133	fission (p)	20.800 H	1.006	W-187	activation	23.720 H	0.932
I-135	fission (p)	6.570 H	1.030	Y-88	activation	106.650 D	1.169
IR-190	activation	11.780 D	1.878	Y-93	fission (p)	10.100 H	1.054
IR-192	activation	73.831 D	1.325	ZN-65	activation	243.900 D	1.066

Trendvue

Further improvements were made to *Trendvue* in addition to the enhancements included in the R3U software. These enhancements include:

- A new plot was added to the pull down menu that plots nuclide concentrations reported in the IDC-generated Automatic Radionuclide Report (ARR) and Reviewed Radionuclide Report (RRR).
- A second Y-axis was added to the *Trendvue* graph. Right-clicking the plot legend opens a dialog box that allows the user to choose the axis on which the graph will be plotted.
- A pop-up dialog box has been added that allows users to specify the minimum and maximum values for the X-axis and both Y-axes.
- Users are now able to choose the format in which the time and date are displayed in *Trendvue*.
- *Trendvue* can now plot data from flat files. The software uses description files that have information about the number of columns and column names for parsing flat files. The description files give *Trendvue* the flexibility to handle new formats in the future.
- Right-clicking the mouse on the legend of a plot gives the user the ability to change the color of the plot.

CONCLUSIONS AND RECOMMENDATIONS

The software suites described are effective and robust. It is recommended that the RMS 5.0 software enter into operational use at the NDC and that work continue on developing further capabilities and applications of the RMS software especially in the area of the newly developed RRAT.

REFERENCES

[1] Fission Product Isotopic Activity Ratios as Event Characterization Tools, Draft Technical Report prepared for the Provisional Technical Secretariat, Y. Finkelstein, February 2000.

[2] Oak Ridge Isotope Generation/Standardized Computer Analyses for Licensing Evaluation, Version 4.4a, Oak Ridge National Laboratory – Radiation Safety Information Computational Center, 2000.

[3] Yields Evaluated and Compiled for Los Alamos report LA-UR-94-3106 (ENDF-349), T.R. England and B.F. Rider October, 1994

[4] Nuclear Sources and Assets Database (NUSAD) Development, J. C. Rynes and D. Leussing, 23rd Annual DoD/DOE Seismic Research Symposium Proceedings, 2001

[5] IDC Processing of Radionuclide Data, Documentation for the International Data Center, K.M.F. Biegalski and H. Magyar, December 2001.

[6] Automatic And Interactive Analysis Software For Beta-Gamma Coincidence Systems Used In CTBT Monitoring, J. Rynes, K.M.F. Biegalski, and P. Donohoe, 22nd Annual DoD/DOE Seismic Research Symposium Proceedings, 2000

RADIONUCLIDE DETECTION THRESHOLD IN THE LOP NOR REGION

Daniel J. Robbins, Joel Rynes, and Michael Eisenbrey

Veridian

Sponsored by Defense Threat Reduction Agency

Contract No. DTRA01-99-C-0031

ABSTRACT

A study was conducted to explore the capability to estimate the threshold for measuring radionuclides escaping from a hypothetical nuclear test within the boundaries of the nuclear test site near Lop Nor, China. A point near the geographic center of the test site, 41.6º north by 86.6º east, was chosen as the hypothetical point of release. The Hybrid Single-Particle Lagrangian Integrated Transport Model (HYSPLIT) was used to model airflow from that point outward for several days for start dates on the first and sixteenth of each calendar month in 2001. HYSPLIT results were compared to Operational Multi-scale Environment Model with Grid Adaptivity (OMEGA). The dilution of the air masses from the site at various contour intervals was calculated and combined with the stipulated minimum detectable concentrations of xenon-135 and barium-140 to produce estimates of the minimum detectable yield (MDY). The minimum estimate of the MDY for each planned sampling location in the International Monitoring System (IMS) in the vicinity of Lop Nor was obtained to provide an overall assessment of the environmental sampling array. Because the fraction of fission products that escape to the environment from a nuclear test is an intuitive estimate, the MDY is only accurate to order of magnitude, at best, but can be used as a figure-of-merit for comparison purposes. The fraction of particulates that escape to the environment was estimated as 0.1 percent. The fraction of noble gasses that escape to the environment was estimated as 10 percent. The MDY ranged from less than 0.1 kiloton to more than 1000 kilotons, depending on location, elapsed time, and the fission product measured. Using the assumptions described above, the planned IMS particulate station array was found to be capable of detecting debris from low yield nuclear explosions during every period analyzed.

OBJECTIVE

Estimate the minimum detectable yield (MDY) for a hypothetical nuclear test at Lop Nor given that 10 percent of the noble gas fission products and 0.1 percent of the particulate fission products escape the test cavity and that the planned international monitoring system sensors are in place and achieving the minimum detectable concentration (MDC) specified in the Comprehensive Nuclear-Test-Ban Treaty (CTBT), 30 µBq for ^{140}Ba and 1 mBq for ^{135}Xe.

RESEARCH ACCOMPLISHED

Background and Assumptions

It is well known that nuclear explosions produce fission products and that the mix of fission products, the relative amounts of various radionuclides, is peculiar to particular fission processes. Fission products found in the environment, therefore, can be attributed to a nuclear explosion or other nuclear fission processes with a high degree of confidence.

Fission products released into the environment have readily detected nuclear explosions that have occurred in the atmosphere. The first nuclear explosion by a country other than the United States was detected by the collection of radioactive fission products thousands of miles downwind of the test site. However, a nuclear device buried deeply enough underground to avoid making a crater will release many fewer fission products into the atmosphere.

Finding information on fission products collected following underground nuclear explosions is difficult. The United States has conducted a robust program that analyzes air samples for the presence of fission products; however, the results are classified. Other countries have also collected environmental samples and analyzed them for fission products, but data from underground nuclear explosions is sparse. This creates severe difficulties in estimating the fraction of fission products that escape the test cavity in an underground explosion. In addition, the conditions for any particular underground nuclear explosion can vary widely and affect the amount of fission products that reach the atmosphere by orders of magnitude.

Fission products in the form of noble gasses, such as xenon, are highly mobile and not chemically reactive. They can reasonably be expected to percolate through porous earth and escape the cavity of an underground nuclear explosion. Particulate fission products are less likely to escape the test cavity. The fireball will release energy to the surrounding material and rapidly cool. If the hot gasses are trapped underground long enough to cool, the fission products that are solid at environmental temperatures will precipitate and tend to collect on the walls of the test cavity. They are likely to escape to the environment only if they remain gaseous long enough to pass through the porous ground or if the explosion ejects the soil overburden resulting in a crater. Xenon-135 was used to represent noble gas fission products because it is strongly indicative of a recent nuclear explosion. Barium-140 was used to represent particulates because it is used as a standard for assessing detector performance.

The Nuclear Treaty Programs Office selected the known Chinese nuclear test site near Lop Nor as the area of interest for our analysis. No historic, empirical data on which to base estimates of the fraction of fission products that would escape an underground test cavity were available. Therefore, the fraction of fission products that escape to the environment from a particular test is an intuitive estimate. The value used for xenon, ten percent, is thought to be conservative, but the value used for particulates, 0.1 percent, is probably quite high. A device deeply buried and properly stemmed might exceed the MDY estimated in this paper significantly and go undetected, depending on the fraction of the fission products that actually escape to the environment. That is, if the device is properly buried and stemmed, no particulate will escape. If the testing agency buries the device too shallowly or uses improper stemming techniques, then heavy venting will occur and a large fraction of the particulate fission products will escape to the environment. Therefore, the MDY is accurate to order of magnitude, at best, and should be used only as a figure of merit for comparison purposes. The detection limits of the radioisotopes were obtained by using the CTBT stipulated values, 30 µBq for ^{140}Ba and 1 mBq for ^{135}Xe.

Atmospheric Transport

Seismologists at the Center for Monitoring Research (CMR) selected a point near the geographic center of the Chinese test site near Lop Nor as the location to focus their efforts at improving analysis. For consistency, the nuclear scientists chose the same point. This point, 41.6º north by 86.6º east, was chosen as the point of release for a hypothetical plume of debris from an underground nuclear test. HYSPLIT[1] was chosen as the application for modeling atmospheric transport from the test site to planned IMS sampler locations. It was compared to OMEGA[2], a more precise atmospheric transport model. HYSPLIT was used for the bulk of the analysis because it is easier to operate and produces results in a fraction of the time that OMEGA requires.

Model plumes were started at 0600 Universal Time Coordinated (UTC) on the first and 16th day of each calendar month in 2001. Default values were used for all HYSPLIT options except pollutant release rate. The default pollutant release rate in HYSPLIT is one unit in one hour and this was thought to be not representative of a plume release from an underground nuclear explosion. The release rate was chosen as 0.0833 units per hour for 12 hours, so that one unit was released over 12 hours at a constant rate. It is not known whether this approximately represents a typical plume from an underground nuclear explosion. However, it was deemed to be more representative than the default value.

Each run was continued for ten days or 240 hours. HYSPLIT provided contour plots of the average, normalized pollutant concentration every 12 hours. These concentration contours were translated into MDY contours using the algorithm described under Minimum Detectable Yield.

International Monitoring System (IMS) Sensor Array

Particulate and gaseous radionuclide sensors planned to be deployed for the International Monitoring System (IMS) were treated as existing in there planned locations for the purposes of determining detectability of the hypothetical nuclear explosion. Relevant, planned IMS sensors are listed in Table 1 and their geographic locations are displayed in Figure 1.

Table 1. Planned International Monitoring Stations in East Asia

Station Code	Location			Sensor Type	IMS stipulated Minimum Detectable Concentration
	Latitude	Longitude	Place Name		
MNG45	47.9	105.3	Ulan Bator, Mongolia	Noble Gas	1 mCi for Xe-135
MNP45	47.9	105.3	Ulan Bator, Mongolia	Particulate	30 µCi for Ba-140
RUP56	59.6	112.6	Peleduy, Russia	Particulate	30 µCi for Ba-140
RUP59	53.9	84.8	Zalesovo, Russia	Particulate	30 µCi for Ba-140
CNP21	36.0	104.2	Lanzou, China	Particulate	30 µCi for Ba-140
CNG21	36.0	104.2	Lanzou, China	Noble Gas	1 mCi for Xe-135
CNP20	40.0	116.4	Beijing, China	Particulate	30 µCi for Ba-140
CNG20	40.0	116.4	Beijing, China	Noble Gas	1 mCi for Xe-135
CNP22	23.1	113.3	Guangzhou, China	Particulate	30 µCi for Ba-140
CNG22	23.1	113.3	Guangzhou, China	Noble Gas	1 mCi for Xe-135
RUP58	43.7	131.9	Ussuriysk, Russia	Particulate	30 µCi for Ba-140
THP65	14.1	100.6	Bangkok, Thailand	Particulate	30 µCi for Ba-140
THG65	14.1	100.6	Bangkok, Thailand	Noble Gas	1 mCi for Xe-135
PHP52	14.5	121.0	Quezon City, Republic of the Philippines	Particulate	30 µCi for Ba-140
JPP37	26.5	127.9	Okinawa, Japan	Particulate	30 µCi for Ba-140
JPP38	36.3	139.1	Takasaki, Japan	Particulate	30 µCi for Ba-140
JPG38	36.3	139.1	Takasaki, Japan	Noble Gas	1 mCi for Xe-135

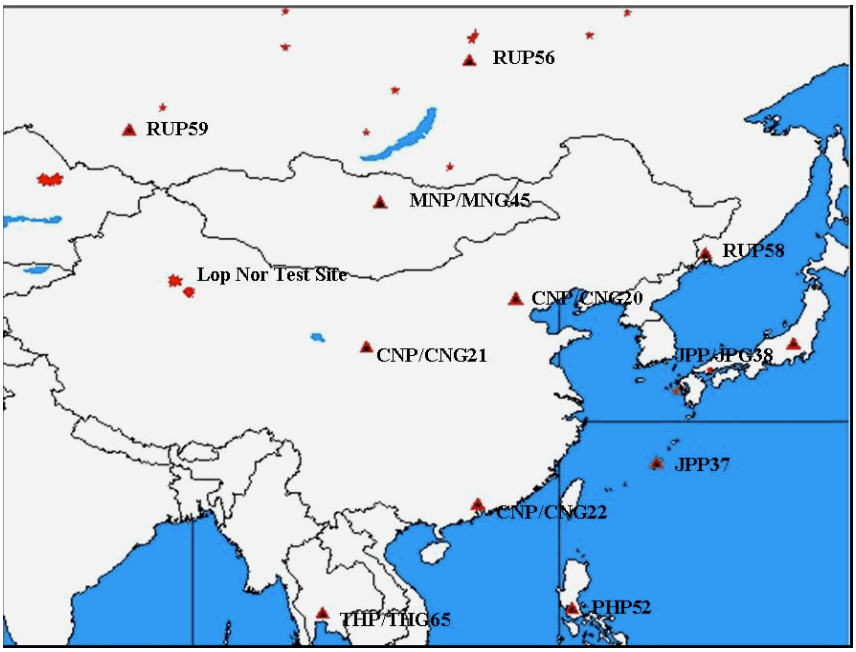

Figure 1. The Lop Nor Test Site and Relevant IMS Sensor Locations

Minimum Detectable Yield

Let *MDY* be the minimum detectable yield, *FPY* be the fission product yield of the isotope for which *MDY* is to be calculated, $t_{1/2}$ be the half-life of the isotope, *f* be the fraction of the fission product that escapes the test cavity to the environment, *Conc* be the diluted concentration of the plume at the sampling site based on HYSPLIT calculations, _*T* be the time elapsed between the source event and the collection of the sample, and *MDC* be the minimum detectable concentration of the isotope activity at the sampling site. Then, since there are 1.45×10^{23} fissions per kiloton of yield[3], the event will be detected if:

$$MDY \geq \frac{MDC}{1.45¥10^{23} * FPY * \frac{\ln 2}{t_{1/2}} * f * EXP(- \frac{\ln 2}{t_{1/2}} * DT) * Conc} \quad (1)$$

The half-lives used were obtained from the CMR radionuclide library used in radionuclide sample analysis. The fission product yield was obtained from Los Alamos report LA-UR-94-3106 (ENDF-349), the England and Rider tables of compiled fission product yields. The normalized concentration, *Conc*, was entered into equation 1 and the resulting MDY was calculated for each 12-hour period.

The fission products are decaying and the center of the air mass from the plume is moving. As shown in Figure 2, for points some distance from the source, the MDY will start infinitely large then drop in a delta function to some value as the leading edge of the air mass reaches the point of collection. The MDY may then decrease as the concentration at that point increases with the approach of the center of the air mass, before increasing again either because of decreasing concentration of the plume or because the fission product activity is decaying away.

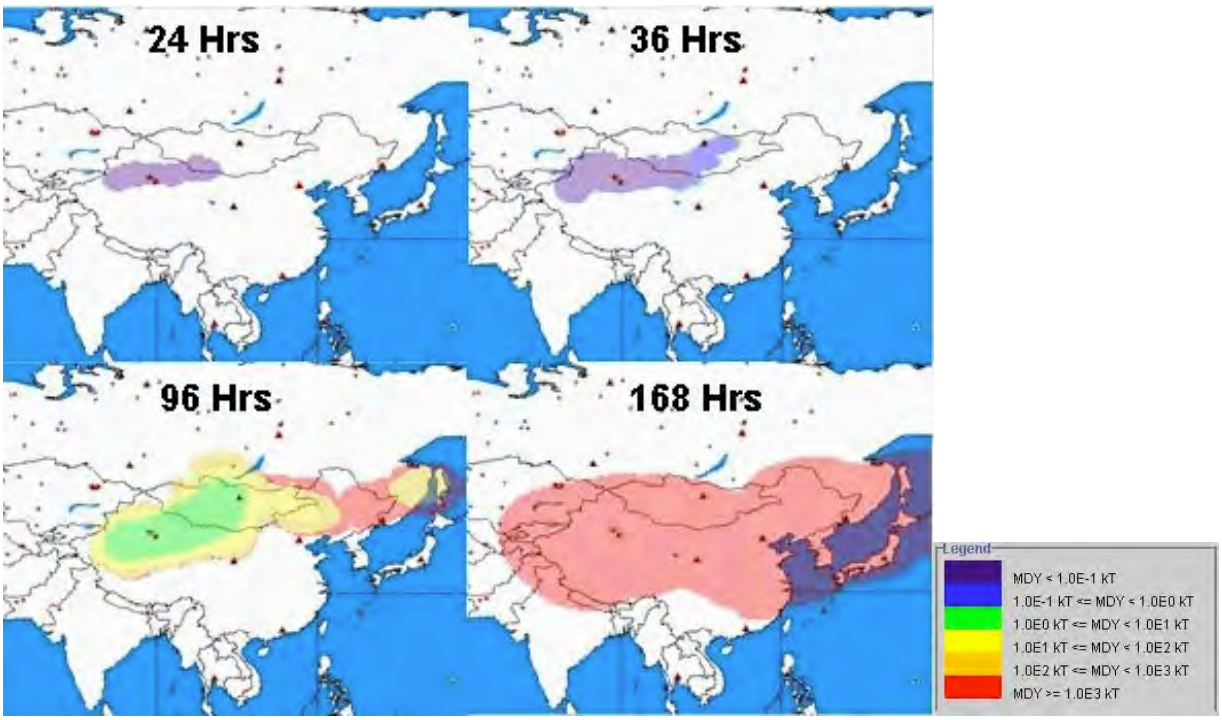

Figure 2. Progression of ^{135}Xe plume from hypothetical underground nuclear test at Lop Nor China.

The twice-daily plots were compiled to make a plot of the minimum MDY obtainable over the region around the hypothetical source location for each particular release and for each of the radionuclides being analyzed, as in Figure 3. The minimum MDY reached at planned sampling locations throughout 2001 was studied to obtain an overall assessment of the efficacy of the planned air-sampling network.

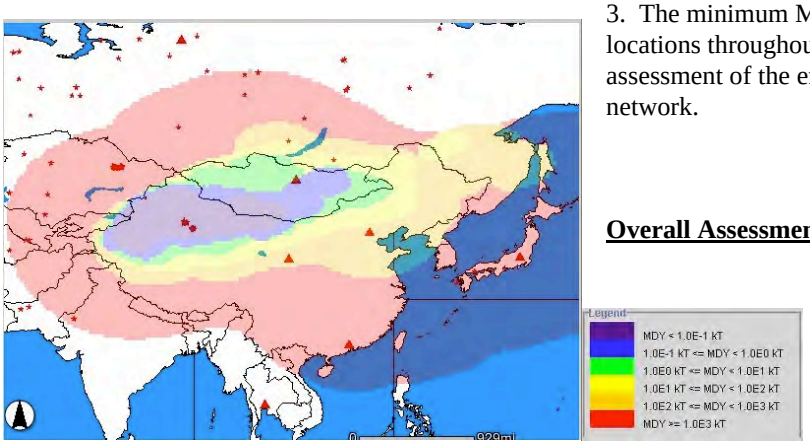

Figure 3. Example of MDY plot for ^{135}Xe.

Overall Assessment

Comparison of OMEGA and HYSPLIT Results

OMEGA is considered by many to be the most accurate atmospheric transport model available. It uses a fine scale grid and Lagrangian dispersion methods in both the horizontal and vertical planes. Its algorithms include calculations to account for planetary boundary layer effects that occur near the Earth's surface. The planetary boundary layer has a significant effect on atmospheric transport in rough terrain. However, it takes a long time to run a problem using OMEGA. HYSPLIT is considered to be less accurate than OMEGA, but it has the advantage of running much faster so that several problems can be modeled in a day. OMEGA was used to provide a baseline comparison for HYSPLIT, improving confidence in HYSPLIT results. HYSPLIT was then used to model the remaining problems.

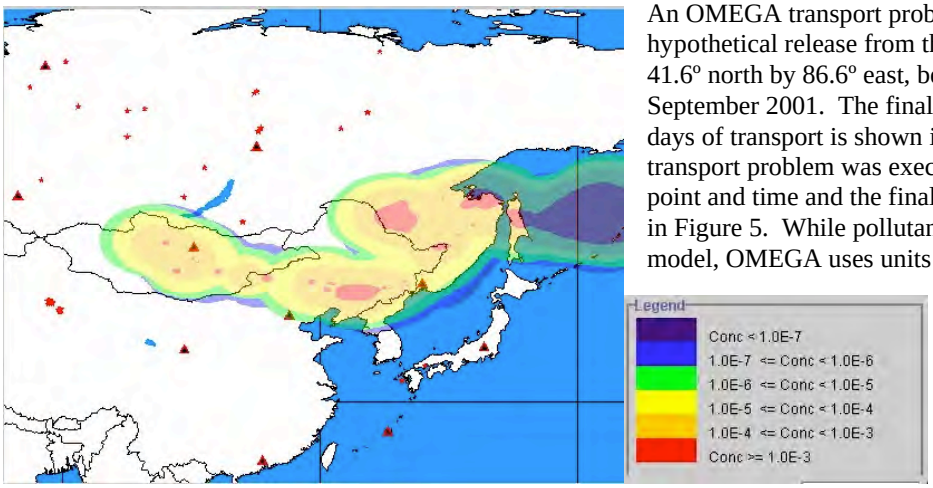

Figure 4. Plot of OMEGA predicted concentrations from plume emanating

An OMEGA transport problem was executed on a hypothetical release from the Lop Nor origin point, 41.6º north by 86.6º east, beginning at 0600 UTC on 10 September 2001. The final concentration plot after ten days of transport is shown in Figure 4. A HYSPLIT transport problem was executed with the same release point and time and the final concentration plot is shown in Figure 5. While pollutant mass is normalized in each model, OMEGA uses units of ng/m^3 while HYSPLIT uses kg/m^3, therefore, the HYSPLIT concentration values must be multiplied by a factor of 10^{12} to compare to OMEGA concentration values. In both models the center of the plume proceeded eastward at approximately the same rate. The centerline of the two plumes followed approximately the same path, however, the OMEGA plume separated into multiple globules while the HYSPLIT plume remained one continuous mass. Also, the centerline of the OMEGA model plume followed a path to the north of the HYSPLIT model. The centerline of the OMEGA model plume passed over Sakhalin Island while the centerline of the HYSPLIT model plume passed over Honshu, the largest island of Japan. In addition, the HYSPLIT plume diffused much more north and south of the centerline of travel compared to the OMEGA plume. Finally, the concentration values of the HYSPLIT plume are an order of magnitude smaller than the OMEGA values.

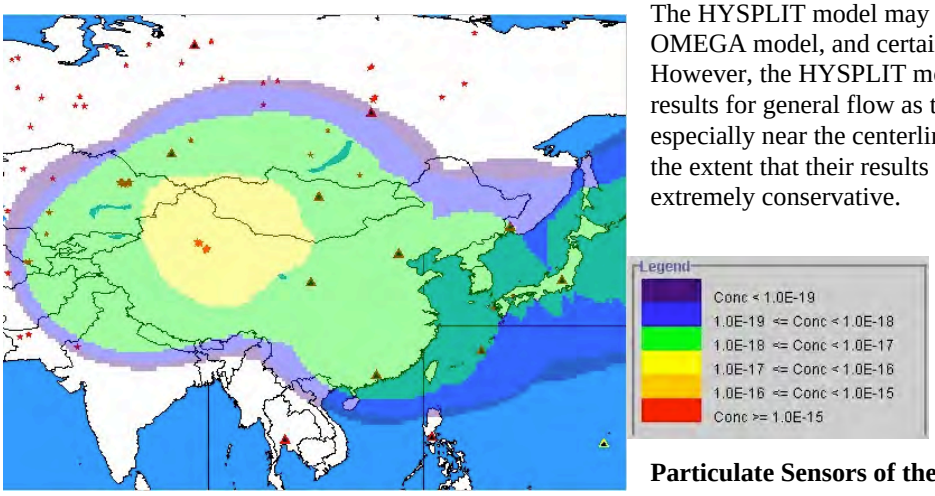

Figure 5. Plot of HYSPLIT predicted concentrations from plume emanating from Lop Nor, China on

The HYSPLIT model may not be as accurate as the OMEGA model, and certainly the results are different. However, the HYSPLIT model provides similar results for general flow as the OMEGA model, especially near the centerline of the plume flow and to the extent that their results are different, HYSPLIT is extremely conservative.

Particulate Sensors of the IMS Array

The planned array of particulate sensors should provide sufficient coverage of the Lop Nor region. The HYSPLIT model shows that a plume emanating from a test site in the Lop Nor region and carrying as little as 0.1 percent of the ^{140}Ba produced by a nuclear detonation can be detected down to less than 1 kiloton TNT equivalent yield during all months of 2001, the year for which atmospheric transport was modeled. Figure 6 shows the composite MDY for the Lop Nor ACD baseline. It must be emphasized that the technology almost certainly exists among countries with experience in nuclear weapons testing to test underground in a way that provides a high level of confidence that no particulate debris will escape the test cavity. The 0.1 percent debris release was chosen for comparison purposes and much less, or even no, particulate debris may escape. However, over the years there have been reports of accidental and intentional releases of significant amounts of debris from the cavities of

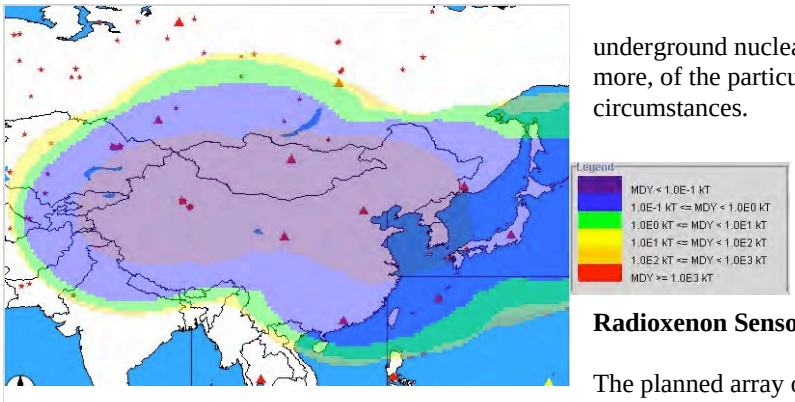

Figure 6. Plot of MDY for Ba-140 from hypothetical test at Lop Nor on 10

underground nuclear tests.[4] A tenth of a percent, or much more, of the particulate debris may escape under the right circumstances.

Radioxenon Sensors of the IMS Array

The planned array of noble gas, or radioxenon, sensors is not sufficient to provide reliable coverage of the Lop Nor region. Although a plume escaping from a test cavity near the center of the test range would reach several sensors, the travel time involved will often allow the ^{135}Xe to decay below the minimum detectable activity before samples can be collected and measured. Figure 7 shows the composite MDY for the Lop Nor ACD baseline. The planned IMS radioxenon station array was found to be capable of detecting debris from a nuclear explosion of 1 kiloton or greater during 9 out of 24 periods analyzed, 10 kilotons or greater 5 out of 24 periods, and 100 kilotons or greater 8 periods out of 24 analyzed. The planned array of radioxenon stations could not be relied on to detect an explosion of 1000 kilotons during 2 of the 24 periods analyzed. The twice-monthly assessment of the capability to detect effluent from underground nuclear explosions is summarized in Table 2 below.

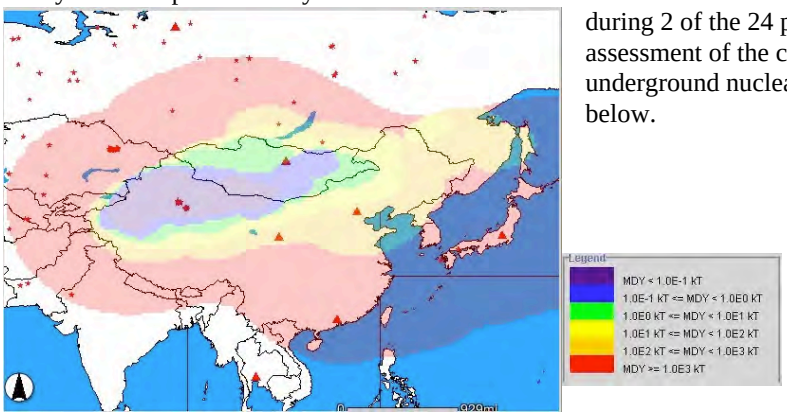

Figure 7. Plot of MDY for Xe-135 from hypothetical test at Lop Nor on 10

Table 2. Twice-monthly assessment of sensor detection capability for 2001.

Probability of Detection										
	MDY ^{135}Xe, IMS Sensor Array					MDY ^{140}Ba, IMS Sensor Array				
Month	Good	Marginal	Poor	MDY (kt TNT)	No. of Stations	Good	Marginal	Poor	MDY (kt TNT)	No. of Stations
1 Jan	X			<1	1	X			<0.1	2
16 Jan	X			<1	1	X			<0.1	2
1 Feb			X	<100	2	X			<0.1	2
16 Feb			X	<1000	1	X			<1	3
1 Mar	X			<0.1	1	X			<0.1	2
16 Mar	X			<1	1	X			<1	2
1 Apr		X		<10	2	X			<1	3
16 Apr		X		<10	1	X			<1	2
1 May	X			<1	1	X			<0.1	1
16 May			X	<100	1	X			<0.1	1
1 Jun		X		<10	2	X			<1	2
16 Jun			X	<1000	1	X			<1	2
1 Jul		X		<10	2	X			<1	2
16 Jul			X	<100	2	X			<1	4
1 Aug		X		<10	1	X			<1	3
16 Aug			X	<100	1	X			<0.1	1
1 Sep	X			<1	1	X			<1	3
16 Sep			X	<100	1	X			<1	2
1 Oct			X	<100	2	X			<1	3
16 Oct	X			<0.1	1	X			<0.1	1
1 Nov		X		<10	1	X			<1	1
16 Nov			X	<100	1	X			<0.1	3
1 Dec			X	<100	1	X			<1	3
16 Dec	X			<1	1	X			<0.1	1

Optimization of Future Station Deployments

Additional radioxenon sampling sites were selected and analyzed to see if the detection capability could be improved. Adding stations in Mongolia at 45.4 degrees north latitude by 91.1 degrees east longitude and at 43.0 degrees north latitude by 96.6 degrees east longitude, along with a station in Kazakhstan at 42.7 degrees north latitude by 79.9 degrees east longitude would improve detectability significantly. The sensors are listed in Table 3 and shown in Figure 8. With these additional stations the sensor array would be assessed as detecting effluent from nuclear explosions below 1 kiloton yield during every period analyzed, as shown in Table 4.

Table 3. Recommended sensor locations to enhance IMS Radioxenon array.

Station Code	Location			Sensor Type	IMS stipulated Minimum Detectable Concentration
	Latitude	Longitude	Place Name		
MNGX1	45.4	91.1	Chinese Border, Mongolia	Noble Gas	1 mCi for Xe-135
MNPX2	43.0	96.6	Chinese Border, Mongolia	Noble Gas	1 mCi for Xe-135
AZGX3	42.7	79.9	Chinese Border, Kazakhstan	Noble Gas	1 mCi for Xe-135

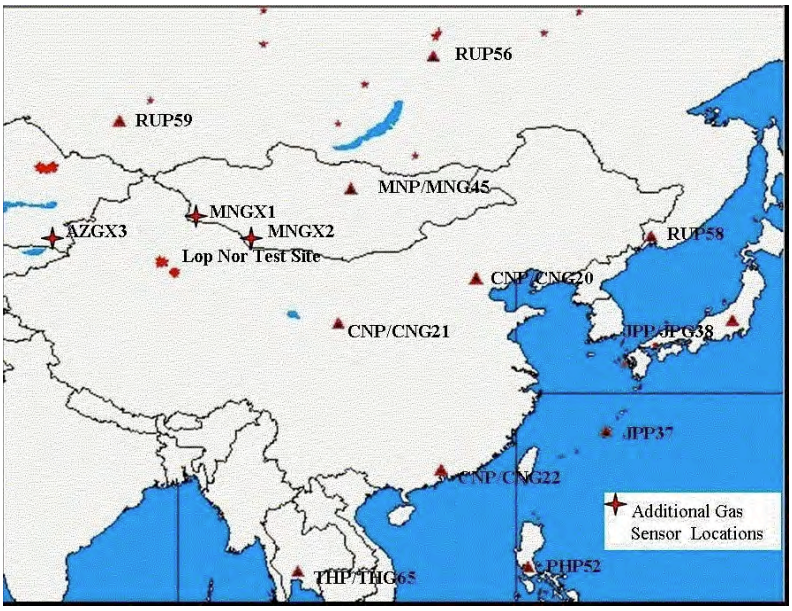

Figure 8. Recommended additional sensors to enhance detection capability of IMS network for Lop Nor.

Table 4. Twice-monthly assessment of sensor detection capability for 2001 with additional sensors.

Probability of Detection										
	MDY ^{135}Xe, Recommended Enhanced Array					MDY ^{140}Ba, IMS Sensor Array, No Enhancements Recommended				
Month	Good	Marginal	Poor	MDY (kt TNT)	No. of Stations	Good	Marginal	Poor	MDY (kt TNT)	No. of Stations
1 Jan	X			<0.1	2	X			<0.1	2
16 Jan	X			<0.1	2	X			<0.1	2
1 Feb	X			<0.1	1	X			<0.1	2
16 Feb	X			<0.1	1	X			<1	3
1 Mar	X			<0.1	2	X			<0.1	2
16 Mar	X			<0.1	1	X			<1	2
1 Apr	X			<0.1	2	X			<1	3
16 Apr	X			<0.1	1	X			<1	2
1 May	X			<0.1	1	X			<0.1	1
16 May	X			<0.1	1	X			<0.1	1
1 Jun	X			<1	1	X			<1	2
16 Jun	X			<0.1	1	X			<1	2
1 Jul	X			<0.1	1	X			<1	2
16 Jul	X			<0.1	1	X			<1	4
1 Aug	X			<0.1	2	X			<1	3
16 Aug	X			<0.1	1	X			<0.1	1
1 Sep	X			<0.1	1	X			<1	3
16 Sep	X			<0.1	2	X			<1	2
1 Oct	X			<1	1	X			<1	3
16 Oct	X			<0.1	4	X			<0.1	1
1 Nov	X			<0.1	1	X			<1	1
16 Nov	X			<0.1	1	X			<0.1	3
1 Dec	X			<0.1	1	X			<1	3
16 Dec	X			<1	3	X			<0.1	1

CONCLUSIONS AND RECOMMENDATIONS

Planned Radionuclide Monitoring Array

The planned IMS radionuclide monitoring array is insufficient to provide reliable coverage of the Lop Nor region, unless particulates escape the test cavity. Xenon-135, the fission product most likely to provide proof of a nuclear detonation, will frequently decay to below detectable limits before it can be collected and measured, because of the length of time required for transport. While the array of particulate sensors is probably as good as achievable, it is also true that it is much easier to contain particulate fission products within the test cavity.

The most effective solution for the Lop Nor region would be the addition of three radioxenon collection and measuring stations. Two should go in Mongolia near the Chinese border and near the coordinates 45.4 degrees north by 91.1 east and 43 degrees north by 96.5 east. The third should go in Kazakhstan, also near the Chinese border and near the coordinates 42.7 degrees north by 79.9 degrees east. A less expensive alternative may be to substitute one of the additional stations in Mongolia for the planned station near Ulan Bator. However, both additional stations in Mongolia would be needed to lower the estimated MDY to less than 10 kt under the conditions described in this paper. No cost/benefit analysis was attempted in this study and issues affecting the positioning of sampling sites at the specified locations has not bee examined.

Future Work

Two major efforts need to be accomplished to expand and refine the analysis performed so far. The period reviewed needs be expanded over several years in an effort to see any seasonal variation and to determine if the monthly airflow does follow a predictable pattern. In addition, the HYSPLIT diffusion model needs to be optimized for particulates and rerun for ^{140}Ba.

It has been implicitly assumed that the airflow in each period examined during calendar year 2001 is typical of that period for any calendar year. This may or may not be true. Several years of data have been processed with the HYSPLIT model to assess this issue. The current availability of archived meteorological data was sufficient to allow five years, from 1997 through 2001, to be analyzed. This period of time will also permit identification of seasonal patterns. The model runs have been completed; however, the large volume of data could not be analyzed in time to be included in this paper.

HYSPLIT can be run as a diffusion model, more applicable to gaseous pollutants, or as a dispersion model, more applicable to particulate pollutants. Since the debris will not escape a properly stemmed test cavity unless it is a gas, it seemed sensible to run HYSPLIT as strictly a diffusion model. Late in the analysis it was recognized that a particulate such as ^{140}Ba might escape the test cavity as a gas then soon precipitate. It would then behave as other particulates and its atmospheric transport might be better modeled that way. It is not clear whether running HYSPLIT in the dispersion mode would provide a better representation of particulate debris dispersal. Consideration should be given to running the HYSPLIT model in the dispersion mode with values entered for dry deposition of barium particulates.

REFERENCES

[1] HYSPLIT4 (HYbrid Single-Particle Lagrangian Integrated Trajectory) Model, 1997. Web address: http://www.arl.noaa.gov/ready/hysplit4.html, NOAA Air Resources Laboratory, Silver Spring, MD.

[2] The Operational Multiscale Environment model with Grid Adaptivity (OMEGA), David P. Bacon, et al., DNA-TR-95-30, Defense Special Weapons Agency, 6801 Telegraph Rd., Alexandria, VA 22310-3398.

[3] The Effects of Nuclear Weapons, 3rd Ed, .S. Glasstone and P. J. Dolan, US DOD and US DOE, 1977.

[4] Radiological Effluents Released from U.S. Continental Tests 1961 through 1992, DOE/NV-317 (Rev. 1) UC-702, United States Department of Energy, Nevada Operations Office, August 1996.

Infrasound Monitoring

INFRASOUND SIGNAL LIBRARY

Eric P. Chael[1] and Rodney W. Whitaker[2]

Sandia National Laboratories[1] and Los Alamos National Laboratory[2]

Sponsored by National Nuclear Security Administration
Office of Nonproliferation Research and Engineering
Office of Defense Nuclear Nonproliferation

Contract No. DE-AC04-94AL85000[1] and W-7405-ENG-36[2]

ABSTRACT

The International Monitoring System (IMS) proposed for verifying compliance with the Comprehensive Nuclear-Test-Ban Treaty will include an infrasound network for detecting and identifying explosions in the atmosphere. As is the case with seismic monitoring, data collected from historic events of interest are vital for improving infrasonic monitoring capabilities. Unfortunately, however, infrasonic recordings of such events are rare and thus any additional data sets that might be available should be pursued. Towards that end, we will digitize, as a result of the ROA01-38 award, paper records and extract from 9-track tapes several unique data sets from Sandia National Laboratories and Los Alamos National Laboratory that have not been available to the monitoring community. These data sets include recordings of surface and atmospheric explosions representing different yields, altitudes and weather conditions, as well as bolides and other natural phenomena that may be detected by the international infrasound monitoring network. Once the data are all in digital form, we will convert them to the standard CSS format, including event and station information. The complete set of database tables and binary waveform files will be the ultimate product of our work.

OBJECTIVES

Our objectives are to generate digital versions of relevant waveform data from older infrasound monitoring activities and distribute them to researchers and analysts, and to demonstrate a reasonably efficient digitizing system useful for retrieving additional data of similar type. In this joint Sandia National Laboratories (SNL) and Los Alamos National Laboratory (LANL) effort, we will make available in a common digital format four valuable sets of infrasound event recordings (including explosions and other types of events) which have hitherto been largely unavailable to explosion monitoring researchers. This collection of data can be exploited to address a number of issues for infrasonic monitoring by the IMS. Information on yield scaling, source functions, regional-distance propagation and variability due to weather could all be derived from such a collection.

RESEARCH ACCOMPLISHED

At the time of preparation of this paper for submission to the SRR Proceedings, neither Sandia nor Los Alamos had received any funds for this work. This proposal was accepted in the FY 2002 phase of the ROA01 process. The funding had been transferred to DOE in Albuquerque and was making its way to each lab. Thus we have not yet begun working on this project, and will report here on what we are planning to do. Candidate records for digitizing include those from atmospheric, surface and shallow underground nuclear tests at the Nevada Test Site, along with earthquakes, conventional ammonium nitrate and fuel oil explosions and bolide signals measured by the older operational infrasound network.

During atmospheric testing, Sandia personnel made numerous microbarograph recordings of the acoustic signals from nuclear tests at several stations surrounding the Nevada Test Site at approximately first bounce distances (Reed, 1969). These data exist only as paper strip-chart records and would make up the bulk of the Sandia contribution to the digital library. Other Sandia records include some acoustic data from underground tests (UGTs) and Plowshare events. These latter two sets were also taken with Sandia microbarographs. Sandia has tested a software package for digitizing these paper traces. This software comes from the well logging community and has the potential to handle most of the data in an efficient and accurate manner.

Los Alamos has been operating infrasound arrays in the southwest since 1983 on a continual basis. Acoustic signal data have been collected from UGTs, earthquakes and conventional explosion tests at White Sands Missile Range. Regrettably, most of the original digital data from the Los Alamos arrays were lost. Some tapes exist, and the first part of the Los Alamos work will be to search the tapes for events and send them to Sandia for reading. The second part would be to find paper records of selected events for digitizing with the Sandia software. Los Alamos has numerous paper records of atmospheric tests and bolides, recorded at various infrasound stations around the world from the 1950's to the 1970's.

CONCLUSIONS AND RECOMMENDATIONS

Based on our preliminary examinations of the early infrasound data available in the Sandia and Los Alamos archives, we believe the recordings are of good quality and offer a valuable resource to infrasound researchers. Under this project we will digitize a representative sample of the records, spanning a range of source sizes and altitudes. We will then distribute the resulting data sets within the monitoring community either on CDs or via the Web.

REFERENCE

Reed, J. W., 1969, Climatology of Airblast Propagations from Nevada Test Site Nuclear Airbursts, Sandia Laboratories Report SC-RR-69-572.

APPLICATION OF PHYSICS-BASED UNDERWATER ACOUSTIC SIGNAL AND ARRAY-PROCESSING TECHNIQUES TO INFRASOUND SOURCE LOCALIZATION

Gerald D'Spain, Michael Hedlin, John Orcutt, Bill Kuperman,
Catherine deGroot-Hedlin, Lewis Berger, and Galina Rovner

Scripps Institution of Oceanography, University of California, San Diego

Sponsored by Defense Threat Reduction Agency

Contract No. DTRA01-00-C-0061

ABSTRACT

The purpose of this project is to apply physics-based signal and array-processing techniques, recently developed in the area of underwater acoustics, to atmospheric infrasound data and co-located seismic field data. The infrasound data are collected by the eight microbarometers comprising the International Monitoring System (IMS) infrasound station at Pinon Flat (PFO) plus an additional five microbarometer/space filter sensor systems installed for a 6-week period at five Anza seismic station sites located within 40-km range of PFO. The co-located Anza seismic sensors as well as the Incorporated Research Institutes for Seismology (IRIS) seismic station at PFO provide the data needed to perform a comparison between infrasound and seismic recordings of atmospheric events across a very wide horizontal aperture. During the 6-week period, four rocket launches occurred at Vandenberg Air Force Base: an Atlas 2AS, a Taurus, a Titan 4B, and a Delta II. The arriving signals from three of these four launches were recorded with high signal-to-noise ratio. High-quality ground truth information on rocket trajectories and other quantities measured during two of the launches have been acquired from the Vandenberg and Los Angeles Air Force Bases.

OBJECTIVE

The purpose of this project is to apply physics-based signal and array processing techniques, recently developed in the area of underwater acoustics, to atmospheric infrasound data and co-located seismic station field data. The hypothesis to be tested is that advanced underwater acoustic signal and array-processing techniques, with some modifications, can provide more accurate source locations and source signature estimates of low-level events of interest in nuclear explosion and treaty monitoring than conventional methods. In addition, the joint use of infrasonic and seismic data from co-located sensor systems has the potential to significantly increase phase identification and source localization capability, and reduce unwanted background noise.

Basic research questions we are addressing in this project include:

- What are the effects of range-dependent, heterogeneous, and time-variable media on infrasound propagation and source localization?
- How can the location of caustics in infrasound be exploited for source localization? Can the location of these caustics be predicted accurately with available environmental data?
- Can waveguide invariant techniques, which have proven to provide robust and simple approaches to analyses of underwater waveguide propagation, be used effectively with infrasound data?
- What are the important sources of infrasonic noise and signals in the southern California environment? How will these measurements be translated into other areas of the world?
- What acoustic propagation codes (e.g., ones based on a parabolic equation (PE) solution to the acoustic wave equation which includes the effect of winds) incorporate the important propagation physics and so can be used for effective forward modeling in the inverse problems of localizing sources and inferring atmospheric properties?
- A question related to the inverse problem is how effective are sources of opportunity, e.g., mining and quarry blasts, bolides and rocket launches, in calibrating the atmospheric propagation characteristics?
- What are the spatial correlation lengths of various infrasound signals and noise at frequencies of interest scientifically and operationally? How do these correlation lengths vary with topography, weather, humidity, background noise, and other environmental variables?
- How can seismic and acoustic data be used in parallel to understand infrasonic wave excitation and propagation and to localize the source? In particular, how do seismic and acoustic waves couple at the interface between the earth and atmosphere and can this coupling be used to both identify the many wave types observed and infer source location?

The primary goal of this paper is to use high-fidelity numerical modeling methods along with the launch trajectory information and environmental data collected at the time of the launches to determine the predictability of the arrival structure of the signals across the PFO/ANZA array from these 400-km-distant rocket launches. The predictions take into account the signal-distorting effects caused by phase delays across the spatial aperture of the space filters (i.e., each microbarometer/space filter system is not omni-directional over the frequency band of interest). A second goal is to search for any possible phase coherence between the output of a microbarometer and a co-located sonic anemometer.

RESEARCH ACCOMPLISHED

Focused Experiment

A focused infrasound experiment was conducted over the 6-week period from 7 September to 18 October 2001. The 8-element International Monitoring System (IMS) infrasound station (I57US) at the Pinon Flat Observatory (PFO), in the high desert 125 km northeast of San Diego, was the source of much of the data. In addition, data were collected from the co-located, three-component, broadband IRIS (Integrated Research Institutions for Seismology)

seismic station at PFO (an IMS auxiliary seismic station) to permit studies of the relationship between the atmospheric infrasound and seismic wave fields. Fig. 1 shows a map of the 8 I57US microbarometer sensors (H1 thru H4 and L1 thru L4), and the IRIS station, along with a line indicating the back azimuth to Vandenberg Air Force Base. The H-type microbarometers, spaced 100 to 200 m apart, had 18-m rosette space filters attached and the L-type sensors, forming a centered triangle with nominal 1.4-km-long sides, had 70-m diameter space filters. The space filters cause each of the infrasound sensors to become a directional receiver with frequency-dependent characteristics; this issue will be discussed further below.

As part of the focused experiment, a microbarometer/space filter sensor system was installed at each of five Anza seismic station sites located within 40-km range of PFO. The space filters at these stations were composed of 4 porous tubes of 15-m length each, arranged in a "plus" (+) pattern as symmetrically as the layout of each site allowed. Fig. 2 is a map of the topography along with the locations of the 5 Anza stations (RDM, KNW, CRY, WMC, and SND) and PFO. A line indicating the back azimuth to Vandenberg Air Force Base again is included in the figure.

Data from the Titan 4B Launch

During the 6-week focused experiment, four rocket launches were conducted at Vandenberg Air Force Base, 400 km to the west-northwest of PFO. The rockets were an Atlas 2AS, a Taurus, a Titan 4B, and a Delta II. Fig. 3 shows a 10-min time series of the arrivals from the Titan 4B as recorded by all 13 infrasound sensors. The data were band-filtered between 1 and 3 Hz. Time 0 on the plot corresponds to 21:40:00 GMT, 5 October, 2001 (JD 278), which is 19 min after the announced launch time. Assuming that the first arrival was created when the rocket first reached supersonic speed, then it has a group velocity of approximately 300 m/s. The waveforms at each of the stations are dominated by three major arrivals, occurring at 22.5 min, 24 min, and 25.4 min after launch in the uppermost traces. Numerical modeling results discussed below indicate that the first arrival is the stratospheric refracted arrival, the first part of the second arrival is also the stratospheric refracted arrival when the rocket reaches the upper regions of the stratosphere whereas the second part is the refracted arrival from the lower part of the thermosphere, and the third arrival initially reflects from the ground and then refracts from higher altitudes in the thermosphere. Therefore, the spread in arrival structure is associated both with the motion of the rocket through the atmosphere and the propagation characteristics through the stratospheric waveguide.

Variations in arrival structure across the 40-km aperture of the array are clearly visible. In addition, the arrival structure recorded by the sensors with 18-m space filters (the uppermost 4 "I57H" traces) is different than that recorded by the sensors with 70-m filters (the "I57L" traces). The corresponding spectrogram of the time series recorded by the temporary infrasound station at Anza station Red Mountain (IRDM) is presented in Fig. 4. The arrivals from the rocket launch have energy that extends up to 5 Hz. However, this higher frequency energy is strongly attenuated by the 70-m space filters, as discussed below.

White-noise-constrained adaptive plane-wave beam forming (Gramann, 1992; Cox, Zeskind, and Owen, 1987) has been applied to the Titan 4B arrivals. Fig. 5 shows the results of the processing on the second part of the second, main arrival (just after the 5-min mark in the upper traces in Fig. 4) using just the data collected by the 8 I57US sensors. The analysis was done only up to 2.5 Hz to avoid the higher frequencies where the 18-m and 70-m space filters have significantly different response characteristics. The white-noise-constraint value used for the results in the figure is 2.5 dB down from 10*log(N) where N is the number of array elements. (Using a constraint value of 10*log(N) is equivalent to conventional array processing). The two-dimensional (2-)D array frequency/wave number processing output is a function of frequency, time, wave number (or slowness), and azimuth. Fig. 5 presents a plot of frequency vs. wave number at a fixed azimuth of 285 deg, the back azimuth having greatest energy for the second arrival. The slope of the dark ridge of energy in the plot passing through the origin equates to a phase velocity of around 359 m/s. A similar plot for the first arrival indicates a phase velocity of 350 m/s. Both estimates are accurate to within about 5 m/s, so the difference in the two results appears to be significant. This phase velocity difference is consistent with the numerical modeling results where the stratospheric refracted arrival has an apparent phase velocity of around 345 m/s (it depends somewhat upon the altitude of the rocket) and the lower thermospheric refracted signal arrives with nearly a 355 m/s phase velocity.

In addition to searching for differences in the arriving phase velocities of the major arrivals in the time series in Fig. 3, several additional adaptive beam forming calculations were done to look for possible differences in azimuth of arrival. The trajectory of the rocket took it to the southwest from the launch site, so that an evolution in azimuth

might be evident in the data. The results showed that all arrivals had back azimuths within 1 or 2 deg of 285 deg. The second part of the second arrival in Fig. 3, i.e., the energy just after the 5-min mark in the upper traces, may have arrived a degree or two from a more southerly direction than the first part just prior to the 5-min mark, but this difference probably is within the beam former resolution.

Numerical Modeling using CASS/GRAB

The Comprehensive Acoustic System Simulation (CASS) program (Weinberg *et al*, 2001; Weinberg and Keenan, 1996) is being used to perform the numerical modeling. The CASS program, developed at the Naval Undersea Warfare Center, Division Newport, is a US Navy-standard code that has been approved by the Navy's Oceanographic and Atmospheric Master Library (OAML). To obtain OAML accreditation, the code underwent extensive testing and has been thoroughly documented. CASS actually is a modular collection of codes that allow all aspects of sonar system performance to be modeled. One of the acoustic propagation models in CASS is the Gaussian Ray Bundle (GRAB) model (Weinberg and Keenan, 1996), which was used in this work. Gaussian ray bundles and Gaussian beam tracing represent recent advances in ray theoretically based modeling, which provides more accurate wave field amplitude results (Jensen *et al*, 1994; see also Cerveny *et al*, 1982). GRAB allows for range dependence of the sound speed profiles and range dependence in the bottom interface (which is either the ocean bottom in hydroacoustic modeling or the Earth topography in atmospheric infrasound), so that propagation in a 3-D varying medium is done using an N X 2-D approximation.

In addition to its more advanced amplitude modeling capability and extensive testing and documentation, the advantages of using CASS/GRAB are that it includes several options for modeling a variety of physical phenomena, the source code is included with the distribution, and it can easily be run in batch mode. Although CASS/GRAB was developed for the underwater sonar problem, the only significant adaptation required for modeling infrasound propagation in the atmosphere was to place an artificial, flat, pressure release upper boundary at 150-km altitude (i.e., zero "depth"). The program is run to search for eigenrays in the ± 60 deg about horizontal launch angle interval, but no rays are allowed in the solution that interact with the artificial interface at 150 km.

Information on the position of the rocket as a function of time at 1-sec intervals after launch was provided by the personnel at Los Angeles Air Force Base, with valuable assistance from individuals at Vandenberg Air Force Base. According to the trajectory information, the rocket became supersonic 8 sec after launch at an altitude of about 300 m. The numerical modeling starts at this position (see McLaughlin *et al*, 2000) and continues for the 242 sec it takes for the rocket to exceed 150 km in altitude. The results presented here are limited to the 8- to 200-sec interval after launch.

The sound speed profile information used as input to the propagation modeling was derived from data from two sources. First, Douglas Drob at the Naval Research Laboratory provided us with profiles of temperature and the meridional and zonal wind profiles at 1-km increments up to 170-km altitude and at approximately 10-km-spaced points along two great circle paths, from PFO to the rocket launch point and from PFO to the splash down point of one of the jettisoned components. Profiles were provided for two different time periods, 1800 GMT and 2400 GMT, 5 Oct, which bracket the launch time. The modeling presented here uses only the profiles along the great circle path from PFO to the launch position, and only from the 2400 GMT, 5 Oct time period. The second source of sound speed information came from the empirical atmospheric models (the Horizontal Wind Model and the Extended Mass Spectrometer - Incoherent Scatter Radar temperature model) contained in the Infrasonic Modeling of Atmospheric Propagation (InfraMAP) tool kit (Norris *et al*, 1999).

Range-dependent modeling, both range dependence of the sound speed profiles and of the topography over land, has been performed. However, only the range dependence of the topography has been incorporated in the modeling results presented here. Effective range-independent sound speed profiles were obtained by first averaging the temperature, meridional, and zonal wind profiles along the great circle path separately. Then, an effective profile was derived by adding the projection of the horizontal wind vectors along the great circle path to the sound speed profile based on the temperature data alone. The left panel in Fig. 6 shows a comparison of the effective range-averaged sound speed profiles from the Drob data (solid curve) and from InfraMAP (dashed curve). The Drob-derived profile has more structure in the stratospheric waveguide (0-50 km altitude), almost forming two ducts, than the InfraMAP profile. This structure has a strong effect on the predicted signal arrival structure, as discussed below. The right hand panel shows the attenuation profile for a frequency of 1 Hz used in the modeling. This profile was extracted from the InfraMAP output (0 - 120 km) and then extrapolated to 150 km.

A fundamental property of propagation in a waveguide is its dispersive characteristics. By providing a measure of the relationship between the group and phase velocities of the various multi-path components in a wavefield, the waveguide invariant quantifies in a single scalar parameter these dispersive characteristics (e.g., D'Spain *et al*, 2000; D'Spain and Kuperman, 1999). Plots of the invariant ("inverse beta") for the two range-averaged sound speed profiles in Fig. 6 are presented in Fig. 7. Again, the solid curve pertains to the profile obtained from the Doug Drob data and the dotted curve is for the InfraMAP-derived profile. The horizontal line at the invariant value of zero indicates where no dispersion occurs (i.e., a broadband pulse remains a pulse) whereas increasingly larger positive and negative values signify increasing amounts of dispersive spreading (and pulse distortion). Two transitions appear in the curves: between 5.5 and 6 deg and between 13.0 and 13.5 deg in the solid curve. The first transition occurs when the ray angles become sufficiently steep that the lower boundary of the waveguide no longer is created by refraction, but by reflection from the ground. (The receiver altitude is taken to be the 1280-m altitude of PFO). The second transition between 13.0 and 13.5 deg is more relevant to the rocket launch data and occurs when the ray angles become sufficiently great that the energy is no longer trapped in the stratospheric waveguide. The important difference between the solid and dotted curves occurs just prior to this transition. That is, the solid curve shows an asymptotic approach to the horizontal line at zero, whereas the InfraMAP curve crosses over it. The implication of this asymptotic approach is that the dispersion is very small over a fairly wide interval of ray angles, so that focusing of broadband pulse energy will occur (Kuperman *et al*, 2001).

The CASS/GRAB 1-Hz modeling results of the eigenray amplitudes as a function of time after rocket launch for the two sound speed profiles in Fig. 6 are shown in Figs. 8 and 9. The predicted arrival structure for the two cases is remarkably different. Whereas the InfraMAP profile (Fig. 9) yields only two major arrivals with the first arrival being the largest in amplitude and having a duration longer than 2 min, the Drob-derived profile (Fig. 8) predicts a small amplitude first arrival followed by a 1-min gap and then a large-amplitude second arrival. This large-amplitude arrival is the result of the broadband focusing evident from the waveguide invariant plots in Fig. 7(as discussed in the previous paragraph). Both sound speed profiles indicate a short duration arrival at the 25-min mark surrounded by low-level "coda". They also both predict that a gap occurs around the 24 min mark, although it is significantly shorter for the Drob-derived profile than for the InfraMAP profile. A comparison with Fig. 3 shows that the Drob-derived profile results provide a much better match to the main features in the actual measurements. That is, they reproduce the relative amplitudes of the first and second arrivals, the 1-min gap between the first and second arrivals, the short duration nature of the gap at the 24-min mark, and the fact that three or four arrivals are present.

To better identify the components of the arrival structure in the Drob-derived predictions, and in the actual data, the eigenray arrivals are plotted as a function of both time after launch and rocket altitude. (Note that the time scale is from 20 to 34 min after launch rather than 19 to 29 min as in Figs. 8, 9, and 3). This plot represents a rocket trajectory travel-time curve. Two different sizes of dots are used to provide an indication of eigenray amplitude. (Fig. 8 is the result of integrating along each vertical line in Fig. 10). Three different branches are evident in the figure. The first, starting at the 21-min mark, is the stratospheric refracted path, the second is the lower thermospheric refracted arrival, and the third, which bifurcates from the second as the rocket altitude increases, is the path that reflects first from the ground and then refracts from higher altitudes in the thermosphere.

Therefore, the first arrival in Figs. 3 and 8 is the stratospheric refracted path that exists when the rocket is at low altitudes. This path disappears as the rocket passes through the upper troposphere and lower stratosphere because of the small medium sound speeds at these altitudes, leading to the 1-min gap between first and second arrivals. The first part of the second arrival actually is the reappearance of this path as the rocket ascends into the upper stratosphere where medium sound speeds are greater. The received amplitudes at PFO are largest from this portion of the rocket trajectory. The short gap around the 24-min mark is the time separation between the latest arriving stratospheric refracted path energy and the lower thermospheric refracted energy. That is, the arrivals just on either side of the 5-min mark in Fig. 3 represent these two different phases. The trailing energy arriving last has reflected from the ground before refracting in the thermosphere.

Plane Wave Response of Space Filters

Each inlet port of the space filters acts as an omni-directional point receiver. The outputs from each of these receivers are summed together at the microbarometer without any relative phase delay since the distance from each port to the microbarometer is the same. This summation is equivalent to forming a broadband beam in the vertical

direction whose character is determined by the 2D spatial distribution of the ports. (In some deployments, the 3D distribution should be taken into account). The plane wave response of the directional receiver characteristics of a 70-m space filter as a function of frequency and elevation angle are shown in Fig. 11. The incoming plane wave is assumed to have unity amplitude so that its mean squared amplitude is 0.5 (-3 dB). Because of the relative phase delays due to propagation across the horizontal aperture of the space filter, the signal amplitude becomes increasingly attenuated with increasing frequency above 1 Hz at the smaller elevation angles. Complete destructive interference occurs along an arc in the frequency/elevation angle plane starting at 5 Hz and 0 deg elevation angle (horizontal). Similar plots show little variation as a function of azimuth so that the response is effectively isotropic in the horizontal plane. Also, no shift in signal phase occurs due to the space filter response so that only its effects on amplitude need to be taken into account. All of the various issues associated with the distorting effects of the rosette space filters are discussed in Hedlin *et al*, 2002.

(No) Phase Coherence Between Wind Velocity and Infrasonic Wind Noise

A focused experiment was conducted at PFO to examine the coherence between the time series from an MB 2000 microbarometer without a space filter and the three components of wind velocity as measured by a co-located sonic anemometer. The goal was to investigate the possibility of using adaptive noise cancellation processing (Widrow, 1976) to remove wind noise contamination in the microbarometer time series. These types of processing schemes allow the phase correlated component (as measured by coherence) between two time series to be separated from the uncorrelated component. Therefore, if sufficient coherence exists between the anemometer and microbarometer time series, then an anemometer could replace a space filter, thus minimizing land use and saving deployment costs.

A total of 166 hours (nearly 7 days) of continuous data were recorded from 4-11 Mar (JD 063-070) 2002. An MB 2000 was placed at a height of 2 m above ground and adjacent to a sonic anemometer at the same height. All six channels of data - two from the microbarometer and four from the sonic anemometer - were digitized at a 20 samples/sec rate and recorded on the same data acquisition system. Fig. 12 shows a plot of 20 min of time series from the two output channels from the MB 2000 (lower-most two panels with the second-from-bottom trace being the output high-pass filtered above 0.05 Hz) and the four channels of output from the sonic anemometer (upper four panels). Although some similar features can be seen in the time series for the three components of wind velocity (upper-most three traces) and the microbarometer infrasound output (second-from-bottom trace), no statistically significant coherence between the infrasound time series and any wind velocity component time series was found at any frequency at any time over the full 166 hours of the experiment.

CONCLUSIONS AND RECOMMENDATIONS

Infrasound signals with large signal-to-noise ratio were recorded by 13 sensors, including the 8 I57US elements at PFO, during a Titan 4B rocket launch at Vandenberg Air Force Base, 400 km distant. Numerical modeling was performed with the CASS/GRAB program, a US Navy standard Gaussian ray bundle-based code, with rocket trajectory information from Los Angeles Air Force Base. The results using profiles of temperature and horizontal winds provided by Douglas Drob at the Naval Research Laboratory show good agreement with the main features of the measured arrival structure. The first arrival is a stratospheric refracted return when the rocket is at low altitudes, followed by a 1-min gap as the rocket passes through the upper troposphere and lower stratosphere where the medium sound speeds are too small to support this path. However, once the rocket ascends into the upper stratosphere where the sound speeds are greater, this path reappears. Its reappearance is marked by large received amplitudes due to broadband focusing, as predicted by waveguide invariant techniques. A short gap in time follows, terminated by the arrival of lower thermospheric-refracted energy. These arrivals have detectable amplitudes also because of broadband focusing. The signals arriving last traveled paths that reflected from the ground before refracting in the thermosphere at higher altitudes. All these components of the arrival structure are clearly illustrated by a rocket trajectory travel-time curve. White-noise-constrained adaptive beam forming on the first arrival and on the thermospheric-refracted arrival yield phase velocity estimates that differ by 10 m/s, consistent with the difference expected from the numerical modeling results.

The 2-D spatial distribution of the individual ports of the space filters acts like a beam former to point a beam in the vertical direction. Therefore, each microbarometer is converted into a directional receiver. The signal-attenuating effects of this vertical beam must be taken into account at frequencies above 1 Hz for the 70-m filters.

Finally, no statistically significant coherence was found between the infrasound time series from an MB 2000 microbarometer and the three wind velocity components as measured by a co-located sonic anemometer.

ACKNOWLEDGEMENTS

We would like to thank the personnel at Los Angeles and Vandenberg Air Force Bases for their efforts in providing us with the rocket launch data. Anton Dainty of the Defense Threat Reduction Agency assisted in acquiring these data. Special thanks to Doug Drob of the Naval Research Laboratory for sending us the environmental data. Clint Coon and Frank Vernon at Scripps provided assistance in installing the temporary infrasound stations and Clint set up the microbarometer/anemometer experiment. In addition, Ruth Keenan of SAIC and Dave Ensberg at Scripps provided help with running the CASS/GRAB code.

Finally, we want to extend a warm thank you to the landowners who allowed us to install our sensors and porous hoses on their land.

REFERENCES

Cerveny, V., M. M. Popov, and I. Psencik (1982), Computation of Wave Fields in Inhomogeneous Media - Gaussian Beam Approach, Geophys. *J. R. Astr. Soc.*, **70**, 109-128.

Cox, H., R. M. Zeskind, and M. M. Owen (1987), Robust Adaptive Beamforming, IEEE Transactions of Acoustics, Speech and Signal Processing ASSP-35 (10).

D'Spain, G. L., W. A. Kuperman, J. A. Orcutt, and M. A. H. Hedlin (2000), Long-Range Localization of Impulsive Sources in the Atmosphere and Ocean from Focus Regions in Single Element Spectrograms, Proc. of 22nd Annual Seismic Research Symposium: Technol. for Monitoring the Comprehensive Nuclear-Test-Ban Treaty, 8 pgs.

D'Spain, G. L. and W. A. Kuperman (1999), Application of Waveguide Invariants to Analysis of Spectrograms from Shallow Water Environments that Vary in Range and Azimuth, *J. Acoust. Soc. Am.*, **106** (5), 2454-2468.

Gramann, R. A. (1992), ABF Algorithms Implemented at ARL-UT, ARL Tech. Letter ARL-TL-EV-92-31, Applied Research Laboratories, The University of Texas at Austin, Austin, TX.

Hedlin, M. A. H., B. Alcovarro, and G. L. D'Spain (2002), Evaluation of Rosette Infrasonic Noise-Reducing Spatial Filters, submitted to *J. Acoust. Soc. Am.*, 28 pgs.

Jensen, F. B., W. A. Kuperman, M. B. Porter, and H. Schmidt (1994), *Computational Ocean Acoustics.* American Inst. Physics, New York, 168-170.

Kuperman, W. A., G. L. D'Spain, and K. D. Heaney (2001), Long Range Source Localization from Single Hydrophone Spectrograms, *J. Acoust. Soc. Am.*,**109** (5) pt. 1, 1935-1943.

McLaughlin, K. L., A. Gault, and D. J. Brown (2000), Infrasound Detection of Rocket Launches, Proc. of 22nd Annual Seismic Research Symposium: Technol. for Monitoring the Comprehensive Nuclear-Test-Ban Treaty, 219-230.

Norris, D., R. Nadel, and R. Gibson (1999), User's Guide for InfraMAP, v. 1.4, BBN Tech. Memo. W1353a, BBN Technologies, Arlington, VA.

Weinberg, H., R. L. Deavenport, E. H. McCarthy, and C. M. Anderson (2001), Comprehensive Acoustic System Simulator (CASS) Reference Guide, NUWC-NPT TM 01-016, Naval Undersea Warfare Center Division Newport, RI.

Weinberg, H. and R. E. Keenan (1996), Gaussian Ray Bundles for Modeling High-Frequency Propagation Loss under Shallow-Water Conditions, *J. Acoust. Soc. Am.*, **100** (3), 1421-1431.

Widrow, B., J. M. McCool, M. G. Larimore, and C. R. Johnson (1976), Stationary and Nonstationary Learning Characteristics of the LMS Adaptive Filter, *Proc. IEEE*, **64** (8), 1151-1162.

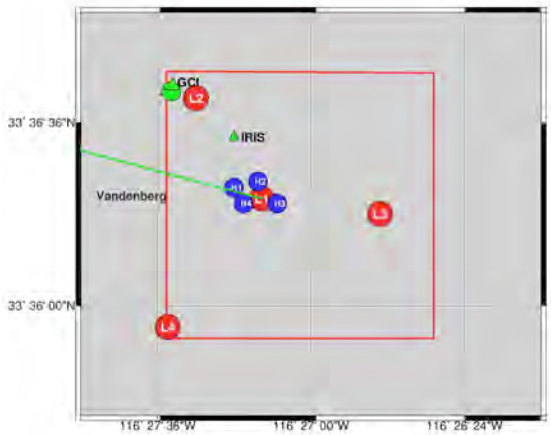

Figure 1. Map of the I57US infrasound station at Pinon Flat Observatory (PFO).

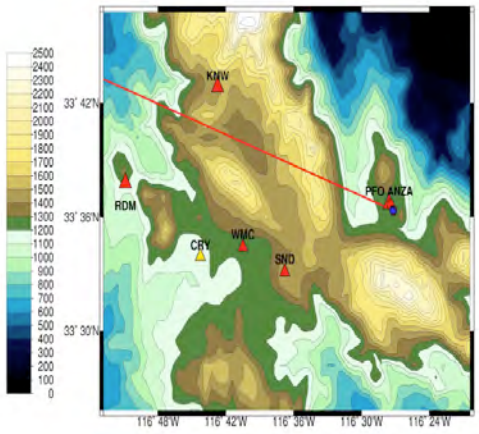

Figure 2. Map of PFO and the five ANZA stations where infrasound sensors were temporary installed for the focused experiment, along with the surrounding topography

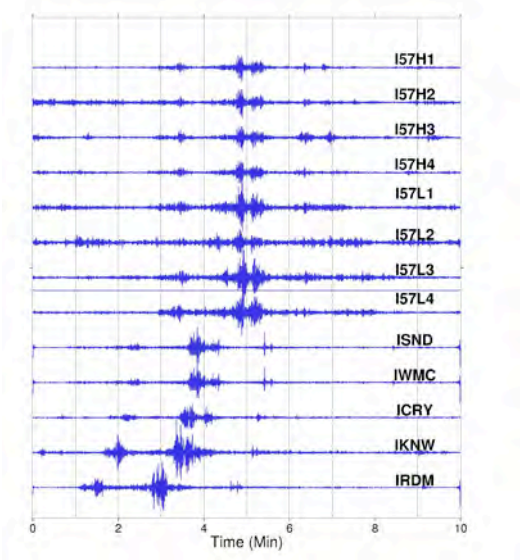

Figure 3. Time series of arrivals from the Titan 4B launch recorded by all 13 infrasound sensors, band-pass filtered from 1 to 3 Hz.

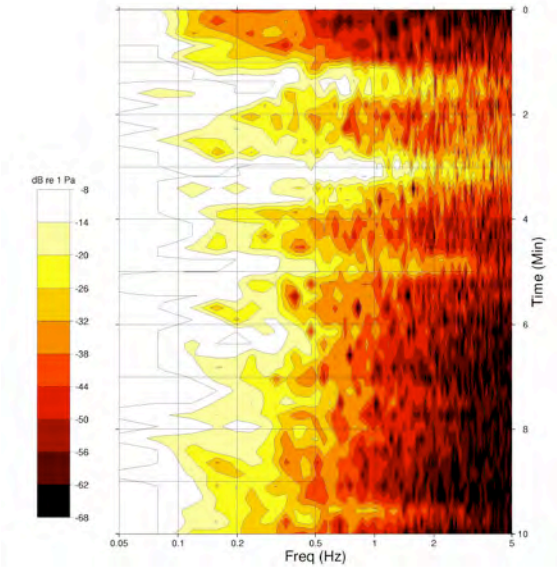

Figure 4. Spectrogram of data recorded by station IRDM over the same 10-min period as Fig. 3 (lower-most trace).

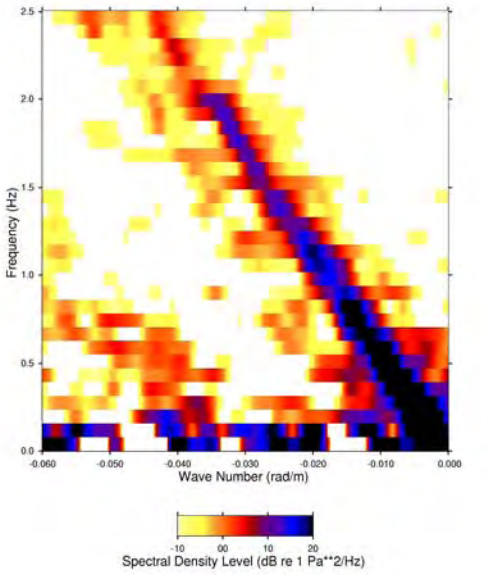

Figure 5. White-noise-constrained adaptive beam forming on the 2nd part of the 2nd (main) arrival from the Titan 4B launch at 285 deg back azimuth.

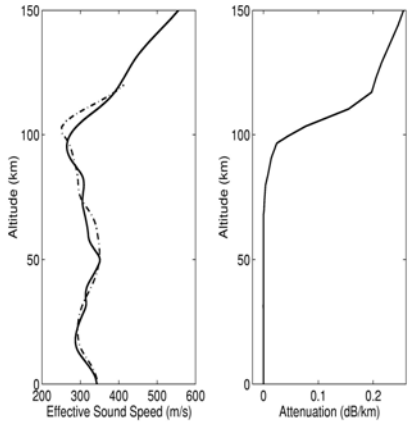

Figure 6. Effective range-averaged sound speed profiles (left panel) derived from NRL data (solid curve) and from InfraMAP databases (dashed curve), and the attenuation profile at 1 Hz (right panel) used in the modeling.

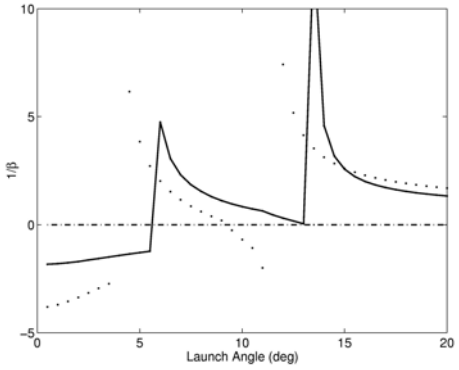

Figure 7. The waveguide invariant as a function of arrival angle for the two sound speed profiles in Fig. 6 and for an altitude corresponding to I57US.

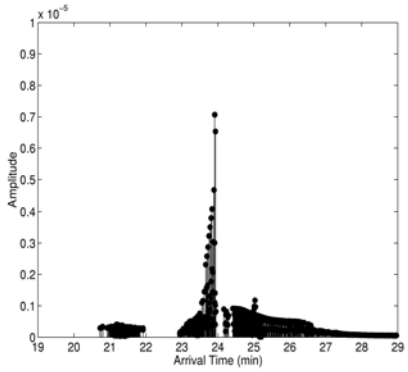

Figure 8. The amplitude vs. arrival time at PFO of the CASS/GRAB eigenrays created in the 8- to 200-sec time interval by the Titan 4B rocket modeled as a moving point source for the NRL-data-derived sound speed profile (solid curve in Fig. 6).

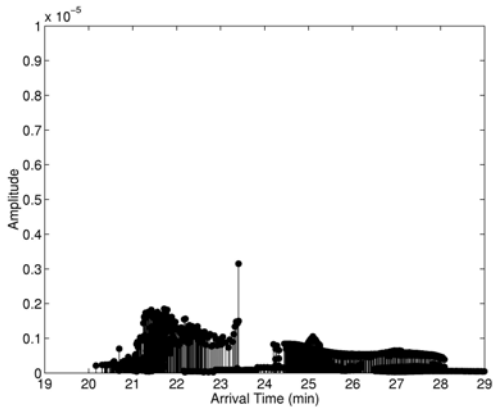

Figure 9. CASS/GRAB-modeled eigenray amplitude vs. arrival time at PFO for the InfraMAP-derived sound speed profile (dashed curve in Fig. 6).

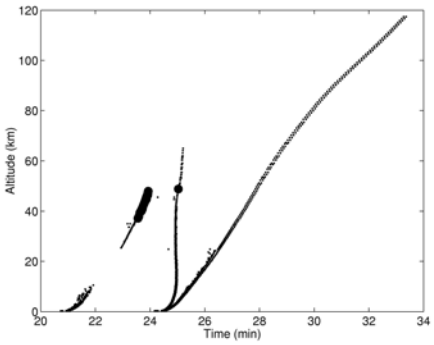

Figure 10. The CASS/GRAB-modeled eigenray arrival times at PFO as a function of rocket altitude. The large and small circles signify eigenray amplitudes greater or less than 1.0 x 10-6, respectively.

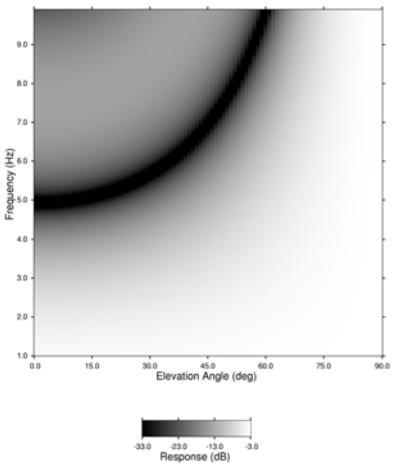

Figure 11. Plane wave response of the 70-m rosette space filters as a function of frequency and elevation angle of arrival.

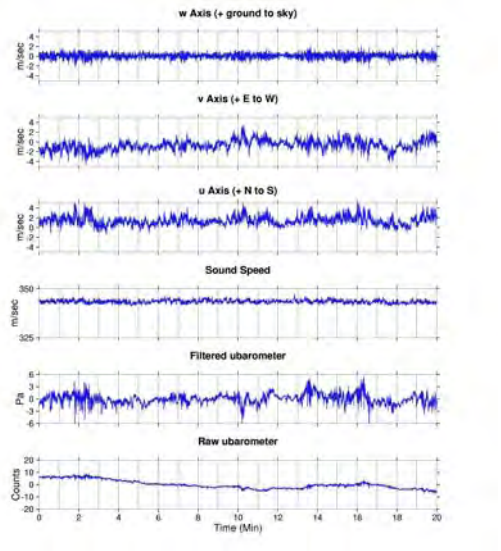

Figure 12. 20-min time series of the 4 output channels of a sonic anemometer (3 components of wind velocity, and sound speed, respectively) and the 2 channels of a co-located microbarometer.

EVALUATION OF INFRASONIC DETECTION ALGORITHMS

Milton A. Garcés and Claus H. Hetzer

University of Hawaii, Manoa

Sponsored by Defense Threat Reduction Agency

Contract No. DTRA01-00-C-0106

ABSTRACT

Infrasound array IS59, Hawaii, also known as the KONA array, started operations on May 25, 2000, and was certified into the International Monitoring System in December of 2001. In order to interpret the KONA data, various analysis tools have been acquired, developed, and evaluated at the Infrasound Laboratory (ISLA) of the University of Hawaii. These include modified versions of Sandia National Laboratories' MatSeis, Los Alamos National Laboratory's InfraTool, STA/LTA-based automatic detectors, and the Progressive Multi-Channel Correlation (PMCC) method. Evaluation of various detection algorithms during routine analysis of the KONA array data demonstrated that PMCC was not as vulnerable to spatial aliasing as frequency-domain detection methods, and it allowed detection of signals below the noise level, which is not possible with a STA/LTA detector. PMCC is presently used to produce automatic bulletins of signals detected by KONA. Phase names based on source identification have been devised to aid in classification. Detector results are subjected to a minimum-correlation/minimum-family-size filter, and both filtered and unfiltered bulletins are produced. The bulletins, which are not subjected to analyst review, provide Phase, Date and Time UT, Azimuth, Slowness, Correlation, Median Frequency of Detection, RMS Amplitude, and Family Size. Filtered detector results are written to CSS .arrival tables, which are subject to analyst review. Future work should concentrate on the development of an automatic, intelligent event identification algorithm that can screen the large amount of events picked by automatic detectors.

OBJECTIVE

The aim of this paper is to discuss the infrasonic signal detection algorithms that have been tested at the Infrasound Laboratory (ISLA), which operates the KONA array. The detection parameters for the signals that are routinely recorded will also be discussed.

RESEARCH ACCOMPLISHED

Summary of Analysis Techniques

In the first two years of the project, a suite of array-processing algorithms was evaluated. Initially, a combination of STA/LTA, F-K, and correlation analyses was used to obtain the arrival azimuth and trace velocity of high-frequency signals. Long-duration, emergent arrivals were detected using the Los Alamos National Laboratory's (LANL) InfraTool. Automatic detections were performed with these algorithms, and the methods and types of signals observed by the KONA array were presented in Garcés and Hetzer (2001). In December 2001, evaluation of the Progressive Multi-Channel Correlation (PMCC) detector (Cansi, 1995) was initiated. The PMCC detector has been automated and is the primary detection system presently implemented at the ISLA.

Description of the PMCC detector

PMCC is a time-domain detector that uses the correlation between various groupings of three sensors, *i*,*j*,*k*, to obtain an estimate of the consistency of the closure relation

$$r_{ijk} = \Delta t_{ij} + \Delta t_{jk} + \Delta t_{ki}\,, \tag{1}$$

where Δt_{ij} is the time delay between the arrival of a signal at sensors *i* and *j* (Cansi and Klinger, 1997). If the consistency is below a certain threshold, a detection is registered. This detector has performed well in KONA for signal-to-noise ratios (S/N) that are close to unity and for all signal frequencies.

The PMCC algorithm is based on analysis of overlapping windows of data. The cross-correlation function of the data from two stations determines a time delay Δt_{ij}; and the mean quadratic residual of the closure relations (Eq. 1) of the sub array triplets yields the consistency of the signal. A subset or all of the array elements can be used for an initial time-delay calculation, which yields an initial value of arrival azimuth and slowness. Using these values, the consistency for additional elements can be progressively calculated. These additional array elements are directed into the calculation by examining a shorter section of the time window determined by a specified bearing and slowness range. If the point of maximum correlation requires a significant variance in azimuth, velocity, or time, the arrival is discarded. This optimizes computation time over a large array, and also allows initial false alarms caused by the presence of correlated noise in the first array subset to be eliminated when not present in further subsets (Cansi, 1995).

During the PMCC calculation, each time window is filtered into a number of frequency segments using a specified suite of filters, and the results are analyzed individually for similarity in azimuth, slowness, and consistency. A detection must satisfy specified trace velocity limits, arrival azimuth variation limits and duration limits, and must appear on a specified minimum number of stations. Each frequency band within each time window represents a "pixel" of data (Figure 1a) and each pixel is analyzed independently. Pixels adjacent in time and/or frequency are compared, and nearest-neighbor groups of pixels with similar characteristics are classified as "families" (Figure 1b). Families that conform to a specified range of sizes are placed in a table of detections.

In order to run the algorithm in near real time, a simple script must be used to generate an initialization file that contains all of the parameters necessary to determine the detection thresholds, as well as the names of and paths to the data files. This initialization file can then be passed to the PMCC executable file, which processes the waveform data and generates a file containing the aforementioned table of families. Each variation in the detection parameters requires a separate run of the detector with a unique initialization file.

For the KONA array, ISLA runs PMCC on all four elements using two sets of detection parameters ("high-frequency" and "microbarom" sets) for routine event processing, with two additional sets ("high-speed" and "very-low-frequency") in development (Table 1a). Each set uses a suite of second-order Chebyshev filters, with passbands shown in Table 1a. Detection parameters include analysis-window length and overlap, maximum consistency, minimum and maximum frequency and trace velocity, and maximum azimuthal variation permissible for inclusion in a family. Other parameters are dependent on these. The PMCC parameters act as logical "and" constraints, where all conditions must be satisfied for the detection to be registered. The resulting table of detection families is sorted and recorded in the "unfiltered" PMCC bulletin, then analyzed and filtered using various parameter thresholds (Table 1b), which act as logical "or" constraints, where satisfaction of any is sufficient for acceptance. A "filtered" bulletin and a Center for Seismic Studies (CSS) arrival table containing arrival time, azimuth, slowness, amplitude, and phase are created using the detections that are within the thresholds. The waveform data in the local CSS database is stored in 4-hour segments, and the PMCC detector processes an entire segment at once, two hours after its normal ending time (to ensure maximum data inclusion). The four iterations through the waveform data currently require about 20-30 minutes of computation time per 4-hour segment on a dual-processor 900-MHz SunBlade 2000 running Solaris 8. Both filtered and unfiltered bulletins of detections are produced weekly (Table 2).

Event Detection Parameters

The *high-frequency* parameter set uses a passband of 0.5-4 Hz, which effectively screens out the dominant low-frequency energy and allows comparatively low-amplitude events to be detected. Before being written to the arrival database, the arrivals are classified by phase. Currently ISLA personnel use a simple azimuth-based classification scheme derived from past observations of similar high-frequency events (Garces and Hetzer, 2001). Azimuthal ranges that include a known or hypothesized source are given a phase identification based on that source. Current phase classifications include surf noise, signals from the Pohakuloa Training Area, and possible volcanic signals; other signals are given a phase identification that signifies "origin unknown". Events that are believed to be local to the Big Island and its shoreline tend to show higher median frequencies than events that are not associated with specific regions (Figure 2). This is to be expected due to the higher attenuation of high-frequency energy with increasing range.

Surf Arrivals

Detections from azimuths of 234±10° and 320±10° are classified as surf events, with assigned phase names of "ik" and "iws" respectively. The signals generally occur as sets of impulsive, evenly spaced arrivals (Figure 3) with relatively high (> 2 Hz) frequency content (Figure 2). These arrivals are believed to be produced by ocean waves trapped within specific bays along the coast of the Big Island, and have an average root-mean-square (RMS) amplitude of 2.99 mPa. During periods of high activity, groups of surf signals will often be sufficiently closely spaced in time such that the PMCC detector will treat them as a single, long-duration event. Other azimuths may also contribute surf signals, but not with the consistency of the two areas specified above.

Pohakuloa Training Area Arrivals

Detections from 65±30° are identified as coming from the Pohakuloa Training Area and are assigned to the "ip" phase. Pohakuloa events generally occur as clusters of one or more irregularly spaced impulsive arrivals (Figure 4), and tend to have fairly high (> 2 Hz) frequency content (Figure 2). They have an average RMS amplitude of 4.99 mPa. Other signals from this azimuth may be more emergent with poor S/N.

Volcanic Arrivals

Detections from 110±10° are identified as coming from the general direction of Pu'u O'o, the active vent of Kilauea Volcano. These signals are tentatively assigned to the "iv" phase and have a RMS amplitude of 7.13 mPa.. To date the majority of these events have featured a S/N of approximately unity. Despite their relatively high amplitude, the events tend to occur at lower frequencies (mean frequency of detection is 0.9 Hz), where the noise floor is higher. This precludes visual analysis of the arrivals. Some tentative correlations have been found between infrasonic events and peaks of thermal activity in the Pu'u 'O'o crater.

Microbarom Arrivals

Detections in the 0.1- to 0.5-Hz frequency band are assigned the "im" phase and are believed to be generated by ocean wave interactions caused by severe weather, often at distances of several thousand kilometers. The arrivals have an average RMS amplitude of 12.57 mPa. Correlation has been drawn between the arrival azimuth of microbarom events (Figure 5) and areas of increased surface wave height. Microbarom energy has been shown to have promise in the field of storm tracking; for a more detailed treatment of this topic see Garcés *et al*. (2002).

Other Detection Parameters

The bands that are currently under development will contain events of a less general nature. For example, the "high-speed" band should be mostly useful for events propagating oblique to the ground, such as bolides or aircraft passing overhead, and for events that exhibit seismic phase velocities, such as earthquakes that disturb the microphone. The "very-low-frequency" band will be used for detecting mountain-associated waves that may be generated by Hawaii's and Maui's massive volcanic peaks. Currently the events in these bands are not recorded in the arrival tables or the filtered bulletins, but are present in the unfiltered bulletins (Figure 6).

CONCLUSIONS AND RECOMMENDATIONS

The detections of infrasonic signals in Hawaii have been improved through the evaluation of various array-processing algorithms. The effectiveness of the PMCC event detection algorithm at KONA has been demonstrated. Further research on this topic should include the development of real-time event detection and identification algorithms. Real-time detection could include implementation of the Antelope system, which can be run concurrently with the PMCC software for comparative evaluation. Event identification procedures could incorporate neural network techniques, and may permit the construction of a more concise automatic bulleting.

REFERENCES

Cansi, Y. (1995). An automatic seismic event processing for detection and location: The P.M.C.C. method. *Geophysical Research Letters*, **22**, 1021-1024.

Cansi, Y., and Y. Klinger (1997). An automated data processing method for mini-arrays. Newsletter of the European-Mediterranean Seismological Center, **11**, 2-4.

Garces, M, and C. Hetzer (2001). Infrasonic signals detected by the Kona array, Hawaii. *23rd Annual DTRA/NNSA Seismic Research Review*, Jackson Hole, 1-5 October 2001.

Garces, M., C. Hetzer, S. Businger and M. Willis (2002). Modeling of microbarom signals in the Pacific. *This volume.*

Garces, M., C. Hetzer, K. Lindquist, and D. Drob (2002). Source location algorithm for infrasonic monitoring. *This volume.*

Table 1. a) Parameters for the two active and two developing sets of detection constraints. b) The secondary constraints used to filter detections into confirmed arrivals. Columns for "High-Frequency" and "Microbarom" sets are currently active and in use at IS59; columns for "High-Speed" and "Very-Low-Frequency" sets are in development.

PMCC Parameter	High-Frequency	Microbarom	High-Speed	Very-Low-Frequency
Window Length	30 sec	90 sec	30 sec	300 sec
Window Overlap	5 sec	20 sec	5 sec	50 sec
Max Consistency	0.2 sec	0.5 sec	0.2 sec	5 sec
Passband	0.5-4.0 Hz	0.1-0.5 Hz	0.5-4.0 Hz	0.033-0.1 Hz
Trace Velocity	0.3-0.45 km/s	0.3-0.45 km/s	0.5-0.8 km/s	0.25-0.45 sec
Min # of Sensors	3	3	3	3
Max Interpixel Time Variation	2 x Window Overlap	2 x Window Overlap	2 x Window Overlap	2 x Window Overlap
Max Interpixel Frequency Variation	0.8 Hz	0.1 Hz	0.8 Hz	0.02
Max Interpixel Azimuth Variation	10°	10°	10°	10°
Max Interpixel Velocity Variation	10%	10%	10%	10%

ISLA Parameter				
Correlation	0.6	0.7	N/A	N/A
Family Size	14	N/A	N/A	N/A

Table 2. Sample filtered bulletin from the high-frequency parameter set showing information typically stored for each arrival. These arrivals satisfy one or both of the ISLA parameters shown in Table 1b.

Date	Time	Azimuth	Slowness (s/deg)	Correlation	Median Frequency	RMS Amplitude (mPa)	Family Size	Phase
9-Jul-02	00:02:15	323.2	311.65	0.32	2.96	0.8	37	iws
9-Jul-02	00:04:25	323	313.44	0.44	3.15	0.8	53	iws
9-Jul-02	00:06:45	322.7	312.54	0.45	3.07	0.9	46	iws
9-Jul-02	00:08:25	322.7	314.34	0.33	3.31	0.6	15	iws
9-Jul-02	00:09:15	323	314.34	0.45	3.35	0.7	27	iws
9-Jul-02	00:14:15	322.5	314.34	0.36	3.05	0.7	25	iws
9-Jul-02	00:22:25	316.6	312.54	0.66	2.45	2.1	24	iws
9-Jul-02	00:32:40	40.3	305.54	0.46	3.3	0.8	18	ip
9-Jul-02	00:59:45	48.5	297.21	0.48	2.52	1.5	38	ip
9-Jul-02	01:25:35	49.6	300.49	0.78	0.88	8.4	7	ip
9-Jul-02	01:34:20	57.6	314.34	0.31	2.31	1.2	18	ip
9-Jul-02	01:35:30	59	313.44	0.33	2.45	1.2	42	ip
9-Jul-02	01:37:55	57.3	312.54	0.28	2.39	1.2	19	ip
9-Jul-02	01:39:10	58.9	312.54	0.23	2.47	0.9	15	ip
9-Jul-02	02:15:20	308.1	317.09	0.47	2.3	2	43	iu
9-Jul-02	02:35:20	232.5	326.58	0.52	3.51	0.4	21	ik
9-Jul-02	02:38:15	232.4	324.63	0.44	3.55	0.4	20	ik
9-Jul-02	02:46:55	232.3	325.6	0.41	3.46	0.4	26	ik
9-Jul-02	02:59:15	231.8	322.71	0.32	3.54	0.3	21	ik
9-Jul-02	03:02:30	114.4	303.84	0.65	0.73	7.8	6	iv
9-Jul-02	03:53:45	232.4	324.63	0.44	3.3	0.5	24	ik
9-Jul-02	04:03:20	234.4	327.56	0.4	3.61	0.3	23	ik
9-Jul-02	04:08:15	232	323.67	0.36	3.5	0.3	16	ik
9-Jul-02	04:12:05	234.6	329.54	0.4	3.66	0.3	15	ik
9-Jul-02	04:13:25	232.6	325.6	0.46	3.46	0.9	59	ik
9-Jul-02	04:30:30	232.4	325.6	0.41	3.5	0.4	37	ik
9-Jul-02	04:40:55	75.3	281.85	0.5	3.31	0.5	23	ip
9-Jul-02	04:45:25	232.6	325.6	0.47	3.54	0.5	29	ik
9-Jul-02	04:53:00	232.4	327.56	0.48	3.37	0.5	24	ik
9-Jul-02	05:01:05	233.2	325.6	0.4	3.5	0.4	39	ik
9-Jul-02	05:02:30	232.4	323.67	0.38	3.57	0.4	26	ik
9-Jul-02	05:06:00	233	326.58	0.47	3.45	0.5	16	ik
9-Jul-02	05:08:35	232.7	329.54	0.44	3.55	0.5	19	ik
9-Jul-02	05:29:45	232.8	324.63	0.39	3.52	0.4	29	ik
9-Jul-02	05:41:45	232.5	326.58	0.38	3.55	0.4	14	ik
9-Jul-02	05:53:45	232.6	326.58	0.44	3.28	0.6	191	ik
9-Jul-02	06:01:35	232.2	320.82	0.41	3.6	0.5	34	ik
9-Jul-02	06:05:30	115	309.88	0.61	0.73	9.8	6	iv
9-Jul-02	06:12:25	232.6	325.6	0.42	3.59	0.5	36	ik
9-Jul-02	06:21:55	233.1	327.56	0.46	3.5	0.5	14	ik
9-Jul-02	06:43:20	234	327.56	0.39	3.58	0.5	17	ik

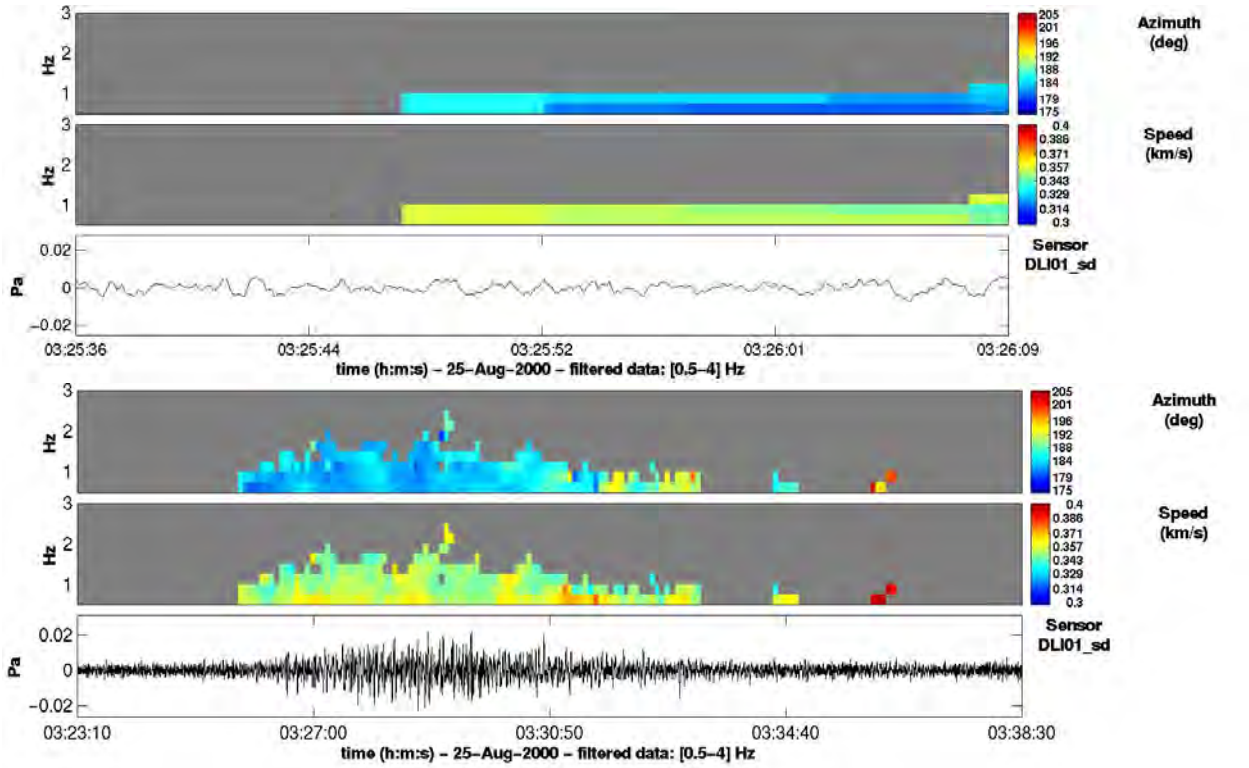

Figure 1. Graphical PMCC windows showing a) the pixel-like nature of an event family (above) and b) a large event family (below). Images are from the bolide event of August 25, 2000 (Garces *et al.*, 2002).

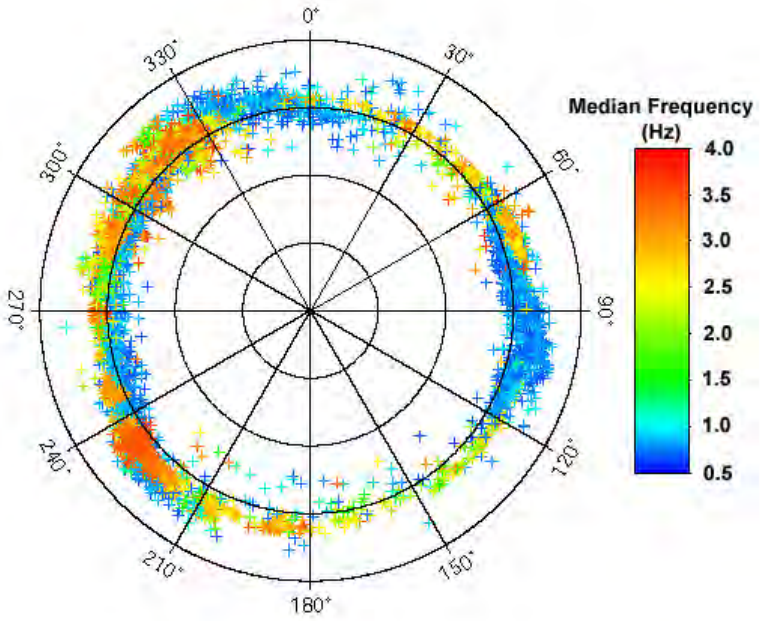

Figure 2. Polar diagram showing azimuth, slowness, and median frequency for arrivals in the "high-frequency" passband detected from January 1-June 30, 2002. Groups of arrivals at 75° (ip phase), 235° (ik phase), and 320° (iws phase) are believed to originate within 50 km of the array. Radial units are seconds/degree, increments of 100.

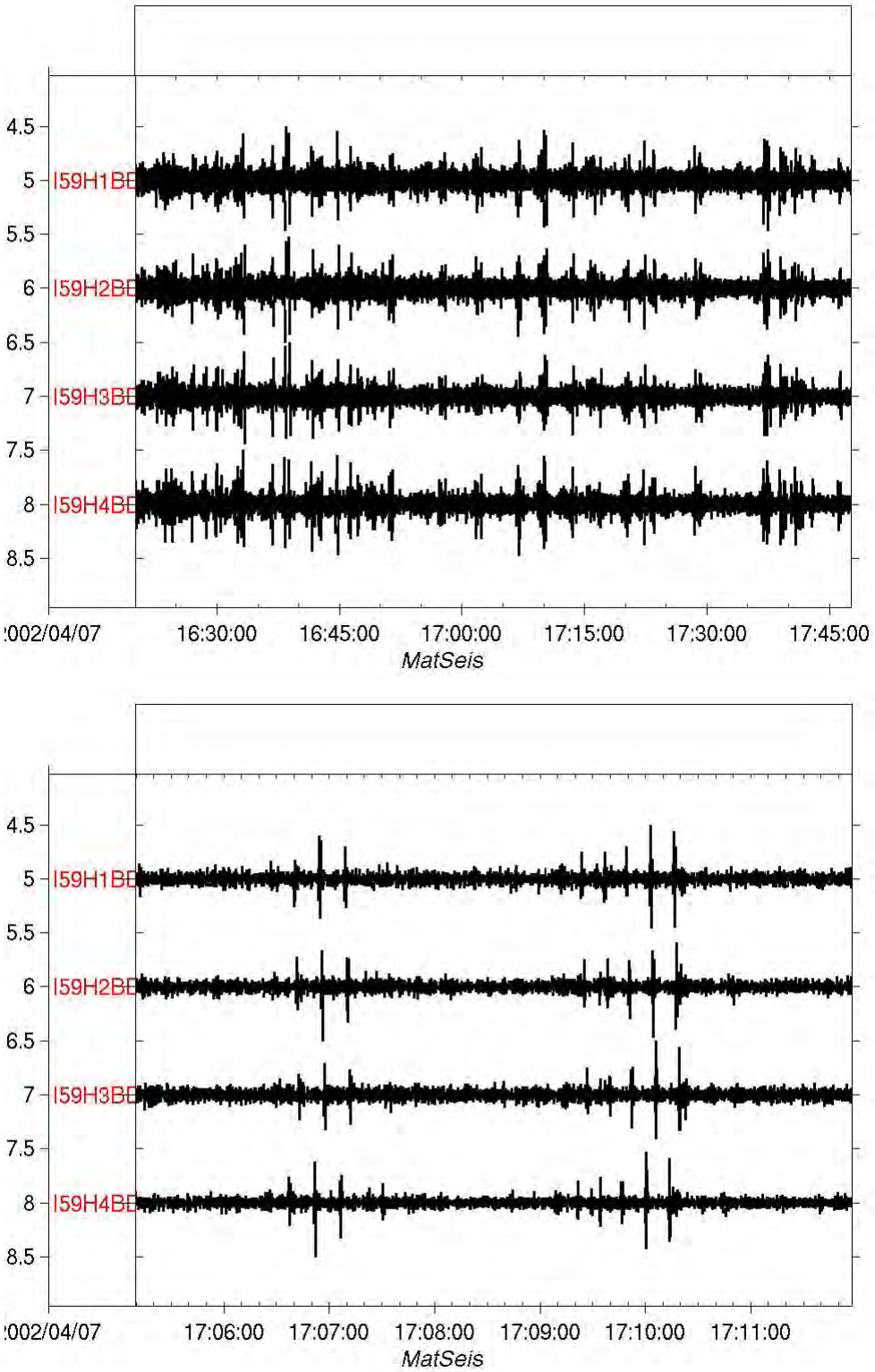

Figure 3. Bandpass-filtered waveform of typical "ik" surf arrival showing regular spacing in time both of groups of arrivals (above) and of individual arrivals (below).

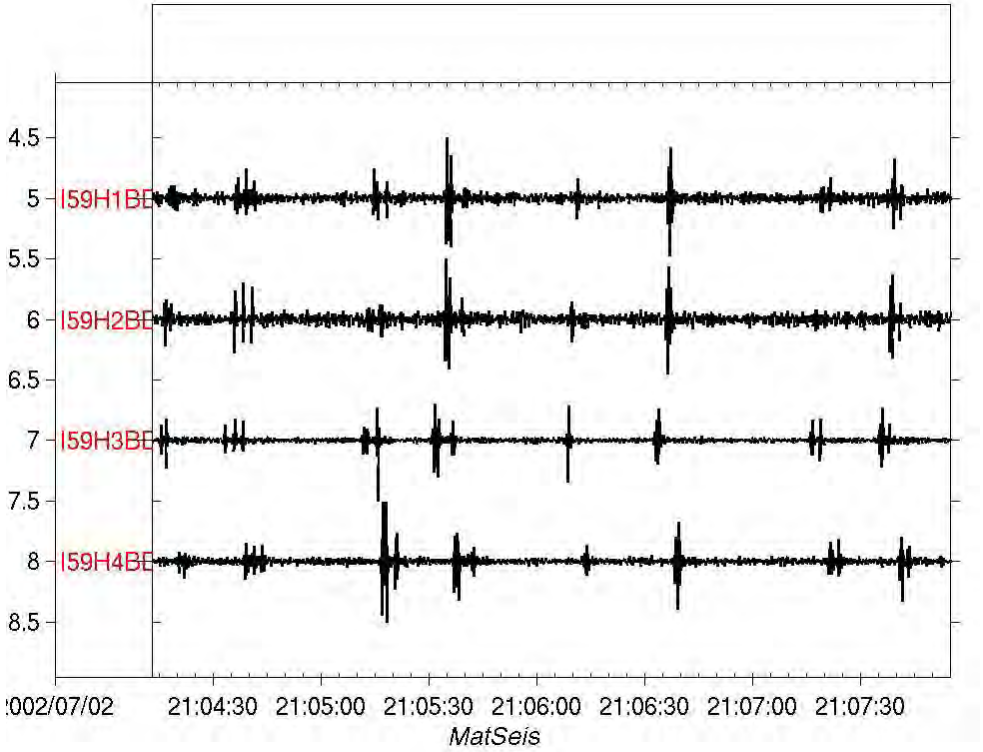

Figure 4. Bandpass-filtered waveform of typical "ip" events showing impulsive quality and irregularity in time.

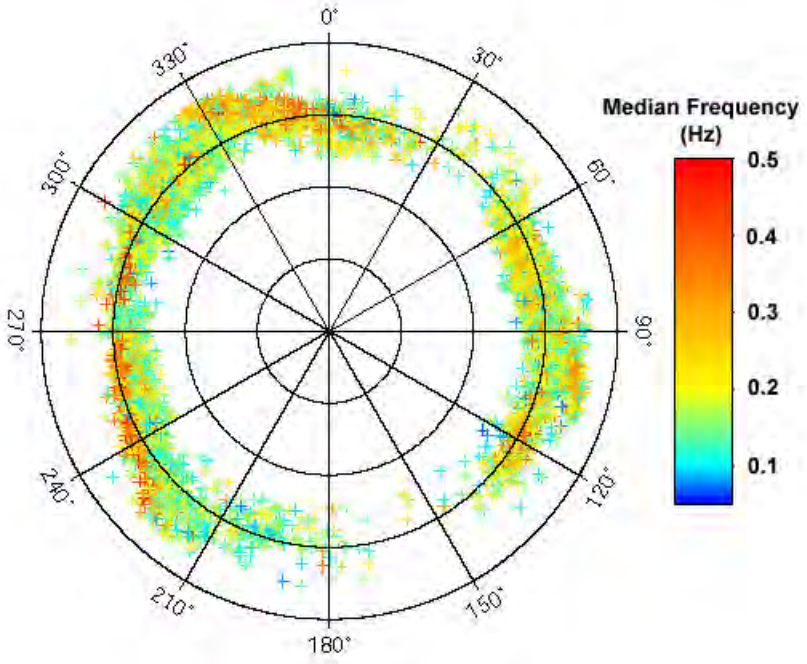

Figure 5. Polar diagram showing arrival azimuth, trace slowness, and median frequency of microbarom events detected from January 1-June 30 2002. Radial units are seconds per degree, increments of 100.

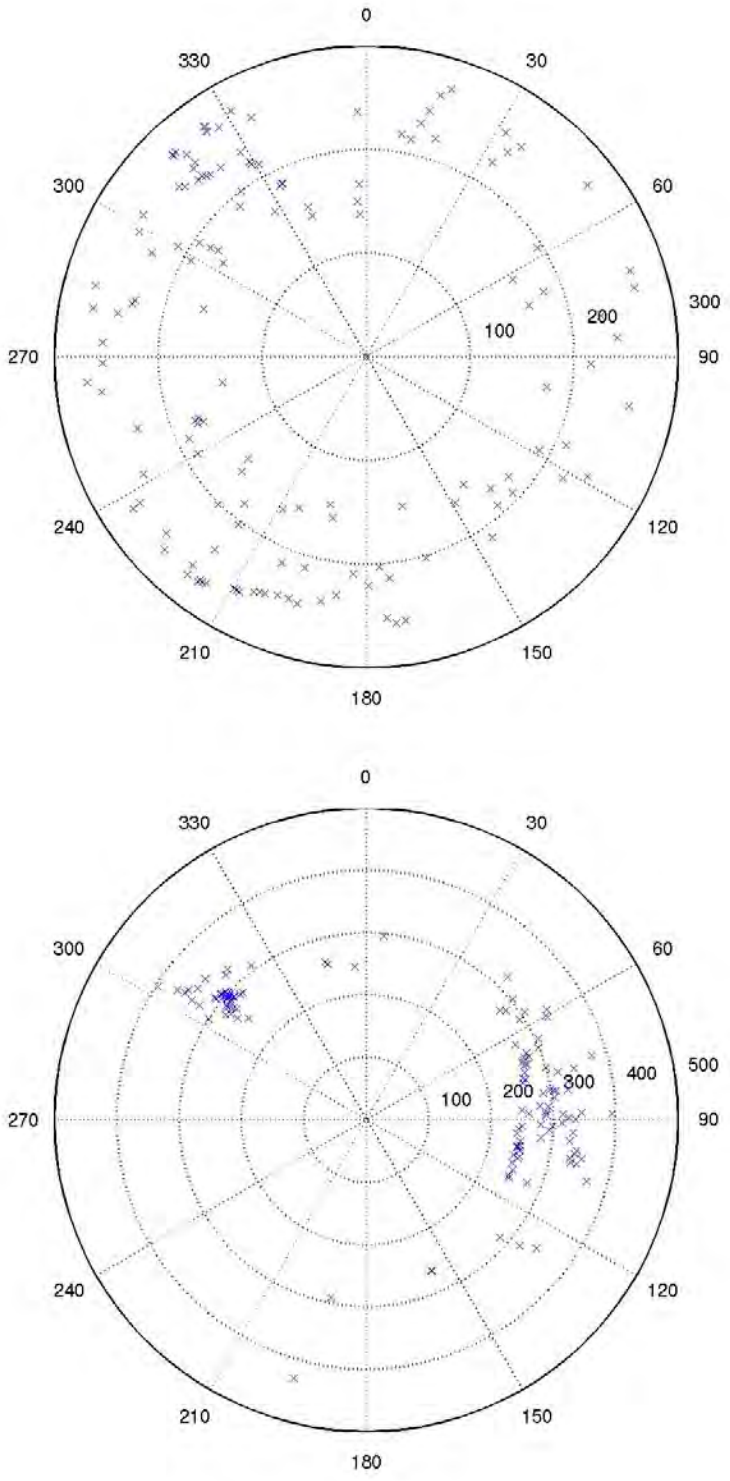

Figure 6. Polar diagrams showing arrival azimuth and trace slowness for detections made by high-speed (above) and very-low-frequency (below) detection parameter sets. Radial units are seconds per degree.

SOURCE LOCATION ALGORITHM FOR INFRASONIC MONITORING

Milton Garces,[1] Claus Hetzer,[1] Kent Lindquist,[2] and Douglas Drob[3]

University of Hawaii Manoa,[1] Lindquist Consulting,[2] and Naval Research Laboratory[3]

Sponsored by National Nuclear Security Administration
Office of Nonproliferation Research and Engineering
Office of Defense Nuclear Nonproliferation

Contract No. DE-FC04-98AL79801

ABSTRACT

Two large bolides have been recorded by International Monitoring System (IMS) infrasound stations in Hawaii and Alaska. On 25 August 2000 at 01:12:25 UTC, Department of Defense and Department of Energy satellites observed an object at 14.45 North and 106.13 West, with a total visible estimated energy of 1.4×10^{12} joules. This object, known as the Acapulco bolide, was observed by IMS stations in Hawaii, Alaska, Bolivia, Canada, and French Guiana, as well as by DLIAR in New Mexico. On 23 April 2001, at 06:12:35 UTC, satellites observed an object at an altitude of 28.5 km at 27.9 North and 133.89 West, with a total visible energy estimate of 4.6×10^{12} joules. This bolide explosion was observed by IMS stations in Hawaii, Alaska, California, Canada, and Germany. We use these two events to study the capabilities and limitations of source location procedures based on travel times and azimuth deviations that are derived from ray tracing formulations. A software algorithm has been developed to ingest accurate atmospheric profiles, which may be provided in near-real-time, use the tau-p method to compute the effective speed, or celerity, of specified infrasonic phases, and export these model results into any standard location algorithm, such as the Generic Locator (genloc) module within the Antelope software platform. This implementation is flexible as well as computationally efficient, and allows the exploitation of Center for Seismic Studies (CSS) (now Center for Monitoring Research) database structures and analysis tools.

OBJECTIVE

The aim of this work is to describe a ray-tracing algorithm for locating infrasonic sources, and to apply this algorithm to the determination of the position and origin time of two bolides detected by infrasound arrays in Hawaii and Alaska.

RESEARCH ACCOMPLISHED

Introduction

The tau-p method of Garcés *et al*. (1998, 2001, 2002) has been refined to clearly identify propagating infrasonic phases. Broadband infrasonic array measurements can be used to extract the amplitude, arrival time, apparent horizontal phase velocity, and azimuth of an arrival. All parameters can be estimated as a function of frequency using the PMCC method (Garcés and Hetzer, 2002). These detection parameters can be used to identify a phase, which is a prerequisite for estimating a source location. Given an atmospheric model, travel-time curves and azimuth deviations can be computed for each phase at any specified arrival azimuth. The apparent speed, or celerity, of a guided arrival is defined as the ratio of the range to the travel time for one or more multi-path bounces. Infrasonic phases identified to date are defined in Table 1, and are compatible with Brown's (1999) nomenclature and the IAVCEI list of propagating seismic phases.

Initial studies concentrated on an exact specification of the propagation path (Le Pichon *et al*., 2002a,b; Liszka and Garcés, 2002), and these works were successful in cases when the range from the source to the receiver was not too large or along the dominant stratospheric wind direction. However, the detection of signals with high celerity propagating against the dominant stratospheric wind direction and the observation of apparent horizontal phase velocities lower than the speed of sound at the ground suggest that the interaction of infrasonic waves with atmospheric or topographical structures may scatter and diffract energy from elevated wave guides into the ground. We illustrate the critical issue of phase identification and the application of the location algorithm by using the bolide explosions of April 23, 2001, and August 25, 2000, as case studies. Because of its greater simplicity, we begin with an analysis of the 2001 bolide.

Event Selection and Array Detections of the April 23, 2001, Bolide

Infrared sensors aboard US Department of Defense (DOD) satellites detected the impact of a bolide on 23 April 2001 at 06:12:35 UTC (988006355 Epoch time). The bolide appeared to explode at an altitude of 28.5 km above the coordinates of 27.9 North and 133.89 West. The impact was simultaneously detected by space-based visible wavelength sensors operated by the US Department of Energy (DOE). The total energy in the visible band was 4.6 X 10^{12} joules. The location for the April 23 event determined by the optical systems is referred to as LO1. Since bolides often propagate at speeds of a few tens of kilometers per second, and there is no guarantee that the infrared detection coincided with the infrasonic signal generation, we postulate that the time of the LOI is more precise than the location of the detection.

The locations of the three nearest IMS arrays that detected the April 23 event are given in Table 2.1, and are shown in the upper panel of Figure 1. The upper panels of Figures 2-5 shows the PMCC (Garcés and Hetzer, 2002) detections for all three arrays. Comparison with the InfraTool detections for IS59 (Garcés *et al*., 2001) shows that the first arrivals for PMCC are 226 seconds (4.4 minutes) earlier than the InfraTool first arrivals. This is an important result, as the first arrival time and the phase identification of that first arrival are essential to the location of infrasonic sources. Table 2.2 shows the maximum celerity values for select propagating phases. The list of Table 1 outlines all candidate phases, but for propagating ranges greater than a few thousand kilometers, it is difficult to sustain the *iw* phases and the *Iw*, *Is*, and *It* phases are not applicable. For long ranges, *is* phases are also found to be unstable, as the stratospheric winds can vary significantly along a meridian. However, the *it*, *itd*, and *isd* phases are found to exist for almost all azimuths and geographic locations. Only when an *is* phase exists does the *itd* phase disappear. For long ranges, the time contribution from the source height to the ground or the source height to the upper waveguide boundary is negligible, multiple bounces produce overlapping travel-time curves that begin to appear as a continuous curve, and shadow zones disappear. The *itd* and *isd* phases (Table 1) correspond to leaky wave guides that are suspended above the ground, but either scatter or diffract acoustic energy to the ground. Sources that explode at heights of ~30 km, such as the April 23 bolide, place acoustic energy in the middle of the low-velocity zone of the stratosphere, and thus efficiently trap energy in the stratospheric duct. This waveguide would be able to duct energy with minimal attenuation, and most first arrivals with high celerity may be attributed to *isd* phases. Due to the continuous appearance of travel-time curves and the further degradation of shadow zones by

scattering and diffraction, we opt to use the celerity as the key propagation model output for the source location iteration.

Infrasonic Location Procedure for April 23 Event

From intersecting back azimuths, it is possible to produce a seed location for the source inversion procedure. However, as can be seen in Figure 1, the back azimuth location may be expected to be in error. An initial origin time can be obtained from the seed location by assuming a constant celerity of 0.3 km/s and computing the great circle paths to the source. Alternatively, if ground truth is known on an event, such as the epicentral location issued by the DoD release, the range of each station to the source and the expected azimuth of the incoming signal can be readily computed. Once an initial azimuth from source to receiver is determined, the tau-p method of Garcés *et al*. (1998, 2002) can be used to compute the celerity of each propagating phase. The lower panels of Figures 2-4 show the celerity computed at each array for the April 23 bolide using the Naval Research Laboratory's (NRL) SAGE atmospheric profiles that include accurate specifications of the troposphere and stratosphere (Garcés *et al*., 2001). The estimated times of arrival of the first or second arrival at the station were used to compute the residuals from a grid search around the seed source location and origin time. Various locations were made assuming different phase identifications for both first and second arrivals (when present), but only two solutions (with the minimal residuals) are shown in Table 2.3. The first solution, LA_S1, assumes all first arrivals correspond to *isd* phases, and produced a very good match to the origin time provided by the satellite observation (LO1). Although in seismic location an 8-s time differential is unacceptable, when scaled to the total travel time of the signal, the percent error is small and comparable to the best seismic location accuracies (Table 2.4). The difference in the source location between LO1 and LA_S1 may be attributed to the high speed of the bolide and could correspond to a difference in where the peak sound and infrared energy are radiated. This result suggests that *isd* phases can be used to explain the arrival of signals in the upstream stratospheric direction, and the relatively higher frequency of the first arrivals observed in Figure 2 and 3 suggest that scattering is an important factor. A second solution, LA_S2, assumed that the first arrival at IS53 was an *isd* phase, the second arrival at IS57 was an *itd* phase, and the second arrival at IS59 was an *isd* phase. These phases were selected in an attempt to match the source location at the expense of the origin time. However, we favor the first solution because we believe the uncertainty in time (~10 s) may be less than the uncertainty in position for the satellite location LO1.

Infrasonic Location Procedure for the August 25, 2000, Event

The August 25, 2000, bolide, known as the Acapulco bolide, is more difficult to unravel. Table 3.1 shows the infrasonic observations for the Acapulco bolide. The arrival information for the stations in South America was derived from PMCC results (Le Pichon, personal communication, 2000). The lower panel of Figure 1 shows the station locations and back azimuths, again showing a poor azimuth fit of some of the stations to the actual source location. In general, it appears that the worst azimuth deviations occur in stations with extreme topography along the propagation path, specifically IS53 (Alaska) and IS08 (Bolivia). From the seed locations, azimuths from the stations to the source were estimated and the celerity computed at each station. Table 3.2 shows the maximum celerity for each phase. Figure 6 shows the PMCC detection at DLIAR, the closest station, and the change in detection azimuth with time. Following the same procedure as for the April 23 event, we computed locations for various permutations of phase identifications for the first and second arrival times. An attempt was also made to separate the detections into two events, one recorded by the US stations and another by the South American stations. However, two-station locations are inherently unstable, and even the solution using the three US stations was unstable because of the near parallel alignment of the DLIAR and IS53 propagation paths from the source. Three solutions are shown in Table 3.3. The first solution, LA_DL1, assumes all first arrivals are *isd* phases, and yielded a large error on the origin time estimate as well as in the time differentials for some of the stations (Table 3.4). The second solution, LA_DL2, assumed a combination of *it*, *itd* and *isd* phases (Table 3.5) and yielded a good fit to the origin time, although the time differentials per station are not as good as the April 23 solution. A source location west of the LO1 location is consistent with the DLIAR observations. Further work is needed to determine whether this event consists of a single bolide or more than one bolide arriving at different times, as suggested by the infrasound detections from IS25.

CONCLUSIONS AND RECOMMENDATIONS

Infrasonic estimates of the origin time and location of the April 23 event were performed using realistic atmospheric profiles and the tau-p method to estimate the celerity of propagating phases in the atmosphere. Arrivals corresponding to phases propagating in leaky stratospheric ducts produced the best fit to the origin time obtained from the satellite infrared detection. This existence of these leaky stratospheric ducts may explain how stratospheric

phases can be observed along both the upstream and downstream dominant stratospheric wind directions. Further work is needed on how topography and perturbations in the atmosphere can scatter and diffract infrasonic energy into and out of elevated wave guides. The next generation of the tau-p software will address propagation in range-dependent environments.

REFERENCES

Brown, D.J. (1999). Summary of infrasound source location meeting: San Diego, November 9-10, 1998, *Center for Monitoring Research*, Arlington, VA.

Garcés, M, and C. Hetzer (2002). Evaluation of infrasonic detection algorithms. *This volume.*

Garcés, M., D. Drob, and M. Picone (2002). A theoretical study of the effect of geomagnetic fluctuations and solar tides on the propagation of infrasonic waves in the atmosphere. *Geophys. J. International*, **148**, 77-87.

Garcés, M, C. Hetzer, K. Lindquist, and R. Hansen, J. Olson, C. Wilson, D. Drob, M. Picone, (2001). Infrasonic location of the April 23, 2001, Bolide event. *23nd Annual DTRA/NNSA Seismic Research Review*, Jackson Hole, 1-5 October 2001.

Garcés, M, D. Drob, M. Picone, K. Lindquist, and R. Hansen (2000). Characterization Of Infrasonic Waves Observed In Hawaii During Summer, *22nd Seismic Research Symposium: Planning for Verification of and Compliance with The Comprehensive Nuclear-Test-Ban Treaty*, New Orleans.

Garcés, M. A., R. A. Hansen, and K. Lindquist (1998). Travel times for infrasonic waves propagating in a stratified atmosphere, *Geophys. J. International*, **135**, 255-263.

Le Pichon, A. M. Garcés, E. Blanc, M. Barthélémy, D. Drob (2002). Acoustic propagation and atmosphere characteristics derived from infrasonic waves generated by the Concorde. *J. Acoust. Soc. Am*., **111**, 629-641.

Le Pichon, A., J. Guilbert, A. Vega, and M. Garcés (2002), Ground-coupled air-waves and diffracted infrasound from the Arequipa earthquake of June 23, 2001, *Geophysical Research Letters* (in press).

Liszka, L., and M. Garcés (2002), Infrasonic Observations of the Hekla Eruption of February 26, 2000. *Journal of Low Frequency Sound* (in press).

Kulichkov, S. N. (1998). On problems of infrasonic monitoring of small energy explosions, *Proceedings of the Informal Workshop on Infrasound*, Bruyers-Le-Chatel, France.

Table 1. Preliminary phase identification nomenclature for long-range infrasonic propagation

Phase ID	Description	Typical celerity of first arrival, m/s
iw	Guided wave propagating between the tropopause and the ground.	330-340
is	Guided wave propagating between the stratopause and the ground.	310-330
isd	Guided wave propagating in elevated waveguide between stratopause and the troposphere, and diffracted or scattered to the ground. May have higher frequency.	310-330
it	Guided wave propagating between the lower thermosphere and the ground.	280-300
itd	Guided wave propagating in elevated waveguide between the lower thermosphere and the troposphere, and diffracted or scattered to the ground.	280-300
It, Is, Iw	Direct arrival from the source to the receiver. May have high apparent phase velocity	N/A

Table 2.1. First arrival observations of April 23, 2001, bolide by three nearest IMS infrasound stations

Station	Lat (N)	Lon (E)	Speed (m/s)	Azimuth	ETA (epoch)
IS53	64.87	-147.84	322	150.6	988020690
IS57	33.6	-116.5	349	256.1	988012060
IS59	19.59	-155.9	348	63.6	988013790

Table 2.2. Predicted first arrival celerity (km/s) for select phases: April 23, 2001

	it	itd	isd
IS53	0.268	0.284	0.292
IS57	0.278	0.292	0.328
IS59	0.284	0.3	0.311

Table 2.3. Source location and errors relative to satellite location (LO1): April 23, 2001

Source	Lat (N)	Lon (E)	Origin Time (Epoch)	Lat error (deg)	Lon error (deg)	Time error (s)
LO1	27.9	-133.89	988006355	0	0	0
LA_S1	28.07	-135.09	988006347	0.17	-1.2	-8
LA_S2	27.79	-133.42	988006145	-0.11	0.47	-210

Table 2.4. Phase selection and time error for LA_S1 solution: April 23, 2001
PA = predicted arrival; ETA = first arrival time; OT = origin time

Station	Selected Phase	Range to LA_S1	X/T (km/s)	Predicted arrival	Time Error /Travel Time	PA-ETA	PA-OT	Ratio (%)
IS53	isd	4191	0.292	988020700	-0.06%	10	14353	0.07
IS57	isd	1877	0.328	988012070	-0.14%	10	5723	0.17
IS59	isd	2313	0.311	988013784	-0.11%	-6	7437	0.08

Table 3.1. First arrival observations of August 25, 2000, bolide by infrasound stations.

Station	Lat (N)	Lon (E)	Speed (m/s)	Azimuth	ETA (epoch)
IS08	-16.3	-68.1	340	298	967184490
IS25	5.2	-52.7	344	283	967187730
IS53	64.87	-147.84	355	144	967187230
IS59	19.59	-155.9	346	88	967182900
DLIAR	35.87	-106.33	360	180	967173900

Table 3.2. Predicted first arrival celerity (km/s) for select phases: August 25, 2000

	it	itd	isd
IS08	0.289		0.298
IS25	0.263	0.285	0.29
IS53	0.292	0.303	0.31
IS59	0.281	0.297	0.308
DLIAR	0.278		0.309

Table 3.3. Source location and errors relative to satellite location (LO1): August 25, 2000

Source	Lat (N)	Lon (E)	Origin Time (Epoch)	Lat error (deg)	Lon error (deg)	Time error (s)
LO1	14.45	-106.13	967165945	0	0	0
LA_DL1	13.68	-108.21	967166247	-0.77	-2.08	302
LA_DL2	13.37	-107.74	967165950	-1.08	-1.61	5

Table 3.4. First arrival phase selection and time error for LA_DL1 solution: August 25, 2000

Station	Selected Phase	Range to LA_DL1	X/T (km/s)	Predicted Arrival	Time Error / Travel Time	PA-ETA	PA-OT	Ratio (%)
IS08	isd	5513	0.298	967184747	1.63%	257	18500	1.39
IS25	isd	6149	0.290	967187450	1.39%	-280	21203	-1.32
IS53	isd	6432	0.310	967186995	1.42%	-235	20748	-1.13
IS59	isd	5110	0.308	967182838	1.78%	-62	16591	-0.37
DLIAR	isd	2464	0.309	967174221	3.80%	321	7974	4.03

Table 3.5. First arrival phase selection and time error for LA_DL2 solution: August 25, 2000

Station	Selected Phase	Range to LA_DL2	X/T (km/s)	Predicted Arrival (PA)	Time error / Travel time	PA-ETA	PA-OT	Ratio (%)
IS08	it	5452	0.289	967184815	0.03%	325	18865	1.72
IS25	itd	6096	0.285	967187339	0.02%	-391	21389	-1.83
IS53	itd	6481	0.303	967187339	0.02%	109	21389	0.51
IS59	isd	5168	0.308	967182729	0.03%	-171	16779	-1.02
DLIAR	isd	2495	0.309	967174024	0.06%	124	8074	1.54

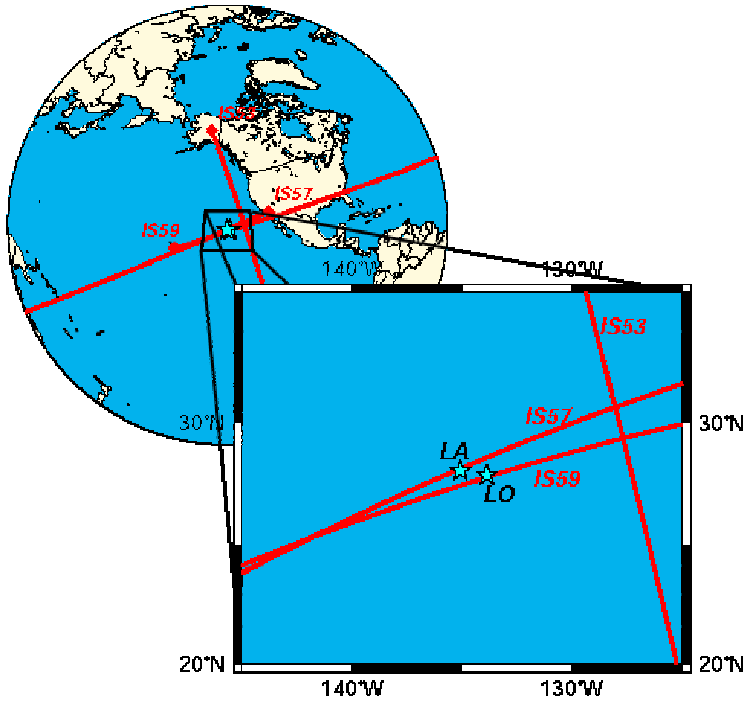

Figure 1. Satellite (LO) and infrasonic (LA_S1) location for the April 23, 2001, bolide. The observed arrival azimuths at infrasound arrays IS53, IS57, and IS59 are shown as red lines.

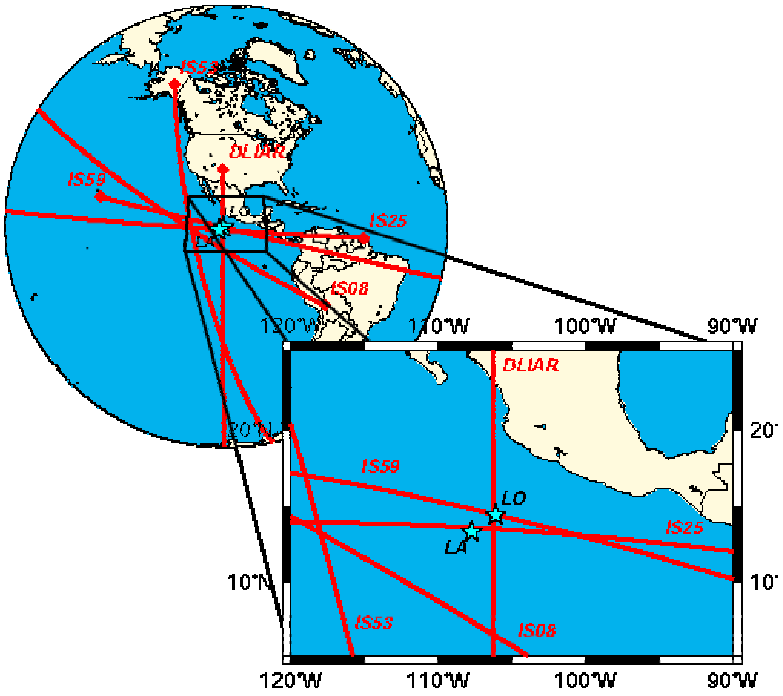

Figure 2. Satellite (LO) and infrasonic (LA_DL2) location for the Acapulco bolide. The observed arrival azimuths at infrasound arrays IS08. IS25, IS53, DLIAR, and IS59 are shown as red lines.

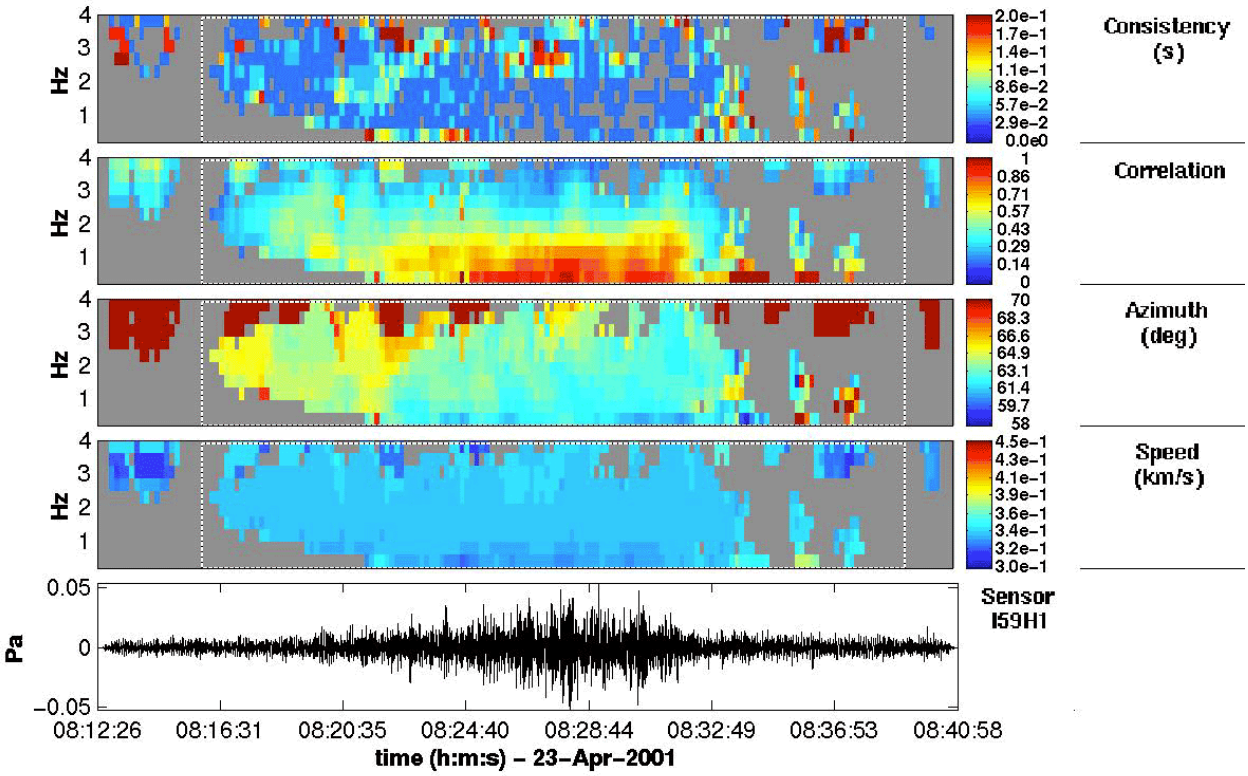

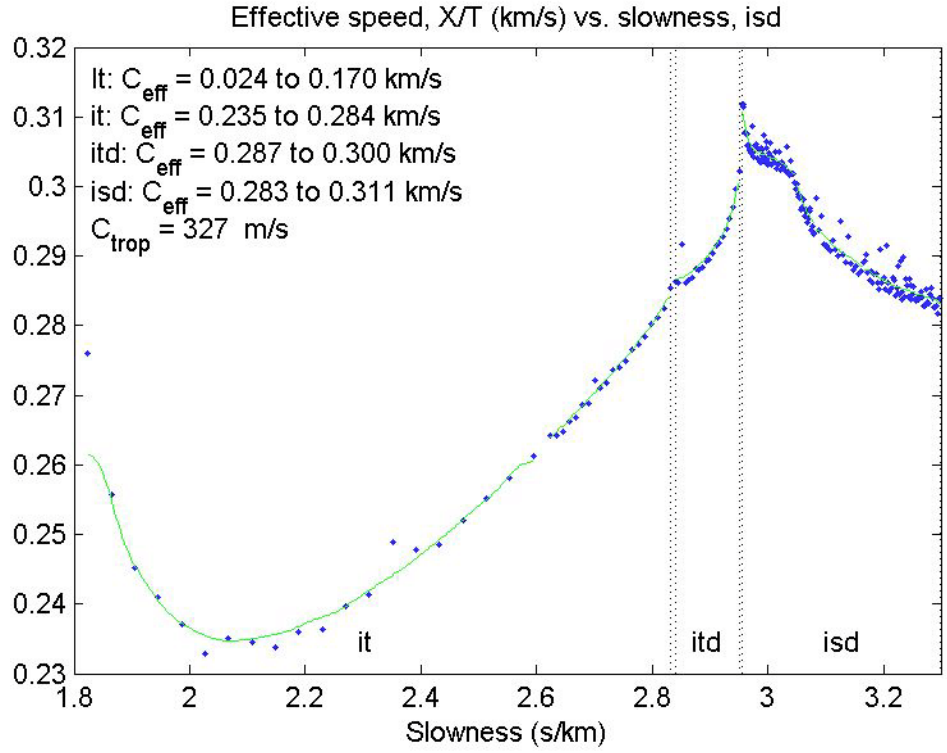

Figure 3. Detection and predicted celerity at IS59, Hawaii, for April 23, 2001, bolide.

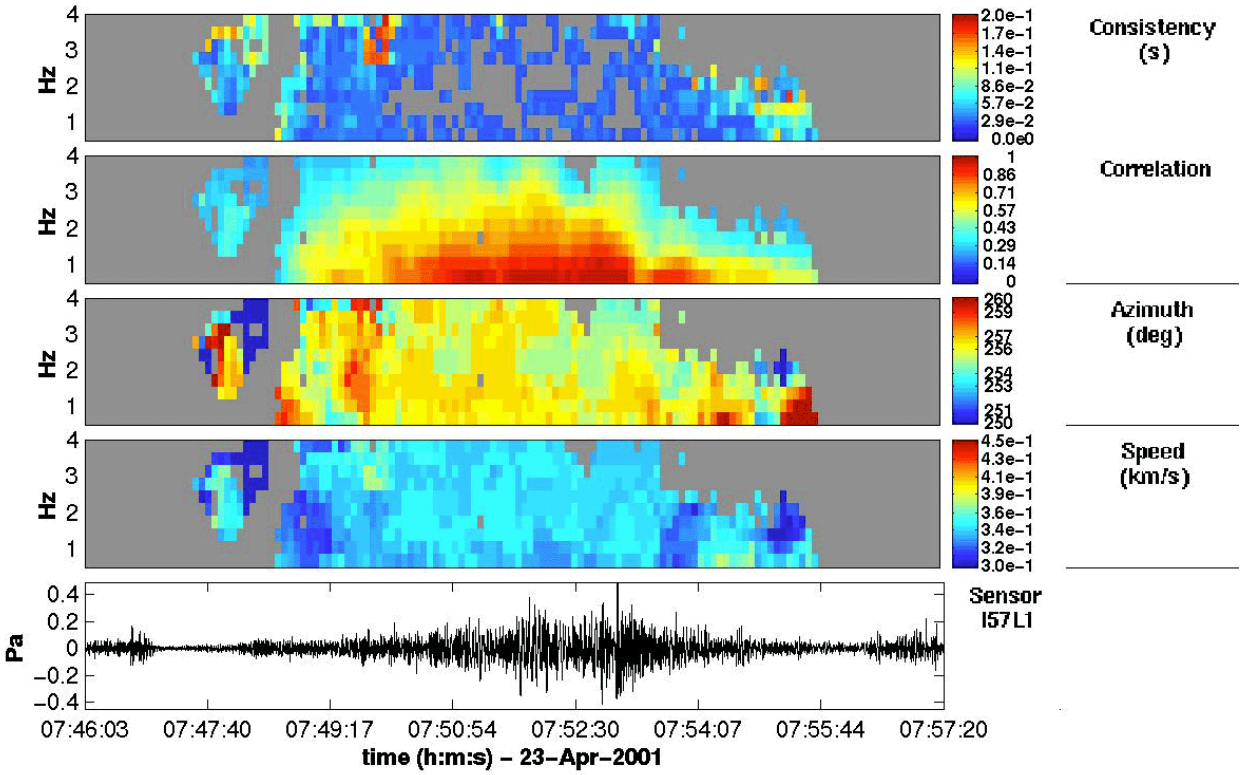

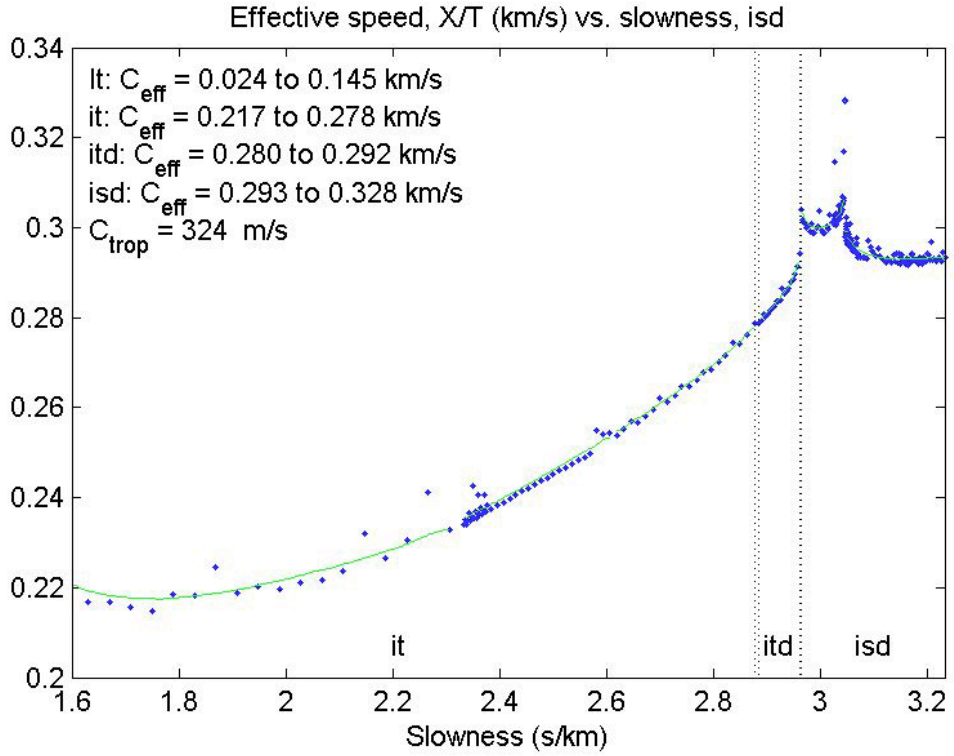

Figure 4. Detection and predicted celerity at IS57, Piñon Flats, for April 23, 2001, bolide.

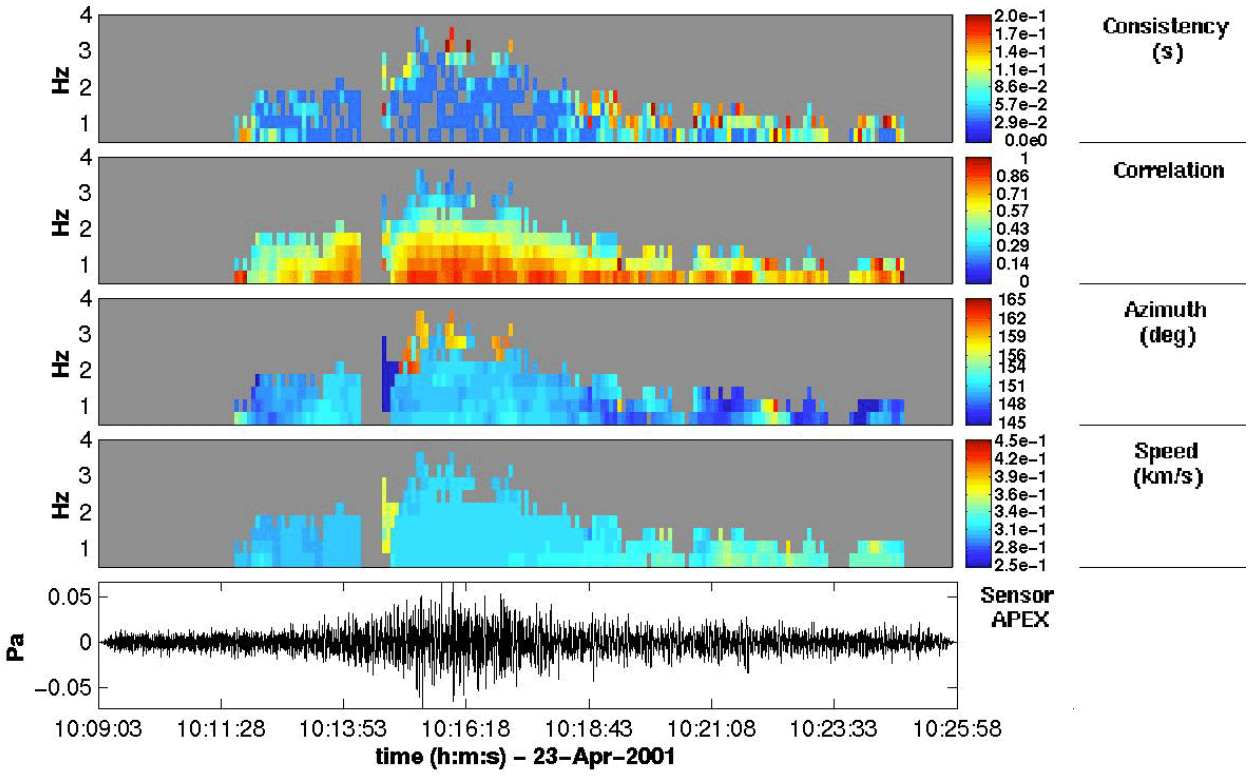

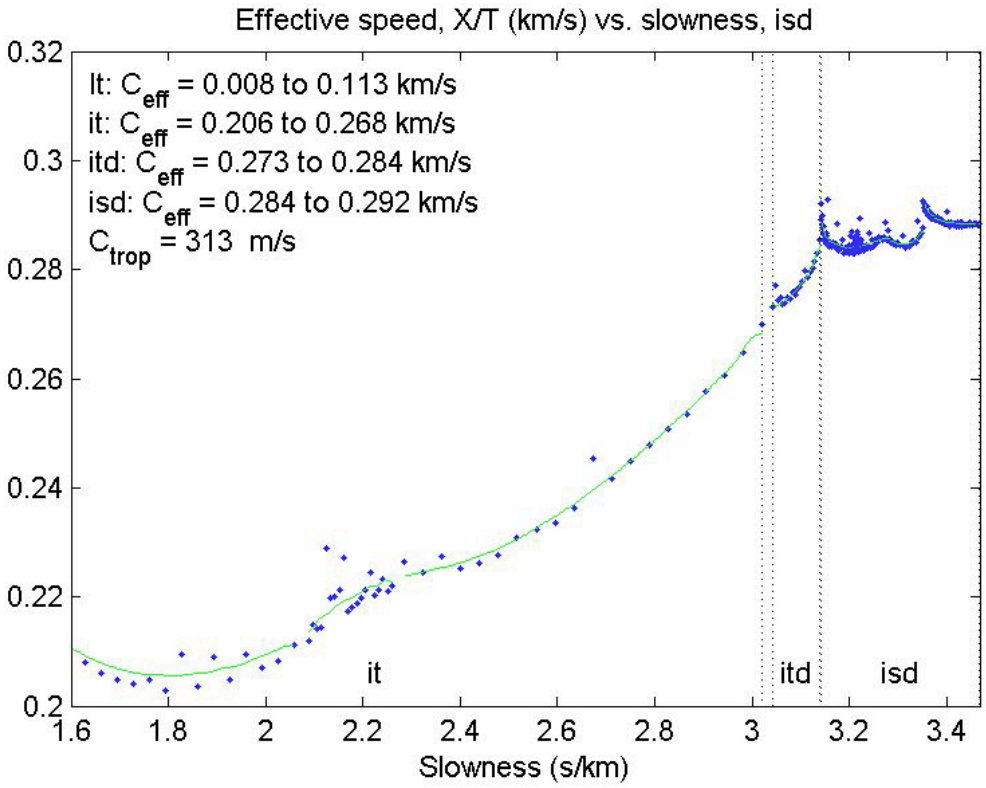

Figure 5. Detection and predicted celerity at IS53, Fairbanks, Alaska, for April 23, 2001, bolide.

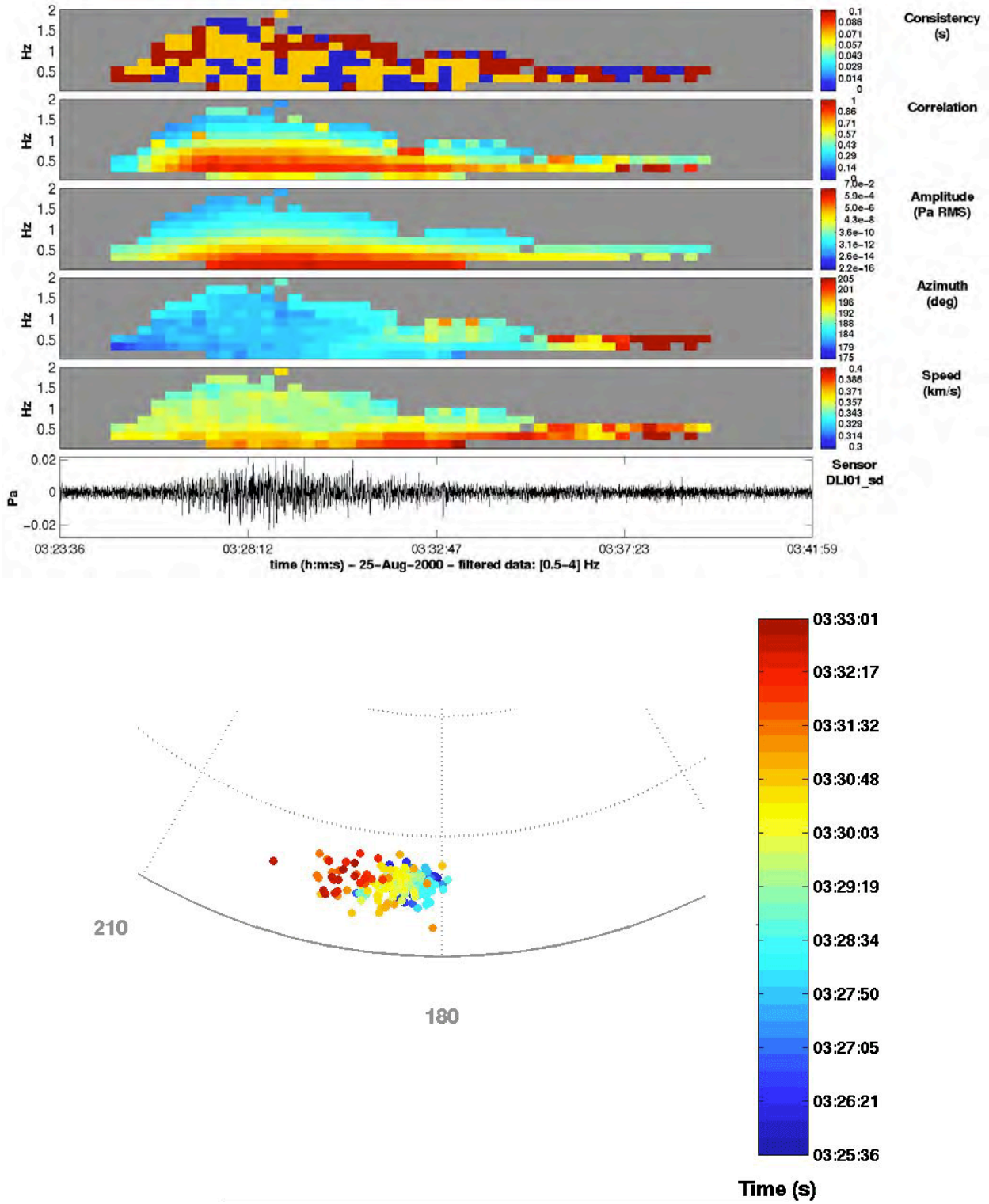

Figure 6. Detections and azimuth changes as a function of time observed at DLIAR, New Mexico, for the Acapulco bolide.

MODELING OF MICROBAROM SIGNALS IN THE PACIFIC

Milton Garcés, Claus Hetzer, Steven Businger, and Mark Willis

University of Hawaii, Manoa

Sponsored by Defense Threat Reduction Agency

Contract No. DTRA01-01-C-0077

ABSTRACT

Severe weather in the ocean generates infrasonic signals in the 0.1- to 0.5-Hz frequency band that can propagate for thousands of kilometers. The source generation mechanism for microbaroms is believed to be the same as for microseisms, and is attributed to the nonlinear interaction of surface ocean waves. We compare theoretical predictions with infrasonic observations of Hurricane Daniel in July of 2000. The nonlinear interaction of the ocean wave field is predicted to radiate sound waves only if the ocean waves are almost opposite in direction and of a near identical frequency. However, perfectly opposing wave trains of the same frequency radiate vertically, and this acoustic energy never returns back to the earth. Only opposing wave trains that are slightly off line or with slightly different frequencies will result in isotropic acoustic radiation, even for highly directional ocean wave fields. The slowness of the infrasonic waves observed by International Monitoring System (IMS) array IS59, or KONA, suggests that these waves were propagating close to the horizontal. The observed azimuth of the incident sound waves corresponds to the most energetic stage of Daniel's lifespan, and suggests that the acoustic signals were radiated during the interaction of surface gravity waves in the open ocean. Using the known dispersion relation for deep water waves, the median detection frequency corresponds to ocean wave speeds that are slower than the known hurricane track speed of Daniel, a condition that would encourage the nonlinear interaction.

OBJECTIVE

The aim of this work is to characterize microbarom signals observed in the Pacific and model the source processes that generate these signals, with the aim of determining infrasonic detection thresholds in the microbarom frequency range.

RESEARCH ACCOMPLISHED

1. Introduction

Infrasonic signals known as microbaroms consist of pressure oscillations with dominant periods of 4-7 s, and they can appear as energy bursts or as a continuous oscillation that can last for hours or days. In the frequency domain, microbaroms appear as a broad frequency peak centered around 0.2-0.3 Hz (Figure 1). Like microseisms in seismology (Kibblewhite and Wu, 1996), microbaroms are thought to be generated by the nonlinear interaction of ocean surface waves. For infrasonic stations near the ocean, microbaroms determine the noise floor in the 0.1-0.5 Hz frequency band, and thus determines the detection thresholds in that band. In Hawaii, microbarom signals are determined from all azimuths (Garces and Hetzer, 2002), and the dominant signal is usually corresponds to either the closest storm to the recording station or the largest wave heights associated with severe weather in the Pacific.

2. Theoretical background

Our starting assumption is that the source generation mechanisms for microbaroms is similar to that of microseisms. However, microseisms and microbaroms will have very different propagation paths. Energy launched near a vertical angle to the ocean surface and towards the ocean floor couples well with the bedrock, and energy launched just below the ocean surface may not reach the ground. In contrast, energy launched near a vertical angle into the atmosphere never returns back to the Earth, and most of the infrasonic signals recorded by ground stations correspond to energy launched near the horizontal angle at the source. The radiation pattern of microbarom sources is discussed below.

For a specified ocean surface wave velocity u_z, the far-field acoustic pressure, p, in a homogeneous atmosphere can be expressed as (Arendt and Fritz, 2000),

$$p\left(x, y, z, t - \frac{R}{c}\right) = -\frac{\rho_0}{8\pi c}\frac{\partial}{\partial t}\int \frac{z}{R^2} u_z^2 \, dx' \, dy'$$

$$R^2 = (x - x')^2 + (y - y')^2 + z^2$$

where x,y, and z are the spatial coordinates in a Cartesian reference frame, x' and y' are the Cartesian coordinates of integration over the ocean surface, ρ_o is the atmospheric density, and c is the atmospheric sound speed. Note that the acoustic pressure is proportional to the integral of the square of the ocean surface velocity. After expressing the ocean surface velocity as sinusoidal terms corresponding to propagating surface wave trains, we find propagating acoustic solutions only exist for surface waves that interact with each other at near the same frequency and nearly anti-parallel directions. All other solutions are non-propagating.

The period and amplitude of an ocean wave depend on the wind speed and fetch of a severe weather disturbance. Although high wind speeds are possible in a hurricane, such winds are usually highly localized, have a relatively small fetch, and thus do not efficiently generate large ocean waves. Ocean surface waves that propagate for long ranges usually have periods of 8-12 seconds. Due to the nonlinear interaction introduced by the square of the velocity, the acoustic solution will have approximately twice the ocean wave frequency (frequency doubling). This can be understood as an acoustic coupling, as for sound to be efficiently radiated in the atmosphere it is necessary for the horizontal wavelength of the ocean wave field to match the acoustic wavelength. Due to the slow propagation speed of deep water waves, their wavelength tends to be too small for acoustic coupling unless two surface wave trains are propagating nearly opposite to each other, in which case one of the nonlinear terms allows the existence of a large horizontal wavelength (small horizontal wave number) that encourages efficient coupling to the atmosphere. This nonlinear term corresponds to an acoustic frequency that is the sum of the frequencies of the interacting surface wave trains, or approximately twice the dominant frequency of the ocean wave. Figure 2 shows the real part of the vertical component of the acoustic wave number as a function of ocean surface wave number (upper panel) and acoustic wave number (lower panel).

The wave number solution space for the surface wave velocity corresponds to two waves propagating in almost parallel but opposite directions. However, the acoustic solution space is isotropic, which implies that even a very directional surface wave field can generate infrasonic waves along all azimuths. This isotropic acoustic radiation pattern helps explain the pervasiveness of the microbarom signals. When ocean waves propagate exactly against each other at the same frequency, the nonlinear interaction produces a piston-like displacement of the ocean surface, and launches sound straight up to the atmosphere. Maximum acoustic energy is radiated in the vertical direction, and although it may contribute to the atmosphere's heating (Rind, 1977), this energy is lost to space and cannot be recorded by ground-based stations. Infrasound arrays would only record microbarom signals that are launched close to the horizontal, corresponding to ocean waves interacting at slightly dissimilar frequencies and slightly off the anti-parallel directions. Thus, only a small fraction of the total acoustic energy launched into the atmosphere by microbarom sources reaches the ground.

3. Case study: Hurricane Daniel

Approximately two months after the initiation of operations of IMS array I59US in Hawaii, Hurricane Daniel formed in the eastern Pacific and steadily moved towards Hawaii. Figure 3 shows the track history of Daniel, and the arrival azimuth of infrasonic signals detected by I59US, also referred to as KONA. All microbarom detections were computed using the PMCC method described in Garces and Hetzer (2002). We see that infrasonic detection of Daniel started before it was designated a hurricane (Figure 3, red), and the detected azimuth matches the actual azimuth of Daniel up to August 1, when Daniel began to dissipate. Figure 4 shows the frequency content of the microbarom signals recorded by KONA. Most of the energy is in the 0.1-0.4 Hz band, and there is a bifurcation in the microbarom band from late July 30 to early August 1. The track speed and maximum wind speed of Daniel is shown in Figure 5. The frequency of the optimal detection at KONA and the range of Daniel from KONA is plotted in the upper panel of Figure 6. Using the dispersion relation for deep water ocean waves, the propagation group velocity for surface waves at the frequency of optimal detection is shown in the lower panel of Figure 6, superposed with the track velocity of Daniel. For a 10 s ocean wave period, the acoustic period will be 5 s, corresponding to a frequency of 0.2 Hz. The group velocity for a 10 s ocean wave is ~ 8m/s. As mentioned in the previous section, a prerequisite for acoustic radiation is the presence of surface waves interacting nearly anti-parallel to each other. Two scenarios in which this condition may be maintained involve (1) a storm system that is propagating faster than the group velocity of surface waves, and (2) surface waves reflected from continents or island. The lower panel of Figure 6 suggest that the initial source of microbarom generation involved the first mechanism, but the later detections involved both mechanisms. Reflections of the storm-generated ocean waves from the islands may also explain the frequency bifurcation in the spectral content of the signals, which correspond to the close proximity of Daniel after July 30.

CONCLUSIONS AND RECOMMENDATIONS

Initial work has been performed in the evaluation of the infrasonic field predicted from storm activity in the Pacific. The theoretical results are consistent with infrasonic observations of Hurricane Daniel as it approached Hawaii. Infrasound from Daniel appears to be initially generated by the interaction of ocean waves generated behind and ahead of the hurricane core as it moved faster than the propagation speed of the ocean waves. As Daniel approached Hawaii, some higher frequency infrasound may have been generated by the interaction of the direct ocean waves with reflections from the island chain. Further work is needed on quantifying the relationships between hurricane dynamics, surface ocean wave generation, and infrasound generation.

REFERENCES

Arendt, S., and D. Fritts (2000). Acoustic radiation by ocean surface waves. *J. Fluid Mech*, **415**, 1-21.

Garces, M., and C. Hetzer (2002). Evaluation of infrasonic detection algorithms. This volume.

Kibblewhite, A., and Cheng Y. Wu (1996). Wave interactions as a seismo-acoustic source. Lecture Notes in Earth Sciences, Springer-Verlag, Berlin.

Rind, D. (1977). Heating of the lower thermosphere by the dissipation of acoustic waves. *J. Atmospheric and Terrestrial Physics*, **39**, 445-456.

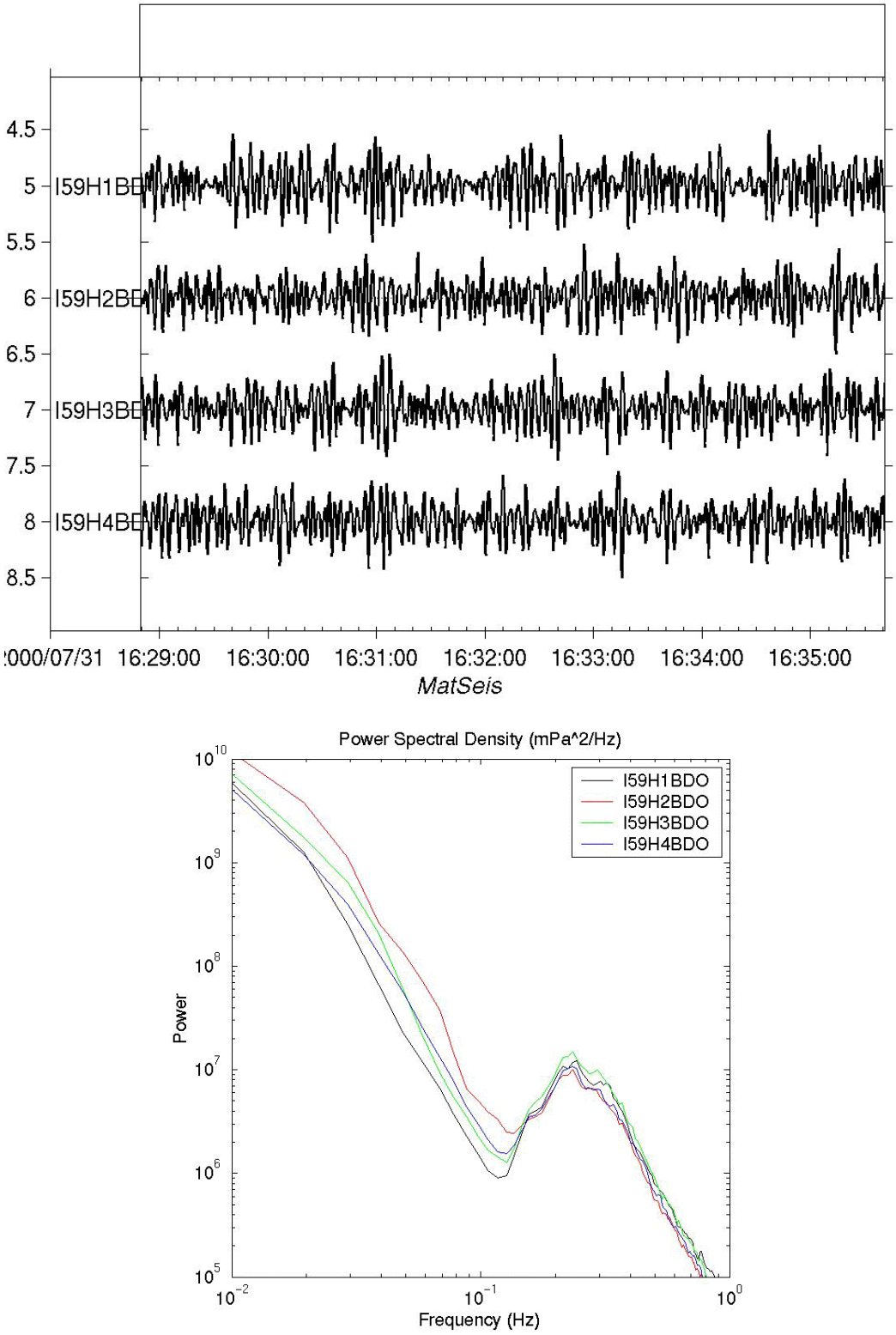

Figure 1. Example of microbarom signals recorded in Hawaii on July 31, 2000, and power spectral density for the same time period.

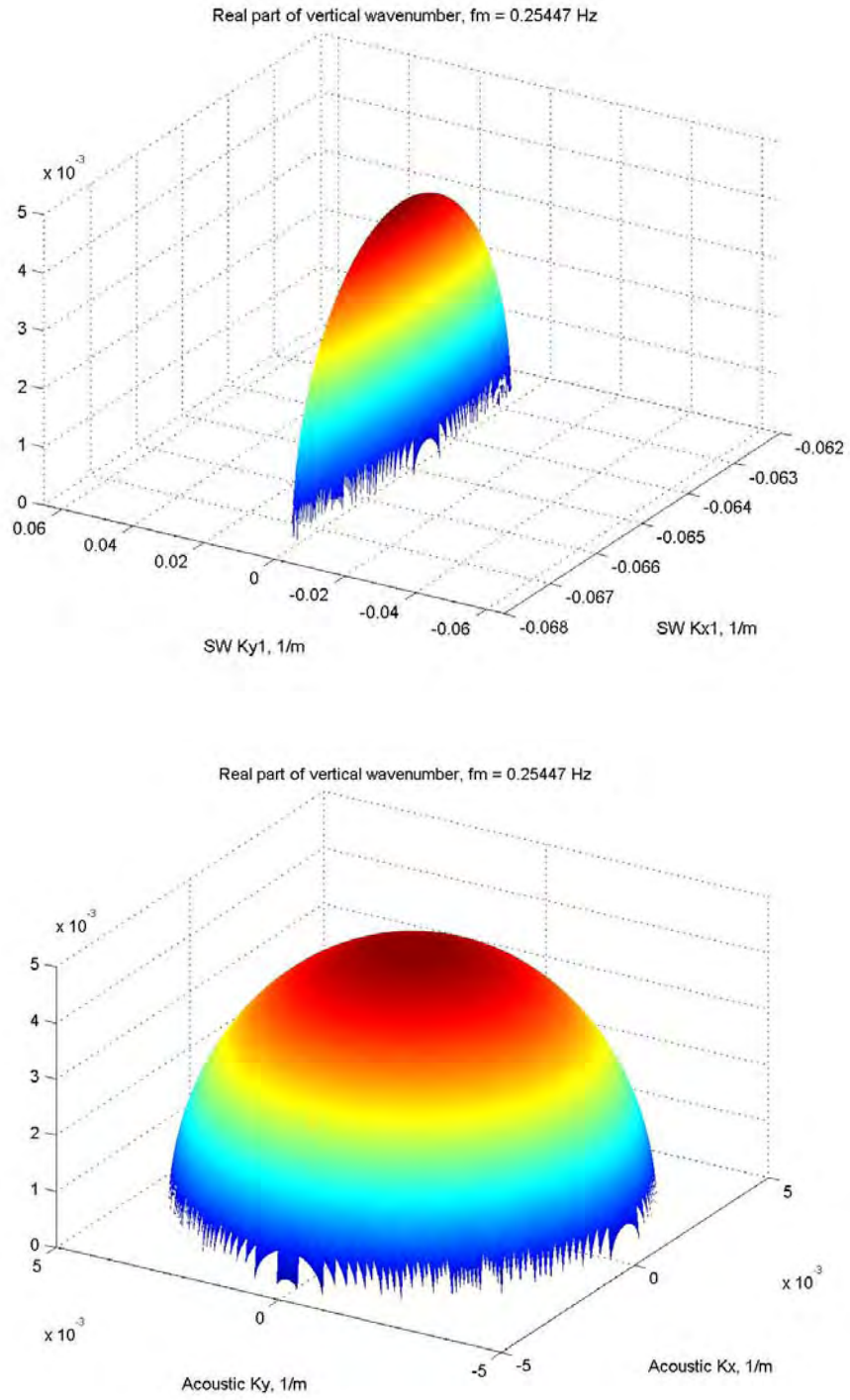

Figure 2. Real part of the vertical wave number of the acoustic solution of Arendt and Fritz (2000) for a surface wave period of ~8 s propagating along the horizontal direction (ky = 0, kx>0) and interacting with a second ocean wave of arbitrary direction. The upper panel shows the acoustic solution only exists for a small range of ocean wave numbers corresponding to the second surface wave propagating nearly anti-parallel (ky << kx, kx <0) to the first wave. The lower panel shows the real part of the acoustic vertical wave number as a function of the horizontal wave number, illustrating the isotropic nature of the acoustic radiation pattern.

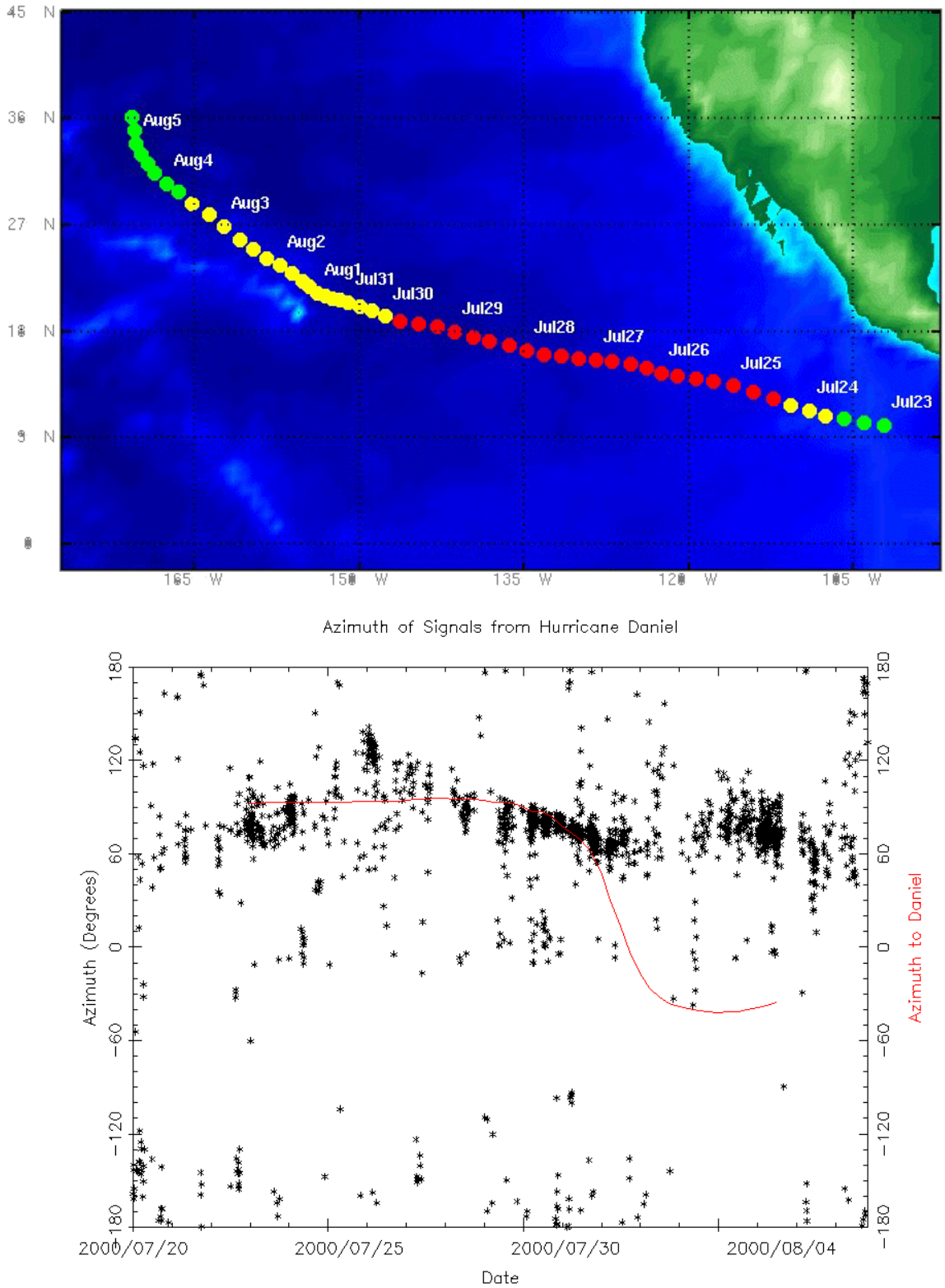

Figure 3. Track of Daniel (upper panel) and observed infrasonic arrival azimuth (lower panel), measured clockwise from N, for microbarom signals observed in KONA for the same period. The red line in the lower panel marks the azimuth from Hawaii to Daniel's core.

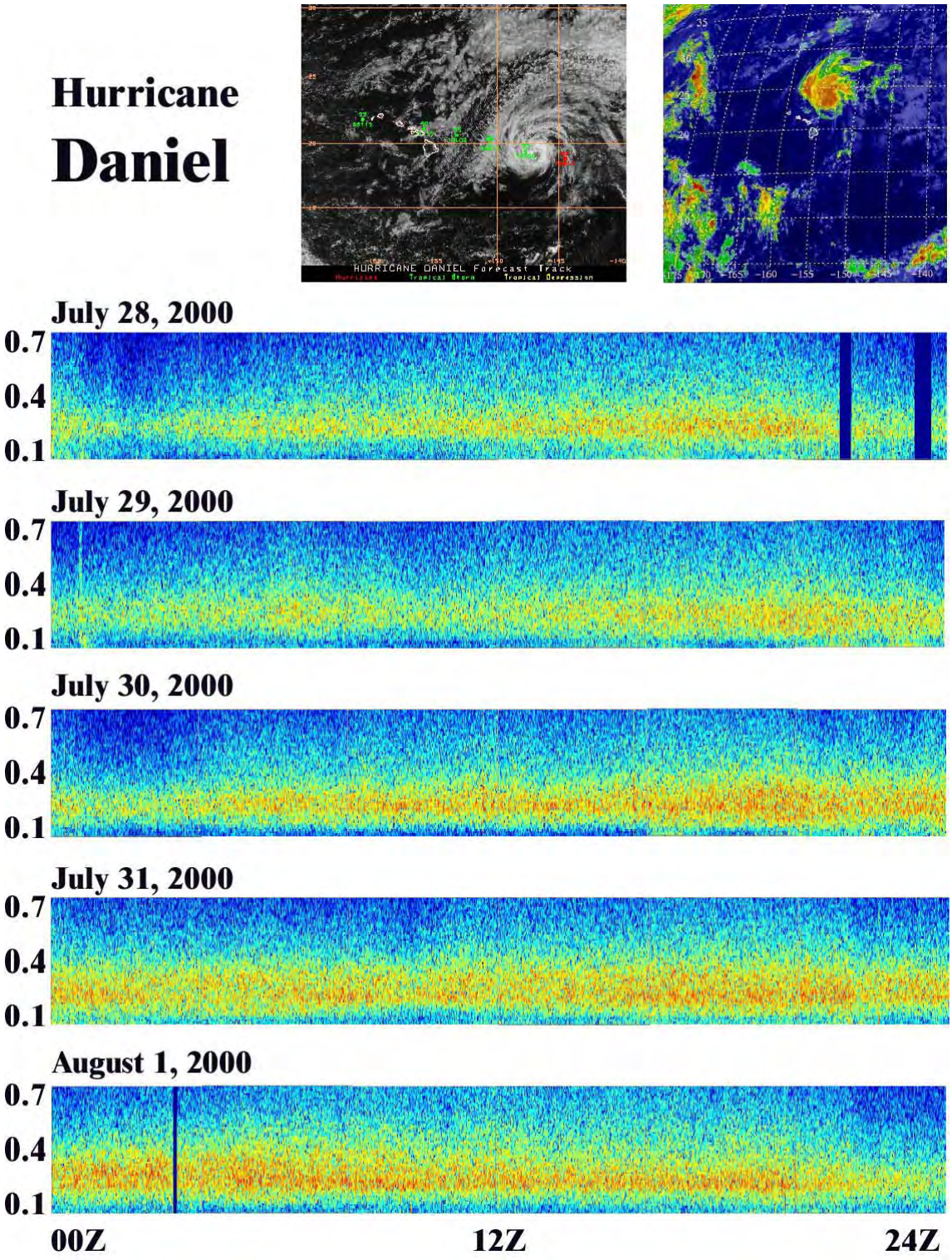

Figure 4. Spectrograms in the microbarom range for Daniel, showing initial diurnal fluctuations in the microbarom levels, which disappear as Daniel approached Hawaii. Note the frequency bifurcation starting after 12Z on July 30 and ending around 12Z on August 1.

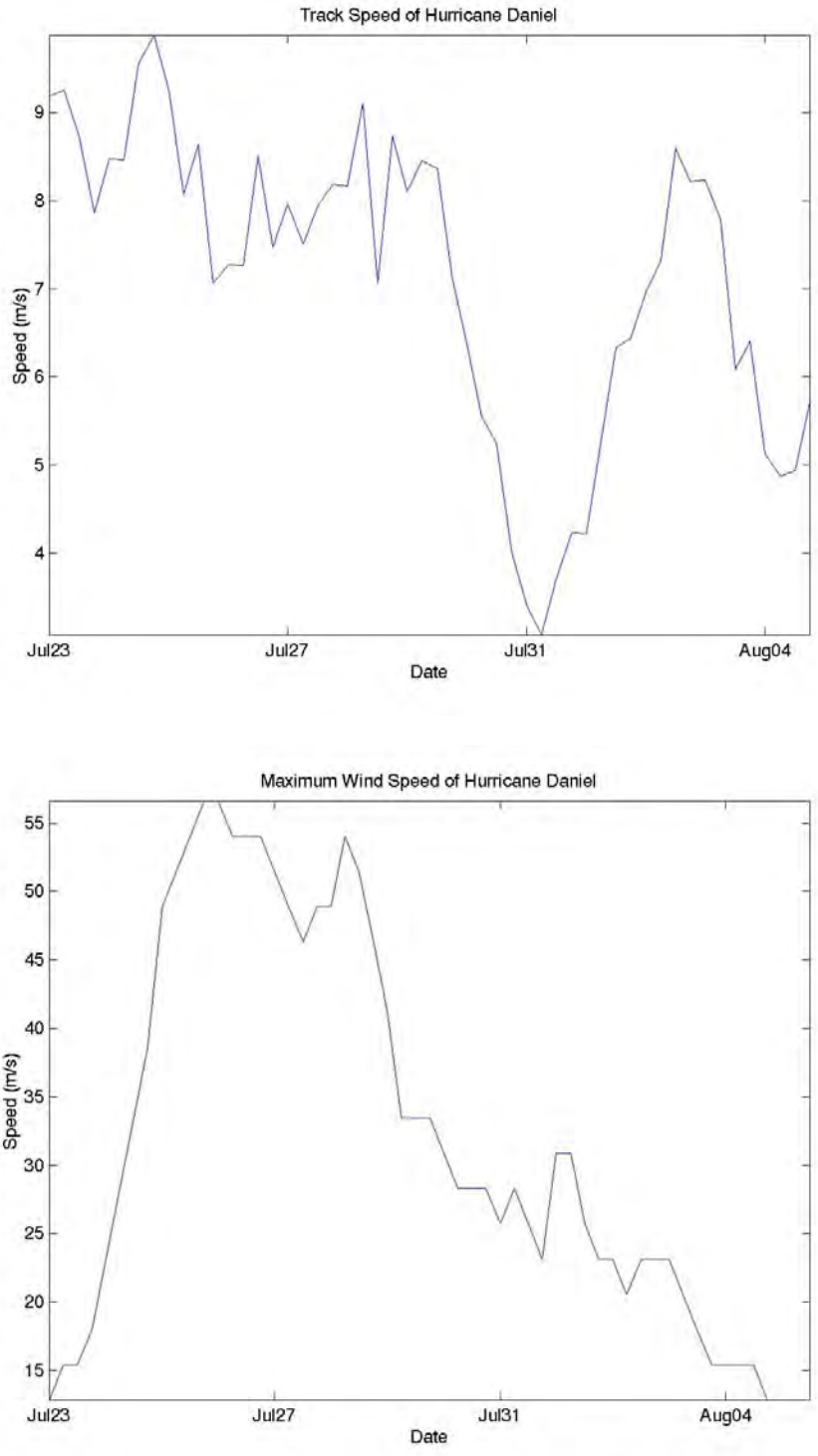

Figure 5. Track speed and maximum wind speed for Daniel.

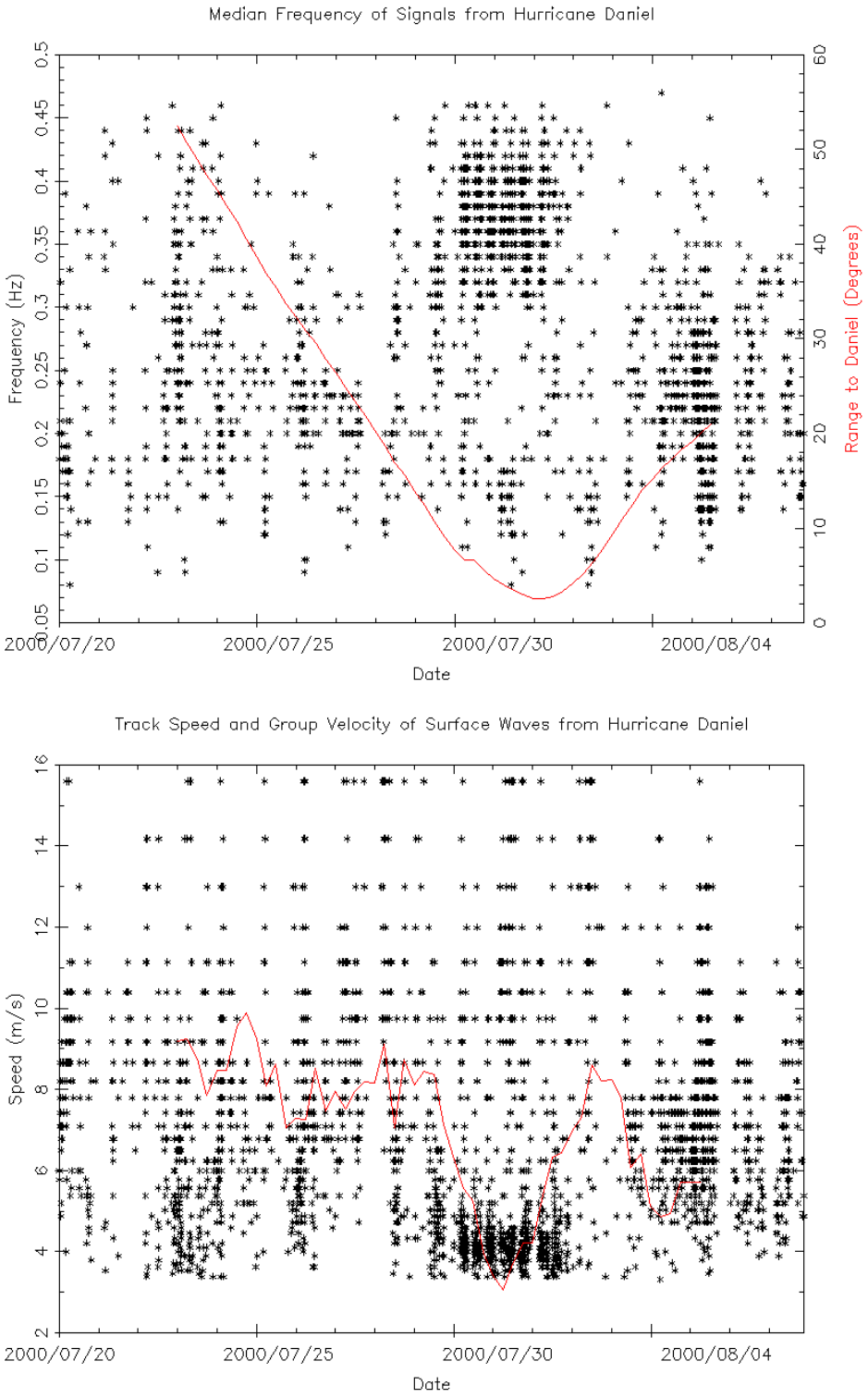

Figure 6. The upper panel shows the median frequency of peak detection and the range from KONA to the core of Daniel, and the lower panel shows Daniel's track speed (as in Figure 4) and the group velocity of surface waves corresponding to the acoustic median frequency. The track speed of Daniel exceeded the mean group velocity of the ocean waves up to the end of July 30, when Daniel is sufficiently close to Hawaii. From July 31-August 2, higher-frequency energy dominates, possibly due to the closer proximity of Daniel and the reflection of ocean waves from the island chain.

INTEGRATION OF NEAR-REAL-TIME ATMOSPHERIC MODELS WITH INFRAMAP AND APPLICATIONS TO MODELING INFRASOUND FROM ROCKETS

Robert G. Gibson and David E. Norris

BBN Technologies

Sponsored by Defense Threat Reduction Agency

Contract No. DTRA01-01-C-0084

ABSTRACT

The accuracy of infrasound propagation modeling depends on the fidelity of the environmental characterization. The analysis tool kit InfraMAP (*Infra*sound *M*odeling of *A*tmospheric *P*ropagation) utilizes the empirical environmental models MSISE and HWM to model temperature and wind, respectively. Opportunities for improved specification of the propagation environment are discussed. Of particular interest is the incorporation of near-real-time atmospheric updates, such as numerical weather prediction models or *in situ* radiosonde measurements, to supplement climatological characterization of the environment.

Approaches to integrating the output of meteorological synoptic models with infrasound propagation modeling codes are under development. Prognostic models such as the Navy Operational Global Atmospheric Prediction System (NOGAPS) provide near-real-time, global grids of temperature and wind over three spatial dimensions. To propagate three-dimensional rays through gridded data, wind and temperature values and their spatial derivatives must be estimated at each point along a ray path. Because ray models are highly sensitive to sharp changes in sound speed, the estimation approach must avoid introducing gradient variability that is not inherent in the original data grid. A natural cubic spline algorithm is being developed to interpolate data for use with ray modeling.

Validation efforts are essential to build confidence in the modeling procedures and are used to assess the value of potential improvements to the atmospheric specification. Observed infrasound events with known ground truth represent valuable sources of opportunity for use in validating propagation modeling techniques. Infrasound signals have been observed at several infrasound arrays in North America following launches of the space shuttle and of other large rockets. InfraMAP has been used to model propagation of infrasound originating from shuttle launches. The moving vehicle is modeled as a series of discrete infrasound sources separated in space and time. Launch ascent trajectory models are used to estimate source locations of the orbiter and solid rocket boosters during flight. Predictions of infrasound arrival times and azimuths resulting from three-dimensional ray tracing through empirical environmental characterizations are compared with observed data.

OBJECTIVES

The primary objective of this research effort is development of an enhanced InfraMAP software tool kit that enables higher fidelity infrasound propagation modeling by making use of linkages to near-real-time atmospheric characterizations. This effort is intended to support improved event localization and phase identification. An extensive validation effort is also being undertaken, using a diverse set of observations and ground truth, in order to improve confidence in the modeling techniques and provide calibration in support of operational needs. Anticipated uses of the software include: in-depth analysis of events and scenarios of particular monitoring interest; sensitivity analyses; and detailed infrasound localization and detection studies.

RESEARCH ACCOMPLISHED

Near-real-time environmental updates to InfraMAP

The InfraMAP software tool kit is composed of research-grade propagation models (3-D ray tracing, normal modes and parabolic equation) and upper-atmospheric characterizations, integrated to allow for user-friendly model execution and data visualization. InfraMAP can be applied to predict travel times, bearings, and amplitudes from potential event locations worldwide. Such predictions can be used to identify infrasound phases and to define travel-time and bearing corrections, which can improve localization performance (Gibson and Norris, 1999).

Temporal and spatial variability of the atmosphere is addressed by modeling range-dependent temperature and winds and incorporating them into the propagation models. The baseline atmospheric characterizations in InfraMAP are two empirical models: the horizontal wind model, HWM-93 (Hedin *et al.*, 1996), and the extended mass spectrometer-incoherent scatter radar temperature model, MSISE-90 (Picone *et al.*, 1997). Wind, temperature, and densities are modeled from the surface into the thermosphere and include spatial, diurnal, and seasonal effects. The models are climatological in that they predict the mean environmental profiles based on assimilation of multiple years of data. The HWM and MSISE models were chosen for use in InfraMAP due to their high fidelity over a wide range of altitudes and temporal scales, their global domain, and the relative ease of software integration. Validation studies conducted to date using InfraMAP with the HWM-93 and MSISE-90 characterizations indicate generally good agreement between modeled propagation paths and infrasound measurements. However, there exist cases in which measured infrasound phases are not adequately predicted using the baseline InfraMAP.

Global climatological models such as HWM and MSISE that are based solely on historical data do not capture local temporal and spatial atmospheric structure. The ability to add near-real-time sources of information will significantly improve the estimate of the infrasound propagation environment. Classes of near-real-time atmospheric updates include:

- *in situ* observations, such as measured profiles from radiosondes, and
- physics-based synoptic models that assimilate observations from a number of sources.

Models generally produce gridded output, whereas observed profiles (e.g., radiosondes) are not gridded; i.e., the observations are not uniformly sampled geographically or in altitude. However, none of the updated sources of data provide the complete set of temperature and wind speed profile information needed for infrasound modeling. In particular, most available data pertain to altitudes less than approximately 35 km, whereas propagation modeling requires information well into the thermosphere (approx. 120 km).

Therefore, empirical atmospheric models remain an essential tool for estimating the environment, particularly at high altitudes. Supplementing the climatological models with available near-real-time updates is likely to yield improved infrasound predictions, particularly for propagation paths that dwell primarily in the lower and middle atmosphere, where updated data are more readily available. The incorporation of updated atmospheric information, in the form of synoptic models or *in situ* measurements, will allow estimates of the propagation environment to be improved over the baseline climatology. Furthermore, it is desired to increase the capability of the InfraMAP software by offering greater flexibility in the range of data sources that can be accommodated.

Investigations have begun into the improvements attainable in propagation modeling by incorporating near-real-time atmospheric updates. The first steps are to develop links to near-real-time atmospheric observations or grids and to import the files for use in InfraMAP in conjunction with the HWM and MSISE empirical characterizations.

Based on the early success of empirical models at defining the propagation environment in the baseline InfraMAP software, automated integration of *in situ* data sources with propagation models has so far been determined not to be a high priority. However, the software provides a capability to incorporate updated atmospheric profiles, for purposes of evaluating potential improvements in propagation modeling. InfraMAP currently provides an option for user-defined atmospheric profiles for range-independent propagation modeling. Thus, updated wind and temperature data, such as from radiosonde observations, can be incorporated with the propagation models. Radiosonde observations are currently available twice a day from over a thousand weather stations worldwide. However, many regions of the world, particularly in the southern hemisphere, do not have dense radiosonde coverage. Available measurements consist of temperature, wind speed and direction from the ground up to approximately 35-km altitude (10-mb atmospheric pressure). Examples of observed temperatures from several radiosondes in the southwestern US on 23 April 2001, corresponding to observation of the Pacific bolide, are presented along with corresponding MSISE-90 characterizations in Figure 1. Observed zonal and meridional winds for the same radiosondes are shown along with corresponding HWM-93 characterizations in Figure 2.

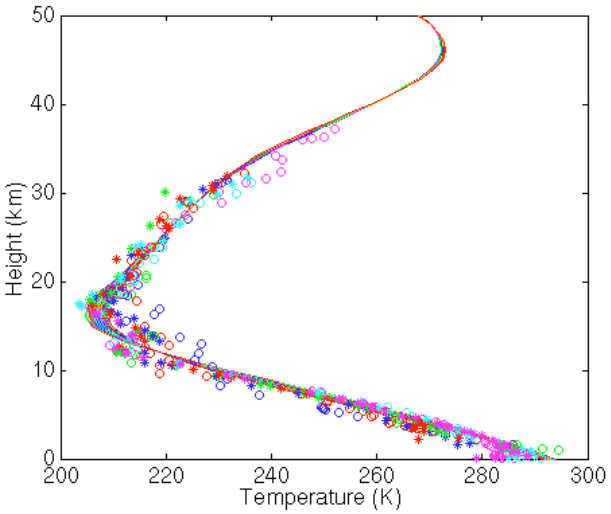

Figure 1. Radiosonde observations of temperature in the southwestern US on 23 April 2001 (shown as symbols) and corresponding MSISE-90 characterizations (shown as lines).

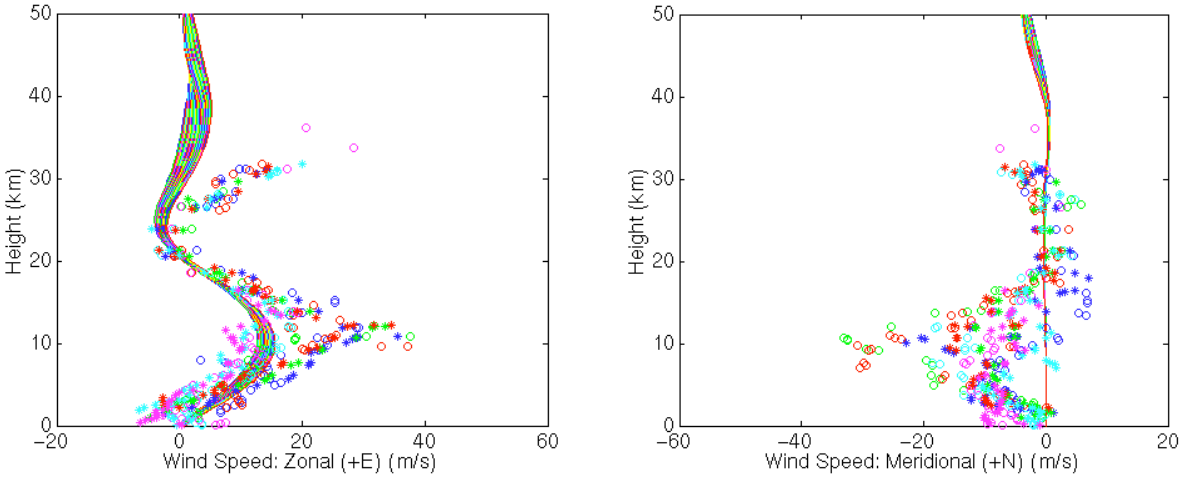

Figure 2. Radiosonde observations of zonal wind (left) and meridional wind (right) in the southwestern US on 23 April 2001 (shown as symbols) and corresponding HWM-93 characterizations (shown as lines).

In this instance, observed temperatures are well represented by the climatological model. The model of mean wind does not capture all of the features of the radiosonde wind observations, particularly the magnitude of the jet stream at approximately 10 km.

Prognostic models such as the Navy Operational Global Atmospheric Prediction System (NOGAPS) provide near-real-time, global grids of temperature and wind over three spatial dimensions. NOGAPS, originated by the Navy's Fleet Numerical Meteorology and Oceanography Center (FNMOC), is a numerical weather prediction model that utilizes not only profiles measured by radiosondes, but also an extensive data set of ship-based, land-based and satellite measurements to provide gridded temperature and wind speed at a range of altitudes. NOGAPS is a promising environmental model for use with infrasound propagation models due to its global domain and relatively high altitude coverage. The NOGAPS integration domain is from the ground to the 1-mb pressure surface (approximately 50 km), and output data are readily available up to the 10-mb pressure surface (approx. 30-35 km). Output products from NOGAPS have been obtained and decoded for purposes of integration and testing.

An example of a subset of gridded zonal wind profiles from NOGAPS is shown in Figure 3. The profiles are for a fixed time and date at the grid points defined in a 7.7 degree by 6.5 degree region over the southwestern US. These are compared to HWM-93 model output, over the same region, date and time. Mean zonal winds in the region are well predicted by the climatological model, but greater variability is shown in the NOGAPS model output.

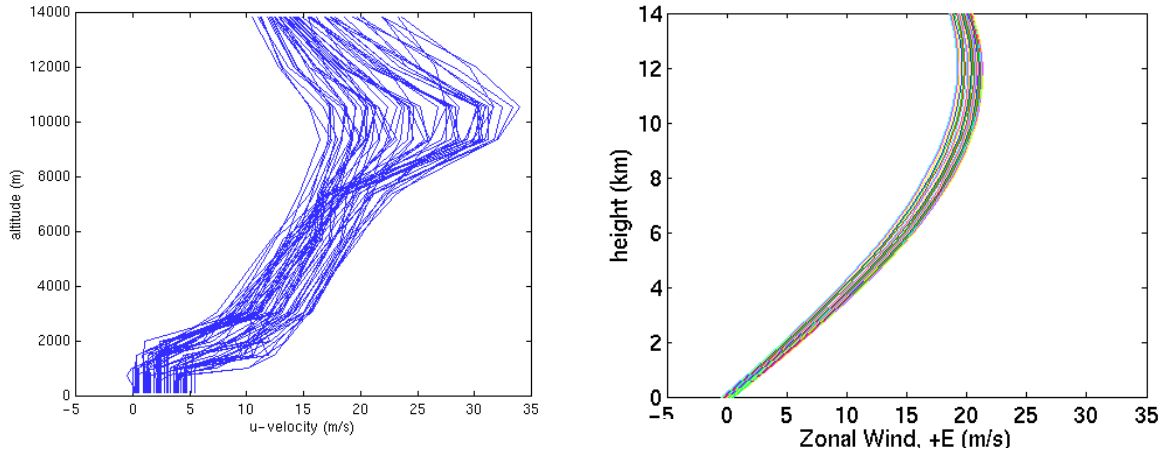

Figure 3. Predictions of zonal wind over a region in the southwestern US using NOGAPS (left) and HWM-93 (right).

Propagation models in InfraMAP interface with environmental characterizations in three ways:

- Range dependent, using the empirical atmospheric model functions to determine the environment at each step;
- Range independent, using average profiles determined from the empirical models evaluated along the propagation path;
- Range independent, using user-defined profiles.

In order to accommodate an environment defined by a gridded database such as NOGAPS, modifications must be made to InfraMAP's interface between propagation and environmental software modules, particularly in order to allow range dependence. There are a number of technical issues to be addressed, including: interpolation and extrapolation techniques; formation of consistent, repeatable representations; and evaluation of prediction sensitivity to interpolation methods. To propagate three-dimensional rays through gridded data, wind and temperature values and their spatial derivatives must be estimated at each point along a ray path. Because ray models are highly sensitive to sharp changes in sound speed, the estimation approach must avoid introducing gradient variability that is not inherent in the original data grid. A natural cubic spline algorithm is being developed to interpolate data for use with ray modeling. Cubic spline interpolation provides a smooth first derivative and continuous second derivative, ensuring compatibility with the ray model. Algorithms are currently being tested for integration into InfraMAP.

The enhanced InfraMAP capabilities that are being developed in this effort are shown schematically in Figure 4. The baseline InfraMAP functionality is shown in light gray, the capabilities that are currently being developed in a

separate effort (Norris and Gibson, 2002) are shown in dark gray, and the new components under development in this effort are shown in blue.

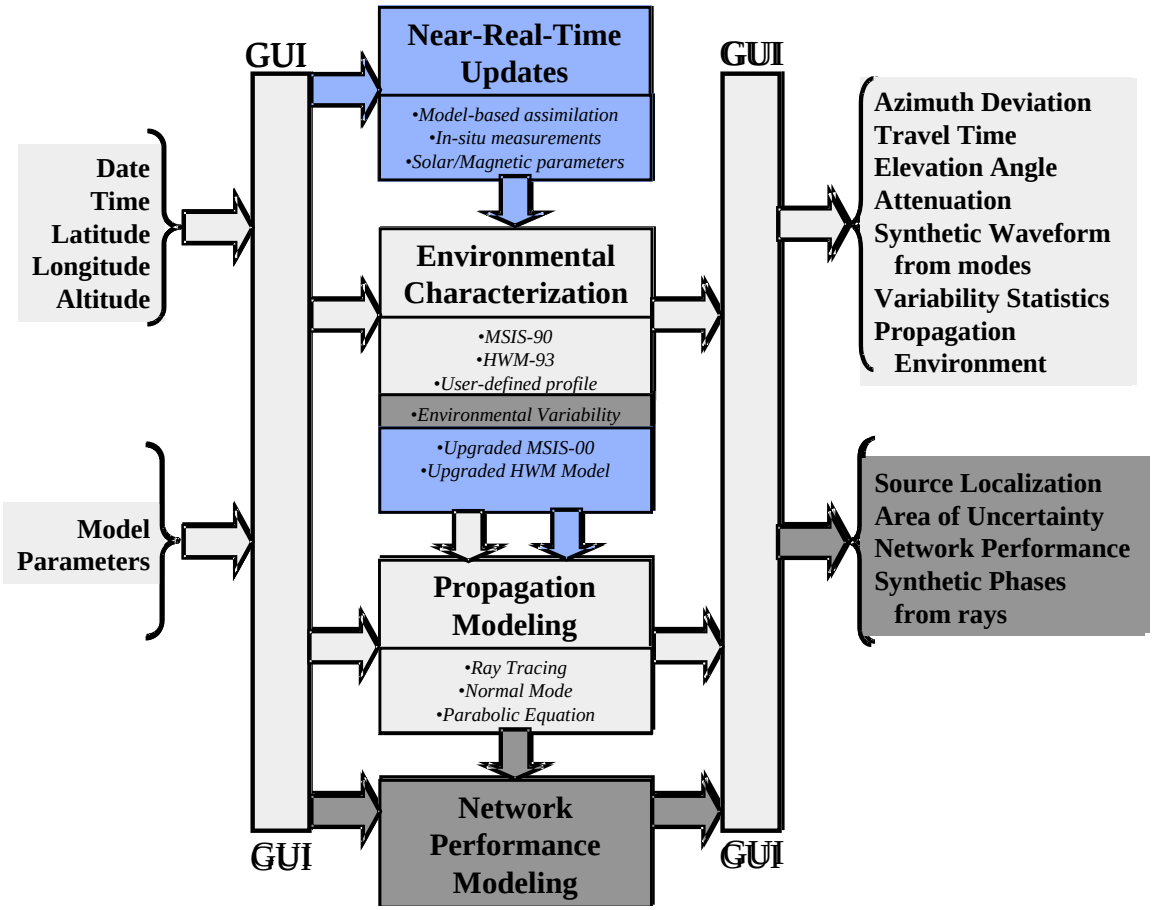

Figure 4. Schematic representation of InfraMAP functionality, with capabilities being developed in this effort shown in blue.

Model validation using infrasound from rocket launches

Validation efforts are essential to build confidence in the modeling procedures and to identify areas where further refinements are required. Where ground truth is available, validation results support event localization, phase identification and calibration efforts.

Rocket launches may serve as useful ground truth data for infrasound (McLaughlin *et al*., 2000) and also represent an excellent source of opportunity for model validation. Space shuttle launches from Cape Kennedy, Florida, have recently been observed at infrasound arrays at Los Alamos, New Mexico, (DLIAR prototype array) and at Lac du Bonnet, Canada (IS10 array). Rocket and missile launches from the eastern US were observed extensively in the 1960's and 1970's by infrasound arrays at Palisades, New York, and elsewhere, and Balachandran and Donn (1971) and other scientists at Lamont-Doherty Geological Observatory and the US Army Electronics Command issued a series of reports. A number of important findings resulted from this early work, including identification of two distinct source regions, one near the launch site and one near the re-entry location of the first stage.

Trajectories for specific shuttle missions have been modeled using actual launch parameters. Trajectories for the shuttle's solid rocket boosters, which are released from the orbiter approximately two minutes into the ascent, have also been estimated. Modeled trajectories for two observed shuttle missions, STS-96 (27 May 1999) and STS-93 (23 July 1999) are shown in Figure 5. Launch ascent trajectories for a typical mission of shuttle orbiter and solid rocket boosters (SRB) are shown in Figure 6.

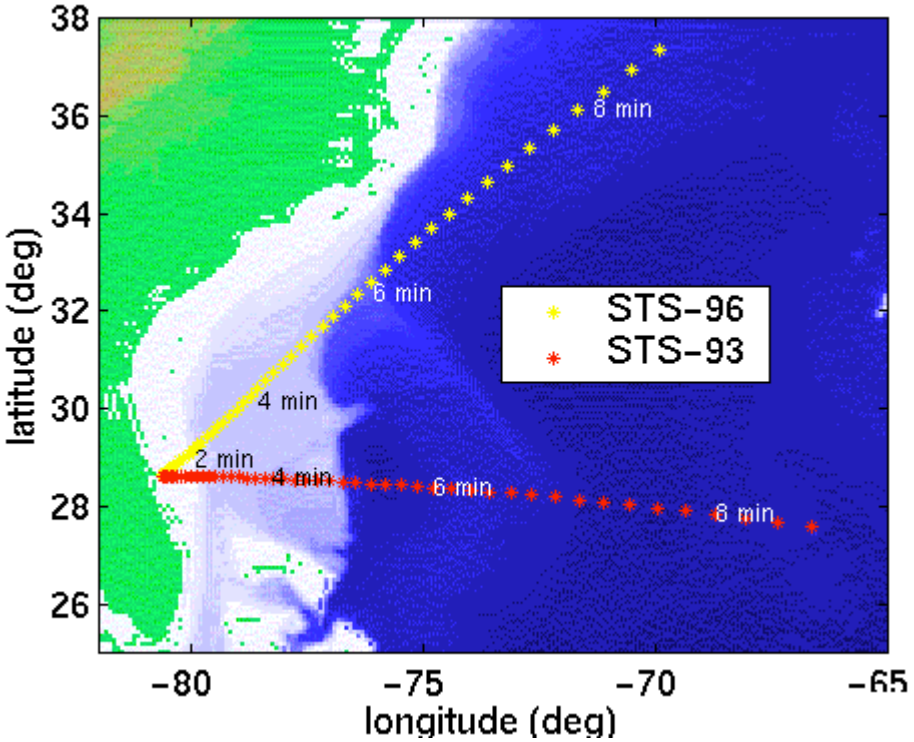

Figure 5: Space shuttle trajectories for two missions.

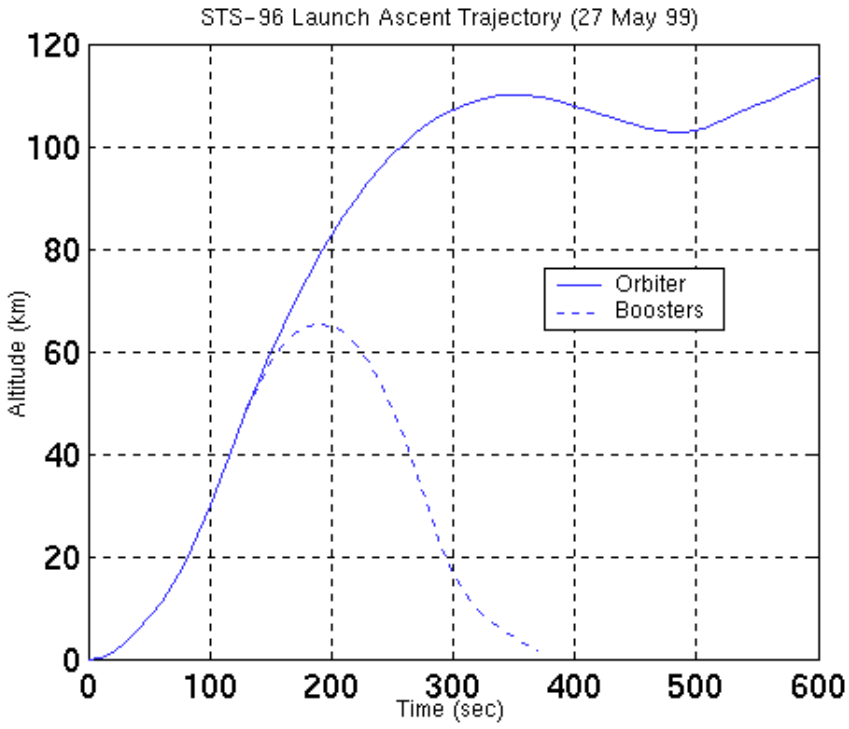

Figure 6: Space shuttle orbiter and solid rocket booster trajectories.

InfraMAP was used to determine eigenrays to DLIAR from points along the STS-96 trajectory, with HWM-93 and MSISE-90 used for environmental characterization. The continuously moving source was modeled as a series of discrete sources separated in space and time. A source was modeled every 10 seconds from the launch time out to 5 minutes after launch for the orbiter and from 200 seconds out to 6 minutes after launch for the solid rocket boosters. For each eigenray, an arrival azimuth and an arrival time (referenced to the launch time) were determined. Results are shown in Figure 7. Stratospheric rays and thermospheric rays are depicted separately for both the orbiter and the SRB. Also shown in the figure (as red asterisks) are results from the observation at DLIAR, determined by analysis using the InfraTool component of the MatSeis software package (Harris and Young, 1996).

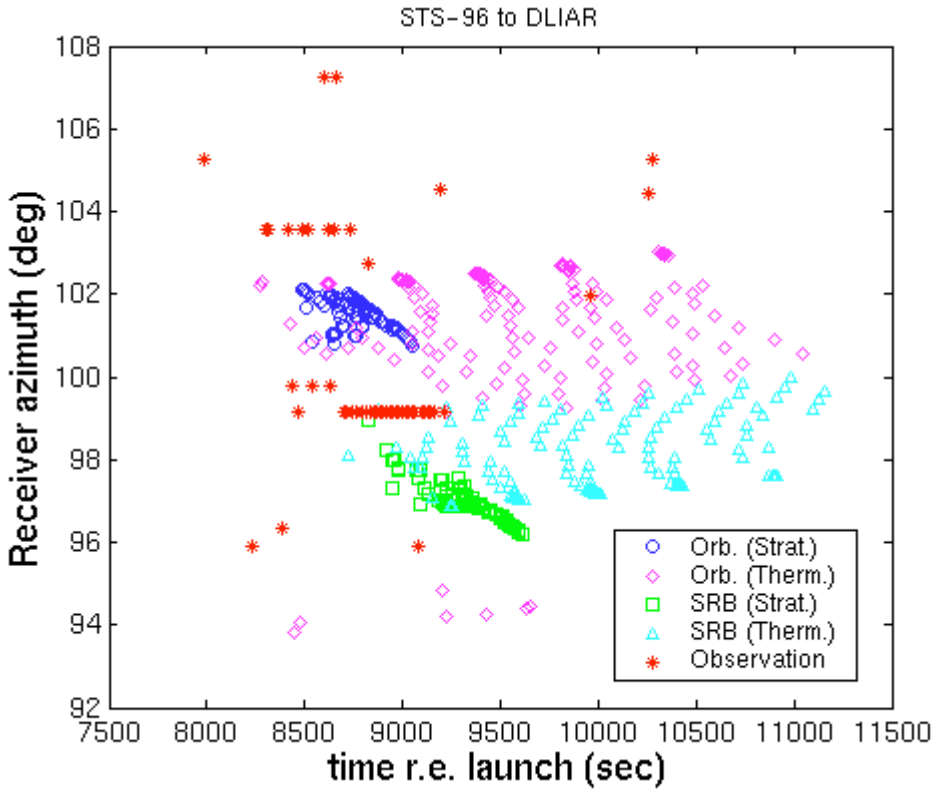

Figure 7: Predicted and observed infrasound arrivals from STS-96 to DLIAR.

The two primary observed arrivals (at approximately 103.5 and 99 degrees) are reasonably well modeled by the stratospheric rays from the orbiter (blue circles) and boosters (green squares), respectively. However, a bias in azimuth of approximately 2 degrees can be seen for both primary arrivals. Further modeling of the launch event using an updated atmospheric characterization, in order to see if travel-time and azimuth predictions could be improved, is of interest in this case.

Further investigation into this and other rocket launches, such as those of the Titan IVB, is underway. Data have been collected and trajectories modeled for several missions from 1998 to the present. Trends of observability, arrival time, and azimuth are being analyzed. Propagation model results are compared with observations and biases quantified. Several technical issues are of interest during this study, including:

- The modeling improvements achievable with near-real-time updates as compared to HWM and MSISE;
- Further understanding of the infrasound source mechanism in order to identify the regions of the trajectory (altitude, velocity, etc.) that contribute most strongly to observed signals;
- Quantifying attenuation along the ray paths to support identification of observed phases;
- The use of propagation modeling to predict observability of events.

The results of the analyses will serve to validate the environmental and propagation modeling techniques.

CONCLUSIONS AND RECOMMENDATIONS

The InfraMAP tool kit is used to predict the critical propagation characteristics that affect infrasound localization and detection. Adequate atmospheric characterization is necessary to correct for biases in travel time and azimuth that result from the propagation environment in order to avoid large location errors. *In situ* observations of winds and temperature can be used in InfraMAP for range-independent propagation modeling. Techniques are being developed to integrate output from the NOGAPS numerical weather prediction model with range-dependent propagation models. InfraMAP's integrated set of models will allow for higher fidelity propagation modeling than has previously been available to the infrasound monitoring community. As new high-fidelity environmental characterizations become available, they should be considered for integration into an enhanced version of the InfraMAP software.

Rocket launches generate infrasound signals for use in model validation studies. Infrasound is generated by both rocket ascent and booster descent. Launch trajectory models provide useful approximations of ground truth for use in conjunction with propagation modeling. Comparisons of measured and modeled arrival times and azimuths suggest that baseline infrasound modeling techniques are good but that higher fidelity would likely be obtained with the use of near-real-time wind and temperature characterizations. Further modeling of a large set of observed events, using updated atmospheric characterizations, is recommended in order to quantify the improvements in travel-time and azimuth predictions that are achievable.

REFERENCES

Balachandran, N. and W. Donn (1971), Characteristics of infrasonic signals from rockets, *Geophys. J. R. Astr. Soc*., **26**, 135-148.

Gibson, R. and D. Norris (1999), Development of an Infrasound Propagation Modeling Tool Kit, DTRA-TR-99-47.

Harris, J. M. and C. J. Young (1996), MatSeis: A Seismic Toolbox for MATLAB, *Proceedings of the 18th Annual Seismic Research Symposium on Monitoring a Comprehensive Test Ban Treaty*, Phillips Laboratory (7/96).

Hedin, A. E, E. L. Fleming, A. H. Manson, F. J. Schmidlin, S. K. Avery, R. R. Clark, S. J. Franke, G. J. Fraser, T. Tsuda, F. Vial, and R. A. Vincent (1996), Empirical wind model for the upper, middle, and lower atmosphere, *J. Atmos. Terr. Phys*., **58**, 1421-1447.

McLaughlin, K. L., A. Gault, and D. Brown (2000), Infrasound detection of rocket launches, *Proceedings of the 22nd Annual DoD/DOE Seismic Research Symposium: Planning for Verification of and Compliance with the Comprehensive Nuclear-Test-Ban Treaty (CTBT)*, New Orleans.

Norris, D. E. and R. G. Gibson (2002), InfraMAP enhancements: environmental/propagation variability and localization accuracy of infrasonic networks, in this volume.

Picone, J. M., A. E. Hedin, S. L. Coffey, J. Lean, D. P. Drob, H. Neal, D. J. Melendez-Alvira, R. R. Meier, and J. T. Mariska (1997), The Naval Research Laboratory program on empirical models of the neutral upper atmosphere, in *Astrodynamics: Advances in the Astronautical Sciences*, Vol. 97, edited by F. R. Hoots, B. Kaufman, P. J. Cefola, and D. B. Spencer, American Astronautical Society, San Diego, Ca.

EXPERIMENTS WITH INFRASONIC NOISE-REDUCING SPATIAL FILTERS

Michael A.H. Hedlin and Jon Berger

Scripps Institution of Oceanography; University of California, San Diego

Sponsored by Defense Threat Reduction Agency

Contract No. DTRA01-00-C-0085

ABSTRACT

As development of the International Monitoring System (IMS) infrasound network progresses, there remains much to learn about reducing noise due to atmospheric turbulence while preserving signals from distant sources. The spatial filter currently preferred for use at new IMS infrasound array sites consists of an array of low-impedance inlets connected by solid tubes to a microbarometer. Acoustic signals and noise enter the "rosette" pipe system via the inlets and are summed in manifolds or at the sensor. Acoustic energy that is incoherent at wavelengths less than the aperture of the filter is attenuated, and the ratio of coherent signal to incoherent noise is increased. We have tested two designs of rosette filters that span 18 and 70 meters to estimate the signal-to-noise ratio (SNR) gain as a function of wind speed and to look for artifacts of the filtering process. Empirical observations compare well with theoretical predictions. The 70-m filter provides noise reduction of up to 20 dB over a band from 0.02 Hz to 0.7 Hz. The 18-m filter does not suppress noise below ~ 0.2 Hz. The corner frequency of both spatial filters scales directly with wind speed. Resonance is observed in data from both filters but is most pronounced in data from the 70-m filter. Modeling of data from both filters clearly indicates that the reflections occur at all points inside the filters at which the impedance changes. Although a large impedance change occurs at the low-impedance inlets, the resonance that is first observed at 0.7 Hz in data from the 70-m filter, and at 3 Hz in data from the 18-m filters occurs between the primary and secondary summing manifolds. Experiments show that this resonance can be largely, or entirely, removed by installing impedance matching capillaries adjacent to the secondary summing manifolds in the pipes leading to the primary summing manifold. Adding capillaries at the inlets is less effective as those points are linked with high-frequency resonance at the upper limit, or beyond, the passband of interest to the monitoring community.

Rosette filters are tuned to vertically incident energy. Energy arriving at other incidence angles is not summed in phase. The problem is acute at high frequencies, at near-horizontal arrival angles, and scales directly with the aperture of the filter. Total cancellation of the horizontally propagating signals recorded via the 70-m rosette filter is predicted to occur at 5 Hz. Recordings of a large bolide that exploded west of the infrasound test bed in southern California on April 23, 2001, were made by co-located reference systems and the large and small rosette filters. The data validate the phase and amplitude response predicted by a theory that takes into account the resonance of energy inside the filters and the phase delays of the energy entering the filters.

This paper will report these results and our experiments with noise reducing barriers.

OBJECTIVE

Our objective is to build, model and test infrasonic noise reduction systems to assess the utility of the different devices as a function of frequency and wind speed. Our goal is to test systems that are being deployed at International Monitoring System (IMS) array sites and to test new devices (such as the new fiber optic sensor under development at the University of California San Diego [UCSD], Zumberge et al., 2002) and spatially compact filters (such as the wind barrier, a sensor buried at a shallow depth in a porous medium) in our search for systems that are more economical, require less space, or have a better response than currently preferred designs. We identify shortcomings of filters (e.g. resonance in large pipe filters) and search for ways to improve the filters.

RESEARCH ACCOMPLISHED

Preliminary evaluation of rosette filters

We have conducted tests of rosette infrasonic noise-reducing spatial filters (Alcoverro, 1998) at the Pinon Flat Observatory in southern California (Figure 1; Hedlin et al., 2002). Data from 18- and 70-m-aperture rosette filters (Figure 2) and a reference port have been used to gauge the reduction in atmospheric wind-generated noise levels provided by the filters and to examine the effect of these spatial filters on spatially coherent acoustic signals in the 0.02- to 10-Hz band. At wind speeds up to 5.5 m/s, the 18-m rosette filter reduces wind noise levels above 0.2 Hz by 15 to 20 dB. Under the same conditions, the 70-m rosette filter provides noise reduction of up to 15 to 20 dB between 0.02 and 0.7 Hz. Standing wave resonance inside the 70-m filter degrades the reception of acoustic signals above 0.7 Hz. The fundamental mode of the resonance, 15 dB above background, is centered at 2.65 Hz and the first odd harmonic is observed at 7.95 Hz in data from the large filter (Alcoverro and LePichon, 2002; Hedlin et al., 2002). Synthetics accurately reproduce the noise reduction and resonance observed in the 70-m filter at all wind speeds above 1.25 m/s (Figures 3 and 4). Resonance theory indicates that internal reflections, which give rise to the resonance observed in the passband, are occurring at the summing manifolds, and not at the inlets. Rosette filters are tuned to acoustic arrivals with infinite phase velocity. Attenuation of signals by the 70-m rosette filter at frequencies above 3.5 Hz arriving at grazing angles of less than 15° from the horizontal are predicted to range upward from 10 dB to total cancellation at 5 Hz (Figure 5). Theoretical predictions of the phase and amplitude response of 18- and 70-m rosette filters that take into account internal resonance and time delays between the inlets compare favorably with observations derived from a cross-spectral analysis of signals from the explosion of a large bolide (Figure 6).

Experiments with impedance-matching capillaries

We have conducted three experiments with impedance-matching capillaries to remove the problem with resonance in the rosette spatial filters (Hedlin and Alcoverro, 2002). In the first test, we sought confirmation that the reflections that give rise to the resonance peaks observed at 2.65 and 7.95 Hz in the data from the 70-m rosette filters are occurring at the secondary summing manifolds, and not at the inlets. We constructed three filters that consist of 8- to 27-m-long pipes. We fitted the open ends of the pipes with different capillaries to assess the utility of acoustic resistance for removing the resonance problem. The test reproduced the resonance peaks and confirmed that the reflections that give rise to the spectral peak at 2.65 Hz occur at the primary and secondary summing manifolds. The test, and subsequent modeling, also confirmed that the resonance peaks could be completely removed by installing capillaries at the inlets of these simplified filters. The appropriate acoustic resistance of each capillary is the characteristic impedance of the pipe that connects the inlet with the primary summing manifold. Modeling also confirms that the same capillaries will remove the resonance problem in the complete rosette filters. Installing eight capillaries adjacent to the secondary summing manifolds in the pipes leading to the primary manifold will be far more effective than installing the capillaries at the 144 inlets (Figure 7). Data collected from a filter in the infrasound array I57US that was modified with capillaries, with acoustic resistance equal to the characteristic impedance of the 27-m pipes connecting the primary and secondary summing manifolds, revealed that the main resonance peak at 2.65 Hz is completely removed, as predicted by theory, and the first sign of resonance, due to resonance in the pipes between the secondary summing manifolds and the inlets, is observed at 5 Hz (Figure 8). A separate test of capillaries in the 18-m rosette filters produced similar results. All filters in the IMS infrasound array I57US have been modified with capillaries as a result of this research. Modeling indicates that a modest improvement of the response of the 70-m rosette filter can be achieved by installing capillaries at the inlets, but this

is not recommended because of the plane wave response, mentioned in the previous section, that degrades the response of these filters above 3 Hz.

Tests of noise-reducing wind barriers

This section reports empirical observations of wind speed and infrasonic noise reduction inside a wind barrier. The barrier has been compared with "rosette" spatial filters and with a reference site that uses no noise reduction system. The barrier is investigated for use at IMS infrasound array sites where spatially extensive noise-reducing systems cannot be used because of a shortage of suitable land. Wind speed inside a 2-m-high 50% porous hexagonal barrier coated with a fine wire mesh is reduced from ambient levels by 90%. If the infrasound wind noise level reductions are all plotted versus the reduced frequency given by $f*L/v$, where L is the characteristic size of the array or barrier, f is the frequency and v is the wind speed, the reductions at different wind speeds are observed to collapse into a single curve for each wind-noise-reduction method. The reductions are minimal below a scale size of 0.3 to 1, depending on the device; then spatial averaging over the turbulence structure leads to increased reduction. Above the corner frequency, the fence reduces infrasonic noise by up to 20 to 25 dB (Figure 9). Below the corner frequency the barrier displays a small reduction of about 4 dB. The rosettes display no reduction below the corner frequency. One other advantage of the wind barrier over rosette spatial filters is that the signal recorded inside the barrier enters the microbarometer from free air and is not integrated, possibly out of phase, after propagation through a system of narrow pipes.

CONCLUSIONS AND RECOMMENDATIONS

Rosette filters

We have found that modeling theory, which takes into account reflection and attenuation of acoustic energy in the rosette filters and includes the response of the microbarometer, accurately reproduces recorded data. We have also determined that impedance matching capillaries, installed at the secondary summing manifolds, will remove the resonance problem. We have noted that the rosette filters are tuned to vertically incident acoustic waves and the reception of signals that arrive within 15° of the horizontal is limited. The plane wave response is most significant in the large, 70-m-aperture rosette filter.

We recommend that all rosette filters used at IMS infrasound arrays are modified as described in the earlier section.

Future research with rosette filters

The theory that accounts for internal resonance and external phase delays can be applied to any rosette filter design and therefore, in principle, can be used to search for better designs. This could be accomplished by defining optimization criteria (e.g. lack of resonance peaks in the band below 10 Hz; flat plane wave response in the same band) and systematically searching for designs that optimally satisfy these criteria. It remains to be determined if the combined theory can be used to correct the amplitude and phase of signals filtered through rosette filters.

Real rosette filters do not adhere perfectly to the specified designs shown in Figure 2. Most sites present obstacles that require some modifications to the placement of the inlets in the rosette clusters. Most sites are not perfectly horizontal but are tilted. An important question that we can now begin to address is what the rosette filters do to the overall performance of an infrasound array. What asymmetries in the placement of the inlets and what tilts at the different elements can exist before unacceptable bias will be introduced into the back-azimuth derived from processing data from all elements. If these imperfections in the locations of the inlets and in the tilts of the filters are known, this work might lead to a means to remove this bias.

Arrivals from naturally occurring infrasound sources such as bolides can be used as signals of opportunity to calibrate *in situ* the amplitude and phase response of the IMS space filters. The derived "calibration" curves can be used to help remove the system response from the recorded data. These calibration curves are a function of arrival angle (apparent phase slowness) as well as frequency so that a collection of events in various directions is required to obtain a complete set of empirically derived curves. Alternatively, one or two events can be used to validate a theory of the spatial and frequency dependence of the rosette filter response, as is done in Hedlin, Alcoverro and D'Spain (2002), so that theoretically derived calibration curves then can be applied. Changes in conditions at the

recording site can result in changes in the filter response. For example, variations in atmospheric temperature result in changes in sound speed that, in turn, cause a shift in the frequencies of the resonances and in the location of the spatial response null associated with phase delays. Likewise, a change in the number, location, and effective impedance of individual ports in a rosette filters will affect the resonance and spatial nulling characteristics. The impact of such changes on the filter response can be evaluated using the methods described in Hedlin, Alcoverro and D'Spain (2002).

Theoretical tests of capillaries are needed to determine the effect of one or more of the capillary plugs becoming partially or fully blocked by water, insects, etc., on the response of the individual filters and of the entire array. The long-term maintenance of these systems might involve periodic inspection and clearing of the capillary plugs.

Wind barriers

Comparison of the scaled reductions in wind noise produced by the rosettes and wind barrier with the reductions afforded by a spherical wind screen hold promise for significant wind-noise reduction with a smaller footprint device (Hedlin and Raspet, 2002). The rosettes only produce reductions if the scale size of the turbulence is smaller than the size of the rosette since such devices rely on the incoherence of the turbulence at each port. The wind barrier displayed large reductions only when the scale size of the turbulence is smaller than the height of the barrier. However, a small reduction of about 4 dB was realized when the scale size was larger than the barrier. This reduction may correspond to the large reductions realized by foam windscreens. In the spherical windscreens, these reductions occur since the pressure measured at the center is the area average of the pressures generated at the surface of the sphere. For large turbules, the pressure generated by an increase in wind speed is positive at the front of the sphere and negative at the back, and the average is less than the pressure measured at a bare sensor. This result holds promise that a properly designed windscreen on or near the ground surface may achieve significant reductions even for turbulence scales greater than the size of the screen.

ACKNOWLEDGEMENTS

Our research was conducted collaboratively with Rich Raspet (University of Mississippi), Benoit Alcoverro (DASE France), and Gerald D'Spain (UCSD). We would like to acknowledge pioneering work on the wind barrier by Ludwik Liszka (Swedish Institute of Space Physics). The design of the wind barrier and insights into how the barrier reduces infrasonic noise were provided by Doug Revelle (Los Alamos National Laboratory). We thank Hank Bass (University of Mississippi) for constructive comments on our research with the wind barrier. The authors are indebted to Chris Hayward (SMU) and Doug Christie (CTBTO) for suggesting that we experiment with capillaries. Frank Vernon, Jennifer Eakins and Glen Offield provided the real-time data link. Clint Coon provided field assistance. Funding was provided by the Defense Threat Reduction Agency under contract DTRA01-00-C-0085. Funding for the rosette filters used in this study was provided by the Defense Threat Reduction Agency, the Provisional Technical Secretariat (PTS) of the Comprehensive Nuclear-Test-Ban Treaty Organization in Vienna, and the US Army Space and Missile Defense Command (SMDC) University Research Initiative (URI).

REFERENCES

Alcoverro, B. (1998) Acoustic filters design and experimental results, Proceedings: Workshop on Infrasound, Commissariat à l'Energie Atomique, Bruyères-le-Châtel, France, July 21-24, 1998.

Alcoverro, B. and A. Le Pichon (2002) Design & optimization of a noise reducer system for infrasound measurements using elements with low acoustic impedance, submitted to *J. Acoust. Soc. Am*.

Hedlin, M.A.H., B. Alcoverro, and G. D'Spain (2002) Evaluation of rosette infrasonic noise-reducing spatial filters, manuscript in review with the *J. Acoust. Soc. Am*.

Hedlin, M.A.H. and B. Alcoverro (2002) The use of impedance matching capillaries for reducing resonance in rosette spatial filters, manuscript in preparation for the *J. Acoust. Soc. Am*.

Hedlin, M.A.H. and R. Raspet (2002) Evaluation of an infrasonic noise-reducing barrier, in preparation for *J. Acoust. Soc Am.*, submitted June 14, 2002.

Zumberge, M.A., J. Berger, M.A.H. Hedlin, R. Hilt, S. Nooner, and R. Widmer-Schnidrig (2002) An optical fiber infrasound sensor: a new lower limit on atmospheric pressure noise between 1 Hz and 10 Hz, in preparation for *J. Acoust. Soc Am.*, submitted June 14, 2002.

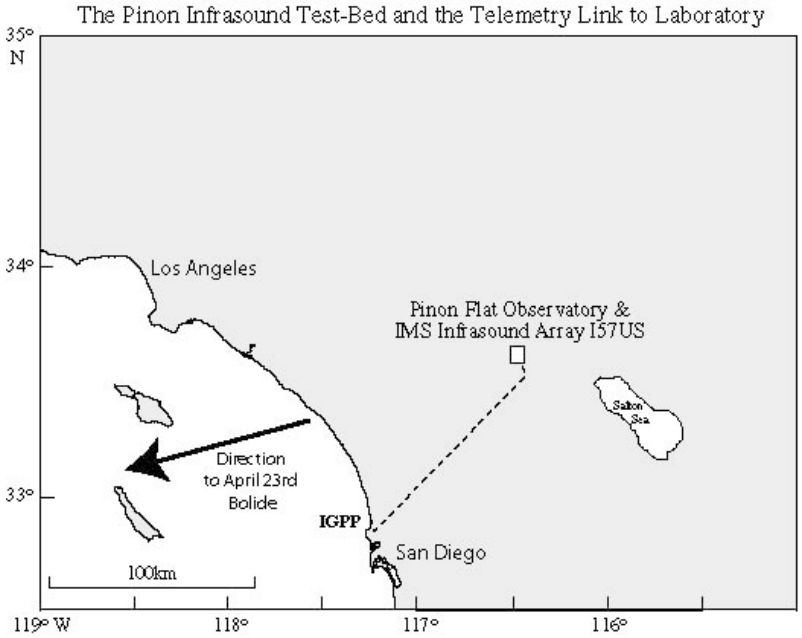

Figure 1. The IMS infrasound array, I57US, is located in the Anza Borrego desert at the Cecil H. and Ida M. Green Pinon Flat Observatory (PFO). The infrasound test-bed is located at PFO. The real-time radio-telemetry link to the laboratory (IGPP) is also shown. Signals from a large bolide that exploded to the SW of the observatory are used in this paper to calibrate the rosette filters.

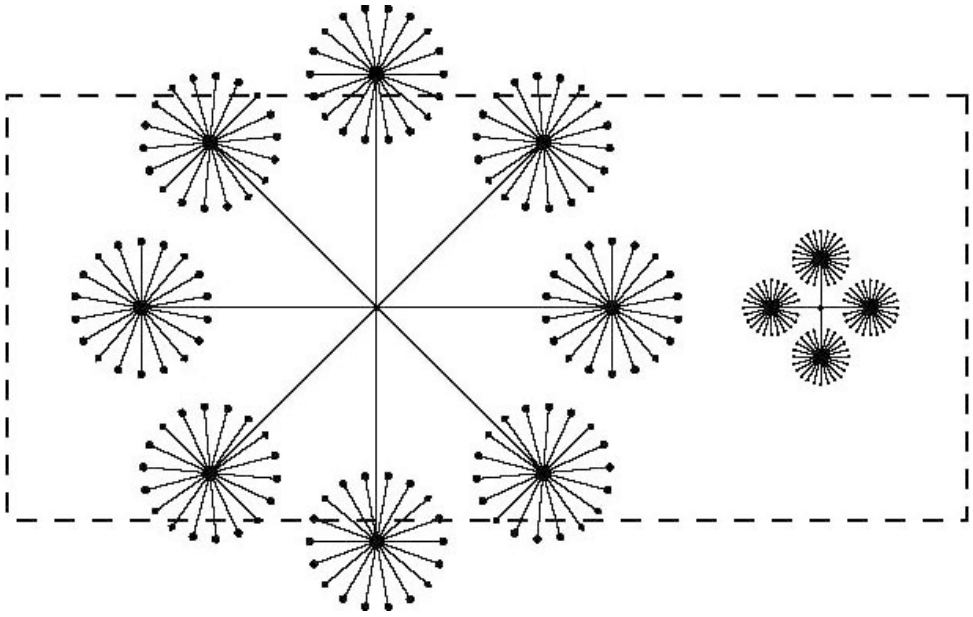

Figure 2: Two rosette filters considered in this paper are shown to scale with a National Football League playing surface. The 18-m filter comprises 92 low-impedance inlets in four rosettes. The 70-m filter comprises 144 inlets arranged in eight rosettes.

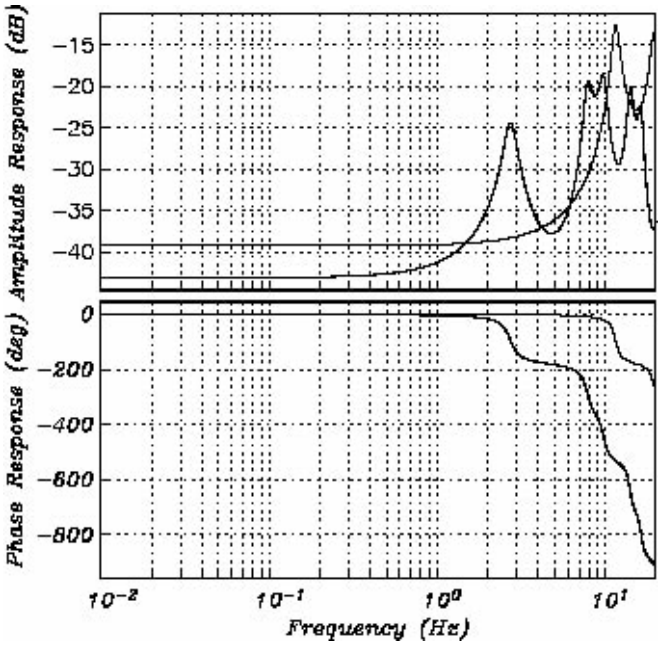

Figure 3: Predicted amplitude and phase response of the 18-m/92 rosette filter (light curve) and the 70-m/144 rosette filter (bold curve) for one inlet. The resonance peaks coincide with significant change in the phase response of the filter. The long-period response is given by -20 log10(N), where N is the number of inlets.

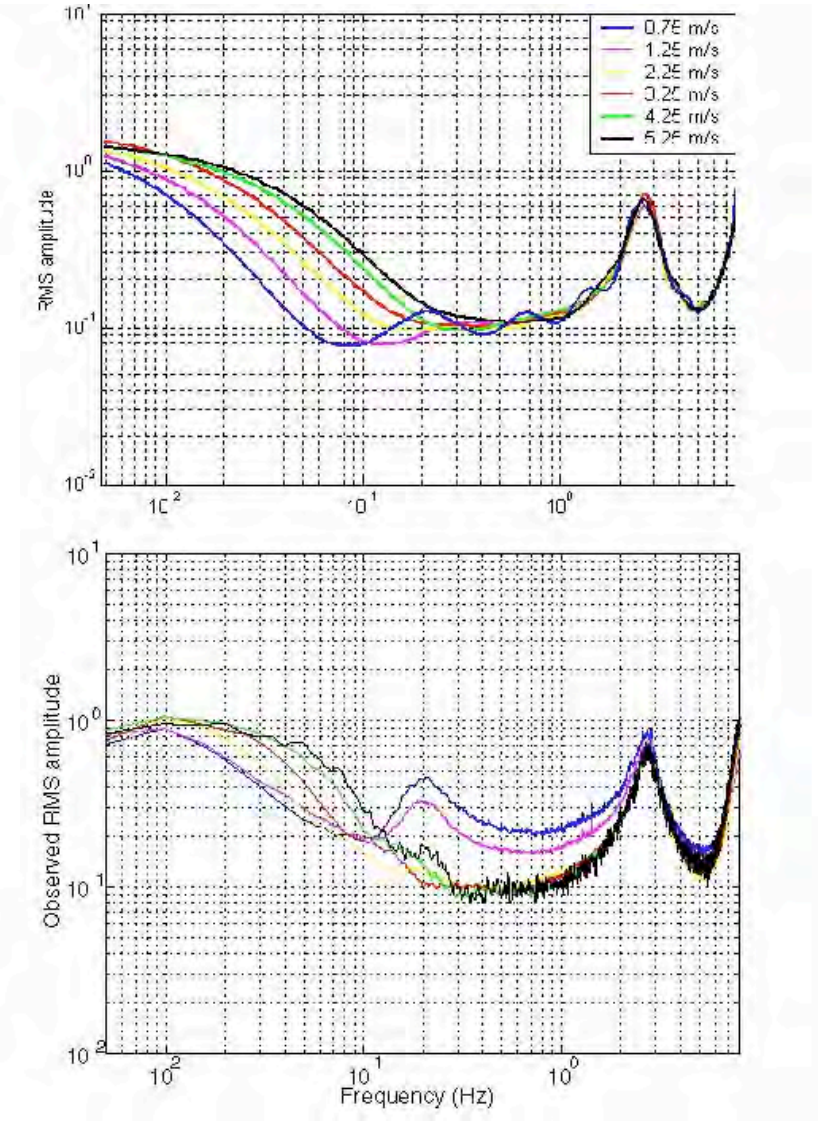

Figure 4: Simulated noise reduction of the 70-m/144-port rosette filter for various mean wind speeds is shown in the upper panel. Each curve represents the ratio between the noise spectrum observed at the reference port and the noise spectrum of the rosette system. The corner frequency of the 70-m rosette filter is predicted to increase with increasing wind speed. Observed noise reduction is shown in the lower panel.

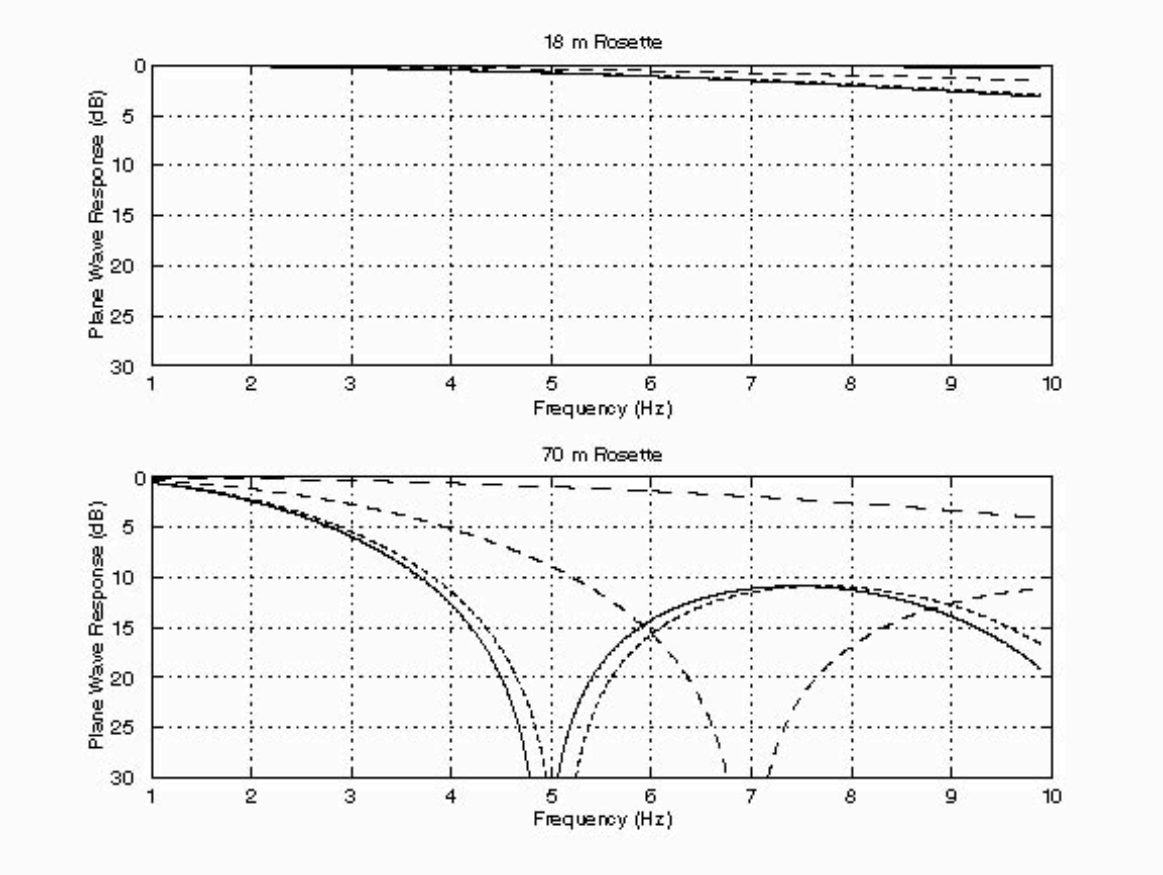

Figure 5: The rosette filter integrates pressure variations from the inlets simultaneously regardless of the angle of incidence of the arriving energy. The rosette filter is tuned to vertically incident signals. Attenuation of signals increases with increasing arrival angle from the horizontal and with increasing frequency. The attenuation is strongly dependent on the aperture of the filter. For example, in the upper and lower panels we show the plane wave response for the 18- and 70-m rosette filters respectively at four arrival angles. The solid curves in each panel represent an arrival with an arrival angle of 0° above the horizontal. The finely to coarsely dashed curves represent signals propagating across the two filters at 15, 45 and 75° above the horizontal. The elevation angles, θ_e, are calculated assuming a sound speed, c, of 347 m/s. The phase velocity, c_p, is given by c/cos (θ_e). The phase velocities corresponding to the arrival angles at the four arrival angles are 347, 359, 491 and 1341 m/s. In both panels, the response for a vertically incident signal is 0 dB at all frequencies.

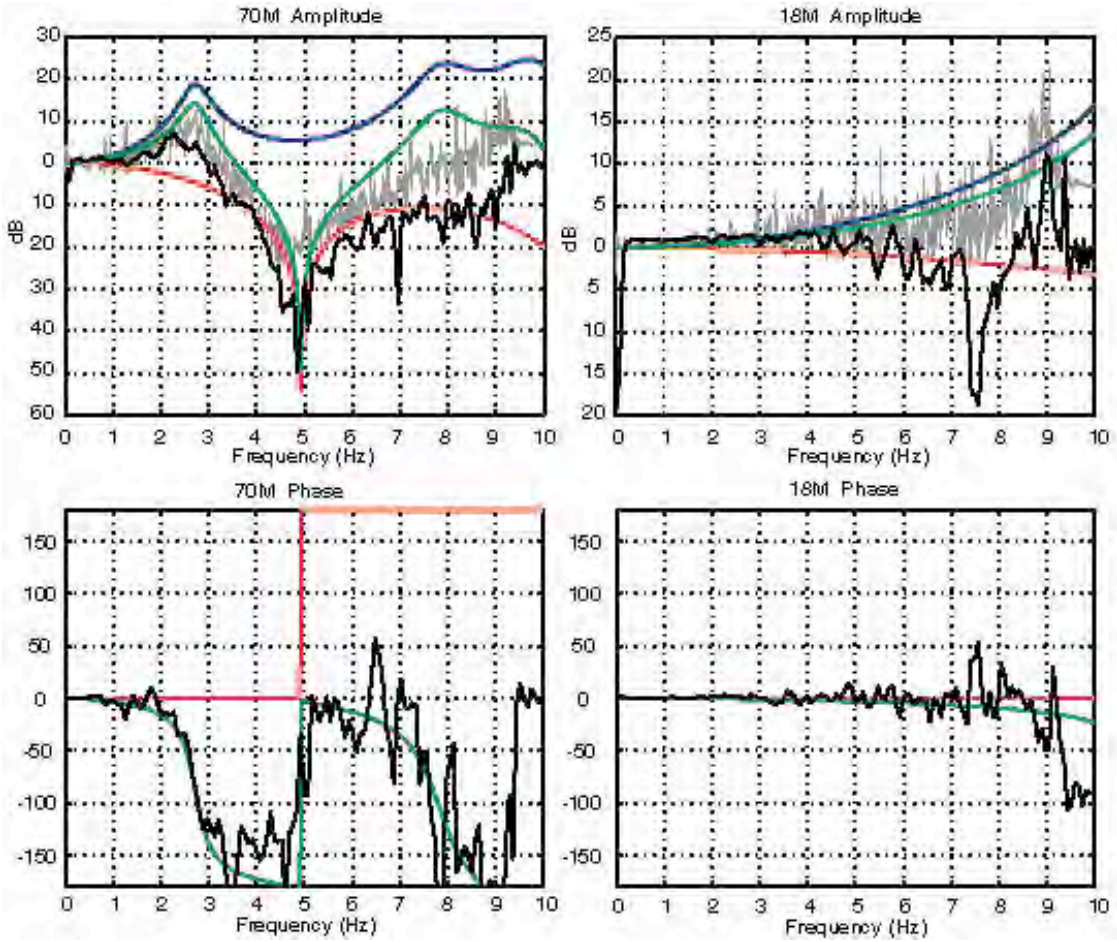

Figure 6: Amplitude and phase response of 18- and 70-m rosette filters are shown in this figure. The blue curves in all panels represent the response due to internal resonance inside the pipe systems. The red curves represent the plane wave response. The plane wave response of the filters, which is dependent on the phase velocity of the incoming energy, has been calculated at 330 m/s. This is the phase velocity of the energy from the April 23rd bolide as determined by processing data from the I57US array. The green curves represent the total response due to time delays between inlets and to resonance inside the filters. As shown in Figure 9, the 18-m filter attenuates the incident signal by less than 5 dB at all frequencies up to 10 Hz. The attenuation caused by the 70-m filter is strongly frequency dependent at this low phase velocity. A pronounced notch is predicted to exist at 5 Hz. Amplitude and phase from a phase-coherent cross-spectral analysis of data from the April 23rd bolide are shown in black. The theory accurately predicts the phase of the signal but under-predicts the amplitude at all frequencies. A spectral ratio of the filtered to unfiltered data (gray curves in the upper panels) closely match the theoretical predictions.

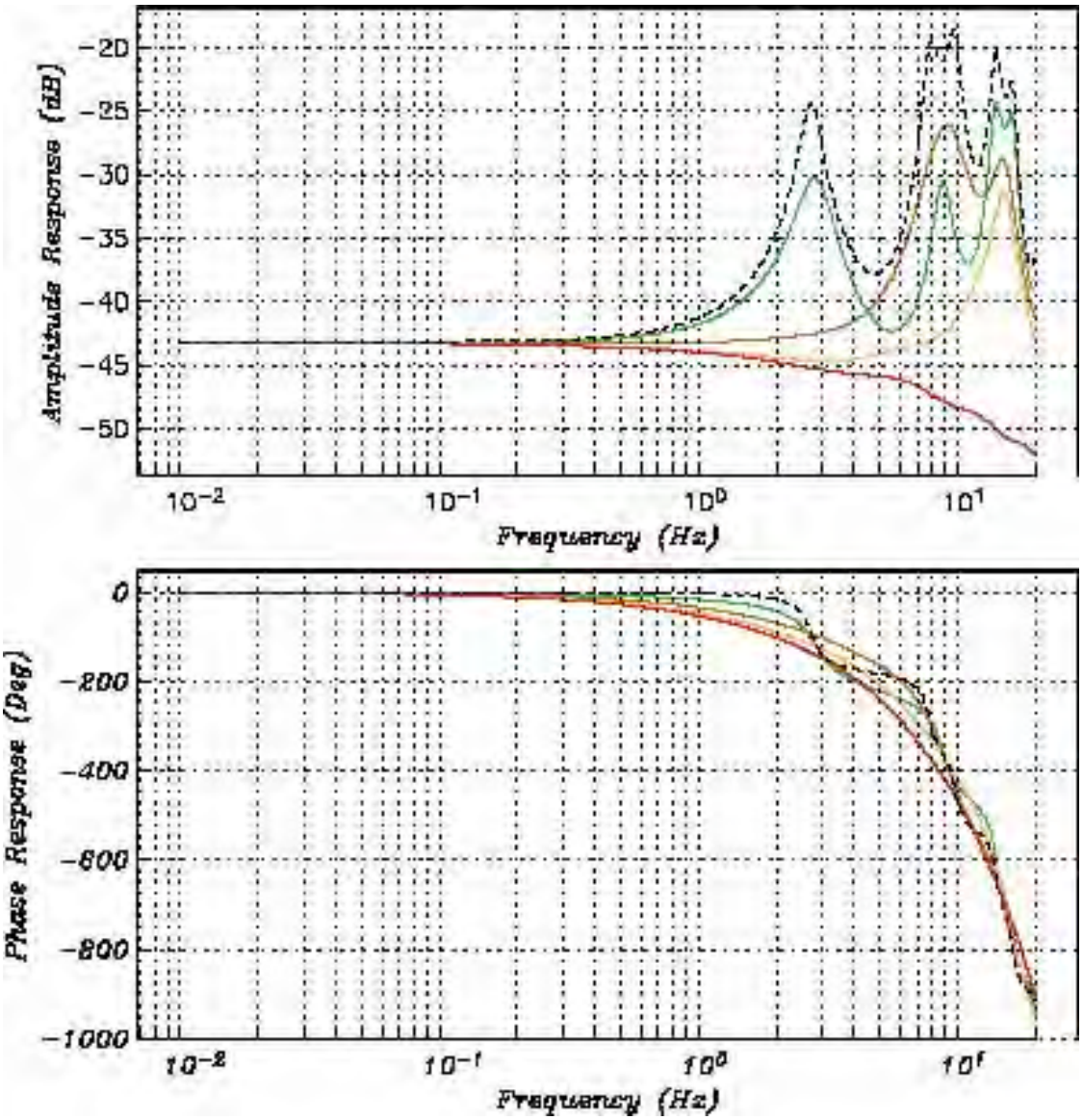

Figure 7: Simulations on the original and modified 70-m-aperture rosette filters are shown in this figure. The systems with capillaries at the inlets, secondary summing manifolds, both the inlets and the secondary summing manifolds, at the inlets and both summing manifolds are represented by the brown, green, gold and red curves. The unmodified system is represented by the dashed curves.

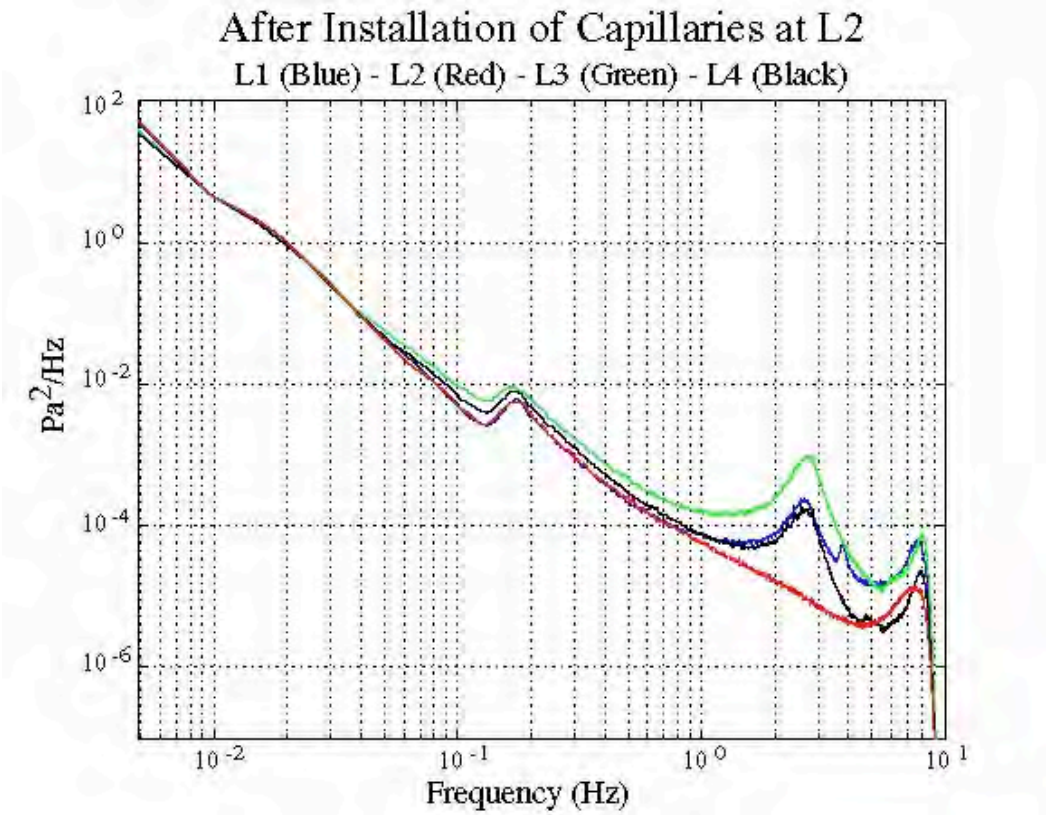

Figure 8: Spectral density estimates taken from data collected after the capillary plugs were installed at site "L2" (red curve). The capillaries have removed the resonance peak at 2.65 Hz.

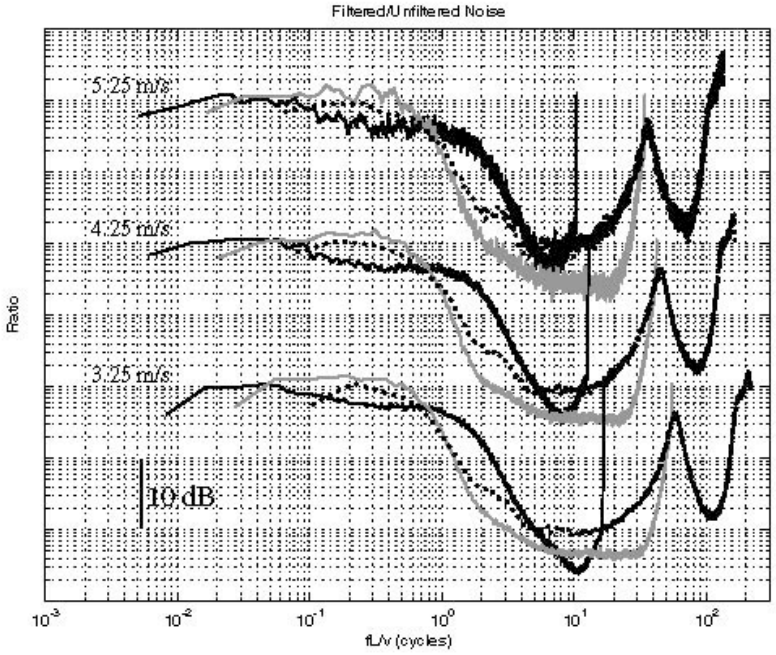

Figure 9. Wind-noise reduction versus scaled frequency at 3.25m/s, 4.25m/s, and 5.25m/s for the 70- rosette (bold dots), the 18-m rosette (bold gray) and the 5.5-m wind barrier (solid curves).

OPTIMUM FILTRATION OF ACOUSTIC PULSES CAUSED BY UNDERGROUND NUCLEAR AND ABOVE-GROUND CHEMICAL EXPLOSIONS

V. Krasnov and Ya. Drobzheva

Institute of the Ionosphere, Ministry of Science and Education, Republic of Kazakhstan

Sponsored by Defense Threat Reduction Agency

Contract No. DTRA01-99-C-0025

ABSTRACT

For identification of acoustic pulses from explosions, we devised a method using optimum filtration of signals. As a reference signal we use the calculated form of an acoustic pulse. To describe the propagation of an acoustic pulse through the inhomogeneous atmosphere, we developed a new equation and corresponding computer simulation code. The model takes into account nonlinear effects, inhomogeneities of the atmosphere, absorption, expansion of a wave acoustic front, etc. At present the model is developed for the ascending part of a trajectory of an acoustic ray: from a ground surface up to the height of a reflection point (ionospheric height). Data from parachute measurements of acoustic pulses, and measurement of acoustic pulses at different heights in the ionosphere along with Doppler radio soundings were used to test the model.

The program includes the following subroutines:

1. Subroutine of the vertical movement of the earth's surface during an underground nuclear explosion (we use an empirical model).
2. Subroutine of a calculation of atmospheric parameters (we use an MSIS model).
3. Subroutine of a calculation of wind profile along an acoustic ray trajectory (we use a HWM model).
4. Subroutine of an acoustic pulse generation by a spall zone.
5. Subroutine of acoustic pulse generation by an above-ground chemical explosion (we developed a new initial form of an acoustic pulse).
6. Subroutine of the propagation of an acoustic pulse from the earth's surface up to the ionospheric height.
7. Subroutine of the calculation of the ionospheric profile (we use an IRI model and data of an ionogram).
8. Subroutine of acoustic wave influence on the ionospheric plasma.
9. Subroutine of the trajectory of radio wave propagation in the ionosphere (we account for the geomagnetic field).
10. Subroutine of the ionospheric perturbation influence on the Doppler frequency of a radio wave.
11. Subroutine of the optimum filtration.

We used data from the Mill Race experiment (an above-ground chemical calibration explosion for which the yield was 500 ton TNT) to test the model calculations simultaneously at eight different locations in the low atmosphere and ionosphere. The correlation coefficient between the calculated and the experimental form of the acoustic pulse was in the range of 0.85 to 0.98. The average mean yield of the explosion was 531 ton TNT with a standard error of ± 34 ton. We also estimated the yield of the Flixborough explosion using the data from six independent measurements of acoustic pulses at ionospheric heights. The reconstructed oblique radio soundings agree remarkably well with experimental results when a ground source explosion yield of 283 ± 38 tons of TNT is utilized. We used the data from the Soviet – US experiment (underground nuclear calibration explosion at the Semipalatinsk test site in 1988, the yield of which was about 150 kiloton TNT) to test the model calculations simultaneously at three different locations in the ionosphere. The correlation coefficients between the calculated and experimental forms of the acoustic pulse were 0.83, 0.8 and 0.68. The probability of detection of a signal was equal to one with the threshold of acceptance of the cross-correlation set equal to 0.4.

OBJECTIVE

The manner in which infrasound monitoring can aid in remote detection and identification of underground nuclear explosions has been the subject of some exploration. We propose the theory of optimum filtration as a way for infrasound to be applied to this problem. The optimum analysis should include: a correlation device and a reference signal such that:

$$R(\tau) = \int_0^T f_s(t)\, f_p(t-\tau)dt\ ;$$

where $f_s(t)$ input is the infrasonic signal and $f_p(t)$ is the reference signal – the infrasonic "portrait" or analysis of an explosion.

To produce analyses of explosions, we can use theoretical calculations. Obviously, the correlation between physical and numerical models and experimental results should be sufficiently high. The model should take into account the following factors:

- Process of generation of an acoustic impulse by an explosion.
- Oblique propagation of acoustic impulses in the real atmosphere.
- Reflection of an acoustic wave from the atmosphere.
- Propagation of acoustic impulses back down to the receiver.

Each of the four parts of this model should be experimentally verified. For long distances, acoustic pulses (infrasound) are propagated from the earth's surface to an altitude about 100-120 km (ionospheric heights). Thus, it is possible to use experiments on radio sounding in the ionosphere (for example, Doppler radio sounding) for testing a model at these heights. As a result we have developed new theoretical models and corresponding computer simulation codes that account for the entire range of atmospheric and ionospheric phenomena involved in the technique, from the generation of acoustic pulses by surface ground motions during underground nuclear explosions to the synthesis of radio frequency signatures recorded by ionospheric radar systems (Drobzheva and Krasnov, 2002). The model accounts for non-linear effects, atmospheric and ionospheric vertical inhomogeneity, absorption, diffraction effects, geomagnetic field, horizontal wind, etc.

The purpose of our work: to show the efficiency of the optimum filtration method for detection of acoustic impulses from chemical and underground nuclear explosions from the ionosphere.

RESEARCH ACCOMPLISHED

The first and second parts of the model were tested with experimental data obtained during the Mill Race experiment (Banister and Hereford, 1991; Warshaw and Dubois, 1981) and the Soviet – US experiment (09/14/88). In the Mill Race experiment, data collected during the surface burst of a 500-ton TNT equivalent chemical explosion represented a unique opportunity to assess the credibility of calculations used to evaluate the yield of surface explosions from atmospheric and ionospheric measurements. The evaluation of the model used the results of atmospheric pressure variation measured by probes suspended by four parachutes at an altitude of about 10 km at horizontal distances of 1.9 to 16.3 km from a vertical line through the explosion point. Doppler shift records (f_d), made when radio waves were reflected from the altitudes of about 151, 222, 242 (vertical sounding) and 263 km (oblique sounding) were also used. It was therefore possible to test the model calculations simultaneously at eight different locations in the atmosphere and ionosphere. To estimate the yield of the explosion, the forms of the calculated and experimental acoustic and Doppler disturbances for a variety of explosion yields were compared. This comparison took the form of determining the correlation coefficient (K) between calculated and experimental values and choosing the value of the explosion yield when the correlation coefficient achieved its maximum value. Figure 1 and Table 1 indicate the results of these comparisons.

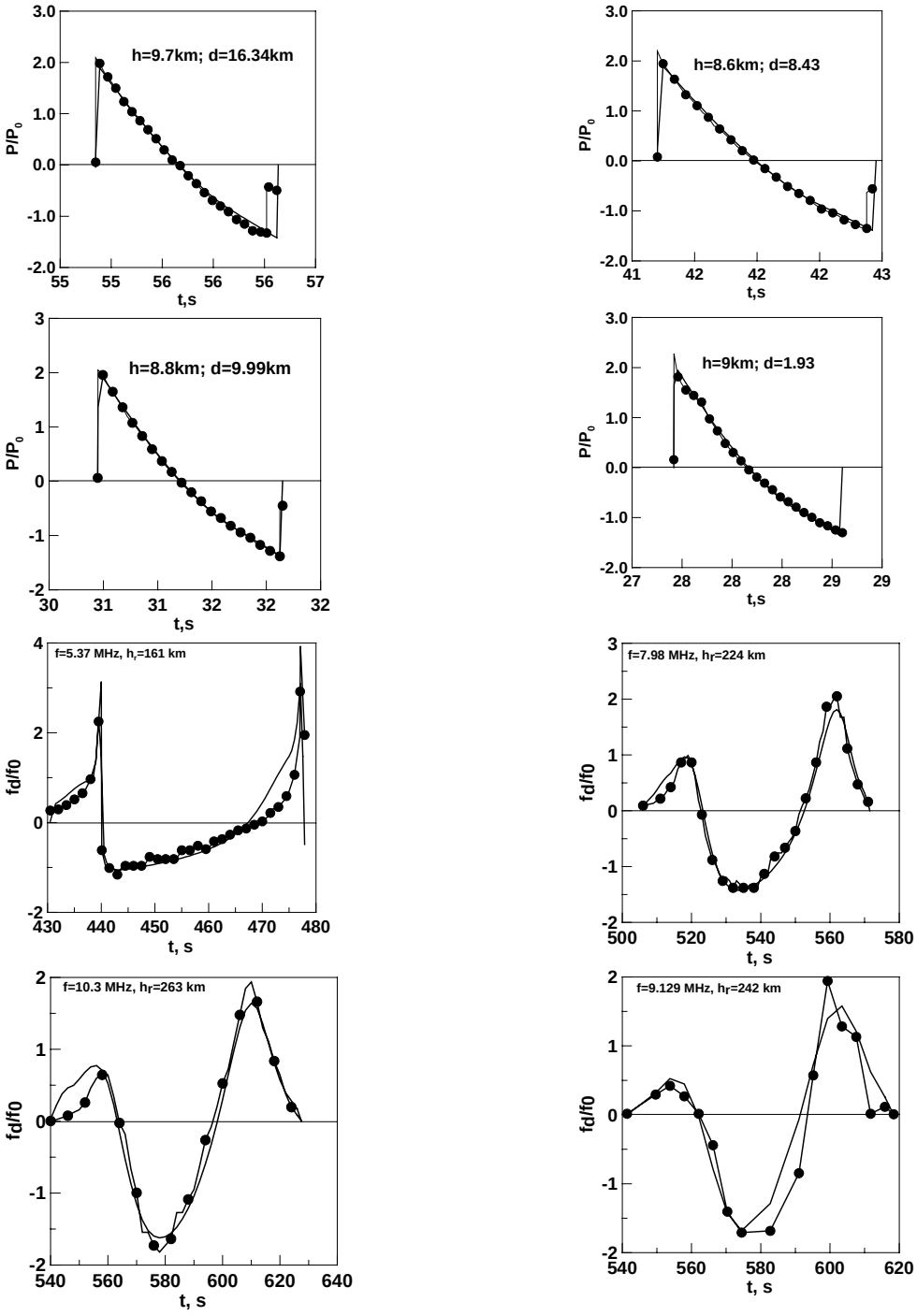

Figure 1. Comparison of calculation results of acoustic and ionospheric perturbations for the Mill Race experiment. Calculations are represented by solid lines and experimental results by dots; h – altitude of observation, d – horizontal distance from the site of explosion, f - frequency of radio sounding.

Table 1. Mill Race Explosion Yield; comparison of experiment to theory.

h (km)	K (correlation coefficient)	Q (ton TNT)	Error in Q (%)
8.6	0.95	450	10
8.8	0.973	550	10
9.0	0.964	550	10
9.7	0.943	450	10
161	0.85	700	40
224	0.989	600	20
242	0.952	400	20
263	0.982	550	10
mean	-	531	6.4

It is necessary to note that there are some differences between the experimental and calculated arrival times of the disturbances. However, to show the agreement between the experimental and calculated waveforms, these were matched by arrival time; any error in the calculation of the arrival time does not exceed 5%.

The average mean of the explosion determined in this manner is 531 ton TNT with a standard error of the mean of ±34 ton. The calculated result agrees well with the experimental value. It is important to note that in spite of using numerous input data (profiles of atmospheric pressure, density, sound speed, ionosphere, etc.), the calculation results show only a small spread in values of yield; ±6.4%. The reason for this is that the parameters of acoustic disturbances depend critically on explosion yield and the altitude profile of atmospheric density (Drobzheva and Krasnov, 2001; Drobzheva and Krasnov, 2002). In turn, any error in the determination of the model of atmospheric density is small – about a few per cent.

In the Soviet – US experiment, data collected during the calibrated underground nuclear explosion of 150 kiloton TNT equivalent represented a unique opportunity to assess the credibility of calculations from ionospheric measurements. Doppler shift records were recorded when radio waves were reflected from the altitudes of about 179, 210-213, 221 km (oblique sounding). It was therefore possible to test the model calculations simultaneously at three different locations in the ionosphere. Figure 2 indicates the results of the comparisons.

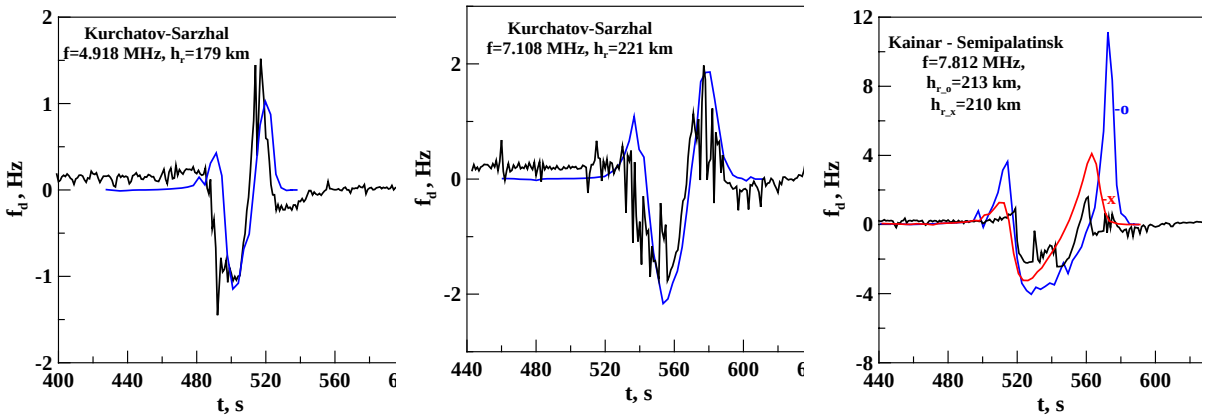

Figure 2. Comparison of calculation results of ionospheric perturbations for the Soviet - US experiment. Black line = experiment, dark blue line = calculation for an ordinary radio wave and red line = calculation for an extraordinary radio wave. h = altitude of observation, f = frequency of radio sounding.

A coefficient of cross-correlation between calculated and experimental curves produced the following results: 0.83 (for Fig. 2a), 0.8 (for Fig. 2b), 0.61 (for Fig.2c - for an ordinary radio wave), 0.68 (for Fig. 2c - for an extraordinary radio wave). The smaller coefficient of correlation for the case in Figure 2c is caused by the fact that the heights of a reflection of ordinary and extraordinary radio waves only differed slightly. As a result, perturbations on the Doppler

record were almost simultaneous for both types of waves. This caused an interference in the Doppler record. The model developed does not take into account interference effects.

During the Soviet-US experiment, the ratio of the signal to noise on Doppler records was more than one. Thus, it was not a problem to detect the signal. A more difficult task was encountered during an underground nuclear explosion on 12/27/87. Figure 3a, b represents initial Doppler records for two radio waves. Figure 3c, d represents the corresponding records after the optimum filtration; the signal considerably exceeds noise. If we determine the threshold of decision-making as a correlation coefficient of 0.4, then the probability of correct detection of the signal is equal to 100 %.

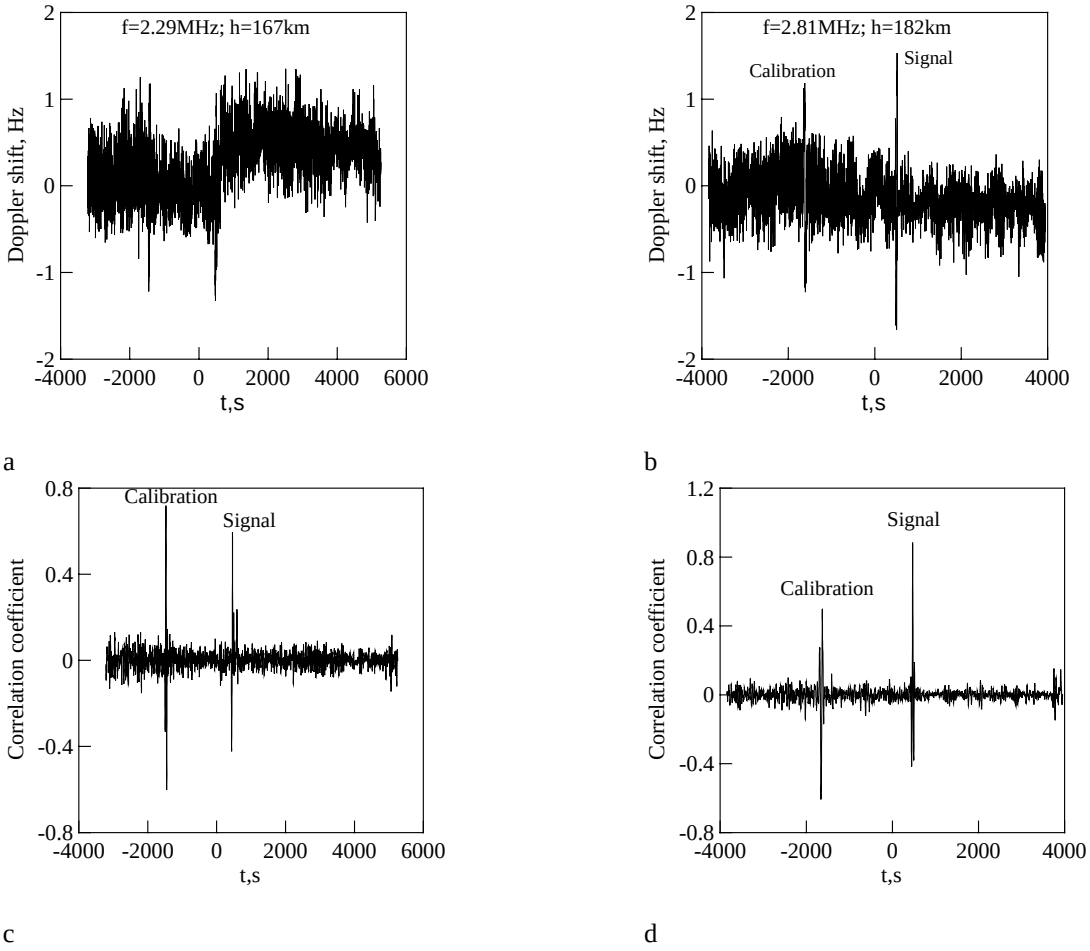

Figure 3. Doppler records before (a,b) and after (c,d) the optimum filtration for two radio trace.

Because the physical model agrees well with experimental results, it allows us to investigate the dependence of the form and magnitude of the Doppler response on the length of a radio trace during an underground nuclear explosion. The result of calculations for an approximately 210-km height of a radio sounding is represented in Figure 4 where it is shown that the form and magnitude of the Doppler response practically do not depend on the length of a radio trace. At the same time, these parameters are highly dependent on the height of radio wave reflection and horizontal distance between the radio wave reflection point and the explosion site. Because radio waves of short wave range can propagate all around the globe, the ionospheric method of detecting acoustic impulses due to explosions has no distance restrictions.

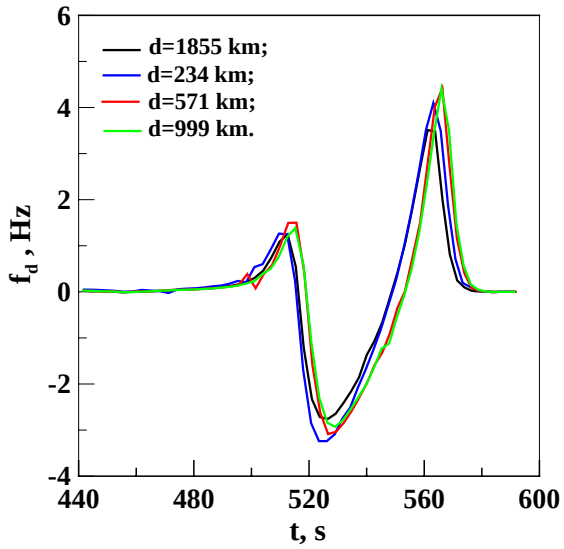

Figure 4. Dependence of Doppler response on length (d) of a radio sounding trace

CONCLUSIONS AND RECOMMENDATIONS

The method of optimum filtration can be effectively used for remote detection of "signals" due to explosions, at least, for detection of infrasound signals at ionospheric heights. It is interesting to test this method using ground-based infrasonic measurements. However, we need to develop the theory and corresponding computer simulation codes for acoustic wave reflection from an atmospheric layer and propagation of acoustic pulses from the point of reflection back to the earth's surface.

ACKNOWLEDGEMENTS

Financial support for this study was provided by the Division of Scientific and Environmental Affairs of NATO under reference #SST.CLG.978353 and the National Nuclear Centre, Republic of Kazakhstan.

REFERENCES

Banister J.R. and W. V. Hereford (1991), Observed high altitude pressure waves from an underground and surface explosion. *J. Geophys. Res.*, **96**, No.D3, p.5185-5193.

Drobzheva Ya.V. and V. M. Krasnov (2002), The acoustic field in the atmosphere and ionosphere caused by a point explosion on the ground. *J.Atmos.Solar-Terr. Phys.*, in press.

Drobzheva Ya.V., and V. M. Krasnov (2001), The spatial structure of the acoustic wave field generated in the atmosphere by a point explosion. *Acoustical Physics*, **47**, No. 5, pp. 556-564.

Warshaw S. I. and P. F. Dubois (1981), Preliminary theoretical acoustic and RF sounding calculation for Mill Race. Report Lawrence Livermore National Laboratory, UCID-19231, USA, 20p.

THE BOLIVIAN ALTIPLANO INFRASOUND ARRAY IS08

Estela Minaya, Guido Avila, Cristina Condori, Alejandro Córdova, and Francisco Vega

Observatorio San Calixto

Sponsored by Defense Threat Reduction Agency

Grant No: F49620-97-1-0214

ABSTRACT

The main purpose of an infrasound station is to detect acoustic waves generated and transmitted in the atmosphere that are associated with nuclear explosions, volcanic eruptions, meteorological processes, and some large earthquakes such as the one that occurred on the Peruvian coast on June 23 of 2001 with magnitude Mw 8.4. That earthquake was recorded in the IS08 (International Monitoring System [IMS] designation) infrasound array located in the Bolivian Altiplano, 63 km from La Paz City, Bolivia. That array includes four microbarographs – three located at the vertices of a 1-km equilateral triangle and the fourth at the middle of the triangle. Transmission is via satellite communication to Departament Analyse Surveillance Environnement, France (DASE) and from there to the International Data Centre (IDC) in Vienna. Communication to the National Data Center (NDC) at the Bolivian Observatorio San Calixto is by a telemetric system with three relays.

Monitoring started in November 2001 and the first observations indicated some apparent anomalies. We compared to the infrasound data reported in the bulletin of CEA (Commissariat a l'Energie Atomique, France), and we found that 57 signals recorded by the array were not reported in that bulletin. To understand the discrepancy, we have analysed the monthly statistical data obtained by our transmission and the data received at CEA to see if the signal loss could be due to transmission gaps. The time at which the data losses occurred does not coincide with those recorded at the CEA, so we are trying to see what could be the cause of that difference. Our monitoring shows a signal that coincides with a small earthquake (magnitude 3) that occurred on March 23, 2002, and was located 84 km away from the array. This signal was recorded by only three elements of the array. We are still working to find the cause. We are applying software to determine the frequencies of that signal and other parameters that allow us to find some associations with any known source that generates acoustic infrasound waves.

OBJECTIVE

The objective of this research is to study all aspects related to the acoustic waves generated in the atmosphere and recorded by the infrasound array IS08 and to determine waveform, origin or cause of generation.

RESEARCH ACCOMPLISHED

Introduction

The installation of the infrasound array in the town of Peñas in the Bolivian Altiplano, approximately 63 km to the northwest of La Paz City, was completed in December 1999 and complements the other South America stations that form part of the International Monitoring System (IMS) of the Preparatory Commission for the Comprehensive Nuclear-Test-Ban Treaty Organization (CTBTO). Station IS08 began infrasound monitoring and transmitting data in December 2001. The monitoring consists of the routine analysis of the microbarographs, obtained by the four elements that comprise the infrasound array IS08. The monitoring allows us to determine any type of physical interruption to the equipment and the quality of transmissions to data analysis centres. This routine analysis has allowed us to do

1. statistical analysis of the telemetric transmission of the signals;
2. comparison of the telemetric transmission (to OSC - CND, La Paz - Bolivia) and VSAT (to DASE); and
3. signal discrimination that corresponds to an acoustic source or other types that are not yet defined.

The previous experience that we have consist of investigations with data recorded by an infrasound acoustic array installed in 1966 as an asymmetric array with seven microbarographs, with more than 2 km of separation between the elements (Table 1).

The major part of this previous analysis covers nuclear explosions, large earthquakes, volcanic eruptions and some signals generated on the surface area of the south Pacific (Fernández, 1969) that the infrasound array in the Bolivian Altiplano registered effectively, especially for waves from large distances. Escobar (1971) indicated that this effect was caused by a small attenuation factor due to large wavelength. These results are influenced by several factors that exist in the area, i.e., the altitude, 4000 m.a.s.l. and low air density, aspects that have a beneficial effect on the signal/noise ratio. Because of the meteorological conditions in the Bolivian Altiplano, the infrasound noise at night is 20 times lower than the noise during the day. The asymmetric distribution of the first array was a factor in the study of events with long periods and large distances between the focus of the events and the locations in the array.

Those studies did not consider local events because at short they distances do not generate long-period waves. But it is very important to know about the process of generation of that kind of infrasound wave. For example La Paz City, on February 19, 2002, suffered a sudden and very severe storm that lasted for 45 minutes (about 70 people dead and great structural damage). The distance from the city to the array is 63 km, but this natural phenomenon (severe storm) apparently was not recorded by the infrasound array IS08. On the other hand, a large earthquake that occurred in Peru on June 23 of 2002 was recorded very clearly due to the generation of long-period waves as shown by Le Pichon (2002).

Table 1. Former infrasound array located in Peñas

CODE	DATE	LATITUDE	LONGITUDE	ALTITUDE (mt)
A	1966-1975	16.2135°	68.4397°	4120
B	1966-1975	16.2885º	68.4186º	4005
C	1966-1975	16.2659º	68.4717º	3960
D	1966-1975	16.2397°	68.4735°	3970
E	1970-1975	16.1996°	68.3268°	4660
F	1970-1975	16.2944°	68.2585°	4680
G	1970-1975	16.3922°	68.3074°	4300
LP1B	1999-	16.2173º	68.4442º	4071
LP2B	1999-	16.2022º	68.4559º	4032
LP3B	1999-	16.2150º	68.4552º	4042
LP4B	1999-	16.2215º	68.4636º	4017
Relay				
Patamanta		-16.3182º	-68.2962º	4480
Cruce Chacaltaya		-16.3833º	-68.1666º	4628
El Alto		-16.4814º	-68.1677º	4020
OSC (Reception)		-16.4905º	-68.1325º	3658

IS08 infrasound array

The infrasound station IS08 is located in the Peñas region, specifically in the area of Isquillani and Tuquia, Department of La Paz, at about 63 km La Paz City. It was installed at the end of 1999. The array has a symmetric distribution. It is composed of four sensors (Figure 1) and has three at the vertices of an equilateral triangle and one at the center with a separation between them of 1 km. There are two modes of data transmission, one through telemetry to the Observatorio San Calixto, La Paz Bolivia, and the other by VSAT (Figure 2) to Champagne (east of Paris) then to DASE and finally to the International Data Centre in Vienna, Austria. The telemetry transmission is performed by relay (Figure 2).

Each station has a sensor and an acquisition system and transmission unit, with a 12-V power supply and the transmission antenna. The sensor, model MB2000, was built by DASE. The sensor measures small variations of atmospheric pressure and also those generated at large distances. The sensitivity of the output is 1 MV/Pa, the frequency response is 0.001 to 40 Hz, and, for filtered output, 100 s to 27 Hz, electronic noise is less than 2 mPa rms (0.02~4 Hz).

The weather sensor is located next to LPN1 (Figure 1). The wind direction, speed, air humidity and temperature are recorded by telemetry in the Bolivian NDC, Observatorio San Calixto.

The data are transmitted from the central station LPN4 (Figure 1) to OSC to check and to validate the digital signals. Remote monitoring is performed by CRISTAL software at DASE and OSC.

Array environment

It is necessary to have a clear picture of the topography in the array environment; i.e., the region of the array and the relays. We need to know if the variation in topography can be the cause of generated infrasound waves, and how much the infrasound variations can be attributed to small changes in temperature near the array.

Local Geology

Geomorphologically, the station array is located on glacial lacustrine to fluvio lacustrine deposits, constituted of blocks of sand, slime and clay. Microthermal ground covered with moss and straw can be found on these sediments that form the Altiplano. There are small mountainous areas with some rivers in different directions.

Topography and average altitude

The topography of the area of the stations is quite moderate and almost flat with an average elevation of 4000 m.a.s.l. The infrasound stations are surrounded by a series of peaks; to the North is the hill Huari Umaña with a height of 4484 m.a.s.l., to the Southwest the hill Allkamarini and the hill Pucuni Arc with an elevation of 4156 m.a.s.l., and to the South the hill Peñas consists of a pair of peaks, Chucecani and Peñas with a height of 4333 m.a.s.l.

To the east of the station is a plain with elevations that rise as we approach the mountain Huayna Potosí and the relay station Patamanta (Figure 3), which is located on the hill Cotan Kkollu with an altitude of 4400 m.a.s.l., and finally the relay station Cruce Chacaltaya that is located at an altitude of 4500 m.a.s.l.

Analysis of signals

The parameters observed on the microbarograms do not show great regularity in periodicity or amplitude, they appear as isolated events with a specific arrival time and direction. This was confirmed by routine analysis that detected 57 signals from December 2001 to February 2002. The signals acquired by the array were not reported by the Infrasound Bulletin of IS08 published by CEA. Two signals are shown in Figure 4.1 and 4.2 and Table 2. The first signal is impulsive; has SE direction and 6.8 second duration, but an amplitude of only a few Pa. The second signal has SW direction, four second duration and is less clear than the first, especially on the LP4B sensor.

Table 2. Signal recorded by infrasound array IS08

Date	Origin Time	Duration (s)	Azimuth	Speed	Filter (Hz)
10/02/2002	09:24:43	6,38	NO CEA		0,1-9
11/02/2002	20:26:10	4	NO CEA		0,1-9
23/03/2002	21:11:00	4	NO CEA		0,3-3,5
12/04/2002	09:54:40	1.31	118,8	0,639	0,1-9
14/04/2002	18:59:20	4.7	74,9	0,383	0,1-9

NO CEA: Signals not reported by CEA Bulletin.

The main cause of those differences between the local analysis and the CEA bulletin was attribued to data transmission. To confirm this situation and to determine its cause, we compared the transmission of the data sent through telemetry and the data sent through satellite communication for each element of IS08 array (Figure 2) Statistical analysis was conducted of data losses during transmission reported each month. Figure 5 shows the analysis for February and no correlations were found between the comparative statistical analyses. We can say that the signals discussed above are very small and probably are local.

In this analysis the topography was considered as a probable generator of infrasound waves at short distances. The topography near to the array is almost flat, but the surrounding area has elevation differences due to the presence of the Cordillera Oriental. More work is needed to verify this hypothesis .

The third signal in Table 2 corresponds to a local earthquake with magnitude Ml 3, and 84 km distance from the source to the array. A filter of 0.8 to 3.5 Hz was applied. Figure 6 shows the seismic and infrasound waves recorded by three barographs. On LP1B, the signal is unclear, the arrival is emergent, and the spectrum shows a frequency of 2 Hz, which confirms the presence of a long-period wave.

Two signals are shown in Figures 7 and 8 that could be generated by local effects. Both records are local and the arrival waves are impulsive; the difference between them is the duration. The spectrum does not show considerable variation between frequencies, and there is background noise.

CONCLUSIONS AND RECOMMENDATIONS

Many of the signals recorded up to now should be considered a consequence of small vibrations with displacements or very small variations of temperature and pressure in the atmosphere that usually accompany infrasound waves.

The analysis shows that signals could give enough information to conduct more precise research. It will be necessary as a second step of this research to use software such as the Progressive Multi-Channel Correlation (PMCC, Cansi, 1995) to determine parameters such as velocity, phase, and azimuth and provide a classification of infrasound waves (Bass, 2001).

REFERENCES

Bass, H.E., K. Gilbert, M. Garces, M. Hedlin, J. Berger, J.V. Olson, C.W. Wilson and D. Osborne. (2001), Studies of microbaroms using multiple infrasound arrays, 23rd Seismic Research Review: Worldwide Monitoring of Nuclear Explosions, Jackson Hole, Wyoming, p. 73-104.

Brown, D.J., C.N. Katz, R. LeBras, J. Wang and A. Gault. (1998), Infrasonic processing at the Prototype International Data Center. In Proceedings of 20th Annual Seismic Research Symposium On Monitoring A Comprehensive Test Ban Treaty (CTBT), Santa Fe, New Mexico, pp. 555-562.

Brown, D.J., C.N. Katz, R. LeBras, J. Wang and A. Gault. (1999), Infrasonic processing at the Prototype International Data Center. In Proceedings of 21st Annual Seismic Research Symposium On Monitoring A Comprehensive Test Ban Treaty (CTBT), Las Vegas, Nevada, II pp.86-95.

Brown, D.J., C.N. Katz, J. Wang and R.W. Whitaker. (2000), Tuning of automatic signal detection algorithms for IMS style infrasound arrays. In 'Proceedings of the 22nd Seismic Research Symposium: Planning for Verification of and Compliance with the Comprehensive Nuclear-Test-Ban Treaty', 12-15 September, New Orleans, Louisiana.

Cansi, Y.(1995), An automatic seismic event processing for detection and location: the P.M.C.C. method. *Geophys. Res. Lett.*, **22**, 1021-1024.

Escobar, G. (1971), *Ondas Infrasónicas: Ruido y Señales Observadas en la Estación Geofísica de Peñas*. Thesis, Universidad Mayor de San Andrés, La Paz, Bolivia.

Fernández, L.M. (1968), Infrasonic Research – Peñas Acoustic Array. Final Report, Grant No. AFOSR-67-1177C, Observatorio San Calixto, La Paz, Bolivia.

Fernández, L.M. (1969). Spectral Characteristics of Infrasonic Acoustic Waves and Related Seismic Research. Interim Scientific Report, Publication, Observatorio San Calixto, La Paz, Bolivia.

LePichon, A., Y. Cansi and B. Alcoverro. (1999). International Monitoring System. Infrasound Technical Training Program. CEA – Bruyères-le-Châtel – Département Analyse Surveillance Environnement DASE/LDG – France.

LePichon, A., J. Guilbert and M. Van de Walle. (2002), Ground – Coupled air wave and diffracted Infrasound from the Arequipa, earthquake by June 23, 2001, CEA, Lavoratoire de Détection et de Géophisyque, France. Poster

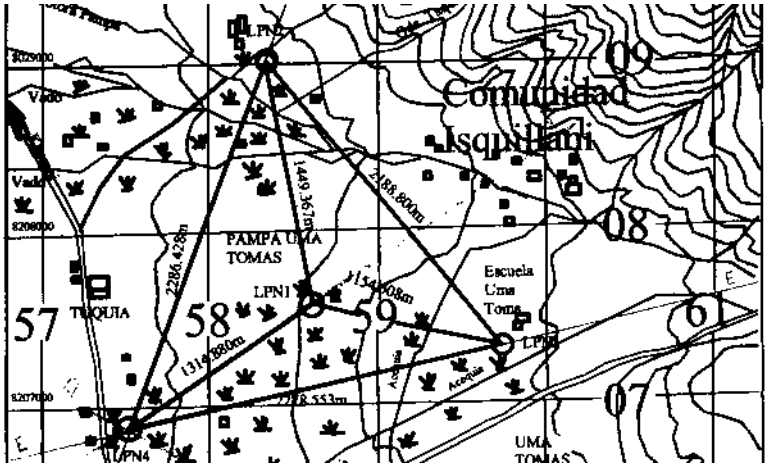

Figure 1: Map that shows the location of the infrasound array

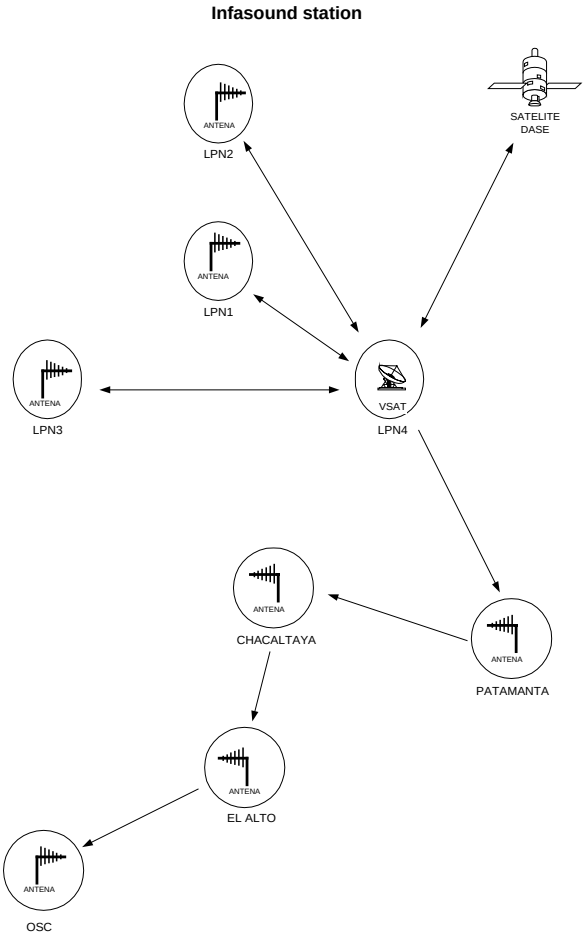

Figure 2: Diagram of the communication network.

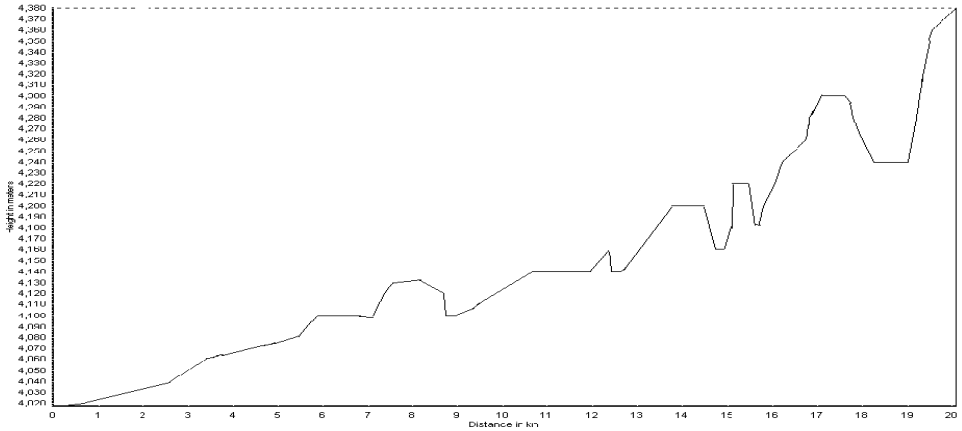

Figure 3: Topographical profile of the infrasound transmission from Peñas to Patamanta relay.

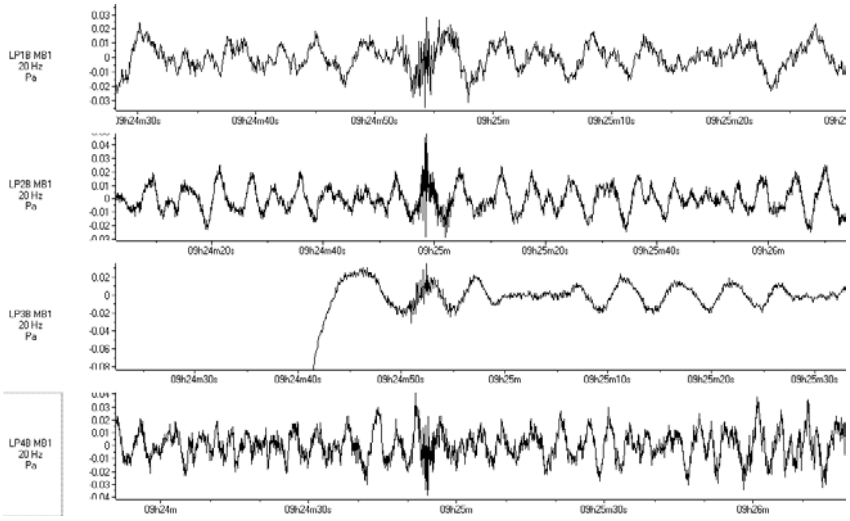

Figure 4.1: Signal of the 10/02/2002, 9:14 am, event, not reported by the CEA bulletin, with filter 0.1 to 9 Hz

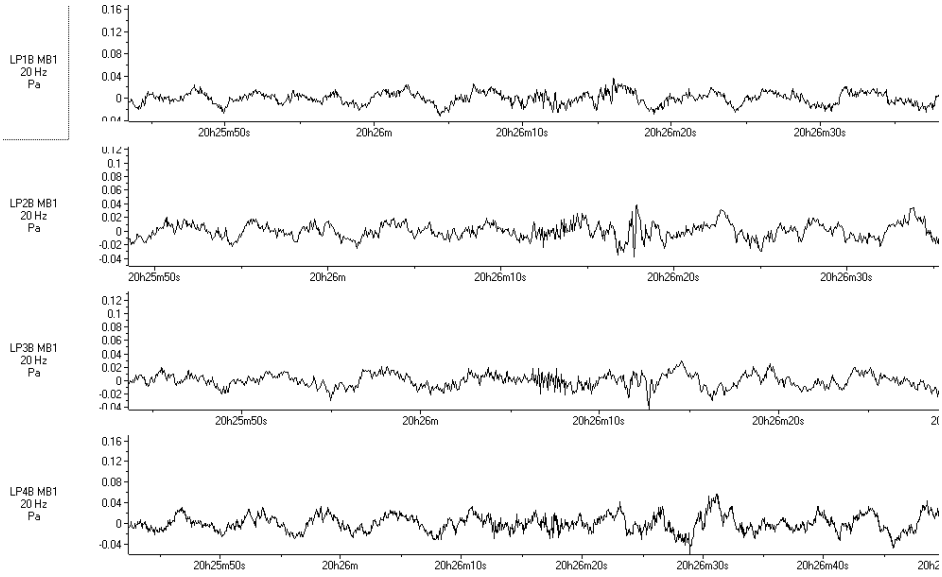

Figure 4.2: Signal of the 10/02/2002, 20:25 am event, not reported by the CEA bulletin, with filter 0.1 to 9 Hz

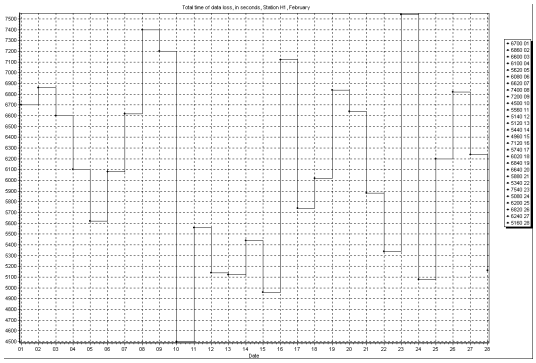

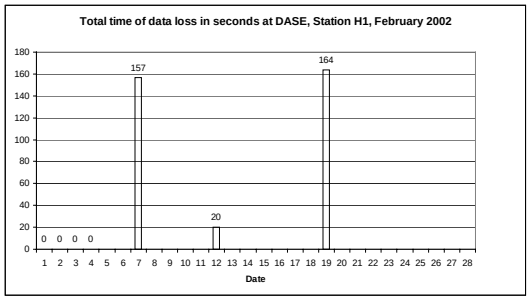

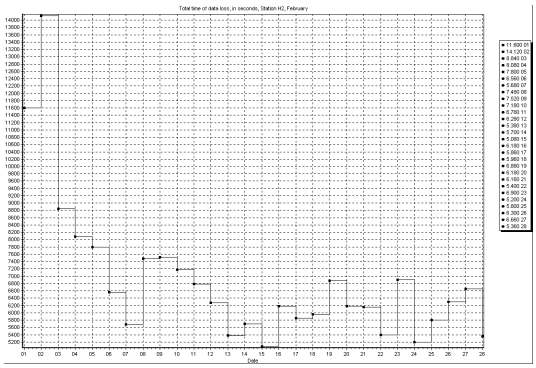

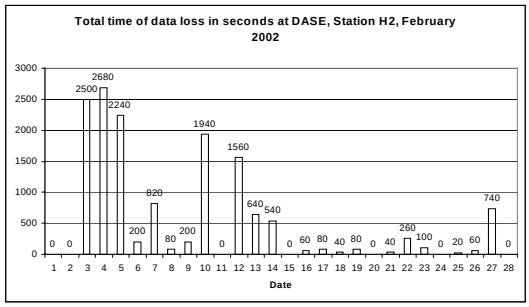

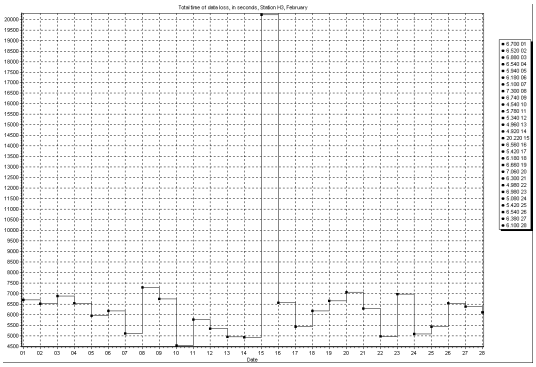

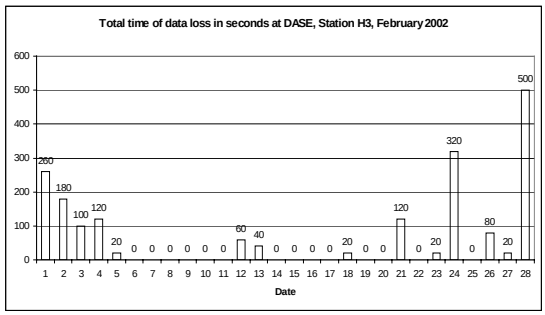

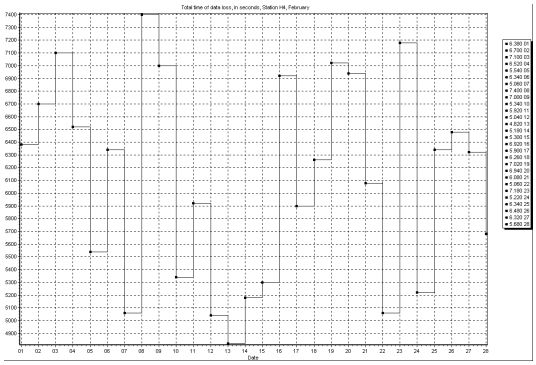

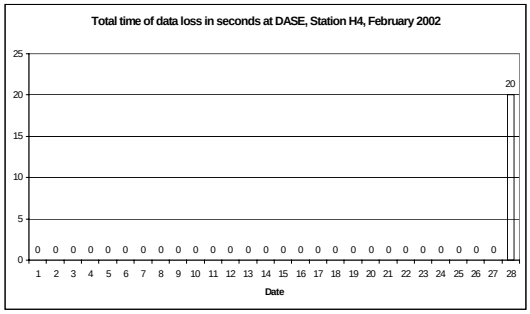

Figure 5: Comparative statistical analysis of data loss at the OSC and at DASE

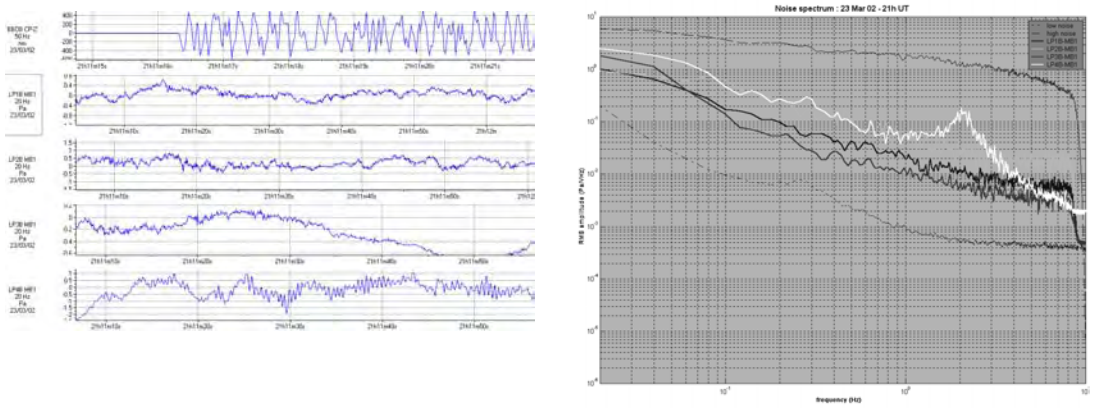

Figure 6: Local earthquake of 23/03/02, detected by the infrasound array, and its corresponding spectrum.

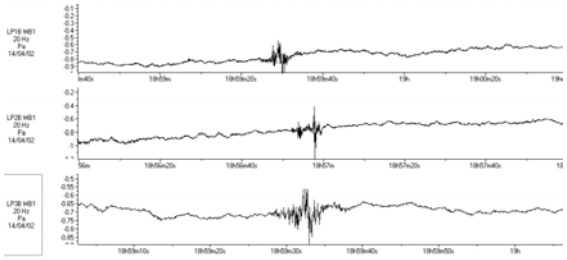

Figure 7: Signal recorded 14/04/02, 18:59

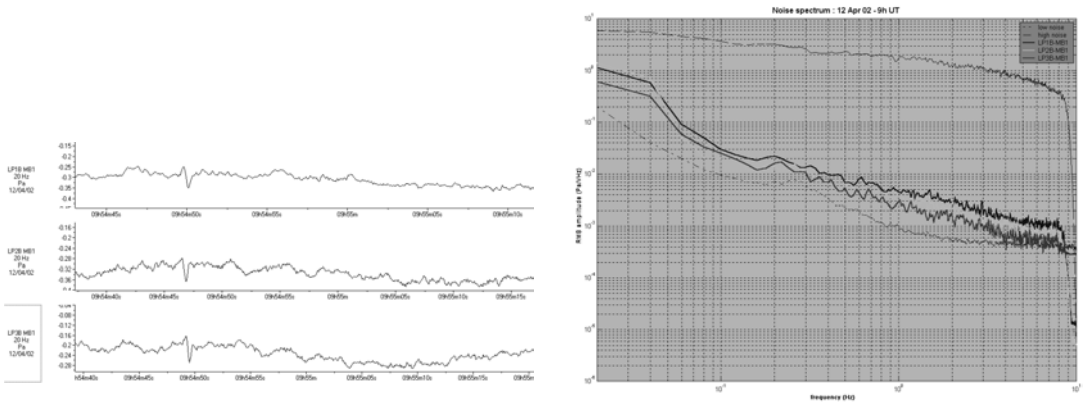

Figure 8: Signal recorded 12/04/02, 9:54 am, direction SE, speed 0.639 m/sec

INFRAMAP ENHANCEMENTS: ENVIRONMENTAL/PROPAGATION VARIABILITY AND LOCALIZATION ACCURACY OF INFRASONIC NETWORKS

David E. Norris and Robert G. Gibson

BBN Technologies

Sponsored by Defense Threat Reduction Agency

Contract No. DTRA01-00-C-0063

ABSTRACT

Enhancements to the propagation modeling capabilities of the InfraMAP analysis tool kit are reported in three areas. InfraMAP (Infrasound Modeling of Atmospheric Propagation) consists of three infrasound propagation models (3-D ray trace, normal mode, and parabolic equation), two atmospheric characterizations (HWM and MSISE), a global topography database, and user interfaces for model execution and data visualization. InfraMAP has been delivered to the Defense Threat Reduction Agency's (DTRA's) research and development test bed and is currently being utilized by nuclear-explosion-monitoring researchers and analysts.

First, improvements have been made to the environmental variability analysis capabilities. Wind and temperature variability covers a wide spectrum, in both space and time. The dominant source of variability affecting infrasonic propagation is believed to result from gravity waves. A gravity wave spectral model based upon scale-independent diffusive filtering theory has been integrated into InfraMAP. The model is used to predict the horizontal wind perturbations as a function of height. As height increases, the spectral model amplitude increases, and there is an overall shift in energy towards lower wave numbers. Fourier inversion using random phase is applied to generate realizations of wind perturbation profiles. A dominant horizontal length scale and Gaussian weighting functions are used to generate range-dependent perturbation fields.

Second, the enhanced environmental modeling capabilities are used to evaluate the resulting variability in propagation. Multiple wind perturbation realizations are generated, and a Monte Carlo simulation is executed where multiple rays are traced through the sum of mean and perturbed environmental fields. Two ray parameters (travel time, azimuthal deviation) are calculated for each perturbation. The sensitivity of ray tracing calculations to variability in wind profiles is then quantified by computing the mean and variance of the predicted distributions.

Finally, prediction of propagation variability induced by the environment is used to evaluate the performance of infrasonic networks. Source localization is first computed from the measured station data. Then, modeled variance in travel time and azimuthal deviation, along with the uncertainty introduced by measurement error, are used to calculate the confidence bounds of the localization. These bounds are expressed as an area of uncertainty (AOU) for which there is a 90% probability that the actual source location is contained. For locations based upon travel time and azimuth, the AOU takes the shape of an ellipse. Network performance modeling is applied to data from the April 2001 Pacific bolide and compared to the satellite source localization.

OBJECTIVE

InfraMAP is a software tool kit designed for researchers and analysts who are interested in modeling infrasound in the atmosphere. Model output includes ray tracing, wind (HWM) and temperature (MSIS-E) mean atmospheric profiles, and wind perturbation profiles based upon power-law spectra. InfraMAP has been delivered to DTRA's research and development test bed, and enhancements that improve the model characterizations are under development. The ultimate goal is to accurately predict the achievable performance of infrasonic networks under various scenarios and environmental conditions.

Model enhancements and studies are reported in three areas. A gravity-wave spectral model has been integrated into the wind perturbation module; a propagation variability study has been completed using range-independent wind perturbation profiles; and, a network performance analysis of the April 23, 2001, bolide has been completed using both station measurements and propagation modeling.

RESEARCH ACCOMPLISHED

Environmental variability model

The baseline environmental variability model in InfraMAP is based on a power-law wind perturbation spectrum, and it provides realizations of wind perturbation profiles. This spectrum is applicable for small-scale turbulence, even though atmospheric turbulence covers a wide spectrum of spatial scales (Figure 1). The dominant source of variability affecting infrasonic propagation is believed to result from gravity waves. Gravity waves result from oscillations of air parcels displaced by buoyancy and restored by gravity. The oscillations have time scales ranging from minutes to tens of hours. Vertical length scales of gravity waves are in the range of 0.1 to 10 km, and horizontal scales can span from 100 to 10,000 km.

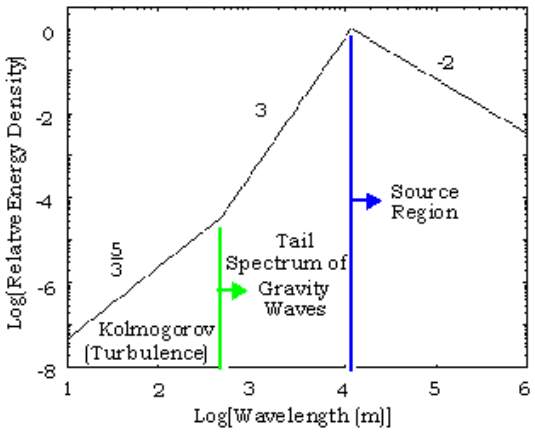

Figure 1. General form of horizontal wind spectrum versus vertical wavelength (from R. J. Sica, University of Western Ontario).

A significant body of research has been carried out to define the spectral character of gravity waves. The spectral model of Gardner (Gardner 1995, 1993) has been selected for integration into the environmental variability module. This model is based on scale-independent diffusive filtering theory. A source spectrum is defined near the ground. As the spectrum is propagated up in height, attenuation is modeled by introduction of diffusive damping. The key spectral properties are:

- an increase in energy with height
- a shift towards larger length scales with height
- an attenuation of smaller length scales with height

The Gardner Spectral model is evaluated at five discrete heights, as shown in Figure 2. These heights capture the dominant gravity wave variability from the troposphere up to the lower thermosphere. Below the troposphere, gravity waves are not fully developed. In the thermosphere, diffusion increases dramatically and gravity waves are damped out.

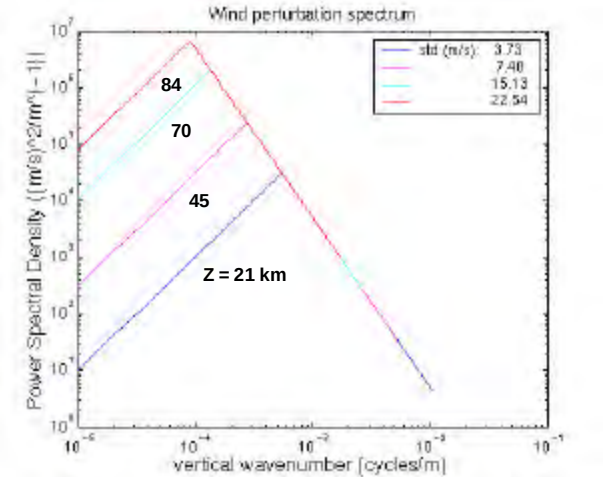

Figure 2. Gardner wind spectral model evaluated at five discrete heights.

Fourier inversion using random phase is applied to the spectra to generate realizations of wind perturbation profiles. A wind perturbation profile is generated for each of the five spectra. A composite profile is then computed by shading each profile spatially with a Gaussian filter and then summing them together, where Gaussian filter half-power points are set to the midpoint between each of the spectral heights. To model range-dependent variability, a dominant horizontal length scale is defined, and Gaussian weighting functions are used to combine the wind perturbation profiles. Figure 3 gives an example realization of a wind perturbation field generated from the gravity wave spectral model.

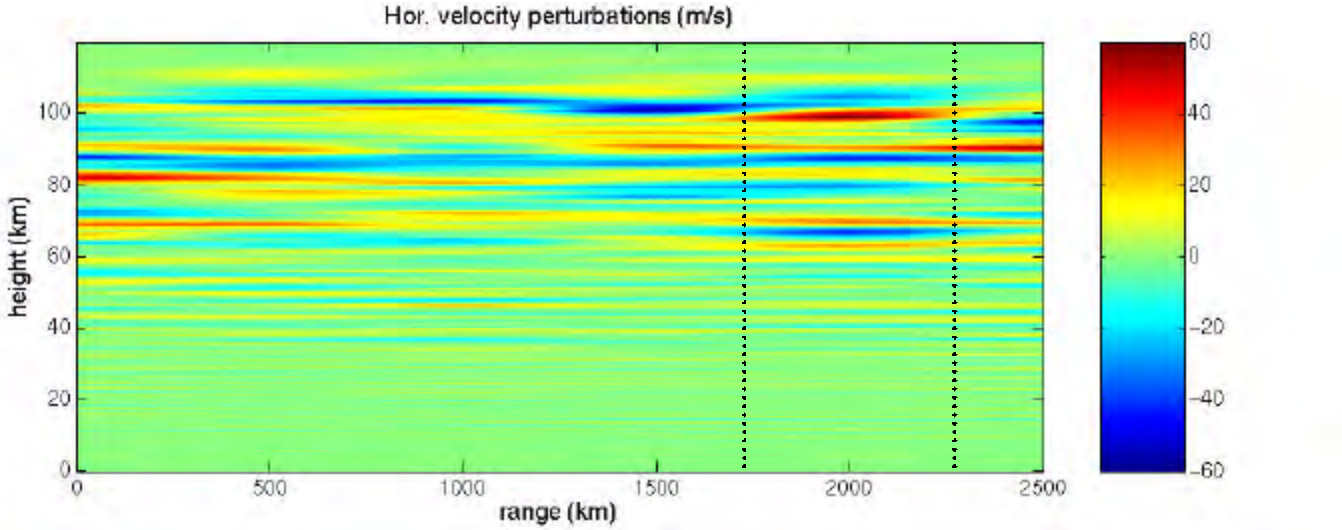

Figure 3. Range-dependent wind perturbations using horizontal correlation length of 500 km.

Propagation variability study

The goal of the propagation variability study is to quantify the bounds in travel time and azimuthal variability that can be expected. Different scenarios are evaluated over different diurnal and seasonal periods. The effects on both stratospheric and thermospheric rays are analyzed.

To perform the study, multiple wind perturbation realizations are generated, and a Monte Carlo simulation is executed where multiple rays are traced through the sum of mean and perturbed environmental fields. Two ray parameters (travel time, azimuthal deviation) are calculated for each perturbation. The sensitivity of ray tracing calculations to variability in wind profiles is then quantified by computing the mean and variance of the predicted distributions. Figure 4 gives an example of the predicted distribution of azimuth deviation of a thermospheric ray over a 500-km path. In this case, the deviation was under 0.2 degree.

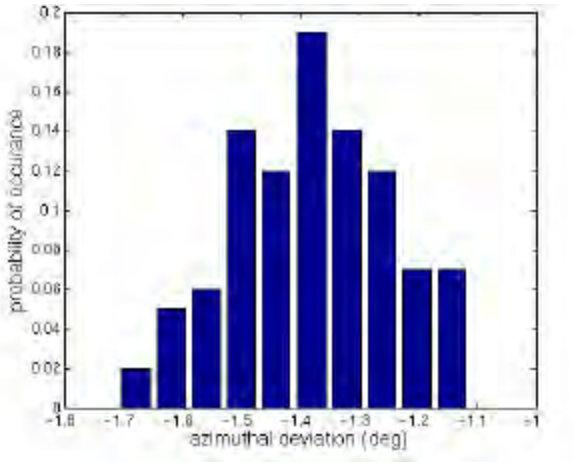

Figure 4. Example probability distribution of azimuthal deviation from Monte Carlo analysis of thermospheric ray along 500-km path.

Network performance study

A network performance model is integrated into InfraMAP that includes the effects of environmentally driven propagation variability. For a selected network of sensors, source localization is computed from measured travel times and azimuths. Predicted uncertainty in ray azimuthal deviation and travel time is added to user-defined station measurement error, and confidence bounds for the localization are computed. These bounds are expressed as an area of uncertainty (AOU) for which there is a 90% probability that the actual source location is contained. For locations based upon travel time and azimuth, the AOU takes the shape of an ellipse. Network performance modeling is applied to data from the April 2001 Pacific bolide and compared to the satellite source localization. Figure 5 illustrates a sample localization and associated AOU ellipse.

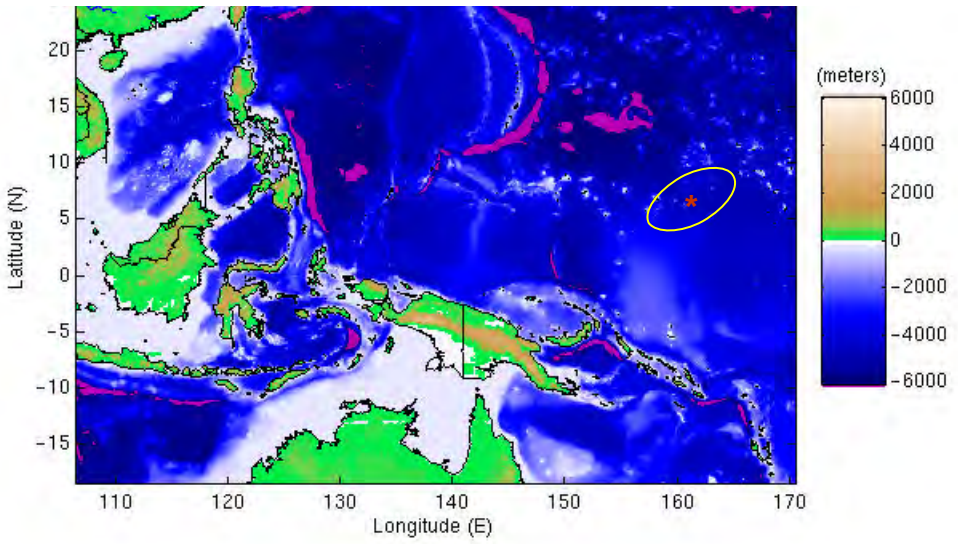

Figure 5. Sample network localization and AOU ellipse.

CONCLUSIONS AND RECOMMENDATIONS

Gravity waves are believed to be the dominant source of environmental variability that affects infrasonic propagation. A gravity wave spectral model has been integrated into InfraMAP based upon scale-independent diffusive filtering arguments. From the model, realizations of wind perturbation profiles are generated. The profiles are based upon five separate spectra in the vertical direction and one dominant Gaussian length scale in the horizontal direction.

Propagation variability is studied by propagating rays through the perturbed profiles, and Monte Carlo statistics are found for travel time and azimuthal deviation. These characterizations are applied to network performance, and AOU confidence bounds are calculated for source localizations.

Network performance studies need to be done over a variety of scenarios and environmental conditions. In areas of high station density, the localization AOU will be small, while in areas of sparse coverage they can become quite large. Defining these regions of best and worst localization accuracy is critical to evaluating the overall performance of an infrasound network.

REFERENCES

Gardner, C. (1995), Scale-Independent Diffusive Filtering Theory of Gravity Wave Spectra in the Atmosphere, The Upper Mesosphere and Lower Thermosphere: A Review of Experiment and Theory, Geophysical *Monograph* 87, AGU.

Gardner, C. (1993), Gravity Wave Models for the Horizontal Wave Number Spectra of Atmospheric Velocity and Density Fluctuations, *JGR*, 98, D1, 1035-1049.

ANALYSIS OF INFRASOUND SIGNALS FROM EKIBASTUZ MINING BLASTS AT KURCHATOV, KAZAKSTAN

Golam Sarker and Won-Young Kim

Lamont-Doherty Earth Observatory of Columbia University

Sponsored by Defense Threat Reduction Agency

Contract No. DTRA01-00-C-0077

ABSTRACT

Infrasound signals have been detected from large mining blasts in Kazakstan by the infrasound arrays at Kurchatov and Borovoye. For one month of data (March 1999) from the Kurchatov cross-array, we have recorded 163 events from the Ekibastuz mining region (Δ= 245 km, B-Az: 296°) in seismic channels, of which 63 (~43%) were detected in infrasound channels. For the same period of data, we have detected 122 events from the Kuzbass region (Δ= 740 km, B-Az: 58°) in seismic channels. Of these, 10 events have ground truth information. No corresponding infrasound detection is found. We also have detected four events in seismic channels at Kurchatov from a relatively less active mine in the Novotaubinka area (Δ= 197 km, B-Az: 123°). Infrasound signals from the Ekibastuz mining area at the Kurchatov array show two arrivals separated by about 60 s, though these arrivals can range between 40 and 90 s. The second arrival is observed in about 65% of the events (41 out of 63 infrasonically detected events). A simple ray tracing scheme through a suitable atmospheric model suggests that the first arrival that has a travel time of about 750 s propagates through the troposphere and is followed 60 s later by a stratospheric arrival. Best beams have been calculated for infrasound signals recorded at Kurchatov from the Ekibastuz and Novotaubinka regions. For Ekibastuz events, although the average best-beam azimuth from first arrivals varies within 3° to 7° from the seismically predicted azimuth, the phase velocity emerges slightly slower (about 280 m/s) than typical sound velocity of 330 m/s. The phase velocity for the second arrival, when present, is slightly higher, around 300 m/s.

For two months of data from Borovoye (December 1999 through January 2000), we have recorded 161 events from the Ekibastuz mining region (Δ= 381 km, B-Az: 113°) in seismic channels. The corresponding infrasound detection is very low (only 4). Infrasound detection is relatively high from nearby mines located NW of the array (Δ= 65 km, B-Az: 326°). From this period of data, we have recorded 36 events from the Kuzbass mining region (Δ= 1123 km, B-Az: 77°) in seismic channels. All of them have ground truth information. We were not able to detect positively any infrasound signals from the Kuzbass region at Borovoye. The infrasound signals that were recorded at Borovoye from the mines northwest and southeast of the array show one simple pulse with about 2- to 3-s duration. Best beams calculated from these infrasound signals show that predicted velocity is slightly slower than nominal sound speed, although predicted azimuth is similar to or slightly off from the seismically calculated azimuth. Best beam for signals from the Kuzbass region could not be resolved with confidence.

OBJECTIVE

The main objective of this project is to evaluate and characterize digital seismic and infrasound data from array sites in Kazakstan in order to improve event location and screening for nuclear explosion and Comprehensive Test-Ban-Treaty (CTBT) monitoring.

RESEARCH ACCOMPLISHED

Since spring of 1999, we have been acquiring infrasound signals from the Kurchatov and Borovoye arrays using available microphones. Several large mines in these areas routinely carry out large explosions that are detected seismically and with infrasound sensors. We have analyzed one month of data from the Kurchatov array and two months of data from the Borovoye array to better understand infrasound propagation in this region.

Station Deployment

We deployed infrasound arrays on the premises of Kurchatov and Borovoye Geophysical Observatories in Kazakstan (Figure 1). The Kurchatov Geophysical Observatory operates a 21-element short-period seismic borehole

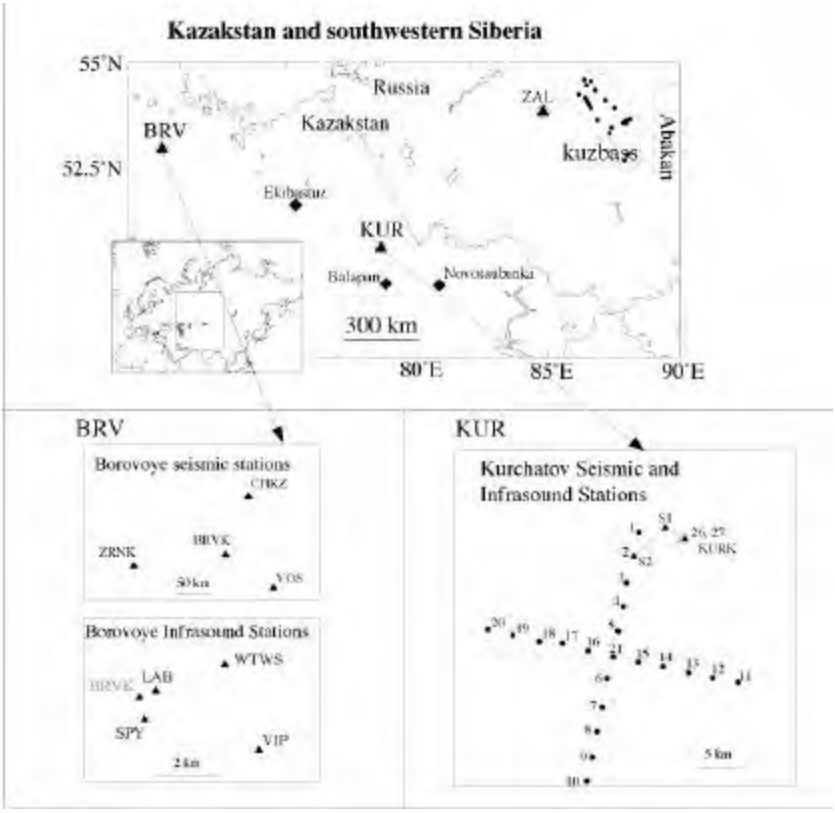

Figure 1. (top) map of Kazakstan and southwestern Siberia showing location of broadband seismic stations (solid triangle), active mining areas (diamond), Kuzbass and Abakan mining regions, and the Kurchatov (KUR) and Borovoye (BRV) Geophysical Observatories, where seismic and infrasound monitoring systems are deployed. (bottom) shows seismic and infrasound system configuration at both observatories (labelled). At KUR, 1 through 21 are short-period seismographic stations (spacing 2.25 km), KURK is a three-component broadband station, and S1, S2, 26, and 27 are infrasound stations.

array (cross-array) and a three-component broadband seismic station. A 4-component large aperture infrasound array (S1, S2, 26, and 27 in Figure 1) was constructed in the spring of 1999 at the Kurchatov Geophysical Observatory.

Each sensor is connected to six 70-m-long underground pipes extending radially from a central chamber that act to reduce wind noise. Sensor spacing varies between 2 and 4 km. Two types of capacitor microphones have been utilized with the pipe arrays configuration; Globe microphones at sites S1 and S2, and Soviet-built K301's at sites 26 and 27. The Globe microphone has a flat amplitude response between 0.1 and 300 Hz (ReVelle *et al*., 1997).

At the Borovoye Geophysical Observatory, we deployed a 4-element infrasound array (Figure 1). The spacing between infrasound stations is 2-3 km, and they are located within 2 km of central seismic station BRVK. The broadband seismic stations are recording signals in a continuous mode at 40 samples per second (sps), and have a flat response to velocity between 0.08 and 16 Hz. Globe microphones have been utilized to record infrasound signals. The microphones use a pipe array configuration to reduce local wind noise, similar to the Kurchatov infrasound system. The signals are recorded at 20 sps in a continuous mode. Infrasound signals in the frequency band of 0.8 - 3 Hz have been used for detection and array processing.

Seismic and Infrasound Observations at Kurchatov

Several large mines in Ekibastuz and surrounding areas generate explosions that are routinely detected seismically, and in many cases, are also detected with infrasound sensors. The Ekibastuz mine, 250 km northwest of the Kurchatov cross-array, regularly produces between four and six seismic detection per days. The location of these events are set to a central location of the Ekibastuz mine (51.61°N and 75.36°E) as determined by satellite photographs (Thurber et al., 1989), and their origin time is calculated from the IASPEI91 model.

For one month of data (March 1999) from the Kurchatov cross-array, we have detected 163 events in seismic channels from the Ekibastuz mine, of which 63 (~39%) were detected in infrasound channels. The infrasound signals of these events are visually examined for accurate picks and are bandpass filtered at 0.8-3 Hz for enhancing signal-to-noise ratio. For noisy data, signals are often Hilbert transformed to make them stand out from surrounding noise. The infrasound detection rate from this large aperture array is about four times larger than that detected from the small aperture array operated at Kurchatov between 1995-1997 (Hagerty *et al*., 2002).

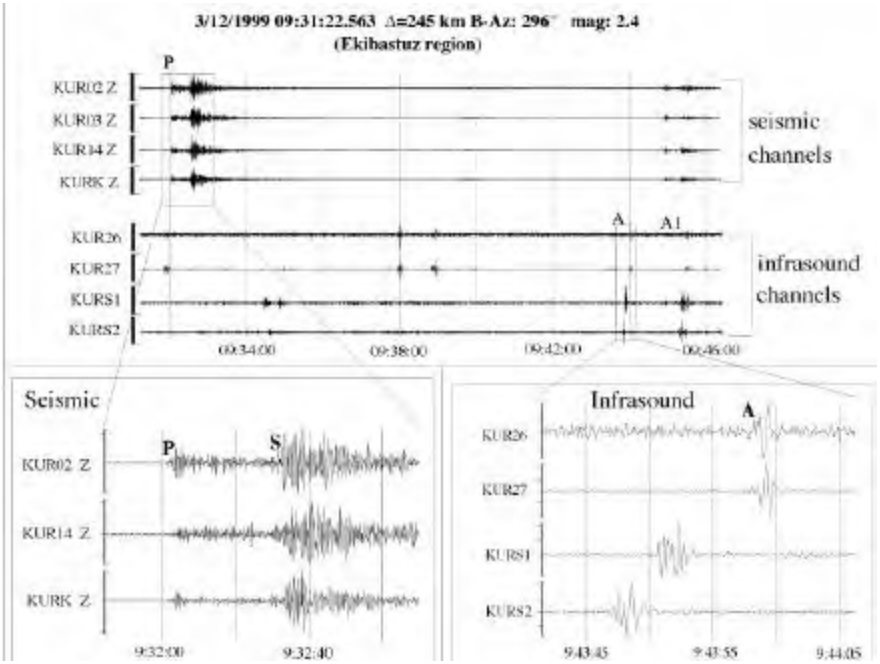

Figure 2. (top) showing a 15-min. time window of selected seismic and infrasound arrivals at the Kurchatov array. The event is located about 250 km NW of the network at the Ekibastuz mining area. Note two infrasound arrivals for this event (A and A1); the first arrival has a travel time of 756 s, and the second a travel time of 843 s. Simple ray tracing indicates this second arrival as wavetrains reflected back from the Stratospheric layer. (bottom) The figure displays close-up views of seismic and infrasound channels (labelled).

The infrasound wavetrain generated by Ekibastuz explosions exhibits two arrivals separated by about 60 s, though the separation time of arrivals can range between 40 and 90 s (Figure 2). The first arrivals show multiple pulses of 2- to 3-s duration, while the second arrivals show two pulses separated by 10 s. The travel time of the first arrival is about 750 s, corresponding to an apparent group velocity of 330 m/s. The second arrival is observed in about 65% of the events (41 out of 63 infrasonically detected events). The time difference between first and second arrivals exhibits great variation for Ekibastuz events, indicating that infrasound signals traverse through varying atmospheric conditions such as transient propagation ducts (Georges and Beasley, 1977).

For the same month of data, we also have detected four events in seismic channels from a relatively less active mine in the Novotaubinka region, of which, one was detected in infrasound channels (Figure 3). The region is 200 km

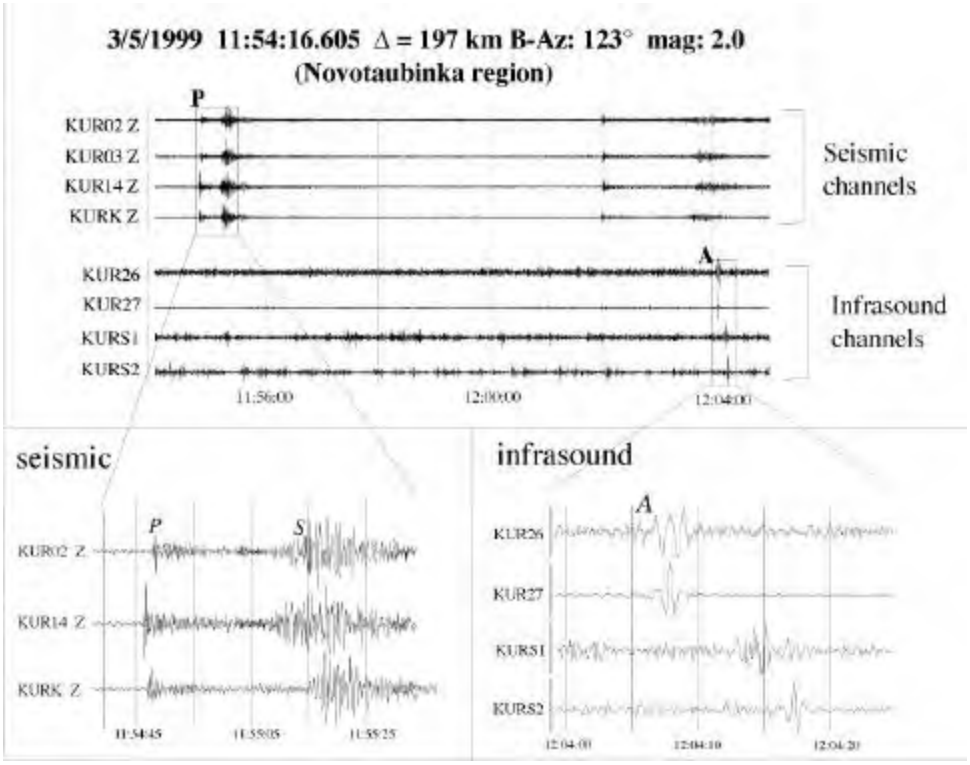

Figure 3. (top) Showing selected seismic and infrasound waveforms recorded at Kurchatov from an event at the Novotaubinka mining region (about 195 km SE of the network). P-wave travel time at KUR02 is 31.7 s, and infrasound (A) travel time at KUR26 is 629 s. This travel time corresponds to 330 m/s acoustic speed. No second infrasound arrival is detected at this distance and direction of propagation. (bottom) Close-up displays of selected seismic and infrasound channels (labelled) are shown.

southeast of the Kurchatov cross-array. The signals from the Novotaubinka region exhibit one single arrival at an apparent phase velocity of 330 m/s. For the same period of data, we have detected 122 events from the Kuzbass region in seismic channels at Kurchatov. The Altay-Sayan Experimental and Methodical Seismological Expedition (ASEMSE) collected ground truth information for 10 events from the Kuzbass and Abakan regions for this time period (Table 1). Signals from all those events are recorded in seismic channels at Kurchatov and the International Monitoring System (IMS) broadband station at Yeltsovka (ELT) (Figure 4). No corresponding infrasound detection is found. The Kuzbass mining area is about 700 km northeast of the Kurchatov cross-array, and about 120 km from the ELT station.

Best beams of infrasound arrivals calculated by slant stacking the traces for a given slowness grid show that the predicted azimuth is slightly off from the seismologically calculated azimuth (Figure 5). For a set of selected events

Table 1: Mining blasts in the Kuzbass and Abakan Regions with Ground Truth Data

Date yr-mo-dd	Time hh:mm:ss	Lat (°N)	Lon (°E)	K	mb	Yield (ton)	name
99-03-03	08:21:38.9	53.85	88.10	9.2	3.59		Oldgerasky
99-03-05	10:45:22.60	53.60	91.37	9.3	3.64		Abakan-2
99-03-06	06:38:39.10	54.32	86.78	8.8	3.41	239.4	Karakansky
99-03-07	10:57:14.80	54.45	86.88	9.0	3.50		Kolmogovsky-2
99-03-10	09:48:52.00	53.71	87.86	9.4	3.68		Krasnogorsky
99-03-12	08:59:46.90	54.53	86.60	8.6	3.32		Kolmogorovsky-1
99-03-19	10:51:12.30	54.08	87.39	8.7	3.36	194.1	Badaevsky
99-03-24	09:11:57.70	53.71	87.83	9.3	3.64	209.4	Sibirginsky
99-03-30	06:55:31.80	53.85	88.15	8.9	3.45		Oldgerasky
99-03-31	09:03:11.60	54.54	86.62	8.9	3.45		Kolmogorovsky

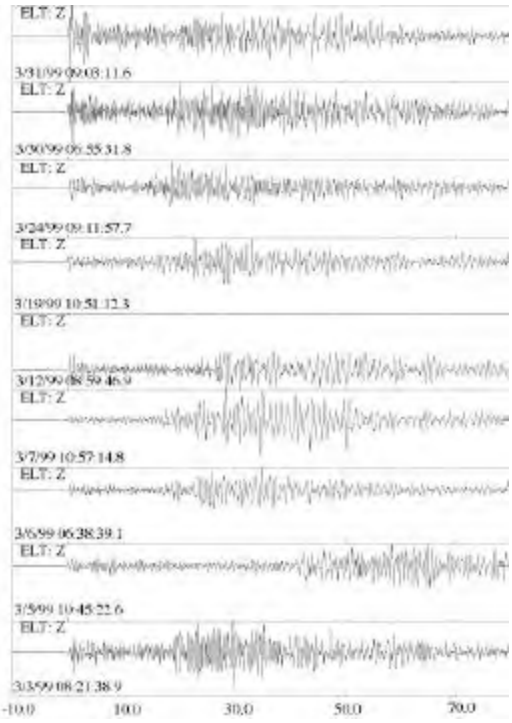

Figure 4. Waveforms of mining events listed in Table 1 recorded at ELT. Records are bandpass filtered at 1-5 Hz. Only vertical component data are shown. P-waves are aligned at 0.0. Origin times are shown in the box.

from one month of data from the Ekibastuz area, maximum power occurs when the traces for first infrasound arrivals are aligned with an average horizontal phase slowness of 3.76± 0.41 s/km (equivalent velocity of 266 m/s) and a back-azimuth of 303°± 5.5 (Figure 6). Although the average best-beam azimuth varies within 3° to 7° from the seismically predicted azimuth, the phase velocity emerges slightly slower than the nominal sound velocity of 330 m/s.

To ascertain whether the size of the mining blasts helps in detecting infrasound signals, we calculated the magnitude of the Ekibastuz events from seismic channels using a *Lg*-based regional magnitude formula (Nuttli, 1973). For Ekibastuz events, the magnitudes of all mining blasts detected range between 1.3 and 2.8, with a mean value of 2.0. The distribution resembles a Gaussian with a standard deviation of 0.30. The magnitude distribution of events that are only detected by infrasound channels also exhibits similar variations (mean 1.9 and standard deviation 0.26),

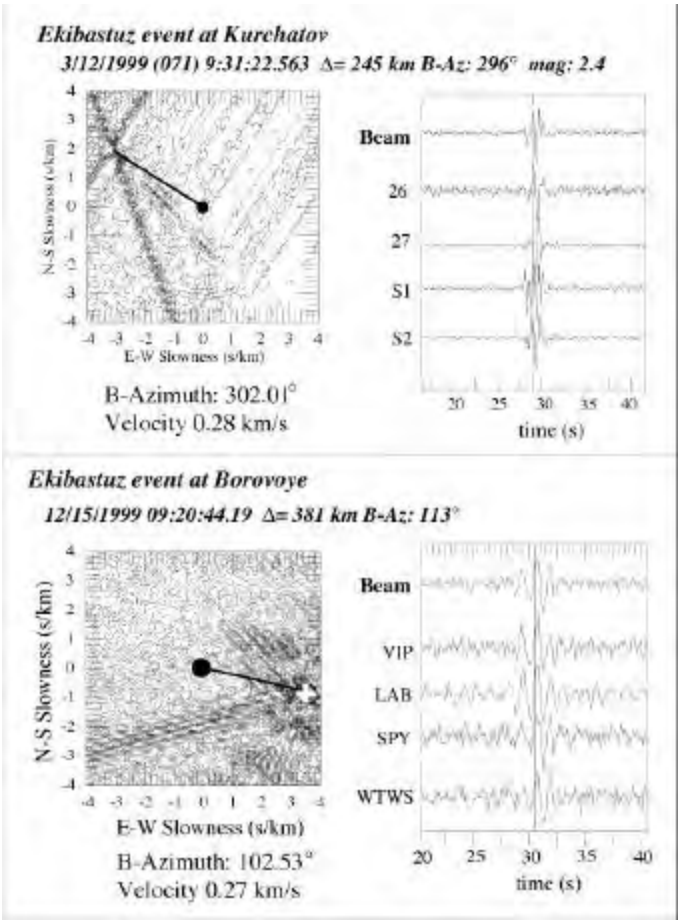

Figure 5. (top) Best beam (right) and contour plot of normalized maximum beam power (left) for an Ekibastuz event recorded at Kurchatov. The waveforms are that of Figure 2. Predicted azimuthal direction is about 7° off of seismologically calculated azimuth. (bottom) Same plot for another event from Ekibastuz recorded at Borovoye. The waveforms are that of Figure 6. In this case, the predicted azimuth is off by 5° from the seismological one. Solid circle is the location of the array, + is the predicted source, and thick solid line is the azimuthal direction. Times are relative to the beginning of the processed window length.

indicating that the magnitudes of seismic signals do not play a significant role in infrasound detection. Should magnitude contribute to infrasound detection, we would have seen a positively biased distribution of magnitude where the higher ends of distribution would only be coincident, not the lower ends.

Seismic and Infrasound Observations at Borovoye

For two months of data from the Borovoye seismic and infrasound array (December 1999 - January 2000), we have detected 161 coal mine events from the Ekibastuz area in seismic channels. The corresponding infrasound detection

is low -- only four. The Ekibastuz mining region is about 300 km southeast of the array. The infrasound wavetrains from Ekibastuz are simple, comprising a wave packet of 3-5 s long (Figure 7). The infrasound travel time is about 1150 s, which corresponds to an apparent group velocity of 300 m/s. For recordings at Borovoye, no second arrivals are seen in the infrasound channels for any events from Ekibastuz.

For the same months of data, we have positively identified six events from the Kokchetav mining region, located about 60 km northwest of the Borovoye array. The infrasound travel time is about 10.5 s, giving an apparent group

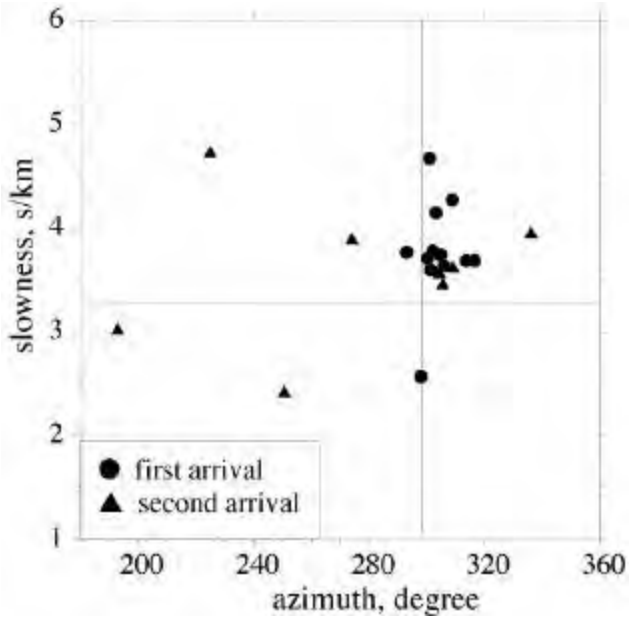

Figure 6. Plot showing predicted azimuth and slowness values from best beam analyses of infrasound arrivals from the Ekibastuz mining region. Circles depict measurements from first infrasound arrivals, and triangles from second arrivals, when present. The plot is made from 17 quality records where signal-to-noise ratio is greater than 3.The mean slowness of first arrivals is 3.76± 0.41 s/km (equivalent velocity 266 m/s) and azimuthal value is 303.2°± 5.5. The mean slowness and azimuth values for second arrivals are not determined because of large outliers in the data.

velocity of 310 m/s. Records from these events are seen in both seismic and infrasound channels. The infrasound waveforms comprise multiple pulses with about 2- to 3-s duration (Figure 8). ASEME collected the ground truth information for 49 events from the Kuzbass and Abakan regions for this time period. We have detected 36 events in seismic channels out of these 49 events. The Kuzbass mining region is about 1150 km east of the network. No corresponding infrasound signals have been positively identified.

Ground Truth Data From Large Mining Blasts in the Kuzbass and Abakan Regions

The Kuzbass and Abakan regions in southwestern Siberia conduct large mining operations. These mining regions are probably the largest that routinely conduct mining operations in Eurasia. The average size of the blasts is over 3 on the seismic magnitude scale. We obtained ground truth data for several mining blasts in the Kuzbass and Abakan regions for 1999-2000. ASEMSE located 367 blasts using data from regional seismic stations (Figure 9). The events located by ASEMSE have location errors ranging from about 5-10 km.

CONCLUSIONS AND RECOMMENDATIONS

Infrasound and seismic data recorded at the Kurchatov and Borovoye arrays from the Ekibastuz, Nobotuabinka, Kokchetav, Kuzbass, and Abakan mining regions have been analyzed. At Kurchatov, this data period covers March

of 1999, and at Borovoye, it covers December, 1999 - January, 2000. Results indicate high infrasound detection capability for large aperture arrays. The Ekibastuz mine produces 4-6 seismic detections per day, while there are 2-3 detections from the Kuzbass and Abakan mining region. For Ekibastuz events, about 65% of events that are detected by seismic channels are seen by infrasound channels at Kurchatov, while less than 1% of seismically

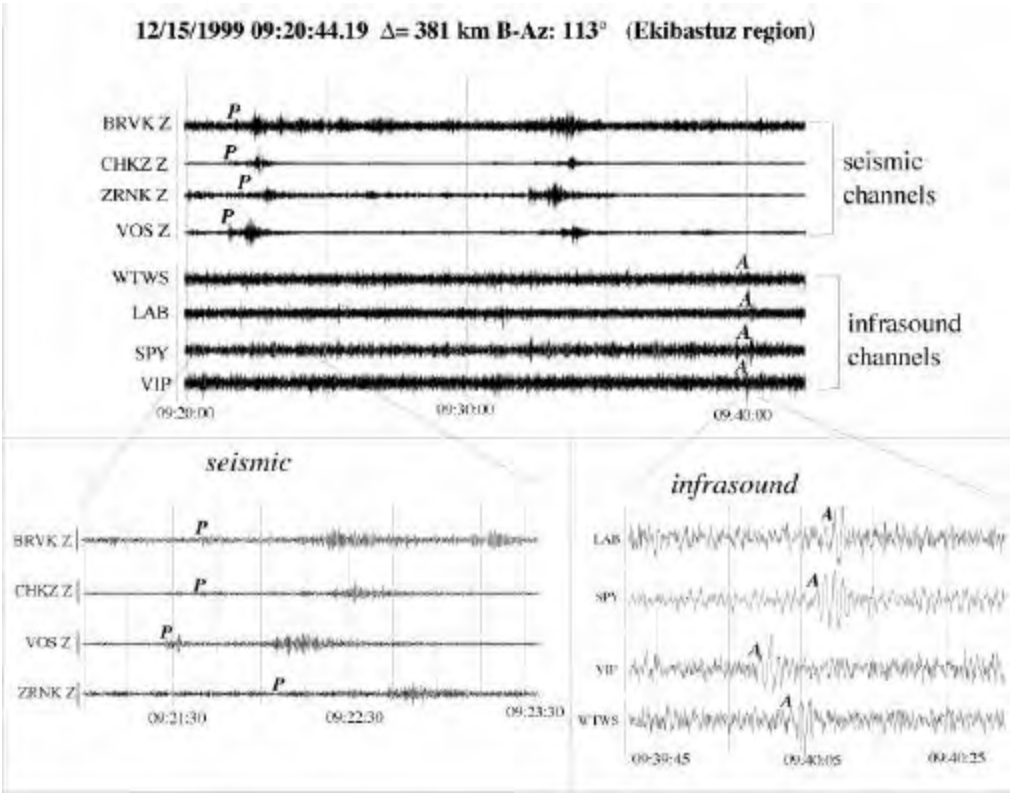

Figure 7. (top) showing selected seismic and infrasound recordings for an event from the Ekibastuz mining area recorded at Borovoye. The P-wave travel time at BRVK is 54.6 s, and the corresponding infrasound (A) travel time at LAB is 1163.8 s. This travel time corresponds to 300 m/s apparent acoustic speed. Bottom figure displays close-up views of selected seismic and infrasound arrivals (labelled).

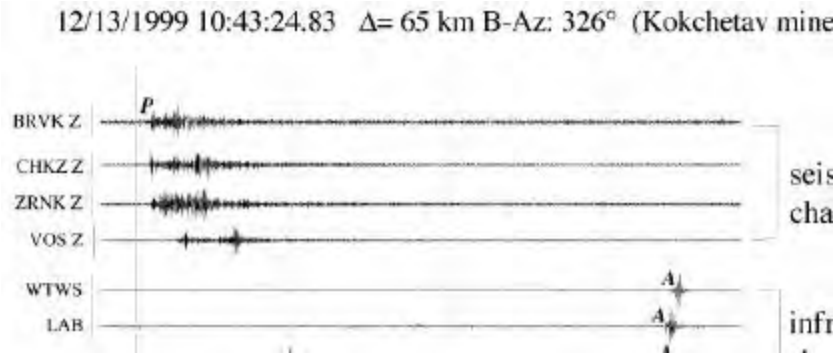

Figure 8. Plot showing selected seismic and infrasound waveforms recorded at Borovoye for an event from the Kokchetav mining region (65 km NW of the array). The P-wave travel time at BRVK is 10.7 s, and the corresponding infrasound (A) travel time at LAB is 208 s. This travel time gives an apparent acoustic velocity of 310 m/s.

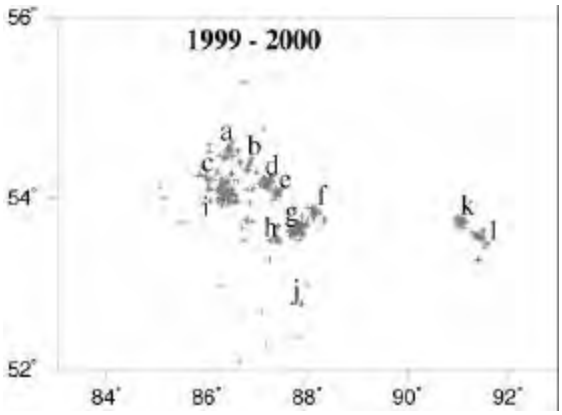

Figure 9. Mining events from the Kuzbass and Abakan regions during 1999-2000. Events were located by the ASEMSE group. Large mines are indicated by clusters of events. a: Kolmogorovsky-1, b: Kolmogorovsky-2, c: Kiselevsk, d: Taldinisky, e: Badaevsky, f: Oldgerasky, g: Mezhdurechensk, h: Kaltansky, i: Listvyansky, j: Tashtagol, k: Abakan-1, l: Abakan-2.

detected events from Ekibastuz are associated with infrasound channels at Borovoye. This may be related to wind direction and directivity of blasts. A simple ray tracing scheme using an appropriate atmospheric model for this region indicates that the first arrival propagates through the troposphere and is followed 60 s later by a stratospheric arrival. Such phenomenon of wave propagation is not seen in any channels that are located against the zonal wind direction. A second arrival appears in the infrasound sensor about 60s after the first arrival for Ekibastuz events that are recorded at Kurchatov. The second arrival, when present, also shows multiples pulses in the recordings, indicating strong positive sound speed gradients in the troposphere and, especially, in the upper stratosphere. Array analyses for data from the Ekibastuz, Novotaubinka, and Kokchetav regions show that predicted azimuthal direction is about 3°-7° off from the seismologically calculated azimuth.

REFERENCES

Donn, W.L. and E. Posmentier (1968), Infrasonic waves from natural and artificial sources. In *Acoustic-gravity Waves in the Atmosphere* (ed. T.M. Georges) (Boulder, CO.) 195-208.

Georges, T.M. and W.H. Beasley (1977), Infrasound refraction by upper-atmospheric winds, *J. Acoust. Soc. Am.*, **61**, 28-34.

Hagerty, M.T., W-Y Kim, P. Martysevich (2002) Infrasound Detection of Large Mining Blasts in Kazakstan, *Pure and Applied Geophysics*, **159**.

Kim, W-Y. and G.M. Sarker (2001), Infrasound Detection of Large Mining Blasts in Kazakstan, *Proceedings of the 23rd Seismic Research Review: Worldwide Monitoring of Nuclear Explosions*, October 2-5, 140-149.

Nuttli, O. (1973), Seismic wave attenuation and magnitude relations for eastern North America, *J. Geophys. Res.*, **78**, 876-885

ReVelle, D.O., R.W. Whitaker, and W.T. Armstrong (1997), Infrasonic observations of Bolides on October 4, 1996, Los Alamos National Laboratory Report: LA-UR-972481, 1-12.

Thurber, C., H. Given, and J. Berger (1989) Regional seismic event location with a sparse network: application to Eastern Kazakstan, USSR, *J. Geophys. Res*., **94**, 17767 - 17780.

DETECTION AND LOCATION CAPABILITIES OF MULTIPLE INFRASOUND ARRAYS

Robert H Shumway

University of California, Davis

Sponsored by Defense Threat Reduction Agency

Contract No. DTRA01-00-C-0082

ABSTRACT

We have developed an integrated approach to locating an infrasound source that fuses local-array wave-number parameters and uncertainties into an overall location procedure. For local estimation of the velocity and azimuth, a small-array theory, based on maximum likelihood, has been given in earlier work that characterizes the large-sample uncertainty of the estimates and evaluates the theoretical missed-signal and false alarm probabilities. We have verified the theoretical uncertainties by computing empirical estimates using the frequency domain bootstrap on a gas-pipe explosion, a Titan IV B missile launch, and a Hawaii meteorite. Detection probabilities and wave-number uncertainties are then integrated into a Bayesian nonlinear regression procedure for evaluating the location capabilities of the particular global infrasound array that is proposed for the International Monitoring System (IMS).

We show contour maps for the average expected areas of the 90% confidence ellipses produced by the overall fusion procedure. The results indicate that for a single-array false alarm probability of 10^{-4}, the standard proposed IMS 4-element array will detect over 90% of the signals at signal-to-noise ratios as low as .6, with sufficient bandwidth. Location accuracies will require higher signal-to-noise ratios on the order of 2-4 and high single-array detection probabilities (>.90) to guarantee reasonable coverage (1000 km^2) for the 90% posterior probability ellipses. Eastern Hemisphere and Western Hemisphere 90% contour plots show almost complete coverage by expected uncertainty areas of 1000 km^2 or less.

OBJECTIVES

The objectives of this project have been to (1) develop the detection and estimation capabilities of small infrasound arrays and (2) to integrate these single-array directional estimation statistics into a procedure for assessing the predicted global performance of the infrasound component of the proposed International Monitoring System (IMS).

In support of (1), our sub-objectives were to develop local-array performance capabilities for estimating velocities and azimuths of propagation and to characterize single-array signal detection probabilities at low false alarm rates. In support of (2), our sub-objectives were to develop fusion posterior-probability ellipses for location and to incorporate single-array detection probabilities into a procedure for developing a global coverage map giving expected areas of 90% uncertainty regions.

RESEARCH ACCOMPLISHED

We have investigated a number of proposed procedures based on plane wave models for detecting infrasound signals at small arrays and for estimating velocities and azimuths, along with their predicted uncertainties. Velocities and azimuths are functionally related to the coordinates in the wave-number plot, say $\boldsymbol{\theta}=(\theta_1 ,\theta_2)'$ and their predicted uncertainties. The estimated wave numbers and their covariance matrices for the detecting sub-arrays are fused into an overall location and its posterior probability ellipse. A large scale simulation using predicted detection probabilities and locations then is used to develop contour plots of the areas of the 90% error ellipses for the Eastern and Western Hemispheres.

Detection of Infrasound Signals

We have investigated three wave-number detectors from the literature, the Capon (1969) *high-resolution estimator*, the F-detector suggested by Shumway (1971), and the MUSIC estimator suggested by Schmidt (see Stoica, 1989).

The high-resolution estimator of Capon is the inverse of a Hermitian form in the probe vector, $\mathbf{x}(\boldsymbol{\theta})$, involving the inverse of the covariance matrix (see Shumway, 2001). Difficulties are in estimating the covariance matrix and in using the statistical distribution, which depends on the unknown theoretical covariance matrix. The multiple signal characteristic (MUSIC) estimator keeps the same form but replaces the inverse spectral matrix by the spectral matrix of the noise, approximated by an inner product of the residual eigen vectors (see Shumway, 2001). The difficulties with this detector relate to the intractability of its distribution under the *noise-alone* and the *signal-plus-noise* hypotheses.

The usual F-detector is defined as the ratio of the scaled beam power to the scaled error power, $F(\theta)$, where θ is the two-dimensional wave-number vector corresponding to a given velocity and azimuth (Shumway, 2001). In contrast to the high-resolution and MUSIC detectors, the performance is determined by observing that $F(\theta)$ is distributed as $(1+rN)F_{2L,2L(N-1)}$, i.e., as an F-statistic with 2L and 2L(N-1) degrees of freedom, where L=BT is half the bandwidth and N is the number of elements in the array. The parameter r is the signal to noise ratio on a single channel. Since the distribution under the noise-alone and signal-plus –noise hypotheses both involve the F, with r=0 under the noise-alone hypothesis, the preceding theory allows us to predict the detection probability as a function of any given false alarm probability. The result also allows unbiased estimation of the signal-to-noise ratio r by equating the value of the F-statistic to the expectation of $(1+rN)F_{2L,2L(N-1)}$.

Figure 1 shows the predicted detection probability for two hypothetical combinations of bandwidth (2L/n) and sub-array size, where L is the number of frequencies smoothed to obtain the test statistic and n is the total number of time points. Note that even with the smaller size array characteristic of those used in this paper, the signal detection is very high for relatively low signal-to-noise ratios and a false alarm probability of 10^{-4}. Extremely low false alarm probabilities are of interest in order to maintain an overall false alarm rate that is sufficiently low when there are many wave-numbers to test. For example, if 100 wave numbers are potentially of interest in this case, Bonferonni's inequality guarantees that the overall false alarm probability will be less than .01.

For illustration purposes, we show a contour plot in Figure 2 exhibiting the behavior of the three statistics given above and the beam power. Note that all statistics give comparable results for the Hawaiian bolide observed on April 23, 2001 from the Pinion Flat Array (shown in Table 1). This array was chosen because, with N=6 elements, it

represents a likely result from processing an event using an array that is close to the IMS configuration We simply note here that all processors detect the event and that F=172 is highly significant. It should also be noted that the signal to noise ratio was extremely high here and the plots are unusually unambiguous. The apparently superior resolution of the Capon and MUSIC estimators does not lead to lower variances or to better resolution of multiple signals (Shumway, 2001) Comparable plots from the Los Alamos, Lac du Bonnet and Mina , Nevada showed multiple maxima that sometimes corresponded to velocities in the neighborhood of .3 km/sec and sometimes at unreasonable velocities. We note also that these arrays, for various reasons, only recorded on N=3 channels. To resolve some of these ambiguities, a general nonlinear optimization was employed that started in the neighborhood of a velocity and azimuth corresponding to the Hawaii location.

Estimation of Velocity and Azimuth Parameters

Figure 2 suggests that we simply read the wave-number coordinates corresponding to the maximizing value of the appropriate statistic and specify the velocity and azimuth corresponding to these wave-numbers as our estimated values. For the F-detector, the maximizers are equivalent to the maximum likelihood estimators, as was shown in Shumway *et al* (1998). Using the Cramer-Rao lower bound, they obtained variance-covariance matrices for the estimated wave-number parameters in Figure 2 and for the derived velocities and azimuths.

It was recognized early in the investigation that analytical computations for the variance-covariance matrices of the Capon and MUSIC estimators would be difficult and a version of the frequency domain bootstrap (see Shumway and Stoffer, 200, p244) was employed for these cases. This involves drawing a random sample from the frequencies determining the maximum likelihood estimator repeatedly and computing the mean and variance over a large number of bootstrap samples. This was not only done for the Capon and MUSIC estimators but was used to check the large-sample covariance matrices computed for the maximum likelihood estimators.

Table 1. Estimated azimuths and uncertainties (bootstrap std. dev.) for sample events. LANL denotes value given by Los Alamos National Laboratories

Event	F	S/N	Capon	Music	LANL
Gas Pipe Explosion	256(1.3)	3.15	258(1.8)	257(1.3)	
Titan IV Missile	267(1.0)	.75	263(.4)	263(.4)	
4/23 Hawaiian Bolide					
Los Alamos	263(.3)	1.91	263(.4)	263(.4)	259
Lac du Bonnet	240(.1)	2.86	240(.2)	240(.1)	244
Pinion Flat	256(.8)	28.7	256(.8)	256(.8)	247
Hawaii	61(.6)	.83	59(1)	61(.6)	61
Mina, NV	237(.9)	3.79	238(1.3)	237(.9)	236
St. George, UT	278(2.3)	23.1	269(2.4)	276(2.3)	252

Preliminary results are shown in Table 1 for a 1998 gas pipe explosion and a Titan IV missile launch, both were recorded on four elements at the Los Alamos array. Additionally, we show results from a suite of arrays that recorded the April 23, 2001 Hawaii bolide. All events reside in the CMR R&D Test Bed Infrasound Waveform Library. As mentioned earlier, in order to handle severe aliasing that resulted in multiple maxima for the Los Alamos, Lac du Bonnet, and Mina arrays, non-linear optimization was used, starting in the vicinity of the assumed location. Because the asymptotic likelihood theory will not apply with multiple maxima, we used the frequency domain bootstrap to estimate the variances and covariances. The results for the bolide show estimated azimuths that are comparable with those obtained by Los Alamos National Laboratories with the exception of St. George Utah, where the angle should have been in the neighborhood of 246 degrees, LANL was close but we were off by 17-25 degrees

For the case where more than one array records a single event such as given by Table 1, one would be interested in the estimated location made by combining or fusing the results of the single-array wave-numbers and their covariance matrices into and overall location. The location theory is summarized in the next subsection.

Location Using Fused Array Wave-Number Parameters

Location results, given previously in Shumway (2000), require estimated wave-number coordinates $\boldsymbol{\theta}_k(\mathbf{x})$ for k=1,2,…,n sub-arrays and their respective estimated covariance matrices, $\sum_k$, computed from one of the procedures in the previous section. The estimated wave-number coordinates are assumed to be a function of the location $\mathbf{x}=(x_1, x_2)'$. Linearizing $\boldsymbol{\theta}_k(\mathbf{x})$ about an initial location $\mathbf{x}_0$, and performing the exact Bayesian analysis with a uniform diffuse prior on $\mathbf{x}$ and an inverted chi-square distribution for the location variance σ^2 in the location covariance matrix $\sigma^2 \sum$, we obtain the posterior probability distribution of the location vector $\mathbf{x}$ as a bivariate t-distribution. Then, using the fact that the posterior probability distribution of the quadratic form in $\mathbf{x}$ will have an F-distribution with 2 and 2(n-1)+m degrees of freedom, we obtain a posterior probability ellipse with a given posterior coverage area. Note that m degrees of freedom are associated with the chi-squared random variable defining the uncertainty in the scaling variance. The solution for independent errors ($\sum=\sigma^2 I$) was given by Jordan and Sverdrup (1981).

Global Array Performance of Proposed IMS Array

In order to develop a reasonable measure of global performance we considered incorporating the infrasound recording arrays proposed for the infrasound part of the IMS. For these plots, we used the asymptotic covariance matrix implied from maximum likelihood, as given by Shumway *et al* (1999) and in a previous SRS report (Shumway, 2000). For this simulation, we need the assumed signal-to-noise ratio (r=4) at a single station, the smoothing constant (L=51 frequencies), and the number of channels in a sub-array, assumed to be N=7, composed of 1km outer triangles with 1km sides and an inner inverted triangle with 2km sides. For location capability, we look at various simulated random configurations of detecting stations. For this initial simulation, we were lacking precise information on detection probabilities for single arrays although from Figure 1, we can infer that they will generally be high, with malfunctions excepted. Overall, we might optimistically expect an average of 9 out of 10 stations to detect and this was assumed for the simulation. We summarize the simulation procedure as:

1. Fix a hypothetical event location
2. Set input parameters as N=7 elements, signal to noise ratio r=4, and a bandwidth of .1 Hz.
3. Simulate a configuration of detecting stations (3<n<28, 3<n<32) for Western and Eastern Hemispheres respectively and P=.9, the probability for single sub-array detection. Assign the chi-squared distribution for the scaling variance as chi-squared with m=10 and expectation 1.
4. Compute the Bayesian posterior probability ellipse and area.
5. Repeat 3.and 4. 500 times, averaging the areas obtained.
6. Record average on grid and increment the hypothetical event location in 1. by 5 degrees.
7. Contour the results for the 90% posterior probability areas separately for the Eastern and Western Hemispheres.

Figure 3 shows the resulting contours in thousands of km^2 separately for the Western and Eastern Hemispheres. We note that doing the computation this way leaves out the possible detections between hemispheres and will distort the performance at the edges of both plots. We note that the 1000 km^2contours include the majority of regions of interest (-80 degrees to 50 degrees for the Western Hemisphere and –80 degrees to 80 degrees for the Eastern Hemisphere). One could obtain a better index of performance for the western Pacific by folding in some of the Eastern Hemisphere sub-arrays and re-doing the computation. We tried relaxing the signal-to-noise ratio to r=2 or decreasing the detection probabilities to P=.5. Either strategy increases the 1000 km^2 to 3000 km^2.

CONCLUSIONS AND RECOMMENDATIONS

Theoretical computations have shown that the wave-number F-detector at a single array can be expected to perform very well for low signal-to-noise ratios and false alarm probabilities as low as 10^{-4}. We have not been able to collect enough historical detections from IMS stations to know that the empirical false alarm and signal detection probabilities will be equally impressive. Historical precedents set by seismic detections would imply that the empirical false alarm rates will be higher than the theoretical ones, implying that thresholds will need to be set high

to avoid significant numbers of false alarms. Every attempt should be made to develop empirical rates based on real events.

For the fused location estimators, theory suggests that we need higher signal-to-noise levels for the purposes of locating accurately with the seven element sub-arrays. The theoretical covariances for the conditions that guaranteed the good worldwide coverage for the 90% 1000 km^2 area contours were on the order of 10^{-4} km^2 whereas the bootstrap simulations using the Hawaiian bolide suggested that the covariance matrix would be on the order of 10^{-3} km^2. An indication of the overall scale variance that multiplies the covariance matrix can possibly be inferred by computing a location and a 90% posterior probability ellipse for the Hawaiian bolide. We intend to try this before the end of the contract.

REFERENCES

Capon, J. (1969). High-resolution frequency-wavenumber spectrum analysis. *Proc. IEEE*, **57**, 1408-1418.

Jordan, T.H. and K. A. Sverdrup (1981). Teleseismic location techniques and their application to earthquake clusters in the South-Central Pacific. *Bull. Seismolog. Soc. Amer.*, **71**, 1105-1130.

Shumway, R.H.(1971). On detecting a signal in N stationarily correlated noise series. *Technometrics*, **13**, 499-519.

Shumway, R.H. (2000). Detection and location capabilities of multiple infrasound arrays. *Proc. 22nd Seismic Research Symposium, 12-15 September*, New Orleans, Louisiana, Chapter 7, 7-12.

Shumway, R.H. (2001). Detection and location capabilities of multiple infrasound arrays. *Proc. 23rd Seismic Research Symposium, 2-5 October, Jackson Hole, Wyoming*, Chapter 7, 7-10.

Shumway, R.H., S.E. Kim and R.R. Blandford (1999). Nonlinear estimation for time series observed on arrays. Chapter 7, Ghosh ed. *Asymptotics, Nonparametrics and Time Series*, 227-258. New York: Marcel Dekker.

Shumway, R.H. and D.S. Stoffer (2000). *Time Series Analysis and Its Applications*. New York: Springer Verlag..

Stoica, P. and A Nehorai (1989). Music, maximum likelihood, and Cramer-Rao lower Bound. *IEEE Trans. Acoustics, Speech and Signal Processing*, **37**, 720-741.

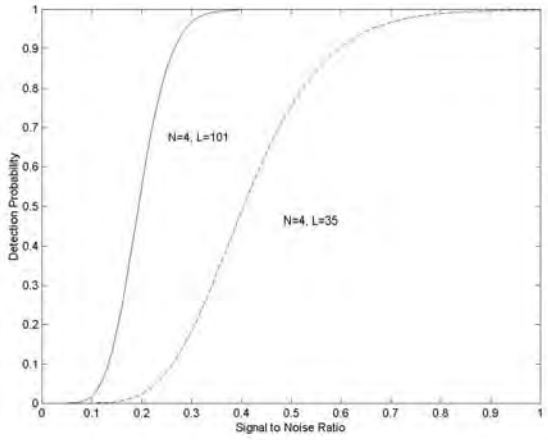

Figure 1. Detection probabilities for different signal-to-noise and smoothing options.

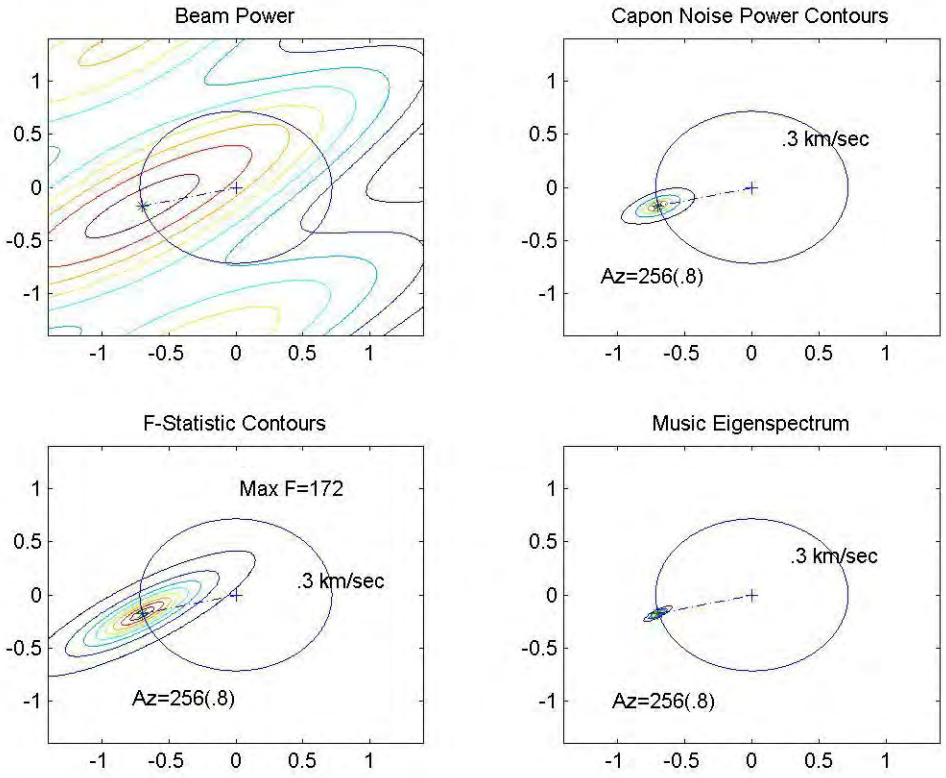

Figure 2. Wave-number analysis for the Hawaii bolide observed at Pinion Flat.

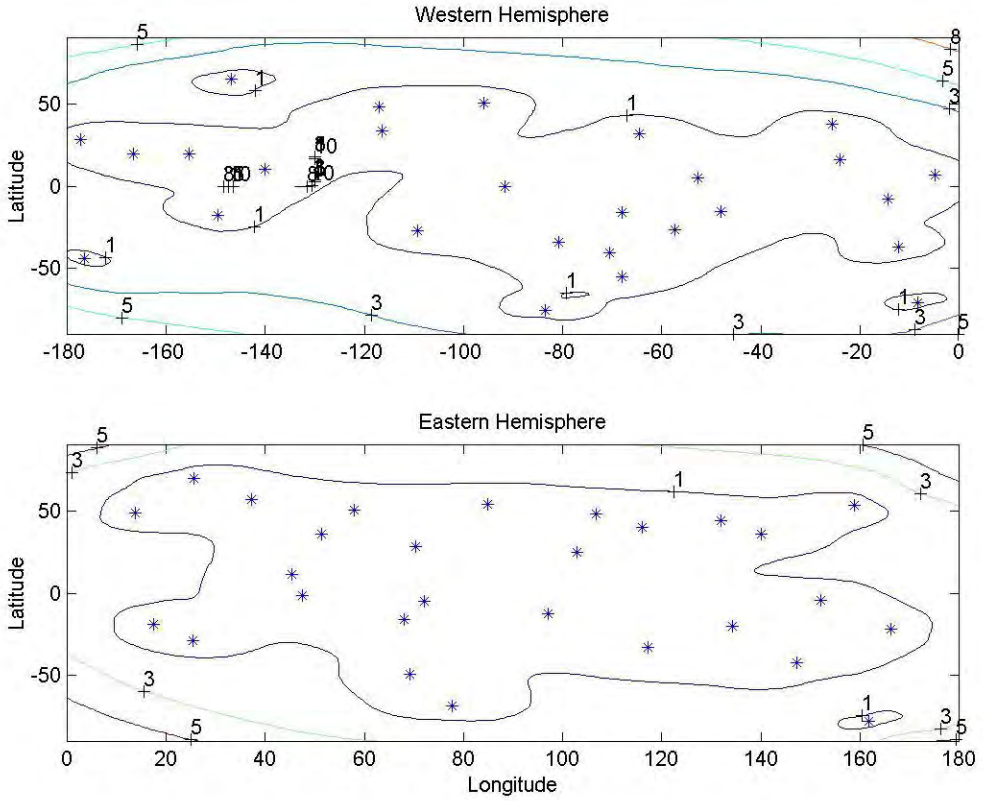

Figure 3. Contoured 90% posterior probability areas for a signal-to-noise ratio of 4 and a single array detection probability .9. Note that the 1000 square km contour includes most of both hemispheres. Array locations are shown as *.

ON INFRASOUND DETECTION AND LOCATION STRATEGIES

Rodney Whitaker, Douglas ReVelle, and Tom Sandoval

Los Alamos National Laboratory

Sponsored by National Nuclear Security Administration
Office of Nonproliferation Research and Engineering
Office of Defense Nuclear Nonproliferation

Contract No. W-7405-ENG-36

ABSTRACT

Routine processing of infrasound array data has been ongoing at relatively few locations during the recent past, and at these locations there has been little to no processing of data from large infrasound networks. As more infrasound monitoring stations become operational, data from them will take on more importance, especially with regard to automated processing routines. We discuss various ideas on detection and location strategies based on our operational experience and input from infrasound researchers. This presentation is directed toward stimulating the discussion about the best approaches to the infrasound data-processing task. This discussion applies to the monitoring task, and it should be noted that this is not the same as the research task. A good research program improves the monitoring function.

Aspects of existing automated processing, other approaches that can aid in the identification of interesting events, and simple criteria that can screen out uninteresting events are considered. The value of wide band processing for sparse arrays is discussed. Implementation of standard location techniques for infrasound monitoring is considered using simple travel-time data. Guidelines for comparison of different approaches are discussed and illustrated with data from bolides and earthquakes.

OBJECTIVE

The last US infrasound network was almost entirely closed out by about 1974 after 20 years of service detecting atmospheric nuclear explosions. In the mid 1970s, digital signal processing was just beginning to be used in a variety of disciplines, and infrasound benefitted only a little from this new processing. Routine processing of infrasound data, prior to 1998, was or had been done at only a few locations, including: Los Alamos National Laboratory (LANL); the National Oceanographic and Atmospheric Administration in Boulder CO; University of Alaska, Fairbanks AK; and Columbia University NY. Our objective here is to stimulate thought and discussion about signal processing applicable for analysis of the developing infrasound network of the International Monitoring System. The presentation will draw on our experience and will be an overview rather than an exhaustive analysis.

RESEARCH ACCOMPLISHED

As a waveform technology, infrasound can benefit from some of the existing processing infrastructure developed during the long monitoring period of seismic research. After all, there is similarity in frequency content and sampling rates; many concepts apply straightaway. But there are differences as well. In traditional infrasound work, little use is made of power detectors because, in part, the wind backgrounds can be quite variable. Rather, because the signals from distant sources are usually well correlated, cross-correlation detectors are far more common in infrasound and acoustic processing. LANL found that the algorithm developed by Young and Hoyle (1975) to be highly valuable in their work from 1983 to the present. Of course one might work with an F detector, rather than cross-correlation, where, for ideal conditions, the F statistic is related to the correlation coefficient, C, as, $F = n C /(1-C) + 1$, where n is the number of sensors. Normalized cross-correlation is bounded, 0 to 1, while the F statistic is unbounded.

The processor discussed by Young and Hoyle (1975) has some differences from traditional FK processing, and they describe their approach as frequency slowness S(ω). One point they present is that for wide-band non-dispersive signals, the S(ω) processor mitigates against side lobe alignment in different frequency planes and reduces their importance. Ferguson (1999) and Katz (2001) also discuss this point from a different perspective but show the value of wide-band processing in many cases. Below we show traditional FK results for some data from the four-element LANL array at the Nevada Test Site for a correlated signal. The strongest values are deep red with the peak at (x=8, y=23). Other strong cells are apparent over the 40 x 40 FK plane.

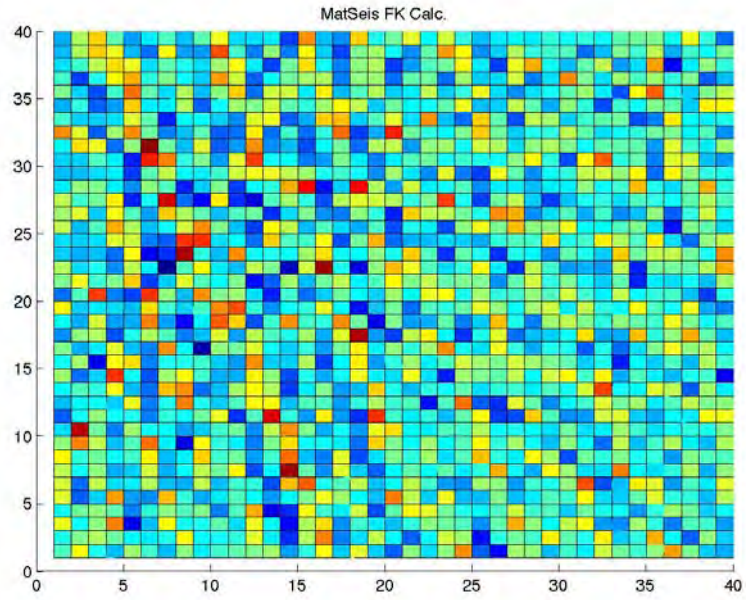

Figure 1. Traditional FK results for some data from the four-element LANL array at the Nevada Test Site for a correlated signal

Figure 2 gives the equivalent result for the same data segment computed with the S(ω) correlation processor. Here the peak is well defined at (8,24) and is clearly the peak value with no competition from other cells. The same window size and passband were used in both cases, and the processing was done with MatSeis.

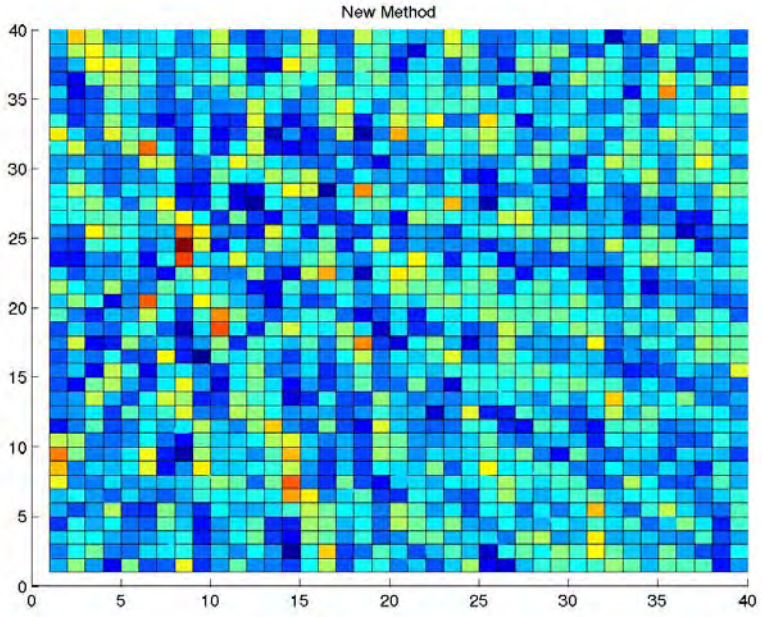

Figure 2. Equivalent result (to that in Fig. 1) for the same data segment computed with the S(ω) correlation processor.

The FK results use the FK tool in MatSeis, and the correlation slowness processing was done with Infra_tool. The results above for S(ω) processing with four elements indicate that the alias problem, with four elements, may not be as serious as first thought. However, there are still good reasons that added elements are needed for improved performance. Added elements provide better array gain as well as redundancy against sensor loss. They will enable better broadband response. In recent work we found another example of how added elements can aid the detection capability.

We recently processed data from DLIAR and LSAR for the shuttle launch of 5 June 2002, expected at around 23:50 UT. LSAR is a smaller baseline array sitting inside the prototype DLIAR array. Spring and summer shuttle launches have been detected by DLIAR, but in this case, as displayed in the figure to the right, DLIAR got very weak correlation, albeit with localization of azimuth and trace velocities. The data were processed with MatSeis and Infra_Tool, and the figure is part of the Infra_Tool Graphical User Interface (GUI) display. From the top, the panels display correlation, trace velocity, azimuth and one channel of data. Twenty-second windows were used with a band pass of 1.0 to 4.0 Hz. The LSAR results show much better correlation, azimuth and trace velocity trends, as is obvious in the next panel. This is an extreme case of the loss of correlation over the larger baseline of the DLIAR (~1.2 km) array as compared to the small baseline (~0.2 km) of the LSAR array. In looking at numerous cases of the same signal on both arrays, we often find a loss of 0.15 to 0.20 units in normalized cross-correlation values due to larger

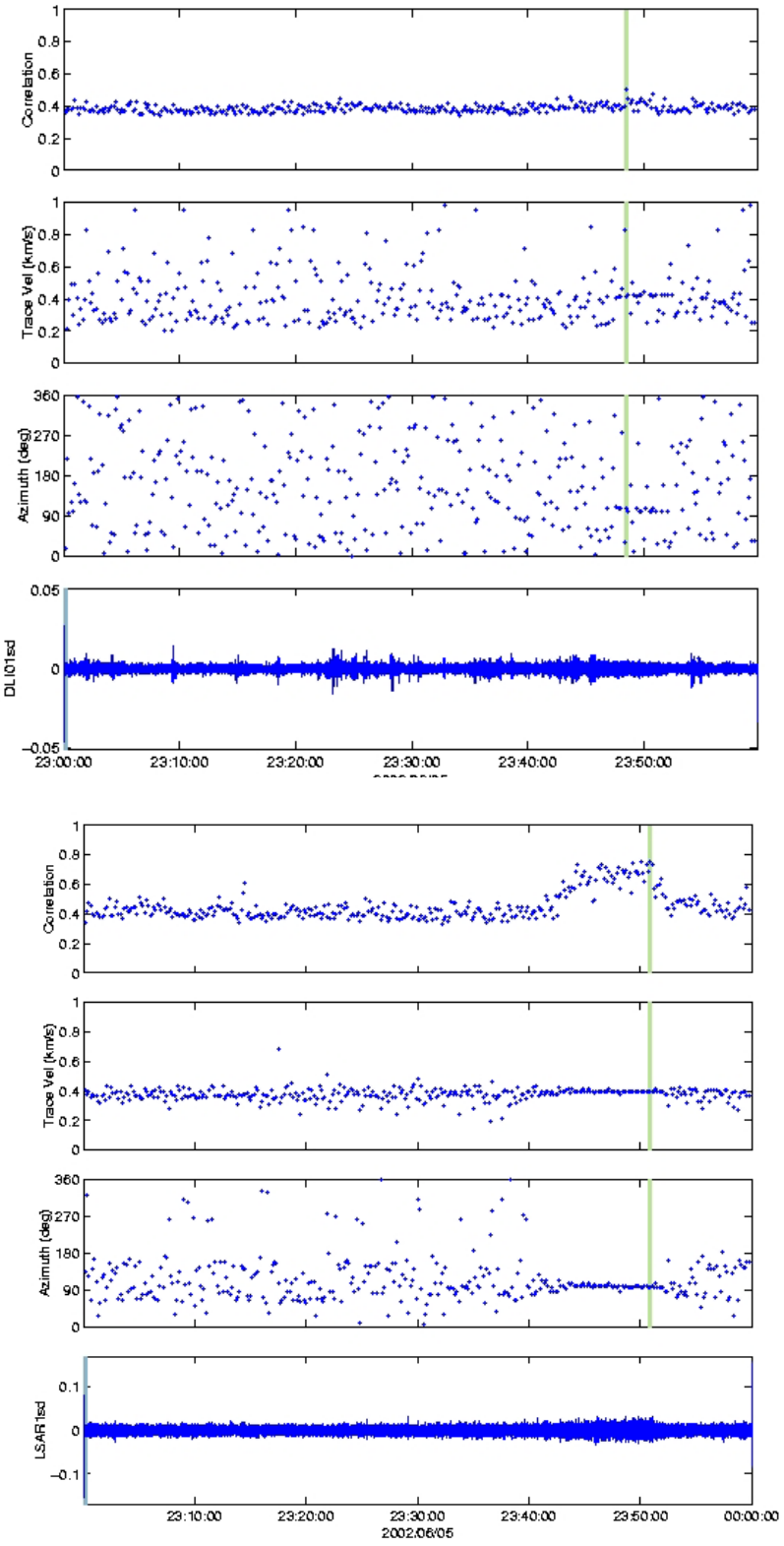

Figure 3. Data from DLIAR (top) and LSAR (bottom) for the shuttle launch of 5 June 2002

baseline. Another example of the correlation loss is given by the DLIAR and LSAR results for a California earthquake on 22 February 2002. Both arrays had good results with the azimuth for DLIAR coming out at 245.9 degrees and that for LSAR at 244.5 degrees. The peak cross-correlation for DLIAR was 0.718 and that for LSAR was 0.944. We are beginning to look again at common DLIAR and LSAR signals now that LSAR has been restored after the Cerro Grande fire.

One could envision a detector based upon the type of processing used in Infra_Tool wherein one would look for constant azimuth signals having some correlation above a threshold and duration longer than some minimum. These results could then be passed onto a global association scheme combining other infrasound stations as well as seismic and hydroacoustic stations.

One of the biggest differences between seismic and infrasound analysis occurs because the atmosphere is dynamic on a variety of time scales, and the solid earth is relatively static. Thus concepts such as travel times with really small variations, on teleseismic distances, are not possible in the atmospheric domain. Location uncertainty in atmospheric acoustics will be larger than in seismic because the travel times will have larger variation, due to the influence of winds. Nevertheless, some average properties of propagation are quite reliable. In the older monitoring period, the main acoustic arrival was associated with energy that arrived with an average travel velocity of 0.290 km/s $\pm$ 0.015 km/s for favorable propagation conditions. In a ray-acoustic picture, this condition represented energy refracted from altitudes of around 50 km and was referred to as a stratospheric return. Higher altitude refractions would, often, show lower average travel velocities of approximatey 0.25 km/s. With atmospheric travel-time variations, locations using only timing would have rather large areas of uncertainty. But because infrasound signals are well correlated, quite good bearings, back azimuths, can be derived, and for two stations, intersecting back azimuths give an estimate of location and distance. With these in hand, one can begin to identify parts of the waveform associated with specific atmospheric phases. Then, among two or more stations, one could examine the results for consistency. Ray-mode theory can aid in location by confirming, if some atmospheric data are available from models or observations, and by showing if signals from the intersection of two or more bearings really can get signals to the stations.

Another difference between infrasound and seismic monitoring is that infrasound uses timings from peak correlation whereas seismic uses first arrival (or onset) time for location. Some infrasound signals emerge slowly out of the background, making onset difficult to determine. Peak correlation can easily be found and the timing can be taken as the time of the middle of the processing window in which correlation peaks. At LANL we have determined this to be an effective approach.

The roles of research and monitoring need to be kept in mind and their differences understood. Analysis for research purposes will be different from that for monitoring. For example, very short impulsive signals are of research interest but can probably be ignored in monitoring as being due to small local events. Events with varying azimuth may be of research value but are not signals from point explosions and thus of little monitoring interest. Over time, results from the research arena will improve the monitoring capability making it more effective. Indeed, it will be the targets of opportunity, cultural and natural, that will provide the events around which the processing can be tested and improved. Both aspects need to be pursued to ensure that the processing is of the highest quality and that signals of interest are not missed.

In comparing results from different tools, one must be careful to be sure that processing parameters are, to the extent possible, the same, or as similar as they can be. A difference in azimuth of five or six degrees may or may not be a real difference. As the processing of infrasound data in the network matures, various schemes will be compared and discussed. We need to be careful to make the comparisons as meaningful as possible.

CONCLUSION

This short contribution has discussed some aspects of infrasound processing based largely on the operational experience at LANL. It has been our desire to stimulate thought and discussion

REFERENCES

Ferguson, Brian G., 1999, Time-delay estimation techniques applied to the acoustic detection of jet arrival transits, JASA**, 106,** 255.

Ham, Fredric M., 2001, Neural Network Classification of Infrasound Events Using Multiple Array Data, Infrasound Technology Workshop, Kona, HI.

Katz, Charles N., 2001, private communication.

Young, Jessie M., and Wayne A. Hoyle, 1975, Computer Programs for Multidimensional Spectra Array Processing, NOAA Technical Report ERL 345-WPL 43.

Data Processing and Analysis

DEVELOPING REGIONAL SEISMIC DATABASES FOR IMPROVING EVENT LOCATION AND GROUND TRUTH DATA SETS IN ASIA

Michael L. Begnaud, Julio C. Aguilar-Chang, Aaron A. Velasco, Lee K. Steck

Los Alamos National Laboratory

Sponsored by National Nuclear Security Administration
Office of Nonproliferation Research and Engineering
Office of Defense Nuclear Nonproliferation
Contract No. W-7405-ENG-36

ABSTRACT

Seismic event location remains one of the most crucial elements in monitoring for nuclear explosions. Recent development of a two-dimensional (2-D) empirical travel-time technique allows for correcting for unmodeled velocity structure, thus improving typical seismic event location using station corrections and/or a 1-D velocity model. However, this technique requires ground truth information, which can be in the form of known explosion locations and well located teleseismic events. To develop a ground truth data set, we rely on existing catalogs and our own travel-time information.

Many global and regional seismic catalogs with earthquake information for Asia are used in location studies. Each catalog contains origin and arrival information that may or may not overlap with the other catalogs. In order to obtain the most accurate earthquake locations, all available arrival information should be combined into a single data set, including derived travel times from digital stations. We have developed a seismic location database for the China region, combining origin and arrival information from a number of global catalogs, including the prototype International Data Center (pIDC) Reviewed Event Bulletin (REB), United States Geological Survey (USGS) Earthquake Data Reports (EDR), International Seismic Centre (ISC), as well as several regional catalogs. Regional arrivals obtained from digital data in Asia are also included. We also include ground truth information from previous research efforts for nuclear test sites and regional mining information. This merged database will provide detailed arrival data from which to produce more accurate locations.

Global and regional origin and arrival catalogs are merged using ORLOADER, a software package developed at Lawrence Livermore National Laboratory for combining individual seismic event catalogs into a master database. The program keeps identification numbers unique and uses a hierarchy table to select preferred origins. The master arrival table will also be analyzed for redundant arrivals based on a pre-approved author hierarchy. Certain catalogs are known to have errors in arrival times from truncation and machine versus manual picking. Traits such as this form the basis for determining a suitable hierarchy of criteria to allow removal of duplicate information. The final location database will thus have the most accurate arrival information available and be used to select appropriate information for various seismic location studies and/or ground truth catalogs.

We will determine how this new database improves location in the China region by relocating the events and observing how many arrivals remained defined in the solution versus the number from the original catalogs. Preliminary analysis indicates that locations will be improved for those events with few original defining phases and/or a large azimuthal gap.

OBJECTIVE

With the multitude of earthquake catalogs available to researchers, a determination of which catalog to use for locations, depths, arrivals, etc. is necessary. Errors are observed in many global and regional catalogs that can propagate into earthquake relocations and cause numerous problems with related research. Separate catalogs also contain varying degrees of accuracy on such data as arrival picks and station coordinates.

Of crucial importance to monitoring for nuclear explosions all over the earth is the process of event location/relocation. The use of empirical travel-time correction surfaces has greatly improved the accuracy of regional seismic locations. However, adequate ground truth information is required to create these surfaces. Global earthquake catalogs may rely on many common stations for their data, but many do not include similar stations of interest. By combining arrival information from many catalogs and using only the "best" information, ground truth information should be improved, resulting in more accurate seismic locations.

We have developed a seismic location database for the China region, combining origin and arrival information from many common global catalogs [e.g., International Data Center (IDC) Review Event Bulletin (REB), International Seismic Centre (ISC), United States Geological Survey (USGS) Earthquake Data Reports (EDR)] as well as regional and local catalogs from various institutions and researchers. Also included is ground truth information from research efforts around nuclear test sites and mines in the region of interest.

RESEARCH ACCOMPLISHED

Data Acquisition and Merging

As a first step in the merging of global catalogs and the compilation of arrival time information, new seismic information is automatically downloaded in the form of daily and weekly seismic bulletins (ASCII text files) via FTP transfers from open sources, such as the USGS EDR and IDC REB. These text files are parsed through a number of programs to convert the seismic data from their original catalog formats to CSS3.0 format flat data files. For example, we use modified versions of programs EDR2DB and REB2DB (distributed by BRTT as the Antelope software) to convert the EDR and REB seismic bulletins to CSS3.0 style flat files. After the data are converted and loaded into the database, several SQL scripts are run to quality control (QC) the data, identifying and correcting any problems with the data. Such QC checks include verifying that all data were loaded, fixing any duplicate entries based on pre-determined database table constraints, and enabling database table constraints (primary and unique keys) to ensure data integrity.

A method is needed to merge the origin information so each event has only one preferred location. We use the database utility ORLOADER (developed at Lawrence Livermore National Laboratory) to merge all of the bulletin data into a global table. This utility analyzes origin information and combines different catalog origins into an event and preferred origin based on location and origin time. All of the database identification numbers are renumbered and kept consistent with the arrival information also included in the seismic bulletins.

The merged event and origin information is now used to tie all of the in-house digital waveform files (formatted as Seismic Analysis Code, or SAC, files) to the events in the global merged database. All of the waveform holdings are QC'd and duplicate and incomplete/missing waveforms and SAC header information are dealt with. The SAC headers contain information on the arrival, station, and event location associated with the waveform and are updated using Perl scripts to correspond with the global tables.

Once the waveforms are tied to the database, in-house Perl scripts are run to create WFDISC, WFTAG, ASSOC, and ARRIVAL database tables that contain data about our waveform holdings and Los Alamos National Laboratory (LANL)-generated phase picks. ORLOADER is then run to merge LANL phase arrivals and waveform information with the global tables. A schematic of the data acquisition and merging process is shown in Figure 1.

Developing the Location Database

The majority of earthquake location programs that utilize some type of CSS3.0 schema tables (database or flat file) require there to be one origin entry per event in the ORIGIN table. In addition, all of the arrivals should point to one origin via the ASSOC table. The process of merging catalogs results in EVENT and ORIGIN tables, where there are several origins for any given event. Many ARRIVAL tables, which have duplicate phase picks for the same event but different origins, are now merged. In order to correctly relocate any of these events, specific rules for arrivals must be adhered to, such one *P* phase used per station, per event. With the large number of duplicate arrivals, a method needs to be developed to select appropriate phases from robust catalogs.

Using merged global tables, we developed a method to create ASSOC and ARRIVAL database tables that have the proper phase names for use with location programs such as EvLoc (Bratt and Bache, 1988; Nagy, 1996) and MatSeis (Harris and Young, 1997). The ASSOC table contains only the preferred origin location for a given event (one event can have one or more origin locations; each location corresponds to a different author, such as USGS EDR, IDC REB; etc.), based on a pre-determined LANL-generated ranking table, which ranks preferred authors to origin locations based on that author's location and time estimate uncertainties. The ASSOC table also has the phase arrivals from all sources (global bulletins, regional catalogs, LANL picks) associated with the preferred origin of an event.

Seismic phases in the ASSOC table are renamed so that all phases associated with a given event have unique descriptive names [this is a requirement of the EvLoc (libloc) program used in the location effort]. The renaming of the seismic phases follows a pre-determined ranking scheme, in which LANL arrival picks are ranked highest, and takes place following the ranking based on phase pick author and phase names.

A common problem is the phase-naming convention for *P* and *S* arrivals. Many catalogs name the *P* phases just *P*, not necessarily a *Pn* if needed (same for the *S* arrivals). Originally, we assumed we could group all of the *P* phases, all of the *Pn*, etc. and remove duplicates. However, many times one catalog would name the same *P* phase a *P* and another would name it a *Pn*, even if the arrival times were the same or very similar for that station. Therefore, it is necessary to analyze the *P*, *Pn*, *S*, and *Sn* phases and choose the correct arrival to rename to *P* or *S*.

To account for these phase discrepancies, all of the *P*, *Pn*, and *Pg* phases for a given station/event are grouped by author rank and time. If, by chance, there were any combination of the three phases for the same station/event, the phase with the minimum time for that author (if it was the highest ranking) would be selected as the "*P*", including any azimuth and/or slowness measurements. We assume that the first P-type arrival was made from the first break in the waveform and, therefore, has the best chance of being an accurate pick. By renaming the phase to *P*, we allow the velocity model in the location program to determine if the time corresponds to a *P*, *Pn*, or *Pg* phase.

We did not want to actually remove the other P-type phases from the table, so they were renamed to append the rank number at the end of the phase, thereby removing the phase from the location procedure, but leaving it in the database for possible later use or comparison. For more complex phases such as pP, PmP, etc., this process of renaming the duplicate phase to add the rank number was all that was modified. The user could later choose whether or not to include more complex phases in the solution. An example of the phase renaming method is shown in Table 1. The renaming of phases is necessary in order to provide the best distinct phase arrival times to the programs used in the location effort. By doing this, we are compiling a database with the "best" phase arrivals, so that for a given event at a given station, there is only one *P*, *Pn*, and *Pg* phase.

After phases have been renamed and distinct names given, we create synthetic arrival times based on the preferred origin. These times are then used to modify the time residual field in the ASSOC table so it is accurate for the given origin. The field for number of defining phases is also updated to be consistent with the actual number of phase chosen for location. The azimuth and slowness measurements are also updated. These updates permit the researcher to choose events for relocation that have a minimum number of defining phases, time residual, and/or azimuthal gap.

Relocation Results

We will utilize the location database to test effectiveness in relocating large sections of the LANL merged catalog. A first test will relocate approximately 156 events for a region around the Mw=7.5 Tibet event of 08NOV1997, with

manually-picked LANL *P* and *S* arrivals as well as global catalog arrivals having a station-event distance ranging from 5.5 to over 30 degrees. The Tibet event provides a unique ground truth test due to the presence of a related surface rupture identified by Inferometric Synthetic Aperture Radar (InSAR) (Peltzer *et al*., 1999) and the determination of the Tibet event as associated with a vertical strike/slip fault (Velasco *et al*., 2000). We will test whether the location database produces relocations that better align with this surface rupture.

Figures 2 and 3 show preliminary relocations using *P* and *S* travel-time correction surfaces for USGS EDR origins/arrivals only and LANL location database origins/arrivals, respectively. The main shock is located at the center area of the surface rupture. Using the EDR arrivals only, the main shock does not transfer to the surface rupture. However, in other studies, the main shock does transfer to the rupture, using and correcting only the *P* phases (Steck *et al*., 2001).

For the location database, the number of events has increased as well as the number of stations and phases. Typically, improvement is readily observed for those events that, in standard catalogs, had few defining phases and/or large azimuthal gap. Relocating using the correction surfaces appears to produce events that align more on the rupture, and moves the main shock closer to the rupture. Again, the shear phases have inconsistencies through most catalogs and do tend to introduce more error in the locations. There is still considerable scatter in the relocations, but this probably is due in large part to the sparse nature of the data.

Other location methods have been tested with the location database, including application of the double-difference location algorithm HYPODD (Waldhauser and Ellsworth, 2000), using the location produced with the *P* and *S* corrections as the starting point (see *Steck et al*, this Proceedings).

CONCLUSIONS AND RECOMMENDATIONS

With the multitude of global, regional, and local catalogs, it is necessary to develop methods to incorporate all available arrival time data into one main catalog in order to create the most accurate set of travel times for use in seismic location. Merging datasets permits all available arrivals to be accessible to the researcher, where specific choices can be made about which authors and arrivals to use for the location process. Duplicate and/or redundant arrival information must be removed from the database so location algorithms have distinct phases for events and stations. The location database typically results in improved origin accuracy as well as an increased number of arrivals for an event. This method can improve locations considerably for events with few arrivals and/or large azimuthal gap.

REFERENCES

Bratt, S. R. and T. C. Bache (1988). Locating events with a sparse network of regional arrays, *Bull. Seism. Soc. Am.*, **78**, 780-798.

Harris, M. and C. Young (1997). MatSeis: a seismic GUI and toolbox for MATLAB, *Seis. Res. Lett.*, **68**, 267-269.

Nagy, W. (1996). New region-dependent travel-time handling facilities at the IDC: Functionality, testing, and implementation details, *SAIC Tech Rep. 96/1179*, 57 pp.

Peltzer, G., F. Crampé, and G. King (1999). Evidence of nonlinear elasticity of the crust from the Mw7.6 Manyi (Tibet) earthquake, *Science*, **286**, 272-276.

Steck, L. K., A. A. Velasco, A. H. Cogbill, and H. J. Patton (2001). Improving regional seismic event location in China, *Pageoph*, **158**, 211-240.

Velasco, A. A., C. J. Ammon, and S. L. Beck (2000). Broadband source modeling of the November 8, 1997 Tibet (Mw = 7.5) earthquake and its tectonic implications, *J. Geophys. Res.*, **105**, 28,065-28,080.

Waldhauser, F., and W. L. Ellsworth (2000). A double-difference earthquake location algorithm: Method and application to the Northern Hayward Fault, California, *Bull. Seism. Soc. Am.*, **90**, 1353-1368.

Table 1. Example of phase renaming for example event #100 at example station XYZ.

Phase pick author	Rank	Original phase			Renamed phase		
		time 1	time 2	time 3	time 1	time 2	time 3
LANL	1	Pn	Pg		P	Pg	
REB	2	Pg	P	Pn	Pg2	P2	Pn
EDR	3	Pn	P	Pg	Pn3	P3	Pg3

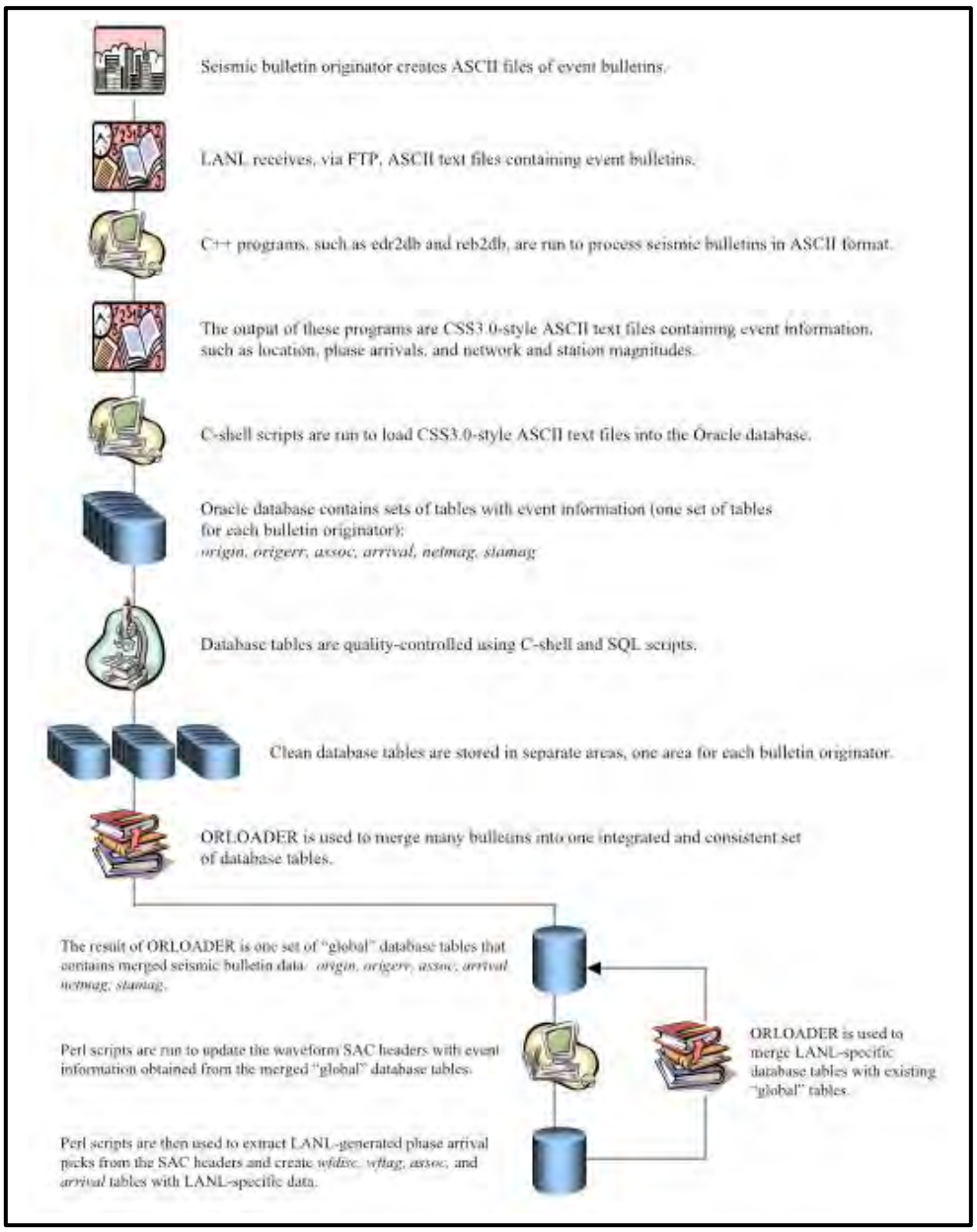

Figure 1. Flow chart for LANL seismic catalog merging process.

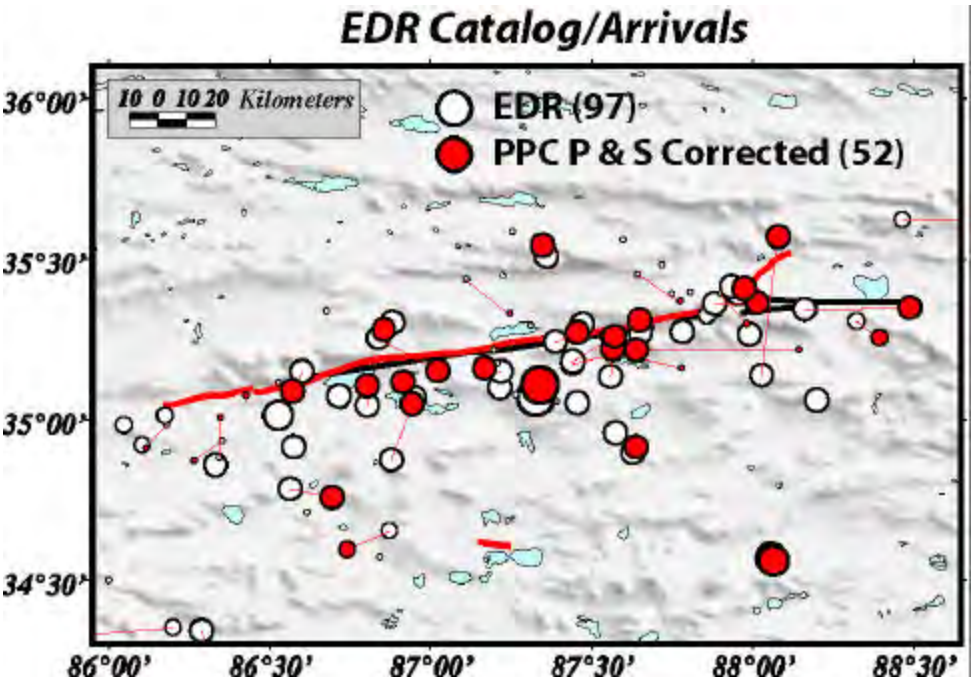

Figure 2. Relocations of Tibet events around a surface rupture using EDR catalog locations and arrivals only. Red line is surface rupture, black line is mapped fault. Both P and S phase travel time correction surfaces were used in the relocation. The main shock (largest event near center of rupture) does not relocate on the rupture (the event was determined to be a vertical strike/slip mechanism, see text).

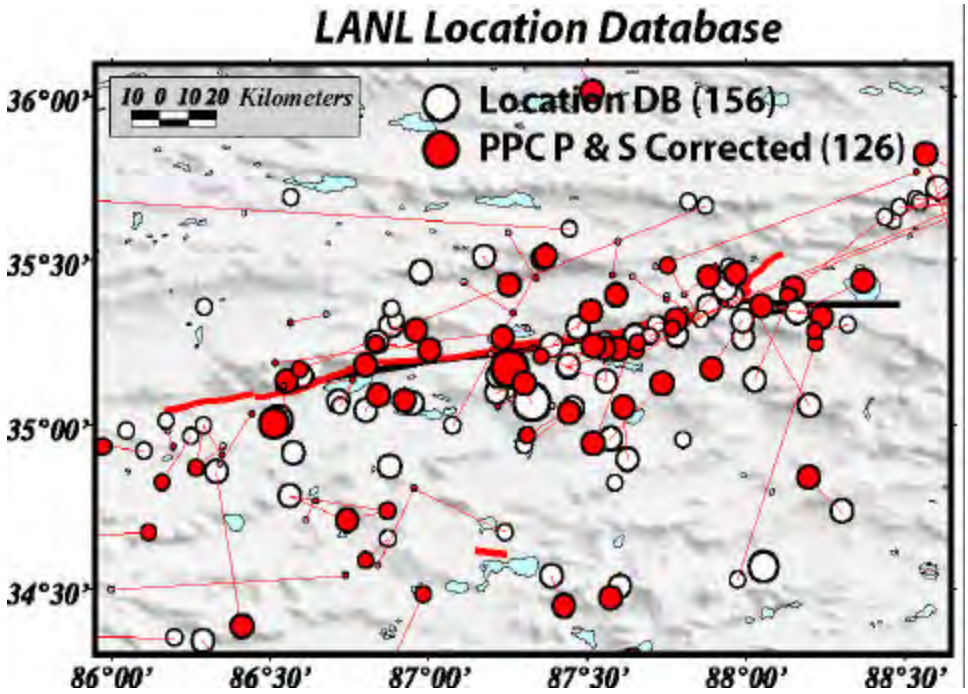

Figure 3. Relocations of Tibet events around a surface rupture using LANL location database origins and arrivals. Refer to Figure 2. The number of events in the area has increased relative to the EDR catalog. The main shock relocates much closer to the surface rupture and many other events align more along the rupture and produce more event clusters.

DEVELOPMENT OF AUTOMATED MOMENT TENSOR SOFTWARE AT THE PROTOTYPE INTERNATIONAL DATA CENTRE

Margaret Hellweg,[1] Douglas Dreger,[1] Barbara Romanowicz,[1] Jeffry Stevens[2]

University of California, Berkeley, Seismological Laboratory;[1] Science Applications International Corporation[2]

Sponsored by Defense Threat Reduction Agency

Contract No. DTRA01-00-C-0038

ABSTRACT

We are implementing the seismic moment tensor software used at the Berkeley Seismological Laboratory (BSL) for routinely monitoring earthquake strain release (Romanowicz *et al*., 1993; Pasyanos *et al*., 1996) on the test bed at the Center for Monitoring Research (CMR, formerly the Prototype International Data Centre (PIDC). The discrimination of nuclear explosions from naturally occurring earthquakes is difficult, particularly for moderate magnitude events. By providing a general representation of the seismic source, the moment tensor allows us to characterize its radiation in terms of isotropic and compensated linear vector dipole (CLVD) patterns in addition to the double couple radiation expected from typical tectonic earthquakes. The software package from BSL determines moment tensors for an event using two separate procedures: a complete waveform (CW) time-domain method as well as a spectral method applied to the surface wave (SW) recordings. During the past year, we have completed the implementation of the code package at CMR. This has involved major reworking of the waveform extraction package *mtisshell* to provide data pre-processing so that other programs such as the Seismic Analysis Code (SAC) or sapling ([a BSL processing module], Pasyanos, 1996) are no longer necessary. In addition, we have improved the estimation of signal-to-noise ratio for data used in the surface wave inversion to exclude noisy data that skews the inversion results. To illustrate the application, we present the inversion results from both methods for events with mb 5.4 in a test interval occurring between 19 July 1999 and 16 October 1999. The waveform data for input are taken from the very sparse network of the primary stations of the International Monitoring System (IMS), while the Greens functions (CW) are calculated using the IASPEI-91 velocity model and mode information for the SW code is derived from model 1066. We compare the results of both inversion methods with information given in the Harvard Centroid Moment Tensor (CMT) catalog and that in the moment tensor catalog of the US Geological Survey (USGS).

To improve its integration into the routine system, we are continuing to test and tune the procedure. Although the results for events in the test interval in some regions of the Earth are good, there are several regions where they could be improved. We show the effects of performing the inversions using theoretical information calculated on the basis of other Earth models. In addition, for selected events, we show how the addition of data from auxiliary stations improves the station coverage and thus the inversion results. On the basis of velocity structure and waveform data collected as part of the Advanced Concept Demonstration (ACD) centered on Lop Nor, we intend to investigate and demonstrate the advantages of Greens functions and mode calculations based on a regional velocity model and investigate the resolution of the two methods for moderate events, recorded well in the ACD region.

OBJECTIVE

Through moment tensor inversion, we can use broadband waveforms from modern broadband digital seismic stations to derive a robust estimate of source magnitude (M_w) for an event as well as information about its mechanism and its depth. In addition, the moment tensor results that are obtained using either primary stations of the International Monitoring System (IMS) or both primary and auxiliary stations will provide an important database of details about the seismic sources. This information will benefit other programmatic objectives such as the calibration of velocity and attenuation structure at both global and regional scales. Thus seismic moment tensors are a potentially powerful method for screening observed seismicity to identify anomalous events, those which are shallower than is typical and which have unusual, non-double couple radiation patterns (e.g. Patton 1988; Dreger and Woods, 2002). Such events may be flagged to be analyzed in greater detail. While previous work has demonstrated that moment tensors of nuclear explosions are different than those of tectonic earthquakes (Patton, 1988; Stump and Johnson, 1984; Vasco and Johnson, 1989), it was often difficult to resolve a purely isotropic source with regionally recorded long-period data (Patton, 1988). In contrast, recent experience indicates that anomalous radiation from nuclear explosions or non-tectonic seismic events may be identified with a relatively sparse network of broadband stations (e.g. Dreger and Woods, 2002; Dreger *et al*., 2000). These studies have identified significant deviation from double-couple type seismic radiation, but come up short in actually resolving the physical processes which give rise to the non-double-couple seismic radiation.

The moment tensor formalism was first developed more than 20 years ago (e.g. Mendiguren, 1977), and has been since applied successfully in various settings for the study and/or routine cataloguing of moderate to large earthquakes on the global scale, using either waveforms in the time-domain (e.g. Dziewonski *et al*., 1981) or surface-wave spectra in the frequency domain (e.g. Romanowicz, 1982; Romanowicz and Guillemant, 1984). When the signal-to-noise ratio is good, data from a single, three-component station are sufficient to obtain a moment tensor solution for a large, purely double-couple earthquake at teleseismic distances (Ekstrom *et al*., 1986). The same is true for regional distances, where a robust estimate of the seismic moment tensor of a moderate earthquake may be determined with data from a single, three-component station (e.g. Dreger and Helmberger, 1991; Fan and Wallace, 1991; Walter, 1993). For large earthquakes recorded teleseismically, relatively low frequency data can be used. In such cases, it is not necessary to know the propagation corrections with great accuracy. The use of standard 1D reference models of the Earth and, more recently, 3D models obtained from global tomography generally give acceptable solutions. More recently, as sparse regional broadband networks become more common, moment tensor inversion procedures have been adapted for application to smaller events observed at regional distances. In such cases, waves with periods between 15 and 40 s are used in the inversions. They are more sensitive to complex crustal structure, and propagation corrections must therefore be estimated more accurately using appropriate regional models. At U.C. Berkeley, we have developed and implemented two independent approaches for estimating the moment tensor of moderate earthquakes at regional distances (Romanowicz *et al*., 1993). They have been automated within the framework of our real-time program (Gee *et al*., 1996) to routinely provide reliable estimates of earthquake size, mechanism and depth in quasi-real time (Pasyanos *et al*., 1996).

In the time-domain moment tensor inversion procedure, the CW method, the complete long-period waveform from the initial P-wave through the surface wavetrain is used (Dreger and Romanowicz, 1994; Pasyanos *et al*., 1996; Fukuyama *et al*., 1998; Fukuyama and Dreger, 2000). This method functions quite well in a region as complex as California for monitoring seismicity 30 to 700 km from stations with only a few calibrated velocity models. One of the models we use describes the relatively fast wave propagation in the thick Sierra block, the second describes propagation through the relatively slow and thin California Coast Ranges (Pasyanos *et al*., 1996). Recently, a third model has been developed to improve results for events occurring offshore of Cape Mendocino (Tajima *et al*, 2000). While a satisfactory solution may often be derived using three-component data from a single station, in practice we use data from several stations to improve the azimuthal coverage of the focal sphere (Pasyanos *et al*., 1996).

The second moment tensor method used at U.C. Berkeley, the SW method, is a frequency-domain, surface wave approach, adapted from the two-step method of Romanowicz (1982). The use of surface waves, the largest of the regional phases, allows us to extend the analysis to smaller seismic events. For this procedure, calibrated fundamental-mode surface wave phase velocities between 10-60 sec period are used to calculate propagation corrections (Pasyanos *et al*., 1996). We are able to analyze events down to magnitude 3.5 using data from stations of the Berkeley Digital Seismic Network between 100 to 500 km from the epicenter. When azimuthal coverage is acceptable this method performs quite well.

The purpose of this project is to adapt and implement the two procedures in use at U.C. Berkeley for nuclear monitoring purposes. The initial goal for this software is the automatic determination of moment tensors on a global scale for events with magnitudes greater than M = 5.5. For a specific region, we will attempt to achieve reliable results for lower magnitudes through the use in the inversions of velocity structures adapted for the region as well as data from additional regional broadband stations. Later releases of the software will incorporate calibration information for several regions of interest, which will allow moment tensors to be determined for events with magnitudes greater than M ~ 4.

RESEARCH ACCOMPLISHED

We have developed and installed an automated processing system for the moment tensor package on the testbed at the Center for Monitoring Research (CMR). The flowchart in Figure 1 gives an overview of the automatically executed processing steps. For a given Julian date, events are selected for processing on the basis of information extracted from the database tables containing the reviewed event bulletin (REB). For our tests, we have chosen the interval from 19 July (day 200) to 16 October (day 290) 1999. If an event has a body-wave magnitude greater than 5.4 and depth shallower than 200 km, it is included in the processing. Table 1 lists the events in the testbed database with these characteristics. In addition to hypocentral information, the process automatically extracts from the database tables a list of the primary stations equipped with broadband sensors, which were used in producing the REB, along with event-station azimuths and distances. Several important events with REB $m_b < 5.4$ have been added to improve coverage, and to improve the testbed dataset for calibration purposes.

For those seismic stations, waveform data are extracted separately for the two inversion routines and preprocessed using the program *mtisshell*. The data intervals are chosen on the basis of group velocity. For the CW method, data lie within an interval having group velocities between 200 km/s and 2 km/s, and only includes stations located less than 5000 km from the epicenter. Data for the SW method are in an interval defined by group velocities between 4.5 km/s and 2 km/s. During the data extraction process, basic data quality tests are performed. If one or more components from a station has gaps in the selected interval or the interval for which data is present is shorter than requested, data from that station are excluded. For data to be used in the SW inversion, a second quality check is performed after they have been extracted. The power for the surface waves in the band of interest, usually between 100 s and 20 s, is compared with the power of the noise in an interval before the arrival of the P-wave from the event (group velocities between 200 km/s and 15 km/s). If the signal-to-noise ratio in power is lower than 100 for the Z, R or T components, data from that station are excluded from the inversion. The maps in Figure 2 show the primary stations, which provided waveform data for the events in the test. As is shown in Figure 1, the preprocessing depends on the inversion algorithm. For both methods, means and trends are removed from the data and they are then resampled to 1 sps. The instrument response is deconvolved and the records are rotated to directions radial (R) and transverse (T) to the event-station direction. While the data for the CW inversion is bandpass-filtered to extract the band to be used in the inversion, the filter limits for the SW data lie well outside the band of interest in order to exclude very long period noise without affecting the data to be inverted.

In addition to the waveform data, the CW method requires Greens function files for the fundamental fault orientations and movements (Dreger and Helmberger, 1991). The Greens functions used at U.C. Berkeley are calculated from the regional velocity models using *FKPROG*, a program for frequency-wavenumber calculation regional waveforms (Saikia, 1994). *FKPROG* treats the velocity model as a planar, not spherical structure, which is an acceptable assumption for near-regional distances of up to 700 km as in California. For the application of *FKPROG* to event-station distances up to 5000 km, as in the testbed implementation, the assumption is no longer valid. Initial tests of the CW method with Greens functions calculated directly from the radially symmetric iasp91 velocity model for the Earth (Kennett and Engdahl, 1991) were unsuccessful. Typically, time differences between phases in the Greens functions were too short to achieve good fits. We applied a flattening algorithm (Müller, 1973, Müller, 1977) to the iasp91 velocity model before calculating a new set of Greens functions. The agreement between the travel times in the Greens function synthetics for a given distance and the data for events at that distance from a station improved. Our analysis of the broadband waveform fits, and comparisons of derived moment tensor solutions with those reported by either Harvard or the USGS indicate that this flattening correction produces a robust set of Greens functions.

The upper map in Figure 2 shows the moment tensors calculated using the CW method and Greens functions based on a flattened iasp91 velocity model (blue) and on a flattened PREM velocity model (green, Dziewonski and Anderson, 1981). For comparison, the moment tensors given for these events in the Harvard CMT (brown) and USGS (red) catalogs are also shown. For events in the southwest Pacific Ocean, the moment tensors derived by the CW method differ from those given by both the Harvard and USGS catalogs. However, data for each of these events were only available for one primary station less than 5000 km from the epicenter, STKA. The solutions calculated by the CW method are consistent with the waveforms from this station. Were data from one or more other stations available, the additional constraints would probably improve the agreement with the standard catalogs. Figure 3A shows the moment tensor difference function (Pasyanos *et al*, 1996) comparing the results from the CW inversions using iasp91 and PREM Greens functions with Harvard CMT catalog moment tensors and with each other, while Figure 3B plots the ratios of the calculated moments to the catalogs' moments and between the different Greens functions. While there is some variation between the ratios of the moments, they cluster around 1. This indicates that the estimate of the moment using the CW method is reliable. On the whole, the agreement between the moment tensors from the CW method and Harvard CMT are not very good when described using the moment tensor difference function (Figure 3A).

The Hector Mine event (Origin ID 20595122, October 16, 1999) is a good example on which to investigate these differences. The map in Figure 4A shows the location of the Hector Mine event (star) and the primary stations of the network of the International Monitoring System (IMS) for which broadband data was extracted from the testbed database (filled blue inverted triangles). Data from the two broadband primary stations closest to the epicenter, NV32 and PD31 (open blue inverted triangles), were excluded because the interval stored in the waveform database was too short. Figure 4B shows the waveform fits and the moment tensor resulting from the automatic inversion of data filtered in a passband between 20 s and 50 s using Greens functions derived from the iasp91 velocity model. While the waveform fits do not look very bad, the moment tensor is the opposite of those given by the Harvard CMT and USGS catalogs and the total reduction in variance is only 18 percent. We investigated the waveforms and instrument information given for the four primary stations. It appears that the instrument response functions stored in the database for the stations ULM and IL31 have reversed polarity. Figure 4C shows the results for the same four stations, when the instrument response has been corrected. In addition, we have used a filter passband between 33 s and 100 s, more appropriate for the size of the Hector Mine earthquake, and less susceptible to the influence of lateral heterogeneity.. The new moment tensor result agrees well with the catalog results and the variance reduction is better than 50 percent. For Figure 4D we have added data from three auxiliary stations of the IMS network (filled red inverted triangles) to the inversion. The data for stations ANMO and CCH was extracted from the database of the Incorporated Research Institutions in Seismology (IRIS), while data from YBH came from the archives of the Berkeley Seismological Laboratory. The stations YBH and ANMO are approximately the same distance from the epicenter as PD31. This inversion shows how the auxiliary stations can supply data from locations close to the epicenter while improving the coverage of the focal sphere.

Figure 2 also shows the moment tensors calculated using the SW method (lower map). Again, the moment tensors calculated using modes derived from two velocity models, 1066b (blue, Gilbert and Dziewonski, 1975) and the PREM velocity model (green) can be compared with the moment tensors given in the Harvard CMT (brown) and USGS (red) catalogs. Fewer of the events selected from the catalog are present on this map than the upper map for the CW method. Moment tensors were calculated only for events if high quality, three-component data were available for more than 2 stations, that is data with no gaps, of a sufficient length between group velocities of 4.5 km/s and 2.0 km/s, and with a signal-to-noise ratio in power greater than 100. Figure 3C shows the moment tensor difference function comparing the results from the SW inversions using 1066b and PREM modes with Harvard CMT catalog moment tensors and with each other, while Figure 3D compares the calculated moments. While the mechanisms for some events agree well with the catalog values, for others, they are completely different. This is also apparent in the plot of the moment tensor difference function (Figure 3C), where it is clear that the results from the 1066b inversion are basically the same as those from the PREM inversion (plusses). Clearly, the values of the moments determined for these events are low, compared with the Harvard CMT catalog (Figure 3D), on average a factor of 7 lower. This is independent of the model used, as the average for the ratios of the moments determined using the 1066b model and PREM is about 1 (plusses).

Figure 5 shows the results of the surface wave inversion of the Hector Mine event (origin ID 20595122, 16 October 1999). The phase and amplitude fits are shown for all stations and frequencies used to produce the result given on the right hand side of the figure. Just as the reversed polarity of the instrument correction for stations ULM and IL31

affected the solution for the CW method, it will have an effect on the results of the surface wave method. We must determine which other stations may have similar problems. We are also investigating the cause of the low estimate of events' moments calculated in the course of the inversion.

CONCLUSIONS AND RECOMMENDATIONS

The automatic procedure to determine moment tensors has been implemented on the testbed at the Center for Monitoring Research. The procedure selects events from the reviewed event bulletin and calculates moment tensors, the events' depths and moments using the complete waveform and surface wave methods developed at U.C. Berkeley. Results from a set of earthquakes with $m_b > 5.4$ and depth shallower than 200 km that occurred between 19 July and 16 October 1999 demonstrate both the effectiveness of the procedure, as well as the areas where improvement is necessary. We have calculated the results of each method, the CW method and the SW method, using synthetic information calculated from two global velocity models. We are investigating solution differences that are apparently due to the choice of velocity model. Initial observations suggest that for the CW method, the differences in the automatic solutions usually result from incorrect alignment with the Greens function. When solutions are reviewed, and the alignment of the waveforms and the Greens function adjusted, the results are much more consistent for the two models.

One of the most basic problems we encountered in the development process relates to the amount and quality of the data used in the inversions. For the methods to function well, the waveform data must have a high signal-to-noise ratio and no gaps or glitches. In many regions of the world, for example the southwest Pacific Ocean, there are very few primary stations. The results of the inversion could be improved by using recordings from auxiliary stations of the IMS network equipped with broadband instruments. Unfortunately, for the test interval, it is impossible to go back and retrieve such data to add in to the inversion. We have been using recent events to test feasibility of using data from auxiliary stations in the moment tensor procedure. In practice, data from auxiliary stations are used in producing the REB, however, generally only very short intervals of data are requested from the stations. These intervals are not long enough to be useful for moment tensor inversions. We recommend that intervals starting at the event origin time and ending with the end of the surface wave train be requested from auxiliary stations with broadband instruments within 50 degrees of the event and stored in the waveform database for use with the moment tensor code. If it is not possible to handle the resulting volume of data, we suggest that at least 1 sps data be stored.

Recently, the Center for Monitoring Research has been collecting waveform data from earthquakes and nuclear explosions in and around Lop Nor as part of an advanced concept demonstration (ACD). Figure 6 shows a set of 175 earthquakes recorded between 1995 and 2002 as well as 25 nuclear explosions dating from 1966 to 1996. As an example of the calibration of the automatic moment tensor procedures for a specific region, we are planning to use this data along with the 3D velocity structure given by CUB1.0 (Anatolik *et al*, 2001). We will compare the moment tensor results with those determined by Bukchin *et al* (2001).

REFERENCES

Anatolik, M., G. Ekström, A. M. Dziewonski, L. Boschi, B. Kustowski, and J Pan (2001), Multi-Resolution Global Models for Teleseismic and Regional Event Location, *23rd Seismic Research Review: Worldwide Monitoring of Seismic Explosions*, Jackson Hole, WY, October 1-5.

Kukchin, B. G., A z. Mostinsky, A. A. Egorkin, A. L. Levshin, and M. H. Ritzwoller (2001), Isotropic and Nonisotropic Components of Earthquakes and Nuclear Explosions on the Lop Nor Test Site, China, *Pure Appl. Geophys.*, **158**, 1497-1515.

Dreger, D. and D. V. Helmberger (1991), Complex Faulting Deduced from Broadband Modeling of the 28 February 1990 Upland Earthquake (M_L=5.2), *Bull. Seism. Soc. Am.*, **81**, 1129-1144.

Dreger, D. and B. Romanowicz (1994), Source Characteristics of Events in the San Francisco Bay Region, *USGS Open-file report, 94-176*, 301-309.

Dreger, D. (1997), The Large Aftershocks of the Northridge Earthquake and their Relationship to Mainshock Slip and Fault Zone Complexity, *Bull. Seism. Soc. Am.*, **87**, 1259-1266.

Dreger D. and B. Woods (2002), Regional Distance Seismic Moment Tensors of Nuclear Explosions, *Tectonophysics*, in press.

Dreger, D. S., H. Tkalcic, and M. Johnston (2000), Dilational Processes Accompanying Earthquakes in the Long Valley Caldera, *Science*, **288**, 122-125.

Dziewonski, A. M., T.-A. Chou, and J. H. Woodhouse (1981), Determination of Earthquake Source Parameters from Waveform Data for Studies of Global and Regional Seismicity, *J. Geophys. Res.*, **86**, 2825-2852.

Dziewonski, A. M. and D. L. Anderson (1981), Preliminary Reference Earth Model, *Phys. Earth Plan. Int.*, **25**, 297-356.

Ekstrom, G., A. M. Dziewonski, and J. Steim (1986), Single station CMT:Application to the Michoacan, Mexico, Earthquake of September 19, 1985, *Geophys. Res. Lett.*, **13**, 173-176.

Fan, G. and T. Wallace (1991), The Determination of Source Parameters for Small Earthquakes from a Single, very Broadband Seismic Station, *Geophys. Res. Lett.*, **18**, 1385-1388.

Fukuyama, E., M. Ishida, D. Dreger, and H. Kawai (1998), Automated Seismic Moment Tensor Determination by Using OnLine Boadband Seismic Waveforms, *Jishin*, **51**, 149-156.

Fukuyama, E. and D. Dreger (2000), Performance Test of an Automated Moment Tensor Determination System, *Earth Planets Space*, **52**, 383-392.

Gee, L., D. Dreger, D. Neuhauser, R. Uhrhammer, and B. Romanowicz (1996), The REDI program, *Bull. Seism. Soc. Am.*, **86**, 936-945.

Gilbert, F. and A. M. Dziewonski (1975), An Application of Normal Mode Theory to the Retrieval of Structural Parameters and Source Mechanisms from Seismic Spectra, *Phil. Trans. Roy. Soc. Lon.*, **278**, 187-269.

Kennett, B. L. N. and E. R. Engdahl (1991), Traveltimes for Global Earthquake Location and Phase Identification, *Geophys. J. Int.*, **105**, 429-465.

Mendiguren, J. (1977), Inversion of Surface Wave Data in Source Mechanism Studies, *J. Geophys. Res.*, **82**, 889-894.

Müller, G. (1973), Theoretical Body Wave Seismograms for Media with Spherical symmetry; Discussion and Comparison of Approximate Methods, *J. Geophysics*, **39**, 229-246.

Müller, G. (1977), Earth-Flattening Approximation for Body waves Derived from Geometric Ray Theory; Improvements, Corrections and Range of Applicability, *J. Geophysics*, **42**, 429-436.

Pasyanos, M. (1996), Regional Moment Tensors and the Structure of the Crust in Central and Northern California, *Ph.D. Thesis, University of California, Berkeley*, 261p.

Pasyanos, M., D. Dreger and B. Romanowicz (1996), Toward Real-Time Estimation of Regional Moment Tensors, *Bull. Seism. Soc. Amer.*, **86**, 1255-1269.

Patton, H. J. (1988), Source Models of the Harzer Explosion from Regional Observations of Fundamental-Mode and Higher Mode Surface Waves, *Bull. Seism. Soc. Am.*, **78**, 1133-1157.

Pechmann, J. C., W. R. Walter, S. J. Nava, and W. J. Arabasz (1995), The February 3, 1995, ML 5.1 Seismic Event in the Trona Mining District of Southwestern Wyoming, *Seis. Res. Lett.*, **66**, 25-34.

Romanowicz, B. (1982), Moment Tensor Inversion of Long Period Rayleigh Waves: A New Approach, *J. Geophys. Res.*, **87**, 5395-5407.

Romanowicz, B. and Ph. Guillemant (1984), An Experiment in the Retrieval of Depth and Source Parameters of Large Earthquakes Using Very Long Period Rayleigh Wave Data, *Bull. Seism. Soc. Am.*, **74**, 417-437.

Romanowicz, B., M. Pasyanos, D. Dreger, and R. Uhrhammer (1993), Monitoring of Strain Release in Central and Northern California Using Broadband Data, *Geophys. Res. Lett.*, **20**, 1643-1646.

Saikia, C. (1994), Modified Frequency-Wavenumber Algorithm for Regional Seismograms using Filon's Quadrature: Modeling of Lg Waves in Eastern North America, *Geophys. J. Int.*, **118**, 142-158.

Stump, B. W., and L. R. Johnson (1984), Near-Field Source Characterization of Contained Nuclear Explosions in Tuff, *Bull. Seism. Soc. Am.*, **74**, 1-26.

Tajima, F., D. S., Dreger, and B. Romanowicz (2000), Modeling of the Transitional Structure from Ocean to Continent in the Mendocino Region using Broadband Waveform data, *EOS*, **81**, no. 48 (Fall meeting supplement).

Vasco, D. and L. Johnson (1989), Inversion of Waveforms for Extreme Source Models with Application to the Isotropic Moment Tensor Component, *Geophys. Journ. Royal Astr. Soc.*, **97**, 1-18.

Walter, W. R. (1993), Source Parameters of the June 29, 1992 Little Skull Mountain Earthquake from Complete Regional Waveforms at a Single Station, *Geophys. Res. Lett.*, **20**, 403-406.

Table 1. Events of test interval, July 19 – October 16, 1999

OriginID	Date	Lat	Lon	Depth	m_b %	Region
20537870	1999 7 19 2:17:09.150	-28.561	-177.424	70	5.64	Kermadec
20541908	1999 7 26 1:33:15.178	-5.210	152.076	16	5.68	New Britain
20542430	1999 7 28 0:16:59.480	-28.606	-177.322	34	5.47	Kermadec
20542756	1999 7 28 10:08:18.210	-30.239	-177.774		5.81	Kermadec
20553840	1999 8 12 5:44:56.157	-1.595	122.667		5.56	Sulawesi
20555310	1999 8 14 0:16:54.100	-5.840	104.674	102	5.87	S. Sumatra
20559538	1999 8 17 0:01:37.795	40.772	30.092		5.59	Turkey
20560647	1999 8 20 10:02:18.146	9.260	-84.165		5.46	Costa Rica
20561207	1999 8 22 12:40:42.345	-16.095	168.213		5.94	Vanuatu
20568654	1999 9 7 11:56:49.481	38.161	23.544		5.50	Greece
20576492	1999 9 18 21:28:34.048	51.264	157.499	50	5.61	Kamchatka
20576889	1999 9 17 14:54:46.930	-13.815	167.446	169	5.72	Vanuatu
20577664	1999 9 20 17:47:29.732	23.548	121.012		5.94	Taiwan MS*
20577672	1999 9 20 17:57:19.559	23.852	121.217	43	5.42	Taiwan AS*
20578273	1999 9 20 18:11:50.377	23.811	121.136		5.83	Taiwan AS*
20578492	1999 9 22 0:14:42.005	23.747	121.091	33	5.45	Taiwan AS
20581262	1999 9 25 23:52:53.459	23.774	121.158	37	5.46	Taiwan AS
20582713	1999 9 29 4:42:55.319	1.907	125.195	158	5.37	Molucca Passage
20582842	1999 9 29 18:01:28.201	-30.763	-71.902		5.43	Central Chile
20583432	1999 9 30 16:31:09.188	16.083	-96.800		5.95	Oaxaca
20590301	1999 10 10 7:03:01.547	-1.960	134.100		5.48	W. Irian
20591829	1999 10 13 1:33:38.755	54.691	-161.136	13	5.54	Alaska Pen
20595122	1999 10 16 9:46:45.597	34.541	-116.361		5.35	Hector Mine

% Given in the testbed database

* No MT solutions determined due to data overlap

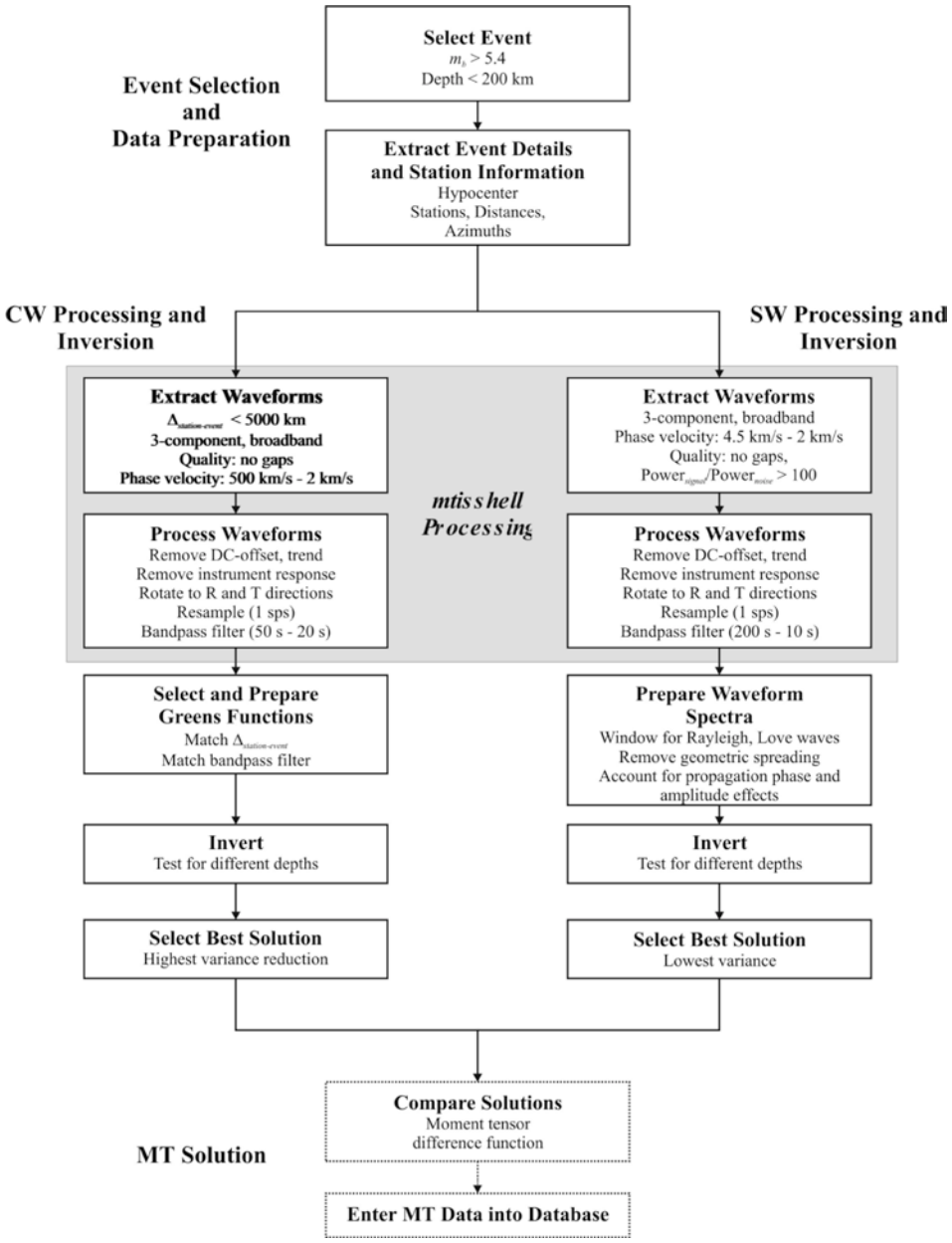

Figure 1. Flowchart describing the automated moment tensor data selection and processing procedure. Event selection parameters are given which characterize the events described in the following text.

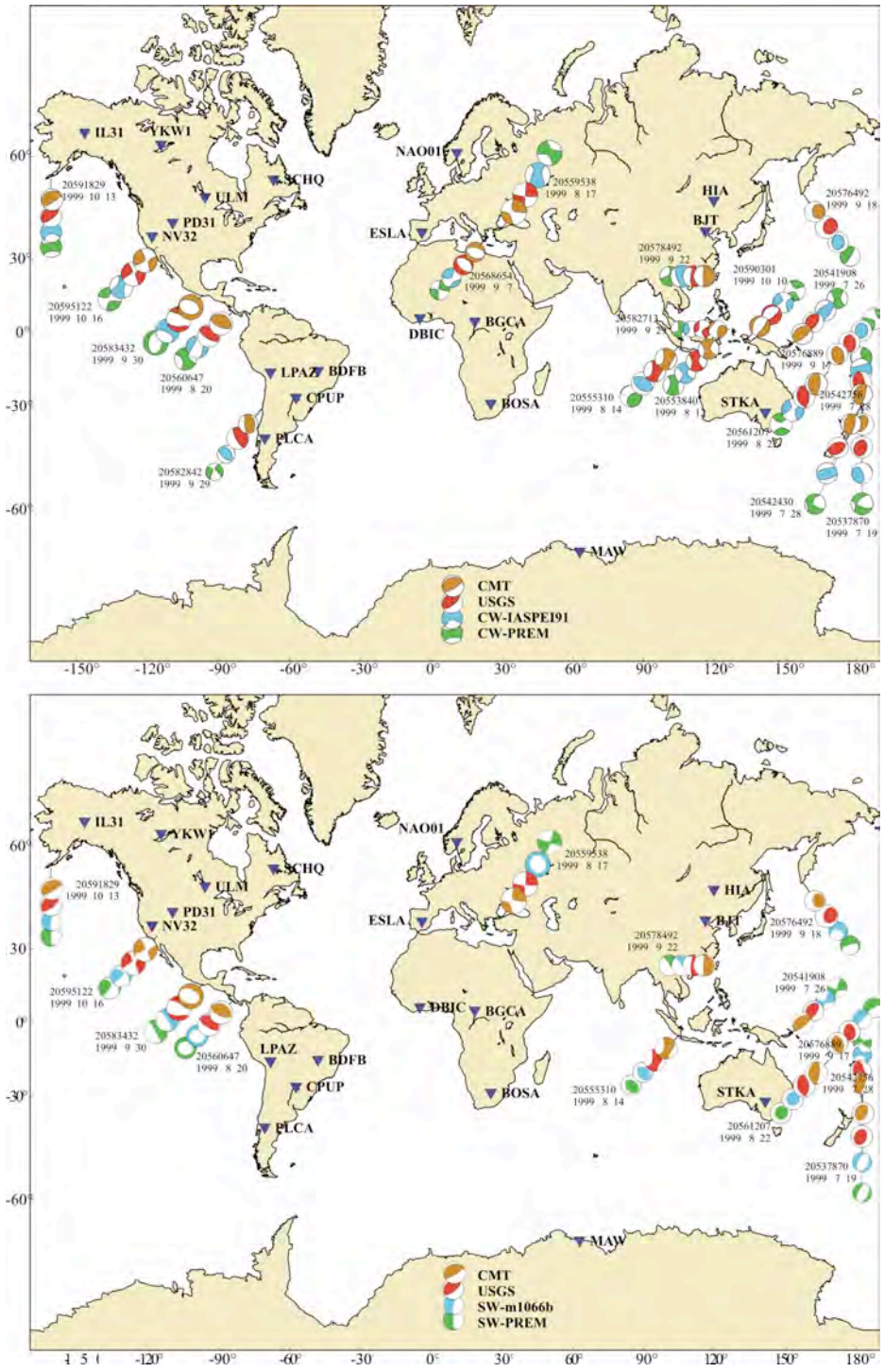

Figure 2. Maps showing the inversion results for the events of the test interval. Inverted triangles mark the locations of stations used in the inversions. The upper map compares results from the CW method using Greens functions based on the iasp91 **(blue) and the PREM (green) velocity models with moment tensors from the Harvard CMT (brown) and USGS (red) catalogs. The lower map compares moment tensors generated by the SW method using modes calculated from the velocity models 1066b (blue) and PREM (green) with those from the Harvard CMT (brown) and USGS (red) catalogs.**

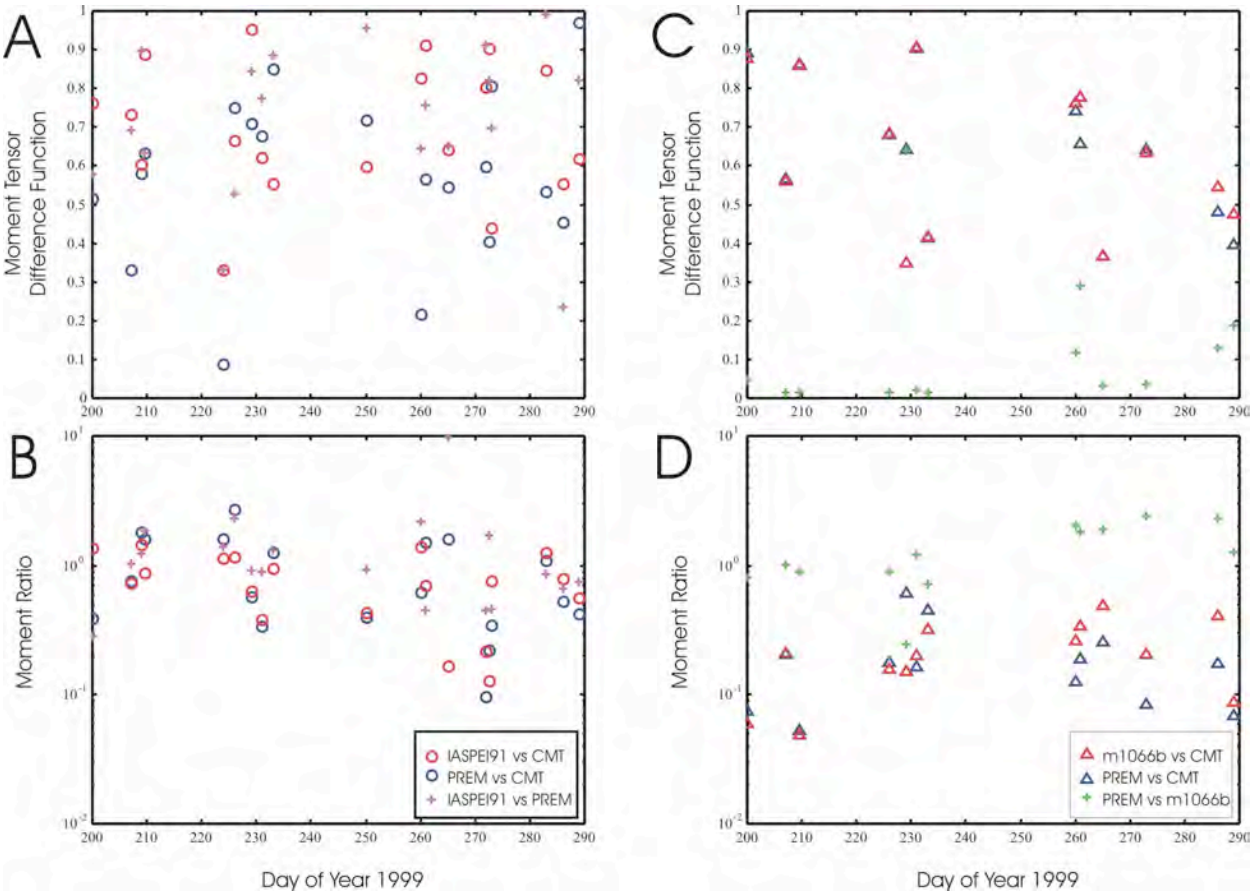

Figure 3. Quantitative comparison of moment tensor solutions from CW (A, B) and SW (C, D) with Harvard CMT results. A and C show the moment tensor difference function (Pasyanos *et al*, 1996). If the difference function is less than 0.5, the moment tensors are similar. B and D show the ratio between the moment of the event calculated using the various methods.

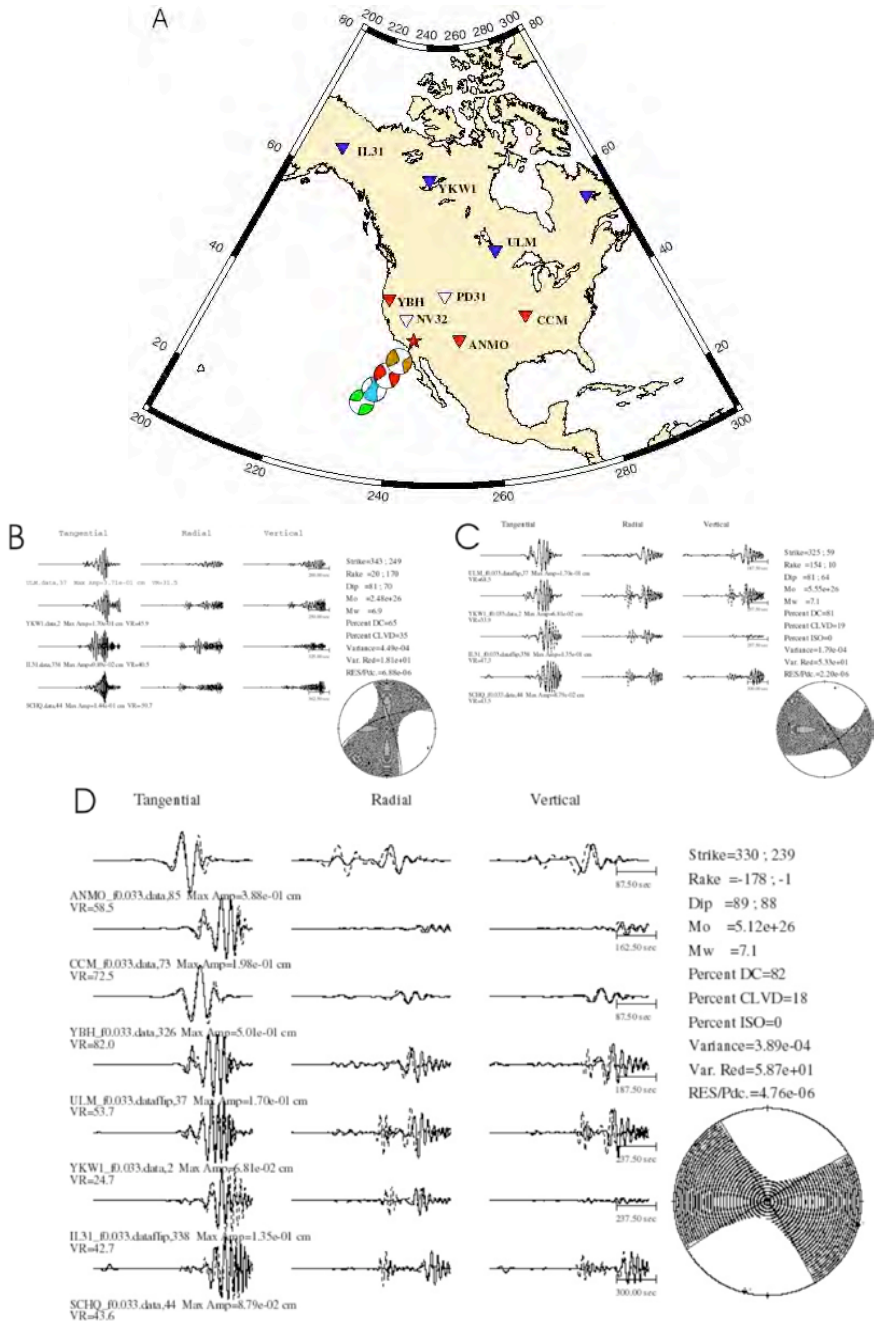

Figure 4. Complete waveform inversion of the Hector Mine event (origin ID 20595122, October 16, 1999). (A) The star shows the epicentral location. Data for the primary stations (filled blue inverted triangles) IL31, YKW1, ULM and SCHQ were extracted from the database. Data from primary stations (open blue inverted triangles) NV32 and PD31 were rejected as being too short. To improve and check the CW inversion, we requested data from the auxiliary stations (filled red inverted triangles) YBH, ANMO and CCM. This data was not available in the testbed database. The moment tensors are as given in Figure 2. (B) Automatic moment tensor solution. (C) Revised moment tensor solution. (D) Moment tensor solution including data from auxiliary stations. See text for discussion.

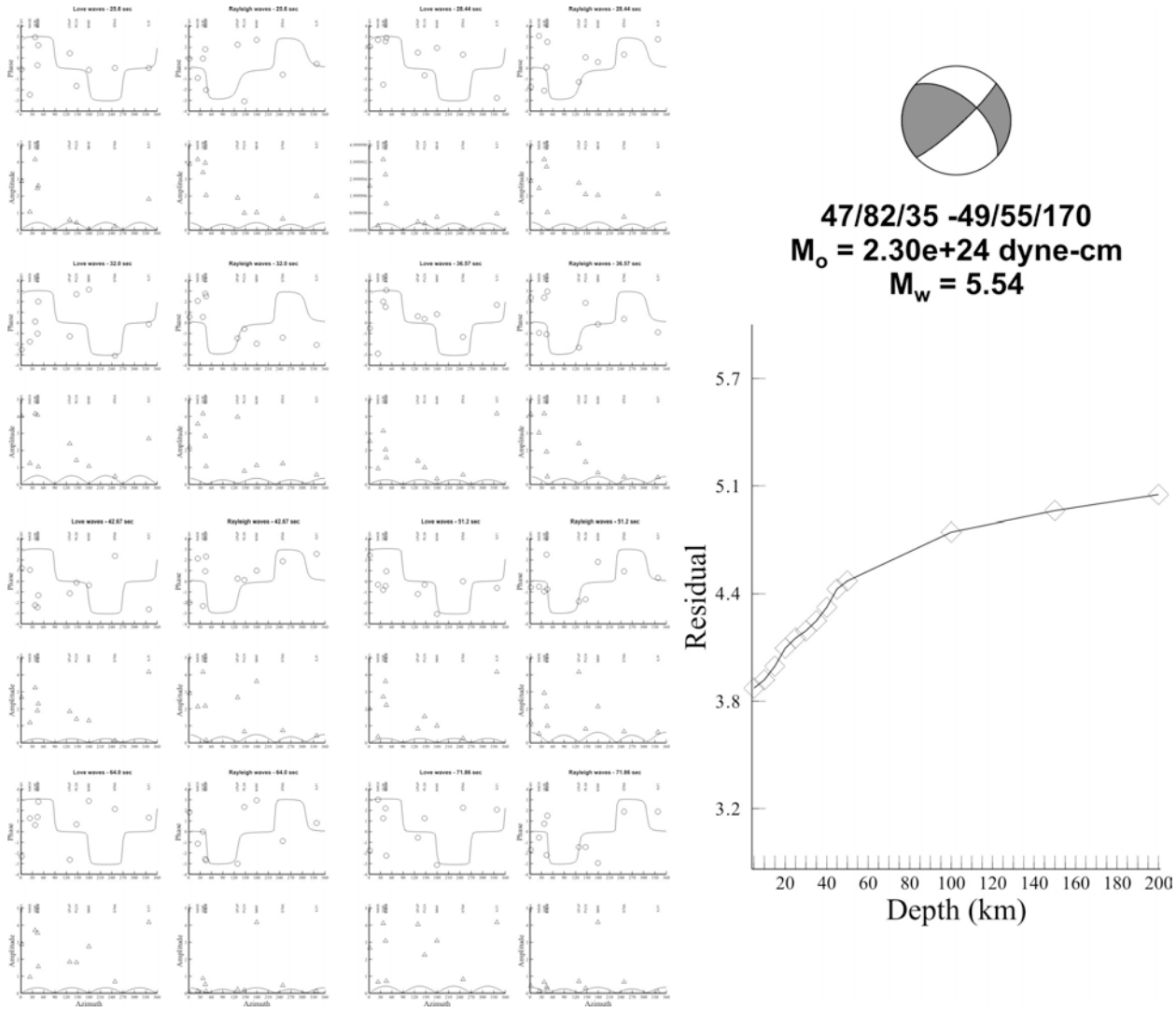

Figure 5. Surface wave inversion of the Hector Mine event (origin ID 20595122, October 16, 1999). The plots on the left show the phase and amplitude fits for the stations and frequencies used to generate the automatic solution. The plot on the right shows the source mechanism and the residuals. For this event, the best solution is found for a depth of 5 km, the shallowest depth used.

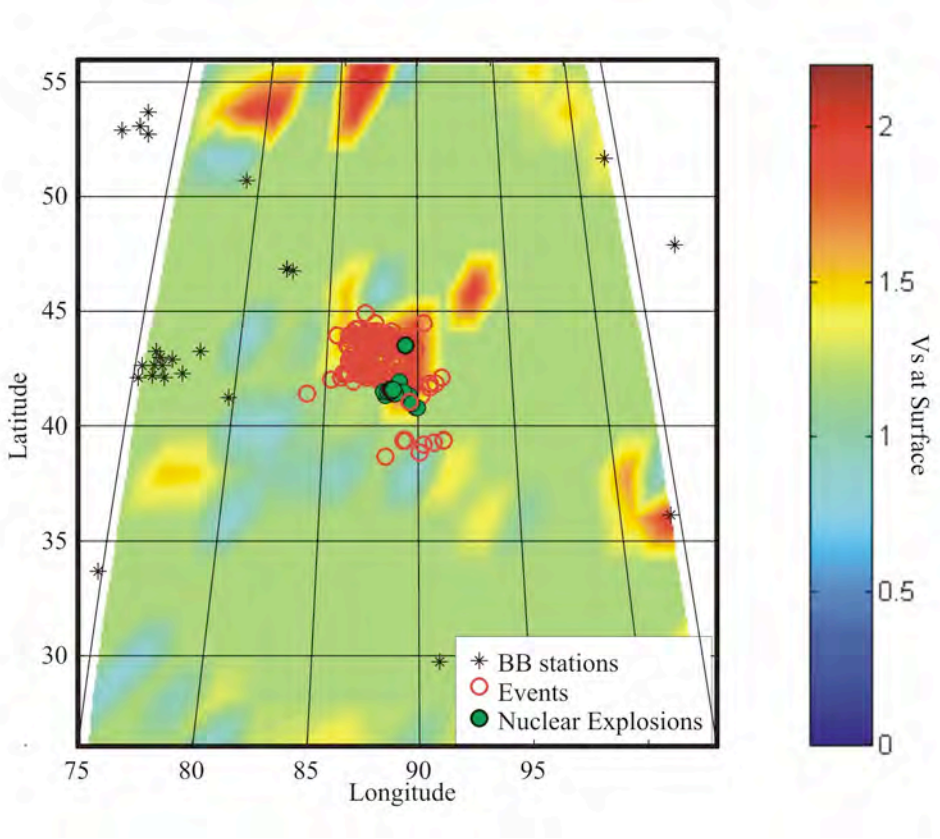

Figure 6. Lop Nor, the advanced concept demonstration region. Waveforms for 200 events, among them 25 nuclear explosions, have been collected for this region. The recordings come from 54 stations equipped with broadband instruments. The color map shows the S-wave velocity at the surface given by the model CUB1.0.

REGIONAL SEISMIC THRESHOLD MONIORING

T. Kværna, E. Hicks, J. Schweitzer, and F. Ringdal

NORSAR

Sponsored by Defense Threat Reduction Agency

Contract No. DTRA01-00-C-0107

ABSTRACT

A database comprising a total of 45 events, selected to provide the best possible ray path coverage of the Barents Sea and adjacent areas, was compiled and reanalyzed in a consistent manner. This resulted in new regional attenuation relations for Pn and Sn, together with a preferred average velocity model to be used for predicting the travel times of regional phases. We have now applied these attenuation relations to investigate a regional threshold monitoring scheme for the Barents Sea area.

A grid system with an approximately 100-km grid spacing was deployed for the Barents Sea region, and the observations at the arrays, ARCES, SPITS, FINES and NORES, were then used for calculating threshold magnitudes for each of the grid points. During an interval without seismic signals, the threshold magnitudes showed large variations over the region, and, in particular, in the vicinity of each array. However, for the region around the island of Novaya Zemlya, the variations are modest, varying around a mean of magnitude 2.1-2.2.

In order to investigate in more detail the variations in threshold magnitudes for the Novaya Zemlya region, we deployed a dense grid with an areal extent of about 500 x 500 km around the former Novaya Zemlya nuclear test site. For each of the grid nodes, we calculated magnitude thresholds for the two-hour time interval 00:00 - 02:00 on 23 February 2002. At 01:21:12.1 there was an event with a magnitude of about 3, located about 100 km northeast of the former nuclear test site.

Regions of different sizes were constructed by selecting grid points within different radii from the former nuclear test site. Average, minimum and maximum threshold magnitudes were calculated for circular regions with radii of 20, 50, 100 and 200 km, respectively.

The most important result is that even for a target region with radius as large as 100 km, the variations in threshold magnitudes are all within 0.2 magnitude units. This applies both for the time interval with the event and for background noise conditions. For the investigated station geometry, it will therefore be meaningful to represent the monitoring threshold of the entire Novaya Zemlya region with the values of a single target point, together with the *á priori* determined uncertainty bounds.

We can therefore conclude that the experimental site-specific threshold monitoring which has been run daily by NORSAR for the past 5 years, aiming at the Novaya Zemlya test site, can be used with only minor adjustments to assess the threshold within 100 km of the site. This monitoring has shown that between 16 August 1997 and 23 February 2002, the threshold level has been consistently below 2.5, except during “interfering” large regional or teleseismic events located well outside the target region.

For areas with larger variations in threshold magnitudes, like in the vicinity of the arrays, a 100-km radius target region will obviously show larger differences between the maximum and minimum values. Examples illustrating this point will be shown.

OBJECTIVE

The main objective of this research is to develop and test a new, advanced method for applying regional seismic array technology to the field of nuclear-test-ban monitoring. To that end, we address the development and testing of a method for optimized seismic monitoring of an extended geographical region, using a sparse network of regional arrays and three-component stations. Our earlier work on optimized site-specific threshold monitoring serves as a basis for the development of this new method. Emphasis of the research is on algorithms that can be efficiently applied in a real-time monitoring environment, that are using primarily automated processing, and that can be readily implemented in an operational Comprehensive Nuclear-Test-Ban Treaty (CTBT) monitoring system.

RESEARCH ACCOMPLISHED

Travel times and attenuation relations for regional phases in the Barents Sea region

A database containing 45 events in the Barents Sea region (Figure 1) has been compiled and analyzed with the aim of evaluating crustal models, travel times, and attenuation relations in the context of performing regional detection threshold monitoring of this region. The 45 events are mostly located around the circumference of the study area due to the virtually aseismic nature of the Barents Sea itself. Regional Pn and Sn phases were observable for most events in the database, while Pg and Lg phases were only observable for events with ray paths that do not cross the tectonic structures in the Barents Sea. This corroborates a number of previous observations of Lg-wave blockage within the Barents Sea.

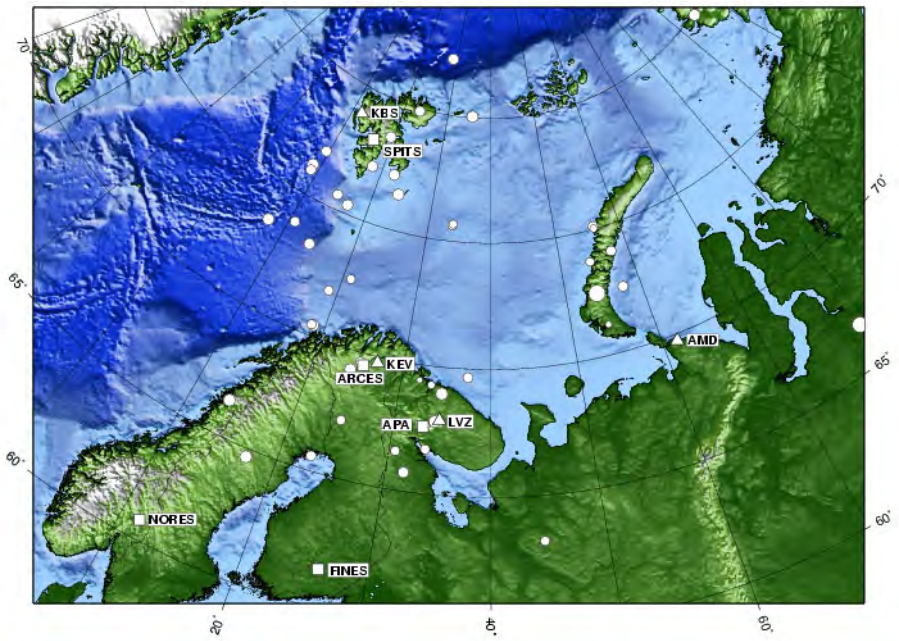

Figure 1. EVENTS (circles) and seismic stations used for deriving wave propagations characteristics of the Barents Sea and surrounding areas. Array stations are shown as squares, while three-component stations are shown as triangles. The symbol sizes for the events are proportional to the network magnitudes.

In order to estimate magnitudes, short-term average (STA) and spectral amplitude values were calculated in several frequency bands for all phase arrivals in the data base. There were no significant differences between spectral and STA amplitudes, so the latter were used since this parameter is more efficient to calculate in real-time processing. A joint inversion of the regional phases Pn, Pg, Sn and Lg was performed in order to determine attenuation relations specific for this region according to the relation given in Equation 1.

$$\mathbf{M_L} = \log\mathbf{A} - \log\mathbf{e} \cdot \alpha_{\mathbf{i}}^{0} \cdot \mathbf{f} + (\mathbf{a_i f} + \mathbf{b_i})\log\left(\frac{200}{\Delta}\right) + \delta_{\mathbf{ik}} + 1.66 \qquad (1)$$

where A is observed STA amplitude within a frequency band with logarithmic center frequency f, Δ is epicentral distance, the α^0_i term represents the total attenuation for phase i out to the reference distance of 200 km, and a_i and b_i are phase-dependent attenuation constants. The inversion results for the parameters α^0, a and b are given in Table 1.

Table 1. The inversion results for the a, b and a0 coefficients (±1s) for Pn, Sn, Pg and Lg phases used in the attenuation relation (Equation 1).

Phase	a	b	α
P_n	-0.002 ± 0.023	2.340 ± 0.099	0.584 ± 0.030
S_n	0.141 ± 0.028	2.021 ± 0.110	0.419 ± 0.037
P_g	0.091 ± 0.084	0.851 ± 0.366	-0.538 ± 0.035
L_g	0.534 ± 0.062	-0.186 ± 0.123	-0.609 ± 0.063

Figure 2 shows a comparison between the phase magnitude residuals calculated using the relations and parameters of Jenkins *et al*. (1998) and our inversion results. Our results using the relations and parameters of Jenkins *et al*. (1998) revealed a relatively high scatter between individual station and phase magnitudes, and also some systematic inconsistencies, most notably magnitudes calculated from different frequency bands at the same station. Magnitudes calculated from STA values in the 2- to 4-Hz passband are mostly higher than magnitudes calculated in the 3- to 6-Hz passband, which again are generally higher than magnitudes calculated from the 4- to 8-Hz passband. The coefficients used in this case were determined using data from eastern North America, central Asia, and Australia. However, this relation is not primarily intended for local magnitude calculation, and some of the scatter in the magnitudes from Pg and Lg arrivals in particular may be due to the small distance for some of these observations, below the lower distance limit of 1.8° used by Jenkins *et al.* (1998).

Phase magnitudes calculated using Equation 1 and the parameters of Table 1 are shown to the right of Figure 2. These results show that the scatter (expressed as standard deviation) was significantly reduced compared to the original calculations. There is also no apparent frequency dependency in the magnitude residuals.

As an example we show in Table 2 the individual phase magnitude estimates of the 23 February 2002 event located on the northeastern coast of Novaya Zemlya. The consistency of these phase magnitudes is remarkably high.

Table 2. Phase magnitudes and network magnitudes for the 23 February 2002 event located on the northeastern coast of Novaya Zemlya, using the attenuation relations developed in this study.

Station	Phase	Distance	Magnitude
AMD	Pn	509	3.19
AMD	Sn	509	3.15
LVZ	Pn	1055	3.22
LVZ	Sn	1055	3.01
SPITS	Pn	1095	3.44
SPITS	Sn	1095	3.11
ARCES	Pn	1144	2.97
ARCES	Sn	1144	3.08
KBS	Pn	1197	3.16
KBS	Sn	1197	3.19
FINES	Pn	1850	3.17

Magnitude Type	Magnitude
Network Pn	3.19
Network Sn	3.11
Network All	3.15

Figure 3 shows comparisons of corrected network magnitudes compared to magnitudes calculated from individual phases. Although relative P and S magnitudes could be used as an aid in discriminating earthquakes and explosions, Figure 3 shows that regional path effects in this area also give rise to substantial differences in magnitude. This is particularly visible for Pn and Sn magnitudes, as they are available for events covering the entire region. Events that predominantly have ray paths within Fennoscandia have larger Sn magnitudes, while the opposite is true for events that have ray paths crossing the sediment basins of the Barents Sea (Novaya Zemlya/Kara Sea and the western Barents Sea/Mid-Atlantic ridge areas).

From this study, it is clear that Pn and Sn are the most useful phases for calculating magnitudes for events in the Barents Sea. In fact, Figure 3 shows that Pg and Lg are mainly observed at close epicentral distances (< 300 km). This situation is quite different from what we have previously found for the Scandinavian Peninsula and the Baltic Shield, where Lg is the dominant phase on the seismogram out to at least 1000 km. Thus, even for a stable continental region, one may expect quite significant regional variations in the magnitude correction factors.

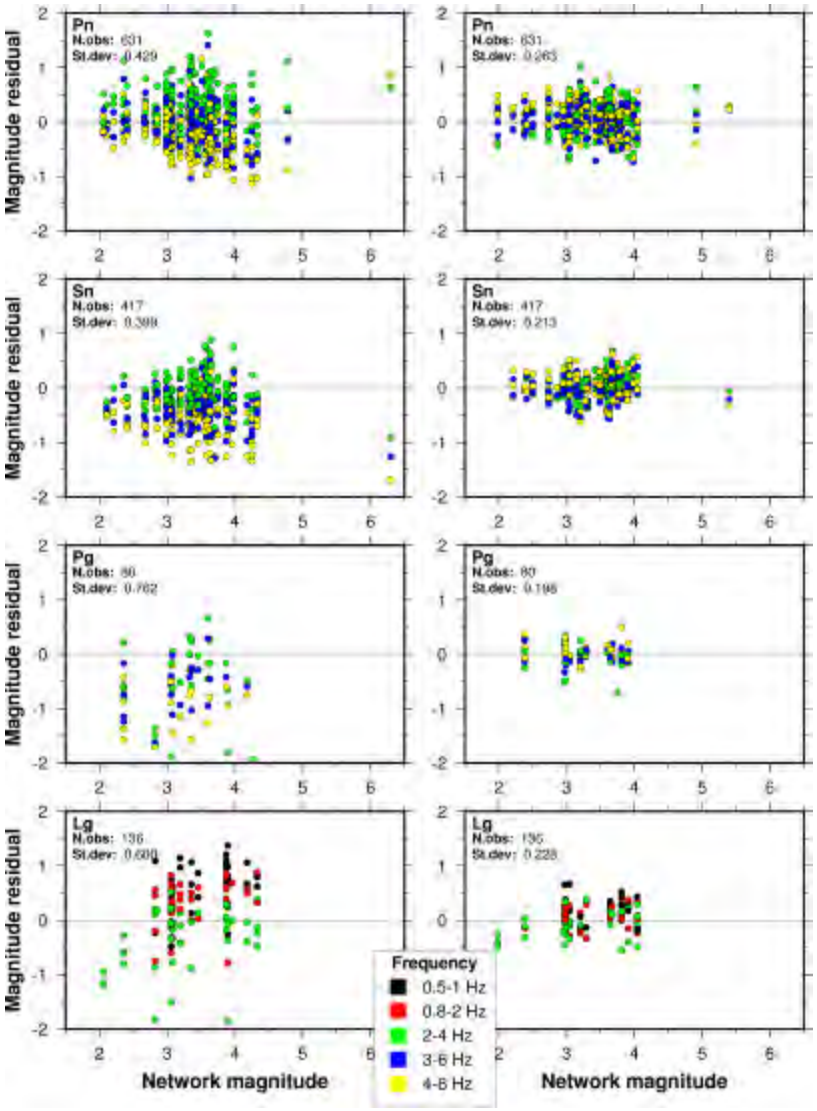

Figure 2. Magnitudes calculated using the relation from Jenkins *et al*. (1998) (left) and this study (right) from individual amplitude readings, plotted vs. network magnitudes for the 45 events. Note the significant reduction in scatter (St. Dev.) and also the absence of frequency-dependent effects when the relation from this study is used.

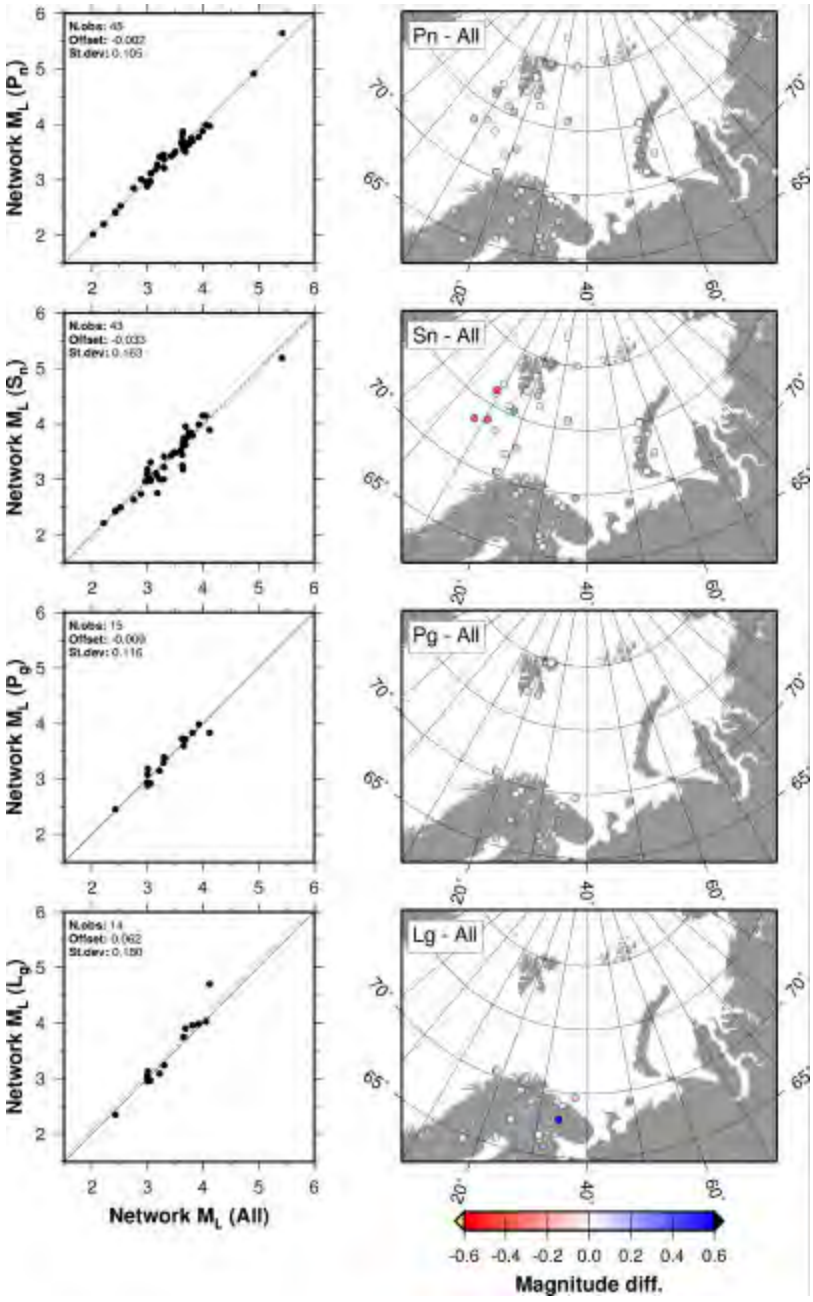

Figure 3. Network event magnitude comparisons and maps of the geographical distribution of the magnitude differences for individual phase magnitudes compared to network magnitudes. Note that Sn magnitudes are overestimated for events that have paths predominantly within the Baltic Shield, while events with paths that cross the Barents Sea have lower Sn magnitudes. Pg and Lg magnitudes appear to be quite stable within the limited distance range from which readings are available.

Regional Threshold Magnitudes

Using the developed attenuation relations described above, observations at the arrays ARCES, SPITS, FINES and NORES were used for calculating threshold magnitudes for a grid system covering the entire Barents Sea region. The grid spacing was approximately 100 km. Figure 4 shows the threshold magnitudes during a time instant without seismic signals. We find large variations over the region, and in particular when approaching each of the arrays. However, for the region around the island of Novaya Zemlya (NZ) the variations are modest, varying around a mean of magnitude 2.2.

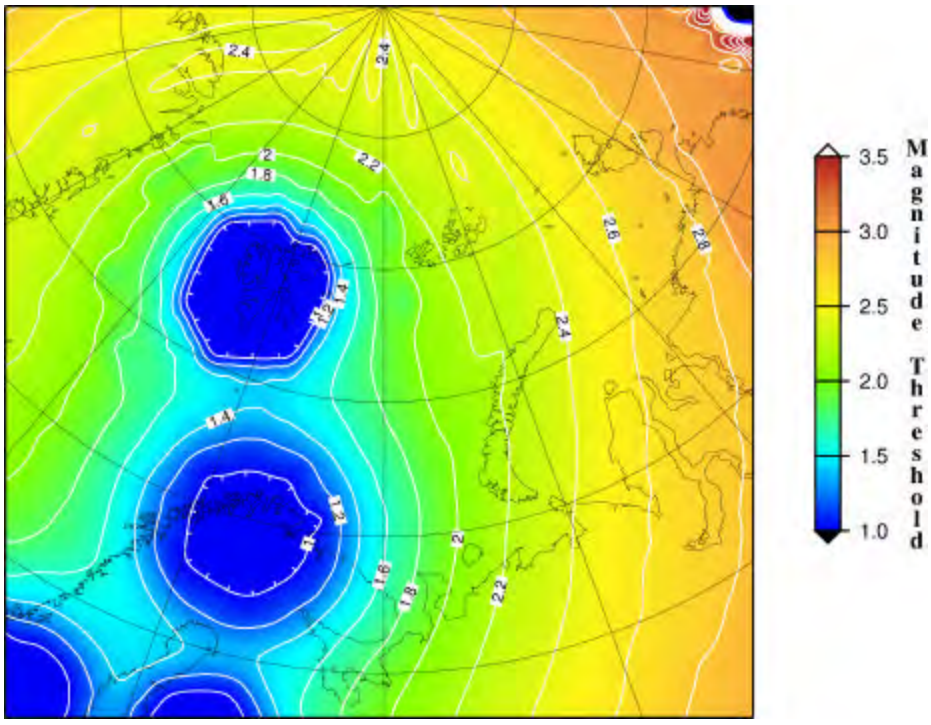

Figure 4. Threshold magnitudes for the time instant 2002-054:01.11.20.0. Notice the improved monitoring capability in the vicinity of each station. For distances above 1.5 degrees of each station, we have considered the Pn and Sn phases, whereas Pg and Lg have been used for distances less than 1.5 degrees.

In order to investigate in more detail the variations in threshold magnitudes for the Novaya Zemlya region, we deployed a dense grid with an areal extent of about 500 x 500 km as shown in Figure 5. For each of the grid nodes, we calculated magnitude thresholds for the two-hour time interval 00:00 - 02:00 on 23 February 2002. At 01:21:12.1 there was an event with a magnitude of about 3.2 (see Table 2), located about 100 km northeast of the former nuclear test site.

Regions of different sizes were constructed by selecting grid points within different radii from the former nuclear test site. Figure 6 (left) shows the variations in threshold magnitudes for a circular region with a radius of 20 km around the test site. The blue line shows the average threshold, whereas the red lines represent the minimum and maximum values. Figure 6 (right) shows similar curves for a region with radius 100 km.

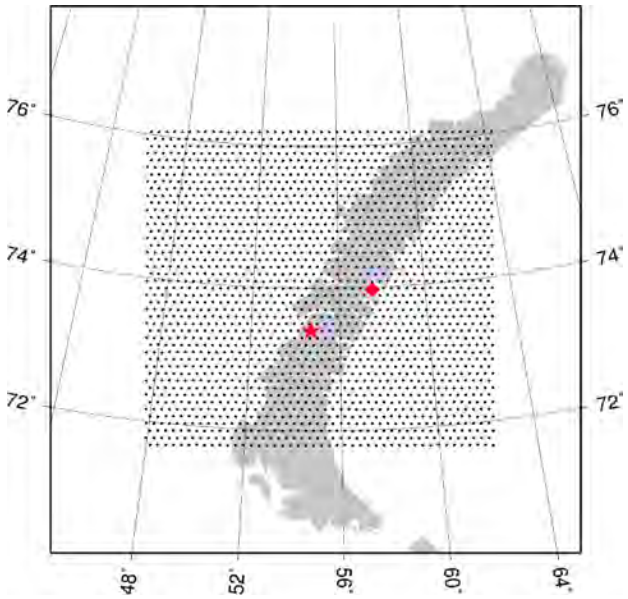

Figure 5. Dense grid deployment around Novaya **Z**emlya (grid spacing 11 km). The red star shows the location of the former nuclear test site, whereas the red diamond shows the location of the event on 23 February 2002 with origin time 01:21:12.1.

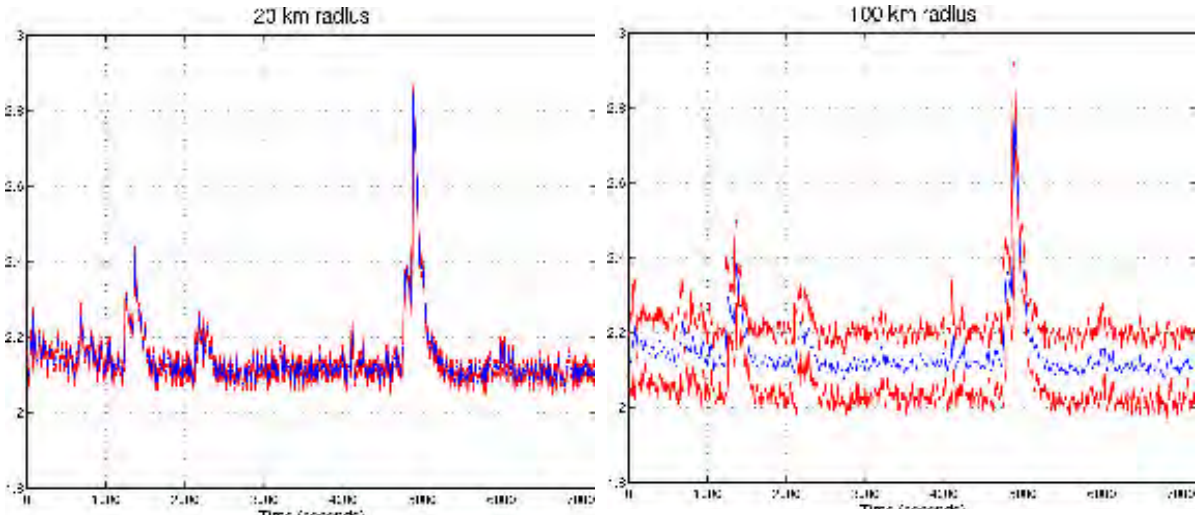

Figure 6. Threshold magnitudes for the time interval 00:00 - 02:00 on 23 February 2002 for 20-km (left) and 100-km (right) radius target regions centered around the former nuclear test site. The peak at about 5000 seconds corresponds to signals for the 3.2 event located about 100 km northeast of the test site.The blue line shows the average threshold, whereas the red lines represent the minimum and maximum values.

It is interesting to notice that even for a region with 100-km radius, the variations in threshold magnitudes are all within 0.2 magnitude units. For this particular configuration of the monitoring network relative to the target area, it will therefore be meaningful to represent the monitoring threshold of the entire region with the values of a single target point, together with uncertainty bounds as shown in Figure 6. For areas with larger variations in threshold magnitudes, like in the vicinity of the arrays, a 100-km radius target region will obviously show larger differences between the maximum and minimum values.

We would like to comment on the threshold magnitude of the peak corresponding to the event located northeast of the test site. In cases where an event actually occurs in the target region, the magnitude thresholds will often be biased slightly low. In Figure 6 we find a maximum value of about 2.9, whereas the event magnitude is estimated to be 3.15. In such cases a maximum-likelihood magnitude estimation algorithm should be activated. However, for small events with a size close to the threshold magnitudes, this bias will not be significant.

Regional threshold monitoring including the Amderma Station

The Kola Regional Seismic Center (KRSC) group in Apatity, Russia, has provided us with about three days of continuous data from the station in Amderma, located on mainland Russia, just south of the island of Novaya Zemlya. The data interval is centered around the origin time of the 23 February 2002 event located on the northeastern coast of Novaya Zemlya. In addition, data from the array in Apatity on the Kola Peninsula were included.

Figure 7 shows the threshold magnitudes during an instant without seismic signals, using the developed attenuation relations for Pn, Pg, Sn and Lg. We find large variations over the region, and in particular when approaching each of the arrays. With the Amderma Station included, we also find significant variations for the island of Novaya Zemlya, ranging from 1.4 at the southern tip to 2.2 at the northern tip. This implies that a regional threshold monitoring scheme for the NZ region has to be divided into geographical sub-regions having similar threshold magnitudes during background noise conditions.

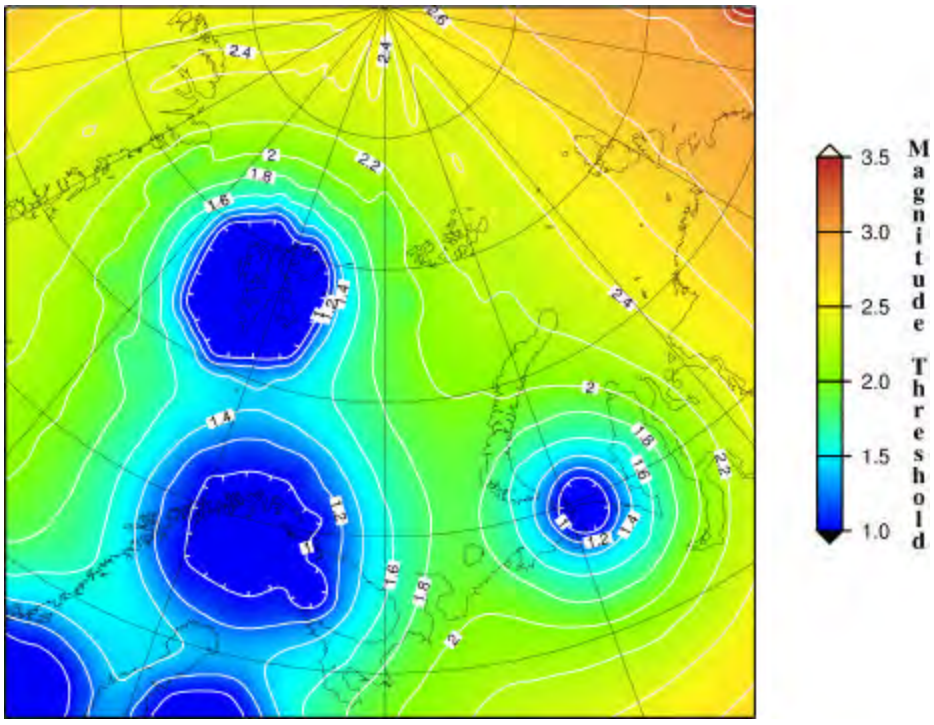

Figure 7. Threshold magnitudes for the time instant 2002-054:01.11.20.0, including data from the Amderma Station and the Apatity Array. Notice the improved monitoring capability in the vicinity of the Amderma Station as compared to the thresholds shown in Figure 4.

CONCLUSIONS AND RECOMMENDATIONS

The pattern of Lg arrivals and associated amplitudes supports the previously published indications that the deep sediment basins and Moho topography under the Barents Sea efficiently block Lg wave energy from crossing. From this, it is clear that Pn and Sn are the most useful phases for calculating stable and consistent magnitudes for events in the Barents Sea.

The 'BAREY' model from Schweitzer and Kennett (2002), based on a model for the Barents Sea area from Kremenetskaya *et al*. (2001), provides the smallest overall travel-time residuals when locating events within the vicinity of the Barents and Kara Seas.

The attenuation in the Barents Sea region differs somewhat from that observed in other stable tectonic regions, as evidenced by the fact that the coefficients given by Jenkins *et al.* (1998) for such regions do not give consistent magnitudes across frequencies, phases and stations for our amplitude observations from the events in the Barents Sea region.

Amplitude inversion has been used in this study to resolve new attenuation coefficients and station corrections for estimating magnitudes from STA amplitude observations for Pn, Pg, Sn and Lg phases in the Barents Sea region. The distance range of observations on which the Pg and Lg relations are based is limited; a future study using a greater number of continental events could most likely provide a relation for STA-based Lg magnitudes that is applicable at larger distances, albeit limited to paths within Fennoscandia.

The seismic station in Amderma can be tied in to the regional network in Fennoscandia and on the Svalbard Archipelago using an appropriate crustal model, and is able to provide important information regarding the location of events in the eastern parts of the Barents Sea and the Kara Sea (Schweitzer and Kennett, 2002). Magnitudes calculated at this station are, on the whole consistent, with the other observations.

For the time interval under study, the seismic arrays ARCES, SPITS, FINES and NORES provide an average monitoring capability of about magnitude 2.2 for the island of Novaya Zemlya. For a region with a 100-km radius around the former nuclear test site, the variations in threshold magnitudes are all within 0.2 magnitude units. It will therefore be meaningful to represent the monitoring threshold of the entire region with the values of a single target point, together with uncertainty bounds as shown in Figure 6.

In cases when data from the Amderma Station can be retrieved, we find significant variations in threshold magnitudes over the island of Novaya Zemlya, ranging from 1.4 at the southern tip to 2.2 at the northern tip. For the actual time interval, the monitoring capability for the former nuclear test site is lowered by about 0.3 magnitude units to about 1.9. This implies that a regional threshold monitoring scheme for the NZ region has to be divided into geographical sub-regions having similar threshold magnitudes during background noise conditions.

REFERENCES

Jenkins, R.D., T.J. Sereno, and D.A. Brumbaugh (1998), Regional attenuation at PIDC stations and the transportability of the S/P discriminant. AFRL-VS-HA-TR-98-0046, Science Applications International Corporation, San Diego, CA, USA.

Kremenetskaya, E., V. Asming, and F. Ringdal (2001). Seismic location calibration of the European Arctic, *Pure Appl. Geophys.* **158**, 117-128.

Schweitzer, J. and B.L.N. Kennett (2002), Comparison of location procedures - the Kara Sea event 16 August 1997, Semiannual Technical Summary, 1 July - 31 December 2001, NORSAR Sci. Rep. 2-2001/2002, Kjeller, Norway, 97-114.

GROUND TRUTH DATA IN INDIA AND CHINA FROM DENSE LOCAL NETWORKS AND CALIBRATION EXPERIMENTS

Walter D. Mooney and Shane Detweiler

US Geological Survey, Menlo Park

Sponsored by National Nuclear Security Administration
Office of Nonproliferation Research and Engineering
Office of Defense Nuclear Nonproliferation

Contract No. DE-A104-98Al79758

ABSTRACT

Obtaining and interpreting qualified, regional geologic and geophysical data from countries such as India and China has been an important scientific and technical goal for many years. To aid in this effort, the U.S. Geological Survey has been building relationships with comparable government organizations throughout Asia. Here we present preliminary results from this interaction in the form of ground truth and crustal structure information for India and China.

We have successfully developed a cooperative program with Indian scientists over the past several years. During that time, delegations from Indian geophysical laboratories have made multiple visits to Menlo Park, CA, bringing with them new seismic data and crustal structure information. We have been very pleased to achieve such unprecedented access to data and their interpretation. During the most recent visit, shallow seismic refraction data from NE India (Kutch region), near the epicenter of the 2001 Bhuj earthquake and in close proximity to the Indian nuclear test site, were processed and interpreted. Another highlight of this cooperation has been the release of aftershock data. This data has relocated hypocenters determined from 18 local seismic stations and were obtained during a visit to India.

We continue our ongoing program of collecting crustal structure and ground truth information from China as well. This effort has likewise been a great success as delegations from many organizations within China have shared data and offered cooperation over the years. We are currently reprocessing data from a 1000-km-long seismic refraction profile centered at 36° N and 104° E. There are 9 borehole chemical shots on this profile, each with 3000-4000 kg charges. The resulting P-wave and S-wave arrivals are excellent. The large borehole explosions will likely have been recorded at seismic monitoring sites, and will serve as valuable ground truth events. In addition, we are working with Chinese seismic network catalog data that provide excellent ground truth seismic events.

OBJECTIVE

This research is aimed at continued cooperation between the U.S. Geological Survey and counterpart agencies in Asia to exchange data and interpretations of crustal structure, and hypocentral locations. With our colleagues from the National Geophysical Research Institute (Hyderabad, India) and the China Seismological Bureau (Beijing, China), we have been successful at initiating and completing a number of seismic studies in areas that are of great importance for nuclear test monitoring. The 2001 Bhuj (western India) earthquake has triggered widespread discussion in the scientific community about the nature and the causes behind such intra-plate earthquakes, and this, in turn, has led to joint work agreements between the USGS and NGRI. This is fortuitous as the Kutch region is just south of the Indian nuclear test site, and the joint study has yielded access to previously unavailable data in the region. In China, we have focused on obtaining the crustal structure of the 1000-km-long Project 973 profile through central China. In addition, large explosions along this line at close proximity to receivers provide excellent ground truth events.

Here, we first make an effort to summarize the available information about the destructive 2001 Bhuj and other major earthquakes in Kutch and their tectonic setting. We shall also try to assess the basic data gaps that need to be filled for understanding the Kutch crustal structure, and thereby will be in a better position to characterize events that occur in the region. Following this, we will describe the area of China where we have newly available information.

RESEARCH ACCOMPLISHED

India

The Kutch region forms a crucial geodynamic part of western continental margin of the Indian sub-continent, and falls in the seismically active Zone-V outside the Himalayan seismic belt. It extends for approximately 250 km (E-W) and 150 km (N-S), and is flanked by Nagar Parkar Fault in the north and the Kathiawar Fault in the south (Fig. 1). The portion bounded between these two faults also contains several E-W trending major faults including the Katrol Hill Fault, Kutch Mainland Fault, Banni Fault, Island Belt Fault and Allah Bund Fault (Biswas, 1987).

The Kutch tectonic setting owes its origin to Mesozoic tectonic events initiated during the break-up of Gondwanaland and the northward drift of the Indian plate. The rift basin evolved as a consequence of this break-up and was controlled by a series of normal faults, which are still exposed in the region. Movement along these faults under an extensional regime produced a number of horsts and grabens.

The Kutch landscape can be categorized into four major E-W trending geomorphic zones (Malik *et al*., 2000). They are: the coastal zone - demarcating the southern fringe, the Kutch mainland - forming the central portion of the rocky uplands, Banni-Plains marked by raised mud flats, and the Great Rann in the north and the Little Rann in east comprising vast saline-waste land. The boundaries of these geomorphic zones are bounded by major faults. The rocky mainland is characterized by the uplifts exposing folded Mesozoic rocks. All the major uplifts are bounded, at least on one side, by a fault or a sharp monoclinal flexure, on the other side by gently dipping Tertiary strata and the peripheral plains that merge gently into the surrounding residual depression.

The Kutch Mainland Fault marks the northern fringe of the rocky mainland. This fault is a vertical to steeply inclined normal fault, but changes upwards into a high angle reverse fault (Biswas, 1987). The central part of the rocky mainland has been upthrown along the longitudinal Katrol Hill Fault (Malik *et al*., 2000).

The Mw=7.6 Bhuj, western India earthquake occurred early in the morning of January 26, 2001. The epicentral coordinates of the main shock obtained from teleseismic data as reported by the USGS to be 23.36°N and 70.34°E. The focus of the earthquake was placed at 22 km. Aftershocks outline an ENE trending south-dipping thrust (45°-50° dip) to great depths (20-30+ km). Later results show concentrated patches of relocated aftershocks that dip to the south between 6 and 37 km deep (Raphael *et al*., 2001). The long-period source time function shows a relatively simple source of about 15 seconds duration. Mori *et al*., (2001) report that the largest area of slip was close to the hypocenter. This asperity is about 10 km x 20 km with a maximum slip of about 10 meters for a rupture velocity of 2.9 km/s. The area of the fault is small for such a large event.

It is interesting to note that Antolik and Dreger's (2001) waveform inversion results also favor the presence of a second sub-event located at shallower depth above and slightly west of the rupture initiation containing as much as 6 m of slip. This sub-event occurs near an area of intense lateral spreading and ground deformation observed in the field, indicating the possible presence of shallow slip although the fault rupture appears not to have reached the surface. They, however, found the overall source parameters (short duration, high stress drop) in line with observations from other intra-plate earthquakes.

The recent Kutch event is about 50 km southeast of the 1819 Kutch (i.e. Allah Bund) event (Mw=7.8), which also originated on a thrust fault (Bilham, 1998). The inferred 50-70 deg N-dipping fault plane (slip>11m) beneath Allah Bund was unfavorably steep for reverse faulting, presumably requiring high fluid pressure in the nucleation zone, according to Bilham (1999). Rajendran and Rajendran (2001) concluded occurrence of another similar sized event 800-1000 years ago from paleo-liquefaction studies. Kaila *et al*. (1972) from statistical analysis computed a return period of 200 years, which is quite close to the time interval between 1819 and 2001 events. More recently, in 1956, a Mw=6.0 event occurred near Anjar town, which also had a thrust mechanism (Chung and Gao, 1995).

Looking at the possible origin of Kutch seismicity, we find that the focal mechanism studies of all the major earthquakes indicate thrust motions on nearly westerly striking planes and, as such, appear to reflect an approximately northerly compressive stress in the crust that would be expected with the ongoing northward collision of India into Eurasia. A change from rift-related extension to north-south compression probably occurred about 40 Ma ago, subsequent to the collision of India with Asia. Low-angle reverse faults exposed in this region provide geologic evidence for such a tectonic reversal, which is indicated also by the thrust-type focal mechanisms. The stress field oriented in the N-S to NNE-SSW direction is considered to be responsible for this reversal of movement and the ongoing deformation (Rajendran and Rajendran, 2001). As well, the Kutch region may be subjected to high and complex stress because of its proximity to the India, Arabia, Asia triple junction, which is located about 500km to the west (Gupta *et al*., 2001). An additional source of stress in the Kutch area might be loading by the Indus delta (Seeber *et al*., 2001).

A good velocity model will improve the hypocenter locations, and thereby identification of active faults. A well-planned seismic reflection study may also image the causative lower crustal fault of the 2001 event, which might have propagated down. If we can image the proper geometry of the fault system, we will be able to assess how the disposition of faults and their interconnection affect/perturb the ambient plate tectonic stress field.

At present, there is far too little information about the Kutch region to completely define the tectonic setting, however this has afforded us an excellent opportunity to share data and research techniques with our Indian counterparts. The data we present here are considered a continuing step in our efforts to work with the Indians. Several issues must be settled before an acceptable model for Kutch seismicity emerges, which will satisfy various observational data sets. We still lack a first order crustal velocity model of the Kutch region. Though we have some knowledge about the geologically mapped faults, we are totally unaware of the disposition of blind faults and thrusts in the crust. Very first information of immense importance is about the thickness, geometry and velocities of this complicated rifted crust. This information may tell us about the age of the crust and its later orogenic history. This will also tell us if there is any systematic difference in the crust between the seismogenic and non-seismogenic parts of the Kutch region. In turn, this information will aid us a great deal in creating accurate crustal models of the area for the purposes of nuclear test monitoring.

Velocity Modeling

In the Kutch region, seismic refraction data was collected, using two 60-channel DFS V recording stations up to a maximum shot-receiver distance of 48 km. The receiver spacing was maintained at 100 m, while the shot point interval was kept as 7 to 8 km. The shot holes drilled up to 20-30 m have been utilized to detonate high-energy explosives. The charge size varied from 50 to 500 kg, depending upon shot-receiver distance.

The data that had been selected for processing at USGS was initially processed at NGRI by utilizing only first arrival refraction data. No attempt was made to utilize near vertical and wide-angle reflection data. The hypocenters of the main and aftershocks of 2001 Bhuj earthquake reportedly lie mainly in the lower crust. After a detailed discussion, we have initiated an effort to reexamine data of some shot points, particularly for the seismic signatures coming from sub-basement features and the base of the crust. We have enhanced the signals of post 5s seismograms

by applying automatic gain control (AGC) and suitable band-pass filters. A few intra-crustal reflections and the reflections from the Moho could be clearly identified. As an experiment, we have subjected this data to stacking, and Kirchhoff pre-stack depth migration. This experiment was done for a small segment with 4 shot points in the vicinity of the 2001 epicentral area (segment C), in addition to the other two segments (B, A) shown in Fig. 1. For depth migration, the aftershock derived sub-basement velocity-depth function (Rastogi *et al*., 2001) has been utilized for the main segment between Anjar and Adhoi, falling in the epicentral area. The average velocity model derived from first arrival refraction data has been used for the column down to the basement. Since one can expect shallower depths to the Moho near the coast, some alterations have been made in the velocity models of other segments for depth migration. Care has been taken to only process subbasement reflection data, as the upper sectional details are restricted.

The 35-km-long main segment (C) of refraction profile between Anjar and Adhoi, shows significantly good reflectivity in the entire mid and lower crustal column (Fig. 2) with prominent reflection horizons at an average depth of 10 km,18-20 km and 30 km. The strong reflection horizon, identified as Moho, has a significant northward dip with depth of about 37 km at the southern end of the segment to almost 47 km at the northern end. At around common depth point (CDP) 200, one can notice a significant change in the pattern of Moho, with Moho assuming a thick lens-like structure. At the southern end of this lens, one can notice the emergence of a possible fault/thrust. From the surface this fault has a southward dip. Also, at the southern end of the segment one can notice the presence of a strong subcrustal reflector at a depth of ~ 57 km. The diffused and disturbed nature of reflectivity at the northern region of the profile has obliterated this reflector. The nearly 35-km-long southern coastal segment (A), depicts good reflectivity in the entire crust (Fig. 3), with the most prominent reflections occurring at an average depth of 5-6 km, and in patches at 10 km and 20 km. The third reflector horizon as a strong band of reflections has a clear eastward updipping trend, with the depth varying from 26 km at the western end to about 18 km at the eastern end of the profile. The Moho, identified as thick zone of 2-3 km thickness, is nearly horizontal all through the profile with an average depth of 35 km. As in the case of the main segment (C) one can notice reflectivity even at sub-Moho depths, with a reflection horizon at an average depth of ~ 47 km.

A close look at the Moho configuration along the three segments suggests that the subhorizontal Moho observed along segments A and B changes the pattern abruptly in the middle part of segment C, where the subsurface crustal structure is disturbed. Perhaps the most striking feature of segment C is the indication of two steeply dipping faults, which extend down to Moho (Fig. 2). The epicenter of 2001 main shock with a fault plane dipping south and a focal depth of 22 km lies very close to this segment.

Thin crust in the aseismic southern segment and a thick crust in the main segment suggest that the Kutch mainland uplift is probably associated with a crustal root, suggesting the significant role played by extensional and compressional tectonic activity. Data from the Banni basin is needed to have detailed subsurface configuration across the area.

China

We also investigate the tectonic process in the northern border of the Tibetan Plateau and the genetic mechanism of the 1920 M=8.6 Haiyuan earthquake, the largest earthquake in recent time in China. To accomplish this, we have interpreted data from what is known as “Project 973” (Funding for this project was established in 1997, March; thus “973.”). This project incorporated a 1000-km-long deep seismic sounding, teleseismic observation, and magnetotelluric sounding profiles. This “tri-combination profile” was the first profile of its kind in China.

The formation and evolution of the Tibetan Plateau is closely related to the convergence of the Indian and Eurasian continental plates. At about 45 Ma, the Indian subcontinent collided with Asia, and has since continued to underthrust at a rate of about 5 cm per year (Molnar and Tapponnier, 1975). As a result, the widest and highest continental deformation zone in the world has been formed. In contrast to the few tens of km wide oceanic deformation zones, the Tibetan Plateau extends into the interior of the plate for more than one thousand km from the plate boundary. The mechanisms of these two kinds of deformation zones are completely different. Therefore, it is of great interest to study the crustal structure of the Tibetan continental deformation zone.

Many investigations in the Tibetan region have been conducted with the efforts of Earth scientists from around the world. As a result, many models have been proposed to describe the evolution of Tibetan Plateau, including the

escape model (Molnar and Tapponnier, 1975; Tapponnier *et al*., 1990), the hydraulic pump model (Zhao and Morgan, 1985, 1987; Westaway, 1995), the underthrust model (Argand, 1924; Barazangi, 1989; Beghoul *et al*., 1993) and the accordion model (Dewey and Burke, 1973; England and Houseman, 1986; Wu *et al*., 1990). However, up to now, most of the field observations have been concentrated in the southern Tibetan region, and therefore most models are based on the data there. In northern Tibet, both observational and theoretical works are sparse and insufficient. Thus, the question remains as to the tectonic process that occur in the northern border of the Tibetan Plateau.

To investigate this question, the China Seismological Bureau, Research Center in Zhengzhou conducted a 1000-km-long geophysical profile crossing the northeastern border in 1999 (Fig. 4). Striking NE-SW, the seismic profile crosses the northeastern corner of Tibetan Plateau and penetrates into the Ordos Block, a very rigid and stable block in the North China Platform. Within the Tibetan Plateau, the profile passes across the Kunlun Fault that is bounded by the Kunlun and Qilian Blocks. The profile also passes through the epicentral area of the M=8.6 Haiyuan earthquake. Here we present the preliminary results from deep seismic sounding data of this profile.

Twelve shots were carried out at each of the 9 shot points along the profile, and for each shot 200 seismometers were deployed with 1-3 km spacing. Thus, a perfect overlapping and reversed observational system was formed.

Based on the characteristics of the recorded P-wave data, the following wave groups were identified: a diving wave (Pg) from the upper crust, reflected waves Pc and Pm from interface C and Moho discontinuity, respectively, and refracted wave Pn which penetrates into top of the upper mantle. The Pc wave, second only to the Pm wave in intensity, can be traced continuously. This indicates that interface C is a major interface of the crust. On these grounds, we deem that the crust can be vertically divided into the upper crust and the lower crust. In addition, we have observed some minor reflected phases, i.e. Pc1, Pc3, Pc4 and Pc5. However, most of these phases are weaker and less continuous than Pc, so the upper and lower crust can be further subdivided into inhomogeneous secondary layers.

The travel times of seismic waves were used to invert for the crustal velocity structures. First, the x^2-t^2 method was used to calculate the depth and average velocity of interface C and Moho discontinuity corresponding to each shot point. Then, the depth-velocity function for each shot point was extracted by 1-D inversion. On this basis, the initial model of 2-D velocity structure along the profile was constructed. The final 2-D velocity structure was ultimately revealed by travel time inversion. In the 2-D model calculation, a joint inversion technique was used for both interface location and velocity values (Zelt and Smith, 1992).

Since apparent seismic velocities are directly measured while the depth of refracting horizons are consecutively calculated (from the shallowest to deepest layer), seismic velocities generally have lower percent errors than interface depths. As is discussed by Mooney (1989), the errors for velocities and interface depths are about 3% and 10% respectively. Even so, the relative variation of velocities and interface depths, and the main features of the crustal structures can be seen from the velocity model.

Figure 5 presents the final 2-D velocity structure. The crust can vertically be divided into an upper crust and a lower crust, with interface C as the boundary. Lateral variation of the crust along the profile is considerable. On the whole, the crust gets gradually thicker from northwest to southwest. As the depth of interface C does not vary greatly along the profile, the variation of crustal thickness is mainly attributed to the gradual thickening of the lower crust from northwest to southwest. The Moho fluctuates significantly in the areas of the Maqin and Haiyuan blocks.

The number of secondary interfaces that exist in the upper and lower crust clearly varies along the profile. It increases gradually from northeast to southwest along the profile, indicating an increase of vertical heterogeneity of the crust.

Figure 5 also shows that a number of low velocity layers exist in the crust in the Maqin Region and one velocity layer exists near interface C in the Haiyuan Region. Moreover, in the vicinities of Maqin and Haiyuan anomalies also appear in the Moho and interface C. The two interfaces are no longer velocity interfaces, but they are complicated transitional layers. Furthermore, there are large offsets of the Moho in these two regions.

As can be readily seen from the record sections and the 2-D velocity model, several distinct anomalies exist in the crustal structure of the Maqin and Haiyuan regions. Two very large strike-slip faults, the Kunlun Fault and the Haiyuan Fault cross these regions respectively. These two faults are closely related to the large thrusts and growing mountain range, and play a very important role in accommodating Indo-Asia convergence (Tapponnier *et al*., 1990; Meyer *et al*., 1998). Their tectonic activity can be seen from the large slip-rates and strong seismicities. The average slip-rates of the Kunlun and Haiyuan faults in Late Pleistocene-Holocene are 11.5 mm/a (Woerd *et al*., 2002) and 11.7-19.2 mm/a (Deng *et al*, 1990) respectively.

As mentioned previously, several models have been proposed to interpret the tectonic evolution of the Tibetan Plateau. In general, these models can be classified into two groups (Tapponnier *et al*., 2001): (1) Continuous thickening and widespread viscous flow of the soft crust and mantle of the entire plateau, (2) Successive oblique subduction of Asian lithosphere mantle, leading to the growth of crustal accretion wedges.

The first model, the viscous Tibetan lithosphere model, ignores the existence of a series of large strike-slip faults within the plateau and at its border. Recent results from surface wave inversion are also not consistent with the soft Tibet paradigm (Griot *et al*., 1998). The phase velocities of Raleigh- and Love-waves show that between the depths of 100 and 300 km, the mantle is faster, and therefore colder, under Tibet than under adjacent regions.

It seems that recent studies of deformation, magnetism and seismic structure beneath the Tibetan plateau support the second model (Tapponnier *et al*., 2001). One important piece of evidence is the existence of magmatic belts becoming younger to the north. This implies that slabs of Asian mantle subducted one after another north of the Zongbo suture. The driving mechanism may be the compression of Indian and Pacific Plates, which results in sufficient stress to reactivate weakly-welded sutures, and thus cause new narrow shears within the Asian lithosphere.

Our 2-D velocity structure appears to support this time-dependent, localized shearing model. This evolution model can easily explain the anomalies of crustal structures in the Haiyuan and Magin Regions. In location, these two regions correspond to two mantle subducted slabs related to the Qilian and Kunlun Sutures. From our results we infer that the detachment zone may be shallower than suspected. One possibility is that the upper crust is decoupled along the top of low velocity layer in the middle crust. Due to subduction, the Moho is no longer a sharp discontinuity, but a very complicated transitional zone. The subduction zones also result in the large offsets of the Moho in these two regions. As the underthrusting action in the Kunlun Region lasted longer than that in the Qilian Region, the crustal structure is more complicated; there are more crustal low velocity layers in the Maqin Region than those in the Haiyuan Region. Furthermore, the crust is thicker and the average velocity is lower in the Maqin Region.

According to the result of Zeng *et al*. (1998) from teleseismic receiver functions and Pn waves, the Moho in the Kunlun and Qilian Blocks dips southward while that in the Qangtang Block dips northward, which is consistent with the evolution model mentioned above. Results from reflection profiling in young (post-Mesozoic) orogens also show that the lower crust usually dips toward the center of the root from both sides and shows seismic laminated structures (Mooney and Meissner, 1992). The long durations of Pc and Pm waves in our Haiyuan and Maqin record sections may therefore reflect a laminated lower crust.

CONCLUSIONS AND RECOMMENDATIONS

The available data from the Kutch, India, region shows the deep-seated effect of the recent seismic activity. We suggest proper imaging of the deep-seated blind thrusts/faults is essential to obtain a meaningful seismicity model for the region.

The Bhuj earthquake has placed the Kutch peninsula and the Little Rann of Kutch west and east of the Bhuj epicenter under increased stress, and it is anticipated that these regions are likely to experience heightened seismicity in the next several decades. Thus, it is imperative that we continue to monitor seismicity and understand the crustal structure so that we will be able to discriminate seismic events. The mapping of potentially active faults with likely increased stress concentration thereby assumes great importance from a monitoring point of view, and seismic surveys are needed to refine the determination of crustal structure in Kutch mainland.

Further experiments are also needed to define the P- and S-wave velocity structure of China. In addition to limited information in other regions of China, we would also seek to verify the step-wise underthrusting evolution model of the Tibetan Plateau. We need better definition of deeper structures, especially within the lithospheric mantle in the northeastern corner of the Tibetan Plateau. Due to the limited observational distance in our refraction profile, we could not image the structures below the Moho. Therefore, further experiments based on teleseismic methods are needed. One possible way is to deploy dense seismic stations in this region for teleseismic observation. By seismic tomography, a 3-D velocity model to a sufficient depth can be obtained which will permit us to refine geologic models of the evolution of this region.

REFERENCES

Antolik, M. and D.S. Dreger, 2001 Source Rupture Process of the 26 January 2001 Bhuj, India, Earthquake (M 7.6), *Eos Trans. AGU, 82*(47), Fall Meet. Suppl., Abstract: S52G-03.

Argand,E., 1924, La tectonique de I'Asie, *Int. Geol. Cong. Rep. Sess.* **13** (1), 170-372.

Barazangi, M., 1989, Continental collision zones: seismotectonics and crustal structure. In James, D. H. (Ed.), *The Encyclopedia of the Solid Earth Geophysics,* Van Nostrand Reinhold, New York, 58-75.

Beghoul, N., M. Barazangi, and B. L. Isacks, 1993, Lithospheric structure of Tibet and western North America: Mechanism of uplift and a comparative study, *J. Geophys. Res.*, **98**, 1997-2016.

Bilham, R., 1998. Slip parameters for the Rann of Kachchh, India, 16 June 1819 earthquake quantified from contemporary accounts. In: *Coastal Tectonics* (Eds: Stewart, L.S. and Vita-Finzi, C.), Geol. Soc. London, Spl. Pub.,146, 295-319.

Bilham, R., K. Wallace, and R. Bendick, 2001. Seismicity Following Deep Reverse-Faulting in the Indian Plate: Implications for Gujarat, *Eos Trans. AGU*, **82** (47), Fall Meet. Suppl., Abstract : S52G-09
Biswas, S.K., 1987.Regional tectonic framework, structure, and evolution of the western marginal basins of India, *Tectonophysics*, 135, 307-327.

Chung, W.P. and H. Gao, 1995. Source parameters of the Anjar earthquake of July 21, 1956, India and its seismotectonic implications for the Kutch rift basin. *Tectonophysics*, **242**, 281-292.

Dewey, J. F. and K. C. A.. Burke, 1973, Tibetan, Variscan and Precambrian reactivation: Products of continental collision, *J. Geol.*, **81**, 683-692.

Deng, Q. and W. Zhang (editors in chief), 1990, *Haiyuan Active Fault*, Seismological Press, Beijing, China, 286 p. (in Chinese).

England, P. and G. Houseman, 1986, Finite strain calculation of continental deformation, 2. Comparison with the India-Asia collision zone, *J. Geophys. Res*., **91**, 3664-3676.

Griot, D., J. P. Montagner, and P. Tapponnier, 1998, Phase velocity structure from Rayleigh and Love waves in the Tibet and its neighboring regions, *J. Geophys. Res*., **103**, 21 215-21 232.

Gupta, H.K., N. Purnachandra Rao, B.K. Rastogi, and D. Sarkar, 2001. The deadliest intra-plate earthquake, *Science*, **291**, 2101-2102.

Kaila, K.L., V.K. Gaur, and H. Narain, 1972. Quantitative seismicity maps of India, *Bull. Seism. Soc. Am*., **62**, 1119-1132.

Karanth, R.V., P.S. Sohoni, G. Mathew, and A.S. Kadkikar, 2001. Geological observations of the 26 January 2001 Bhuj earthquake, *J. Geol. Soc. Ind..*, **58**, 193-202.

Ma, X. Y., 1989, *Lithospheric Dynamic Atlas of China*, Beijing: China Cartographic publishing House.

Malik, J.N., P.S. Sohoni, S.S. Merh, and R.V. Karanth, 2000. Paleoseismology and neotectonism of Kachchh, western India. In: *Active Fault Research for the New Millennium*, Proceedings of the Hokudan International Symposium and School on Active Faulting (Eds. Okumura, K., Goto, H., and Takada, K.).

Mereu, R. F., 1990, The complexity of the crust from refraction/wide angle reflection data, *Pure Appl. Geophys*., **132** (1/2), 269-288.

Meyer, B., P. Tapponnier, L. Bourjot, F. Metivier, Y. Gaudemer, G. Peltzer, G. Shunmin, and C. Zhitai, 1998, Crustal thickening in Gansu-Qinghai, Lithospheric mantle, and oblique, strike-slip controlled growth of the Tibet plateau, *Geophys. J. Int.*, **135**, 1-47.

Molnar, P. and P. Tapponnier, 1975, Cenozoic tectonics of Asia: effects of a continental collision, Science, **189**, 419-426.

Mooney, W. D., 1989, Seismic methods for the determination of earthquake source parameters and lithospheric structure, in Geophysical Framework of the Continental United States, edited by L. C. Pakiser and W. D. Mooney, Geol. Soc. Am. Mem., **172**, 11-34.

Mooney, W. D. and R. Meissner, 1992, Multi-genetic origin of crustal reflectivity: a review of seismic reflection profiling of the continental lower crust and Moho, in: Continental Lower Crust, edited by D. M. Fountain, R. Arculus and R. W. Kay, Elsevier, Amsterdam, 45-79.

Mori, J., T. Sato, and H. Negishi, 2001. Slip Distribution of the 2001 West India Earthquake, *Eos Trans. AGU,* **82** (47), Fall Meet. Suppl., Abstract S51B-0604.

Rajendran, K., C.P. Rajendran, M. Thakkar, and M.P. Tuttle, 2001. The 2001 Kutch (Bhuj) earthquake: Coseismic surface features and their significance, *Current Science*, **80**, 1397-1405.

Rajendran, C.P. and K. Rajendran, 2001. Characteristics of deformation and past seismicity associated with the 1819 Kutch earthquake, northwestern India, *Bull. Seism. Soc. Am*., **91**, 407-426.

Raphael, A., P. Bodin, S. Horton,, and J. Gomberg, 2001. Preliminary Double-Difference Relocations of Bhuj Aftershocks *Eos Trans. AGU*, **82** (47), Fall Meet. Suppl., Abstract : S51B-0605.

Rastogi, B.K., 2001. Personal communication

Seeber, N., B. Senthil, R. Briggs, and S.G. Wesnousky, 2001. Field observations bearing on the genesis of the January 26, 2001 Republic Day Earthquake of India resulting from a field survey of the epicentral region. http://neotectonics.seismo.unr.edu/Bhuj/Report.html

Talwani, P. and A. Gangopadhyay, 2001. Tectonic framework of the Kachchh earthquake of 26 January 2001, *Seism. Res. Lett*., **72**, 338 –341.

Tapponnier, P., 1990, The Ailao Shan-Red River metamorphic belt: Tertiary left-lateral shear between Indochina and south China, *Nature*, **343**, 431-437.

Tapponnier, P., B. Meyer, J. P. Avouac, G. Peltzer, Y. Gaudemer, S. Guo, H. Xiang, K. Yin, Z. Chen, S. Cai, and H. Dai, 1990, Active thrusting and folding in the Qilian Shan, and decoupling between upper crust and mantle in northeastern Tibet, *Earth Planet. Sci. Lett*., **97**, 382-403.

Tapponnier, P., Z. Xu, F. Roger, B. Meyer, N. Arnaud, G. Wittinger, and J. Yang, 2001, Oblique stepwise rise and growth of the Tibet Plateau, *Science*, 294, **23**, 1671-1677.

Westaway, R., 1995, Crustal volume balance during the India-Eurasia collision and altitude of the Tibetan plateau: a working hypothesis, *J. Geophys. Res*., **100**, 15 173-15 192.

Woerd, J. V. D., P. Tapponnier, F. J. Ryerson, A. S. Meriaux, B. Meyer, Y. Gaudemer, R. C. Finkel, M. W. Caffee, G. G. Zhao and Zh. Q. Xu, 2002, Uniform postglacial slip-rate along the central 600 km of the Kunlun Fault (Tibet), from 26Al, 10Be and 14C dating of riser offsets, and climatic origin of the regional morphology, *Geophys. J. Int*., **148**, 356-388.

Wu, G., X. Xu,, and T. Li, 1990, The Yadong-Golmud geoscience transect in the Qinghai-Tibet plateau, *Acta Geol. Sin*., **3,** 115-127.

Zhao, W. J. and W. J. Morgan, 1985, Uplift of Tibetan Plateau, *Tectonics*, **4**, 359-369.

Zhao, W. J. and W. J. Morgan, 1987, Injection of Indian crust into Tibetan lower crust: a two-dimensional finite element model study, *Tectonics*, **6**, 489-504.

Zelt, C. A. and R. B. Smith, 1992, Seismic traveling inversion for 2-D crustal velocity structure, *Geophys. J. Int.*, **108**, 16-34.

Zeng, R. S., Z. F. Ding, and Q. J. Wu, 1998, The crustal structures from Himalaya to Qilian and its implications for continent collision process, Chinese Journal of Geophysics *Acta Geophys. Sin.*, **41**, 49-60 (in Chinese).

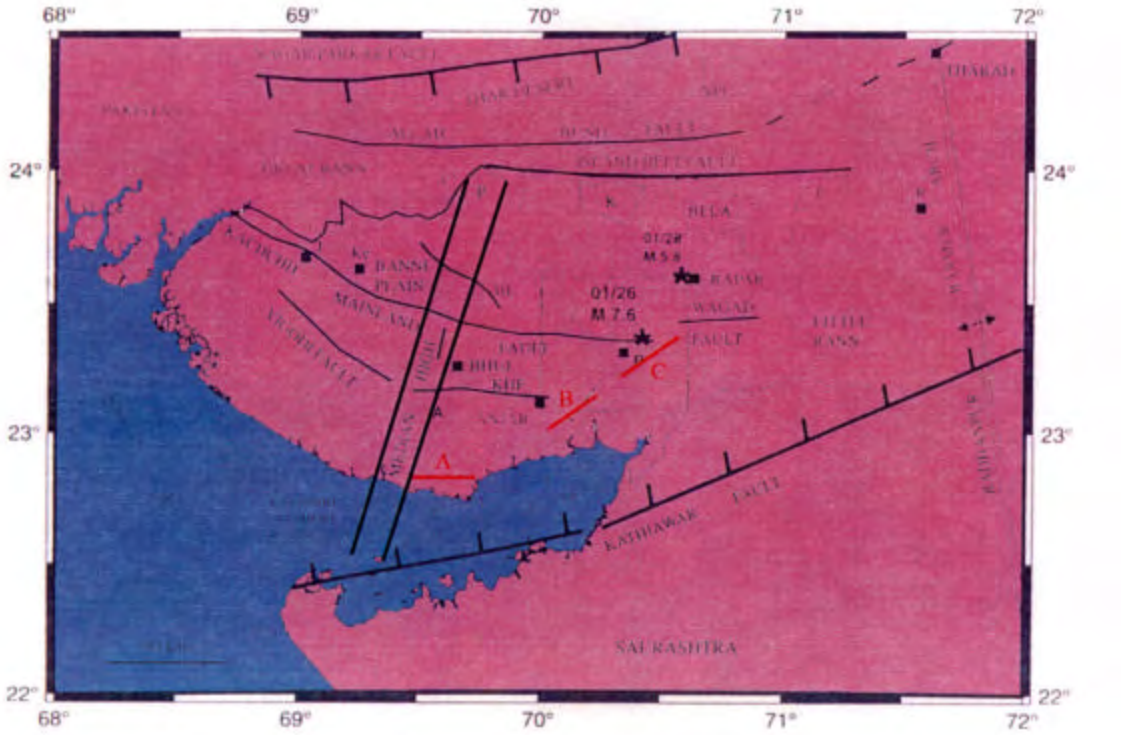

Figure 1. Structural elements in the Kutch basin. Asterisks show the USGS location of the 2001 main and one aftershock events (after Talwani and Gandopadhyay, 2001). Three seismic refraction segments (A, B, and C) are shown in red.

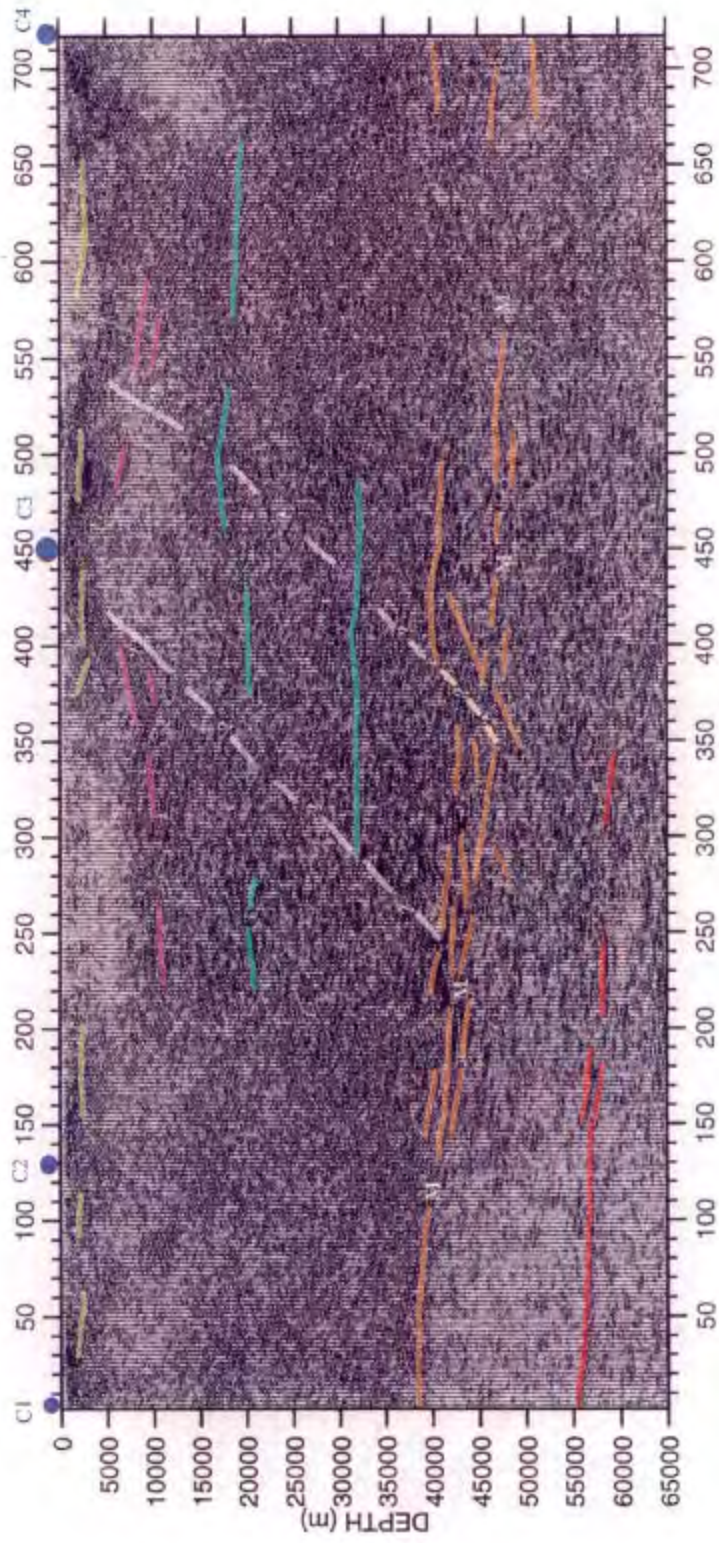

Figure 2. Kirchhoff pre-stack depth migrated crustal cross-section along segment C. CDP interval is 50 m. Interpreted horizonas are superimposed. Dots above represent shot point locations.

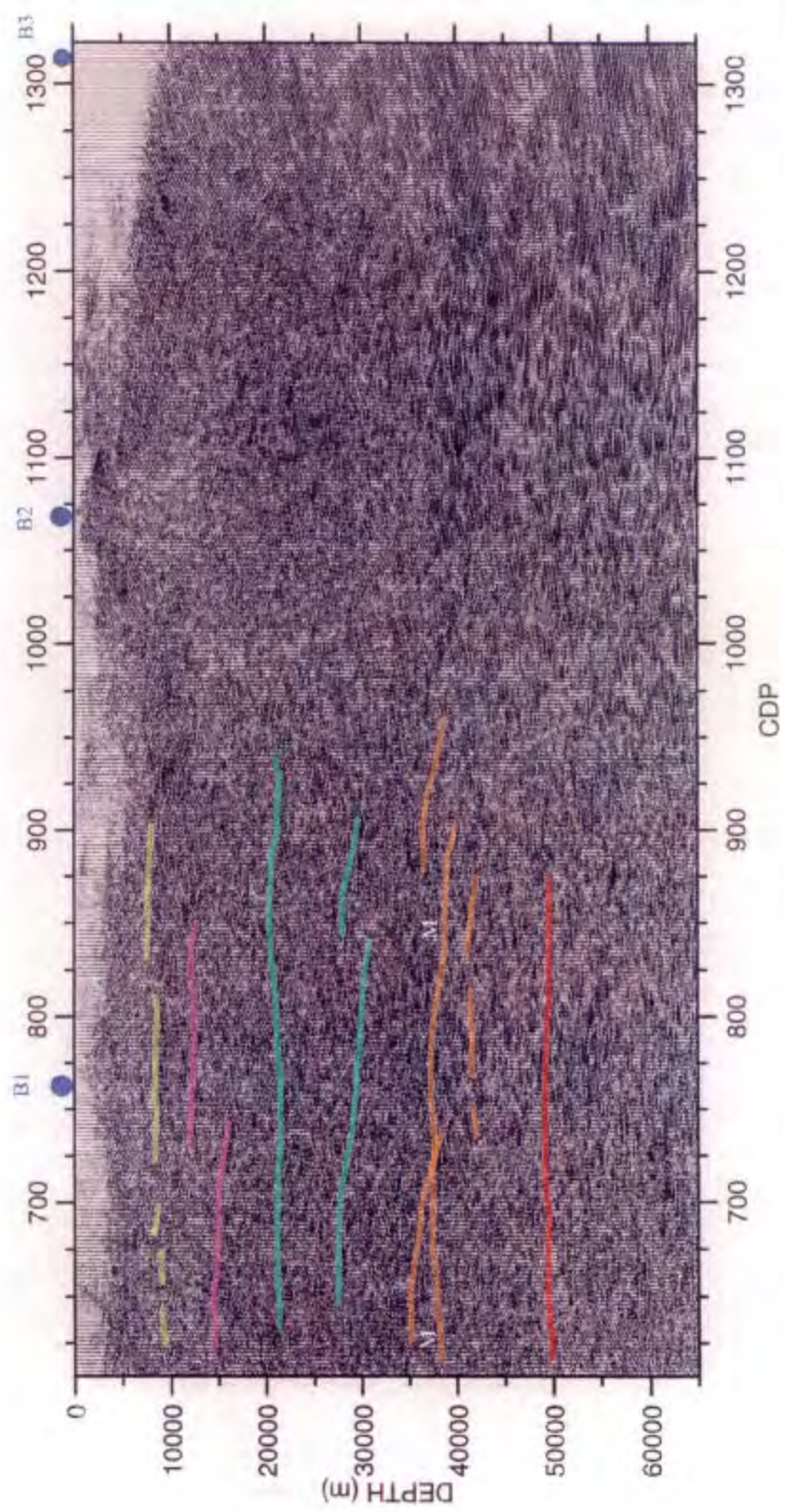

Figure 3. Kirchhoff pre-stack depth migrated crustal cross-section along segment B. CDP interval is 50 m. Interpreted horizons are superimposed. Dots above represent shot point locations.

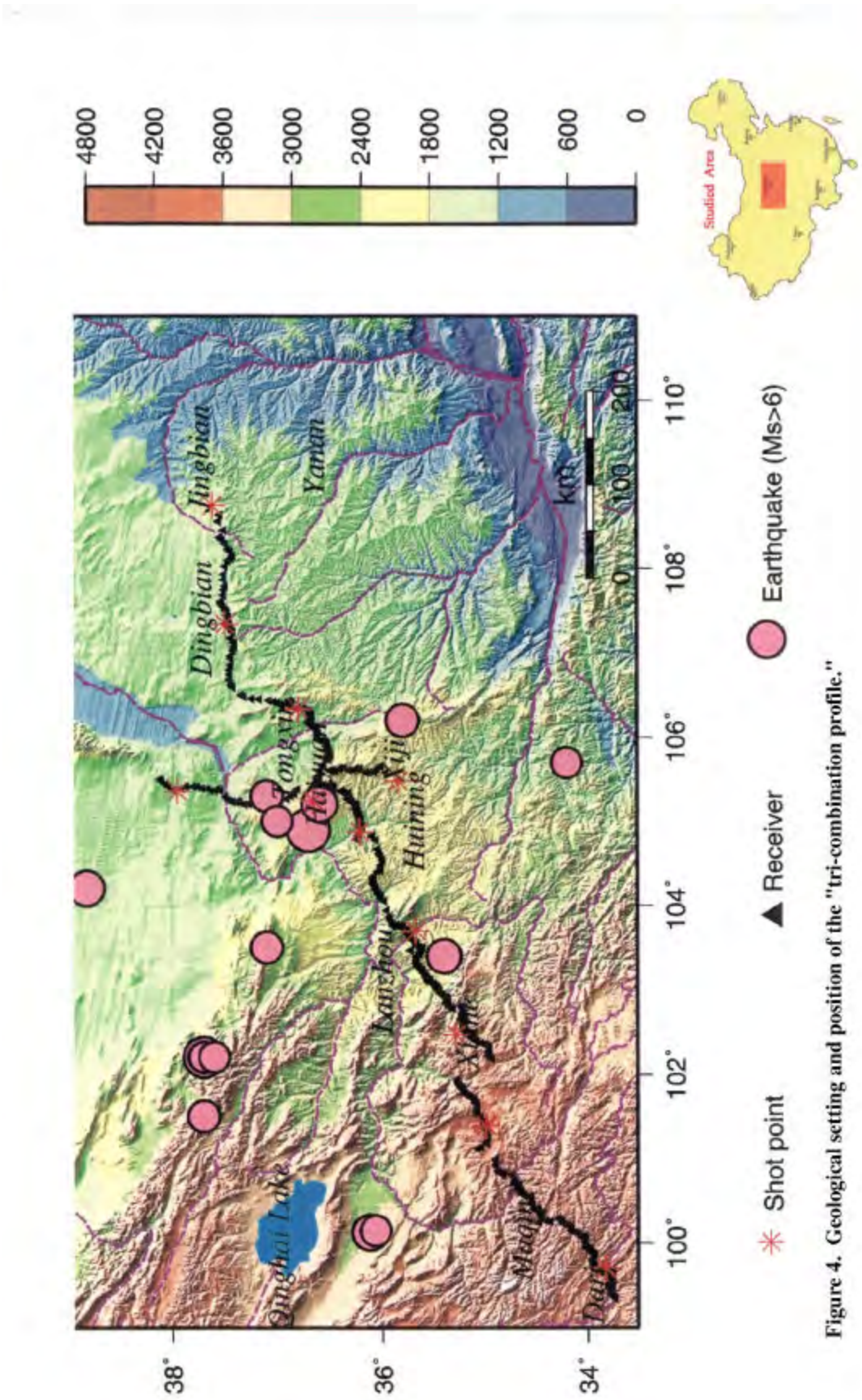

Figure 4. Geological setting and position of the "tri-combination profile."

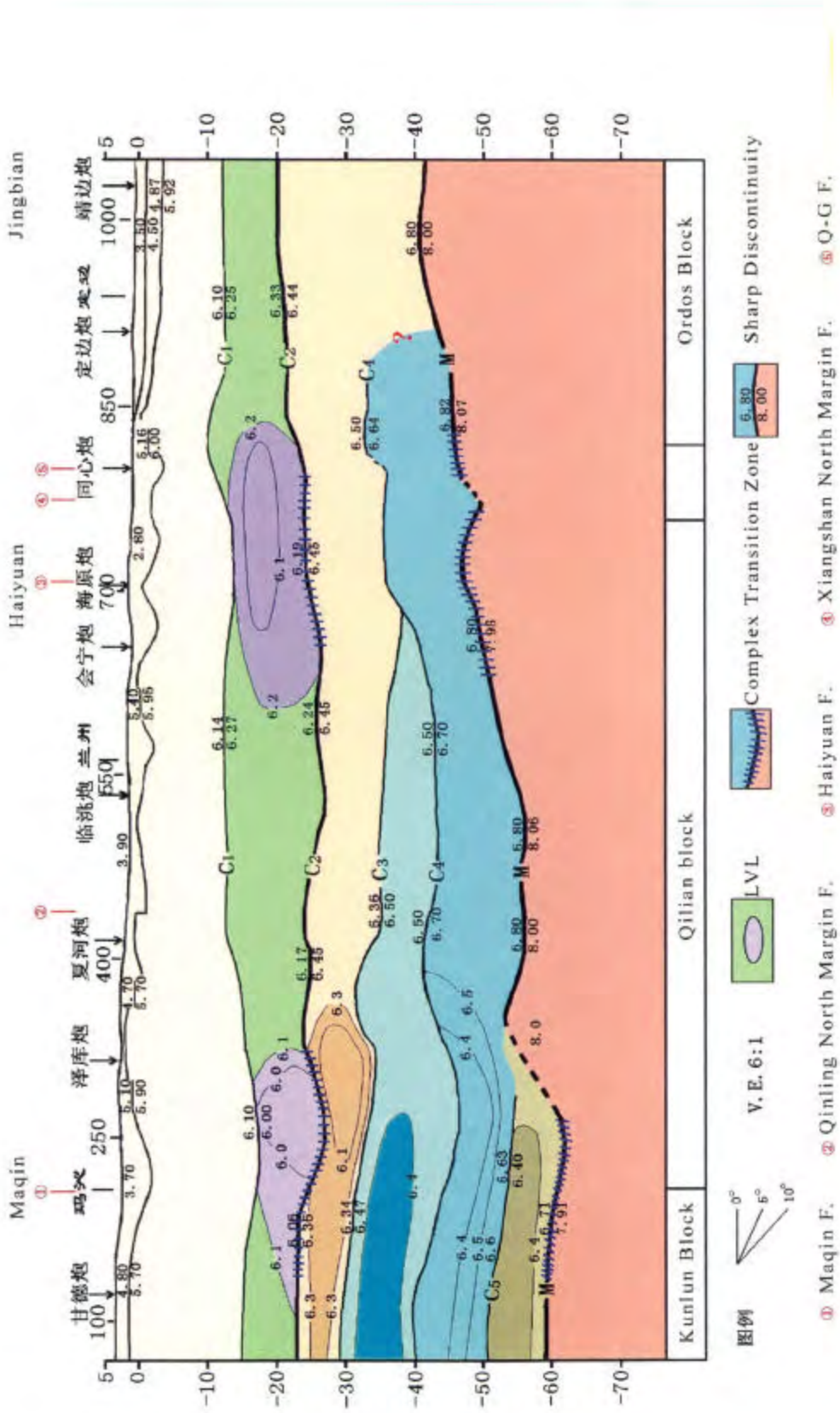

Figure 5. 2-D crustal seismic velocity structure of the Maqin-Jingbian DSS profile.

EFFICIENT INTEGRATION OF OLD AND NEW RESEARCH TOOLS FOR AUTOMATING THE IDENTIFICATION AND ANALYSIS OF SEISMIC REFERENCE EVENTS

D. Wilmer Rivers,[1] Craig A. Schultz,[2] and Douglas A. Dodge[2]

Multimax, Inc.,[1] Lawrence Livermore National Laboratory[2]

Sponsored by National Nuclear Security Administration
Office of Nonproliferation Research and Engineering
Office of Defense Nuclear Nonproliferation

Contract No. DE-FG02-01ER83218[1] and W-7405-ENG-48[2]

ABSTRACT

The selection and study of reference events for inclusion in the National Nuclear Security Administration (NNSA) Knowledge Base requires the application of a much broader suite of seismic analysis software than does either the routine production of a seismic bulletin or the subsequent preliminary screening of those bulletin events to conduct nuclear explosion monitoring. For either of those latter applications, a large program designed explicitly for that single purpose can be applied in a set analysis procedure for every one of the many events that will be processed daily, but to study the much smaller number of reference events in adequate detail, it is necessary to use many separate specialized programs, including new routines that may still be in the testing phase or even some that were developed or modified specifically to study the particular event at hand. In order to make the most effective use of this software suite, the individual programs must communicate with one another in an efficient and flexible manner, so that a scientist can select which programs to run and in what order, thereby improvising a data-processing pipeline of programs passing their results from one to the next.

We have explored the technical feasibility of constructing such a reference event analysis system by using the Common Object Request Broker Architecture (CORBA) as the data communications tool for passing data among programs and for allowing them to make Remote Procedure Calls (RPCs) to invoke one another's services. We have extended the standard seismic analysis program *geotool* to incorporate a CORBA interface, and through it, we can send data and RPC messages to other programs for processing, and then back again to *geotool* for interactive graphics display of the results. The communications take place through separate Object Request Brokers (ORBs) for *geotool* and for the analysis programs. We demonstrate this procedure by using the C-language program *geotool* as server software on Linux and a Java application for waveform filtering as client software in MS Windows. The two programs on the separate platforms are able to function together just as if the remote Java application were actually a local C-language routine within *geotool* called via a pull-down menu. All data communications take place within memory, and no new disk files or database records need be generated as output from one program and then read as input to the other. It is this type of seamless data communications that should form the infrastructure for integrating the many separate programs that will be needed to analyze seismic reference events thoroughly.

Although the work performed to date has used CORBA as the mechanism for inter-process communications, we have monitored the software industry's increasing acceptance within the last year of "Web services" as an alternative approach to the integration of distributed software components. Web services technology is based on Simple Object Access Protocol (SOAP) invocations of remote procedures, and the SOAP calls are transmitted through XML-formatted text messages sent via HTTP. Since the messages are text-based, and since they are handled by a SOAP-enabled Web server rather than by an ORB, inter-platform data communications are simpler (but more bandwidth intensive) through Web services than through CORBA. The potential for integrating native Windows applications with UNIX applications through Web services is particularly appealing, so in our future work, we intend to investigate the use of Web services as an alternative to CORBA for transmitting data and RPCs among the programs that will be used to analyze reference events. In particular, the XML messages invoking the remote processing offer a means for creating a metadata tracking system that can be used to record the data-processing history of each parameter measurement made by the distributed system of independent software components, so the metadata for the entire suite of data analysis procedures for each waveform can be archived for repeating (or undoing) any or all of the measurements.

OBJECTIVE

Scientists use a variety of stand-alone computer programs to analyze and identify seismic events for nuclear explosion and treaty monitoring, and an especially wide selection of software tools is needed for the detection and intensive study of reference events that will be included in the NNSA Knowledge Base for use in future event comparisons. Some of these stand-alone programs are large software packages that offer many tools for routine seismic analysis, but they are difficult to modify to include additional tools for specialized tasks. Others of these stand-alone programs offer the capability of performing only specific operations, and they must be used in conjunction with other programs such as interactive waveform graphics displays that offer more general analysis capabilities. In most cases neither the large software packages nor the specialized analysis programs can communicate adequately from one to another without the tedious creation and input of temporary data files and other awkward techniques. Since the stand-alone programs cannot exchange data easily, it is difficult to use them in a data-processing pipeline that could add new capabilities to those offered by the large software packages or that could allow the specialized analysis programs to rely on other software for tasks such as graphics displays.

A reference event analysis system should therefore be built by using a system architecture that facilitates data flow among these stand-alone programs, including any new programs that will be developed in the course of future research and that may be especially valuable for the identification and characterization of reference events. This new architecture should allow the results of one program to be sent easily to another one, as chosen on a case-by-case basis by the seismic analyst, without the creation of temporary files and database tables. Because many of the stand-alone seismic analysis programs that need to communicate with one another are written in different computer languages, and many are written for use under different operating systems, it will be important for this architecture to be as nearly platform-independent as possible. Furthermore, the communications among the separate programs should allow access to remote resources for data retrieval or specialized computations. The reference event analysis system should therefore be constructed as a distributed system of individual software components rather than as a single large software package. The first objective of our study is to examine software architectures and communications protocols that will allow existing and newly developed programs to be used as the components in this distributed system. Our next objective is to select and modify those programs so that they can be integrated into a reference event analysis system using that distributed system architecture.

RESEARCH ACCOMPLISHED

This project is divided into two phases: a six-month proof-of-concept phase, which has recently been completed, and a two-year implementation phase, which has now begun. The proof of concept was intended to explore the architectural underpinnings of a software system for analyzing seismic reference events, and it was not intended in this first stage to design and construct any of the graphics, signal processing, geophysical, communications and other modules that would be the constituent parts of such a system. Our study has not focused so much on the construction of a new seismic analysis package that is intended to replace the ones currently in use as it has focused on the integration of separate modules, including both existing code and newly developed routines, into a flexible software system. We shall select the individual modules to use for analyzing reference events, and we shall build certain new data processing tools as required, during the two-year implementation phase that is now underway.

In examining possible architectures for a reference event analysis system, our choices have been guided strongly by the differences between routine seismic analysis performed for constructing event bulletins and the more nearly *ad hoc* analysis that is required to identify and characterize reference events for inclusion in the Knowledge Base. Software packages for routine seismic analysis are designed to facilitate the repetitive performance of a pre-determined series of tasks. Although a data analyst engaged in constructing an event bulletin will have some flexibility in choosing to perform certain ones of those analysis tasks for every waveform under consideration while reserving other analysis tasks for use only in unusual circumstances (such as using a polarization filter to help separate the sources of mixed signal arrivals), by and large the processing of every new event will conform to set procedures. In particular, if the analyst makes any choice of data processing tools at all, the selection of those tools will be limited to only those modules that are included within the seismic analysis software package, so the designer of that package must therefore foresee all the tasks that the analyst may need to perform. For screening all seismograms recorded by a network and pre-processed by an automated system, and especially for making a specified set of measurements that are agreed upon for international data exchange, this approach is, in fact, a suitable one. A number of software packages such as Seismic Analysis Code (SAC2000; *viz.* Goldstein, 1998),

Analyst Review Station (ARS; *viz.* Wang, 1996), *geotool* (Henson, 1993), and MatSeis (Young, 2001), among others, are commonly used for these analysis tasks. These same packages can also be used satisfactorily for the analysis of reference events, but we feel that the use of any one of these packages, or for that matter the use of any other single large program that we could design and build *ab initio* as a product of our current study, may not be the best possible approach for this purpose. We shall now discuss some shortcomings of that approach and describe alternatives to it.

For identifying and characterizing possible reference events for use within the Knowledge Base, it is critical that the scientist have maximum flexibility in choosing what algorithms and data processing routines should be used in any particular case. The purpose of a reference event is to exemplify the seismograms that are to be expected from a particular type of event, in a particular region, as recorded at particular stations, and the tools needed to characterize those seismograms will be as varied as the waveforms themselves. A wavetrain from a small strike-slip earthquake in the upper mantle in a region of low anelastic attenuation will, of course, be markedly different from the waveform of a large thrust-fault earthquake at shallow depth in a tectonically active region, and a scientist may wish to choose to apply a different suite of tools depending on certain features that are exhibited by one of these events but not by the other. In fact, highlighting these differences in order to categorize patterns that can be used to distinguish one type of event from another is one of the goals of reference event analysis. Even for conventional applications such as picking arrival times, determining epicenters and confidence regions, measuring signal amplitudes and periods, etc., when studying a reference event, a scientist may well wish to apply unusual tools that would not conventionally be applied during routine event screening. For instance, elaborate de-ghosting algorithms may be used to identify multiple small echoes within reference signals propagating along paths characterized by strong multipath arrivals, a procedure that is unlikely to be applied to signals not intended for inclusion in the Knowledge Base. It is even possible that a scientist may wish to develop special software for application to a particular signal, if no tool that is available seems appropriate for the purpose. Applying specialized tools would require making modifications or extensions to the seismic analysis software packages. Another reason that these packages could need to be modified for reference event analysis is that it can be the software itself, rather than the seismogram, that is the subject of the analysis. This would happen because a scientist who is developing a new analysis routine will likely want to test it by applying it to reference signals in conjunction with the existing tools that already exist in those packages. For instance, a scientist who has developed some variant on the conventional computation of the complex signal cepstrum will want to test only that algorithm and not have to write new graphics code for the display of the waveforms, spectra, cepstra, etc., capabilities that are already offered by the existing seismic analysis packages. For processing reference events, then, it will be necessary for a scientist to make modifications to SAC, ARS, *geotool*, etc., by incorporating unusual or newly developed analysis tools into the software package.

Although most of these seismic analysis software packages can be modified to some extent, the process is usually not an easy one. In some cases modifications can be made to the software through the resource files it processes as data, and in other cases new libraries can be linked in and operated from existing callbacks, but often it is necessary to modify (and thus have access to) the source code to make some desired changes. Even when it is possible to do this, it is dangerous to do so, since modifying code in the huge single programs that form the basis of most of these packages is liable to result in unanticipated "side effects" that cause existing functionality in the program to break or to behave in a different manner than before. Another major problem is that often a scientist who is working with a large seismic analysis program written in the C programming language, for example, will want to implement a processing routine that is written in Java or some other language. Although software programs can be constructed to invoke routines written in one language from main programs written in another, the process is not so straightforward that a scientist or data analyst could rig it together in short order as an improvised addition to the analysis of a specific event. Scientists who are running a program like *geotool* that is intrinsically hard coded with calls to a particular graphics platform (in this case, Motif) are furthermore constrained to work within a particular operating system such as UNIX and therefore cannot take advantage of seismic analysis codes written to run on another platform such as Windows. To overcome these problems associated with adding functionality to large software systems for seismic analysis, we have decided to take a different approach to constructing the reference event analysis system. Instead of augmenting an existing large program, or writing a new one that would be more nearly comprehensive but that would itself eventually become inadequate when future research results in new analysis algorithms and new software tools, we have chosen to implement a distributed architecture that will permit existing code as well as new code to be invoked remotely from the large programs currently used for seismic analysis.

The distributed system architecture that we have investigated during the recently concluded proof-of-concept phase is based on CORBA, a technology that was developed in the mid-1990s for client/server data communications between desktop computers and corporate mainframes. Our scheme for implementing CORBA as the backbone for a distributed seismic analysis software system is illustrated in Figure 1. We are using the C-language program *geotool* as the server software, running under the Linux operating system, and for the proof of concept, we have used a simple Java program called "WaveformViewer" as a client application, running under the Windows 2000 operating system on a separate computer within the same local area network (LAN). As its name implies, WaveformViewer does little more than display waveforms using Java graphics, but it does offer a limited functionality, such as digital filtering, that will suffice to demonstrate how the reference event analysis system should work. WaveformViewer is, in fact, assembled from only a few of the many Java classes that make up a much more comprehensive seismic analysis system (Henson *et al.*, 2000), but rather than use that full system, thereby linking together two large programs that offer many duplicate capabilities, we wish to show how a single server can drive data analysis by communicating with a number of small client programs, each of which perform only a small number of particular tasks, perhaps only a single function. This is the system design that we intend to implement in the reference event analysis system.

As is shown in the diagram in Figure 1, we have modified *geotool* by adding new callback functions that allow it to communicate with an ORB. (Since *geotool* is running under Red Hat's distribution of Linux, we can make use of the open-source ORB known as "ORBit" that is bundled as a part of the distribution. For a *geotool* server running instead under Solaris, we could use one of a number of commercial ORBs for UNIX.) Using the X Resources file for *geotool*, we can then add a new pull-down menu item that will allow the user to send data to our client program, WaveformViewer. To expedite the process (external to *geotoo*l) of setting up the data connection, we have written a utility called "CORBA Center" that effectively acts as a switchboard for choosing a server side and a client side of the data flow. This utility registers the IP addresses with the CORBA Naming Service (to associate object references with symbolic names) so that the two programs can exchange data across the LAN as easily as if they were both running on the same computer. CORBA's data communication across the LAN takes place using the Internet Inter-ORB Protocol (IIOP). This is an official internet protocol (like FTP and HTTP) that allows an ORB on one platform to communicate with one on another platform. Note that it is irrelevant that the server-side software is in C and the client-side software is in Java, since IIOP is platform independent. We have modified the WaveformViewer client application by adding callback functions that allow it to communicate with a new "Agent" Java class, which, in turn, handles the communication with the ORB that is included within the Java platform under release JDK 1.2. The data messages that are exchanged through this client/server communication consist of seismograms and the metadata that describe them, in conformance with the standard CSS data schema (Carter *et al.*, 2001). To allow this communication, we have translated the CSS-schema data structures such as *.wfdisc*, *.arrival*, *.origin*, etc., into CORBA's Interface Definition Language (IDL). An IDL routine does not know whether the application with which it is communicating is written in C or Java (or one of several other languages). All it knows is that the application on the other side of the data stream expects to receive a message conforming to a particular IDL argument list, and we have therefore translated all the standard CSS data tables into a single IDL interface so that we can re-use that same interface for as many different *geotool* client/server applications as possible.

Figure 2 shows a server-side view of how this system can be used in practice. Once the program "CORBA Center" has been run to specify that *geotool* on the Linux computer will be a server and that WaveformViewer on the Windows computer will be a client, the data analyst starts up *geotool* in the normal manner. To make it readily apparent on the screen what is happening within the client/server data flow, in Figure 1 the analyst has used *geotool*'s own data-processing functionality to apply a high-pass filter to two seismograms. Those two seismograms are thus now different within *geotool* from the versions that were read in from the disk file, and (depending on what processing was applied) perhaps they are no longer correctly described by the CSS-schema tables residing in the database. The analyst will now use a new menu item that we have added to *geotool* to send to the client whichever seismograms are selected on the screen. In this case we shall send to WaveformViewer five seismograms, including the two that we have changed within *geotool*. These waveforms will be sent to the client directly from memory, so the analyst will not have to write the new waveforms to disk, then store new CSS-schema tables in the database, and then send those new disk-resident data to the Windows computer via FTP, where they would next have to be written to that computer's disk and finally read in by WaveformViewer. Instead, the data are sent directly between the programs through the IDL interfaces. This is in effect a client/server RPC, but it is considerably easier to implement using the high-level CORBA architecture than it would be by using a low-level interface such as code for sockets.

Figure 3 is a screen shot from the Java program WaveformViewer running on the Windows platform, showing a callback we have added that displays the *.wfdisc* description of the waveforms received through the IDL interface, just as if they had been read from the disk. The analyst can select which seismograms to display within the Java-graphics WaveformViewer display (which mimics the Motif waveform display used by *geotool*), and in this case we choose to display all five waveforms. In Figure 5 the analyst has applied WaveformViewer's own filtering routine to apply a different high-pass filter to two of the seismograms that were received from geotool as unfiltered waveforms. The analyst will then use a menu item we have added to WaveformViewer to send data back to the server program. Figure 5 shows that the waveforms newly modified by WaveformViewer are indeed now present within *geotool*. The whole process is as simple for the analyst to use as it would be if all the digital filtering had been performed within *geotool* itself. All that is required is to make a few mouse clicks, just as if WaveformViewer were simply a function that is part of *geotool* instead of its being in fact a separate program, written in a different language, running on a different computer and under a different operating system.

This proof of concept demonstrates that a distributed software architecture built using CORBA can form the basis of a reference event analysis system. Instead of having a single huge program, which is hard and/or dangerous to modify, as the tool to use for identifying and characterizing reference events, it is possible to modify *geotool* (or ARS, or SAC, etc.) to be used as a data server and then to perform the actual seismic analysis externally to *geotool* by using a host of separate applications, including both existing code and programs yet to be written, running on whatever platform is most appropriate. In particular, the analyst should be able to use seismic data centers and supercomputers located at remote facilities accessible via the Internet, just as if those capabilities were offered by the server platform itself. The data communications should be performed as easily as possible without requiring the analyst to go through intermediate steps of creating, exporting, and importing temporary files and database records. This flexibility will be required for the intensive study of reference events, where new algorithms not ordinarily used for routine seismic analysis may be required in order to perform specialized investigations in individual cases. The analyst should be able to select which programs to run, and in what order to run them, and in many cases it may well be necessary to construct new programs. The analysis programs that run as client applications should perform only one or two specific tasks, and they can be written to perform only those particular functions without reproducing all the overhead capabilities for data management that are required by the server program.

The example that is illustrated in Figures 2 – 5 should serve to demonstrate the need for certain features in a distributed processing architecture that are not conventionally part of a software system like *geotool* that runs as a single program on one computer (albeit within multiple windows). In Figure 2 data channels 6 and 8 are unfiltered, in Figure 4 they have been filtered by the client application, and in Figure 6 they have been returned to the *geotool* server in their filtered form. What, then, should the *geotool* server program do with the unfiltered versions of these channels, which, of course, are still resident in the program's RAM, and are still displayed on the Linux computer screen, once the client program is ready to send the filtered versions back to the server? Should the process of returning the filtered data from the client automatically cause the server to delete the unfiltered data? Should the *geotool* window instead now display the presence of two different versions of these waveforms, and if so, should it change the waveform identification label *.wfid* to reflect that there are now two different waveforms for the same time windows on these particular data channels? Should the return of the filtered data from the server be blocked until the analyst has hit a "receive" button in *geotool* indicating that the original data should now be overwritten? (Blocking the transmission of a data message from the client until the server specifies that it is ready to receive it makes the data stream function in many ways like an Instant Messenger service such as AOL IM or ICQ.) What happens if the data analyst sends the unfiltered data to one client application for filtering and then chooses to send those same data to a different client program for some other processing, such as polarity reversal, *before* the first client program has returned its results? Clearly, the distributed processing architecture presents a number of issues related to the data's referential integrity, versioning, and configuration management. Establishing and enforcing policies for handling these issues will be an important part of the design of the reference event analysis system.

It is also clear that the system must use some sort of metadata audit trail for tracking the distributed processing. Regardless of whether the unfiltered data are deleted from the server's memory and screen display when the filtered data are returned from the client, how will the system distinguish between the filtered waveforms and the original ones that reside on the disk? In the particular case of the interactive WaveformViewer client application, the analyst was required to input the filter parameters by using a GUI, so it is known (at least by the analyst, if not by *geotool*) what sort of filter was applied. In general, however, it is far more likely that the client code will run automatically, and the analyst will have no knowledge of the exact parameters that govern the algorithm implemented by the client

program, which, after all, is likely to be running on a different computer, perhaps even at a different facility. The client must therefore return not only the processed data but also a metadata message describing just what operations it performed and the parameters it used. The server must construct a database archive of these metadata records as a tool to use for the data versioning and configuration management so that any one or all of the data processing routines executed by the distributed client applications can later be repeated or undone.

Finally, although our work has shown that CORBA can be used as the backbone for the reference event analysis system, we have now begun an investigation into the use of an alternative technology. Within the last year the software industry has begun to move from using CORBA for client/server applications to an Internet- or Intranet-hosted approach based on Web services. This technology relies on Web servers, rather than ORBs, for data communications, and the data (including SOAP's RPC invocations to process the data) are sent as XML messages via HTTP rather than as binary data sent via IIOP. There are a number of advantages to this approach. Because XML messages are alphanumeric data, they can be sent through firewalls more easily than can binary data (although more bandwidth is required). XML and SOAP are easier to use than CORBA (even though we have made that process easier by the construction of the "CORBA Center" program that facilitated the *geotool*-to-WaveformViewer connection). Because XML is just alphanumeric data, it is truly platform independent. In particular, it is quite difficult to use CORBA to communicate with applications that are running under Windows as native code (as opposed to applications like WaveformViewer that run under Windows but within Java's own platform), since the standard Windows platform uses the Component Object Model (COM), which is incompatible with the CORBA object model. Software bridges can be constructed, but the process is difficult. XML bypasses this problem, and so Web services that are developed for UNIX work perfectly with those that are developed for Windows. Microsoft has made the construction of Web services especially easy by now replacing COM with a new platform called ".NET" that automates much of the use of SOAP. We feel that this platform will be an important one, and the reference event analysis system should be able to make use of it. Using XML as the basis for data communications has further advantages, including the fact that in a real sense, XML is itself metadata. Database vendors are therefore making sure that new releases of their software can store and transmit XML. We feel that this would be a good approach for constructing the metadata archive that will be an important component of the planned system.

CONCLUSIONS AND RECOMMENDATIONS

We conclude that the best system architecture for a reference event analysis system is likely to be one that is based on distributed stand-alone software components (which can all be on the same computer or distributed across a network) rather than on a single large program. Our proof of concept study has shown that CORBA technology can be used to connect a server program for seismic analysis (like *geotool*) to client programs developed for specialized applications, even if they are written in other languages and run under different operating systems. We recommend, however, that Web services technology be investigated thoroughly as an alternative to the use of CORBA as the backbone for the distributed processing. We shall implement that recommendation during the next phase of work, and then we shall begin incorporating both existing and new programs into that distributed processing system

REFERENCES

Carter, J., R. Bowman, K. Biegalski, J. Bohlin, M. Fisk, R. Carlson, W. Farrell, B. MacRitchie, and H. Magyar (2001), IDC Documentation Database Schema Revision 3, Center for Monitoring Research User Guide on-line document (available at http://www.pidc.org/librarybox/idcdocs/downloads/511r3ab.pdf).

Goldstein, P. (1998), SAC Tutorial Guide for New Users, Lawrence Livermore National Laboratory report UCRL-MA-112836 (available at http://www.llnl.gov/sac/).

Henson, I. (1993), The *geotool* Seismic Analysis System, in: Proceedings of the 15th Annual Seismic Research Symposium 8-10 September 1993, Phillips Laboratory report PL-TR-93-2160.

Henson, I., R. Wagner, and W. Rivers (2000), Automated Seismic Event Monitoring System, U.S. Nuclear Regulatory Commission report NUREG/CR-6625.

Wang, J. (1996), Analyst Review Station's User Manual, Science Applications International Corporation report SAIC-96/1100.

Young, C. (2001), MatSeis User's Manual, Version 1.3, Sandia National Laboratories on-line document (available at http://www.nemre.nn.doe.gov/nemre/data/matseis/matseis_manual.pdf).

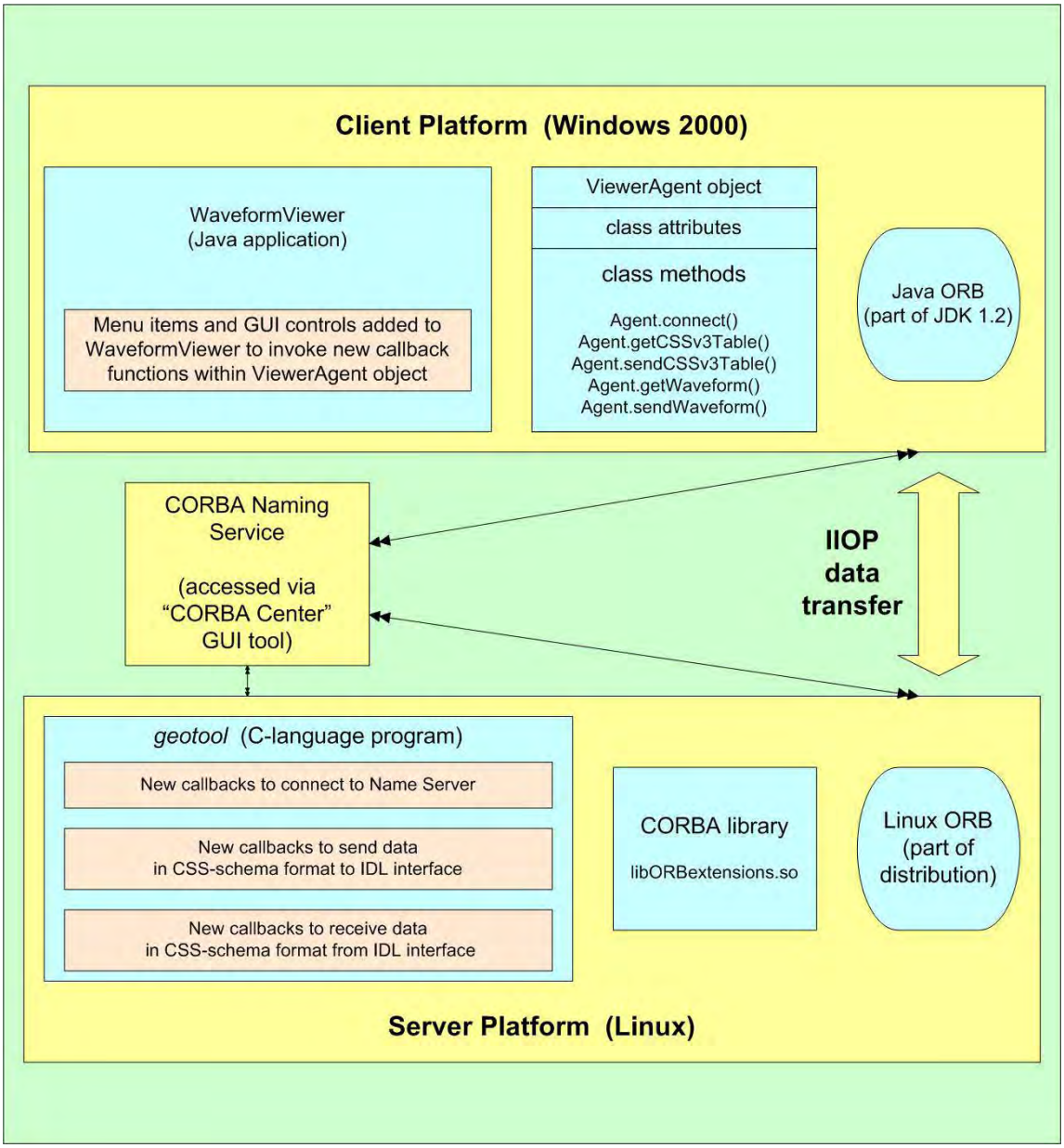

Figure 1. Using CORBA to enable client/server data communications between the C-language program *geotool*, running as a server on a Linux platform, and the Java program WaveformViewer, running as a client application on a Windows 2000 platform. The data communication takes place between the Object Request Brokers on each platform via the Internet Inter-ORB Protocol, which is an internet standard. We have modified the client code and the server code so that they link to CORBA, and that link can now be used to permit data communications between the sever and additional client applications that are invoked by the user through items added to the *geotool* pull-down menus. The data that are exchanged between the client and server programs are translated from the standard CSS database table schema to CORBA Interface Definition Language. We have written a utility called "CORBA Center" that makes it easier for the user to set up the client/server link (which requires the *geotoo*l server to register itself with the CORBA Name Server).

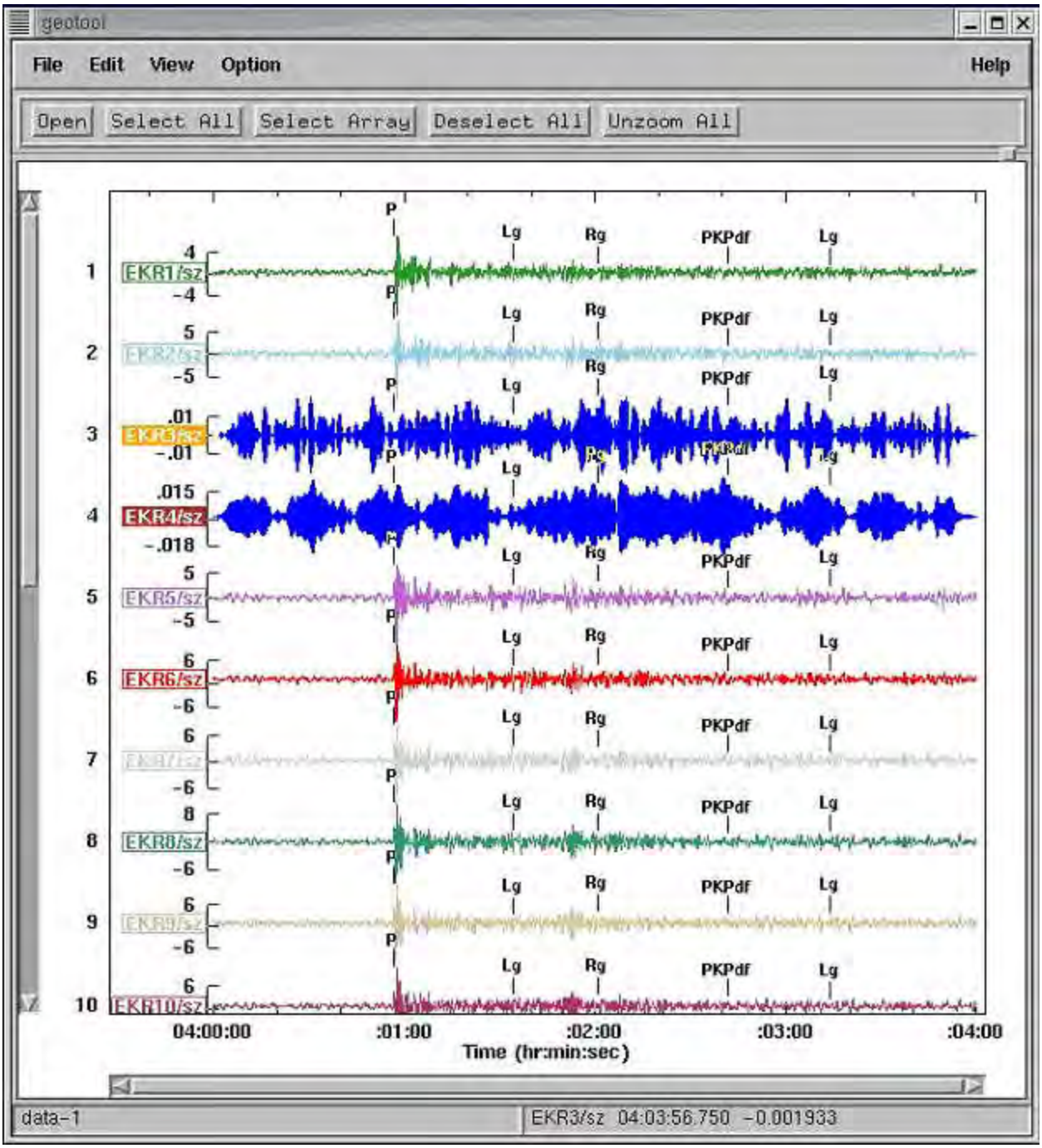

Figure 2. Screen shot of the C-language program *geotool* running on a Linux computer and displaying ten short-period vertical channels recorded by the seismic array EKA. The waveforms on channels 3 and 4 have been passed through a very high-pass filter by a Butterworth-filtering function in *geotool*. These two seismograms are therefore different in this screen image, and in the Linux computer's active memory, from the original versions that still reside on the hard disk. These two altered seismograms and the unaltered ones on channels 1, 6, and 8, along with the *.wfdisc* data structures that describe the seismograms, will be transmitted via CORBA to the Java-language program WaveformViewer running on a Windows 2000 computer. Rather than the disk-resident version of these waveforms, it is the memory-resident version, including the changes made within *geotool* by applying the high-pass filter, which will be transmitted from *geotool* to WaveformViewer.

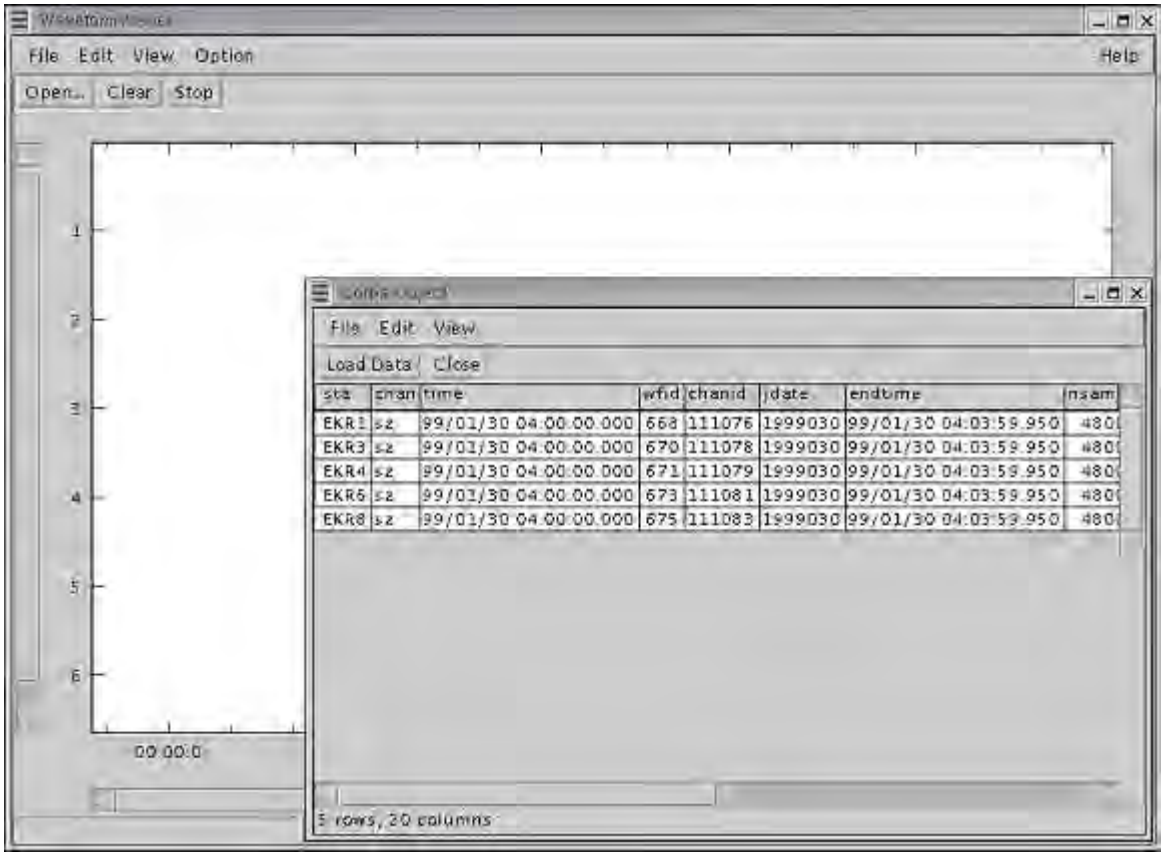

Figure 3. On the Windows 2000 computer running the Java-language program WaveformViewer, the CORBA connection causes a window to pop up that displays the *.wfdisc* record that was sent across from *geotool* on the Linux computer. From that pop-up window, the user selects which waveforms to display. We shall choose to display all five channels that were exported from *geotool*.

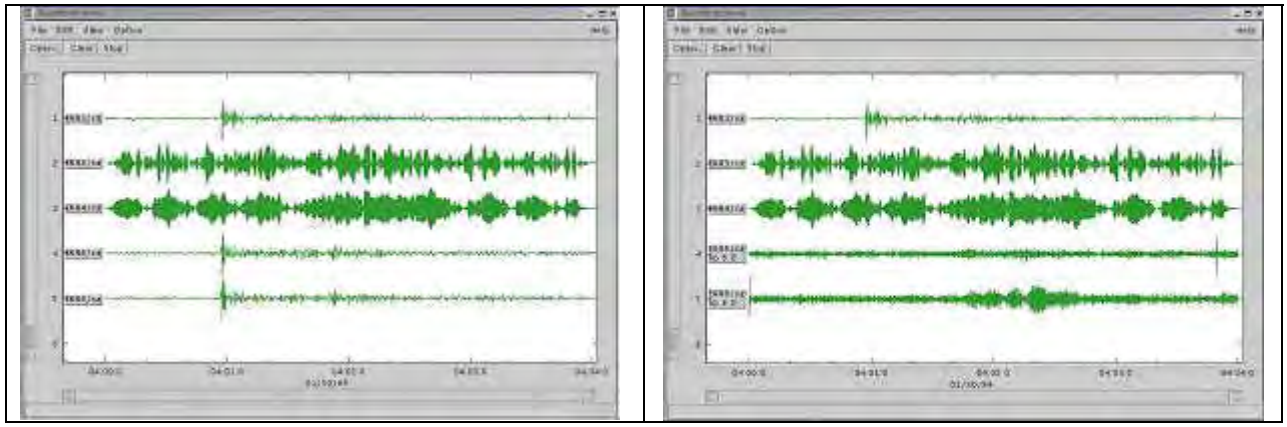

Figure 4. (a) Waveforms imported into WaveformViewer from *geotool*. Note that two of the waveforms reflect the filtering applied by *geotool* and thus show that they have been sent to the Windows computer directly from memory on the Linux computer and not from the disk files. (b) The bottom two waveforms in the display (channels 6 and 8) have now been filtered with WaveformViewer's own Butterworth high-pass filtering routine. A different bandpass was selected in WaveformViewer than in *geotool*, so we can recognize which waveforms were filtered by which program. The waveforms filtered by the WaveformViewer client program will now be sent back from Windows to Linux via the CORBA connection so that they can be displayed within the *geotool* server program.

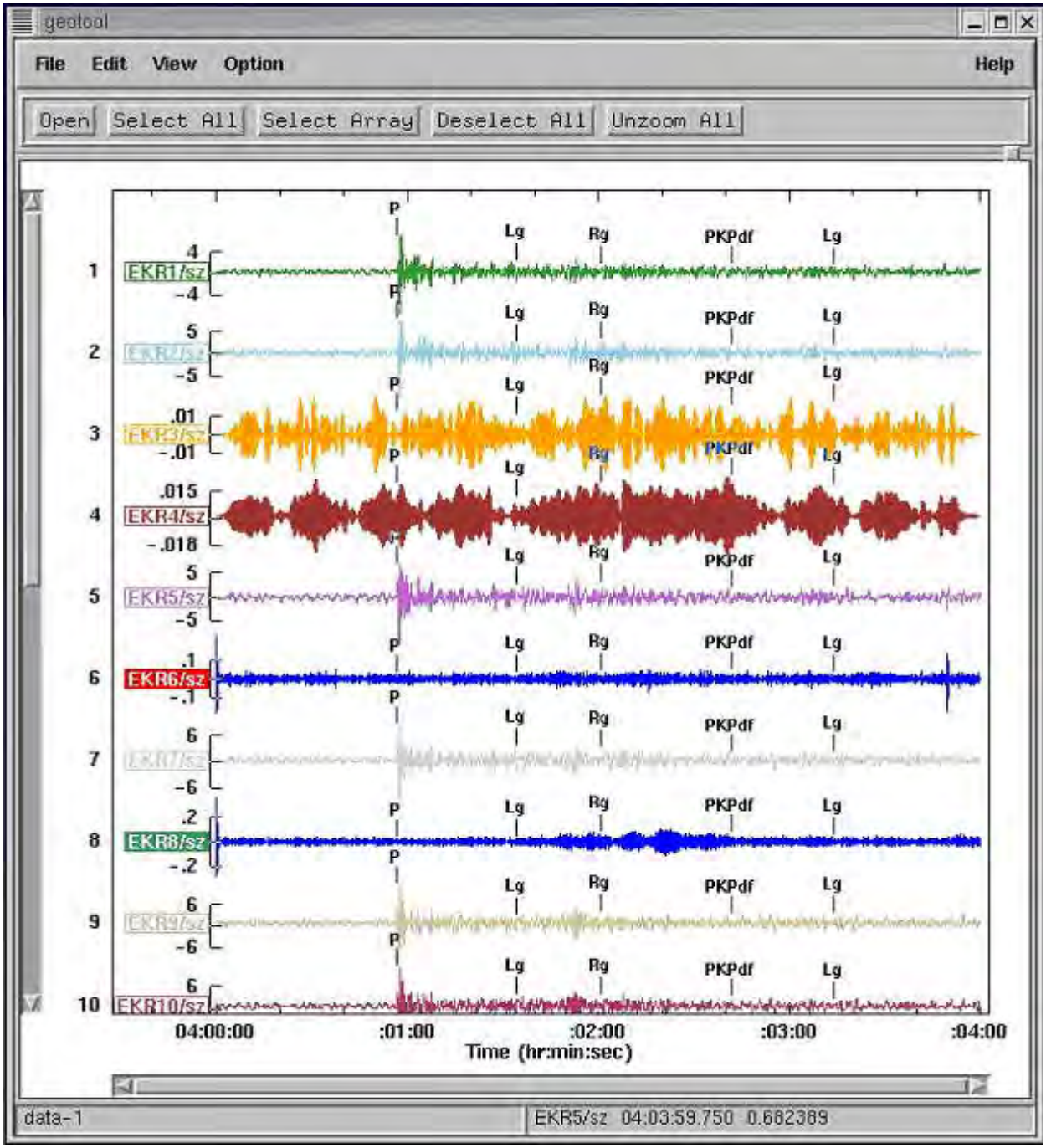

Figure 5. The waveform display that has been running within the *geotool* server program running under Linux is now updated with the seismograms for channels 6 and 8 that were filtered by the WaveformViewer client program running under Windows 2000. Just as with the data transmission from the server to the client, the data that were transmitted back were sent dynamically from the computer's memory rather than being written out as disk files. The whole process shows how a filter could be applied in the reference event analysis system: the data analyst can apply either a filter using a routine that is part of *geotool* or a filter that is part of a separate application (in this case, one written in Java and running on a different computer under a different operating system). This demonstrates the technical feasibility of constructing a reference event analysis system by using CORBA to link stand-alone seismic data analysis programs that are distributed across a network.

IMAGERY ASSETS FOR SUPPORTING NUCLEAR EXPLOSION MONITORING RESEARCH AND DEVELOPMENT

Michael Skov, Benjamin Kohl, and Robert L. Woodward

Science Applications International Corporation

Sponsored by Defense Threat Reduction Agency

Contract No. DTRA01-99-C-0025

ABSTRACT

The Defense Threat Reduction Agency's (DTRA) Center for Monitoring Research (CMR) maintains a wide range of technical capabilities to support nuclear explosion monitoring research and development. Within the CMR the Research and Development Support System (RDSS) operates as the vehicle to both digest and distribute data and research results of value to both DTRA authorized researchers and the general research community, in particular providing access to processed commercial imagery.

In recent years, commercial products, such as the 1-m-resolution panchromatic products of IKONOS, have enabled the nuclear explosion monitoring research community to benefit from satellite-based imagery acquisition systems. CMR maintains a library of imagery products ranging from the recently acquired, freely available (www.visibleearth.nasa.gov) low-resolution (1-km) composite images of the entire Earth, to 4-m multispectral and 1-m panchromatic (IKONOS) images of selected regions. Supplementing the high-resolution imagery products are 10-m panchromatic (SPOT) and 30-m multispectral (Landsat) images. Even higher resolution (0.7-m) commercial services (Digital Globe) are becoming available and high-resolution images will be acquired by the CMR to extend current holdings.

Within the CMR, research is conducted to determine methodologies for integrating enhanced event location and characterization techniques for nuclear explosion monitoring systems. One aspect of this effort is the utilization of imagery products to provide geographic context for event solutions, and, in some cases, to validate event location hypotheses.

The RDSS makes available selected imagery holdings via http://www.cmr.gov/rdss . Assets include interactive Portable Document Format (PDF) files of annotated images of Novaya Zemlya, Russia; Lop Nor, China; Pakistan; and India. Other imagery assets may be made available to the research community subject to the license agreement of the imagery vendor.

OBJECTIVE

The Defense Threat Reduction Agency (DTRA) sponsors the Center for Monitoring Research's (CMR) effort to improve nuclear explosion monitoring. Within the CMR, the Research and Development Support System (RDSS) (Woodward and North, 2002) supports the DTRA PRDA and general R&D communities with assistance ranging from data and research product dissemination to integration and testing of research and development results. Also within the CMR, the Technical Verification and Analysis Support project provides an environment to demonstrate nuclear explosion monitoring advances applied to generalized conditions. More focused efforts, such as the Lop Nor Advanced Concept Demonstration (Kohl *et al*, 2002), provide environments to develop, integrate and demonstrate advanced techniques applied to specific nuclear explosion monitoring regimes. Despite the broad scope of CMR activities, one common component is the application of imagery assets to the nuclear explosion monitoring research and development effort.

RESEARCH ACCOMPLISHED

The CMR maintains an assortment of imagery products to support research and development. Products range in scale and scope from high-resolution (1-m) geographically registered images (IKONOS) of small regions (~100 sq. km per scene) to low-resolution (1-km) composite images covering the entire Earth. The CMR employs these assets in a variety of ways, including validation and refinement of ground truth locations, event analysis and context visualization, and site identification. Additionally a selection of the imagery assets has been annotated and packaged as interactive Portable Document Format (PDF) documents for use by the general R&D community. In the sections below, each of these areas will be described, and we will close with a summary of planned imagery acquisitions.

Imagery to support ground truth

Many R&D efforts rely on the existence of well-located reference events. Such events, categorized by their absolute location uncertainty in kilometers as GT1 (ground truth, 1 km), GT2, GT5 and so on, are highly valuable for the establishment of regional travel-time corrections and for use as master events when applying Joint Hypocentral Determination (JHD) and Master Event Location techniques. Fisk (2002) demonstrates the advantage of applying high-resolution imagery to the task of establishing ground truth for nuclear explosions at the Lop Nor, China nuclear weapons testing facility.

CMR imagery assets covering the tunnel (western) and vertical-borehole (eastern) areas of the Lop Nor facility were analyzed for surface features associated with nuclear explosions. Features such as adits, boreholes, roads, and structures were identified. Subtler features, such as erosional characteristics, were utilized to establish the relative age of the surface features. Using these features, Fisk (2002) determined precise locations for three nuclear explosions. Using these three events as master events, eight other explosions were relocated. Semi-major axis error estimates for these events were less than about 0.65km. Event locations could be associated with observed features to provide an absolute accuracy of 300 m or less – the registration accuracy of the satellite imagery.

Figure 1 demonstrates the clarity of surface features visible in the tunnel region of the Lop Nor facility. The image is a panchromatic (1-m) sharpened, multispectral (4-m) image producing an approximately 1-m-resolution natural color image. This image, covering approximately ¼ of a square kilometer, highlights two (areas 'A' and 'B') of the four tunnel adits described by Fisk (2002). Also visible in the scene are numerous road and support structures. Figure 2 similarly displays the anthropogenic features associated with a portion of the vertical borehole region of the Lop Nor facility.

Using imagery to support the determination of ground truth locations, 11 nuclear explosions, detonated between May 1990 and July 1996 have been relocated and established as GT1 events. These events were utilized during the Lop Nor Advanced Concept Demonstration (Kohl *et al*, 2002) to illustrate the advantage of employing Master Event Location techniques to locate small (mb 2.5-3.5) events.

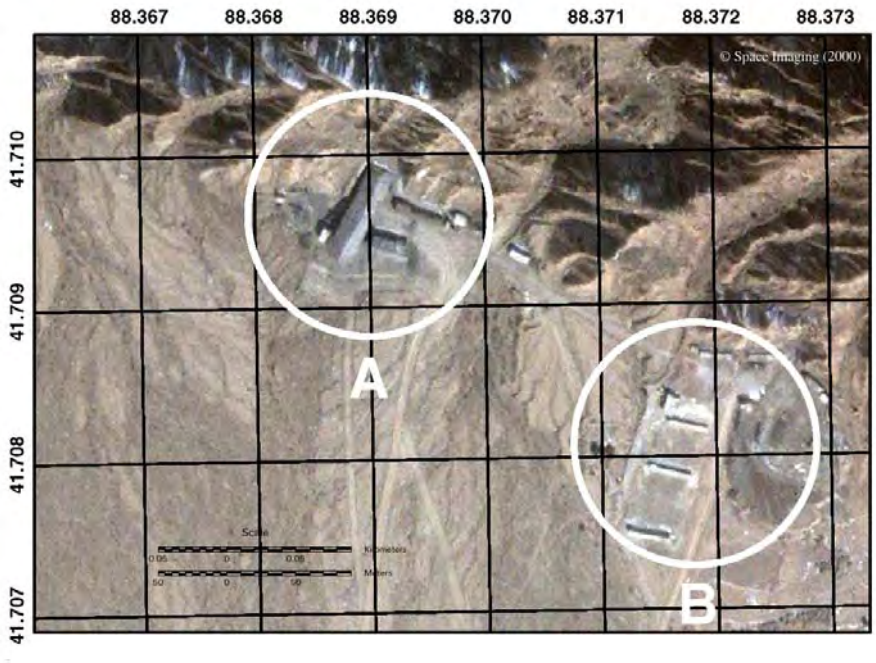

Figure 1. IKONOS imagery from CMR's collection showing two tunnel adits in the Lop Nor complex. The regions labeled 'A' and 'B' correspond to tunnel adits 'A' and 'B' as described by Fisk (2002).

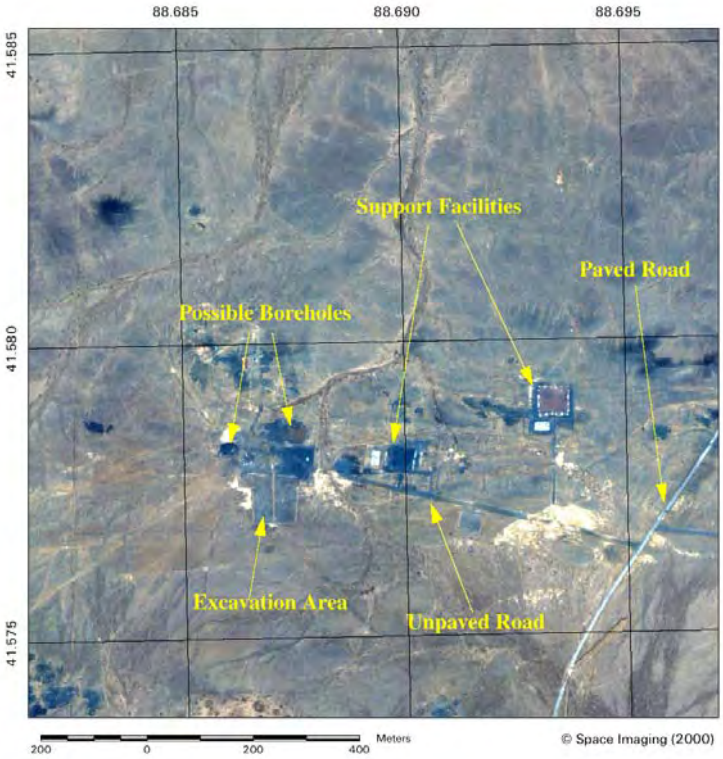

Figure 2. Surface features associated with vertical borehole emplacements in the Lop Nor complex. The IKONOS imagery was acquired, processed and archived by CMR analysts; the annotations are from Fisk (2002).

Imagery to support event analysis and context visualization

Satellite imagery can provide a rich backdrop for conveying information relevant to event analysis or to an event location. High-resolution images such as those shown in Figures 1 and 2 are often required to identify small-scale surface features associated with an event. In some situations, however, broader coverage is desired. Figure 3 shows the Novaya Zemlya, Russia region including several hypothesized locations for a February 23, 2002, seismic event. Also shown, for additional context, are the locations of several historical events of interest (blue triangles) and of underground nuclear explosions (red stars). The larger coverage area provides better visual clues as to the separation of this event from known nuclear tests and places the event in the overall geographic context. Displaying larger coverage areas is neither technically practical nor financially feasible using high-resolution products such as IKONOS. Figure 3 is based on lower resolution (~40 m) MODIS imagery freely available from NASA's Earth images web site (http://visibleearth.nasa.gov).

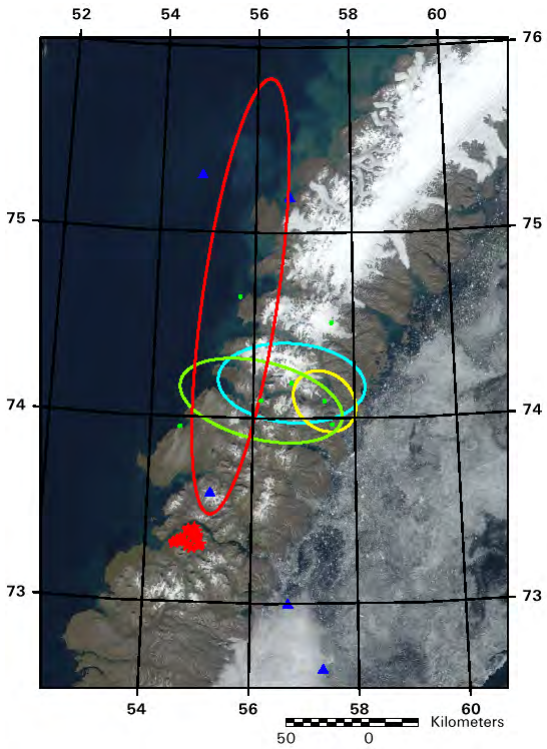

Figure 3. NASA MODIS imagery of Novaya Zemlya, Russia (http://visibleearth.nasa.gov).

NASA maintains a substantial catalog that CMR staff utilize to identify images of potential value to nuclear explosion monitoring research and development. Also available from NASA (http://visibleearth.nasa.gov) are low-resolution (1-km) composite images covering the entire Earth. CMR has acquired this collection of images and is currently assembling relevant regional composite images.

CMR's usage of imagery also includes sophisticated visualization techniques such as imagery draping. Figure 4 illustrates the technique. The region shown in Figure 1 is draped over digital terrain elevation data to produce a three-dimensional (3-D) transformation of IKONOS imagery. This specific example shows non-exaggerated surface elevation features associated with two of the adits in the western portion of the Lop Nor, China, nuclear weapons testing facility. Of particular note is the extent of the overburden provided by the ridge. The extent and relative isolation of the overburden is further illustrated through the creation of "flyby" animations. Two such animations were constructed to support the Lop Nor Advanced Concept Demonstration (Kohl *et al*, 2002). One such animation toured the western tunnel region; the second illustrated the features around the vertical borehole complex in the eastern portion of the Lop Nor facility.

Figure 4. IKONOS imagery of the region shown in Figure 1 draped over terrain data.

Imagery for site identification

Supporting the efforts of ground truth determination and event context visualization is an effort to maintain imagery holdings for regions of particular interest. Recent imagery acquisitions can obviously aid research and development by providing the most up-to-date view possible of surface features in a region of interest. However, other benefits, such as resolving surface features obscured by clouds or shadows, can also be realized through routine acquisition of imagery.

Most sites of interest are best imaged by acquisitions in mid to late summer. These times provide high sun angles and minimize cloud and snow cover. For this reason, most images commissioned by CMR have acquisition dates of July, August, and September (images of sites in the northern hemisphere dominate current holdings). The subtle changes in acquisition date and time can be beneficial for altering sun angles, but often the more overt changes seen year-to-year are the most interesting.

Identification of changes can be highly valuable for tasks such as establishment of ground truth. Fisk (2002) used substantially more subtle features, such as relative erosional characteristics, to establish the relative age of various components of the Lop Nor, China, facility. Clear changes observed in sequential images, such as those illustrated in Figure 5, can provide substantially better temporal information than can be inferred by interpretation of erosional features. The region highlighted with the white box in Figure 5 illustrates the substantial development that occurred in the 14 months between the acquisition dates of July 2000 and September 2001 of high-resolution (~1 m) IKONOS imagery and illustrate the advantage of maintaining and refreshing imagery holdings.

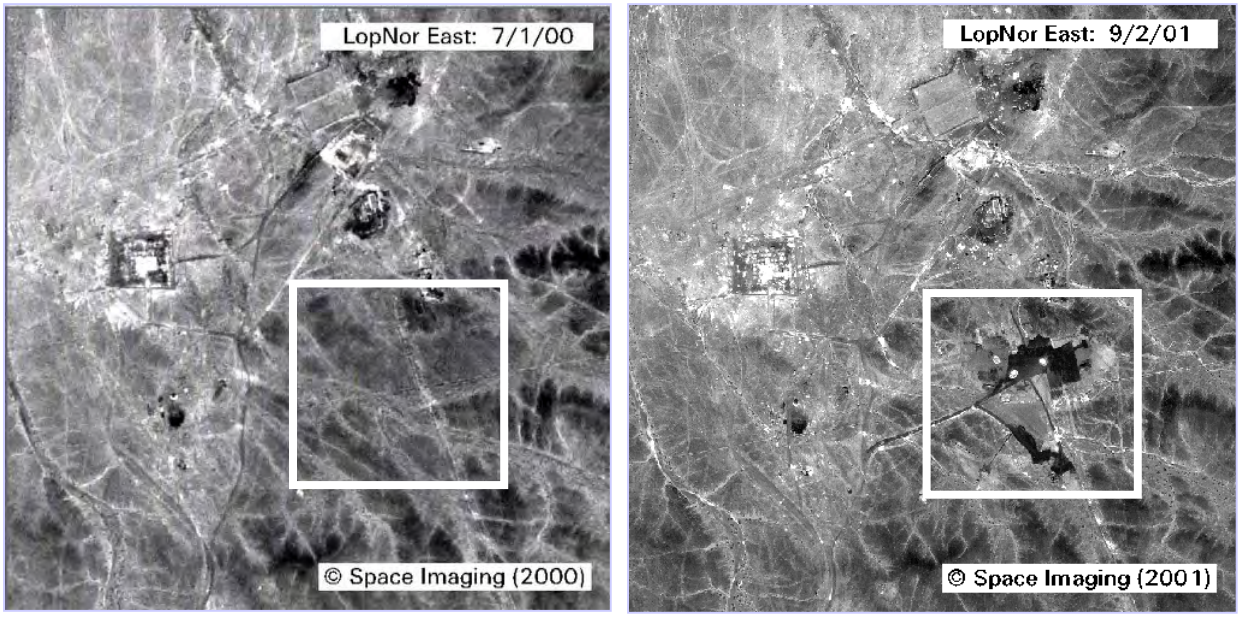

Figure 5. Two IKONOS images of Lop Nor, China taken approximately 14 months apart illustrating the substantial observable changes occurring at the site.

Detailed analysis of the changes has not been conducted; however, current plans include the acquisition of higher-resolution (~0. 7-m) Digital Globe imagery for this site in 2002. A more detailed study may be initiated pending the initial analysis of new imagery and a determination of need.

Imagery for the research community

CMR provides annotated satellite imagery products for use by the research community. Subject to the end user license agreement of the image provider, selected imagery is packaged in PDF format and made available from the RDSS portion of the CMR web site at http://www.cmr.gov/rdss . The PDF documents provide mechanisms to zoom on features of interest and navigate the region. Figure 6 shows a snapshot of the portion of the RDSS web content that provides a high-level view of the Novaya Zemlya, Russia, region. Annotations include structures, roads and rivers, as well as features more directly related to nuclear weapons testing, such as tailings and subsidence craters. The images viewable directly on the web site are reduced resolution; however, the PDF format documents available for download provide full resolution versions of the imagery.

Currently available imagery includes a mosaic of three images of Novaya Zemlya, Russia, (Figure 6), two images of Lop Nor, China, showing both the tunnel and vertical borehole regions, one image of the site of the May 5, 1974, and May 11, 1998, underground nuclear tests in India, and two images of the test facility in Pakistan, including the site of the May 28, 1998, underground nuclear test. Each of these is available via the CMR web site. Also available are examples of typical features associated with nuclear weapons testing, such as support infrastructure and collapse features. The main entry point for the CMR web site may be accessed at http://www.cmr.gov .

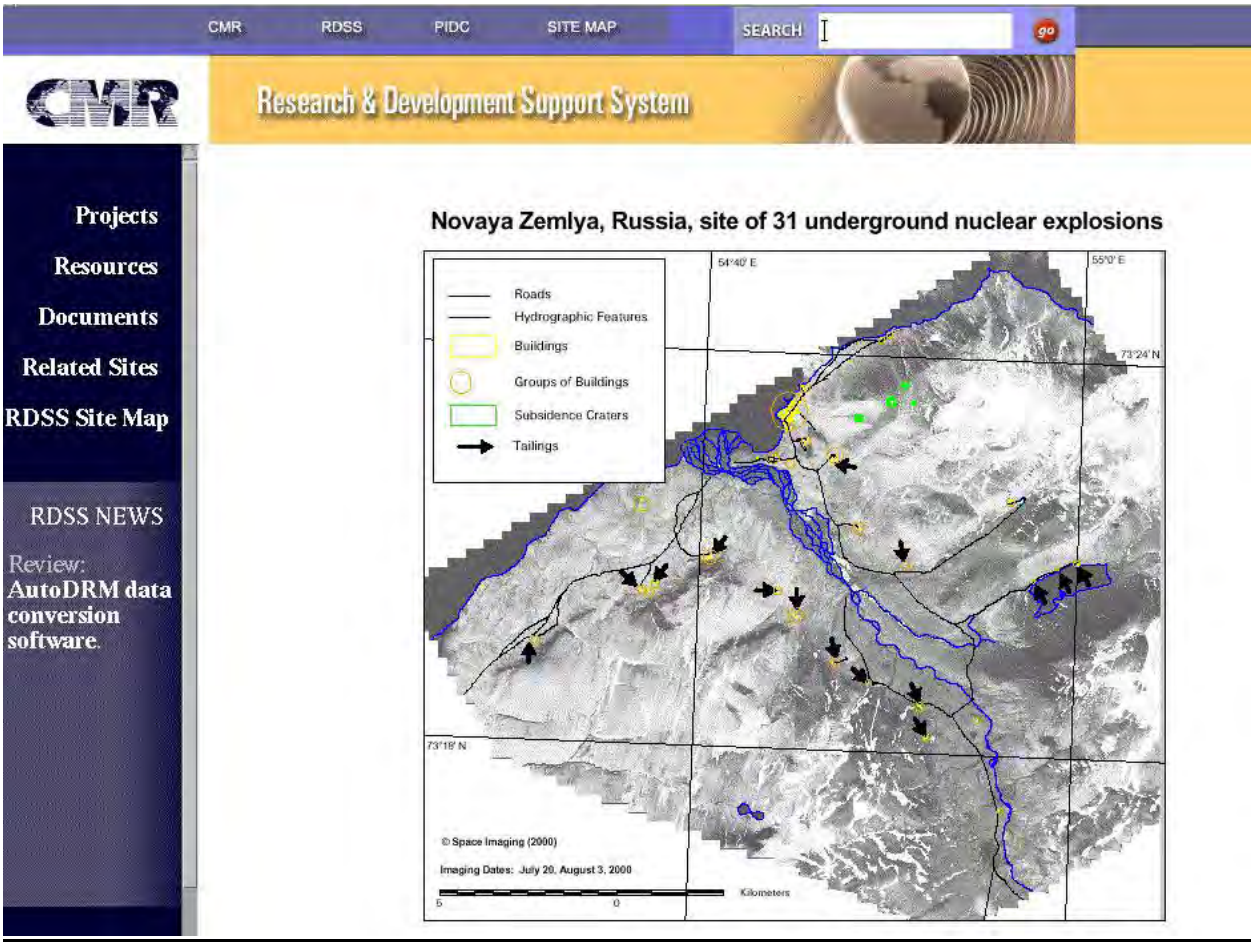

Figure 6. Screenshot of a portion of the CMR web site showing one of the images (Novaya Zemlya, Russia) available from the RDSS.

Planned 2002 acquisitions

As of this writing, the Technical Verification and Analysis Support component of CMR has initiated imagery acquisitions for 2002. Pending the outcome of the price quote process, CMR is considering new acquisitions for four regions of interest. For all sites, CMR is considering the acquisition of higher-resolution panchromatic (0.7-m) Digital Globe products. Multispectral images may be acquired for selected sites. Two images covering the Novaya Zemlya, Russia, test facility are being considered. Three new images of the Lop Nor, China, region are being considering, including one of the western (tunnel) area, one of the eastern (vertical borehole) area including the altered region identified in Figure 5, and possibly an image of the region southwest of this complex where two tests are reported to have been conducted many years ago. Also under consideration are updates to the imagery holdings for India and Pakistan.

CONCLUSIONS AND RECOMMENDATIONS

CMR's imagery acquisition program has proven a valuable aid to efforts such as the establishment of ground truth locations and for the visualization of research and development results. Additional, commercial, high-resolution imagery will be acquired on a periodic basis to ensure CMR's imagery holdings remain current. These commercial products will be supplemented with freely available products whenever possible.

ACKNOWLEDGEMENTS

The authors would like to thank Mark Fisk for providing a pre-publication version of his upcoming paper describing the use of satellite imagery to establish ground truth locations. Many thanks to Brenda Zuzolo for her continuing work to acquire, register, catalog, and interpret imagery products for CMR. Special thanks to Elizabeth Eaton of SAIC's Imagery Central (http://www.imagery-central.com), who provides continuing logistical support for CMR's commercial imagery acquisition program. Finally, the authors would like to recognize the effort and support of the Defense Threat Reduction Agency and of the Nuclear Treaty Program Office.

REFERENCES

Fisk, M. D. (2002), Accurate Locations of Nuclear Explosions at the Lop Nor Test Site Using Alignment of Seismograms and IKONOS Satellite Imagery, in press, *Bull. Seism. Soc. Am.*

Kohl, B., R. North, J. R. Murphy, M. Fisk, and G. Beall (2002), Demonstration of Advanced Concepts for Nuclear Test Monitoring Applied to the Nuclear Test Site at Lop Nor, China, *24th Seismic Research Review*, September 17-19.

Woodward, R. L. and R. G. North (2002), A Support System for Nuclear Explosion Monitoring Research and Development, *24th Seismic Research Review*, September 17-19.

THE GNEM R&E SPATIAL DATA INTERFACE

Lisa K. Wilkening, Matthew N. Chown, and Bion J. Merchant

Sandia National Laboratories

Sponsored by National Nuclear Security Administration
Office of Nonproliferation Research and Engineering
Office of Defense Nuclear Nonproliferation

Contract No. DE-AC04-94AL85000

ABSTRACT

In the course of developing contextual data products for the Ground-based Nuclear Explosion Monitoring Research & Engineering (GNEMR&E) program, a need for rapid spatial analysis of seismic events has been realized. To this end, Sandia National Laboratories is working to develop a Spatial Data Interface (SDI) application, which will assist in the identification of these events. The SDI is supported by contextual data and reference seismic information produced by the GNEM R&E program.

The Spatial Data Interface is designed to be a generic application, which can be accessed from any of the GNEM monitoring tools (ArcView, the MatSeis package and associated regional seismic analysis tools, etc.), and which could be accessed by processes within an automated event monitoring pipeline. Contextual data is stored in a relational database, Oracle, and is accessed via an Environmental Systems Research Institute (ESRI) software package, ArcSDE. A suspicious seismic event may be submitted to the SDI, which in turn evaluates the event against a set of criteria using reference contextual data. These criteria consist of a set of spatial queries, which are the basis upon which an event may be tagged for further analysis or dismissed.

OBJECTIVE

The objective of the Sandia National Laboratories (SNL) Spatial Data Interface (SDI) is to provide a generic interface designed to enhance the processing of seismic events, which can be used either in automated or interactive processing pipelines for treaty monitoring. An application using SDI will process these events through a series of spatial queries, specifically formulated to assist in their identification and analysis. SDI will be developed using an existing programming interface for ArcSDE, an Environmental Systems Research Institute (ESRI) product. This product facilitates rapid access and query functions for spatial data stored in an Oracle database. It can take advantage of the availability of contextual and reference information properly stored within a database, and complement the capabilities of existing tools, data sets, and infrastructure.

RESEARCH ACCOMPLISHED

Introduction

Meeting the GNEM R&E program monitoring goals implies the detection, location, identification, and characterization of possibly hundreds of seismic events daily. Automated processing procedures are in place to perform this duty. As an event moves through the automated system, various software applications are accessed, which draw upon reference information stored in Oracle databases and flat files on the operating system.

Occasionally, a suspicious event is detected. An automated monitoring system may have embedded logic with which it can determine the priority of this event. This logic is based on select criteria, coupled with existing reference data sets. An event may then be dismissed as irrelevant to the monitoring mission, or tagged for further seismic analysis.

Development of the SDI is intended to enhance the automated system processing of questionable events by referring to spatially referenced datasets. Most applications support special event identification, but are somewhat limited. By incorporating access to additional detailed spatial data and enhanced query logic, monitoring analysis may be more efficiently accomplished, providing robust results for event prioritization and reporting efforts.

Spatial Data Interface Application Development

The Spatial Data Interface will be prototyped using ArcSDE 8.2 (formerly SDE, Spatial Database Engine) from ESRI. ArcSDE is an interface, which resides on top of any supported relational database (in this case Oracle), and is capable of serving spatial data to different applications. Via ArcSDE, spatial data is loaded into Oracle where it is stored and managed as tables. This application will also take advantage of the Oracle Spatial extension for spatial data types. ArcSDE can either use these data types or provide its own mechanisms for managing the feature geometry (West, 2001). In addition, ArcSDE provides fast, flexible querying capabilities by spatially indexing the data features. These indexes can be fine-tuned for maximum performance in concert with the Oracle Spatial tuning guidelines.

The SDI application itself will be designed and implemented using ArcSDE's open, high-level C programming language API. The C API allows a developer to build a custom application for ArcSDE, incorporating many advanced geographic information system (GIS) functions for spatial querying (West, 2001). The C API is also the means by which all applicable ESRI software products access ArcSDE. This flexibility would allow the SDI application to be coupled with other customized GIS applications along the monitoring pipeline, such as ArcView GIS for graphic display of SDI results. The ArcView GIS application is customized using its own object-oriented programming language, Avenue, which also allows access to ArcSDE's functionality.

The SDI interface is intended to be generic and independent. Therefore, it could theoretically reside anywhere on the system and be called from any application providing that a valid interprocess communication interface is in place. The SDI will operate with minimal input from the user beyond some key information to initiate processing. This information can either be provided by the user via a GUI or can be contained in a message delivered to the SDI from another application. This information can include the error ellipse information for the event, point location information for the event, and a dataset of interest against which the spatial analysis will be made. A set of canned queries will be accessible for processing. The user will also have the ability to customize the query set or iterate the

process as necessary. A user may also elect to perform spatial analysis between any of the contextual datasets available, or against a spatial feature stored in seismic database holdings (such as stations, arrival paths, etc.).

The output of the SDI will be passed back to the calling application, which can be archived, displayed (Figure 1) or used to trigger further processing. For example, a message may be passed to ArcView for viewing the selected event on a map, or to MatSeis to view associated waveform information, or to a web-based bulletin generation tool for event reporting. The goal is to provide an output format that can be easily incorporated into any monitoring task.

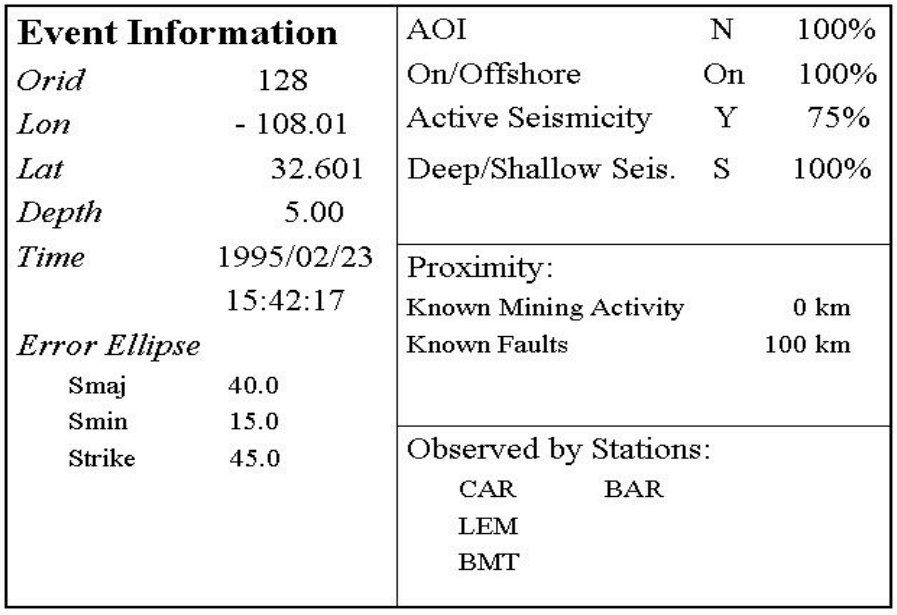

Figure 1. Example of an event identification application, which has used SDI to characterize an event.

Data Sets

A given monitoring system architecture will generally incorporate software and interfaces to perform seismic analysis and data visualization, either for automated or interactive processing components. Depending on the sources, the architecture will likely manage data as a mix of relational databases and flat files stored on the operating system. Therefore, the calling application must be able to access and incorporate either data storage method, or have an interface, which formats the data accordingly.

As noted above, the customized SDI interface utilizes data stored in Oracle tables. Seismic database holdings include event data and associated attribute information. Generally speaking, events have an implied spatial attribute associated with them (a latitude and a longitude), which will form the basis for many of the spatial queries. However, the remainder of contextual data holdings is stored in flat file format at present, and must be loaded into Oracle.

A wide variety of reference information may be used in order to analyze a seismic event. In order to account for the nature and location of an event anywhere across the globe, the contextual data holdings must be diverse. Spatial contextual information may include:

- Political Boundaries
- Coastlines
- Continental shelf
- Roads/railroads
- Topography/bathymetry contours
- Mines

- Seismic stations
- Regions of seismicity
- Faults
- Volcanoes

The ArcSDE software also allows spatial data to be stored with internal behaviors or relationships. The SDI can take advantage of these relationships, and other non-spatial information submitted to it, when evaluating a spatial query against these data.

Spatial Queries

Spatial data is generally stored in one of two models, raster and vector. Raster data are represented as cells of a uniform size, each containing a single numeric value. They are often used for modeling surfaces, such as elevation or depth to basement. For the purposes of this prototype, raster data are not utilized, but may be incorporated in future iterations of this application.

The contextual data sets listed previously are stored as vector data in the SDI's prototype monitoring system. Vector data is made up of a series of features with explicit geometry. Attributes, behavioral, and relationship information may also be stored for each feature. Queries can be based on the spatial relationship of features' geometries as easily as on specific attributes or behaviors. For example, a query may select for a political boundary, which contains features of a global seismic activity data set. The query can then be modified to subselect a particular political boundary that contains only shallow seismic activity and return the results (see Figure 2).

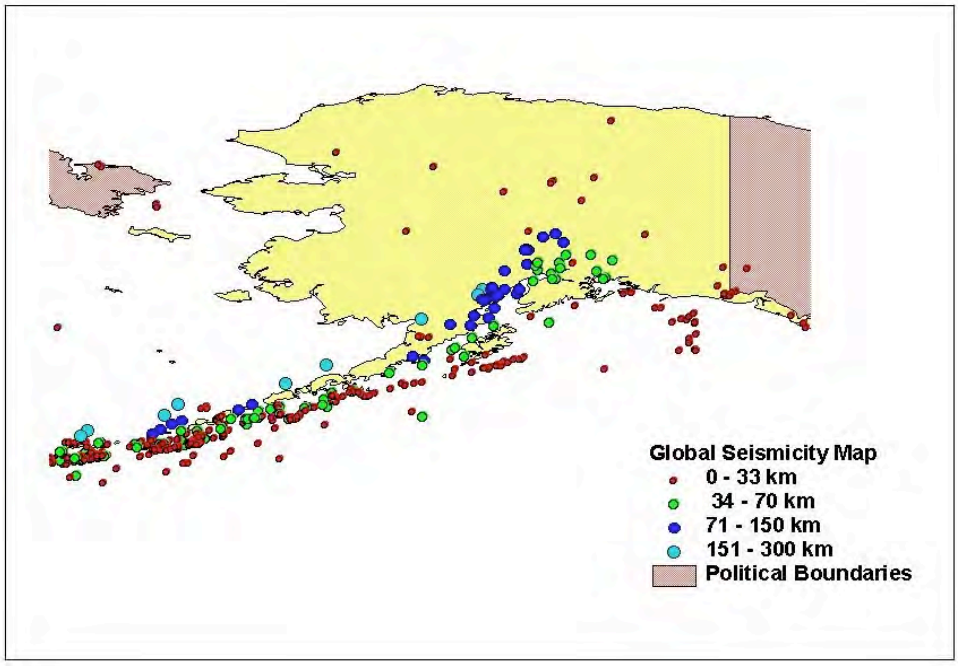

Figure 2. Graphic display of a query depicting a shallow depth seismic activity features within a political boundary.

The SDI application must be able to analyze spatial relationships between a target feature and any feature of a comparison data set. It may do this by performing any one of a basic set of built-in spatial querying capabilities that test a spatial relationship (see Figure 3), using the C API functions. SDI will also take advantage of basic GIS functions such as finding the distance and bearing between features, buffering features or generating new data sets from query results.

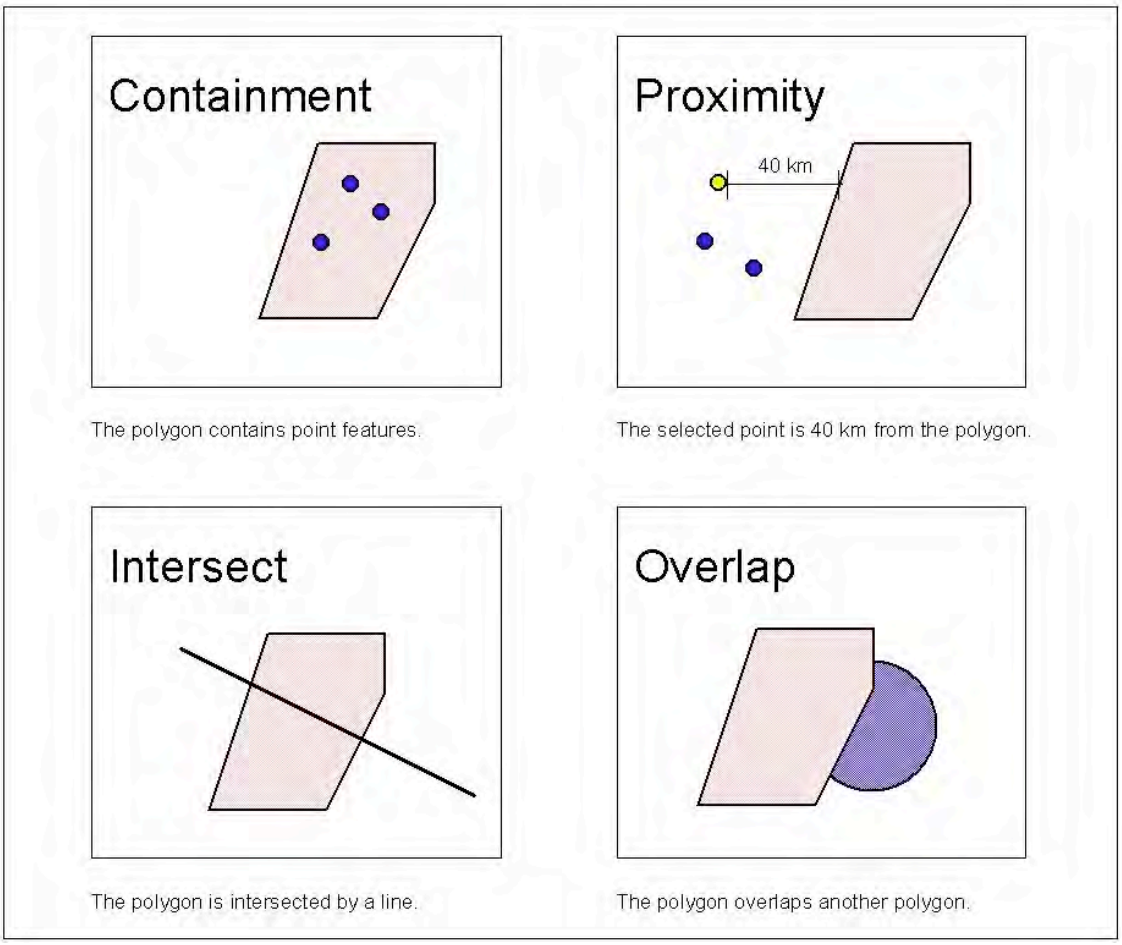

Figure 3. Examples of common spatial relationships between features.

While an automated procedure may have existing logic for defining priorities of seismic activity monitoring, performing spatial analysis on suspicious events can enhance the process by finding relationships between contextual features. Figure 1 gave an example of simple, first-cut analysis. Many times, this may be all that is required to dismiss an event. However, for those suspicious events, which are not immediately dismissed, the SDI can add another dimension to the process, strengthening confidence in the event analysis. The utility of this application is most apparent when placed in the context of normal event processing. An example is depicted in Figure 4.

Figure 4 models an automated processing system within which decisions are made regarding a suspicious event. In this case, an event, which occurs beyond realistic testing depths, will be dismissed immediately. This decision will have been made outside the SDI application. If the answer is yes, a spatial query is submitted to the SDI, which evaluates the overlap of the event's error ellipse with the predefined area of interest data set. The result is returned to the calling application. The next call may be to check the event's error ellipse against seismic data sets of the region, or its proximity to dams or roadways. Specific contextual data, such as depth values ("Deep" in Figure 4), may be queried repeatedly as the event is more accurately defined and characterized. This process can iterate as necessary through the automated analysis pipeline, querying the event against a series of contextual data sets until either a decision is reached, or the event is kicked out to an interactive processing pipeline for special event analysis. SDI analysis may then be reapplied.

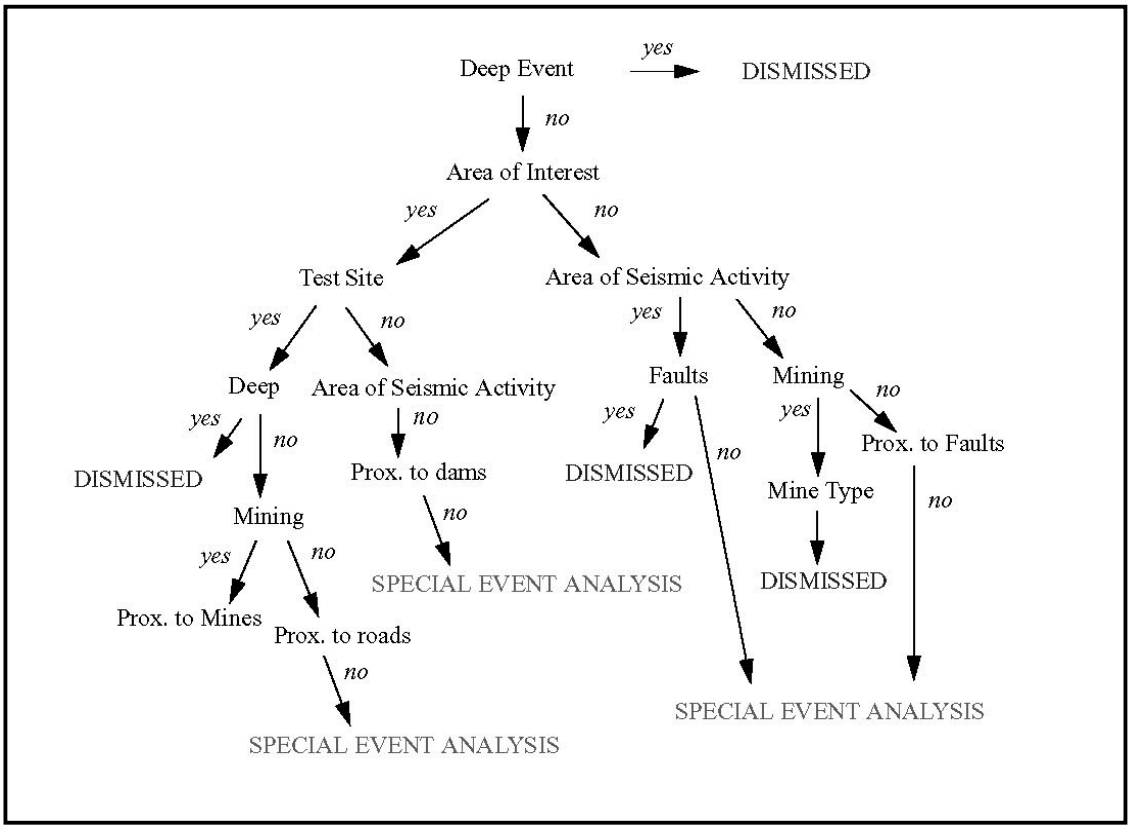

Figure 4. Example of an automated processing decision tree. Event processing moves through the tree, interfacing with SDI for spatial analysis where applicable.

Interactive event processing may require entirely new spatial querying capability. For example, the automated procedure will have established the initial key criteria that an event is shallow, in an area of active deep seismicity, and close to, but not inside, an area of interest. The SDI may then be called upon to answer spatial questions, which provide the analyst with context about the geographic and geophysical attributes of the region. These may include questions about the predominant geologic features in the region, topographic elevations, proximity to faults, types of materials mined in the area, or proximity to human habitation and other man-made features.

CONCLUSIONS AND RECOMMENDATIONS

The application developers recognize that there may be several iterations of the SDI before it is considered a "complete" tool. Future developments will likely focus on creating the "front-end" application to structure the processing rule-set and handle information passing between monitoring system components. As its use grows, new datasets may be developed and new spatial relationships defined. The questions will continue to define the system requirements. Given the availability of and confidence in the spatial contextual data, the SDI should prove to be both an efficient and effective analysis tool, and it should be considered for use as part of an automated event monitoring pipeline.

REFERENCES

West, R. (2001), Understanding ArcSDE, Environmental Systems Research Institute, Inc. (ESRI), Redlands, CA.

A SUPPORT SYSTEM FOR NUCLEAR-EXPLOSION MONITORING RESEARCH AND DEVELOPMENT

Robert L. Woodward and Robert G. North

Science Applications International Corporation

Sponsored by Defense Threat Reduction Agency

Contract No. DTRA01-99-C-0025

ABSTRACT

A comprehensive support system for Research and Development (R&D) efforts funded by the Defense Threat Reduction Agency that address nuclear-explosion monitoring and verification research and development is provided by the Research and Development Support System (RDSS) at the Center for Monitoring Research (CMR). The RDSS provides resources to support ongoing research and development, most importantly through extensive data sets and testing environments at appropriate scales, and identifies important technical issues for achieving improved nuclear monitoring capability.

The RDSS provides researchers with access to a ten terabyte data archive containing current International Monitoring System (IMS) seismic, hydroacoustic, infrasound, and radionuclide data, as well as data archives spanning several years; past and present products of the International Data Centre (IDC) and Prototype IDC, including Reviewed Event Bulletins and various radionuclide reports; test environments; a variety of special purpose data sets and databases, such as the Nuclear Explosion, Ground Truth, and Infrasound databases; and an on-line technical library.

Defense Threat Reduction Agency (DTRA)-sponsored researchers actively deliver results of their research contracts to the RDSS. These results are archived and are available for download from the RDSS web site (see below) to authorized researchers. Recent deliveries include infrasound recordings of atmospheric nuclear explosions, earthquake bulletins for various parts of the world, Geographic Information System databases, and reports on a wide range of seismic, hydroacoustic, and infrasound research topics.

The RDSS supports and collaborates on integration and testing of R&D results. Recent examples include testing of station-specific source corrections (SSSCs) produced by DTRA-sponsored calibration consortia for IMS stations in Eurasia and North Africa. We also highlight a collaborative effort with researchers at the University of California, Berkeley (UCB) to establish a platform with direct access to near-real-time data for testing and developing Automatic Moment Tensor Analysis software.

The RDSS actively develops tools and products to better serve the nuclear-explosion-monitoring R&D community, as well as to provide a gateway to a wide range of CMR resources. A variety of commercial imagery for nuclear test sites is available on the RDSS web site. We have also recently developed a remote user interface to our EvLoc event location software. Authorized members of the nuclear monitoring R&D community can submit any combination of seismic, hydroacoustic, and infrasound arrival and amplitude information and the EvLoc software running at the CMR (the same software as delivered to the IDC) will compute an event location and magnitude. Comprehensive guides to CMR hydroacoustic and infrasound resources are also available. Further information on RDSS resources and services may be found by researchers on the RDSS web sites (http://www.cmr.gov/rdss).

OBJECTIVE

The purpose of the Research and Development Support System (RDSS) at the Defense Threat Reduction Agency's (DTRA) Center for Monitoring Research (CMR) is to improve nuclear-explosion monitoring capability by supporting the R&D community with a broad range of activities and resources.

RDSS activities include providing environments for testing and evaluating promising research results at a range of scales. Such testing provides the US government with quantitative measures of current monitoring capability, identifying obstacles and establishing expectations for achieving improved capability. The RDSS organizes and archives research results produced by the R&D community in a manner that facilitates the access to these results for the entire research community. Finally, a wide range of CMR internal resources is made available to the R&D community via the RDSS.

RESEARCH ACCOMPLISHED

The Center for Monitoring Research (CMR) provides many unique resources to support basic and applied research and development. CMR maintains a large and growing archive of seismic, hydroacoustic, infrasound, and radionuclide data, as well as special tools and functionality built to maximize information available for each data technology. In addition, a wide variety of special data products (both databases and data sets) has been assembled to support monitoring research. These data sets are routinely augmented with new data as they become available.

Researchers may also take advantage of the results of the DTRA PRDA research program that are delivered to the RDSS. These results are reviewed, archived and redistributed by the RDSS. The PRDA results are distributed in their raw (as delivered) form and if appropriate, in value-added form (e.g. added to related data to create a new product).

Finally, researchers may take advantage of the facilities and test capabilities provided by the RDSS. Testing environments can be arranged at any scale, from the full data-load of the IMS network and the full-processing environment of the IDC monitoring system, to highly specific experimental arrangements with historical data sets. Supporting facilities include a large UNIX-based computing environment, databases, and data archives.

In the remainder of this paper, we describe some of the data, data products, and capabilities that are available to the R&D community via the CMR RDSS.

Data Resources

The CMR has been continuously acquiring and archiving time-series and radionuclide data since 1992. Currently, the CMR receives data from a variety of international stations, including stations of the International Monitoring System (IMS) network. The data archive consists of over 10 terabytes of waveform data from seismic, hydroacoustic, and infrasound stations and is growing at a rate of approximately 1.5 Tb per year. Detailed guides describing the hydroacoustic, infrasound, and radionuclide resources have been prepared and these are available on-line at the RDSS web site. These guides provide detailed descriptions of the stations, instructions on accessing data, and detailed information on data availability. A guide to CMR seismic resources will be prepared in the future, though usage patterns for the data archive indicate that the R&D community is generally more familiar with the existing CMR seismic resources than either the hydroacoustic or infrasound data resources.

CMR data are easily accessed from remote sites by using the AutoDRM (Automatic Data Request Manager) interface, an e-mail-based request mechanism. RDSS users are also provided access to bulletins and other data products obtained from the International Data Centre (IDC) in Vienna, Austria. The RDSS is presently developing a streamlined, web-based graphical user interface to the data archive. We expect this new interface to be online in the fourth quarter of 2002.

Special Databases

The RDSS produces a variety of special databases and data products that are useful to nuclear explosion monitoring research and development, and these are summarized in Table 1. These data products provide data and metadata

assembled in a manner to maximize their utility for research purposes. Where appropriate, data being delivered to the RDSS by DTRA-sponsored contractors are added to these databases, such that the value of both the delivered data, and the database, are increased.

Table 1. Research databases available to R&D community via the RDSS.

Radionuclide	• High-resolution gamma-ray spectroscopy • Beta-gamma coincidence spectroscopy
Ground Truth	• Nuclear and chemical explosions, industrial events, earthquakes, mixed data sets
Reference Event	• Small- to medium-sized, well located, uniformly globally distributed events
Nuclear Explosion	• Nuclear explosions (1945 – 1993), announced nuclear explosions since 1984, and Australian Geological Survey Organization database (1945 – 1996)
Lop Nor	• An extensive compilation of seismic data for events in and around the Lop Nor nuclear test site region, China

Recently, an Advanced Concept Demonstration (ACD) was performed at CMR (Kohl *et al*, 2002). This ACD focused on improving the capability for monitoring the Chinese nuclear test site at Lop Nor. As part of this ACD, an extensive data set was assembled. The RDSS has now integrated the Lop Nor ACD data set into a data product for public distribution, referred to as the Lop Nor Database (LNDB). The LNDB includes nuclear explosions and earthquakes, as well as various synthetic events. All relevant information, including parameters, waveforms, and extensive metadata, are collected together in this product. As for the other RDSS research databases, all information is loaded into a centralized relational database, with waveforms and metadata stored on local disks. Database tables have been created to store metadata that do not fit within the standard IDC database schema.

The Lop Nor Database consists of 421 events (Figure 1) in the Lop Nor ACD "box" (defined as 39°--44° N and 86°--92° E), with approximately 43,000 arrivals. For each event there are multiple data sources, and a preferred origin is chosen based on the location accuracy. Data sources for events and arrivals include:

- ACD analysis results
- PIDC Reviewed Event Bulletins (REBs)
- IDC REBs
- CMR Nuclear Explosion Database
- CMR Ground Truth Database
- International Seismological Centre
- Annual Bulletin of Chinese Earthquakes (ABCE)
- PIDC GAMMA bulletin

A total of 205 events were thoroughly analyzed during the ACD work, including 25 out of all 45 nuclear explosions. Waveform data were obtained from the CMR archive system, CMR Nuclear Explosion Database, Incorporated Research Institutions for Seismology (IRIS) Data Management Center, and Blacknest UK data archives. Synthetic seismograms for small nuclear tests were obtained by applying frequency dependent scaling relations to actual recordings of large nuclear tests and embedding the result in noise recordings. Ground truth information is available for most of the nuclear explosions and for the scaled/embedded events. There are approximately 100 Gb of waveform data in total.

There are 37 tables in the LNDB providing detailed metadata for waveforms and events. Metadata tables are developed to document data sources, references to data sources, and various computational results. This database uses unique event identifiers (evid) to identify all related solutions for an event and the associated waveforms. Metadata are also associated with each event through the metadata tables. Arrivals from the ACD analysis and from bulletin collections are associated with their corresponding origins. Additional details about the Lop Nor database, including a complete description of the schema, will be published as a CMR Technical Report (to be completed in fourth quarter, 2002).

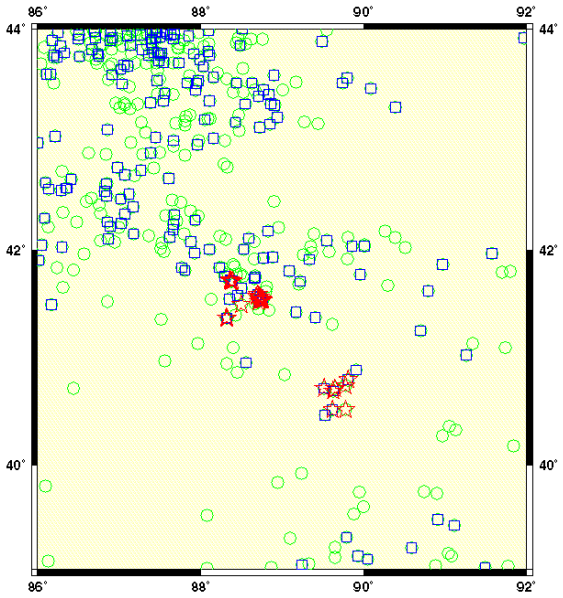

Figure 1. Preferred origin of 421 events (green circles) in the Lop Nor Database, including nuclear explosions (red stars) and events for which waveform data were analyzed (blue squares).

Commercial Satellite Imagery

A variety of high-resolution commercial satellite images are available through the RDSS (Skov *et al*, 2002). Images include 1-m panchromatic and 4-m multi-spectral satellite imagery obtained from commercial vendors. At CMR these images have been used in conjunction with re-analysis of seismic data to obtain definitive locations of historical nuclear explosions with accuracy suitable for designations as Ground Truth 1 (GT1) or GT2 events. Images have been obtained for the test sites at Novaya Zemlya, Lop Nor, India, and Pakistan.

The imagery has been analyzed to identify features in one of three categories: 1) direct evidence of disturbances resulting from nuclear detonations, typically collapse features; 2) direct evidence of test site artifacts highly correlated with locations of nuclear tests; 3) direct evidence of test site artifacts constrained to the vicinity of nuclear detonations. To estimate uncertainties, highly visible and distinct but spatially constrained features, such as the intersections of major roadways, are identified on a number of different sources. Older imagery from lower resolution sensors (SPOT, LANDSAT, KVR), digital terrain elevation data, and high resolution maps available through the National Imagery and Mapping Agency were registered with respect to one another, demonstrating variations of no more than several hundred meters.

The results of the imagery analysis are assembled in a series of imagery products that are available through the RDSS web site. The imagery products are provided in Portable Document Format (PDF) to ensure maximum portability. Table 2 presents a list of the imagery products presently available through the RDSS web site. This collection will continue to grow as new images are acquired as part of CMR's imagery acquisition program. A comprehensive discussion of the use and analysis of satellite imagery at CMR can be found in Skov *et al*. (2002).

Table 2. List of imagery products available through the RDSS web site.

Site	Acquisition Dates	Imagery Type	# of Nuclear Tests Within Area of Imagery
Novaya Zemlya	June 26, 2000 July 20, 2000 August 3, 2000	1-m panchromatic, mosaic of 3 images	31
Lop Nor	February 26, 2000	1-m pan + 4-meter multi-spectral	6
	July 1, 2000	1-m pan + 4-meter multi-spectral	13
India	August 10, 2000	1-m pan + 4-meter multi-spectral	2
Pakistan	July 9, 2000	1-m pan + 4-meter multi-spectral	1
	July 9, 2000	1-m panchromatic	1

Hypocenter Location Server

The RDSS has recently developed the Hypocenter Location Server (HLS) to provide a remotely accessible interface to the powerful hypocenter location program *EvLoc*. The *EvLoc* software is a core element of the CMR processing system and is part of the complete system provided to the IDC. *EvLoc* is capable of using any combination of seismic, hydroacoustic, and infrasound arrivals to determine hypocenters and to compute magnitudes (seismic only). The HLS is accessed by sending formatted e-mail messages to the server (in this sense it looks much like an AutoDRM server), as illustrated in Figure 2. The user provides data files, configuration files, and custom parameter files via FTP (using a flat-file structure or using XML). The HLS processes requests, with their associated input files, and then e-mails the results to the user.

EvLoc is a complex software component that relies heavily on a carefully configured database environment (e.g. Oracle) to function properly. As such, *EvLoc* is not readily portable. By providing access to *EvLoc* functionality through the Application Service Provider model as described here, researchers can readily use *EvLoc* in their analysis without worrying about software portability or configurability. Further, the capability provided by the HLS completely supercedes that provided by CMR's stand-alone hypocenter determination program *LocSAT*. Note that the HLS is fully backward compatible with *LocSAT* input files.

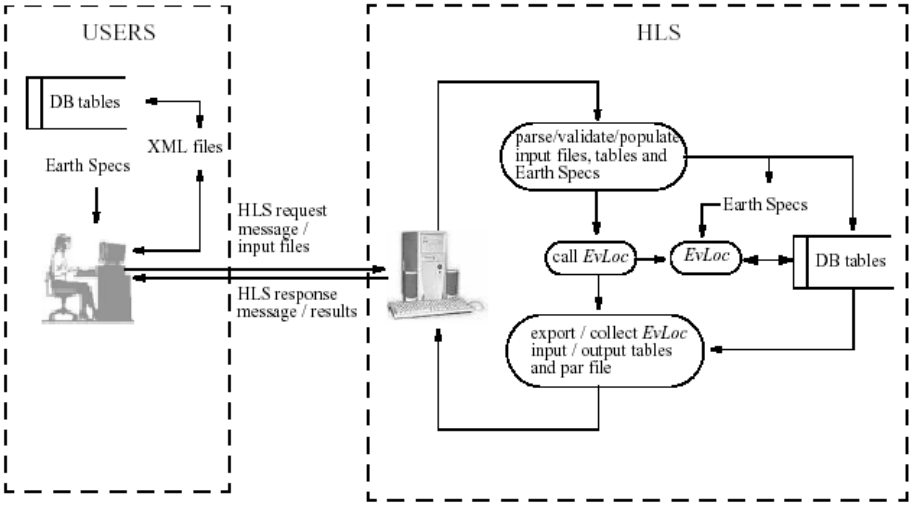

Figure 2. Data flow for the Hypocenter Location Server, showing the relationship between the user and the server.

DTRA Contract Results

A key activity of the RDSS is receiving, accepting, and testing results from the R&D community. In general, the RDSS receives three types of deliveries: technical reports, data to receive and store, and software components or parametric results to evaluate and possibly integrate into a monitoring system. All of the R&D products received by

the RDSS are archived and are made available for redistribution to the entire R&D community via the RDSS web site. Table 3 summarizes the deliveries from DTRA-sponsored researchers that have been received to date. To learn more about any of the products listed in Table 3, please consult the RDSS web site.

Table 3. Summary of research products received by the RDSS.

	Contract/Task Title	Performing Org.	P.I.	Products Received
1	Development of a Dynamic Infrasound Knowledge Database	BBN Tech.	Farrell	Software and User's Guide
2	Enhanced Depth Determination Using Cepstral Techniques	Weston Geophysical	Reiter	Report ; Software for cepstral F-stat analysis
3	Characterization of Reflected Arrivals for Hydroacoustic Test Ban Monitoring	BBN Tech.	Gibson	Final Report; database 15 events between 1965 and 1970
4	Feasibility of the Use of 3D Models to Improve Regional Locations in W. China, Central Asia, and Parts of the Middle East	Univ. of Colorado at Boulder	Ritzwoller	Final Report; database of KNET and CAB bulletins
5	Long-Period Surface Wave Dispersion and NDC Global Association Database	Boston College	Harkrider	Final Report; FORTRAN versions of travel time codes
6	Infrasound Excitation and Propagation Research	Maxwell Tech.	Stevens	Final Report; database of infrasound recordings; IDG Final Report
7	Statistical Calibration & Regionalization of China & Surrounding Region	New Mexico State Univ.	Hearn, Ni	Annual Bulletin of Chinese Earthquakes 1985, 1986, and 1991-1995
8	Collection and Analysis of Regional Seismic Data for Underground Explosions	Mission Research Corp.	Fisk	Final Report; waveform database
9	Reconnaissance of Backgound Infrasound at Selected Future IMS Locations, Atlantic Ocean	UC San Diego	Hedlin	Final Report
10	Development of Ultrahigh Sensitivity Xenon Detectors for Enhancement of Ability to Monitor Nuclear Testing	Univ. of Cincinnati	Valentine	Final Report
11	Discr., Det., Dep., Loc., and Wave Propagation Studies Using Intermed. Period Surface Waves in the Mid-East, C. Asia, and the Far East	Univ. of Colorado at Boulder	Levshin	Final Report
12	Advanced Regional Array Studies	NORSAR	Kvaerna	Final Report
13	Source Char. and Reg. Discr. of N. Idaho Rockbursts and Earthquakes	Univ. of Idaho	Sprenke	Final Report
14	Signal Det. and Estimation Directional Parameters for Multiple Arrays	UC Davis	Shumway	Final Report
15	CTBT Seismic Monitor Issues at Local Distance Ranges	Univ. Bergen	Husebye	Technical Report
16	Regionalized Velocity Models and Improved Locations for Pakistan and the Surrounding Area	Weston Geophysical	Reiter	Technical Report
17	Joint Inversion of Receiver Function and Surface Wave Dispersion for Local Crustal Structure in the Mideast	St. Louis Univ.	Herrmann, Ammon	Final Report
18	Various contracts	Columbia Univ., LDEO	Kim, Richards	Report; Borovoye digital seismogram archive
19	Development of Event Screening Procedures	Australian Geol. Survey Org.	Jepsen	Summary report; database of nuclear and chemical events, CSS3.0 format
20	Path Corrections for Regional Phase Discriminants	UC Santa Cruz	Lay	Final Report
21	Improve Monitoring of the CTBT in Middle East by Israel SeisNet	Geophysical Institute Israel	Gitterman	Final Report; data, video, etc.
22	A Ground Truth Database for Regional Seismic Research	Multimax	Henson	313 CEB events China, FSU, and N. Am
23	A Damage Mechanics Model for Underground Nuclear Explosions	Univ. Southern CA	Sammis	Final Report
24	Basic Research on Seismic Monitoring Problems	UC Berkeley	Johnson	Final Report
25	Auto Interpretation of Seismic Signals Using CUSUM-SA Algorithm	ENSCO	Der	Final Report; software – Matlab M-scripts
26	Global & Regional GIS Database Development in Support of CTBT	Cornell	Barazangi	Final Report
27	Probabilistic Integration of Seis, Hydro & Infra Data in Disc Sch	ENSCO	Der	Final Report

	Contract/Task Title	Performing Org.	P.I.	Products Received
28	Seismic Calibration for IMS Stations in North Africa and Western Asia (Group 2)	SAIC	McLaughlin	Reports; SSSCs and numerous data products
29	Integration of Enhanced Propagation, Environmental Variability, and Network Performance Models into the InfraMAP Software Toolkit	BBN Tech.	Norris	InfraMAP Users Guide, V2.1; InfraMAP V2.1 (available from BBN)
30	Constraining Depth and Source Mechanisms of Small Events at Far-regional to Teleseismic Distances	ANU	Kennett	Final Report
31	Regional GIS Databases in Support of CTBT Monitoring	Cornell	Barazangi	Final Report; GIS digital data sets
32	Physical Basis and Improved Criteria for Phase Spectral Ratio Discrimination	Columbia Univ., LDEO	Xie	Final Report
33	Integrated Study of Seismic and Infrasonic Signals from Sources in Southern Siberia, Eastern Kazakhstan, and Western China	Columbia Univ., LDEO	Kim	Final Report
34	Seismic Calibration for IMS Stations in Eastern Asia (Group 1)	Columbia Univ., LDEO	Richards	Pn SSSCs for subset of group 1 IMS stations
35	Application of Joint Inversion of Receiver Functions and Surface-Wave Dispersion for Local Crustal Structure	St. Louis University	Herrmann	Seismological software
36	Development of Improved Capabilities for Depth Determination and Research on the Frequency Dependence of Regional Seismic Phases	MRC	Fisk	Final Report; software
37	Statistical Calibration & Regionalization of China & Surrounding Region	New Mexico State Univ.	Hearn, Ni	Final Report; velocity models,; Annual Bulletin of Chinese Earthquakes, 1984-1999
38	Seismic Calibration for IMS Stations in Eastern Asia (Group 1)	SAIC	Murphy	SSSCs for group 1 IMS stations
39	Enhanced Depth Determination Using Cepstral Techniques	Weston Geophysical	Reiter	Final Report; software

Integration and Testing

Many of the deliveries to the CMR R&D Support System comprise software components, parametric results, or other components that are to be tested to determine their potential for use in large-scale monitoring systems. To perform such tests, a test plan, with evaluation criteria, is generated by the researcher in collaboration with RDSS staff.

Deliveries that require full-scale testing require special planning. For example, the DTRA IMS Location Calibration Program is funding three consortia to provide SSSCs for stations of the IMS. In this endeavor, integration, testing, and evaluation are required at CMR to ensure that the results produced by the three consortia are compatible with the CMR nuclear-explosion-monitoring system software. To date, the RDSS has performed testing for two of the consortia (Yang *et al,* 2001; Richards *et al,* 2002).

Part of the DTRA tasking to the location consortia has been to develop depth-dependent SSSCs. In the past, SSSCs have only been specified for a single source depth, typically either 0 km or 10 km. To support the consortia activities, the RDSS has now developed a new version of *EvLoc* that can utilize SSSCs that are specified for multiple source depths (Figure 3). Additionally, the new *EvLoc* will be available to the R&D community via the Hypocenter Location Server discussed earlier.

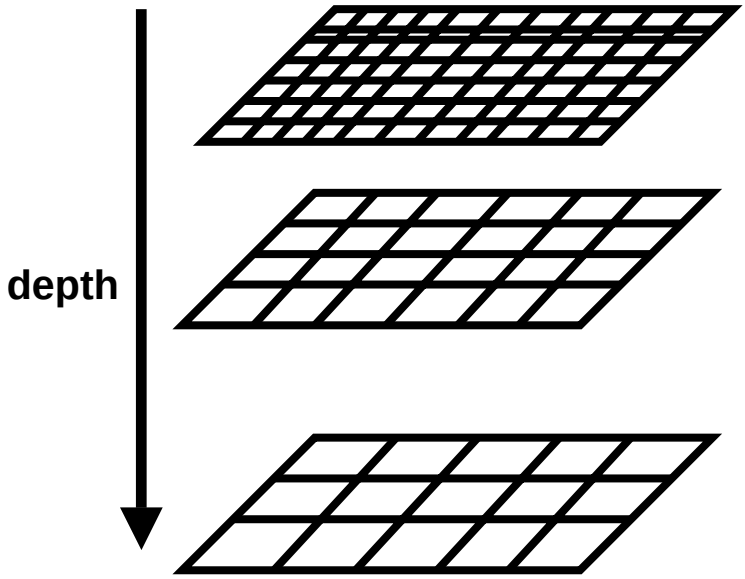

Figure 3. Depth-dependent SSSCs are parameterized as a sequence of horizontal 2-D grids at various depths. The software supports arbitrary depth sampling and variable horizontal gridding. The software is backward compatible with non-depth-dependent SSSC files.

In another testing effort at the RDSS, investigators at the University of California, Berkeley, and RDSS staff are working on a plan for integrating UCB's automated moment tensor software (Dreger *et al*, 2001) into the nuclear monitoring system developed at CMR. The purpose of the UCB effort is to develop software to automatically determine moment tensors for seismic events recorded at the IMS network stations. To support UCB, the RDSS staff have configured a dedicated test platform, with direct access to the near-real time disk loops at CMR (kept online for 20 days) and to the database containing the Reviewed Event Bulletins produced by the IDC. In this way the UCB software can access the bulletins to cue their processing and can take advantage of the high-speed access to full waveform data that is provided by the online diskloops. This dedicated test platform will allow UCB researchers to refine and tune their software by experimenting with large numbers of events in different parts of the world. Ultimately, the software will be integrated into the CMR processing pipeline architecture and will provide improved source characterization capabilities for the nuclear-explosion monitoring system.

CONCLUSIONS AND RECOMMENDATIONS

The RDSS supports R&D aimed at improving nuclear-explosion monitoring and treaty verification capabilities by drawing on the facilities, resources, and expertise of the CMR.

In summary, basic RDSS activities include:

- Supporting the R&D community, from the inception of research through to testing and archiving of results.
- Archiving research results to ensure important work is not lost and results can be shared readily amongst the R&D community.
- Providing a mechanism for the test, evaluation, and integration of R&D results.

A wide range of CMR staff, including scientific, software development, testing, and infrastructure support teams, are available to support all phases of R&D activity. Please watch for news and developments (or contact us) at: http://www.cmr.gov/rdss . The web site contains a wide range of information, such as listings of current DTRA

contracts, contract deliverables received, documents describing the access and use of the RDSS, and information on available RDSS resources.

REFERENCES

Dreger, D., B. Romanowicz, G. Clitheroe, P. Hellweg, J. Stevens (2001), Development of Automated Moment Tensor Software at the Prototype International Data Center, Proceedings of the 23rd Seismic Research Review, Vol. I, 500-508.

Kohl, B., R. North, J. Murphy, M. Fisk, and G. Beall (2002), Demonstration of Advanced Concepts for Nuclear Test Monitoring Applied to the Nuclear Test Site at Lop Nor, China, 24th Seismic Research Review (this volume).

Richards, P., R. Burlacu, M Fisk (2002), Pn SSSCs for IMS and Surrogate Stations in Asia, proposal to CMR Configuration Control Board, CCB-PRO-02/04, http://www.cmr.gov/cmrlibrarybox/ccb/ccb0204.pdf .

Skov, M., B. Kohl, R. Woodward (2002), Imagery Assets for Supporting Nuclear Explosion Monitoring Research and Development, 24th Seismic Research Review (this volume).

Yang, X., K. McLaughlin, I. Bondár, J. Bhattacharyya, H. Israelsson (2001), Pn & Sn SSSCs in Europe, North Africa, Middle East, and Western Asia, proposal to CMR Configuration Control Board, CCB-PRO-01/15, http://www.cmr.gov/cmrlibrarybox/ccb/ccb0115a.pdf.

VERSION 1.7 OF MATSEIS AND THE GNEM R&E REGIONAL SEISMIC ANALYSIS TOOLS

Christopher J. Young, Eric P. Chael, and Bion J. Merchant

Sandia National Laboratories

Sponsored by National Nuclear Security Administration
Office of Nonproliferation Research and Engineering
Office of Defense Nuclear Nonproliferation

Contract No. DE-AC04-94AL85000

ABSTRACT

To improve the nuclear event monitoring capability of the U.S., the NNSA Ground-based Nuclear Explosion Monitoring Research & Engineering (GNEM R&E) program has been developing a collection of products known as the Knowledge Base (KB). Though much of the focus for the KB has been on the development of calibration data, we have also developed numerous software tools for various purposes. The Matlab-based MatSeis package and the associated suite of regional seismic analysis tools were developed to aid in the testing and evaluation of some Knowledge Base products for which existing applications were either not available or ill-suited. This presentation will provide brief overviews of MatSeis and each of the tools, emphasizing features added in the last year.

MatSeis was begun in 1996 and is now a fairly mature product. It is a highly flexible seismic analysis package that provides interfaces to read data from either flatfiles or an Oracle database. All of the standard seismic analysis tasks are supported (e.g. filtering, 3 component rotation, phase picking, event location, magnitude calculation), as well as a variety of array processing algorithms (beaming, FK, coherency analysis, vespagrams). The simplicity of Matlab coding and the tremendous number of available functions make MatSeis/Matlab an ideal environment for developing new monitoring research tools (see the regional seismic analysis tools below). New MatSeis features include: addition of *evid* information to events in MatSeis, options to screen picks by author, input and output of *origerr* information, improved performance in reading flatfiles, improved speed in FK calculations, and significant improvements to Measure Tool (filtering, multiple phase display), Free Plot (filtering, phase display and alignment), Mag Tool (maximum likelihood options), and Infra Tool (improved calculation speed, display of an F statistic stream).

Work on the regional seismic analysis tools (CodaMag, EventID, PhaseMatch, and Dendro) began in 1999 and the tools vary in their level of maturity. All rely on MatSeis to provide necessary data (waveforms, arrivals, origins, and travel time curves). CodaMag Tool implements magnitude calculation by scaling to fit the envelope shape of the coda for a selected phase type (Mayeda, 1993; Mayeda and Walter, 1996). New tool features include: calculation of a yield estimate based on the source spectrum, display of a filtered version of the seismogram based on the selected band, and the output of codamag data records for processed events. EventID Tool implements event discrimination using phase ratios of regional arrivals (Hartse et al., 1997; Walter et al., 1999). New features include: bandpass filtering of displayed waveforms, screening of reference events based on SNR, multivariate discriminants, use of *libcgi* to access correction surfaces, and the output of discrim_data records for processed events. PhaseMatch Tool implements match filtering to isolate surface waves (Herrin and Goforth, 1977). New features include: display of the signal's observed dispersion and an option to use a station-based dispersion surface. Dendro Tool implements agglomerative hierarchical clustering using dendrograms to identify similar events based on waveform correlation (Everitt, 1993). New features include: modifications to include arrival information within the tool, and the capability to automatically add/re-pick arrivals based on the picked arrivals for similar events.

OBJECTIVE

MatSeis was originally developed to support signal-processing research for the GNEM R&E program at Sandia Labs. The initial goal was simple: to develop a graphical user interface (GUI) to help a user bring data from an Oracle database into Matlab. Once the data was in Matlab, researchers could then run various scripts and/or functions to test algorithms. This goal was quickly accomplished thanks to the tremendous range of existing Matlab functionality, but Sandia chose to extend development because it became apparent that the package had potential to be much more useful than had been expected. Within a year we had developed a simple, interactive seismic analysis package built around 4 basic data types: waveforms, arrivals, origins, and travel time curves. However, because the bulk of Sandia's development work went towards signal processing, early versions of MatSeis had an odd look and feel: the package had an extensive set of signal processing capabilities (e.g. filtering, rotation, beaming, FK, coherency, vespagrams), while at the same time it lacked many of the more common seismic analysis utilities (e.g. a locator, magnitude calculations, a quick and easy phase picker) because these were not needed for Sandia's research efforts at that time.

The second MatSeis development phase began when Sandia began to use the package as a base upon which to develop specialized regional seismic analysis tools. Over the past few decades, many studies have suggested ways to improve regional monitoring, yet relatively few of the ideas presented have found their way into operational software. The reason is that those who actually monitor have limited time and resources to put towards evaluating these ideas, and so generally only the most sure-fire get implemented. What is needed is a prototyping environment in which promising analysis techniques can be implemented and evaluated quickly and with relatively little effort. Sandia recognized that MatSeis/Matlab offered just such an environment, and taking advantage of this we began to build a set of prototypes for various regional analysis tasks, focusing first on the techniques and data sets generated by the research of our colleagues at Lawrence Livermore National Lab (LLNL) and Los Alamos National Lab (LANL). Currently the tools support phase match filtering, regional magnitude calculations, discrimination, and event clustering using waveform correlation.

An unplanned but welcome side effect of the development of these tools has been the improvement of MatSeis itself. To properly use the tools, it is necessary to add new picks, re-time picks, re-locate events, etc. Thus, Sandia was forced to fill in many of missing basic seismic analysis utilities, and to improve many of the existing ones. The result is that MatSeis is now a significantly more complete, more robust package.

RESEARCH ACCOMPLISHED

The following sections describe MatSeis, and the four regional seismic analysis tools. The important new features for Version 1.7 are highlighted for each.

MatSeis

The main MatSeis graphical window is a standard time vs. epicentral distance plot that can display waveforms, arrivals, origins, and travel time curves (Figure 1). The user can interact with this display by clicking directly on the displayed objects, by using the buttons along the bottom, by using the menus along the top, or by typing commands at the Matlab prompt. MatSeis is predominantly written as Matlab m-file functions, which are organized in a set of directories according to the general purpose of each. However, the package also includes a set of compiled C functions linked to the m-files via the Matlab cmex utility. Typically the C functions are introduced where performance of an m-file is too slow (e.g. FK calculations).

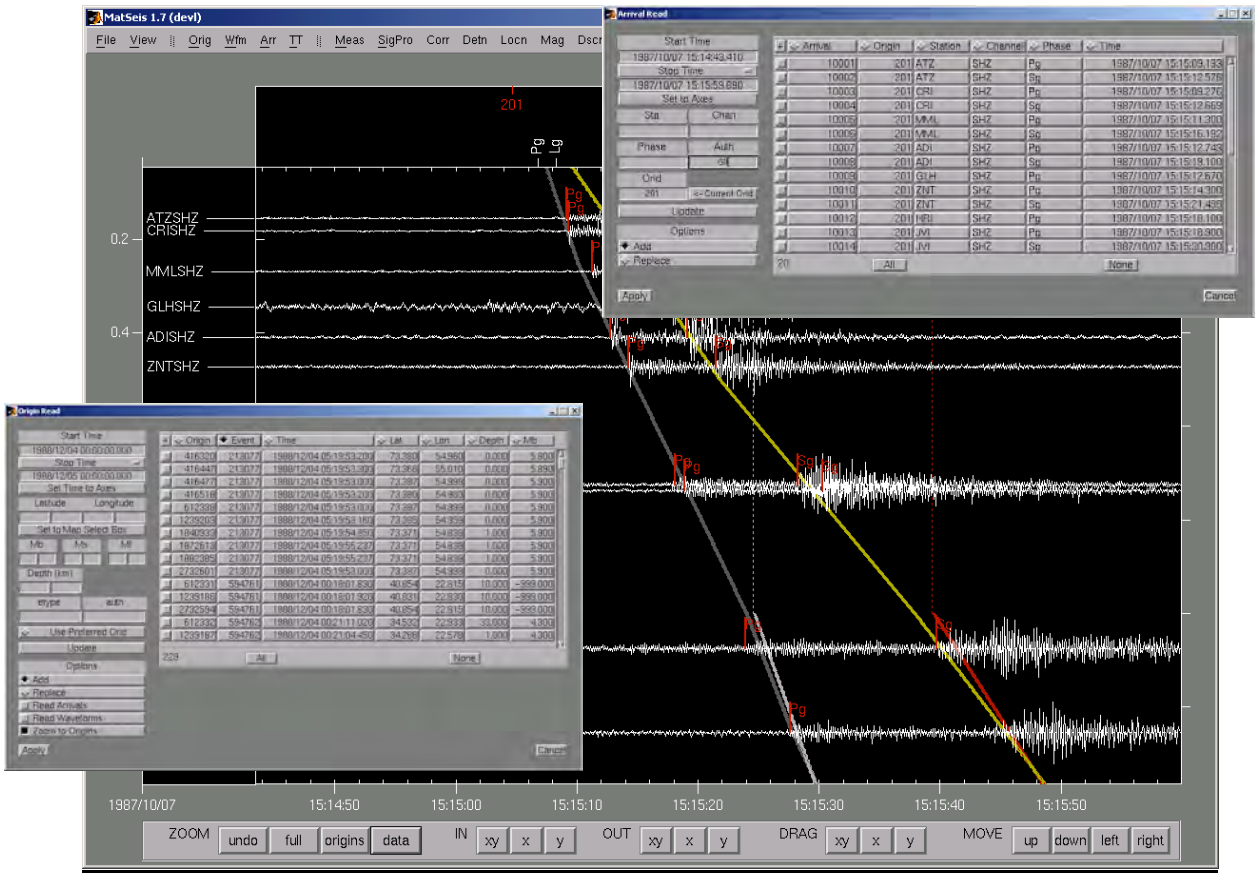

Figure 1. The main MatSeis display is a standard time vs. epicentral distance waveform profile. This figure shows all 4 data objects: waveforms, arrivals, origins, and travel time curves. Also shown are the re-designed popups to read in arrivals (upper right) and origins (lower left).

Data IO

MatSeis can read CSS3.0 format data from either an Oracle database, or flatfiles. Output is restricted to flatfiles only. The number of tables used by MatSeis has steadily expanded and now includes: *affiliation, amplitude, arrival, assoc, event, instrument, nextid, netmag, network, origerr, origin, remark, sensor, site, sitechan, stamag, wfdisc,* and *wftag*. In Version 1.7, flatfile data reads have been greatly sped up, making it practical to work with larger data sets than has been the case in the past. In order to allow the user to better control the data read into MatSeis, Version 1.7 has an extensive set of filters for both origins (*lat, lon, magnitude, etype, auth*) and arrivals (*sta, chan, phase, auth, orid*). In the origin read popup, *evid* is now displayed, which makes it more convenient to work with multiple origins for the same event.

Arrival Picking and Amplitude Measurement

Arrivals can be added, deleted, renamed, and retimed in the main MatSeis display, but it is a cumbersome process and impractical when editing more than a few arrivals. The recommended method is to use an auxiliary utility called Measure Tool (Figure 2) that can be launched from the main display. Measure Tool is designed to help analysts quickly and efficiently pick arrivals and measure amplitudes for an event. The theoretical arrival times for the TT curves in MatSeis, are shown for reference. Version 1.7 includes a set of controls to filter the waveforms, and the filtering can be toggled on or off. Once an arrival has been picked, the user can choose from a set of amplitude measurements (e.g. Peak-Peak, Zero-Peak, RMS), and the measurement is automatically made after the user sets the window. A toggle allows the user to choose whether or not to correct the measurements for instrument response.

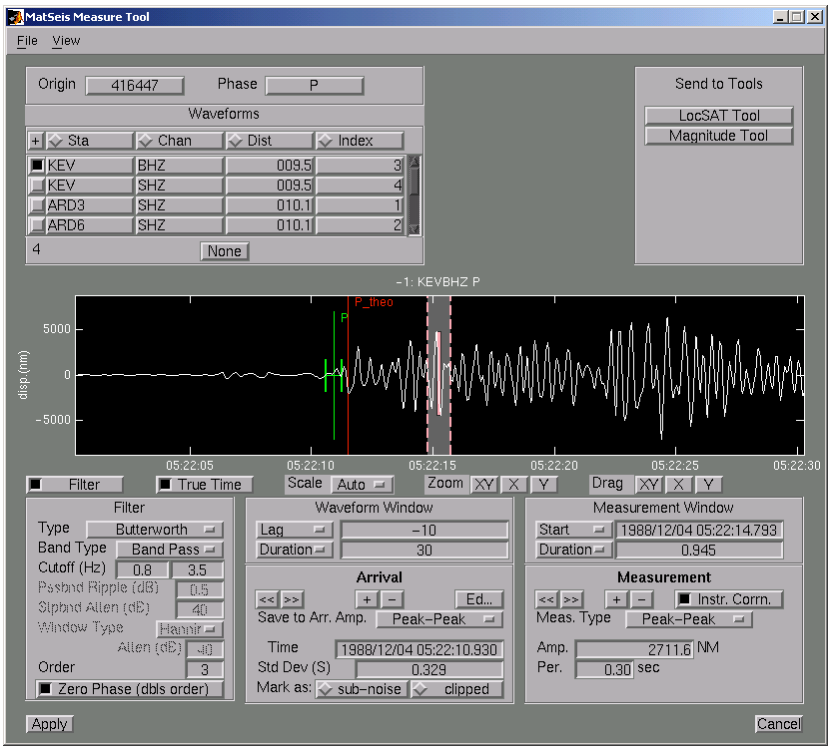

Figure 2. Measure Tool has been designed specifically to allow the analyst to quickly pick, retime, and measure amplitudes for arrivals.

Magnitude

Magnitudes can be calculated in MatSeis using either of two tools. The Magnitude Tool (Figure 3) offers a variety of standard amplitude-based magnitude formulas for local, regional, and teleseismic data. The user can screen the data used by phase, period, and distance.

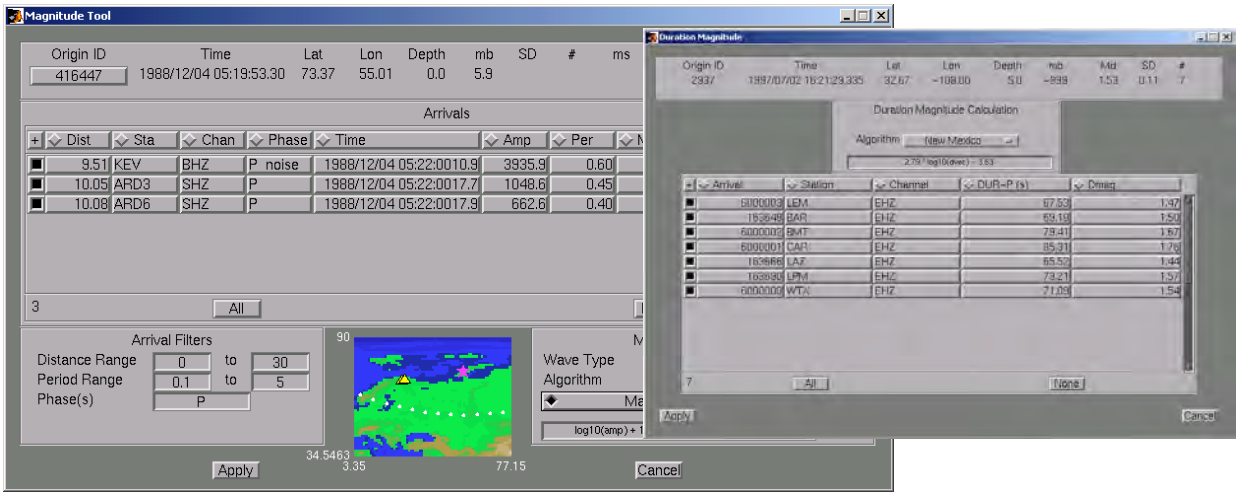

Figure 3. The Magnitude Tool (left) and Duration Mag Tool (right) allow the user to select the type of magnitude formula , and provides a clickable list to control which station measurements are used for the network magnitude.

Individual measurements can be turned on or off by clicking on their rows in a table, and a small map shows the positions of the stations relative to the source location. A new feature in Version 1.7 is an option to calculate a maximum likelihood magnitude, if some of the arrivals have been designated as sub-noise or clipped (Blandford & Shumway, 1993; Ringdal, 1976).

The Duration Magnitude Tool has a similar look and feel, but calculates magnitude base on duration of signal above noise, as picked by an analyst. The tool includes a default formula for New Mexico, and can be easily modified to include calibrated formulas for any number of other regions.

Infra Sound Analysis

MatSeis-1.7 includes Infra Tool, a tool for analysis of infrasound array data. This tool uses cross-correlations of the array channels to derive azimuth and velocity for incoming signals. The calculation is made for a short user-defined moving window, so the result is a stream of azimuth, velocity, correlation, and fstat. The tool displays these streams, along with the filtered data channels (Figure 4). The user can change the filter parameters and/or the moving window parameters (length, %overlap), and re-calculate the streams.

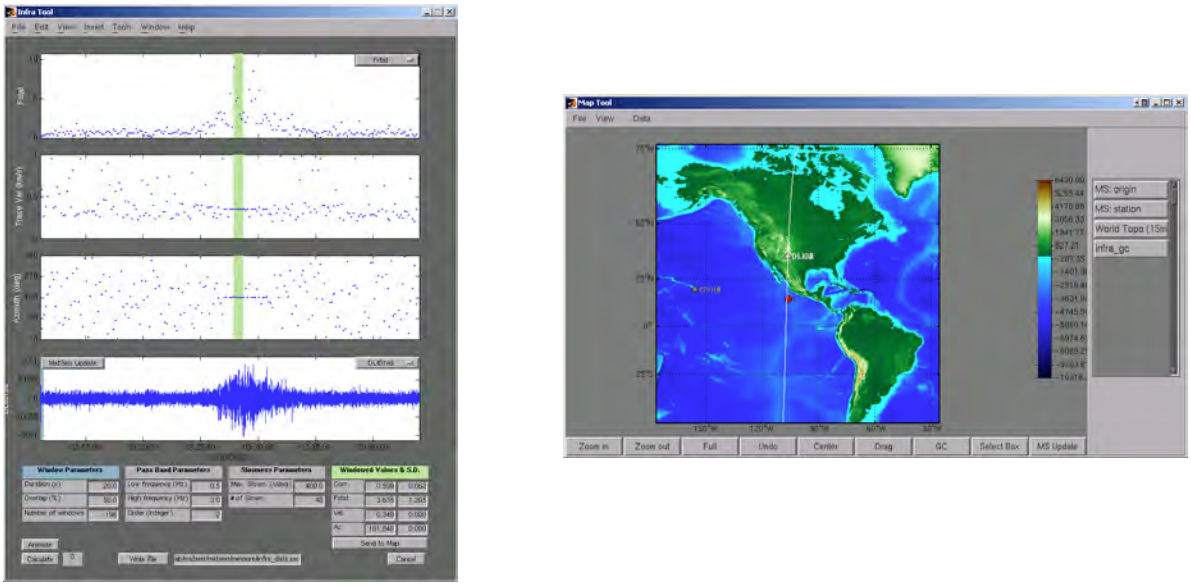

Figure 4. The Infra Tool helps the user derive great circle path information from infrasound array data (left). Great circles can be plotted using the Map Tool (right).

Once the streams have been calculated, the user can set an analysis window to measure average values and standard deviations for each of the calculated streams. The average azimuth value can then be sent to the map and plotted as a great circle. Using data from two or more infrasound arrays, events can be located by crossing the great circles.

<u>Regional Seismic Analysis Tools</u>

Phase Match Tool

PhaseMatch Tool is a waveform analysis interface launched from MatSeis that allows the user to calculate the predicted surface wave dispersion for a given source to receiver path by ray tracing through a model, and then use the model dispersion to generate and apply a matched filter (Herrin and Goforth, 1977). The tool (Figure 5) allows the user to view the observed waveform, the model dispersion, the predicted waveform, the cross-correlation of the predicted and observed waveforms, and the match-filtered waveform. The user can control the frequency range of the model dispersion used, as well as the time limit of the portion of the cross-correlated waveform from which the match-filtered waveform is taken. Once a satisfactory filtering has been achieved, the user can send either the

observed waveform or the filtered waveform to Measure Tool to measure surface wave amplitudes, which can then be used to determine event magnitude.

New features for the Version 1.7 include an option to display the signal's observed dispersion, and an option to use a station-based dispersion surface.

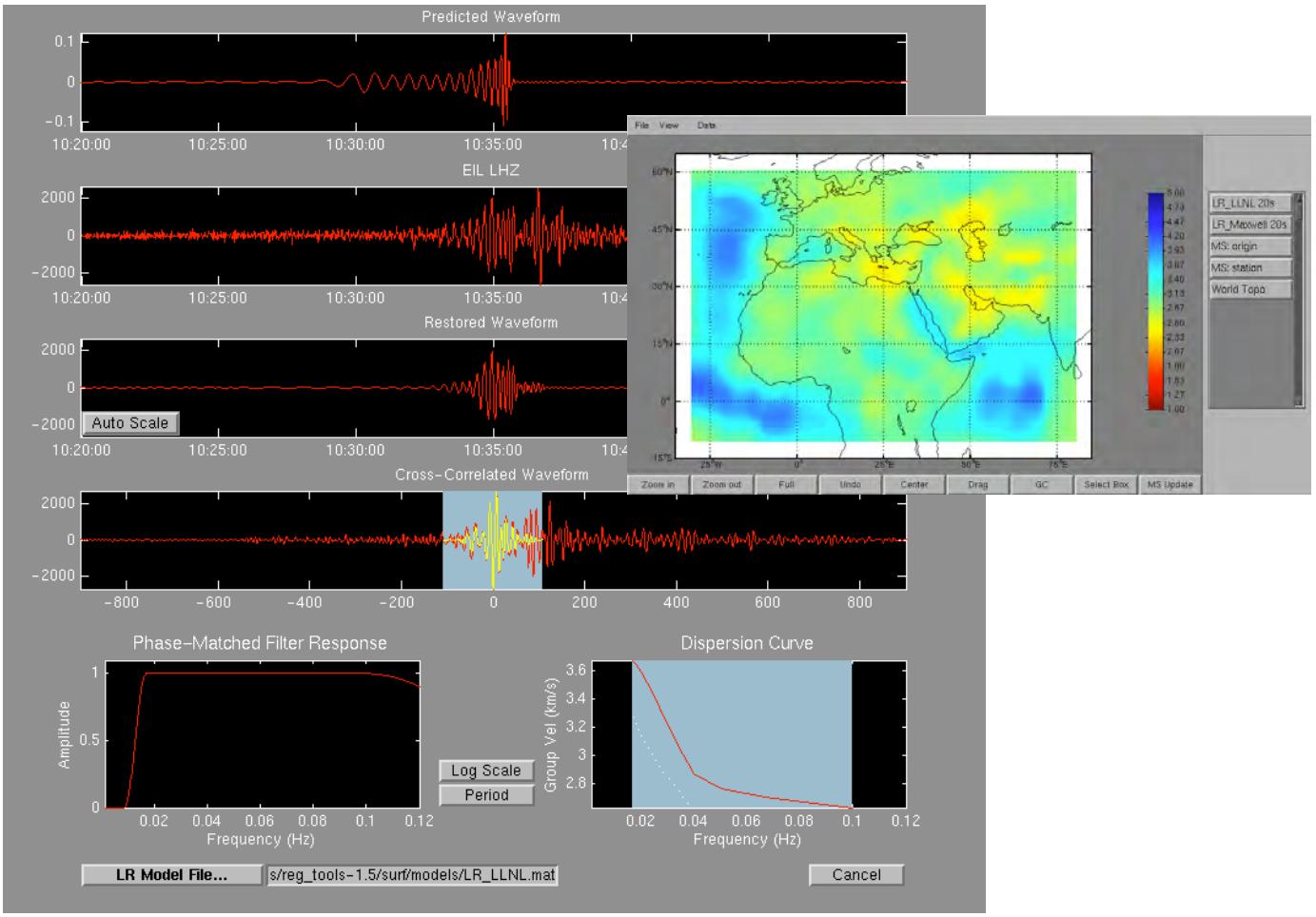

Figure 5. Phase Match Tool allows the user to use the information from a dispersion model (upper right) to design a phase-match filter to isolate surface waves.

Coda Magnitude Tool

CodaMag Tool is a waveform analysis interface launched from MatSeis that allows the user to calculate magnitudes and source spectra for an event of interest by fitting empirical decay functions to narrow-band coda envelopes of a given phase (currently Lg). The technique was developed by Mayeda and has been described in detail in several papers (Mayeda, 1993; Mayeda and Walter, 1996; Mayeda, et al., 1999). The tool consists of two displays. The main one shows the calculated moment spectrum and the derived magnitudes. The second display shows how the spectrum was derived. The user can adjust the Lg arrival window, examine the fit between the observed and synthetic envelopes, and control which frequency bands are used for the magnitude calculations. The various required parameters (frequency bands, groups velocity windows, decay curves, etc.) are read from parameter files unique to each station.

Important new features in Version 1.7 include a yield estimate based on the source spectrum, an option to display filtered seismograms in addition to the Hilbert envelopes, and the capability to write out data records to capture results.

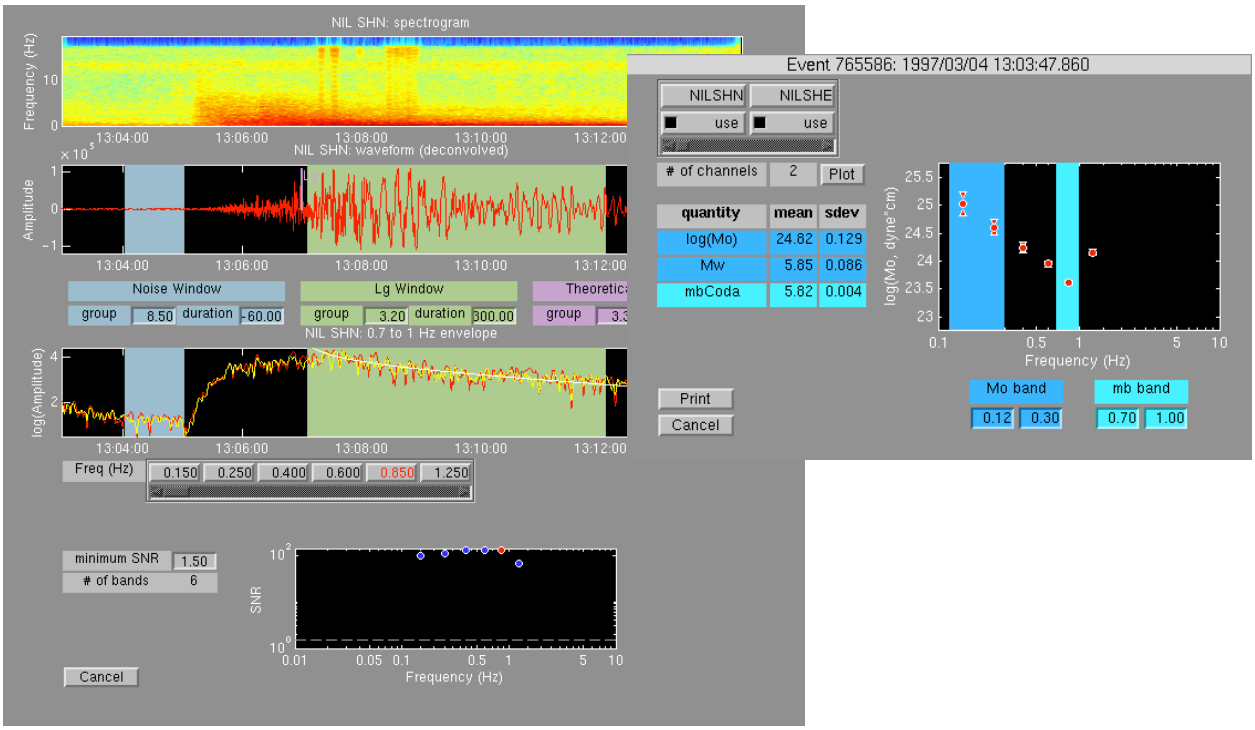

Figure 6. The Coda Mag Tool implements the methodology developed by Mayeda. Coda envelopes are fit for a series of narrow frequency bands (left), and the scaling factors are then used to derive a moment spectrum, from which various magnitudes can be taken (right).

Event Identification Tool

EventID Tool is a waveform analysis interface launched from MatSeis that allows the user to identify an event of interest (i.e. explosion or earthquake) using spectral ratios of standard regional arrivals (see Hartse et al., 1997; Walter et al., 1999). The tool (Figure 7) consists of three displays. The main display plots the phase ratio for the current event against a backdrop of the same ratio for archived events that have already been identified. The user can choose different phases and/or frequency bands to ratio to try to improve the separation of the earthquake and explosion populations, and the display will immediately update. A second display shows the user a plot of an "MDACogram" (i.e. the MDAC corrected measurements at all of the phase/frequency combinations) for the current event along with all of the archived events. This can be useful in deciding which ratio will yield the best separation. If there are questions about the amplitude measurements themselves, a third display can be brought up, and the user can easily examine group velocity windows for the phases and change them if necessary. If they are changed, the measurements will automatically be re-made and the ratios updated in the main display.

Version 1.7 has several important new features including the ability to apply MDAC2 corrections (Walter and Taylor, 2002) to the spectral measurements, as well as kriged corrections from Ground Truth events, the option to use multi-variate discriminants, the capability to screen the reference events shown, based on signal-to-noise ratio, and the capability to write out data records for processed events.

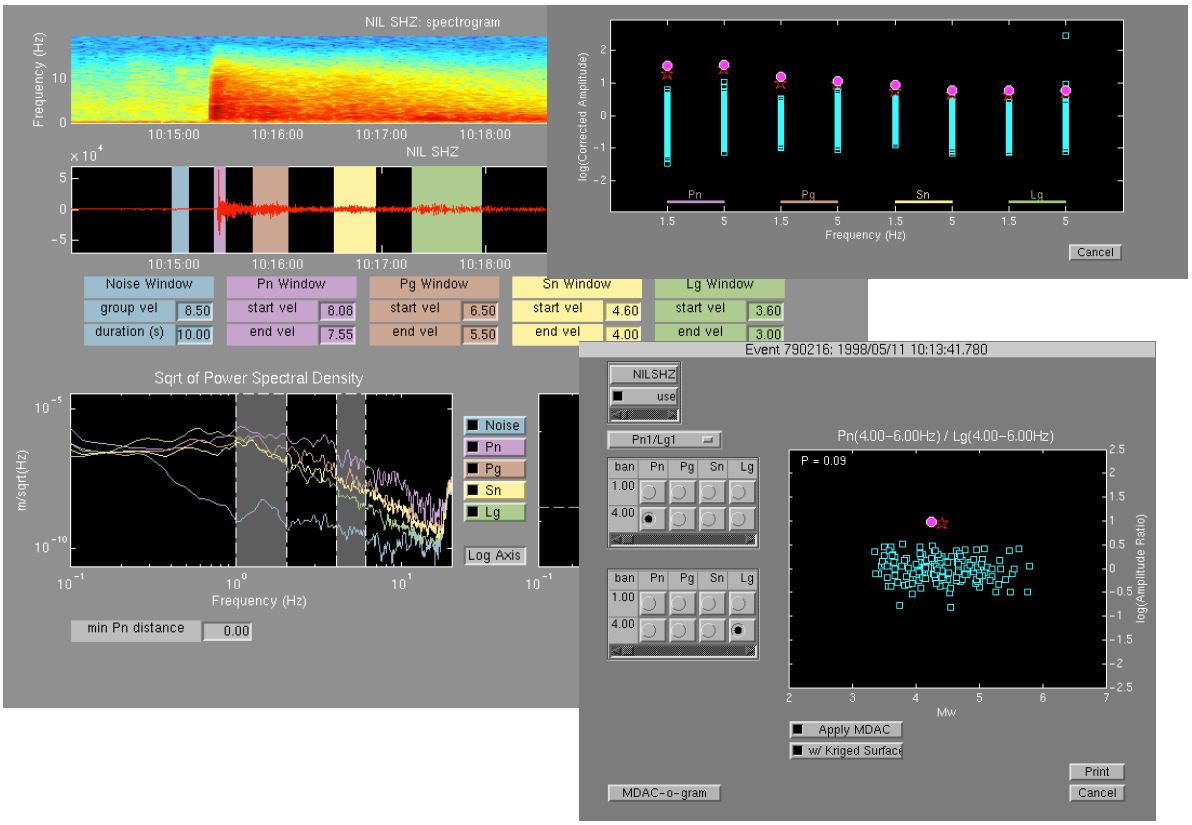

Figure 7. The EventID Tool helps the user discriminate explosions from earthquakes using standard phase-ratio methods. The user can view the overall results (lower right) or an "MDACogram" (upper right), or examine and change how the measurements for each phase were made (left).

Dendrogram Tool

The DendroTool provides a tool to perform waveform correlation-based cluster analysis techniques on seismic data. The purpose of Dendro Tool is quite simple: to allow a user to quickly and efficiently determine whether a waveform of interest matches any in the available archives. By arranging the correlations in a hierarchical dendrogram, rather than just determining the most similar waveform, the user gets a much more complete picture of how the current event fits with the archived events. For example, in regions with repeated mining explosions, the mines are often easily identified as distinct clusters, and new mining events can be readily identified as such by association with those clusters.

Dendro Tool consists of many interfaces to help the user assess the effectiveness of the clustering and to use the clusters to identify the events. The main display shows the dendrogram, along with a set of metrics that can be used to determine the correlation level to use to identify the families of events. Once a level has been chosen, the families are assigned separate, distinct colors to make them easier to see. Parameters controlling filtering and windowing of the waveforms, the method used to build the dendrogram, etc. can be set using another display, and the dendrogram will then be updated. The color-coded waveforms for any or all of the families in the dendrogram display can be sent to the MatSeis utility Free Plot for viewing to assess the validity of the families. The color-coded locations of the events in any or all of the families can be sent to the MatSeis Map Tool to see how the families agree with the locations. Within the Dendro Tool, origin times for any or all of the families can be used to generate color-coded histograms by year, month, day of year, day of week, or hour of day.

Dendro Tool can form dendrograms based on a single-phase window for a single station, or the user can choose to use multiple windows and/or multiple stations. The method of combining the multiple correlations (minimum, maximum, mean, median) is user controlled.

The significant new features for Version 1.7 are related to the newly added support for arrivals. The user can now view the picks along with the waveforms when examining the structure of the dendrograms. It is now also possible to use Dendro Tool to re-time arrivals based on lags calculated from the waveform cross-correlations. Once the current event has been added to a dendrogram, the user can then re-time the picks for that event based on the lags with other events in that group. Once the arrivals have been adjusted, they can then be sent back to MatSeis for other uses (e.g. re-locating the event).

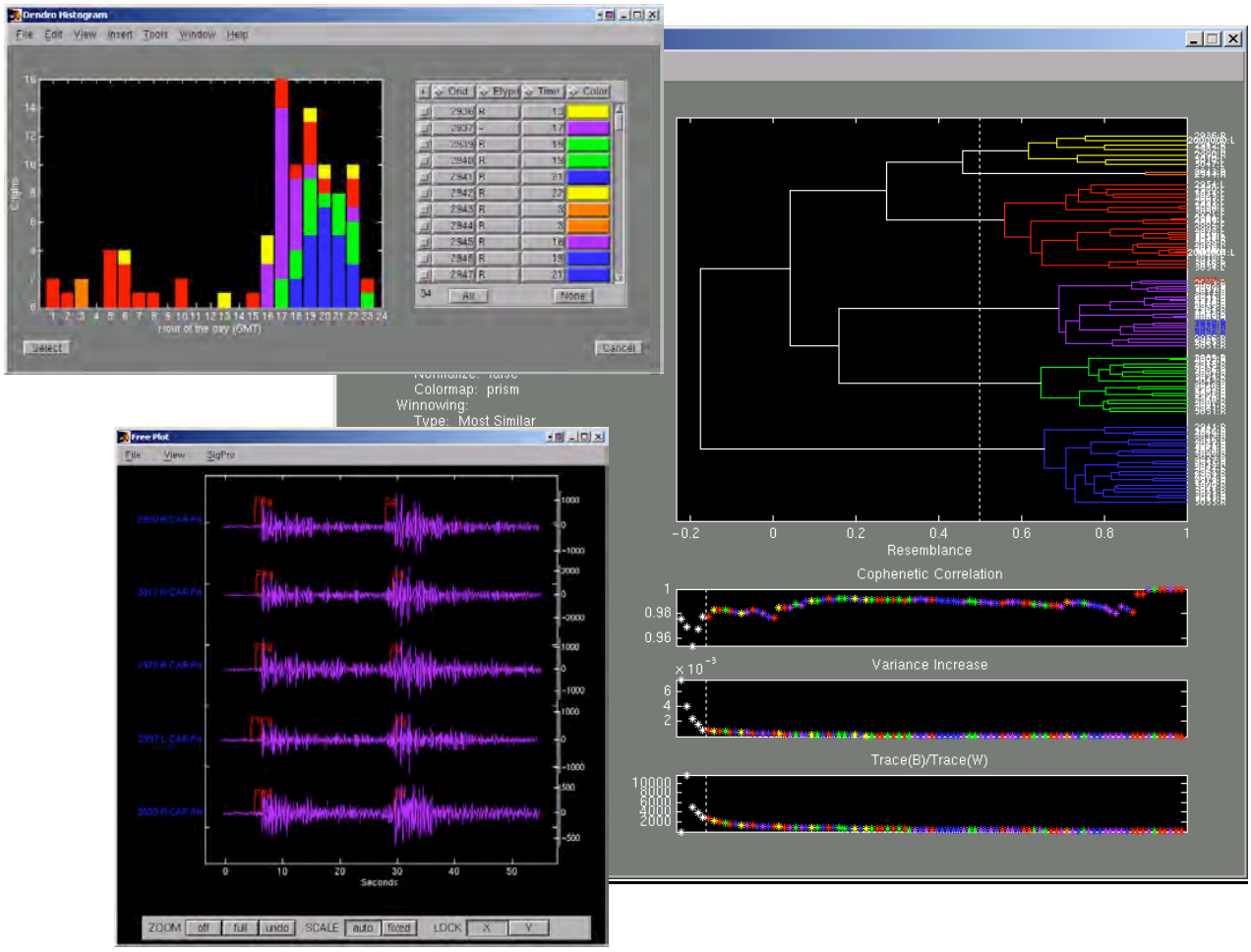

Figure 8. The Dendrogram Tool employs hierarchical cluster analysis to group similar waveforms. The main display is a dendrogram (right). The user can also view the waveforms (lower left) or histograms (upper left) for all or part of the dendrogram.

CONCLUSIONS AND RECOMMENDATIONS

Though started specifically to support signal-processing research in the GNEM program at Sandia Labs, MatSeis has now become an important part of the overall GNEM R&E program. It provides a much needed bridge between research results and operational monitoring. The ability of researchers to generate interesting new data sets and ideas continues to overmatch the resources available for testing them in an operational or quasi-operational setting. This is unfortunate both because using some of these products could immediately improve monitoring capabilities, and because feedback on the products could be used to guide further research.

To improve the situation, what is needed is a means to quickly develop realistic prototype software to test products. We believe that MatSeis offers one of the best, if not the best, platforms to do this. MatSeis handles all of the data I/O with the standard CSS3.0 format, it provides a broad range of basic seismic analysis functions, and perhaps most

importantly, it runs on top of the well-vetted, powerful, flexible, commercial Matlab product. So far, we have used MatSeis as a base to develop a suite of 4 regional seismic analysis tools – Phase Match Tool, Codamag Tool, EventID Tool, and Dendro Tool – which are being used to evaluate some of the analysis methodologies and regional calibration products produced by the GNEM R&E program. We expect to expand the use of MatSeis in the future and develop other prototype tools, where appropriate, to help evaluate promising research products.

The basic MatSeis package is available to all as a data product on the GNEM R&E web site: http://www.nemre.nn.doe.gov/nemre/

Matlab and the Signal Processing Toolbox are required to run MatSeis. Version 6.1 of Matlab or later is recommended, but the software should run with Matlab versions back as far as 5.3. MatSeis will run on Sun workstations, Windows PC's, and Linux PC's. It should run on other platforms as well, but the C code will need to be re-compiled.

ACKNOWLEDGEMENTS

We thank all of the MatSeis users who have helped us to debug and improve the software, particularly our colleagues at LANL and LLNL.

REFERENCES

Blandford, R. R. and R. H. Shumway (1982). Magnitude: yield for nuclear explosions in granite at the Nevada Test Site and Algeria: joint determination with station effects and with data containing clipped and low-amplitude signals, *Report VSC-TR-82-12*, Teledyne Geotech, Alexandria, Virginia.

Everitt, B. S. (2001). Cluster analysis, Arnold, London.

Hartse, H. E., Taylor, S. R., Phillips, W. S., and G. E. Randall (1997). A preliminary study of regional seismic discrimination in central Asia with emphasis on western China, *Bull. Seism. Soc. Am.*, 87, 551-568.

Herrin, E. and T. Goforth (1977). Phase-matched filters: application to the study of rayleigh waves, *Bull. Seism. Soc. Am.*, 67, 1259-1275.

Mayeda, K. (1993). Mb(LgCoda): a stable single station estimator of magnitude, *Bull. Seism. Soc. Am.*, 83, 851-861.

Mayeda, K. and W. R. Walter (1996). Moment, energy, stress drop, and source spectra of western United States earthquakes from regional coda envelopes, *J. Geophys. Res.*, 101, 11,195-11,208.

Mayeda, K., R. Hofstetter, A. J. Rodgers and W. R. Walter (1999). Applying coda envelope measurements to local and regional waveforms for stable estimates of magnitude, source spectra, and energy, *21st Annual Seismic Research Symposium on Monitoring a CTBT*, Vol I, 527-533.

Ringdal, F. (1976). Maximum-likelihood estimation of seismic magnitude, *Bull. Seism. Soc. Am.*, 66, 789-802.

Walter, W. R. and S. R. Taylor (2002). A revised magnitude and distance amplitude correction (MDAC2) procedure for regional seismic discriminants: theory and testing at NTS, *LLNL Report UCRL-ID-146882*.

Walter, W. R., A. J. Rodgers, A. Sicherman, W. Hanley, K. Mayeda, S. C. Myers and M. Pasyanos (1999). LLNL's regional seismic monitoring research, *21st Annual Seismic Research Symposium on Monitoring a CTBT*, Vol I, 294-302.

Other Topics

THE UPGRADE OF THE INTERNATIONAL MONITORING SYSTEM PRIMARY STATION AT SONSECA, SPAIN, (PS-40): A BEFORE AND AFTER COMPARISON OF THE SHORT-PERIOD ARRAY

Michael Hasting and Sergio Barrientos

Sponsored by Comprehensive Nuclear-Test-Ban Treaty Organization

ABSTRACT

In early November 2001 the PS-40 Array, located at Sonseca, Spain, underwent a major upgrade of the short-period array elements by the station operators, the Instituto Geografico Nacional (IGN), under contract to the International Monitoring System (IMS) of the Comprehensive Nuclear-Test-Ban Treaty Organization (CTBTO). This upgrade was required to bring the PS-40 array into compliance with the Treaty specifications and for certification of the Station, which was accomplished on 21 December 2001. As part of this upgrade, the older passive Geotech 23900 sensors were replaced with new Güralp CMG-3ESPV sensors, which are themselves broadband sensors with a passband of 0.02 Hz to 50 Hz. These new sensors are flat to acceleration instead of being flat to velocity, like the 23900 sensors, which provides the array with higher sensitivity to short-period data while still being able to record the long-period data and have a sensitivity of 750 v/m/s^2. The 16-bit Remote Terminal (RT) digitizers were replaced with new Nanometrics Inc. Callisto-Europa 24-bit authenticating digitizers with a sensitivity of 2539 nv/count. This combination gives the overall system sensitivity, "NCALIB", of 0.0858 nm/count. Each digitizer is configured with 13 MB of internal data storage that gives a re-request capability at each element of between 16 and 24 hours, depending on compression.

The sample rate for each element was increased from 20 to 40 samples per second, and the 1200-baud private wire modems used by the old system were replaced with 9600-baud modems to handle the increase in data rate and packet size. Three new Sun Spark-5 work station computers were added, each configured the same, having over 20 days of data storage with one designated as the primary data acquisition computer, one the back-up and one the Network Operator Terminal. Each computer is configured with a CD1 sender and AutoDRM, and, at present, they are sending CD1 data to the International Data Centre (IDC) in Vienna, Austria, to IGN and to the Air Force Technical Applications Center (AFTAC). A new broadband element was also added to the array using a Güralp CMG-3T sensor, which has a sensitivity of 1500 v/m/s (flat to velocity) and which is located in a vault near the long-period array element and is designated as ESBB.

Initial data from the new configuration looks good with data availability at 100% for the past several months as measured by the IDC. At first glance, the waveforms look much noisier due to the higher sensitivity to the short-period cultural noise in the local area. This short-period noise was present before the upgrade but, due to the old configuration, was not detected. Because of this noise, several elements are problematic at present and are not being used for beam forming. IGN has also reported a marked increase in the number of false event triggers by their data acquisition system in Madrid used for regional event detection. To resolve this noise issue, the IMS staff is looking into several alternatives that are suitable to all parties, while still keeping the station within compliance of the Treaty.

INTRODUCTION

Location

The primary seismic array PS40 (the Station) is located in central Spain, in and around the town of Sonseca, with a reference location of 39.6744°N, 3.9630°W and an elevation of 752 m. Sonseca is a small town of about 10,000 people and is within the aperture of the array. Due to the size of the SP Array, over 8 km in aperture, it takes in residential and industrial areas, as well as some surrounding agricultural areas (Figure 1). Located about 24 km north of the Station is the city of Toledo with a population of about 75,000. Madrid, the capital of Spain, is located about 120 km north of the Station. The terrain around the Station is rocky, with small hills and farming areas spreading throughout the array. Several manufacturing facilities in and around Sonseca are the cause of much of the high-frequency noise seen in the data above 1 Hz. A highway running through the array also causes a great deal of noise in the data. The official station operator is the Instituto Geográfico Nacional (IGN) located in Madrid, Spain. Technical staff of IGN maintains the Station with five onsite IGN personnel and three contractors.

Brief History of the Station

The Station was installed, and originally operated, under the United States Air Force (USAF) nuclear test monitoring programs and has been in operation for more than 40 years. Over the past few decades, the Station had been modified and upgraded by the USAF to a final configuration of 19 short-period (SP) elements using Geotech 23900A seismometers and 7 long-period (LP) elements using Geotech KS54000 seismometers. All elements at the Station used 16-bit "Remote Terminal" (RT) to digitize the analog signals from the seismometers. The SP elements and the central LP element, LPA, were sampled at 20 samples per second (sps) while the remaining 6 LP elements were sampled at 1sps, with the LPA element also providing 1sps data stream.

In 1991 six LP elements were added to form an LP array using Geotech KS36000 seismometers in 60-m boreholes, with an array radius of 25 km centered on the SP array. These LP elements underwent a further upgrade in 1998 when the KS36000 were replaced with KS54000. Also in 1991 AFTAC upgraded the intra-array power and communications distribution systems by replacing over 600 power poles and installing new power and communication wiring.

A basic topology Global Communication Infrastructure (GCI) satellite link was installed at the Station by CTBTO International Monitoring System (IMS) in 1999 to integrate the Station into the International Data Centre (IDC) Operations (Figure 2). The IMS installed a new computer that was configured to send continuous data to both the IGN at the National Data Center (NDC) in Madrid and to the IDC in Vienna.

In January 2001, at the request of the Spanish Mission to CTBTO, the IMS initiated the upgrade process to bring the Station into compliance with the Treaty requirements for certification. The Provisional Technical Secretariat (PTS) purchased from Nanometrics Inc. three data acquisitions computers (DAC), 22 authenticating digitizers, and intra-array communications hardware and support equipment. A second contract was awarded to Güralp Systems Limited for the procurement of 22 CMG-3ESPV seismometers to replace the Geotech 23900 SP seismometers. A new CMG-3T seismometer was also ordered for a new broadband element ESBB that was installed as part of the upgrade to meet IMS requirements.

The new equipment was delivered mid October 2001 and the upgrade of the Station's SP elements commenced at the end of October. All 19 SP elements were upgraded, the new broadband element installed, and systems were fully operational sending CD1 data to the IMS Lab, AFTAC and IGN, in early November under the new configuration. After review of the Station performance and configuration, PS40 was officially certified on 21 December 2001 by the PTS under the new configuration.

Overview of new hardware and configuration

This system configuration described below provides a data acquisition and storage capability that meets the 98% timely data availability requirement under the Treaty for data availability at the IDC.

Basic Overview of the Station

Under the IMS configuration the SP array has 20 elements with a total of 22 channels, sampled at 40 sps. The aperture of the SP array is just over 8 km and is of a spiral design (Figures 1 and 3). The array consists of 19 vertical SP elements and one three-channel broadband element. Both the digitizers and communications modems are located in new Wellhead Termination Units (WTU) affixed to the top of the borehole casing, which provides protection from weather, as well as security, for the hardware (Figure 4). Each WTU has a tamper detection switch attached to the door that is connected to one of the External State of Health (SoH) channels of the new digitizer. Because of the geographic location of the array, and since the digitizer and communication modems are located in the WTU, a thermostatically controlled exhaust fan was added that would turn on if the inside WTU temperature reaches +40°C. A shade cover was also installed around each WTU to help provide additional protection from the sun and thus reduce the internal heat of the WTU, and help protect the equipment (Figure 5). All cables running to the WTU are housed in flexible or solid metal conduit to provide both security and weather protection.

The SP sensors are installed in the original 4.5-in. steel-cased boreholes at a nominal depth of 30 m below surface. Each SP seismometers is coupled to the borehole casing using a motor-driven three-jaw hole-lock attached to the bottom of the seismometer (Figure 6). The broadband element is a surface-mounted seismometer installed in a vault approximately 4 m below the surface and placed on a concrete pier. The digitizer and modem are also located within the vault. To help dampen the affects of acoustic sound waves in the vault produced by wind blowing across the door, and to provide additional thermal stability, the broadband seismometer has been buried in a box filled with sand.

Seismometer

The Güralp GMG-3ESPV borehole seismometer, with a bandpass of 0.02 to 50Hz and configured to 750 V/m/s^2 sensitivity, was chosen for the SP vertical-component elements due to their force feedback design, size, bandwidth, dynamic range, sensitivity and ease of importation within the European Union (Figure 6). Due to the background noise at the Station and the overall design requirements of the IMS, it was determined that using sensors flat to acceleration would be preferable as they would be more sensitive at higher frequency. The three-component broadband element uses a high-sensitivity Güralp CMG-3T triaxial seismometer that is flat to velocity, has a bandpass of 0.0083 to 50Hz, and is normalized to 20,000 V/m/s. It was chosen primarily for its compatibility with the CMG-3ESPV sensors, the dynamic range, sensitivity and ease of importation. It had been verified before that these two sensors meet the minimum self-noise requirements of the IMS.

Digitizer

The Nanometrics HRD Europa remote digital acquisition system, in a Callisto housing, provides 24-bit digitization, digital signal processing and data frame authentication (Figure 4). Each digitizer has two RS-232 outputs, one for the internal non-authenticated data and one for external authenticated data, as well as having one 10-base-T LAN port for both data output and programming. The output of the digitizer is compressed NMX-X format data and uses a UDP/IP communications protocol, instead of TCP/IP, to reduce communication overhead. Each data package is assigned a unique identification (ID) and also contains information on the oldest data package still in the digitizer's memory.

The HRD digitizer uses a 24-bit delta-sigma processor and, as measured at Sandia National Laboratory, has a "Noise Power Ratio" dynamic range of 125 db (131 db for shorted inputs). Input channel noise levels are generally less than two counts rms at 1.9 uV/bit & 100-sps and a cross-talk of less than –80db. Authentication of data is handled via a PCMCIA hardware token utility attached to the "Communications Controller Board" located inside the digitizer housing. Authentication hardware is protected with an internal tamper indication switch mapped to a SoH channel and incorporated into the data stream.

The digitizers in the array were each configured with a sensitivity of 2539 nV/count giving a nominal overall system sensitivity, "NCALIB", of 0.0858 nm/count for the SP elements and 0.0202 nm/count for the broadband elements. All data channels are sampled at 40 sps, per the IMS requirement, and data are sent over the intra-array communications network to the Central Recording Facility (CRF) using private wire modems and the authenticated RS-232 output of the digitizer. Independent timing for each element is provided by means of a Trimble GPS receiver incorporated into each digitizer and an external antenna mounted on the outside of the new WTU (Figure 5). Each digitizer has 13MB of RAM, which, depending on compression, can store over 20-hr of data in an internal "Ringbuffer". This data can be re-requested by any or all of the DAC in the event of missing data packages, or an interruption in communications between the CRF and the digitizer.

Each digitizer has three "fast" State of Health (SoH) channels and three slow SoH channels. The fast SoH channels sample at 10 Hz and monitor the vault door and internal authenticator tamper detectors and the calibration-enabled channel. These SoH channels are mapped in the data acquisition software to the appropriate CD1 status bits and forwarded to the IDC in the CD1 "Data Frame". The slow SoH channels are sampled at 0.1 Hz with two of the channels used to measure the internal digitizer temperature and input voltage, the third channel-free. Figure 7 shows the basic data flow within the digitizer.

Central Recording Facility Hardware

The CRF Data Acquisition Computers (DAC) consist of three Sun Microsystems Sparc Ultra-5 Workstations running the Solaris 8 (Unix) operating system. One of these computers is designated as the "Primary" IMS DAC and a second as the "Back-up" IMS DAC. Both are configured to send continuous data (CD1) to the IDC via the basic topology GCI. The station operators use the third computer as the Network Operator Terminal (NoT) for routine screening of waveform and SoH data. The NoT is also configured to send CD1 data to IGN in Madrid, Spain, and AFTAC in Florida, USA, via their respective independent sub-networks. The NoT is also capable of sending CD1 data to the IDC via the GCI if needed.

Data flow from each element via the Intra Array Communications equipment to one of four RM-4 Bridge-multiplexers. The RM-4 converts the RS-232 serial data to Internet Protocol (IP) and then multicasts the data over the LAN to the various DAC computers connected to the LAN. For reference, Figures 8, 9 and 10 show the interconnection to all hardware located at the CRF and the data flow for the new hardware and software installed as part of the upgrade. The RM-4 also provides full duplex communication with each digitizer for data recovery and issuing of various commands from the DAC, such as mass centering

and calibration. The data are received by each of the DAC and are stored in independent ringbuffers. Each ringbuffer is set to hold about 14 days of data assuming no compression of the data. Recovery of missing data packages is handled through the data acquisition software, NAQSServer.

The computers, and RM-4s, are each attached to one of two standard 3-Com LAN Hubs. These hubs also provide the physical link to the GCI, IGN, and AFTAC communications equipment for forwarding of data to their respective destinations. The computers, RM-4s, LAN Hubs, and communications equipment are installed in an equipment rack with intrusion detection switches that indicate when either of the doors to the rack has been opened (Figure 11). The switches are mapped into one of the SoH channels of one of the RM-4 and will set a "rack open" bit in the CD1.1 protocol when implemented. This rack also houses two Chrysalis authenticators for signing AutoDRM requests and the intra-array communications equipment.

The CRF itself is a brick building with office space, storage rooms, work rooms, and a separate room for the DAC and other central array equipment (Figure12). The CRF has three additional buildings used for equipment storage, maintenance facility, and the backup generator.

Central Recording Facility Software

Data are sent to the all three data acquisition computers over the Intra-Array Communication system in compressed NMX-X format where they are recorded, stored, converted to CD1 and forwarded on to the respective destination by the data acquisition software. Figures 9 and 10 show an overview of data flow from the seismometer through the DAC to the CD1 receivers. The data acquisition software running on the DAC is the Nanometrics NAQSServer software, which is a Java-based program that can also be run on PC-based computers with minor modifications to the set-up files. The primary role of the NAQSServer software is to acquire continuous error-free data sets for real-time and off-line processing by Nanometrics and third party client software modules. It also serves as the primary interface for receiving real-time seismic data from Nanometrics' remote field digitizers through the RM4 Bridge Multiplexers. Since the digitizers send data using a UDP/IP protocol, the NAQSServer performs all error correction by re-requesting missing data packages. Since each data package is assigned a unique ID, and each data package contains the ID of the oldest package still in the digitizer's memory, NAQSServer can recover most missing data packages, as bandwidth permits, in the event of communication outages.

To provide CD1 data, all three DACs are configured with multiple instances of NMXTOCD1 software. This program is also a Java-based program that connects to the NAQSServer program as a client and builds real-time CD1 data frames and then forwards them on to the appropriate CD1 Receiver. All three computers are configured to send CD1 data to both the IDC and IGN in the event that their respective primary computers should fail. Only the back-up computer and NoT are configured to send CD1 data to AFTAC due to firewall constraints. Both the primary and back-up computers are configured with AutoDRM to provide additional data via e-mail request to the IDC. AutoDRM messages are signed by one of the Chrysalis authenticator tokens installed in the rack and any incoming AutoDRM request must meet appropriate security requirements or the system will not respond.

Additional software is provided for monitoring real-time waveforms and for viewing the various SoH parameters. Calibration and Mass-Centering commands can be issued from any one of the DAC at the CRF using the NAQSView program. All programs can be used over the GCI from work stations and PCs located at the IMS in Vienna to help provide support to the station operator. Various playback programs are also available to the station operator for extracting additional SoH information as well as extracting and converting time-series event data.

Since the software provided under the contract with the equipment supplier, Nanometrics, does not have the capability to look at older waveform data, the IMS has installed additional software for the station operator to use. This software converts the NMX-X data to CSS-formatted data and stores about 5 days of continuous time-series data online. The IMS also installed various other programs developed by the IMS so that the station operator can view the data and perform routine analysis for data quality.

Intra-Array Communications

The intra-array communications between the digitizer and DAC is handled using private wire modems over the existing copper wire network (Figures 3 and 4). The array has over 50 km of cabling with the longest run between element and CRF of just over 8 km and uses the same transmission poles as the A/C power distribution system. Each element within the array has 4 pairs of wire between the CRF and the element: two for data, one for power monitoring, and one spare. Cables were recently checked as part of the IMS upgrade requirements and several bad sections were replaced under the site upgrade contract. New splice connections were made at each end and a new terminal board installed at the CRF during the upgrade.

The private wire modems are connected to each of the digitizers inside the WTU via a short, 1-m, communications cable (Figure 4). The modems are then connected to the private wire network for communications back to the CRF. The wires are attached to the corresponding modem at the CRF and terminate inside the equipment rack and attached to the appropriate RM-4. Each

digitizer/modem pair is configured to send data to the CRF at 9.6-kbaud, which provides ample bandwidth for data recovery and communications requirements between the DAC and digitizer.

Power Systems

The array elements use DC power provided by 24 VDC batteries with over 200 hours of autonomous run-time capability. They are charged by both a solar charging system and 440 VAC to 24 VDC, and are the primary source of power at each element. Power is converted within the modems to 12 VDC using an internal DC/DC converter. The DC/DC converter supplies power to the seismometer and digitizer at the site as well as meeting the modems power requirements.

A private above-ground power transmission network provides commercial 440 VAC power from the CRF and each element within the array (Figure 3). Both a UPS and a back-up generator are located at the CRF and provide back-up power for the 440 VAC power lines. At the CRF commercial power feeds into a new double conversion UPS that conditions power and provides back-up power to the DAC and associated equipment in the event of a power outage until the back-up generator comes on line.

Review of Array Testing

Component Testing

The Nanometrics digitizer underwent formalized testing in May 2000 at Sandia National Laboratories, under the supervision of the IMS Seismic Monitoring Section (IMS/SM), to validate the manufacturer's specifications, and to confirm that it meets IMS requirements. These tests demonstrated that the digitizer met or exceeded all IMS requirements for noise, dynamic range, timing and functionality. Additionally, each system provided to the IMS undergoes a formal "acceptance" testing at the manufacturer's facility before shipment. The acceptance tests are designed to test all aspects of the systems and to ensure that they meet the IMS requirements before shipping and that they are properly configured. They also provide a baseline for each system under a controlled environment.

After the upgrade of the first 10 SP elements and the installation of the new BB element, the CD1 data stream was started to the IMS Lab in Vienna via the Basic Topology GCI. CD1 data frames were checked to see that they met IMS requirements. As additional elements were upgraded throughout the array, they were added to the data flow to the IMS Lab and tested until all elements were functional. As each element was installed, the tamper switches were tested to ensure proper functioning. Calibration and mass centering commands were tested, as well as the GPS timing. Both CD1 sender and receiver logs were checked to ensure that the system was setting the proper status bits in the CD1 data stream. Evaluation of the receiver logs from the IMS Lab confirmed that the station met all IMS requirements for characteristics such as sampling rate, data frame length, proper implementation of the CD1 data format, and authentication signature for each element. After this initial checking by the IMS, data were transferred to the IDC test bed on 26 November 2001 for further analysis by the IDC.

Data Latency and Timely Data Availability

Data from the station under the old configuration were received by the IDC from August 1999 until the upgrade in October 2001 via the basic topology GCI. Data Availability (DA) statistics under the old configuration showed the station routinely performed above the 98% monthly DA requirement of the IMS, but missing data was never refilled. Under the new configuration, results taken from the "stacap" program while in the IDC test bed showed that DA for the station is now above 99.9% with most channels reporting 100% monthly DA. It should be noted that the ES10 element has been having major communication problems due to a faulty and intermittent problem with the intra-array wiring.

Data Latency

An indication of data latency for the station is shown in Figure 13. This figure shows a plot for CD1 data frames received in the IDC test bed over a 24-hour period. The y-axis represents the time that the data acquisition computer recorded the data and the x-axis the time the frames were received by the IDC DLMan program. The difference in these times is a good representation of the overall data latency between the station and the IDC. Frame latencies >300 seconds typically represent periods in which "catch up" occurred from the disk buffer. The mean latency for data sent by the NmxToCD1 software, as recorded in the IMS, from November 26 – December 10 was about 26 seconds.

Timely Data Availability

The IMS requirement for Timely Data Availability (TDA) is that data frames must be received by the IDC within 300 seconds (5 Minutes) of the actual recording time. As an example, an estimate of total TDA from 30 November to 2 December 2001 was made from the frame logs in the IDC. During this period, a total of 26214 CD1 data frames were received by the IDC of which 206 took longer than 300 seconds, giving a TDA of 99.22% of the total data received with 100% DA. Of the 206 frames, 170

were "second pass" frames where only missing data were retransmitted after 12 hours. Due to the way the stacap program reports TDA, these second-pass frames were weighed the same as a first-pass frame. If we correct for this, we see that the true TDA is around 99.98% for this period.

Review of Waveform Data[1]

Perceived Noise

Initial review of waveform data indicates that the station appears much noisier than it was before the upgrade. It should be pointed out that while the data *appear* to be much noisier, in fact it has been this way for many years as the array is centred on the town of Sonseca. There are several factories in the area, some of which are within 100 m of the elements, which produce high-frequency noise. Also a highway running through the middle of the array, and in some cases less than 100 m from the elements, is the source of much of the transient noise and causes many of the false triggers seen by IGN and the IDC. A new bypass highway is currently under construction that will pass within a few hundred meters of four more stations, (ES02, ES07, ES17 and ES18), which will increase the noise problem in the near future.

Because the new station configuration has an increase in gain, dynamic range, sampling rate, a higher sensitivity and sensor response is flat to acceleration, we see what is perceived as an increase in noise within the array. If we look at data from the array under the old configuration, i.e. using the older 16-bit RT and Geotech 23900 sensor, and simply differentiate the data from velocity to acceleration (Figure 14), we now see that the noise was there before the upgrade of the Station. Because we were looking at data relative to velocity, we did not see this noise as easily. Conversely, if we decimate the new data to 20 sps and then integrate it, it looks like the old data. Since the new seismometers and digitizer are more sensitive at higher frequencies, the amplitudes of the high frequency noise in the raw data are much larger. If we integrate the acceleration data to velocity, we can produce a trace that looks very similar to the old data. Decimation of the acceleration data from 40 sps back to 20 sps alone does little to remove the high-frequency noise in the data as much of it is still below 10 Hz.

Looking at just background data for ES01 before and after the upgrade, along with ESLA and ESBB vertical channels, and doing a simple FT analysis of the data, we see that in the raw data, the old data look quieter (Figures 15A and B). However, if we remove the instrument response, we can see that for data above 1Hz, the trace for ES01/BHZ, ESBB and ESLA track nicely (Figures 15C-D). If we first apply a simple Butterworth Low Pass (LP), 1-Hz, causal, first order, filter to the ES01/BHZ data, we now see an improvement in ES01/BHZ. Now the new configuration tracks the older ES01/sz data up to about 5 Hz, where it rolls over, possibly due to anti-alias filtering at the digitizer (Figures 16A-D). In either case it has been shown that the new sensor is performing nicely above 1 Hz and, even without filtering, is as good as the KS54000.

If we apply the simple LP filter described above, we can remove much of the high-frequency background noise while retaining much of the waveform information (Figure 17). With this simple filter we can produce a trace from the ES01/BHZ acceleration data that correlates very well with the new broadband velocity element, ESBB/BHZ. Further this filtered trace also correlates nicely with the integrated data.

Comparison of Event Data

Comparisons of waveforms were made for two sets of events under the old and new array configuration. Data for two each regional and teleseismic events were picked at random based on available data from the IDC database, location and magnitudes. These events are not meant as conclusive evidence as to the overall performance of the array but only given as examples. Comparisons were made using data from ES01, ESBB and ESLA, which are located near the center of town and are very noisy elements within the array. The regional events that occurred on 9 August 2001 and 4 April 2002 with magnitude ML 3.7 and 3.0, respectively, were located 1.3 and 0.8 degrees NNE of the array, depth at about 8 km for both. The teleseismic events occurred in northern Chile near the Bolivian border on 24 July 2001 and 28 March 2002 and were magnitude MW 6.3 and 6.5, respectively. The epicentral distances for these two events to Sonseca were about 85 degrees. The first teleseismic event had a reported hypocentral depth of 33 km while the second event was much deeper (about 125 km).

Regional Events

Comparisons of arrivals were made for old data (ES01/sz), new acceleration data (ES01/BHZ), integrated acceleration data (ES01i/BHZ), LP-filtered acceleration data (ES1lp/BHZ) and the ESBB/BHZ element. The data show that the first motion is very clear for the regional event using just the raw acceleration data and that secondary arrival in the initial part of the trace is clearly present (Figures 18A-D). The raw velocity data for the first event under the old configuration is still good, but does not

[1] *For the purpose of the following sections, ES01/sz and ESLA/bz are from the old configuration, ES01/BHZ is the new acceleration data and ES01i/BHZ is the integrated data of ES01/BHZ, and ES1lp/BHZ is LP data for ES01/BHZ.*

show as clear a first motion or the details for secondary arrivals (Figures 18A-C). It should be noted that these are different events, in a different area and at a different time, and as such a direct comparison is not possible as variation should be expected.

A basic integration of the acceleration data using the SAC software for this event provides significant first and secondary arrival information but is notably smoothed and has lower amplitudes as compared to the raw acceleration data. Applying a very simple LP filter to the acceleration data gives almost an exact match to the integrated data but provides greater amplitude information. The filtered, or integrated, data can be directly compared to the velocity data provided by the CMG-3T vault seismometer at ESBB. Adjusting for the station offset, again a good correlation can be made between the various waveforms, even without integration or filtering (Figure 18D).

Teleseismic Events

For the teleseismic events, we again looked at ES01, ESBB, and added ESLA for comparison. For the two events we can see that for the velocity data, i.e. ES01/sz, ESLA/bz, ES01i/BHZ and ESBB/BHZ, the first arrival is clearly present in the raw waveform data without any processing (Figure 19A). For ES01/BHZ, the first motion is present in the raw acceleration data but because of local noise, i.e. a vehicle driving by, it is hard to pick out if one does not know where to look (Figure 19B). Again, applying LP filtering enhances the first arrival and removes much of the noise in the trace, making it much easier to see (Figures 19A-F). For the second event you can clearly see a pP phase arrival, even in the raw acceleration data (Figure 19D). Using a 3rd order LP filter at 0.1 Hz on both events, we can see that under either configuration, later arrivals are present in all traces (Figures 19C-D). LP filtering of the data at 0.01Hz shows that for the two broadband sensors, ESLA and ESBB, ESLA performs much better and has greater detail in later phase arrivals (Figures 19E-F). This would be expected, as ESLA is located in a borehole at a depth of about 100 m while ESBB is located at the surface. Also, the KS54000 performs much better at longer periods than the CMG-3T but this is well below the design criteria for the IMS.

It should be noted that the performance of the new short-period sensors, the CMG-3ESPV, is very good and these sensors provide additional information on later arrivals (Figures 19E-F). Due to their installation in boreholes, these SP sensors perform, in some respects, even better than the broadband ESBB sensor installed at the surface. When applying the LP filter at 0.01 Hz, the waveform for ES01/sz falls apart under this filtering, and no real useful data are provided, though this is well below the passband of the sensor (Figures 19E-F). This shows that the new SP sensors are indeed broadband sensors, as well as short period, and should provide additional information about seismic waveforms not seen by the array in the past. It has yet to be determined how useful this information will be for verification purposes.

Solutions to Reducing Noise

Various techniques have been looked at by the IMS staff to reduce the high-frequency noise at the site in post-processing and in the hardware itself. The software solutions include decimating the acceleration data from 40 sps to 20 sps after receiving it at the IDC, integration of the data at 40 sps or 20 sps, and applications of various low-pass filters before triggering and beam forming. The most promising is simply applying the 1-Hz, LP, first order, filter to the raw acceleration data. This filter essentially converts the data from acceleration to velocity and removes much of the high frequency noise seen in the data, but still retains all the information in the waveform provided by the sensor.

Several hardware solutions, and combinations, have been looked at. The first alternative would be to reduce the sample rate of the digitizer from 40 sps to 20 sps, like the old system. The second alternative would be to add an integrator into each of the seismometers converting them to be flat to velocity. The third alternative is to move the problem stations away from the noise source. Alternative 1 does little to reduce the actual noise in the traces, as much of the noise is still present after decimating the data and false trigging will still be present. Alternative 2 is possible, but the IMS feels that valuable data will be lost as these elements are providing useful data at the higher frequency. The third alternative may need to be implemented, as the new road construction will further reduce the capability of the array, and it may become necessary in the near future to move elements.

CONCLUSIONS

The station has been shown to meet all requirements for a primary IMS seismic station and as such has been certified by CTBTO. Authentication devices and GCI infrastructure are in place and have been demonstrated to work properly. The station underwent a complete upgrade in Oct and Nov 2001 with equipment purchased by the IMS. New software and hardware have proven to be stable with little or no trouble. The station has been sending CD1 data to the IDC, AFTAC and the NDC via basic topology GCI and independent sub-networks since 10 Nov 2001. Under the upgraded configuration, DA has been well above the Treaty's 98% requirement.

Event data clearly show that the new configuration is more sensitive and is able to record high-quality data for both regional and teleseismic events. With or without filtering, it is the PTS's feeling that the new SP elements are performing better than the old sensors and are capable of providing additional waveform information below 0.05Hz and above 5Hz. Comparisons of spectral noise plots show that the new SP elements are performing within specification and a simple low-pass filter is very effective in

removing high-frequency noise. Utilization of instrument corrections shows that the new SP elements respond better above the microseismic background noise as compared to the broadband element and the old equipment. This holds true with or without first using LP filtering. Comparisons of background data show that the array "appears" to be noisier under the new configuration. However, it has been shown that even under the old configuration the same types of noise sources were present and can be clearly seen when differentiated to acceleration. The new data can be decimated by a factor of two and then integrated to arrive at what looks like the old array.

The new configuration has greater sensitivity to high-frequency signals, which one would expect to see for a "Treaty Relevant Event". It is the PTS's feeling that this type of array configuration is acceptable for new and upgraded arrays as it should provide a better ability to detect small events at greater distances in the future. As such, analysts working with the new data will need to become accustomed to processing acceleration data, as several of the new IMS arrays will be configured the same as PS40, i.e. with sensor response flat to acceleration. While the new configuration is currently causing many false triggers at the IDC and NDC, it is the PTS's view that additional work must be done on software improvements to handle the use acceleration data and not to degrade the new performance of the station. Proper pre-filtering of the data should greatly reduce the number of false triggers.

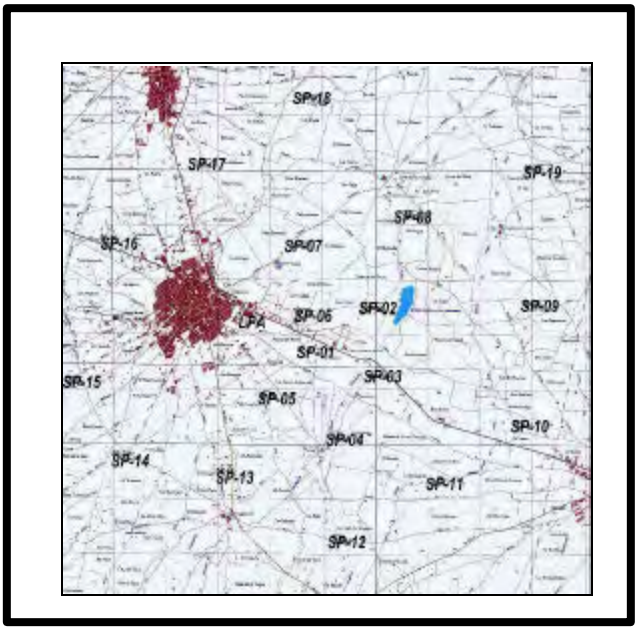

Figure 1. Map of PS40 Array showing the location of array elements and proximity of Sonseca, SP01=ES01.

Figure 2. GCI Dish installed on side of CRF.

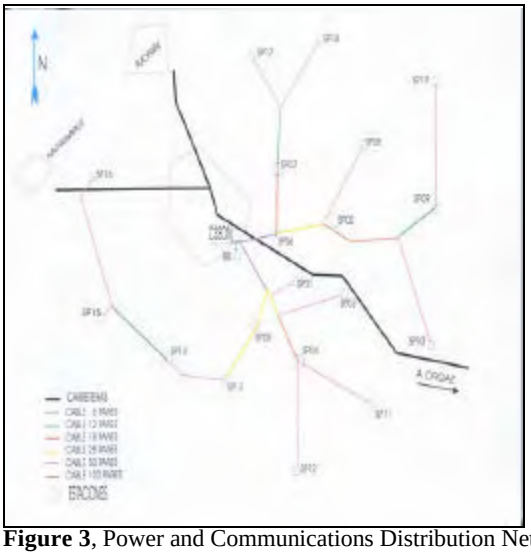

Figure 3, Power and Communications Distribution Network.

Figure 4. New Callisto Digitizer (L) and Modem (R).

Figure 5. New WTU with shade cover, external GPS antenna shown in upper right of picture.

Figure 6. New CMG-3ESPV seismometer with 3-jaw holelock.

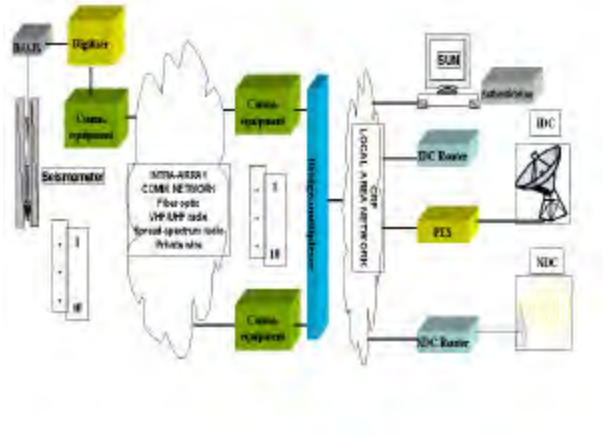

Figure 9. Block diagram of major components of the array.

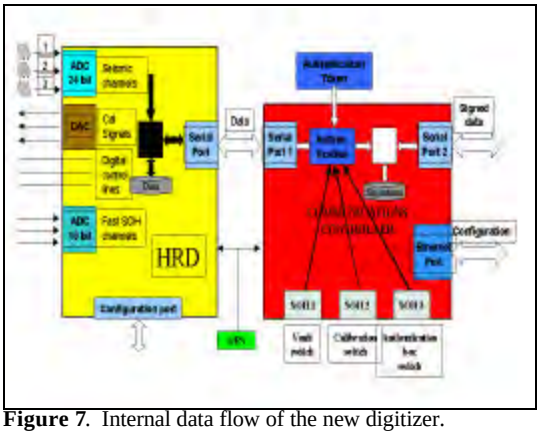

Figure 7. Internal data flow of the new digitizer.

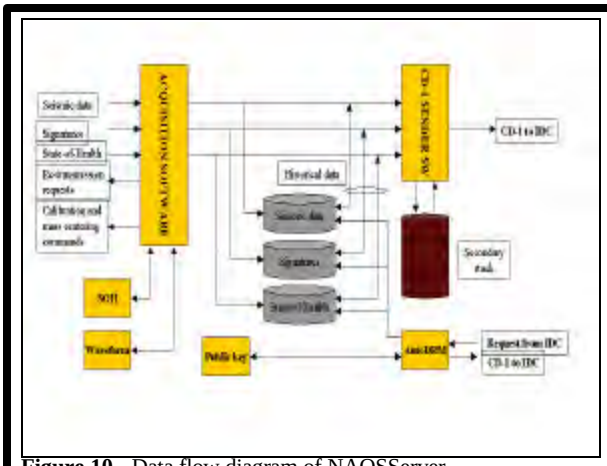

Figure 10. Data flow diagram of NAQSServer.

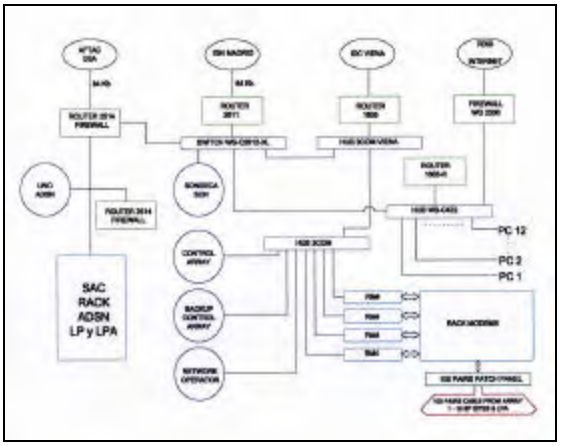

Figure 8. CRF equipment inter-connection showing new equipment configuration and physical connections. Flow to AFTAC still has LP elements going to them.

Figure 11. Front of new equipment rack at CRF, primary and back-up DAC on top, two each authenticators below DAC, 4 each RM-4s below authenticators, CRF communications modems below RM-4s. Older AFTAC rack to the right.

Figure 12. Central Recording Facility at Sonseca

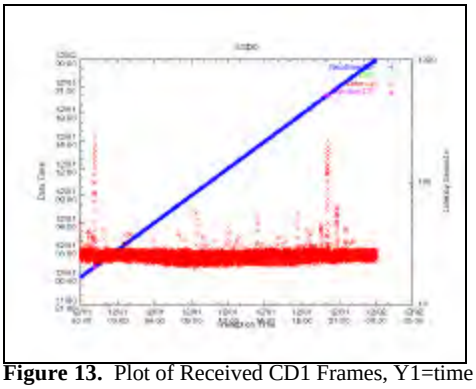

Figure 13. Plot of Received CD1 Frames, Y1=time that the data was recorded, X=time frame was received by IDC, Y2=log of latency time. Blue line plots the "Realtime" frames, red X is the difference of the X-Y1 times.

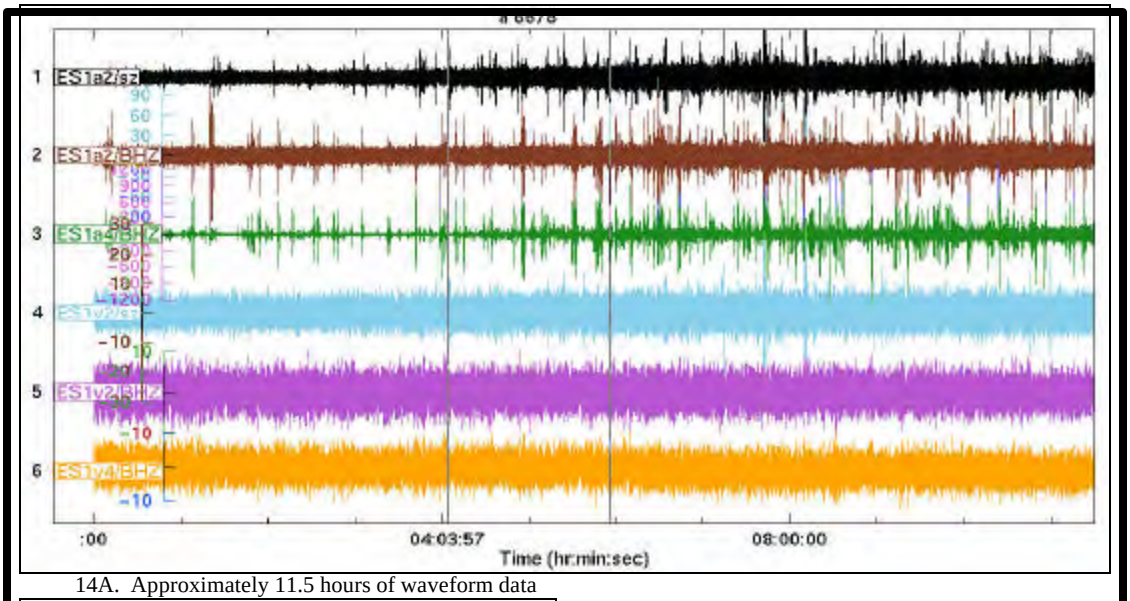

14A. Approximately 11.5 hours of waveform data

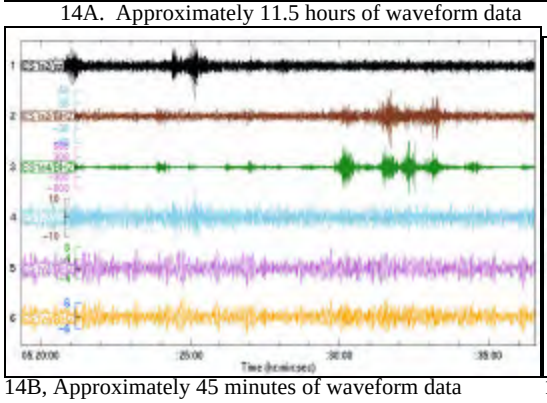

14B, Approximately 45 minutes of waveform data

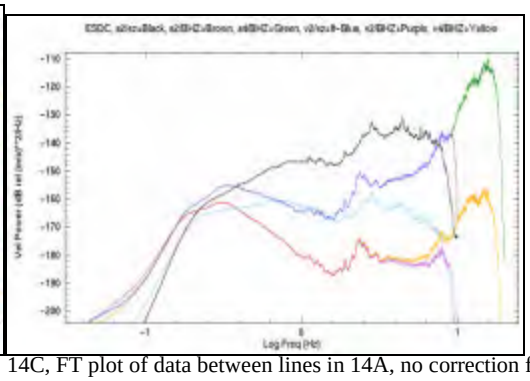

14C, FT plot of data between lines in 14A, no correction for instrument response.

Figure 14 A-C. Old and new ES01 data. Black=ES01/sz (ES1a2) differentiated to acc, brown=ES01/BHZ (ES1a2) decimated to 20 sps, green=ES01/BHZ (ES1a4) raw data (40sps Acc), light-blue= ES01/sz raw data (20sps Vel), purple=ES01/BHZ (ES1v2) integrated acc data decimated to 20 sps, yellow=ES01/BHZ (ES1v4) integrated acc data at 40 sps. 14A, note similarity between traces 1&2 (20 sps acceleration data). 14C-raw FT plot for each trace without instrument correction, only for comparison.

Figures 15 A-D

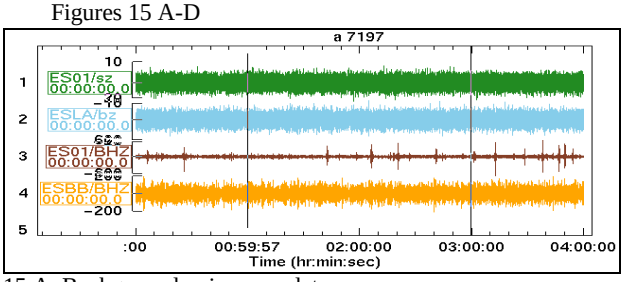

15 A, Background noise, raw data

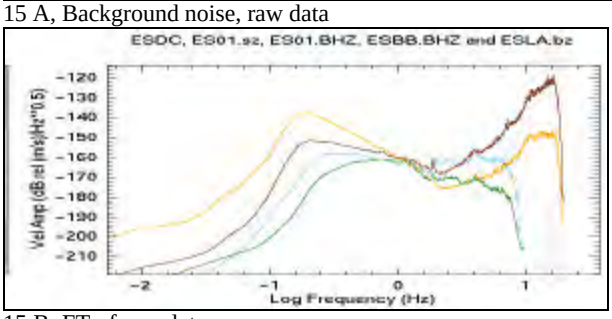

15 B, FT of raw data

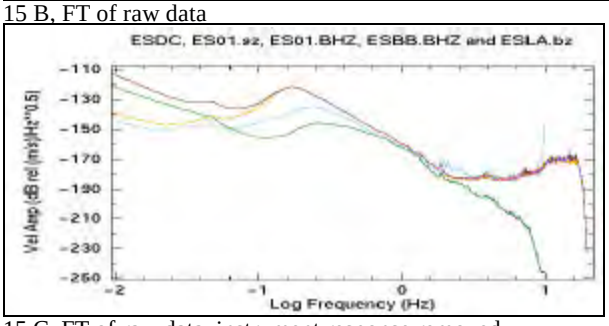

15 C, FT of raw data, instrument response removed

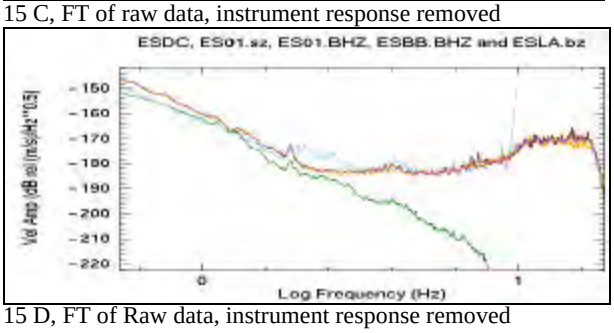

15 D, FT of Raw data, instrument response removed

Figures 16 A-D

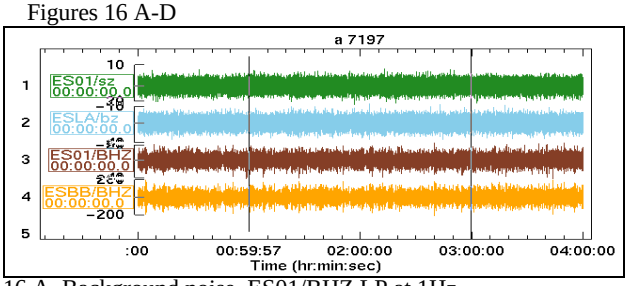

16 A, Background noise, ES01/BHZ LP at 1Hz

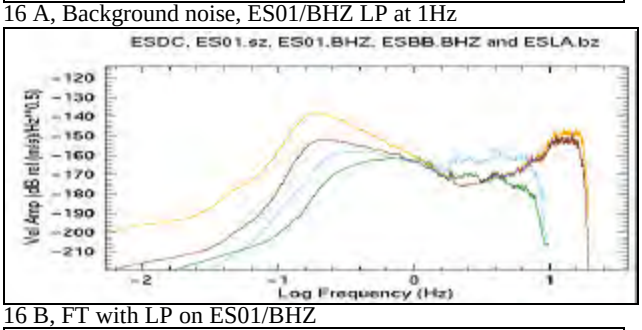

16 B, FT with LP on ES01/BHZ

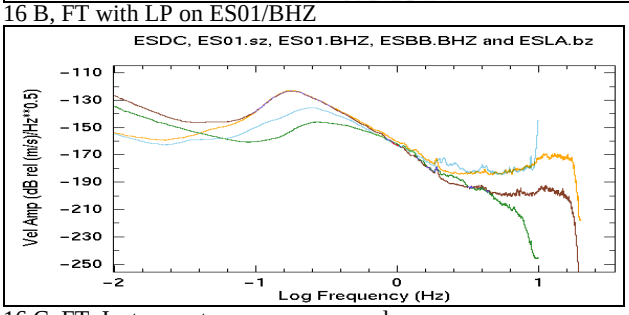

16 C, FT, Instrument response removed

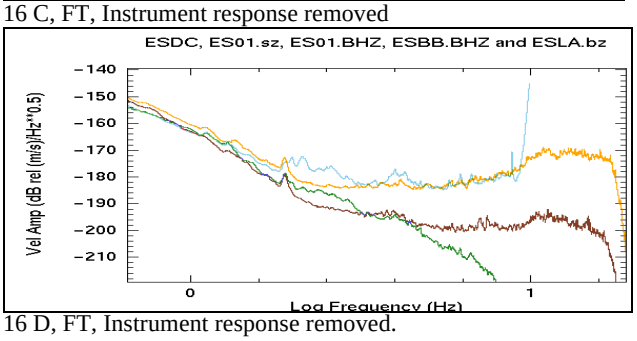

16 D, FT, Instrument response removed.

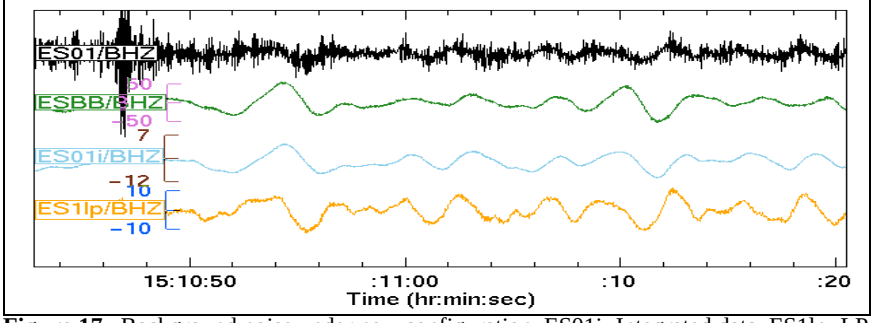

Figure 17. Background noise under new configuration, ES01i=Integrated data, ES1lp=LP at 1Hz

Figure 18 A-D, Comparison of Regional Earthquakes, ES01/sz=Old Vel, ES01/BHZ=New Acc, ESBB=Broadband Vel, ES01i=Integrated to Vel, ES1lp=LP, 1Hz, 1st order

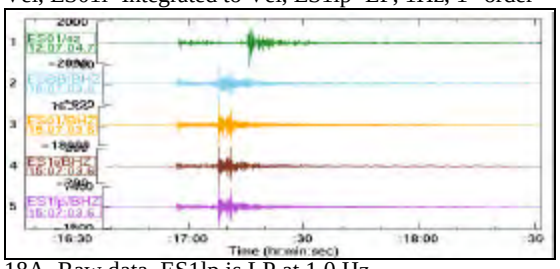

18A. Raw data, ES1lp is LP at 1.0 Hz

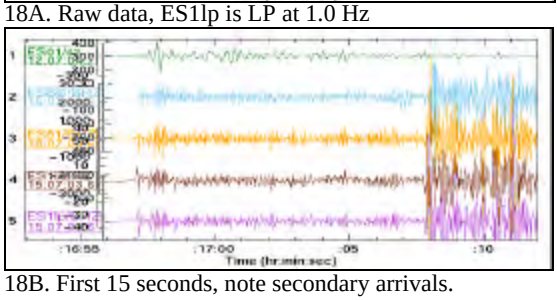

18B. First 15 seconds, note secondary arrivals.

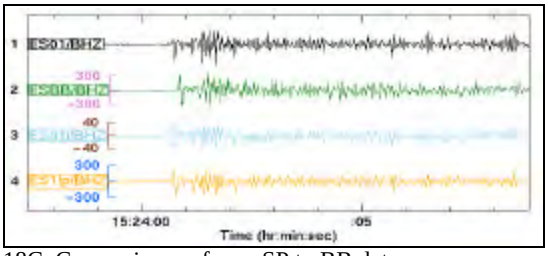

18C. Comparisons of new SP to BB data

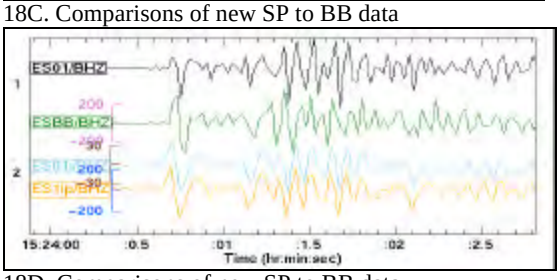

18D. Comparisons of new SP to BB data

Figure 19 A-E, Comparison of Chile earthquakes, ES01/sz=old vel, ESLA/bz=KS54000 vel, ES01/BHZ=new acc,

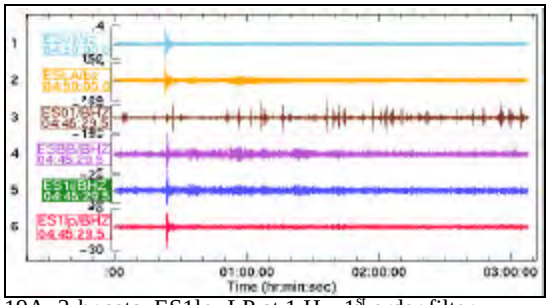

19A. 3-hr sata, ES1lp=LP at 1 Hz, 1st order filter

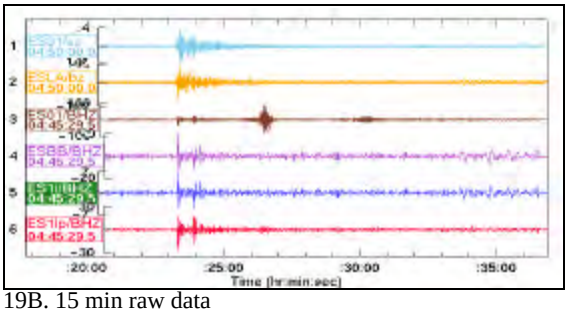

19B. 15 min raw data

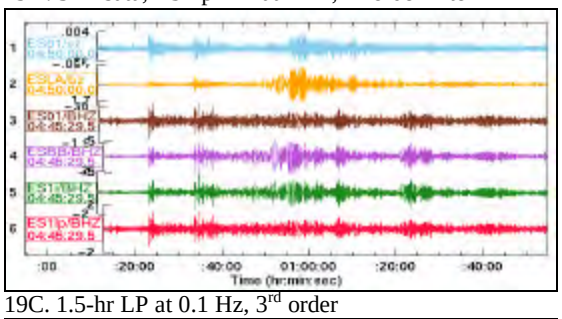

19C. 1.5-hr LP at 0.1 Hz, 3rd order

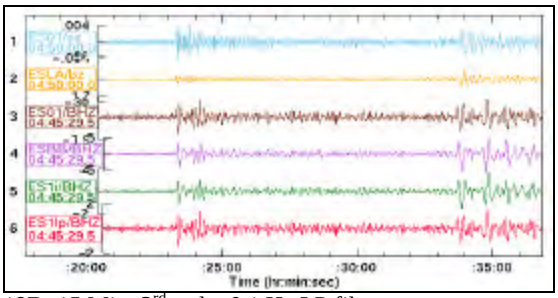

19D. 15 Min, 3rd order 0.1 Hz LP filter

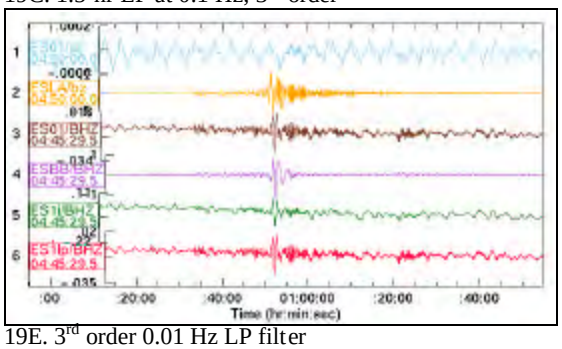

19E. 3rd order 0.01 Hz LP filter

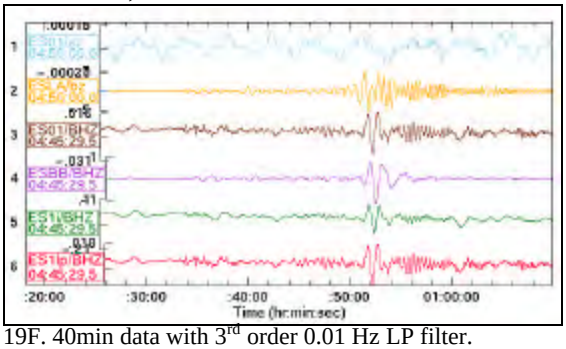

19F. 40min data with 3rd order 0.01 Hz LP filter.

LOCAL SITE EFFECTS AT THE NEVADA SEISMIC ARRAY (NVAR)

Eugene T. Herrin, Petru T. Negraru, Paul Golden, Carl Mulcahy

Southern Methodist University

Sponsored by Defense Threat Reduction Agency

Contract No. DTRA01-00-C-0093

ABSTRACT

In most cases array processing techniques are based on homogeneous structure assumptions, which is not always true. The output of a frequency-wave number analysis, based on the Fourier Transform, which is often used in processing raw data, will be strongly biased if all the stations do not have the same frequency content. In spite of the evidence that individual station corrections must be applied, corrections are not widely used. Often a simple relief correction is believed to account for all the local site effects.

The goal of this study is to present and, if possible, to explain the anomalous amplitude variations that are recorded at the Nevada Seismic Array (NVAR). Narrow-band frequency-dependent amplitudes were measured for both regional and teleseismic phases. Differences in source function (corner frequency) and attenuation account for the frequency content of different phases. Typically regional events allow observation from 0.5 to 16 Hz (0.5-1 Hz, 2-4 Hz, 4-8 Hz and 8-16 Hz) and teleseismic from 0.12 to 4 Hz (0.12-0.25 Hz, 0.25-0.5 Hz, 0.5-1 Hz, 1-2 Hz and 2-4 Hz). Although there are differences, particularly at high frequency, similar patterns are recognized for all phases. The most striking feature is the much larger amplitude exhibited by NV04 at frequencies 1-2 Hz and 2-4 Hz. Across the whole array, the variation in this frequency band can be higher than a factor of 8. The amplitude variation between NV04 and NV01, stations located only 500 meters apart can reach a factor of six. At higher frequency, 4-8 Hz and 8-16 Hz, NV09 dominates, its amplitude being occasionally more than one order of magnitude larger than the rest of the stations. No azimuth and distance dependence was found for these effects, which implies the absence of any organized dipping structure.

Taking advantage of the co-located seismic and experimental infrasound arrays, the seismic responses for propagating pressure waves were analyzed. The effects are larger, possibly because of the higher frequency (shorter wavelength) of the infrasound signals. The presence of the same amplitude effects leads to the conclusion that the structure responsible for these effects is shallow, being up to a few tens of meters.

To better understand the shallow structure, refraction profiles will be carried out in the field. Considering the depth of seismometer emplacement, true velocities can be obtained for the upper 12 meters using the short-period seismometer as a stationary receiver and moving the source further away from it, in a “walk-away” technique. In this way the presence of a low-velocity layer in the first 12 meters that may exist near site NV04 can be determined. It is desired to investigate the structure to a depth of 30 meters, the standard depth used by engineers to classify site characteristics.

OBJECTIVE

The objective of this study is to present and explain the effects that occur at the Nevada Seismic Array (NVAR) due to variations in the local geology. Common array processing techniques are based on homogeneous geological structure assumptions, which is clearly a simplification of the problem. In processing raw data the time-space domain is transformed in frequency-wave number domain by computing two-dimensional Fourier Transforms. The azimuth and phase velocity for the desired time window at the desired frequency are found by looking for the peak in power. Such an approach yields satisfactory results when the input time functions do not exhibit large spectral variations. This is usually the case in areas with uniform geological structure. Therefore, if an array exhibits large spectral variations, the outcome of f-k processing will be biased, and even the detection capability of the array could be lowered. At areas with large topographic variations, sometimes a simple relief correction is applied before processing, to account for the local site effects, but such an approach takes into account the topography rather than the geology.

RESEARCH ACCOMPLISHED

Berteussen (1974) was the first to observe and discuss amplitude variations at a seismic array. Explaining the travel-time anomalies recorded beneath several seismic arrays (NORSAR, LASA) in terms of scattering waves due to lower crust – upper mantle heterogeneities was the focus at the time. Additional papers were published discussing this subject (Aki, 1973; Capon 1974, Berteussen *et al* 1975; Berteussen 1975). More recently, the array calibration work has shifted toward experimental calibration (Tibuleac *et al*, 2001). A set of station corrections is developed empirically, to improve the location capabilities of the array. This approach yields better results, but it won't improve the detection capability for the whole array. Experience gained from the NORSAR array led to the installation of the small aperture NORESS array, which has a detection capability higher than NORSAR, for sources located close to the Semipalatinsk Test Site, although it was built at the location of one of the NORSAR subarrays.

The Nevada Seismic Array (NVAR) was installed in December 1998 by Southern Methodist University. The location of the array was chosen following negotiations between a team of experts from the USA and Russia. It was decided that one of the three-component stations would be located in the Black Butte mine, on the former setting of the station MNV (Mina, Nevada) for which historically recorded nuclear explosions exist (Figure 1). Although the array fulfills its mission very well, to provide coverage for the Nevada Test Site (NTS), the final location in a very

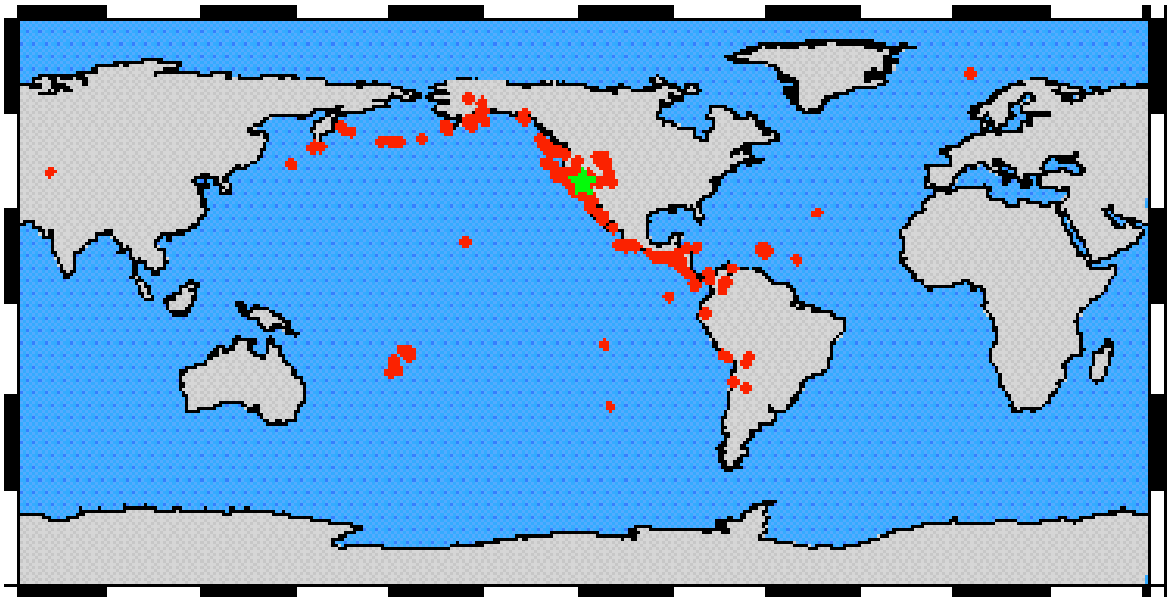

Figure 1. Position of earthquakes used in this study. The green star represents the location of the Nevada Seismic Array (NVAR)

complex geology led to unusual site effects, which raised the problem of determining an optimum array processing technique. The array consists of three broadband, three-component stations and ten short-period vertical stations. A weather station monitoring temperature, wind speed, wind direction, atmospheric pressure and relative humidity is located within the array. The present study is restricted only to the short-period stations, with the main focus on the inner ring of the array whose stations are co-located with an experimental infrasound array. More than half of the stations (stations NV01, NV02, NV03, NV05, NV06 and NV10) are located in the steeply dipping limestone of the Luning formation (Figure 2). These rocks were deposited during the late Triassic Period and can reach a thickness greater than 2 km close to the array. Site NV04 is located in lithified terrace gravels of Tertiary age. Site NV07 is located in the Dunlop formation, which comprises a very fine-grained sandstone, but the formation is variable within the region and can include shale and volcanic assemblages. Site NV09 is located in a Tertiary basalt flow, whereas site NV08 is sited in a Cretaceous granitic intrusive body.

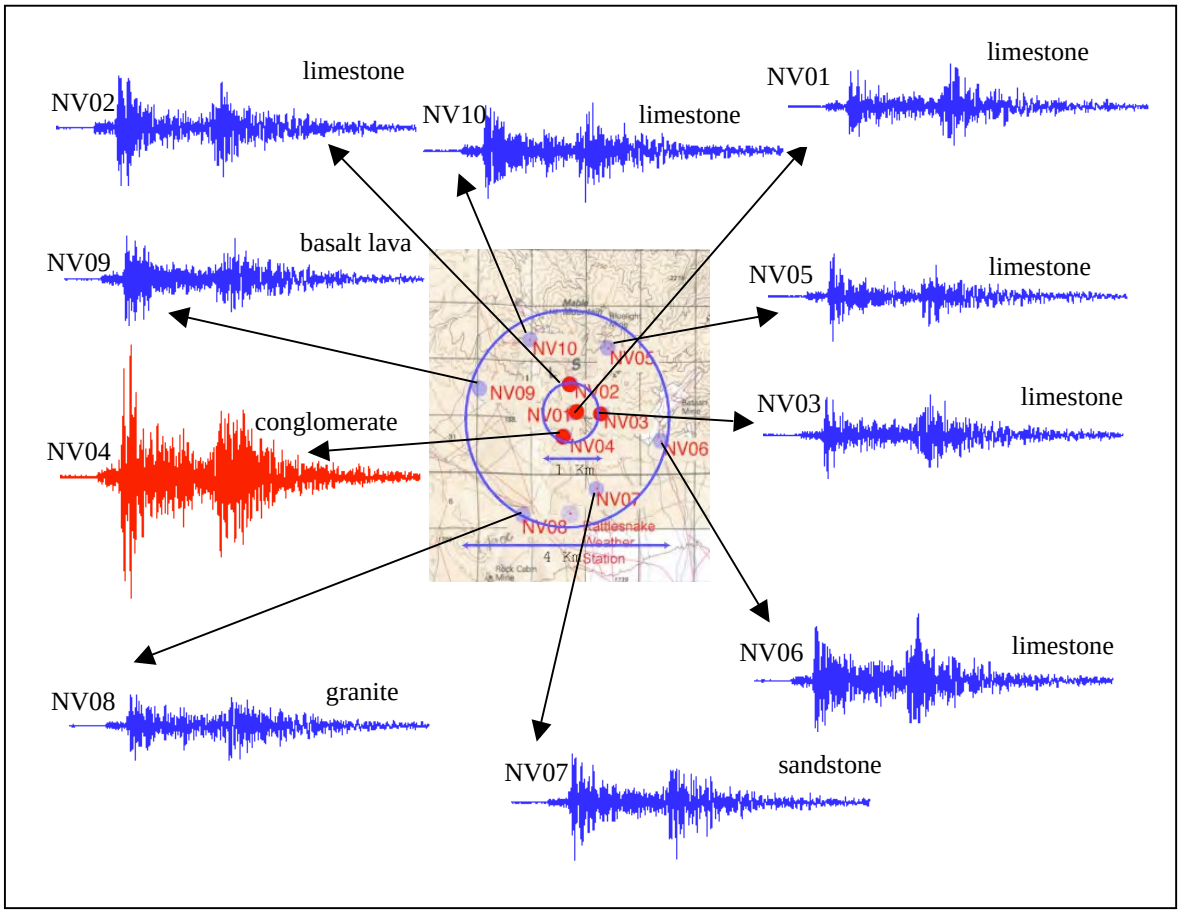

Figure 2. Detailed map of the NVAR array. The waveforms represent raw data recorded at NVAR at each of the short-period stations. The magnitude 5.7 earthquake occurred in California at a distance of 478 km. All the traces shown here are at the same scale. The red trace is channel NV04, located in Tertiary conglomerate, which exhibits the largest amplitude by a factor of three in this particular case.

To illustrate the local site effects encountered at NVAR, narrow-band frequency-peak accelerations were measured for both regional and teleseismic phases (Pn, Pg, Lg and teleseismic P). Although we desired observations in the same frequency band, variations in source functions and attenuation did not always allow this. In order to have a good signal-to-noise (SNR) ratio, most of the teleseismic earthquakes must have a magnitude higher than 5. Because the larger the earthquake, the lower the corner frequency, there is not too much energy above 4 Hz and secondly the high-frequency attenuation is much greater than at lower frequencies. Typically, teleseismic earthquakes, located at distances ranging from 24 to 90 degrees, allow observations from 0.12 to 4 Hz (0.12-0.25, 0.25-0.5, 0.5-1, 1-2 Hz) and regional events from 0.5 to 16 Hz (0.5-1, 1-2, 2-4, 4-8, 8-16 Hz).

In order to have a good azimuthal coverage, some earthquakes with lower magnitudes were included. The data consist of 75 teleseismic events and 213 regional earthquakes with magnitude between 3.5 and 7 (Figure 1). A fourth-order recursive Butterworth filter was applied for each frequency band, and the peak acceleration was measured from the envelope functions computed using Hilbert Transforms. In general the final results are relative to a particular channel, and thus most of the results will be equivalent for displacement, velocity and acceleration.

Taking advantage of the co-located seismic and experimental infrasound arrays, the seismic responses to propagating pressure waves were analyzed. The seismo-acoustic signals were detected by estimating the correlation coefficients at zero lag between seismic and acoustic envelope functions for a sliding 10-s window. Because the shorter the window, the higher the correlation coefficients for seismic and infrasound noise, a trade-off between window length and correlation threshold was achieved. The time length of most signals, which in general do not exceed a few seconds, was also taken into account. Empirically, the 10-s window and a detection threshold of 0.5 gave good results. Typically the noise for such a window length will have correlation coefficients below 0.3. Signals with good SNR have correlation coefficients above 0.5. The maximum correlation coefficient was 0.99, for a signal recorded on channel NV04. A detection was declared if there were correlation coefficients above 0.5 for at least three stations. Although this method works well for NVAR, it is not expected to work in the same way for all stations in the western US, but a similar approach can be used to make a detector at each particular array (or site). From 07/18/2001 to 08/30/2001 there were over 100 signals detected in this manner. Afterwards the amplitude was measured in the same way as the seismic signals, except that instead of peak acceleration, we calculated the root mean square value for the first three seconds of the signal. The bandpass filters used were similar to the filters used for regional events.

Background noise studies were also conducted. Ten-minute-long noise samples were chosen for different wind velocities. The sample was chosen so that the wind velocity had small variation during the time of interest. From every four-hour block, one time frame was chosen. The Welch Block Averaging method (Welch, 1967) was then applied to yield power spectral density estimates. The length of each data block was 512 points to constrain the individual estimates to frequencies greater than 0.1 Hertz. The individual blocks in each sample record were overlapped by 50 % and a Hanning window was used to reduce the variance of the power spectral density estimate.

CONCLUSIONS AND RECOMMENDATIONS

Figure 3 represents the spatial variations in ground motion peak acceleration for teleseismic P, Pn, Pg and Lg phases. Although there are differences, most notably at high frequencies, the patterns are very similar. The common feature for all analyzed phases is the much larger amplitude recorded at channel NV04 for frequency bands 1-2 Hz and 2-4 Hz. For stations NV01 and NV04, located only 500 m apart, the difference in peak acceleration can be as large as a factor of six. The largest difference across the whole array occurs usually for stations NV04 (largest amplitude) and NV05 (smallest amplitude), and could be higher than a factor of eight. At longer periods (0.12 – 0.25 Hz and 0.25 – 0.5 Hz), the signal is very similar, the variations being less than a factor of two. At higher frequencies (4 – 8 Hz and 8 –16 Hz), NV09 exhibits the largest amplitude, its peak acceleration being sometimes more than one order of magnitude larger than NV07.

No significant azimuthal or distance pattern has been found for this effect (Figure 4), which suggests the lack of any organized dipping structure. This conclusion is also supported by a previous calibration study (Tibuleac *et al*, 2001). This would suggest that the anomalous structure is flat to the first order.

The effects are larger for the pressure waves (Figure 5), possibly because of the higher frequency (shorter wavelength) of the infrasound signals. For approximately the same pressure levels, the variations in amplitude can be larger than a factor of 20. In general the amplitude recorded on the seismic channels for NV01 and NV03 are similar, which suggests the presence of the same physical properties beneath these two stations. NV04 always exhibits the largest amplitude and NV02, although located in the same geology as NV01 and NV03 can exhibit amplitudes larger than a factor of 10 when compared with NV02 and NV03.

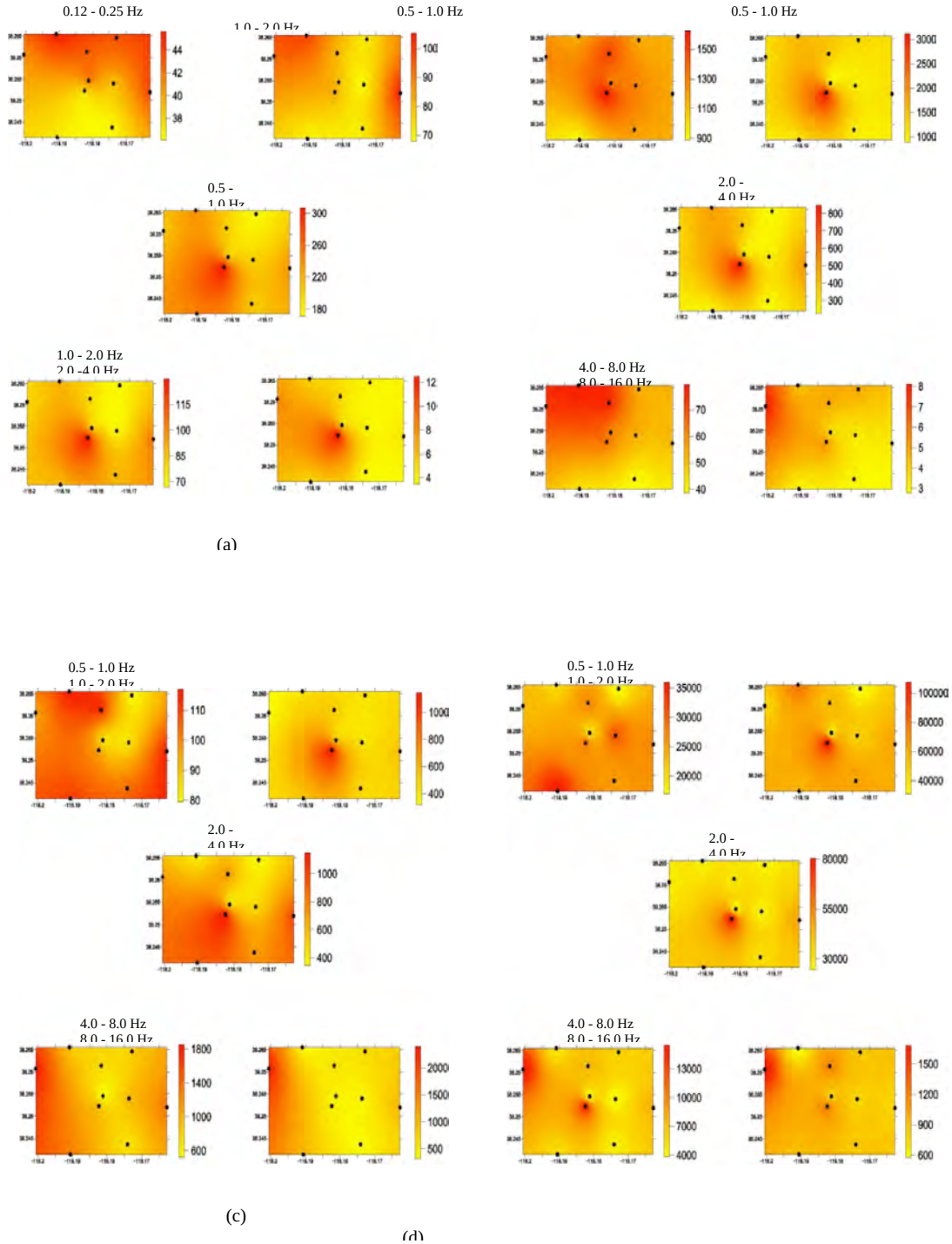

Figure 3. Spatial variations in ground motion peak acceleration of teleseismic P (a), Pn (b), Pg(c) and Lg (d). The black dots represent the position of each individual station. The units of the map are nm/s^2.

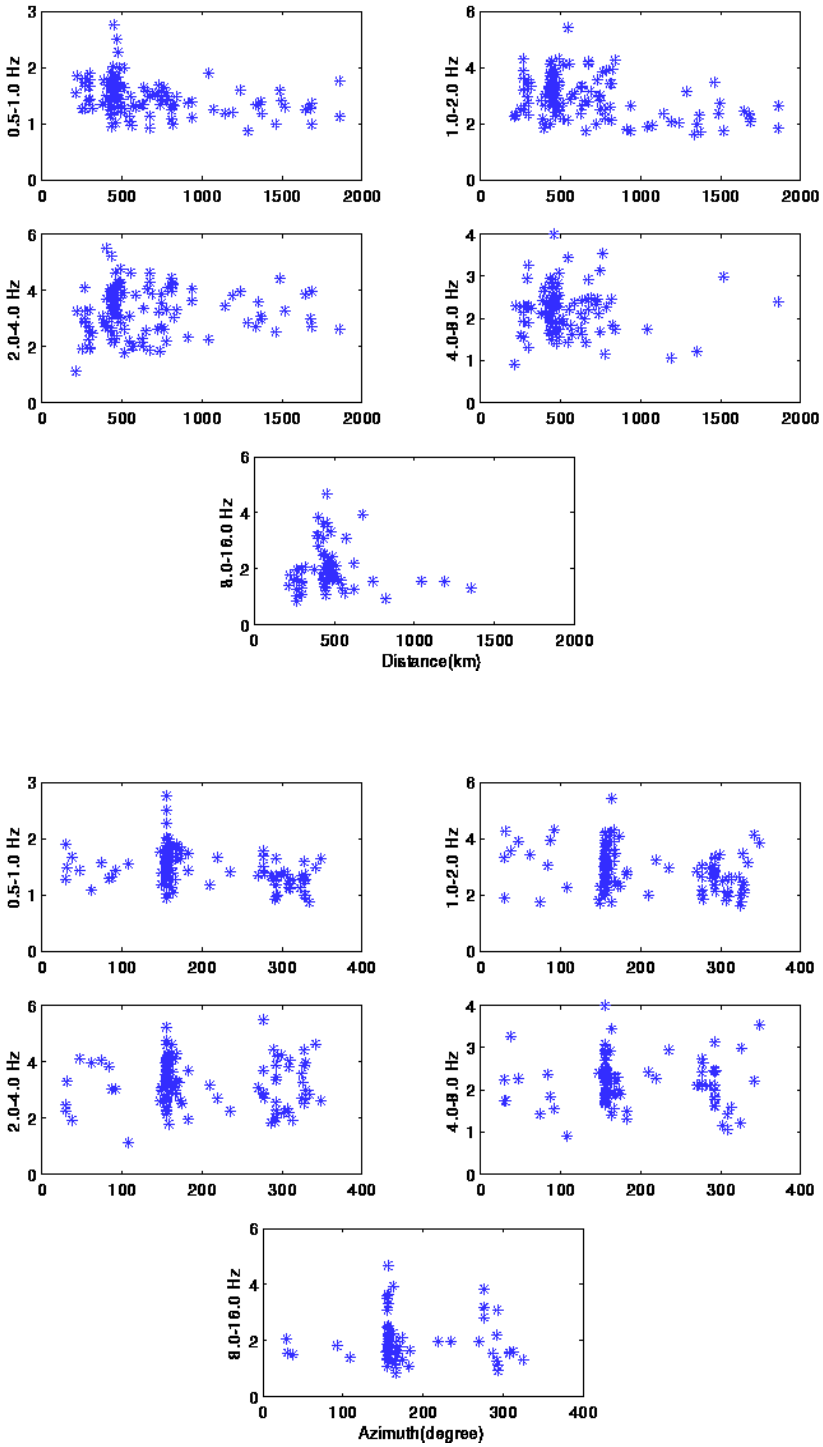

Figure 4. NV04/NV01 peak acceleration ratio for regional events. No pattern has been found as a function of distance (upper plot) or azimuth (lower plot). These two stations situated only 500 m apart exhibit variations as big as a factor of six in peak acceleration. The largest variation across the whole array for this set of events occurred for NV04 (largest acceleration) and NV05 (lowest acceleration) and was more than a factor of eight.

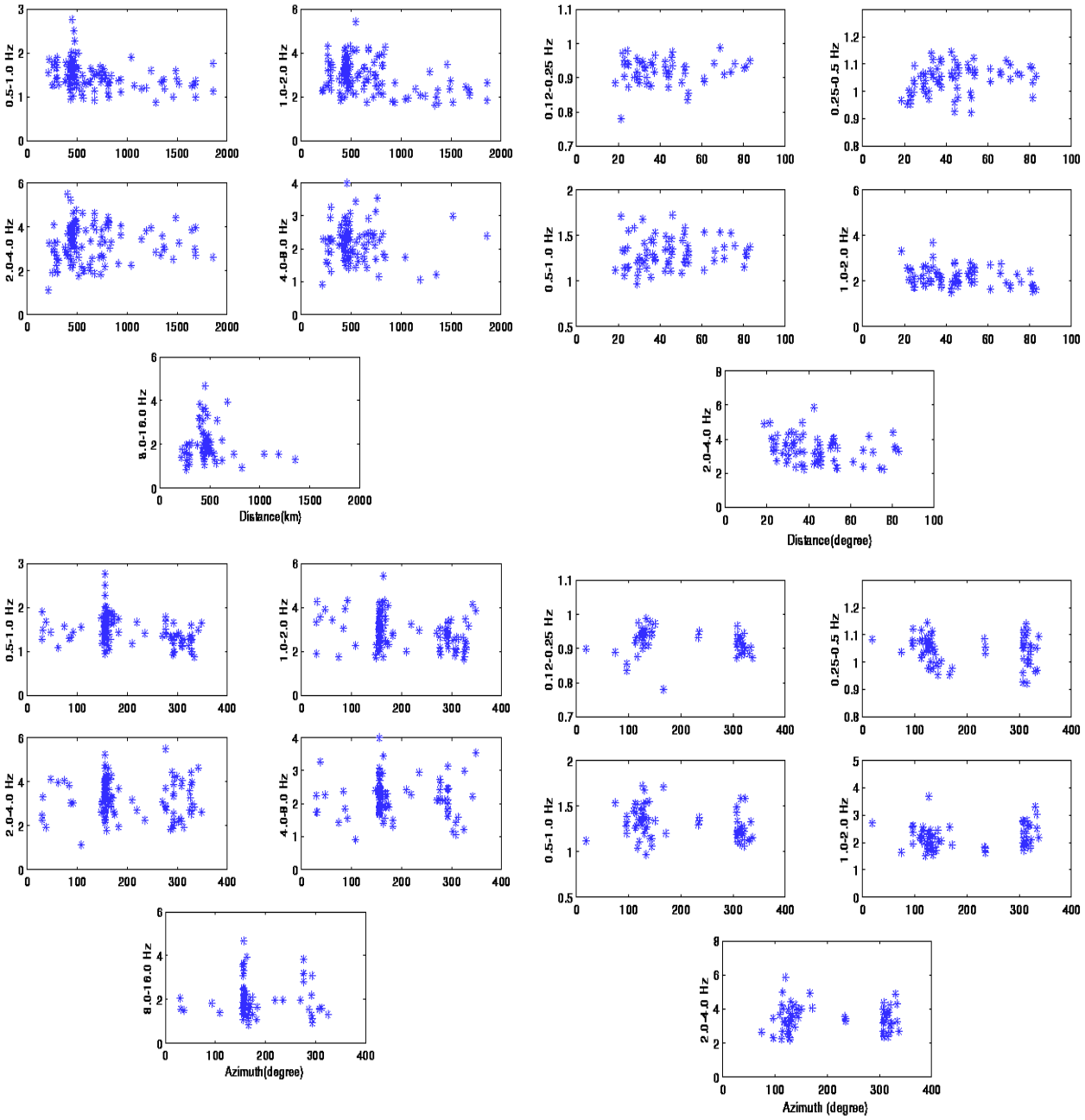

Figure 5. NV04/NV01 peak acceleration ratio for teleseismic events. The results are similar to the regional events. The maximum peak acceleration variations (for stations NV01 and NV04) is close to a factor of six, and the maximum variation across the whole array is close to a factor of eight

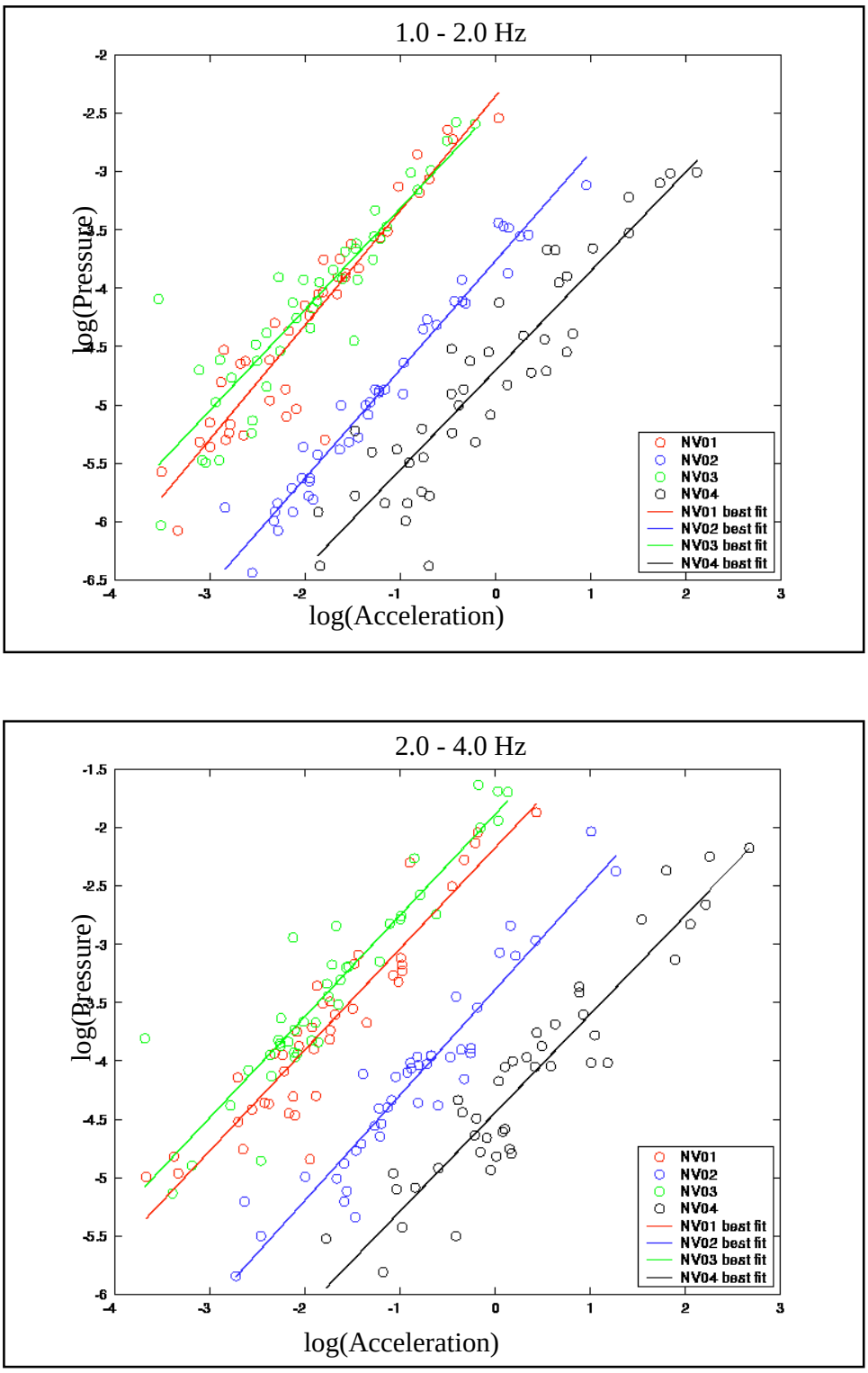

Figure 6. RMS Pressure versus RMS Acceleration for seismo-acoustic events. The data below 1 Hertz is contaminated by noise, and above 4 Hertz the response of the infrasound sensor hoses can further bias the measurements. The difference between NV01, NV03 and NV02 is likely to be due to the weathering effects. The difference between NV04 and the rest of the channels is due to the change in local geology. The Pressure Units are Pa; the acceleration units are nm/s^2.

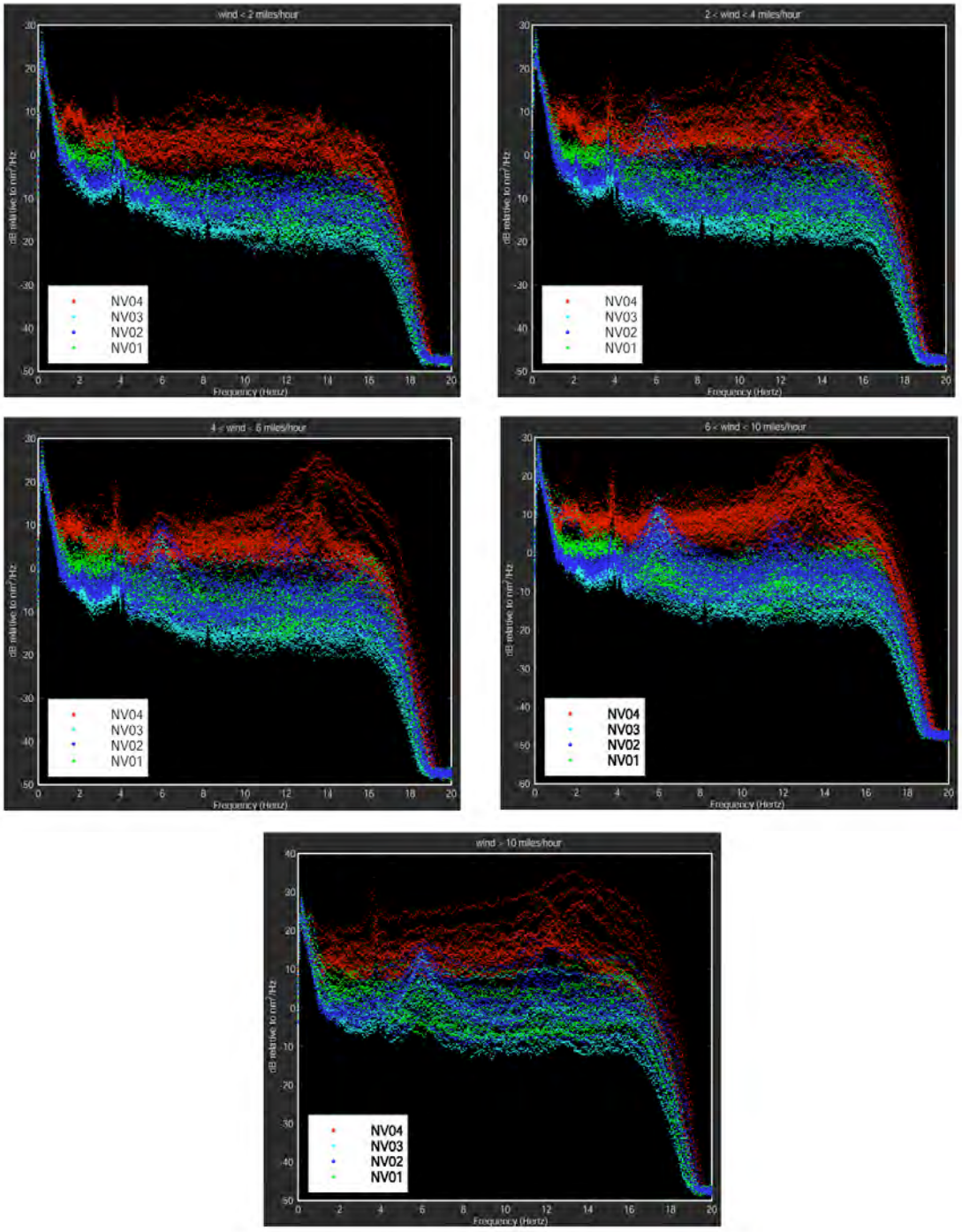

Figure 7. Power Spectrum Density Function for a suite of 160 noise samples. Here are shown only the elements of the inner array (NV01, NV02, NV03 and NV04). The wind velocities are: less than 2 miles/hour (upper plot left), 2-4 miles/hour (upper plot right), 4-6 miles/hour (middle plot left), 6-10 miles/hour (middle plot right), above 10 miles /hour (lower plot).

These effects are not related to or influenced by atmospheric noise. The noise analyses (Figure 7) show that the atmospheric noise is more important at frequencies above 1 Hz. The median noise difference for NV04 and NV01 between the peak at around 6 Hz exhibited by NV01 and the peak at around 14 Hz exhibited by NV04 is approximately constant and is around 10 dB, regardless of wind strength. The maximum difference can reach 25 dB. At 1 Hz the median difference is 5 dB. The broad peaks that appear around 14 Hz (for NV04) and around 6 Hz (for NV03 and NV01) represent the combined effect of geology and topography.

To fully understand the geological structure responsible for these site effects refraction profiles will be carried out in the field. Taking advantage of the depth of the seismometers, true velocities can be obtained for the upper 40 feet using the seismometer as a static receiver and moving the source away from it in a "walk-away" technique. In this way the presence of a low-velocity layer that may exist near site NV04 can be detected. Additionally, shear velocity refraction profiles might be necessary because of the complicated geology. It is desired to investigate the structure to a depth of at least 30 m, the standard depth used by engineers to classify site characteristics.

REFERENCES

Aki K (1973) Scattering of P-waves under the Montana LASA, *J.Geophys. Res*. **78**, 1334-1346

Berteussen (1975) Crustal structure and P-wave travel time anomalies at NORSAR, *J. Geophys*., **41**, 71-84

Berteussen (1975) P-wave amplitude variability at NORSAR, *J. Geophys*. **41**, 595-613

Berteussen K. A., Christoffersson A., Husebye E. S. and Dahles A. (1975), Wave scattering theory in analysis of P-wave anomalies at NORSAR and LASA, *Geophys. J. R astr. Soc*. **42**, 403-417

Capon J. (1973), Characterization of crust and upper mantle structure under LASA as a random medium, *Bull. Seism. Soc. Am*. **64**, 235-266

NVAR Certification Manual (1999) prepared for the Preparatory Commission for the Comprehensive Nuclear-Test-Ban Treaty Organization Provisional Technical Secretariat International Monitoring System Division.

Tibuleac I. M., Herrin E. T. and Negraru P. T. (2001), Calibration studies at NVAR, *Seism. Res. Let*., **72**, 754

SEISMIC DATA ACQUISITION SYSTEM (SDAS) COMPONENT EVALUATION

Richard P. Kromer, J. Mark Harris, and Toby O. Townsend

Sandia National Laboratories

Sponsored by National Nuclear Security Administration
Office of Nonproliferation Research and Engineering
Office of Defense Nuclear Nonproliferation

Contract No. DE-AC04-94AL85000

ABSTRACT

Sandia National Laboratories has tested and evaluated the Geotech DB24 Remote Digitizer and SAIC SAN2000B Authenticator/Formatter as components of the AFTAC Sensor Site Subsystem (SSS) of the Seismic Data Acquisition System (SDAS).

Geotech DB24 tests included response to static and dynamic input signals, data time-tag accuracy and seismic application performance. Configurations tested include:

DB24	3 Channel	40 Samples per second	Geotech KS54000 Broadband Seismometer Gain
DB24	3 Channel	4 Samples per second	Geotech KS54000 Long-Period Seismometer Gain
DB24	1 Channel	20 Samples per second	Geotech 23900 Seismometer Gain

A subset of component tests was performed on multiple Sensor Site Subsystems.

The SDAS equipment is proposed for some stations that may be part of the International Monitoring System (IMS). In these cases, IMS data surety requirements and guidelines must be met for station certification. SAIC SAN2000B data surety was tested to verify correct operation in the station environment and ensure data surety requirements are met. These tests included data authentication (CD-1.1 format), intrusion monitoring, remote command authentication, and remote key management operations.

This paper describes the evaluation of the SDAS digitizer, authenticator/formatter components and performance within the subsystem.

OBJECTIVES

Introduction

The Air Force Technical Applications Center (AFTAC) is tasked with monitoring compliance of existing and future nuclear test treaties. To perform this mission, AFTAC uses several different monitoring techniques to sense and monitor nuclear explosions, each designed to monitor a specific physical domain (e.g. space, atmosphere, underground, oceans, etc.). Together these monitoring systems, equipment and methods form the United States Atomic Energy Detection System (USAEDS). The Seismic Data Acquisition System (SDAS) is part of the USAEDS program. Some USAEDS seismic stations may be included in the International Monitoring System (IMS).

Sandia National Laboratories has tested and evaluated the Geotech DB24 Remote Digitizer and SAIC SAN2000B Authenticator/Formatter as components of the AFTAC Sensor Site Subsystem (SSS) of the SDAS.

Evaluations Performed

Sandia evaluated the overall technical performance of the Geotech DB24 remote digitizer component of the AFTAC SDAS. Distortions introduced by the high-resolution digitizers were measured. Sandia also evaluated the performance of the Geotech DB24 remote digitizer as a component installed in the SSS of the AFTAC SDAS. The additional distortions and noise introduced into the DB24 by the SSS were measured. The results of these evaluations can be compared to relevant AFTAC SDAS and IMS application requirements or specifications.

Sandia evaluated the data surety performance of the AFTAC SDAS for data authentication, command authentication, key management operations, and intrusion monitoring. These tests are intended to verify correct operation of the SAIC SAN2000B Authenticator/Formatter component and the Operation and Maintenance Subsystem (OMS) in an IMS station environment.

RESEARCH ACCOMPLISHED

Geotech DB24 Remote Digitizer

The DB24 borehole remote digitizer was built by Geotech Instruments, LLC, Dallas, TX. Geotech provided ‘dsutil’ data acquisition software for the DB24 digitizer. It operated on a PC Workstation under Windows 2000 and communicated with the DB24 through a direct-connect serial connection. Data were acquired in real-time in CSS 3.0 flat-file records. GPS was provided to the DB24 using a SAIC GPS/splitter.

Testing was performed at Sandia National Laboratories Facility for Acceptance, Calibration and Testing (FACT) Site (Figure 1).

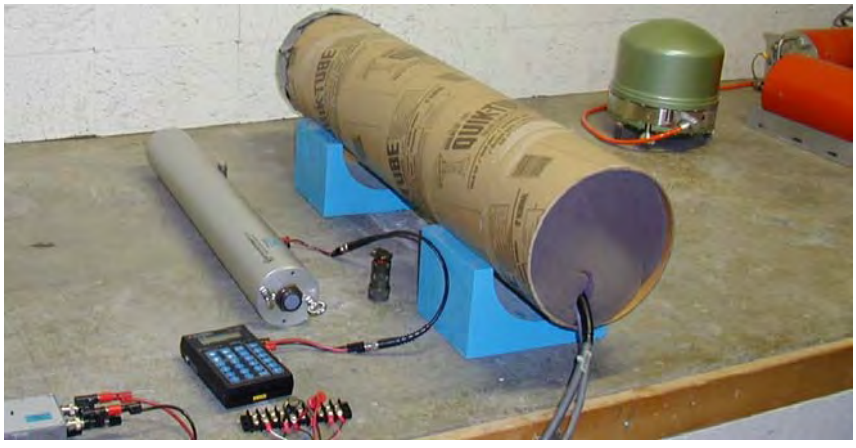

Figure 1. DB24 Testing at FACT Site

Three configurations of the DB24 were tested:

1. DB24, 3-Channel, 40 Samples per Second, Geotech KS54000 Broadband Seismometer Gain [1]
2. DB24, 3-Channel, 4 Samples per Second, Geotech KS54000 Long-Period Seismometer Gain [2]
3. DB24, 1-Channel, 20 Samples per second, Geotech 23900 Short-Period Seismometer Gain [3]

DB24 Digitizer Performance Tests and Results

The following tests were conducted on the DB24. This is a subset of tests as outlined in the Sandia Ground-based Monitoring R and E Technology Report [4].

Static Performance Tests

Input Terminated Noise (ITN) Test: Measure the Input Terminated Noise of the DB24.

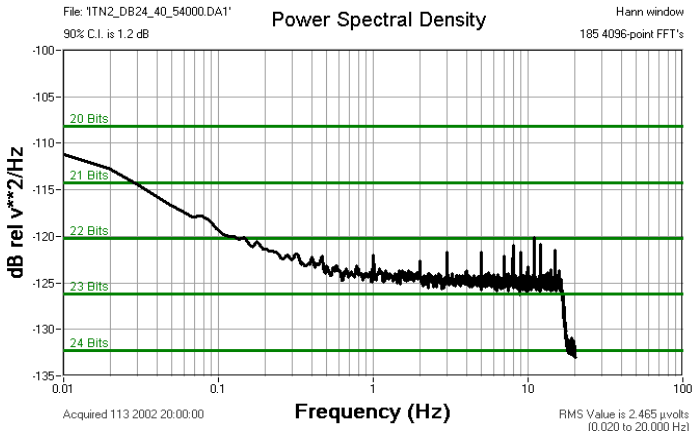

Figure 2. DB24 Channel 1 Input Terminated Noise with Integer Hz Peaks

ITN Test Results: Figure 2 indicates that the DB24 has < 0.7 count RMS noise and integer hertz spurious peaks. There is very little power in these peaks.

Maximum Potential Dynamic Range (MPDR) Test: Compute Maximum Potential Dynamic Range using data from the ITN Test.

Table 1. DB24 Channel 1-3 MPDR

Channel	RMS Noise µV 0.02 to 20 Hz	RMS Full-Scale Volts	MPDR
1	2.465	14.14	135.2 dB
2	2.474	14.14	135.1 dB
3	2.570	14.14	134.8 dB

MPDR Test Results: Table 1 indicates that the DB24 Maximum Potential Dynamic Range is greater than 134.8 dB.

Tonal Dynamic Performance Tests

Total Harmonic Distortion (THD) Test: Measure the linearity of the DB24 digitizers using Total Harmonic Distortion.

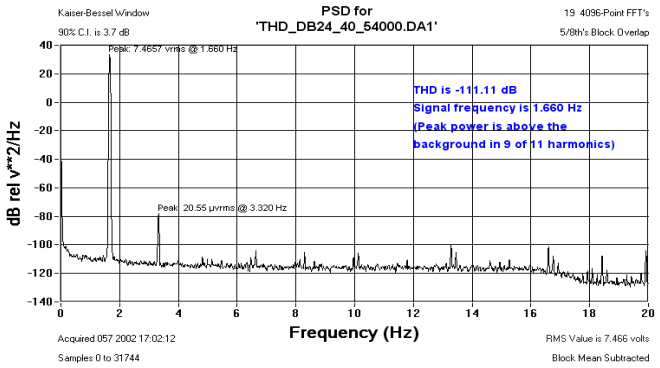

Figure 3. DB24 Channel 1 Total Harmonic Distortion

Table 2. DB24 Channel 1-3 THD

Channel	THD
1	111.11 dB
2	109.09 dB
3	109.88 dB

THD Test Results: Figure 3 and Table 3 indicate that the DB24 Total Harmonic Distortion is better than -109 dB.

Crosstalk (CTK) Test: Measure the amount of digitizer channel-to-channel crosstalk.

Table 3. DB24 Channel 1-3 Crosstalk

Channel	RMS Input	RMS Crosstalk	Crosstalk
1	4.96 V	0.51 µV	-139.8 dB
2	4.94 V	0.61 µV	-138.2 dB
3	4.92 V	0.47 µV	-140.4 dB

CTK Test Results: Table 4 indicates that the DB24 crosstalk is better than –138 dB.

Common Mode Rejection ratio (CMR) Test: Measure the ability of the digitizer to reject common-mode signals.

Table 4. DB24 Channel 1-3 Common Mode Rejection

Channel	Peak Input	Peak Common-mode	CMRR
1	10.0 V	0.512 mV	85.8 dB
2	10.0 V	0.937 mV	80.6 dB
3	10.0 V	0.197 mV	94.1 dB

CMR Test Results: Table 5 indicates that the DB24 CMR is better than –80 dB at 1 Hz.

Broadband Dynamic Performance Tests

Modified Noise Power Ratio (MNPR) Test: Determine DB24 performance using broadband signals.

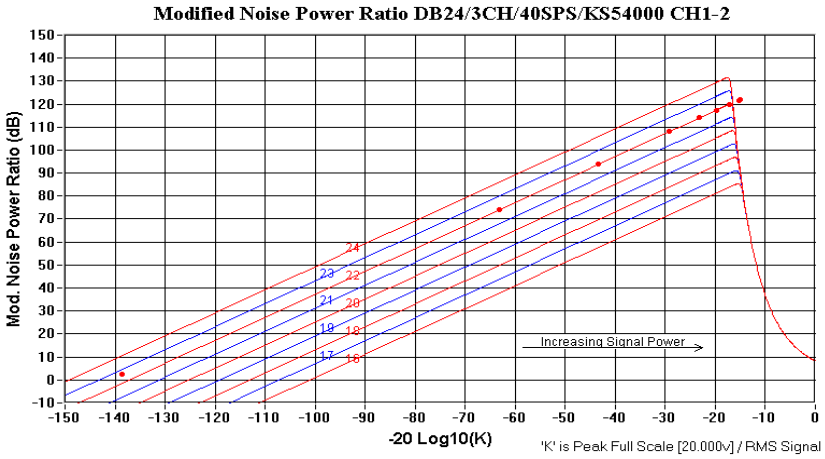

Figure 4. DB24 Channel 1-2 Modified Noise Power Ratio

MNPR Test Results: Figure 4 indicates that the DB24 has 22-bit performance using broadband signals.

Seismic Application Tests

Seismic System Noise (SSN) Test: Determine ability of the DB24 to resolve the expected seismic background using a KS54000 seismometer.

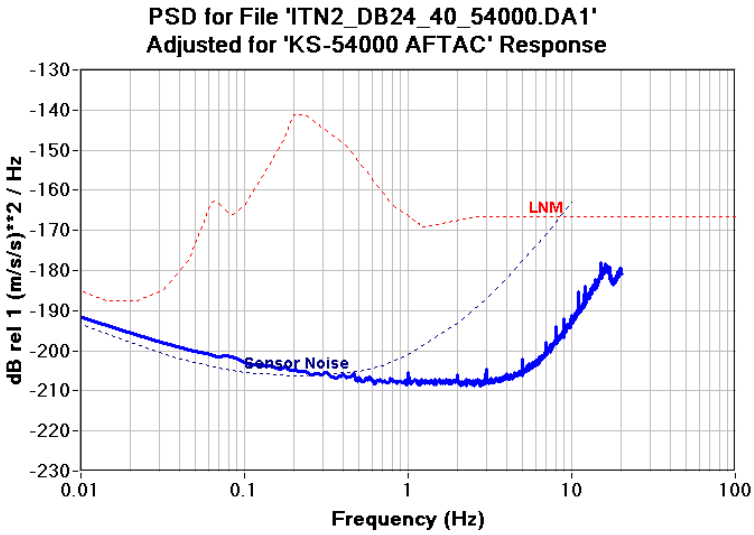

Figure 5. DB24 CH1 Seismic System Noise

SSN Test Result: Figure 5 indicates that the noise of the DB24 digitizer was at least 8 dB below the USGS New Low Earth Noise Model (NLNM) between 0.02 and 16 Hz when used with a Geotech KS54000 seismometer.

Sensor Site Subsystem - Geotech DB24 Remote Digitizer

SSS Testing was performed at the Pinedale Seismic Research Facility (PSRF) (Figure 6).

Figure 6. SSS Testing at PSRF

Three configurations of the DB24 were tested at PSRF:

1. DB24, 3-Channel, 40 Samples per Second, Geotech KS54000 Broadband Seismometer Gain [4]
2. DB24, 3-Channel, 4 Samples per Second, Geotech KS54000 Long-Period Seismometer Gain [4]
3. DB24, 1-Channel, 20 Samples per second, Geotech 23900 Short-Period Seismometer Gain [4]

Input Terminated Noise (ITN) Test: Measure SSS Input Terminated Noise on broadband DB24. Compare to FACT ITN Test.

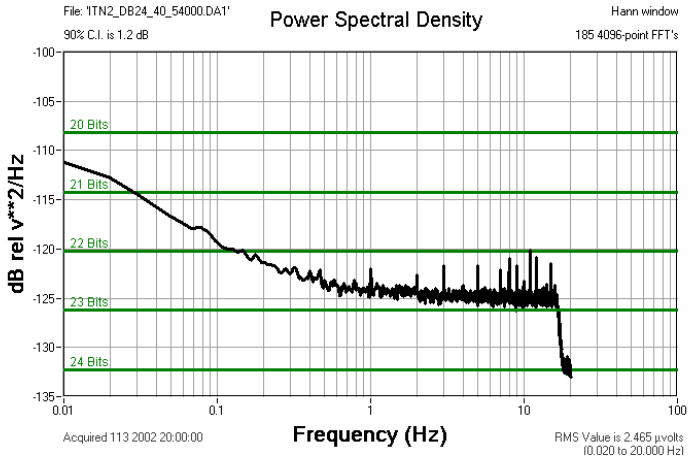

Figure 7. FACT Broadband DB24 Channel 1 Input Terminated Noise with Integer Hz Peaks

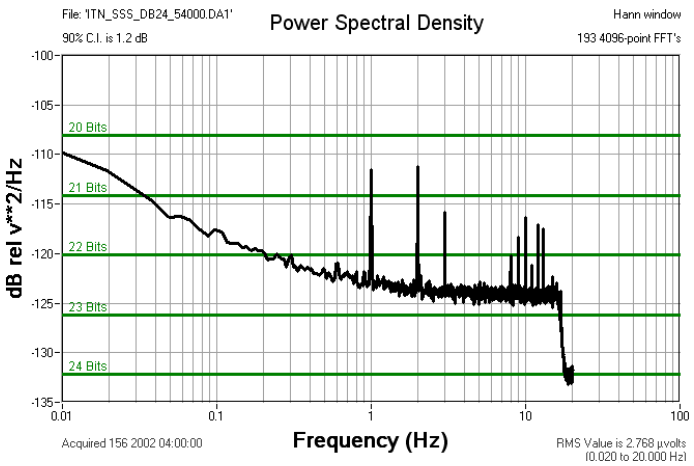

Figure 8. PSRF SSS Broadband DB24 Channel 1 Input Terminated Noise with Integer Hz Peaks

ITN Test Results: Figures 7-8 indicate that DB24 ITN testing at FACT showed < 0.7 count RMS noise with moderate integer hertz spurious peaks. SSS DB24 ITN testing at PSRF showed < 0.75 count RMS noise with increased integer hertz spurious peaks.

Input Terminated Noise (ITN) Test: Measure SSS Input Terminated Noise on short-period DB24. Compare to FACT Test.

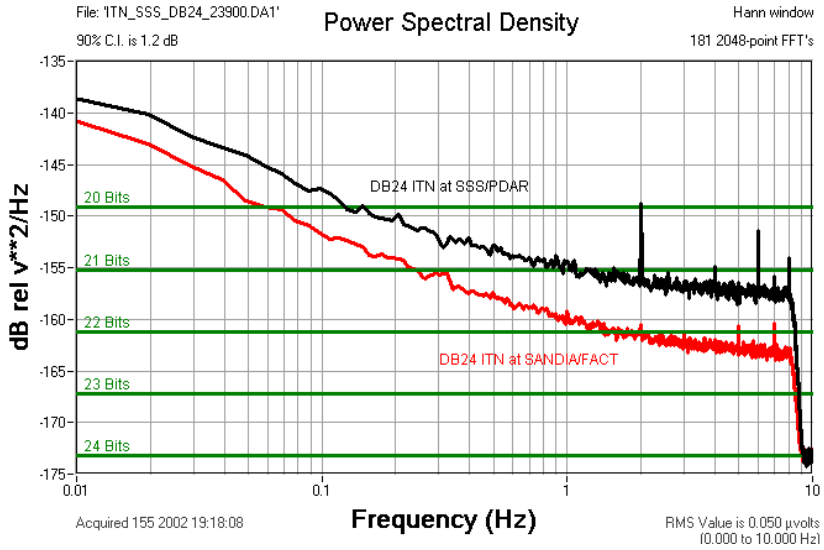

Figure 9. FACT and PSRF Short-period DB24 Channel 1 Input Terminated Noise

ITN Test Results: Figure 9 indicates that DB24 ITN testing at FACT showed < 0.95 count RMS noise with low integer hertz spurious peaks. SSS DB24 ITN testing at PSRF showed increased noise < 1.77 count RMS with increased integer hertz spurious peaks.

SDAS Data Surety

Data Surety Requirements

The PTS has developed requirements to ensure that data from IMS stations is reliable and authentic. These requirements cover data surety aspects of the station, including data authentication, command authentication, key management operations, and intrusion monitoring. Our tests are intended to verify correct operation of the SDAS equipment in an IMS station environment. IMS station data surety requirements, summarized from PTS documents [6], are listed here.

1. All IMS data must be signed at the sensor sites.
2. Data must be digitized and signed within a secure (tamper-detecting) environment.
3. Signature must be calculated within a dedicated, tamper-indicating hardware authentication device.
4. Data must be formatted for signing as specified by an approved protocol.
5. DSS (DSA with SHA-1) must be used with 1024-bit public key.
6. Signature device must generate DSA keys internally.
7. Signature device must provide public key components to user.
8. Signature device must not disclose private key directly to user or leak private key during operation.
9. Commands originating remote from the station must be signed by the originator and verified at the station.
10. A remote key change command must be supported for each authentication device; the authentication device must securely generate a new key pair and securely transmit the new public key.

The PTS strongly recommends that a PC Card device certified to FIPS 140-1 Level 2 be used for DSA operations and private key storage.

Test Configuration

The testing of the SDAS equipment described here was performed during May and June 2002. The following test environment was assembled at the Sandia National Laboratories FACT site (Figure 10, 11).

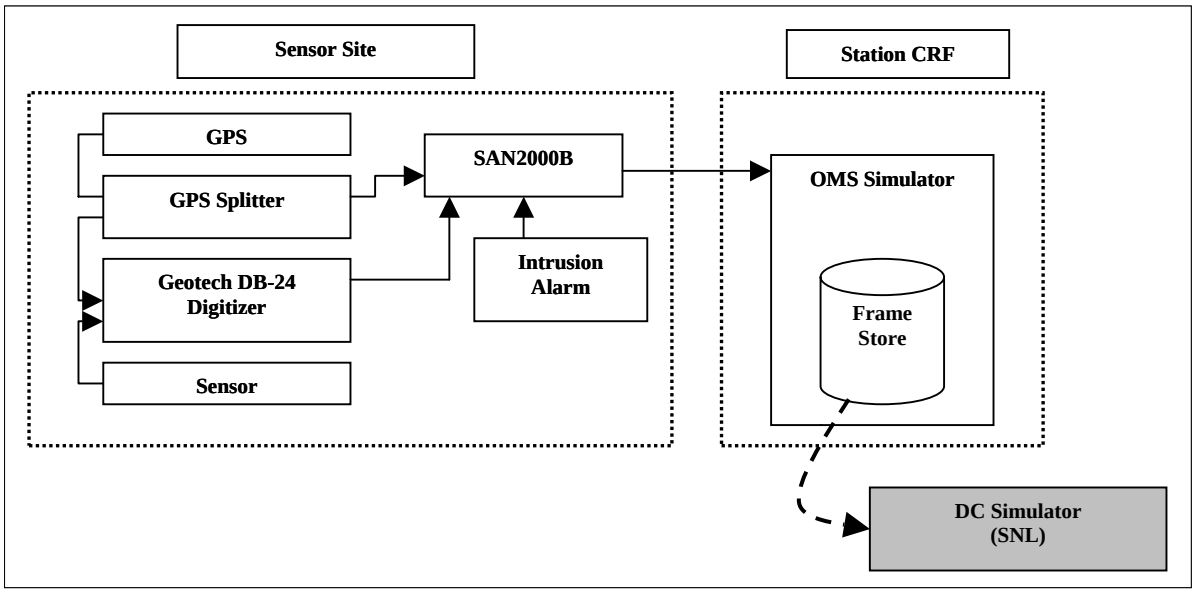

Figure 10. FACT Site Test Configuration

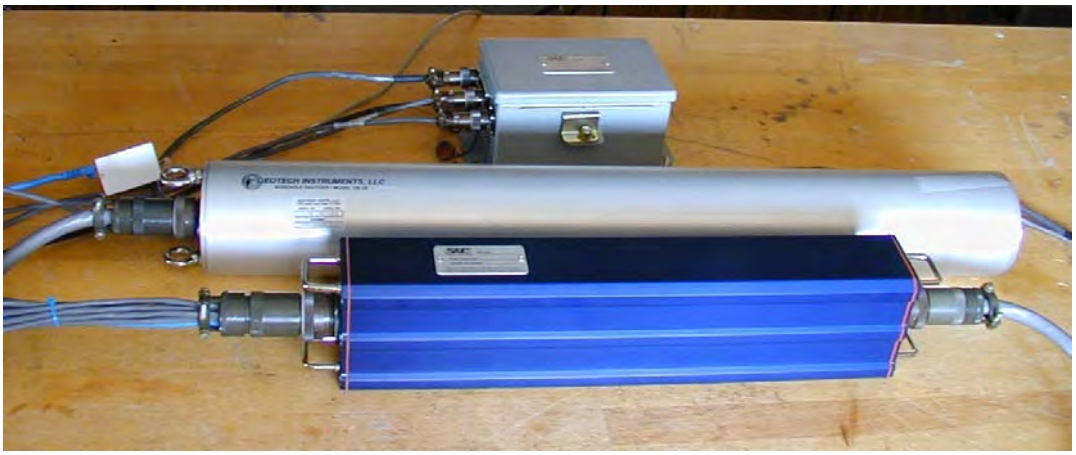

Figure 11. FACT Site Test Configuration

The DC Simulator is a computer at Sandia National Laboratories configured with software to parse the SAIC Frame Store files (the *saic_rip* program). It displays the CD-1.1 format data in a human-readable format, checks the validity of the format, and verifies authentication signatures using the *authd* program. The Station CRF is a Sun Ultra 60. Frame Store files were built on the Station CRF then manually transferred to the DC Simulator using FTP. The SAN2000B and Station CRF were connected on a 10BaseT LAN.

Data Surety Tests and Results

System Design Review Test: Determine that the SAN2000B and OMS, as part of the SDAS station environment, are designed to meet IMS surety guidelines; that system security, data authentication, and command authentication are incorporated in the equipment design and meet minimal criteria.

Test Results: The evaluation of the overall data surety of the station has not been completed. Additional system documentation is needed that describes which components sign, store, and exchange data, how commands are received, verified, and processed, how authentication keys are generated, signed, and distributed, and the physical security of the hardware components.

Data Authentication Test: Determine that the SAN2000B correctly calculates DSA signatures for sensor data in CD-1.1 format; that the station equipment transmits signed data that can be verified using the public key retrieved from the station.

Test Result: CD-1.1 data frames were successfully retrieved and parsed from the SAN2000B. The frames included the correct configuration, status information and were signed correctly. Data signatures were correctly verified using the public key retrieved from the SAN2000B. The SAN2000B has an internal Fortezza card for signature generation and public key protection. The Fortezza card is certified to FIPS 140-1 Level 2, and meets IMS guidelines for security of authentication operations. It has not yet been verified that the Fortezza card is used securely within the SAN2000B.

Intrusion Monitoring Test: Determine that intrusion detection hardware is monitored correctly by the SAN2000B; that the SAN2000B sets the appropriate intrusion flags in the signed data; that the data transmitted from the station has these flags set correctly.

Test Results: The SAN2000B correctly monitored opening of its own enclosure. External intrusion monitoring (vault/wellhead open alarm) could not be tested at the FACT Site with the hardware supplied to date. Procedures are in development to allow access to the external intrusion alarm inputs.

Remote Key Change Command Test: Determine that the key change operation works correctly on the SAN2000B and OMS.

Test Results: It was determined that the SAN2000B will generate a new key pair on command, then start to use the new key on a second command. This was tested by entering commands directly to the SAN, which uses test-mode software in the SAN. A software bug was discovered and has been reported to be fixed. It was also discovered that the key change operation is performed differently when requested from operator software on the OMS workstation. This additional OMS software is needed to test the key change operation in the station environment.

Remote Command Authentication Test: Determine that all commands issued remote from the station are signed at the remote location and verified at the station.

Test Results: SDAS command authentication has not yet been evaluated. Additional software and documentation is needed to test this function.

CONCLUSIONS AND RECOMMENDATIONS

DB24 Digitizer Performance Tests

The DB24 digitizer performed at the 21 to 22 bit performance levels depending on seismometer gain and sample rate. The moderate amount of integer Hertz noise was identified at low levels that will not be seen above the seismic background. It is recommended that the source of these spurious peaks be determined and removed if possible.

The DB24 amplifier configuration for 23900 seismometer application may be insufficient for quiet sites. It is recommended that a DB24 amplifier be developed for quiet site applications.

Data Surety Tests

At the time of this writing, several data surety tests have not been completed. Data authentication performance is acceptable, but command authentication, key management operations, system security, and intrusion monitoring require further evaluation. Additional hardware, software, and documentation are needed to complete the evaluation. We expect to receive these items soon and complete testing of the data surety of the SDAS by October 2002.

REFERENCES

Evaluation of the Geotech DB24 Remote Digitizer for AFTAC SDAS Application: DB24/3CH/40SPS/KS54000 Configuration, Ground-based Monitoring R and E Technology Report, June 17, 2002.

Evaluation of the Geotech DB24 Remote Digitizer for AFTAC SDAS Application: DB24/3CH/4SPS/KS54000 Configuration, Ground-based Monitoring R and E Technology Report, June 17, 2002.

Evaluation of the Geotech DB24 Remote Digitizer for AFTAC SDAS Application: DB24/1CH/20SPS/23900 Configuration, Ground-based Monitoring R and E Technology Report, June 17, 2002.

Test Plan for the Evaluation of Digitizing Waveform Recorder Subsystems for Ground-based Geophysical Monitoring, Ground-based Monitoring R and E Technology Report, February 26, 2002.

Evaluation of the Geotech DB24 Remote Digitizer for AFTAC SDAS Application: Multiple SSS DB24 Elements Configuration, Ground-based Monitoring R and E Technology Report, June 25, 2002.

Implementation Plan for IMS Authentication, CTBT/PTS/INF.100/Rev.1, 4 February 1999.

Acknowledgements

The National Nuclear Security Administration (NNSA) and the Defense Threat Reduction Agency (DTRA) gratefully acknowledge the important contributions of the following people for their work on the *Proceedings of the 24th Seismic Research Review — Nuclear Explosion Monitoring Technology: Innovation and Integration*.

Authors of papers for excellent research, good technical content, and willing cooperation in electronic submission.

Ms. Leslie A. Casey (NNSA) for review and clearance of abstracts and papers related to NNSA contracts and for providing NNSA financial support for the Proceedings.

Ms. Francesca C. Chavez, Los Alamos National Laboratory (LANL), for technical editing of the papers and abstracts and for design of the CD label.

Dr. Anton M. Dainty (DTRA) for review and clearance of abstracts and papers related to DTRA contracts.

Mr. Marvin D. Denny (NNSA/Dichroma) for overall review of the abstracts and papers.

Ms. Mary L. Girven, Sandia National Laboratories (SNL), for making everyone's job easier with web-based technology for abstract and paper submissions, online review and approval tools, and creation of the master files for the hard copy and compact disc versions of the Proceedings.

Mr. Michael Pankratz (LANL) for classification review of the completed Proceedings.

Ms. Ruth N. Robichaud (LANL) for artwork for the CD label.

Dr. Stanley D. Ruppert, Lawrence Livermore National Laboratory (LLNL), for making and jacketing the CD copies.

Dr. Frederick R. Schult, Air Force Technical Applications Center (AFTAC), for review and clearance of abstracts and papers related to AFTAC contracts.

Dr. N. Jill Warren (LANL) for editing of the abstracts and papers.

Dr. John (Jay) Zucca (LLNL), ***Dr. David B. Harris*** (LLNL), ***Mr. Preston B. Herrington*** (SNL), ***Mr. J. Mark Harris*** (SNL), ***Dr. C. L. Edwards*** (LANL), ***Dr. Steven R. Taylor*** (LANL), ***Dr. Ned A. Wogman*** (Pacific Northwest National Laboratory—PNNL), and ***Dr. Dale N. Anderson*** (PNNL) for a myriad of internal management reviews of NNSA laboratory abstracts and papers.